



energies

Special Issue Reprint

Power System Dynamics and Renewable Energy Integration

Volume I

Edited by
Juri Belikov

www.mdpi.com/journal/energies



**Power System Dynamics
and Renewable Energy
Integration—Volume I**

Power System Dynamics and Renewable Energy Integration—Volume I

Editor

Juri Belikov



Basel • Beijing • Wuhan • Barcelona • Belgrade • Novi Sad • Cluj • Manchester

Editor

Juri Belikov
Tallinn University of Technology
Estonia

Editorial Office

MDPI
St. Alban-Anlage 66
4052 Basel, Switzerland

This is a reprint of articles from the Special Issue published online in the open access journal *Energies* (ISSN 1996-1073) (available at: https://www.mdpi.com/journal/energies/special_issues/Power_System_Dynamics_Renewable_Energy_Integration).

For citation purposes, cite each article independently as indicated on the article page online and as indicated below:

Lastname, A.A.; Lastname, B.B. Article Title. <i>Journal Name</i> Year , <i>Volume Number</i> , Page Range.
--

Volume I

ISBN 978-3-0365-8204-7 (Hbk)
ISBN 978-3-0365-8205-4 (PDF)
doi.org/10.3390/books978-3-0365-8205-4

Set

ISBN 978-3-0365-6966-6 (Hbk)
ISBN 978-3-0365-6967-3 (PDF)

Contents

About the Editor	vii
Preface	ix
Alejandro Rubio, Holger Behrends, Stefan Geißendörfer, Karsten von Maydell and Carsten Agert Determination of the Required Power Response of Inverters to Provide Fast Frequency Support in Power Systems with Low Synchronous Inertia Reprinted from: <i>Energies</i> 2020 , <i>13</i> , 816, doi:10.3390/en13040816	1
Ujjwal Datta, Akhtar Kalam and Juan Shi Battery Energy Storage System for Aggregated Inertia-Droop Control and a Novel Frequency Dependent State-of-Charge Recovery Reprinted from: <i>Energies</i> 2020 , <i>13</i> , 2003, doi:10.3390/en13082003	23
Aviad Navon, Gefen Ben Yosef, Ram Machlev, Shmuel Shapira, Nilanjan Roy Chowdhury, Juri Belikov, et al. Applications of Game Theory to Design and Operation of Modern Power Systems: A Comprehensive Review Reprinted from: <i>Energies</i> 2020 , <i>13</i> , 3982, doi:10.3390/en13153982	41
Muhammad Hafeez Mohamed Hariri, Mohd Khairunaz Mat Desa, Syafrudin Masri and Muhammad Ammirul Atiqi Mohd Zainuri Grid-Connected PV Generation System—Components and Challenges: A Review Reprinted from: <i>Energies</i> 2020 , <i>13</i> , 4279, doi:10.3390/en13174279	75
Arkadiusz Adamczyk Sizing and Control Algorithms of a Hybrid Energy Storage System Based on Fuel Cells Reprinted from: <i>Energies</i> 2020 , <i>13</i> , 5147, doi:10.3390/en13195147	103
Constantine Michailides Hydrodynamic Response and Produced Power of a Combined Structure Consisting of a Spar and Heaving Type Wave Energy Converters Reprinted from: <i>Energies</i> 2021 , <i>14</i> , 225, doi:10.3390/en14010225	119
Eric Pareis and Eric Hittinger Emissions Effects of Energy Storage for Frequency Regulation: Comparing Battery and Flywheel Storage to Natural Gas Reprinted from: <i>Energies</i> 2021 , <i>14</i> , 549, doi:10.3390/en14030549	141
Davide Astolfi, Raymond Byrne and Francesco Castellani Estimation of the Performance Aging of the Vestas V52 Wind Turbine through Comparative Test Case Analysis Reprinted from: <i>Energies</i> 2021 , <i>14</i> , 915, doi:10.3390/en14040915	161
Mohammad Seydali Seyf Abad, Jennifer A. Hayward, Saad Sayeef, Peter Osman and Jin Ma Tidal Energy Hosting Capacity in Australia’s Future Energy Mix Reprinted from: <i>Energies</i> 2021 , <i>14</i> , 1479, doi:10.3390/en14051479	187
Antans Sauhats, Andrejs Utans, Jurijs Silinevics, Gatis Junghans and Dmitrijs Guzs Enhancing Power System Frequency with a Novel Load Shedding Method Including Monitoring of Synchronous Condensers’ Power Injections Reprinted from: <i>Energies</i> 2021 , <i>14</i> , 1490, doi:10.3390/en14051490	207

Muhammad Faisal Shehzad, Mainak Dan, Valerio Mariani, Seshadhri Srinivasan, Davide Liuuza, Carmine Mongiello, et al. A Heuristic Algorithm for Combined Heat and Power System Operation Management Reprinted from: <i>Energies</i> 2021 , <i>14</i> , 1588, doi:10.3390/en14061588	229
Roberto Zanasi and Davide Tebaldi Modeling Control and Robustness Assessment of Multilevel Flying-Capacitor Converters Reprinted from: <i>Energies</i> 2021 , <i>14</i> , 1903, doi:10.3390/en14071903	251
Zbigniew Kłosowski and Sławomir Cieślik The Use of a Real-Time Simulator for Analysis of Power Grid Operation States with a Wind Turbine Reprinted from: <i>Energies</i> 2021 , <i>14</i> , 2327, doi:10.3390/en14082327	291
Ming Yang, Wu Cao, Tingjun Lin, Jianfeng Zhao and Wei Li Low Frequency Damping Control for Power Electronics-Based AC Grid Using Inverters with Built-In PSS Reprinted from: <i>Energies</i> 2021 , <i>14</i> , 2435, doi:10.3390/en14092435	319
Sławomir Cieślik Mathematical Modeling of the Dynamics of Linear Electrical Systems with Parallel Calculations Reprinted from: <i>Energies</i> 2021 , <i>14</i> , 2930, doi:10.3390/en14102930	337
Manisha Maharjan, Almir Ekic, Bennett Strombeck and Di Wu An RTDS-Based Testbed for Investigating the Impacts of Transmission-Level Disturbances on Solar PV Operation Reprinted from: <i>Energies</i> 2021 , <i>14</i> , 3867, doi:10.3390/en14133867	361
Jianqiang Luo, Yiqing Zou, Siqi Bu and Ulas Karaagac Converter-Driven Stability Analysis of Power Systems Integrated with Hybrid Renewable Energy Sources Reprinted from: <i>Energies</i> 2021 , <i>14</i> , 4290, doi:10.3390/en14144290	377
Qiguo Han, Xing Wang, Pengfei Hu, Maolin Wang, Xu Luo and Weihua Hou Multi-Mode Voltage Sag/Swell Generator Based on Three-Phase Inverter Circuit Reprinted from: <i>Energies</i> 2021 , <i>14</i> , 6520, doi:10.3390/en14206520	397
Muhammad Riaz, Sadiq Ahmad, Irshad Hussain, Muhammad Naeem and Lucian Mihet-Popa Probabilistic Optimization Techniques in Smart Power System Reprinted from: <i>Energies</i> 2022 , <i>15</i> , 825, doi:10.3390/en15030825	413
Paolo Tenti and Tommaso Caldognetto Generalized Control of the Power Flow in Local Area Energy Networks Reprinted from: <i>Energies</i> 2022 , <i>15</i> , 1416, doi:10.3390/en15041416	453
Sergio Coronas, Jordi de la Hoz, Àlex Alonso and Helena Martín 23 Years of Development of the Solar Power Generation Sector in Spain: A Comprehensive Review of the Period 1998–2020 from a Regulatory Perspective Reprinted from: <i>Energies</i> 2022 , <i>15</i> , 1593, doi:10.3390/en15041593	475

About the Editor

Juri Belikov

Juri Belikov, Ph.D., is an Assistant Professor in the Department of Software Science, Tallinn University of Technology (since 2018). His research interests lie on the edge of nonlinear control theory, power systems, and computer science. He received a BSc (cum laude) in Mathematics from Tallinn University, and MSc and PhD degrees in Computer and Systems Engineering from Tallinn University of Technology in 2006, 2008, and 2012, respectively. In 2015–2017, he was a Postdoctoral Fellow in the Faculty of Mechanical Engineering and The Andrew & Erna Viterbi Faculty of Electrical Engineering, Technion—Israel Institute of Technology.

Preface

As environmental concerns continue to grow and the push for carbon neutrality intensifies, the question is no longer whether renewable energy is a viable solution, but rather how to successfully transition towards it. This raises an intriguing discussion regarding the inherent limitations of traditional power systems. Specifically, there is a clear gap between today's emerging generation technologies and our current understanding of the dynamics of complex power systems—a gap that is partly covered by the research results in this book.

Juri Belikov

Editor

Article

Determination of the Required Power Response of Inverters to Provide Fast Frequency Support in Power Systems with Low Synchronous Inertia

Alejandro Rubio *, Holger Behrends, Stefan Geißendörfer, Karsten von Maydell and Carsten Agert

DLR Institute of Networked Energy Systems, Carl-von-Ossietzky-Str. 15, 26129 Oldenburg, Germany; holger.behrends@dlr.de (H.B.); stefan.geissendoerfer@dlr.de (S.G.); karsten.maydell@dlr.de (K.v.M.); carsten.agert@dlr.de (C.A.)

* Correspondence: alejandro.rubio@dlr.de; Tel.: +49-441-99906-481

Received: 29 December 2019; Accepted: 6 February 2020; Published: 13 February 2020

Abstract: The decommissioning of conventional power plants and the installation of inverter-based renewable energy technologies decrease the overall power system inertia, increasing the rate of change of frequency of a system (RoCoF). These expected high values of RoCoF shorten the time response needed before load shedding or generation curtailment takes place. In a future scenario where renewables are predominant in power systems, the ability of synchronous machines to meet such conditions is uncertain in terms of capacity and time response. The implementation of fast power reserve and synthetic inertia from inverter-based sources was assessed through the simulation of two scenarios with different grid sizes and primary reserve responses. As main results it was obtained that the full activation time for a fast power reserve with penetration above 80% of inverter-based generation would need to be 100 ms or less for imbalances up to 40%, regardless of the synchronous response and grid size, meaning that the current frequency measurement techniques and the time for fast power reserve deployment would not ensure system stability under high unbalanced conditions. At less-unbalanced conditions, the grid in the European scale was found to become critical with imbalances starting at 3% and a non-synchronous share of 60%.

Keywords: fast power reserve; frequency nadir; critical time; low inertia grids

1. Introduction

As part of the international efforts set to counteract global warming, the deployment of renewable energy sources in the electric sector has been considered an energetic priority as a measure to reduce CO₂ emissions. This objective is also reflected in the regulatory energy policies and plans of some countries. For instance, in Germany, the transformation of the electricity sector contemplates achieving a share of electricity generation of 80% from renewable energy by 2050. As part of such transformation, the expansion of renewables and the decommissioning of conventional power plants is regulated by the “Erneuerbare Energien Gesetz” [1]. The commitment of renewable energy plants has dispatch priority in the power market due to its zero marginal cost for power generation. This affects market auctions and also has some technical implications [2]. Balancing of the residual load is provided by conventional units, so curtailment of renewable energy resources is the least preferred option for power balancing [3].

An effect of conventional power plant decommissioning and their replacement with inverter-based renewable power plants is the reduction of system inertia, and consequently the incrementation of the rate of change of frequency (RoCoF) [4,5]. The relevance of the inherent synchronous generator inertia is to avoid rapid changes in frequency as load-generation imbalances take place; in this way, enough time is given for the primary power reserve activation to recover the balanced, stable conditions [6]. In future

power systems dominated by non-synchronous generation, it is expected that the inverters will be able to provide ancillary services such as frequency and voltage regulation [4,6]. Thus, the future inverters must be capable of replacing synchronous machines, operate in a decentralised mode, and provide inertial and damping responses [7].

Some ancillary services have been included in the inverter capabilities. The inverter-based generation has been employed to contribute to frequency and voltage regulation. Through the implementation of the virtual synchronous machine concept, inertial and damping capabilities can be added to the inverters [7,8]. This allows islanded operation as well as frequency control. Another common technique is the emulation of the power-frequency droop characteristic of the synchronous machine [5,9]. This method provides a primary reserve response but lacks an inertial response during transients. Moreover, ramping capabilities of PV plants' inverters were studied in [10] for power reserving. Similarly, highly PV penetrated grids and the inverters' requirements to meet local codes were evaluated in [11,12]. Additionally, modified control strategies in the power electronics allow the controller to extract part of the stored kinetic energy in the rotating masses of the wind turbines [9,13].

In continental Europe, the frequency range between 49.8 Hz and 50.2 should be maintained by reserves after a power imbalance. The primary reserve of the interconnected system can withstand a power imbalance of 3 GW with a system load of 150 GW [14]. The reference incident case scenario with a power loss of 3 GW has been found adequate even with a high penetration of renewables [3,14]. Nevertheless, there will be still many hours with a positive residual load. The decommissioning of conventional power plants diminishes their capacity to provide balancing power services. At low inertia conditions, the system balance must be complemented with a non-synchronous reserve. Additional to the uncertainty of conventional generation availability in the German power system, it is also not clear whether instantaneous reserve services from abroad will be available and whether transmission capacities will be enough [3].

The scope of this investigation is to determine the conditions which should be fulfilled by the fleet of inverters connected in a low inertia grid. The required triggering time and power response to avoid under-frequency load shedding (UFLS) are estimated. The over-frequency phenomenon is treated with the same approach as the under-frequency case. The effectiveness of synthetic inertia is also evaluated. In order to assess the influences of the grid size, synchronous response, and model simplifications, two grid cases are employed. The IEEE 9 bus benchmark grid model and an electric power system in the European scale are considered for said purpose; a methodology to determine the inverter requirements to offer frequency support is developed.

2. Methodology

2.1. Frequency Limits and Inertia Constants

When the global security of the system is endangered and under/above frequency is experienced, the load shedding is activated and the system enters an emergency state. If the frequency exceeds the range between 47.5 and 51.5 Hz, a system blackout can hardly be avoided [14]. Consequently, the system will reach the so-called blackout state and will have to be restored. Before the blackout, the system tries to recover the balance by rejecting a partial load starting at 49 Hz as frequency decreases. On the other hand, curtailment thresholds between 50.2 and 50.5 Hz have been studied by ENTSOE for over-frequency scenarios [14]. In this research, a deviation of ± 1 Hz is used as a threshold before load shedding and curtailment starts. In the case of under-frequency, power is injected in the system, whereas in the over-frequency case, power is extracted from the grid. Hence, to keep frequency within such threshold, the investigated critical time and power response corresponds to the maximum allowed time for fast power reserve activation in both over and under-frequency.

Two terms commonly found in the literature of power system stability will be used in this section:

- **Inertia constant (H):** It has units of seconds (s) and it is the ratio of the stored kinetic energy in the rotating masses of the machine (E_k in MWs) and its nominal capacity (S_{nom} in MVA).

- Acceleration time constant (T_a):** It also has the units of seconds (s), but this is the ratio of double the kinetic energy (MWs) and the generator nominal power output (P_{nom} in MW). The acceleration time constant is a measure of the system’s robustness against disturbances. It could be interpreted as the required time to remove the kinetic energy from the rotating masses at the rate of the supplied power load. Thus, the higher the time constant, the higher the available kinetic energy. As the share of synchronous generation decreases, this constant decreases proportionally.

With f as frequency, f_0 as nominal frequency and ΔP as power imbalance, the swing equation can be expressed as follows [15]:

$$\frac{df}{dt} = \frac{\Delta P * f_0}{2 * H * S_{nom}} = \frac{\Delta P * f_0}{T_a * P_{nom}} = \frac{\Delta P * f_0}{2 * E_k} \tag{1}$$

In this paper, the inertia constant H is used for the description of inertia in wind turbines and single synchronous machine representation, whereas the system acceleration constant T_a is used to express the whole system inertia related to the load in terms of real power.

2.2. Frequency Support from Inverter-Based Generation

In this section, the methodology and considerations for the implementation of inverter-based generation for frequency support are explained.

2.2.1. Synthetic Inertia

Synthetic inertia is one of the techniques that manufacturers and researchers are considering to tackle the low inertia problem in power systems [16,17]. Frequency support through synthetic inertia was considered with the following assumptions [9,18]:

1. The power output from synthetic inertia is limited to 10% of the wind turbine nominal power.
2. Due to mechanical and thermal stresses, the additional power can be delivered only for a maximum time of 10 s.
3. It is assumed that all wind turbines operate at a nominal power output. The value of 1.5 MW was selected for said purpose.
4. The maximum allowable amount of kinetic energy to be extracted from the turbines was limited to half of the kinetic energy while the turbine operates at a nominal speed [19].

A control system is needed so the stored energy in the rotating blades can be extracted from the wind turbine. Equation (2) is obtained from the expression of power as the derivative of the stored energy. The additional extracted power from the wind turbine through the implementation of Equation (2) accounts for the synthetic inertia contribution [19]. Figure 1 represents the implementation of Equation (2) in MATLAB-Simulink. In the figure, the insertion of a filter at the output of the multiplication block can be seen [17,18]. A constant block K_i adjusts the response in the model. Since Equation (2) is given per unit, the output is multiplied by a constant P_{wt} representing the turbine rated power.

$$P_{pu}(t) = 2 * H_{wt} * \omega_{pu}(t) * \frac{d\omega_{pu}(t)}{dt} \tag{2}$$

where H_{wt} is the turbine inertia constant and ω_{pu} the rotational speed per unit.

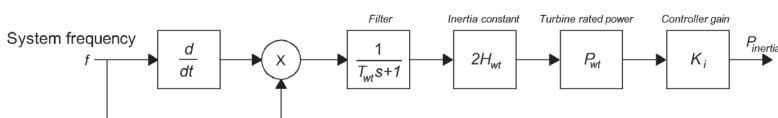


Figure 1. Block representation of Equation (2) in MATLAB-Simulink.

Typical values of inertia constant for wind turbines are not openly available from the manufacturers to the public. The approximate value was calculated with the utilisation of an equation which relates nominal power and inertia constant for wind turbines [20].

$$H_{wt} \approx 1.87 * P_{nwt}^{0.0597} \tag{3}$$

For a wind turbine with a nominal power of 1.5 MW, the value of H corresponds to 4.37 s. Rated rotational speed of 18 rev/min was considered [13]. To avoid the wind turbine stalling, a reduction of 5 revs/min is allowed. This change of rotational speed equals a reduction of 3 MWs on kinetic energy out of a total of 6 MWs. The values of the constants considered in the model are summarised in Table 1.

Table 1. Constants for the implementation of synthetic inertia. n_{wt} represents the number of wind turbines with synthetic inertia control.

T_{wt}	H_{wt} (s)	P_{wt} (MW)	K_i
1	4.37	$1.5 * n_{wt}$	10

2.2.2. Inverter-Based Fast Power Reserve

When a power system is subjected to a negative power imbalance and it is assumed that no load is rejected at UFLS frequency, this continues dropping below 49 Hz. The time at which the system frequency equals the UFLS value is then called critical time. This is the maximum available time for the inverter-based reserve to deploy the required power to the system.

In the critical condition that would lead to load shedding, it is expected from the IBFPR to at least counteract the RoCoF at the critical time, as illustrated in Figure 2b. Recalling Equation (1); it is necessary that the machine accelerating power (power imbalance) becomes zero at the critical time.

$$P_a(t_{cr}) = P_{mech} - P_{elec} + P_{IBFPR} = 0 \tag{4}$$

where P_a is accelerating power, P_{mech} is mechanical power, P_{elec} is electrical power load, t_{cr} is the critical time, and P_{IBFPR} is inverter-based fast power reserve.

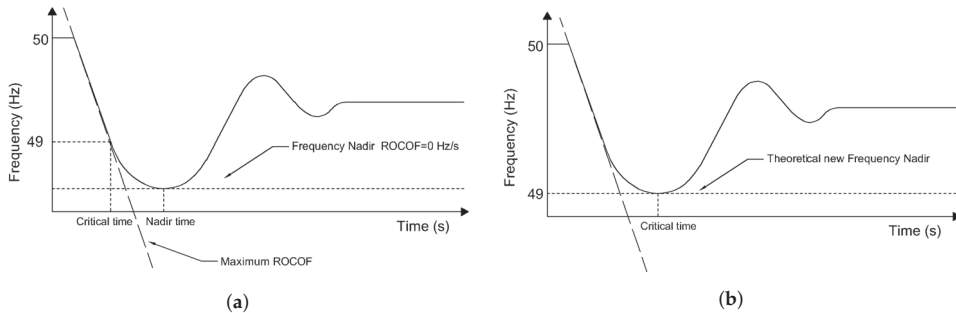


Figure 2. (a) Typical frequency response after a power imbalance leading to under-frequency load shedding (UFLS) at the critical time. (b) Power response with IBFPR applied to compensate power imbalance.

From the assumption of a linear mechanical power deployment of the synchronous machines governors, the rate of change in mechanical power, after a power imbalance ΔP , is given by $\Delta P / t_{nadir}$, where t_{nadir} represents the time at which the frequency nadir occurs. Given the power balance at the critical time, t_{cr} , the IBFPR response must be equal to $P_{elec} - P_{mech}$, P_{elec} being equal to ΔP .

Substituting P_{mech} by $\Delta P * t_{cr}/t_{nadir}$ and P_{elec} by ΔP in Equation (4), the following expression is obtained for the P_{IBFPR} at time t_{cr} :

$$P_{IBFPR}(t_{cr}) = \Delta P * (1 - t_{cr}/t_{nadir}) \quad (5)$$

It is assumed that P_{IBFPR} remains with a constant power output after t_{cr} long enough to stabilise the system frequency. The result of the previous equation represents the slope of the power output from the inception of the incident until the critical time, which with the implementation of IBFPR will not be critical any longer, but rather the new frequency nadir time.

$$P_{IBFPR}(t) = \frac{\Delta P * (1 - t_{cr}/t_{nadir}) * t}{t_{cr}} \quad (6)$$

According to the expression obtained in Equation (6), it can be realised that the desired power response from the inverters depends exclusively on parameters that cannot be directly measured from the grid. In a real situation, the values of ΔP , t_{nadir} , and t_{cr} cannot be known in advance; representing these factors is a challenge in the implementation of this ideal power response. Those values are dependent on the grid characteristics, the primary conventional reserve deployment time, and the overall system inertia [21]. Thus, two main cases are considered for the remaining analysis with the intent of covering a wider range of systems with different characteristics and dimensions.

2.3. Simulation Cases

As presented in the previous section, the values of critical time and frequency nadir depend on the system imbalance and primary reserve deployment time. In spite of assessing the influence of the grid size and the primary reserve characteristics, two main cases are considered. In Table 2, a summary of the simulated scenarios is provided. In both cases it is assumed that the initial steady frequency is the nominal 50 Hz.

- **Small scale grid case:** The IEEE 9 bus model was selected for carrying out the simulations due to its wide acceptance for power system studies and its relatively simple architecture [22,23]. The synchronous reserve deployment is in the order of a few seconds due to governor response [15,24]. In order to assess the typical simplifications made in power system analysis, two approaches of these cases were developed:
 - Scenario A—simplified model: The power system is represented by an equivalent single machine model in which the losses are neglected. In this case, typical governor data is considered [25]. With this model, the critical time and power response are determined. Furthermore, the impact of synthetic inertia is analysed.
 - Scenario B—extended model: All the power system components and their dynamic characteristics are considered in the IEEE 9 bus model for critical time and IBFPR estimation [22].
- **Large scale grid case:** The European grid-scale, in which all the synchronous machines are modelled and simplified as one single machine providing the characteristic expected from the overall system. The synchronous primary reserve deployment is in the order of ≈ 30 s [14,26]. The frequency response is assumed to be the same as the European response analysed by ENTSOE [14]. Similarly, as in the simplified model of the IEEE benchmark, the influence of synthetic inertia and IBFPR is evaluated.

Table 2. Summary of the simulated cases.

Cases	Assessment	
	IBFPR	Synthetic Inertia
Small scale grid		
(a) Simplified IEEE model	X	X
(b) Extended IEEE model	X	
Large scale grid	X	X

Therefore, with the selected cases, the critical and nadir times are estimated through the simulations of different scenarios combining a range of imbalances and shares of non-synchronous generation. In order to assess Equation (6), a fit of the critical time as function of RoCoF is carried out. With the corresponding fitting function for each case, Equation (6) can be easily applied assuming that the system inertia is known and power imbalance can be calculated as:

$$\Delta P(t) = \frac{df}{dt} \frac{T_a P_{LOAD}}{f_0} \quad (7)$$

2.4. Simplified IEEE 9 Bus Model

As a first step to evaluating the impacts of inverter-based generation and power imbalances in the grid, the whole system is simplified as one single generating unit. All the losses in the system (transformers, transmission lines, and generators) are neglected with the assumption that the prime mover output is the same as the electrical power output at the generator terminals. Table 3 provides a summary of the elements comprising the base model.

Table 3. Elements of the IEEE 9 bus model.

	Quantity
Buses	9
Transformers	3
Transmission Lines	6
Generators	3
Load	315 MW

Figure 3 is the block representation of the swing Equation (1); it only differs in the fact that additional blocks representing the inverter-based generation have been included. The mechanical power is represented by the output of a steam turbine governor model, which is used to represent the synchronous machine as depicted in Figure 4. In the figure, R is the turbine droop, P_{ref} is the reference load at nominal frequency, T_1 is the governor delay, T_2 is the reset time constant, T_3 is the servo time constant, T_4 is the steam valve time constant, and T_5 is the steam re-heat time constant [25]. When equilibrium is lost, the accelerating power is multiplied by the transfer function $1/(2HS)$, where H is the machine inertia constant and S is the machine power rating. From Equation (1) this product equals the derivative of frequency; therefore, an integrator block is added to obtain the frequency response [15,27,28]. A feedback loop is added and an error signal obtained from the reference frequency so that the synchronous machine can react as frequency deviates from the nominal value.

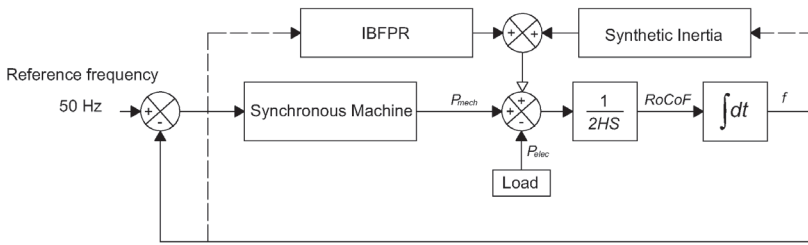


Figure 3. Simplified representation of the IEEE 9 bus model. Blocks linked by the solid line represent the conventional swing equation given by Equation (1). Represented with dashed lines, the respective frequency signals to the blocks of IBFPR and synthetic inertia, which add power to the system.

Typical governor constants are listed in Table 4. The values of kinetic energy and time constants of a synchronous machine with 835 MVA capacity were selected to represent the synchronous response; with a load of 315 MW, the system acceleration time constant is 14 s, which is approximately today’s European acceleration constant [14]. This is the base scenario where a 100% synchronous generation is assumed. For the sake of evaluating the impact of the inverter-based generation penetration in the system, the values of lower capacity generators were selected, diminishing the total system inertia.

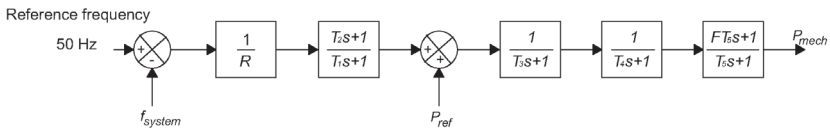


Figure 4. Model of the general-purpose governor for the representation of synchronous machines in the simplified IEEE 9 bus case.

Table 4. Typical generator values and governor settings as function of capacity [25]

Parameters	Generator Capacity (MVA)											
	911	835	590	410	384	192	100	75	51.2	35.29	25	
T ₁ (s)	0.1	0.18	0.08	0.18	0.22	0.083	0.09	0.09	0.2	0.2	0.2	
T ₂ (s)	0	0.03	0	0	0	0	0	0	0	0	0	
T ₃ (s)	0.2	0.2	0.15	0.04	0.2	0.2	0.2	0.2	0.3	0.3	0.3	
T ₄ (s)	0.1	0	0.05	0.25	0.25	0.05	0.3	0.3	0.09	0.2	0.09	
T ₅ (s)	8.72	8	10	8	8	8	0	0	0	0	0	
Kinetic Energy (MWs)	2265	2206.4	1368	1518.7	1006.5	634	498.5	464	260	154.9	125.4	
H (s)	2.486	2.642	2.319	3.704	2.621	3.302	4.985	6.187	5.078	4.389	5.016	
P _{max} (MW)	820	766.29	553	367	360	175	105	75	53	36.1	22.5	
T _a (s)	14.381	14.009	8.686	9.643	6.390	4.025	3.165	2.946	1.651	0.983	0.796	

Even though load imbalances up to 40% were simulated in each inertia scenario, the capacity of the generator was disregarded for the estimation of the critical time. The negative imbalance was simulated by increasing the system load.

2.5. Extended IEEE 9 Bus Model

Since it was desired to compare the obtained results in Section 2.4 with some model that takes into account the whole system components, losses, and dynamics, an extended representation of the IEEE 9 bus model was implemented in MATLAB-Simulink [22]. In this representation, simulations for different values of system inertia and load imbalance were performed, similarly as was done with the simplified representation of the model. Figure 5 shows the extended IEEE 9 bus grid architecture with inverter-based generation added.

To evaluate the validity of the equation describing the IBFPR needed to avoid ULFS, the IEEE model was modified with the insertion of ideal controlled power source blocks. The power sources were set up to inject power into the grid according to the simulated scenario. Therefore, no means of frequency measurement were included, and only IBFPR was assessed. As it was done in Section 2.4, the total acceleration time constant of the system equalled 14 s for a complete synchronous generation share. Hence, the same kinetic energy should be distributed among the three rotating masses. From Equation (8), it can be easily calculated that the system's kinetic energy with 14 s of acceleration time constant is 2205 MWs.

$$T_{sys} = 2 * E_k / P_{load} \quad (8)$$

Since the inverter-based generation reduces the system's kinetic energy, for different levels of IBG, the generator nominal capacity was kept constant and the inertia constant of each machine multiplied by the synchronous share factor f_{ss} . The total system kinetic energy is the summation of all the machines kinetic energy.

To start the simulations in steady-state conditions, a load flow calculation of the grid was carried out to determine the initial conditions for the exciter and prime mover models. Table 5 summarises the main values for setting the system initial conditions from the load flow calculation.

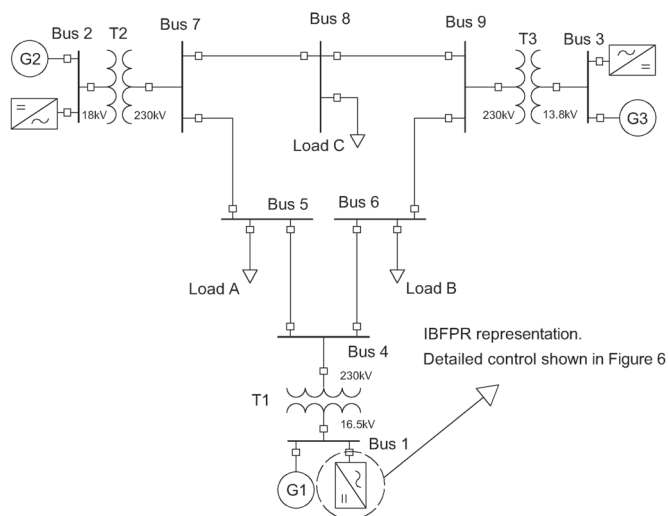


Figure 5. One line diagram of the IEEE 9 bus model. The inverter-based frequency response has been added at the same bus of the generating units.

Table 5. Steady state initial conditions of the system.

Bus Number	Bus Type	Voltage (pu)	Active Power (MW)	Reactive Power (MVAR)
1	Slack	1.04/0°	72.2	25.64
2	PV	1.025/9.83°	163	8
3	PV	1.025/4.63°	85	−9.41
5	PQ	0.9949/−4.42°	125	50
6	PQ	1.01211/−4.16°	90	30
8	PQ	1.0172/0.17°	100	35

IBFPR Representation

The IBFPR was modelled as controlled current sources. These controlled sources inject active power according to the load imbalance and system inertia simulated. The continuous measurement of voltage is required to determine the amount of current needed to supply the requested power. The IBFPR will have symmetrical and balanced characteristics. Due to that reason, the magnitude and angle of the current phasor will be obtained from the positive sequence of the measured voltage. From the definition of complex power and voltage symmetrical components in three-phase systems (9), the positive sequence components of the phase voltage and the line current are obtained [27].

$$S_{3\phi}^1 = 3 * V_{LN}^1 * \bar{I}_L^1 \quad (9)$$

This equation is valid for RMS values in which $S_{3\phi}^1$ is the positive sequence of the three-phase complex power, V_{LN}^1 is the positive sequence of voltage line to neutral, and \bar{I}_L^1 is the conjugation of the positive sequence line current. Nevertheless, the measured voltage values in MATLAB-Simulink are peak voltages, so the equations for power and current become:

$$S_{3\phi}^1 = \frac{3 * V_{LNpeak}^1 * \bar{I}_{Lpeak}^1}{2} \quad (10)$$

$$I_{Lpeak}^1 = \frac{2 * S_{3\phi}^1}{3 * V_{LNpeak}^1} \quad (11)$$

With the help of the a operator ($-0.5 + j\sqrt{3}$ or $1/120^\circ$), the values of the positive sequence component of phase voltage can be obtained.

From $V_a + V_b + V_c = 0$ and $V_a^1 = \frac{V_a + aV_b + a^2V_c}{3}$:

$$\begin{aligned} V_a^1 &= \frac{V_a + aV_b - a^2V_b - a^2V_a}{3} \\ &= \frac{V_a * (1 - a^2) + aV_b * (1 - a)}{3} \end{aligned}$$

Since $V_{an}^1 = \frac{V_a^1}{\sqrt{3}/30^\circ}$, $\sqrt{3}/30^\circ = 1 - a^2$ and $\sqrt{3}/-30^\circ = 1 - a$ then after some algebraic manipulation, the expression for V_{an}^1 becomes:

$$V_{an}^1 = \frac{V_a - a^2V_b}{3} \quad (12)$$

With the obtained expressions in (12) and (10), the current needed (11) to supply the IBFPR related to the measured voltages can be implemented in MATLAB-Simulink, as depicted in Figure 6. From the voltages readings of lines a-b and b-c, the voltage V_{an} is calculated using Equation (12). Then, Equation (11) is implemented to calculate the current to be fed into the system using the complex power response (6) and the previously calculated value of V_{an} . The ramping function will last until the critical time is reached; afterwards, the IBFPR output will remain constant.

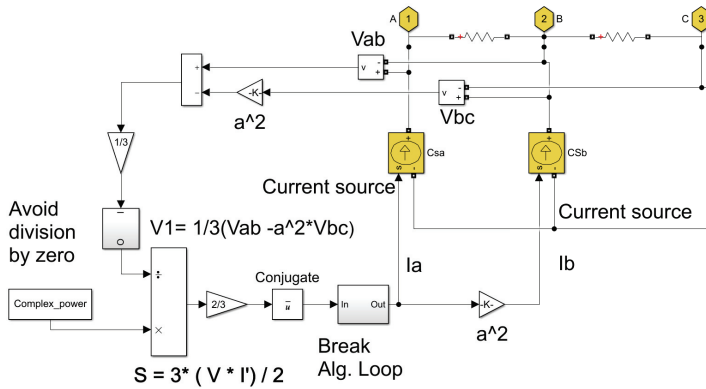


Figure 6. Implementation of IBFPR with ideal current sources and voltage monitoring in the extended IEEE model [29].

It must be noticed that when the IBFPR depicted in Figure 6 was implemented in MATLAB-Simulink, additional blocks were added to run the simulation; such blocks are a break in the algebraic loop just before the conjugate block. Additionally, a block to avoid division by zero was added at the output of the gain of 1/3 [29].

2.6. Large Scale Case: Europe Power System

Under normal operation, ENTSOE has reported values of RoCoF in the range of 5–10 mHz/s for power outages of 1 GW in the current interconnected power system. If an imbalance event of more than 3 GW occurs with depleted primary reserve, extraordinary values of frequency and RoCoF might be reached. After serious disturbances, the continental European power system has experienced RoCoF values between 100 mHz/s and 1 Hz/s. Imbalances of 20% or more along with RoCoFs greater than 1 Hz/s have been determined by experience to be critical [14]. ENTSOE has determined that in the interconnected reference scenario, the reduction of system inertia would not jeopardise the system’s stability. Due to the expected increase of non-synchronous generation in the future, international power trade, and renewables’ variability, ENTSOE estates in its future split reference scenario that the power system must be capable of withstanding imbalances greater than 40% with RoCoF values of 2 Hz/s or higher. Under these circumstances, the resulting islands must avoid load shedding. Hence, the conditions of the split scenario are considered for further analysis. The system representation is illustrated in Figure 7.

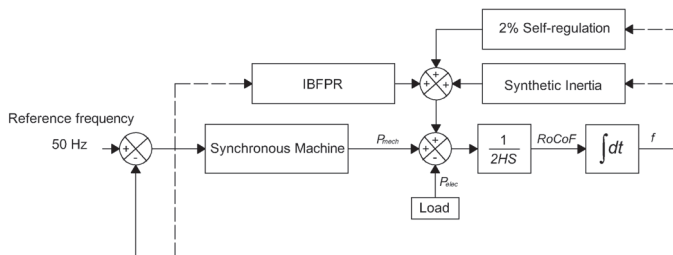


Figure 7. Large scale grid derived from the simplified IEEE model.

To fit the system behaviour to that modelled by ENTSOE, the synchronous representation in the simplified IEEE model shown in Figure 4 was used as a base. This was done with the insertion of an additional block at the output of the governor model, as shown in Figure 8. With this approach, the primary power reserve can be easily tuned with the assistance of the Control System Tuner

application available in MATLAB. In Figure 8, the synchronous machine block represents the governor model used in Section 2.4. The Control System Tuner sets the constants A, B, C, and D of the additional block in the model to have a step response with a rise time of ≈ 30 s by establishing an overshoot of 2% and a time constant of 8 s [28]. The time of utmost interest for analysis is from the inception of the power imbalance until the nadir time. Therefore, the system must perform as similarly as possible in this region compared to the ENTSOE reference, whereas after the nadir time, the disparity between responses can be neglected. On the European scale, the reserves must be completely deployed within 30 s after the occurrence of the disturbance.

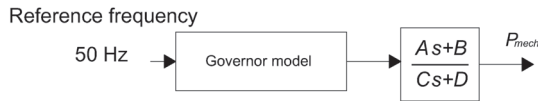


Figure 8. Governor representation for the large grid scale case.

System Parameters

When a power system with n number of synchronous machines is assumed, granting each of them a capacity of S MVA and a nominal power P_{nom} MW, and supposing that each machine operates at a deload factor dl of P_{nom} , with an acceleration constant equal to T_{nom} , then the number of machines n for the load $P_{syncload}$ served by synchronous machines is:

$$n = \frac{P_{syncload}}{P_{nom} * dl} \tag{13}$$

The system time acceleration constant T_{sys} can be obtained as follows:

$$\begin{aligned} T_{sys} &= \frac{\sum_{i=1}^n P_i * T_i}{P_{LOAD}} \\ &= \frac{n P_{nom} * T_i}{P_{LOAD}} \\ &= \frac{P_{syncload} * T_{nom}}{P_{LOAD} * dl} \\ &= \frac{Syncshare * T_{nom}}{dl} \end{aligned} \tag{14}$$

In this sense the system acceleration time constant can be calculated with a synchronous share of 100%, resulting in $T_{sys} = 12.5$ s with values of $T_{nom} = 10$ s [14,25], and a deload factor $dl = 0.8$. Considering only the swing equation, it can be demonstrated that RoCoF, and therefore, the frequency response of the system is only dependent on the percentage of load imbalance and the system acceleration time constant. From the definition of RoCoF as $\frac{df}{dt} = \frac{\Delta P * f_0}{2 * E_k}$ and $T_{sys} = \frac{2 * E_k}{P_{LOAD}}$:

$$\begin{aligned} \frac{df}{dt} &= \frac{\Delta P * f_0}{P_{LOAD} * T_{sys}} \\ &= \frac{\Delta P_{pu} * f_0}{P_{LOAD} * T_{sys}} \end{aligned} \tag{15}$$

In Equation (15) the value of ΔP_{pu} is the normalised value of power imbalance having as base power the value of load P_{LOAD} .

3. Results

3.1. Analysis of Critical Time

When the obtained critical times from the simplified and the extended model of the IEEE benchmark are compared in Figure 9, a higher deviation in the low range of RoCoF is clear. This is because the critical time is long enough to allow for the governor response activation of the respective synchronous machine's representation. Therefore, it can be stated that the simplifications made in the model have a greater influence on the results for low values of IBG penetration and low power imbalances. In this sense, the simplifications become less significant as the RoCoF increases in such a manner that the activated synchronous reserve is not relevant in frequency support. In the range of RoCoF higher than 2 Hz/s, the critical time trend for the European grid-scale and the simplified IEEE model get closer each to other as RoCoF increases.

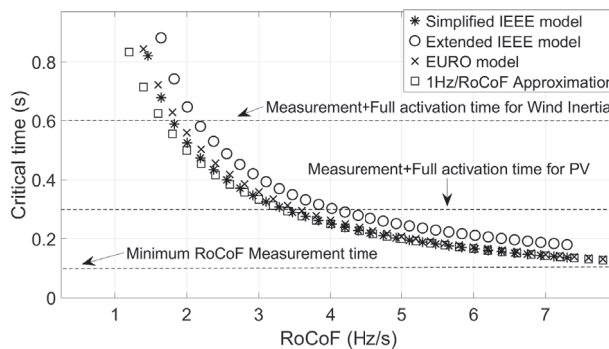


Figure 9. Results for critical time in all simulated models with a penetration of IBG of 80%.

Therefore under high RoCoF conditions in any of the models, the primary reserve does not significantly counteract the frequency drop [3]. Figure 9 demonstrates that primary reserve can be neglected for determining the critical time when the combination of IBG and load imbalances would lead to high RoCoF; as it increases, the approximation of critical time as 1 Hz/RoCoF narrows the difference with the results obtained from the simulations [30]. Nevertheless, such an approximation applies to the simplified IEEE model and the European-scale grid model. Hence, the influences of all the dynamics and machine components, such as the generator exciter and damping windings, seem to improve the critical time. The damping torque was not considered in Equation (1) for the simplified IEEE model; the inclusion of such may lead to more accurate results when compared with the extended model.

Because the European scenario's characteristics provided by ENTSOE were assumed to be the same as the resulting islands after a severe event; the results for the large scale model can be understood as the behaviour of the whole European system with bigger perturbations [14]. If in the future, a bigger reference scenario is utilised, then the synchronous response would not be enough to balance the system before load shedding occurs. Table 6 exhibits the required time when the power imbalance is increased by up to 10% for different IBG penetration.

Table 6. Critical time for European-scale case given in seconds.

IBG Share (%)	Load Imbalance (%)								
	3	4	5	6	7	8	9	10	
20	-	-	6.081	4.517	3.629	3.050	2.638	2.316	
40	-	6.226	4.169	3.215	2.628	2.222	1.934	1.705	
60	7.142	3.639	2.623	2.062	1.698	1.451	1.263	1.122	
80	2.753	1.744	1.277	1.018	0.843	0.722	0.628	0.559	
95	0.697	0.436	0.322	0.254	0.211	0.179	0.157	0.140	

3.2. Analysis of Synthetic Inertia and Fast Power Reserve

3.2.1. The Effect of Synthetic Inertia on Frequency

In this section, the results of the implementation of synthetic inertia in the simplified IEEE model and the European model are presented. The effect of synthetic inertia on the simplified model is illustrated in Figure 10a,b. Similarly, the effect of synthetic inertia on the European model is depicted in Figure 11a,b.

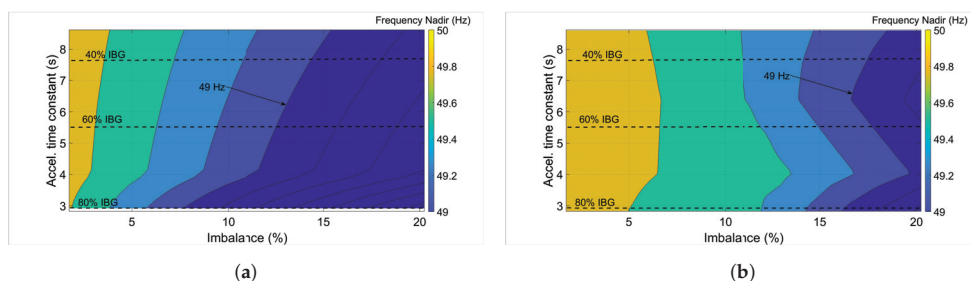


Figure 10. (a) Frequency nadir of the simplified IEEE model with only synchronous reserve. (b) Frequency nadir of the simplified IEEE model with 40% of the IBG equipped with synthetic inertia controls.

In any of the cases, UFLS is not avoided for all combinations of imbalances and acceleration constants with the application of synthetic inertia. It can also be observed in Figure 10b that values of frequency nadir under 49 Hz are reached for imbalances bigger than 14% combined with IBG shares above 80% in the simplified representation of the IEEE model. Nevertheless, enhanced performance is observed in the simplified IEEE model. The reason behind this is the faster response of the synchronous share present in the system, which jointly performs with the synthetic inertia to improve overall frequency response performance. Conversely, the frequency nadir of the European-scale model, depicted in Figure 11b at 80% of IBG, reaches values lower than 49 Hz with an imbalance of 3%. This demonstrates that synthetic inertia is not enough by itself for withstanding severe imbalances under high penetration of inverter-based generation.

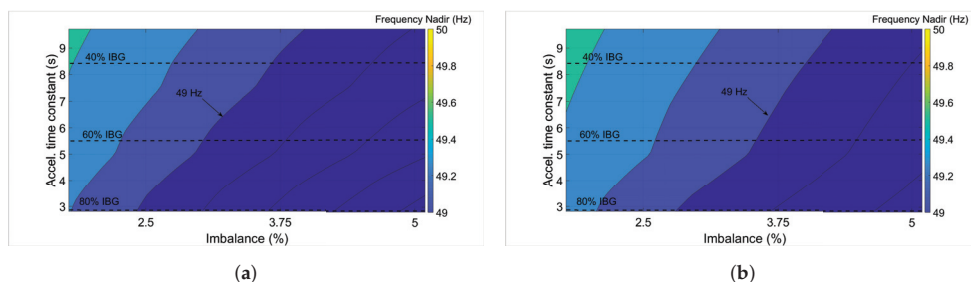


Figure 11. (a) Frequency nadir of the European-scale with only synchronous reserve. (b) Frequency nadir of the European-scale model with 40% of the IBG equipped with synthetic inertia controls.

Figure 12a,b shows the frequency response of the system with wind shares of 40% and 80% out of the total IBG share. Power imbalances of 10% and 15% were considered for each. In Figure 12a it can be observed how the frequency drops below 49 Hz with a 10% of imbalance when no IBFPR or synthetic inertia is used as a frequency support strategy. There is an improvement of the response with the implementation of synthetic inertia. UFLS is avoided for every share of synthetic inertia, assuming that primary reserve takes place after synthetic inertia. As the imbalance increases, the effectiveness of the synthetic inertia decreases. Figure 12b shows how a wind power contribution of 40% from the inverter-based generation is capable of avoiding UFLS. Nevertheless, with the wind share of 80%, the frequency drops smoothly during a short period; then, suddenly, the frequency drops below 49 Hz, since synthetic inertia is switched off after 10 s. This situation leads to UFLS because frequency is sustained during that time by the synthetic inertia power.

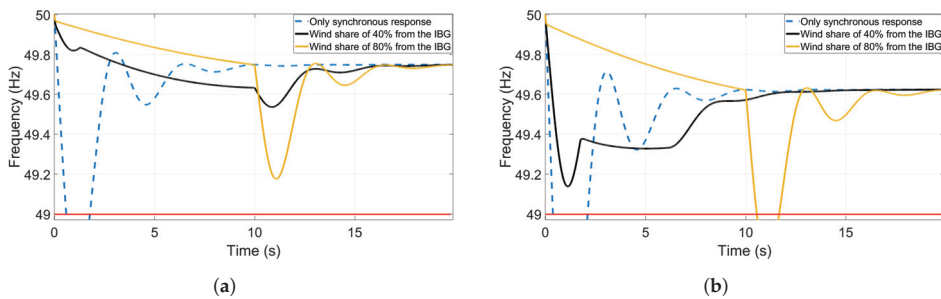


Figure 12. (a) System frequency response and synthetic inertia performance with a power imbalance of 10%. (b) System frequency response and synthetic inertia performance with a power imbalance of 15%.

3.2.2. The Effect of Power Ramp Response on Frequency

The contribution from the ramping power in diminishing system RoCoF from the perturbation inception until the critical time was disregarded when the Equation (5) was calculated. Assuming an instant switch-on of the IBFPR at the critical time, the frequency nadir would be 49 Hz. However, a ramp power response was assumed instead. Therefore, the frequency response of an unbalanced system commonly exhibits a frequency nadir higher than 49 Hz due to the contribution of the ramping period. In this sense, it can be inferred that the longer the ramping period is, the higher the frequency nadir will be.

When a comparison is established between all the calculated power ramp slopes per unit (pu), with a high penetration of non-synchronous power in the system, the required power to ensure no UFLS has a consistent trend between the three models and proximity, is seen in Figure 13. A steeper power ramp slope is needed in all the range of RoCoF for the European case. After inspecting Equation (6), it was noticed that the IBFPR is affected by the factor $1 - t_{cr}/t_{nadir}$; then, as nadir time increases, IBFPR increases as well. The nadir time for the European case, due to the action of the self-regulation and primary reserve deployment of 30 s, is in the range of 3–12 s (6 s for 80% IBG penetration) whereas the nadir time for the simplified IEEE model is between 1 and 3 s.

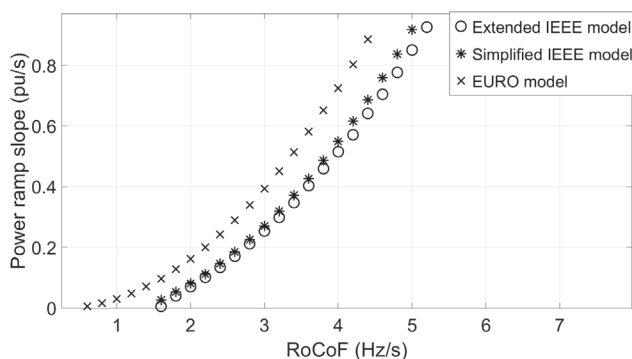


Figure 13. Comparison of the results of the three models in terms of the IBFPR power ramp which is needed at 80% of the share from non-synchronous generation.

3.2.3. Fast Power Reserve

The required power ramp to avoid load shedding has been found for both IEEE 9 bus models and the European-scale model. Hence, the IBFPR at the critical time, which remains constant after the critical time, would be counted as the fast power reserve. In Table 7 the required values for the inverter-based reserve for the European model are listed for imbalances out of the reference case of ENTSOE.

Table 7. Fast power reserve per unit for the European case with the power load as base.

IBG Share (%)	Load Imbalance (%)							
	3	4	5	6	7	8	9	10
20	-	-	0.025	0.038	0.049	0.060	0.070	0.081
40	-	0.016	0.030	0.041	0.052	0.063	0.073	0.083
60	0.005	0.024	0.035	0.045	0.056	0.066	0.077	0.087
80	0.016	0.028	0.039	0.049	0.062	0.070	0.080	0.09
95	0.024	0.035	0.045	0.055	0.065	0.075	0.085	0.096

When IBFPR is implemented in all three cases, the frequency drop below 49 Hz is avoided for almost all values of RoCoF, considering that enough IBFPR is available for the given imbalance. Figure 14a–c shows the frequency nadir for all the cases.

It can be observed that in the IEEE grid models, depicted in Figure 14a,b, UFLS is avoided in all the cases. However, in the simplified IEEE model, a minimum area with a value of 49.1 Hz is found, as indicated in the figure. This is caused because of the selected values of time constants for such inertia scenario. As indicated in Table 4, the generator with a capacity of 590 MVA has a bigger reheat time constant than the other machines, causing a delay in synchronous response. As the imbalance increases, the relevance of the response diminishes; therefore, the frequency nadir increases. In the case of the extended IEEE model, time constants were kept equal for all inertia scenarios, and only generator inertia was changed. In the European-scale model depicted in Figure 14c, UFLS is not avoided in the region of low imbalance and high acceleration time constant. Since the implemented IBFPR was based on a power response as a function of the measured initial RoCoF, the inaccuracy in the fitting function leads to overestimating the critical time in the low region of RoCoF as demonstrated in Figure 15. This has a bigger influence on the European-scale model because of the inaccuracy is not compensated by a faster power response from the synchronous machines.

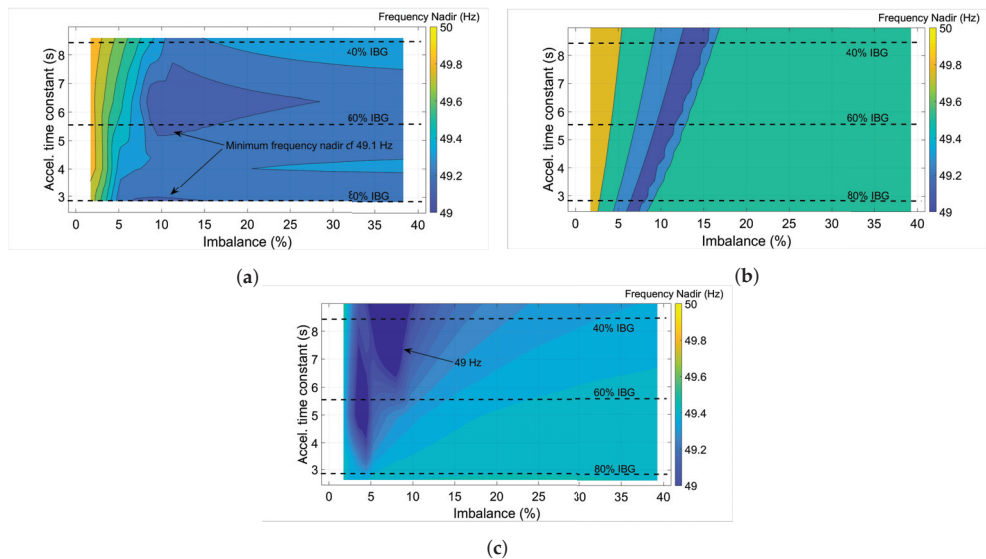


Figure 14. Frequency nadir with the implementation of IBFPR in: (a) The simplified IEEE model; (b) the extended IEEE model; (c) the large scale (European) model.

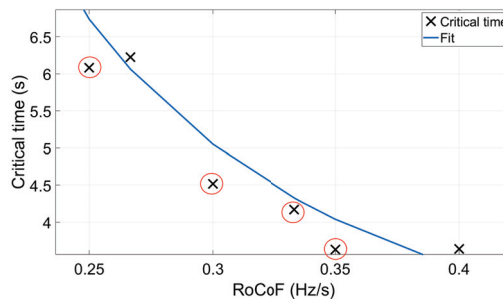


Figure 15. Overestimation of critical time leading to UFLS in the European-scale model.

3.3. Synchronising Effect, Lack of Damping Torque and Implications

The diminishing of synchronous machines in the system leads to a very weak network where synchronising and damping torque, which are inherent characteristics of synchronous machines, are not enough to stabilise the system [15]. Although the implementation of IBFPR contributes to keeping the synchronous machine on step, oscillations in the speed/frequency response of the rotor are observed. These oscillations are created by the lack of damping torque which is provided mainly by the synchronous machines through damping windings, a rotor field exciter, and a power system stabiliser [6,15].

For the simplified IEEE model and the European-scale model, only transfer functions describing an equivalent system governor were considered. Hence in such approaches, the effects and dynamics of a synchronous generator exciter and an inter-machine interaction were not taken into account. The aforementioned factors influence greatly the small-signal stability [15,25]. Even though the scope of this work was to analyse the power-time characteristics needed to avoid frequency collapse, oscillations were observed, but they could not be addressed by the simple injection of power to the system. With inverter-based generation penetration of 95%, and a 2% load imbalance being considered, UFLS is not reached, but the system becomes unstable, as shown in Figure 16a,b. With penetration levels above 85%, complete frequency stability is not ensured with the injection of a fast power reserve. Then, the system becomes unstable with increasing amplitude oscillations. It is important to note that ENTSOE in its EUROPEAN interconnected scenario determined that there is no UFLS when an imbalance of 2% with a high contribution of non-synchronous generation occurs. Nonetheless, no inter-machine interaction was considered, and therefore, a similar effect as observed in Figure 16a could be experienced.

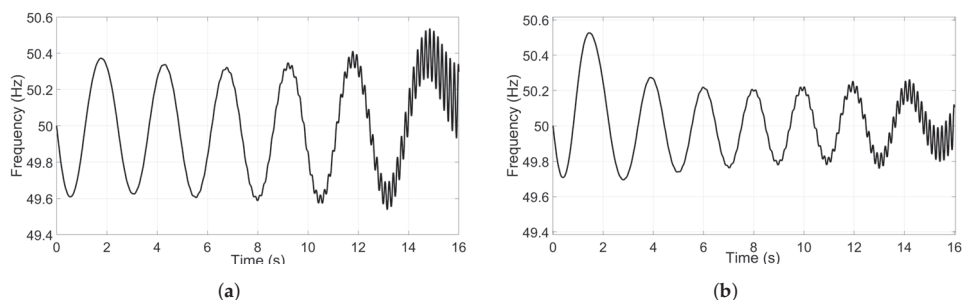


Figure 16. (a) Oscillatory frequency response when no additional frequency support is given by the IBG. (b) Oscillatory frequency response when frequency support is given by the IBG.

Table 8 provides a summary of the main results obtained from the simulations.

Table 8. Summary of results.

Main Results	
European model	<ol style="list-style-type: none"> 1. A load imbalance of 3% with an IBG share of 60% is critical. 2. The power imbalances leading to UFLS must be covered almost completely by the IBFPR. 3. The synthetic inertia does not substantially improve frequency nadir. 4. The inaccuracy in the calculation of RoCoF leads to overestimation of the critical time, and consequently to UFLS.
Simplified IEEE model	<ol style="list-style-type: none"> 1. The approximation of 1 Hz/RoCoF represents a good estimation of the critical time. 2. An extreme power imbalance requires an activation time in the order of 100 ms. 3. The frequency nadir was improved when synthetic inertia was implemented.
Extended IEEE model	<ol style="list-style-type: none"> 1. The IBFPR does not provide damping torque to the system and undamped oscillations occur when the IBG share exceeds 85%. 2. The critical time deviates from the simplified model the most when the RoCoF is low. 3. A power rate in the range of 0.5 pu/s would be needed to avoid UFLS for conditions leading to RoCoF of 4 Hz/s. 4. The faster synchronous response provides robustness when an inaccurate calculation of RoCoF is performed.

4. Discussion

The main results of the simulations are discussed in the following points:

- In the European scenario, the conventional governor response was found not to be able to ensure transient frequency stability in conditions of power imbalance exceeding 2%. A non-synchronous share of 60% with $\approx 3\%$ power imbalance was found to be critical. The governor operation is too sluggish to constitute the unique solution for frequency support during the transient period. As indicated in [5], in real implementations, the governor response varies at each power plant, even having some of the governor response withdrawal. Thus, the inverter-based fast power reserve needs to be activated in an extremely short time.
- A fast power reserve activation between 0.14 and 2.75 s would be required for an inverter-based share above 80% and power imbalances between 3 and 10%.
- The uncertainty of synchronous reserve availability and possible power transmission congestion in future scenarios could lead to higher power imbalances, as occurs nowadays [3]. To avoid load shedding in scenarios with a non-synchronous share above 80% and load imbalances up to 40%, the inverter-based fast power reserve must be deployed in between 100 and 500 ms, independently of the grid size and the primary reserve response.
- Nevertheless, the currently full power activation time of renewable sources without storage is in the range of 200 to 600 ms. Table 9 lists some important and typical time scales of the most common power electronic technologies implemented in modern power systems. (Time required for the measurement, signal transmission, and processing, and the coordination of the power electronic controls [30].) These activation times are adequate for power imbalances leading to values of RoCoF equal or less than 4 Hz/s, as studied by ENTSOE for future scenarios [14].

Table 9. Activation time of non-synchronous technologies [30].

Technology	Full Fast Frequency Response (ms)
Wind turbine-Synthetic inertia	≈ 500
Lithium batteries	10–20
Flow batteries	10–20
Lead-acid batteries	40
Flywheels	<4
Super capacitor	10–20
Solar PV	100–200
HVDC	50–500

- The energy storage technologies will be a key factor to avoid deloading and curtailment of renewables. The fast activation time (<50 ms) and promising price reduction make storage a good strategy to provide power balancing in both over and under-frequency cases [31].
- With a non-synchronous share above 85%, the frequency excursions after a load imbalance do not exceed the stable threshold. Nonetheless, the total system stability is not ensured after a few seconds (≈ 5 s). The reduction of synchronous share provokes undamped oscillations due to the poor damping torque present in the system. Unlike the virtual synchronous machine [7], the proposed fast power reserve based on the initial RoCoF measurement does not provide damping torque, leading the system to become unstable for small perturbations [7,8].
- When a linear system is employed, as with the cases of the simplified IEEE model and the large scale scenario, no difference was found between the critical times for under and over-frequency. On the contrary, when the nonlinearity of the system is included in the extended model, the critical times between under and over-frequency do not match, as illustrated in Figure 17.

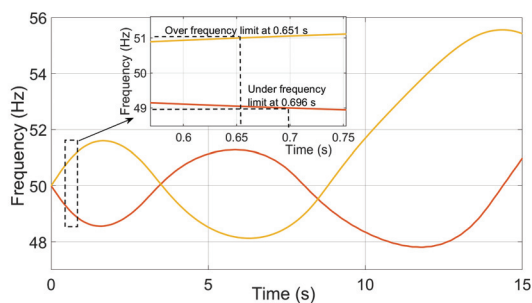


Figure 17. Under and over-frequency events in the extended IEEE model: a difference of 45 ms between each critical time was found.

- The synthetic inertia from wind turbines has a better performance when operated along with a fast synchronous response, as shown in Section 3.2.1. When synthetic inertia is implemented with a slow primary response, such as the case of the European grid, no frequency nadir improvement was obtained. Therefore, synthetic inertia is not able by itself to regulate or restore frequency deviation [13]. This outcome limits its usage just for slowing down the frequency drop after a load event. The influence of the gain K_i is fundamental, since the choice of a specific value can avoid load shedding just for a certain range of imbalances. For instance, in Section 3.2.1 it was demonstrated that the chosen value for K_i is adequate for imbalances of 10%, but as the imbalance increases to 15%, the initial dependency of system to sustain the imbalance from the synthetic inertia makes the frequency rapidly drop after 10 s, when the synthetic inertia has been removed.
- In general, similar behaviour is exhibited from the different models and approaches, even though they differ considerably in size and complexity. Hence, the simplified block representation of the power system seems to be a fair way to sketch overall system's trends and responses. The differences among governor time constants were found not to be relevant in frequency studies. The difference in critical time estimation between a full grid simulation and a simplified model was calculated to differ between 20% and 35%; such a difference could be crucial in fast power reserve studies, and therefore, should be considered when precise applications are implemented. A comprehensive method for estimation of the inverter-based fast power reserve and critical time were developed and proved through the simulation cases.

Author Contributions: Conceptualisation, A.R., H.B., and S.G.; investigation, A.R.; writing—original draft, A.R.; supervision, H.B., S.G., K.v.M., and C.A.; writing—review and editing, A.R., S.G., K.v.M., and C.A. All authors have read and agreed to the published version of the manuscript.

Funding: This research received no external funding.

Conflicts of Interest: The authors declare no conflict of interest.

Abbreviations

The following abbreviations are used in this manuscript:

ENTSOE	European Network of Transmission System Operators for Electricity.
HVDC	high voltage direct current.
IEEE	Institute of Electric and Electronic Engineers.
IBFPR	inverter-based fast power reserve.
IBG	inverter-based generation.
PV	photovoltaic.
RoCoF	Rate of Change of Frequency.
UFLS	under frequency load shedding.
WSCC	Western System Coordinated Council.

References

1. Energiewende: What do the New Laws Mean? Ten Questions and Answers about EEG 2017, the Electricity Market Act, and the Digitisation Act. Available online: https://www.agora-energiewende.de/fileadmin2/Projekte/2016/EEG-FAQ/Agora_FAQ-EEG_EN_WEB.pdf (accessed on 31 July 2019)
2. Energiewende, A. *Flexibility in Thermal Power Plants—With a Focus on Existing Coal-Fired Power Plants*; Agora Energiewende: Berlin, Germany, 2017.
3. Deutsche Energie-Agentur GmbH (dena)—German Energy. *dena Ancillary Services Study 2030: Security and Reliability of a Power Supply with a High Percentage of Renewable Energy*; Deutsche Energie-Agentur GmbH: Berlin, Germany, 2014.
4. Kroposki, B.; Johnson, B.; Zhang, Y.; Gevorgian, V.; Denholm, P.; Hodge, B.M.; Hannegan, B. Achieving a 100% renewable grid: Operating electric power systems with extremely high levels of variable renewable energy. *IEEE Power Energy Mag.* **2017**, *15*, 61–73. [[CrossRef](#)]
5. Miller, N.W.; Shao, M.; Venkataraman, S. California ISO (CAISO) frequency response study. *GE Energy* **2011**, *9*.
6. Lammert, G.; Yamashita, K.; Ospina, L.D.P.; Renner, H.; Villanueva, S.M.; Pourbeik, P.; Ciausiu, F.E.; Braun, M. Modelling and dynamic performance of inverter based generation in power system studies: an international questionnaire survey. *CIREC-Open Access Proc. J.* **2017**, *2017*, 1899–1902. [[CrossRef](#)]
7. D’Arco, S.; Suul, J.A.; Fosso, O.B. A Virtual Synchronous Machine implementation for distributed control of power converters in SmartGrids. *Electr. Power Syst. Res.* **2015**, *122*, 180–197. [[CrossRef](#)]
8. Vorwerk, J. Small-Signal Analysis of Power Systems with Low Rotational Inertia. Master’s Thesis, Swiss Federal Institute of Technology (ETH), Zurich, Switzerland, 2018.
9. Dreidy, M.; Mokhlis, H.; Mekhilef, S. Inertia response and frequency control techniques for renewable energy sources: A review. *Renew. Sustain. Energy Rev.* **2017**, *69*, 144–155. [[CrossRef](#)]
10. Crăciun, B. Grid Support in Large scale PV Power Plants Using Active Power Reserves. Ph.D. Thesis, Aalborg University, Aalborg, Denmark, 2014.
11. Hoke, A.F. *Fast Grid Frequency Support from Distributed Inverter-Based Resources*; Technical Report; National Renewable Energy Lab. (NREL): Golden, CO, USA, 2018.
12. Hoke, A.; Elkhatib, M.; Nelson, A.; Johnson, J.; Tan, J.; Mahmud, R.; Gevorgian, V.; Neely, J.; Antonio, C.; Arakawa, D.; et al. *The Frequency-Watt Function: Simulation and Testing for the Hawaiian Electric Companies*; Technical Report; National Renewable Energy Lab. (NREL): Golden, CO, USA, 2017.
13. Wu, L.; Infield, D.G. Towards an Assessment of Power System Frequency Support from Wind Plant—Modeling Aggregate Inertial Response. *IEEE Trans. Power Syst.* **2013**, *28*, 2283–2291. [[CrossRef](#)]
14. ENTSOE. *Frequency Stability Evaluation Criteria for the Synchronous Zone of Continental Europe*; ENTSOE: Brussels, Belgium, 2016.
15. Kundur, P.; Balu, N.J.; Lauby, M.G. *Power System Stability and Control*; McGraw-Hill: New York, NY, USA, 1994; Volume 7.
16. Gevorgian, V.; Zhang, Y.N. *Wind Generation Participation in Power System Frequency Response*; Technical Report; National Renewable Energy Lab. (NREL): Golden, CO, USA, 2017.
17. First International Workshop on Grid Simulator Testing of Wind Turbine Drivetrains. Available online: https://www.nrel.gov/grid/assets/pdfs/turbine_sim_12_advanced_wind_plant_controls.pdf (accessed on 29 May 2019)
18. Nesje, B. The Need for Inertia in the Nordic Power System. Master’s Thesis, NTNU, Trondheim, Norway, 2015.
19. Muljadi, E.; Gevorgian, V.; Singh, M.; Santoso, S. *Understanding Inertial and Frequency Response of Wind Power Plants*; University of Texas-Austin: Austin, TX, USA, 2012.
20. González Rodríguez, A.G.; González Rodríguez, A.; Burgos Payán, M. Estimating wind turbines mechanical constants. *Renew. Energy Power Qual. J.* **2007**, *1*, 697–704. [[CrossRef](#)]
21. Ørum, E.; Kuivaniemi, M.; Laasonen, M.; Bruseth, A.I.; Jansson, E.A.; Danell, A.; Elkington, K.; Modig, N. *Future System Inertia*; Tech. Rep.; ENTSOE: Brussels, Belgium, 2015.
22. Delavari, A.; Kamwa, I.; Brunelle, P. SImscape power systems benchmarks for education and research in power grid dynamics and control. In Proceedings of the 2018 IEEE Canadian Conference on Electrical & Computer Engineering (CCECE), Quebec City, QC, Canada, 13–16 May 2018; pp. 1–5.

23. Demetriou, P.; Asprou, M.; Quiros-Tortos, J.; Kyriakides, E. Dynamic IEEE test systems for transient analysis. *IEEE Syst. J.* **2015**, *11*, 2108–2117. [[CrossRef](#)]
24. Sundaram, D.; Bhuiyan, M. Comparing and Evaluating Frequency Response Characteristics of Conventional Power Plant with Wind Power Plant. Master's Thesis, Chalmers University of Technology, Göteborg, Sweden, 2008.
25. Anderson, P.M.; Fouad, A.A. *Power System Control and Stability*, 2nd ed.; Wiley: New York, NY, USA; Chichester, UK, 2002.
26. Hultholm, C.; Wägar, N. *Optimal Reserve Operation in Turkey—Frequency Control and Non-Spinning Reserves*; Power-Gen Europe: Milano, Italy, 2015.
27. Grainger, J.J.; Stevenson, W.D. *Power System Analysis*; McGraw-Hill: New York, NY, USA, 1994; Volume 67.
28. Ogata, K. *Ingenieria de Control Moderna (Spanish Edition)*; Prentice Hall: Upper Saddle River, NJ, USA, 1999.
29. Mathworks. Available online: <https://www.mathworks.com/help/phymod/sps/examples/24-hour-simulation-of-a-vehicle-to-grid-v2g-system.html> (accessed on 15 August 2019).
30. Miller, N.; Lew, D.; Piwko, R. *Technology Capabilities for Fast Frequency Response*; Tech. Rep.; GE Energy Consulting: Schenectady, NY, USA, 2017.
31. Ralon, P.; Taylor, M.; Ilas, A.; Diaz-Bone, H.; Kairies, K. *Electricity Storage and Renewables: Costs and Markets to 2030*; International Renewable Energy Agency: Abu Dhabi, UAE, 2017.



© 2020 by the authors. Licensee MDPI, Basel, Switzerland. This article is an open access article distributed under the terms and conditions of the Creative Commons Attribution (CC BY) license (<http://creativecommons.org/licenses/by/4.0/>).

Article

Battery Energy Storage System for Aggregated Inertia-Droop Control and a Novel Frequency Dependent State-of-Charge Recovery

Ujjwal Datta *, Akhtar Kalam and Juan Shi

College of Engineering and Science, Victoria University, P.O. Box 14428, Melbourne 8001, Australia; akhtar.kalam@vu.edu.au (A.K.); juan.shi@vu.edu.au (J.S.)

* Correspondence: ujjwal.datta@live.vu.edu.au

Received: 19 March 2020; Accepted: 11 April 2020; Published: 18 April 2020

Abstract: To deal with the technical challenges of renewable energy penetration, this paper focuses on improving the grid voltage and frequency responses in a hybrid renewable energy source integrated power system following load and generation contingency events. A consolidated methodology is proposed to employ a battery energy storage system (BESS) to contribute to voltage regulation through droop-type control and frequency regulation by assimilated inertia emulation (IE) and droop-type control. In addition, a novel frequency-dependent state-of-charge (SOC) recovery (FDSR) is presented to regulate BESS power consumption within the FDSR constraints and recharge the battery during idle periods whenever needed. The efficacy of the proposed BESS controller is demonstrated in an IEEE-9 bus system with a 22.5% photovoltaics (PV) and wind penetration level. The simulation results obtained manifest the satisfactory performance of the proposed controller in regulating simultaneous voltage and frequency in terms of lower rate of change of frequency and better frequency nadir. Furthermore, the proposed FDSR demonstrates its superiority at the time of SOC recovery compared to the conventional approach.

Keywords: battery energy storage system; frequency control; inertia emulation; voltage control; SOC recovery

1. Introduction

A large amount of renewable energy sources (RESs), mainly wind and photovoltaic (PV) power plants, has been installed throughout Europe, the USA, and Asia. A European Network of Transmission System Operators for Electricity (ENTSO-E) forecast stated that fossil fuelled conventional power plants (CPPs) are closing down following increased RES penetration in the grid [1]. With the replacement of CPPs by fundamentally intermittent wind and PV sources, several inevitable technical challenges are being introduced that can have a significant impact on the stability and security of the power system. The conventional synchronous generators inherently provide inertial response to frequency deviation and can participate in load-frequency control (LFC) according to their droop characteristics, given that sufficient spinning reserves are accessible. Therefore, increased penetration of RESs significantly reduces system inertia as RESs have the limitation of providing fundamental inertial and primary frequency control (PFC) response. This eventually affects the rate of change of frequency (ROCOF) and the maximum/minimum frequency limit during post-contingency periods, and therefore, the provision of frequency control becomes a challenging task.

The smart grid-oriented future power system with dominant infiltration of power electronics has led to a significant amount of research on emulating the behaviour of synchronous machines by exploiting the control mechanism of the power electronics converter at RES farms [2]. Different control strategies are proposed to provide grid frequency control including under-frequency load-shedding [3],

regulating DC voltage in HVDC [4], and demand-side management [5]. Typically, RES plants are regulated to produce the maximum output power at a given wind speed and solar radiation. The research conducted by Engleitner et al. [5] proposed that wind farms can take part in regulating grid frequency through the use of their stored kinetic energy. To some extent, PV systems can also demonstrate frequency response capability [6]. However, such control approaches require curtailing power generation at their terminal, which is not desirable. Moreover, the implicit weather-dependent nature of RESs makes it unreliable to rely on adopting such control approaches. A new research trend of an electric vehicle (EV) acting as a power reserve to regulate frequency was proposed by Aliabadi et al. [7] and Liu et al. [8]; nevertheless, the vehicle-to-grid infrastructure to control grid frequency is not yet accessible. Moreover, different energy storage technologies are available to contribute both inertial [9] and primary frequency control [10].

The power-frequency droop control of BESS has been reported to have significant improvement in primary frequency response [11,12]. Li et al. [13] demonstrated that a droop-controlled hybrid storage system suppressed significant frequency oscillations and offered robust stability responses. Virtual inertia offers an added benefit to the system dynamics by delivering the required power imbalance. An inertia emulation (IE) performance analysis of an energy storage system (ESS) [14] and BESS [9] in a microgrid (MG) was demonstrated to deliver robust frequency stability. A combination of BESS for PFC and an ultra-capacitor for IE was proposed by Fini and Golshan [15] to improve the frequency stability of an MG. Different optimal energy storage methods have been proposed to enhance frequency variation for the required IE [16] and PFC in an MG using battery overloading features [17]. The research by Toma et al. [18] considered BESS to provide virtual inertia and PFC in a two-area power system considering 100% renewable generation. However, the battery state-of-charge (SOC) was completely overlooked in the earlier studies [14,15,18–20]. ESS provides IE and PFC to regulate grid frequency with high wind penetration [20]. Fast acting BESS is utilized for IE and PFC to participate in unit-commitment and improve frequency dynamics under contingencies [21]. The optimal sizing of BESS considering the BESS contribution as IE and PFC was presented in [22]. The study by Brogan et al. [23] demonstrated that improvements in frequency nadir and ROCOF were visible when BESS was activated with less time delay and high BESS power input following the changes. Nevertheless, all the aforementioned studies of IE and IE with PFC were based on active power regulation of BESS and did not provide any insight into the voltage regulation capability of BESS. A charge/discharge management of BESS was proposed by Zeraati et al. [24] via a droop control method in order to regulate distribution network voltage with high PV penetration.

In [25], BESS was proposed to regulate voltage and frequency in an MG. Nonetheless, battery SOC was considered for the droop component only. As demonstrated by Alhejaj and Longatt [26], battery SOC discharge is inversely related to the BESS inertia constant; hence, ignoring SOC for the inertia component is an inaccurate assumption in designing BESS for IE and PFC. An autonomous SOC recovery was proposed in [27] that suggested the regulation of the terminal voltage of the super-capacitor (SC) to maintain SOC defined constraints of SC from the battery. A similar SOC recovery was proposed by Xiao et al. [28] for voltage regulation and SOC recovery as long as the power capacity of energy storage devices was available. Nevertheless, these studies did not provide any insight into the impact of SOC recovery on the frequency of the grid. On the contrary, the study by Zhu and Zhang [29] proposed an SOC recovery strategy that could minimize the penalty costs due to the failure of frequency regulation. Variable SOC recovery strategies were proposed by Datta et al. [30] depending on the value of the charging current. However, the impact of SOC management on the performance of the controller and grid frequency was not considered by Zhu and Zhang [29] and by Datta et al. [30].

This paper therefore proposes an IE-and PFC-regulated BESS to achieve enhanced frequency dynamics in a power system with high shares of non-synchronous renewable generation. In addition, the droop control is selected to regulate reactive power and enhance the voltage dynamics. Hence, the main contributions of this paper include: (1) the proposed combined inertia- and droop-controlled

frequency regulation and droop-controlled voltage regulation, which have not been studied in the earlier literature; (2) a novel frequency-dependent SOC recovery (FDSR) strategy to ensure sufficient SOC is available for future events without affecting the grid frequency. The proposed control approach regulates BESS active and reactive power considering BESS operation within the defined SOC constraints when participating in IE ad PFC.

2. System Inertia and Frequency Response

The inertia of rotating masses of synchronous machines and turbines responds to immediate frequency changes, due to power deficit, by regulating power flows (injection/absorption). There are several stages in frequency control following a power imbalance from a contingency event: the inertia response to regulate ROCOF, which is an uncontrolled response, primary control, secondary control, and tertiary control to mitigate frequency deviations, as shown in Figure 1. In the inertia control stage, power imbalance is met by the implicit kinetic energy release of synchronous machines during periods of 0–10 s [14]. PFC takes over this stage, once the controller is activated, mainly during periods of 0–30 s, and stabilizes the frequency to a new steady-state point. Then, the secondary and tertiary control recovers frequency to the non-operating frequency boundary if required, and the feature is available for a duration of 30 s–30 min [31]. The minimum grid frequency response followed by power imbalance is influenced by the deployment and the intensity of virtual inertia control and PFC, which depends on the available physical inertia and power/energy regulation capability of the system. The overall system inertia constant was defined in [32] as:

$$H_{sys} = \frac{E_{kinetic}}{S_{sys}} = \frac{1}{2} \frac{J \cdot \omega^2}{S_{sys}} \tag{1}$$

where H_{sys} is the total system inertia and $E_{kinetic}$ is the total stored kinetic energy of all rotating machines with their rotational speed (ω), moment of inertia (J), and rated base power of the system (S_{sys}).

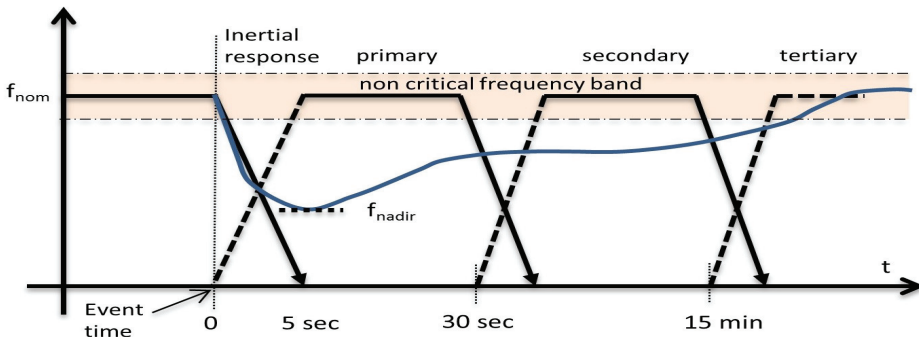


Figure 1. Frequency response stages by the European Network of Transmission System Operators for Electricity (ENTSO-E) [1].

The power imbalance (ΔP_{im}) during a contingency is determined by Equation (2):

$$\Delta P = P_g - P_l = \frac{dE}{dt} = J \omega \frac{d\omega}{dt} \tag{2}$$

where P_g and P_l are total generated and total load power, respectively. Substituting the value of J from (2) into (1), the swing equation describing the relationship of system inertia (H_{sys}) and ROCOF due to power imbalance can be defined as in (3) [32]:

$$\frac{df}{dt} = \frac{\Delta P_{im}}{S_{sys}} \frac{f_{grid}}{2 H_{sys}} \tag{3}$$

where f_{grid} is the nominal system frequency. It can be observed that ROCOF (df/dt) is inversely related to the system inertia, which implies that with a lower inertia value, the grid has a weaker frequency response capability during the abrupt changes in the power balance between power generation and demand and results in higher ROCOF.

At present, the grid code defines the ROCOF value for the Australian Energy Market Operator (AEMO) and ENTSO-E to be ≤ 0.5 Hz/s [33,34]. A faster ROCOF may activate protection relays and may cause tripping of generators [33]. On the other hand, rapid initial ROCOF may contribute a large frequency deviation, which can result in generator trip and load shedding [33]. In the Australian National Electricity Market (NEM), the maximum allowable frequency deviation in the post-fault condition is 50 ± 0.5 Hz for a load event and generation event with 50 ± 0.15 Hz as non-critical frequency operating ranges [35].

Synchronous inertia plays a fundamental role in minimizing the faster changes of frequency (df/dt). Synchronous machines respond to power deficit instantly by releasing kinetic energy as they are coupled with the grid frequency. On the contrary, generators on renewable farms are connected to the grid via a power electronics interface; hence intrinsically, they are not providing inertia response as they are decoupled from the grid frequency. Therefore, with increased penetration of asynchronous renewable generation, the power system has lower inertial response capability.

3. Proposed IE and Droop-Regulated BESS Control Schemes

The proposed BESS structure and its control system are discussed in this section. The control schemes regulate power flow between the battery and the grid via a voltage source converter (VSC). The measurements for voltage and frequency controllers are taken locally to control BESS operation. BESS regulates active and reactive power independently by governing its current controller in the d and q axes, and the total power is delimited by BESS converter capacity.

3.1. Frequency Controller for IE and PFC

BESS contributes towards frequency regulation by altering active power through the point of common coupling (PCC). At PFC, reduced system inertia affects power-frequency droop and thus influences the stability of the power system. Figure 2 illustrates the block diagram of the frequency controller to provide IE and PFC. The goal of the proposed frequency controller is to enhance the damping of frequency oscillations and reduce the value of ROCOF and frequency deviation. BESS is designed to emulate the behaviour of a conventional synchronous generator and provide both the inertial response and primary frequency control.

The expression of the suggested frequency controller can be written as in (4):

$$dP_{ref} = \Delta P_{PFC} + \Delta P_{IE} \quad (4)$$

where dP_{ref} is the total BESS output power reference and ΔP_{PFC} and ΔP_{IE} are the changes in BESS active power output based on power-frequency droop characteristics and inertial response capability following the variation in grid frequency respectively and can be expressed as in (5) and (6):

$$\Delta P_{PFC} = \frac{1}{R_{p-f}} \Delta f \quad (5)$$

$$\Delta P_{IE} = H_{BESS} \cdot \frac{d}{dt} f_{grid} \quad (6)$$

where Δf (pu) is the frequency deviation resulting from a disturbance and calculated as the difference between the reference frequency (f_{ref}) and the grid frequency (f_{grid}), R_{p-f} is the power-frequency droop value, and H_{BESS} is the BESS inertia constant. The positive and negative values of Δf define BESS power injection and absorption, respectively. R_{p-f} in (5) specifies the demand of BESS active power adjustment in response to frequency error. The deadband restricts BESS operation for any minor

frequency changes and within the grid defined inactive region. The PFC feature is activated if the actual frequency differs by $f_{tol} = \pm 150$ MHz from the nominal value according to NEM criteria [35]. The BESS power is regulated linearly with the variation of frequency error, and the droop value R_{P-f} is selected as 0.006 pu in order to activate the nominal BESS power for the frequency deviation of ± 300 MHz. BESS operates at its maximum rated power when frequency deviation exceeds ± 300 MHz.

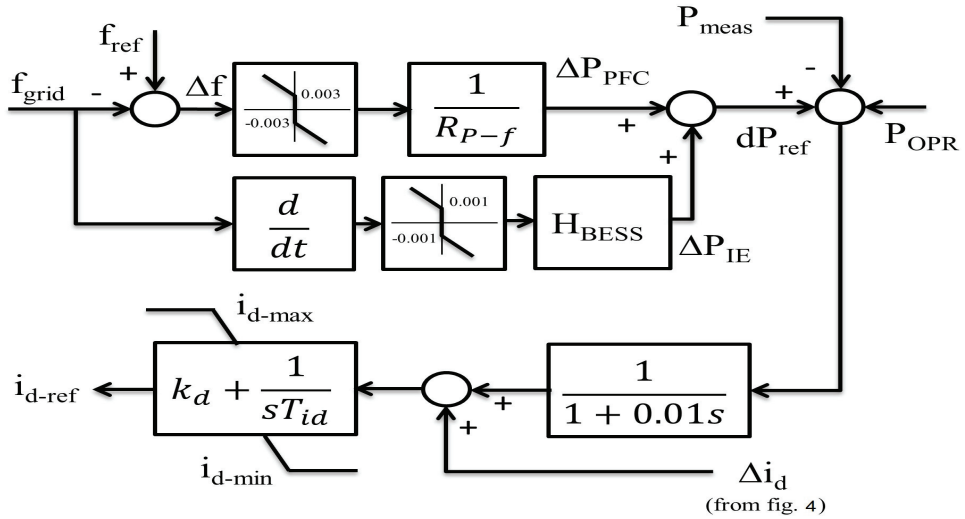


Figure 2. Block diagram of BESS for the inertia emulation (IE)- and primary frequency control (PFC)-regulated frequency controller.

The changes in active power during inertial response are regulated by the derivative of frequency error and the BESS inertia constant as in (6). The value of the inertia constant controls the sensitivity of the BESS controller according to the changes in ROCOF value. Theoretically, H_{BESS} can be infinite as the physical concept of limiting the inertia constant is not applicable for BESS. However, the inertia constant value defines the intensity of active power participation, i.e., an increased H_{BESS} value generates increased BESS power output, as mentioned in [26]; therefore, the value needs to be determined according to the capacity of the BESS converter. Hence, considering an amalgamated application, the value of H_{BESS} was selected as 20 s, which defines the activation of nominal BESS active power for a total df/dt of 0.15 Hz/s. The inertial deadband value was selected as 0.05 Hz/s according to [22]. As the deadband for inertial response is smaller than droop response, BESS inertial power is activated for a small deviation in system frequency. Although Duckwitz and Fischer [36] presented that a certain delay may be essential in the control chain in order to avoid control instability when synthetic inertia (i.e., df/dt) control is performed, this study considered no delay for df/dt as in the studies [22] proposed by Knap et al. and [25] proposed by Serban and Marinescu.

The frequency fluctuations are dealt with by varying BESS active power output in charging, discharging, and inactive modes as shown in (7):

$$Mode/f = \begin{cases} \text{Inactive} & \text{if } f_{ref} - f_{grid} \leq f_{tol} \\ \text{Charge} & \text{if } f_{grid} > (f_{ref} + f_{tol}) \\ \text{Discharge} & \text{if } f_{grid} < (f_{ref} - f_{tol}) \end{cases} \quad (7)$$

The battery storage operates in charging mode if the grid frequency is higher than the reference frequency and in discharging mode if the reference frequency is higher than the grid frequency, considering the SOC of the battery is usable as per the defined battery operating range. The battery

can be charged when BESS remains in the inactive region. A low-pass filter is used to filter out the noise in the BESS active power reference. The error between the active power reference dP_{ref} and active power output at BESS AC terminal P_{meas} generates updated active current reference in the d axis. The difference of the charge controller input and output as Δi_d is added with the d axis current reference. P_{OPR} is the external power reference input by the operator.

3.2. Voltage Controller

The grid voltage is affected by the penetration of inverter-based RESs. As BESS can regulate active and reactive power separately, it can be easily utilized to draw/inject reactive power. The voltage control can be accomplished by regulating reactive power sharing according to conventional reactive power-voltage (Q-V) droop. The block diagram of the proposed voltage controller is shown in Figure 3. The figure shows how the reactive power reference is generated in response to the changes in voltage at the BESS AC terminal. Q_{OPR} is the external power reference input by the operator. The tracking error is used as an input to the PI controller.

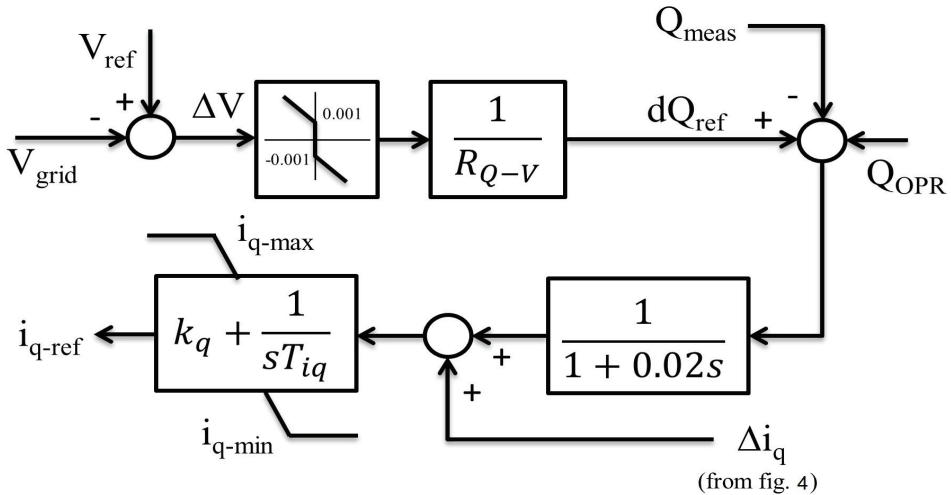


Figure 3. Block diagram of the BESS voltage controller.

The voltage droop controller can be expressed as in (8):

$$dQ_{ref} = \frac{1}{R_{Q-V}} \Delta V \tag{8}$$

where ΔV is the difference between voltage reference V_{ref} (pu) at steady state and grid voltage V_{grid} (pu) and dQ_{ref} defines the reactive power reference according to the Q-V droop characteristics. R_{Q-V} is the measure of reactive power intensity, which was selected as 10, defining the nominal reactive power activation for a voltage deviation of 0.1 pu with a voltage tolerance of $V_{tol} = \pm 0.01$ pu. The lower slope for the reactive power-voltage drop is preferred to avoid overloading of BESS.

BESS absorbs/injects reactive power according to three level structures as shown in (9):

$$Mode/V = \begin{cases} \text{Inactive} & \text{if } V_{ref} - V_{grid} \leq V_{tol} \\ \text{Absorb} & \text{if } V_{grid} > (V_{ref} + V_{tol}) \\ \text{Inject} & \text{if } V_{grid} < (V_{ref} - V_{tol}) \end{cases} \tag{9}$$

A low-pass filter is used to filter out the noise in the BESS reactive power reference, and the current reference in the q axis is generated using a PI controller. The error between the charge controller input and output as Δi_q is added with the updated reactive current reference. This reference is calculated from the error of reactive power reference dQ_{ref} and the reactive power output at the BESS AC terminal Q_{meas} that generates the reactive current reference in the q axis. The associated BESS parameters are given in Appendix A. The initial battery SOC was considered as 0.8 pu. As this study focuses on short-term transients, the smaller size of BESS capacity was selected for simulation purposes. The nominal source voltage and the internal resistance of the battery were selected as in [37]. PI parameters were tuned on a trial-and-error basis.

3.3. Proposed FDSR-Based Charge/Discharge Management

The BESS charge/discharge management (BCDM) encompasses coordinated operation between grid demand and accessible BESS power. BESS participates in frequency control by exchanging energy during over-frequency and under-frequency events resulting from power transients. It is worth noting that an effective control strategy is indispensable to avoid unwanted deep discharge and over-charge operation of BESS. The direction of current flow selects the appropriate SOC condition to fulfil and manage battery charge/discharge to deliver the required BESS output if the SOC condition is met. BESS operates in discharging mode if battery SOC is greater than the minimum SOC and charging mode if present battery SOC is less than the maximum SOC. The minimum and maximum battery SOC were selected as 0.2 pu and 1 pu, respectively. Battery SOC changes throughout the power exchanging periods (increase/decrease). Therefore, BESS functions in SOC recovery charging mode if battery SOC drops lower than the threshold or the minimum SOC value according to the conditions specified in (10). However, according to the proposed FDSR, the battery will only be recharged if the grid frequency is equal to or higher than the minimum limit of the nominal frequency limit, i.e., 0.997 pu. This can avoid the deep discharge of the battery and secure BESS availability for the upcoming events without affecting grid frequency stability.

$$i_{ch} = \begin{cases} i_{ch} & \text{if } i_{d-ref} < 1e-3 \text{ and } SOC \leq 0.5 \\ & \text{or } SOC \leq SOC_{min} \text{ and } f_{grid} \geq 0.997pu \\ 0 & \text{otherwise} \end{cases} \quad (10)$$

Figure 4 illustrates the battery charging or discharging mechanism, highlighting the various control levels of BESS action. BCDM governs the response of BESS to the changes in frequency controller output and mandatory charging recovery, if applicable.

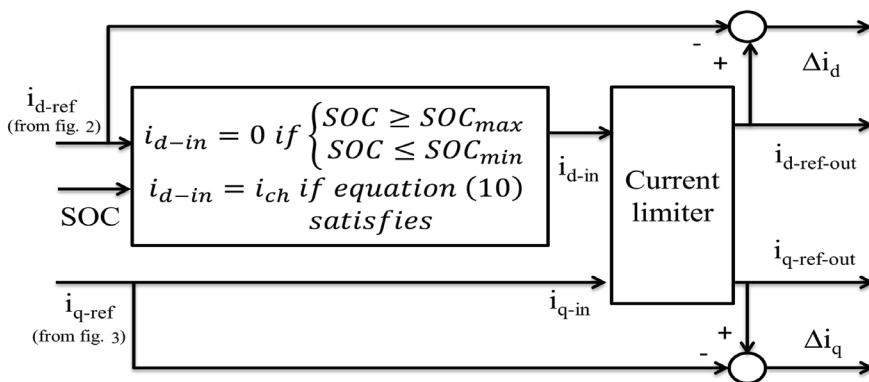


Figure 4. Block diagram of BESS charge/discharge management.

BCDM determines whether the generated active power reference is executable from BESS according to available and specified SOC operating values. BESS operates in power curtailment mode when the SOC of the battery reaches the defined minimum and maximum range. The overall BESS charge/discharge approach can be defined as in (11):

$$i_{d-in} = \begin{cases} i_{d-ref} & SOC \geq SOC_{min} \\ -i_{d-ref} & SOC \leq SOC_{max} \\ -i_{ch} & \text{if Equation (10) is satisfied} \end{cases} \quad (11)$$

As the active and reactive power of BESS is limited by its apparent power, a well regulated power allocation is imperative to avoid competition between these two and thus avoid saturation when the grid demands a large amount of active and reactive power at the same time. The current limiter calculates the total BESS current at its output to make sure active and reactive power do not exceed the rated capacity of BESS and can be calculated as shown in Figure 5. The active power is given preference over the reactive power, which can be calculated as in Figure 5a. The reactive power output is limited by the remaining BESS capacity and can be calculated as illustrated in Figure 5b where the value of y can be calculated as in (12).

$$y = \sqrt{|1 - i_{d-in}^2|} \quad (12)$$

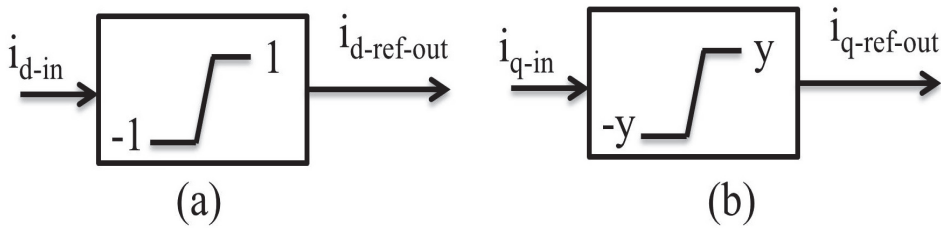


Figure 5. Active (a) and reactive (b) power calculation at converter output.

3.4. Battery Model and SOC Calculation

Unlike the previous work in [25], SOC is calculated based on the total power output of BESS, which is the proper method of calculating battery SOC in this study. The selected battery model is an equivalent R_{int} model, which was widely used in the previous studies [38–40].

The battery SOC can be calculated as follows:

$$SOC_k = SOC_{k-1} + \int_{k-1}^k \frac{\eta I_b}{3600 C_b} dt \quad (13)$$

where η is the Coulomb efficiency, I_b is the battery current, C_b is the rated battery capacity, and k is the time of SOC calculation. Furthermore, $\eta = \eta_C$ at the charging stage and $\eta = \eta_D$ at the discharging stage, which is 0.98 and one, respectively, as in [41], and the temperature dependency for Coulomb efficiency is not considered in this study.

3.5. Current Controller on the d and q Axes

The current control loop, an internal level control, provides the reference voltage at BESS output (AC side) for regulating the VSC. The input of the current controller is the reference current generated in the d ($i_{d-ref-out}$) and q ($i_{q-ref-out}$) axes and the measured d and q axis

current from the internal control loop. The phase-locked-loop (PLL) provides the necessary reference phase angle to the d-q transform value in the three phase reference for regulating DC/AC converter.

4. Attributes of the Test System

The performance of the proposed BESS model was investigated on an IEEE 9 bus standard test network, as shown in Figure 6, with 22.5% renewable energy penetration. The synchronous generator G1 was considered as the reference generator. The generators were dynamically modelled as hydro- (G1), gas- (G2), and coal-type (G3) power plants with a capacity of 250 MW, 255 MW, and 230 MW, respectively. All the generators were designed with a turbine governor and automatic voltage regulator (AVR). The connected RES farms at buses 5 and 9 were solar PV-type, whereas at buses 6 and 8, they were doubly-fed-induction generator-based wind-type. The BESSs farm was integrated with the grid via a step-up transformer. The BESS was connected to the network via a 0.4/230 kV step-up transformer. The studied model was designed and simulated in Powerfactory, and the renewable generation parameters are given in Appendix A.

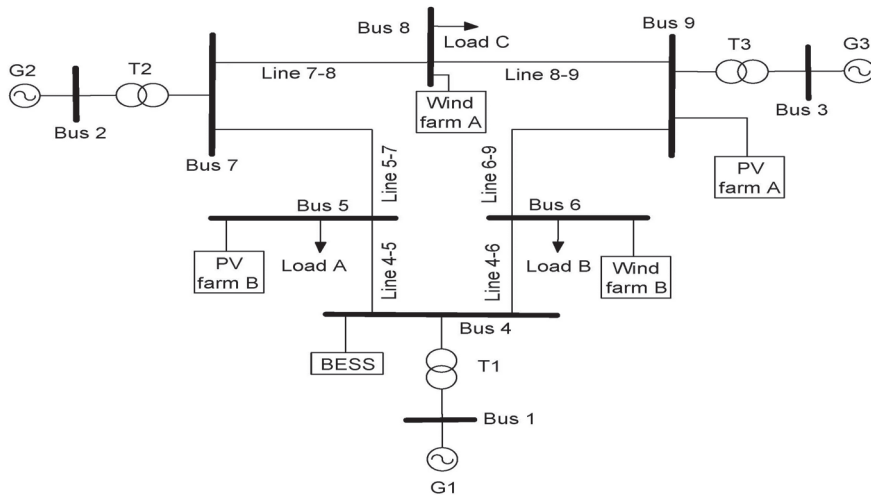


Figure 6. IEEE 9 bus standard test network with installed BESS and RES. G, generator.

Three case studies were investigated to evaluate the performance of the proposed BESS for IE and PFC and to achieve a grid code compatible outcome. The considered case studies were as follows:

1. Case 1: Load change event
2. Case 2: Generation event
3. Case 3: BESS recharging with FDSR
4. Case 4: Single-phase-to-ground fault

BESS was integrated to provide additional system damping and improve the transient response of the system with increased RES penetration.

5. Results and Discussion

The dynamic responses of the proposed BESS were evaluated in a hybrid power system following multiple disturbance scenarios. The performance of the proposed BESS was assessed in accordance with fulfilling the NEM criteria as mentioned in [35].

5.1. Load Change Event

In this section, the objective is to assess BESS efficacy in strengthening the frequency response of the grid following an abrupt change in load demand at a particular bus. A temporary 50% step increase in load demand at Load A (bus 5) was applied during $t = 0-0.75$ s. The applied transient load event would create frequency oscillations due to temporary imbalances between the electrical and mechanical power of each generator.

Figure 7 depicts that without a BESS, the frequency of generator G1 dropped to a value of 49.416 Hz, which was beyond the grid defined limit (49.5–50.5 Hz) for a load event. Therefore, a 27 MW BESS was incorporated at bus 4 to provide added oscillation damping to the system. The frequency response of generator G1 illustrated in Figure 7 demonstrated that BESS in inertia or droop control mode failed to achieve the minimum allowed frequency value for the load event. However, droop control (49.478 Hz) performed better than the inertial control (49.435 Hz) of BESS in terms of lowest frequency drop. On the contrary, combined IE- and PFC-regulated BESS delivered sufficient damping to the system and recovered the frequency response within the minimum grid frequency periphery (49.518 Hz). The frequency responses of generators G2 and G3 demonstrated similar performance. As BESS was connected at the generator G1 terminal, the improvement in the case of G2 and G3 was not as prominent as G1. The ROCOF values for different scenarios are outlined in Table 1. The aim was to provide the same values of the inertia constant and droop to demonstrate comparative performances in different frequency controller configurations. BESS as IE support showed a higher ROCOF value as the considered inertia constant of BESS was small. It could be observed that there was a noticeable improvement in slowing down the frequency drop, i.e., lowest ROCOF and highest f_{min} value that defined the effectiveness of the proposed combined control of BESS.

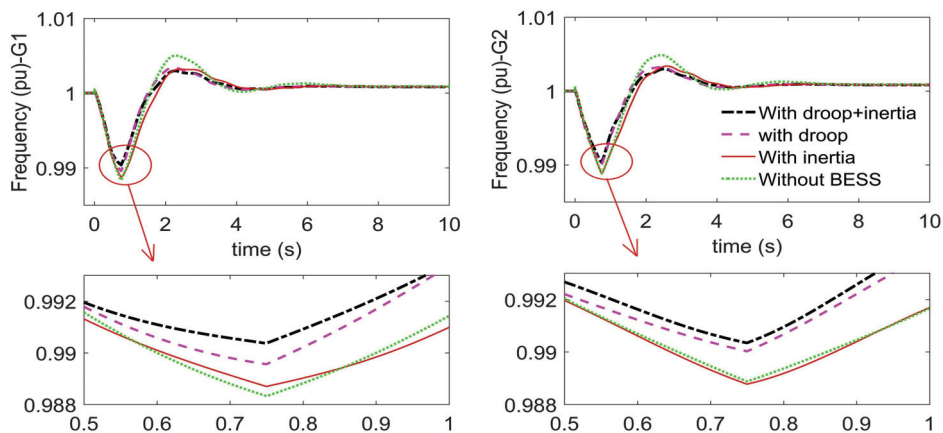


Figure 7. The frequency (pu) oscillation of generators with the load event.

Table 1. The frequency results of G1 with the load event.

Mode	No BESS	IE	PFC	IE + PFC
P_{BESS} (MW)	N/A	12.343	26.589	27.2
Q_{BESS} (MVar)	N/A	4.029	4.389	4.442
E_{BESS} (MWh)	N/A	0.00558	0.0137	0.0241
df/dt (Hz/s)	0.627	0.548	0.473	0.43
f_{min} (Hz)	49.416	49.435	49.478	49.518
SOC (pu)	N/A	0.798	0.774	0.772

The response of PCC voltage presented in Figure 8 shows that BESS with combined control performed better than without a BESS and independent of the IE-/PFC-controlled BESS, resulting in

lower voltage drop during the load event periods. However, droop control demonstrated a slightly better outcome right after the end of the load event. It is worth noting that as voltage was regulated through droop control only, hence, the voltage responses in all three cases were very similar.

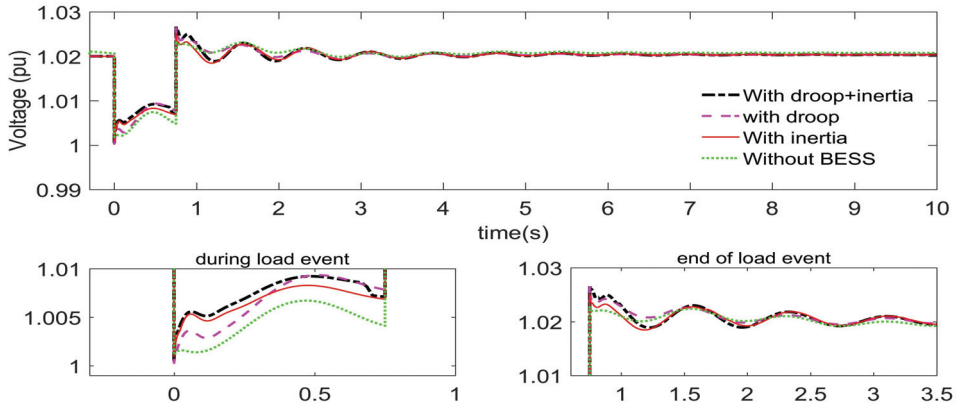


Figure 8. The voltage (pu) at the point of common coupling (PCC) with the load event.

The active and reactive power output of BESS is presented in Figure 9. As demonstrated in Figure 9 and Table 1, BESS with IE and PFC provided better performance by delivering more power to the system during the transient periods. However, the reactive power output was nearly the same for all the control modes as the voltage control was droop-based regulation only. The sum of the total energy exchange of BESS during transient periods (discharging as positive and charging as negative value), as indicated in Table 1, exhibited that IE and PFC mixed control delivered more energy than others and thus reflected lower SOC at the end of the transient periods. Therefore, the results indicated that the proposed BESS control performed better and efficiently regulated the voltage and frequency of the power system following an abrupt load change event.

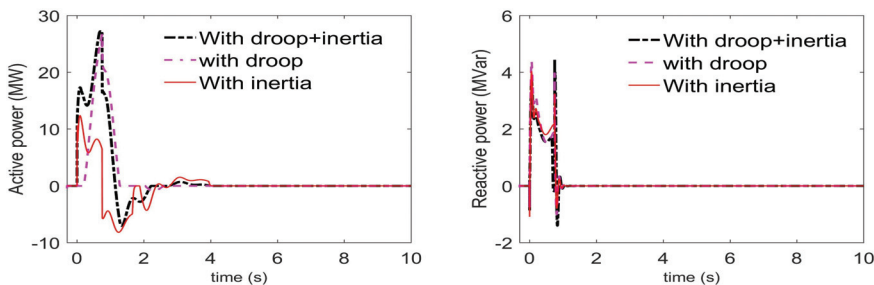


Figure 9. The active and reactive power of BESS with the load event.

5.2. Generation Contingency Event

PV power output is subjected to intermittent and uncertainty, which require a sufficient level of contemplation to maintain system reliability and security. To evaluate further the efficacy of the proposed BESS control, the dynamic behaviour of the network was investigated following a temporary reduction of the largest PV farm output. A 85% reduction of PV farm output was applied for the duration of 0.2–3.2 s, and the comparative performance of the different BESS control modes was evaluated. Figure 10 demonstrates that without a BESS, the minimum frequency reached the lowest value of 49.307 Hz and thus exceeded the grid operating standards. On the contrary, the incorporated BESS effectively supplied additional damping to the system that regulated the frequency deviation of

the generators within ± 0.5 Hz. Nevertheless, IE- and PFC-regulated BESS manifested a slightly better frequency outcome, and this was clearly noticeable by taking a closer look at the lower minimum frequency and ROCOF value, as shown in Table 2. This was an expected result, as IE provided an immediate response to the frequency deviation before the droop controller came into action, and then, the droop controller took control linearly; therefore, the combination of IE and PFC contributed to providing better attenuation of the frequency derivative and minimum frequency nadir.

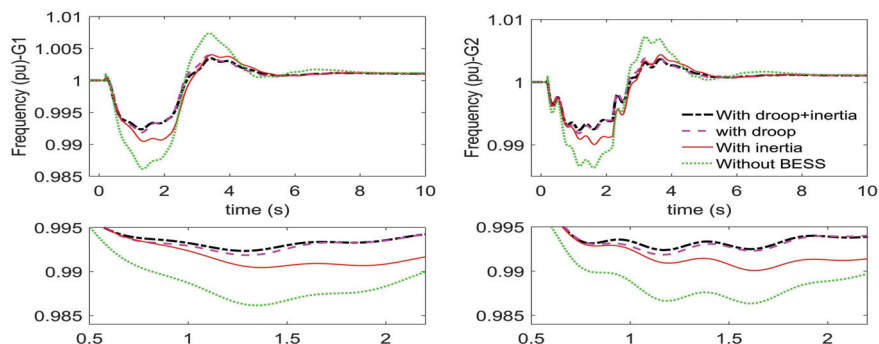


Figure 10. The frequency (pu) oscillation of generators with the generation event.

Table 2. The frequency results of G1 with the load event.

Operation Mode	No BESS	IE	PFC	IE + PFC
P_{BESS} (MW)	N/A	7.01	18.66	17.24
Q_{BESS} (MVar)	N/A	0.145	0.326	0.271
E_{BESS} (MWh)	N/A	-0.00136	0.05772	0.08961
df/dt (Hz/s)	0.833	0.526	0.433	0.394
f_{min} (Hz)	49.307	49.522	49.592	49.617
SOC (pu)	N/A	0.8001	0.7602	0.7501

The voltage response at PCC shown in Figure 11 illustrated that the PCC voltage was not affected much during the generation event. Therefore, the reactive power contribution was relatively small, as illustrated in Figure 12. The BESS active power exhibited in Figure 12 showed that droop-controlled BESS provided the maximum active power (18.66 MW) at a certain time. However, the overall performance was not better than the combined IE- and PFC-regulated BESS control. The sum of total energy supplied by BESS in different operation modes revealed that a higher amount of energy was supplied by the assimilated IE- and PFC-regulated BESS, which also demonstrated better frequency dynamic behaviour.

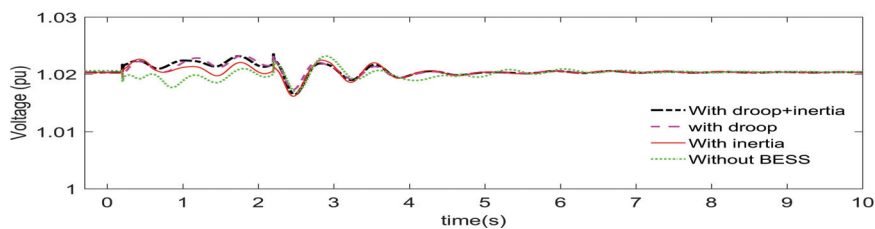


Figure 11. The voltage (pu) at PCC with the generation event.

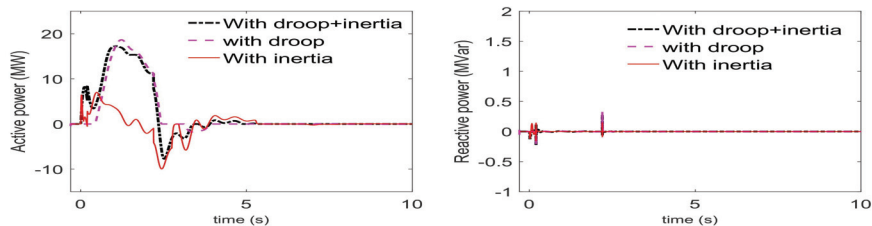


Figure 12. The active and reactive power of BESS with the generation event.

5.3. BESS Recharging with FDSR

Battery SOC changes due to the exchange of BESS power with the grid and also the inherent self-discharging characteristics of the battery. Therefore, SOC recharging facility is required to ensure the battery is charged enough to participate in exchanging power whenever it is needed. A 15 Ah battery capacity and a charging current of 0.05 pu were used to demonstrate the proposed SOC recovery strategy (FDSR). In order to simulate the SOC recovery strategy, a permanent 20% load growth was applied at Load A at time $t = 0$ s. This would result in a reduction in grid frequency, and as the frequency dropped lower than the deadband limit, BESS action took place. BESS would inject power to the grid to improve grid frequency as long as it had sufficient SOC. Once battery SOC reaches the minimum SOC, battery needs to be charged. The comparative results of the conventional approach and the proposed SOC recovery strategy are demonstrated in Figure 13a–d.

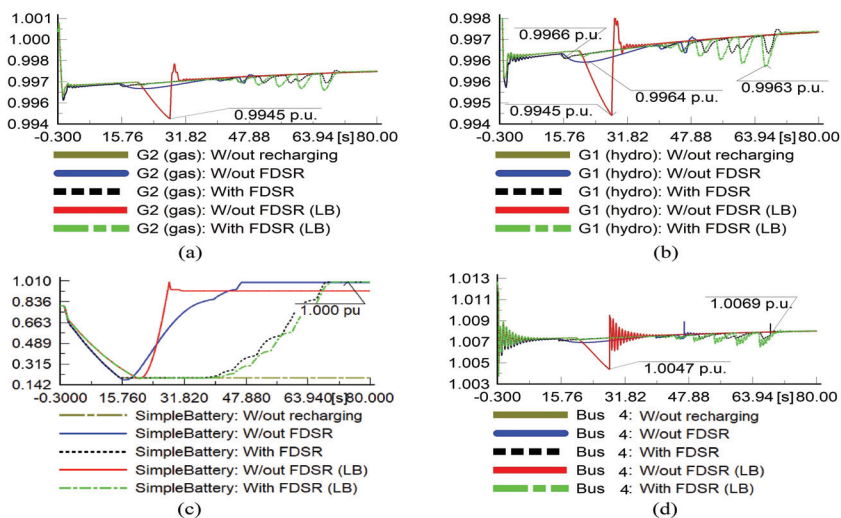


Figure 13. Generator frequency (a,b) and battery SOC (c) and bus voltage (d) with the SOC recharging strategy. FDSR, frequency-dependent SOC recovery; LB, large BESS.

Figure 13c shows that at approximately $t = 15$ s, battery SOC reached the minimum SOC and the battery stopped injecting power to the grid according to the design constraints, as in (11). As the battery reached the minimum SOC, this resulted in a frequency reduction to 49.83 Hz before it finally recovered to the deadband boundary. With the conventional SOC recovery method (w/out FDSR), the battery started to recharge immediately as soon as the battery reached the minimum SOC. The battery would consume energy from the grid to be recharged, and this dragged down more the already lowered frequency to 49.82 Hz for the generators (G1, G2), as illustrated in Figure 13a,b. However, with the proposed FDSR, the battery did not participate in battery recharging, i.e., it consumed energy from

the grid until the grid frequency reached the deadband boundaries ($f_{grid} \geq 0.997$ pu), i.e., within the nominal grid operation limit, which was at about $t = 37.5$ s. It can be seen that there were ups and downs in the frequency response during FDSR-based charging. This was due to the fact that when the frequency was equal to or greater than 0.997 pu, the battery attempted to charge and consumed energy from the grid; this caused the frequency to drop below 0.997 pu, and battery stopped charging immediately and waited until the frequency reached 0.997 pu. This continued until SOC reached the maximum SOC.

In order to further demonstrate the effectiveness of the proposed FDSR approach, a higher charging current and rated BESS power capacity were applied, which exemplified the high power capacity of BESS for SOC recovery. The large BESS (LB) converter (50 MW) with a battery capacity of 2.5 Ah and in response to the same load growth frequency response was slightly better, but at the expense of a faster reduction in battery SOC. With LB and a charging current of 0.5 pu and without FDSR (LB), the battery started consuming energy immediately (approximately at $t = 20.4$ s) for recharging. It can be seen that due to the consumption of higher energy from the grid, the grid frequency considerably reduced to a lower value (49.745 Hz). However, with the proposed FDSR (LB), BESS delayed its battery charging until the grid frequency satisfied the FDSR constraints and thus avoided impacting the grid frequency negatively during SOC recovery. In addition to grid frequency, PCC voltage was also affected by the uncontrolled battery charging (w/out FDSR (LB)). Without the proposed FDSR, the PCC voltage reduced to 1.0047 pu from its pre-charging voltage of 1.0075 pu, as depicted in Figure 13d. On the contrary, PCC voltage drop was limited to 1.0069 with FDSR (LB), which showed a significant improvement in the grid voltage. These observations clearly indicated that without the proposed FDSR, SOC recovery could hamper the performance of the controller and degrade grid performance instead of enhancing it. With larger BESS capacity, the consequences could be severe for the already seriously affected grid in terms of frequency and voltage. On the contrary, FDSR ensured that battery recharging took place when the grid frequency was stable and thus overcame the negative impact of the conventional SOC recovery strategy on both voltage and frequency.

5.4. Single-Phase-to-Ground Fault

In order to demonstrate the efficacy of the proposed BESS control design in fault conditions, a single-phase-to-ground fault event was carried out. The fault was applied at bus 4 for a duration of $t = 0$ –150 ms. The performance of the generators, the bus voltage at bus 4, and BESS power output are illustrated in Figures 14–16. The frequency of generators G1 and G2 as shown in Figure 14 indicated that the system experienced the highest rise and lowest drop in frequency without a BESS. However, it was observed that the comparative performance of various BESS control approaches was a mix of experience in terms of frequency rise and drop throughout the transient periods. The droop and combined control of BESS demonstrated a similar level of superior performance compared to the inertia-controlled BESS in terms of frequency rise and without a BESS condition. It is worth noting that for the studied contingency event, the frequency did not violate the mandatory grid limit of ± 0.5 Hz for both the frequency and df/dt , as illustrated in Table 3.

On the contrary, the inertia and combined control manifested slightly better response in regards to the voltage drop between $t = 0.6$ –0.75 s. In contrast, the droop and combined control exhibited a superior frequency drop response during $t = 1.3$ –1.45 s, as shown in Figure 14. Furthermore, the proposed method established the superior performance for df/dt having the lowest value.

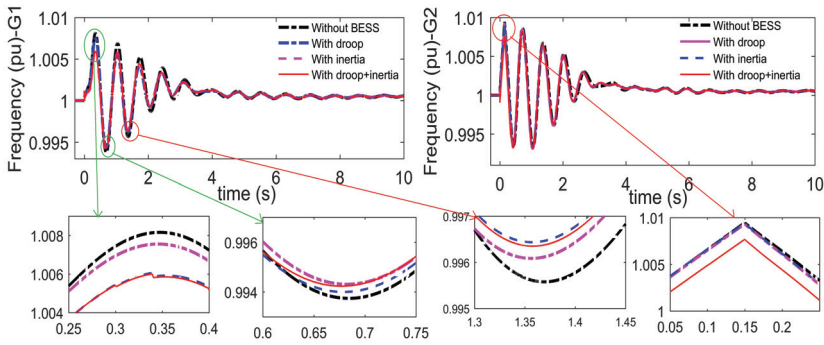


Figure 14. The frequency (pu) oscillation of generators with a single-phase-to-ground fault.

Table 3. The frequency results of G1 with a single-phase-to-ground fault.

Operation Mode	No BESS	IE	PFC	IE + PFC
P_{BESS} (MW)	N/A	26.595	12.98	22.163
Q_{BESS} (MVar)	N/A	26.147	26.781	23.167
E_{BESS} (MWh)	N/A	-1.924	-0.539	-1.922
df/dt (Hz/s)	0.335	0.275	0.307	0.269
f_{min} (Hz)	49.678	49.715	49.7	49.71
SOC (pu)	N/A	0.8001	0.7602	0.7501

The voltage responses as shown in Figure 15 exhibited that BESS provided enhanced performance as compared to without a BESS in all control modes, and the voltage response was almost identical for all control designs throughout the transient periods. Nonetheless, droop-controlled BESS handled the frequency rise more effectively than the combined-controlled BESS. The amount of reactive power participation was substantial as the voltage oscillations were very high for this particular contingency event, as shown in Figure 16. BESS active power as shown in Figure 16 delineated that the inertia and combined control regulated the output more effectively than the droop control, which was reflected in the frequency of generators and df/dt , as shown in Figure 14 and Table 3, respectively.

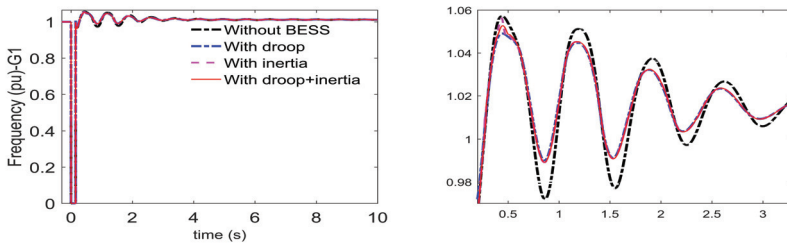


Figure 15. The voltage (pu) oscillation of generators with a single-phase-to-ground fault.

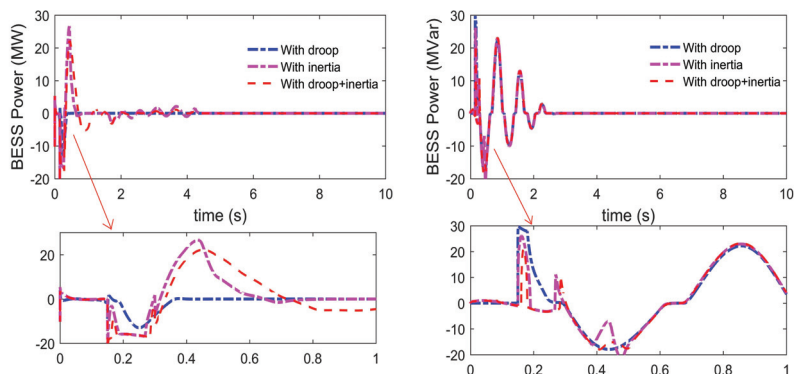


Figure 16. The active and reactive power of BESS with a single-phase-to-ground fault.

6. Conclusions

In this paper, BESS was designed to provide voltage and frequency support and improve the stability of the grid. An enhanced consolidated IE- and PFC-regulated frequency controller and droop-regulated voltage controller were presented for supporting both the frequency and voltage stability with a high penetration of renewable sources. In addition, a novel frequency-dependent battery SOC recovery strategy was also suggested that allowed the battery to be recharged without imposing a negative impact on grid frequency. The battery was recharged when BESS was in idle mode and SOC was above the specified threshold or below the minimum SOC.

The simulation results of the comparative performances demonstrated that in comparison to individual IE or PFC service, the proposed amalgamated frequency controller performed the best in regulating the frequency response. The lower ROCOF and higher minimum frequency values were achieved with the proposed controller. As expected, IE with PFC service entailed a higher energy rating of BESS as this required BESS operation for longer periods. Furthermore, BESS exhibited a lower voltage drop than without a BESS during the contingency periods. Moreover, without FDSR, SOC recovery could have a severe impact on grid frequency and voltage as the battery consumed energy from the grid, which could be severe with high battery capacity and poor grid frequency. Nevertheless, the proposed FDSR demonstrated effective SOC recovery without negatively affecting either the grid frequency or voltage as FDSR delayed the battery recharging until the grid frequency was restored to the nominal operation limit.

Author Contributions: Conceptualization, methodology, software validation, formal analysis, and original draft preparation were done by U.D.; editing and supervision were carried out by A.K. and J.S. All authors read and agreed to the published version of the manuscript.

Funding: This work was supported by the Victoria University International Postgraduate Research Scholarship (IPRS) scheme.

Conflicts of Interest: The authors declare no conflict of interest.

Appendix A

Battery parameters: Initial SOC = 0.8 pu, battery cell capacity = 200 Ah, parallel cells = 65, nominal source voltage = 0.9 kV, internal resistance (Ω) = 0.001 pu. PI parameter: $k_d = 1.5$, $T_{id} = 0.01$, $k_q = 2$, $T_{iq} = 0.01$, $i_{ch} = 0.035$. Current controller PI parameter: $k_d = k_q = 1$, $T_{id} = T_{iq} = 0.001$.

Network parameters: PV Farm A = 69 MW, PV Farm B = 45 MW, Wind Farm A = Wind Farm B = 50 MW.

References

1. *Scenario Outlook & Adequacy Forecast 2014–2030*; European Network of Transmission System 428 Operators for Electricity: Brussels, Belgium, 2014.
2. D’Arco, S.; Suul, J.A.; Fosso, O.B. A Virtual Synchronous Machine implementation for distributed control of power converters in SmartGrids. *Elect. Power Syst. Res.* **2015**, *122*, 180–197. [[CrossRef](#)]
3. Gu, W.; Liu, W.; Shen, C.; Wu, Z. Multi-stage underfrequency load shedding for islanded microgrid with equivalent inertia constant analysis. *Int. J. Elect. Power Energy Syst.* **2013**, *46*, 36–39. [[CrossRef](#)]
4. Zhu, J.; Booth, C.D.; Adam, G.P.; Roscoe, A.J.; Bright, C.G. Inertia Emulation Control Strategy for VSC-HVDC Transmission Systems. *IEEE Trans. Power Syst.* **2013**, *28*, 1277–1287. [[CrossRef](#)]
5. Engleitner, R.; Nied, A.; Cavalca, M.S.M.; da Costa, J.P. Dynamic Analysis of Small Wind Turbines Frequency Support Capability in a Low-Power Wind-Diesel Microgrid. *IEEE Trans. Ind. Appl.* **2018**, *54*, 102–111. [[CrossRef](#)]
6. Nanou, S.I.; Papakonstantinou, A.G.; Papathanassiou, S.A. A generic model of two-stage grid-connected PV systems with primary frequency response and inertia emulation. *Elect. Power Syst. Res.* **2015**, *127*, 186–196. [[CrossRef](#)]
7. Liu, H.; Qi, J.; Wang, J.; Li, P.; Li, C.; Wei, H. EV Dispatch Control for Supplementary Frequency Regulation Considering the Expectation of EV Owners. *IEEE Trans. Smart Grid* **2018**, *9*, 3763–3772. [[CrossRef](#)]
8. Aliabadi, S.F.; Taher, S.A.; Shahidehpour, M. Smart Deregulated Grid Frequency Control in Presence of Renewable Energy Resources by EVs Charging Control. *IEEE Trans. Smart Grid* **2018**, *9*, 1073–1085. [[CrossRef](#)]
9. Gonzalez-Longatt, F.M.; Alhejaj, S.M. Enabling inertial response in utility-scale battery energy storage system. In Proceedings of the 2016 IEEE Innovative Smart Grid Technologies - Asia (ISGT-Asia), Melbourne, Australia, 28 November–1 December 2016; pp. 605–610.
10. Datta, U.; Kalam, A.; Shi, J. Battery energy storage system for transient frequency stability enhancement of a large-scale power system. In Proceedings of the Australasian Universities Power Engineering Conference, Melbourne, Australia, 19–22 November 2017; pp. 1–5.
11. Shotorbani, A.M.; Mohammadi-Ivatloo, B.; Wang, L.; Ghassem-Zadeh, S.; Hosseini, S.H. Distributed secondary control of battery energy storage systems in a stand-alone microgrid. *IET Gen. Trans. Dist.* **2018**, *12*, 3944–3953. [[CrossRef](#)]
12. Vazquez, N.; Yu, S.S.; Chau, T.K.; Fernando, T.; Iu, H.H. A Fully Decentralized Adaptive Droop Optimization Strategy for Power Loss Minimization in Microgrids With PV-BESS. *IEEE Trans. Energy Conv.* **2019**, *34*, 385–395. [[CrossRef](#)]
13. Li, J.; Xiong, R.; Yang, Q.; Liang, F.; Zhang, M.; Yuan, W. Design/test of a hybrid energy storage system for primary frequency control using a dynamic droop method in an isolated microgrid power system. *Appl. Energy* **2017**, *201*, 257–269. [[CrossRef](#)]
14. Kerdphol, T.; Rahman, F.S.; Mitani, Y.; Watanabe, M.; Küfeoğlu, S. Robust Virtual Inertia Control of an Islanded Microgrid Considering High Penetration of Renewable Energy. *IEEE Access* **2018**, *6*, 625–636. [[CrossRef](#)]
15. Fini, M.H.; Golshan, M.E.H. Determining optimal virtual inertia and frequency control parameters to preserve the frequency stability in islanded microgrids with high penetration of renewables. *Elect. Power Syst. Res.* **2018**, *154*, 13–22. [[CrossRef](#)]
16. Yue, M.; Wang, X. Grid Inertial Response-Based Probabilistic Determination of Energy Storage System Capacity Under High Solar Penetration. *IEEE Trans. Sust. Energy* **2015**, *6*, 1039–1049. [[CrossRef](#)]
17. Aghamohammadi, M.R.; Abdolahinia, H. A new approach for optimal sizing of battery energy storage system for primary frequency control of islanded Microgrid. *Int. J. Elect. Power Energy Syst.* **2014**, *54*, 325–333. [[CrossRef](#)]
18. Toma, L.; Sanduleac, M.; Baltac, S.A.; Arrigo, F.; Mazza, A.; Bompard, E.; Musa, A.; Monti, A. On the virtual inertia provision by BESS in low inertia power systems. In Proceedings of the 2018 IEEE International Energy Conference (ENERGYCON), Limassol, Cyprus, 3–7 June 2018; pp. 1–6.
19. Goya, T.; Omine, E.; Kinjyo, Y.; Senjyu, T.; Yona, A.; Urasaki, N.; Funabashi, T. Frequency control in isolated island by using parallel operated battery systems applying H-infinity control theory based on droop characteristics. *IET Renew. Power Gen.* **2011**, *5*, 160–166. [[CrossRef](#)]
20. Li, H.; Wang, J.; Du, Z.; Zhao, F.; Liang, H.; Zhou, B. Frequency control framework of power system with high wind penetration considering demand response and energy storage. *J. Eng.* **2017**, *2017*, 1153–1158. [[CrossRef](#)]
21. Wen, Y.; Li, W.; Huang, G.; Liu, X. Frequency Dynamics Constrained Unit Commitment with Battery Energy Storage. *IEEE Trans. Power Syst.* **2016**, *31*, 5115–5125. [[CrossRef](#)]

22. Knap, V.; Chaudhary, S.K.; Stroe, D.; Swierczynski, M.; Craciun, B.; Teodorescu, R. Sizing of an Energy Storage System for Grid Inertial Response and Primary Frequency Reserve. *IEEE Trans. Power Syst.* **2016**, *31*, 3447–3456. [[CrossRef](#)]
23. Brogan, P.V.; Best, R.J.; Morrow, D.J.; McKinley, K.; Kubik, M.L. Effect of BESS Response on Frequency and RoCoF During Underfrequency Transients. *IEEE Trans. Power Syst.* **2019**, *34*, 575–583. [[CrossRef](#)]
24. Zeraati, M.; Hamedani Golshan, M.E.; Guerrero, J.M. Distributed Control of Battery Energy Storage Systems for Voltage Regulation in Distribution Networks With High PV Penetration. *IEEE Trans. Smart Grid* **2018**, *9*, 3582–3593. [[CrossRef](#)]
25. Serban, I.; Marinescu, C. Control Strategy of Three-Phase Battery Energy Storage Systems for Frequency Support in Microgrids and with Uninterrupted Supply of Local Loads. *IEEE Trans. Power Electron.* **2014**, *29*, 5010–5020. [[CrossRef](#)]
26. Alhejaj, S.M.; Gonzalez-Longatt, F.M. Investigation on grid-scale BESS providing inertial response support. In Proceedings of the 2016 IEEE International Conference on Power System Technology (POWERCON), Wollongong, Australia, 28 September–1 October 2016; pp. 1–6.
27. Xu, Q.; Xiao, J.; Wang, P.; Pan, X.; Wen, C. A Decentralized Control Strategy for Autonomous Transient Power Sharing and State-of-Charge Recovery in Hybrid Energy Storage Systems. *IEEE Trans. Sustain. Energy* **2017**, *8*, 1443–1452. [[CrossRef](#)]
28. Xiao, J.; Wang, P.; Setyawan, L. Hierarchical Control of Hybrid Energy Storage System in DC Microgrids. *IEEE Trans. Ind. Electron.* **2015**, *62*, 4915–4924. [[CrossRef](#)]
29. Zhu, D.; Zhang, Y.A. Optimal Coordinated Control of Multiple Battery Energy Storage Systems for Primary Frequency Regulation. *IEEE Trans. Power Syst.* **2019**, *34*, 555–565. [[CrossRef](#)]
30. Datta, U.; Kalam, A.; Shi, J. Battery Energy Storage System Control for Mitigating PV Penetration Impact on Primary Frequency Control and State-of-Charge Recovery. *IEEE Trans. Sustain. Energy* **2019**, *11*, 746–757. [[CrossRef](#)]
31. ENTSO. P1—Policy 1: Load-Frequency Control and Performance. Available online: http://kom.aau.dk/project/smartcool/restricted_files/2012.11.06-AAU/ENTSOE_UCTE_frequency_reserves.pdf (accessed on 1 October 2018).
32. Kundur, P.; Balu, N.J. *Power System Stability And Control*; McGraw-Hill: New York, NY, USA, 1994.
33. Australian Energy Market Operator. Integrating Renewable Energy—Wind Integration Studies Report. Available online: <http://www.aemo.com.au/-/media/Files/PDF/Integrating-Renewable-Energy--Wind-Integration-Studies-Report-2013pdf.pdf> (accessed on 2 October 2018).
34. Operator, A.E.M. International Review of Frequency Control. Available online: https://www.aemo.com.au/-/media/Files/Electricity/NEM/Security_and_Reliability/Reports/2016/FPSS---International-Review-of-Frequency-Control.pdf (accessed on 31 March 2020).
35. AEMC. The Frequency Operating Standard Stage One Final-for-Publi. Available online: <https://www.aemc.gov.au/sites/default/files/content/ce48ba94-b3a9-4991-9ef9-e05814a78526/REL0065-Review-of-the-Frequency-Operating-Standard-Final-for-publi.pdf> (accessed on 15 September 2018).
36. Duckwitz, D.; Fischer, B. Modeling and Design of df/dt -Based Inertia Control for Power Converters. *IEEE J. Emerg. Sel. Top. Power Electron.* **2017**, *5*, 1553–1564. [[CrossRef](#)]
37. Datta, U.; Kalam, A.; Shi, J. Battery Energy Storage System to Stabilize Transient Voltage and Frequency and Enhance Power Export Capability. *IEEE Trans. Power Syst.* **2019**, *34*, 1845–1857. [[CrossRef](#)]
38. Shen, P.; Ouyang, M.; Lu, L.; Li, J.; Feng, X. The Co-estimation of State of Charge, State of Health, and State of Function for Lithium-Ion Batteries in Electric Vehicles. *IEEE Trans. Veh. Tech.* **2018**, *67*, 92–103. [[CrossRef](#)]
39. Mukherjee, N.; De, D. A New State-of-Charge Control Derivation Method for Hybrid Battery Type Integration. *IEEE Trans. Energy Conv.* **2017**, *32*, 866–875. [[CrossRef](#)]
40. Zhang, R.; Hredzak, B.; Morstyn, T. Distributed Control with Virtual Capacitance for the Voltage Restorations, State of Charge Balancing and Load Allocations of Heterogeneous Energy Storages in a DC Datacenter Microgrid. *IEEE Trans. Energy Conv.* **2018**, *34*, 1296–1308. [[CrossRef](#)]
41. Hu, X.; Yuan, H.; Zou, C.; Li, Z.; Zhang, L. Co-Estimation of State of Charge and State of Health for Lithium-Ion Batteries Based on Fractional-Order Calculus. *IEEE Trans. Veh. Tech.* **2018**, *67*, 10319–10329. [[CrossRef](#)]



Review

Applications of Game Theory to Design and Operation of Modern Power Systems: A Comprehensive Review

Aviad Navon ¹, Gefen Ben Yosef ¹, Ram Machlev ¹, Shmuel Shapira ¹,
Nilanjan Roy Chowdhury ¹, Juri Belikov ², Ariel Orda ¹ and Yoash Levron ^{1,*}

¹ The Andrew and Erna Viterbi Faculty of Electrical Engineering, Technion—Israel Institute of Technology, Haifa 3200003, Israel; aviad.nav@gmail.com (A.N.); jeffbenyo@gmail.com (G.B.Y.); ramm@campus.technion.ac.il (R.M.); shmuel@campus.technion.ac.il (S.S.); nilanjan2008@gmail.com (N.R.C.); ariel@ee.technion.ac.il (A.O.)

² Department of Software Science, Tallinn University of Technology, Akadeemia tee 15a, 12618 Tallinn, Estonia; juri.belikov@taltech.ee

* Correspondence: yoashl@ee.technion.ac.il

Received: 3 July 2020; Accepted: 27 July 2020; Published: 2 August 2020

Abstract: In this work, we review papers that employ game theoretic tools to study the operation and design of modern electric grids. We consider four topics in this context: energy trading, energy balancing, grid planning, and system reliability, and we demonstrate the advantages of using game-theoretic approaches for analyzing complex interactions among independent players. The results and conclusions provide insights regarding many aspects of design and operation, such as efficient methodologies for expansion planning, cyber-security, and frequency stability, or fair-benefit allocation among players. A central conclusion is that modeling the system from the perspective of one entity with unlimited information and control span is often impractical, so correct modeling of the selfish behavior of independent players may be critical for the development of future power systems. Another conclusion is that correct usage of incentives by appropriate regulation or sophisticated pricing mechanisms may improve the social welfare, and, in several cases, the results obtained are as good as those obtained by central planning. Using an extensive content analysis, we point to several trends in the current research and attempt to identify the research directions that are currently at the focus of the community.

Keywords: game theory; power systems; control; management; electrical grids; review; survey; energy balancing; energy trading; grid planning; expansion planning; electric vehicles; renewable energy; reliability

1. Introduction

Recently, there has been a wide interest in game-theoretic approaches for studying modern electric grids, which are going through a transformative change due to the penetration of new disruptive technologies. This transformation, which is sometimes referred to as ‘The Energy Transition’, mainly refers to two major changes: the increasing integration of renewable energy sources and the increasing use of electric vehicles [1,2]. Legacy electric grids were not planned with these technological innovations in mind, so they have to significantly change in order to support them [3–5]. Furthermore, these technologies can be purchased and managed by any citizen; hence, the way they will develop depends on the opinions of many people. For example, they may be integrated in a centralized manner by big companies or crowd funding, or in a distributed small scale manner in residential areas. As a result, the private sector is becoming a key player in the energy market, and its influence on the

development of electrical grids is gradually growing. Consequently, electric utilities and governments that have worked in a centralized manner for over a century have to fundamentally change the ways they plan and operate the electric grid, and they need to find new ways to predict and control the behavior of multiple entities operating within a single system.

The research community currently understand quite well the behavior of each player in the power system, be it a grid operator, a consumer, an energy source, or a storage system. Yet, recent studies show that the interactions among these players are at least as important as the individual behavior of each of them [6–8]. The current approach of most studies is to forecast the development of power systems by solving optimization problems from the perspective of one entity with unlimited knowledge and control span [9–13]. While this approach might have been relevant for many years, it is gradually becoming unrealistic due to the decentralization and deregulation of the energy market. A major challenge is therefore to predict the development of a power system, taking into account the different objectives of the many players. This can be done based on game theory, which studies strategic interaction among rational players.

The seminal results of game theory were established in the 1950s, whereas the first application of game theory for studying power systems can be found in the 1970s [14–16]. Game theory can be divided into two branches: non-cooperative game theory and cooperative game theory [17]. Additional classification can be made in accordance with certain properties, such as the number of stages (static or dynamic games), the structure of information (perfect or imperfect, complete or incomplete), type of strategies (pure or mixed), and so forth [18]. Figure 1 shows the number of publications in applications of game theory in the fields of energy markets and power systems. The search was done in Scopus, which is Elsevier’s abstracts and citations database, and was divided to three different topics: the energy market, power systems management and control, and power systems planning.

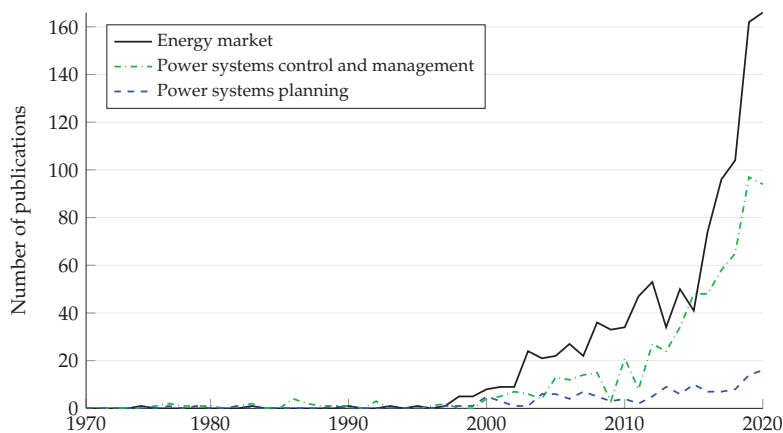


Figure 1. Scopus search results for publications related to game theory and power systems.

As can be seen in Figure 1, the study of energy markets and power systems from a game theoretic perspective started gaining popularity in the early 2000s. This can be attributed to two major developments in the 1990s: the first was the establishment of deregulated networks and free markets in the energy sector, and the second was the introduction of new technologies, such as distributed energy sources, energy storage devices, and controllable loads. Due to these developments, multiple players with different interdependent objectives currently participate in the energy market and influence the development of electrical grids. Consequently, game theory is a natural choice to study decision making in modern power systems.

Few papers review how game theory may be used in the context of power systems. A comprehensive review of game theoretic approaches for solving power system problems is

provided in Reference [19]. The reviewed studies are divided according to the type of game they use: non-cooperative (both static and dynamic), cooperative or evolutionary. Moreover, a summary of different objective functions, methods and case studies is presented. Based on this summary, the authors suggest several topics for future research, such as interaction among electric vehicles and storage devices for energy balancing, fairness aspects in fully-competitive distributed energy trading scenarios, and the impact of renewable energy sources on demand side management, when dynamic pricing techniques are utilized. Over the years many of the suggestions for future research were indeed realized, as we demonstrate in this study. In addition, Reference [20,21] survey studies that employ game theory to investigate smart-grid related problems. Reference [20] surveys a variety of smart-grid related topics, such as demand side management, plug-in hybrid electric vehicles, and smart-grid security, whereas Reference [21] focuses on studies that use non-cooperative game theory to study energy trading. Reference [21] also provides an overview of smart-grid architectures. The similarities and differences among the studies are presented, focusing on the type and number of players, the players' incentives, and the method used, e.g., analytic versus numeric. Moreover, studies that use game theoretic approaches to research micro-grids are surveyed in Reference [22,23]. Reference [22] focuses on cooperation among micro-grids, and presents the advantages of using game theory to study this field. Reference [23] provides an overview of game-theoretic methods for three problems in the context of micro-grids: micro-grid systems (focusing on energy exchange and control), demand side management, and smart-grid communications. Reference [24] surveys works that use game theory for studying demand-response mechanisms. Here the studies are divided according to the type of game: (1) non-cooperative, (2) cooperative, (3) evolutionary, (4) Stackelberg, and (5) Bayesian. One of the main conclusions is that, due to the increasing complexity of electricity markets, future research would focus on game theoretic approaches that harness intelligent algorithms, such as machine learning techniques, for more efficient solutions of realistic games. Moreover, the authors suggest that Bayesian games, which may be used when information is limited, and evolutionary games, which attempt to describe the behavior of non-rational players, will increasingly be used to model transactions among private companies and citizens, since, in these situations, there are many unknown factors, and spontaneous decisions may be common.

Contrary to these comprehensive review papers, which focus on applications of game theory in energy markets [24], smart-grids [20,21], micro-grids [22,23], and power systems from a broad perspective [19], this study focuses on recent applications of game theory that are specifically related to operation and design of modern electric grids. We review four topics in this context: energy trading, energy balancing, grid planning, and system reliability, and demonstrate the advantages of using game-theoretic approaches for analyzing complex interactions among independent players. The results and conclusions of the reviewed papers provide insights regarding many aspects of design and operation, such as fair-benefit allocation among players, or efficient methodologies for expansion planning, cyber-security, and frequency stability. A central conclusion is that modeling the system from the perspective of one entity with unlimited information and control is often impractical, so correct modeling of the selfish behavior of independent players allows to develop efficient control algorithms, which may be critical for the development of future power systems. Another conclusion is that correct usage of incentives by appropriate regulation or sophisticated pricing mechanisms may improve the social welfare, and in several cases the results obtained are almost as good as can be obtained by central planning.

The paper is organized as follows. Sections 2–5 review papers that focus on the following applications: energy trading, energy balancing, grid planning, and grid reliability. In Section 6, we discuss the advantages and disadvantages of employing different types of games for studying various power system applications, whereas, in Section 7, we discuss current trends and provide suggestions for future work. Finally, in Section 8, we conclude the paper.

2. Energy Trading

The deployment of decentralized generation and storage devices in the past two decades allows many players in the modern power grids to participate in energy trading. These players include consumers, generators and utilities, which all have the same main objective—to maximize their own profit. Since in many situations the players' actions influence one another, more often than not conflicts arise. For this reason, game theoretic approaches are common for formulating energy trading problems.

As shown next, energy trading problems are investigated using different types of games, such as evolutionary, cooperative, and non-cooperative games, the latter being the most popular approach. In most works, the players are defined as sellers or buyers of electric energy, and the challenge is to find an equilibrium in a power market, considering various objectives and constraints. One main conclusion is that, even in competitive markets, the government should apply some profit distribution mechanism to ensure fairness. Moreover, it is concluded that reasonable bidding rules should be considered for limiting high pricing and for preventing market manipulation by generation companies. As many of the reviewed papers show, game theoretic approaches are suitable for analyzing complex trading interactions among different independent market players. However, the use of game theory for studying energy trading has its own challenges and limitations. For example, most of the studies assume that each player has complete information of the opponents' available strategies, yet, in reality, energy companies often sign business confidentiality agreements. Another main challenge is that game-theoretic models tend to be hard to analyze and have a high computational complexity. As a result, most studies consider up to four types of players, whereas real-life energy markets are obviously more complex. The section is organized according to specific applications, and all of the reviewed works are summarized in Table 1.

2.1. General Energy Market Applications

Various works from the recent literature that employ game theory to study trading in modern energy markets are overviewed in this subsection. The works are divided according to the type of game that is modeled, as follows: non-cooperative, cooperative, and evolutionary.

Most works use a non-cooperative game to model the interactions among trading entities. For example, in Reference [25], a non-cooperative game is developed for plug-in hybrid electric vehicles that seek to sell their stored energy in an energy market. Each group can sell a desired amount of energy surplus in order to maximize a utility function that reflects a trade-off between the economic benefits from the trade and the physical costs (e.g., reduction in the batteries' life-time). A Nash Equilibrium is reached using an iterative algorithm, and simulation results show an improvement in the average utility of the players when compared to a greedy algorithm. From the same authors, Reference [26] formulates a non-cooperative game among energy storage units that trade their stored energy in a double-auction market with multiple buyers and sellers. Each storage unit operator decides how much energy to sell in order to maximize a utility function that reflects the trade-off between the trading profits and the associated costs. A novel algorithm that guarantees convergence to equilibrium is proposed, and again the results demonstrate that the performance of each storage unit is improved when compared to a greedy approach. In the same line of thinking, Reference [27] proposes a retail electricity market model that consists of a utility company and prosumers, which locally operate and manage their own distributed resources. Here, the day-ahead electricity market price is determined based on game-theoretic algorithms, and a numerical simulation demonstrates the effectiveness of the proposed electricity market clearing schemes. In Reference [28], a Stackelberg game is suggested to model the interactions between a power station, which is considered the "leader", and several prosumers, who are the "followers". The rules of the game are that the station decides how much total energy to buy from the prosumers, and then each prosumer decides how much energy to sell to the station. It is shown that the game reaches a Stackelberg equilibrium, which consists of the socially optimal energy for the consumers and minimal total cost to the station. In addition, the performance of the game has been established via simulation that shows a reduction in the average total cost over a

conventional feed-in-tariff scheme. Similarly, Reference [29] formulates a Stackelberg game between a power company, the leader, who defines a pricing strategy to maximize its profits, and prosumers, the followers, who choose the amount of energy to buy or sell in order to optimize their future earnings. The behavior of the prosumers is modeled according to prospect theory. The game is shown to have a unique Nash equilibrium in pure strategies, which emerges from classical game-theoretic analysis.

Studies [30,31] have used the Nash bargaining concept to study energy trading related problems. Reference [30] analyzes Nash bargaining settlement outcomes for a financial bilateral contract negotiation between a generation firm and a load-serving entity, considering risk management, strategic gaming, and multi-market interactions. It has been shown through both theoretical analysis and simulation that the negotiation outcomes vary in response to changes in risk preferences and price biases. Reference [31] proposes a cooperative-game-based bargaining scheme for an energy trading problem between demand response aggregators and a distribution company that collaboratively decide on the costs and amounts of traded energy. Based on the Nash bargaining solution, a fair and Pareto optimal outcome is achieved, which means that the players have an incentive to cooperate. Simulation results show that the suggested framework may improve the profits of the players and maximize the social welfare when compared to the non-cooperative game-based approach.

In addition, several works formulate their games using evolutionary algorithms. For example, Reference [32] proposes a non-cooperative game to analyze strategic interactions among energy suppliers in deregulated electricity markets based on competitive co-evolutionary algorithms. The suppliers are represented by their behavior strategies, and an evolutionary algorithm is used as a learning method that enables players find the best strategy according to past behavior of their opponents. The co-evolutionary algorithm is used to find a Nash equilibrium, and several case studies demonstrate the effectiveness of these algorithms to find optimal strategies in different market situations.

2.2. Micro-Grid Applications

Papers that focus on micro-grids in energy trading related problems mainly use non-cooperative games, and can be divided into two categories: (1) trading among consumers inside a single micro-grid, and (2) trading among interconnected micro-grids. Several of the latest works of the first category are [33–36]. In Reference [33], a multi-agent based reverse auction model for micro-grid market operations is proposed. The goal is to obtain the cheapest power supply for the micro-grid's loads. The proposed model promotes competition between distributed energy resources and determines their unit commitment within an hour-ahead market framework. This approach has been tested in a micro-grid that fully complies with industrial protocols. Based on these results, the authors recommend applying such multi-agent based models in future micro-grids. Reference [34] proposes a pool strategy for a micro-grid trading with a distribution electricity market. This is done by formulating a Stackelberg game in which the micro-grid is the leader, proposing a price offering, and the competitors and consumers are the followers, choosing how to trade. It is shown that the proposed strategy creates a fair environment for all players, and that utilizing micro-grids as price makers promotes competition. Reference [36] develops a game theoretic model for real time energy trading using interactions among prosumers in a micro-grid. The interaction among the prosumers who sell energy (leaders) and prosumers who buy energy (followers) is modeled as a Stackelberg game. Furthermore, the authors formulate a non-cooperative game to model the pricing competition among sellers, and an evolutionary game to model the competition among buyers when selecting sellers. Simulation results show that the suggested model can effectively handle energy trading in a micro-grid, and that the power imported from the main grid to the micro-grid is reduced compared to conventional trading, since all the available energy within the micro-grid is efficiently allocated. The authors in Reference [35] suggest a model of economic incentives for market participants who cooperate in developing a micro-grid. The authors model a cooperative game with three types of players—a micro-grid developer, a utility company, and consumers. An analysis on how the development of a micro-grid affects prices and

costs for all players under different assumptions is presented. Based on different scenarios, the study offers energy policy recommendations on how to efficiently promote micro-grids and specifies market failures that should be addressed in order to maximize the benefits of micro-grid development.

Works [37–39] have used game theory to study trading among interconnected micro-grids. Reference [37] suggests an energy trading mechanism among micro-grids in a competitive market where each micro-grid can be an energy provider or a consumer, according to their energy generation and local demand. The problem is formulated as a non-cooperative game among the micro-grids and the Nash equilibrium solution is given in closed-form. Based on numerical results, it is concluded that the suggested mechanism is fast enough for real-time applications. Reference [38] analyzes energy trading among micro-grids where several micro-grids have surplus energy that can be sold or stored, while other micro-grids want to buy surplus energy. A Stackelberg game is formulated where the sellers lead the competition by deciding the amount of energy for sale and the buyers follow the sellers' actions by submitting a price bid. It is shown that the game has a unique equilibrium and that the proposed game-based trading mechanism maximizes profits for all players. Reference [39] proposes a mechanism that is based on the Nash bargaining theory to encourage proactive energy trading and fair benefit sharing among interconnected micro-grids. A Nash bargaining problem is solved as two consecutive problems: social cost minimization and trading benefit sharing. Based on several case studies, it is shown that, through the suggested mechanism, each individual micro-grid can achieve an increase in profit and the total operation cost of the interconnected micro-grids can be reduced by up to 13% compared to its performance without cooperation.

2.3. Electricity Pricing Models

In recent years, a variety of electricity pricing models that are based on electricity demand profiles have been implemented by utility companies worldwide. The pricing models mainly differ in their resolution and in the frequency in which prices change. Several known models are: Time-of-use pricing, Critical peak pricing, and Real-time pricing. Many use game theory to offer novel pricing models, where non-cooperative game theory is the leading approach. For example, Reference [40] suggests a game theoretic approach to optimize time-of-use electricity pricing strategy for utility companies and their users. The authors formulate a multi-stage non-cooperative game between utility companies, who set the pricing mechanism, and consumers, who set their demand accordingly. Through simulations, the proposed pricing mechanism is shown to increase the utilities' profits and level the users' demand in comparison to a scenario with flat prices. In Reference [41], a game theory based dynamic pricing model is evaluated for Singapore's electricity market in order to achieve an efficient demand response. The game is designed to maximize benefits for both utility companies and consumers, with a focus on the residential and commercial sectors. Simulations that are based on real data show that, when a half-hourly real-time pricing strategy is used, there is maximum peak load reduction and increase in profits. Similarly, Reference [42] proposes a pricing mechanism for an electricity supply chain that consists of a single generation company, multiple consumers and competing utility companies. The interactions among the utility companies, who set retail prices, is characterized through a non-cooperative game, and an iterative algorithm is developed to obtain a Nash equilibrium. Moreover, the authors show that a revenue sharing contract among the utility companies and the generation company can be set to obtain maximal profits and social welfare. Another example is Reference [43], which formulates a real-time pricing scheme for demand response management. This is done by modeling the interactions between an energy provider (leader) and multiple energy hub operators (followers) as a Stackelberg game. The equilibrium of the game is found using a novel distributed algorithm, and the optimal strategies for each player are determined in order to balance the energy. Numerical results show that the method can improve the payoffs for all players with good convergence performance. Finally, Reference [44] analyzes an electricity market with a time-of-use electricity pricing using an evolutionary game. The game is between power generation companies, power grid companies, power supply entities, and power consumers. Based on the results,

the authors describe policy implications that can assist governments in defining policies for electricity markets. A principal suggestion is that the government should promote fairness by establishing a profit distribution mechanism among all players in the market. Furthermore, the government should make reasonable bidding rules in order to limit high pricing and prevent market manipulation by the generation corporations.

2.4. Bidding Strategies

Many employ game theory to study and design bidding strategies in energy markets. An intelligent bidding strategy is crucial for generation companies that participate in a competitive energy market and aim to maximize their profits. Since a good bidding strategy has to take into account the rational and objectives of other players, game theory is a natural choice. As an example, Reference [45] presents Nash equilibrium bidding strategies in a bilateral market in which generators submit bids to consumers. Network optimization techniques are used to calculate Nash equilibrium points, and it is shown that for all solutions an efficient allocation is achieved with equal revenue for all generators. In Reference [46], conjectural variation-based bidding strategy methods are used to help generation firms maximize their profits in electricity spot markets with imperfect information. Formal analysis shows that the system equilibrium that is reached via conjectural variation-based bidding is a Nash equilibrium. Reference [47] proposes a bidding strategy for wind power producers to maximize profits. In this model, wind power producers buy energy from conventional power producers in a bilateral reserve market to minimize the risk caused by uncertainties in generation. The interaction among them is modeled through a non-cooperative game where the price is settled by finding a Nash Equilibrium. Case studies with real-world market data and different types and numbers of players are performed to show the effectiveness of the model. Reference [48] suggests a framework for implementing a retail energy market with a high distributed energy resources penetration and demand side management of prosumers. The distributed energy resources take into account uncertainties in production and try to maximize their profit by undertaking strategies through the price bidding strategy that is obtained in the Nash equilibrium. Different scenarios show that it is more profitable for the players to collaborate with one another. Reference [49] proposes an evolutionary imperfect information game for analyzing bidding strategies in electricity markets with price-elastic demand. The main observation is that the strategies of the generation companies in this imperfect information game eventually converge to the Nash equilibrium in the perfect information game.

2.5. Profit Allocations

Both the Shapley value and the Nucleolus are solution methods in cooperative game theory that describe profit allocation among cooperating entities, and many authors use these concepts to study energy trading related problems. For example, Reference [50,51] use these concepts to suggest profit allocation strategies. Reference [50] studies cooperation among independent power producers in a retail market. Based on the Shapley value and the Nucleolus solution concepts the authors propose a profit allocation among producers. Comparison between a non-cooperative game and a cooperative one shows that cooperation among power producers, with the suggested profit allocation, leads them to higher profits. Reference [51] suggests a novel stochastic programming approach to model the participation of a virtual power plant in a day-ahead market and a balancing real-time market. The virtual power plant aggregates distributed energy sources and manages them to reduce the risk caused by intermittent generation. The contribution of each resource to the virtual power plant is assessed and the Shapley value and Nucleolus solutions are used to determine the profit allocation among them. Moreover, it is shown that, when the risk-aversion level of the resources is high, their profits increase when they are coordinated by an external entity, e.g., a virtual power plant.

Table 1. Summary of works focusing on energy trading application using game-theory.

	Ref.	Game Method	Players	Application
General trading applications	[25]	Non-cooperative	Hybrid electric vehicles	Energy Trading
	[25]	Non-cooperative	Hybrid electric vehicles	Energy Trading
	[26]	Non-cooperative	Batteries	Trading in a double-auction market
	[27]	Non-cooperative	Utility company, prosumers	Retail electricity market with prosumers
	[28]	Stackelberg	Power station, consumers	Energy Trading
	[29]	Stackelberg	Generation company, prosumers	Pricing strategy for energy trading
	[30]	Cooperative	Generation companies, load-serving entity	Financial bilateral contract negotiation
	[31]	Cooperative	Demand response aggregators, distribution company	Bargaining-based cooperative energy trading
Micro-grid applications	[32]	Evolutionary	Power suppliers, consumers	Suppliers' optimal strategies in a deregulated electricity market
	[33]	Non-cooperative	A Micro-grid's distributed energy sources	Reverse auction model for micro-grid market operations
	[37]	Non-cooperative	Micro-grids	Trading mechanism in a competitive market
	[34]	Stackelberg	Micro-grid, consumers	Pool strategy for a micro-grid trading with a distribution electricity market
	[38]	Stackelberg	Micro-grids	Distributed mechanism for energy trading among microgrids
	[36]	Stackelberg + non-cooperative + evolutionary	Prosumers	Energy trading in a micro-grid considering demand response
	[35]	Cooperative	Utility, Micro-grid developer, customers	Model of economic incentives for market participants who cooperate to develop a micro-grid
Pricing models	[39]	Cooperative	Micro-grids	Energy trading and fair benefit sharing among interconnected micro-grids
	[40]	Non-cooperative	Utility companies, consumers	Time-of-use electricity pricing strategy
	[41]	Non-cooperative	Utility companies, consumers	Dynamic pricing model for Singapore electricity market
	[42]	Non-cooperative	Utility companies, consumers, generation company	Electricity supply chain
	[43]	Stackelberg	Energy provider, energy hub operators	Demand response management
Bidding strategies	[44]	Evolutionary	Utility companies, consumers, generation companies, suppliers	Stability analysis of electricity markets
	[45]	Non-cooperative	Generation companies, loads	Bidding strategies in a bilateral market
	[46]	Non-cooperative	Generation companies	Conjectural variation-based bidding strategy method for generation companies
	[47]	Non-cooperative	Conventional and wind power producers	Wind power producers profit maximization
	[48]	Non-cooperative	Prosumers	Retail energy market with distributed energy resources and demand side management
Profit allocation	[49]	Evolutionary	Generation companies	Bidding strategies in electricity markets with price-elastic demand
	[50]	Cooperative	Power producers	Cooperation among independent power producers in a retail market
	[51]	Cooperative	Distributed energy resources	Profit allocation among distributed energy resources

3. Energy Balancing

The operation of modern power systems, and specifically the balance between generation and demand, is affected by multiple decisions makers, including system operators, generators, and consumers, who may have different objectives. Thus, game theory is a popular tool for designing control algorithms that address energy balancing problems.

As shown in this section, game theory plays a pivotal role in addressing numerous energy balancing problems, which include demand side management, energy sharing in and among micro-grids, and optimal charging of electric vehicles. Different non-cooperative and cooperative games are used for modeling the selfish or cooperative behavior of utility providers, energy hubs, energy generators and electricity consumers. Several studies show that efficient regulation may result in equilibrium points in which customers distribute their load throughout the day and shift their peak consumption. This in return reduces the peak-to-average ratio of the overall load, and improves the overall efficiency of the system. In addition, different game-theoretic algorithms are proposed as solutions for consumers that have their own energy sources and storage devices. These solutions allow consumers to share energy over the grid efficiently while operating in equilibrium. A few cooperative games are proposed as tools of analysis for energy management problems in smart grids. These solutions typically provide profit-sharing schemes that ensure that all consumers are financially rewarded by minimizing the energy cost of the joint coalition. In the category of electric vehicles, non-cooperative games are used to model interactions between the aggregator and electric vehicles, and are employed to solve optimal charging problems. In many papers, exhaustive analysis illustrates that these games have a unique equilibrium that allows development of distributed control strategies for each vehicle. More specifically, it is shown that by correctly modeling the driver's behavior, one may design incentives to influence his or her decisions, such that the social welfare is maximized.

In this section, we explore several state-of-the-art studies in which game-theoretic paradigms are deployed in order to solve energy-balancing problems. The overall section is categorized into three parts that include demand response and demand side management problems, energy management in micro-grids, and electric vehicle applications. The considered studies are also summarized in Table 2.

3.1. Demand Side Management

Demand-side management strategies are often used to balance generation and demand, by giving customers economic incentives and encouraging them to adjust their demand by leveraging the flexibility of their loads. When this technique is implemented in short time scales, it is named demand-response. Works [52–54] have formulated a non-cooperative game to study demand side management of residential loads. In Reference [53,54], the consumers are assumed to be selfish, and compete with each other to minimize their individual energy costs. Reference [53] proposes a distributed algorithm to solve this problem, and shows that this algorithm efficiently distributes the load and achieves lower electricity bills compared to uncontrolled energy consumption of the consumers. Similarly, in Reference [54], the selfish behavior of the consumers is modeled as a non-cooperative aggregative game, and sufficient conditions are derived for the existence and uniqueness of a Nash equilibrium. In addition, the paper develops three distributed algorithms to obtain the equilibrium of the formulated game in two scenarios: in the first scenario, consumers can access real-time information regarding the aggregated load, whereas in the second scenario they cannot. It is further revealed that these algorithms encourage the consumers to shift their peak consumption, which could be beneficial for the consumers and the grid. To control the flexible demand of consumers, a control algorithm is proposed in Reference [52] in which consumers are aiming to maximize their electricity consumption while satisfying certain constraints. To that end, the consumers propose a bid at each time interval, and based on this bid a price signal is computed by a central control authority using a proportional allocation mechanism. Following this, Reference [52] focuses on two scenarios in which the total demand is allocated among consumers: in the first, an optimization problem is solved by the central control authority, while in the second the selfish behavior of the consumers is modeled using a non-cooperative Cournot game. The authors first evaluate the Nash equilibrium of this game, and then show that the selfish behavior of the consumers may lead to reduced efficiency. The authors further explain that this loss is typically affected by the number of consumers and their functions.

Works [55–57] have used non-cooperative games to model demand side management in which the end users own an energy storage system. In Reference [55,57], interactions among the users are

modeled as a non-cooperative game where the users aim to minimize their energy payments by controlling the charging and discharging of their storage systems. Reference [55] studies a demand side management problem in a smart grid that includes users with distributed energy sources and storage units. The authors model this problem as a non-cooperative game and prove the existence of a Nash equilibrium. Moreover, the authors suggest a distributed and iterative algorithm based on the proximal decomposition method that allows to compute the optimal strategies of the users with minimum information exchange between the central unit and the users. In Reference [57], consumers with a storage device convey their energy demand to an energy provider who determines the energy payments based on their load profiles. The authors compare two methods: a centralized and a decentralized one. In the centralized approach, the energy provider controls the user's demand with the goal of minimizing the difference between the instantaneous and average energy demand of the system. In the decentralized approach, each user independently tries to minimize their energy payment. The second method is described as a non-cooperative game and the authors propose two distributed algorithms in which users define their demand according to a signal from the control center regarding the total load profile. In the first algorithm the users update their consumption sequentially, whereas in the second one they do so simultaneously. The authors show that both distributed algorithms achieve the global optimal solution of the centralized approach. Reference [56] formulates two games. The first one is a non-cooperative game played among residential energy consumers with storage who aim to minimize their energy consumption. The second is a Stackelberg game played between an energy provider and the consumers, where the energy provider sets the prices to maximize its profit knowing that consumers will respond by minimizing their cost. It is shown that both games have a unique equilibrium. The authors analyze the influence of the storage capacity, energy requirements and number of users on the overall cost and peak-to-average power ratio.

Reference [58] proposes demand side management algorithms for solar photovoltaic (PV) systems, where demand is scheduled in accordance with the expected power generation from the PV panels. The authors present three control schemes named centralized control, decentralized open-loop control and decentralized feedback control. The centralized control is formulated as an optimal control problem, whereas the distributed control schemes are based on differential games. Results show that the decentralized open-loop control scheme manages the power consumption efficiently when weather data is available, whereas the decentralized feedback controller performs well when such data is unavailable. Perhaps most interestingly, both decentralized control schemes outperform the centralized one whether data is available or not.

Several works study demand response problems through non-cooperative games [59–63]. Reference [59] proposes a game-theoretic model to manage the demand in a smart grid. The authors use a non-cooperative game to model the interaction among energy providers and consumers. In this model, the players can exchange information with one another to determine the amount of energy produced or consumed. A 0–1 mixed integer linear programming method is used to find Pareto-optimal solutions. In Reference [61], the model is extended from a single-period to a multi-period game. Moreover, the ability of the consumers to produce and store energy is added. Computation analysis shows that a Nash equilibrium can be computed in a few hundreds of seconds for even thousands of users. The authors claim that this is a reasonable time for the application of demand response.

The demand response management problem can also be formulated as a non-cooperative Stackelberg game where energy providers, as leaders, set the electricity price and consumers, as followers, adjust their energy use accordingly [60,62,63]. This is done in Reference [60] by formulating a game among utility companies and consumers. The Nash equilibrium is computed analytically and the necessary and sufficient conditions on the budget of a consumer for participating in the demand response program are given. The results show that a multi-period demand response program provides more incentive to participate in the program than a single-period one. Reference [62] addresses a real-time demand response problem and formulates a game between an energy management center and consumers. Analysis of this game reveals the existence and uniqueness of Stackelberg equilibrium

and provides optimal energy demands for each customer. Reference [63] studies a demand-response problem for geographically distributed loads that represent data centers in a power grid. The problem is formulated as a two-stage Stackelberg game, where in the first stage each utility sets a price to maximize its own profit and then based on these prices, in the second stage, data centers aim to minimize its cost via work load shifting. Results show that this game has a unique equilibrium and it significantly reduces the energy demand of the data centers and improves the grid's reliability and robustness.

3.2. Energy Management in Micro-Grids

Several recent papers use game theory to design energy management algorithms for operating and coordinating loads, distributed energy sources, and storage devices in micro-grids. These algorithms are used to optimally allocate the power output among distributed generation units and to efficiently manage stored energy to provide reliable and sustainable energy in a cost-effective way. The works are divided according to the type of game used: non-cooperative or cooperative.

Several works use non-cooperative games to study energy management of residential users in a micro-grid. For example, Reference [64] formulates a non-cooperative game among residential users for optimizing their battery capacity and scheduling their energy consumption. Results show that the game has a Nash equilibrium that is Pareto-optimal in terms of energy cost. Moreover, it assists in reducing the peak-to-average ratio of overall energy demand. Likewise, Reference [65] proposes a coupled-constraint game to solve the residential energy consumption scheduling problem. First, this game is transformed into a decoupled game by dual decomposition, and then the best response is computed employing the gradient projection method. Numerical results show that the proposed approach enhances the welfare of each user and minimizes the demand peak-to-average ratio.

Non-cooperative games are further explored to address energy management of storage devices and PV arrays in micro-grids. For instance, Reference [66] considers a hybrid energy storage system that includes an engine-generator, battery and an ultra-capacitor, and formulates the energy management problem as a non-cooperative current control game. The authors analytically derive the Nash equilibrium of the game and provide a distributed control update, which significantly improves the flexibility, scalability, and reliability of the hybrid storage systems. Similarly, given a multi-micro-grid system, Reference [67] formulates the energy management problem as a multiple leader and multiple follower Stackelberg game. In this game, micro-grids are leaders who decide the minimum generated energy, with the help of a central energy management unit, and aim to maximize their profit. Consumers with energy storage devices are the followers who choose their energy demand. The authors provide three different algorithms by which the micro-grids determine the minimum amount of energy to be generated and its price, and the customers request energy based on their real-time price. In Reference [68], a method for energy sharing among neighboring PV prosumers is provided, where the engagement of energy is done through a third party, named energy-sharing provider, that is equipped with energy storage. The key problem is formulated as a hybrid optimization problem that consists of a day-ahead energy storage scheduling and real-time internal pricing. In the day-ahead scheduling, the storage provider attempts to maximize its profit and improve the net power profile of the energy network. In addition, the real time pricing is modeled as a Stackelberg game where the storage provider is the leader who sets the energy prices considering the utilization of the storage system, and the prosumers are the followers, who respond to the energy prices by optimizing their energy consumption. A practical case study reveals that the proposed method is beneficial to improve the economic benefits of the grid and PV energy sharing. Reference [69] promotes solar PV installations in apartment buildings by studying energy sharing models between an owner of a solar PV and storage systems and the residents of the building. The first model is an optimization problem with the objective of maximizing welfare, whereas in the second model a Stackelberg game between the PV owner and the consumers is formulated. Results show that in both cases welfare may be maximized, however it is allocated differently between the PV owner and the consumers.

Several works study the utilization of components in the micro-grid through cooperation. The idea is that, through cooperation, underused resources can be utilized more efficiently, thus lowering the overall cost for the group. For example, Reference [70–72] study cooperation among players to purchase and manage storage systems together. Reference [70] investigates two scenarios in this context. In the first scenario, each player has a storage device and the players may cooperate and manage all devices together in order to maximize the overall profit. In the second scenario, players can purchase a common storage device and then manage it together. The authors show that, in both scenarios, sharing storage is beneficial by proving that the core of the game is non-empty, meaning that no player can benefit from forming a smaller coalition than the coalition that includes all the players. Moreover, in both scenarios, they find an allocation of the overall cost that is satisfactory for all users. Reference [71] extends the model formulated in Reference [70] by adding ramp constraints to the storage devices. While Reference [70] uses a two period time-of-use electricity tariff and takes into consideration only the peak consumption of the players, in Reference [71], the model takes into account inter-day consumption patterns and a realistic tariff. The authors show how consumption patterns and ramp constraints affect both the feasibility of forming a grand coalition and the allocation of cost among them. They prove the existence of a solution in the core for a set of cooperative games that are equivalent to a well-known class of games named ‘unitary glove market’ and demonstrate the analytic results using real data from the ‘Pecan street’ project. In their subsequent Reference [72], the authors augment the model by adding two extensions: stochasticity of the load and discreteness of the storage device capacity. They prove that, for the stochastic yet continuous case, a solution of the game always exists and they provide an efficient algorithm to find it. On the other hand, they show that the discrete case may fail to admit a solution. Accordingly, for that case, they provide an approximate solution that appears to be satisfactory for real-world deployments. In addition, they provide numerical simulations in which the cooperative scheme achieved an increase between 100% and 250% in the amount of storage hosted in residential premises compared to the setting in which consumers invest individually, when it was profitable for them to do so. In Reference [73], a cooperative energy scheduling problem is addressed for multiple neighboring energy hubs. These hubs may have different supply and load profiles, and they can exchange power to minimize their own operational costs. For ensuring cooperation among these hubs, bargaining game theory is utilized to compute a Pareto solution to the minimization problem. Further analysis illustrates that the cooperative operation of these hubs has better economic benefits than the non-cooperative operation. In Reference [74], a cooperative game is proposed to study an energy management problem in which distributed energy storage systems operate collaboratively under a centralized control strategy to minimize the joint conditional energy cost. The core of the cooperative game is shown to be non-empty, that is, the players benefit from all cooperating together. Moreover, case studies show that the cooperation among the players leads to a more leveled overall load in the local network.

3.3. Electric Vehicle Applications

Game theory is a popular tool for modeling interactions between electric vehicles and the grid, and allows to establish novel energy management and charging policies. As part of this trend, a variety of non-cooperative games are utilized to solve optimal charging problems in electric vehicles [75–80]. For example, Reference [75,76] employed Stackelberg games to research optimal charging problems in electric vehicles. In both works there is a charging service provider, who leads the game by defining the charging price, and electric vehicle owners, who follow by deciding when to charge. Reference [75], proposes a combination of non-cooperative and cooperative approaches. In the non-cooperative game, each vehicle selects its own demand strategy to optimize its benefit selfishly, while in the cooperative model, a distributed energy scheduling algorithm is proposed to optimize the overall benefit of the vehicles. Theoretical analysis proves the existence and uniqueness of an equilibrium in both approaches. Moreover, algorithms are developed in both frameworks to ensure convergence to a global optimum, and it is shown that the solutions are robust against demand uncertainty. Likewise,

Reference [76] shows that the formulated game always reaches an equilibrium point where the vehicle charging requirements are satisfied and the aggregator's profit is maximized. Moreover, the authors analyze the influence of the costumers' weighted utility function on the results of the game, and show that they are maintained at a certain level between the optimum solution in terms of minimum generation cost and the optimal solution in terms of an equal rate-of-charge during a given period.

Apart from the Stackelberg game, several other non-cooperative games are deployed in Reference [77–79] to solve electric vehicle charging problems. Reference [77] proposes a stochastic mean-field theoretic framework to solve a distributed charging problem for a large-number of electric vehicles, and considers a scenario where a large number of vehicles charge simultaneously from a charging station. The proposed solution to this problem enables each vehicle to dynamically control its charging process and finish the process within an appropriate time so that the total cost of charging is minimized. A similar charging problem is addressed in Reference [78], where it is formulated as a non-cooperative game, and a Newton-type fixed-point algorithm is developed to compute the Nash equilibrium. It is shown that, in theory, this algorithm can achieve a super-linear convergence rate, and that the vehicle's best response can be quickly implemented in a distributed way to minimize the charging cost of each vehicle.

Reference [79] suggests an electric vehicle scheduling scheme to solve the problem of variable wind generation. In the suggested model, a virtual power plant operator aims to balance the mismatch between wind generation and demand by offering electric vehicles monetary incentives to charge when needed. The key idea is that the incentives are proportional to the power needed, and the electric vehicle owners decide when to charge according to these incentives and other considerations, such as their battery's state-of-charge and their daily schedule. The distributed approach reduces computational time since the operator only has to set the incentives, according to the overall wind generation and load, rather than to control each vehicle separately. Moreover, it provides the electric vehicle owners more freedom and prevents privacy issues. Regarding the balancing between wind generation and load, it is shown that the difference between the results of the distributed approach and the centralized one are negligible.

Reference [80] combines game theory with microeconomics to study the charging scheduling problem among a family of electric vehicle aggregators. In the proposed model, each aggregator considers the actions of their neighboring aggregators, and attempts to minimize their vehicle charging costs by determining charging start times and profiles. The interaction among these aggregators is modeled using a two-stage non-cooperative game. Next, the game is studied using two user behavioral models: expected utility theory and prospect theory. This is done in order to study the influence of irrational decisions of the aggregators on the results of the game. An exhaustive analysis reveals that the proposed charging strategy reduces electric vehicle charging cost and the peak-to-average ratio of the load in the system, and that it is resilient to irrational actions of the aggregators.

Table 2. Summary of works focusing on energy balance application using game-theory.

	Ref.	Game Method	Players	Application
Demand Response	[59]	Non-cooperative	Energy retailers, customers	Single period demand response management
	[60]	Stackelberg	Utility companies, energy consumers	Multi-period demand response management
	[61]	Non-cooperative	Residential consumers, electricity providers	Multi-periodic demand response management
	[62]	Stackelberg	Energy management center and its customers	Optimal control of customers' load
	[63]	Stackelberg	Utility company, data centers	Demand response for geographically distributed data centers
Demand Side Management	[52]	Cournot	Energy consumers	Demand side management for balancing residential loads
	[55]	Non-cooperative	Users with storage devices	Demand side management for smart-grids with storage
	[53]	Non-cooperative	Energy consumers	Demand side management for residential loads
	[54]	Aggregative	Energy consumers	Energy consumption scheduling
	[56]	Non-cooperative + Stackelberg	Energy providers, customers	Demand side management for consumers with storage systems
	[57]	Non-cooperative	Users with storage devices	Demand side management for consumers with storage systems
[58]	Differential	PV systems	Demand side energy management for PV systems	
Energy management in micro-grids	[64]	Non-cooperative	Residential users with storage systems	Evaluation of energy consumption
	[65]	Coupled constrained	Residential users	Energy consumption scheduling for residential users
	[66]	Non-cooperative current control game	Generator, battery, ultracapacitor	Energy management in hybrid storage systems
	[67]	Stackelberg	Micro-grids, consumers	Energy management of residential consumers with storage devices
	[81]	Non-cooperative	Multiple micro-grids	Energy consumption scheduling
	[68]	Stackelberg	Storage provider, prosumers	Energy sharing for PV prosumers in the smart grid
	[69]	Stackelberg	Storage system owner, consumers	Energy allocation in a residential building
	[73]	Cooperative bargaining game	Energy hubs	Cooperative energy scheduling for neighboring energy hubs
	[70]	Coalitional Game	Consumers with storage systems	Sharing storage systems among consumers
	[71]	Coalitional Game	Consumers with storage systems that have ramp constraints	Sharing storage systems among consumers
[72]	Coalitional Game	Consumers with storage systems that have ramp constraints	Sharing storage systems among consumers	
[74]	Cooperative	Energy storage systems	Coalitional energy management for storage systems	
Electric vehicle applications	[75]	Stackelberg	Aggregator, electric vehicles	Optimal charging scheduling of multiple vehicles
	[76]	Stackelberg	Aggregator, electric vehicles	Optimal charging in the presence of demand uncertainty
	[77]	Stochastic mean field game	Aggregator, electric vehicles	Optimal charging in electric vehicles
	[78]	Non-cooperative	Aggregator, electric vehicles	Optimal charging in electric vehicles
	[79]	Incentive-based game	Wind generator, electric vehicles	Minimizing energy imbalance between a wind generator and its connected vehicles
	[80]	Non-cooperative	Multiple aggregators	Coordinated electric vehicle charging

4. Grid Planning

Modern electric grids include new components, such as energy storage devices, renewable energy sources, and electric vehicle charging stations. Such components may be owned and managed by different entities with contradicting objectives; nevertheless, grid planning procedures today tend to ignore these contradictions and assume the existence of one entity with complete knowledge and control span. Since this fundamental assumption is gradually becoming unrealistic, several authors suggest new grid planning procedures that take these different objectives into account. Naturally, game-theory plays a major role in these works.

For instance, since modern grids include multiple generation assets that are owned by private entities, it is often a challenge to coordinate the development of these assets alongside the on-going expansion of the transmission system. As a simple example, in many countries large photovoltaic plants require development of the transmission system, which may not be optimal in view of increasing loads in other areas. To address this problem, several works formulate non-cooperative games between transmission system planners and competing generation firms, in order to study the behavior of each player at equilibrium. Furthermore, as a guideline for transmission expansion planning, theoretic concepts from cooperative game theory are used to determine the benefits obtained by different users of the transmission system and the most efficient and fair way to allocate the cost among them. A similar problem is to plan the portfolio of energy resources and storage devices, including their size, location and preferred technology. Both non-cooperative and cooperative games are used in this context. For example, to find the optimal technology for a generation asset, several papers formulate a non-cooperative game in which different technologies compete with one another. However, when planning a combination of different sources, it seems that cooperative games are more popular for finding the optimal mix. For example, many studies employ a cooperative game to find the optimal combination of renewable energy sources and storage devices in a hybrid power plant or a micro-grid. In addition, non-cooperative games are often used for optimal allocation of electric-vehicle charging stations.

In this section, we present papers that address grid planning problems in the following order: generation and transmission expansion, micro-grid design, resource sizing, and electric vehicle charging station planning. In each sub-section, we further categorize the papers according to the game theoretic approach they employ. All of the considered studies are summarized in Table 3.

4.1. Generation and Transmission Expansion Planning

Generation and transmission expansion planning requires long-term investments and coordination among multiple entities. The following papers introduce game-theory based algorithms to optimize the planning procedure and overcome inherent conflicts. Several of them suggest methods to estimate and reduce the overall costs of planned projects, while others propose methods to select an optimal deployment for different technologies. Works [82–85] have studied generation and transmission expansion planning problems using non-cooperative games. Reference [82] formulates a game among available power plant technologies to identify the ideal one in terms of profits, reliability and degree of expansion. Using the Cournot model of oligopoly behavior, it is shown that generation resources grow faster when they are distributed among competitors than when they are managed in a traditional monopolistic manner. Moreover, the formation of a coalition among the competitors, namely, a cartel, yields the greatest profits, but results in the lowest expansion rate and reliability. Reference [83] models a game between generation and transmission companies, each trying to maximize their profits while maintaining the voltage stability of the power system. Comparison of several expansion scenarios shows that simultaneous expansion is the most profitable one. Similar to this, Reference [84] formulates a game between a transmission company and a wind farm, allocating energy storage to smooth power fluctuations while meeting a governmental target of wind power curtailment rate. Based on a case study, it is shown that the companies will fail to find an equilibrium point without the government's interference in the game, i.e., changes in regulations that may result in a sub-optimal

solution. Reference [85] models a Stackelberg game between transmission (leader) and generation (follower) companies, and compares two planning models in which the incentives of the transmission operator are different: in the first, the operator maximizes profits, whereas, in the second, it maximizes welfare (thus reducing the electricity price). The results show that, if the transmission network is non-congested, there are no significant differences between the models. However, if the network is congested, then the incentive of the transmission company has major impact on the overall welfare. In such cases, the conclusion is that a regulated transmission company is more efficient for developing the grid and enhancing welfare than when it solely relies on profit incentives.

Studies [86–88] have employed a cooperative game for studying conflicts between generation and transmission expansion projects. Reference [86] considers expansion projects as the players of an Aumann-Shapley cooperative game, trying to minimize their costs. It is shown that the suggested method can overcome some major drawbacks of other existing planning methods. These include the inability to capture the dependency of the benefits of a projects on: (1) the interactions among different projects in the expansion plan, (2) the order of deployment of projects, (3) grouping different projects within the expansion plan, e.g., considering two new transmission lines as one project or two. Moreover, it is shown to be superior in computation time. In Reference [87], a cooperative game between a transmission company and a renewable energy (RE) generation company to maximize their profits is formulated. The suggested methodology models a negotiation between the players for the cost sharing and recovery of investment of a new transmission line permitting delivery of RE to the grid. This work also discusses the ability of RE subsidies to steer the negotiated solution towards a transmission plan that maximizes total net benefits for all market participants. Reference [88] formulated a cooperative game among flexibility providers—demand side management through flexible loads, fast-ramping gas turbines, hydro-power plants and high voltage cross-border transmission lines (inter-connectors). To this end, the Shapley value accounts for different sequences, in which technologies are deployed, from a perspective of uncertainty regarding learning and innovation, as well as lead-time. For instance, some components, e.g., transmission lines, might require a longer lead-time from day of decision to day of operation, compared to other alternatives, e.g., gas turbines. The results demonstrate the disadvantages of long lead-time of grid investments and the advantage of cost-efficient demand side management solutions.

4.2. Micro-Grids and Resource Sizing

Many studies employ game theory for planning the portfolio of resources in modern electrical grids. The planning procedure includes determining the size, location and technology of the resources, in either a micro-grid or the main grid. The following papers use game theory for predicting the behavior of the resources' owners, for optimizing the planning procedure while taking into account the owner's independence and private objectives, and for studying opportunities for cooperation.

Reference [89–92] used non-cooperative games for planning the portfolio of different resources in the grid. In Reference [89], a non-cooperative game among residential owners of solar photovoltaic (PV) sources and energy storage (ES) devices is formulated to optimize their capacities while minimizing the overall costs. The suggested model, which considers the varying electricity price that is a result of the individual load management of the customers, indicates that there is an optimal ratio between the user's load and the capacity of its PV source and ES device. Reference [90] investigates the optimal sizing and siting of distributed generation sources (DGs) using a bi-level approach. The first level is used to locate the DGs while maintaining power quality parameters using multi-objective optimization. In the second level, a Stackelberg game is formulated between the DGs owners (leaders) who maximize their profits and a distribution company (follower), which selects the best pricing contract to minimize its power payments, taking into account network constraints. The results show that DGs are optimally located far from the substations, and that the profit at the equilibrium point is inversely proportional to the number and capacity of the DGs due to competition among DGs.

Several studies focus on capacity planning of components in micro-grids. For example, in Reference [92], a non-cooperative game among MGs, buying and selling electricity, is used to optimize the capacity of their renewable sources. The suggested method indicates that the needed capacity can be reduced when taking into account the participation of MGs in the electricity market. Reference [91] investigates a unique form of a MG, namely an industrial MG, that has generation surplus during weekends and a fairly neutral generation to load ratio the rest of the week. The authors use a dual non-cooperative game—an external game among MGs and an internal one among renewable energy sources that aim to maximize their profits. The results show that PV owners who are part of an industrial MG have a shorter return of investment period and that the best compromise among players is obtained when prices for internal exchanges follow the prices of the external ones.

Several works employ cooperative games to study planning of resources and interactions among micro-grids. Works [93–95] have used a cooperative game to size and select the most cost effective technology for renewable energy sources and energy storage systems. In Reference [96], hybrid renewable power plants are investigated using both cooperative and non-cooperative games in which the players are optional sources—wind turbines, photovoltaic panels, and batteries, which are trying to maximize their profit. A comparison between the results of the games reveals that the equilibrium point achieved in a cooperative game, when two or more sources cooperate, increases the overall profits. In addition, this work tests the stability of the equilibrium and its sensitivity to various uncertainties and correlations. The main conclusion is that the profits and performance of hybrid plants with more than one source are more stable. Similar to this, in Reference [93], the authors model a cooperative game among renewable energy sources—wind turbines, solar panels and batteries, which try to maximize their profits while meeting the electrical load requirements. The results are that the profit is maximized when wind turbines and solar panels cooperate. Reference [94] formulates a cooperative game among battery technologies—lead-acid, lithium-ion and vanadium redox flow (VRB) to maximize the profits of an energy storage system. The results indicate that a combination of lithium-ion batteries (70%) and VRBs (30%) feature the economically optimal solution. Reference [95] uses a cooperative game between a power-to-gas (P2G) stations and the electricity network to maximize their profits. P2G technology has a two-step process: convert excess electricity generated from renewable sources (such as wind or solar energy) into methane, and then use this gas to generate electricity. Using the Nash Bargaining cooperative game between P2Gs, the electricity network and the natural gas system, it is shown that cooperation gives a good distribution of the profits among the different participants compared to other methods. In Reference [97], a cooperative game is used to solve the conflicts between micro-grids' internal (among components) and external (with the grid and other MGs) interactions. It establishes a cooperative game among MGs, built of renewable energy resources, to minimize their overall costs. A benchmark is set using a non-cooperative game and it is shown that the cooperative game provides better results. Moreover, it is shown that additional cost reduction can be achieved by adding an incentive mechanism that encourages cooperation among interconnected MGs towards a socially optimal planning, and by distributing the total investment cost in a fair manner.

4.3. EV Charging Stations

The increasing presence of electric vehicles (EV), which have limited traveling range and long charging periods, requires careful sizing and placement of their charging stations. Moreover, there are different types of stations, which are usually divided according to their charging time: rapid, fast and slow. The optimal portfolio of charging stations in an electrical grid is affected by the behavior of the drivers and traffic patterns, both spatial and temporal, and has to be coordinated with the distribution network. Since there are many players with different objectives that influence the optimal portfolio, game theory is used in many studies to investigate this problem. We divide them by the type of game that is used: non-cooperative and cooperative.

Several papers propose a non-cooperative game for planning the placement and sizing of electric vehicle charging stations [98–100]. Reference [98] formulates a charging stations placement problem

as a bi-level optimization problem with the goal of maximizing social welfare. The social welfare is measured as the overall travel cost of electric vehicles to charging stations and queuing cost at the stations. The behavior of the vehicle owners is modeled as a non-cooperative congestion game in which the congested elements are the roads and the charging stations. The optimal distribution of charging stations is determined by the equilibrium that yields the minimum social cost. Through experimental evaluation, the authors compare their method to three baseline methods and illustrate that this proposed method leads to a solution with less traffic congestion and queuing in charging stations. Similar to this, Reference [99] uses a Bayesian non-cooperative game in which the players are charging service providers who aim to locate their charging stations in a manner that maximizes profits, while ensuring the quality of service. The effects of the charging stations on the power grid is modeled through a penalty fee for disturbances that the grid operator gives to the charging service provider. These disturbances are represented by the load imbalance caused from charging electric vehicles. The main conclusions are that the location of charging stations is highly consistent with traffic flow, and that charging service providers prefer clustering stations, rather than separating them. Reference [100] formulates a Stackelberg game in which the leader is a distribution company setting a time-based electricity tariff, and the followers are costumers that participate in a demand response program and adjust their electricity consumption with accordance to the price. The consumption patterns are used to plan the optimal distribution of micro-turbines and electric vehicle parking lots in a distribution system, in a way that minimizes the cost for the distribution company. The results demonstrate that the reduction in consumption has a direct and positive effect on the planning cost of the distribution system.

Concepts from cooperative game theory are used both to allocate profit among stakeholders, as well as to allocate electric vehicles to charging stations. In Reference [101], the problem of planning fast charging stations in a distribution network is modeled as a mixed-integer non-linear problem. A concept from cooperative games theory, namely, the Nash bargaining solution, is used to allocate profits among the charging service providers and the electrical distribution company. In Reference [102], a pricing mechanism for charging electric vehicles and the allocation of electric vehicles among charging stations are modeled as a bi-level optimization problem. In the upper level, a coordinate descent optimization algorithm is used to define a time-based pricing mechanism of charging in different stations. In the lower level, a matching game between electric vehicles and charging stations is solved using the Gale-Shapley matching algorithm. It is shown through numerical analysis that the utility of the electric vehicle owners is improved by using the matching algorithm. Moreover, the overall utility increases when the amount of electric vehicles increases. This is true until the system capacity is nearly full, and afterwards the overall utility starts to decline since the charging service providers raise their prices.

Table 3. Summary of works focusing on grid planning application using game-theory.

	Ref.	Game Method	Players	Application
Transmission and generation expansion planning	[82]	Non-cooperative	Power plants of different technologies	Planning a new power plant with multiple technology options available
	[83]	Non-cooperative	Generation, Transmission	Planning generation and transmission expansion
	[84]	Non-cooperative static	Wind farm, Transmission	Transmission line planning between a wind farm and the grid
	[85]	Stackelberg	Generation, Transmission	Coordination between generation and transmission expansion planning
	[86]	Cooperative	Transmission expansion projects	Study of the benefits obtained by users of the transmission network (consumers, generators and transmission owners) from expansion projects
	[87]	Cooperative	Renewable energy sources, transmission	Transmission expansion planning
	[88]	Cooperative	Demand side management participants, fast-ramping generators, energy storage devices	Planning the integration of flexibility providers into the grid
Micro-grids design and resources siting and sizing	[91]	Non-cooperative	Consumers and prosumers in a micro-grid	Investment planning of industrial micro-grids
	[92]	Non-cooperative	Micro-grids	Optimal sizing of distributed renewable energy sources in micro-grids
	[89]	Non-cooperative	PVs and ESs owners	Optimal sizing of residential PV sources and energy storage devices
	[90]	Bi-level, multiobjective optimization + Stackelberg	DG owners, distribution company	Planning the optimal location and operation of Distributed Generation
	[96]	Cooperative + non-cooperative	Wind Turbines, solar panels, batteries	Planning a hybrid power plant
	[97]	Cooperative	Micro-grids	Planning of renewable energy sources in a distribution network of micro-grids
	[93]	Cooperative	Wind turbines, Solar panels, Storage batteries	Capacity planning of generation sources and batteries for clustered micro-grids
	[94]	Cooperative	Battery technologies	Planning a battery system with optimized economic features and capacity
EV charging stations	[95]	Cooperative	Electricity system, natural gas system, Power to gas station	Planning an integrated electricity-gas system with power to gas (P2G) technology
	[98]	Non-cooperative	EV owners	Planning placement of fast EV charging stations
	[99]	Bayesian	Charging stations	Planning placement of EV charging stations
	[100]	Stackelberg	Distribution company, customers	Planning EV charging stations in parking lots
	[101]	Cooperative	Distribution company, Fast Charging Stations	Planning placement and sizing of fast EV charging stations
	[102]	Cooperative	Electric vehicles, charging stations	Allocation of electric vehicles among charging stations

5. Power System Reliability

Power system reliability refers to the ability of a system to deliver power to consumers under acceptable standards [103]. In recent years, the on-going deregulation of power markets alongside the continuing integration of renewable energy sources have led to increasing number of independent entities that operate within the same power system. Since power production is not always controlled directly by the system operator, maintaining an adequate level of reliability is becoming a serious challenge. This challenge may become more severe when independent entities have contradicting

objectives. To address this challenge, game theory is used in various works to design incentive mechanisms that encourage players with energy sources and flexible loads to enhance the reliability of a system. It is shown that in many cases this approach is more efficient in stabilizing the system than a centralized approach, in which a single entity is solely responsible for system reliability. This is especially true in situations in which this single entity has limited resources.

In this section, we refer to real-time reliability, whereas planning for reliability in the long-term is considered in Section 4 (grid planning). We review papers that address three aspects of power system reliability: (1) frequency stability, (2) voltage stability, and (3) cyber attacks. These aspects are affected by interactions between at least two independent entities: cyber attacks involve an attacker and a defender, while frequency and voltage stability-related problems may involve all of the system's operators, generators, and consumers. In this light, it is natural to use game theory to study such interactions. The considered studies are summarized in Table 4.

5.1. Frequency Stability

The frequency stability of a power system is strongly connected to the power balance between generation and demand and to the availability of frequency response services, such as spinning reserves and load frequency control (LFC). The power balance and the frequency response services are mostly affected by actions of active system players, such as system operators, generators, and loads. Due to the great number of such players and the interactions among them, game theory receives much attention in the literature. Reference [104,105] uses Bayesian games to study frequency reserve allocation. Reference [104] studies a game between a system operator, and frequency constrained electricity market participants. In this market, frequency reserve constraints are set in order to limit the frequency nadir of the grid, following a loss of renewable energy sources. Two types of market participant players are considered: (a) a price-taker, who cannot influence the prices, and (b) a price-maker, who is able to affect the prices. Results show that, in the game's equilibrium point, the available frequency reserve of the system is maximized. Reference [105] proposes a game that models spinning reserve trading between neighboring power systems in order to achieve reserve requirements. These requirements increase together with wind turbine power capacity and wind uncertainty. The trading price is the mean between the price of the buyer and the seller at the Nash equilibrium. Once the trading price is set, the players set the quantities to be traded. The mechanism is decoupled from the system unit dispatch process and, as a result, it minimizes the changes to the existing optimal dispatch. Moreover, it allows each system to individually determine its reserve dispatch, instead of solving a multi-area reserve dispatch problem, and leads to higher wind power generation.

Mean-field games are useful for analyzing the coordination among a large number of agents. For example, Reference [106] proposes to coordinate a large number of thermostatically controlled loads (TCLs) in order to provide frequency response support. The coordination is based on a non-cooperative mean-field game between TCLs that receive two price signals, which are the price of electricity and the price of frequency response availability. Based on the price signals, the TCLs schedule their energy consumption and allocate frequency response provision in order to minimize their operational costs. Assuming that a single TCL is too small to significantly impact the prices, the TCLs influence the price signals through their aggregated power consumption and total frequency response availability. The equilibrium is computed numerically using an iterative algorithm. The authors compare the mean-field game based mechanism to a "business as usual" scenario, where loads do not exploit their flexibility to support the frequency, and to a centralized approach, in which the loads are controlled by a central unit. Results show that the game-based approach and the centralized one reduce system costs by 0.4% and 0.6%, respectively. Although the centralized approach achieves better results, the game-based approach promises the satisfaction of the users, since no player can achieve a better result.

Several papers use differential games to analyze power and frequency related problems that are described by differential equations, using either non-cooperative, or cooperative games. LFC is one example for a mechanism that is based on differential equations. Reference [107] analyzes an LFC

mechanism through a non-cooperative differential game between suppliers and consumers, and proposes a real-time pricing mechanism. The objective is to increase the stability of LFC and to guarantee the supply-demand balance. The real-time mechanism is individually-rational in the sense that it attempts to be overall more beneficial to each player compared to their profit in a fixed-price market. In order to guarantee the supply-demand balance, the mechanism explicitly considers this dynamic balance as a constraint. The proposed mechanism converges to a Nash equilibrium that maximizes the social welfare, and, under certain conditions, its solution conforms with that of the system operator's centralized optimization. Reference [108] considers a non-cooperative differential game to address the problem of frequency regulation in a power system with large scale wind power clusters. The power system is divided into areas, where each one has both conventional generators and wind turbine farms. The areas coordinate among themselves the active power generation in order to minimize each tie-line power fluctuations and frequency deviations. Each area regulates its own active power dispatch according to frequency and power injection measurements. This regulation is based on a distributed model predictive controller, which considers wind power fluctuations and critical frequency regulation parameters of generation units. Simulation results indicate that in cases of load step disturbances, the coordination may achieve smaller frequency deviations. Reference [109] considers a two-area LFC system and proposes several differential games to model the interaction between the areas while considering load and power fluctuations. The utility function of each area considers frequency and tie-line power errors, as well as control efforts, such as commands for active power output. The authors analyze a non-cooperative game, and two cooperative games, and conclude that the cooperative games lead to more stable system operation. Reference [110] also considers a multi-area LFC system and a differential game to model the interaction between the areas, with a similar payoff function. Differently from the previous papers, this one proposes a co-evolutionary algorithm to solve the game. The authors conclude that the proposed algorithm has a better suppression effect on the frequency and tie-line power deviations, and a shorter settling time compared to several other algorithms.

Finally, cooperative evolutionary game theory is used in Reference [111] to formulate a mechanism for controlling primary frequency control of hydro power plants. The main objective of the mechanism is to reduce the frequency nadir and the settling time following a power imbalance disturbance. The governors cooperate by sharing their measurements of frequency deviations, and are all coordinated through a central controller, which sends them a signal that is proportional to the rate of change of frequency (RoCoF). The authors conclude that the proposed RoCoF based control mechanism is effective for arresting the frequency response.

5.2. Voltage Stability

Power system voltage stability refers to the ability of the system to maintain voltage metrics at each bus within certain boundaries. We survey papers that address this problem and try to improve the voltage stability by coordinating between different entities, such as system operators, generators, and consumers. We divide these works into two types of non-cooperative games: static and sequential.

Several papers analyze non-cooperative static games, in which the players play simultaneously. Reference [112] proposes methods for power system operators to encourage PV owners to participate in voltage regulation, and coordinate among them to do so efficiently. The coordination is done through a pricing mechanism, and its objective is to minimize the operator's cost of maintaining voltage stability, while maximizing the PV owners' profit. The owners profit by providing two services: voltage regulation and active power input. The owners compete for the provision of these services; thus, a non-cooperative game is formulated among them. The proposed pricing mechanism is designed in a way that leads to a potential game among the owners, where the actions benefiting a single owner benefit all the others, as well.

Several papers formulate sequential games to describe voltage stability related problems that include multiple stages. Reference [113] introduces a game among buses in a HVDC grid who influence the voltage stability through the power they produce. Each bus aims at minimizing the

voltage deviations, power drawn from the grid, and losses in its surroundings. Since the buses decisions influence one another, they iteratively update their decisions until they reach an equilibrium. This approach allows the general power dispatch optimization problem to be solved locally at each bus. Reference [114] proposes a dynamic game among prosumers in a distribution network. At each time step, the prosumers decide how much power to consume, generate or store. These decisions affect the power flows in the system; thus, the players affect one another. Moreover, their utility functions capture costs of power trading and penalties of violating voltage constraints, which encourage the players to comply with voltage constraints. Numerical analysis shows that the proposed mechanism can maintain the stability of the grid and can be implemented in practice. A non-cooperative differential game is proposed in Reference [115]. This paper discusses voltage magnitude and angle regulation during a transient in islanded micro-grids with parallel-connected inverters. In order to improve the voltage performance during a transient, a game between the inverters is proposed. Reference [116] introduces a Stackelberg game in order to solve a power dispatch problem between generators, which are the leaders, and micro-grids with generation capabilities, which are followers. The generators lead by determining their power generation, and the micro-grids follow by setting their power generation. The players' cost function includes the costs of generation and penalties for voltage angle deviations. The authors show the existence and uniqueness of an equilibrium, and conclude that for players to reach their decisions, they mainly require to know the voltage angle at local buses. This may suggest that the proposed mechanism can be simply implemented without much resources.

5.3. Cyber Attacks

The digital evolution of the power grid and the increasing number of active participants increases its vulnerability to cyber attacks. Adequate analysis of such attacks can guide decision making on security measures that may increase the reliability of power systems and lower related economic losses. Cyber attacks generally involve two agents with counteracting objectives: an attacker, whose goal is to damage or destabilize the system, and a defender, whose goal is to maintain a reliable system with minimum investments. This leads to interactions among the agents that make game theory especially useful for modeling and analyzing cyber attacks. We survey papers that model cyber attacks and are mostly based on various types of non-cooperative games. While several papers consider the static versus the sequential nature of the game, other papers consider the information that the players are able to acquire before choosing their strategies.

Several papers consider a static game in which the attacker and the defender play simultaneously. For example, a static zero-sum and incomplete information game is presented in Reference [117] in order to analyze attack-defense interactions over load frequency control (LFC). The utility function of both the attacker and the defender takes into account the frequency deviations and the probability of the defender to detect the attack. The model considers two types of attackers and two defensive schemes. The attackers can be either damage oriented or detection-evasion oriented, while the defenders can follow an immediate or a cumulative false data detection scheme to identify compromised signals. A numerical analysis shows that detection-evasion oriented attackers can maintain a low probability of detection, whereas damage-oriented attackers can trigger emergency frequency controllers that cause severe damage.

Several papers utilize various types of sequential games to describe and analyze more complicated attacks. Reference [118] uses a Stackelberg game in a multi-level framework which models the relationships between defenders, attackers, and system operators, considering false data injection attacks, such as load redistribution attacks. The defenders start by allocating defensive resources, after which the attackers choose their strategy, and finally the operators react to the new state. The proposed defense mechanism is shown to be effective against false data injection attacks, and may be extended to address other types, as well. Reference [119] proposes a repeated game to analyze a framework where each synchronous generator in the system has a local energy storage that regulates the rotors' speed. The game is between an attacker and a defending utility that reacts to their attacks. The

attacker attempts to control the power injections from the storage unit towards the generators, while the defender attempts to stabilize the generators' rotor speed by controlling their power injections. The players' payoff function is based on the rotor speed deviation and on their control efforts. The attacker actions are stochastic, and as a result, the analysis focuses on the long term average outcome to the defender. The authors conclude that, if the defender acts at each repeated game, ignoring the control efforts penalties, then its long-term average payoff can be better compared to the game-theoretic strategy in which it attempts to optimize its actions at each repeated game. Reference [120] proposes a differential game where attackers try to control a subset of distributed energy resources (DERs) in order to destabilize the system, while a defending utility aims to stabilize it by using another subset of system resources. The cost function includes deviations from a stable state. The paper demonstrates that, if the utility is able to identify uncompromised DERs, then it can take countermeasures that will effectively reduce the impact of an attack. On the other hand, if uncompromised DERs are not identified, then a coordinated attack can lead to instabilities. Reference [121] offers a game model where both the defender and the attacker can affect the overall system damage by identifying critical substations and the chronological order in which they can be attacked. The authors conclude that subsequent attacks can incur a significantly higher damage compared to simultaneous attacks, and that the models are effective in improving the system resilience under such chronological attacks.

Several papers consider the players' information on the system state or the other players' strategies. A player that has no information is considered static, whereas one that has some information is considered dynamic. Reference [122] considers both a static and a dynamic attacker and proposes to analyze the worst possible outcome. During the game, the defenders allocate their budget between protection and recovery measures. Two different problems are considered: (a) how to allocate a limited budget in order to maintain low losses, and (b) how much budget is needed in order to limit the losses to an expected value. The authors conclude that the loss to the defender can be predicted and limited, and that for large systems the algorithms might take long time to compute. Reference [123] uses a non-cooperative game in order to establish a probabilistic defensive algorithm and to reduce the power system vulnerability to a cascading failure. Different types of attackers are considered that are either static or dynamic. The attacker chooses its strategy, then the possible cascading failures are identified, and finally the defender takes countermeasures based on the identification of the cascading failures and the components which are likely to be attacked. The authors suggest that highly capacity-constrained systems are especially vulnerable to cascading failures.

In addition, several papers use cooperative games to examine whether cooperation among defenders can improve their cyber protection. For example, Reference [124] proposes a game that examines cooperation among consumers to locate abnormalities in the system due to false metering and power blackouts events. It is assumed that the consumers are willing to pay in order to detect these abnormalities and reduce monetary losses. This is done by finding load changes during normal conditions, false metering events and power blackout events.

Table 4. Summary of works focusing on reliability applications using game-theory.

	Ref.	Game Method	Players	Application
Frequency stability	[104]	Non-cooperative Bayesian	System operator, generators, consumers	Frequency reserve allocation
	[105]	Non-cooperative Bayesian	Power systems	Frequency reserve allocation
	[106]	Non-cooperative mean-field	Thermostatically controlled loads	Frequency reserve allocation
	[107]	Non-cooperative differential	Suppliers and consumers	Supply-demand balancing
	[108]	Non-cooperative differential	Power system areas	Active power regulation
	[109]	Cooperative and non-cooperative differential	Power system areas	Active power regulation
	[110]	Cooperative differential	Power system areas	Primary frequency control
	[111]	Cooperative evolutionary	Hydro plants	Active power regulation
Voltage stability	[113]	Non-cooperative	High-voltage DC (HVDC) buses	Voltage regulation
	[112]	Non-cooperative static	PV owners	Voltage regulation
	[115]	Non-cooperative differential	Power inverters	Voltage regulation during transients
	[114]	Non-cooperative dynamic	Prosumers	Voltage regulation
	[116]	Non-cooperative Stackelberg	Generators and micro-grids	Voltage regulation
Cyber attacks	[117]	Non-cooperative incomplete information	Attacker and defender	False data injections
	[118]	Non-cooperative Stackelberg	Attacker, defender, system operator	Hijacking and false data injections
	[119]	Non-cooperative repeated	Attacker and defender	Hijacking
	[120]	Non-cooperative differential	Attacker and defender	Hijacking
	[121]	Non-cooperative static	Attacker and defender	Disable elements
	[122]	Non-cooperative static and dynamic	Attacker and defender	Disable elements
	[123]	Non-cooperative static and dynamic	Attacker and defender	Disable elements
	[124]	Cooperative	Attacker and defender	Locating abnormalities in the electric grid

6. Discussion

Power system management and control problems are often studied as optimization problems, in which the underlying assumption is that there exists one entity with unlimited knowledge and control span [9–13]. While this approach might have been relevant for many years, it is gradually becoming unrealistic due to the decentralization and deregulation of energy markets. A major challenge is therefore to predict the development of a power system, taking into account the different objectives of many players. As many of the reviewed papers demonstrate, game theoretic approaches are especially suitable for analyzing complex interactions among different independent players. However, the type

of game that is being used and the accuracy of the model are crucial for obtaining control mechanisms and policy recommendations that are both efficient and applicable.

Most studies consider non-cooperative games and address situations in which multiple players with conflicting objectives interact. In many cases formal analysis reveals that the game has a unique equilibrium, hence allowing to predict the players' behavior and to design the system accordingly. In case of multiple equilibria the typical approach is to define appropriate regulations, in order to stir the players to the most desired outcome. In the majority of studies, this is done by designing a pricing mechanism that provides incentives for players to perform the actions needed to reach a certain goal, such as maximizing the profits of all players, balancing supply and demand, or regulating the voltage. The reviewed studies also show that taking into consideration the objectives of all players is key for designing effective mechanisms. For instance, several studies propose pricing models for demand side management, in which utility companies set prices to maximize their revenues or to improve the stability of the system, and customers respond accordingly, with an attempt to optimize their own objectives. It has been shown that in some cases such pricing mechanisms efficiently steer customers to shift their peak consumption and distribute their load throughout the day, thus reducing the peak-to-average ratio of the overall load and improving the system's efficiency. In another example, it has been found that a competitive voltage regulation market is efficient in maintaining voltage levels within normal limits and can be designed to benefit all players who participate in voltage regulation, as well as the system operator. Based on these and similar works, several studies conclude that the results obtained using a game-theoretic model are almost as good as those obtained by central planning, even when it is assumed that full knowledge is available to the central planner. Moreover, several studies show that the results obtained from game-theory-based mechanisms for supply-demand balancing and load frequency control coincide with centralized system operator optimization.

Non-cooperative game theory is also very useful for deciding on an effective energy policy. The main challenge of policy makers is to set rules that improve the overall social welfare, without diminishing the advantages of a free market. In this context, various studies employ non-cooperative game theory to examine the influence of regulation in a competitive environment, on both the overall social welfare and on each player as an individual. For example, in energy trading problems, many studies define a non-cooperative game with competing players, typically sellers and buyers, and investigate equilibrium points of the power market under various constraints. In several cases the results may help shape suitable policies. For example, it is suggested that even in competitive markets governments should apply some profit distribution mechanisms to ensure fairness. Moreover, it has been concluded that reasonable bidding rules should be considered for limiting high prices, and for preventing market manipulations by large generation companies.

Interesting results also arise from studies that employ cooperative game theory. The reviewed studies show clearly that cooperation among different entities in power system markets often improves the benefits of all cooperating players and leads to a higher social welfare. This conclusion is true for all types of applications that have been reviewed in the present work. In energy trading problems it is shown that when players can bargain directly with each other to reach binding decisions, cooperative models can improve their profits and lead to higher social welfare. For example, it is shown that distributed energy sources or interconnected micro-grids can cooperate in competitive electricity markets to increase their profits. Moreover, in energy balancing problems, cooperation is shown to be beneficial for both generators and consumers. Cooperation is found to be especially beneficial for energy sources with variable power output and uncertainties in generation, e.g., wind turbines and solar PV sources. Through cooperation the sources gain more control over their generation, and may adjust it according to the market's needs, to the benefit of all players. Moreover, it is shown that shared purchasing and management of energy storage devices allows to utilize them better, thus reducing the cost for all consumers.

Recent papers also shows that cooperation among players can be used to improve the stability of a power system. Several studies show that cooperation among generating companies can be

designed to improve the frequency stability, thus benefiting all the participants. For example, it has been shown that RoCoF-based control, in which hydro-power plants share their frequency data to regulate the speed of their rotors, can effectively regulate frequency in the interconnected system. With regard to grid planning problems, when planning the portfolio of energy sources and storage devices, including their size, location and technology, cooperative games are useful for finding the optimal mix. For example, many studies use cooperative games to find the optimal combination of renewable energy sources and storage devices in a hybrid power plant or a micro-grid. Specifically, cooperation seems to be extremely beneficial for expansion-planning problems, as several papers show that cooperation between transmission and generation expansion projects maximizes the profits of all participants and improves the utilization of the network. Other studies use a non-cooperative approach, in which a regulated transmission company is the leader, defining the expansion of the transmission system, and the generating companies react accordingly. This approach enables to define the expansion of the transmission system based on the expected reactions of the generating companies. The role of regulation in this case is to ensure that the planning of the transmission system is done to maximize the overall social welfare, rather than solely the profits of the transmission companies.

Another important conclusion of many studies is that choosing a relevant scenario and fine-tuning the assumptions of a model are crucial for the applicability of the suggested solution. Several papers show that their assumptions regarding the regulation and market rules, such as legal limitations, governmental incentives, and the business model of the utility company, have a strong impact on the results. Moreover, in some cases the suggested solutions are not feasible in certain markets, highlighting the need to define beforehand a relevant market and regulatory framework. In addition, game theoretic models that are highly accurate often lead to complex results that are hard to implement in practice. Competitive energy markets in modern electrical grids may include a significant number of players, each having a large variety of decisions, which influence a great number of components in the system. Solving such problems from a game-theoretic perspective often leads to iterative algorithms that are too complex. In such cases, many studies take an analytical approach to find equilibrium points, thus avoiding the computational burden incurred by iterative algorithms. In addition, several studies employ evolutionary game theory due to its computational efficiency.

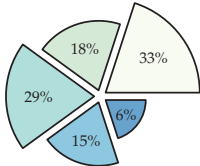





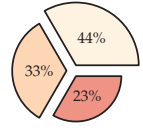



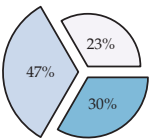



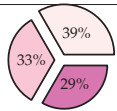



7. Current and Future Trends

We show here the results of a content analysis that targets applications of game theory in power systems. The analysis focuses on the four main applications reviewed in this paper and uses the Scopus and IEEE Xplore databases. To cover a large variety of relevant papers, we searched for the expression “game*” (the asterisk is used as a wild-card, allowing the search-engine to capture both game and games) and a combination of synonyms that describe the relevant applications. The search was also restricted to the fields title, abstract, and keywords, thus capturing only studies that use game theoretic concepts as a main approach. The search results and statistical analysis are summarized in Table 5. The first column denotes the category, the second and third columns depict the proportion of publications in a specific application area over a 7-year period, and the fourth column visualizes linear trends over the same period. The remaining columns summarize statistical data. We show trend lines, which were calculated via individual one-sample 2-sided *t*-tests, using a linear regression tool from the software “R”. Based on the results, we divide the application areas into two groups with strong ($p < 0.05$) and weak statistical significance (Note that some data cannot be accurately described using linear regression; hence, nonlinear tools have to be used instead to reveal more complex trends. However, for simplicity, we report here only explicit linear trends). We further divide the strong trend group to application areas with rapidly rising interest (slope > 3) and moderately rising interest (slope < 3):

- Strong trends-rapidly rising interest:
 - energy trading & general market, or micro-grid applications;
 - energy balancing & energy management in micro-grids;

- Strong trends—moderately rising interest:
 - energy trading & bidding strategies;
 - grid planning & generation or transmission expansion;
 - power system reliability & cyber-attacks or frequency stability;
- Weak trends—fluctuating interest:
 - energy trading & electricity pricing or profit allocation;
 - energy balancing & electric vehicles or demand side management;
 - grid planning & resource sizing, or power system reliability, or voltage stability.

Table 5. Historical trends for typical applications of game theory in power systems.

	Proportion of Publications over 2013–2019	Application Area	Trends over 2013–2019	Statistical Data		
				#	Slope	<i>p</i> -Value
Energy trading		General market		118	4.7140	0.0053
		Micro-grids		64	3.9643	0.0032
		Electricity pricing		106	0.8214	0.2578
		Bidding strategies		54	1.4643	0.0241
		Profit allocations		20	0.6429	0.2320
Energy balancing		Demand side management		126	0.8929	0.5837
		Energy management in micro-grids		94	4.4643	0.0003
		Electric vehicles		65	1.0714	0.0990
Grid planning		Generation and transmission expansion		43	1.0357	0.0369
		Micro-grids and resource sizing		90	1.9643	0.0842
		Electric vehicle charging stations		57	2.5710	0.0610
Power system reliability		Cyber attacks		47	2.1429	0.0020
		Frequency stability		40	0.3571	0.0268
		Voltage stability		35	0.9643	0.1309

The rising trends are now in the focus of the community, probably due to global initiatives targeting the development of low-carbon and energy efficient power systems, and due to more active involvement of the end-consumers in beyond-the-meter technologies. It is the authors’ opinion that several of the weak trends are the most interesting ones. For instance, generation and transmission expansion planning or voltage stability may be under-evaluated topics, which fits nicely in line with the game-theoretical formalism.

8. Conclusions

This study reviews recent papers that employ game theoretic tools to study the operation and design of modern electric grids, with a focus on four application areas: energy trading, energy balancing, grid planning, and power systems reliability. One central conclusion is that modeling the system from the perspective of one entity with unlimited information and control span is often impractical; hence, correct modeling of the selfish behavior of independent players may be critical

for the development of future power systems. In this context, game theoretic approaches seem to be particularly suitable for analyzing complex interactions among different independent players that participate in energy markets, and response to energy policies. Most studies consider non-cooperative games, in which it is consistently shown that proper incentives and regulations are crucial for optimizing the social welfare. In addition, several studies show that correct usage of incentives by appropriate regulation or sophisticated pricing mechanisms may improve the social welfare, and in several cases the results obtained are almost as good as those obtained by central planning. Interesting results also arise from studies that employ cooperative game theory, which clearly show that cooperation among different entities in power system markets often improves the benefits of all cooperating players. This conclusion holds for all types of applications that have been reviewed in the present study.

Based on an extensive content analysis, we point to several trends in the current research, and offer directions for new research. First, it is the authors' opinion that several of the weak trends identified in Section 7 might have been overlooked and deserve more attention. More specifically, some of the less explored topics are multi-stage planning problems, profit allocation among aggregators of distributed energy sources and flexible loads, and voltage regulation in smart grids. Concerning the type of game, most works formulate a static game with a single stage, which may be used to reflect a situation in which players decide simultaneously. However, in reality, many processes are dynamic and develop over many stages; hence, there is room for additional studies that focus on multi-stage games.

Moreover, to ensure the accuracy of the results and feasibility of the suggested solutions, future studies may emphasize the operational constraints imposed by electricity and natural gas networks. In addition, a key limitation of game theory is the resulting computational complexity, which increases exponentially with the number of players. Therefore, developing algorithms that reduce the computational burden may be a promising research direction. In the context of electric vehicles, when implementing energy charging scheduling schemes that require real-time data, it may be of interest to consider the privacy of electric vehicle owners. A possible direction to tackle this problem could be employing tools from Bayesian game theory. In addition, uncertainties in the arrival and departure times of electric vehicles in charging stations can be studied in the context of dynamic or stochastic games. Regarding the topic of cyber-attacks, there seems to be a shortage of models that consider cooperation among players with common goals. Indeed, several papers study cooperation among defenders, however cooperation among attackers should be considered, as well, when evaluating cyber-security. Lastly, only a few studies use game theory, in particular cooperative game theory, in order to explore the issue of voltage stability. This may become an important topic due to the ongoing deregulation of power markets and the continuing integration of renewable energy sources.

Author Contributions: All authors have worked on this research together and they have approved the paper. All authors have read and agreed to the published version of the manuscript.

Funding: This research was funded by Israel Science Foundation, grant number 1227/18.

Conflicts of Interest: The authors declare no conflict of interest.

Abbreviations

The following abbreviations are used in this manuscript:

DER	Distributed energy resource
DG	Distributed generation
ES	Energy storage
EV	Electric vehicle
HVDC	High-voltage direct current

LFC	Load frequency control
MG	Micro-grid
PV	Photovoltaic
RES	Renewable energy sources
TCL	Thermostatically controlled load

References

1. Leach, G. The energy transition. *Energy Policy* **1992**, *20*, 116–123. [[CrossRef](#)]
2. Strauch, Y. Beyond the low-carbon niche: Global tipping points in the rise of wind, solar, and electric vehicles to regime scale systems. *Energy Res. Soc. Sci.* **2020**, *62*, 101364. [[CrossRef](#)]
3. Klessmann, C.; Held, A.; Rathmann, M.; Ragwitz, M. Status and perspectives of renewable energy policy and deployment in the European Union—What is needed to reach the 2020 targets? *Energy Policy* **2011**, *39*, 7637–7657. [[CrossRef](#)]
4. Huang, Y.W.; Kittner, N.; Kammen, D.M. ASEAN grid flexibility: Preparedness for grid integration of renewable energy. *Energy Policy* **2019**, *128*, 711–726. [[CrossRef](#)]
5. Zhang, Y.; Chen, J.; Cai, L.; Pan, J. Expanding EV Charging Networks Considering Transportation Pattern and Power Supply Limit. *IEEE Trans. Smart Grid* **2019**, *10*, 6332–6342. [[CrossRef](#)]
6. Soares, J.; Pinto, T.; Lezama, F.; Morais, H. Survey on Complex Optimization and Simulation for the New Power Systems Paradigm. *Complexity* **2018**, *2018*, 1–32. [[CrossRef](#)]
7. Quijano, N.; Ocampo-Martinez, C.; Barreiro-Gomez, J.; Obando, G.; Pantoja, A.; Mojica-Nava, E. The Role of Population Games and Evolutionary Dynamics in Distributed Control Systems: The Advantages of Evolutionary Game Theory. *IEEE Control Syst.* **2017**, *37*, 70–97. [[CrossRef](#)]
8. Gholizad, A.; Ahmadi, L.; Hassannayebi, E.; Memarpour, M.; Shakibayifar, M. A System Dynamics Model for the Analysis of the Deregulation in Electricity Market. *Int. J. Syst. Dyn. Appl.* **2017**, *6*, 1–30. [[CrossRef](#)]
9. Weitemeyer, S.; Kleinhans, D.; Siemer, L.; Agert, C. Optimal combination of energy storages for prospective power supply systems based on Renewable Energy Sources. *J. Energy Storage* **2018**, *20*, 581–589. [[CrossRef](#)]
10. Child, M.; Bogdanov, D.; Breyer, C. The role of storage technologies for the transition to a 100% renewable energy system in Europe. *Energy Procedia* **2018**, *155*, 44–60. [[CrossRef](#)]
11. Haas, J.; Cebulla, F.; Nowak, W.; Rahmann, C.; Palma-Behnke, R. A multi-service approach for planning the optimal mix of energy storage technologies in a fully-renewable power supply. *Energy Convers. Manag.* **2018**, *178*, 355–368. [[CrossRef](#)]
12. Limpens, G.; Jeanmart, H. Electricity storage needs for the energy transition: An EROI based analysis illustrated by the case of Belgium. *Energy* **2018**, *152*, 960–973. [[CrossRef](#)]
13. Esteban, M.; Zhang, Q.; Utama, A. Estimation of the energy storage requirement of a future 100% renewable energy system in Japan. *Energy Policy* **2012**, *47*, 22–31. [[CrossRef](#)]
14. Breton, A.; Haurie, A.; Kalocsai, R. Efficient management of interconnected power systems: A game-theoretic approach. *Automatica* **1978**, *14*, 443–452. [[CrossRef](#)]
15. Martin, R.W.; Dillon, T.S. Solutions of the problem of stochastic optimal control of hydro-thermal power systems. *IFAC Proc. Vol.* **1977**, *10*, 257–264. [[CrossRef](#)]
16. Bobrowski, W. Some Problems Connected with Arriving at a Decision as to the Selection of Protection for a Power Plant. *Arch Elektrotech* **1972**, *21*, 669–674.
17. Fadlullah, Z.M.; Nozaki, Y.; Takeuchi, A.; Kato, N. A survey of game theoretic approaches in smart grid. In Proceedings of the 2011 International Conference on Wireless Communications and Signal Processing (WCSP), Nanjing, China, 9–11 November 2011. [[CrossRef](#)]
18. Mei, S.; Wei, W.; Liu, F. On engineering game theory with its application in power systems. *Control Theory Technol.* **2017**, *15*, 1–12. [[CrossRef](#)]
19. Abapour, S.; Nazari-Heris, M.; Mohammadi-Ivatloo, B.; Hagh, M.T. Game Theory Approaches for the Solution of Power System Problems: A Comprehensive Review. *Arch. Comput. Methods Eng.* **2018**, *27*, 81–103. [[CrossRef](#)]
20. Eslahi-Kelorazi, M.; Parand, F.A. Game theoretic approaches in modeling and solving smart grid issues. In Proceedings of the 2015 2nd International Conference on Knowledge-Based Engineering and Innovation (KBEI), Tehran, Iran, 5–6 November 2015. [[CrossRef](#)]

21. Pilz, M.; Al-Fagih, L. Recent Advances in Local Energy Trading in the Smart Grid Based on Game-Theoretic Approaches. *IEEE Trans. Smart Grid* **2019**, *10*, 1363–1371. [[CrossRef](#)]
22. Loni, A.; Parand, F.A. A survey of game theory approach in smart grid with emphasis on cooperative games. In Proceedings of the 2017 IEEE International Conference on Smart Grid and Smart Cities (ICSGSC), Singapore, 23–26 July 2017. [[CrossRef](#)]
23. Saad, W.; Han, Z.; Poor, H.; Basar, T. Game-Theoretic Methods for the Smart Grid: An Overview of Microgrid Systems, Demand-Side Management, and Smart Grid Communications. *IEEE Signal Process. Mag.* **2012**, *29*, 86–105. [[CrossRef](#)]
24. Cheng, L.; Yu, T. Game-Theoretic Approaches Applied to Transactions in the Open and Ever-Growing Electricity Markets From the Perspective of Power Demand Response: An Overview. *IEEE Access* **2019**, *7*, 25727–25762. [[CrossRef](#)]
25. Saad, W.; Han, Z.; Poor, H.V.; Basar, T. A noncooperative game for double auction-based energy trading between PHEVs and distribution grids. In Proceedings of the 2011 IEEE International Conference on Smart Grid Communications (SmartGridComm), Brussels, Belgium, 17–20 October 2011. [[CrossRef](#)]
26. Wang, Y.; Saad, W.; Han, Z.; Poor, H.V.; Basar, T. A Game-Theoretic Approach to Energy Trading in the Smart Grid. *IEEE Trans. Smart Grid* **2014**, *5*, 1439–1450. [[CrossRef](#)]
27. Su, W.; Huang, A.Q. A game theoretic framework for a next-generation retail electricity market with high penetration of distributed residential electricity suppliers. *Appl. Energy* **2014**, *119*, 341–350. [[CrossRef](#)]
28. Tushar, W.; Zhang, J.A.; Smith, D.B.; Poor, H.V.; Thiebaux, S. Prioritizing Consumers in Smart Grid: A Game Theoretic Approach. *IEEE Trans. Smart Grid* **2014**, *5*, 1429–1438. [[CrossRef](#)]
29. Rahi, G.E.; Etesami, S.R.; Saad, W.; Mandayam, N.B.; Poor, H.V. Managing Price Uncertainty in Prosumer-Centric Energy Trading: A Prospect-Theoretic Stackelberg Game Approach. *IEEE Trans. Smart Grid* **2019**, *10*, 702–713. [[CrossRef](#)]
30. Yu, N.; Tesfatsion, L.; Liu, C.C. Financial Bilateral Contract Negotiation in Wholesale Electricity Markets Using Nash Bargaining Theory. *IEEE Trans. Power Syst.* **2012**, *27*, 251–267. [[CrossRef](#)]
31. Fan, S.; Ai, Q.; Piao, L. Bargaining-based cooperative energy trading for distribution company and demand response. *Appl. Energy* **2018**, *226*, 469–482. [[CrossRef](#)]
32. Ladjici, A.; Tiguercha, A.; Boudour, M. Nash Equilibrium in a two-settlement electricity market using competitive coevolutionary algorithms. *Int. J. Electr. Power Energy Syst.* **2014**, *57*, 148–155. [[CrossRef](#)]
33. Cintuglu, M.H.; Martin, H.; Mohammed, O.A. Real-Time Implementation of Multiagent-Based Game Theory Reverse Auction Model for Microgrid Market Operation. *IEEE Trans. Smart Grid* **2015**, *6*, 1064–1072. [[CrossRef](#)]
34. Wu, Y.; Barati, M.; Lim, G.J. A Pool Strategy of Microgrid in Power Distribution Electricity Market. *IEEE Trans. Power Syst.* **2020**, *35*, 3–12. [[CrossRef](#)]
35. Prete, C.L.; Hobbs, B.F. A cooperative game theoretic analysis of incentives for microgrids in regulated electricity markets. *Appl. Energy* **2016**, *169*, 524–541. [[CrossRef](#)]
36. Paudel, A.; Chaudhari, K.; Long, C.; Gooi, H.B. Peer-to-Peer Energy Trading in a Prosumer-Based Community Microgrid: A Game-Theoretic Model. *IEEE Trans. Ind. Electron.* **2019**, *66*, 6087–6097. [[CrossRef](#)]
37. Park, S.; Lee, J.; Bae, S.; Hwang, G.; Choi, J.K. Contribution-Based Energy-Trading Mechanism in Microgrids for Future Smart Grid: A Game Theoretic Approach. *IEEE Trans. Ind. Electron.* **2016**, *63*, 4255–4265. [[CrossRef](#)]
38. Lee, J.; Guo, J.; Choi, J.K.; Zukerman, M. Distributed Energy Trading in Microgrids: A Game-Theoretic Model and Its Equilibrium Analysis. *IEEE Trans. Ind. Electron.* **2015**, *62*, 3524–3533. [[CrossRef](#)]
39. Wang, H.; Huang, J. Incentivizing Energy Trading for Interconnected Microgrids. *IEEE Trans. Smart Grid* **2018**, *9*, 2647–2657. [[CrossRef](#)]
40. Yang, P.; Tang, G.; Nehorai, A. A game-theoretic approach for optimal time-of-use electricity pricing. *IEEE Trans. Power Syst.* **2013**, *28*, 884–892. [[CrossRef](#)]
41. Srinivasan, D.; Rajgarhia, S.; Radhakrishnan, B.M.; Sharma, A.; Khincha, H. Game-Theory based dynamic pricing strategies for demand side management in smart grids. *Energy* **2017**, *126*, 132–143. [[CrossRef](#)]
42. Ma, K.; Wang, C.; Yang, J.; Hua, C.; Guan, X. Pricing Mechanism With Noncooperative Game and Revenue Sharing Contract in Electricity Market. *IEEE Trans. Cybern.* **2019**, *49*, 97–106. [[CrossRef](#)]
43. Ma, T.; Wu, J.; Hao, L.; Yan, H.; Li, D. A Real-Time Pricing Scheme for Energy Management in Integrated Energy Systems: A Stackelberg Game Approach. *Energies* **2018**, *11*, 2858. [[CrossRef](#)]

44. Cheng, L.; Yu, T. Nash Equilibrium-Based Asymptotic Stability Analysis of Multi-Group Asymmetric Evolutionary Games in Typical Scenario of Electricity Market. *IEEE Access* **2018**, *6*, 32064–32086. [[CrossRef](#)]
45. Song, H.; Liu, C.C.; Lawarree, J. Nash equilibrium bidding strategies in a bilateral electricity market. *IEEE Trans. Power Syst.* **2002**, *17*, 73–79. [[CrossRef](#)]
46. Song, Y.; Ni, Y.; Wen, F.; Hou, Z.; Wu, F.F. Conjectural variation based bidding strategy in spot markets: fundamentals and comparison with classical game theoretical bidding strategies. *Electr. Power Syst. Res.* **2003**, *67*, 45–51. [[CrossRef](#)]
47. Dai, T.; Qiao, W. Trading Wind Power in a Competitive Electricity Market Using Stochastic Programming and Game Theory. *IEEE Trans. Sustain. Energy* **2013**, *4*, 805–815. [[CrossRef](#)]
48. Marzband, M.; Javadi, M.; Domínguez-García, J.L.; Moghaddam, M.M. Non-cooperative game theory based energy management systems for energy district in the retail market considering DER uncertainties. *IET Gener. Transm. Distrib.* **2016**, *10*, 2999–3009. [[CrossRef](#)]
49. Wang, J.; Zhou, Z.; Botterud, A. An evolutionary game approach to analyzing bidding strategies in electricity markets with elastic demand. *Energy* **2011**, *36*, 3459–3467. [[CrossRef](#)]
50. Jia, N.; Yokoyama, R. Profit allocation of independent power producers based on cooperative Game theory. *Int. J. Electr. Power Energy Syst.* **2003**, *25*, 633–641. [[CrossRef](#)]
51. Dabbagh, S.R.; Sheikh-El-Eslami, M.K. Risk-based profit allocation to DERs integrated with a virtual power plant using cooperative Game theory. *Electr. Power Syst. Res.* **2015**, *121*, 368–378. [[CrossRef](#)]
52. Chakraborty, P.; Baeyens, E.; Khargonekar, P.P. Distributed control of flexible demand using proportional allocation mechanism in a smart grid: Game theoretic interaction and price of anarchy. *Sustain. Energy, Grids Networks* **2017**, *12*, 30–39. [[CrossRef](#)]
53. Yaagoubi, N.; Mouftah, H.T. User-aware game theoretic approach for demand management. *IEEE Trans. Smart Grid* **2014**, *6*, 716–725. [[CrossRef](#)]
54. Chen, H.; Li, Y.; Louie, R.H.; Vucetic, B. Autonomous demand side management based on energy consumption scheduling and instantaneous load billing: An aggregative game approach. *IEEE Trans. Smart Grid* **2014**, *5*, 1744–1754. [[CrossRef](#)]
55. Atzeni, I.; Ordóñez, L.G.; Scutari, G.; Palomar, D.P.; Fonollosa, J.R. Demand-side management via distributed energy generation and storage optimization. *IEEE Trans. Smart Grid* **2012**, *4*, 866–876. [[CrossRef](#)]
56. Soliman, H.M.; Leon-Garcia, A. Game-theoretic demand side management with storage devices for the future smart grid. *IEEE Trans. Smart Grid* **2014**, *5*, 1475–1485. [[CrossRef](#)]
57. Nguyen, H.K.; Song, J.B.; Han, Z. Distributed demand side management with energy storage in smart grid. *IEEE Trans. Parallel Distrib. Syst.* **2014**, *26*, 3346–3357. [[CrossRef](#)]
58. Arai, R.; Yamamoto, K.; Morikura, M. Differential game-theoretic framework for a demand side energy management system. In Proceedings of the 2013 IEEE International Conference on Smart Grid Communications (SmartGridComm), Vancouver, BC, Canada, 21–24 October 2013; pp. 768–773. [[CrossRef](#)]
59. Belhaiza, S.; Baroudi, U. A game theoretic model for smart grids demand management. *IEEE Trans. Smart Grid* **2014**, *6*, 1386–1393. [[CrossRef](#)]
60. Alshehri, K.; Liu, J.; Chen, X.; Başar, T. A Stackelberg game for multi-period demand response management in the smart grid. In Proceedings of the 54th IEEE Conference on Decision and Control, Osaka, Japan, 15–18 December 2015; pp. 5889–5894. [[CrossRef](#)]
61. Belhaiza, S.; Baroudi, U.; Elhallaoui, I. A Game Theoretic Model for the Multiperiodic Smart Grid Demand Response Problem. *IEEE Syst. J.* **2019**. [[CrossRef](#)]
62. Yu, M.; Hong, S.H. A real-time demand-response algorithm for smart grids: A stackelberg game approach. *IEEE Trans. Smart Grid* **2015**, *7*, 879–888. [[CrossRef](#)]
63. Tran, N.H.; Tran, D.H.; Ren, S.; Han, Z.; Huh, E.N.; Hong, C.S. How geo-distributed data centers do demand response: A game-theoretic approach. *IEEE Trans. Smart Grid* **2015**, *7*, 937–947. [[CrossRef](#)]
64. Bingtuan, G.; Xiaofeng, L.; Cheng, W.; Yi, T. Game-theoretic energy management with storage capacity optimization in the smart grids. *J. Mod. Power Syst. Clean Energy* **2018**, *6*, 656–667. [[CrossRef](#)]
65. Deng, R.; Yang, Z.; Chen, J.; Asr, N.R.; Chow, M.Y. Residential energy consumption scheduling: A coupled-constraint game approach. *IEEE Trans. Smart Grid* **2014**, *5*, 1340–1350. [[CrossRef](#)]
66. Yin, H.; Zhao, C.; Li, M.; Ma, C.; Chow, M.Y. A game theory approach to energy management of an engine-generator/battery/ultracapacitor hybrid energy system. *IEEE Trans. Ind. Electron.* **2016**, *63*, 4266–4277. [[CrossRef](#)]

67. Mondal, A.; Misra, S.; Obaidat, M.S. Distributed home energy management system with storage in smart grid using game theory. *IEEE Syst. J.* **2015**, *11*, 1857–1866. [[CrossRef](#)]
68. Liu, N.; Cheng, M.; Yu, X.; Zhong, J.; Lei, J. Energy-sharing provider for PV prosumer clusters: A hybrid approach using stochastic programming and stackelberg game. *IEEE Trans. Ind. Electron.* **2018**, *65*, 6740–6750. [[CrossRef](#)]
69. Fleischhacker, A.; Auer, H.; Lettner, G.; Botterud, A. Sharing solar PV and energy storage in apartment buildings: resource allocation and pricing. *IEEE Trans. Smart Grid* **2018**, *10*, 3963–3973. [[CrossRef](#)]
70. Chakraborty, P.; Baeyens, E.; Poolla, K.; Khargonekar, P.P.; Varaiya, P. Sharing Storage in a Smart Grid: A Coalitional Game Approach. *IEEE Trans. Smart Grid* **2018**, *10*, 4379–4390. [[CrossRef](#)]
71. Kiedanski, D.; Orda, A.; Kofman, D. The effect of ramp constraints on coalitional storage games. In Proceedings of the Tenth ACM International Conference on Future Energy Systems-e-Energy 19, Phoenix, AZ, USA, 25–28 June 2019; ACM Press: New York, NY, USA. 2019.
72. Kiedanski, D.; Orda, A.; Kofman, D. Discrete and stochastic coalitional storage games. In Proceedings of the Tenth ACM International Conference on Future Energy Systems-e-Energy 20, Virtual Event, Melbourne, Australia, 23–26 June 2020; ACM Press: New York, NY, USA. 2020.
73. Fan, S.; Li, Z.; Wang, J.; Piao, L.; Ai, Q. Cooperative economic scheduling for multiple energy hubs: A bargaining game theoretic perspective. *IEEE Access* **2018**, *6*, 27777–27789. [[CrossRef](#)]
74. Han, L.; Morstyn, T.; McCulloch, M. Incentivizing prosumer coalitions with energy management using cooperative game theory. *IEEE Trans. Power Syst.* **2018**, *34*, 303–313. [[CrossRef](#)]
75. Yang, H.; Xie, X.; Vasilakos, A.V. Noncooperative and cooperative optimization of electric vehicle charging under demand uncertainty: A robust Stackelberg game. *IEEE Trans. Veh. Technol.* **2015**, *65*, 1043–1058. [[CrossRef](#)]
76. Yoon, S.G.; Choi, Y.J.; Park, J.K.; Bahk, S. Stackelberg-game-based demand response for at-home electric vehicle charging. *IEEE Trans. Veh. Technol.* **2015**, *65*, 4172–4184. [[CrossRef](#)]
77. Zhu, Z.; Lambbotharan, S.; Chin, W.H.; Fan, Z. A mean field game theoretic approach to electric vehicles charging. *IEEE Access* **2016**, *4*, 3501–3510. [[CrossRef](#)]
78. Li, J.; Li, C.; Xu, Y.; Dong, Z.Y.; Wong, K.P.; Huang, T. Noncooperative game-based distributed charging control for plug-in electric vehicles in distribution networks. *IEEE Trans. Ind. Inform.* **2016**, *14*, 301–310. [[CrossRef](#)]
79. El-Moaty, A.M.A.; Mesbah, W.; Al-Awami, A.T. Incentive-Based Game Theoretic Approach for Wind Power Balancing Using Electric Vehicles. In Proceedings of the 9th IEEE-GCC Conference and Exhibition, Manama, Bahrain, 8–11 May 2017; pp. 1–9. [[CrossRef](#)]
80. Mediawathe, C.P.; Smith, D.B. Game-theoretic electric vehicle charging management resilient to non-ideal user behavior. *IEEE Trans. Intell. Transp. Syst.* **2018**, *19*, 3486–3495. [[CrossRef](#)]
81. Liu, X.; Gao, B.; Zhu, Z.; Tang, Y. Non-cooperative and cooperative optimisation of battery energy storage system for energy management in multi-microgrid. *IET Gener. Transm. Distrib.* **2018**, *12*, 2369–2377. [[CrossRef](#)]
82. Chuang, A.; Wu, F.; Varaiya, P. A game-theoretic model for generation expansion planning: problem formulation and numerical comparisons. *IEEE Trans. Power Syst.* **2001**, *16*, 885–891. [[CrossRef](#)]
83. Jahromi, M.Z.; Bioki, M.M.H.; Rashidinejad, M.; Fadaeinedjad, R. Transmission and generation expansion planning considering loadability limit using game theory & ANN. In Proceedings of the 2012 11th International Conference on Environment and Electrical Engineering, Venice, Italy, 18–25 May 2012. [[CrossRef](#)]
84. Sun, C.; Chen, L.; Wang, L.; Wei, W.; Zheng, T.; Mei, S. Energy Storage-Transmission Line Planning Based on Complete Information Static Game Model. In Proceedings of the 2019 IEEE Innovative Smart Grid Technologies—Asia (ISGT Asia), Chengdu, China, 21–24 May 2019. [[CrossRef](#)]
85. Jenabi, M.; Ghomi, S.M.T.F.; Smeers, Y. Bi-Level Game Approaches for Coordination of Generation and Transmission Expansion Planning Within a Market Environment. *IEEE Trans. Power Syst.* **2013**, *28*, 2639–2650. [[CrossRef](#)]
86. Banez-Chicharro, F.; Olmos, L.; Ramos, A.; Latorre, J.M. Beneficiaries of transmission expansion projects of an expansion plan: An Aumann-Shapley approach. *Appl. Energy* **2017**, *195*, 382–401. [[CrossRef](#)]
87. Zhou, Q.; Tesfatsion, L.; Liu, C.C.; Chu, R.F.; Sun, W. A Nash Approach to Planning Merchant Transmission for Renewable Resource Integration. *IEEE Trans. Power Syst.* **2013**, *28*, 2086–2100. [[CrossRef](#)]

88. Kristiansen, M.; Korpås, M.; Svendsen, H.G. A generic framework for power system flexibility analysis using cooperative game theory. *Appl. Energy* **2018**, *212*, 223–232. [[CrossRef](#)]
89. Jung, S.; Kim, D. Pareto-Efficient Capacity Planning for Residential Photovoltaic Generation and Energy Storage with Demand-Side Load Management. *Energies* **2017**, *10*, 426. [[CrossRef](#)]
90. Moradi, M.H.; Abedini, M.; Hosseini, S.M. A Combination of Evolutionary Algorithm and Game Theory for Optimal Location and Operation of DG from DG Owner Standpoints. *IEEE Trans. Smart Grid* **2015**, *1*. [[CrossRef](#)]
91. Stevanoni, C.; Greve, Z.D.; Vallee, F.; Deblecker, O. Long-Term Planning of Connected Industrial Microgrids: A Game Theoretical Approach Including Daily Peer-to-Microgrid Exchanges. *IEEE Trans. Smart Grid* **2019**, *10*, 2245–2256. [[CrossRef](#)]
92. Hakimi, S.M.; Bagheritarbar, H.; Hasankhani, A.; Shafie-khah, M.; Lotfi, M.; Catalao, J.P.S. Planning of Smart Microgrids with High Renewable Penetration Considering Electricity Market Conditions. In Proceedings of the 2019 IEEE International Conference on Environment and Electrical Engineering and 2019 IEEE Industrial and Commercial Power Systems Europe (EEEIC/I&CPS Europe), Genova, Italy, 11–14 June 2019. [[CrossRef](#)]
93. Ali, L.; Muyeen, S.; Bizhani, H.; Ghosh, A. Optimal planning of clustered microgrid using a technique of cooperative game theory. *Electr. Power Syst. Res.* **2020**, *183*, 106262. [[CrossRef](#)]
94. Han, X.; Ji, T.; Zhao, Z.; Zhang, H. Economic evaluation of batteries planning in energy storage power stations for load shifting. *Renew. Energy* **2015**, *78*, 643–647. [[CrossRef](#)]
95. Zhang, X.; Chan, K.; Wang, H.; Hu, J.; Zhou, B.; Zhang, Y.; Qiu, J. Game-theoretic planning for integrated energy system with independent participants considering ancillary services of power-to-gas stations. *Energy* **2019**, *176*, 249–264. [[CrossRef](#)]
96. Mei, S.; Wang, Y.; Liu, F.; Zhang, X.; Sun, Z. Game Approaches for Hybrid Power System Planning. *IEEE Trans. Sustain. Energy* **2012**, *3*, 506–517. [[CrossRef](#)]
97. Wang, H.; Huang, J. Cooperative Planning of Renewable Generations for Interconnected Microgrids. *IEEE Trans. Smart Grid* **2016**, *7*, 2486–2496. [[CrossRef](#)]
98. Xiong, Y.; Gan, J.; An, B.; Miao, C.; Bazzan, A.L.C. Optimal Electric Vehicle Fast Charging Station Placement Based on Game Theoretical Framework. *IEEE Trans. Intell. Transp. Syst.* **2018**, *19*, 2493–2504. [[CrossRef](#)]
99. Luo, C.; Huang, Y.F.; Gupta, V. Placement of EV Charging Stations—Balancing Benefits Among Multiple Entities. *IEEE Trans. Smart Grid* **2015**, *1*–10. [[CrossRef](#)]
100. Salyani, P.; Abapour, M.; Zare, K. Stackelberg based optimal planning of DGs and electric vehicle parking lot by implementing demand response program. *Sustain. Cities Soc.* **2019**, *51*, 101743. [[CrossRef](#)]
101. Pahlavanhoseini, A.; Sepasian, M.S. Optimal planning of PEV fast charging stations using nash bargaining theory. *J. Energy Storage* **2019**, *25*, 100831. [[CrossRef](#)]
102. Yu, Y.; Song, T.; Su, C.; Tang, X.; Han, Z. Hierarchical Game for Electric Vehicle Public Charging Market. In Proceedings of the 2019 IEEE International Conference on Communications, Control, and Computing Technologies for Smart Grids (SmartGridComm), Beijing, China, 21–23 October 2019. [[CrossRef](#)]
103. Shahidehpour, M.; Tinney, F.; Fu, Y. Impact of Security on Power Systems Operation. *Proc. IEEE* **2005**, *93*, 2013–2025. [[CrossRef](#)]
104. Rayati, M.; Toulabi, M.; Ranjbar, A.M. Optimal Generalized Bayesian Nash Equilibrium of Frequency-Constrained Electricity Market in the Presence of Renewable Energy Sources. *IEEE Trans. Sustain. Energy* **2020**, *11*, 136–144. [[CrossRef](#)]
105. Xu, Q.; Zhang, N.; Kang, C.; Xia, Q.; He, D.; Liu, C.; Huang, Y.; Cheng, L.; Bai, J. A Game Theoretical Pricing Mechanism for Multi-Area Spinning Reserve Trading Considering Wind Power Uncertainty. *IEEE Trans. Power Syst.* **2016**, *31*, 1084–1095. [[CrossRef](#)]
106. Paola, A.D.; Trovato, V.; Angeli, D.; Strbac, G. A Mean Field Game Approach for Distributed Control of Thermostatic Loads Acting in Simultaneous Energy-Frequency Response Markets. *IEEE Trans. Smart Grid* **2019**, *10*, 5987–5999. [[CrossRef](#)]
107. Namerikawa, T.; Okubo, N.; Sato, R.; Okawa, Y.; Ono, M. Real-Time Pricing Mechanism for Electricity Market With Built-In Incentive for Participation. *IEEE Trans. Smart Grid* **2015**, *6*, 2714–2724. [[CrossRef](#)]
108. Sun, B.; Tang, Y.; Ye, L.; Chen, C.; Zhang, C.; Zhong, W. A Frequency Control Strategy Considering Large Scale Wind Power Cluster Integration Based on Distributed Model Predictive Control. *Energies* **2018**, *11*, 1600. [[CrossRef](#)]

109. Chen, H.; Ye, R.; Wang, X.; Lu, R. Cooperative Control of Power System Load and Frequency by Using Differential Games. *IEEE Trans. Control. Syst. Technol.* **2015**, *23*, 882–897. [[CrossRef](#)]
110. Wang, N.; Zhang, J.; He, Y.; Liu, M.; Zhang, Y.; Chen, C.; Gu, Y.; Ren, Y. Load-Frequency Control of Multi-Area Power System Based on the Improved Weighted Fruit Fly Optimization Algorithm. *Energies* **2020**, *13*, 437. [[CrossRef](#)]
111. Chamorro, H.R.; Sanchez, A.C.; Pantoja, A.; Zelinka, I.; Gonzalez-Longatt, F.; Sood, V.K. A network control system for hydro plants to counteract the non-synchronous generation integration. *Int. J. Electr. Power Energy Syst.* **2019**, *105*, 404–419. [[CrossRef](#)]
112. Wu, C.; Hug, G.; Kar, S. Smart Inverter for Voltage Regulation: Physical and Market Implementation. *IEEE Trans. Power Syst.* **2018**, *33*, 6181–6192. [[CrossRef](#)]
113. del Nozal, A.R.; Orihuela, L.; Millan, P. A Game-Theoretic Framework for Distributed Voltage Regulation over HVDC grids. In Proceedings of the 2018 European Control Conference (ECC), Limassol, Cyprus, 12–15 June 2018. [[CrossRef](#)]
114. Ghosh, A.; Aggarwal, V. Penalty Based Control Mechanism for Strategic Prosumers in a Distribution Network. *Energies* **2020**, *13*, 452. [[CrossRef](#)]
115. Dissanayake, A.M.; Ekneligoda, N.C. Game theoretic transient control of parallel connected inverters in islanded microgrids. In Proceedings of the 2018 IEEE Power & Energy Society Innovative Smart Grid Technologies Conference (ISGT), Washington, DC, USA, 19–22 February 2018. [[CrossRef](#)]
116. Chen, J.; Zhu, Q. A Stackelberg Game Approach for Two-Level Distributed Energy Management in Smart Grids. *IEEE Trans. Smart Grid* **2018**, *9*, 6554–6565. [[CrossRef](#)]
117. Bi, W.; Chen, C.; Zhang, K. Optimal Strategy of Attack-Defense Interaction Over Load Frequency Control Considering Incomplete Information. *IEEE Access* **2019**, *7*, 75342–75349. [[CrossRef](#)]
118. Abusorrah, A.; Alabdulwahab, A.; Li, Z.; Shahidehpour, M. Minimax-Regret Robust Defensive Strategy Against False Data Injection Attacks. *IEEE Trans. Smart Grid* **2019**, *10*, 2068–2079. [[CrossRef](#)]
119. Farraj, A.; Hammad, E.; Daoud, A.A.; Kundur, D. A Game-Theoretic Analysis of Cyber Switching Attacks and Mitigation in Smart Grid Systems. *IEEE Trans. Smart Grid* **2016**, *7*, 1846–1855. [[CrossRef](#)]
120. Srikantha, P.; Kundur, D. A DER Attack-Mitigation Differential Game for Smart Grid Security Analysis. *IEEE Trans. Smart Grid* **2016**, *7*, 1476–1485. [[CrossRef](#)]
121. Hasan, S.; Dubey, A.; Karsai, G.; Koutsoukos, X. A game-theoretic approach for power systems defense against dynamic cyber-attacks. *Int. J. Electr. Power Energy Syst.* **2020**, *115*, 105432. [[CrossRef](#)]
122. Chen, G.; Dong, Z.Y.; Hill, D.J.; Xue, Y.S. Exploring Reliable Strategies for Defending Power Systems Against Targeted Attacks. *IEEE Trans. Power Syst.* **2011**, *26*, 1000–1009. [[CrossRef](#)]
123. Tas, S.; Bier, V.M. Addressing vulnerability to cascading failure against intelligent adversaries in power networks. *Energy Syst.* **2014**, *7*, 193–213. [[CrossRef](#)]
124. Zhan, T.S.; Kuo, C.L.; Chen, S.J.; Chen, J.L.; Kao, C.C.; Lin, C.H. Non-technical loss and power blackout detection under advanced metering infrastructure using a cooperative game based inference mechanism. *IET Gener. Transm. Distrib.* **2016**, *10*, 873–882. [[CrossRef](#)]



© 2020 by the authors. Licensee MDPI, Basel, Switzerland. This article is an open access article distributed under the terms and conditions of the Creative Commons Attribution (CC BY) license (<http://creativecommons.org/licenses/by/4.0/>).

Review

Grid-Connected PV Generation System—Components and Challenges: A Review

Muhammad Hafeez Mohamed Hariri ^{1,*}, Mohd Khairunaz Mat Desa ¹, Syafrudin Masri ² and Muhammad Ammirul Atiqi Mohd Zainuri ³

¹ School of Electrical and Electronic Engineering, Engineering Campus, Universiti Sains Malaysia (USM), Nibong Tebal, Penang 14300, Malaysia; khairunaz@usm.my

² Faculty of Science and Technology, Universitas Muhammadiyah Bandung (UMB), Bandung 40614, Indonesia; syafrudin@umbandung.ac.id

³ Department of Electrical, Electronic and System Engineering, Faculty of Engineering and Built Environment, Universiti Kebangsaan Malaysia (UKM), Bangi 43600, Malaysia; ammirulatiqi@ukm.edu.my

* Correspondence: mhmh14_eee069@student.usm.my

Received: 8 June 2020; Accepted: 11 August 2020; Published: 19 August 2020

Abstract: Renewable energy (RE) has become a focal point of interest as an alternative source of energy to the traditional fossil fuel and other energy sources due to the fact that it is more environmentally friendly, abundant and economically feasible. Many countries aggressively promote feed-in tariff schemes and solar photovoltaic (PV) systems have become one of the fastest growing RE sources that can be integrated into the grid distribution network. This paper reviews the recent development of grid-connected PV (GPV) generation systems comprising of several sub-components such as PV modules, DC-DC converter, maximum power point tracking (MPPT) technique, and an inverter. In addition, various grid synchronization and islanding detection methods are elaborated. The future key challenges to build a smart and efficient GPV generation system were also presented.

Keywords: renewable energy (RE); photovoltaic (PV); maximum power point tracking (MPPT); grid synchronization; phase locked loop (PLL)

1. Introduction

As both world population and standard of living increase, the demand for commercial energy is projected to continue its ascending trend [1]. The United Nations estimates the world population will further upsurge to 11.2 billion in the year 2100 [2]. Energy is the key determinant of the expansion of industrialization, a prerequisite for social development and its availability, as well as the pattern of consumption, plays an important role in sustainable development. According to the report of World Energy Outlook 2018 by International Energy Agency (IEA), world primary energy demand for the year 2017 led by oil accounting 31.74% and followed by coal 26.84%, natural gas 22.24%, renewables 9.55%, nuclear 4.92%, and solid biomass 4.71% as presented in Figure 1. The world RE consumptions has grown very rapidly in terms of electricity generation with the total share of 25% (6351 TWh—hydro 65%, wind 17%, PV 7%) in the year 2017 and is expected to achieve 41% (16,753 TWh—hydro 37%, wind 28%, PV 23%) in the year 2040 with implementation of New Policies Scenario [3]. Meanwhile, Energy Information Administration, (EIA) projects 48% increment in the world energy consumption from 2012 to 2040 (815 quadrillions Btu) [4]. Meeting rising energy demands pose a challenge to the utility planners and policymakers on managing this issue as it could result in insurmountable difficulties for energy security, air protection, and CO₂ emission reductions.

It is recognized and acknowledged that renewable and non-conventional forms of energy will play a crucial role in the future as they are environmentally friendly, easy to use and are bound to become economically more feasible with increased usage [5]. RE term is derived from a broad range of

resources all of which are based on self-renewing energy sources such as sunlight, flowing water, wind, the earth's internal heat and biomass comprised of energy crops, agricultural, industrial and municipal waste. RE sources generate little if any greenhouse gases, waste, or pollutants that contribute to acid rain, urban smog, and health problems and do not require an environmental cleanup cost. In addition, these resources can be used to produce electricity for all economic sectors, fuels for transportation, heat for building and industrial processes [6].

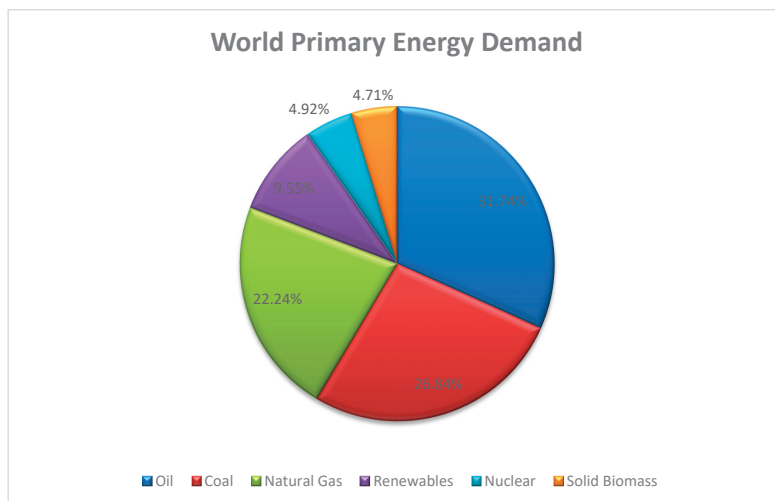


Figure 1. World primary energy demand for the year 2017.

Among all the various RE technologies, solar photovoltaic or precisely PV is the most exploited RE source alongside with hydro and wind power in terms of the pace of deployments and as it is considered a very promising source of future electrical power generation due to the abundance of sunlight over a large area of the earth surface thus giving rise to several applications of PV systems [7]. It also offers continuous cost reduction over the years, a stable system, fast technological progress, being maintenance and pollution-free [8]. There are two classes of the solar energy system, namely stand-alone and grid-connected PV (GPV) generation systems. Both systems have several similarities and differences in their implementations and purposes. By general definition, a stand-alone PV system produces power independently of the grid and a GPV system is an independent decentralized power system that is connected to an electricity transmission and distribution system [9]. The stand-alone PV system consists of PV modules or arrays together with converter and battery storage. Meanwhile, GPV system comprises two controllers as one is for MPPT and the other for inverter controls and grid synchronization. The stand-alone PV system is more favorable as compared to GPV system in areas where the extension of the national power grid is impracticable. The stand-alone PV system is used in off-grid applications together with battery storage. There are several applications in which stand-alone PV system is preferable as compared to GPV systems such as farm's ventilation fans, water pumps, small circulation pumps for thermal water heating systems and even more advanced applications such as lighthouses, auxiliary power units for emergency services and others. The current set-up cost for a stand-alone PV system is high. The main disadvantage regarding the stand-alone PV system is the fluctuation of its output power due to the intermittence nature of solar irradiation and temperature. Therefore, battery storage elements are needed as a buffer system in order to compensate for this power instability and ensures steady power to the load. Moreover, this system suffers from low capacity factor, excess battery costs and finite capacity to store electricity consequently forcing them to dissipate the extra energy generated [10].

Meanwhile, recently the GPV system is playing an increasingly significant role as an electrical supply resource as well as an integral part of the electrical grid generation network. Single-phase, as well as a three-phase GPV system, poses some notable challenges to researchers. The challenges include the maximum power extraction from PV modules, rapid output variation, and daily variability of the output, the effect on power quality especially voltage and current harmonics, current backflow and a mismatch between PV output and grid demand. Contrary to single-phase system, the three-phase GPV generation system is commonly preferred in high-power applications as its ability to provide almost constant power flow and able to avoid excessive asymmetry in the grid current [11]. The maximum power transfer is the utmost objective regarding developing the GPV generation system. The optimization scheme based on the parameters customization on each of individual system components as well as recognizable challenges able to propel PV researchers to build a smart and efficient grid-connected PV generation system. In Figure 2 shows a single line diagram of a general structure for a GPV generation system.

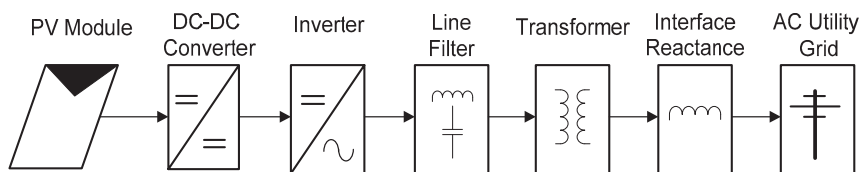


Figure 2. Single line diagram of the GPV generation system.

There are several review papers reported in the literature which covers almost similar topic. Nevertheless, there are still some differences in the scope coverage. Details comparison between these papers is tabulated in Table 1.

Table 1. Comparative analysis of review papers covers a similar topic.

Parameters	1st Review Paper [12]	2nd Review Paper [13]	3rd Review Paper [14]
Scope of the review	1st paper covers almost similar in content and structure. Details analysis on each section of GPV generation system.	2nd review paper mostly focused on the modeling of the PV, MPPT methods, converter’s topologies and control algorithms.	3rd paper presents a review of the recent technological development and trends in the GPV generation system.
Advantages	1st Paper emphasis on prevailing technology along with the techno-economic comparison of commercial available components in the market.	The authors highlight the importance of continuous research in the field of material and power electronics technologies which able to reduce overall cost and increases the system efficiencies.	The main intention of 3rd paper are on the economic growing of GPV generation system as well as the technical challenges posed by mass proliferation.
Drawbacks	Details study on PV cell development is not covered. Moreover, it does not stated the recent and future challenges faced by the GPV generation system. In addition to that, there is no mention on fire protection and disposable standard.	Recent update on PV cell, MPPT technique not well reported. The description on the types of filters, switching techniques, grid synchronization and islanding detection methods were also missing.	3rd paper merely focuses on PV installation cost and smart inverters. It is totally lack of details explanation on the other sub-topics within the GPV generation system.
Focus Group	Young Researcher PV Researcher Project Engineer	Young Researcher PV Researcher Project Engineer	Young Researcher PV Researcher

Based on the outcomes from comparative analysis as in Table 1, this paper fills some of those gaps by providing a comprehensive overview on the development of each of the main components in GPV generation system. The review of the latest publications as well as current PV technological development allows the researchers especially in the field of PV to explore the new opportunity and initiate an innovative state-of-the-art ideals. The maximum power transfer, stability, safety, immunization against all types of disturbances, and power quality issues are still the main concerns regarding the reliability of GPV generation system. A collective summary of key challenges which covers almost a full range of

spectrum on the topic sphere provides a preliminary conceptual framework to the development of future GPV generation system. In addition, this paper hopefully able to offers a valuable exposure not limited to young or future PV researcher nevertheless able to assist a wider group of researcher from different research background such as mechanical, civil and environmentalist to get a quick glance regarding the overall components of GPV generation system and furthermore able to help them to smoothly adapt to the current technological progress in GPV field.

The paper's structure is as follows: Section 2 reveals the relationship between the irradiation and temperature with the generation of PV current; Section 3 presents the classification of DC-DC converters as Section 4 describes the fundamental concept of MPPT; Section 5 surveys a list of MPPT control techniques; Section 6 outlines the classification of an inverter; Section 7 overviews line filter and coupling transformers; Section 8 outlines grid-synchronization methods; Section 9 summaries the latest hierarchy of islanding detection methods; Section 10 provides standards and guidelines; Section 11 reviews the future key challenges posed by GPV system and lastly, Section 12 concludes the overall system.

2. Characteristics of Photovoltaic (PV)

PV exhibits numerous merits such as cleanness, low maintenance, no noise and regarded as one of the most essential RE sources. A PV cell is basically a semiconductor diode whose p - n junction is exposed to light. The irradiation level and temperature are the focal factors for the characteristic of the PV cell. Generally, the equivalent circuit of a PV cell is represented by a single diode model. The single-diode model composes of four components namely a photocurrent source I_{ph} , a diode parallel to the sources, a series resistor, R_s and a shunt resistor, R_{sh} as displayed in Figure 3.

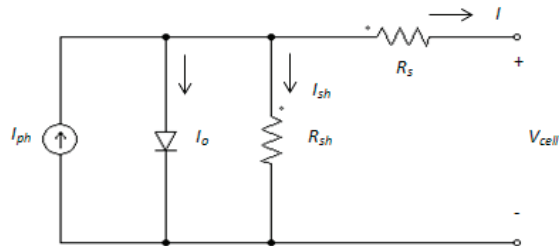


Figure 3. PV cell modeled as a diode circuit.

The series resistance, R_s is the internal resistance of the cell and it depends on the resistance of the semiconductor. The shunt resistance, R_{sh} is due to leakage at the junction. The I - V characteristic of a PV cell is governed by the following equations:

$$I = I_{ph} - I_s \left[\exp\left(\frac{q(V_{cell} + R_s I)}{BkT}\right) - 1 \right] - \frac{V_{cell} + R_s I}{R_{sh}} \quad (1)$$

where I_{ph} is the light current, I_s as reverse saturation current of the diode, k is Boltzmann constant, B is ideality factor of the junction, V_{cell} is the output voltage of the PV cell and T is the temperature in Kelvin and I is the PV cell output current. PV cells are then combined in series and parallel connection to form larger units called PV modules, which are further interconnected in a series-parallel configuration created PV arrays.

Nowadays, there are various types of PV modules available in the market, which can be classified into several main categories [15]. Mono and polycrystalline silicon PV modules type are well-known matured technologies that dominate the commercial PV market. They are known as the first generation of PV technology which reached a conversion efficiency of more than 20% recently [16]. The second generation of PV is thin-film technologies. Thin-film PV modules have a lower efficiency as compared to the first generation yet still offer cheaper cost to manufacture. Moreover, this kind of module deals

with much more flexible design as it includes amorphous silicon (a-Si) and microcrystalline silicon materials. The main goal for each of the PV module manufacturers is to continue to develop a lower cost, highly reliable and simultaneously, attain great conversion efficiency. Figure 4 illustrates the highest PV module conversion efficiency according to the type of materials and technology used. The efficiency of the PV module is a closer indication to the commercial PV efficiency value in comparison to cell efficiency value. This is due to the fact that the wider area was used, and the technology is more ready for commercialization. For silicon types of PV technology, the highest module conversion efficiency is achieved by SunPower and Panasonic through Interdigitated Back Contact (IBC) and Heterojunction IBC structure at 22.8% and 24.4% respectively. The IBC structure allow more light capture by eliminating front busbar that common in silicon PV module structure [17]. For type III–V material category, highest efficiency was attained at 25.1% and 31.2% for single and three junctions respectively at non-concentrating irradiation. Emerging PV technology like Perovskite is currently at 16.1%. While highest PV efficiency was recorded more than 40% from hybrid four junction PV technology (UNSW), it is very complex structure and measured at concentrated level of irradiation. The usage of high efficiency PV module has the advantage of reducing the active installation area, material use and balance of system although initial cost might be expensive.

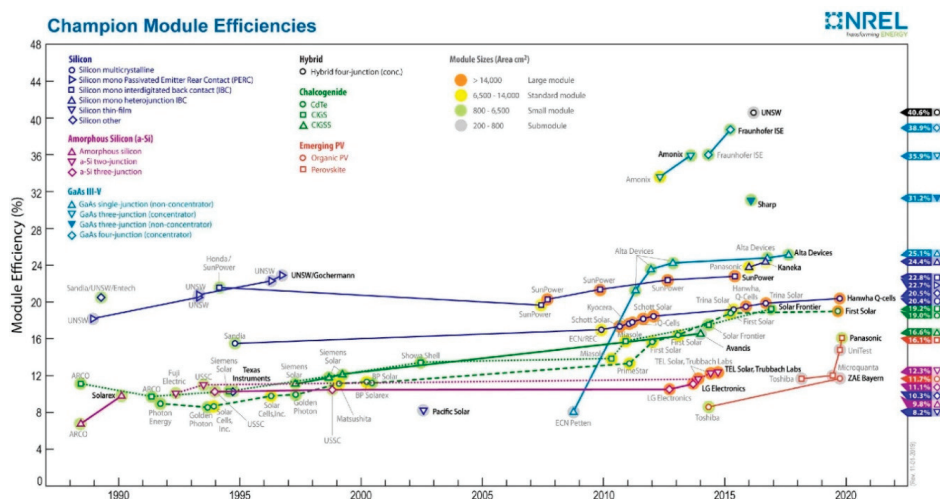


Figure 4. PV module efficiency chart [16].

3. Topology of DC-DC Converter for GPV System

The amount of PV array output voltage depends on the individual arrangement of PV modules. Due to the intermittence characteristic of PV source, load specification and the need to provide a constant DC voltage with high efficiency, a regulator or a DC-DC converter is required in most PV applications in order to regulate or control the DC output voltage that PV arrays generate [18]. Figure 5 shows the classification of isolated and non-isolated DC-DC converters. As the installation trend of PV system moves towards large scale plant and grid-connected scheme, it is crucial to further enhance the capabilities of the DC-DC converter so as to achieve a higher power rating and a higher voltage level at the point of common coupling (PCC).

Theoretically, a conventional DC-DC boost converter is able to deliver high voltage gain. However, when it comes to hardware implementation, the voltage gain of the DC-DC boost converter is insufficient due to the losses associated with the switching devices and the passive elements integrated into the circuitry. To overcome these issues, three different types of high voltage gain interleaved DC-DC converters have been developed [19]. The results show the proposed converter topologies works well with PV and Fuel Cell (FC) systems. Moreover, a comparative analysis of various converter topologies

relates to high voltage gain DC-DC converters have been reported by the authors [20]. Most of the topologies mentioned are based on the structure of conventional boost converter are specifically categorized under their ability to provide fixed or multiple times voltage gain.

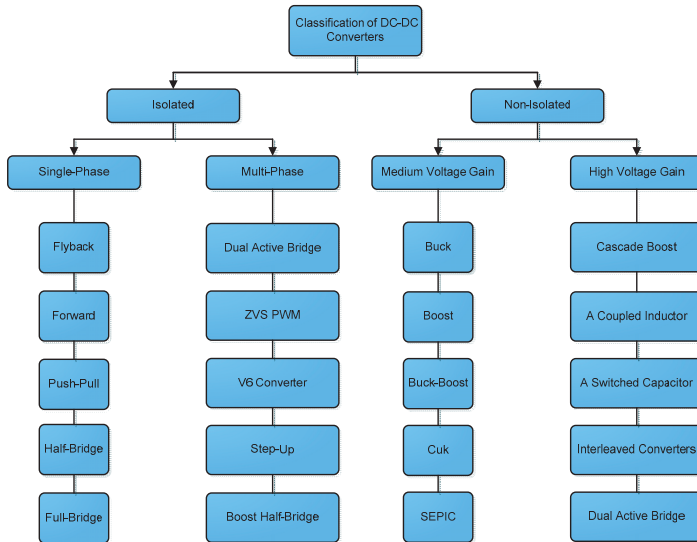


Figure 5. Isolated and non-isolated DC-DC converters.

4. Maximum Power Point Tracking (MPPT)

Currently, the average efficiency rating of PV modules available on the market today is close around 20 % [21]. In order to extract maximum power that PV modules could harvest; researchers have come out with numbers of the MPPT technique. MPPT is a power control technique that operates the PV modules in such a way allows the modules to deliver all the available power it has. Examine a graph of PV array battery charging power transfer as illustrated in Figure 6. This chart is able to give a better understanding of how MPPT works.

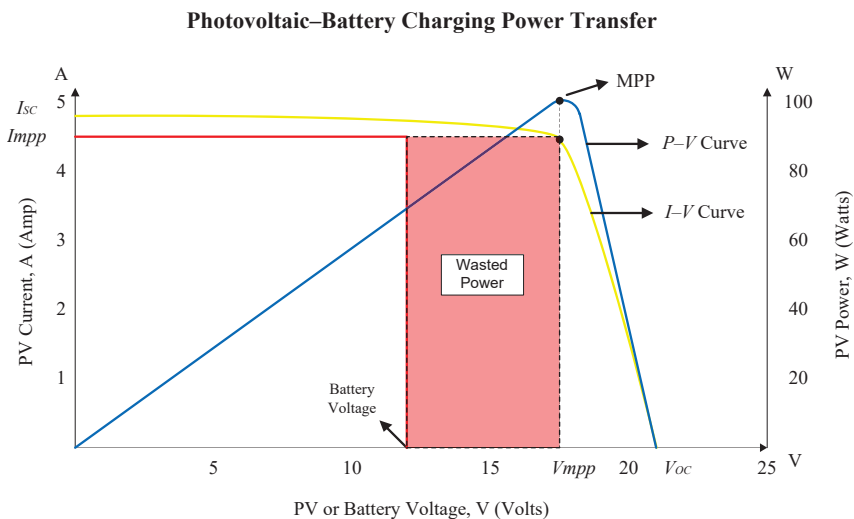


Figure 6. Graph of PV array battery charging power transfer.

Suppose that when a conventional PV module connects directly to the battery, it will force the module to operate at battery's voltage level of 12 V which is not an ideal operating voltage level for the available maximum power that a PV module is capable of generating. Therefore, there is a portion of power that could not be extracted from the module and it is wasted power. The implementation of MPPT will vary the electrical operating point of the PV module so that the module is capable to deliver the maximum available power at the optimal value (maximum power point, MPP) of its voltage and current rated level.

5. MPPT Control Strategy

Recently, there are numerous MPPT control strategies presented in the literature. These control methods vary in complexity, cost, sensor required, convergence speed, implementation of hardware circuits, and other aspects. However, according to the development history of techniques, they can be classified into two categories, namely conventional techniques and artificial intelligent (AI) techniques [22]. The most significant conventional techniques are hill climbing (HC), perturbation and observation (P&O), incremental conductance (INC), fractional open-circuit voltage (FOCV) and fractional short-circuit current (FSCC). Meanwhile, the most applicable AI techniques are Fuzzy Logic (FL), artificial neural network (ANN) and soft computing methodologies. The main obstacle raised by MPPT techniques is to automatically find the real voltage V_{mpp} at which a PV module should operate to attain the maximum power output P_{mpp} under a given PV surface temperature and irradiation [23]. Several techniques as mentioned previously are discussed in detail in an arbitrary order.

5.1. Hill Climbing (HC)

HC is a popular MPPT technique ever developed due to its simplicity and easy implementation [24]. The flow diagram of a classical HC technique as well as Power-Duty (P - D) curve as illustrated in Figures 7 and 8 respectively, operated with a fixed duty cycle size which controls the sign of the P - D curve's slope on each calculation step and makes the appropriate voltage alteration.

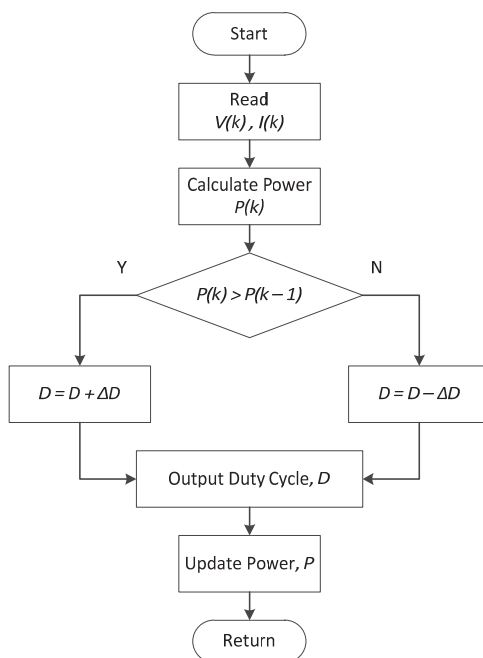


Figure 7. Flow diagram of HC.

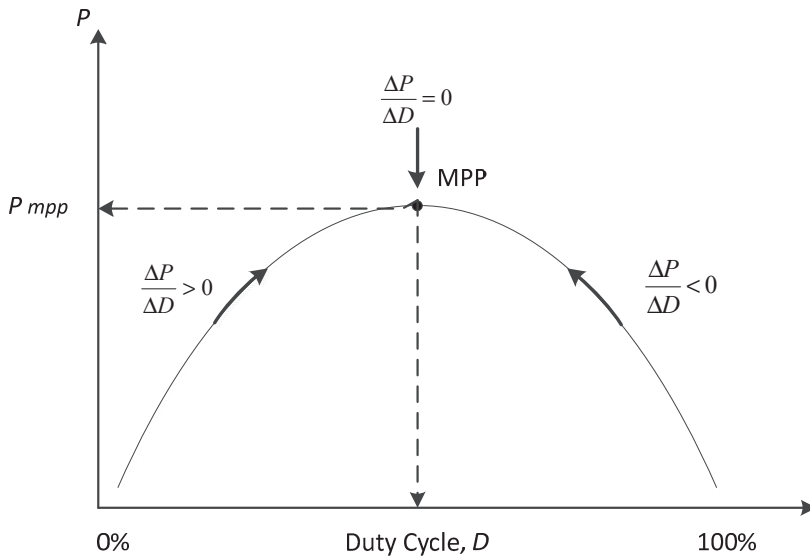


Figure 8. P - D curve of the HC.

The duty cycle, D , in every sampling period is determined by the comparison of the power at the present time and previous time. If the incremental power $\Delta P > 0$, then the duty cycle should be increased in turn to make $\Delta D > 0$. Then if $\Delta P < 0$, the duty cycle is reduced to make $\Delta D < 0$. Shortcomings of the HC method are described below. Figure 8 is the P - D curve diagram of PV modules when the power interface device is a DC-DC buck converter. If the initial operating point of the PV system is located on the left side of the MPP, the duty cycle has to be continuously increased on the basis of the judgment procedure of the HC method in order to track the maximum power point. When the operating point of the PV module is located on the right side of the MPP, the duty cycle should be continuously reduced to return back to the maximum power point. However, if the operating point wants to move toward the MPP ($\Delta P > 0$), the incremental duty cycle should be greater than zero ($\Delta D > 0$) according to the judicial procedure of the HC method. This will cause the operating point to move farther away from the MPP. Therefore, a misjudgment of tracking direction during changing weather condition may happen under this kind of situation. For the HC method, this misjudgment is a fatal weak point [25].

5.2. Perturbation and Observation (P&O)

The P&O algorithm control technique like HC is widely used in the MPPT controllers due to its simple structure and fewer required parameters [26]. This method finds the MPP of PV modules by means of iteratively perturbing, observing and comparing the power generated by the PV modules. The P&O technique comprises a perturbation in the operating voltage of the PV module, while HC strategies involve a perturbation in the duty ratio of the power converter [27]. The flow chart of the typical P&O algorithm is shown in Figure 9.

The algorithm is started by reading the value of current, I and voltage, V from the PV module. The power, P is then calculated from the measured voltage and current. The value of voltage and power at the k th instance is stored. Then next values at $(k + 1)$ th instance is measured again and power is calculated from the measured values. The power and voltage at $(k + 1)$ th instant are subtracted with the values from the k th instant. In the P - V curve of the PV module, it is inferred that in the right-hand side curve where the voltage is almost constant and the slope of power voltage is negative ($\Delta D/\Delta V < 0$) whereas in the left-hand side, the slope is positive ($\Delta P/\Delta V > 0$). Therefore, the right side of the curve

is for the low duty cycle (near to zero) whereas the left side curve is for the higher duty cycle (nearer to unity). Depending on the sign of $\Delta P(P(k+1) - P(k))$ and $\Delta V(V(k+1) - V(k))$ after subtraction, the algorithm decides whether to increase or to decrease the duty cycle of the converter. P&O and HC techniques can malfunction under rapidly changing atmospheric conditions [28]. As illustrated in Figure 10, the starting point is point A, and a $+\Delta V$ voltage perturbation will move the operating point from A to B and cause a decreasing power when the weather condition is steady. According to the judging rules of the P&O method, the next perturbation should be changed to $-\Delta V$ in the opposite direction. However, if the irradiation increases and shifts the power curve from P_1 to P_2 within one sampling period, the operating point will move from A to C instead of A to B. This represents an increase in power and the perturbation is kept the same. Consequently, the operating point diverges from the MPP and will keep diverging if the irradiation steadily increases and vice versa. The power loss of PV modules will increase and therefore, the efficiency of the PV system eventually will fall.

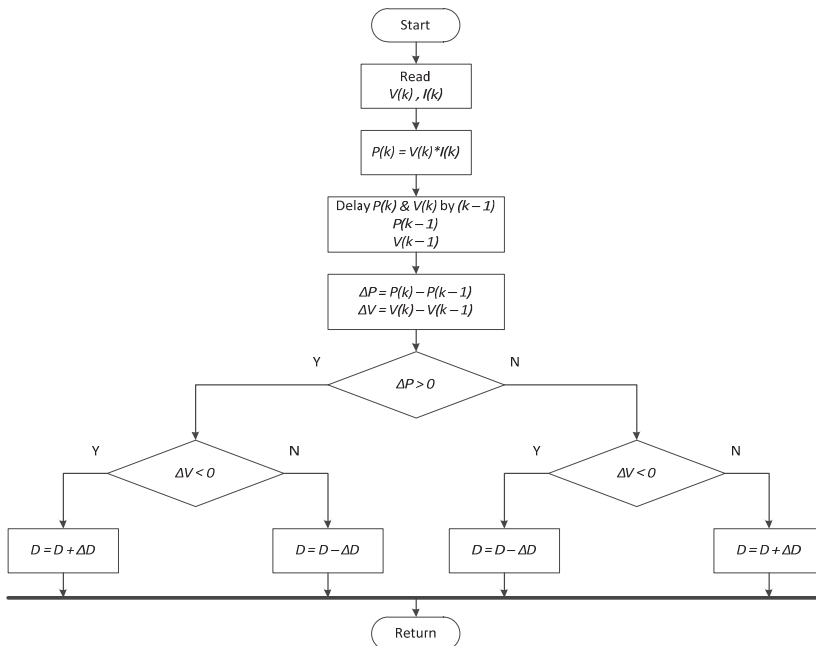


Figure 9. Typical P&O MPPT algorithm.

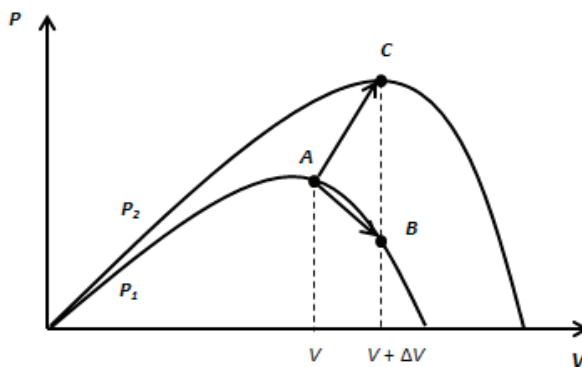


Figure 10. Divergences of HC and P&O from MPP.

Another drawback of the P&O method is that, as the MPP is reached, the power tracked by the P&O method will oscillate and perturb up and down near the MPP as the module terminal voltage is perturbed for every MPPT cycle resulting in a loss of PV power especially in cases of constant or slowly varying atmospheric conditions. The magnitude of the oscillations is determined by the degree of variations of the output voltage or duty cycle [29].

5.3. Modify P&O

The modified P&O is presented [30]. The experimental result work shows that the adopted proposed modified MPPT control algorithm improved the accuracy as well as a fast response as compared to conventional P&O method [31]. The authors [32] came out with the estimate perturb-perturb (EPP) method that uses one estimate mode between two perturb mode. Furthermore, in order to minimize the negative effects associated with the classical P&O method especially during rapidly changing atmospheric conditions, the P&O MPPT parameters should be customized to the dynamic behavior of the specific converter adopted as reported [33]. Precisely, the MPPT parameters which contains the fixed duty cycle step size, ΔD and sampling time, T_a are customized to the dynamic behavior of the specific converter and PV module adopted.

On the other hand, the oscillation around MPP can be minimized by reducing the perturbation step size. However, a smaller perturbation size slows down the MPPT and the system shows poor dynamic response. A larger perturbation step size could cause large fluctuations of output power resulting in energy dissipation. A solution to this conflicting circumstances is to have a variable perturbation step size that gets smaller towards the MPP as discussed [34]. By varying the step size value as well as the sampling time reduces the oscillation around the MPP and steers to a faster response. Meanwhile, [35], a linearization around the MPP leads to a good selection of the sampling period, T_a and the duty cycle variation, ΔD in order to reduce the number and the amplitude of oscillation around MPP in the typical P&O algorithm. It can be concluded that, the stability of the PV system and rapidity of the MPPT algorithm is to compromise by having a good selection of the adaptive sampling period as well as perturbation step size towards the MPP.

5.4. Incremental Conductance (INC)

The INC MPPT technique is based on the fact that the slope of the P - V curve as in Figure 8 is zero at the MPP, positive on the left of the MPP and negative on the right. The flow diagram of the INC method and INC conditions is illustrated in Figure 11 and mentioned in Equations (2)–(4) respectively.

$$\frac{\Delta P}{\Delta V} = 0, \text{ at MPP} \quad (2)$$

$$\frac{\Delta P}{\Delta V} > 0, \text{ left of MPP} \quad (3)$$

$$\frac{\Delta P}{\Delta V} < 0, \text{ right of MPP} \quad (4)$$

The advantage of the INC MPPT method, which is superior to those of the other two HC and P&O algorithms, is that it can calculate and find the exact perturbation direction for the operating voltage of PV modules. In theory, when the MPP is found by the judgment conditions ($\Delta I/\Delta V = -I/V$ and $\Delta I = 0$) of the INC method, it can avoid the perturbation phenomenon near the maximum power point which usually happens to the previous MPPT algorithms. The value of operating voltages is then fixed. However, it indicates that the perturbation phenomenon is still happening near the MPP under non-uniform weather conditions during experimental tests [36]. This is due to the reason that the probability of meeting condition $\Delta I/\Delta V = -I/V$ is extremely small plus the deterministic process of INC algorithm is more complicated, therefore the simulation time spent by INC MPPT algorithm is a little bit longer than that of HC and P&O.

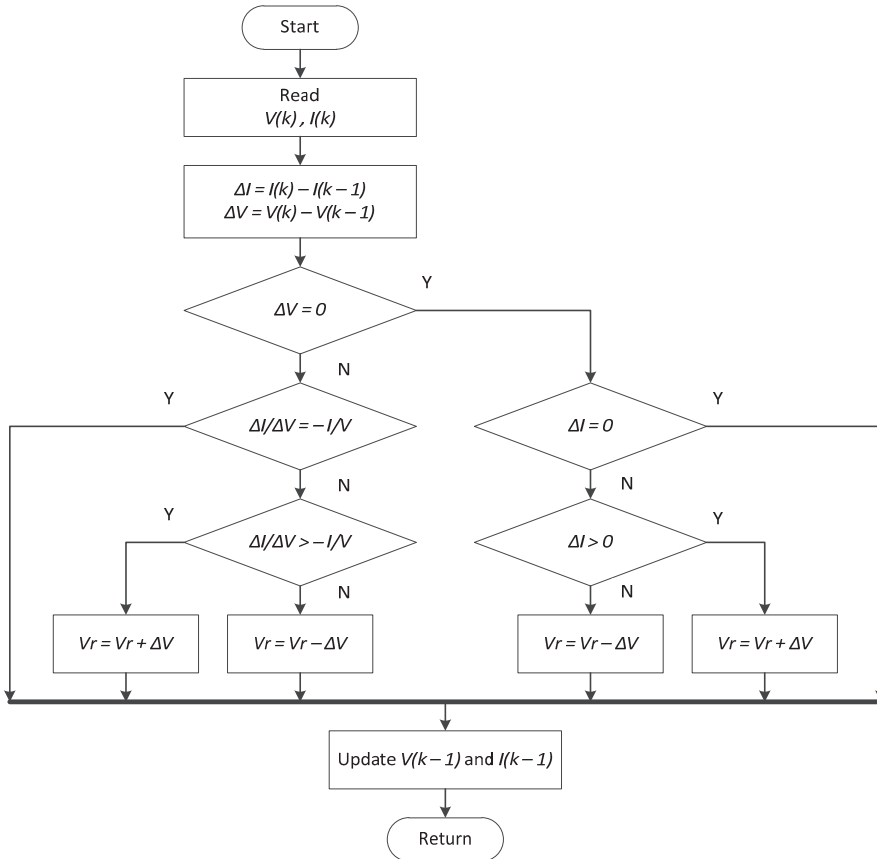


Figure 11. The flow diagram of the INC method.

5.5. Fractional Open-Circuit Voltage (FOCV)

This method is based on the observation that, the ratio between module voltage at maximum power, V_{mpp} to its open-circuit voltage, V_{oc} is nearly constant [37].

$$V_{mpp} = k_i V_{oc} \tag{5}$$

Although the execution of this method is simple and easy, its tracking efficiency is relatively low due to the utilization of inaccurate values of the constant k_i in the computation of V_{mpp} . Once the constant k_i is known, V_{mpp} is computed by measuring V_{oc} periodically. This factor k_i has been reported to lie between 0.71 and 0.78.

5.6. Fractional Short-Circuit Current (FSCC)

This method results from the fact that the current at the maximum power point I_{mpp} is approximately linearly related to the short-circuit current I_{sc} of the PV array [38].

$$I_{mpp} \approx k_i I_{sc} \tag{6}$$

The MPP tracking is completed by measuring the short-circuit current I_{sc} . However, k_i is not constant. It lies between 0.78 and 0.92. The accuracy of the method and tracking efficiency depends on the accuracy of k_i are the periodic measurement of short-circuit current.

5.7. Fuzzy Logic (FL), Artificial Neural Network (ANN) and Other Algorithms

The PV module's MPP varies with the irradiation and surface temperature since the module exhibits a non-linear current-voltage or power-voltage characteristic. Some artificial intelligent prediction tools, such as FL or ANN, control with non-linear and adaptive in nature is introduced in the PV MPPT control mechanism. By knowledge-based Fuzzy rules, Fuzzy control can track the MPP of the PV module [39]. On the other hand, an ANN control executes like a black-box model, requiring no detailed information about the PV system. After learning the relation between maximum power point voltage and open-circuit voltage or irradiation and temperature, the ANN control can track the MPP during a real-time scenario. Since most PV arrays have different characteristics, ANN has to be specifically trained for the PV module with which it will be used. The characteristics of the PV module also change with time, implying that the ANN has to be periodically trained to guarantee accurate MPPT [40]. Ref. [41] presents a high-performance tracking of maximum power delivered from PV systems using adaptive neural Fuzzy inference systems (ANFIS). This method combines the learning abilities of ANN and the ability of FL to handle imprecise data. Moreover, due to the emerging technology especially on the computing-based, enormous MPPT techniques are developed in order to overcome some limitation occurred in previous approaches. Most of the newly emerged MPPT techniques are able to relocate the true MPP effectively even under partial shading condition. However, the main disadvantage of these controls is the high cost of accomplishment owing to complex algorithms that usually need a digital signal processor (DSP) as their interface platform.

Comparison of major MPPT techniques found in the literature is tabulated in Table 2. RCC stands for ripple correlation control, FL, ANN, particle swarm optimization (PSO), genetic algorithm (GA), radial movement optimization (RMO), biological swarm chasing algorithm (BSCA), ant colony optimization (ACO), cuckoo search (CS), salp swarm algorithm (SSA) and grey wolf optimization (GWO). Among these MPPT techniques, the modified variable-step INC is found to be the best promising technique among other conventional approaches in the literature. On the other hand, PSO proved to be an effective method among new generations of MPPT techniques which are based on soft computing. PSO is able to provide accurate, fast convergence speed and able to work effectively even under partial shading conditions. Furthermore, detailed analysis carried out by the authors [42] demonstrated the superiority of GWO among other distinctive meta-heuristic optimization algorithms in terms of speed and reaction time to reach MPP.

Table 2. Comparison of major MPPT techniques and their limitations [43–64].

MPPT Technique	Parameters						
	PV Array Dependent	Analog or Digital	Convergence Speed	Implementation Complexity	Input Sensors	Tracking Approach	Under Partial Shading Condition
HC	No	Both	Slow	Low	V, I	Iteration	Ineffective
P&O	No	Both	Medium	Low	V, I	Iteration	Ineffective
INC	No	Digital	Varies	Medium	V, I	Mathematical Calculation	Ineffective
FOCV	Yes	Both	Medium	Low	V	Constant Parameters	Ineffective
FSCC	Yes	Both	Medium	Medium	I	Constant Parameters	Ineffective
RCC	No	Analog	Fast	Medium	V, I	Mathematical Calculation	Ineffective
A voltage or Current Sweep	Yes	Digital	Slow	High	V, I	Mathematical Calculation	Ineffective
DC-Link Capacitor Droop	No	Both	Medium	Low	V	Iteration	Ineffective
The load I or V Maximization	No	Analog	Fast	Low	V, I	Measurement and Comparison	Ineffective
dP/dV or dP/dI Feedback Control	No	Digital	Fast	Medium	$V \& I$	Mathematical Calculation	Ineffective
FL	Yes	Digital	Fast	High	Varies	Intelligent Prediction	Partially Effective
ANN	Yes	Digital	Fast	High	$T, G \& I$	Intelligent Prediction	Partially Effective
PSO	No	Digital	Fast	High	$V \& I$	Soft Computing	Effective
GA	No	Digital	Fast	High	Varies	Soft Computing	Effective

Table 2. Cont.

MPPT Technique	Parameters						
	PV Array Dependent	Analog or Digital	Convergence Speed	Implementation Complexity	Input Sensors	Tracking Approach	Under Partial Shading Condition
RMO	No	Digital	Fast	Medium	Varies	Soft Computing	Effective
BSCA	No	Digital	Medium	High	V, I, G, T	Soft Computing	Effective
ACO	No	Digital	Fast	High	V, I	Soft Computing	Effective
CS	No	Digital	Fast	High	V	Soft Computing	Effective
SSA	No	Digital	Fast	High	V, I	Soft Computing	Effective
GWO	No	Digital	Fast	High	V, I	Soft Computing	Effective

6. Inverter

Inverter is an electronic device or circuitry that changes a DC input voltage to asymmetric AC output voltage of desired magnitude and frequency [65]. Inverters can be broadly classified into two main classes which are line-commutated and self-commutated inverters as shown in Figure 12. It furthermore can be structured into many sub-categories which are based on the types of input source, output characteristics, method of connections, types of load, pulse-width modulation (PWM) switching techniques and also based on the number of output voltage level.

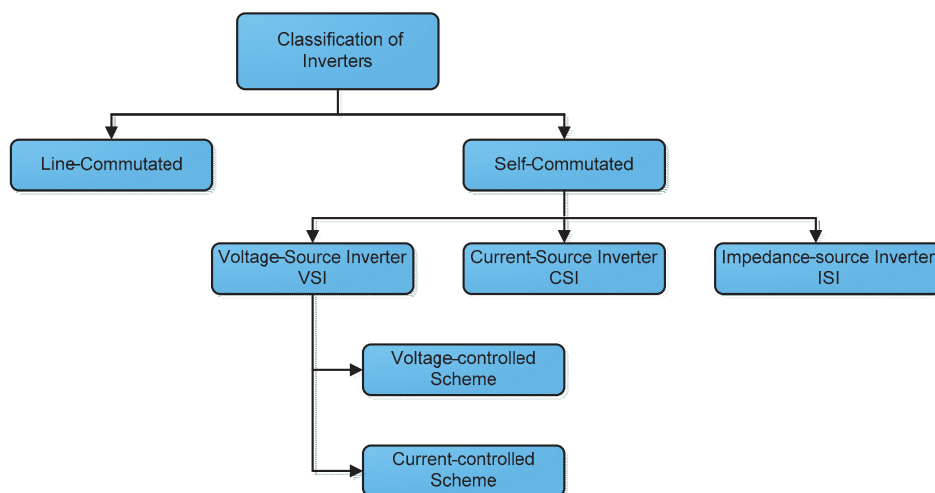


Figure 12. Classifications of inverters [66–69].

The line-commutated inverter (LCI) depends on the grid parameters that dictate the commutation process. In addition, it requires some additional circuitry to turn-off the switching devices. On the other hand, the self-commutated inverter (SCI) is a fully controlled device. The potential at the gate terminal controls the whole operation of the switching device. Since the SCI is controllable, it is able to control both the current as well as voltage waveform at the output side of the inverter. Furthermore, it is well recommended for GPV system as it is highly robust to grid disturbances, able to suppress current harmonics and therefore able to improve the grid power quality. SCI can be further divided into three sub-categories which are Voltage-Source Inverter (VSI), Current-Source Inverter (CSI) and Impedance-Source Inverter (ISI). The two most common type of SCI for grid-connected operation is VSI and CSI. VSI is fed from a DC voltage input having small or negligible impedance and the output voltage does not depend on the load. Meanwhile, CSI is fed with adjustable current from a DC voltage input source having high impedance. The amplitude of the output current is independent of the load impedance [70]. VSI is a more preferable converter scheme over CSI for several reasons such as it offers better loss reduction, easy to control, reduction in filtering requirement, and provide improved quality of the produced voltages and currents especially for the grid-connected system.

7. Line Filter and Coupling Transformer

Power electronic circuit such as DC-DC converters or an inverter produces high order harmonic that flow into the grid will create harmonic pollution thus affecting the power quality of the grid [71]. Passive and active harmonic power filters (APF) are used to reduce voltage distortion, current harmonics and able to act as a reactive power compensation in distributed generation systems [72]. A passive filter contains passive elements such as a resistor, capacitor, and inductor connected in several arrangements which responses to a frequency range of 100 Hz to 300 MHz. On the other hand, APFs have different configurations which are shunt, series, and hybrid as illustrated in Figure 13. APFs are capable of dealing with low-frequency range as well as able to provide flexible gain.

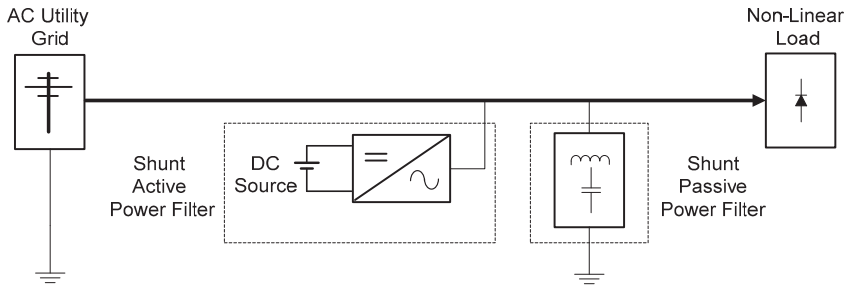


Figure 13. Circuit configurations of hybrid power filters.

The introduction of the coupling transformer in a GPV system is based on two main reasons. A large 50 Hz coupling transformer is often paired at the inverter output as it works as galvanic isolation and to prevent DC current injection into the distribution grid. Excessive DC current injection into the grid network creates corrosion in underground equipment and leads to transformer saturation [73]. Moreover, a coupling transformer’s role as an interface to the magnitude of the PV array voltage could minimize the effect of leakage current. The implementation of a transformer, however, will lead to additional circuitry losses and consequently bring down the overall system efficiency. Meanwhile, the use of solid-state transformer offers size and weight reduction as it works on a high frequency [74]. The grid-connected PV system without coupling transformer raises another complication which is the creation of leakage current components. The occurrence of ground leakage current as presented in Figure 14 exist in transformer-less GPV system as the parasitic elements within the system is not properly grounded.

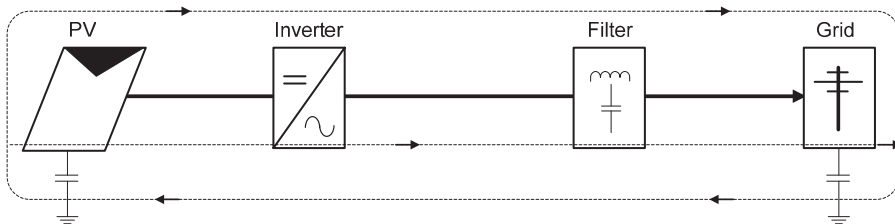


Figure 14. Path of ground leakage current in transformer-less GPV System [75].

8. Grid Synchronization

As discussed earlier, the GPV generation system received extensive attention as more researchers focus on the integrated and smart-grid distribution power system. The implementation of these systems requires deep understanding, critical evaluation and detail analysis in case of normal and abnormal operation. In order to synchronous single-phase or three-phase inverter system to the grid distribution network, four vital conditions must be met as tabulated in Table 3.

Table 3. Grid-synchronization Parameters [76,77].

Parameters	Description
Phase Sequence	The phase sequence or phase rotation of the three-phase inverter must be matching as the phase sequence of the three phases of the grid.
Voltage Magnitude	The magnitude of the sinusoidal voltage produced by the inverter must be equivalent to the magnitude of the sinusoidal voltage of the grid
Frequency	The frequency of the sinusoidal voltage produced by the inverter must be equal to the frequency of the sinusoidal voltage of the grid.
Phase Angle	The phase angle between the sinusoidal voltages produced by the inverter and the sinusoidal voltage generated by the grid must be zero.

The synchronization must occur in the first place before connecting the PV system to the grid. The main purpose of grid synchronization is to allow and automatically take the control action to prevent the abnormalities of parameters between the PV system, and the grid. Moreover, the variables such as phase sequence, voltage magnitude, frequency, and phase angle should be continuously monitored within the permissible limits in order to guarantee a safe and effective synchronization operation of PV power converters connected to the grid.

A GPV system can be modeled as having two sources on each side with intermediate reactance in between as shown in Figure 15a.

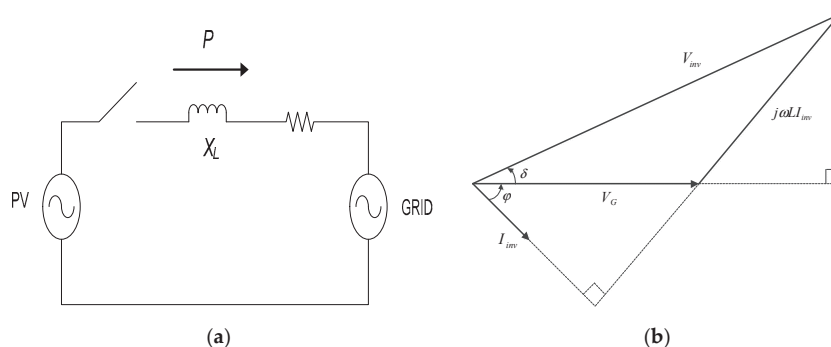
**Figure 15.** GPV system; (a) Equivalent circuit diagram (b) Phasor diagram.

Figure 15b represents the phasor diagram of the fundamental components including the inverter output voltage V_{inv} , the inverter output current I_{inv} , the voltage drop on the line reactance $j\omega LI$ and the fundamental component of the grid voltage V_G . The symbol φ represents the power angle between the grid and inverter output current meanwhile δ represents as the phase difference or load angle between the grid and the inverter output voltage. These relationships are governed by Equations (7) and (8) respectively,

$$P = |V_G||I_{inv}| \cos \varphi = \frac{|V_{inv}||V_G|}{X_L} \sin \delta \quad (7)$$

$$Q = \frac{|V_G|}{X_L} (|V_{inv}| \cos \delta - |V_G|) \quad (8)$$

The direction of power flow from an inverter to the grid or vice versa can be controlled by fine-tuning the inverter output voltage magnitude $|V_{inv}|$ and phase difference δ with respect to the grid while the inverter phase sequence as well as its frequency are monitored closely. The summary of the operation is presented in Table 4. It is clear that maximum power delivery can be made when the phase difference between inverter and grid voltage is 90° . However, if $\delta = 90^\circ$, these two voltages are unable to synchronous and are unstable. Therefore, the angle difference should be slightly lower than 90° in order to achieve maximum power transfer from the PV source to the grid.

Table 4. Direction of Power Flow [78–80].

Parameter	The Direction of Power Flow	
Phase Difference, δ	$\delta > 0$	The real power, P flows from inverter to Grid
	$\delta < 0$	The real power, P flows from Grid to Inverter
Voltage Magnitude, V	$V_{inv} > V_{grid}$	The reactive power, Q flows from Inverter to Grid
	$V_{inv} < V_{grid}$	The reactive power, Q flows from Grid to Inverter

8.1. Control Mechanism for GPV System

The power transferred or injected from the PV system into the grid must be continuously monitored, controlled and analyzed. Designing a GPV system employs two control loops which are external voltage and internal current control loop respectively. The voltage control loop is used to regulate the output power from PV modules to the grid as well as to balance the power flow, whereas the current control loop is used to regulate the injected current to the grid and keep it in phase with grid voltage to achieve unity power factor [81]. Many control mechanisms have been proposed in the literature to regulate the inverter output current that is injected into the grid. Among these control mechanisms are hysteresis controller, predictive and linear proportional-integral (PI) controller, Fuzzy proportional-integral (FPI) and others [82]. Among all, the PI controller is the most common control algorithm used for current error compensation [83]. A PI controller calculates an error value as the difference between a measured inverter output current and a desired injected current to the grid, then the controller attempts to minimize the error between them.

Current control in a synchronous (rotating) reference frame (SRF) using PI controllers is the typical solution, especially in the three-phase grid-connected inverters [84]. As shown in Figure 16, Clark’s transformation transforms three-phase grid quantities vector from ABC natural reference frame into balanced two-phase quantities ($\alpha-\beta$) and then converting to two-phase rotating reference frame by using Park’s transformation which defined as the direct (d) and quadrature (q) components respectively.

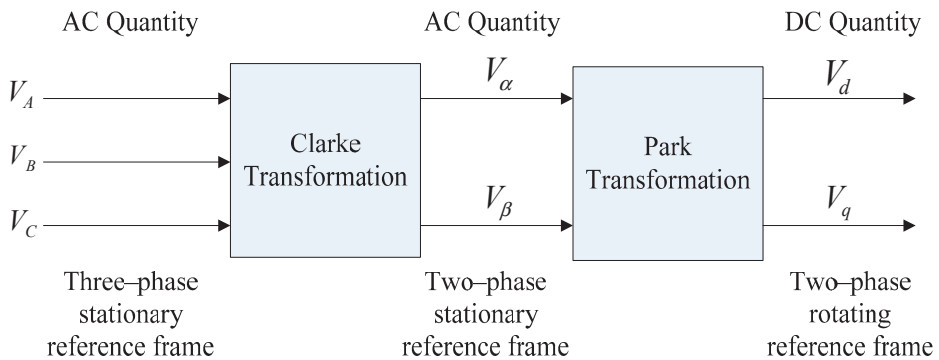


Figure 16. Transformation of the reference frame.

Transforming natural frame AC variable quantities into a DC quantity two-phase rotating reference frame makes filtering and controlling easily achievable [85].

The transformation from three-phase stationary reference frame into two-phase rotating reference frame has also been called as D - Q transformation and it is governed by Equations (9)–(11) respectively.

$$\begin{bmatrix} V_d \\ V_q \\ V_0 \end{bmatrix} = [T] \begin{bmatrix} V_a \\ V_b \\ V_c \end{bmatrix} \tag{9}$$

$$\begin{bmatrix} i_d \\ i_q \\ i_0 \end{bmatrix} = [T] \begin{bmatrix} I_A \\ I_B \\ I_C \end{bmatrix} \tag{10}$$

$$[T] = \sqrt{\frac{2}{3}} \begin{bmatrix} \sin \alpha & \sin\left(\alpha - \frac{2\pi}{3}\right) & \sin\left(\alpha + \frac{2\pi}{3}\right) \\ \cos \alpha & \cos\left(\alpha - \frac{2\pi}{3}\right) & \cos\left(\alpha + \frac{2\pi}{3}\right) \\ \frac{1}{\sqrt{2}} & \frac{1}{\sqrt{2}} & \frac{1}{\sqrt{2}} \end{bmatrix} \tag{11}$$

According to the mathematical model of the three-phase GPV system as discussed [86], the output voltages of the inverter in the SRF are given by Equations (12) and (13) respectively.

$$V_d^* = K_p(I_d^* - I_d) + K_i \int (I_d^* - I_d)dt - \omega L I_q + V_d \tag{12}$$

$$V_q^* = K_p(I_q^* - I_q) + K_i \int (I_q^* - I_q)dt + \omega L I_d + V_q \tag{13}$$

where V_d^* , V_q^* , I_d^* and I_q^* are DC components of the grid voltage and current respectively whereas V_d , V_q , I_d and I_q are DC components of the inverter output. These DC quantities are then transformed back into the ABC natural frame where they will be used as a reference signal for sinusoidal pulse-width modulation (SPWM) to generate proportional duty-cycle switching sequence to the three-phase inverter. By referring to Equation (11), the transformation of the reference frame from AC quantities into DC quantities require a value of α which is the information of phase angle of grid. There are numerous methods used to obtain the grid information especially phase angle value. Among the methods available in the literature, phase-locked loop (PLL) is the most acknowledged owing to its simplicity, effectiveness and robustness in various grid conditions [87].

8.2. Phase-Locked Loop (PLL)

The role of the PLL is to provide the rotation frequency (ω), direct (d) and quadrature (q) voltage or current components by resolving the grid ABC natural components. It synthesizes the frequency and phase of grid voltage and current correspondingly. Moreover, it is able to provide the frequency and phase angle of the grid voltage correctly even though in the event of disturbance [88]. The principle operation of three-phase PLL is based on the closed-loop control system as displayed in Figure 17 which regulates V_d to zero and locks θ^* to the phase angle of the input signal θ .

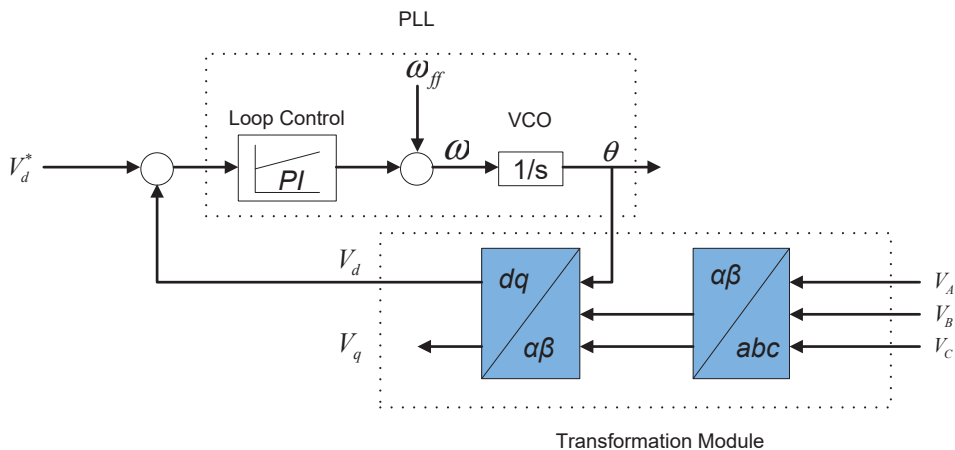


Figure 17. Three-phase SRF-PLL for grid synchronization.

The gains of the PI controller are designed in such a way that V_d follow the reference value V_d^* . This results in an estimated phase angle that equals the phase angle original, therefore, a phase difference of zero [89]. The general structure with the entire components of the three-phase GPV system is presented in Figure 18. There are two controller blocks employed in this system. The first controller block implements MPPT on the input side of the converter. Normally the voltage and current of PV modules are set as the input and duty cycle is the output parameter. The next controller generates PWM to the three-phase inverter. The extraction of the phase angle from the grid voltage is vital. There are three technical aspects that are very crucial for the effective grid synchronization scheme. The primary one is to regulate the DC link voltage to make it constant. The next one is a controller which control active power injected into the grid. The third one is to control reactive power compensation. [90], a full working three-phase PLL for GPV system with coupling transformer has been designed. Furthermore, there are studies that compare the performance of a GPV generation system with and without coupling transformer. Both system's configurations have its own advantages and disadvantages as detail analysis regarding this implementation are provided by the authors [91].

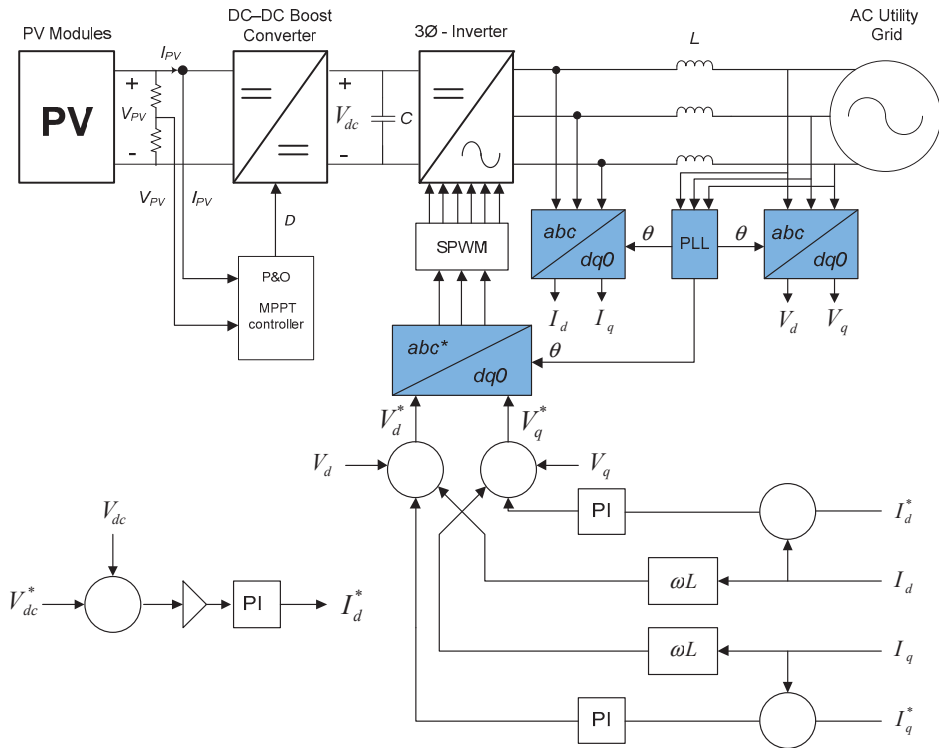


Figure 18. The general structure of the three-phase GPV generation system with transformation blocks.

The designing of a synchronization control algorithm must be able to cope with the disturbances of grid parameters such as voltage, frequency, and phase angle. It is expected that the faster and the more accurate these measurements are the better the synchronization and therefore the more efficient the control actions. It is well-known that PLL is the most popular synchronization technique available in the literature. However, recently there is a vast spectrum of grid synchronization techniques available which can be divided into two categories which are for open-loop and closed-loop system. Open-loop systems directly detect the magnitude, phase, and frequency of the input signal whereas closed-loop systems adaptively update the detected parameters through a loop mechanism. Artificial intelligence (AI),

zero-crossing detection (ZCD), adaptive notch filtering (ANF), delayed signal cancellation (DSC), nonlinear least square (NLS), discrete Fourier transform (DFT), Kalman filter (KF), and frequency-locked loop (FLL) are among numerous grid synchronization control techniques available in the literature. Figure 19 shows the classification of synchronization up-to-date techniques. [92] elaborate in detail some of the mentioned synchronization control techniques together with their applications. The authors emphasize that more attention is required to focus on hybrid techniques for robust grid synchronization especially in adverse grid conditions.

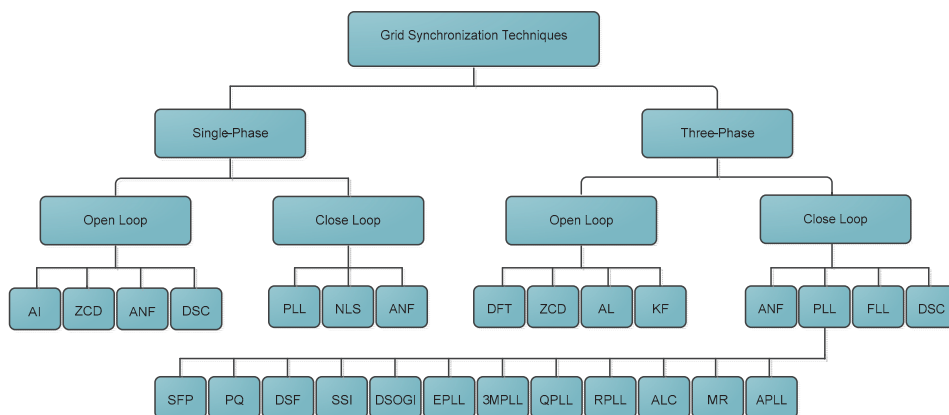


Figure 19. Classification of grid synchronization techniques.

Since PLL is the most common grid synchronization technique, there is plenty of derivation generated from this method. A comprehensive review of major PLL techniques has been carried out in [93] which includes synchronous reference frame (SRF), instantaneous real and imaginary power theory (PQ), double synchronous frame (DSF), sinusoidal signal integrator (SSI), double second-order generalized integrator (DSOGI), enhance PLL (EPLL), three-phase magnitude (3MPLL), quadrature method (QPLL), robust PLL (RPLL), adaptive linear combiner (ALC), multi-rate (MR), and as well as adaptive PLL (APLL). Each of these techniques depends strongly on the system specifications and requirements. Some of the proposed schemes did not provide the corresponding results or hardware verifications. Yet, the main goals are it should be able to provide fast and accurate synchronization information along with the high degree of immunity and insensitivity towards disturbances in the input signal thus making the grid synchronization as well as power transfer mechanism working effectively within the given standards and regulations.

9. Islanding Detection Methods

Apart from the grid synchronization mechanism, a protection scheme against islanding is another crucial issue in the GPV generation system. The IEEE standards defined islanding as the condition in which a portion of an area of electric power system (EPS) is energized solely by one or more local EPS through the associated point of common coupling (PCC) while that portion of the area EPS is electrically isolated from the rest of the area EPS. Generally, there are two types of islanding circumstances which are intentional and unintentional cases. The unintentional islands pose more tangible risks with high possibilities of damaging the electrical device due to the asynchronous re-closure, potential fire hazards to the personnel on-duty and safety issues. Up to date, there are various islanding detection methods have been reported in the literature [94–96]. Figure 20 classified the islanding detection methods in two main categories comprise of local and remote methods.

The major problems lie in the installation cost, effective communications between supervisory controllers and computational accuracy. In addition, extra considerations need to take into account

especially in the event of improper disconnection and reclosing events. Moreover, the introduction of the latest islanding detection methods should look for uniformity and comply with international standards and regulations. A suitable coordination procedure between synchronization with the islanding detection techniques, controller accuracy and efficiency are the key determinants for the smooth operation of GPV generation system.

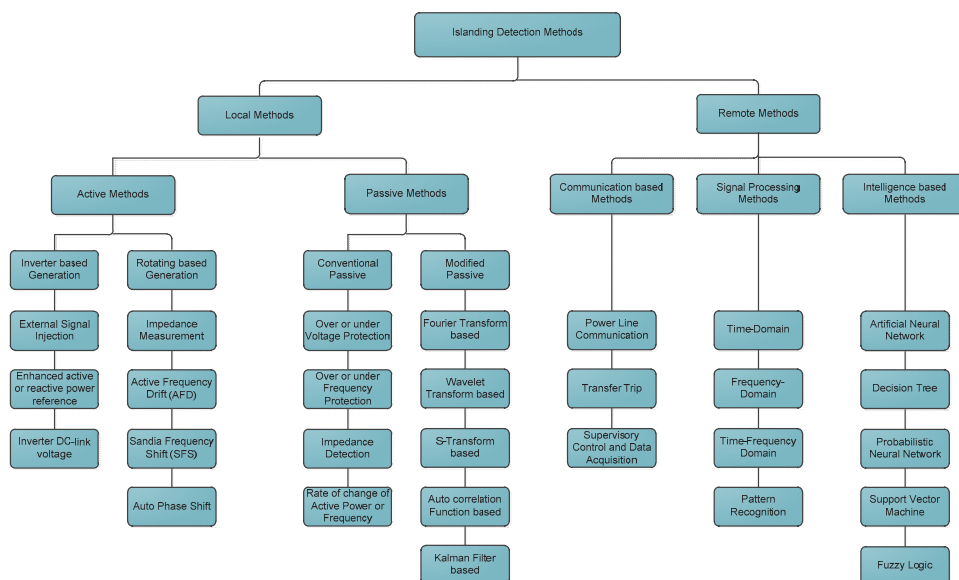


Figure 20. Classification of islanding detection methods.

10. Standards and Guidelines

Interconnecting PV system to the grid poses a major challenge in the development of the modern smart grid and distribution power systems. The awareness about the environment, safety, energy disturbance and the reliability of the integrated power system raise concerns on proper preventive measures and protective equipment resulting in the creation of the international standards and guidelines for the GPV system. Standards and guidelines are able to provide researchers and engineer around the globe with a basis for mutual technical understanding regarding the GPV system. Up to date, there are various standards that govern the interconnections of the PV system. The most widely recognized and used are the Institute of Electrical and Electronics Engineers (IEEE 1547) and the International Electrotechnical Commission (IEC 61,727). The IEEE 1547 standard covers technical specifications and tests for the interconnection of distributed resources below 10 MVA meanwhile IEC 61,727 relates to GPV systems with a rated capacity below 10 kVA. On the other hand, IEEE 929–2000 was created specifically for GPV systems [97–99].

11. Future Key Challenges

There are several key challenges that need to be addressed in order to build efficient GPV generation system. Table 5 summarizes future key challenges and obstacles for the researcher in the field of the GPV system.

Table 5. Future key challenges on GPV generation system [100–131].

Main Components on GPV Generation System							
PV Module	MPPT	DC-DC Converter	Inverter	Line Filter	Synchronization Control Technique	Coupling Transformer	Interface Impedance
Material on high energy conversion efficiency and low-cost implementation	The exact and variable step size of Duty Cycle and Voltage.	High gain DC-DC Converters.	DC-AC Ratio Optimization	Impact on power quality, protection, and operation of distribution feeders.	Protection scheme against Islanding, transient fault condition, rapidly changing reactive power demand by grid.	The single-stage transformer-less conversion system.	An optimization technique for Inverter-Grid Interface Impedance.
Protection against the high intensity of irradiation, fire hazard, haze, and extreme climatic changes	The exact and variable step size of the perturbation period.	Resonant Converters with soft-switching technique.	Three-level neutral point clamp Topologies.	Hybrid Passive Filter configurations.	Supervisor controller to control of multiple distributed generation plants.	High-Frequency (HF) Transformer.	Characteristic of interface impedance for maximum power transfer.
Potential Induced Degradation (PID) effect	Partially shaded condition.	Multi-level DC-DC Converters.	Multi-level Modular Central Inverter.	Double line frequency pulsating power issue.	Smart grid and smart energy storage system.	Effect of Core Losses and Saturation to Power transfer.	
Development of advance Sun Tracking PV Panel	Sensor-less MPPT Algorithm.	Multiple Input Multiple Output DC-DC Converters.	Modulation control technique.	Shunt Active Power Filter for Three-phase system.	Control strategy for Unbalanced, distorted and Non-linear load conditions.	Leakage current in Transformer-less system.	
Booster application to intensify the Irradiation and Temperature	The introduction of artificial intelligence i.e., Heuristic search methods.	Control technique for non-isolated DC-DC Converters.	Single-stage Transformer-less Inverters.	Hybrid Active and Passive Filter configuration.	The introduction of artificial intelligence in the synchronization of the grid-connected PV system.	Study on the Construction and Core Design of Transformer.	

Each main component on the GPV generation system poised several key challenges that required extensive understanding on the subject sphere. Every section is at different stages of technological development. The major challenges on PV modules technical developments can be divided into two main classifications which lie on material fabrication and electromechanical advancement. The main aim is to achieve an optimal energy conversion from the sunlight to electrical energy. Another crucial aspect with regards to the construction of PV systems is the proper protection against fire hazards. As reported [132], there are various factors that may contribute to fire risks especially to the PV modules installed on buildings such as the use of low-quality electrical components, imperfection of construction standards and lack of relevant protocols on installation. A standardized fire mitigation procedure should be established to overcome these issues. Other setbacks are the deficiency of disposable procedure on aging PV modules. PV modules mostly constructed based on material which may cause harm to human health and safety. Greater awareness of the environment and effective PV recycling process plays a vital impact on the management of PV waste. Alongside the progressions in power electronics technology, the research direction of the hardware prototype is moving towards creating a highly efficient power converter. Replacing and reducing the number of physical electrical elements such as analogue circuitry and bulky passive components with digital means becomes part of the interest among researches to optimize the overall performance of the GPV generation system. The transient analysis on grid-interfaced inverter due to the presence of a different type of faults, voltage sag, voltage swell and rapidly changing power demand by the grid becomes the main concern for researchers in assessing the ability, characteristic and response of the designated power inverter to compensate the changes. Meanwhile, the introduction of computational algorithms techniques made a huge breakthrough in the PV controller architectures. Apart from its complexity, the development of so-called smart controllers able to improve the speed, accuracy, robustness and reliability of the GPV system. Effective grid synchronization as well as islanding detection methods are the key principle for the successful operation of GPV generation system. In the near future, a smart, intelligent and efficient GPV system will be a prominent part in grid electricity generation.

12. Conclusions

A GPV generation system offers abundant opportunities for the researcher to build a smart and efficient integrated system in order to meet future energy demand. The increased number of GPV generation systems gave rise to problems concerning the stability, safety, as well as power quality issues. This paper provided a detailed review on recent findings, development and future key challenges of each sub-component of the system, which hopefully will be able to assist the future researcher in the field of PV to explore new state-of-the-art ideas. There are numerous approaches, topologies, and architectures of GPV generation systems that have been implemented in the literature. Some of the new techniques are found to perform better than the classical ones yet the scheme which were constructed based on conventional VSI topologies, SPWM switching technique and PLL control algorithms are still well-accepted for its simplicity. The emerging challenges for these systems lie in the use of high-efficiency PV materials, MPPT against partial shading condition, modular central inverter, APF, the introduction of AI for both synchronization and anti-islanding state, smart energy storage system and the development of supervisory controller for the integration of multiple PV generation plant within the same buses. By identifying, analyzing and tackling these challenges will further nourish the development of a smart and efficient integrated GPV generation system.

Author Contributions: All authors equally contributed to this work. All authors have read and agreed to the published version of the manuscript.

Funding: The authors wish to thank Universiti Sains Malaysia (USM) under Research University Grant (RUT)-RCMO scheme with Account No: 1001/PELECT/8014028 for providing computational facilities to carry out this research at the School of Electrical and Electronic Engineering USM.

Conflicts of Interest: The authors declare no conflict of interest.

References

1. BP Statistical Review of World Energy. BP Statistical Review of World Energy 2016 No. June. pp. 1–48. Available online: <http://oilproduction.net/files/especial-BP/bp-statistical-review-of-world-energy-2016-full-report.pdf> (accessed on 11 August 2020).
2. WEO-2017 Special Report: Energy Access Outlook; International Energy Agency: Paris, France. Available online: <https://webstore.iea.org/download/summary/274?fileName=English-Energy-Access-Outlook-2017-ES.pdf> (accessed on 11 August 2020).
3. World Energy Outlook 2018: The Future Is Electrifying. 2018. Available online: <https://www.iea.org/reports/world-energy-outlook-2018> (accessed on 11 August 2020).
4. EIA. International Energy Outlook 2016: U.S.; Energy Information Administration (EIA): Washington, DC, USA, 2016; Volume 1.
5. Owusu, P.A.; Asumadu-Sarkodie, S. A review of renewable energy sources, sustainability issues and climate change mitigation. *Cogent Eng.* **2016**, *3*, 1–14. [CrossRef]
6. Bishoge, O.; Zhang, L.; Mushi, W. The Potential Renewable Energy for Sustainable Development in Tanzania: A Review. *Clean Technol.* **2018**, *1*, 6. [CrossRef]
7. Raheem, A.; Abbasi, S.A.; Memon, A.; Samo, S.R.; Taufiq-Yap, Y.H.; Danquah, M.K.; Harun, R. Renewable energy deployment to combat energy crisis in Pakistan. *Energy Sustain. Soc.* **2016**, *6*. [CrossRef]
8. Kabir, E.; Kumar, P.; Kumar, S.; Adelodun, A.A.; Kim, K.H. Solar energy: Potential and future prospects. *Renew. Sustain. Energy Rev.* **2018**, *82*, 894–900. [CrossRef]
9. Karthikeyan, V.; Rajasekar, S.; Das, V.; Pitchaivijaya, K. Grid-Connected and Off-Grid Solar Photovoltaic System. *Green Energy Technol.* **2017**. [CrossRef]
10. Hamza, H.A.; Auwal, Y.M.; Sharpson, M.I. Standalone PV System Design and Sizing for a Household in Gombe, Nigeria. *Int. J. Interdiscip. Res. Innov.* **2018**, *6*, 96–101.
11. Isen, E.; Bakan, A.F. Highly efficient three-phase grid-connected parallel inverter system. *J. Mod. Power Syst. Clean Energy* **2018**, *6*, 1079–1089. [CrossRef]
12. Chatterjee, S.; Kumar, P.; Chatterjee, S. A techno-commercial review on grid connected photovoltaic system. *Renew. Sustain. Energy Rev.* **2018**, *81*, 2371–2397. [CrossRef]
13. Kumar, A.; Gupta, N.; Gupta, V. A Comprehensive Review on Grid-Tied Solar Photovoltaic System. *J. Green Eng.* **2017**, *7*, 213–254. [CrossRef]
14. Rani, A.; Sharma, G. A Review on Grid-Connected PV System. *Int. J. Trend Sci. Res. Dev.* **2017**, *1*, 558–563. [CrossRef]
15. Luceño-Sánchez, J.A.; Díez-Pascual, A.M.; Capilla, R.P. Materials for photovoltaics: State of art and recent developments. *Int. J. Mol. Sci.* **2019**, *20*, 976. [CrossRef] [PubMed]
16. Champion Photovoltaic Module Efficiency Chart. Available online: <https://www.nrel.gov/pv/module-efficiency.html> (accessed on 25 July 2020).
17. Mat Desa, M.K.; Sapeai, S.; Azhari, A.W.; Sopian, K.; Sulaiman, M.Y.; Amin, N.; Zaidi, S.H. Silicon back contact solar cell configuration: A pathway towards higher efficiency. *Renew. Sustain. Energy Rev.* **2016**, *60*, 1516–1532. [CrossRef]
18. Baharudin, N.H.; Mansur, T.M.N.T.; Hamid, F.A.; Ali, R.; Misrun, M.I. Topologies of DC-DC converter in solar PV applications. *Indones. J. Electr. Eng. Comput. Sci.* **2017**, *8*, 368–374. [CrossRef]
19. Choi, H.A. *High-Gain Interleaved DC-DC Converters for Renewable Energy Systems*; The University of New South Wales Sydney: Sydney, Australia, 2016.
20. Amir, A.; Amir, A.; Che, H.S.; Elkhateb, A.; Rahim, N.A. Comparative analysis of high voltage gain DC-DC converter topologies for photovoltaic systems. *Renew. Energy* **2019**, *136*, 1147–1163. [CrossRef]
21. Meehan, C. Solar Panel Efficiency Rankings. Available online: <https://www.solarreviews.com/blog/what-are-the-most-efficient-solar-panels-for-2019> (accessed on 11 August 2020).
22. Shareef, H.; Mutlag, A.H.; Mohamed, A. Random Forest-Based Approach for Maximum Power Point Tracking of Photovoltaic Systems Operating under Actual Environmental Conditions. *Comput. Intell. Neurosci.* **2017**, *2017*, 1–17. [CrossRef]
23. Abdul-Kalaam, R.; Muyeen, S.M.; Al-Durra, A. Review of Maximum Power Point Tracking Techniques for Photovoltaic System. *Glob. J. Control Eng. Technol.* **2016**, *2*, 8–18.
24. Bahari, M.I.; Tarassodi, P.; Naeini, Y.M.; Khalilabad, A.K.; Shirazi, P. Modeling and simulation of hill climbing MPPT algorithm for photovoltaic application. In Proceedings of the 2016 International Symposium on Power Electronics, Electrical Drives, Automation and Motion, Capri, Italy, 22–24 June 2016; pp. 1041–1044.

25. Balakumar, N.; Prabhu, B. Performance Evaluation of Maximum Power Point Tracking Principle for PV Systems. *Int. J. Res. Electron. Commun. Technol.* **2016**, *3*, 21–24.
26. Mutlag, A.H.; Mohamed, A.; Shareef, H. An Improved Perturbation and Observation based Maximum Power Point Tracking Method for Photovoltaic Systems. *J. Teknol.* **2016**, *78*, 19–25. [[CrossRef](#)]
27. Liu, F.; Kang, Y.; Zhang, Y.; Duan, S. Comparison of P & O and Hill Climbing MPPT Methods for Grid-Connected PV Converter. In Proceedings of the 3rd IEEE Conference on Industrial Electronics and Applications, Singapore, 3–5 June 2008; pp. 804–807.
28. Haque, A. Maximum Power Point Tracking (MPPT) Scheme for Solar Photovoltaic System Maximum Power Point Tracking (MPPT) Scheme for Solar Photovoltaic System. *Energy Technol. Policy* **2014**, *1*, 115–122. [[CrossRef](#)]
29. Bounechba, H.; Bouzid, A.; Nabti, K.; Benalla, H. Comparison of perturb & observe and fuzzy logic in maximum power point tracker for PV systems. *Energy Procedia* **2014**, *50*, 677–684. [[CrossRef](#)]
30. Piegari, L.; Rizzo, R.; Spina, I.; Tricoli, P. Optimized adaptive perturb and observe maximum power point tracking control for photovoltaic generation. *Energies* **2015**, *8*, 3418–3436. [[CrossRef](#)]
31. Ahmed, J.; Member, S.; Salam, Z. A Modified P & O Maximum Power Point Tracking Method with Reduced Steady State Oscillation and Improved Tracking Efficiency. *IEEE Trans. Sustain. Energy* **2016**, *7*, 1506–1515. [[CrossRef](#)]
32. Samantara, S.; Roy, B.; Sharma, R.; Choudhury, S.; Jena, B. Modeling and simulation of integrated CUK converter for grid connected PV system with EPP MPPT hybridization. In Proceedings of the IEEE Power, Communication and Information Technology Conference, PCITC 2015—Proceedings, Bhubaneswar, India, 15–17 October 2015; pp. 397–402.
33. Shankar, G.; Mukherjee, V. MPP detection of a partially shaded PV array by continuous GA and hybrid PSO. *Ain Shams Eng. J.* **2015**, *6*, 471–479. [[CrossRef](#)]
34. Firmansyah, E.; Suharyanto, S. Variable Step Size P&O MPPT Algorithm on 250 W Interleaved Flyback Converter. *Int. J. Inf. Technol. Electr. Eng.* **2018**, *1*, 132–138. [[CrossRef](#)]
35. Mumtaz, S.; Ahmad, S.; Khan, L.; Ali, S.; Kamal, T.; Hassan, S.Z. Adaptive feedback linearization based neurofuzzy maximum power point tracking for a photovoltaic system. *Energies* **2018**, *11*, 606. [[CrossRef](#)]
36. Hahm, J.; Kang, H.; Baek, J.; Lee, H.; Park, M. Design of incremental conductance sliding mode MPPT control applied by integrated photovoltaic and proton exchange membrane fuel cell system under various operating conditions for BLDC motor. *Int. J. Photoenergy* **2015**, 1–14. [[CrossRef](#)]
37. Suresh, E. Design and implementation of improved fractional open circuit voltage based maximum power point tracking algorithm for photovoltaic applications. *Int. J. Renew. Energy Res.* **2017**, *7*, 1108–1113.
38. Kumari, J.S.; Babu, C.S. Comparison of Maximum Power Point Tracking Algorithms for Photovoltaic System. *Int. J. Adv. Eng. Technol.* **2011**, *1*, 133–148.
39. Menadi, A. Real time implementation of a fuzzy logic based Mppt controller for grid connected photovoltaic system. *Int. J. Renew. Energy Res.* **2015**, *5*, 236–244. [[CrossRef](#)]
40. Rezvani, A.; Izadbakhsh, M.; Gandomkar, M.; Vafaei, S. Investigation of ANN-GA and Modified Perturb and Observe MPPT Techniques for Photovoltaic System in the Grid Connected Mode. *Indian J. Sci. Technol.* **2015**, *8*, 87–95. [[CrossRef](#)]
41. Mlakić, D.; Majdandžić, L.; Nikolovski, S. ANFIS used as a maximum power point tracking algorithm for a photovoltaic system. *Int. J. Electr. Comput. Eng.* **2018**, *8*, 867–879. [[CrossRef](#)]
42. Mohamed, M.A.; Zaki Diab, A.A.; Rezk, H. Partial shading mitigation of PV systems via different meta-heuristic techniques. *Renew. Energy* **2019**, *130*, 1159–1175. [[CrossRef](#)]
43. Zainuri, M.A.A.M.; Azari, E.A.; Ibrahim, A.A.; Ayob, A.; Yusof, Y.; Radzi, M.A.M. Analysis of adaptive perturb and observe-fuzzy logic control maximum power point tracking for photovoltaic boost DC-DC converter. *Int. J. Adv. Trends Comput. Sci. Eng.* **2019**, *8*, 201–210. [[CrossRef](#)]
44. Mohammad, A.N.M.; Radzi, M.A.M.; Azis, N.; Shafie, S.; Zainuri, M.A.A.M. An enhanced adaptive perturb and observe technique for efficient maximum power point tracking under partial shading conditions. *Appl. Sci.* **2020**, *10*, 3912. [[CrossRef](#)]
45. Verma, D.; Nema, S.; Shandilya, A.M.; Dash, S.K. Maximum power point tracking (MPPT) techniques: Recapitulation in solar photovoltaic systems. *Renew. Sustain. Energy Rev.* **2016**, *54*, 1018–1034. [[CrossRef](#)]
46. Sudheer, P.; Chengaiah, C.; Engineering, S.V.U.C.; Pradesh, A.; Engineering, S.V.U.C.; Pradesh, A. Maximum Power Point tracking algorithms for solar power system- Review. *Int. Res. J. Eng. Technol.* **2017**, *4*, 1507–1514.

47. Liu, Y.H.; Chen, J.H.; Huang, J.W. A review of maximum power point tracking techniques for use in partially shaded conditions. *Renew. Sustain. Energy Rev.* **2015**, *41*, 436–453. [[CrossRef](#)]
48. Husain, M.A.; Tariq, A.; Hameed, S.; Arif, M.S.B.; Jain, A. Comparative assessment of maximum power point tracking procedures for photovoltaic systems. *Green Energy Environ.* **2017**, *2*, 5–17. [[CrossRef](#)]
49. Singh, O.; Gupta, S.K. A review on recent Mppt techniques for photovoltaic system. In Proceedings of the 2018 IEEMA Engineer Infinite Conference (eTechNxT), New Delhi, India, 13–14 March 2018; pp. 1–6. [[CrossRef](#)]
50. Hadji, S.; Gaubert, J.P.; Krim, F. Real-time Genetic Algorithms-based MPPT: Study and comparison (theoretical an experimental) with conventional methods. *Energies* **2018**, *11*, 459. [[CrossRef](#)]
51. Seyedmahmoudian, M.; Horan, B.; Soon, T.K.; Rahmani, R.; Than Oo, A.M.; Mekhilef, S.; Stojcevski, A. State of the art artificial intelligence-based MPPT techniques for mitigating partial shading effects on PV systems—A review. *Renew. Sustain. Energy Rev.* **2016**, *64*, 435–455. [[CrossRef](#)]
52. Karami, N.; Moubayed, N.; Outbib, R. General review and classification of different MPPT Techniques. *Renew. Sustain. Energy Rev.* **2017**, *68*, 1–18. [[CrossRef](#)]
53. Titri, S.; Larbes, C.; Toumi, K.Y.; Benatchba, K. A new MPPT controller based on the Ant colony optimization algorithm for Photovoltaic systems under partial shading conditions. *Appl. Soft Comput. J.* **2017**, *58*, 465–479. [[CrossRef](#)]
54. Ahmed, J.; Salam, Z. A Maximum Power Point Tracking (MPPT) for PV system using Cuckoo Search with partial shading capability. *Appl. Energy* **2014**, *119*, 118–130. [[CrossRef](#)]
55. Rezk, H.; Eltamaly, A.M. A comprehensive comparison of different MPPT techniques for photovoltaic systems. *Sol. Energy* **2015**, *112*, 1–11. [[CrossRef](#)]
56. Yang, B.; Zhong, L.; Zhang, X.; Shu, H.; Yu, T.; Li, H.; Jiang, L.; Sun, L. Novel bio-inspired memetic salp swarm algorithm and application to MPPT for PV systems considering partial shading condition. *J. Clean. Prod.* **2019**, *215*, 1203–1222. [[CrossRef](#)]
57. Ahmad, R.; Murtaza, A.F.; Sher, H.A. Power tracking techniques for efficient operation of photovoltaic array in solar applications—A review. *Renew. Sustain. Energy Rev.* **2019**, *101*, 82–102. [[CrossRef](#)]
58. Alik, R.; Jusoh, A.; Sutikno, T. A Review on Perturb and Observe Maximum Power Point Tracking in Photovoltaic System. *Int. Res. J. Eng. Technol. (IRJET)* **2016**, *13*, 745. [[CrossRef](#)]
59. Pakkiraiah, B.; Sukumar, G.D. Research Survey on Various MPPT Performance Issues to Improve the Solar PV System Efficiency. *J. Sol. Energy* **2016**, *2016*, 1–20. [[CrossRef](#)]
60. Rai, A.; Awasthi, B.; Singh, S.; Dwivedi, C.K. A review of Maximum Power Point Tracking Techniques for Photovoltaic System. *Int. J. Eng. Res.* **2016**, *5*, 539–545. [[CrossRef](#)]
61. Sher, H.A.; Murtaza, A.F.; Noman, A.; Addoweesh, K.E.; Chiaberge, M. An intelligent control strategy of fractional short circuit current maximum power point tracking technique for photovoltaic applications. *J. Renew. Sustain. Energy* **2017**, *7*, 1–15. [[CrossRef](#)]
62. Srinivas, C.L.S.; Sreeraj, E.S. A Maximum Power Point Tracking Technique Based on Ripple Correlation Control for Single Phase Photovoltaic System with Fuzzy Logic Controller. *Energy Procedia* **2015**, *90*, 69–77. [[CrossRef](#)]
63. Oulcaid, M.; El Fadil, H.; Yahya, A.; Giri, F. Maximum Power Point Tracking Algorithm for Photovoltaic Systems under Partial Shaded Conditions. *Int. Federation Autom. Control* **2016**, *49*, 217–222. [[CrossRef](#)]
64. Dhande, D.P.; Chaudhari, A.P.; Mahajan, G.K. A Review of Various Mppt Techniques for Photovoltaic System. *Int. J. Innov. Eng. Res. Technol.* **2015**, *2*, 1–11.
65. Rashid, M.H. *Power Electronics: Circuits, Devices, and Applications*, 3rd ed.; Pearson Prentice Hall: Upper Saddle River, NJ, USA, 2004.
66. Mahela, O.P.; Shaik, A.G. Comprehensive overview of grid interfaced solar photovoltaic systems. *Renew. Sustain. Energy Rev.* **2017**, *68*, 316–332. [[CrossRef](#)]
67. Jana, J.; Saha, H.; Das Bhattacharya, K. A review of inverter topologies for single-phase grid-connected photovoltaic systems. *Renew. Sustain. Energy Rev.* **2017**, *72*, 1256–1270. [[CrossRef](#)]
68. Zeb, K.; Uddin, W.; Khan, M.A.; Ali, Z.; Ali, M.U.; Christofides, N.; Kim, H.J. A comprehensive review on inverter topologies and control strategies for grid connected photovoltaic system. *Renew. Sustain. Energy Rev.* **2018**, *94*, 1120–1141. [[CrossRef](#)]
69. Pillai, S.; Thale, S. Design and Implementation of a Three Phase Inverter for Renewable Energy Source with Unified Control Strategy. *Energy Procedia* **2015**, *90*, 673–680. [[CrossRef](#)]

70. Srivastava, A.K.; Tripathi, S.M. Current source inverter fed induction motor drives: A survey. *Int. J. Electr. Syst.* **2011**, *1*, 14–27.
71. Kadir, A.F.A.; Khatib, T.; Elmenreich, W. Integrating photovoltaic systems in power system: Power quality impacts and optimal planning challenges. *Int. J. Photoenergy* **2014**, *2014*, 1–7. [[CrossRef](#)]
72. Chauhan, A.; Thakur, R. Power Quality Improvement using Passive & Active Filters. *Int. J. Eng. Trends Technol.* **2016**, *36*, 130–136. [[CrossRef](#)]
73. Sundar, D.J.; Kumaran, M.S. Common mode behavior in grid connected DC and AC decoupled PV Inverter topologies. *Arch. Electr. Eng.* **2016**, *65*, 481–493. [[CrossRef](#)]
74. Borgaonkar, A. Solid State Transformers: A Review of Technology and Applications. 2015. Available online: File:///C:/Users/MDPI/AppData/Local/Temp/Solid_State_Transformer-TechnologyReview.pdf (accessed on 11 August 2020). [[CrossRef](#)]
75. Shayestegan, M. Overview of grid-connected two-stage transformer-less inverter design. *J. Mod. Power Syst. Clean Energy* **2018**, *6*, 642–655. [[CrossRef](#)]
76. Raturaj, V.; Shinde, P.D.B. A Review on Generator Grid Synchronization Needs Effects, Parameters and Various Methods. *Int. J. Res. Appl. Sci. Eng. Technol.* **2016**, *4*, 715–723.
77. Rajan, J.D.; Supriya, S. Kadam Synchronization of Three Phase Inverter with Electrical Grid. *Int. J. Eng. Res.* **2015**, *4*, 1024–1031. [[CrossRef](#)]
78. Nguyen, X.T.; Nguyen, D.Q.; Tran, T. Power control of a photovoltaic system connected to a distribution frid in Vietnam. *Vietnam Acad. Sci. Technol. J. Sci. Technol.* **2015**, *53*, 331–336.
79. Dragicevic, T.; Meng, L.; Blaabjerg, F.; Li, Y. Control of Power Converters in ac and dc Microgrids. *IEEE Trans. Power Electron.* **2019**, *27*, 4734–4749. [[CrossRef](#)]
80. Hassaine, L.; Ollás, E.; Quintero, J.; Barrado, A. Digital control based on the shifting phase for grid connected photovoltaic inverter. In Proceedings of the Conference Proceedings—IEEE Applied Power Electronics Conference and Exposition—APEC, Austin, TX, USA, 24–28 February 2008; pp. 945–951.
81. Elbaset, A.A.; Hassan, M.S.; Ali, H. Performance analysis of grid-connected PV system. In Proceedings of the 2016 Eighteenth International Middle East Power Systems Conference (MEPCON), Cairo, Egypt, 27–29 December 2016; pp. 675–682. [[CrossRef](#)]
82. Abdalrahman, A.; Inverters, G.; Abdalrahman, A.; Alshazly, A. Simulation and Implementation of Grid—Connected Inverters, Simulation and Implementation of. *Int. J. Comput. Appl.* **2012**, *60*, 41–49. [[CrossRef](#)]
83. Abdalrahman, A.; Zekry, A. Control of the grid-connected inverter using dsPIC microcontroller. In Proceedings of the 2013 2nd International Japan-Egypt Conference on Electronics, Communications and Computers, JEC-ECC 2013, Cairo, Egypt, 17–19 December 2013; pp. 159–164.
84. Althobaiti, A.; Armstrong, M.; Elgendy, M.A. Current Control of Three Phase Grid—Connected PV Inverters using Adaptive Controllers. *Int. J. Res. Comput. Commun. Technol.* **2017**, *6*, 256–262.
85. Blaabjerg, F.; Teodorescu, R.; Liserre, M.; Timbus, A.V. Overview of control and grid synchronization for distributed power generation systems. *IEEE Trans. Ind. Electron.* **2006**, *53*, 1398–1409. [[CrossRef](#)]
86. Naderipour, A.; Zin, A.A.M.; Habibuddin, M.H.B.; Miveh, M.R.; Guerrero, J.M. An improved synchronous reference frame current control strategy for a photovoltaic grid-connected inverter under unbalanced and nonlinear load conditions. *PLoS ONE* **2017**, *12*, e0164856. [[CrossRef](#)]
87. Golestan, S.; Monfared, M.; Freijedo, F.D. Design-Oriented Study of Advanced Synchronous Reference Frame Phase-Locked Loops. *IEEE Trans. Power Electron.* **2013**, *28*, 765–778. [[CrossRef](#)]
88. Harrison, W.P.M.J.; Duke, R.M. Three-Phase Phase-Locked Loop Control of a New Generation Power Converter. In Proceedings of the ICIEA, Singapore, 24–26 May 2006.
89. Shaikh, F.; Joseph, B. Simulation of synchronous reference frame PLL for grid synchronization using Simulink. In Proceedings of the International Conference on Advances in Computing, Communication and Control 2017, ICAC3 2017, Mumbai, India, 1–2 December 2017.
90. Refaat, A.; Kalas, A.; Daoud, A.; Bendary, F. A Control Methodology of Three Phase Grid Connected PV System. In Proceedings of the Clemson University Power Systems Conference (PSC 2013), Clemson, SC, USA, 12–15 March 2013.
91. Santhoshi, B.K.; Sundaram, K.M.; Padmanaban, S.; Holm-Nielsen, J.B.; Prabhakaran, K.K. Critical review of PV grid-tied inverters. *Energies* **2019**, *12*, 1921. [[CrossRef](#)]
92. Jaalam, N.; Rahim, N.A.; Bakar, A.H.A.; Tan, C.K.; Haidar, A.M.A. A comprehensive review of synchronization methods for grid-connected converters of renewable energy source. *Renew. Sustain. Energy Rev.* **2016**, *59*, 1471–1481. [[CrossRef](#)]

93. Guo, X.; Wu, W.; Gu, H. Phase locked loop and synchronization methods for grid-interfaced converters: A review. *Prz. Elektrotechniczny (Electr. Rev.)* **2011**, *87*, 182–187.
94. Li, Y.; Lu, N.; Wang, X.; Jiang, B. Islanding fault detection based on data-driven approach with active developed reactive power variation. *Neurocomputing* **2019**, *337*, 97–109. [[CrossRef](#)]
95. Mastromauro, R.A. Grid Synchronization and Islanding Detection Methods for Single-Stage Photovoltaic Systems. *Energies* **2020**, *13*, 3382. [[CrossRef](#)]
96. Kim, M.S.; Haider, R.; Cho, G.J.; Kim, C.H.; Won, C.Y.; Chai, J.S. Comprehensive review of islanding detection methods for distributed generation systems. *Energies* **2019**, *12*, 837. [[CrossRef](#)]
97. IEEE. IEEE Recommended Practice for Utility Interface of Photovoltaic (PV) Systems. *IEEE Std.* **2000**, *2000*, 32.
98. Schwartfeger, L.; Santos-Martin, D. Review of Distributed Generation Interconnection Standards. In Proceedings of the EEA Conference & Exhibition 2014, Auckland, New Zealand, 18–20 June 2014.
99. Wu, Y.; Lin, J.; Lin, H. Standards and Guidelines for Grid-connected Photovoltaic Generation Systems: A Review and Comparison Yuan-Kang Wu Jhih-Hao Lin Huei-Jeng Lin. *IEEE Trans. Ind. Appl.* **2017**, *53*, 3205–3216. [[CrossRef](#)]
100. Dhass, A.D.; Senthil Kumar, R.; Lakshmi, P.; Natarajan, E.; Arivarasan, A. An investigation on performance analysis of different PV materials. *Mater. Today Proc.* **2019**, *22*, 330–334. [[CrossRef](#)]
101. Agüera-Pérez, A.; Palomares-Salas, J.C.; González de la Rosa, J.J.; Florencias-Oliveros, O. Weather forecasts for microgrid energy management: Review, discussion and recommendations. *Appl. Energy* **2018**, *228*, 265–278. [[CrossRef](#)]
102. Wang, B.; Xian, L.; Manandhar, U.; Ye, J.; Zhang, X.; Gooi, H.B.; Ukil, A. Hybrid energy storage system using bidirectional single-inductor multiple-port converter with model predictive control in DC microgrids. *Electr. Power Syst. Res.* **2019**, *173*, 38–47. [[CrossRef](#)]
103. Hema Rani, P.; Navasree, S.; George, S.; Ashok, S. Fuzzy logic supervisory controller for multi-input non-isolated DC to DC converter connected to DC grid. *Int. J. Electr. Power Energy Syst.* **2019**, *112*, 49–60. [[CrossRef](#)]
104. Pourbehzadi, M.; Niknam, T.; Aghaei, J.; Mokryani, G.; Shafie-khah, M.; Catalão, J.P.S. Optimal operation of hybrid AC/DC microgrids under uncertainty of renewable energy resources: A comprehensive review. *Int. J. Electr. Power Energy Syst.* **2019**, *109*, 139–159. [[CrossRef](#)]
105. Faraji, F.; Mousavi, G.S.M.; Hajirayat, A.; Birjandi, A.A.M.; Al-Haddad, K. Single-stage single-phase three-level neutral-point-clamped transformerless grid-connected photovoltaic inverters: Topology review. *Renew. Sustain. Energy Rev.* **2017**, *80*, 197–214. [[CrossRef](#)]
106. González, M.; Cárdenas, V.; Miranda, H.; Álvarez-Salas, R. Modular multilevel converter for large-scale photovoltaic generation with reactive power flow and unbalanced active power extraction capabilities. *Math. Comput. Simul.* **2019**, *162*, 135–154. [[CrossRef](#)]
107. Sinha, A.; Chandra Jana, K.; Kumar Das, M. An inclusive review on different multi-level inverter topologies, their modulation and control strategies for a grid connected photo-voltaic system. *Sol. Energy* **2018**, *170*, 633–657. [[CrossRef](#)]
108. Sahoo, S.K.; Sukchai, S.; Yanine, F.F. Review and comparative study of single-stage inverters for a PV system. *Renew. Sustain. Energy Rev.* **2018**, *91*, 962–986. [[CrossRef](#)]
109. Yazdaninejadi, A.; Hamidi, A.; Golshannavaz, S.; Aminifar, F.; Teimourzadeh, S. Impact of inverter-based DERs integration on protection, control, operation, and planning of electrical distribution grids. *Electr. J.* **2019**, *32*, 43–56. [[CrossRef](#)]
110. Asha Rani, M.A.; Nagamani, C.; Saravana Ilango, G. A versatile method for computation of power pulsations in DFIG under grid imperfections. *Renew. Energy* **2016**, *88*, 143–153. [[CrossRef](#)]
111. Lakum, A.; Mahajan, V. Optimal placement and sizing of multiple active power filters in radial distribution system using grey wolf optimizer in presence of nonlinear distributed generation. *Electr. Power Syst. Res.* **2019**, *173*, 281–290. [[CrossRef](#)]
112. Zhang, J.; Cao, D.; Diahm, S.; Zhang, X.; Yin, X.; Wang, Q. Research on potential induced degradation (PID) of polymeric backsheets in PV modules after salt-mist exposure. *Sol. Energy* **2019**, *188*, 475–482. [[CrossRef](#)]
113. Mulla, M.A.; Chudamani, R.; Chowdhury, A. A novel control method for series hybrid active power filter working under unbalanced supply conditions. *Int. J. Electr. Power Energy Syst.* **2015**, *64*, 328–339. [[CrossRef](#)]

114. Chandak, S.; Bhowmik, P.; Mishra, M.; Rout, P.K. Autonomous microgrid operation subsequent to an anti-islanding scheme. *Sustain. Cities Soc.* **2018**, *39*, 430–448. [[CrossRef](#)]
115. Singh, B.; Sharma, J. A review on distributed generation planning. *Renew. Sustain. Energy Rev.* **2017**, *76*, 529–544. [[CrossRef](#)]
116. Meral, M.E.; Çelik, D. A comprehensive survey on control strategies of distributed generation power systems under normal and abnormal conditions. *Annu. Rev. Control* **2019**, *47*, 112–132. [[CrossRef](#)]
117. Balamurugan, M.; Sahoo, S.K.; Sukchai, S. Application of soft computing methods for grid connected PV system: A technological and status review. *Renew. Sustain. Energy Rev.* **2017**, *75*, 1493–1508. [[CrossRef](#)]
118. Kim, K.-S.; Lee, S.-H.; Cha, W.-J.; Kwon, B.-H. Three-level three-phase transformerless inverter with low leakage current for photovoltaic power conditioning system. *Sol. Energy* **2017**, *142*, 243–252. [[CrossRef](#)]
119. Jurisic, B.; Uglesic, I.; Xemard, A.; Paladian, F. Difficulties in high frequency transformer modeling. *Electr. Power Syst. Res.* **2016**, *138*, 25–32. [[CrossRef](#)]
120. Ramírez-Niño, J.; Haro-Hernández, C.; Rodríguez-Rodríguez, J.H.; Mijarez, R. Core saturation effects of geomagnetic induced currents in power transformers. *J. Appl. Res. Technol.* **2016**, *14*, 87–92. [[CrossRef](#)]
121. Kirthiga, S.; Jothi Swaroopan, N.M. Highly reliable inverter topology with a novel soft computing technique to eliminate leakage current in grid-connected transformerless photovoltaic systems. *Comput. Electr. Eng.* **2018**, *68*, 192–203. [[CrossRef](#)]
122. Samimi, M.H.; Hillenbrand, P.; Tenbohlen, S.; Shayegani Akmal, A.A.; Mohseni, H.; Faiz, J. Investigating the applicability of the finite integration technique for studying the frequency response of the transformer winding. *Int. J. Electr. Power Energy Syst.* **2019**, *110*, 411–418. [[CrossRef](#)]
123. Bahrami, A.; Okoye, C.O.; Atikol, U. Technical and economic assessment of fixed, single and dual-axis tracking PV panels in low latitude countries. *Renew. Energy* **2017**, *113*, 563–579. [[CrossRef](#)]
124. Wang, J.; Tyuryukanov, I.; Monti, A. Design of a novel robust current controller for grid-connected inverter against grid impedance variations. *Int. J. Electr. Power Energy Syst.* **2019**, *110*, 454–466. [[CrossRef](#)]
125. Kolesnik, S.; Sitbon, M.; Gadelovits, S.; Suntio, T.; Kuperman, A. Interfacing renewable energy sources for maximum power transfer—Part II: Dynamics. *Renew. Sustain. Energy Rev.* **2015**, *51*, 1771–1783. [[CrossRef](#)]
126. Pranesh, V.; Velraj, R.; Christopher, S.; Kumaresan, V. A 50 year review of basic and applied research in compound parabolic concentrating solar thermal collector for domestic and industrial applications. *Sol. Energy* **2019**, *187*, 293–340. [[CrossRef](#)]
127. Messalti, S.; Harrag, A.; Loukriz, A. A new variable step size neural networks MPPT controller: Review, simulation and hardware implementation. *Renew. Sustain. Energy Rev.* **2017**, *68*, 221–233. [[CrossRef](#)]
128. Mohapatra, A.; Nayak, B.; Das, P.; Mohanty, K.B. A review on MPPT techniques of PV system under partial shading condition. *Renew. Sustain. Energy Rev.* **2017**, *80*, 854–867. [[CrossRef](#)]
129. Meddour, S.; Rahem, D.; Cherif, A.Y.; Hachelfi, W.; Hichem, L. A novel approach for PV system based on metaheuristic algorithm connected to the grid using FS-MPC controller. *Energy Procedia* **2019**, *162*, 57–66. [[CrossRef](#)]
130. Sri Revathi, B.; Mahalingam, P.; Gonzalez-Longatt, F. Interleaved high gain DC-DC converter for integrating solar PV source to DC bus. *Sol. Energy* **2019**, *188*, 924–934. [[CrossRef](#)]
131. Salem, M.; Jusoh, A.; Idris, N.R.N.; Das, H.S.; Alhamrouni, I. Resonant power converters with respect to passive storage (LC) elements and control techniques—An overview. *Renew. Sustain. Energy Rev.* **2018**, *91*, 504–520. [[CrossRef](#)]
132. Zhao, G.; Li, M.; Jian, L.; He, Z.; Shuang, J.; Yuping, S.; Zhang, Q.; Zhongxian, L. Analysis of Fire Risk Associated with Photovoltaic Power Generation System. *Adv. Civ. Eng.* **2018**, *2018*, 1–7. [[CrossRef](#)]



© 2020 by the authors. Licensee MDPI, Basel, Switzerland. This article is an open access article distributed under the terms and conditions of the Creative Commons Attribution (CC BY) license (<http://creativecommons.org/licenses/by/4.0/>).

Article

Sizing and Control Algorithms of a Hybrid Energy Storage System Based on Fuel Cells

Arkadiusz Adamczyk

Faculty of Mechanical and Electrical Engineering, Institute of Electrical Engineering, Polish Naval Academy, Śmidowicza 69 Str., 81-127 Gdynia, Poland; a.adamczyk@amw.gdynia.pl

Received: 1 July 2020; Accepted: 24 September 2020; Published: 2 October 2020

Abstract: Growing consciousness of the threat posed by man-made climate change has spurred government institutions, industry, and science to find clean fuels to power economic activity. Fuel cells powered by hydrogen are one of the steps in gaining clean energy. To improve the efficiency of the fuel cell, the hybrid solutions are required. This article shows a new approach to the design and control of a hybrid energy storage system for portable applications. The methodology allows us to optimize the desired physical parameters of the elements (weight or size) in order to withstand the connected load power demand. Such an approach allows us to minimize weight, which is essential in portable systems. The methodology was proven by building a technology demonstrator. The measurements of physical objects verified the electrical parameters received during simulation and allowed a lower weight of the system, compared to the system based only on Li-ion batteries.

Keywords: energy storage; fuel cell; hybrid batter; optimal sizing; power management

1. Introduction

The international community is trying to develop new technologies and solutions allowing a reduction in greenhouse gas production [1–7]. Fossil fuels and oil used on a global scale are one of the major reasons for air pollution [8–13]. Renewable energy is key in the modern stationery industry [14–17]; however, overcoming these issues becomes more difficult when one wants to downsize the system. The use of fuel cells running on hydrogen seems to be one of the most sufficient and environmentally friendly solutions for mobile/portable applications [18–23]. Unfortunately, the physical limitations of the fuel cells require a new hybrid approach that involves Li-ion batteries or supercapacitors in order to fulfil the electrical power requirements of modern equipment [24–28]. Electrical boats, cars, electrical bikes, and scooters are something we have become used to in our everyday life. Such miniaturization creates new challenges regarding the mass and size of the designed systems [29–34]. The author’s goal was to design and build a portable device useful mostly in military applications, therefore the total system’s mass and size were the main issues. By applying new mathematical apparatus, the author was able to prepare methodology allowing us to estimate the size of each power source in the Hybrid Energy Storage System. Using fuel cells along with other energy sources also requires new control algorithms [35–39], which will support a complex power distribution system. Most of the power management algorithms used in modern hybrid solutions are rule-based strategies, which are quite vulnerable to dynamic changes in load. The author’s algorithm is also rule-based, but by considering the energy profile of the load it was possible to overcome the problem of power fluctuations. Such solutions comprise one or more power converters, several types of secondary energy sources, a fuel cell, several control loops, and protections, among other things. The aim of this paper is to present a new approach to designing hybrid energy sources suitable for portable applications based on energy profiles with the use of the Proton Exchange Membrane (PEM) fuel cell, Li-ion battery, and supercapacitor. Furthermore, the author presents the physical model of

the hybrid power system designed and build accordingly to the simulation, based on the presented mathematical model.

2. System Elements Selection

In this section, the author describes a new approach to estimate the mass of the elements for the hybrid energy source. Based on the purpose of the device, the group of loads intended to be connected is tested to create energy profiles. The energy profiles bring information about the current power demand and dynamics of the connected load. More specific information on how the energy profiles were created can be found in previous publications [40,41].

Using the energy profiles (Figure 1) generated according to the methodology described in [40,41], one can determine the electrical parameters (including mass) of the system that will be able to power the considered group of loads. Assuming that the random nature of the load is closest to the phenomena occurring in real situations, one should adopt the energy profile randomly generated for this stage of considerations.

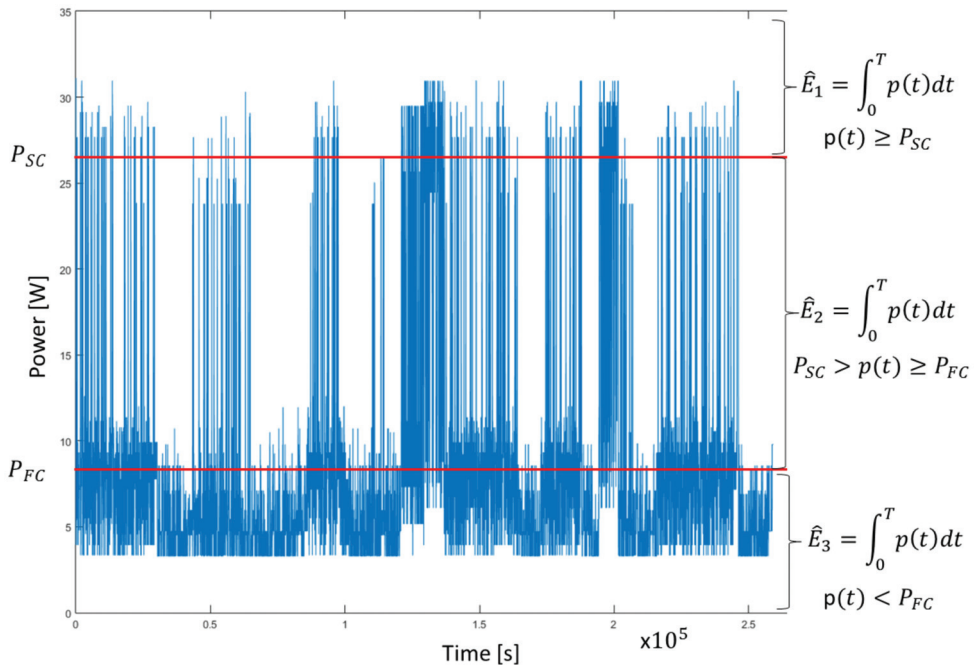


Figure 1. The energy profile generated in the random mode, with the marked power level and energy gathered in each threshold. P_{SC} stands for the power level at which supercapacitor starts to work in normal conditions, and P_{FC} stands for the power level at which the fuel cell starts to work in normal conditions.

During the selection of individual elements of the hybrid power supply system, no optimization criteria were adopted, and only a general condition of mass reduction was taken into account to compare it to the mass of the primary and secondary cells used in portable applications. Therefore, the parameters that taken into account are the mass of the cells and the electricity stored in them.

Describing the electrical energy emitted by the supercapacitor as E_1 , the PEM fuel cell as E_2 , and the Li-ion battery as E_3 , the energy and mass can be found with the equations:

$$1E_1 = f(m_1), \tag{1}$$

$$E_2 = f(m_2), \tag{2}$$

$$E_3 = f(m_3), \tag{3}$$

where:

m_1 : the mass of the supercapacitor.

m_2 : the mass of the fuel cell.

m_3 : the mass of the Li-ion battery.

In each example, the relationship between the mass and energy of the cell is non-linear (Figure 2), and can be described as:

$$E_1 = \alpha_1 m_1^{\beta_1}, \tag{4}$$

$$E_2 = \alpha_2 m_2^{\beta_2}, \tag{5}$$

$$E_3 = \alpha_3 m_3^{\beta_3}, \tag{6}$$

where the non-linearity coefficient $\alpha, \beta > 0$.

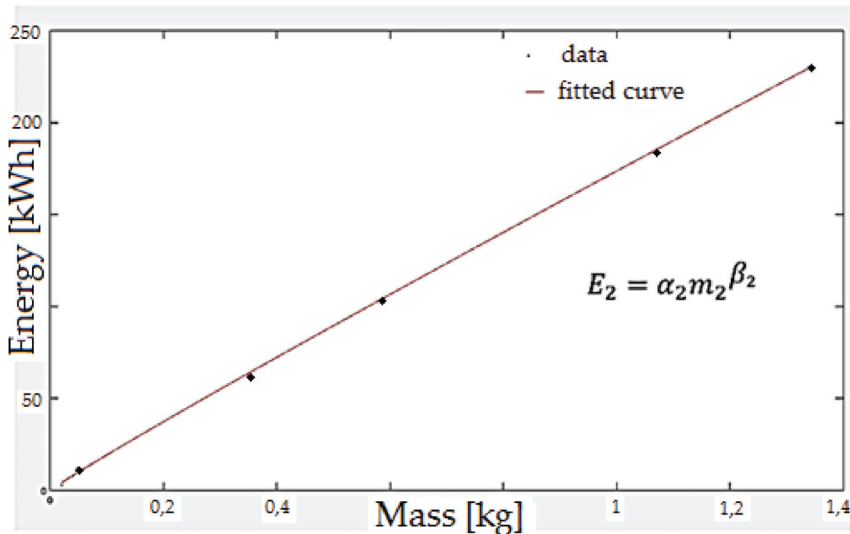


Figure 2. Non-linear relationship between energy and mass (Li-ion battery) with a fitted curve calculated in the Matlab environment. Coefficient α and β are given in Section 5.

In order to determine the proportions between individual elements that allow us to regulate the physical dimensions of the hybrid energy storage system, the proportionality factors (r) were created:

$$r_{12} = \frac{\alpha_1 m_1^{\beta_1}}{\alpha_2 m_2^{\beta_2}}, \tag{7}$$

$$r_{23} = \frac{\alpha_2 m_2^{\beta_2}}{\alpha_3 m_3^{\beta_3}}, \tag{8}$$

$$r_{31} = \frac{\alpha_3 m_3^{\beta_3}}{\alpha_1 m_1^{\beta_1}}. \tag{9}$$

Taking into account the equations from (4)–(9) this can be transformed to:

$$\frac{E_1}{E_2} = \frac{\alpha_1 m_1^{\beta_1}}{\alpha_2 m_2^{\beta_2}} = r_{12}, \tag{10}$$

$$\frac{E_2}{E_3} = \frac{\alpha_2 m_2^{\beta_2}}{\alpha_3 m_3^{\beta_3}} = r_{23}, \tag{11}$$

$$\frac{E_3}{E_1} = \frac{\alpha_3 m_3^{\beta_3}}{\alpha_1 m_1^{\beta_1}} = r_{31}. \tag{12}$$

Integrating in the time domain the energies of the individual power sources of the hybrid energy storage system, one can obtain an energy \hat{E} for individual thresholds (Figure 1).

$$\hat{E}_1 = \int_0^T P(t)dt \text{ for thresholds } P(t) \geq P_{SC}, \tag{13}$$

$$\hat{E}_2 = \int_0^T P(t)dt \text{ for thresholds } P_{SC} > P(t) \geq P_{FC}, \tag{14}$$

$$\hat{E}_3 = \int_0^T P(t)dt \text{ for thresholds } P(t) < P_{FC}. \tag{15}$$

The thresholds in equations from (13)–(15) were obtained from the functions in Equations (16)–(18):

$$(P_{SC}, P_{FC}) \in \operatorname{argmin}_{P_{SC}, P_{FC}} \left| \frac{\hat{E}_1}{\hat{E}_2} - r_{12} \right|, \tag{16}$$

$$(P_{SC}, P_{FC}) \in \operatorname{argmin}_{P_{SC}, P_{FC}} \left| \frac{\hat{E}_2}{\hat{E}_3} - r_{23} \right|, \tag{17}$$

$$(P_{SC}, P_{FC}) \in \operatorname{argmin}_{P_{SC}, P_{FC}} \left| \frac{\hat{E}_3}{\hat{E}_1} - r_{31} \right|. \tag{18}$$

3. Control Algorithms

The power generated by the hybrid energy storage system should cover the needs of the connected loads, taking into account the properties of the individual sources (Table 1). When designing control algorithms, one of the most important elements is to take into account the dynamics of load changes connected to the hybrid energy storage system.

Table 1. Comparison of properties for selected types of cells. On a scale from one (+) to three (+++), the advantages of the cell for the described parameters were determined [42].

	Response Time	High Temperature Performance	Low Temperature Performance	Energy Density	Power Density	Work Cycles	Single Cell Voltage	Control System Requirements
Li-ion battery	++	+	++	++	++	++	+++	+
Supercapacitor	+++	+++	+++	+	+++	+++	+	+
PEM Fuel cell	+	++	+	+++	++	++	++	++

Nevertheless, to understand the basic concept of the control algorithm it is easier to start with the simplified control algorithm. The fuel cell delivers power not only to the load but also to collaborating power sources, which are charged each time they drop below initially set voltage. The power demand

of the external load defines which power source is turned on or turned off according to the scheme shown in Figure 3. Due to the dynamic character of the load changes, it is necessary to distinguish short time fluctuations to avoid unnecessary switching between the power sources.

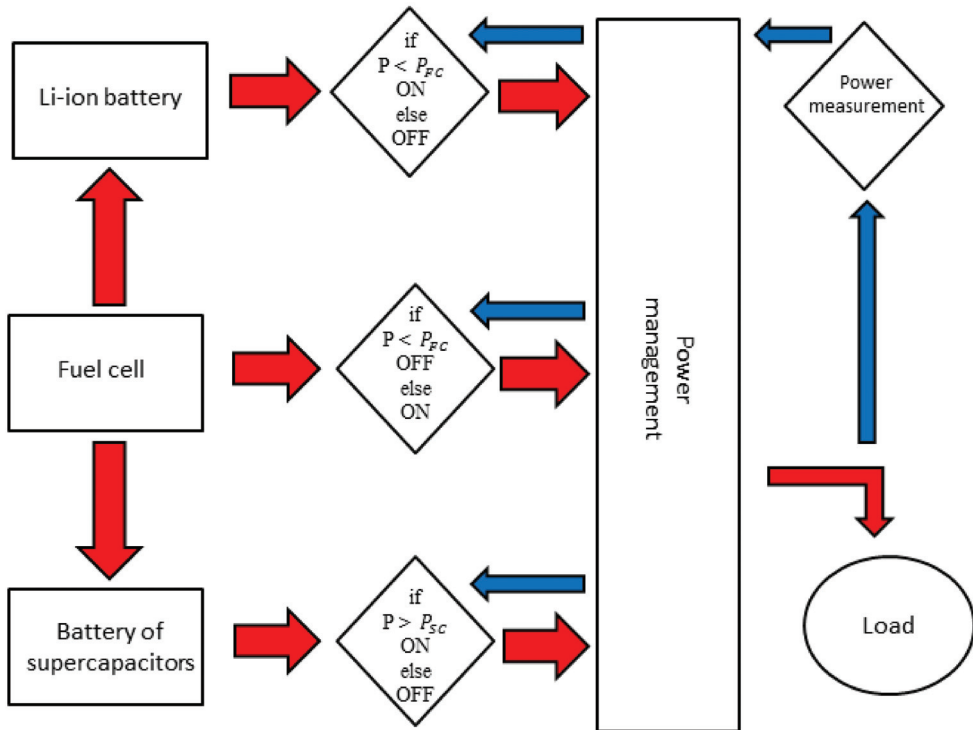


Figure 3. Simplified control algorithm of the hybrid power system. Red arrows indicate the power flow, blue arrows indicate the information signal flow.

The function of power-versus-time $p(t)$ is known (as a sample):

$$p(t_k) = p_k, \text{ where } k = \overline{1, N}. \tag{19}$$

When considering the dynamics of the hybrid energy source, the slowest element is the fuel cell (FC), which will set the main limitation for the operation of the entire system. By marking the dynamics of power changes as ε and assuming that a change in the operating states of individual cells included in the hybrid energy source requires exceeding the assumed threshold, one can write:

$$\left| \frac{dp(t)}{dt} \right| \leq \varepsilon. \tag{20}$$

The condition described by Equation (20) describes the state in which there will be no switching between cells due to sufficiently slow power dynamics. Moreover, if condition (20) holds, any current state is not shifted, whether it has been the FC or another element. The opposite state is represented by Equation (21), which will condition the switching.

$$\left| \frac{dp(t)}{dt} \right| > \varepsilon. \tag{21}$$

Note that conditions (20) and (21) are purely theoretical. Practically, we can use an approximation for the derivative. With the forward difference,

$$\left. \frac{dp(t)}{dt} \right|_{t=t_k} \approx \frac{p_{k+1} - p_k}{t_{k+1} - t_k} \tag{22}$$

This is an approximation of the power derivative at time t_k . For distinguishing real power jumps from short-time fluctuations, we need to estimate the short-time energy \tilde{E}_k for a standardized power:

$$\begin{aligned} \tilde{E}_k &= \int_{t_k}^{t_{k+2}} |p(t) - p(t_k)| dt \approx \\ &\approx (t_{k+1} - t_k) \frac{|p_{k+1} - p_k| + |p_{k+2} - p_k|}{2} + (t_{k+2} - t_k) \frac{|p_{k+1} - p_k| + |p_{k+2} - p_k|}{2} = \\ &= (t_{k+1} - t_k) \frac{|p_{k+1} - p_k|}{2} + (t_{k+2} - t_{k+1}) \frac{|p_{k+1} - p_k| + |p_{k+2} - p_k|}{2}, \end{aligned} \tag{23}$$

where the trapezoidal rule for integral approximation is used. Hence, if \tilde{E}_k is negligible, then a fluctuation has been registered on the interval $[t_k; t_{k+2}]$, so any state of the hybrid power source should not be shifted. Denoted by E_0 is a negligible part of energy occurring due to short-term fluctuations. In Table 2, one can see how the elements of the hybrid energy storage system are shifted, if at all, depending on the short-time power dynamics (22) and residual short-time energy (23). This table is considered at time $[t = t_{k+2}]$ only if:

$$\left| \frac{P_{k+1} - P_k}{t_{k+1} - t_k} \right| > \varepsilon. \tag{24}$$

Table 2 has an additional power level, marked as P_{Li} , which includes the state reserved for the Li-ion battery.

Therefore, the power value $p(t)$ in each next step $p(t_1) = p_1$ depends on the parameters ε and E_0 . This can be described as (25):

$$p_k = \psi\left(\left\{P_{jj}\right\}_{j=1}^{k-1}, \varepsilon, E_0\right) \text{ where } k = \overline{2, N}. \tag{25}$$

The switching problem boils down to finding the maximum energy for the period T depending on the ε and E_0 (26):

$$\begin{aligned} E_T^* &= \max_{\varepsilon} \max_{E_0} \int_{t_1}^{t_N} P(t, \varepsilon, E_0) dt \approx \\ &\max_{\varepsilon} \max_{E_0} \sum_{k=1}^{N-1} (t_{k+1} - t_k) \frac{P_k + P_{k+1}}{2} = \\ &= \max_{\varepsilon} \max_{E_0} \left((t_2 - t_1) \frac{P_1 + \psi(P_1, \varepsilon, E_0)}{2} + \right. \\ &\quad \left. + \sum_{k=2}^{N+1} (t_{k+1} - t_k) \frac{\psi\left(\left\{P_{jj}\right\}_{j=1}^{k-1}, \varepsilon, E_0\right) + \psi\left(\left\{P_{jj}\right\}_{j=1}^k, \varepsilon, E_0\right)}{2} \right). \end{aligned} \tag{26}$$

The presented mathematical apparatus allows us to determine both the size of the individual cell used in the hybrid energy storage system and to create the algorithm controlling the operation of the system.

Table 2. A scheme of the shifting algorithm between elements of the hybrid energy storage system at time $t = t_{k+2}$.

State	Short-Time Power Dynamics	Residual Short-Time Energy	Shift to the State
1 (SC)	$\frac{p_{k+1}-p_k}{t_{k+1}-t_k} > \varepsilon$	$\tilde{E}_k > E_0$	No shift
1 (SC)	$\frac{p_{k+1}-p_k}{t_{k+1}-t_k} > \varepsilon$	$\tilde{E}_k \leq E_0$	No shift
1 (SC)	$\frac{p_{k+1}-p_k}{t_{k+1}-t_k} < -\varepsilon$	$\tilde{E}_k \leq E_0$	No shift
1 (SC)	$\frac{p_{k+1}-p_k}{t_{k+1}-t_k} < -\varepsilon$	$\tilde{E}_k > E_0$ for $P_{SC} < P_{k+1}$	No shift
1 (SC)	$\frac{p_{k+1}-p_k}{t_{k+1}-t_k} < -\varepsilon$	$\tilde{E}_k > E_0$ dla $\frac{P_{Li}+P_{SC}}{2} \leq P_{k+1} \leq P_{SC}$	2 (FC)
1 (SC)	$\frac{p_{k+1}-p_k}{t_{k+1}-t_k} < -\varepsilon$	$\tilde{E}_k > E_0$ dla $P_{k+1} < \frac{P_{Li}+P_{SC}}{2}$	3 (Li-ion)
2 (FC)	$\frac{p_{k+1}-p_k}{t_{k+1}-t_k} > \varepsilon$	$\tilde{E}_k > E_0$	1 (SC)
2 (FC)	$\frac{p_{k+1}-p_k}{t_{k+1}-t_k} > \varepsilon$	$\tilde{E}_k \leq E_0$	No shift
2 (FC)	$\frac{p_{k+1}-p_k}{t_{k+1}-t_k} < -\varepsilon$	$\tilde{E}_k \leq E_0$	No shift
2 (FC)	$\frac{p_{k+1}-p_k}{t_{k+1}-t_k} < -\varepsilon$	$\tilde{E}_k > E_0$	3 (Li-ion)
3 (Li-ion)	$\frac{p_{k+1}-p_k}{t_{k+1}-t_k} > \varepsilon$	$\tilde{E}_k > E_0$ for $\frac{P_{Li}+P_{SC}}{2} \leq P_{k+1}$	1 (SC)
3 (Li-ion)	$\frac{p_{k+1}-p_k}{t_{k+1}-t_k} > \varepsilon$	$\tilde{E}_k > E_0$ for $P_{k+1} < \frac{P_{Li}+P_{SC}}{2}$	2 (FC)
3 (Li-ion)	$\frac{p_{k+1}-p_k}{t_{k+1}-t_k} > \varepsilon$	$\tilde{E}_k \leq E_0$	No shift
3 (Li-ion)	$\frac{p_{k+1}-p_k}{t_{k+1}-t_k} < -\varepsilon$	$\tilde{E}_k \leq E_0$	No shift
3 (Li-ion)	$\frac{p_{k+1}-p_k}{t_{k+1}-t_k} < -\varepsilon$	$\tilde{E}_k > E_0$	No shift

Note that we use the forward difference to estimate the derivative instead of the central difference in order to have interval $[t_{k+1}; t_{k+2}]$ to accomplish the integration. For instance, if condition (24) is not true, then we literally do nothing on the interval $[t_{k+1}; t_{k+2}]$ (“waiting”, wherein the corresponding memory of microprocessor controller is empty). If condition (24) is true, then a very short interval $[t_{k+1}; t_{k+2}]$ is occupied for the microprocessor preparation to integrate over interval $[t_k; t_{k+2}]$ and make a decision on the shift.

4. Mathematical Model

The mathematical model of the hybrid power system was designed and tested in the Matlab Simulink environment. In Simulink, it is very straightforward to represent and then simulate a mathematical model representing a physical system. Models are represented graphically in Simulink as block diagrams. A wide array of blocks are available to the user in provided libraries for representing various phenomena and models in a range of formats. The multilayer model was divided into few sections (Figure 4). Taken from the left, the “Digital Clock” and “MATLAB function GEN_LOS_NIEB” are responsible for operating the connected load. This block turns on and off selected elements of the load according to the chosen scenario. The next block, “Load”, represents the physical load connected to the hybrid power system. The “Stab” block represents the dc/dc converter and the “hybrid” block is the hybrid power system.

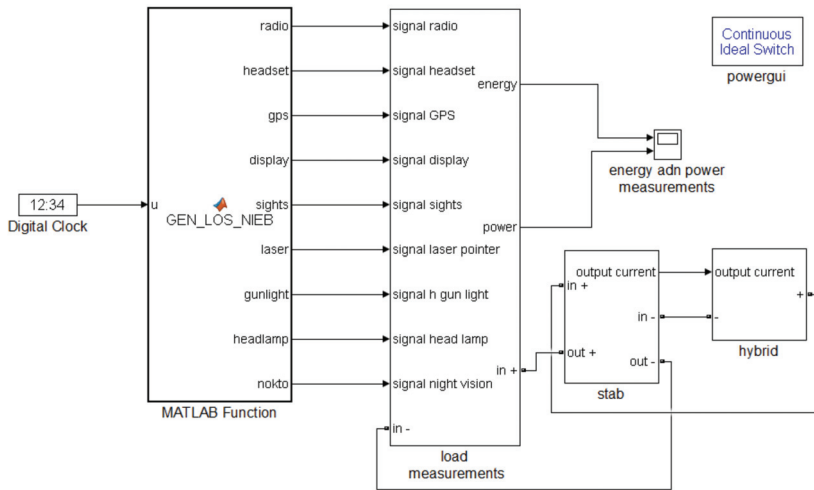


Figure 4. Base layer of the hybrid.

The first layer of the hybrid power system (Figure 5) consists of the “Logic” block responsible for the harmonic work of the fuel cell (“Fuel cell”), the Li-ion battery (“Li-ion”)k and the supercapacitor (“Supercap”), which are controlled with controlled relays (“Switch”).

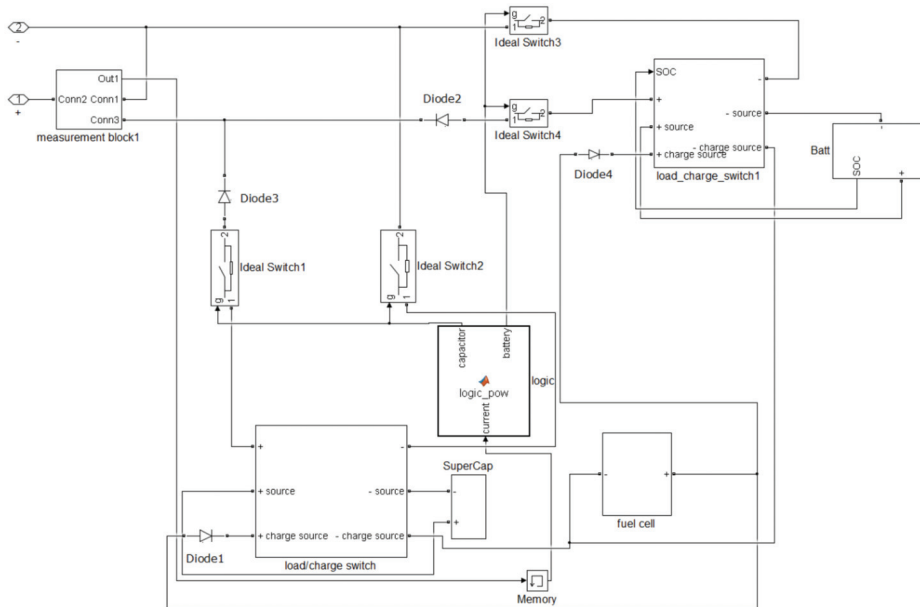


Figure 5. Hybrid power system first layer.

5. Physical Realization of the Mathematical Model

To ensure that the presented mathematical apparatus is valid, a simulation in the Matlab-Simulink environment was performed. All the elements used in the simulation were taken from the standard

Simulink Simscape library. However, both the loads and control systems were custom-made by the author in order to fully reflect the complex working principal of the hybrid power system.

The hybrid energy storage system was designed with the use of multiple electronic devices, which allowed us to support loads of up to 35W. A DSPIC33EP256MU810-I/PT microcontroller was used as the main engine, and it allowed us to support most of the algorithms implemented in the system. Other significant elements are the LTC4412 MOSFET controllers, the ZXCT1082 current output monitors, the ADUM1250 I2C isolator, and the LT3650-8.4 Li-ion charger.

The coefficient values received with use of the methodology shown in the first paragraph (Equations (4)–(6)) for the tested battery of supercapacitors (Maxwell 5F), PEM fuel cell (Horizon PEM 20W), and Panasonic 18,650 Li-ion 2P2S battery (4 Ah) are as follows:

Coefficients for the supercapacitor (with 95% confidence bounds):

- $\alpha = 7.934$ (7.038, 8.831),
- $\beta = 1.152$ (1.115, 1.189).

Coefficients for the fuel cell (with 95% confidence bounds):

- $\alpha = 52.1$ (37.56, 66.64),
- $\beta = 1.684$ (1.523, 1.845).

Coefficients for the Li-ion battery (with 95% confidence bounds):

- $\alpha = 173.7$ (169.6, 177.8),
- $\beta = 0.9565$ (0.9042, 1.009).

The thresholds that separate the areas of responsibility of cells working in the hybrid power system (Equations (13)–(15)) are as follows:

- $P_{SC} = 23.85$ (W),
- $P_{FC} = 5.68$ (W).

After computer simulation, which resulted in a steady output voltage (24V) across all ranges of loads, changing accordingly to various scenarios of energy profiles, a physical model was made (Figure 6). The 3D model (Figure 7) presents the main elements of the physical model. The PEM fuel cell module holds the mentioned fuel cell with the controller and system of valves responsible for the hydrogen flow. Two hydrogen cartridges store hydrogen in the metal hydride to ensure the uninterrupted work of the fuel cell. The Li-ion/supercapacitor module holds a battery of supercapacitors and Li-ion batteries.

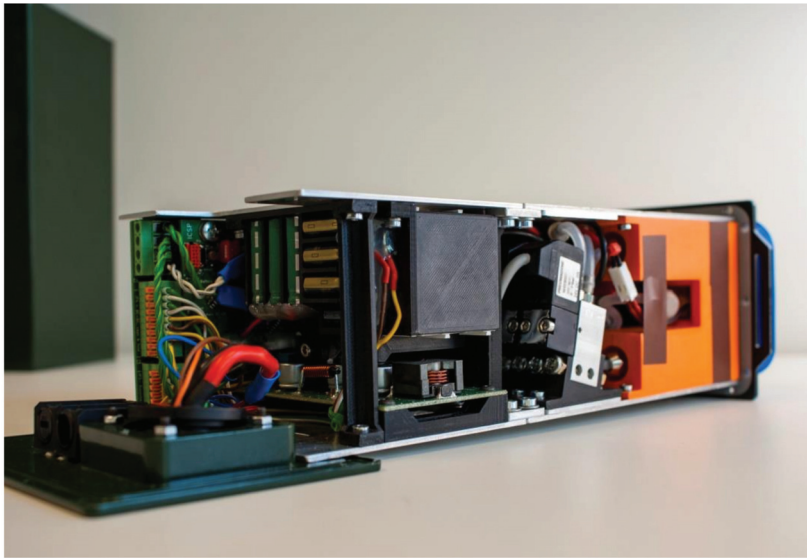


Figure 6. Physical model of the hybrid energy storage system.

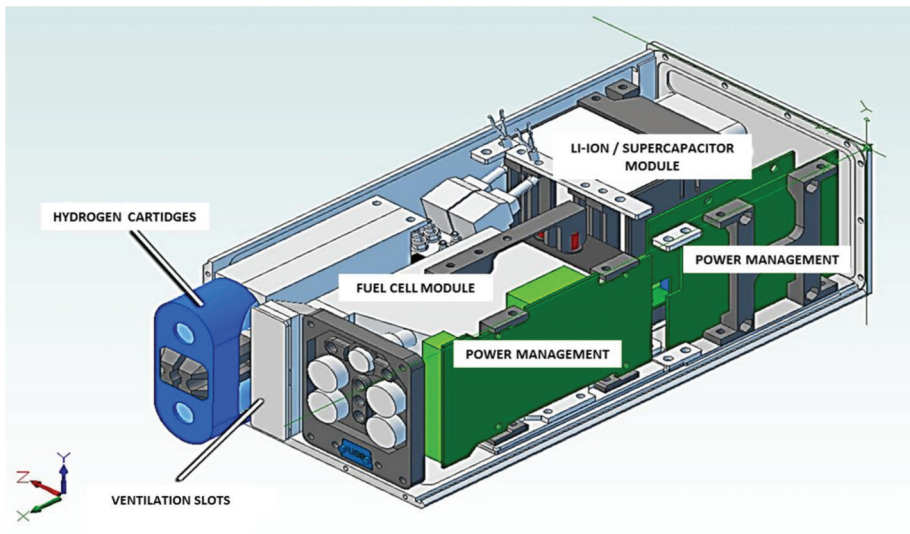


Figure 7. 3D model of the hybrid power system.

The power management modules are responsible for the control of the hybrid power system and load-displacement among all modules (Figure 7). The output voltage rises up to 24V with the DC-DC step-up converter. The control algorithm of the physical model is shown in Figure 8.

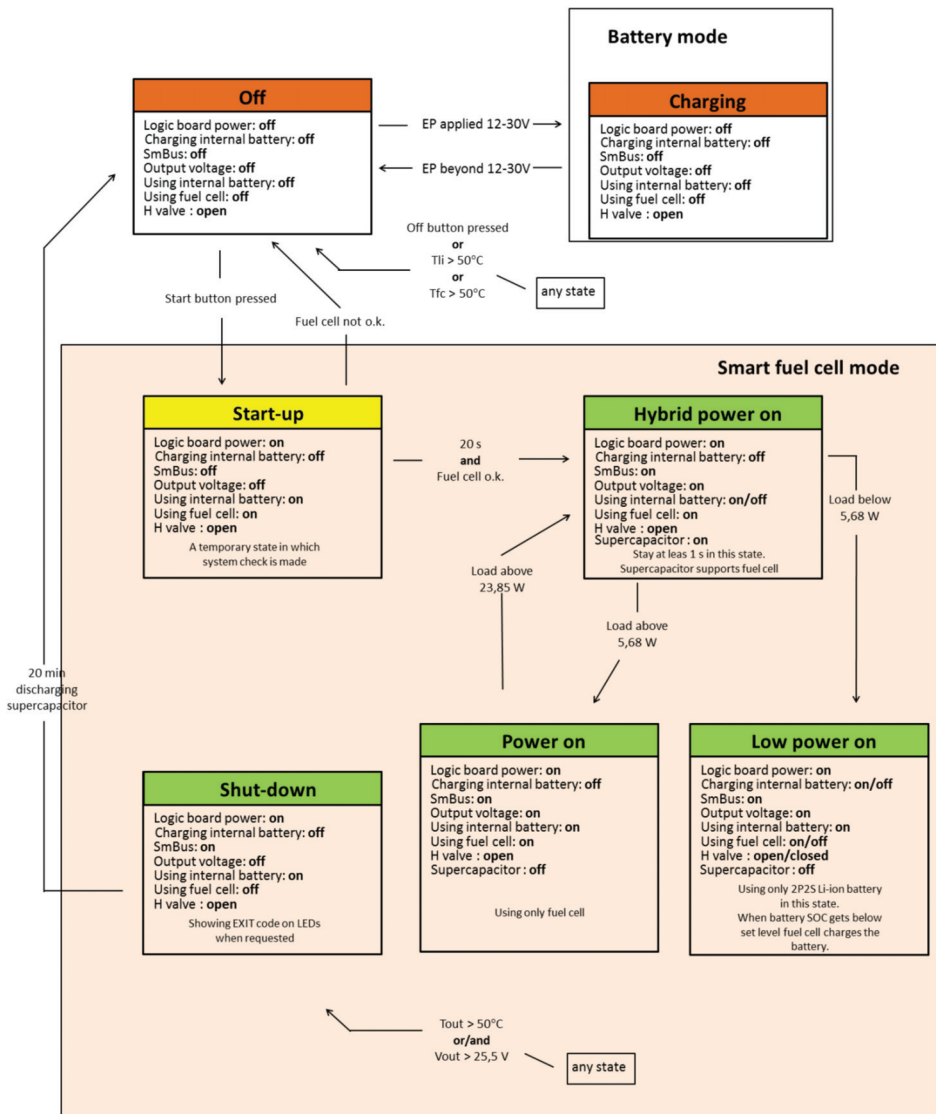


Figure 8. Physical model control algorithm.

6. Measurements and Simulation

Measurements and data acquisition for the physical model (Figure 6) were carried out with the use of the analog-digital converter NI USB-6289 and Labview ver. 2017 software. Variable loads changing according to the energy profiles were simulated with the digital load array 3711A. The tests were carried out with the use of energy profiles (Figure 1) reflecting several scenarios, which covered various conditions and the possible usage of electronic equipment, represented by the above-mentioned variable load. The PEM fuel cell along with the Li-ion battery and battery of supercapacitors were operating in a temperature of 23 °C and with a 50% humidity. The simulation was made with help of the Simulink Matlab environment, where basic mathematical models of the supercapacitor, fuel cell,

and Li-ion battery were modified according to data taken from physical objects. The experiment as well as the simulation resulted in a steady output voltage (24 V) across all ranges of loads.

Comparing the response of each cell during the simulation and the measurement results for the physical objects, one can notice few differences which did not influence the overall performance of the hybrid power system. Data acquired during the measurements on the physical object were used to correct the simulation parameters. Such modifications resulted in very similar cell responses both in the simulation and in the measurements of the physical object. Major differences can be noticed in two situations: first, when a steady state was not reached by the fuel cell (Figure 9), and, second, during the normal operation of the Li-ion battery (Figure 10).

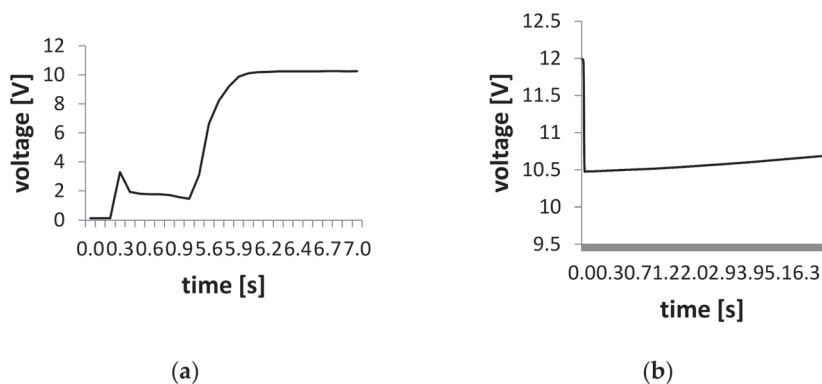


Figure 9. Fuel cell voltage characteristic during start-up. Measurements of the physical object (a), simulation (b).

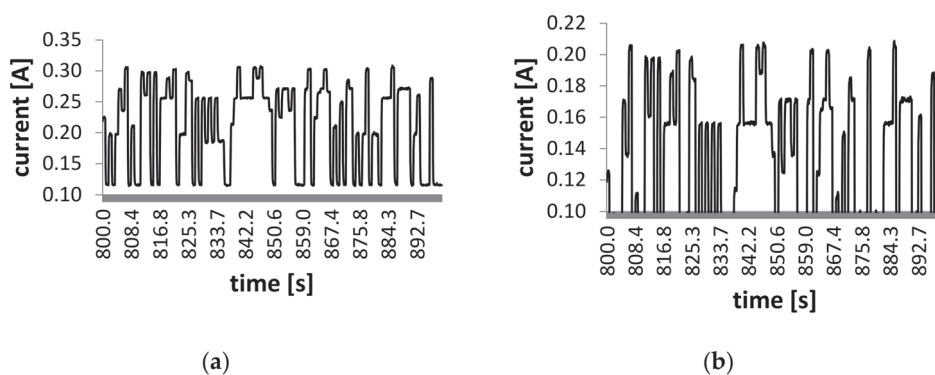


Figure 10. Li-ion battery current characteristics during its normal operation in a chosen period of time. Measurements of the physical object (a), simulation (b).

The differences between both fuel cell voltage characteristics (during the start-up) are the result of the insufficient accuracy of the mathematical model. It is very difficult to predict the unstable state of the fuel cell during its start-up.

These differences were caused by a few factors, in which the most significant one was placing the current measurement point on the hybrid energy storage system's output. This way, the power consumption of the electronic elements is not considered by the algorithm responsible for switching between the cells. Electronic elements are connected to the most stable and reliable power source in the system, which is the Li-ion battery. The current measurement presented in Figure 10 was taken directly from the Li-ion battery.

Further differences between the simulation and the measurements of the physical object were insignificant and noticeable only in the fuel cell (Figure 11). One can notice bigger voltage drops during the simulation, as well as voltage peaks (only one in this time frame).

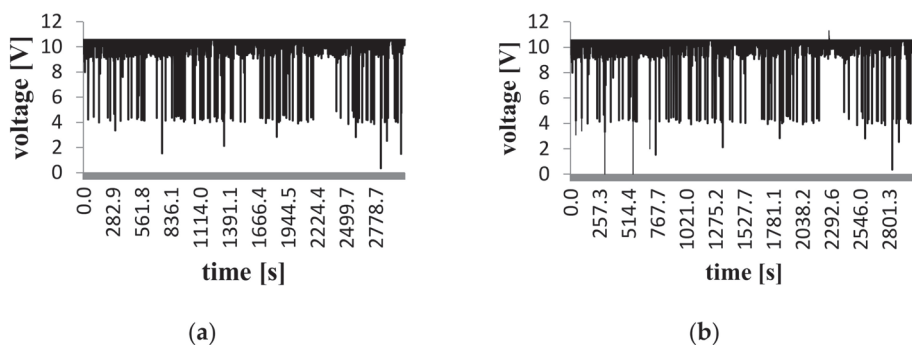


Figure 11. Fuel cell voltage characteristics during normal state. Measurements of the physical object (a), simulation (b).

The power management system ensures that the energy distribution in the hybrid power system sustains the required output parameters. At this point, the system should be analyzed as a whole, where, despite minor differences between the simulation and the measurements, one receives the same steady output voltage in both cases. The detailed behavior of each cell along with the mathematical model of the system will be a subject of another publication.

7. Conclusions

Considering the results obtained by comparing the measurements results of the mathematical model and the physical object, it can be concluded that the presented approach to sizing elements for a hybrid energy source is correct. This method can be customized regarding optimization criteria, which makes it universal. Furthermore, despite the fact that physical model was built mainly from commercially available elements (Horizon PEM fuel cell 20W, Li-ion 18,650–3400 mAh and VEC6R0505QG supercapacitor 6V/5F), the total weight of the hybrid power system (8325 g) was almost 20% smaller than a set of Li-ion batteries (10280 g) storing the same amount of energy (890 Wh). The total mass of the system includes hydrogen cartridges, which allow operating for 72 h. Measurements were taken from real-life objects during laboratory tests. The detailed behavior of each cell during the test along with its responses, both in the physical object and the simulation, is a subject of another publication. The results show some minor differences between the mathematical model and the physical elements, especially in the transient states in the hybrid power system. However, the overall results give a solid basis for using a Matlab environment in this kind of simulation.

Taking into account the results of the simulation and the measurements proves that the presented mathematical apparatus is correct and the use of the hybrid system with fuel cells is not only possible but justified in portable applications.

Funding: This research received no external funding.

Conflicts of Interest: The author declares no conflict of interest.

References

- Greenblatt, J.B.; Saxena, S. Autonomous taxis could greatly reduce greenhouse-gas emissions of US light-duty vehicles. *Nat. Clim. Chang.* **2015**, *5*, 860–863. [[CrossRef](#)]
- Cheah, L.; Evans, C.; Groode, T.; Heywood, J.; Kassaris, E.; Kromer, M.; Weiss, M. Reducing the fuel use and greenhouse gas emissions of the US vehicle fleet. *Energy Policy* **2008**, *36*, 2754–2760. [[CrossRef](#)]

3. Brown, M.A.; Levine, M.D.; Romm, J.P.; Rosenfeld, A.H.; Koomey, J.G. Engineering-economic studies of energy technologies to reduce greenhouse gas emissions: Opportunities and challenges. *Ann. Rev. Energy Environ.* **1998**, *23*, 287–385. [[CrossRef](#)]
4. Toy, J. Delivery by drone: An evaluation of unmanned aerial vehicle technology in reducing CO₂ emissions in the delivery service industry. *Transp. Res. Part D Transp. Environ.* **2018**, *61*, 58–67. [[CrossRef](#)]
5. Wang, A.; Stogios, C.; Gai, Y.; Vaughan, J.; Ozonder, G.; Lee, S.; Posen, I.D.; Miller, E.J.; Hatzopoulou, M. Automated, electric, or both? Investigating the effects of transportation and technology scenarios on metropolitan greenhouse gas emission. *Sustain. Cities Soc.* **2018**, *40*, 524–533. [[CrossRef](#)]
6. Aschilean, I.; Rasoi, G.; Raboaca, M.S.; Filote, C.; Culcer, M. Design and Concept of an Energy System Based on Renewable Sources for Greenhouse Sustainable Agriculture. *Energies* **2018**, *11*, 1201. [[CrossRef](#)]
7. Schäfer, A.W.; Barrett, S.R.H.; Doyme, K.; Dray, L.M.; Grandt, A.R.; Self, R.; O’Sullivan, A.; Synodinos, A.P.; Torija, A.J. Technological, economic and environmental prospects of all-electric aircraft. *Nat. Energy* **2019**, *4*, 160–166. [[CrossRef](#)]
8. Perera, F. Pollution from Fossil-Fuel Combustion is the Leading Environmental Threat to Global Pediatric Health and Equity: Solutions Exist. *Int. J. Environ. Res. Public Health* **2017**, *15*, 16. [[CrossRef](#)]
9. Pan, Y.; Tian, S.; Liu, D.; Fang, Y.; Zhu, X.; Gao, M.; Gao, J.; Michalski, G.; Wang, Y. Isotopic evidence for enhanced fossil fuel sources of aerosol ammonium in the urban atmosphere. *Environ Pollut.* **2018**, *238*, 942–947. [[CrossRef](#)]
10. Parry, I. Fossil-fuel subsidies assessed. *Nature* **2018**, *554*, 175–176. [[CrossRef](#)]
11. Zhang, Y.; El-Haddad, I.; Huang, R.; Ho, K.; Cao, J.; Han, Y.; Zotter, P.; Bozzetti, C.; Daellenbach, K.R.; Slowik, J.G.; et al. *Atmospheric Chemistry and Physics: From Air Pollution to Climate Change*; John Wiley & Sons Ltd: Chichester, UK, 2018; Volume 18, pp. 4005–4017. [[CrossRef](#)]
12. Martins, F.; Felgueiras, C.; Smitkova, M. Fossil fuel energy consumption in European countries. *Energy Proced.* **2018**, *153*, 107–111. [[CrossRef](#)]
13. Hartfoot, M.B.J.; Tittensor, D.P.; Knight, S.; Arnell, A.P.; Brooks, S.B.S.; Butchart, S.H.M.; Hutton, J.; Johnes, M.I. Present and future biodiversity risks from fossil fuel exploitation. *Conserv. Lett.* **2018**, *11*. [[CrossRef](#)]
14. Liang, Y.; Yu, B.; Wang, L. Costs and benefits of renewable energy development in China’s power industry. *Renew. Energy* **2019**, *131*, 700–712. [[CrossRef](#)]
15. Almezia, A.A.; Al-Masri, H.M.K.; Ehsani, M. Integration of Renewable Energy Sources by Load Shifting and Utilizing Value Storage. *IEEE Explor* **2019**, *10*. [[CrossRef](#)]
16. Kuik, O.; Branger, F.; Quirion, P. Competitive advantage in the renewable energy industry: Evidence from a gravity model. *Renew. Energy* **2019**, *131*, 472–481. [[CrossRef](#)]
17. Kaberger, T. Progress of renewable electricity replacing fossil fuels. *Glob. Energy Interconnect.* **2018**, *1*, 48–52. [[CrossRef](#)]
18. Wang, J.; Wang, H.; Fan, Y. Techno-Economic Challenges of Fuel Cell Commercialization. *Engineering* **2018**, *4*, 352–360. [[CrossRef](#)]
19. Ali, R.; Pasha, A. Fuel Cells-A signpost to future. In Proceedings of the IOP Conference Series: Materials Science and Engineering, Kocierz, Beskid Mały, Poland, 16–19 September 2019.
20. Kheirandish, A.; Akbari, E.; Nilashi, M.; Dahari, M. Using ANFIS technique for PEM fuel cell electric bicycle prediction model. *Int. J. Environ. Sci. Technol.* **2019**, *16*, 7319–7326. [[CrossRef](#)]
21. Manoharan, Y.; Hosseini, S.E.; Butler, B.; Alzahrani, H.; Fou, B.T.; Ashuri, T.; Krohn, J. Hydrogen Fuel Cell Vehicles; Current Status and Future Prospect. *Appl. Sci.* **2019**, *9*, 2296. [[CrossRef](#)]
22. Reddy, B.M.; Samuel, P.; Reddy, N.S.M. Government Policies Help Promote Clean Transportation in India: Proton-Exchange Membrane Fuel Cells for Vehicles. *IEEE Electr. Mag.* **2018**, *6*, 26–36. [[CrossRef](#)]
23. Nawotny, J.; Dodson, J.; Fiechter, S.; Gur, T.M.; Kennedy, B.; Macyk, W.; Bak, T.; Sigmund, W.; Yamawaki, M.; Rahman, K.A. Towards global sustainability: Education on environmentally clean energy technologies. *Renew. Sustain. Energy Rev.* **2018**, *81*, 2541–2551. [[CrossRef](#)]
24. Gonzales, E.L.; Cuesta, J.S.; Fernandez, F.J.V.; Lierena, F.I.; Carlini, M.A.R.; Bordons, C.; Hernandez, E.; Elfes, A. Experimental evaluation of a passive fuel cell/battery hybrid power system for an unmanned ground vehicle. *Int. J. Hydrogen Energy* **2019**, *44*, 12772–12782. [[CrossRef](#)]
25. Wang, Y.; Moura, S.J.; Advani, S.G.; Prasad, A.K. Power management system for a fuel cell/battery hybrid vehicle incorporating fuel cell and battery degradation. *Int. J. Hydrogen Energy* **2019**, *44*, 8479–8492. [[CrossRef](#)]

26. Wang, Y.; Sun, Z.; Chen, Z. Energy management strategy for battery/supercapacitor/fuel cell hybrid source vehicles based on finite state machine. *Appl. Energy* **2019**, *254*, 113707. [[CrossRef](#)]
27. Fathabadi, H. Combining a proton exchange membrane fuel cell (PEMFC) stack with a Li-ion battery to supply the power needs of a hybrid electric vehicle. *Renew. Energy* **2019**, *130*, 714–724. [[CrossRef](#)]
28. Thunthong, P.; Rael, S.; Davat, B. Energy management of fuel cell/battery/supercapacitor hybrid power source for vehicle applications. *J. Power Sour.* **2009**, *193*, 376–385. [[CrossRef](#)]
29. Dyer, C.K. Fuel cells for portable applications. *J. Power Sour.* **2002**, *106*, 31–34. [[CrossRef](#)]
30. Patil, A.S.; Dubois, T.G.; Sifer, N.; Bostick, E.; Gardner, K. Portable fuel cell systems for America’s army: Technology transition to the field. *J. Power Sour.* **2004**, *136*, 220–225. [[CrossRef](#)]
31. Younghyun, K.; Donghwa, S.; Jueun, S.; Naehyuck, C. System integration of a portable direct methanol fuel cell and a battery hybrid. *Int. J. Hydrogen Energy* **2010**, *35*, 5621–5637. [[CrossRef](#)]
32. Moore, J.M.; Lakeman, J.B.; Mepsted, G.O. Development of a PEM fuel cell powered portable field generator for the dismantled soldie. *J. Powersour.* **2002**, *106*, 16–20. [[CrossRef](#)]
33. Meyers, J.P.; Maynard, H.L. Design considerations for miniaturized PEM fuel cells. *J. Power Sour.* **2002**, *109*, 15. [[CrossRef](#)]
34. Davis, M.W.; Lototsky, M.; Malinowski, M.; van Schalkwyk, D.; Parsons, A.; Pasupathi, S.; Swanepoel, D.; van Niekerk, T. Metal hydride hydrogen storage tank for light fuel cell vehicle. *Int. J. Hydrogen Energy* **2019**, *44*, 29263–29272. [[CrossRef](#)]
35. Lei, T.; Yang, Z.; Lin, Z.; Zhang, X. State of art on energy management strategy for hybrid-powered unmanned aerial vehicle. *Chin. J. Aeronaut.* **2019**, *32*, 1488–1503. [[CrossRef](#)]
36. Weyers, C.; Bocklish, T. Simulation-based investigation of energy management concepts for fuel cell—battery—hybrid energy storage systems in mobile applications. *Energy Proced.* **2018**, *155*, 295–308. [[CrossRef](#)]
37. Raga, C.; Barrado, A.; Lazaro, A.; Martin-Lozano, A.; Quesada, I.; Zumel, P. Influence of the Main Design Factors on the Optimal Fuel Cell-Based Powertrain Sizing. *Energies* **2018**, *11*, 3060. [[CrossRef](#)]
38. You, Z.; Wang, L.; Han, Y.; Zare, F. System Design and Energy Management for a Fuel Cell/Battery Hybrid Forklift. *Energies* **2018**, *11*, 3440. [[CrossRef](#)]
39. Snoussi, J.; Ben Elghali, S.; Benbouzid, M.; Mimouni, M.F. Auto-Adaptive Filtering-Based Energy Management Strategy for Fuel Cell Hybrid Electric Vehicles. *Energies* **2018**, *11*, 2118. [[CrossRef](#)]
40. Adamczyk, A. A concept of minimizing an electric power supply system for portable gear and amrs. *Sci. J. Pol. Nav. Acad.* **2016**, *206*. [[CrossRef](#)]
41. Adamczyk, A.; Grzeczka, G. Hybrid power supply system model for offshore floating platforms. *J. Mar. Eng. Technol.* **2018**, *16*, 392–399. [[CrossRef](#)]
42. Ehrlich, G.M. *Handbook of Batteries*, 3rd ed.; Chapter 1; The McGaw-Hill Companies: New York, NY, USA, 2002.



© 2020 by the author. Licensee MDPI, Basel, Switzerland. This article is an open access article distributed under the terms and conditions of the Creative Commons Attribution (CC BY) license (<http://creativecommons.org/licenses/by/4.0/>).

Article

Hydrodynamic Response and Produced Power of a Combined Structure Consisting of a Spar and Heaving Type Wave Energy Converters

Constantine Michailides

Department of Civil Engineering and Geomatics, Cyprus University of Technology, Limassol 3036, Cyprus; c.michailides@cut.ac.cy; Tel.: +357-2500-2396

Abstract: During the past years, researchers have studied both numerically and experimentally multibody wave-wind combined energy structures supporting wind turbines and different types of Wave Energy Converters (WECs); rigid body hydrodynamic assumptions have been adopted so far for the development of their numerical models and the assessment of their produced power. In the present paper a numerical model that is based on the use of generalized modes addressing wave-structure interaction effects for the case of a multibody wave-wind combined structure is developed and presented. Afterwards, the developed numerical model is used for the assessment of the hydrodynamic response and the prediction of the produced power of different possible configurations of the updated WindWEC concept which consists of a spar supporting a wind turbine and one, two, three or four heaving type WEC buoys. The combined effects of the center-to-center distance of the WEC and spar platform, the number of the WECs and the grid configuration of spar and WECs on the hydrodynamic interaction between the different floating bodies, spar and WEC buoys, and consequently on their response and wave power production are examined for regular and irregular waves. Strong hydrodynamic interaction effects exist for small distance between spar and WECs that result to the decrease of the produced power. Power matrices of the updated WindWEC concept are presented for all examined configurations with different number of WECs. Moreover, the annual produced power of the updated WindWEC in two sites is estimated and presented. The generalized modes analysis presented in this paper is generic and can be used for the early stage assessment of wave-wind combined energy structures with low computational cost. The updated WindWEC can be used in sea sites with different environmental characteristics while extracting valuable amount of wave power.

Citation: Michailides, C. Hydrodynamic Response and Produced Power of a Combined Structure Consisting of a Spar and Heaving Type Wave Energy Converters. *Energies* **2021**, *14*, 225. <https://doi.org/10.3390/en14010225>

Received: 30 November 2020

Accepted: 29 December 2020

Published: 4 January 2021

Publisher's Note: MDPI stays neutral with regard to jurisdictional claims in published maps and institutional affiliations.



Copyright: © 2021 by the author. Licensee MDPI, Basel, Switzerland. This article is an open access article distributed under the terms and conditions of the Creative Commons Attribution (CC BY) license (<https://creativecommons.org/licenses/by/4.0/>).

Keywords: generalized modes; hydrodynamic analysis; combined energy structures; offshore wind turbines; wave energy converters; WindWEC

1. Introduction

Offshore Wind Turbines (OWTs) technology can be considered as the leading technology in the ocean renewable energy sector, which has the greatest potential for being developed extensively in the years to come and become the backbone of the global energy system. New offshore wind farms are now in operation or are scheduled for development in the coming years [1]. Floating OWTs can be effectively used as an alternative to the fixed bottom OWTs in intermediate and deep water areas. Among several concepts proposed so far Hywind is a successful example already in operation off the north-east coast of Scotland [2] in the world's first floating wind farm.

On the other hand, Wave Energy Converters (WECs) after forty years of unsuccessful wide industrialization are in a reconsideration phase as far as numerical analysis and design methods that should be used. Many different types of WECs have been proposed so far by a big number of researchers during the past decades [3–5]. Wavestar [6,7] is a good WEC example that may efficiently produce electricity due to the simple mode

of operation. Although the WECs were proposed earlier than OWTs, offshore wind technology experienced a very rapid and intense growth. The maturity of OWTs and WECs is different although both are subjected to similar challenges related with the harsh marine environment and hydrodynamic loadings.

It might be beneficial to investigate the possibility of extracting ocean energy resources, offshore wind and wave energy, simultaneously by sharing common marine infrastructures aiming to reduce the overall cost to increase the advantage use of the resources to ensure the efficient use of the ocean space [8–11]. Combining WECs with OWTs may result in several advantages including the possible reduction of construction, installation and maintenance costs related with infrastructures, equipment, mooring and anchoring systems, subsea power cables, survey and monitoring methods, and power storage. Also, the combined production of wind and wave energy may result in power output smoothing and in zero produced power reduction as the frequency range of the fluctuation in mean produced power by the OWTs greatly differs from the relevant range produced by WECs. Moreover, the WECs may act as a damper for the OWT system while harnessing the incoming wave loads. Several researchers [12–18] have studied numerically and experimentally wave-wind combined energy concepts utilizing different floating support platforms with different WEC types. An innovative wave-wind combined concept that consists of the Hywind spar and one Wavestar type WEC has been introduced in [19] and named as WindWEC is very critical at the beginning of the development of a specific concept basic questions about the effect of the number of the WECs as well as the effect of the distance between the different bodies to be on the hydrodynamic response of both spar and WECs and produced power to be addressed.

The design and analysis of combined energy structures present increasing complexity and require efficient computational models and numerical analysis methods as well as suitable physical model tests to ensure structural integrity and efficient performance. For the implementation of the numerical analysis of the combined concept that is a multibody marine structure, in time or in frequency domain, rigid body hydrodynamic assumptions and interconnected bodies with flexible or rigid elements have been very commonly adopted and used [14–17]. Excitation wave loads and hydrodynamic coefficients between the different interconnected bodies are calculated based on the six rigid body degrees of freedom for each body and relevant hydrodynamic analysis.

Generalized modes analysis has been developed by [20] and is mainly used to describe structural deformations of floating structures [21], motions of hinged and/or interconnected bodies [22–24], hydroelasticity of floating structures [25,26] and viscous dissipation in relation with marine engineering problems [27].

In the present paper, the dynamic characteristics and the wave power performance of the updated wave-wind combined concept WindWEC is presented for different possible design configurations. Updated WindWEC consists of a spar supporting a wind turbine and one, two, three or four heaving type WECs in different grid configurations. For estimating the hydrodynamic response and the produced wave power, a numerical model has been developed and presented which is based on the use of generalized modes. Spar oscillates in the six rigid body degrees of freedom while WECs are oscillating in two additional generalized modes, one of which related to the produced wave power. Details about the development of the generic generalized modes analysis are presented at the beginning of the paper. Afterwards with the use of the proposed numerical model, the effects of the total number of floating bodies comprising WindWEC, and consequently its grid configuration, and of the center-to-center distance between the bodies on the hydrodynamic interaction effects and on the produced wave power are examined. Strong hydrodynamic interaction effects exist for small distance between the spar and WECs resulting to the decrease of the produced power and should be avoided. The examined configuration with four WECs results to the largest produced wave power. Power matrices of the updated WindWEC concept are presented for all examined configurations with different number of WECs. The increase of the number of the bodies, and consequently the increase of the hydrodynamic

interaction between the different bodies, results to the decrease of the produced power if the distance between the spar and the different bodies remains the same. Moreover, the annual produced power of the updated WindWEC in two different sea sites is estimated and presented in order a direct estimation of the expected annual produced power of the updated WindWEC to be presented. An early-stage assessment of the updated combined concept WindWEC with low computational cost has been achieved with the use of the generalized modes analysis developed and presented in this paper.

2. Numerical Modeling of Wave-Wind Combined Structures with the Use of Generalized Modes

The numerical modeling that will be presented in this section is generic and can be applied for combined concepts consisting of different bodies for the evaluation of their wave-structure interaction effects and produced power. Also, it can be used if hydroelasticity is important for one or more of the bodies of the combined structure. In the present paper the developed numerical modeling is used for the case of the WindWEC concept combining the technologies of Hywind OWT and a heaving type WEC. WindWEC was introduced in [19] and originally analyzed as a two-body structure consisting of the spar platform and one WEC in time domain with rigid body hydrodynamic assumptions for everybody. A schematic layout of the original design configuration of WindWEC combined concept is presented in Figure 1.

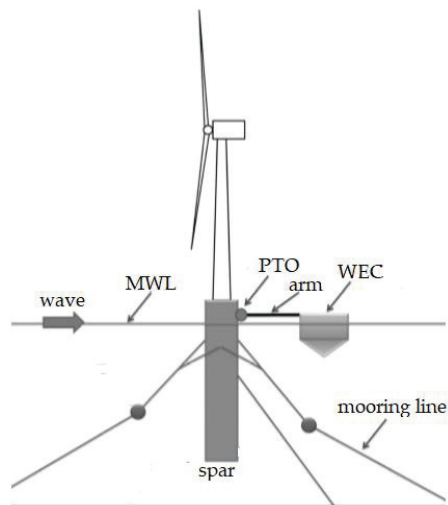


Figure 1. WindWEC combined concept as originally proposed.

In the present paper and contrary to the original design of WindWEC [19] the combined concept consists of the moored spar-type floating wind turbine Hywind OWT and one, two, three or four heaving type WECs. Four different possible grid configurations of WindWEC have been examined consisting of two, three, four and five bodies in total. The spar platform is capable to carry the NREL 5MW wind turbine for offshore applications. The WEC used in the present paper has a cylindrical geometry with a conical bottom end and its relative dimensions compared to the spar floating structure are small (2.2% of the total spar displacement and 2.1% of the spar mass); it is noted that this type of WEC is based on the design philosophy of Wavestar but is not exactly the same. Details and characteristics about the platform, wind turbine and WECs are presented in Table 1. For both spar and WECs similar design characteristics have been used compared to the unit characteristics as proposed in the original design of this combined concept in [19]. It should be noted that for the calculation of the characteristics, and when it is necessary, the

coordinate system in which the characteristics are calculated is at the mean water level of each body with the Z-axis pointing upward and X-axis to the right. For the calculation of the characteristics the hull of the spar (including ballast and steel weight), rotor, nacelle and tower are accounted for.

Table 1. Characteristics of different components of the WindWEC [19].

Spar		WEC	
Displacement	8016 m ³	Diameter	10 m
Diameter (free surface)	6.5 m	Draft	3 m
Diameter (bottom)	9.4 m	Conic length	1 m
Entire mass	8216 × 10 ³ kg	Entire mass of WEC	180 × 10 ³ kg
Center of gravity	−78.5 m	Center of gravity	−1.5 m
Center of buoyancy	−62.0 m	Center of buoyancy	−1.17 m
Mass moment of inertia, I _{XX}	69.84 × 10 ⁹ kg·m ²	Mass moment of inertia, I _{XX}	1.690 × 10 ⁶ kg·m ²
Mass moment of inertia, I _{ZZ}	16.78 × 10 ⁷ kg·m ²	Mass moment of inertia, I _{ZZ}	3.018 × 10 ⁶ kg·m ²

The spar platform and the WEC buoys are interconnected through a rigid structural arm (e.g., a frame structure or a rigid bar) that allows the WECs to move relatively with the spar platform in different degrees of freedom that can be adjusted. In the present paper we consider that WECs can move freely related with the spar's motions in heave and pitch degrees of freedom. The structural configuration (e.g., connectors, steel thickness, dimensions), as well as the final engineering design of the arm, is out of the scope of the present paper. Moreover, it is assumed that the arm can withstand all the internal loads without any structural integrity problems and behaves rigidly. The Power Take-Off (PTO) that transforms the relative heave motion of the two bodies, WEC and spar, into useful power is positioned at the edge of the rigid structural arm and behaves as a linear damper. It is stated that PTO stiffness effects have not been examined in the present paper. On the other hand, the spar is considered to move in six rigid body degrees of freedom.

The multibody hydrodynamic analysis of the WindWEC subjected to incident regular waves is conducted in the frequency domain and is based on the three-dimensional linear wave diffraction theory appropriately modified to account generalized modes for the representation of the motions of WECs. The hydrodynamic analysis of the WindWEC is taking into account the hydrodynamic interaction between the WECs and spar. The six degrees of freedom of the spar, namely, surge (ξ_1), sway (ξ_2), heave (ξ_3), roll (ξ_4), pitch (ξ_5) and yaw (ξ_6) are numerically simulated as six rigid body degrees of freedom while the two degrees of freedom of each of the WECs are numerically simulated as: (a) two additional generalized modes ξ_j , $j = 7$ and 8 , for the case that WindWEC consists of one WEC, (b) four additional generalized modes ξ_j , $j = 7, 8, 9$ and 10 , for the case that WindWEC consists of two WECs, (c) six additional generalized modes ξ_j , $j = 7, 8, 9, 10, 11$ and 12 , for the case that WindWEC consists of three WECs and (d) eight additional generalized modes ξ_j , $j = 7, 8, 9, 10, 11, 12, 13$ and 14 , for the case that WindWEC consists of four WECs. As a result, and for the grid configuration that WindWEC consists in total of two bodies, spar and one WEC, the total degrees of freedom of the numerical model are eight, namely, the six rigid body degrees of the spar platform, $\xi_1, \xi_2, \xi_3, \xi_4, \xi_5$ and ξ_6 , and the two generalized modes of each WEC, ξ_7 and ξ_8 , representing heave and pitch of the WEC, respectively. Same considerations apply to the rest examined configurations with three, four and five bodies with eight, ten, twelve and fourteen total degrees of freedom, respectively.

Based on linear potential theory, the flow is assumed irrotational and incompressible. The fluid is considered inviscid while its motion can be described with the use of the

velocity potential. The velocity potential, φ , satisfies the Laplace equation, and is described as below:

$$\varphi = \varphi_D + i\omega \sum_{j=1}^N \xi_j \varphi_j = \varphi_0 + \varphi_S + i\omega \sum_{j=1}^N \xi_j \varphi_j \tag{1}$$

where φ_0 is the potential of the incident waves, φ_D is the diffraction potential, φ_S is the scattered potential due to WECs and spar, $\varphi_j, j = 1, \dots, N$, is the radiation potential of each mode associated with the waves that are radiated due to the forced motions of the floating bodies (six rigid body degrees of freedom of spar and additional generalized modes of WECs), $\xi_j, j = 1, \dots, N$, are the complex amplitudes of the degrees of freedom of the combined structure, ω is the wave frequency, g is the gravitational acceleration, and N is the number of the total degrees of freedom (e.g., $N = 8, 10, 12$ and 14 for two, three, four and five bodies, respectively, as discussed previously). For $\varphi_j, j = 1, \dots, 6$, the radiation potential corresponds to the rigid body degrees of freedom of the spar. While, for $\varphi_j, j = 7, \dots, N$, the potential is related only with the additional generalized modes that correspond to the heave and pitch motions of the WECs.

The boundary value problem is solved based on the three-dimensional panel method utilising Green’s theorem. Appropriate boundary conditions are used on the free surface, on the sea bottom, and on the floating body, and the radiation condition for the outgoing waves is adopted [20,24]. The velocity potential ϕ should satisfy the Laplace equation and the following linearized boundary conditions (2–5):

$$\frac{\partial \varphi}{\partial z} - k\varphi = 0 \tag{2}$$

$$\frac{\partial \varphi}{\partial z} = 0 \text{ for } z = -d \tag{3}$$

$$\frac{\partial \varphi_D}{\partial n} = 0 \tag{4}$$

$$\frac{\partial \varphi_j}{\partial n} = n_j \tag{5}$$

where Equation (2) is the combined kinematic and dynamic free-surface condition, k is the wave number, Equation (3) is the bottom boundary condition for depth d , and Equations (4) and (5) are the Neumann conditions, which should hold on the wet surfaces of all the bodies of the combined structure with n_j denoting the normal unit vector of the bodies for all j degrees of freedom in the vertical direction.

The additional generalized degrees are numerically defined as a unit deformation of all panels of the wet surface of the WEC in the specific degree of freedom; e.g., for the 7th degree of freedom all the panels of the wet surface of the WEC obtain a value equals to one in heave direction only. The radiation potential for all modes, $\varphi_j, j = 1, \dots, N$, is subjected to the following boundary condition on the WECs and spar body [20]:

$$\frac{\partial \varphi_j}{\partial n} = n_j = u_j n_x + v_j n_y + w_j n_z \tag{6}$$

where n_x, n_y, n_z are the unit normal vectors on the wet surface of the body and u_j, v_j, w_j are the components of the displacement vector of the generalized mode $\varphi_j, j = 1, \dots, N$ in x, y, z directions, respectively; e.g., for the 7th degree of freedom the displacement vector is $u_7 = 1, v_7 = 0$ and $w_7 = 0$.

For both the spar and the WEC bodies, uniform mesh is used for the panel model discretization of their wet surface. The number of panels is selected after an appropriate convergence study. The amplitudes of all body’s motions, $\xi_j, j = 1, \dots, N$, (rigid body and

additional generalized) are calculated from the solution of the following linear system of equations (for $i = 1, \dots, N$):

$$\sum_{j=1}^N \left[-\omega^2 (M_{ij} + A_{ij}) + i\omega (B_{ij} + B_{ij}^E) + (C_{ij} + K_{ij}) \right] \xi_j = X_i \tag{7}$$

where M_{ij} and K_{ij} , $i, j = 1, \dots, N$, are the entire mass of the system and stiffness elements in all degrees of freedom. With regards to the hydrodynamic coefficients, namely, added mass, A_{ij} , $i, j = 1, \dots, N$, radiation damping, B_{ij} , and wave excitation loads, X_i , are calculated after the solution of the first-order boundary value problem according to the following equations:

$$A_{ij} - \frac{i}{\omega} B_{ij} = \rho \iint_{S_B} n_i \varphi_j dS \quad i, j = 1, \dots, N \tag{8}$$

$$X_i = -i\omega\rho \iint_{S_B} n_i \varphi_D ds \quad i = 1, \dots, N \tag{9}$$

where n_i , $i = 1, \dots, N$, is the normal component of the i -th mode shape (both rigid body and generalized degrees of freedom) on the mean body wetted surface, S_B , and ρ is the mass density of the water. Moreover in Equation (4), C_{ij} , $i, j = 7, \dots, N$, are the coefficients of the hydrostatic stiffness matrix given with the use of the following equation [20]:

$$C_{ij} = \rho g \iint_{S_B} n_j (w_i + d_r D_i) ds \tag{10}$$

where d_r is the draft of the floating body, D_i is the divergence of the displacement vector, and ρ_s and ρ are the mass density of the structure and the water, respectively.

With regard to the PTO damping elements, B_{ij}^E , and since the PTO function is related with the heave motion of the WECs, the B_{ij}^E coefficients that are nonzero are related with the heave degree of freedom of the WECs. It is stated that the present paper emphasizes on the hydrodynamic analysis of this type of the combined structure; aerodynamic damping loads or structural viscous loads are not considered during the analysis. In the present paper four different configurations of the combined concept will be examined consisting of one, two, three and four WECs. As a result, and for the case that the combined concept consists of four WECs and the spar, the degrees of freedom of the numerical model that correspond to the heave motion of the WECs are the 7th, 9th, 11th and 13th. Similar considerations can be made for the case that the combined concept consists of different number of WECs. The B_{ij}^E elements depending to the number of WECs that are used are calculated as follow:

$$B_{ij}^E = B_{PTO} \quad i = j = 7, 9, 11, 13 \tag{11}$$

or

$$B_{ij}^E = 0 \quad i \neq j \tag{12}$$

The response of the floating body in all the examined degrees of freedom, rigid and additional generalized modes, is expressed in terms of the Response Amplitude Operator, RAO, (Equation (13)):

$$RAO_j = \frac{|\xi_j|}{A}, \quad \text{with } j = 1, \dots, N \tag{13}$$

where $|\xi_j|$ is the amplitude of the complex quantity ξ_j and A is the amplitude of the incident waves defined at the beginning of the analysis equal to one.

The time-averaged produced wave power, P_{WECk} , of the k -th WEC extracted from the regular waves is calculated with the following Equation [28]:

$$P_{WECk} = 0.5 B_{PTO} \omega^2 |\xi_3 - \xi_j|^2 \quad \text{with } j = 7 \text{ and/or } 9 \text{ and/or } 11 \text{ and/or } 13 \tag{14}$$

where j depends upon the WEC that produces power. The total produced power, P_{tot} , of the WindWEC is:

$$P_{tot} = \sum_{k=1}^n P_{WECk} \text{ with } n = 1, 2, 3 \text{ or } 4 \quad (15)$$

where n is the total number of WECs that are used for the examined configuration of WindWEC. The time averaged power output for irregular waves is calculated as:

$$P_{irr}(H_s, T_p) = \int_0^\infty P_{tot}(\omega) S_\omega(\omega) d\omega \quad (16)$$

where $P_{tot}(\omega)$ is the total produced power of WindWEC for ω wave frequency, $S_\omega(\omega)$ is a power spectrum, H_s is the significant wave height and T_p is the peak wave period. For the purposes of the present paper the Pierson-Moskowitz spectrum is adopted as below:

$$S_\omega(\omega) = \beta_j H_s^2 T_p^{-4} \omega^{-5} \exp[-1.25(T_p \omega)^{-4}] \gamma \exp[-(T_p \omega - 1)^2 / 2\sigma^2] \quad (17)$$

where β_j is a factor that depends upon the γ factor that is considered equal to 3.3 and σ a constant value depends upon the wave frequency.

Finally, the annual averaged produced power of WindWEC for a specific sea site is calculated as follows:

$$P_{annual} = \sum_{H_s} \sum_{T_p} p(H_s, T_p) P_{irr}(H_s, T_p) \quad (18)$$

where $p(H_s, T_p)$ is the probability of occurrence that corresponds to the wave climate at a specific ocean site defined as a set of sea states related with the significant wave height and wave energy period.

3. Examined Configurations of WindWEC

As far as the examined wave environment, the combined multibody structure is placed in infinite water depth (deep water approximations) while the incident wave direction equals to 0° (surge motion of spar aligns with wave direction) (Figure 2). Forty-seven wave periods are totally examined between 3 and 24 s and the amplitude of incident waves, A , is considered equals to 1.

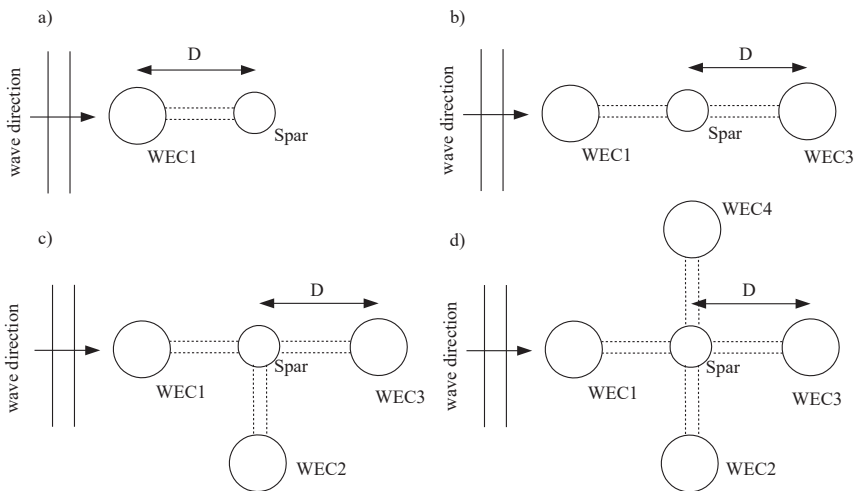


Figure 2. (a) CF1 examined configuration of WindWEC, (b) CF2 examined configuration of WindWEC, (c) CF3 examined configuration of WindWEC and (d) CF4 examined configuration of WindWEC.

Four different configuration cases of the WindWEC, CF_i , $i = 1\sim 4$ are examined (Figure 2). The examined configuration CF1 consists of the spar platform and WEC1, configuration CF2 consists of the spar platform, WEC1 and WEC3, CF3 consists of the spar platform, WEC1, WEC2 and WEC3, and CF4 consists of the spar platform, WEC1, WEC2, WEC3 and WEC4. In all the examined cases, D is the center-to-center distance between the spar platform and WECs. Four different D values are examined for each of the configurations equal to 10 m, 20 m, 30 m and 40 m in order to study the combined effect of the D value and grid configuration on the hydrodynamic response of WindWEC and the produced wave power. In total four configurations and four D values have been examined in the present paper resulting to 16 different examined cases; one of the examined configurations corresponds to the original design of WindWEC. The examined configurations, as well as their total degrees of freedom, are presented in Table 2. The examined configurations correspond to the case with two, three, four and five bodies with eight, ten, twelve and fourteen degrees of freedom, respectively. In all examined cases the first six degrees of freedom correspond to the rigid body degrees of freedom of spar. The natural periods of heave and pitch motions of both spar and WEC are presented in Table 3.

Table 2. Examined configurations of the WindWEC.

WindWEC Configuration	Utilized WECs	Total Degrees of Freedom, N
CF1	WEC1	8
CF2	WEC1 and WEC3	10
CF3	WEC1, WEC2 and WEC3	12
CF4	WEC1, WEC2, WEC3 and WEC4	14

Table 3. Natural periods of heave, T_{n3} , and pitch, T_{n5} , motions of spar and WEC.

Examined Body	Heave (sec)	Pitch (sec)
Spar	20.50	30.50
WEC	4.25	4.00

A constant value of B_{PTO} has been selected for all the examined cases which is equal with the radiation damping of the WEC for its natural period in heave degree of freedom, T_{n3} [29] in order maximum energy absorption to be achieved at the natural period of a single WEC. Based on relevant hydrodynamic analysis the heave radiation damping that corresponds to $T_{n3} = 4.25$ s is used. The damping coefficient that is used for all the examined cases in the present paper equals to $B_{PTO} = 88,482.7$ Nm/s.

4. Results and Discussion

With the examined configurations studied in the present paper the effect of the position of the WECs concerning the spar and the effect of grid configuration are intended to be highlighted. Those configurations will be feasible with an appropriate mooring system design in order to stabilize the combined structure. In the following subsections the results of the generalized modes based numerical model are presented and discussed. Initially hydrodynamic coefficients, namely, the added mass, radiation damping and excitation wave loads, are presented for different WindWEC configurations and D values. Next, results are presented for the motions of WECs and spar as well as for the produced wave power by the WECs focusing on examining the effects of the D values between spar and WECs for a specific configuration, as well as, of the different grid configurations of the WindWEC.

In Figure 3 the heave added mass coefficients are presented for different WECs and examined configurations. The 7th degree of freedom corresponds to the heave generalized mode of the WEC1 for all the examined configurations. The heave added mass coefficient

of the WEC considered as a single body (without any interaction effect) is also presented in Figure 3 with a black solid line. For WEC1 (Figure 3a,b) and for all examined cases a large interaction effect of the A_{77} added mass coefficient exists for all examined wave periods and for the case where the center-to-center distance D equals to 10 m. For the same D value and compared to the heave added mass coefficient of the single WEC the differences are large for all examined configurations CF1, CF2, CF3 and CF4. For $D = 10$ m and as the number of the bodies consisting WindWEC increases, the effects on the A_{77} added mass coefficient are larger for all examined wave periods attributed to the intense hydrodynamic interaction. For the rest examined center-to-center distances, namely, 20 m, 30 m and 40 m the A_{77} coefficients are different compared to the added mass coefficient of a single WEC for wave periods smaller than 14 s. Large differences are observed close to the natural period T_{n3} of the WEC; as the distance D increases the resonant effects become smaller.

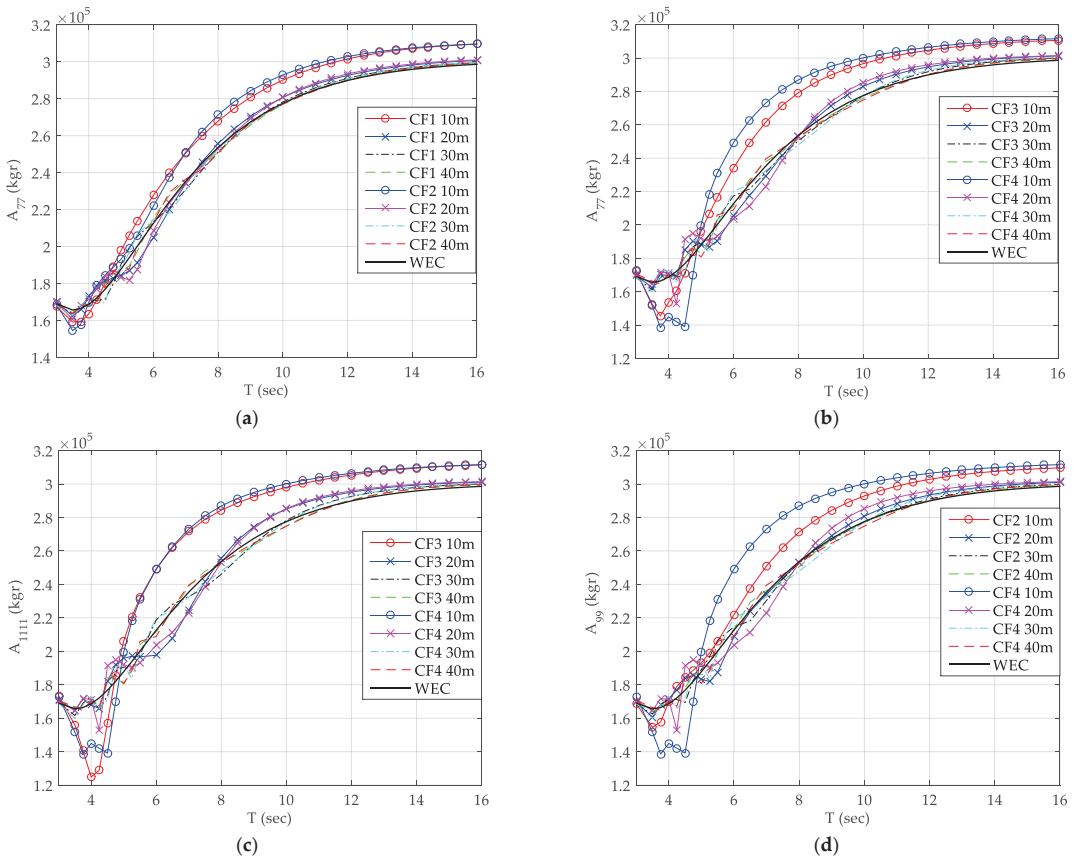


Figure 3. Heave added mass coefficients for the: (a) WEC1 of CF1 and CF2, (b) WEC1 of CF3 and CF4, (c) WEC2 of CF3 and CF4 and (d) WEC3 of CF2 and CF4.

Similar observations exist for WEC2 of CF3 and CF4 configurations (Figure 3c), and WEC3 of CF2 and CF4 configurations (Figure 3d) regarding the heave added mass coefficient of the WECs; for $D = 10$ m the effects are large and observed for all the examined wave periods while for the rest examined D values the interaction effects exist for wave periods smaller than 14 s. As far as the heave added mass coefficients of the spar, A_{33} , of the combined concept WindWEC the effect of the configuration and number of bodies of WindWEC on the A_{33} coefficient (Figure 4a) is large only for the case of CF4 configuration

consisting of five bodies and mainly for $D = 10\text{ m}$ and $D = 20\text{ m}$, while for the pitch degree of freedom (Figure 4b) the effect of the number of bodies of WindWEC on the A_{55} coefficient is not significant even for the case of small D values and CF4 where strong interaction effects exist. With regards to the pitch motion of WEC1 which is the 8th degree of freedom in the numerical analysis model of WindWEC, the A_{88} coefficient of CF1 and CF4 (Figure 4c) is largely affected mainly for small center-to-center distances, $D = 10\text{ m}$ and $D = 20\text{ m}$, between WECs and spar.

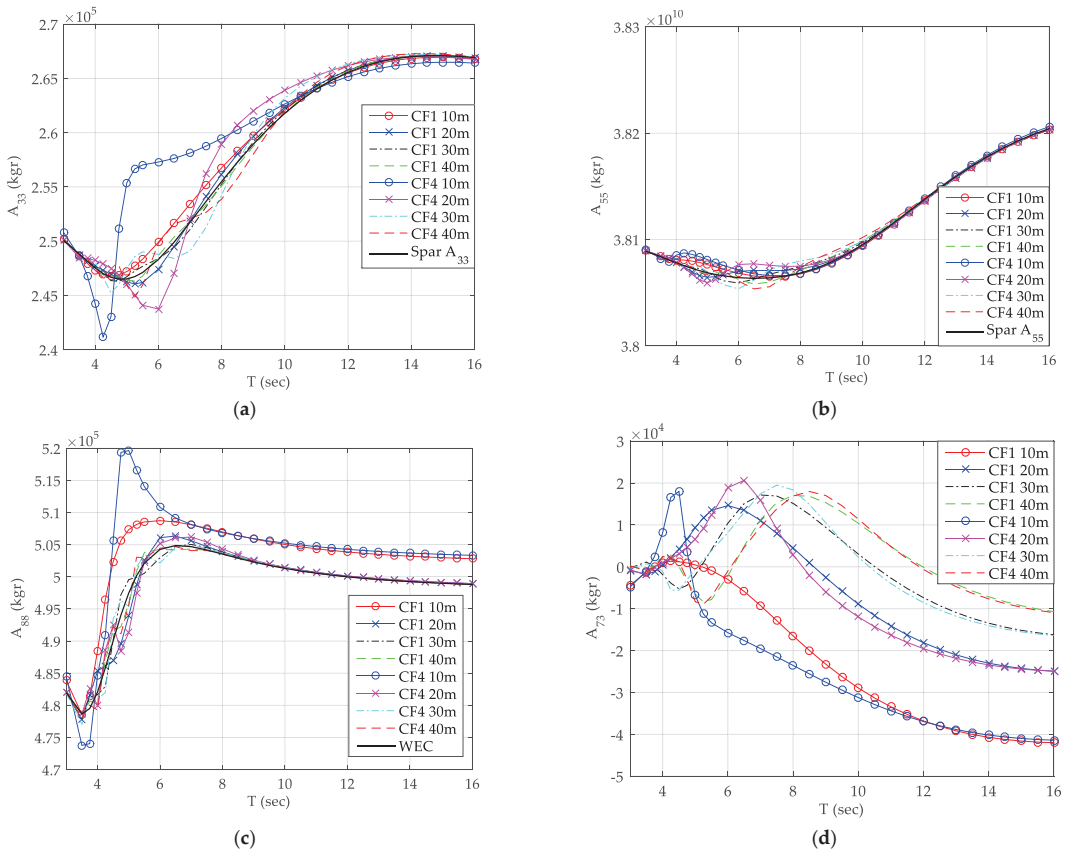


Figure 4. (a) A_{33} of spar for CF1 and CF4, (b) A_{55} of spar for CF1 and CF4, (c) A_{88} of WEC1 for CF1 and CF4 and (d) A_{73} of WEC1 for CF1 and CF4.

Apart from the diagonal terms of the added mass matrix that are affected by the WindWEC configuration and distance between the different bodies comprising the combined structure, the non-diagonal terms of the added mass matrix are affected too and should be accounted when dealing with the analysis of wind-wave combined structures. In Figure 4d the A_{73} coefficient for WEC1 of CF1 and CF4 are presented for all examined D values; A_{73} is the added mass coefficient of heave motion of WEC1 due to the heave motion of the spar. Large effects exist for all examined wave periods attributed to both the D value and the configuration of WindWEC.

In Figure 5a,b the heave radiation damping coefficients are presented for WEC1 and all examined configurations. It is stated that in all the Figures the heave radiation damping coefficient of the WEC calculated for the WEC considered as a single body without any interaction is also presented with a black solid line. For all the examined WindWEC

configurations and irrespectively of the examined D value, the effect of the D value for a specific configuration on the heave radiation damping coefficient exists only for wave periods up to 10 s. The interaction effects on the B_{77} value are larger for all the examined configurations with $D = 10$ m and are observed for wave periods close to the T_{n3} natural period of WEC. Similar trends are observed for WEC3 of CF2 and CF4 configurations (Figure 5c); for the case where five bodies are comprising WindWEC the heave radiation damping coefficients obtain very large values for wave periods close to the natural period of the WEC in heave degree of freedom. With regard to the second additional generalized degree of freedom of the numerical analysis (pitch motion of the WEC1) of CF1 and CF4, the B_{88} coefficient (Figure 5d) is largely affected mainly for $D = 10$ m, while the interaction effects on the B_{88} values are larger for CF4 configuration compared to the rest examined configurations.

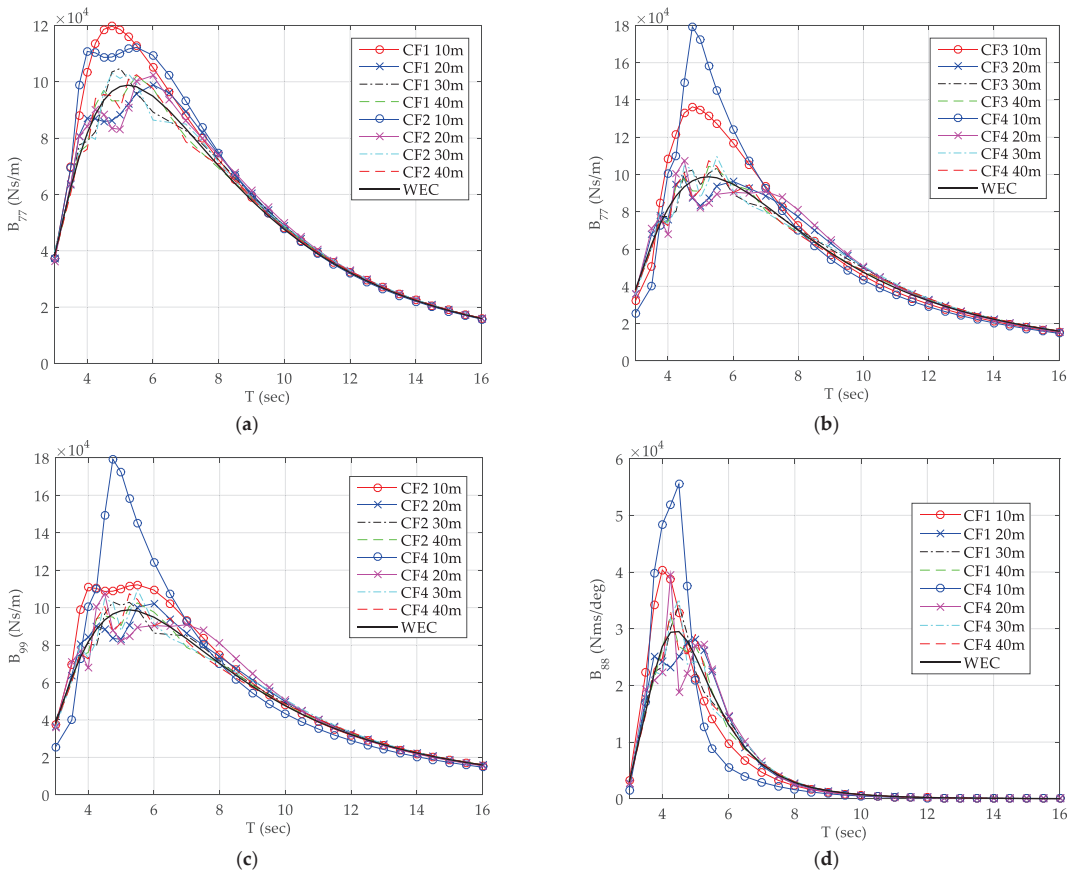


Figure 5. Radiation damping coefficients for: (a) WEC1 of CF1 and CF2, (b) WEC1 of CF3 and CF4, (c) WEC3 of CF2 and CF4, and (d) B_{88} coefficient for WEC1 of CF1 and CF4 configurations.

The effect of the D value between the different bodies as well as of the number of bodies of WindWEC on the wave excitation loads, X_i , applied on WECs and spar are presented in Figure 6. Compared to the heave excitation loads of a single WEC body (black solid line), as the number of the bodies increases the interaction effects on the X_7 excitation loads of WEC1 (Figure 6a,b) become more intense and for wider wave period range. Irrespectively of the number of the bodies and WindWEC configurations, the effects on the excitation loads are more intense as the D value decreases. Regarding the WEC3

and heave generalized mode excitation load (Figure 6c) the interaction effects are smaller compared to WEC1 and X_7 . However, for the presented interaction effects the larger values are observed for the smaller examined D value and configuration CF4. As far as the spar heave excitation loads (Figure 6d), the interaction effects are small for most of the examined configurations and D values, apart from CF4 and D = 10 m where large interaction effects exist resulting to a decrease of the excitation loads for periods close to spar’s natural period in heave, as well as a second peak is presented related with the natural period of the WECs and coupling between the two motions.

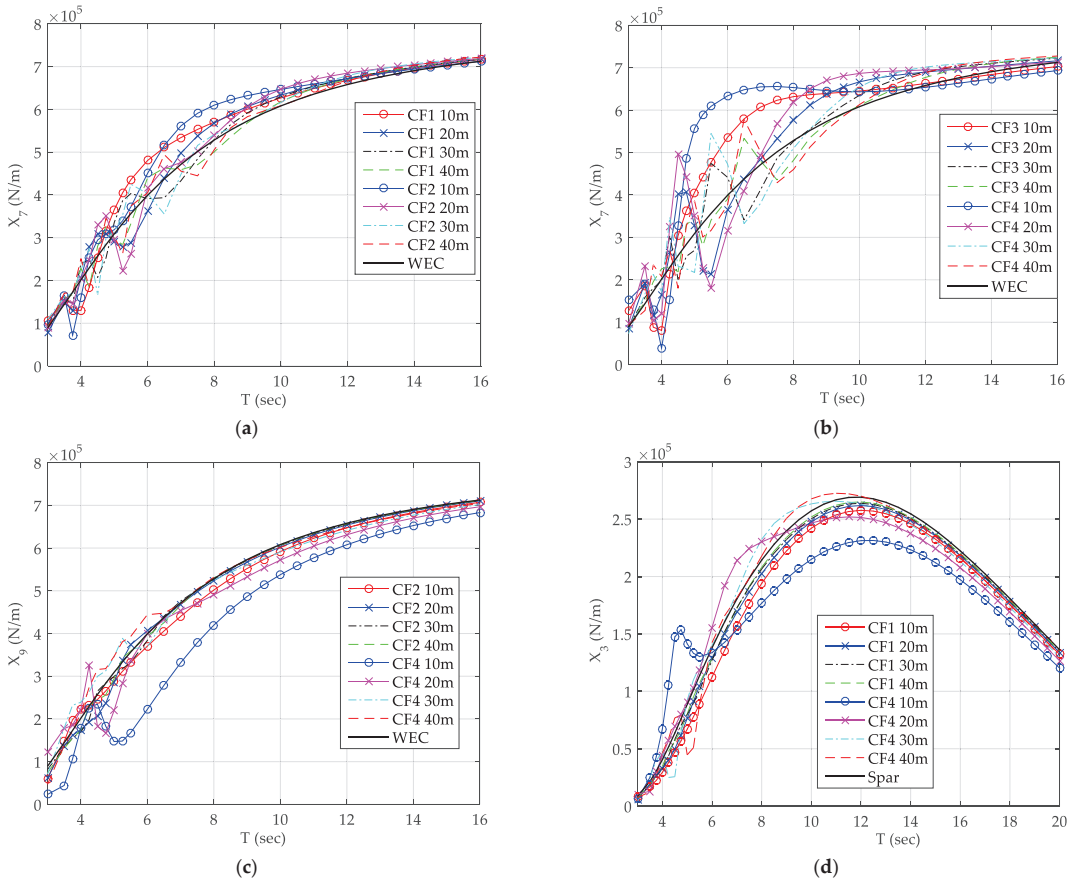


Figure 6. Heave excitation loads of WECs and spar for: (a) WEC1 of CF1 and CF2, (b) WEC1 of CF3 and CF4, (c) WEC3 of CF2 and CF4, and (d) spar of CF1 and CF4.

The effect of the D value and of the grid configuration on the motion responses is shown in Figure 7, where the variation of RAOs of WECs and spar of the WindWEC configuration as a function of wave period is presented. For the case of WEC1 and RAO₇ (heave motion of WEC1 in Figure 7a,b), in most of the presented curves the variation of RAO₇ is characterized by the existence of two distinctive peaks one attributed to the occurrence of the resonance in heave motion and the other to the rapid increase of relevant wave exciting forces in heave. The existing large interaction effects on added mass and excitation loads for the examined cases with D = 10 m, do not result to the largest heave RAO values. For all the examined configurations the largest values of RAO₇ are observed for D value equals to 20 m followed by a rapid decrease and a second peak.

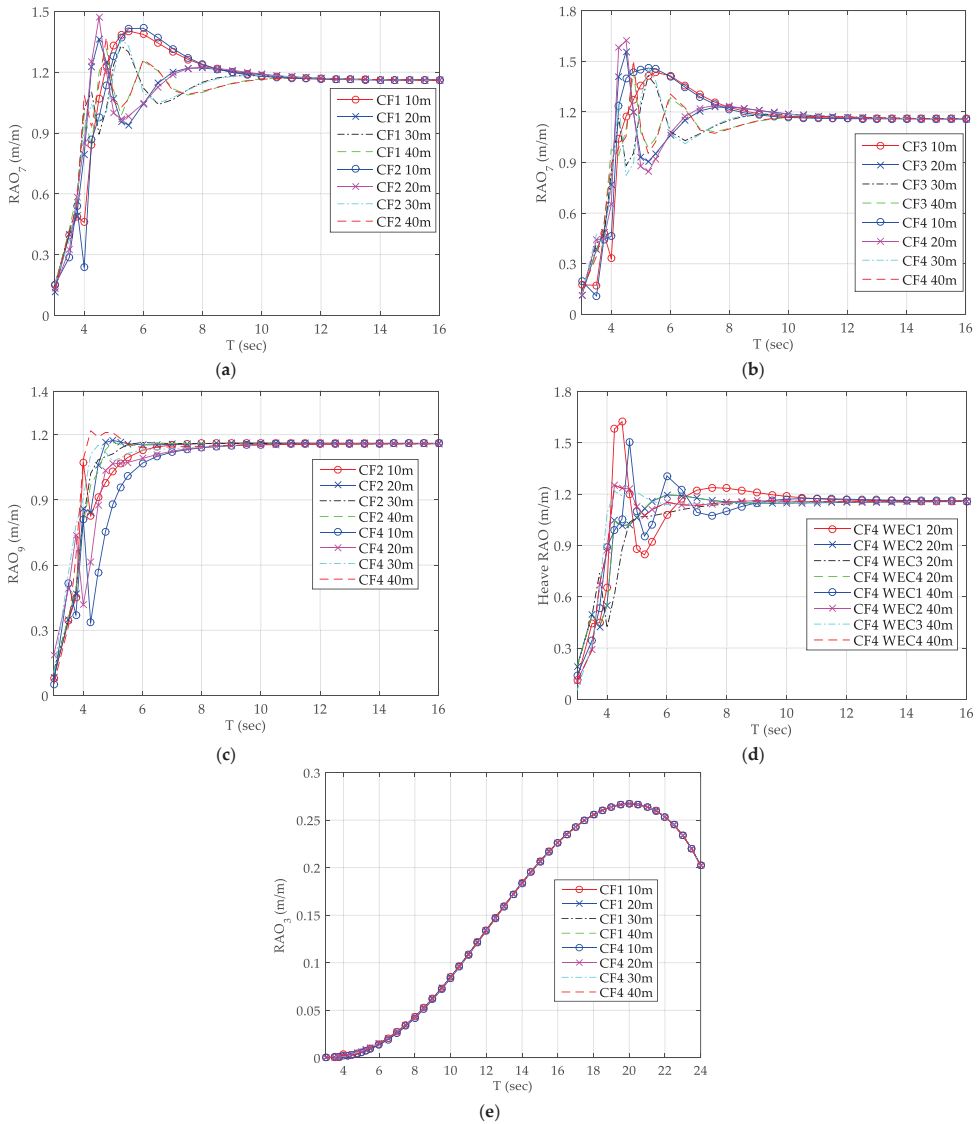


Figure 7. Heave RAOs of WECs, for: (a) WEC1 of CF1 and CF2, (b) WEC1 of CF3 and CF4, (c) WEC3 of CF2 and CF4, (d) WEC1, WEC2, WEC3 and WEC4 of CF4 and (e) spar of CF1 and CF4.

With regards to the heave RAO of WEC3 (Figure 7c) of CF2 and CF4 examined configurations, the amplitudes of heave RAOs are presenting intense variations only for the case where $D = 10$ m and for examined wave periods smaller than 8 s, attributed to relevant intense excitation loads for this wave period range. For the rest examined cases in Figure 7c, the heave RAO curves are increasing smoothly and obtaining their largest values for wave periods larger than 8 s. The values of WEC3 heave RAOs are smaller compared to the relevant heave RAOs values of WEC1 for wave periods close to the T_{n3} of WEC attributed to the wake hydrodynamic interaction effects between the different bodies of the examined configurations resulting to the decrease of the heave amplitudes of the WEC3. The effect of the D value on the response of heave motion of WECs is presented

in Figure 7d; the increase of the D value from 20 m to 40 m results to the decrease of the heave motion in most WECs for wave periods smaller than 10 s. With regards to the RAOs of spar of CF1 and CF4 and specifically for the heave motion of spar, RAO_3 , (Figure 7e) the effect of the D value and of the grid configuration results to insignificant changes of the amplitudes of the heave motion of spar.

As far as the produced wave power of the WECs of WindWEC, in Figure 8 the total produced power, as calculated by Equation (14), is presented. For CF1 configuration (Figure 8a) and for all examined D values the peaks of the produced wave power curves exist close to the resonance of the WECs in the heave degree of freedom. The largest produced power is observed for distance value $D = 20$ m. The curve of the produced power varies smoothly and obtains one peak value. Similar observations exist for the examined configuration CF2 (Figure 8b). It is clear that a linear trend between the increase of the D with the produced power does not exist. For the case of $D = 40$ m and for all examined configurations a quite irregular pattern of the produced power curves exist with multiple peaks and minima. For $D = 10$ m and $D = 30$ m the examined configuration CF2 is not producing large amount of wave power since heave RAO of WEC3 obtains small values even in examined wave periods close to heave motion resonance. For both CF3 and CF4 examined configurations, WindWEC produces similar amount of wave energy irrespective of the examined D value apart from the smallest D value equals to 10 m, attributed to the strong interaction effects that result to smaller heave motion amplitudes close to the resonance period of WECs for the heave motion. For both examined configurations CF3 and CF4 the largest values of the produced wave power are presented for D value equals to 40 m, but with small difference compared to the rest maximum values of produced power for $D = 20$ m and $D = 30$ m.

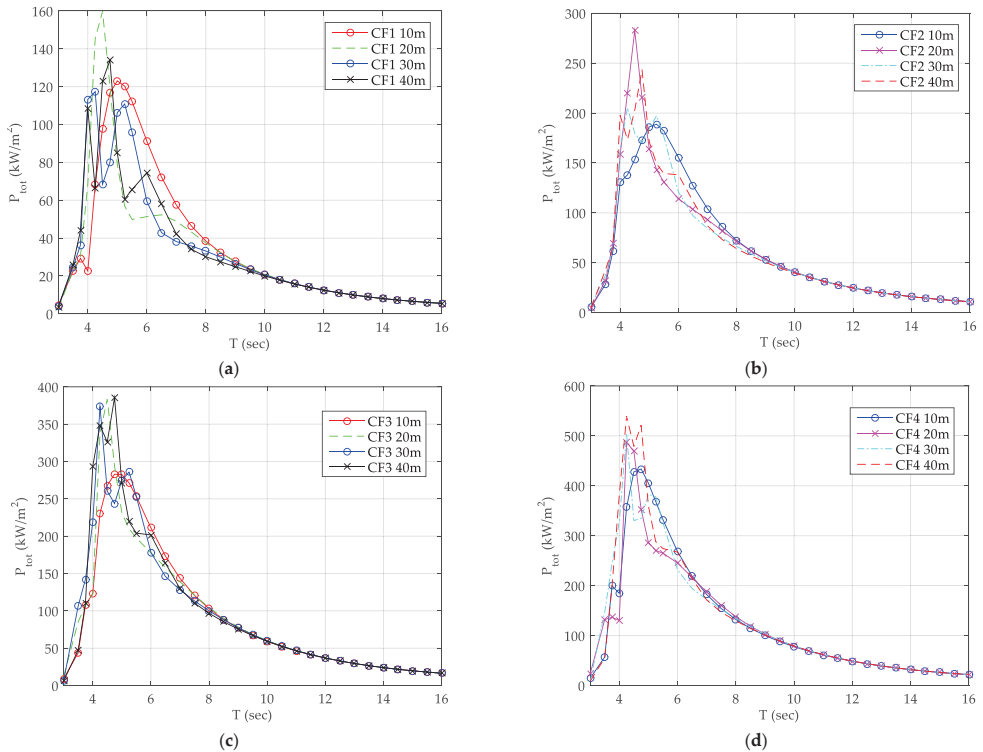


Figure 8. Produced wave power P_{tot} of WindWEC for: (a) CF1 and all D examined values, (b) CF2 and all D examined values, (c) CF3 and all D examined values, and (d) CF4 and all D examined values.

In Figure 9a comparison is presented of the produced wave power, P_{tot} , for CF1, CF2, CF3 and CF4 configurations and for $D = 20$ m (Figure 9a), and of the P_{WECk} of all the WECs of CF4 configuration with $D = 20$ m. The curve of P_{tot} for CF4 is obtaining not only the largest value of the wave power but also the curve has wider characteristics and large values up to wave periods equal to 16 s; this curve pattern results to more effective use of WindWEC in a larger number of sea sites that possibly WindWEC can be placed and produce power effectively. For CF4 and $D = 20$ m, the larger contribution of wave power is produced by WEC1 for wave periods close to the resonance of the WEC in heave motion while for the rest wave periods all the WECs are contributing in the total produced power of WindWEC similarly. WEC3 has a small contribution on the total produced wave power due to hydrodynamic wake effects and wave direction; but in order WindWEC to have produced wave power independent of the wave direction all WECs should be used.

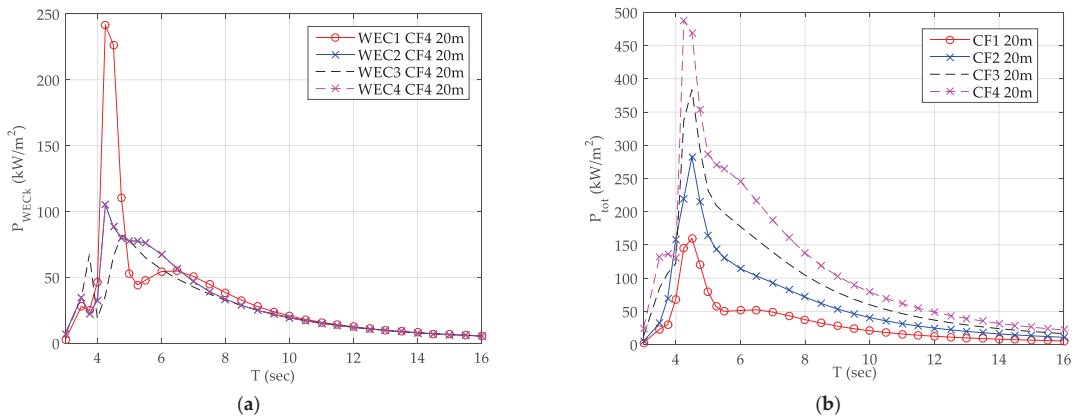


Figure 9. (a) Produced wave power P_{tot} of WindWEC for CF1, CF2 CF3 and CF4 for $D = 20$ m and (b) P_{WECk} of WECs of CF4 configuration and $D = 20$ m.

In Figures 10–13 we can see the produced wave power (kW) contours (power matrix) for irregular waves, P_{irr} , of WindWEC for CF1, CF2, CF3 and CF4 examined configurations, respectively, for all the examined values of the distance between the spar and the WECs. For the calculation of the P_{irr} Equation (16) has been used and applied. It is noted that no control has been used for the damping B_{PTO} of the PTO and a constant damping has been selected equal with the radiation damping of the WEC for its natural period in heave degree of freedom. Based on relevant hydrodynamic analysis the heave radiation damping that corresponds to $T_{n3} = 4.25$ s is used. As it is expected the increase of the number of the WECs results to the increase of the produced power of the combined concept for similar irregular wave conditions. For both CF3 and CF4 examined configurations WindWEC produces power for mild wave conditions. The value of the distance between the spar and WECs plays a dominating factor for the power matrices. For each of the CF1 and CF2, the examined case with $D = 20$ m results to the larger produced power while for each of the CF3 and CF4 the examined case with $D = 40$ m has the better performance in terms of produced power for different examined irregular wave cases. The increase of the number of the bodies, and consequently the increase of the hydrodynamic interaction between the different bodies, results to the decrease of the produced power if the distance between the spar and the different bodies remains the same. For the case that a large number of WECs are utilized the distance between the spar and WECs should increase in order the interaction effects not to have negative impact on the produced power.

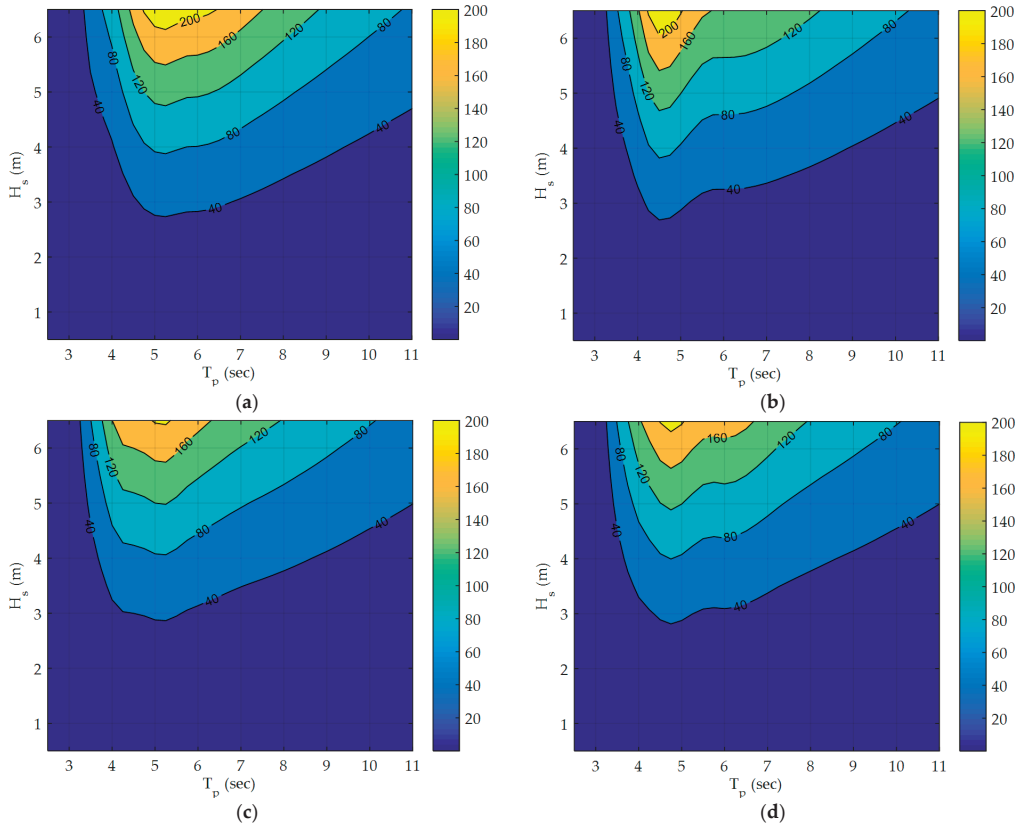


Figure 10. Produced wave power P_{IRR} contour of WindWEC for CF1 examined configuration and: (a) $D = 10$ m, (b) $D = 20$ m, (c) $D = 30$ m and (d) $D = 40$ m.

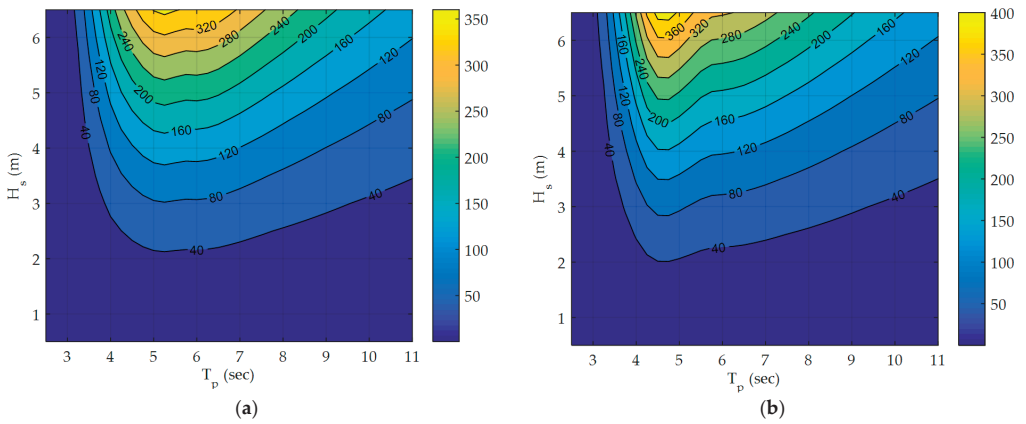


Figure 11. Cont.

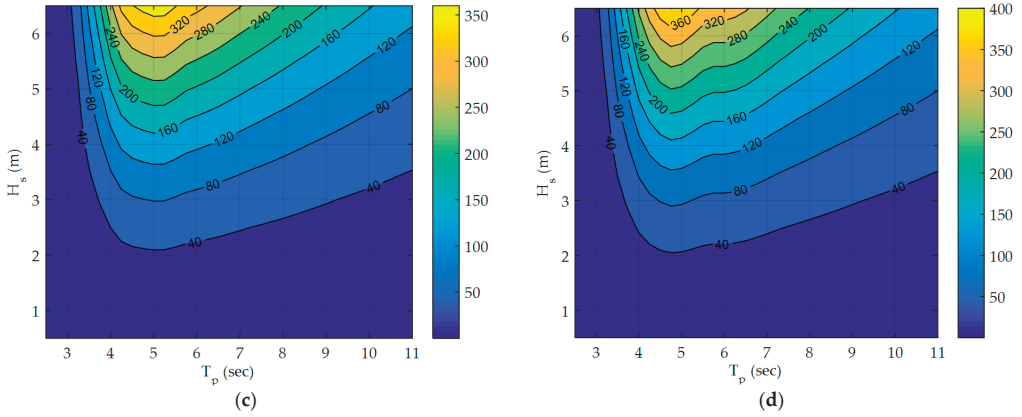


Figure 11. Produced wave power P_{irr} contour of WindWEC for CF2 examined configuration and: (a) $D = 10$ m, (b) $D = 20$ m, (c) $D = 30$ m and (d) $D = 40$ m.

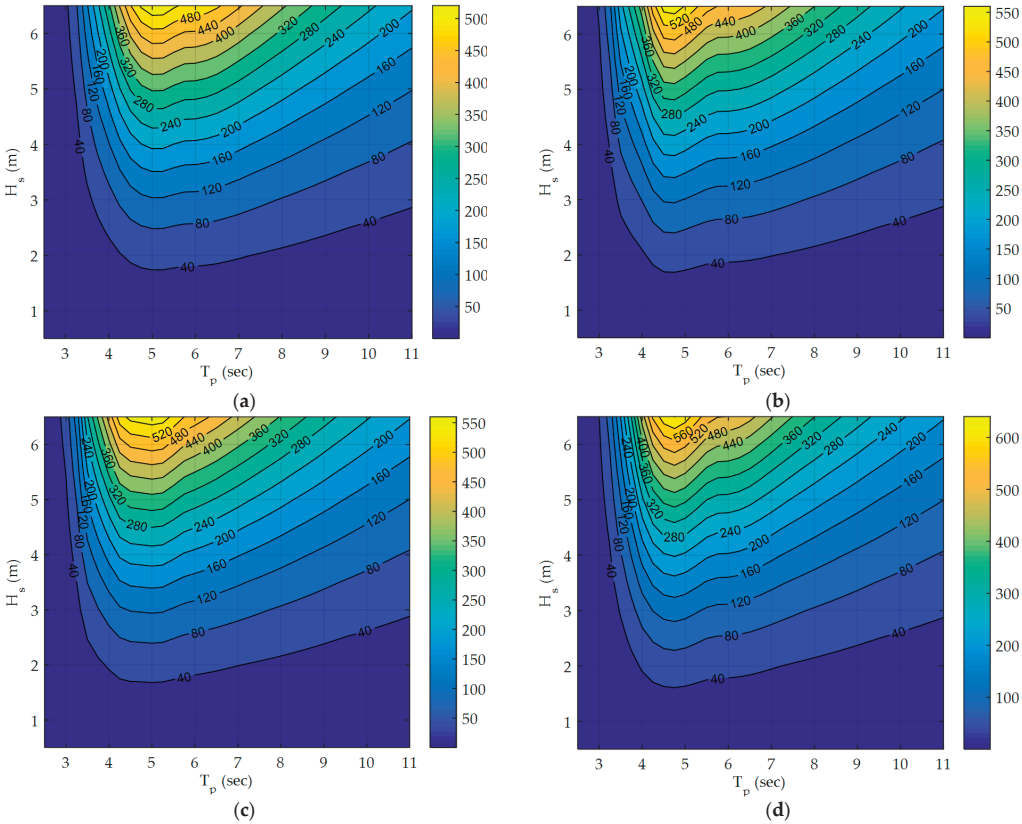


Figure 12. Produced wave power P_{irr} contour of WindWEC for CF3 examined configuration and: (a) $D = 10$ m, (b) $D = 20$ m, (c) $D = 30$ m and (d) $D = 40$ m.

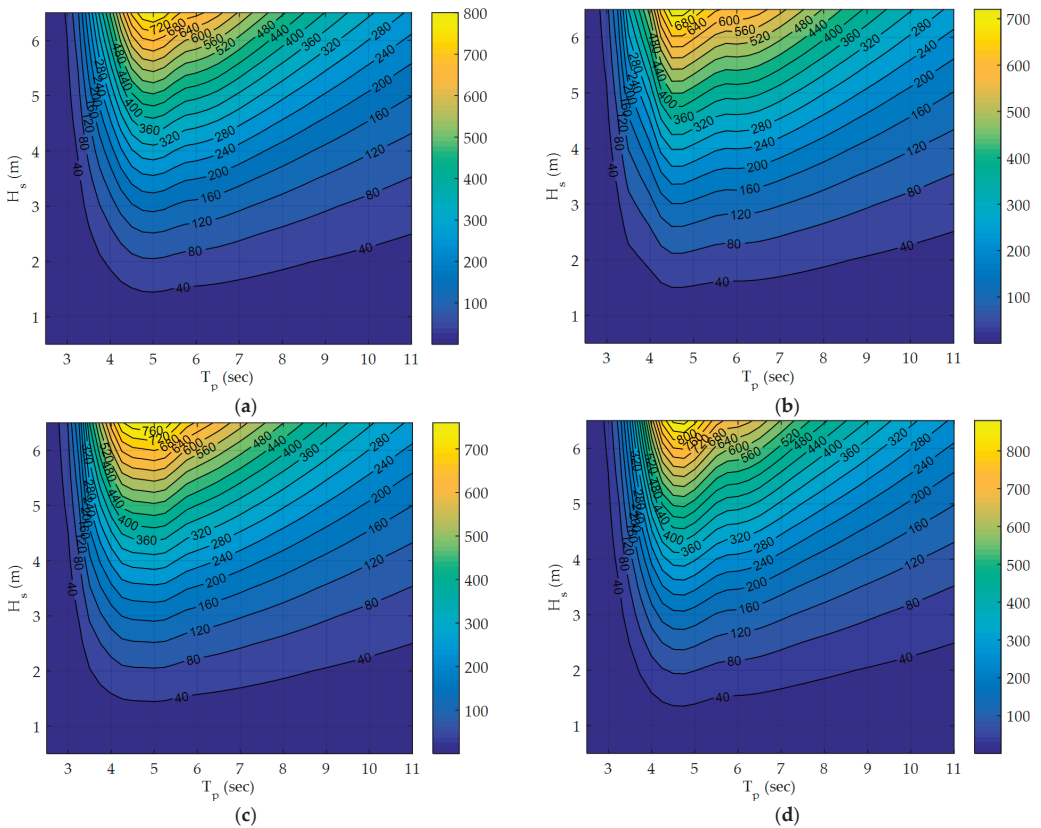


Figure 13. Produced wave power P_{irr} contour of WindWEC for CF4 examined configuration and: (a) $D = 10$ m, (b) $D = 20$ m, (c) $D = 30$ m and (d) $D = 40$ m.

In order to compare the produced power of the different examined configurations of WindWEC in real sea conditions, the annual-averaged produced wave power, P_{annual} , (Equation (18)) for two sea states is calculated and presented. The first examined site (Site 1) is presented in [30] and is based on Danish Hydraulic Institute (DHI) MetOcean data portal for the case of a Danish small island in the Baltic Sea while the second one (Site 2) corresponds to the National Wave Energy Test site located off the Annagh Head west of Belmullet [31]. It is stated that the wave climate at a specific site is defined by a set of sea states, defined by their significant wave height, H_s , and peak period, T_p , values, and the probability of occurrence $p(H_s, T_p)$ in one year period. For the examined sites the wave climate matrices are presented in Tables 4 and 5 below. In Table 6 the annual averaged produced power, P_{annual} , in kWh/year for all examined configurations and two examined sites are presented. In the same Table it is also presented the value P_{annual} /number of WECs in kWh/year. For the case that one and two WECs are utilized the largest annual produced power corresponds for D value equals to 20 m, while, for the case that three and four WECs are used the D value that corresponds to the largest annual produced power corresponds to 40 m. The largest produced power is presented for the CF4 configuration with $D = 40$ m and equals to 191,260 kWh for Site1 and 653,340 kWh for Site2.

Table 4. Wave climate matrix of the examined Site1.

	Tp (sec)											Total (%)
	1.5	2.5	3.5	4.5	5.5	6.5	7.5	8.5	9.5	10.5	11.5	
Hs (m)	0.25	0.75	1.25	1.75	2.25	2.75	3.25	3.75	4.25	4.75	Total (%)	27.3679
	0.02277	0	0	0	0	0	0	0	0	0	0.02277	32.3998
	3.21038	0	0	0	0	0	0	0	0	0	0.03415	19.3078
	12.3179	4.61066	0	0	0	0	0	0	0	0	0.04554	10.6557
	7.57058	15.255	1.54827	0	0	0	0	0	0	0	0.01138	6.42077
	2.9827	7.82104	12.2154	1.5255	0	0	0	0	0	0	0.02277	2.45902
	1.10428	2.4704	3.9276	7.61612	2.43625	0.18215	0	0	0	0	0.03415	0.77414
	0.13661	1.1612	1.03597	0.9449	3.44945	1.42304	0.10246	0	0	0	0.02277	0.22769
	0	0.67168	0.43261	0.43261	0.50091	0.80829	0.5123	0.13661	0.02277	0	0	0.20492
	0.01138	0.3643	0.148	0.07969	0	0	0.05692	0.17077	0	0	0	0.18215
	0.01138	0.04554	0	0.05692	0.17077	0	0.13661	0.04554	0	0	0.03415	100

Table 5. Wave climate matrix of the examined Site2.

	Te (sec)											Total (%)											
	5.5	6.5	7.5	8.5	9.5	10.5	11.5	12.5	13.5	14.5													
Hs (m)	0.25	0.75	1.25	1.75	2.25	2.75	3.25	3.75	4.25	4.75	5.25	5.75	6.25	6.75	7.25	7.75	8.25	8.75	9.25	9.75	10.25	Total (%)	
	0.1	0.8	0.8	0.1	0	0	0	0	0	0	0	0	0	0	0	0	0	0	0	0	0	0	1.3
	0.5	2.8	3.8	2.8	0.7	0	0	0	0	0	0	0	0	0	0	0	0	0	0	0	0	0	11
	0.6	4.4	4.8	4.4	2.4	0.5	0	0	0	0	0	0	0	0	0	0	0	0	0	0	0	0	16.8
	0.1	2.8	3.7	3	3.3	1.4	0.3	0	0	0	0	0	0	0	0	0	0	0	0	0	0	0	14.6
	2.8	0.7	3.4	3	2.5	1.8	0.6	0.1	0	0	0	0	0	0	0	0	0	0	0	0	0	0	12.1
	0.1	0.1	1.6	2.8	2	1.8	0.9	0.1	0	0	0	0	0	0	0	0	0	0	0	0	0	0	9.3
	0.4	0	0.4	2.1	1.7	1.5	1.2	0.5	0.1	0	0	0	0	0	0	0	0	0	0	0	0	0	7.5
	0.1	0	0.1	1.4	1.9	1.4	1	0.5	0.2	0	0	0	0	0	0	0	0	0	0	0	0	0	6.5
	0	0	0	0.4	1.5	1.4	1	0.5	0.3	0	0	0	0	0	0	0	0	0	0	0	0	0	5.1
	0	0	0	0.1	0.9	1.3	0.9	0.4	0.2	0.1	0	0	0	0	0	0	0	0	0	0	0	0	3.9
	0	0	0	0	0.3	1.1	0.9	0.5	0.2	0.1	0	0	0	0	0	0	0	0	0	0	0	0	3.1
	0	0	0	0	0.2	0.7	0.6	0.5	0.2	0.1	0	0	0	0	0	0	0	0	0	0	0	0	2.3
	0	0	0	0	0	0.4	0.5	0.4	0.2	0.1	0	0	0	0	0	0	0	0	0	0	0	0	1.6
	0	0	0	0	0	0.2	0.4	0.3	0.2	0.1	0	0	0	0	0	0	0	0	0	0	0	0	1.2
	0	0	0	0	0	0.1	0.3	0.4	0.2	0.1	0	0	0	0	0	0	0	0	0	0	0	0	1.1
	0	0	0	0	0	0	0.2	0.2	0.2	0.1	0	0	0	0	0	0	0	0	0	0	0	0	0.7
	0	0	0	0	0	0	0.1	0.2	0.2	0.1	0	0	0	0	0	0	0	0	0	0	0	0	0.6
	0	0	0	0	0	0	0	0.1	0.1	0	0	0	0	0	0	0	0	0	0	0	0	0	0.2
	0	0	0	0	0	0	0	0	0.1	0.1	0.1	0	0	0	0	0	0	0	0	0	0	0	0.3
	0	0	0	0	0	0	0	0	0	0.2	0.1	0	0	0	0	0	0	0	0	0	0	0	0.3
	0	0	0	0	0	0	0	0	0	0	0.1	0	0	0	0	0	0	0	0	0	0	0	0.1

Table 6. Annual averaged produced power, P_{annual} , for all examined configurations and two examined sites.

WindWEC Configuration	P_{annual} (kWh per Year)	P_{annual} /Number of WECs (kWh per Year)	P_{annual} (kWh per Year)	P_{annual} /Number of WECs (kWh per Year)
	Site1		Site2	
CF1 10 m	46,576	46,576	167,420	167,420
CF1 20 m	54,437	54,437	176,150	176,150
CF1 30 m	46,050	46,050	161,620	161,620
CF1 40 m	46,674	46,674	161,520	161,520
CF2 10 m	91,739	45,870	328,790	164,395
CF220	94,684	47,342	341,230	170,615
CF2 30 m	90,014	45,007	321,230	160,615
CF2 40 m	91,957	45,979	322,800	161,400
CF3 10 m	136,190	45,397	490,990	163,663
CF3 20 m	134,020	44,673	483,820	161,273
CF3 30 m	137,440	45,813	483,080	161,027
CF3 40 m	140,690	46,897	492,960	164,320
CF4 10 m	186,000	46,500	650,520	162,630
CF4 20 m	177,100	44,275	640,620	160,155
CF4 30 m	185,560	46,390	646,110	161,528
CF4 40 m	191,260	47,815	653,340	163,335

5. Conclusions

In the present paper the hydrodynamic response and the prediction of the produced power of different possible configurations of the updated WindWEC concept based on generalized modes analysis is presented for regular and irregular waves. Updated WindWEC consists of a spar and one, two, three or four heaving type WEC buoys. Initially the development of the generalized modes numerical model is presented. With the use of the developed numerical model the effects of structural design parameters on the hydrodynamic response and produced wave power are examined. The structural design parameters are the center-to-center distance of the WECs and spar platform, the number of the WECs and the grid configuration of spar and WECs. Numerical analysis is made in frequency domain and power matrices of the updated WindWEC concept are presented for all examined configurations with different number of WECs. Moreover, the annual produced power of the updated WindWEC in two sites is estimated and presented.

Based on the results the main findings can be summarized in this paragraph. The decrease of the distance between the different bodies results to the decrease of the produced power due to strong hydrodynamic interaction effects. The value of natural period of WEC dominates both the hydrodynamic response and produced power. The combined concept with larger number of WECs in use results to increase of produced power in wider number of wave characteristics; in this case the WECs should be placed in large distance from the central spar body. Hydroelastic analysis can be used efficiently when dealing with combined structures for early-stage assessment of the hydrodynamic response and produced power of WECs. The updated WindWEC can be used in sea sites with different environmental characteristics while extracting valuable amount of wave power.

Moreover, and based on the findings it can be concluded that, the effect of the center-to-center distance between the spar and WECs is large on the hydrodynamic response of, mainly, the WECs for all the examined configurations of updated WindWEC. For the smaller examined value of center-to-center distance, intense hydrodynamic interaction

effects exist but are not resulting to the larger produced wave power of updated WindWEC. It is very critical the assessment of the effects of the center-to-center distance on the power performance of the combined concepts.

Large interaction effects exist not only for the diagonal coefficients of added mass and radiation damping matrices but also for the nondiagonal coefficients. Those coefficients should be accounted and used when dealing with the analysis of combined energy concepts consisting of different floating bodies.

The effect of the grid configuration, and consequently of the number of the spar and WECs bodies, is large on the hydrodynamic response for all the examined center-to-center distance values. As the number of the bodies increases the interaction effects are larger.

Irrespectively of the examined center-to-center distance value and grid configuration, the interaction effects on the motions of the WECs are large close to the heave natural period value of WECs, while the interaction effects on the motions of spar platform are insignificant for all examined cases.

With regards to the total produced power of updated WindWEC, CF4 results to the larger maximum total produced power as well as to a wider produced power curve. The smaller examined center-to-center distance value results to the small, produced wave power for all examined configurations attributed to the strong hydrodynamic interaction effects. For the case that a large number of WECs are utilized the distance between the spar and WECs should increase in order the interaction effects not to have negative impact on the produced power.

The generalized modes analysis that is presented in this paper is generic and can be used for the early-stage assessment of combined energy concepts.

The updated WindWEC can be used in sea sites with different environmental characteristics while extracting valuable amount of wave power.

Different possible future studies may arise from this paper related to the WindWEC combined concept; the design of the mooring line system and the design of the arm of the WindWEC for the CF4 configuration is prioritized in relevant fully coupled time domain analysis models. Moreover, the shape optimization of the WEC of the WindWEC for maximizing the produced wave power is also prioritized as a future study.

Author Contributions: The author has read and agreed to the published version of the manuscript.

Acknowledgments: The author would like to acknowledge the “CUT Open Access Author Fund” for covering the open access publication fees of the paper.

Conflicts of Interest: The author declares no conflict of interest.

References

1. European Wind Energy Association. *Offshore Wind in Europe Key Trends and Statistics 2019*; Wind Europe: Brussels, Belgium, 2020.
2. Hywind Scotland. Available online: https://en.wikipedia.org/wiki/Hywind_Scotland (accessed on 25 May 2020).
3. Falcao, A. Wave energy utilization: A review of the technologies. *Renew. Sustain. Energy Rev.* **2010**, *14*, 899–918. [CrossRef]
4. Falnes, J. A review of wave-energy extraction. *Mar. Struct.* **2007**, *20*, 185–201. [CrossRef]
5. Michele, S.; Buriani, F.; Renzi, E.; van Rooij, M.; Jayawardhana, B.; Vakis, A.I. Wave Energy Extraction by Flexible Floaters. *Energies* **2020**, *13*, 6167. [CrossRef]
6. Wave Star Energy. Available online: <http://wavestarenergy.com> (accessed on 25 May 2020).
7. Hansen, R.H.; Kramer, M.M.; Vidal, E. Discrete Displacement Hydraulic Power Take-Off System for the Wavestar Wave Energy Converter. *Energies* **2013**, *6*, 4001–4044. [CrossRef]
8. TROPOS. Available online: <http://www.troposplatform.eu/> (accessed on 25 May 2020).
9. Marina Platform. Available online: <https://www.msp-platform.eu/projects/marina-platform> (accessed on 25 May 2020).
10. Lavidas, G.; Venugopal, V. Energy Production Benefits by Wind and Wave Energies for the Autonomous System of Crete. *Energies* **2018**, *11*, 2741. [CrossRef]
11. Pham, T.D.; Shin, H. A New Conceptual Design and Dynamic Analysis of a Spar-Type Offshore Wind Turbine Combined with a Moonpool. *Energies* **2019**, *12*, 3737. [CrossRef]
12. Soulard, T.; Babarit, A.; Borgarino, B.; Wyns, M.; Harismendy, M. C-HYP: A combined wave and wind energy platform with balanced contributions. In Proceedings of the 32nd International Conference on Ocean, Offshore and Arctic Engineering, Nantes, France, 4–9 June 2013.

13. Aubult, A.; Alves, M.; Sarmento, A.; Roddier, D.; Peiffer, A. Modeling of an oscillating water column on the floating foundation WindFloat. In Proceedings of the 30th International Conference on Ocean, Offshore and Arctic Engineering, Rotterdam, The Netherlands, 19–24 June 2011.
14. Muliawan, M.J.; Karimirad, M.; Moan, T. Dynamic response and power performance of a combined spar-type floating wind turbine and coaxial floating wave energy converter. *Renew. Energy* **2013**, *50*, 47–57. [[CrossRef](#)]
15. Michailides, C.; Gao, Z.; Moan, T. Experimental study of the functionality of a semisubmersible wind turbine combined with flap-type Wave Energy Converters. *Renew. Energy* **2016**, *93*, 675–690. [[CrossRef](#)]
16. Wang, Y.; Zhang, L.; Michailides, C.; Wan, L.; Shi, W. Hydrodynamic Response of a Combined Wind–Wave Marine Energy Structure. *J. Mar. Sci. Eng.* **2020**, *8*, 253. [[CrossRef](#)]
17. Gao, Z.; Moan, T.; Wan, L.; Michailides, C. Comparative numerical and experimental study of two combined wind and wave energy concepts. *J. Ocean Eng. Sci.* **2016**, *1*, 36–51. [[CrossRef](#)]
18. Ren, N.X.; Zhu, Y.; Ma, Z.; Wu, H.B. Comparative study of hydrodynamic responses of two combined wind turbine and wave energy converter systems under typical operational sea cases. In Proceedings of the 37th International Conference on Ocean, Offshore and Arctic Engineering (OMAE), Madrid, Spain, 17–22 June 2018.
19. Karimirad, M.; Koushan, K. WindWEC: Combining Wind and Wave Energy Inspired by Hywind and Wavestar. In Proceedings of the International Conference on Renewable Energy Research and Applications, Birmingham, UK, 20–23 November 2016.
20. Newman, J.N. Wave Effects on Deformable Bodies. *Appl. Ocean Res.* **1994**, *6*, 47–59. [[CrossRef](#)]
21. Riggs, H.R.; Ertekin, R.C.; Mills, T.R.J. A Comparative study of RMFC and FEA models for the wave-induced response of a MOB. *Mar. Struct.* **2000**, *13*, 217–232. [[CrossRef](#)]
22. Fu, S.; Moan, T.; Chen, X.; Cui, W. Hydroelastic Analysis of Flexible Floating Interconnected Structures. *Ocean Eng.* **2007**, *34*, 1516–1531. [[CrossRef](#)]
23. Fu, S.; Weicheng, C.; Chen, X.; Cong, W. Hydroelastic analysis of a nonlinearly connected floating bridge subjected to moving loads. *Mar. Struct.* **2005**, *18*, 85–107.
24. Karimirad, M.; Michailides, C.; Nematbakhsh, A. *Offshore Mechanics: Structural and Fluid Dynamics for Recent Applications*, 1st ed.; John Wiley & Sons, Inc.: Hoboken, NJ, USA, 2018.
25. Lee, C.H.; Newman, J.N. An Assessment of Hydroelasticity for Very Large Hinged Vessels. *J. Fluids Struct.* **2000**, *14*, 957–970. [[CrossRef](#)]
26. Michailides, C.; Loukogeorgaki, E.; Angelides, D.C. Influence of Connectors’ Stiffness on the Performance of Flexible Floating Breakwaters. In Proceedings of the Nineteenth International Offshore and Polar Engineering Conference, Osaka, Japan, 21–26 July 2009; Volume 3, pp. 1094–1101.
27. Lee, C.H.; Zhu, X. Application of Hyper-Singular Integral Equations for a Simplified Model of Viscous Dissipation. In Proceedings of the 28th International Ocean and Polar Engineering Conference, Sapporo, Japan, 10–15 June 2018.
28. Falnes, J. Wave-energy conversion through relative motion between two single-mode oscillating bodies. *J. Offshore Mech. Arct. Eng.* **1999**, *121*, 32–38. [[CrossRef](#)]
29. Falnes, J. *Ocean Waves and Oscillating Systems: Linear Interactions Including Wave-Energy Extraction*, 1st ed.; Cambridge University Press: Cambridge, UK, 2002; pp. 17–20.
30. Margheritini, L.; Kofoed, J.P. Weptos Wave Energy Converters to Cover the Energy Needs of a Small Island. *Energies* **2019**, *12*, 423. [[CrossRef](#)]
31. Cahill, B.G.; Lewis, T. Weptos Wave energy resource characterisation of the Atlantic Marine Energy Test Site. *Int. J. Mar. Energy* **2013**, *1*, 3–15. [[CrossRef](#)]

Article

Emissions Effects of Energy Storage for Frequency Regulation: Comparing Battery and Flywheel Storage to Natural Gas

Eric Pareis¹ and Eric Hittinger^{1,2,*}

¹ Department of Public Policy, Rochester Institute of Technology, 92 Lomb Memorial Dr., Rochester, NY 14623, USA; egp5082@rit.edu

² Arts et Métiers Institute of Technology, University of Lille, Centrale Lille, Yncrea Hauts-de-France, ULR 2697–L2EP, F–59000 Lille, France

* Correspondence: eshgpt@rit.edu

Abstract: With an increase in renewable energy generation in the United States, there is a growing need for more frequency regulation to ensure the stability of the electric grid. Fast ramping natural gas plants are often used for frequency regulation, but this creates emissions associated with the burning of fossil fuels. Energy storage systems (ESSs), such as batteries and flywheels, provide an alternative frequency regulation service. However, the efficiency losses of charging and discharging a storage system cause additional electrical generation requirements and associated emissions. There is not a good understanding of these indirect emissions from charging and discharging ESSs in the literature, with most sources stating that ESSs for frequency regulation have lower emissions, without quantification of these emissions. We created a model to estimate three types of emissions (CO₂, NO_x, and SO₂) from ESSs providing frequency regulation, and compare them to emissions from a natural gas plant providing the same service. When the natural gas plant is credited for the generated electricity, storage systems have 33% to 68% lower CO₂ emissions than the gas turbine, depending on the US eGRID subregion, but higher NO_x and SO₂ emissions. However, different plausible assumptions about the framing of the analysis can make ESSs a worse choice so the true difference depends on the nature of the substitution between storage and natural gas generation.

Keywords: flywheel; battery; frequency regulation; emissions; natural gas

Citation: Pareis, E.; Hittinger, E. Emissions Effects of Energy Storage for Frequency Regulation: Comparing Battery and Flywheel Storage to Natural Gas. *Energies* **2021**, *14*, 549. <https://doi.org/10.3390/en14030549>

Academic Editor: Juri Belikov
Received: 27 December 2020
Accepted: 15 January 2021
Published: 21 January 2021

Publisher's Note: MDPI stays neutral with regard to jurisdictional claims in published maps and institutional affiliations.



Copyright: © 2021 by the authors. Licensee MDPI, Basel, Switzerland. This article is an open access article distributed under the terms and conditions of the Creative Commons Attribution (CC BY) license (<https://creativecommons.org/licenses/by/4.0/>).

1. Introduction

Traditional fossil fuel energy sources are used extensively for energy generation, but they emit greenhouse gases and other pollutants that are changing the planet's climate. Other negative effects, such as acid rain and air pollution, can also be attributed to fossil fuel consumption. These issues cause both economic and health concerns to the world population, including the United States. Energy use will continue to increase, potentially increasing the rate of emissions and their negative effects [1]. To combat this, the government needs to enforce policies which decrease the emissions of energy generating technologies while maintaining a sufficient supply of energy for its citizens in the future.

Both state and federal governments have sought to incentivize a higher share of renewable energy systems in the market. Many states have developed energy plans for reducing their greenhouse gas emissions and increasing renewable energy generation. Some states have ambitious plans in place, such as New York's plan to completely decarbonize the power system by 2050 and achieve an 85% reduction in all energy-related greenhouse gases by 2040 [2]. However, some generation technologies, such as solar and wind energy systems, are intermittent and do not supply constant power. To counteract the intermittent nature of these energy sources and to meet the goals of energy plans, a significant increase in frequency regulation of the energy grid is needed to keep the electrical grid stable [3].

Today, frequency regulation in the United States typically uses plants that burn fossil fuels [4]. Fast-response natural gas power plants are a common method of fossil fuel fre-

quency regulation. In addition to natural gas, coal is also used for frequency regulation [5]. Pumped hydro storage and demand response can also be used for frequency regulation [6].

There are issues with many of these frequency regulation methods which make them less ideal for regulation. Coal plants may not always accurately follow the control signal and can have difficulties providing precise frequency regulation services [7]. Natural gas and other combustion turbines must run continuously while providing frequency regulation. This can cause the combustion turbines providing frequency regulation to operate at times when it is less profitable for the plant. In addition, forced baseload generation from the combustion plants could force other generation to be taken offline to avoid generating too much electricity [8]. Pumped hydro storage requires a location for water storage with higher and lower elevations to work and cannot be easily installed in many areas. Demand response requires significant coordination with the grid and consumers which makes demand response frequency regulation more complex than other profitable uses for demand response.

To facilitate a cleaner energy grid, frequency regulation technology may need to evolve along with electrical generation technology. An alternative to the technologies listed above is an energy storage system (ESS), which either discharges by releasing energy into the grid or recharges by drawing energy from the grid as needed. Some ESSs, such as batteries and flywheels, are already in use for frequency regulation services and avoid the issues associated with other frequency regulation technologies.

As an alternative to fossil fuel consumption, ESSs could offer lower emissions. However, there is uncertainty over the emission differences between ESSs and traditional frequency regulation plants. The operation of an ESS has an emissions footprint due to the inefficiency of charging from and discharging to the energy grid with the ESS, which requires more energy to be produced in total. While the emissions from fossil generators are clear, attributing them to “energy” versus “services” is harder.

Existing literature has considered the economics of applying energy storage for frequency regulation services. In 2016, Lucas and Chondrogiannis evaluated vanadium redox flow batteries for frequency regulation and concluded that this technology was economically feasible, though it could still be more expensive than traditional frequency regulation methods and will need policy intervention to be implemented across the grid [9]. Du found that the lifecycle costs of lead acid batteries will never be positive for regulation, indicating that lead acid batteries are not economically viable [10]. Zakeri and Syri disagreed, stating that lead acid batteries could have positive life cycle benefits [11]. However, in both cases, other battery energy storage system (BESS) and flywheel energy storage system (FESS) technologies were superior. Zakeri determined that FESS is cheaper and more effective than both lead acid and lithium ion BESSs [11]. Du compared lithium ion batteries and lead acid batteries to FESS technologies and found that flywheels performed significantly better in terms of economic viability [10]. However, despite their high efficiency and effectiveness, the startup cost of these systems is higher, which discourages investors. This high initial capital investment is another area where government intervention through policy is needed [11].

Investigations of the emission effects of storage for frequency regulation are rare, with two important studies relevant to this work. The first is a 2007 report from KEMA, offering an emissions comparison analysis for the proposed 20 MW flywheel-based frequency regulation power plant at Stephentown, NY, concluding that flywheels produce net emissions benefits [12]. This analysis differs from our methodology, specifically by using a simple test “cycle” (which is quite different from the signal from the PJM Independent System Operator) and the method for emissions calculations (presuming specific generators are displaced due to lack of marginal emissions data at the time). The second is a more recent work by Ryan et al. that provided a broad life-cycle assessment of storage for frequency regulation, including considerations such as manufacturing of storage, grid dispatch and operation, and end-of-life treatment [13]. They use an IEEE 9-bus system to model the operational phase, and concluded that adding storage will increase emissions in

all scenarios. The contribution of our work is in the application of more realistic modeling of displaced emissions (based on data from the EPA Continuous Emissions Monitoring Systems) and a method that allows us to compare results for locations across the US. This analysis modernizes and broadens the basic idea of the KEMA study and complements Ryan et al. by providing an analysis based on historical data for grid emissions rather than modeled values from a 9-bus system.

This analysis estimates the CO₂, NO_x, and SO₂ emissions generated by three different frequency regulation technologies: natural gas, flywheel energy storage (FESS), and battery energy storage (BESS). The goal of the analysis is to determine what conditions result in ESS systems having lower emissions than natural gas for frequency regulation.

2. Materials and Methods

We created a MATLAB model to simulate CO₂, NO_x, and SO₂ emissions from a battery energy storage system (BESS), flywheel energy storage system (FESS), and natural gas plant providing 20 MW of frequency regulation service in 22 US EPA eGRID subregions. The US EPA eGRID database breaks the US into 26 subregions with borders that approximate the historical boundaries of electricity systems. We work with the 22 eGRID regions within the Continental US. Energy losses from transfer inefficiencies in the ESS and the emissions associated from the losses were calculated using marginal emission factors (MEFs), which vary across the US. The natural gas emissions were calculated from a regression analysis by Katzenstein and Apt based on the operation of a 501FD natural gas turbine [14]. The CO₂, NO_x, and SO₂ emissions from the ESS and natural gas plant were then compared. Because of the complexity and uncertainty in production, maintenance, and decommissioning footprint of the technologies involved, the analysis is limited to operational emissions for both ESSs and gas turbines. The analysis is focused solely on the emission effects of switching from gas turbines to stationary storage for frequency regulation services regardless of the motivation for the change (economic, policy-driven, or otherwise). Storage economics and policy certainly affect the amount of storage added to the grid and what services it provides, but that is outside the scope of the current investigation.

The transfer efficiencies assumed for BESS and FESS were the average of overall system efficiencies found in the literature: 88.8% for BESS roundtrip efficiency and 89.1% for FESSs. Details of the transfer efficiency calculation and sources can be found in the supplementary information (Supplementary Materials), Section S1, including Figures S1–S3 showing literature-reported efficiency values for energy storage and Table S1 showing the final figures used in this work. The charge and discharge efficiencies were assumed to be equal and were thus each the square root of the roundtrip efficiency so that the full cycle (charge and discharge) results in the round-trip efficiency figures above (Example: BESS round-trip efficiency = 88.8% = 94.2% charging efficiency X 94.2% discharging efficiency).

A key piece of information for both storage technologies and the natural gas turbine was the frequency regulation control signal, the second-by-second signal that describes the changing energy output requested from the ISO. The best available regulation signal data was from PJM [15]. PJM provides two frequency regulation signals, the traditional Reg A signal, and the faster-responding Reg D signal. Reg A is the standard frequency regulation service and Reg D was designed more recently to better reflect the capabilities of energy storage assets. Reg D services pay out more on a per MW/hour basis but also require faster and more frequent ramping. In this work, we used the Reg A signal for direct “apples to apples” analysis as the natural gas plant is unable to adequately provide Reg D service. Even though real-life storage is more likely to choose the Reg D service, having it do so in this analysis would unfairly disadvantage storage as it attempts to follow a more challenging signal. The same frequency regulation signal was used in all three emissions calculations: the PJM regulation signal from May 4th to May 10th in 2014 [15].

The BESS operates as a net electricity consumer: it requires more energy input than it provides later because of efficiency losses. This net energy demand comes from the electric grid. The energy requirements for discharging to the grid from the BESS were calculated at

each timestep using Equation (1). The amount of energy sent from the BESS to the grid ($E_{sent, discharging}$) was calculated using the timestep of the regulation signal (T) of 4 s for all analyses and the BESS service capacity was 20 MW ($Capacity$). To deliver the desired amount of energy to the grid, the BESS sends more than the required amount of energy to compensate for discharge losses. Therefore, the required energy according to the PJM signal was divided by the discharging efficiency of 94.2% for the BESS ($\eta_{discharging}$). The calculation for the amount received by the grid follows a similar logic (Equation (2)).

$$E_{sent, discharging\ BESS} = \frac{Signal(i) \times T_{discharging} \times Capacity}{\eta_{discharging}} \quad (1)$$

$$E_{received, discharging\ BESS} = Signal(i) \times T_{discharging} \times Capacity \quad (2)$$

The model was subdivided into increments that allowed energy purchases every 15 min so that the ESS could maintain state of charge. When charging the BESS from the grid, the amount of energy desired depends on the charge level of the BESS. When the BESS was above the target charge level of 50% it is not charged, and no energy is purchased from the grid for the BESS. When the BESS is below the desired state of charge, the grid sends energy to it equal to the net amount of energy the BESS discharged during the last 15-min period. The amount of energy sent from the grid to the BESS ($E_{sent, charging}$) varied due to changes in the regulation signal over the one-week period. The energy required by the BESS was then divided by the charging efficiency ($\eta_{charging}$) to compensate for transfer loss. The amount received by the BESS from the grid was calculated in Equation (4), where the net energy was summed over 225 4-s periods to get a 15-min energy estimate.

$$E_{sent, charging\ BESS} = \frac{1}{\eta_{charging}} \times \sum_{i=1}^{225} \left(\frac{Signal(i) \times T_{discharging} \times Capacity}{\eta_{discharging}} \right) \quad (3)$$

$$E_{received, charging\ BESS} = \sum_{i=1}^{225} \left(\frac{Signal(i) \times T_{discharging} \times Capacity}{\eta_{discharging}} \right) \quad (4)$$

The ESS state of charge is based on the sum of energy discharged and received in each 15-min period as shown in Equation (5). The energy purchased for recharging is spread evenly over the 15-min charging period.

$$E_{stored, BESS}(j) = E_{stored, BESS}(j-1) + E_{sent, discharging\ BESS}(j-1) - E_{received, charging\ BESS}(j) \quad (5)$$

The final output of the BESS model was the energy losses caused by the operation of the BESS in frequency regulation. The BESS loss is defined as the energy lost from charging and discharging inefficiencies in the system. The charging and discharging efficiency losses were calculated separately and then added together to find the total loss for each charging timestep. Equation (6) shows the equation used to find the BESS losses. The difference between the amount of energy sent to the grid and the amount received by the grid is the discharging efficiency loss. The difference between the amount of energy sent to the BESS and the amount received by the BESS is the charging efficiency loss. The energy loss in each hour was then multiplied by that hour's marginal emissions factor (MEF) to calculate the BESS emissions.

$$E_{loss, BESS}(j) = (E_{sent, BESS} - E_{received, BESS}) + (E_{sent, grid} - E_{received, grid}) \quad (6)$$

MEFs provide a metric by which additional or avoided emissions can be determined by representing the emission rates of the generator that will respond to small increases or decreases in demand. MEFs are not constant and change as different generation sources are used to meet the changing demand of the grid. The MEFs for different locations in the United States were taken using the methods from Siler-Evans and Azevedo [16] and taken

for the year 2017 from the Electricity Marginal Factor Estimates database from the Center for Climate and Energy Decision Making [17].

The model for the flywheel emissions used the same input variables as the BESS, with the addition of a self-discharge rate and a different round-trip efficiency of 89.1%. The self-discharge rate of 1.145% per hour was found by taking the average self-discharge rate of the high-speed flywheel products listed in the Electric Power Research Institute (EPRI) Handbook of Energy Storage with similar characteristics to the one we wanted to model [18]. This was used in conjunction with charging and discharging efficiencies of 94.4% ($\eta_{\text{discharging}}$) to determine the total energy losses from the FESS. The self-discharge rate of batteries was also investigated but was found to be negligible for this application and was assumed to be zero.

Although energy lost in self-discharge was not sent to the grid, it was lost by the FESS and is included in the discharging equation. The self-discharge rate (η_{self}) used was 0.00127% at each timestep ($T_{\text{discharging}}$). The calculation for the amount of energy sent to the grid is shown in Equation (7), while Equation (8) calculates the amount of energy received by the grid from the FESS. The self-discharge loss was a function of the 20 MW service capacity (Capacity) of the FESS and independent of the stored energy level and was therefore unaffected by the control signal or operation of the FESS. The other FESS emission calculations were identical to the BESS emission calculations.

$$E_{\text{sent, discharging FESS}} = \frac{\text{Signal}(i) \times T_{\text{discharging}} \times \text{Capacity}}{\eta_{\text{discharging}}} + \eta_{\text{self}} \times \text{Capacity} \quad (7)$$

$$E_{\text{received, discharging FESS}} = \text{Signal}(i) \times T_{\text{discharging}} \times \text{Capacity} + \eta_{\text{self}} \times \text{Capacity} \quad (8)$$

2.1. Natural Gas Operation and Emissions

The natural gas frequency regulation service used the same signal as the ESS and offers the same frequency regulation capacity of 20 MW. The main difference lies in the operation of 180 MW of base generation produced continuously from the natural gas plant. When frequency regulation services are required, the gas plant will start burning additional fuel to meet the demand of the grid up to the 200 MW capacity of the natural gas plant. The natural gas power output is the sum of the base power and the frequency regulation power and the total power output from the plant will vary between 180 and 200 MW. A simple cycle gas turbine was chosen for this application because this type of generator is designed to handle the frequent and rapid changes in power output required for frequency regulation service. The 200 MW scale for the gas turbine was selected so that it would provide an equal quantity of frequency regulation service as the stationary storage and to be in line with the scale of modern gas turbine sizes (for example, the 501FD turbine on which we base our emissions analysis is a 180 MW turbine). Importantly, the scale of the turbine should not affect the results in any way because there are not any scaling factors in either the storage or gas turbine model. This means, for example, that a modeled gas turbine of 100 MW (with 10 MW dedicated to regulation) would have the same emissions per unit of frequency regulation service. The proportion of the turbine's capacity dedicated to regulation is relevant, however, and we treat it as such in the sensitivity analysis (see Section 4—Discussion Section).

The desired result of our analysis is a calculation of the emissions from providing frequency regulation services. As such, the emissions from the 180 MW of baseload generation of the natural gas plant needs to be excluded from the emission results. To do this, for each emission type, the emissions from the baseload generation were subtracted from the total calculated emissions, leaving only the emissions associated with frequency regulation, though we also considered two alternative methods of allocating frequency regulation emissions from natural gas turbines (described in Section 2.2 below).

For this work, we used a model of gas turbine CO₂, NO_x, and SO₂ emissions based on measurements of a 501FD turbine. Emissions can be calculated directly using Equations (9)–(12) from Katzenstein and Apt's 2009 analysis [14] and we describe and discuss the emissions

model in greater detail in the Supplementary Materials, Section S2, including Figure S4 showing the emission curves for the gas turbine. An important note about this model: while it does account for the effect of partial load on emissions rate, it does not account for the effect of rapidly changing power output. Katzenstein and Apt do address this issue in their work and we find that the effect is likely small given that the gas turbine is only ramping $\pm 5\%$ from the nominal output of 190 MW. Greater details on the data, analysis, and equations used for this emissions model are available in the Supplementary Materials, Section S2.

$$\text{CO}_2 \text{ Emissions} = 1.746 \times 10^1 + 2.528 \times 10^{-1} \times \text{Power} \quad (9)$$

$$\begin{aligned} \text{NO}_x \text{ Emissions Region 1 (0 – 53MW)} \\ = 8.03 \times 10^{-1} + 2.45 \times 10^{-2} \times \text{Power} - 3.49 \times 10^{-4} \times \text{Power}^2 \end{aligned} \quad (10)$$

$$\begin{aligned} \text{NO}_x \text{ Emissions Region 2 (53 – 105MW)} \\ = -9.48 \times 10^{-1} + 6.12 \times 10^{-2} \times \text{Power} - 3.95 \times 10^{-4} \times \text{Power}^2 \end{aligned} \quad (11)$$

$$\begin{aligned} \text{NO}_x \text{ Emissions Region 3 (105 – 200MW)} \\ = 1.18 \times 10^{-1} - 5.76 \times 10^{-4} \times \text{Power} + 4.1 \times 10^{-6} \times \text{Power}^2 \end{aligned} \quad (12)$$

$$\begin{aligned} \text{NO}_x \text{ Emissions Region 3 Plateau} \\ = -5.8572 \times 10^{-4} + 2.9661 \times 10^{-3} \times \text{Power} \\ - 3.5211 \times 10^{-5} \times \text{Power}^2 + 1.9211 \times 10^{-7} \times \text{Power}^3 \\ - 3.4885 \times 10^{-10} \times \text{Power}^4 \end{aligned} \quad (13)$$

2.2. Attributing Natural Gas Emissions

Because a natural gas turbine and a storage device provide a different set of services (as well as net energy production and associated emissions), the attribution of emissions is a critical question for fair comparison between the two technology types. The simplest way to estimate the emissions of the gas turbine providing frequency regulation is to calculate the difference between the estimated emissions while providing frequency regulation and while providing zero regulation service (180 MW flat output). We call this method “Raw Emissions”. On average, the ESS technologies consume energy while providing frequency regulation services. However, the natural gas turbine, even when deducting the 180 MW of base power output, produces net energy (of approximately 10 MW, for an average output of around 190 MW) when providing frequency regulation. Since the natural gas plant is generating energy, it is displacing energy that would have to be generated elsewhere if an ESS was performing the frequency regulation service. Because of this, there is a benefit to the natural gas plant regulation service that is not captured in the “Raw Emissions” case. We thus examined two alternative methods that can account for this generated energy and provide a fairer comparison of emissions.

In the “Compensated Generation” case, it was assumed that, in the absence of providing frequency regulation services, the natural gas plant would operate at full capacity (200 MW), where its operation is most efficient. By having the natural gas plant provide frequency regulation, it is forced to run at less efficient conditions. Thus, to account for the plant’s electricity generation, we compared the annual tonnes of emissions and energy produced for frequency regulation to the energy and emissions produced if the turbine were operated at optimal (maximum) output. The amount of energy being generated for frequency regulation (E_{reg}) was multiplied by the emission rates at full capacity (Emission Rate) and subtracted from the raw natural gas emissions from the 20 MW of regulation ($\text{NG Emissions}_{\text{raw}}$). Therefore, the natural gas frequency regulation emissions under “Compensated Generation” are the emissions that result from the less efficient operation of a natural gas plant as it operates at a partial load to meet a variable control signal, as calculated in Equation (14). We also propose that this is the most appropriate of the three

comparison cases used to determine the natural gas emissions for a typical plant and use it for baseline results.

$$NG\ Emissions_{full} = NG\ Emissions_{raw} - E_{reg} \times Emission\ Rate \quad (14)$$

In the “Marginal Replacement” case, the marginal emission factors (MEFs) were used to calculate emissions from marginal generation replacing the reduced natural gas plant output as shown in Equation (15). This method is the same as in the compensated generation case, except instead of multiplying the energy generated by the emissions rate of this gas turbine at full capacity, the generated energy was multiplied by the MEFs for each corresponding region. This represents a scenario where the portion of the generation from the natural gas plant dedicated to frequency regulation must be compensated for by marginal generation facilities. In this comparison case, the natural gas frequency regulation emissions are the difference in emissions from the natural gas plant generating the electricity used to provide 20 MW of frequency regulation and the emissions from marginal generation producing that amount of electricity instead. An example calculation can be seen in Figure 1.

$$NG\ Emissions_{full} = NG\ Emissions_{raw} - E_{reg} \times MEF \quad (15)$$

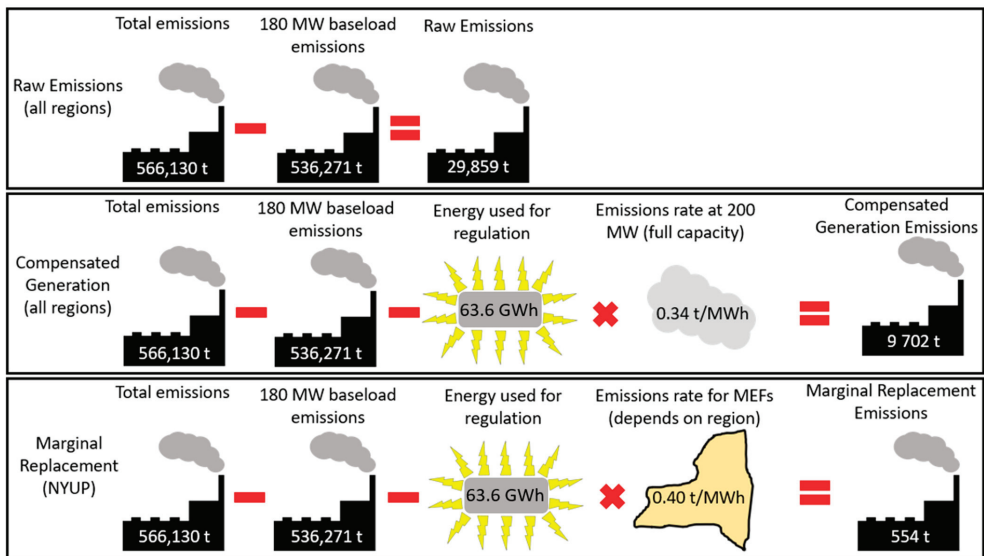


Figure 1. Example of calculations for three methods of estimating annual natural gas CO₂ emissions attributable to frequency regulation. The raw emissions method is the simplest but neglects that the gas turbine produces 63.6 GWh of energy annually in association with the regulation service. The compensated generation case credits those emissions at the full capacity emissions rate for the gas turbine. The marginal replacement method credits those MWhs at the marginal emissions rate for the electricity grid. Upstate New York (NYUP) was used as an example since there are different marginal emissions in each region.

For all three methods of attributing natural gas emissions, there is a question about the emissions effect of having an extra 63 GWh of energy that comes from the gas turbine but not the energy storage. The raw emissions method assumes that this energy has no particular emissions value or use. Compensated generation assumes that it displaces 63 GWh of additional use of the gas turbine in question, while marginal replacement

assumes that it displaces 63 GWh of energy production from other marginal generators on the grid.

3. Results

We calculated annual total emissions of CO₂, NO_x, and SO₂ from a natural gas plant, BESS, and FESS providing frequency regulation using the PJM Reg A signal under several scenarios. A determination of the lowest emission frequency regulation technology was made for each eGRID subregion. There were significant differences between the eGRID subregions, so the best choice changed based on geographic location for some of the emission types. We present the compensated generation results below and provide the results for the raw emissions and marginal replacement scenarios, along with a variety of other outputs, in the Supplementary Materials, Section S3, including Figures S5–S28.

The compensated generation case “compensates” the natural gas plant for generated electricity based on the emissions it would have produced operating at full capacity, which we believe is the fairest treatment of emissions. The total annual CO₂ emissions for the natural gas plant is 566,000 tonnes when providing Reg A frequency regulation service. However, 536,000 tonnes of the CO₂ emissions is attributable to the 180 MW of unvarying generation. The other 30,000 tonnes of CO₂ emissions per year are attributable to the frequency regulation service of the natural gas plant, though this 20MW of regulation service also produces around 10MW of generation. Under the compensated generation assumptions, producing that amount of energy would emit an additional 20,000 tonnes of CO₂, which is subtracted from the natural gas plant frequency regulation emissions, resulting in approximately 10,000 tonnes of CO₂ emissions attributable to frequency regulation.

Figure 2 shows the comparison between the CO₂ emissions for the different frequency regulation technology types in upstate New York (NYUP), California (CAMX), Texas (ERCT), and the upper Midwest (MROW). The storage technologies have lower CO₂ emissions than the natural gas plant in all eGRID subregions when meeting the Reg A frequency regulation requirement using compensated generation, with batteries showing slightly lower emissions than flywheels.

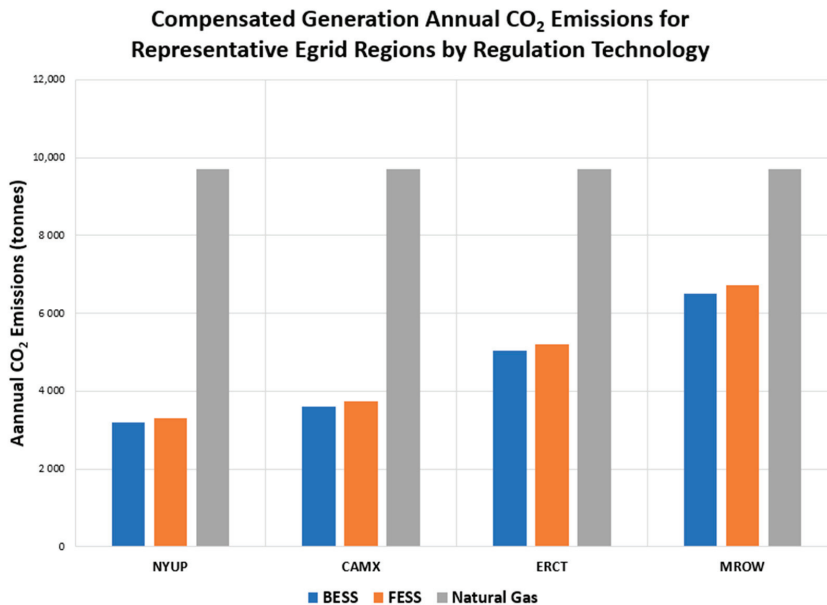


Figure 2. Annual CO₂ emissions with compensated generation when providing Reg A frequency regulation service for upstate New York (NYUP), California (CAMX), Texas (ERCT), and the upper Midwest (MROW). The battery energy storage system (BESS) and flywheel energy storage system (FESS) emissions are similar for all regions with the BESS having slightly lower emissions. The ESS has lower CO₂ emissions than the compensated generation natural gas plant in all eGRID subregions.

Figure 3 shows how much lower the BESS emissions were for each eGRID subregion when providing Reg A frequency regulation service, using the compensated generation assumptions. The lighter regions had higher BESS emissions and had a smaller difference between the natural gas and BESS emissions. With the compensated generation comparison case, the BESS had lower CO₂ emissions than the natural gas plant in each eGRID subregion, varying from 33% lower in the upper Midwest to 68% lower in Upstate NY.

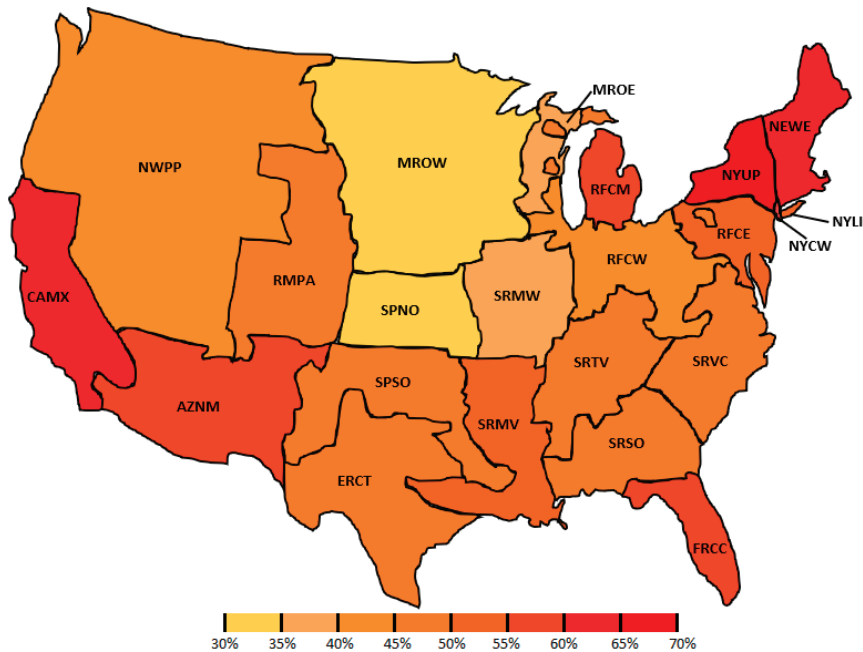


Figure 3. Percent reduction in CO₂ emissions from 20 MW of Reg A frequency regulation operating 24 h a day for a year using the BESS instead of the natural gas plant, with compensated generation assumptions.

The total annual NO_x emissions for the natural gas plant is 80.76 tonnes when using the Plateau Equation to provide Reg A frequency regulation service. However, 78.90 tonnes of the NO_x emissions are due to the 180 MW of unvarying generation. The other 1.86 tonnes of NO_x emissions are attributable to the frequency regulation service of the natural gas plant. With compensated generation, 1.81 tonnes of NO_x emissions were subtracted from the natural gas plant frequency regulation emissions, resulting in 0.05 tonnes of NO_x emissions.

Figure 4 shows the comparison between the NO_x emissions for the different frequency regulation technology types in the NYUP, CAMX, ERCT, and MROW eGRID subregions. With compensated generation, the natural gas plant had lower NO_x emissions than both storage technologies in all eGRID subregions. With the Plateau Equation, almost none of the natural gas plant NO_x emissions were attributed to frequency regulation. This result (and the similar result for SO₂ below) occurs because the modeled gas turbine is a “low NO_x” design, while the emissions associated with the storage technologies are based on the marginal grid mix.

Compensated Generation Annual NO_x Emissions for Representative Egrid Regions by Regulation Technology

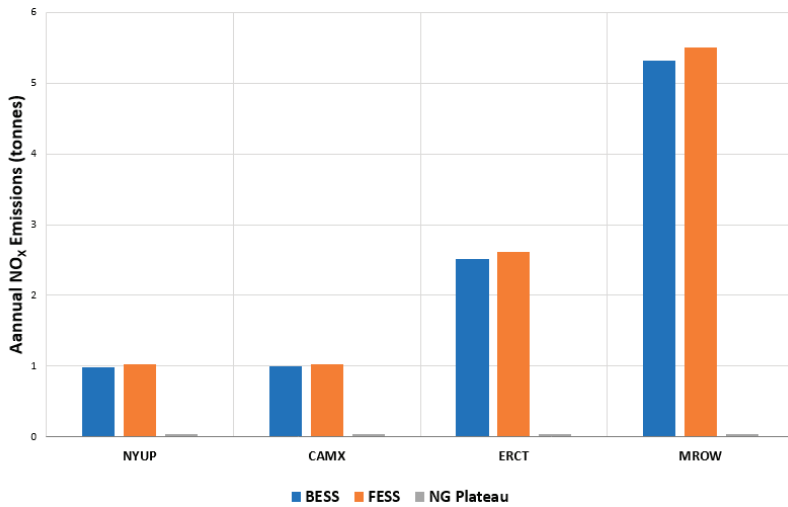


Figure 4. Annual NO_x emissions when providing Reg A frequency regulation service with compensated generation for upstate New York (NYUP), California (CAMX), Texas (ERCT), and the upper Midwest (MROW). The BESS and FESS emissions are similar for all regions with the BESS having slightly lower emissions. The compensated generation natural gas plant has significantly lower NO_x emissions than the two types of ESS.

The modeled natural gas plant had 0.05 tonnes of NO_x emissions per year attributed to the 20 MW of frequency regulation service (using the Plateau Equation). Figure 5 shows the difference between the NO_x emissions of the BESS and natural gas plant. With the Plateau Equation, the BESS produced 20 times or more NO_x emissions than the natural gas plant in all eGRID subregions.

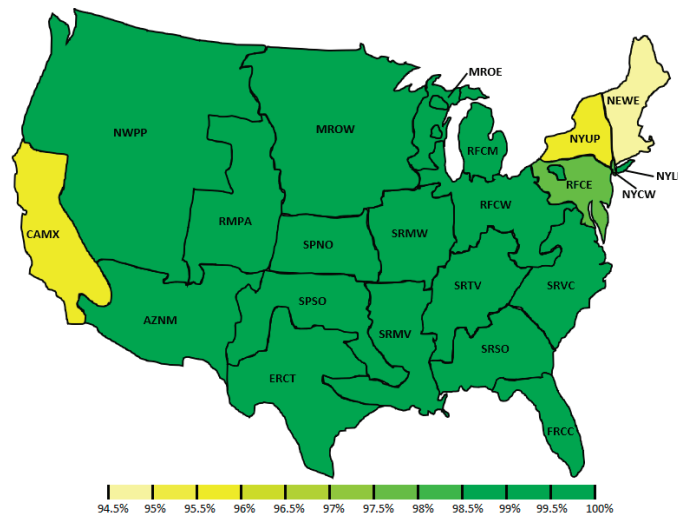


Figure 5. Percent reduction in NO_x emissions from 20 MW of Reg A frequency regulation operating 24 h a day for a year using the compensated generation natural gas plant instead of the BESS.

The total annual SO₂ emissions for the natural gas plant are 2.83 tonnes when providing Reg A frequency regulation service. However, 2.68 tonnes of the SO₂ emissions are due to the 180 MW of unvarying generation. The other 0.15 tonnes of SO₂ emissions per year for the 20 MW of frequency regulation service are attributable to the frequency regulation service of the natural gas plant. With compensated generation, 0.10 tonnes of SO₂ emissions are subtracted from the natural gas plant frequency regulation emissions resulting in 0.05 tonnes of SO₂ emissions being attributed to the frequency regulation.

Figure 6 shows the comparison between the SO₂ emissions for the different frequency regulation technology types in upstate NYUP, CAMX, ERCT, and MROW. In the case of the compensated generation natural gas plant, there are almost no SO₂ emissions. This was expected because of the low rate of SO₂ production from natural gas combustion.

Compensated Generation Annual SO₂ Emissions for Representative Egrid Regions by Regulation Technology

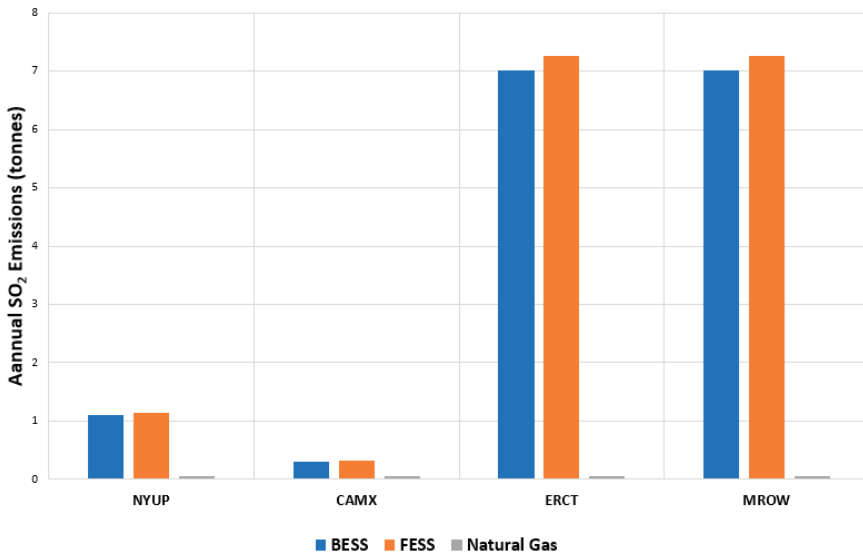


Figure 6. Annual SO₂ emissions when providing Reg A frequency regulation service with compensated generation for upstate New York (NYUP), California (CAMX), Texas (ERCT), and the upper Midwest (MROW). The BESS and FESS emissions are similar for all regions with the BESS having slightly lower emissions. The compensated generation natural gas plant has significantly lower SO₂ emissions than the ESS technologies.

Figure 7 shows how much lower the natural gas SO₂ emissions were than the BESS emissions for each eGRID subregion. The darker regions had higher BESS emissions and had a larger difference between the natural gas and BESS emissions. In 18 of the 22 eGRID subregions, the natural gas plant resulted in at least 20 times lower SO₂ emissions than the BESS. However, in NYCW, the natural gas plant has only 11% lower SO₂ emissions than the ESS with compensated generation due to the low sulfur emissions in that region.

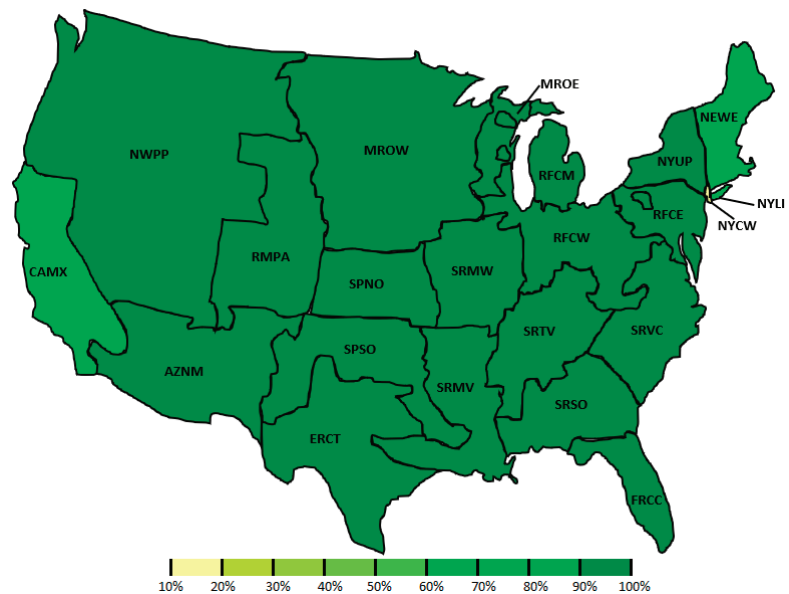


Figure 7. Percent reduction in SO₂ emissions from 20 MW of Reg A frequency regulation operating 24 h a day for a year resulting from using the compensated generation natural gas plant instead of the BESS.

Sensitivity Analysis

We performed several sensitivity analyses on the model to test different assumptions and inputs. The most important of these were the three methods for crediting the natural gas turbine's energy production (two of which are presented in full in the Supplementary Materials). Figure 8 shows the CO₂ emissions in Upstate NY (NYUP) for the three methods of crediting the natural gas plant. Going from raw emissions to compensated generation reduces the CO₂ emissions of the natural gas plant by 68%. The marginal replacement CO₂ emissions from the natural gas plant were lower than the compensated generation case and were actually slightly below zero due to the gas plant having lower emissions than the marginal generator in this region. This pattern of large reductions between raw emissions, compensated generation, and marginal replacement is consistent throughout all the eGRID subregions, demonstrating the critical importance of the assumption about crediting back emissions.

The most appropriate crediting method depends on the individual plant location and situation. Our assessment is that the compensated generation assumption (using the Plateau Equation for NO_x emissions) was the fairest method. The raw emissions case neglects the relevance of the electricity produced by the gas plant when providing regulation services (10 MW on average), which ought to displace some other generator in a real system. On the other hand, the marginal replacement approach essentially assumes that the gas plant is built new for the purpose of frequency regulation, which also seems unlikely. The compensated generation case assumes that without providing frequency regulation the natural gas plant would operate at its maximum capacity where its operation is most efficient. Although there are specific scenarios where these other cases could be used (discussed further in the Supplementary Materials, end of Section S3), they seem to be less representative scenarios.

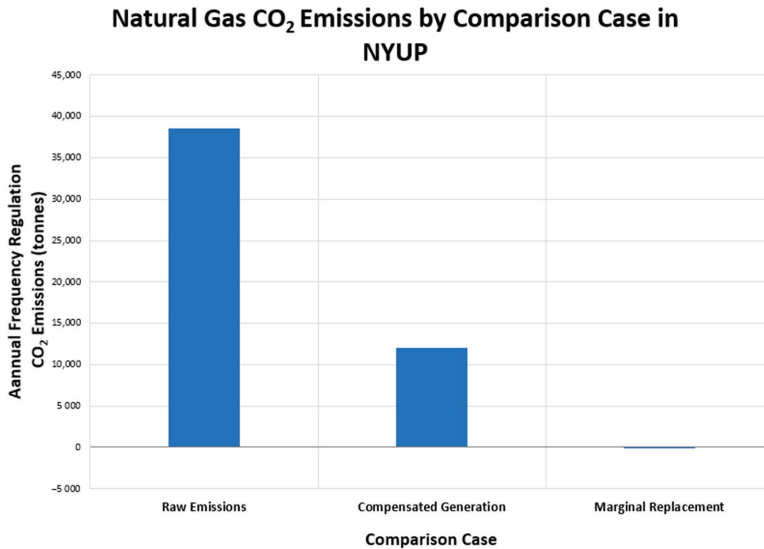


Figure 8. The annual CO₂ frequency regulation emissions in Upstate NY (NYUP) by method of crediting natural gas energy generation. Both the compensated generation case and the marginal replacement case have significantly lower emissions than the raw emissions case.

The self-discharge rate of the flywheel was an uncertain input variable to the model. The self-discharge rate used, 1.145% per hour, was found by taking the average self-discharge rate of the high-speed flywheel products listed in the Electric Power Research Institute (EPRI) handbook [18]. The 2002 EPRI handbook was used as the EPRI handbooks from later years did not list specific self-discharge rates, instead stating that the self-discharge rate is between 1% and 2% per hour. This average was not based on many products, and a slightly different self-discharge rate for any specific FESS is likely.

Using the model, the self-discharge rate of the flywheel would have to be reduced to 0.2% for the FESS overall efficiency to be the same as the BESS, when using the base-case roundtrip energy efficiency of 88.8% for the BESS and 89.1% for the FESS. An efficiency of 0.2% may be possible with specific highly efficient flywheel systems but this seems to suggest that the lithium ion BESS is a slightly lower emission energy storage option for frequency regulation under the parameters of our analysis. The range of self-discharging efficiencies found in the handbook result in a range of effective overall system efficiencies from 82.0% to 88.9%. Nearly all of this range is lower than the efficiency of 88.8% used for the BESS. Using a FESS with a high rate of discharge, corresponding to a system efficiency of 82.0%, will result in nearly twice the FESS emissions of the version that we modeled. This is a major difference and would change the results from FESS having lower emissions in every eGRID subregion to natural gas having lower CO₂ emissions in every eGRID subregion. If a FESS is to be used for frequency regulation service, it must have a low rate of self-discharge to be a viable alternative to natural gas for frequency regulation services with the goal of emission reduction.

Our results are based on the 501FD high efficiency combined cycle turbine with low NO_x emissions, and the results will vary depending on the turbine used. We used the 501FD turbine emissions for our analysis because of the availability of detailed emission rates from operational data for a range of potential operation power output levels. When comparing our emission results from the 501FD turbine to emission rates of representative natural gas turbines according to the EPA in 2015 [19], the 501FD turbine had between a 32% and 55% lower CO₂ emission rate. The NO_x emission rates also varied significantly based on factors involved with the individual natural gas plant. The 501FD combustion turbine

is a low NO_x turbine, with NO_x emissions 78% to 91% lower than the representative turbines studied by the EPA. However, since the 501FD plant is a low NO_x emission plant, it makes more sense to compare the 501FD emission rates to the representative turbines with NO_x emission reduction methods. When compared to the 501FD plant, the EPA representative natural gas plants with emission reduction technology had between 22% and 57% lower NO_x emissions than the 501FD plant. This makes sense because the 501FD design studied by Katzenstein is older than modern turbines with dedicated NO_x emission aftertreatment methods.

To determine the changes that result from using an alternate turbine, we reran the emission results using the highest and lowest emission rates of the five representative turbines described in the EPA Combined Heat and Power Partnership report [19]. Using the EPA representative turbines instead of the 501FD did not improve the CO₂ results for natural gas since the EPA representative turbines have on average 57% more CO₂ emissions than the 501FD. This was similar for the EPA representative turbines with NO_x emissions control technologies: because they have up to 56% lower NO_x emissions than the 501FD turbine, the natural gas plant continues to have lower NO_x emissions than BESS and FESS in all eGRID subregions. Overall, because of the large differences in emissions, using a different turbine would not change the results of which technology has lower frequency regulation emissions.

Our analysis was based on the case of a 200 MW plant providing 20 MW of frequency regulation and 180 MW of unvarying generation. If more of the plant is dedicated to frequency regulation services, the emissions from the natural gas plant change. As the baseload generation is decreased, the emissions per unit of energy generated increase due to a lower operational efficiency. To investigate this, simulations were run with an unvarying “baseload” at 120, 140, and 160 MW in addition to the base case of 180 MW. Lower baseloads were not considered, as the 501FD turbine’s low-NO_x operation only occurs above 105 MW. There were some differences between different baseload generation results, but the trend of the BESS and FESS having lower CO₂ emissions than natural gas and the natural gas plant having lower NO_x and SO₂ emissions remained the same as in the base case. The largest difference in emissions is for the case where the gas plant provides 80 MW of regulation services. For the compensated generation comparison case, the BESS and FESS continued to have lower CO₂ emissions when providing 80 MW of regulation service, while the natural gas plant had lower NO_x and SO₂ emissions. However, compared to the 20 MW base case where the natural gas plant had at least 94% lower NO_x emissions than the BESS/FESS, with 80 MW of frequency regulation service the ESS and natural gas emissions were much closer at 37% or lower. As the amount of frequency regulation from the gas plant increased, the ESS generally performed better in terms of emissions, especially NO_x emissions, but there is not a large enough difference to change which technology has lower emissions.

4. Discussion

FESS was repeatedly identified as a high efficiency option for frequency regulation in the literature, but in our results the FESS generated 1.8% more emissions than the BESS for CO₂, NO_x, and SO₂. This is because in our model the emission results account for the self-discharge of the flywheel in addition to the round-trip efficiency of the energy transfer. However, both the BESS and FESS roundtrip efficiencies are averages found in the literature and an individual storage system would likely differ somewhat, so the proper conclusion is that BESS and FESS perform similarly, and the individual system efficiency of the battery or flywheel will determine which system has lower emissions.

A key factor for a plant operator when considering the use of natural gas plants for frequency regulation is the potential profit. Although a natural gas plant can provide frequency regulation services, this competes with other potential services. If there is more profit to be made by providing energy or spinning reserves, a natural gas plant would not want to perform frequency regulation services. For a natural gas plant to choose to provide

frequency regulation over baseload generation, it would have to have enough financial incentive to run at a reduced power level and less efficiently. This is assumed in the results above but does not hold at all times and locations.

Another real-world consideration that did not factor into our analysis is the requirement for the natural gas plant to run continuously when providing frequency regulation services. Although the natural gas plants used for frequency regulation can ramp up and down quickly enough to meet the requirements of the regulation signal, they must already be running to do so. Because the natural gas plant would want to be running as close to full capacity as possible while still leaving enough potential to increase output and meet the frequency regulation requirements, it would be continuously running near maximum capacity which may not be profitable at all hours of the year. If the natural gas plant is providing frequency regulation services, it may not have the opportunity to stop generating electricity during less profitable time periods. This makes frequency regulation provision for the natural gas plant more of an inconvenience than for the ESS technologies.

In the analysis above, we used the traditional Reg A signal from PJM, but the newer Reg D signal was designed for fast-response regulation providers such as BESS and FESS. There are significant differences between the regulation signals, but we found that the advantages or disadvantages of BESS/FESS when compared to the natural gas plant are similar between the two signals, though there are relevant shifts in emissions between the Reg D and Reg A results. Additionally, there is a difference in the ability of the technology to provide the services required by the control signal: our fast-ramping natural gas plant cannot meet the requirements of the Reg D signal. These are summarized in Figure 9, which shows that the ESS emission advantages are lower under Reg D, but the modeled natural gas plant is unable to reliably meet the Reg D signal. There were only minor differences in the NO_x and SO_2 emissions when comparing the Reg A and Reg D results.

Compensated Generation ESS CO_2 Emission Advantage Over Natural Gas for Representative Egrid Regions for Reg A and Reg D

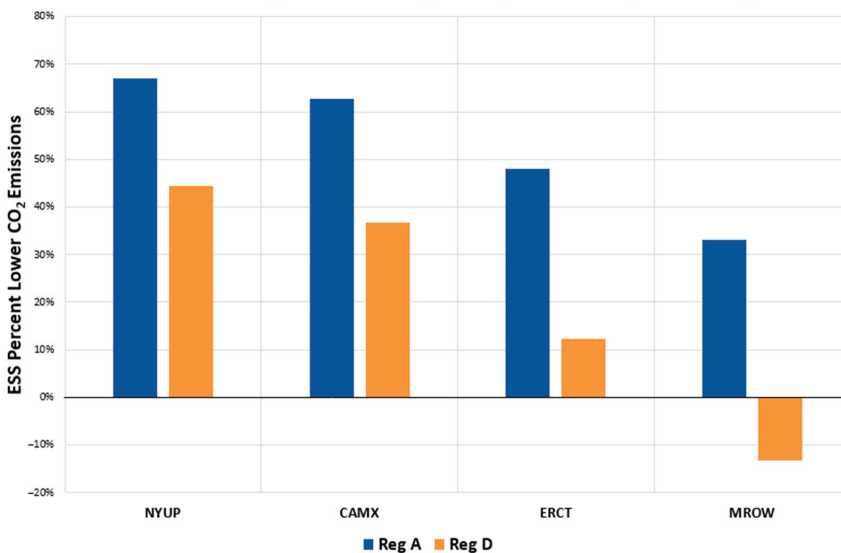


Figure 9. Comparison of the CO_2 emission advantage for ESSs over a natural gas plant providing 20 MW of frequency regulation service using both the Reg A and Reg D signals. The advantage of ESS is reduced when following the Reg D signal. Despite this, the ESS still had lower CO_2 emissions than the natural gas plant in 17 of 22 eGRID subregions under the Reg D signal.

Overall, it is important to state that frequency regulation service is not a major contributor to emissions. Currently, the PJM Regional Transmission Operator (RTO) from which the frequency regulation signal was taken requires 700 MW of frequency regulation at peak hours [20]. When compared to the installed capacity of PJM electricity generation that this stabilizes (178,500 MW in 2017), regulation makes up only 0.39% of the installed generation capacity in PJM [21]. Consequently, large scale changes to the installed generation, such as transitioning from fossil fuels to renewable generation, will have much larger effects on emissions than changes to frequency regulation technology.

A final consideration is the trend over time as the grid mix shifts. Because the BESS and FESS technologies have emission effects that are related to the marginal generation sources, a shift in generation mix can affect estimates of their emissions, presumably improving as the grid becomes cleaner. We investigated historical changes in MEFs for the years in which consistent MEF data were available, focusing on CO₂ because the difference between the BESS/FESS and natural gas plant CO₂ emissions was the smallest. The CO₂ MEFs from 2006–2017 are quite consistent, as shown in Figure 10. None of the eGRID subregions had an annual change of more than 13% in the CO₂ MEFs. The largest overall change can be seen in NYUP where there is a 29% decrease in the CO₂ MEFs from their peak in 2009 to their low in 2017, but the year-to-year change did not exceed 13%. Applying the largest percent difference over the analyzed time period in MEFs to our analysis does not change which emission technology had lower emissions for CO₂ in any eGRID subregion.

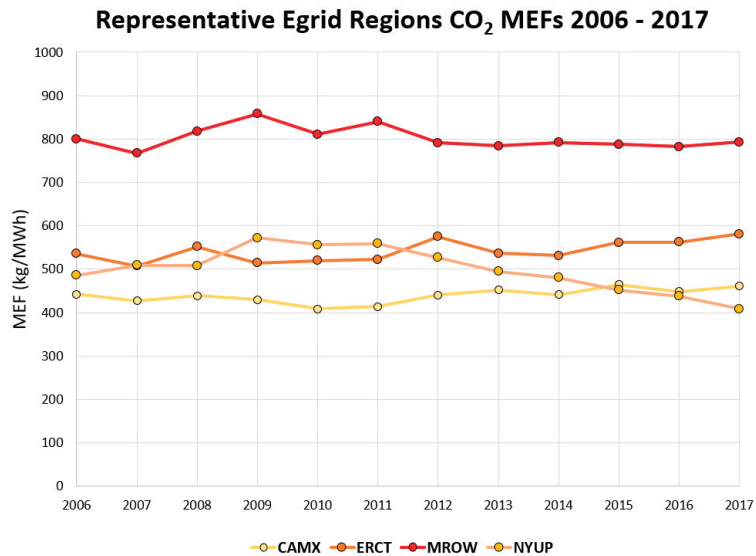


Figure 10. Change in CO₂ marginal emissions factor (MEF) from 2006 to 2017 for Upstate New York (NYUP), California (CAMX), Texas (ERCT), and the Upper Midwest (MROW). The MEFs have remained fairly constant in the eGRID subregions, with NYUP demonstrating the largest change over the 12 years analyzed.

The MEFs would have to change significantly for the ESS emissions to be the same as the natural gas emissions. A MEF of 1.21 tonnes of CO₂ per MWh would result in equal ESS and natural gas CO₂ emissions. This is three times higher than the current CO₂ MEFs for the average eGRID subregion. A MEF of 5.2 kg of NO_x per MWh would result in equal ESS and natural gas NO_x emissions. This is at least 22 times lower than the current NO_x MEFs for all the subregions. A MEF of 6.6 kg of SO₂ per MWh would result in equal ESS and natural gas SO₂ emissions—eight times lower than the current SO₂ MEFs for all the subregions.

In a similar sense, electricity grids in other parts of the world may demonstrate varying net emission effects from using energy storage for frequency regulation service. The electricity grids where storage has the strongest benefit will be those that have clean electricity generation on the margin and currently use dirtier generation to provide frequency regulation. While the analysis in this work applies only to the US, the results may be informative for other countries, while similar methods could be applied for different grids for greater accuracy.

5. Conclusions

This work attempts to determine the emission effects of providing frequency regulation services from batteries or flywheel energy storage relative to the current common approach of ramping natural gas plants. There are both strengths and weakness in using BESS/FESS for frequency regulation in terms of emissions. Our preferred accounting method (compensated generation) suggests that utilization of BESS/FESS for frequency regulation would reduce CO₂ emissions from frequency regulation when compared to the 501FD natural gas plant providing the same service. However, using BESS/FESS would result in higher NO_x and SO₂ emissions for each eGRID subregion, relative to using a low-NO_x natural gas power plant. Therefore, the net benefit of storage depends on what type of emissions is more important to decisionmakers. Despite advantages for NO_x and SO₂ emissions for the natural gas plant, there are real-world inconveniences related to using a natural gas plant for frequency regulation that are not captured in our emissions analysis, such as performance accuracy and the ability to meet faster control signals such as the PJM Reg D. If the MEFs decrease in the future because of changes to the electric grid generation, using ESS for frequency regulation will result in lower emissions. As many states in the US pursue a goal of lower CO₂ emissions, the use of ESS for frequency regulation can be an option to meet that objective. However, it is important to note that frequency regulation is a small percentage of US electricity usage, meaning that changes to the generation fleet can have a far larger impact on overall emission levels.

Supplementary Materials: The following are available online at <https://www.mdpi.com/1996-1073/14/3/549/s1>, Figure S1: Efficiencies of lead acid battery storage from the literature. For studies that reported a range of values, the mean value was used, Figure S2: Efficiencies of Lithium Ion Battery storage from the literature. For studies that reported a range of values, the mean value was used, Figure S3: Efficiencies of Flywheels from the literature. For studies that reported a range of values, the mean of the range was used, Figure S4: NO_x emissions rate per unit power calculated by the Katzenstein Equation and the Plateau Equation, Figure S5: Annual CO₂ emissions from 20 MW of Reg A frequency regulation operating 24 h a day for a year using BESS for the different eGRID regions in tonnes, Figure S6: Annual NO_x emissions from 20 MW of Reg A frequency regulation operating 24 h a day for a year using BESS for the different eGRID regions in tonnes, Figure S7: Annual SO₂ emissions from 20 MW of Reg A frequency regulation operating 24 h a day for a year using BESS for the different eGRID regions in tonnes, Figure S8: Annual CO₂ emissions from 20 MW of Reg A frequency regulation operating 24 h a day for a year using FESS for the different eGRID regions in tonnes, Figure S9: Annual NO_x emissions from 20 MW of Reg A frequency regulation operating 24 h a day for a year using FESS for the different eGRID regions in tonnes, Figure S10: Annual SO₂ emissions from 20 MW of Reg A frequency regulation operating 24 h a day for a year using FESS for the different eGRID regions in tonnes, Figure S11: Annual CO₂ emissions from Reg A frequency regulation service with no crediting for upstate New York (NYUP), California (CAMX), Texas (ERCT), and the Midwest (MROW), Figure S12: Comparison of CO₂ emissions from 20 MW of Reg A frequency regulation operating 24 h a day for a year using BESS and natural gas without any emission crediting. Figure S13: Annual NO_x emissions when providing Reg A frequency regulation service with no crediting for upstate New York (NYUP), California (CAMX), Texas (ERCT), and the Midwest (MROW), Figure S14: Comparison of NO_x emissions from 20 MW of Reg A frequency regulation operating 24 h a day for a year using BESS and natural gas without any emission crediting using the Plateau Equation. Figure S15: Annual SO₂ emissions when providing Reg A frequency regulation service with no crediting for upstate New York (NYUP), California (CAMX), Texas (ERCT), and the Midwest (MROW), Figure S16: Comparison of SO₂ emissions from

20 MW of Reg A frequency regulation operating 24 h a day for a year using BESS and natural gas without any emission crediting. Figure S17: Annual CO₂ emissions with full capacity crediting when providing Reg A frequency regulation service for upstate New York (NYUP), California (CAMX), Texas (ERCT), and the Midwest (MROW), Figure S18: Comparison of CO₂ emissions from 20 MW of Reg A frequency regulation operating 24 h a day for a year using BESS and natural gas with full capacity emission crediting. Figure S19: Annual NO_x emissions when providing Reg A frequency regulation service with full capacity crediting for upstate New York (NYUP), California (CAMX), Texas (ERCT), and the Midwest (MROW), Figure S20: Comparison of NO_x emissions from 20 MW of Reg A frequency regulation operating 24 h a day for a year using BESS and natural gas with full capacity emission crediting and the Plateau Equation. Figure S21: Annual SO₂ emissions when providing Reg A frequency regulation service with full capacity crediting for upstate New York (NYUP), California (CAMX), Texas (ERCT), and the Midwest (MROW), Figure S22: Comparison of SO₂ emissions from 20 MW of Reg A frequency regulation operating 24 h a day for a year using BESS and natural gas with full capacity emission crediting. Figure S23: Annual CO₂ emissions when providing Reg A frequency regulation service with full capacity crediting for upstate New York (NYUP), California (CAMX), Texas (ERCT), and the Midwest (MROW), Figure S24: Comparison of CO₂ emissions from 20 MW of Reg A frequency regulation operating 24 h a day for a year using BESS and natural gas with MEF crediting. Figure S25: Annual NO_x emissions when providing Reg A frequency regulation service with full capacity crediting for upstate New York (NYUP), California (CAMX), Texas (ERCT), and the Midwest (MROW), Figure S26: Comparison of NO_x emissions from 20 MW of Reg A frequency regulation operating 24 h a day for a year using BESS and natural gas with MEF crediting and the Plateau Equation. Figure S27: Annual SO₂ emissions when providing Reg A frequency regulation service with full capacity crediting for upstate New York (NYUP), California (CAMX), Texas (ERCT), and the Midwest (MROW), Figure S28: Comparison of SO₂ emissions from 20 MW of Reg A frequency regulation operating 24 h a day for a year using BESS and natural gas with MEF crediting. Table S1, Model inputs.

Author Contributions: Conceptualization, E.P. and E.H.; methodology, E.P. and E.H.; software, E.P. and E.H.; validation, E.P.; formal analysis, E.P.; investigation, E.P.; data curation, E.P.; writing—original draft preparation, E.P.; writing—review and editing, E.P. and E.H.; visualization, E.P.; supervision, E.H.; project administration, E.H.; funding acquisition, E.H. All authors have read and agreed to the published version of the manuscript.

Funding: This research was funded by the Environmental Sustainability program of the National Science Foundation under award number 1706228.

Institutional Review Board Statement: Not Applicable.

Informed Consent Statement: Not Applicable.

Data Availability Statement: The data presented in this study are available on request from the corresponding author.

Conflicts of Interest: The authors declare no conflict of interest.

References

1. Denchak, M. Are the Effects of Global Warming Really that Bad? Available online: <https://www.nrdc.org/stories/are-effects-global-warming-really-bad> (accessed on 12 November 2017).
2. The New York State Energy Research and Development Authority. Advances Framework to Implement the State’s Climate Law and Decarbonize its Power Sector. Available online: <https://www.nyserda.ny.gov/About/Newsroom/2020-Announcements/2020-06-18-New-York-Advances-Framework-to-Implement-the-States-Climate-Law-and-Decarbonize-its-Power-Sector>. (accessed on 7 September 2020).
3. Bae, H.; Tsuji, T.; Oyama, T.; Uchida, K. Frequency regulation method with congestion management using renewable energy curtailment. In Proceedings of the 2016 IEEE Power and Energy Society General Meeting (PESGM), Boston, MA, USA, 17–21 July 2016.
4. General Electric. What Every Generation Executive Should Know About the Impact of Ancillary Services on Plant Economics. Available online: <https://www.ge.com/power/transform/article.transform.articles.2019.aug.ancillary-services-gas-power-plants> (accessed on 19 January 2021).
5. Cannon, G.; White, J.M.; Whites, S. FERC Orders on PJM’s Frequency Regulation Market Give Energy Storage Providers Another Recent Win. Available online: <https://www.akingump.com/en/experience/industries/energy/speaking-energy/ferc-orders-on-pjm-s-frequency-regulation-market-give-energy.html> (accessed on 3 December 2020).

6. PJM. Regulation Market. Available online: <https://learn.pjm.com/three-priorities/buying-and-selling-energy/ancillary-services-market/regulation-market.aspx> (accessed on 3 December 2020).
7. Frequency Regulation Basics and Trends. Available online: <https://www.osti.gov/biblio/885974-frequency-regulation-basics-trends> (accessed on 19 January 2021).
8. Deign, J. When batteries beat traditional power. Available online: <http://energystoragereport.info/frequency-regulation-battery-energy-storage/#sthash.ddRcwygr.uj5Fv1W.dpbs> (accessed on 3 November 2018).
9. Lucas, A.; Chondrogiannis, S. Smart grid energy storage controller for frequency regulation and peak shaving, using a vanadium redox flow battery. *Int. J. Electr. Power Energy Syst.* **2016**, *80*, 26–36. [[CrossRef](#)]
10. Du, P. Application of Energy Storage for Fast Regulation Service in Energy Market. In *Energy Storage for Smart Grids: Planning and Operation for Renewable and Variable Energy Resources (VERs)*; Academic Press: London, UK, 2015; pp. 97–113.
11. Zakeri, B.; Syri, S. Electrical energy storage systems: A comparative life cycle cost analysis. *Renew. Sustain. Energy Rev.* **2015**, *42*, 569–596. [[CrossRef](#)]
12. Keuring van Elektrotechnische Materialen te Arnhem (KEMA). Emissions Comparison for a 20 MW Flywheel-based Frequency Regulation Power Plant. Available online: https://jointventure.org/images/stories/pdf/kema_flywheel_report_co2_reductions.pdf (accessed on 1 December 2020).
13. Ryan, N.A.; Lin, Y.; Mitchell-Ward, N.; Mathieu, J.L.; Johnson, J.X. Use-Phase Drives Lithium-Ion Battery Life Cycle Environmental Impacts When Used for Frequency Regulation. *Environ. Sci. Technol.* **2018**, *52*, 10163–10174. [[CrossRef](#)] [[PubMed](#)]
14. Katzenstein, W.; Apt, J. Air Emissions Due To Wind And Solar Power. *Environ. Sci. Technol.* **2009**, *43*, 253–258. [[CrossRef](#)] [[PubMed](#)]
15. PJM. Ancillary Services. Available online: <https://www.pjm.com/markets-and-operations/ancillary-services.aspx> (accessed on 25 February 2018).
16. Siler-Evans, K.; Azevedo, I.L.; Morgan, M.G. Marginal Emissions Factors for the U.S. Electricity System. *Environ. Sci. Technol.* **2012**, *46*, 4742–4748. [[CrossRef](#)] [[PubMed](#)]
17. Azevedo, I.L.; Deetjen, T.A.; Donti, P.L.; Horner, N.C.; Siler-Evans, K.; Vaishnav, P.T. Electricity Marginal Factor Estimates. Available online: <https://cedm.shinyapps.io/MarginalFactors/> (accessed on 19 January 2021).
18. Electric Power Research Institute. Handbook of Energy Storage for Transmission or Distribution Applications. Available online: <https://www.epri.com/#/pages/product/1007189/?lang=en> (accessed on 17 April 2018).
19. Darrow, K.; Tidball, R.; Wang, J.; Hampson, A. Combined Heat and Power Partnership. Available online: <https://www.epa.gov/chp/catalog-chp-technologies> (accessed on 17 October 2018).
20. PJM. Regulation. Available online: <https://www.pjm.com/-/media/training/nerc-certifications/markets-exam-materials/mkt-optimization-wkshp/regulation-market.ashx?la=en> (accessed on 20 October 2018).
21. PJM. Capacity by Fuel Type. Available online: <https://www.pjm.com/-/media/markets-ops/ops-analysis/capacity-by-fuel-type-2017.ashx?la=en> (accessed on 20 October 2018).

Article

Estimation of the Performance Aging of the Vestas V52 Wind Turbine through Comparative Test Case Analysis

Davide Astolfi ^{1,*}, Raymond Byrne ² and Francesco Castellani ¹

¹ Department of Engineering, University of Perugia, Via G. Duranti 93, 06125 Perugia, Italy; francesco.castellani@unipg.it

² Centre for Renewables and Energy-Dundalk Institute of Technology, Dublin Road, A91 V5XR Louth, Ireland; raymond.byrne@dkit.ie

* Correspondence: davide.astolfi@studenti.unipg.it; Tel.: +39-075-585-3709

Abstract: It is a common sense expectation that the efficiency of wind turbines should decline with age, similarly to what happens with most technical systems. Due to the complexity of this kind of machine and the environmental conditions to which it is subjected, it is far from obvious how to reliably estimate the impact of aging. In this work, the aging of five Vestas V52 wind turbines is analyzed. The test cases belong to two different sites: one is at the Dundalk Institute of Technology in Ireland, and four are sited in an industrial wind farm in a mountainous area in Italy. Innovative data analysis techniques are employed: the general idea consists of considering appropriate operation curves depending on the working control region of the wind turbines. When the wind turbine operates at fixed pitch and variable rotational speed, the generator speed-power curve is studied; for higher wind speed, when the rotational speed has saturated and the blade pitch is variable, the blade pitch-power curve is considered. The operation curves of interest are studied through the binning method and through a support vector regression with a Gaussian kernel. The wind turbine test cases are analyzed vertically (each in its own history) and horizontally, by comparing the behavior at the two sites for the given wind turbine age. The main result of this study is that an evident effect of aging is the worsening of generator efficiency: progressively, less power is extracted for the given generator rotational speed. Nevertheless, this effect is observed to be lower for the wind turbines in Italy (order of -1.5% at 12 years of age with respect to seven years of age) with respect to the Dundalk wind turbine, which shows a sharp decline at 12 years of age (-8.8%). One wind turbine sited in Italy underwent a generator replacement in 2018: through the use of the same kind of data analysis methods, it was possible to observe that an average performance recovery of the order of 2% occurs after the component replacement. It also arises that for all the test cases, a slight aging effect is visible for higher wind speed, which can likely be interpreted as due to declining gearbox efficiency. In general, it is confirmed that the aging of wind turbines is strongly dependent on the history of each machine, and it is likely confirmed that the technology development mitigates the effect of aging.

Citation: Astolfi, D.; Byrne, R.; Castellani, F. Estimation of the Performance Aging of the Vestas V52 Wind Turbine through Comparative Test Case Analysis. *Energies* **2021**, *14*, 915. <https://doi.org/10.3390/en14040915>

Academic Editor: Juri Belikov

Received: 28 January 2021

Accepted: 7 February 2021

Published: 9 February 2021

Publisher's Note: MDPI stays neutral with regard to jurisdictional claims in published maps and institutional affiliations.

Keywords: wind energy; wind turbines; technical systems aging; performance analysis; power curve



Copyright: © 2021 by the authors. Licensee MDPI, Basel, Switzerland. This article is an open access article distributed under the terms and conditions of the Creative Commons Attribution (CC BY) license (<https://creativecommons.org/licenses/by/4.0/>).

1. Introduction

It is a well-known fact that machines and technical systems are affected by aging [1–6], but it is difficult to theoretically estimate this kind of effect.

In particular, the power production of a wind turbine has a very complex dependence on ambient conditions [7–10], on the stochastic nature of the source [11,12], on the working parameters [13,14], on the wake interactions [15,16], and on the health status and on the efficiency [17,18] of the sub-components. On these grounds, it is a common sense expectation that the efficiency of wind turbines declines with age, but there are no standards about how much and in how much time the performance should decline.

Therefore, a uniquely conceivable approach to the analysis of wind turbine aging consists of learning from experience, which is feasible because a vast number of industrial wind turbines of different sizes and technologies are reaching the end-of-life expectancy. For example, in [19], it was reported that in 2020, 28% of wind turbines installed in Europe were older than 15 years of age, with peaks in the order of 50% in Spain, Germany, and Denmark.

The analysis of wind turbine aging results in being a very complex problem because a vast number of wind turbines should be considered, in order to obtain statistically robust results: from this point of view, the only possibility is considering cumulative data, as for example average yearly capacity, yearly production, and so on. Unfortunately, due to the fact that wind turbines operate under non-stationary conditions and that failure rates are not irrelevant [20], the use of cumulative data is equivalent to losing the control details of the behavior of the wind turbines under consideration. It should also be noticed that in wind energy practice, it has become common to refurbish wind turbines by adopting aerodynamic and/or control technology innovations [21]; therefore, in general, it should be concluded that without knowing in detail the history of the analyzed wind farms, it is likely that the effects of aging are incorrectly estimated.

Despite the above summarized critical points, some remarkable analyses have been conducted. In [22], two-hundred-eighty-two wind farms in the U.K. were considered, and the mismatch between the theoretical and measured load factor was analyzed by attempting a linear regression between the age and the measured load. In [22], it was estimated that the output of the considered test cases diminished by $1.6 \pm 0.2\%$ per year: this implies a 9% increase of the levelized cost of electricity over twenty years. An important point of [22] was that the hypothesis was formulated that wind turbine performance decline with age should be mitigated by innovation in wind turbine technology. In [23], a similar methodology was proposed based on the analysis of wind farms in Sweden: a linear regression between the capacity factor of wind turbines and their age. The methods in [22,23] contain some hints about the fact that a linear trend might be too simple for taking into account the complexity given by the fact that the source (the wind) is stochastic and the response of the machine (i.e., the measured load) depends on several factors; for this reason, some corrections in the linear regression were included, which were an adjustment for the on-site conditions in [22] and sine-cosine fluctuations of the dependency on the age in [23].

The critical points of the approaches based on cumulative data can be overcome through an in-depth analysis of wind turbines' operation data and operation curves [24,25], which allows disentangling the aging effects from reliability degradation or ambient effects. In a nutshell, aging can be distinguished with respect to reliability by considering the behavior of operation curves when the wind turbines are running. Aging can be distinguished with respect to ambient effects by analyzing operation curves such as the generator speed-power, rotor speed-power, and blade pitch-power curves [25]. The drawback of this approach is that it is costly from the point of view of data analysis: for example, the studies in [24–26], which constitute the premise of this work, dealt with a unique wind turbine.

In particular, the results in [24,25] constitute the motivation of the present work: in those studies, a Vestas V52 wind turbine was studied, which is sited at the Dundalk Institute of Technology in Ireland. The wind turbine has been operating since 2005, and operation data from 2008 to 2019 were analyzed. The generator speed-power curve was analyzed when the wind intensity was between 5 and 9 m/s (indicated as Region 2), because in that regime, the wind turbine control is based on variable rotor and generator speed and fixed pitch. When the wind speed was between 9 and 13 m/s (indicated as Region 2 ^{1/2}), the blade pitch-power curve was studied, because the wind turbine operates at rated rotational speed and the blade pitch varies with the wind intensity. The earliest data set available was employed for training a support vector regression for the curves of interest, and the aging was quantified through the analysis of how the residuals between measurements and model estimates evolve as years pass by. The main result of [25] was that the performance decline with the age of the test case wind turbine can be ascribed mainly to the decline of generator performance: in Region 2, it is observed that progressively, the wind turbine extracts less

power for a given generator rotational speed. Comparing the average performance after ten years of operation (2008 vs. 2018), a worsening in the order of 8% is observed. It is further observed that in Region 2 $1/2$ in general, the gearbox efficiency decline contributes almost negligibly to the aging, but in the proximity of the gearbox end of life, it is possible to detect an average performance decline of the order of 1.3%.

The aging estimate obtained in [24,25] was lower with respect to the results in [22], but is in general a non-negligible amount. On these grounds and given the ubiquitous deployment of the Vestas V52 wind turbine model, in [24,25], the importance of analyzing how general the obtained results were was noticed. This involves analyzing further test cases of the same wind turbine model, and the present work deals with this objective: four Vestas V52 wind turbines are studied, which are sited in southern Italy in a complex terrain. Data from 2013 to 2020 are analyzed, courtesy of the Lucky Wind company. The objective of this study is twofold:

- Analyzing the rate of performance decline with age for the wind turbines sited in Italy and comparing against the results in [24];
- Inquiring if the operation curves, and therefore the aging, of the four Italian wind turbines are comparable to those of the test case in [24] when the wind turbines have the same age.

The points of strength of the present work are therefore several:

- Four test case wind turbines of the same model as [24] (Vestas V52) are added to the literature;
- The four wind turbines sited in Italy can be compared among themselves and against the reference of [24]: the analysis is therefore vertical (each turbine against itself) and horizontal (each wind turbine against the others in the farm and against the reference in [24]). This investigation provides additional information, with respect to the existing literature, about the extent to which it is possible to individuate recurring patterns in the aging of wind turbines of a certain model.
- The generator of one wind turbine sited in Italy reached its end of life in 2018. Therefore, a devoted analysis is performed in this study in order to understand how the performance of the wind turbine changes after the replacement of the generator with respect to the yearly data set immediately before. This analysis, on the one hand, represents a crosscheck of the proposed methodologies and, on the other hand, provides an estimate of the amount of performance recovery that can be expected by replacing an aged main component, as the generator of a wind turbine.
- It is possible to inquire at least qualitatively if there is a connection between the wind turbine site and aging: the wind turbine in [24] is placed in a peri-urban site (in proximity to the Dundalk Institute of Technology in Ireland), while the other four wind turbines considered in this study are placed in an industrial wind farm in a mountainous area.

The methodologies employed in this study are similar to those in [24,25], but were adapted to the case of multiple wind turbines from two different sites. In particular, the operation curves are analyzed qualitatively, through the generalization of the binning method, which is recommended for power curve analysis [27], and quantitatively, through support vector regression with a Gaussian kernel. The analysis is conducted in parallel for the two sites, by considering the age of the wind turbines.

It should be noticed that the above summarized methodologies, and in particular the horizontal analysis of the operation curves of the two test cases, represent also a contribution to the more general problem of wind turbine performance analysis and to the problem of comparing the performance of wind turbines of the same model that are sited in different environments: it is known from the literature, and widely discussed in Section 3, that environmental factors (shear, turbulence, atmospheric stability) have an impact on the wind turbine nacelle transfer function and on the measured power curve [28,29]. Therefore, it is more reliable to compare operation curves that do not depend on nacelle wind speed

measurements, as is done in the present work and in [14], where several operation curves were analyzed in detail through a data-driven regression.

The manuscript is organized as follows: Section 2 is devoted to the description of the test case wind farms and the materials at our disposal for the study; in Section 3, the methods are described; the results are reported in Section 4; and finally, in Section 5, the conclusions are summarized.

2. The Test Cases and the Data Sets

The former test case is the same as in the previous studies [24,25]: it is a Vestas V52 installed in 2005 at the Dundalk Institute of Technology, indicated as Test Case 1 (or IREwind turbine) and shown in Figure 1.



Figure 1. Vestas V52 wind turbine at Dundalk Institute of Technology [24].

The latter test case is constituted by four Vestas V52 wind turbines, from a wind farm sited in southern Italy in a mountainous area, which were installed in 2007: these are indicated as Test Case 2 (or ITA1, ITA2, ITA3, ITA4 wind turbines).

The different climatologies at the two sites are summarized by Figure 2, where the average yearly turbulence intensity (per wind speed interval of 0.5 m/s) is reported. There were no meteorological mast data at our disposal for the present study, and therefore, Figure 2 was constructed using the nacelle anemometer data of each wind turbine. The critical points as regards the use of nacelle anemometers for estimating turbulence intensity are well known, but the intention of Figure 2 is mainly qualitative and aimed at indicating that both environments can be considered complex; the mountainous area of the ITA wind turbines is very complex, with an impressively high level of turbulence. As regards the wind intensity distributions, the same sample year as in Figure 2 was considered, and the average wind intensities are respectively 6.2 m/s (IRE), 6.4 m/s (ITA1), 6.7 m/s (ITA2), 6.3 m/s (ITA3), and 6.3 m/s (ITA4).

For the purposes of this study, it is sufficient to indicate that the average yearly intensities are similar (order of 6 m/s), with a slightly higher average for the ITA site.

The gearbox and the generator models are the same for all the test case wind turbines. The model of the generator in this case is a Weier 850 kW, shown in Figure 3, and the main features are reported in Table 1. It should be noted that the generator of wind turbine ITA4 reached its end of life in February 2018; this represents an interesting test case, because the performance before and after the generator replacement can be analyzed. For this reason, a devoted analysis is performed for ITA4.

The gearbox of the wind turbines is Metso PLH-400V52; it is shown in Figure 4, and the principal specifications are reported in Table 2. This information was reported in [24].

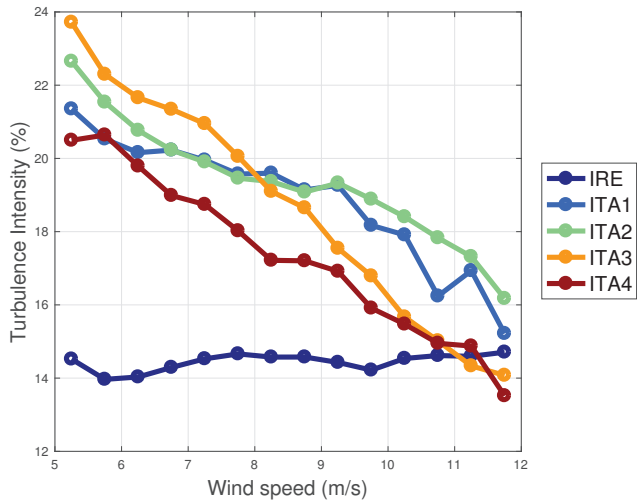


Figure 2. Average yearly turbulence intensity per wind intensity interval at the IRE and ITA sites.

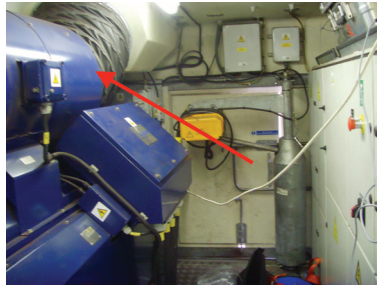


Figure 3. Weier DVSGF 400/4L SP 850 kW generator.

Table 1. Generator principal specifications.

Specification	Data
Model	DVSGF 400/4L SP
Rated power	850 kW
Rated stator voltage	690 V
Rated stator frequency	50 Hz
No. of poles	4
Weight	3755 kg
Moment of inertia	35.7 kgm ²

Table 2. Gearbox principal specifications [24].

Specification	Data
Model	PLH-400V52
Rated power	935 kW
Rated RPM (low speed shaft)	26 min ⁻¹
Gearing ratio	61.799
Weight	5400 kg

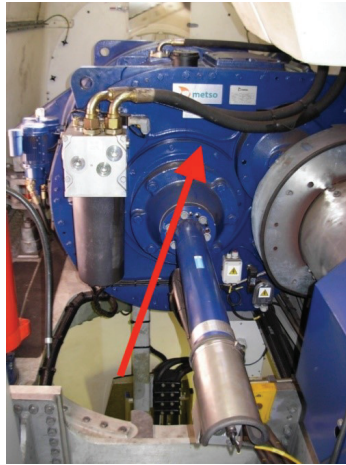


Figure 4. Metso PLH-400V52 gearbox [24].

The data sets at our disposal are from 2008 to 2019 for Test Case 1 (except 2016) and from 2013 to 2020 for Test Case 2; these were organized in yearly packets to be analyzed in parallel, which are characterized by the wind turbines having the same age. This is represented in Table 3.

Table 3. Organization of the data sets.

Test Case 1	Test Case 2	Age (Years)
D_{2012}^1	D_{2014}^2	7
D_{2013}^1	D_{2015}^2	8
D_{2014}^1	D_{2016}^2	9
D_{2015}^1	D_{2017}^2	10
D_{2017}^1	D_{2019}^2	12

On the grounds of the above considerations about the ITA4 wind turbine and the generator replacement, a separate analysis was conducted using the data sets D_{2017}^2 , D_{2018}^2 , and D_{2019}^2 . The data set D_{2018}^2 started since the replacement date of the generator at ITA4 (in March).

The measurements at our disposal are reported in Table 4.

Table 4. SCADA parameters analyzed.

Parameter	Units	Symbol
Wind speed	(m/s)	v
Wind speed standard deviation	(m/s)	σ_v
Wind direction	(deg)	θ
Ambient temperature	(°C)	T_{ext}
Rotor speed	(rpm)	ω
Blade pitch angle	(deg)	β
Generator speed	(rpm)	Ω
Power	(kW)	P
Gear oil temperature	(°C)	T_{oil}

In order to correctly interpret the performance of the wind turbines, it is fundamental to filter the operation data appropriately. The first filter that was applied to the data of both

test cases was based on the run time counter. For Test Case 2, where the wind turbines operate under possible limitations dictated by the grid, the measurements corresponding to curtailment were filtered out through the analysis of the outliers with respect to the average wind speed-blade pitch curve.

For the objectives of the present study, it is important to distinguish the data sets on the basis of the operation regions, which respectively are fixed pitch-variable rotational speed and vice versa. In order to do this, on the grounds of the qualitative analysis of the wind speed-generator speed and wind speed-blade pitch curves, it was decided to employ the nacelle wind intensity v to discriminate the two working regions, as indicated in Table 5 and shown in Figure 5 on a sample power curve (IRE wind turbine). The same notation as in [25] was adopted: the regime when the wind turbine operates at full aerodynamic load, with variable rotational speed and fixed pitch, is indicated as Region 2; instead, the regime characterized by rated rotational speed and variable pitch is indicated as Region 2 ¹/₂.

Table 5. Operation regions for the test case wind turbine.

Region	Condition
2	$5 \leq v \leq 9$
2 ¹ / ₂	$9 < v \leq 13$

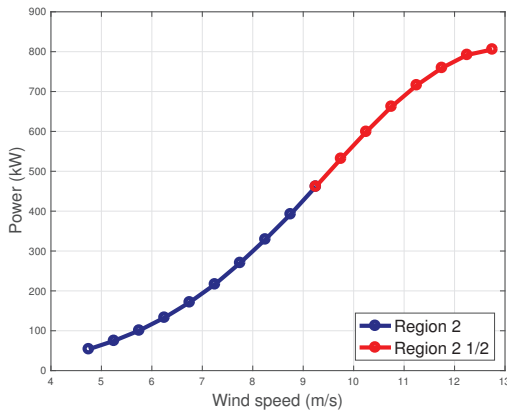


Figure 5. A sample power curve (IRE wind turbine) with the operation regions (2 and ¹/₂) indicated.

3. The Method

In this section, the adopted methodologies are explained: the underlying idea is similar to [25], but the analysis was adapted and generalized in order to consider also the comparisons between wind turbines placed in different sites. On these grounds, there are overlaps between the following section and [25].

3.1. Operation Curve Analysis

The methodology for the analysis of the operation curves is inspired by the recommendations of the International Electrotechnical Commission (IEC) [27] as regards the power curve, which is the observed relation between the wind intensity v and the power output P . The binning method proposed by the IEC is particularly intuitive and consists of dividing the data into wind speed intervals of 0.5 or 1 m/s in amplitude and computing the average power for each interval, thus obtaining an average power curve.

The average wind speed for the i -th interval is defined in Equation (1):

$$\bar{v}_i = \frac{1}{N_i} \sum_{j=1}^{N_i} v_{i,j} \tag{1}$$

and the average power for the bin is computed as in Equation (2):

$$\bar{P}_i = \frac{1}{N_i} \sum_{j=1}^{N_i} P_{i,j}. \quad (2)$$

With this notation, it is intended that there are N_i wind speed measurements for each i -th bin, that $v_{i,j}$ is the j -th wind speed measurement in the i -th bin, and that $P_{i,j}$ is the corresponding power output.

There are some critical points in the analysis of the power curve through the binning method, which are particularly relevant if the objective is comparing wind turbines sited in different environments. The main issue is that the power has a multivariate dependence on ambient conditions, which include atmospheric stability, wind shear, turbulence intensity, and so on; these effects can be particularly relevant in complex terrain [30–33] and affect the nacelle transfer function [28,29]. Therefore, one should not expect that the measured relation between nacelle wind speed and power output is the same in different environments: this expectation would lead to the wrong conclusions, as the comparison between the two test cases in this work indicates. An illustrative example is the power curve reported in Figure 6 for the IRE and ITA1 wind turbines having the same age (seven years): data are averaged per wind speed intervals of 0.5 m/s. From Figure 6, one would conclude that the ITA wind turbine is remarkably under-performing with respect to the IRE one. This conclusion is incorrect, because the wind turbines are placed in different sites and the ambient conditions affect the nacelle wind speed measurements. In particular, Figure 6 is consistent with Figure 2 because higher turbulence means a higher apparent curve in Region 2 and a sensibly lower apparent curve in Region 2 $1/2$. This interpretation is consistent also with Figure 7, where the standard deviation of the IEC-based power curve of Figure 6 is reported: it arises that for the ITA1 wind turbine, the extracted power for given average wind speed varies more than for the IRE wind turbine.

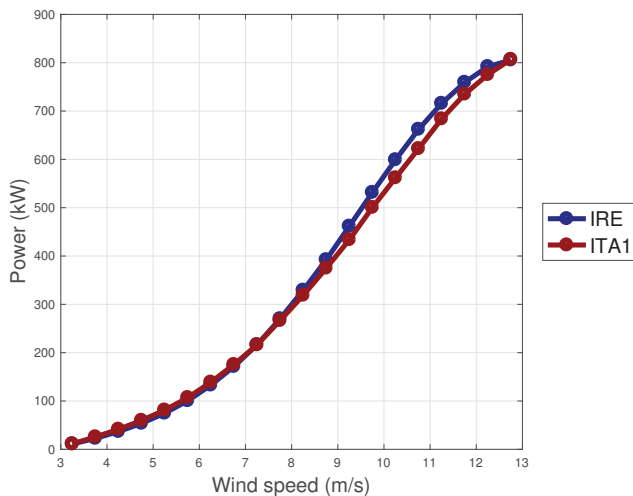


Figure 6. An example of the binned power curve for the IRE and ITA1 wind turbines having the same age (7 years).

For these reasons, in order to compare reliably the performance of the same model of wind turbine placed in different sites, it is more appropriate to compare operation curves that are not based on the nacelle wind speed measurements: in this study, the same curves as in [25] are selected, which are the generator speed-power curve and the blade pitch-power curve. In studies like [34–36], it was observed that operation variables as the rotor speed, generator speed, and blade pitch are important for a reliable multivariate analysis

of the power of a wind turbine [37,38]. In this study, following [38], a step forward with respect to the literature is made because the selected curves involve couples of operation variables and do not involve the nacelle wind speed.

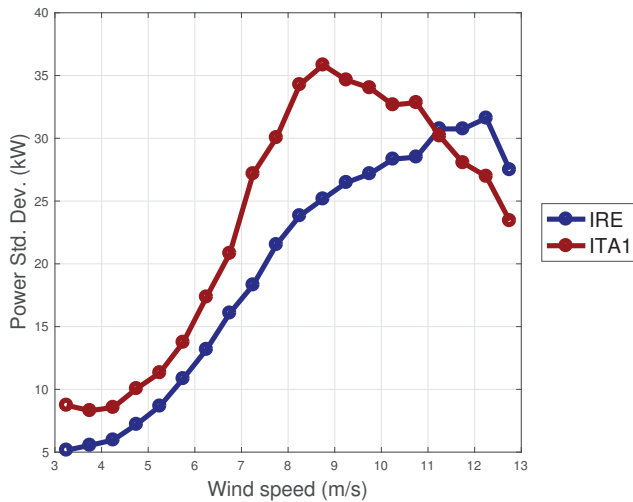


Figure 7. The standard deviation of the IEC-based power curve of Figure 6, for the IRE and ITA1 wind turbines having the same age (7 years).

In [25], it has been observed that the above curves should be interpreted in light of the control of the wind turbines: for moderate wind speed (approximately $5 \leq v \leq 9$ m/s), wind turbines operate with a variable rotational speed and fixed pitch; for higher wind speeds (approximately $9 \leq v \leq 13$ m/s), the rotational speed is rated and the blade pitch varies. These two control regions were indicated as Region 2 and Region 2 $1/2$ in [25] (Table 5), and this notation was also adopted in this study. This means that in the present study, as well as in [25], the rotor equivalent wind speed was used in what here is called Region 2, because rotor speed and generator speed are proportional. It can be said that instead in Region 2 $1/2$, a sort of pitch equivalent wind speed has been introduced, because in that operation region, the rotational speed has saturated and does not provide information about the wind intensity and therefore the amount of power that should be extracted.

In Figures 8 and 9, examples of binned generator speed-power and blade pitch-power curves are respectively reported for Region 2 and Region 2 $1/2$. For the readability of the Figures, the curves are plotted for two sample wind turbines (IRE and ITA1) when they had the same age (7 years). From Figures 8 and 9, it arises that the wind turbines placed in the two different sites respond to the same control logic because the curves are substantially the same: it should be noted that this is not obvious because innovations in the control logic and in the rotational speed management can occur during the lifetime of wind turbines (as analyzed for example in [39]). From Figure 9, in particular, it arises that for the given blade pitch angle, the amount of power extracted by the ITA1 wind turbine is on average a little higher than for the IRE wind turbine: from this curve, one would conclude that the performance of ITA1 is a little better than IRE, while the opposite conclusion would be drawn from the power curve in Figure 6. This observation further supports that power curves of wind turbines sited in different environments should not be compared.

On the grounds of these observations, it is important for this study to generalize the IEC binning method for the analysis of the operation curves of interest. For a generic selection (G_1, G_2) of the quantities to be put in the abscissa and ordinate of the operation curve, Equations (1) and (2) remain, with v substituted by G_1 and P substituted by G_2 . There are no established recommendations about how to select the averaging intervals for

G_1 : a meaningful rule of thumb might be considering intervals of the order of 10% of the range that G_1 can assume. The summary of the curves of interest for each working region is reported in Table 6 and is based on the selections employed in [25].

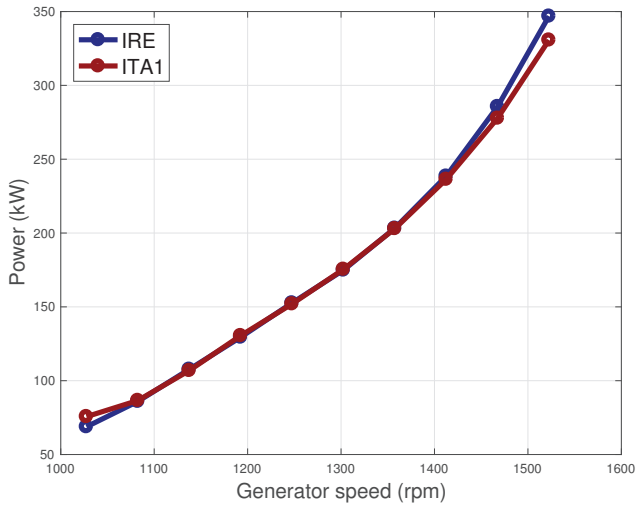


Figure 8. An example of the binned generator speed-power curve for the IRE and ITA1 wind turbines having the same age (7 years): Region 2.

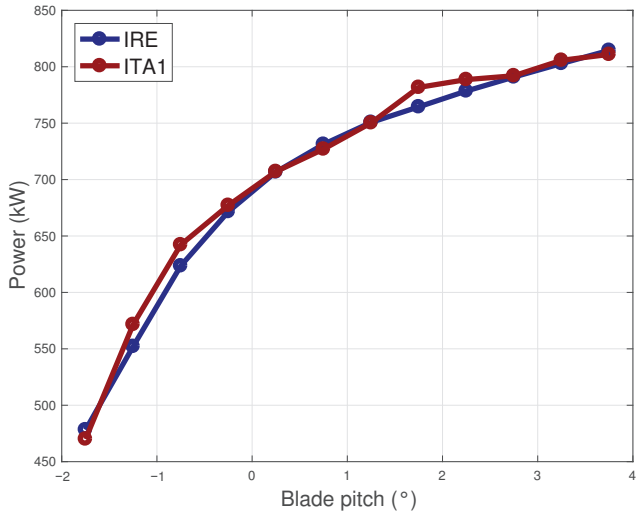


Figure 9. An example of binned blade pitch-power curve for the IRE and ITA1 wind turbines having the same age (7 years): Region 2 1/2.

Table 6. Analyzed operation curves and working range of the variables.

Region	Curve	(G_1, G_2)	G_1 Range	G_1 Bin
2	Generator speed-power curve	(Ω, P)	[1050, 1550] rpm	50 rpm
2 1/2	Blade pitch angle-power curve	(β, P)	$[-2^\circ, 4^\circ]$	0.5°

3.2. Support Vector Regression

The IEC-like analysis of the operation curves indicated in Table 6 provides a qualitative indication of the performance of the wind turbines of interest. In order to achieve a quantitative estimation, a data-driven regression is helpful. The objective is therefore an estimation of the performance worsening with age for each wind turbine (vertical) and the horizontal comparison between the curves of the two test cases at the same age of the wind turbines. In practice, a reference data set is employed for training the regression, which means constructing a digital twin of the curves of interest. The digital twin is subsequently employed for simulating the output, i.e., the power P , given the input variables' measurements in the target data set: the difference between the model estimates and the measurements of the power encode how much the target data set differs from the reference one. Depending on the reference and target data set selection, this same kind of procedure allows performing the vertical and the horizontal analysis, which means analyzing the aging history of each wind turbine and comparing the behavior of the ITA wind turbines with respect to the IRE one for a given age of the wind turbines. The structure of the employed methods can be visualized in Figure 10.

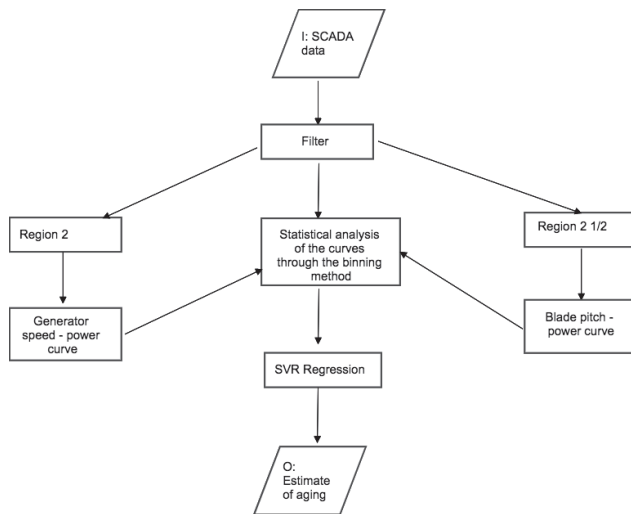


Figure 10. Block diagram for the structure of the methods.

The selected regression is a support vector regression with a Gaussian kernel [40]. The following explanation of the general methodology for the regression has overlaps with the manuscripts [24,25].

Consider at first a linear model (Equation (3)):

$$f(\mathbf{X}) = \mathbf{X}\boldsymbol{\beta} + b. \quad (3)$$

\mathbf{X} is the matrix of the covariates. $\boldsymbol{\beta}$ are the coefficients of the multivariate regression. b are the intercept coefficients. The objective of the regression is using the training data set for estimating $f(\mathbf{X})$ with the minimum norm value $\boldsymbol{\beta}'\boldsymbol{\beta}$, given the constraint that the residuals between the measurement Y and the model estimate $f(\mathbf{X})$ should be lower than a threshold ϵ for each n -th observation (Equation (13)):

$$|Y_n - \mathbf{X}_n\boldsymbol{\beta} + b_n| \leq \epsilon \quad (4)$$

The request that the norm of the regression coefficient vector ($\boldsymbol{\beta}'\boldsymbol{\beta}$) should be minimum consists of searching for models that are as flat as possible, but this request must be compromised with the necessity that the model is as precise as possible (Equation (13)) for

each observation. This kind of optimization problem, where the targets are possibly conflicting, is typically rephrased in the Lagrange dual formulation. The function to minimize is $L(\alpha)$ (Equation (5)):

$$L(\alpha) = \frac{1}{2} \sum_{i=1}^N \sum_{j=1}^N (\alpha_i - \alpha_i^*) (\alpha_j - \alpha_j^*) \mathbf{X}_i' \mathbf{X}_j + \epsilon \sum_{i=1}^N (\alpha_i + \alpha_i^*) + \sum_{i=1}^N Y_i (\alpha_i^* - \alpha_i), \tag{5}$$

with the constraints (Equation (6)):

$$\begin{aligned} \sum_{n=1}^N (\alpha_n - \alpha_n^*) &= 0 \\ 0 &\leq \alpha_n \leq C \\ 0 &\leq \alpha_n^* \leq C, \end{aligned} \tag{6}$$

where C is the box constraint.

The β parameters are given in Equation (7):

$$\beta = \sum_{n=1}^N (\alpha_n - \alpha_n^*) \mathbf{X}_n. \tag{7}$$

If α_n or α_n^* is non-vanishing, the corresponding observation is called a support vector (hence the name of the regression).

Given the input variables matrix and the β coefficients computed on a training data set, the model can be used to predict through the function (Equation (8)):

$$f(\mathbf{X}) = \sum_{n=1}^N (\alpha_n - \alpha_n^*) \mathbf{X}_n' \mathbf{X} + \mathbf{b}. \tag{8}$$

The non-linear support vector regression is obtained by replacing the products between the observations matrix with a non-linear kernel function (Equation (9)):

$$G(\mathbf{X}_1, \mathbf{X}_2) = \langle \varphi(\mathbf{X}_1) \varphi(\mathbf{X}_2) \rangle, \tag{9}$$

where φ is a transformation mapping the \mathbf{X} observations into the feature space.

A Gaussian kernel selection is given in Equation (10) and is widely employed for non-linear problems:

$$G(\mathbf{X}_i, \mathbf{X}_j) = e^{-\|\mathbf{X}_i - \mathbf{X}_j\|^2}. \tag{10}$$

Then, Equation (5) is rewritten as in Equation (11):

$$L(\alpha) = \frac{1}{2} \sum_{i=1}^N \sum_{j=1}^N (\alpha_i - \alpha_i^*) (\alpha_j - \alpha_j^*) G(\mathbf{X}_i, \mathbf{X}_j) + \epsilon \sum_{i=1}^N (\alpha_i + \alpha_i^*) + \sum_{i=1}^N Y_i (\alpha_i^* - \alpha_i), \tag{11}$$

and Equation (8) for predicting is rewritten as in Equation (12):

$$f(\mathbf{X}) = \sum_{n=1}^N (\alpha_n - \alpha_n^*) G(\mathbf{X}_n, \mathbf{X}) + \mathbf{b}. \tag{12}$$

The data sets must be organized appropriately in order to distinguish performance differences. In order to do this, therefore:

- We divide the training data set into two parts: $\frac{2}{3}$ of the data (named D0) are used for training the model; $\frac{1}{3}$ (D1) is used for validating and establishing a reference for the behavior of the residuals between model estimates and measurements.

- The model is subsequently validated on the target data set D2, with the objective of comparing the residuals against the reference for the data set D1.

The general methodology moves from Equation (13) with $i = 1, 2$, which defines the sets of residuals for data sets D1 and D2:

$$R(\mathbf{X}_i) = Y(\mathbf{X}_i) - f(\mathbf{X}_i). \tag{13}$$

For $i = 1, 2$, one computes (Equation (14)):

$$\Delta_i = 100 \frac{\sum_{\mathbf{X} \in \text{Data}_i} (Y(\mathbf{X}) - f(\mathbf{X}))}{\sum_{\mathbf{X} \in \text{Data}_i} Y(\mathbf{X})} \tag{14}$$

and the quantity in Equation (15):

$$\Delta = \Delta_2 - \Delta_1 \tag{15}$$

provides an estimate of the performance deviation from data sets D1 to D2 [39,41].

As discussed above, vertical and horizontal analysis are performed in this work. This translates into the use of the data sets that are summarized in Table 7. As can be argued from Table 7 and from the block diagram in Figure 11, the vertical analysis spans the ages for each wind turbine, while the horizontal analysis constructs the reference at a certain age with IRE data and spans the ITA wind turbines at the same age.

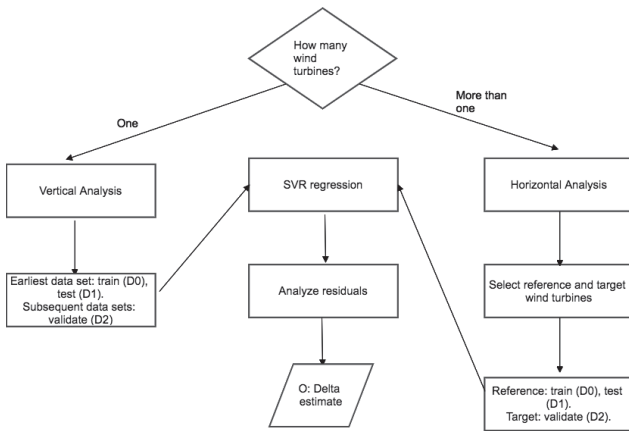


Figure 11. Block diagram of the horizontal and vertical analysis based on the support vector regression.

Table 7. Use of the data sets for vertical and horizontal analysis.

Analysis	D0–D1	D2
Vertical	Age 7 years (D_{2012}^1 IRE– D_{2014}^2 ITA)	Subsequent ages for each WT
Horizontal	IRE data set (from D_{2012}^1 , age 7 years)	ITA at same age (from D_{2014}^2 , age 7 years)

If, for example, the performance of the wind turbine in the data set D2 is worse than in D1 (as is expected for an aging assessment), the residuals of the D2 data set should be lower with respect to those of D1 because the simulated data are obtained with a model that is trained when the wind turbine had better performance with respect to D2.

In Table 8, the setup of the models for each operation region is indicated.

Furthermore, the case of ITA4 and generator replacement was treated by performing a vertical analysis in Region 2, where D0 and D1 were extracted from D_{2017}^2 , and the model as validated against D_{2018}^2 (since March) and D_{2019}^2 . The rationale for this selection was taking as the reference the data set immediately before the generator replacement at ITA4

and as the validation the data sets immediately after generator replacement: a model for each wind turbine was set up, in order to highlight the difference between ITA4 and the other wind turbines in the farm (which have not replaced the generator).

Table 8. Structure of the SVR regressions for each operation region.

Region	Input	Output
2	Generator speed Ω	Power P
2 1/2	Blade pitch angle β	Power P

4. Results

4.1. Operation Curve Analysis

4.1.1. Region 2: Curve Analysis

Figure 12 contains a comparison between the two test cases. The generator speed-power curve is reported, in the form of the difference between the Italian wind turbines and the Irish benchmark at the same wind turbines age. It arises that for seven years of wind turbine age, the difference is negative for all the ITA wind turbines, especially approaching the rated speed. Subsequently, the difference stabilizes around zero and becomes positive when the wind turbines are aged 12 years. These results can be better interpreted in light of Figure 13, which groups for each wind turbine the comparison between the curve at seven years of age and for subsequent years: it arises that for the IRE wind turbine, there is a sharp decline at 12 years of wind turbine age, which does not occur at the ITA wind turbines. This results in the fact that the IRE and ITA wind turbines have comparable performance up to when the wind turbines are aged 12 years, and at 12 years, the performance of the ITA wind turbines is clearly better than the IRE one. The analysis of Figure 13 indicates a trend of aging for wind turbines ITA2 and ITA3 because the amount of extracted power for the given rotational speed slightly decreases in time: it should be noted that this phenomenon is of the order of a few kW, and it would be interesting to analyze its further evolution and inquire if and possibly when a sharp decline as for the IRE wind turbine occurs. Furthermore, it is not surprising to notice that ITA4 is the only wind turbine for which the curve at 12 years of age is better than the one at 10 years of age: the data set at 10 years of age describes the generator at its end of life, while the data set at 12 years describes ITA4 operating with a new generator.

Figure 14 contains an analysis devoted to the case of ITA4: the curves of ITA4 after the generator replacement are considered (data sets D_{2018}^2 and D_{2019}^2 , corresponding to 11 and 12 years of age) and are compared against the data set immediately before the generator replacement (D_{2017}^2 , corresponding to 10 years of age). This kind of plot is reported for ITA4 and for ITA2, which is individuated as being affected by declining performance (Figure 13). From Figure 13e, it arises that for ITA4, after the generator replacement, there is a clear improvement in the amount of power extracted for the given generator speed, which is more visible as the rotational speed increases. The other way round, for ITA2, there is a clear worsening, especially for moderate and high generator speed. In Section 4.2, using support vector regression, it will be possible to estimate quantitatively the average production improvement after the generator replacement at ITA4.

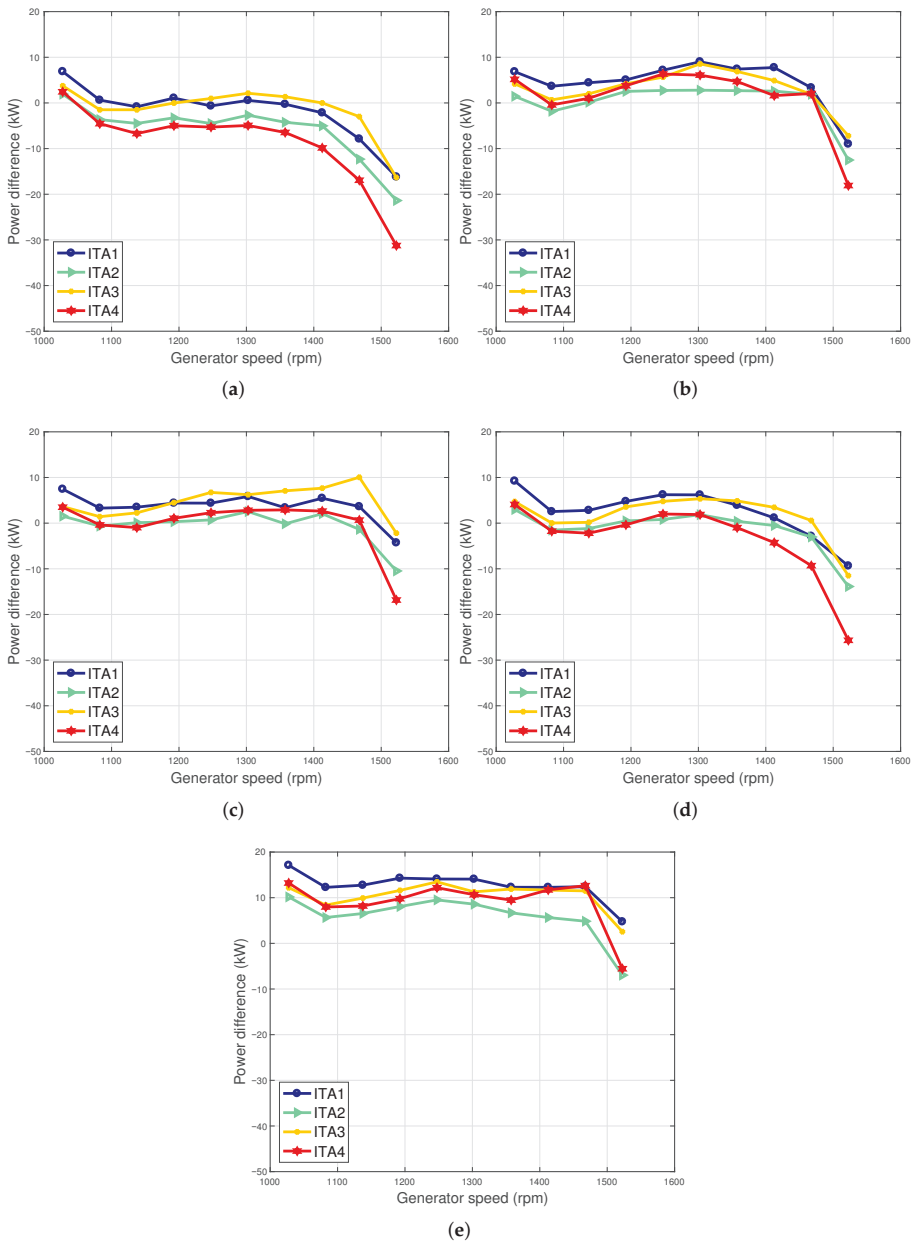


Figure 12. Generator speed–power curve: horizontal analysis, consisting of the comparison between the two test cases. For each data set, the difference between the IRE curve and the ITA wind turbines’ curve is represented. (a) Seven years, (b) 8 years, (c) 9 years, (d) 10 years, and (e) 12 years.

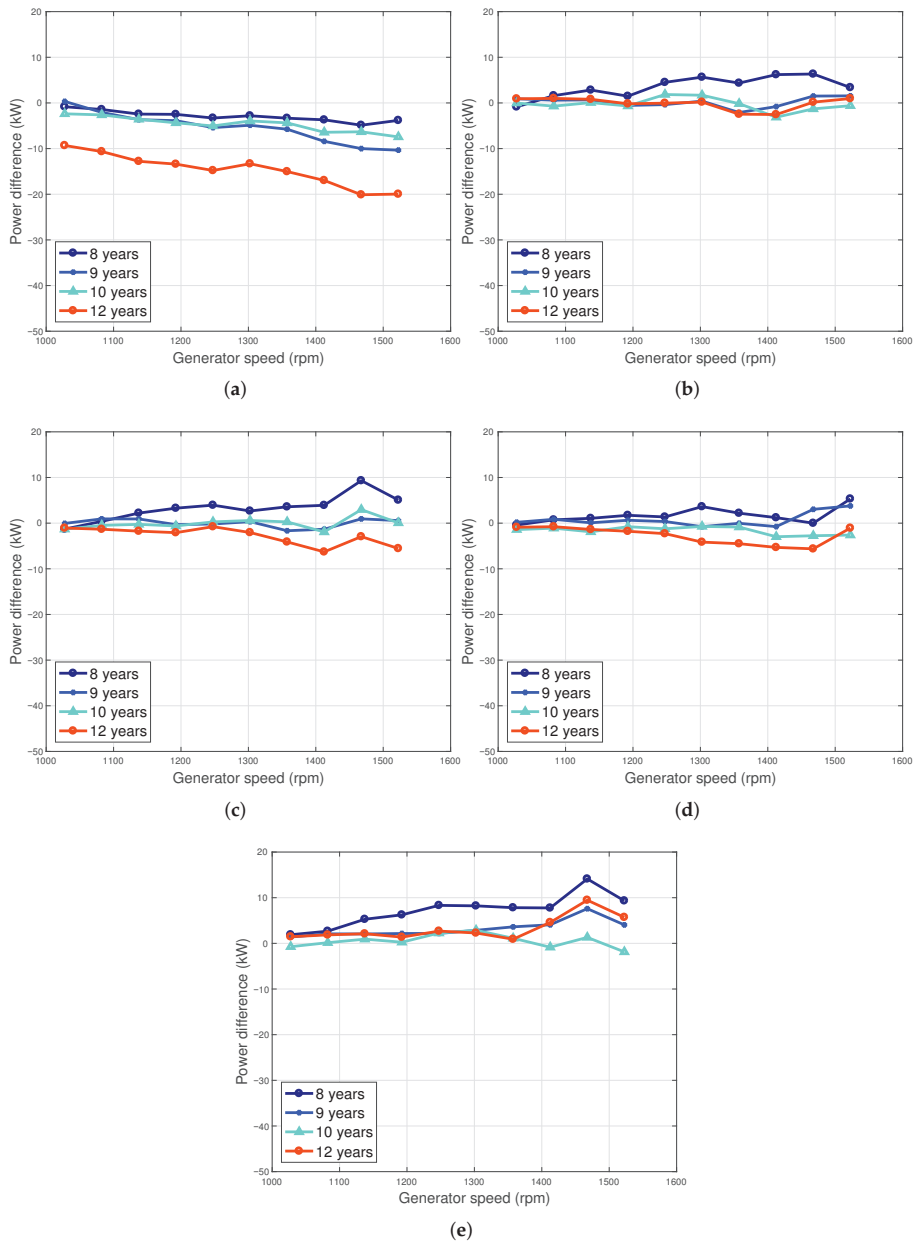


Figure 13. Generator speed–power curve: vertical analysis, consisting of the comparison of each wind turbine against itself in the earliest data set at our disposal (seven years). The difference with respect to the reference curve for each wind turbine is reported. (a) IRE, (b) ITA1, (c) ITA2, (d) ITA3, and (e) ITA4.

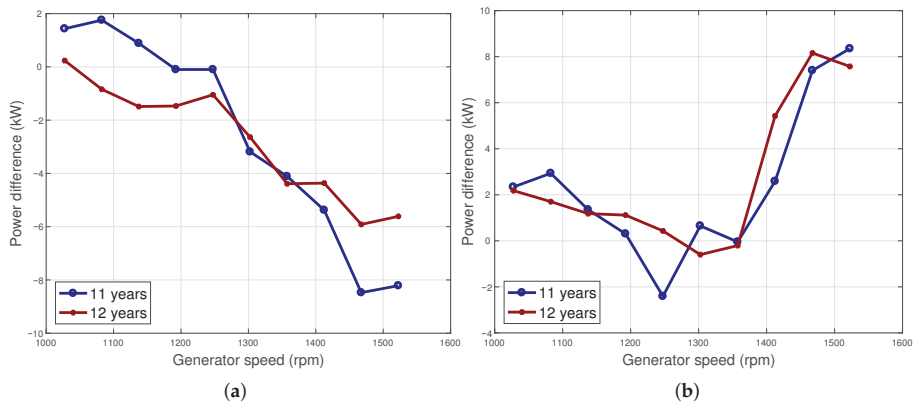


Figure 14. Analysis of generator substitution at the ITA4 wind turbine: the generator speed–power curve is reported, in the form of the difference between the data sets D_{2018}^2 and D_{2019}^2 (after the generator replacement at ITA4) and the reference D_{2017}^2 data set (before generator replacement at ITA4). Results are reported for ITA4 and for a sample wind turbine ITA2. (a) ITA2 and (b) ITA4.

4.1.2. Region 2 $1/2$: Curve Analysis

In Figure 15, the same kind of plot as in Figure 12 is provided for the blade pitch–power curve. The curve is reported in the form of the difference between the IRE benchmark curve and the target ITA wind turbines' curve (each taken at the same wind turbine age). In general, it arises that the behavior is less regular with respect to the generator–power curve: a common feature of the ITA curves is that they are lower than the IRE one near the lower and upper bounds of the pitch angle, while the curves are comparable elsewhere. The evolution in time of the curve of each wind turbine is shown in Figure 16: a declining trend is visible for the IRE wind turbine, and this phenomenon was interpreted in [25] as due to the gearbox approaching its end of life; the behavior is less regular for the ITA wind turbines, despite a decreasing trend being visible in the latest three data sets for ITA1, ITA2, and ITA3 (similarly to what happens for the generator speed–power curve). Furthermore, it can be noticed that the replacement of the generator at ITA4 seems not to influence noticeably the behavior in Region 2 $1/2$. This confirms the observations in [24,25] about the fact that the aging of different components of the wind turbines impacts differently depending on the working region. Finally, it can be observed that, in general, the more complicated behavior of the pitch curves for the ITA wind turbines can likely be interpreted as due to the fact that they are sited in a very complex terrain in a mountainous area.

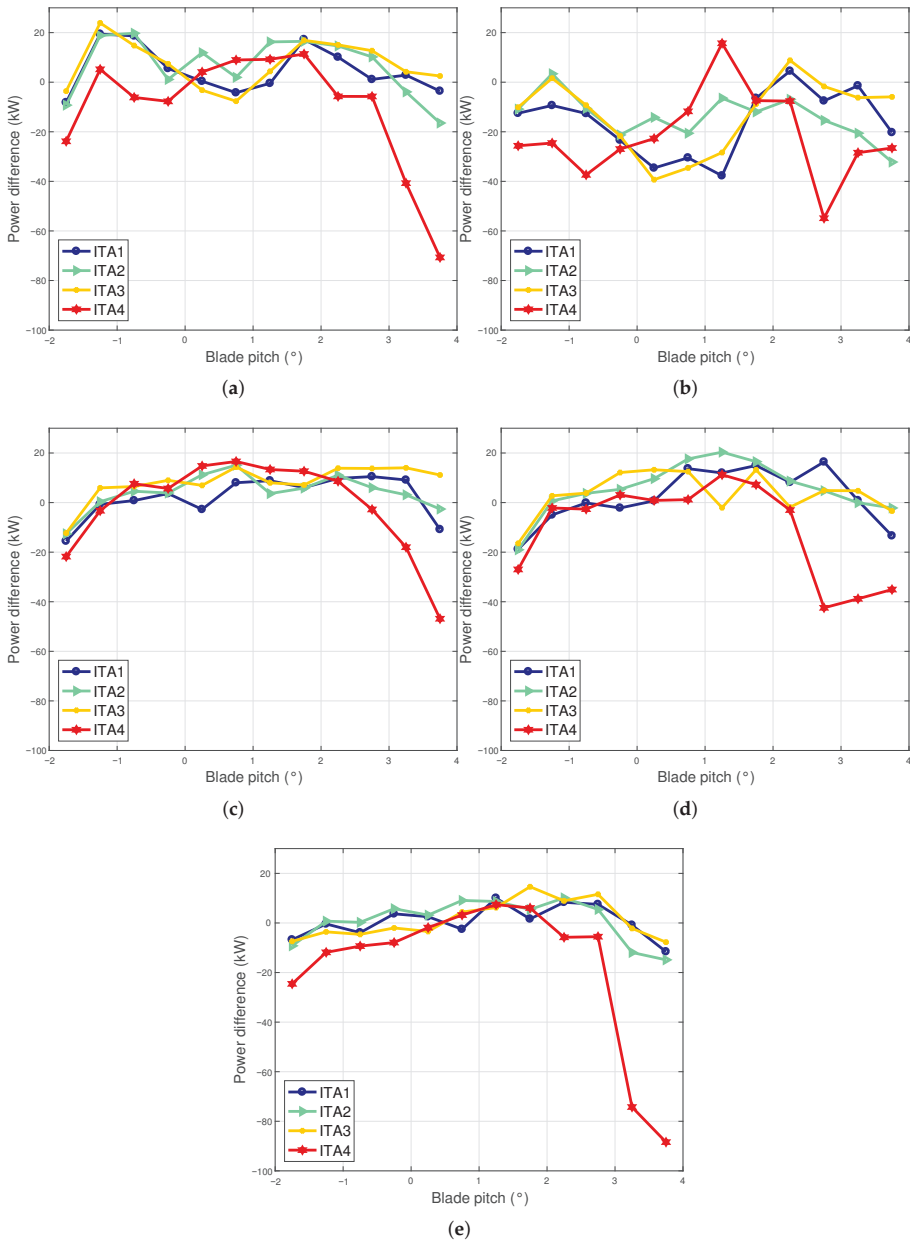


Figure 15. Blade pitch–power curve: horizontal analysis, consisting of the comparison between the two test cases. For each data set, the difference between the IRE curve and the ITA wind turbines curve is represented. (a) Seven years, (b) 8 years, (c) 9 years, (d) 10 years, and (e) 12 years.

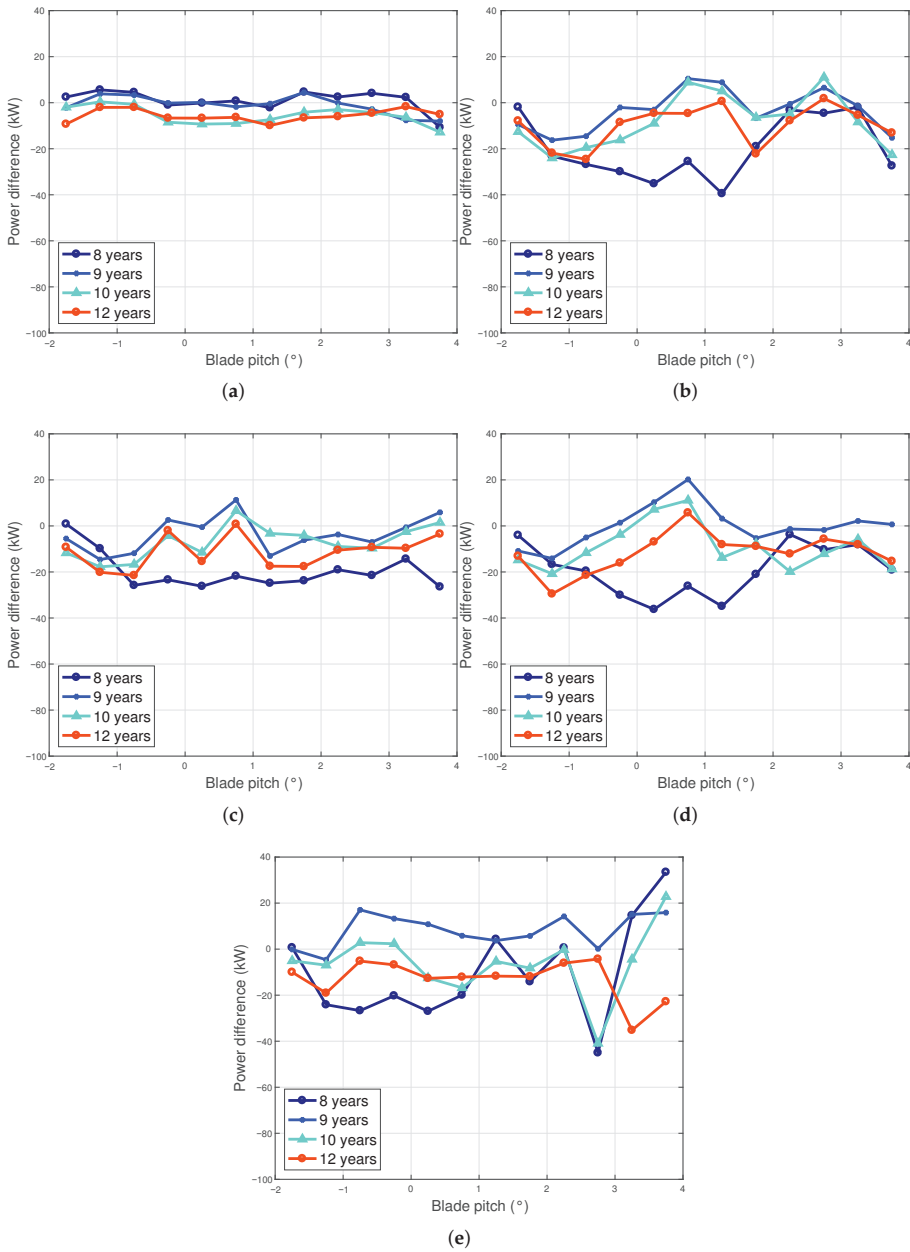


Figure 16. Blade pitch–power curve: vertical analysis, consisting of the comparison of each wind turbine against itself in the earliest data set at our disposal (seven years age). The difference with respect to the reference curve for each wind turbine is reported. (a) IRE, (b) ITA1, (c) ITA2, (d) ITA3, and (e) ITA4.

4.2. Support Vector Regression

In this section, the qualitative results of Section 4.1 are re-interpreted quantitatively by adopting a support vector regression with a Gaussian kernel for constructing a digital twin of the operation curves of interest. The importance of this part of the study is also the

fact that the analysis, similarly to Section 4.1, was conducted vertically and horizontally. In other words, the reference digital twin of the curves was constructed as follows:

- For the vertical analysis, the reference was set by training the regression with the data describing each wind turbine aged seven years. The evolution of the curves was quantified by analyzing how the residuals between model estimates and measurements change in all the posterior data sets for each wind turbine. In practice, this analysis follows the history of each wind turbine and compares each wind turbine against itself. This is equivalent to selecting the D0 and D1 data sets from the seven years age data set for each wind turbine and the D2 data set as each posterior one.
- The objective of the horizontal analysis was inquiring how similar the behaviors of wind turbines of the same model are, which are sited in different environments, when they have the same age. The benchmark was selected as the IRE wind turbine. This means that D0 and D1 were selected from the data sets of the IRE wind turbine. A separate model was trained per each age and was validated against the ITA data sets of the same age (which therefore constitute the D2 data set). For example, if one considers the generator speed-power curve, the behavior of the IRE wind turbine is learned through the regression and is replicated by predicting how much power the IRE wind turbine would extract when the generator speeds are those measured at the ITA wind turbines; the comparison between measurement and model estimates allows quantifying the average performance difference between the IRE and ITA wind turbines at a given age.

A separate vertical analysis was performed for analyzing the effect of generator replacement at ITA4; the details are reported in Section 4.2.1.

4.2.1. Region 2: Regression Analysis

The results of the vertical analysis for the generator speed-power curve are reported in Table 9: the IRE wind turbine underwent an evident decline, which in five years time (7 to 12 years of age) reached 8.8% on average. As shown also in Section 4.1, the ITA2 and ITA3 wind turbines had a slight trend of performance worsening, which is definitely non-comparable with those of the IRE wind turbine because it reached the order of 1% at 12 years age. ITA1 seemed not to be affected by a remarkable aging trend. The case of ITA4 stood apart, because of the generator replacement: at 12 years of age, the performance was visibly better with respect to 10 years of age (when the generator was approaching its end of life) and with respect to the earliest data set at our disposal in this study (the Δ at 12 years with respect to seven years was positive).

Given the different behavior in time of the IRE and ITA wind turbines, the horizontal analysis of Table 10 is particularly interesting: it arises that for seven years of wind turbine age, the performance of the IRE wind turbine is superior to the ITA ones, and this is mainly due to the behavior near rated rotational speed (Figure 12). From eight years of wind turbine age, the difference between the ITA and the IRE wind turbine erodes, and the trend inverts: the ITA wind turbines extract on average a little more power for a given generator speed, except for ITA2 and ITA4, which at 10 years of age, have slightly worse behavior with respect to the IRE wind turbine. At 12 years of wind turbine age, the difference between the IRE and ITA wind turbines is dictated by the sharp decline of the IRE wind turbine's performance: the ITA wind turbines result in having considerably better behavior, despite some differences (the Δ varies from 7.8% to 3.8%).

In general, the analysis of Table 10 and Figure 12 indicates that the behavior of the operation curves of the wind turbines of the same model at the same age is qualitatively similar, but there are some quantitative differences that depend on the history of each wind turbine. For example, the ITA wind turbines have likely less suffered from aging from seven to 12 years of age, but started from an inferior performance at seven years of age. It is likely that the energy balance between the two test cases is tricky to understand up to 10 years of age, while the situation becomes clearer at 12 years of age because of the evident decline of the IRE wind turbine: this indicates that the decline of the generator

efficiency can deteriorate considerably the performance of a wind turbine (as in the IRE case), but the other four wind turbines considered in this study do not show evidence of a similar remarkable behavior.

Table 11 reports the result of a vertical analysis that has been conducted in order to understand how the performance of ITA4 changed after the generator replacement, with respect to immediately before. Similarly to Figure 14, ITA2 and ITA4 are compared. The baseline data set was selected to be D_{2017}^2 , and the target data sets are respectively D_{2018}^2 (after the generator replacement at ITA4) and D_{2019}^2 . It arises that ITA4 improved of the order of 2% with respect to the data set immediately before the generator replacement, while ITA2 instead shows a progressive performance decline. This result not only provides a consistency check of the method, similar to the one obtained in [24,25] as regards the substitution of a gearbox, but also indicates an estimate of the possible profitability of the replacement of aged components, whose performance has declined with the years. A further interesting consideration regards the comparison between ITA4 and IRE and the relation between performance and end of life: the performance of the IRE generator at 12 years of life is worse with respect to that of ITA4 when the generator reaches its end of life. This in general indicates that economic considerations regarding the profitability of components substitution should be read also in light of the expected lifetime, which is a complex topic, beyond the scope of the present study.

Table 9. Vertical analysis: estimates of Δ (%) with respect to the baseline data set (7 years age for each wind turbine).

Age	IRE	ITA1	ITA2	ITA3	ITA4
8 years	−1.6	+2.0	+2.1	1.3	3.9
9 years	−3.0	0.0	0.4	0.6	1.6
10 years	−2.5	−0.3	0.3	−0.7	0.1
12 years	−8.8	0.0	−1.3	−1.2	1.6

Table 10. Horizontal analysis: estimates of Δ (%) with respect to the corresponding IRE baseline data set for each wind turbine age.

Age	ITA1	ITA2	ITA3	ITA4
7 years	−1.5	−2.8	−1.2	−3.0
8 years	2.9	0.2	2.1	1.2
9 years	2.4	0.0	2.8	0.2
10 years	1.6	−0.6	1.2	−1.7
12 years	7.8	3.8	6.5	5.6

Table 11. Vertical analysis for the generator replacement case study: estimates of Δ (%) with respect to the baseline data set (10 years age for each wind turbine).

Age	ITA2	ITA4
11 years	−0.4	2.2
12 years	−0.8	2.4

4.2.2. Region 2 1/2: Regression Analysis

In Table 12, the results of the vertical analysis are reported: it arises that each wind turbine undergoes a performance worsening, which, from seven years to 12 years of age, is of the order of 1–2%. The addition of further test cases to the study substantially confirms the results in [24,25]: a decreasing trend is visible, but it is not as impactful as the generator efficiency decline observed for the IRE wind turbine. The horizontal analysis in Table 13 indicates that the performance of the IRE and ITA wind turbines is comparable in Region 2 1/2 from nine years of wind turbine age, while at seven years of age, three

ITA wind turbines had superior performance with respect to the IRE one; it can be likely concluded that the aging in Region 2 1/2 impacted more the ITA wind turbines, but it should be noticed that the curves for the ITA wind turbines (as shown in Figures 15 and 16) have a less regular behavior, which can be dictated by the complexity of the external environment.

Table 12. Vertical analysis: estimates of Δ (%) with respect to the baseline data set (7 years age for each wind turbine).

Age	IRE	ITA1	ITA2	ITA3	ITA4
8 years	−0.3	−1.1	−0.8	−0.9	+0.2
9 years	0.0	−1.4	−1.0	−0.9	+0.2
10 years	−0.9	−1.4	−1.0	−0.9	+0.2
12 years	−2.0	−1.2	−1.6	−2.1	−0.4

Table 13. Horizontal analysis: estimates of Δ (%) with respect to the corresponding IRE baseline data set for each wind turbine age.

Age	ITA1	ITA2	ITA3	ITA4
7 years	1.2	1.1	0.8	−0.8
8 years	−2.3	−1.0	−1.6	−3.4
9 years	0.0	0.3	0.8	0.2
10 years	0.0	0.5	0.6	−0.4
12 years	0.0	0.2	−0.2	−1.4

4.2.3. Summary of the Results: Aging Estimate

The results from Sections 4.2.1 and 4.2.2 are combined here (Table 14) to give a unique estimate of aging performance, which is obtained through a weighted average of the results from Tables 9 and 12: the weights are selected to be the sizes of the data sets for respectively Region 2 and Region 2 1/2 for each turbine. By doing this, the estimates of Table 14 are obtained by taking into account how much time each wind turbine operates in each working region. It should be mentioned that this estimate corresponds to the sub-rated regime, and to obtain an estimate of annual energy production, the time of operation in the so-called Region 3 (at rated power) should be considered.

From Table 14, the results of [24,25] are substantially confirmed as regards the IRE wind turbine. As regards the ITA wind turbines, it arises that in five years time, ITA1-ITA2-ITA3 underwent a slight worsening (up to the order of 1.5%), while ITA4 even improved its performance thanks to the generator replacement.

Table 14. Vertical analysis: estimates of Δ (%) with respect to the baseline data set (7 years age for each wind turbine): Region 2 and Region 2 1/2 are considered together.

Age	IRE	ITA1	ITA2	ITA3	ITA4
8 years	−1.3	1.2	1.3	0.7	3.1
9 years	−2.3	−0.3	0.0	0.2	1.2
10 years	−2.2	−0.5	0.0	−0.8	0.1
12 years	−7.4	−0.2	−1.4	−1.4	1.2

5. Conclusions

The present work deals with the analysis of wind turbine performance decline with age. Motivated by previous findings in [24,25] about a Vestas V52 wind turbine sited at the Dundalk Institute of Technology in Ireland, in this study, four Vestas V52 sited in a mountainous area in southern Italy are selected as further test cases. The objective of the study was addressing if wind turbines of the same model present similar aging trends.

The employed methodologies consisted of the analysis of appropriate operation curves depending on the working region of the wind turbines and in a support vector regression for constructing digital twins of the curves of interest and for validating them against target data sets. The selected curves are the generator speed-power curve and blade pitch-power curve, and each is analyzed in the working region where it is of most interest: the former curve is analyzed for moderate wind speed, when the wind turbines operate at fixed pitch and variable rotational speed; the latter curve is analyzed for higher wind speed, when the wind turbines operate at rated rotational speed and variable pitch.

The methodologies were employed vertically and horizontally: in other words, for each wind turbine, its history was studied (vertical analysis), and the horizontal analysis consisted of the comparison between the IRE and ITA wind turbines when they had the same age. This approach goes beyond the scope of the present work because it contributes to the general problem of comparing the performance of the same model of wind turbine, installed in different environments: the power curve analysis is not reliable, because the environmental conditions affect the nacelle transfer function differently at each site. Therefore, it is more appropriate to analyze the operation curves, which do not depend on the nacelle wind speed measurements, as the ones selected in this study.

It results that the aging of the generator affects non-negligibly the performance of the wind turbines, and this is highlighted as diminished power extraction for a given generator speed; however, this happens to different extents in the test case wind turbines: from seven to 12 years of age, in Region 2, two wind turbines sited in Italy underwent a performance worsening of the order of 1–2%, while the average performance decrease was –8.8% in the same period for the wind turbine in Ireland. An interesting test case is given by the fact that the generator of one wind turbine sited in Italy reached its end of life in 2018 and was substituted: by comparing the data sets immediately before the ones immediately after the replacement, it can be estimated that the replacement provided a performance improvement of the order of 2%. This provides a consistency check of the proposed methodologies and indicates an estimate of the profitability of substituting aged wind turbine components. In Region 2 ^{1/2}, the behavior of all the test case wind turbines was similar, and a performance decline of the order of 2% was observed. Overall, it can be summarized that after five years of operation (which is the span of the data sets at out disposal for this study), the performance of the IRE wind turbine declined below the rated power of the order of 7.7%, while three ITA wind turbines had slightly worsened performance (from 0.2% to 1.4%) and one (ITA4) improved. Another important aspect is given by the fact that the performance worsening with age seems not to be linear in time: the selected data sets go from seven to twelve years of age of the wind turbines, and in particular for the IRE test case, an evident decline occurs at twelve years of age. Referring to the results in [25] for the IRE wind turbine, if one considers a span of ten years (two years of age against twelve), the estimated worsening is in the order of 8.8%: by comparison, it can be argued that the aging from two to seven years of age is quite low. This ex post supports the rationale of the horizontal and vertical analysis, which were combined in this work: by comparing several test cases, it is possible to analyze the level of performance at a certain age of the wind turbines.

Therefore, on the grounds of what is observed for the four wind turbines in Italy in comparison with the test case in Ireland, it is concluded that it is likely that the effect of aging for the Vestas V52 wind turbines can be in general lower with respect to the estimates provided in [24,25], but it cannot be excluded that a similar decline in the generator efficiency would occur as well for the other test case wind turbines in the future. This motivates that an interesting further direction of this work is the analysis of the electrical parameters of wind turbine generators in order to formulate prognostic models. In addition, the operating condition and response of the hydraulic station that controls the blade pitching system deserves further examination, e.g., if oil pressures in the hydraulic station are not well maintained, the blade pitch response may deviate from the optimum and affect the power performance.

Furthermore, the case of the ITA4 wind turbine, which has undergone a replacement of the generator, inspires further developments as regards a detailed analysis of the economic balance: this could give meaningful indications in general as regards the management of wind turbines.

Another interesting further line of research regards the interpretation of the aging performance in terms of the overall maintenance level of the wind turbines: from this point of view, we expect that a large number of test cases should be analyzed, in order to possibly highlight the dependence on this factor, which can be expected to be relevant, but can not be expected to be the only or the main determinant.

A valuable further development of the present work is investigating in more detail the hypothesis formulated in [22] about the fact that the evolution of wind turbine technology should mitigate the impact of aging: the results reported in [24,25] and in the present work indicate that the hypothesis should be confirmed because the observed decline rate is lower with respect to the estimates reported in [22] for wind turbines installed in the 1990s. At present, further studies are being conducted by the authors on wind turbines of higher size (the order of a 100 m rotor diameter), which were installed in the late 2000s, and the preliminary results indicate that the aging decline is lower with respect to the results of this study.

Author Contributions: Conceptualization, D.A., R.B., and F.C.; data curation, D.A., R.B., and F.C.; formal analysis, D.A., R.B., and F.C.; investigation, D.A.; methodology, D.A.; project administration, R.B. and F.C.; software, D.A.; supervision, R.B. and F.C., validation, D.A., R.B., and F.C.; writing—original draft, D.A.; writing—review and editing, D.A., R.B., and F.C. All authors read and agreed to the published version of the manuscript.

Funding: This research received no external funding.

Acknowledgments: The authors acknowledge Fondazione “Cassa di Risparmio di Perugia” for the funded research project WIND4EV (WIND turbine technology EVolution FOR lifecycle optimization). The authors also wish to acknowledge the support of the INTERREG VA SPIRE2 project. This research was supported by the European Union’s INTERREG VA Programme (Grant No. INT-VA/049), managed by the Special EU Programmes Body (SEUPB). The views and opinions expressed in this document do not necessarily reflect those of the European Commission or the Special EU Programmes Body (SEUPB). The authors acknowledge the IEA-Wind-Task 41-“Enabling Wind to Contribute to a Distributed Energy Future”. The authors thank the company Lucky Wind for the technical support and for providing the data sets employed for the study.

Conflicts of Interest: The authors declare no conflict of interest.

References

1. Kurz, R.; Brun, K. Degradation of gas turbine performance in natural gas service. *J. Nat. Gas Sci. Eng.* **2009**, *1*, 95–102. [[CrossRef](#)]
2. Penrose, H.W.; Frost, N. Aging electric machines. In Proceedings of the 2015 IEEE Electrical Insulation Conference (EIC), Seattle, WA, USA, 7–10 June 2015; pp. 292–296.
3. Giangrande, P.; Madonna, V.; Nuzzo, S.; Galea, M. Moving Toward a Reliability-Oriented Design Approach of Low-Voltage Electrical Machines by Including Insulation Thermal Aging Considerations. *IEEE Trans. Transp. Electrification*. **2020**, *6*, 16–27. [[CrossRef](#)]
4. Blokus, A.; Kolowrocki, K. Reliability and maintenance strategy for systems with aging-dependent components. *Qual. Reliab. Eng. Int.* **2019**, *35*, 2709–2731. [[CrossRef](#)]
5. Scharfenberg, G.; Elis, L.; Hofmann, G. New Design Methodology—Using VHDL-AMS Models to Consider Aging Effects in Automotive Mechatronic Circuits for Safety Relevant Functions. In Proceedings of the 2019 International Conference on Applied Electronics (AE), Pilsen, Czech Republic, 10–11 September 2019; pp. 1–5.
6. Saltas, E.; Bouilly, J.; Geivanidis, S.; Samaras, Z.; Mohammadi, A.; Iida, Y. Investigation of the effects of biodiesel aging on the degradation of common rail fuel injection systems. *Fuel* **2017**, *200*, 357–370. [[CrossRef](#)]
7. Kim, D.Y.; Kim, Y.H.; Kim, B.S. Changes in wind turbine power characteristics and annual energy production due to atmospheric stability, turbulence intensity, and wind shear. *Energy* **2021**, *214*, 119051. [[CrossRef](#)]
8. Bahamonde, M.I.; Litrán, S.P. Study of the energy production of a wind turbine in the open sea considering the continuous variations of the atmospheric stability and the sea surface roughness. *Renew. Energy* **2019**, *135*, 163–175. [[CrossRef](#)]
9. Wen, B.; Wei, S.; Wei, K.; Yang, W.; Peng, Z.; Chu, F. Power fluctuation and power loss of wind turbines due to wind shear and tower shadow. *Front. Mech. Eng.* **2017**, *12*, 321–332. [[CrossRef](#)]

10. Barthelmie, R.J.; Shepherd, T.J.; Aird, J.A.; Pryor, S.C. Power and wind shear implications of large wind turbine scenarios in the US Central Plains. *Energies* **2020**, *13*, 4269. [[CrossRef](#)]
11. Zhang, Y.; Chen, B.; Pan, G.; Zhao, Y. A novel hybrid model based on VMD-WT and PCA-BP-RBF neural network for short-term wind speed forecasting. *Energy Convers. Manag.* **2019**, *195*, 180–197. [[CrossRef](#)]
12. Zhang, Y.; Wang, P.; Ni, T.; Cheng, P.; Lei, S. Wind power prediction based on LS-SVM model with error correction. *Adv. Electr. Comput. Eng.* **2017**, *17*, 3–8. [[CrossRef](#)]
13. Castellani, F.; Garinei, A.; Terzi, L.; Astolfi, D.; Gaudiosi, M. Improving windfarm operation practice through numerical modelling and supervisory control and data acquisition data analysis. *IET Renew. Power Gener.* **2014**, *8*, 367–379. [[CrossRef](#)]
14. Astolfi, D. Wind Turbine Operation Curves Modelling Techniques. *Electronics* **2021**, *10*, 269. [[CrossRef](#)]
15. Barthelmie, R.J.; Jensen, L. Evaluation of wind farm efficiency and wind turbine wakes at the Nysted offshore wind farm. *Wind Energy* **2010**, *13*, 573–586. [[CrossRef](#)]
16. Astolfi, D.; Castellani, F.; Terzi, L. Mathematical methods for SCADA data mining of onshore wind farms: Performance evaluation and wake analysis. *Wind Eng.* **2016**, *40*, 69–85. [[CrossRef](#)]
17. Fernandes, C.M.; Blazquez, L.; Sanesteban, J.; Martins, R.C.; Seabra, J.H. Energy efficiency tests in a full scale wind turbine gearbox. *Tribol. Int.* **2016**, *101*, 375–382. [[CrossRef](#)]
18. Sequeira, C.; Pacheco, A.; Galego, P.; Gorbeña, E. Analysis of the efficiency of wind turbine gearboxes using the temperature variable. *Renew. Energy* **2019**, *135*, 465–472. [[CrossRef](#)]
19. Mishnaevsky, L., Jr.; Thomsen, K. Costs of repair of wind turbine blades: Influence of technology aspects. *Wind Energy* **2020**, *23*, 2247–2255. [[CrossRef](#)]
20. Carroll, J.; McDonald, A.; McMillan, D. Failure rate, repair time and unscheduled O&M cost analysis of offshore wind turbines. *Wind Energy* **2016**, *19*, 1107–1119.
21. Astolfi, D.; Castellani, F.; Terzi, L. Wind Turbine Power Curve Upgrades. *Energies* **2018**, *11*, 1300. [[CrossRef](#)]
22. Staffell, I.; Green, R. How does wind farm performance decline with age? *Renew. Energy* **2014**, *66*, 775–786. [[CrossRef](#)]
23. Olauson, J.; Edström, P.; Rydén, J. Wind turbine performance decline in Sweden. *Wind Energy* **2017**, *20*, 2049–2053. [[CrossRef](#)]
24. Byrne, R.; Astolfi, D.; Castellani, F.; Hewitt, N.J. A Study of Wind Turbine Performance Decline with Age through Operation Data Analysis. *Energies* **2020**, *13*, 2086. [[CrossRef](#)]
25. Astolfi, D.; Byrne, R.; Castellani, F. Analysis of Wind Turbine Aging through Operation Curves. *Energies* **2020**, *13*, 5623. [[CrossRef](#)]
26. Dai, J.; Yang, W.; Cao, J.; Liu, D.; Long, X. Ageing assessment of a wind turbine over time by interpreting wind farm SCADA data. *Renew. Energy* **2018**, *116*, 199–208. [[CrossRef](#)]
27. International Electrotechnical Commission. *Wind Energy Generation Systems—Part 12-1: Power Performance Measurements of Electricity Producing Wind Turbines*; Technical Report, IEC 61400-12-1: 2017; IEC: Geneva, Switzerland, 2007.
28. St Martin, C.M.; Lundquist, J.K.; Clifton, A.; Poulos, G.S.; Schreck, S.J. Atmospheric turbulence affects wind turbine nacelle transfer functions. *Wind Energy Sci.* **2017**, *2*, 295. [[CrossRef](#)]
29. Wagner, R.; Antoniou, I.; Pedersen, S.M.; Courtney, M.S.; Jørgensen, H.E. The influence of the wind speed profile on wind turbine performance measurements. *Wind Energy Int. J. Prog. Appl. Wind. Power Convers. Technol.* **2009**, *12*, 348–362. [[CrossRef](#)]
30. Bulaevskaya, V.; Wharton, S.; Clifton, A.; Qualley, G.; Miller, W. Wind power curve modeling in complex terrain using statistical models. *J. Renew. Sustain. Energy* **2015**, *7*, 013103. [[CrossRef](#)]
31. St Martin, C.M.; Lundquist, J.K.; Clifton, A.; Poulos, G.S.; Schreck, S.J. Wind turbine power production and annual energy production depend on atmospheric stability and turbulence. *Wind Energy Sci. (Online)* **2016**, *1*, 221–236. [[CrossRef](#)]
32. Antoniou, I.; Pedersen, S.M.; Enevoldsen, P.B. Wind shear and uncertainties in power curve measurement and wind resources. *Wind Eng.* **2009**, *33*, 449–468. [[CrossRef](#)]
33. Lange, J.; Mann, J.; Berg, J.; Parvu, D.; Kilpatrick, R.; Costache, A.; Chowdhury, J.; Siddiqui, K.; Hangan, H. For wind turbines in complex terrain, the devil is in the detail. *Environ. Res. Lett.* **2017**, *12*, 094020. [[CrossRef](#)]
34. Pandit, R.K.; Infield, D. Comparative analysis of binning and Gaussian Process based blade pitch angle curve of a wind turbine for the purpose of condition monitoring. *J. Phys. Conf. Ser.* **2018**, *1102*, 012037. [[CrossRef](#)]
35. Pandit, R.; Infield, D. Gaussian process operational curves for wind turbine condition monitoring. *Energies* **2018**, *11*, 1631. [[CrossRef](#)]
36. Pandit, R.K.; Infield, D. Comparative assessments of binned and support vector regression-based blade pitch curve of a wind turbine for the purpose of condition monitoring. *Int. J. Energy Environ. Eng.* **2019**, *10*, 181–188. [[CrossRef](#)]
37. Pandit, R.K.; Infield, D.; Kolios, A. Gaussian process power curve models incorporating wind turbine operational variables. *Energy Rep.* **2020**, *6*, 1658–1669. [[CrossRef](#)]
38. Astolfi, D.; Castellani, F.; Natili, F. Wind Turbine Multivariate Power Modeling Techniques for Control and Monitoring Purposes. *J. Dyn. Syst. Meas. Control* **2021**, *143*, 034501. [[CrossRef](#)]
39. Astolfi, D.; Castellani, F.; Fravolini, M.L.; Cascianelli, S.; Terzi, L. Precision computation of wind turbine power upgrades: An aerodynamic and control optimization test case. *J. Energy Resour. Technol.* **2019**, *141*, 051205. [[CrossRef](#)]
40. Vapnik, V. *The Nature of Statistical Learning Theory*; Springer Science & Business Media: Berlin/Heidelberg, Germany, 2013.
41. Lee, G.; Ding, Y.; Xie, L.; Genton, M.G. A kernel plus method for quantifying wind turbine performance upgrades. *Wind Energy* **2015**, *18*, 1207–1219. [[CrossRef](#)]

Tidal Energy Hosting Capacity in Australia's Future Energy Mix

Mohammad Seydali Seyf Abad ¹, Jennifer A Hayward ^{2,*}, Saad Sayeef ², Peter Osman ² and Jin Ma ³

¹ WSP Australia and New Zealand, Sydney, NSW 2000, Australia; mohammad.seidaliseifabad@wsp.com

² The Commonwealth Scientific and Industrial Research Organisation, Newcastle, NSW 2300, Australia; Saad.Sayeef@csiro.au (S.S.); Peter.Osman@csiro.au (P.O.)

³ School of Electrical and Information Engineering, The University of Sydney, Sydney, NSW 2006, Australia; J.ma@sydney.edu.au

* Correspondence: Jenny.Hayward@csiro.au

Abstract: This paper outlines a methodology to determine the amount of renewable energy that can be accommodated in a power system before adverse impacts such as over-voltage, over-loading and system instability occur. This value is commonly known as hosting capacity. This paper identifies when the transmission network local hosting capacity might be limited because of static and dynamic network limits. Thus, the proposed methodology can effectively be used in assessing new interconnection requests and provides an estimation of how much and where the new renewable generation can be located such that network upgrades are minimized. The proposed approach was developed as one of the components of the AUSTEN project, which was a three-year project to map Australia's tidal energy resource in detail and to assess its economic feasibility and ability to contribute to the country's energy needs. In order to demonstrate the effectiveness of the proposed approach, two wide area networks were developed in DIGSILENT PowerFactory based on actual Australian network data near two promising tidal resource sites. Then, the proposed approach was used to assess the local tidal hosting capacity. In addition, a complementary local hosting capacity analysis is provided to show the importance of future network upgrades on the locational hosting capacity.

Keywords: Australian energy mix; hosting capacity; over-voltage; system strength; thermal capacity; tidal energy

Citation: Abad, M.S.S.; Hayward, J.A.; Saef, S.; Osman, P.; Ma, J. Tidal Energy Hosting Capacity in Australia's Future Energy Mix. *Energies* **2021**, *14*, 1479. <https://doi.org/10.3390/en14051479>

Academic Editor: Juri Belikov

Received: 31 January 2021

Accepted: 1 March 2021

Published: 8 March 2021

Publisher's Note: MDPI stays neutral with regard to jurisdictional claims in published maps and institutional affiliations.



Copyright: © 2021 by the authors. Licensee MDPI, Basel, Switzerland. This article is an open access article distributed under the terms and conditions of the Creative Commons Attribution (CC BY) license (<https://creativecommons.org/licenses/by/4.0/>).

1. Introduction

The penetration level of renewable resources in power systems has been increasing in recent years. However, the increasing penetration of renewable resources entails some technical challenges such as over-voltage, overloading, protection systems maloperation and power quality issues. There are two approaches to address the above-mentioned issues; (i) upgrading the system, which is quite costly, and (ii) the hosting capacity (HC) concept, which is defined as the maximum renewable resource capacity that can be accommodated into a system without any violation in operational constraints. Understanding this concept can assist utilities to make decisions regarding interconnection requests.

The value of the HC depends on the network characteristics, renewable resources' size, location and technology. Therefore, identifying the network HC is not a straightforward process. Further HC is not a single value for any given system. Generally, three regions as shown in Figure 1, can be defined for HC. Region (A) includes all the penetration levels that do not cause any constraint violation, regardless of renewable resource location. Region (B) demonstrates the penetration levels that are acceptable at specific sites. Region (C) includes all renewable deployments that are not acceptable, regardless of distributed energy resources' (DERs') location [1,2]. The border between (A) and (B) is referred as the minimum HC and the border between (B) and (C) is referred as the maximum HC in this paper. Generally, all the existing HC estimation methods can be divided into two

categories; (i) region-B category including the methods that converge to the maximum HC or a value in region (B); (ii) min-HC category including methods that estimate the minimum HC.

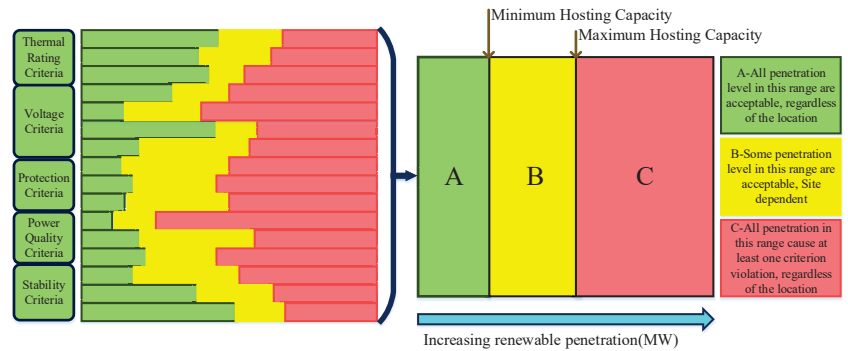


Figure 1. Different regions of the HC in a system.

In terms of HC assessment, studies in [3–18] can be categorized as region-B approach. The HC in region-B methods is usually modelled as the objective of an optimization problem [4,6,9,12–18]. However, there are some other approaches such as analytical [3,7,8,10] and Monte Carlo-based [5,11] methods that belong to the region-B category. In analytical methods, an equation is derived based on technical constraints such as over-voltage [8], overloading [7] and harmonic distortion [10] to estimate the maximum DER that could be connected to a certain location of the system. Nevertheless, the optimization-based methods in the region-B category such as [4,6,9,12–17] are generally more accurate than analytical methods. Further, most of the optimization-based methods such as [6,9,12–15] limit the number of potential locations for DERs to make the model easier to solve. Unlike optimization-based methods, the Monte Carlo-based methods in the region-B category are often based on a traditional power flow calculation. In this approach, numerous power flow calculation are performed to identify the HC of a certain location [5] or an area [11] of a network.

The aim in the second category of the HC methods, i.e., min-HC, is to estimate the minimum HC. Studies in [19–25] belong to this category. These methods are generally based on Monte Carlo simulation, where a high number of DER expansion scenarios are generated. Then, simulation is performed for all generated scenarios over the study period. Next, the minimum HC is defined based on the scenarios that may cause a constraint violation. Although, the general idea of studies such as [21–24] is the same, the implementation details of the Monte Carlo process including generating scenarios, analyzing scenarios over the study period and defining the minimum HC are different. For example, study [21] assumed that the size of DERs is a fixed number. Nevertheless, studies [22,23] used different sizes for DERs. Similarly, the study period and time series impact analysis, which addresses the uncertainties associated with the loads and output power of DERs, could be different. For instance, in [21], it is assumed that the study period could be limited to the worst condition, i.e., maximum DER generation and minimum load consumption. Nevertheless, study [23] randomly allocated the daily load and DER profiles and conducted the analyses. The advantage of min-HC methods is that they could easily be improved to include all network technical criteria.

Studies [3–27] presented different methods to identify the HC. However, they are all focused on estimating the HC of distribution systems considering the voltage and thermal rating criteria. Considering the current trend of renewable energy, the number of renewable power plants connecting to the transmission networks has been growing very fast. Similar to distribution systems, the capacity of transmission networks to host new generation is constrained by different technical issues. Thus, the HC concept is also

applicable for transmission networks. However, unlike distribution systems, transmission networks usually have a meshed structure and their HC highly depends on the location of new generation. Further, the renewable plants in transmission networks entail protection, power quality and stability challenges, which are generally neglected in the existing HC methods. Therefore, it is necessary to propose a comprehensive approach to identify the locational HC in transmission networks based on all static and dynamic constraints. The main contributions of this paper are summarized as follows:

1. As one of the components of Australian Tidal Energy (AUSTEn) project [28,29], we proposed a comprehensive approach based on the thermal rating, voltage, protection, stability and system strength criteria, to identify the locational HC in transmission networks.
2. The proposed approach is applied to Australia networks (Tasmanian and Darwin–Katherine networks) to assess their locational tidal HC. Further, the impact of different renewable resources such as solar and wind on the locational tidal HC has been assessed.

The remainder of this paper is organized as follows: The background information about the AUSTEn project is provided in Section 2. Section 3 describes the technical issues that could limit the penetration level of renewable generation. In Section 4, the proposed approach to identify the locational HC is presented. Network modelling data is discussed in Section 5. Section 6 presents the numerical results and discussion. Finally, the conclusions are summarized in Section 7.

2. Background Information

Australia has some of the largest tides in the world. Nevertheless, insufficient knowledge of Australia’s tidal resource, its spatial extent and technical implementation effectively constrain the tidal energy industry, policy makers and research community to conduct any assessment on risks and benefits of investment in potential tidal generation. AUSTEn was a project to map Australia’s tidal energy resource in detail and to assess its technical and economic feasibility. The project was co-funded by the Australian Renewable Energy Agency (ARENA) Advancing Renewables Program. The AUSTEn project was a joint effort between the Australian Maritime College at the University of Tasmania, the University of Queensland, Commonwealth Scientific and Industrial Research Organisation (CSIRO), MAKO Tidal Turbines, Atlantis Resources, and Sabella. AUSTEn consisted of three inter-linked components as follows:

- Conducting a national Australian high-resolution tidal resource assessment (500 m resolution) and integrating the results into the Australian Renewable Energy Mapping Infrastructure (AREMI).
- Conducting field based and high-resolution numerical site assessments, as well as in-situ environmental measurements at two promising locations for energy extraction.
- Conducting techno-economic feasibility assessment for tidal energy integration into Australia’s electricity infrastructure.

This paper presents some of the assessments conducted for the third component of AUSTEn project. We refer the readers to [28–30] for more details on the outcomes of the AUSTEn project.

3. Technical Criteria

There are quite a few technical issues that limits the higher penetration of renewable generation in power systems with different voltage levels. Some of these issues are specific to networks with a certain voltage level and structure. However, the technical issues can be divided in five general categories as below:

- Thermal rating criteria;
- Voltage criteria;
- Protection criteria;
- Power quality criteria;

- Stability and system strength criteria.
Sections 3.1 to 3.5 provide more details about the above-mentioned criteria.

3.1. Thermal Rating Criteria

Every Power infrastructure element such as lines, cables and transformers is characterized by a current-carrying capacity, which is referred to as thermal rating. If this limit is exceeded for a sufficient time, the element physical and/or electrical characteristics might be permanently damaged. Connecting new renewable generation to the networks would change the current flows in them. Therefore, the thermal rating constraint is one of the criteria that network service providers (NSPs) considers when they want to do their assessment for a query for new connections. As this assessment does not require a very accurate model of the renewable generation, it is usually conducted at the early stages of the studies. Further, the thermal rating constraint is generally assessed under different network configurations and viable contingencies.

3.2. Voltage Criteria

There are quite a few voltage-related criteria that can limit the penetration level of renewable generation. These criteria includes over-voltage, under-voltage, voltage unbalance, voltage deviation and voltage regulation constraints. The normal voltage range in Australia networks is between 0.9 p.u. and 1.1 p.u. Thus, a new renewable generation should not cause a voltage outside of this range. Some of the criteria such over-voltage, under voltage and voltage unbalance are general and network service providers usually consider them in their assessment irrespective of whether it is a transmission or distribution system. However, some criteria such as voltage deviation could be more applicable to distribution networks. For instance, Powercor, which is an Australian distribution company, requires the voltage deviation between voltage profiles for minimum and maximum demand with and without the new renewable generation to stay below a certain level (3% to 4%). In this paper, over-voltage and under-voltage constraints are considered in the assessment.

3.3. Protection Criteria

The protection criteria includes fault level, fault current contribution and relay/fuse mis-coordination. Fault level at a point in a power system is a measure of maximum fault current expected at that point. Fault currents need to be quickly detected and interrupted due to their extensive damage to cables, overhead lines, transformers and other equipment. The circuit breakers' rating limits the fault level in the feeder. This limit is referred to as the design fault level. The design fault level is a limiting factor to the new renewable generation as new connections can increase the fault level. It should be mentioned that renewable resources with directly connected electrical generators would contribute significantly higher fault current than those connected via power electronics interfaces such as solar farms. Therefore, fault level may be much more important for directly connected renewable generations in comparison to the resources connected via power electronics interfaces. Other than fault level, the fault current contribution of generation with power electronic interfaces can also constrain the locational HC. One approach to resolve the fault contribution issue of renewable generation is increasing the impedance of the transformer that connects the plant to the network. However, other factors such as the fault level at the terminal of the turbine/inverter inside the plant should be considered when designing the grid interface transformer. Both turbines and inverters generally provide a better performance when the fault level at their terminals is higher than a certain value. The minimum fault level at the terminal is usually provided by the original equipment manufacturer.

3.4. Power Quality Criteria

A high renewable penetration may raise power quality issues such as voltage fluctuations and harmonics. Although advanced pulse width modulation techniques and

harmonic filters are usually used in converters, voltage distortion limits can be exceeded in high penetration levels. It should be mentioned that the evaluation of harmonic problems is somewhat complicated and requires extensive modelling and simulations. In order to properly conduct the harmonic assessment for a generating system, the detailed design of the plant such as the LV/MV transformer data, the collector system data (i.e., length and type of the cables) and the main grid interface transformer data are required. Further, the Norton impedance of the turbine/inverter and its current harmonics for different operation ranges should be available. Thus, power quality studies are not considered in this paper as detailed design data of the plant is required to conduct the power quality assessment.

3.5. Stability and System Strength Criteria

There are different strategies to control inverter-based power sources (IBPSs), which can cause different dynamic behaviors. Two basic types of control strategies of IBPSs are known as “grid-following” and “grid-forming”. Currently, most IBPSs use a grid-following control strategy, which typically uses a phase-lock-loop (PLL) and a current control loop to control the output currents. Grid-following control strategy makes the IBPSs behave like a current source. The main advantage of this control approach is that the currents can be quickly regulated. However, grid-following control relies on an external voltage source for the voltage and frequency references. Thus, grid-following IBPSs provide poor performance in weak networks. In contrast to grid-following approach, grid-forming IBPSs control the voltage and frequency, making them behave like a voltage source. In comparison to grid-following IBPSs, the grid-forming IBPSs can provide a good performance even in a weak network as they can work in the stand-alone mode and do not rely on the external grid.

High penetration of grid-following IBPSs entails new challenges in power systems. The IBPSs penetration level at which network issues occur is system-specific and depends on the number of synchronous generators (SGs) in service, SGs’ location, the share of SGs relative to IBPSs generation, the size of the largest credible contingency, and the settings of IBPS control systems. Considerable presence of online SGs slows the system dynamic behavior, which allows present grid-following IBPSs with fast controllers to precisely track the grid voltage angle and inject current at the correct phase angle. However, with increasing penetration of IBPSs and retiring the SGs, system dynamics becomes faster. The consequence of faster system dynamic changes is that the fast IBPS controllers potentially fail to track the voltage phase angle and to adequately synchronize with the network. As per control theory, tracking a fast-moving reference requires an even faster controller. Thus, if the IBPS controller is not robust enough to track the changes in the network, even a small disturbance could entail significant consequences such as sustained oscillation in voltage, active and reactive power at IBPSs’ point of connection and IBPSs loss of synchronism from the network. Currently, limiting the IBPSs output, maintaining a sufficient number of SGs in service and installing synchronous condensers are established methods to facilitate the reliable operation of the network in the presence of high IBPSs penetration. Nevertheless, operational constraints and the additional investments required for synchronous condensers could affect further development of IBPSs in the long run.

In order to ensure stable performance of IBPSs, sufficient system strength should be maintained under normal and N-1 contingency. As per [31], system strength is a characteristic of a power system that represents the size of the voltage change following a contingency or disturbance on the power system. Australian Energy Market Operator (AEMO) considers system strength as the ability of a power system to maintain and control the voltage at any location in the network. The system strength at a given node in a power system is proportional to the fault level at that node and inversely proportional to effective grid-following IBPSs penetration observed at that node. Traditionally, system strength at a location has been presented by the fault level available at that location divided by the capacity of IBPS connecting at that location, which is referred to as short circuit ratio (SCR). As close by grid-following IBPSs can reduce the system strength, an aggregated SCR was

recently defined to recognize the cumulative effect of electrically close IBPSs on the system strength. The existing grid-following IBPSs are generally designed to stably operate above a minimum system strength. Unlike synchronous machines that contribute to the system strength, grid-following IBPSs act as sink of system strength (have a negative impact).

Although system strength is an important index when discussing the power system stability with high IBPS penetration, it should not be considered as the only one. Note that grid-following IBPSs could provide a stable operation in networks with low system strength if their control parameters are properly tuned. In fact, to properly discuss the stability of a weak power system, a detailed model of grid-following IBPS and the system is required. Electromagnetic transient simulations based on accurate network and grid-following IBPS models are required to assess the control interaction and stability of grid-following IBPSs in the weak networks. Nevertheless, SCR could be a useful system strength index in steady state feasibility studies. Thus, in this paper, the SCR is used as one of technical constraints of locational HC.

4. Methodology

As discussed in Section 3, there are different technical challenges that constrain the integration of grid-following IBPSs in power systems. A comprehensive approach for identifying the locational HC should include all those constraints. However, due to differences in the nature of the technical issues, it is very difficult if possible to develop a mathematical model for the locational HC. A practical method to estimate the locational HC for grid-following IBPSs is to follow a heuristic algorithm, which is presented in Figure 2. As it can be seen, the algorithm starts with a an initial capacity of zero for the grid-following IBPS. Then, it checks the HC constraints. If there is a violation in any of the constraints, the algorithm stops. Otherwise, it increases the size of the IBPS. Further, it should be noted that:

- It is obvious that the load and the renewable generation are uncertain variables. In order to properly address the uncertainty associated with the loads and the output power of renewable resources, the simulations should be conducted over a time period. In this paper, time-series simulation is conducted with a resolution of one hour.
- In the power system, the total generation is always equal to the summation of total load and the power losses. Thus, when integrating the new IBPS, it is necessary to decrease the generation from other online generators in the system to maintain the load-generation balance. This adjustment should be done for all the time steps.
- As it was mentioned in Section 3, the grid-following IBPSs should be able to provide a stable performance under normal and credible contingencies. Therefore, the proposed algorithm monitors the system strength index under normal and credible contingencies.

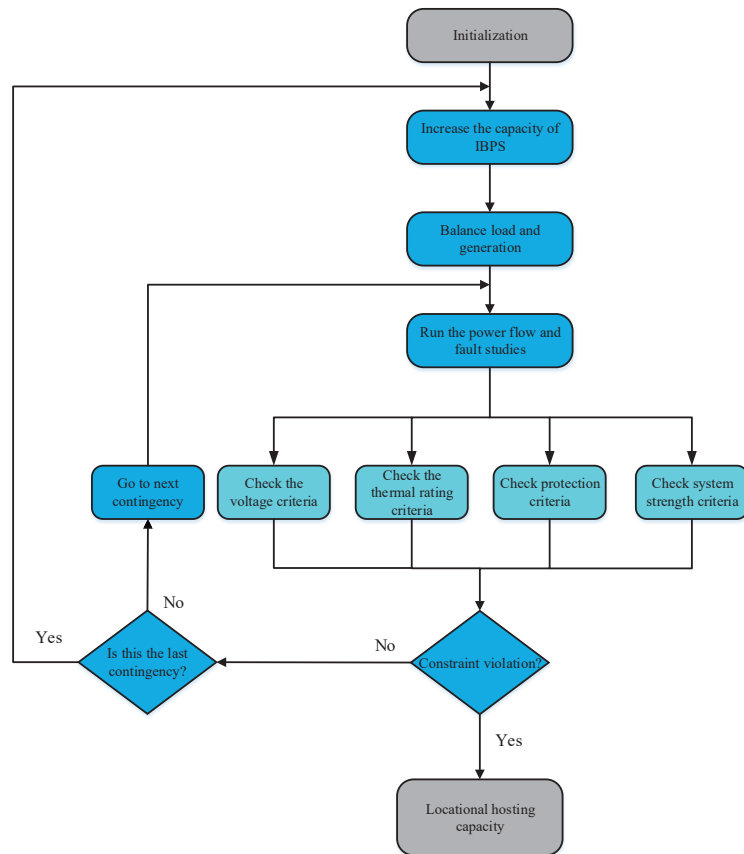


Figure 2. Methodology for identifying the locational HC of grid-following IBPSs.

5. Network Modelling

The purpose of this section is to describe the steps that have been taken to model the power systems in Darwin and Tasmania, which are the prime candidates for installing tidal generators in the AUSTEN project. The modeling in this section is based on information sourced from Power and Water Corporation (PWC), which is the Northern Territory's premier provider of electricity, TasNetworks, which is a Tasmanian Government State owned company that is responsible for electricity transmission and distribution throughout Tasmania, AEMO reports, and publicly available information. The following sections provide the details for modeling the Power system in Darwin and Tasmania, respectively.

5.1. Darwin Network Modelling

Darwin-Katherine interconnected system (DKIS) is the largest power system in the Northern Territory. It supplies Darwin city and its surrounding areas and suburbs, Palmerston, the township of Katherine and its surrounding rural areas. Figure 3 illustrates the Darwin-Katherine network. The only transmission lines in this network are the lines from Katherine to Channel Island and Channel Island to Hudson Creek [32].

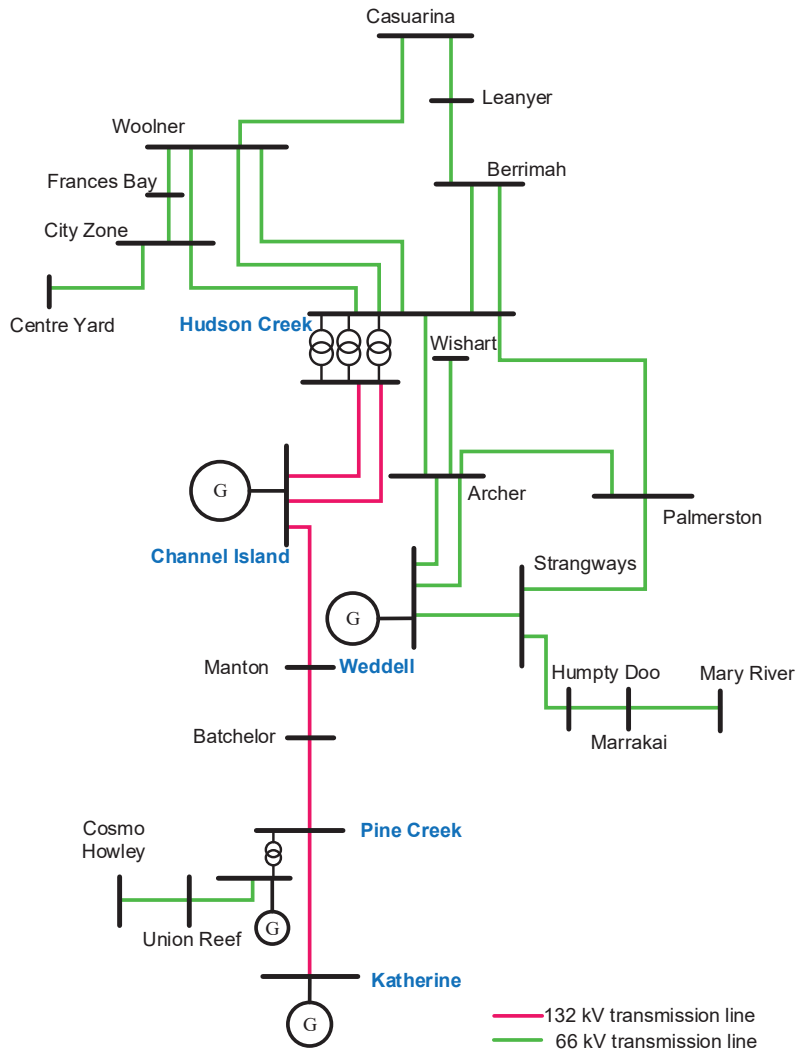


Figure 3. Single line diagram of Darwin–Katherine transmission network.

The information required to build the network model was collected from different sources. The lines and transformers data were provided by PWC. Further, thermal capacity of the lines was extracted from [33]. Daily load profiles with the resolution of 30 min for dry and wet seasons were extracted from [33] for all substations in Darwin–Katherine region. The DKIS has a sustainable installed capacity of just over 500 MW. The fuel type of the generation units is made up of a mix of dual fuel (gas/diesel), gas only, steam and landfill gas. The generation plants are Channel Island (310 MW), Weddell (129 MW), Katherine (35 MW), Pine Creek power station (27 MW) and Shoal Bay (1.1 MW). The details of generation units in the Darwin–Katherine region such as their make, engine type, fuel type and MW rating can be found in [32]. The 30 min generation dispatch of all generating units in Darwin–Katherine region are provided in [34]. The collected

network, load and generation data was used to develop an accurate model of the DKIS in DigSILENT PowerFactory.

5.2. Tasmanian Network Modelling

Tasmania's power system forms a part of the Eastern Australian power system. Basslink, which is a privately-owned undersea cable, connects Tasmania to the mainland network and has the capability to transfer electricity in both directions. The participants of Tasmania's electricity supply chain are as follows:

- Power stations and wind farms.
- A transmission network.
- A distribution network.
- Small-scale generation connected within the distribution network.
- Retailers.
- End-users of electricity.

All large generators sell their generation to a central market, i.e., the national energy market (NEM). The Tasmanian transmission network transfers the power from generators, often in remote areas, to transmission-distribution connection points (substations). Then, the distribution network distributes the energy to smaller industrial and commercial and residential customers. Electricity is sold to end-users, by retailers, who purchase electricity from the NEM and sell it to the consumers. The Tasmanian transmission network comprises [35]:

- A 220 kV, and some parallel 110 kV lines, transferring power from major generation centers to major load centers and Basslink.
- A peripheral 110 kV transmission network that connects smaller load centers and generators to the bulk transmission network.
- Substations that provide transmission connection points for the distribution network and industrial loads.

A summary of the composition of the Tasmanian transmission infrastructure is presented in Table 1.

Table 1. Summary of the Tasmanian transmission infrastructure.

Asset	Quantity
Substations	49
Switching stations	6
Circuit kilometers of transmission lines	3554
Route kilometers of transmission lines	2342
Circuit kilometers of transmission cable	24
Transmission line support structures (towers and poles)	7621
Easement area (Ha)	11,176

In order to build the Tasmanian power system model, the detailed network, load and generation data were collected from different sources. Regarding the network infrastructure, data released by AEMO and Geoscience Australia (GA) provide a substantial amount of information regarding the NEM's participants and topology. Information regarding the locations and attributes of major power stations, substations, and transmission lines in Tasmania were extracted from GA [36–38]. Each data-set (substations, lines and power stations) includes xls, csv, gdb, and kmz file formats. However, coordinates describing the paths of transmission lines can only be found in gdb and kmz files. The kmz files were used to extract the substations, generators and network data. Finally, the extracted network data were validated using the line and transformer information provided by TasNetworks. Regarding the load modeling, TasNetworks provided the load profile for all connection points for 2017. Further, AEMO provided the load forecast for all transmission connection

points in Tasmania up to 2026 in [39]. The yearly load profile and AEMO load forecast were used to model the loads in the Tasmanian network. Information on the capacity of existing, withdrawn, committed, and proposed generation projects in the Tasmanian network is provided in [40]. Further, the actual generation data of different generating systems in the NEM was obtained from the AEMO website [41]. The collected network, load and generation data was used to develop an accurate model of the Tasmanian network in DiGSILENT PowerFactory, which is shown in Figure 4.

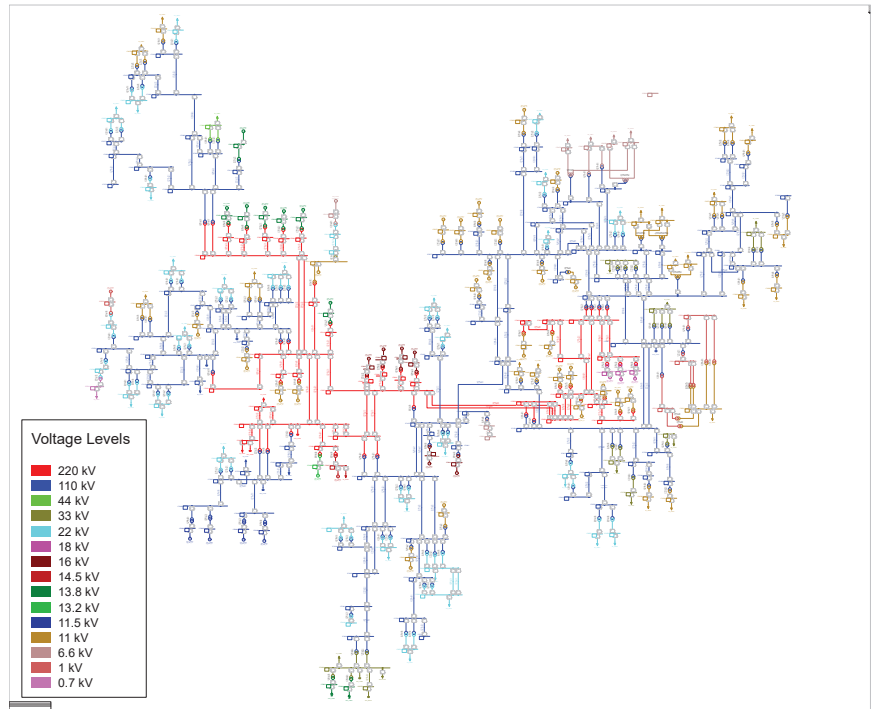


Figure 4. Single line diagram of the Tasmanian network in DiGSILENT PowerFactory.

6. Simulation Results

In this section, simulations were carried out to assess the performance of the proposed methodology. The test systems are described in Section 5. The normal voltage range is between 0.9 p.u and 1.1 p.u. Further, as it was explained before, the grid-following IBPSs generally reduce the system strength. To determine the fault level “consumption” of each grid-following IBPS, the minimum SCR withstand capability of the generating system is multiplied by its nominal capacity. As per [42], a minimum SCR of 3 at the connection point should be used when the minimum SCR withstand capability of the IBPS is unknown.

6.1. Point of Connection for Prospective Tidal Farm

A national tidal energy model, which was developed in component 1 of the AUSTEN project, was used to identify regions in Australia with peak tidal flow rates greater than 1.5 m per second within 100 km of a community or industry with a significant electricity demand. Then, two candidate site were selected from identified regions. One of the selected sites for tidal generation is Clarence Strait in the northern part of Northern Territory, which connects the Beagle Gulf in the west to the Van Diemen Gulf in the east. This strait is approximately located 50 km north of the city of Darwin. The prospective location of tidal generation is very close to the following substations:

- Darwin city substation;

- Snell street (Woolner) substation;
- Casuarina substation;
- Frances Bay substation.

Therefore, these locations are considered as the point of connection for tidal generation in the DKIS. The second candidate for the tidal farm is Banks Strait in east-north of Tasmania, which is located between Cape Portland and Clarke Island. This location is very close to the following substations:

- Musselroe Bay wind farm (WF) substation in Cape Portland;
- Derby substation;
- Scottsdale substation;
- Starwood substation in Bell Bay;
- St Marys substation.

Therefore, these locations are considered as the point of connection for the tidal generation in the Tasmanian network.

6.2. Balance of Load-Generation

As it was explained in the methodology section, the balance of power should always be held in a power system. This means that if a new generator is integrated in a system, the output power of the other generators in that system should be decreased. As a rule of thumb, the market keeps the output of the most expensive generators as low as possible. In Australia, the gas units are amongst the most expensive generators. Therefore, the best candidates for reducing the output power are gas generators. All the generating units in the DKIS are gas generators. Therefore, the following power stations are dispatched in proportion to their size to balance the incoming tidal generation.

- Channel Island (310 MW);
- Weddell (129 MW);
- Katherine (35 MW);
- Pine Creek power station (27 MW).

The situation in the Tasmanian power system is different from the Darwin–Katherine network. Less than 10% of power generation is from the gas units. The first gas generation plant is Tamar Valley Combined Cycle power station with a total capacity of 208 MW, which has been announced withdrawal. The second one is Tamar Valley Peaking with a capacity of 58 MW, which is still in service. The third one is Bell Bay Power Station with a total capacity of 105 MW. As the gas generators might not be enough for balancing the new tidal generators, the hydro generators that are close to the point of connection were also considered. These generators are as follows:

- Trevallyn Power Station with a total capacity of 46.5 MW;
- Palooka Power Station with a total capacity of 33 MW;
- Devils Gate Power Station with a total capacity of 60 MW;
- Cethana Power Station with a total capacity of 85 MW;
- Lemonthyme / Wilmot Power Station with a total capacity of 81.6 MW.

6.3. Grid-Integration Scenarios

The simulations were conducted for a couple of different scenarios. In the first scenario, the locational tidal HC is identified for the existing network. This scenario is referred as “Baseline Scenario” in this paper. In the second scenario, the locational tidal HC is identified considering the future network development and renewable projects. This scenario is referred as “Future Scenario” in this paper. The future upgrades in DKIS is provided by PWC in their network management plan report [43]. Further, the details of the network upgrades required in Tasmania are provided in Appendix D of Integrated System Plan (ISP) 2018 report [44]. As for the future renewable project, solar energy is the most prospective renewable energy resource in the Northern Territory and wind seems to be the dominant renewable resource in Tasmania.

6.4. Simulation Results and Discussions for Baseline Scenario

Table 2 presents the maximum capacity of tidal generators that could be installed at different locations in the DKIS. As can be seen among the considered locations, Casuarina can accommodate 104 MW, which is the highest level of tidal generation among the assessed locations. Further, Frances Bay substation with an allowable capacity of 61 MW is the worst point of connection. Moreover, the main technical constraint that bounded tidal generation at the considered locations is the thermal capacity of the transformers.

Table 2. Locational tidal HC at different locations in DKIS.

Point of Connection	Maximum Allowable Capacity (MW)	Limitation
Darwin city substation	89	Thermal rating (Transformer)
Snell street (Woolner) substation	77	Thermal rating (Transformer)
Casuarina substation	104	Thermal rating (Transformer)
Frances Bay substation	61	Thermal rating (Transformer)

Table 3 presents the maximum tidal capacity that could be installed at different locations in the Tasmanian network. As can be seen among the considered locations, Scottsdale substation can accommodate 65 MW, which is the highest level of tidal generation among the assessed locations. Further, St Marys substation with an allowable capacity of 21 MW is the worst point of connection. Similar to Darwin–Katherine network, the main technical constraint that bounded tidal generation at the considered locations is the thermal capacity.

Table 3. Locational tidal HC at different locations in the Tasmanian network.

Point of Connection	Maximum Allowable Capacity (MW)	Limitation
Musselroe Bay WF substation	59	Thermal rating (line)
Derby substation	24	Thermal rating (Transformer)
Scottsdale substation	65	Thermal rating (Transformer)
Starwood substation in Bell Bay	59	Thermal rating (line)
St Marys substation	21	Thermal rating (Transformer)

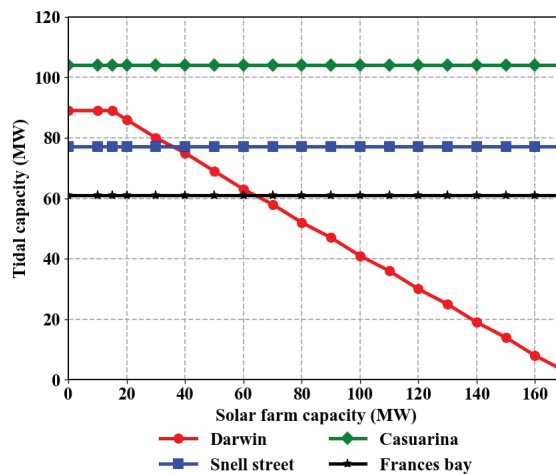
Improving HC generally can be done by employing local solutions. If the limiting constraint is voltage related, employing a reactive power resource such as capacitor bank, reactor and STATCOM (depending on the observed issue) could alleviate the situation. If the limiting constraint is thermal rating violation, upgrading the lines or substation transformer is an effective solution. Further, if the system strength is the limiting constraint, installing synchronous condensers can generally resolve the issue. As shown, thermal rating is the main constraint in the studied cases of both Darwin–Katherine and Tasmanian network. It can be seen in Table 4 that upgrading the transformer capacity could increase the locational HC. Note that the area of interest is quite congested and integrating higher tidal capacity requires a huge amount of investment in upgrading the network.

Table 4. Locational tidal HC at different locations in the Tasmanian network after upgrading nearby transformers.

Point of Connection	Maximum Allowable Capacity (MW)	Limitation
Musselroe Bay WF substation	59	Thermal rating (line)
Derby substation	89	Thermal rating (line)
Scottsdale substation	159	Thermal rating (line)
Starwood substation in Bell Bay	59	Thermal rating (line)
St Marys substation	57	Thermal rating (line)

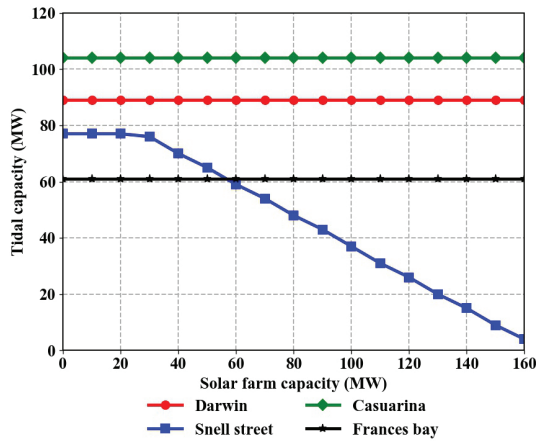
6.5. Simulation Results and Discussions for the Future Scenario

As it was mentioned, solar energy is the dominant resource in the Northern Territory. In this section, the proposed algorithm was used to identify the locational tidal HC in the presence of future solar farm projects in the Darwin–Katherine network. There are different options to be considered as the point of connection (POC) of the new solar farm. In this paper, it was assumed that the POC for the potential solar farm were the same as those defined for the tidal farm. Further, the capacity of the solar farm is changed from 0 MW to 210 MW. Figure 5 demonstrates the locational tidal HC versus solar farm capacity. As it can be seen, the prospective solar farm only affected the tidal HC when the POC of solar and tidal farm are the same. This is mainly because the solar farm power injection did not change the power flow around the tidal farm POC. Another interesting observation is that increasing the solar farm capacity did not have any impact on the locational tidal HC if the solar farm capacity is below 15 MW. However, a solar farm with a capacity in the range of 15 MW to 210 MW would cause a decrease in the locational tidal HC. This is mainly because the tidal generation caused a thermal rating constraint violation at 4 a.m. The output power of the solar farm is zero during this time period. However, the solar farm generated its maximum power at 1:30 p.m. Increasing the capacity of the solar farm eventually shifted the critical time period for the combined generation from 4 a.m. to 1:30 p.m.

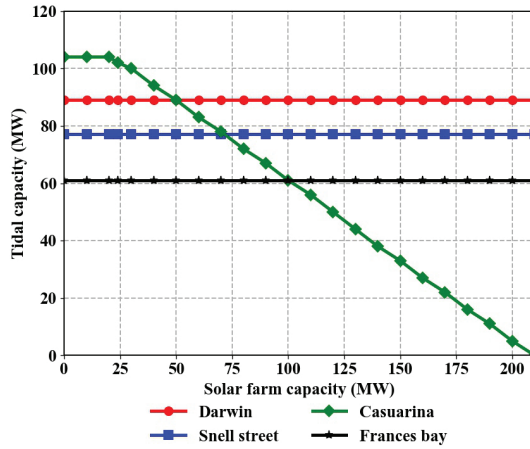


(a) Solar farm connected at Darwin city

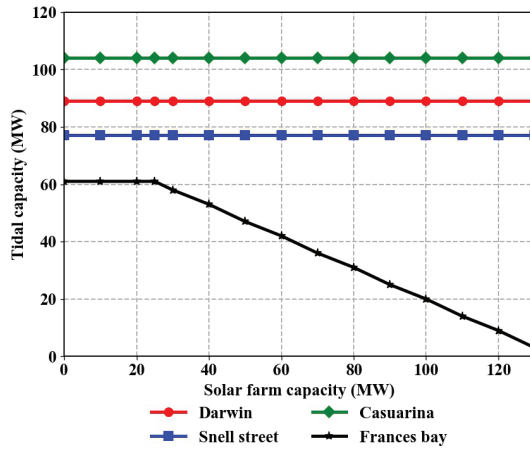
Figure 5. Cont.



(b) Solar farm connected at Snell street



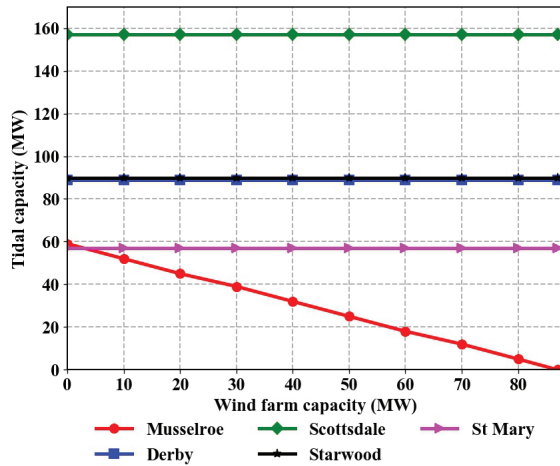
(c) Solar farm connected at Casuarina



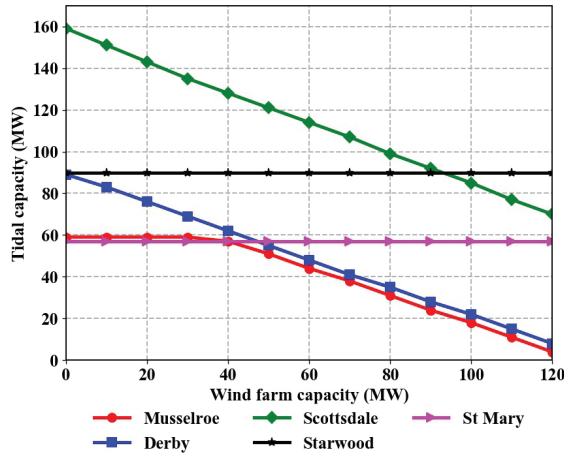
(d) Solar farm connected at Frances Bay

Figure 5. Impact of a potential solar farm on locational tidal HC in Darwin–Katherine network.

Wind energy is quite strong in Tasmania. Thus, the proposed algorithm was used to identify the locational tidal HC in presence of future wind farm projects in the Tasmanian network. There are different options to be considered as the point of connection (POC) of the new wind farm. In this paper, it is assumed that the POC for the potential wind farm are the same as those defined for the tidal farm. Further, the capacity of the wind farm is changed from 0 MW to 120 MW. Figure 6 demonstrates the locational tidal HC versus wind farm capacity. As it can be seen, the prospective wind farm affected the tidal HC when the POC of wind and tidal farm are close to each other. For instance, as can be observed in Figure 6b, increasing the wind farm capacity at Derby substation would result in a decrease in the locational tidal HC at Musselroe, Derby and Scottsdale.

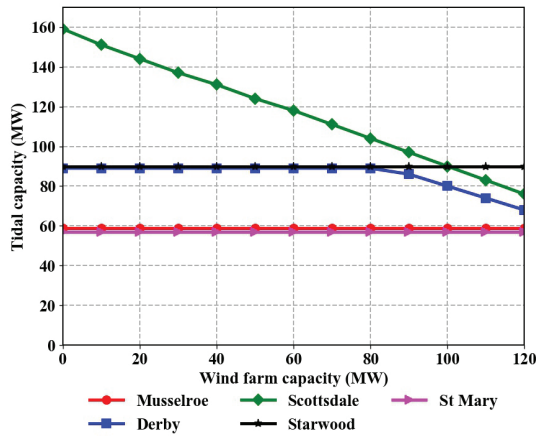


(a) Wind farm connected at Musselroe Bay

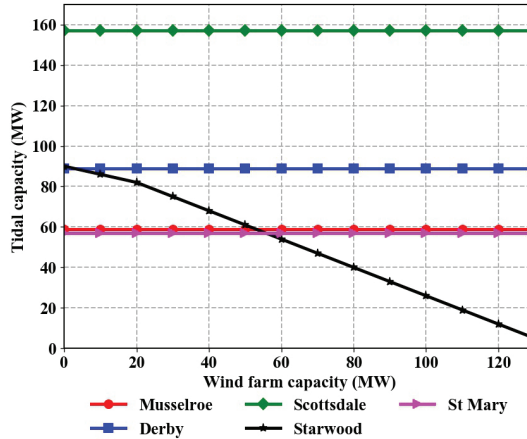


(b) Wind farm connected at Derby

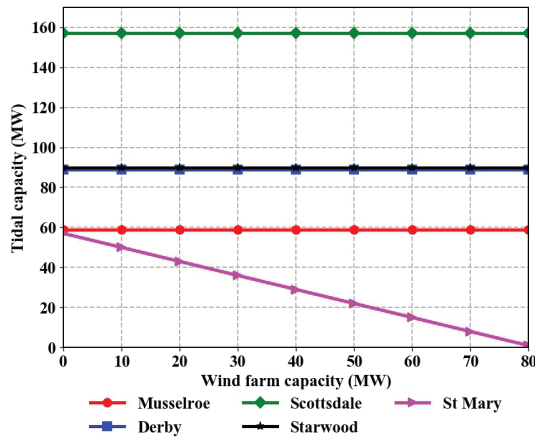
Figure 6. Cont.



(c) Wind farm connected at Scottsdale



(d) Wind farm connected at Starwood



(e) Wind farm connected at St Marys

Figure 6. Impact of a potential wind farm on locational tidal HC in the Tasmanian network.

In both the Darwin–Katherine and the Tasmanian networks, the locational HC of the hybrid generation, i.e., tidal-solar and tidal-wind, was higher than locational tidal HC. This was because the HC at the considered locations was mainly limited due to thermal rating constraint. Further, the generation profile of tidal, wind and solar farms were different and their maximum generation did not occur at the same time. Therefore, if the network is strong and the HC is limited by thermal rating and voltage related constraints, hybrid generation could result in a higher locational HC. Of course, considering this approach depends on the availability of the resources and the feasibility of the project from an economical point of view. However, if the system strength is the limiting constraint of the HC, hybrid generation using grid-following inverters would not improve the locational HC. In such a case, only increasing system strength or employing grid-forming technology could be effective.

7. Conclusions

This paper develops a methodology to estimate the locational HC for grid-following IBPSs. The developed methodology is based on thermal rating, voltage, protection and stability criteria. The uncertainty associated with the load and output power of IBPSs are addressed using time-series simulations. Further, the proposed algorithm monitors the voltage, loading of the elements, fault level as well as system strength index for all credible contingencies. The developed approach was employed in the AUSTEn project to assess the capability of the Tasmanian and Darwin–Katherine networks to host tidal generation. The assessment demonstrated that although both Banks and Clarence straits provide very good tidal resources, the network capacity to transfer the energy from those locations to load centers is limited. In other words, the network capacity is an immediate constraint on future tidal integration into the systems. Further, the sensitivity of the maximum allowable tidal generation to the capacity of a prospective wind and/or solar farm was also assessed. It was observed that a prospective wind and/or solar farm would not impact the locational tidal HC for some cases while they could decrease the maximum allowable tidal generation at some other locations. Moreover, it was demonstrated that improving the IBPSs HC required a local solution. Depending on the limiting constraint, upgrading the lines/transformers and installing reactive power resources such as STATCOM and synchronous condenser could increase the HC.

Author Contributions: Conceptualization, M.S.S.A.; Formal analysis, M.S.S.A.; Investigation, M.S.S.A.; Methodology, M.S.S.A.; Resources, M.S.S.A.; Software, M.S.S.A.; Supervision, J.A.H., S.S., P.O. and J.M.; Validation, M.S.S.A.; Visualization, M.S.S.A.; Writing—Original draft, M.S.S.A.; Writing—Review & editing, J.A.H., S.S. and P.O. All authors have read and agreed to the published version of the manuscript.

Funding: This research received no external funding.

Institutional Review Board Statement: Not applicable.

Informed Consent Statement: Not applicable.

Data Availability Statement: Not applicable.

Acknowledgments: This project was supported by the Australian Renewable Energy Agency (ARENA) Advancing Renewables Program.

Conflicts of Interest: The authors declare no conflict of interest.

Abbreviations

The following abbreviations are used in this manuscript:

AEMO	Australian Energy Market Operator
AREMI	Australian Renewable Energy Mapping Infrastructure
ARENA	Australian Renewable Energy Agency
AUSTEn	Australian Tidal Energy
CSIRO	Commonwealth Scientific and Industrial Research Organisation
DER	Distributed Energy Resource
DKIS	Darwin–Katherine interconnected system
GA	Geo-science Australia
HC	Hosting Capacity
IBPS	Inverter Based Power Resource
ISP	Integrated System Plan
LV/MV	Low Voltage/Medium Voltage
NEM	National Electricity Market
NSP	Network Service Provider
PLL	Phase-Lock-Loop
POC	Point of Connection
PWC	Power and Water Corporation
SCR	Short Circuit Ratio
SG	Synchronous Generators
WF	wind farm

References

- Smith, J.; Rylander, M. Stochastic analysis to determine feeder hosting capacity for distributed solar PV. *Electr. Power Res. Inst. Palo Alto CA Tech. Rep.* **2012**, 1026640, 0885–8950.
- Abad, M.S.S.; Ma, J.; Han, X. Distribution systems hosting capacity assessment: Relaxation and linearization. In *Smart Power Distribution Systems, Control, Communication, and Optimization*; Academic Press: Cambridge, MA, USA, 2018.
- Heslop, S.; MacGill, I.; Fletcher, J. Maximum PV generation estimation method for residential low voltage feeders. *Sustain. Energy Grids Netw.* **2016**, *7*, 58–69. [[CrossRef](#)]
- Chen, X.; Wu, W.; Zhang, B. Robust capacity assessment of distributed generation in unbalanced distribution networks incorporating ANM techniques. *IEEE Trans. Sustain. Energy* **2017**, *9*, 651–663. [[CrossRef](#)]
- Zio, E.; Delfanti, M.; Giorgi, L.; Olivieri, V.; Sansavini, G. Monte Carlo simulation-based probabilistic assessment of DG penetration in medium voltage distribution networks. *Int. J. Electr. Power Energy Syst.* **2015**, *64*, 852–860. [[CrossRef](#)]
- Abad, M.S.S.; Verbič, G.; Chapman, A.; Ma, J. A linear method for determining the hosting capacity of radial distribution systems. In Proceedings of the Universities Power Engineering Conference (AUPEC), Melbourne, Australia, 19–22 November 2017; pp. 1–6.
- Spertino, F.; Di Leo, P.; Cocina, V. Which are the constraints to the photovoltaic grid-parity in the main European markets? *Sol. Energy* **2014**, *105*, 390–400. [[CrossRef](#)]
- Mahmud, M.A.; Hossain, M.J.; Pota, H.R. Voltage variation on distribution networks with distributed generation: Worst case scenario. *IEEE Syst. J.* **2013**, *8*, 1096–1103. [[CrossRef](#)]
- Alturki, M.; Khodaei, A.; Paaso, A.; Bahramirad, S. Optimization-based distribution grid hosting capacity calculations. *Appl. Energy* **2018**, *219*, 350–360. [[CrossRef](#)]
- De Oliveira, T.E.; Carvalho, P.; Ribeiro, P.F.; Bonatto, B.D. PV hosting capacity dependence on harmonic voltage distortion in low-voltage grids: Model validation with experimental data. *Energies* **2018**, *11*, 465. [[CrossRef](#)]
- Hoke, A.; Butler, R.; Hambrick, J.; Kroposki, B. Steady-state analysis of maximum photovoltaic penetration levels on typical distribution feeders. *IEEE Trans. Sustain. Energy* **2012**, *4*, 350–357. [[CrossRef](#)]
- Akbari, M.-A.; Aghaei, J.; Barani, M. Convex probabilistic allocation of wind generation in smart distribution networks. *IET Renew. Power Gener.* **2017**, *11*, 1211–1218. [[CrossRef](#)]
- Akbari, M.A.; Aghaei, J.; Barani, M.; Niknam, T.; Ghavidel, S.; Farahmand, H. Convex models for optimal utility-based distributed generation allocation in radial distribution systems. *IEEE Syst. J.* **2018**, *12*, 3497–3508. [[CrossRef](#)]
- Wang, S.; Chen, S.; Ge, L.; Wu, L. Distributed generation hosting capacity evaluation for distribution systems considering the robust optimal operation of OLTC and SVC. *IEEE Trans. Sustain. Energy* **2016**, *7*, 1111–1123. [[CrossRef](#)]
- Santos, S.F.; Fitiwi, D.Z.; Shafie-Khah, M.; Bizuayehu, A.W.; Cabrita, C.M.; Catalao, J.P. New multistage and stochastic mathematical model for maximizing RES hosting capacity—Part I: Problem formulation. *IEEE Trans. Sustain. Energy* **2016**, *8*, 304–319. [[CrossRef](#)]
- Al-Saadi, H.; Zivanovic, R.; Al-Sarawi, S.F. Probabilistic hosting capacity for active distribution networks. *IEEE Trans. Ind. Inform.* **2017**, *13*, 2519–2532. [[CrossRef](#)]

17. Rabiee, A.; Mohseni-Bonab, S.M. Maximizing hosting capacity of renewable energy sources in distribution networks: A multi-objective and scenario-based approach. *Energy* **2017**, *120*, 417–430. [[CrossRef](#)]
18. Abad, M.S.S.; Ma, J.; Zhang, D.; Ahmadyar, A.S.; Marzooghi, H. Distributionally robust distributed generation hosting capacity assessment in distribution systems. *Energies* **2018**, *11*, 2981. [[CrossRef](#)]
19. Abad, M.S.S.; Ma, J.; Zhang, D.; Ahmadyar, A.S.; Marzooghi, H. Probabilistic Assessment of Hosting Capacity in Radial Distribution Systems. *IEEE Trans. Sustain. Energy* **2018**. [[CrossRef](#)]
20. Abad, M.S.S.; Ma, J.; Zhang, D.; Ahmadyar, A.S.; Marzooghi, H. Sensitivity of Hosting Capacity to Data Resolution and Uncertainty Modeling. In Proceedings of the 2018 Australasian Universities Power Engineering Conference (AUPEC), Auckland, New Zealand, 19–22 November 2017; pp. 1–6.
21. Ding, F.; Mather, B. On distributed PV hosting capacity estimation, sensitivity study, and improvement. *IEEE Trans. Sustain. Energy* **2016**, *8*, 1010–1020. [[CrossRef](#)]
22. Dubey, A.; Santoso, S. On estimation and sensitivity analysis of distribution circuit’s photovoltaic hosting capacity. *IEEE Trans. Power Syst.* **2016**, *32*, 2779–2789. [[CrossRef](#)]
23. Navarro-Espinosa, A.; Ochoa, L.F. Probabilistic impact assessment of low carbon technologies in LV distribution systems. *IEEE Trans. Power Syst.* **2015**, *31*, 2192–2203. [[CrossRef](#)]
24. Torquato, R.; Salles, D.; Pereira, C.O.; Meira, P.C.M.; Freitas, W. A comprehensive assessment of PV hosting capacity on low-voltage distribution systems. *IEEE Trans. Power Deliv.* **2018**, *33*, 1002–1012. [[CrossRef](#)]
25. Arshad, A.; Lindner, M.; Lehtonen, M. An analysis of photo-voltaic hosting capacity in Finnish low voltage distribution networks. *Energies* **2017**, *10*, 1702. [[CrossRef](#)]
26. Ma, Y.; Abad, M.S.S.; Azuatalam, D.; Verbic, G.; Chapman, A. Impacts of community and distributed energy storage systems on unbalanced low voltage networks. In Proceedings of the 2017 Australasian Universities Power Engineering Conference (AUPEC), Melbourne, Australia, 19–22 November 2017.
27. Abad, M.S.S.; Ma, J. Photovoltaic hosting capacity sensitivity to active distribution network management. *IEEE Trans. Power Syst.* **2020**, *36*, 107–117. [[CrossRef](#)]
28. Penesis, I.; Hemer, M.; Cossu, R.; Hayward, J.; Nader, J.R.; Rosebrock, U.; Grinham, A.; Sayeef, S.; Osman, P.; Marsh, P.; et al. Tidal energy in Australia—assessing resource and feasibility to Australia’s future energy mix. In Proceedings of the AWTEC 2018 Proceedings, Taipei, Taiwan, 9–13 September 2018.
29. Penesis, I.; Hemer, M.; Cossu, R.; Nader, J.R.; Marsh, P.; Couzi, C.; Hayward, J.; Sayeef, S.; Osman, P.; Rosebrock, U.; et al. Tidal Energy in Australia: Assessing Resource and Feasibility in Australia’s Future Energy Mix. Australian Maritime College, University of Tasmania. 2020. Available online: <https://arena.gov.au/assets/2020/12/tidal-energy-in-australia.pdf> (accessed on 1 December 2020).
30. Shen, W.; Chen, X.; Qiu, J.; Hayward, J.A.; Sayeef, S.; Osman, P.; Meng, K.; Dong, Z.Y. A comprehensive review of variable renewable energy levelized cost of electricity. *Renew. Sustain. Energy Rev.* **2020**, *133*, 110301. [[CrossRef](#)]
31. AEMO. System Strength for NEM Explained. March 2020. Available online: <https://aemo.com.au/-/media/files/electricity/nem/system-strength-explained.pdf> (accessed on 1 March 2020).
32. Charles Darwin Centre. Power System Review 2015–2016. Available online: <https://utilicom.nt.gov.au/publications/reports-and-reviews/power-system-review-2015-to-2016> (accessed on 1 February 2020).
33. Power and Water Corporation. Network Management Plan 2013/2014 to 2018/2019 Update. 2017. Available online: https://www.powerwater.com.au/__data/assets/pdf_file/0024/29238/Network-Management-Plan-2013-14-to-2018-19-January-2017-Information-Update.pdf (accessed on 1 February 2020).
34. Power and Water Corporation. Daily Price and Trading Data Page. Available online: <https://www.powerwater.com.au/market-operator/daily-price-and-trading-data> (accessed on 1 February 2020).
35. TasNetworks. Annual Planning Report 2018. Available online: <https://www.aer.gov.au/system/files/TasNetworks%20-%20Annual%20Planning%20Report%202018%20-%202029%20November%202018.pdf> (accessed on 1 December 2019).
36. Orr, K.; Allan, B. Electricity Transmission Substations. Geoscience Australia. Dataset. 2015. Available online: <http://pid.geoscience.gov.au/dataset/ga/83173> (accessed on 1 December 2019).
37. Orr, K.; Allan, B. Electricity Transmission Lines. Geoscience Australia. Dataset. 2015. Available online: <http://pid.geoscience.gov.au/dataset/ga/83105> (accessed on 1 December 2019).
38. Orr, K.; Skeers, N. Power Stations. Geoscience Australia. Dataset. 2014. Available online: <http://pid.geoscience.gov.au/dataset/ga/82326> (accessed on 1 December 2019).
39. AEMO. Transmission Connection Point Forecasts for Tasmania: Dynamic Interface for Connection points in Tasmania. 2018. Available online: https://aemo.com.au/-/media/files/electricity/nem/planning_and_forecasting/tcpf/tas/2018/2018_tas_dynamic_interface.xlsm (accessed on 1 December 2019).
40. AEMO. Generation Information Page. 2018. Available online: <https://www.aemo.com.au/Electricity/National-Electricity-Market-NEM/Planning-and-forecasting/Generation-information> (accessed on 1 November 2019).
41. AEMO. Generation and Load Page. Available online: <https://www.aemo.com.au/energy-systems/electricity/national-electricity-market-nem/data-nem/market-management-system-mms-data/generation-and-load> (accessed on 1 October 2019).

42. Operational Analysis and Engineering, AEMO. System Strength Impact Assessment Guidelines. July 2018. Available online: https://www.aemo.com.au/-/media/files/electricity/nem/security_and_reliability/system-security-market-frameworks-review/2018/system_strength_impact_assessment_guidelines_published.pdf?la=en&hash=771B8F6BC8B3D1787713C741F3A76F8B (accessed on 1 October 2018).
43. Power and Water Corporation. Network Management Plan 2013/14 to 2018/19. Available online: https://www.powerwater.com.au/__data/assets/pdf_file/0013/8410/2013-14-to-2018-19-Power-and-Water-Corporation-Network-Management-Plan.pdf (accessed on 1 March 2020).
44. AEMO. Integrated System Plan Appendices. 2018. Available online: https://aemo.com.au/-/media/files/electricity/nem/planning_and_forecasting/isp/2018/isp-appendices_final.pdf?la=en&hash=D52884BF713B2B23EEB3F90BA784CFAD (accessed on 1 November 2019).

Article

Enhancing Power System Frequency with a Novel Load Shedding Method Including Monitoring of Synchronous Condensers' Power Injections

Antans Sauhats ¹, Andrejs Utans ¹, Jurijs Silinevics ^{1,2}, Gatis Junghans ² and Dmitrijs Guzs ^{1,2,*}

¹ Institute of Power Engineering, Riga Technical University, 12-k1 Azenes Street, LV-1010 Riga, Latvia; sauhatas@eef.rtu.lv (A.S.); utan@eef.rtu.lv (A.U.); jurijs.silinevics@ast.lv (J.S.)

² AS Augstsprieguma Tikls (TSO), 86 Darzciema Iela, LV-1073 Riga, Latvia; gatis.junghans@ast.lv

* Correspondence: dmitrijs.guzs@ast.lv; Tel.: +371-67725361

Abstract: Under-frequency load shedding (UFLS) is a classic and a commonly accepted measure used to mitigate the frequency disturbances in case of loss-of-generation incidents in AC power grids. Triggering of UFLS is classically done at frequency thresholds when system frequency collapse is already close to happening. The renewed interest for synchronous condensers due to the global trends on massive commissioning of non-synchronous renewable power generation leading to reduction of system inertia gives an opportunity to rethink the approach used to trigger load-shedding activation. This question is especially relevant for the Baltic states facing a desynchronization from Russian power grid and a necessity to operate in an isolated island mode. The main goal of this paper is to introduce a predictive load shedding (LS) method without usage of either frequency or ROCOF measurements based on the monitoring of active power injections of synchronous condensers and to prove the efficiency of the concept through several sets of case study simulations. The paper shows that the proposed approach can provide a greatly improved frequency stability of the power system. The results are analyzed and discussed, the way forward for the practical implementation of the concept is sketched.

Keywords: power grid; inertia; load shedding; frequency stability; synchronous condensers; frequency collapse; PMU

Citation: Sauhats, A.; Utans, A.; Silinevics, J.; Junghans, G.; Guzs, D. Enhancing Power System Frequency with a Novel Load Shedding Method Including Monitoring of Synchronous Condensers' Power Injections. *Energies* **2021**, *14*, 1490. <https://doi.org/10.3390/en14051490>

Academic Editor: Juri Belikov

Received: 15 February 2021

Accepted: 5 March 2021

Published: 9 March 2021

Publisher's Note: MDPI stays neutral with regard to jurisdictional claims in published maps and institutional affiliations.



Copyright: © 2021 by the authors. Licensee MDPI, Basel, Switzerland. This article is an open access article distributed under the terms and conditions of the Creative Commons Attribution (CC BY) license (<https://creativecommons.org/licenses/by/4.0/>).

1. Introduction

The topic of climate change and the ongoing efforts to combat it and to reduce anthropogenic greenhouse gas emissions have resulted in several high-level policies [1] aimed at reducing the usage of fossil fuels with a massive roll-out of renewable energy generation capacities. As the result the European Union (EU) has introduced and started to implement the 2030 Climate & Energy Framework stating a 55% net greenhouse gas emission reduction target with 1990 as the base year [2]. Under this framework Germany for example as one of largest economies of the EU plans to achieve ca. 190 GW of non-synchronous renewable generation capacity installed in 2030 [3], comparing to 100 GW non-synchronous renewable generation capacity and a peak load of ca. 80 GW in 2018 [4]. These developments leading to higher and higher penetration of alternating current (AC) power systems by non-synchronous renewables are expected to bring a number of challenges as reduction of total system inertia, increasing rates of change of frequency (ROCOF), reduced frequency stability and a decreasing number of generation units providing primary and secondary frequency regulation [5,6].

Frequency stability of AC power systems, together with the voltage and the transient angular stabilities, is a cornerstone of secure and reliable operation of any modern power system. Under-frequency load shedding (UFLS) is a classic and commonly accepted measure used in AC power systems to counteract a potential frequency collapse following a

serious loss-of-generation incidents and instant imbalance between generated and consumed power. The UFLS is typically triggered when the activation of available frequency reserves does not provide a sufficient frequency stabilization. UFLS is usually defined by a list of loads with matching frequency thresholds which are disconnected from the grid by frequency relays when the grid frequency reaches any of the predetermined thresholds in the list. The loads disconnected by UFLS are typically the whole MV side/-s of a HV/MV substation/-s [7].

The importance of the frequency stability for an AC power system increases with decreasing power system size due to decreasing system inertia and increasing ROCOF during loss-of-generation incidents. Equation (1) which is a form of swing equation [8] clearly shows that the change in system frequency $d\omega/dt$ is reverse proportional to the total system inertia H_{tot} in MWs, so that decreasing inertia level will lead to a faster fall in frequency for the same power imbalance ΔP :

$$\frac{d\omega}{dt} = \Delta P \frac{\omega_{syn}}{2H_{tot}}, \quad (1)$$

The importance of UFLS and its response time increases with decreasing power system size and inertia as the UFLS frequency thresholds are reached faster in smaller AC power systems with less inertia. An introduction of faster UFLS triggering would therefore be beneficial especially for AC systems of medium and small sizes.

Equation (1) clearly states that in order to improve $d\omega/dt$ one can either increase the available system inertia H_{tot} —by adding more synchronous machines (as for example synchronous condensers) or introducing synthetic inertia—or reducing the ΔP by improving the existing UFLS algorithms.

Traditional UFLS schemes—triggered solely by a frequency threshold—can be enhanced by more sophisticated UFLS schemes and concepts proposed and described in the literature [9–13]. A semi-adaptive UFLS scheme can use a triggering method utilizing static frequency and ROCOF thresholds instead of a frequency-only approach. An adaptive UFLS scheme can adopt triggering methods employing a dynamic combination of frequency and ROCOF. Another type of dynamic UFLS schemes use algorithms including calculating the system inertia values or the total power imbalance of the system and use these for load shedding triggering together with frequency and ROCOF threshold values [11,12] or even bus voltage threshold values [13]. Some of the adaptive schemes described by the literature propose to use artificial intelligence or neural networks in order to automatically determine the number of loads to be shed for each disturbance, but it is unclear how to educate the neural network without compromising the safety and stability of a real power system [14]. All of the proposed UFLS schemes use frequency measurements in one or another manner.

Despite the advantages of the adaptive approaches over the classic one, the disadvantages of the adaptive UFLS schemes are well known and described [15]. A still ongoing search for new methods or concepts for UFLS is explained by the complexity of using Equation (1) in adaptive approaches due to the complexity of a real power system with many generators, each with own moment of inertia. The frequency in a multi-machine power system becomes a local parameter during the transient power imbalance oscillations and the Equation (1) is then describing the behavior of each generator separately. As a result, to estimate the disturbance ΔP , knowledge of the frequencies and inertia of many generators in the power system is required. This fact indicates that a predictive approach to UFLS, as anticipated in [15], could be the next step in the development of UFLS. A search for improved UFLS approach for low-inertia power systems is the main motivation for authors of this paper and therefore a novel type of a predictive LS algorithm will be presented here.

In order to assess the efficiency of newly proposed UFLS schemes, dynamic simulations on standard test power system models, as for example IEEE XX bus standard test power systems, are usually executed and the results are investigated. The authors of this paper will follow another approach and will test the proposed LS approach through executing dynamic simulations on a specific model depicting the Baltic power system.

This not only due to the origin of the authors—living and working in the Baltics—but also due to the expected rapid shift towards the renewable energy generation also in the Baltic power system due to the previously mentioned EU regulations [2].

Power transmission grid of the Baltic states is a meshed, interconnected 330 kV grid with a peak load of ca. 4000 MW [16]. It has a strong synchronous interconnection with the Unified Power System of Russia (UPS) synchronous power system and has asynchronous HVDC connections to both Finland, Sweden and Poland, see Figure 1. The maximum exchange capacity of all interconnections to the Baltics is around 4700 MW [17], which makes it theoretically possible to supply the peak load of Baltic power grid with imports alone. Main generation assets in the Baltic power grid comprise of thermal oil-shale and wind power generation in Estonia, large river hydro power plants plus a major gas-fired power plant (Riga TEC2) in Latvia and a combination of wind power, small/medium sized CHPs, a major pump-storage and a major gas-fired power plant in Lithuania. Baltic power grid is heavily relying on imported power with the total import comprising in 2019 47,6% of the total consumption, with largest net power exporters to the Baltics in 2019 being Belarus, Finland and Sweden [18].

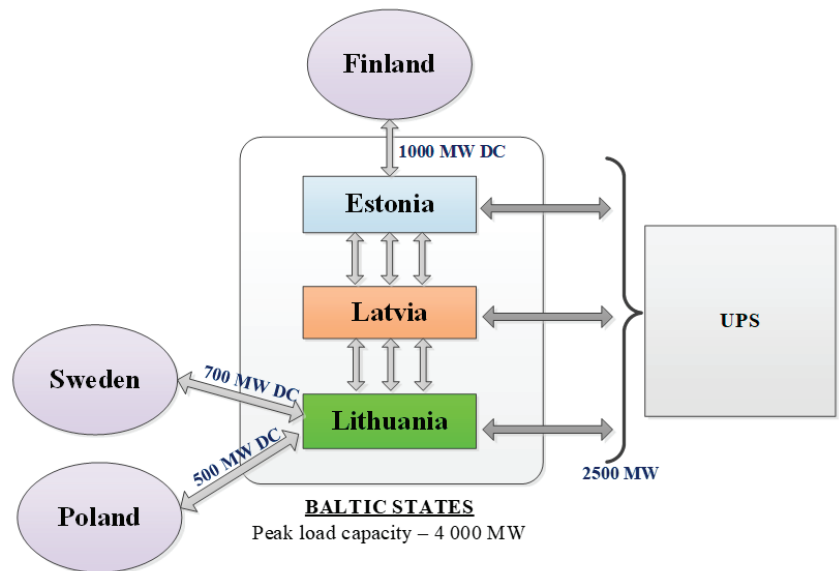


Figure 1. Schematic power system interconnection of the Baltic states.

The interconnection with UPS today provides the Baltic power system with vast frequency and inertia reserves. Frequency stability is not an issue in today's situation due to the size of the UPS synchronous power system. A political decision has been taken to desynchronize the Baltic states from the UPS power system and to synchronously connect it with the European Network of Transmission System Operators (ENTSO-E) power grid in 2025 [19]. Baltic and the UPS power systems are interconnected with nine 330 kV transmission lines with the total thermal capacity of ca. 9000 MW and a nominal transmission capacity of ca. 2500 MW. The upcoming synchronous connection between the Baltic and the ENTSO-E power systems is to succeed through a single double-circuit 400 kV synchronous interconnection on the border Lithuania-Poland with thermal capacity of ca. 2000 MW [17]. Planned or unplanned outages of this interconnection will result in the operation of Baltic states' power grid in an island mode. During this mode of operation the Baltic power system is only to rely on its own inertia reserves which are radically lower than today's available inertia of the UPS power grid. The island mode of operation is to introduce major challenges to the frequency stability of the Baltic power grid.

Another development to impact the inertia level of the Baltic power system is the expected rise in intermittent non-synchronous renewable generation capacity. Around 4000 MW of wind generation capacity is planned in the Baltic states up to year 2034 according to [20]. Separate national renewable energy targets in the scope of the EU 2030 Climate & Energy Framework [2] indicate sharp rise of share of renewable generation in Estonia and Lithuania, while Latvia is already close to fulfilling 2030 renewable electricity targets due to large existing hydropower generation capacity [21–23]. Wind power generators are non-synchronous so they do not contribute to the system inertia. This implies that the total inertia level of the Baltic power system is expected to decline. It is also expected that due to the rise of the share of intermittent generation and the subsequent volatility of the power prices, the operation of the synchronous generators is to be more volatile, with more start-and-stop cycles [24]. This means also volatility in the level of the total inertia of the power system.

To mitigate these developments and to safeguard frequency stability of the Baltic power grid Baltic TSOs have agreed to make investments in three synchronous condensers (SC) rated ca. 305 MVA each—totaling nine synchronous condensers planned in the Baltic power grid by 2025 [17].

Synchronous condenser technology is far from new: SC is a synchronous generator without a prime mover as a steam turbine and therefore it is not a source of active power in a classic manner. A SC has all qualities of a classic synchronous generator, similar design and behavior. SC provides a wide reactive power regulating envelope, large short-circuit current capabilities and inertia which can be additionally increased by means of installing a flywheel on the SC rotor shaft [25]. SC requires some small amounts of active power for its operation. Due to their qualities SC have become increasingly popular again due to a sharp increase in decommissioning of synchronous generation (largely fossil) and in commissioning of non-synchronous renewable generation [26]. SC have become a powerful tool to meet challenges caused by increasing penetration of the grid by non-synchronous renewables, particularly reduction of the system inertia and the grid short-circuit current capabilities.

Summarizing the results of publications on frequency stability of power system with a significant share of renewable energy, we can note the following:

- (1) The importance of the frequency stability for an AC power system increases with decreasing power system size due to decreasing system inertia and increasing rate of change of frequency (ROCOF) during loss-of-generation incidents;
- (2) Synchronous condenser technology can be used to increase the system inertia and simplify the solution to the frequency control problem. In the event of a loss of large generating capacities, the use of SC makes it easier to solve the task of frequency control, but the problem of emergency frequency control remains to be acute;
- (3) Attempts to improve the efficiency of UFLS schemes have until now been based on the use of ROCOF in one or another way. However, to the best of our knowledge, there are no studies aimed at improving UFLS based on the monitoring of the SC response in transient conditions.

This article will present an innovative approach for a new adaptive UFLS method (main contribution of the article). This method is based on the combined simultaneous use of synchronous condensers and their active power control system. Unlike the known adaptive methods, the new method disconnects the load in the amount which is selected depending on the results of measuring not the ROCOF but the active power injections of synchronous condensers. The use of the proposed new parameter eliminates the problems of fast and accurate measuring the rate of change in frequency as also discussed in the next chapter. The remaining part is organized as follows: first theory, method and the principles of the proposed approach are described, then the case studies are portrayed, finally the discussion is conducted and the conclusions are made.

2. Materials and Methods

2.1. Inertia and Inertial Response

Any power system under consideration includes following elements: synchronous generators, synchronous condensers, load with electric motors, renewable energy sources and high-voltage grid tie lines.

An unexpected disconnection of a large generator in the power system causes a transition to a new state—in particular, the rotation frequency of synchronous generators, synchronous condensers and motors is subject to change (decreases). In the process of decelerating of rotating masses of the elements of the power system, the kinetic energy accumulated in them is transformed into electric energy and injected into the electrical network. As result of this injection (inertial response) the balance of generated and consumed electrical energy is maintained even during the transient process. Within a few seconds delay after disturbance, generator's governors, in response to a decrease in frequency, start to react on the frequency decline trying to restore the frequency rated value (primary frequency control). Additionally, diminishing of the frequency causes a decrease in the power consumption of the frequency dependent load. However, the initial period of the considered transient process is mainly determined by the disconnected generator with active power ΔP at the beginning of the process and the inertia of the system. In such case the impact of primary frequency control and the decrease in the power consumption can be neglected. Consequently, we can assert that the volume of the disconnected power ΔP at the very beginning of the process prior to primary frequency control is compensated by the injection of the active power by each element of the power system possessing inertia:

$$\Delta P = \sum_{a=1}^S \Delta P_{SC_a} + \sum_{b=1}^G \Delta P_{G_b} + \sum_{c=1}^L \Delta P_{L_c}, \forall a \in S, \forall b \in G, \forall c \in L \quad (2)$$

where ΔP_{SC_a} , ΔP_{G_b} and ΔP_{L_c} are active power injections of every synchronous condenser, synchronous generator and frequency dependent load (for example electric motors) present in the power grid; where S, G, L are the total numbers of synchronous condensers, synchronous generators and frequency dependent loads in the power grid. To stop the change in frequency, it is enough to restore the balance of generation and consumption by disconnecting, for example, a load equal to ΔP . Estimates of the volume of this load can be carried out on the basis of measuring all ΔP 's included in Equation (2). However, in real power systems, due to the large number of elements, this path is unacceptable. The problem can be simplified by assuming that Equation (2) can be represented as:

$$\Delta P = K_r * \sum_{a=1}^S \Delta P_{SC_a}, \quad (3)$$

where $K_r = \frac{\sum_{b=1}^G \Delta P_{G_b} + \sum_{c=1}^L \Delta P_{L_c}}{\sum_{a=1}^S \Delta P_{SC_a}} + 1$.

If the coefficient K_r is known, to estimate ΔP it is sufficient to measure the power injections of all synchronous condensers $\sum \Delta P_{SC}$. In real life, the coefficient K_r is not a constant value, it depends on the operating mode of the power system, its topology and also of the total system inertia level. However, in any case, we can assert that the measured $\sum \Delta P_{SC}$ can be taken as the basis for disconnecting/shedding the load for frequency stabilization. This load shed must be in a volume not less than $\sum \Delta P_{SC}$. Such disconnection, as will be shown below, can significantly increase the efficiency of systems where the main source of inertia are synchronous condensers. Equation (3) will give an opportunity to rapidly predict the fall in the system frequency and therefore form the basis of the decision to initiate a fast triggering of the proposed LS scheme. Monitoring of SCs only is achievable in practice and can be used as a basis for power imbalance and system frequency prediction. The implementation of such a concept would require usage of a Wide Area Measurement System and dedicated measurement units/terminals.

2.2. Classic/Static UFLS and Its Challenges

UFLS automated systems are used to rescue the power systems facing extreme disturbances to avoid system collapse. In event of sudden loss of generation, a power mismatch lead to frequency decline. In case the primary frequency regulation does not respond quickly enough or in the absence of power reserve, the UFLS sheds a certain amount of load, attempting to prevent frequency drop below the lowest acceptable limit. A classical UFLS has several steps of load disconnection and frequency thresholds and the amount of load disconnected for each step is predefined but may differ from system to system depending on the system specifics. The main disadvantage of such “static” UFLS schemes is their inability to adapt fixed thresholds and the amount of load to be shed by each step to continuously varying load/generation profiles and to severity of power imbalance. These deficiencies may result in late response or excessive load shedding. It is a common understanding that for the load-shedding to be effective it should be activated as quickly as possible and simultaneously it should be resilient to small disturbances so that no excessive load is shed [9].

Several adaptive, response-based UFLS schemes were mentioned earlier and some are also proposed in [27–30] to overcome the deficiencies of the static UFLS. Even probabilistic approaches are proposed for power systems where some loads are not crucial and are allowed to be shed in order to maintain the feed of critical loads [31]. The majority of adaptive UFLS estimate the initial imbalance of power ΔP and then redistributes the total power deficit among several load shedding steps. The total power imbalance could be estimated from Equation (1) when ROCOF of the system is known/measured immediately after disturbance. The problem is that in multi-machine system generators might oscillate at different rates and, therefore, frequency gradient is not homogeneous at different nodes of the system. The concept of frequency of center of inertia (COI) f_{COI} was proposed to avoid this challenge. System with n generators is represented by equivalent COI generator and swing equation takes the form of Equation (4) where inertia constants H_i are in a common system base S_{base} and $f_{COI,p.u.}$ is the system frequency divided by the system nominal frequency. Calculation of the COI necessitate the online knowledge of all generators inertia which is not a trivial task, especially when RES inertia uncertainty is considered:

$$\frac{df_{COI,p.u.}}{dt} = \frac{\Delta P_{COI,p.u.} * f_{COI,p.u.}}{2 \sum_{i=1}^n H_i \left(\frac{S_{rate,i}}{S_{base}} \right)}, \quad (4)$$

A comprehensive overview of the ROCOF-based power imbalance estimation-related problems is given in [32]. It was concluded that besides the inertia, several additional factors may influence the estimation, namely, the initial system loading and the load voltage characteristics need to be taken into account. Ignoring these factors along with some frequency gradient measurement issues [33] may lead to significant inaccuracies in power imbalance calculation and, therefore, may negatively affect UFLS performance.

2.3. The Concept

Earlier simulations conducted for the Baltic grid in island mode [34] have shown that after shortfall of a major generation unit a ROCOF of 0.75 Hz/s (0–500 ms) is observed and the typical classic first UFLS threshold of 49 Hz is reached in approx. 1.75 s from the moment of the contingency. That means that if an alternative UFLS method is to bring added value to the Baltic power grid it should provide triggering considerably faster than 1.75 s. [35] states that a fast response for frequency stabilization should be activated faster than 800 ms in situations with ROCOF of around 1 Hz/s.

We would like to propose a principle of much faster triggering of LS than that of the conventional UFLS—a principle which allows to trigger (not to be confused with activate) LS up to 100 ms from the moment of the contingency without usage of either frequency or ROCOF measurements, activate the LS considerably faster than conventional UFLS and is based on a predictive approach. The principle is based on the monitoring of the active power injections of the SCs. Our hypothesis is following: active power injection

of a SC in an AC power system contains information on the instantaneous shortfall of a major generation unit and the expected fall in frequency. SC active power injections can therefore be used as a set off for rapid LS activation. Execution of such a rapid scheme of LS substantially reduces the frequency fall and the value of frequency nadir, thus greatly reducing the risk of frequency limit violation in the given power grid. The schematic representation of the proposed LS principle is seen in Figure 2.

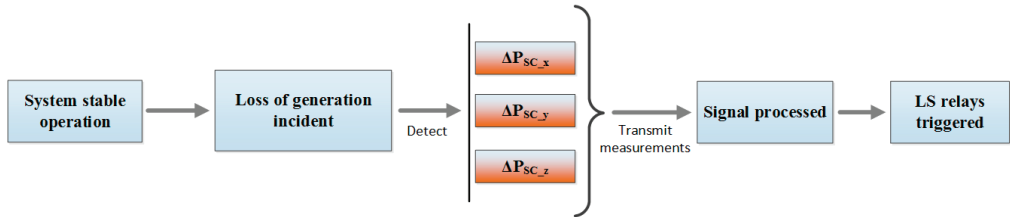


Figure 2. Schematic of the proposed LS principle.

To prove the concept and the hypothesis we will perform two sets of power grid dynamic simulation case studies based on two different Baltic power grid models derived from models found in [34] and presenting a range of scenarios for the Baltic power system: from today’s situation with little non-synchronous renewable generation of considerable size to a scenario with non-synchronous renewable generation supplying a major part of the electricity demand. Two different and independent sets of test cases on two different models depicting the Baltic power system in different simulation environments—Siemens PSSE ver. 34 and ETAP ver. 12.5 [36,37]—are executed in order to cross-check the performance of our proposed LS concept and to prove its efficiency to keep the frequency within the operational limits of the power grid.

3. Case Study

3.1. Methodology and Results. Test Case Set No. 1

The first case study set will be done on a model of the Baltic power grid in island mode already presented in [34] and now enhanced with adding a set of synchronous condensers (SC): 3 SCs rated ca. 305 MVA each added to the busbar of every Baltic country—totaling 9 SC. The SC are of turbogenerator-type with active power set to 0, each having an inertia constant of $H = 6.23$ s, providing a total inertia of 17101 MWs. The other dynamic characteristics of the SCs for the model are provided by [17]. Additionally, three tie lines between Latvian and Lithuanian zones are now present to depict the realities of the Baltic power system. The rest of model characteristics are identical to that in [34]. A diagram of the modelled grid can be seen in Figure 3. An overview of the system parameters in the different modelled scenarios is seen in Table 1.

Table 1. Grid model parameters for different modelled scenarios, test case set 1, MW/MWs in italic.

	Scenario			
	A	B	C	D
Total generation before disruption	2567	2548	2623	2686
-of it renewable non-synchronous	100	700	1500	2500
Total load	3700	3700	3700	3700
Total import	1700	1700	1600	1530
Total export	500	500	500	500
Total post-contingency system inertia H_{tot_post}	29,779	36,739	24,768	18,091
Gen. loss event	TEC2, 800 MW	HVDC, 700 MW	HVDC, 700 MW	HVDC, 700 MW

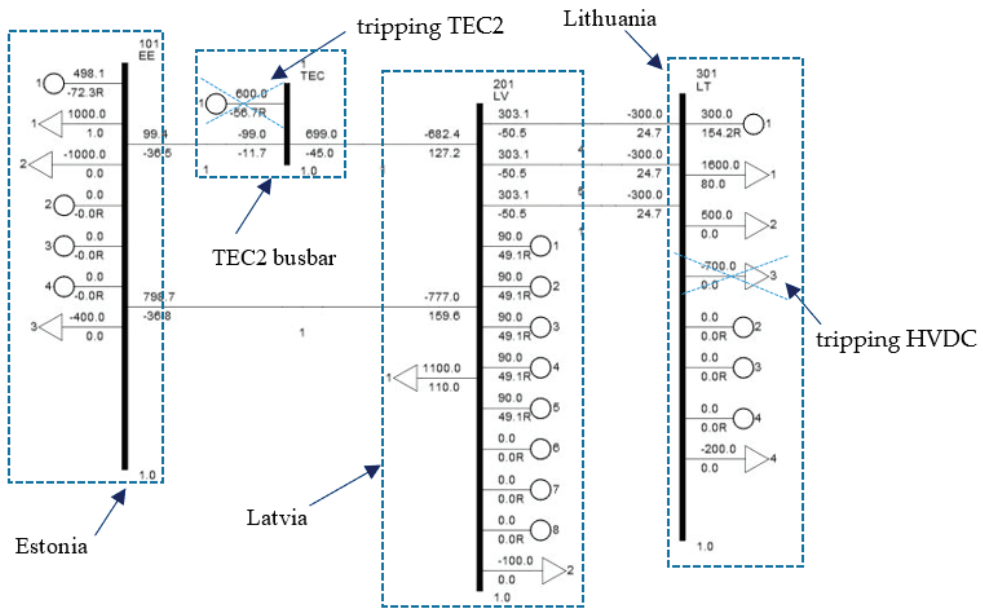


Figure 3. Schematic diagram of the modelled Baltic power grid for test case set No. 1.

For all scenarios of the first test case set the most severe disturbance available will be modelled: tripping of TEC2 with 800 MW or HVDC import cable with 700 MW. Scenarios B, C and D have an increasing wind power generation levels displacing the generation on the top of the merit-order, which for the Baltics is TEC2. This means the tripping of TEC2 with full power is not possible in the scenarios B, C and D and therefore the tripping of the 700 MW HVDC cable becomes the largest incident. Active power injections of the SC on each country busbar will then be examined and used to draw the basics of the proposed LS concept. The total SC active power injections ΔP_{SC} will be monitored from $t \geq 20$ ms from the start of contingency, as 20 ms is one period for a 50 Hz AC grid and measurement accuracy at Δt under 1 period can be problematic due to the function principles of the voltage and current measurement units, as well as due to the sub-transient and transient electromagnetic processes in the rotor-stator pair of any synchronous generator. This will be the procedure for measuring ΔP_{SC} for the test case set No. 2 as well. For all scenarios of the first test case a separate simulation for cases with no LS, with conventional UFLS and with the proposed LS method will be executed in order to compare frequency responses. The parameters for the conventional UFLS for the test case set 1 are given by Table 2 with activation time delay of 0.17 s after threshold has been reached.

Table 2. Conventional UFLS parameters, test case set No. 1.

	Load Shedding Step Number, n					
	1	2	3	4	5	6
Freq. threshold, Hz	48.8	48.6	48.4	48.2	48.0	47.8
$P_{load_UFLS_n}$, %	5.4	6.1	7.5	6.4	5.4	4.4

Note that the implementation of a load shedding using the measured power injection value ΔP_{SC} can be realized in various ways. First, we present results corresponding to one of the simplest schemes (the second scheme will be described in Section 3.2): if a power injection ΔP_{SC} is detected and measured, then the load is disconnected according to the following algorithm:

If $\Delta P_{SC} > P_{load_UFLS_1}$ AND If $\Delta P_{SC} < (P_{load_UFLS_1} + P_{load_UFLS_2})$ then $P_{load_novel_LS} = P_{load_UFLS_1}$;
 If $\Delta P_{SC} > (P_{load_UFLS_1} + P_{load_UFLS_2})$ AND If $\Delta P_{SC} < (P_{load_UFLS_1} + P_{load_UFLS_2} + P_{load_UFLS_3})$ then $P_{load_novel_LS} = P_{load_UFLS_2}$;
 ...

where $P_{load_UFLS_1}, P_{load_UFLS_2}, \dots$ are loads shed carried out by the corresponding step of conventional UFLS (see Table 2). $P_{load_novel_LS}$ is load shed carried out by the proposed LS method. The total load shed by conventional UFLS is the sum of all the relevant steps $P_{load_UFLS} = P_{load_UFLS_1} + P_{load_UFLS_2} + \dots$

For each scenario the volume of load shed by the conventional and new methods is the same. Observance of this equality makes it easier to compare the efficiency of both compared LS schemes. The LS done with the proposed method is activated with time delay of no more than 0.4 s after the triggering of the scheme (up to 0.5 s after the disturbance itself).

3.1.1. Scenario A

An outage of TEC synchronous generation of 800 MW is simulated at $t = 5$ s and the LS activated according to the proposed method. The active power response of SCs can be seen in Figure 4: the SCs in all three countries react instantly with the SC closest to outage location injecting more active power; at $t \approx 5.5$ s the drop of active power injections due to LS activation can be seen. Active power responses are scaled p.u. to the base MVA rating of 1200 MW. Figure 5 shows the frequency responses of all simulations within scenario A, frequency is scaled p.u. to the base of 50 Hz.

In Figure 4 the instantaneous active power response of Estonian and Latvian SCs (red and green curves) being closest to the tripped generator reaches 54 MW each, the response of the Lithuanian SC (blue curve) is around 32 MW and it reacts on the disturbance much slower as being furthest from the tripped generator in the model. The $\Delta P_{SC} = 420$ MW. Figure 5 shows that with conventional UFLS frequency falls to 48.7 Hz and with proposed LS method—to 48.85 Hz.

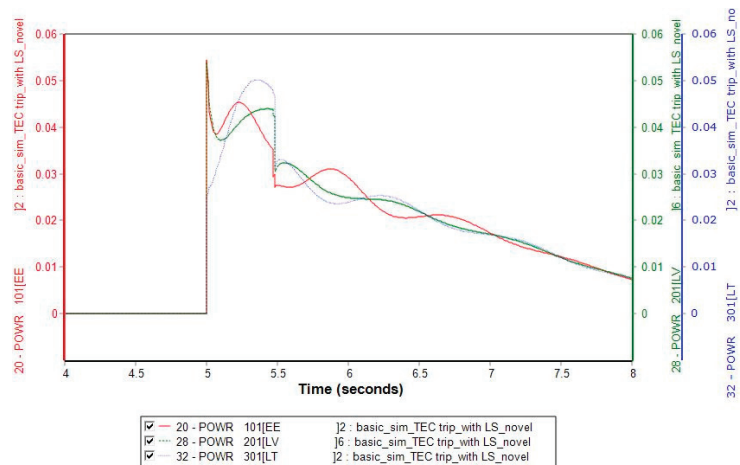


Figure 4. Active power injections of the SC, scenario A with novel LS method.

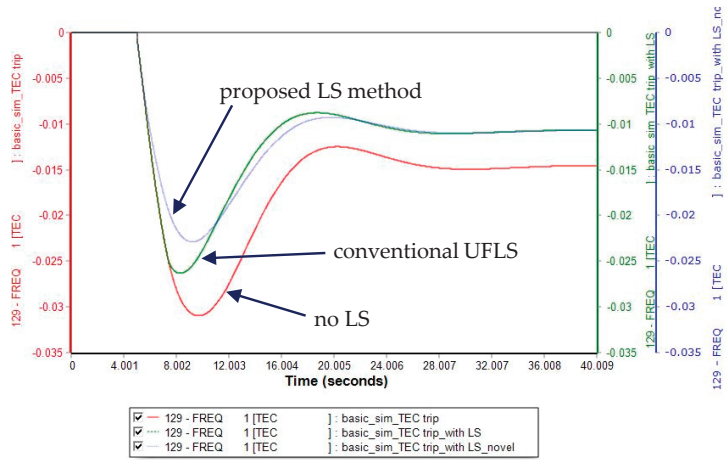


Figure 5. Frequency responses, scenario A.

3.1.2. Scenario B

An outage of HVDC import cable of 700 MW is simulated at $t = 5$ s and no conventional UFLS is activated due to insufficient fall in frequency. In the same way a simulation with the proposed LS method is conducted. The active power response of SCs can be seen in Figure 6: the SCs in all three countries react instantly with the SCs closest to outage location injecting more active power. Active power responses are scaled p.u. to the base MVA rating of 1200 MW. Figure 7 shows the frequency responses of both simulations within scenario B, frequency is scaled p.u. to the base of 50 Hz.

In Figure 6 the instantaneous active power response of Estonian and Latvian SC (red and green curves) are 11 MW and 46 MW, the response of the Lithuanian SC (blue curve) being closest to the tripped HVDC cable is around 89 MW. Estonian SC reacts on the disturbance much slower as being furthestmost from the tripped HVDC cable in the model. The $\Delta P_{SC} = 438$ MW. Figure 7 shows that the frequency falls to 48.81 Hz und is not sufficient to activate the conventional UFLS; with the proposed LS method activated the frequency falls only to 49.1 Hz.

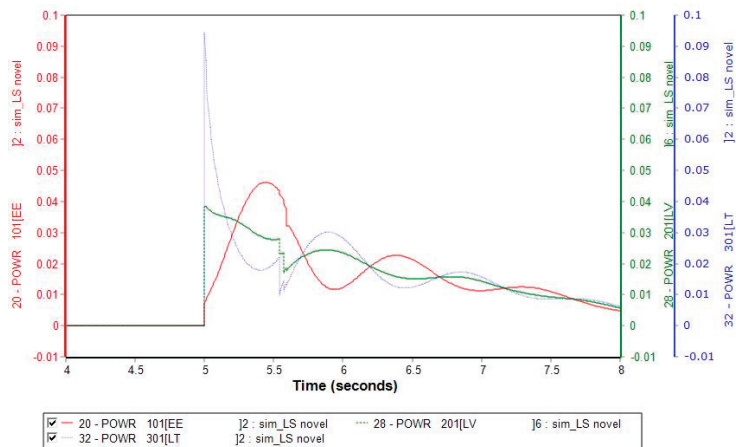


Figure 6. Active power injections of the SC, scenario B with novel LS method.

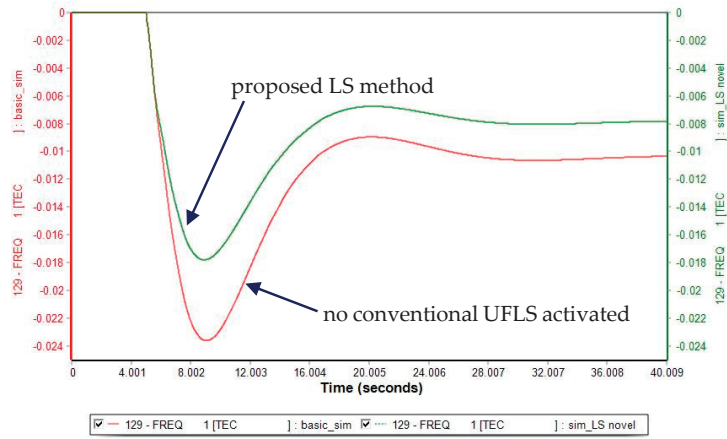


Figure 7. Frequency responses, scenario B.

The scenario B stands out from the other scenarios in the test case set by both a large amount of system inertia and a large amount of available spinning reserves, that also explains the fact that in this scenario the classical UFLS is not activated—the primary regulators of the synchronous generators limit the fall of the frequency. The scenario also shows a potential strength of the proposed LS method for high-inertia cases: it is activated and contributes to limit the fall in frequency also in cases when no conventional UFLS is expected to be activated.

3.1.3. Scenario C

An outage of HVDC import cable of 700 MW is simulated at $t = 5$ s and the LS activated according to the proposed method. The active power response of SCs can be seen in Figure 8: the SCs in all three countries react instantly with the SCs closest to outage location injecting more active power; at $t \approx 5.5$ s the drop of active power injections due to LS activation can be seen. Active power responses are scaled p.u. to the base MVA rating of 1200 MW. Figure 9 shows the frequency responses of all simulations within scenario C, frequency is scaled p.u. to the base of 50 Hz.

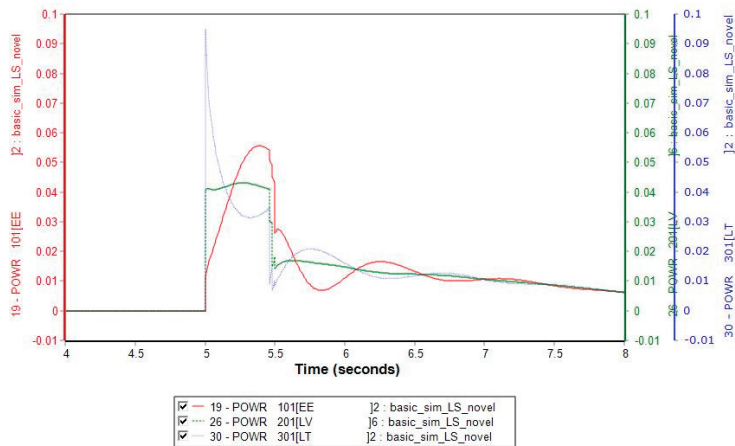


Figure 8. Active power injections of the SC, scenario C with novel LS method.

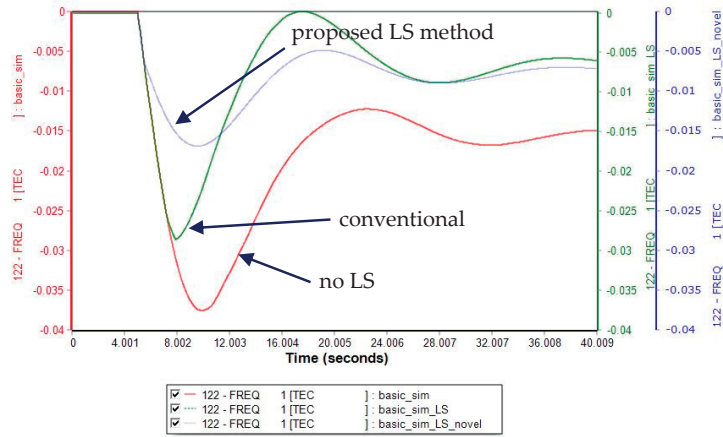


Figure 9. Frequency responses, scenario C.

In Figure 8 the instantaneous active power response of Estonian and Latvian SC (red and green curves) are 18 MW and 49 MW each, the response of the Lithuanian SC (blue curve) being closest to the tripped HVDC cable is around 91 MW. Estonian SC reacts on the disturbance much slower as being furthest from the tripped HVDC cable in the model. $\Delta P_{SC} = 475$ MW. Figure 9 shows that with conventional UFLS frequency falls to 48.6 Hz and with proposed LS method—to 49.15 Hz.

3.1.4. Scenario D

An outage of HVDC import cable of 700 MW is simulated at $t = 5$ s and the LS activated according to the proposed LS method. The active power response of SCs can be seen in Figure 10: the SCs in all three countries react instantly with the SC closest to outage location injecting more active power; at $t \approx 5.5$ s the drop of active power injections due to LS activation can be seen. Active power responses are scaled p.u. to the base MVA rating of 1200 MW. Figure 11 shows the frequency responses of all simulations within scenario D, frequency is scaled p.u. to the base of 50 Hz.

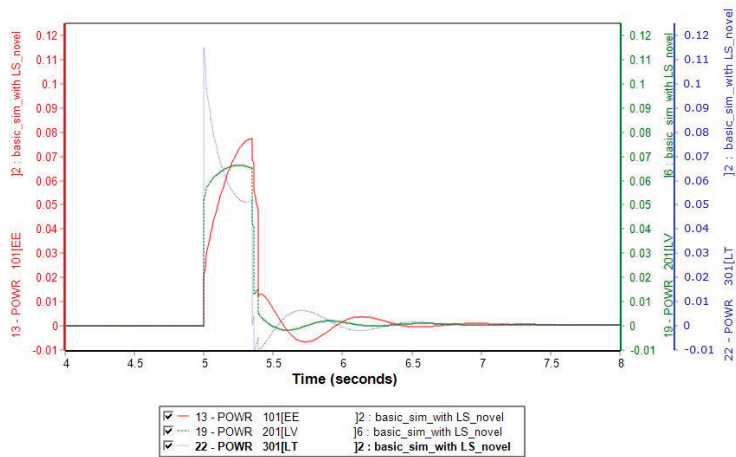


Figure 10. Active power injections of the SC, scenario D with novel LS method.

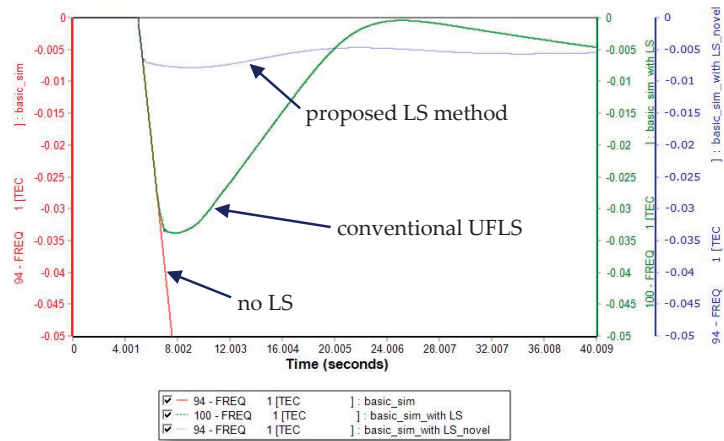


Figure 11. Frequency responses, scenario D.

In Figure 10 the instantaneous active power response of Estonian and Latvian SCs (red and green curves) are 36 MW and 68 MW each, the response of the Lithuanian SC (blue curve) being closest to the tripped HVDC cable is around 118 MW. Estonian SC reacts on the disturbance much slower as being furthestmost from the tripped HVDC cable in the model. $\Delta P_{SC} = 666$ MW. Figure 11 shows that with conventional UFLS frequency falls to 48.3 Hz and with proposed LS method—to 49.6 Hz.

The summary of results of test case set No. 1 can be seen in Table 3.

Table 3. Result summary, test case set No. 1.

	Scenario			
	A	B	C	D
ΔP_{SC} , MW	420	438	475	666
P_{load_UFLS} , MW	200	0	425.5	703
P_{load_UFLS} , % of total load	5.4	0	11.5	19
$P_{load_novel_LS}$, MW	200	200	425.5	703
Frequency nadir when UFLS does not activate (scenario B), Hz	-	48.81	-	-
Frequency nadir conventional UFLS, Hz	48.7	-	48.6	48.3
Frequency nadir novel LS method, Hz	48.85	49.1	49.15	49.6

3.2. Methodology and Results. Test Case Set No. 2

The second test case study set is also based on another model previously presented in [34]. The model (depicted in Figure 12) has a more detailed depiction of Latvian power system but depicts Estonian and Lithuanian power systems as grid equivalents—thus providing a different dynamic response to disturbances than the model in the test case set No. 1. The total rated power of the grid equivalents are 990 MVA for EE and 400 MVA for LT. This model also has 3 SC present (SC1, SC4 and SC6) rated at 305 MVA in the Latvian power grid as in the model of the test case set No. 1. The largest traditional generation plants are cogeneration plant CHP2 and hydro power plant HPP. Some of the traditional generation sources were replaced with wind parks (WTG2, WTG4 and WTG6) in order to imitate the increasing penetration of the non-synchronous renewable sources in the future. Despite this presence of the renewable sources the share of synchronous generation in the total load of scenarios A and B of the test case set are 91% which is exceptionally high for the Baltic power system today. This means the scenarios A and B represent historic rather than future situation. Scenarios C and D on the other hand give a realistic image of today’s situation with a portion

of synchronous generation in the total load around 50%. An overview of the test case set scenario parameters in the different modelled scenarios is seen in Table 4.

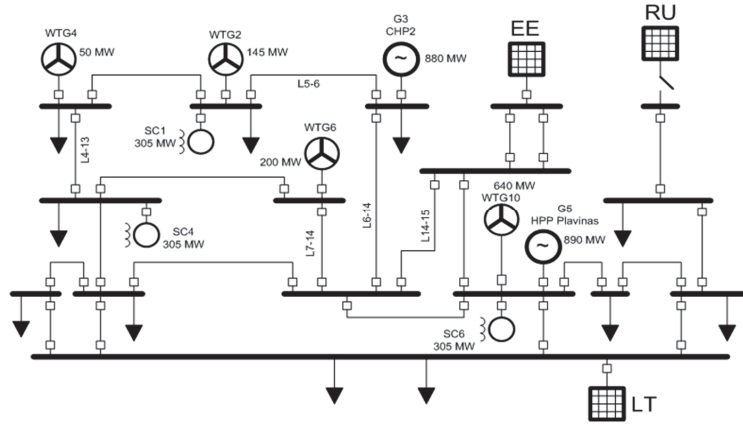


Figure 12. Schematic diagram of the modelled Baltic power grid for test case set No. 2.

Table 4. Grid element parameters for different modelled scenarios, test case set No. 2, MW/MWs in italic.

Scenario	CHP2	HPP	EE	LT	WTG2	WTG4	WTG6	WTG10	Gen. Loss Event	Total System Inertia
A	800	220	670	380	128	40	120	x	EE	15,760
B	x	800	990	400	128	40	120	x	HPP	12,150
C	800	x	50	350	128	40	120	640	CHP2	5790
D	800	x	50	350	128	40	120	640	CHP2	12,148

x = generation source not in operation.

Four scenarios (A–D) were simulated using ETAP 12.5 electrical software [37]. The goal of simulation was to explore the system frequency response under various loss-of-generation events. Total load of the Latvian grid is assumed to be ca. 2400 MW for all cases. Approximately half of the consumption is covered by in-house generation capacity with the remaining power imported from EE and LT. The loss-of-generation events were simulated by disconnecting one of the major generation source. Operation mode with minimal system inertia is simulated in scenario C: CHP2, EE and LT generation sources inertia constants has been reduced to $H = 0.1$ s.

For the second set of tests, simulations were first done with conventional UFLS and then with the proposed LS method. Additionally, now we use a different scheme (compared to the one described in Section 3.1) for choosing the volume of the load to be disconnected. We assume that the volume of the load to be disconnected— $P_{load_novel_LS}$ is proportional to the injection power ΔP_{SC} of all SC according to Equation (5):

$$P_{load_novel_LS} = K * \Delta P_{SC}, \tag{5}$$

where K is the coefficient—which we wish to predict to be as close to the coefficient K_r appearing in Equation (3). The parameters of conventional UFLS are given by the Table 5 with activation time delay of 0.3 s after threshold has been reached. The total amount of load shed by the conventional UFLS is P_{load_UFLS} .

Table 5. Conventional UFLS parameters, test case set No. 2.

	Load Shedding Step Number, n					
	1	2	3	4	5	6
Freq. threshold, Hz	49.0	48.8	48.6	48.4	48.2	48.0
$P_{load_UFLS_n}$, %	5	5	10	10	10	10

The load shed with the novel LS method with time delay of 0.3 s after the disturbance. In cases where the amount of load shed by the novel LS method was not sufficient to limit the fall in frequency the conventional UFLS will kick in according to the thresholds in Table 5.

For each scenario of test case set No. 2 simulations with generation loss event at $t = 0.5$ s were carried out: with conventional UFLS and with novel LS method with coefficient $K = 1$; for scenario B also simulations with coefficients $K = 2$ and $K = 3$ were executed to reach the best frequency result within the criteria of added value of the novel LS method. For simulations with the novel LS method the conventional UFLS scheme was still active and it contributed with additional shed load as we see in the scenarios B and D. The simulation results for all scenarios of the test case set No. 2 are given in Table 6. The frequency responses of the simulations of scenario B are given in the Figure 13.

Table 6. Result summary, test case set No. 2.

Scenario	ΔP_{gen_loss} , MW	ΔP_{load_UFLS} , MW	Conventional UFLS f_{min} , Hz	ΔP_{SC} , MW	Novel Approach LS with $K = 1$ + Additional Load Shed by Conv. UFLS		Novel Approach LS with $K = 2$ + Additional Load Shed by Conv. UFLS		Novel Approach LS with $K = 3$ + Additional Load Shed by Conv. UFLS	
					f_{min} , Hz	Add. Conv. UFLS, MW	f_{min} , Hz	Add. Conv. UFLS, MW	f_{min} , Hz	Add. Conv. UFLS, MW
A	670	120	48.9	150	49.06	-	N/A	-	N/A	-
B	800	960	48.1	280	48.4	480	48.72	240	49.48	-
C	800	720	48.29	800	49.4	-	N/A	-	N/A	-
D	800	480	48.45	330	48.9	120	N/A	-	N/A	-

The scenarios in the test case set No. 2 were very diverse in terms of level of total system inertia and the parameters of the primary frequency control regulators. Scenario A had a high system inertia, which explains the minimal amount of P_{load_UFLS} and ΔP_{SC} . In scenario B the system inertia was high but the power reserves of all of the remaining synchronous generators in the system were zero as the delivered active power of all remaining synchronous machines is equal to their rated apparent power: it is a rather unrealistic scenario but nevertheless included in the test case set. The amount load shed by conventional UFLS P_{load_UFLS} in scenario B was exceptionally large and even with this large amount of load shed the frequency falls down to unacceptable value of 48.1 Hz. This all due to the missing capability of the synchronous generators in the system to contribute with any active power. The response of the SC ΔP_{SC} in this scenario is also almost the double of that in scenario A with a similar level of system inertia. In the scenario B the coefficient K had to be brought up to $K = 3$ so that the $P_{load_novel_LS}$ could match the P_{load_UFLS} for that scenario and prevent the fall of frequency to an unacceptable level. The proposed LS method shows clearly it’s advantage in this particular scenario, but also highlights the fact that the novel approach LS coefficient K may have to possess a dynamic value proportional to the total system inertia. The determination of an algorithm for estimation of K for real system applications will be one of the topics of further research.

Scenarios C and D have also shown that the proposed LS method significantly improves frequency response, especially for the low-inertia scenario C.

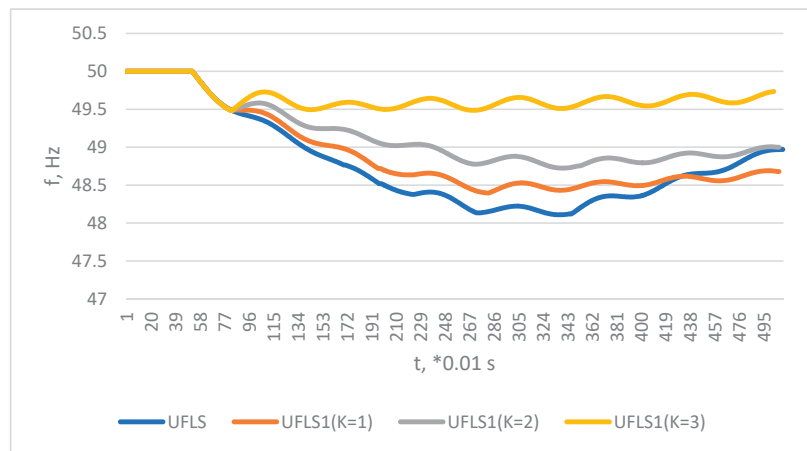


Figure 13. Frequency responses, scenario B.

4. Discussion

A principle of a novel LS method was introduced and two sets of case studies on assessment of the effect of the proposed approach were carried out. The case study sets were executed on two different and independent grid models and simulation software types. For every set and scenario the analysis of the response of SC was examined—active power injections of the SC during such incidents were observed and analyzed; for every set and scenario the effect of the proposed LS method was examined—the frequency responses for conventional UFLS and the novel LS approach were analyzed. Scenarios of the test cases had different system inertia levels, the topology of the grid was constant for every test case set.

Test case set No. 1—based on a simpler model topology—has shown that the response of the SC in case of contingency is related to the total system inertia level. For the highest inertia scenario (scenario B) no UFLS (either classic or novel) is triggered due to the vast contribution of the synchronous generators to the stabilization of frequency. The scenario A with 2nd highest system inertia a moderate response of the UFLS is registered and the novel LS method also provides only a modest contribution to the frequency stability.

Both low inertia scenarios (C and D) of the test case set No. 1 have shown that the proposed LS scheme provides a significantly improved post-contingency frequency response providing an effective measure for frequency stabilization. This verdict provides an important point—the proposed LS method is exceptionally suited for systems where the main source of inertia are synchronous condensers. The threshold of system inertia level at which the proposed LS method provides added value is the subject for further research on this topic.

Test case set No. 2—with a more detailed topology—shows similar results as the test case set No. 1: in high inertia scenarios the amount load shed decreases, which is logical due to the response of the synchronous generators in the system. Once again it is clear that the proposed LS method only provides a limited added value in frequency support in the high inertia scenarios.

As in the test case set No. 1, in the scenario with low system inertia (scenario C) the SC provide an intensive response to the contingency and the proposed LS method shows outstanding results in supporting the system frequency. We confirm once again that the contribution of the proposed LS method increases with decreasing system inertia. This also means that the practical implementation of the proposed LS method should possess a certain system inertia threshold at which the scheme is activated—leaving the ground clear for the conventional UFLS for system inertia levels larger than this threshold. The determination of the system inertia threshold is a matter of detailed simulations using practical topology of the grid the novel LS method is intended to be used for.

The simulations altogether showed that SC actively counteract frequency disturbances caused by tripping of generation by injecting considerable amounts of active power into the grid. These injections are observed almost instantly, are of considerable size and are well measurable. Injections can be measured at $t \geq 20$ ms giving a principal basis for the triggering automation of the proposed LS method and proving the method to be perspective.

SC power injections are found to be mainly dependent on the total inertia amount in the system and on the amount of available spinning reserves. This implies that for the proposed LS method the fact of activation of this novel scheme and the amount of LS to be activated is to be based on a logic taking account of:

- the SC active power injections
- the total system inertia level

For the Baltic power grid a uniform distribution of the SC in the grid is determined. The list of contingencies relevant for this scheme is static, definite, and coherent. This lays a foundation to create a dedicated automation concept for rapid LS scheme to ensure frequency control for Baltic power system in island mode in order to prevent socioeconomic costs caused by restrictions on power generation and imports to ensure safe island mode operation.

To determine the practical thresholds of system inertia level and the SC injection coefficients suitable for the implementation of the novel LS method and its operation algorithm, a detailed dynamic simulation in the relevant practical power grid have to be conducted taking in account the detailed grid topology. Such an analysis has to be done for different generation-load scenarios with varying total inertia levels of the power system. Such an in-depth analysis can provide a foundation for practical implementation algorithms of the proposed LS method in the relevant AC power system.

Several different automation concepts can be used to implement the proposed LS method in practice. The SC active power injection measurements can trigger a SCADA based LS algorithm which will calculate the amount of load-shedding needed and activate the load-shedding relays. The function of measuring the active power can be assigned to the terminals of microprocessor based relay protection (for example as an addition to out-of-step protection automation) since these devices use active and reactive components of the vectors of currents and voltages: U_a, U_r and I_a, I_r . [38,39] The measurements of this values at times t and $t + 1$ allow as to calculate the total active power injection based on elementary arithmetic operations according to Equation (6):

$$\Delta P(t + 1) = U_{a(t+1)}I_{a(t+1)} + U_{r(t+1)}I_{r(t+1)} - (U_{a(t)}I_{a(t)} + U_{r(t)}I_{r(t)}), \quad (6)$$

Figure 14 depicts a potential scheme for the SC measurement arrangement.

A flowchart of the proposed UFLS algorithm is presented in Figure 15. The voltage and current phasors are collected from PMUs as in Figure 14, and $\Delta P_{SC} = \sum_{i=1}^N \Delta P_{SC_i}$ is computed according with Equation (6). Load shedding sequence is triggered when ΔP_{SC} exceeds the minimum allowed imbalance value P_{min} . At next step the amount of load to be shed P_{load_LS} is calculated. The K coefficient is dependent on the percentage the non-synchronous sources constitute in total generated power. For a 100% non-synchronous generation, $K = 1$ and $P_{load_LS} = P_{SC}$. It should be also noted, that for a simplistic case the coefficient could be set to $K = 1$. Such setting suits all configurations of the network and all generation types' scenarios because over-shedding will never happen; but we still benefit from the quick tripping of certain amount of load. The final step is sending a trip commands to appropriate relays/IEDs according with calculated P_{load_LS} .

The proposed here LS scheme triggers (SC injections) can as well be used in the automation algorithms for triggering of fast frequency reserve such as primary reserve provided by battery energy storage units etc.

One of the biggest challenges for the practical implementations of the proposed LS scheme as seen by the authors would be transmitting the disconnection commands to hundreds or even thousands of loads. One of the solutions to this may be involving load aggregators which can be used for a number of purposes, including demand response [40,41].

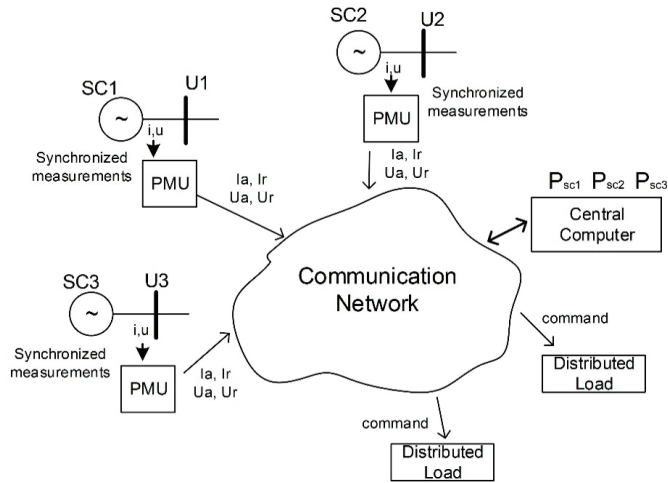


Figure 14. Potential scheme SC measurement arrangement for the proposed LS method tripping.

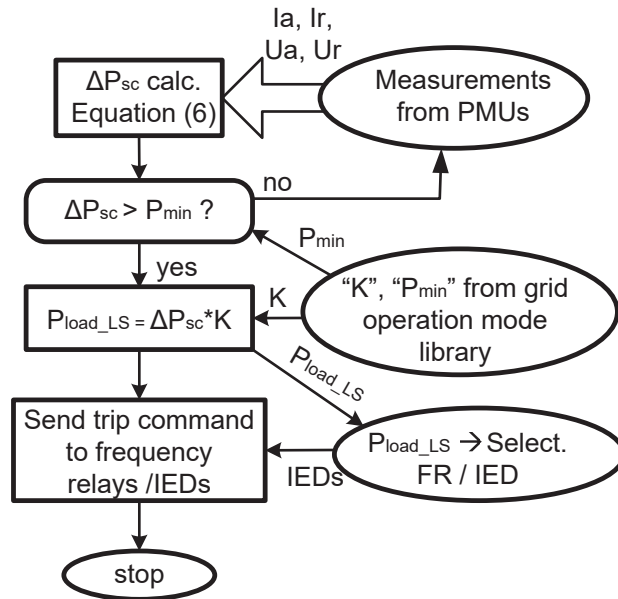


Figure 15. Potential execution algorithm.

5. Conclusions

The study shows that synchronous condensers in an AC power system respond with active power injections during a loss-of-generation incident. These injections are almost instant and are of considerable size and well measurable. The injections vary with the size of the tripped generator and are affected by the electrical distance between the SC itself and the tripped generator.

The test case set simulations show that the proposed LS method is best suited for low system inertia power systems and the proposed LS approach significantly improves the post-contingency frequency response and the frequency stability of low inertia power systems.

The study concludes that a proposed LS method based on the active power injections by the SC can have a right to be used. To develop the proposed LS concept further studies on the relevant power system topology, with real SC locations in the HV grid and on different total system inertia levels are needed. This will help to determine all the relevant parameters for the design and operation of a practical LS algorithm based on the proposed LS method.

Author Contributions: The contributions of the authors to this paper are as follows: the main idea was proposed by all the authors. A.S. and G.J. contributed to the methodology and data supervision. D.G., A.U. and J.S. performed the simulations for the case study and the paper writing—original draft preparation. All authors have read and agreed to the published version of the manuscript.

Funding: This article has been supported: by Latvian Council of Science, project: Management and Operation of an Intelligent Power System (I-POWER) (No. Izp-2018/1-0066) and by the Ministry of Economics of the Republic of Latvia, project “Future-proof development of the Latvian power system in an integrated Europe (FutureProof)”, project No. VPP-EM-INFRA-2018/1-0005 and project “Innovative smart grid technologies and their optimization (INGRIDO)”, project No. VPP-EM-INFRA-2018/1-0006.

Institutional Review Board Statement: Not applicable.

Informed Consent Statement: Not applicable.

Data Availability Statement: The data presented in this study are available on request from the corresponding author.

Conflicts of Interest: The authors declare no conflict of interest.

Abbreviations

LS	Load shedding
UFSL	Under-frequency load shedding
ROCOF	Rate of change of frequency
AC	Alternating current
EU	European Union
MV/HV	Medium voltage/high voltage
UPS	Unified Power System of Russia
HVDC	High voltage direct current
CHP	Combined heat and power
ENTSO-E	European Network of Transmission System Operators for Electricity
TSO	Transmission systems operator
SC	Synchronous condenser
COI	Centre of inertia
TEC2	Riga TEC2 CHP power plant
HPP	Hydro power plant

References

1. UN Framework Convention on Climate Change. *The Paris Agreement*; UN Framework Convention on Climate Change: Rio de Janeiro, Brazil, 2016.
2. European Union. *2030 Climate & Energy Framework*; European Union: Brussels, Belgium, 2020.
3. European Union. *Integrated National Energy and Climate Plan*; European Union: Brussels, Belgium, 2020.
4. Germany Trade & Invest. *Business Opportunities in Germany*; Germany Trade & Invest: Berlin, Germany, 2018; p. 4.
5. Dreidy, M.; Mokhlis, H.; Mekhilef, S. Inertia response and frequency control techniques for renewable energy sources: A review. *Renew. Sustain. Energy Rev.* **2017**, *69*, 144–155. [[CrossRef](#)]
6. Tielens, P.; van Hertem, D. Grid Inertia and Frequency Control in Power Systems with High Penetration of Renewables. In *Proceedings of the Young Researchers Symposium in Electrical Power Engineering, Delft, The Netherlands, 16–17 April 2012*.
7. Moser, A. *Planung und Betrieb von Elektrizitätsversorgungssystemen, Skriptum zur Vorlesung*; IAEW: Aachen, Germany, 2012; pp. 151–153.
8. Machowski, J.; Bialek, J.W.; Bumby, J.R. *Power System Dynamics*, 2nd ed.; John Wiley & Sons: Aachen, Germany, 2008; p. 171.

9. Delfino, B.; Massucco, S.; Morini, A.; Scalera, P.; Silvestro, F. Implementation and comparison of different under frequency load-shedding schemes. In Proceedings of the 2001 Power Engineering Society Summer Meeting (Cat. No.01CH37262), New York, NY, USA, 16–18 October 1989; IEEE: Piscataway, NJ, USA, 2001; Volume 1, pp. 307–312.
10. Rudez, U.; Mihalic, R. Comparison of adaptive UFLS schemes in modern power systems. In Proceedings of the 2010 IEEE Electrical Power & Energy Conference, San Diego, CA, USA, 22–26 July 2012; IEEE: Piscataway, NJ, USA, 2011; pp. 233–238.
11. Ben Kilani, K.; Elleuch, M.; Hamida, A.H. Dynamic under frequency load shedding in power systems. In Proceedings of the 2017 14th International Multi-Conference on Systems, Signals & Devices (SSD), Marrakech, Morocco, 28–31 March 2017; IEEE: Piscataway, NJ, USA, 2017; pp. 377–382.
12. Zare, F.; Ranjbar, A.; Faghihi, F. Intelligent topology-oriented load shedding scheme in power systems. In Proceedings of the 2019 27th Iranian Conference on Electrical Engineering (ICEE), Yazd, Iran, 30 April–2 May 2019; IEEE: Piscataway, NJ, USA, 2019; pp. 652–656.
13. Jianjun, Z.; Dongyu, S.; Dong, Z.; Yang, G. Load Shedding Control Strategy for Power System Based on the System Frequency and Voltage Stability (Apr 2018). In Proceedings of the 2018 China International Conference on Electricity Distribution (CICED), Tianjin, China, 17–19 September 2018; IEEE: Piscataway, NJ, USA, 2018; pp. 1352–1355.
14. Talaat, M.; Hatata, A.; Alsayyari, A.S.; Alblawi, A. A smart load management system based on the grasshopper optimization algorithm using the under-frequency load shedding approach. *Energy* **2020**, *190*, 116423. [[CrossRef](#)]
15. Rudez, U.; Mihalic, R. Trends in WAMS-based under-frequency load shedding protection. In Proceedings of the IEEE EUROCON 2017-17th International Conference on Smart Technologies, Ohrid, Macedonia, 6–8 July 2017; IEEE: Piscataway, NJ, USA, 2017; pp. 782–787.
16. European Commission. *The Baltic Power System Between East and West Interconnections*, JRC Science for Policy Report; European Commission: Brussels, Belgium, 2016.
17. AS Augstsprieguma Tikls; Latvian TSO; Riga, Latvia. Personal communication, 2020.
18. NordPoolSpot. Available online: <https://www.nordpoolgroup.com/> (accessed on 15 December 2020).
19. European Commission. *Energy Security: The Synchronisation of the Baltic States' Electricity Networks—European Solidarity in Action*; European Commission: Brussels, Belgium, 2019.
20. Junghans, G.; Silis, A.; Marcina, K.; Ertmanis, K. Role of Balancing Markets in Dealing with Future Challenges of System Adequacy Caused by Energy Transmission. *Latv. J. Phys. Tech. Sci.* **2020**, *57*, 48–56. [[CrossRef](#)]
21. Republic of Estonia. *Estonia's 2030 National Energy and Climate Plan*; Republic of Estonia: Talin, Estonia, 2019.
22. Republic of Latvia. *Latvia's National Energy and Climate Plan 2021–2030*; Republic of Latvia: Riga, Latvia, 2020.
23. Republic of Lithuania. *National Energy and Climate Action Plan of the Republic of Lithuania for 2021–2030*; Republic of Lithuania: Vilnius, Lithuania, 2021.
24. Ivanova, P.; Sauhats, A.; Linkevics, O. Towards optimization of combined cycle power plants' start-ups and shut-down. In Proceedings of the 2016 57th International Scientific Conference on Power and Electrical Engineering of Riga Technical University (RTUCON), Riga, Latvia, 13–14 October 2016; IEEE: Piscataway, NJ, USA, 2016; pp. 1–6.
25. Payerl, C. *Introduction to ABB Synchronous Condenser Offering—A Solution to Improve Grid Strength*; IEEE: Piscataway, NJ, USA, 2020.
26. Szaba, C. Synchronous condensers. An old tool rediscovered to address new grid challenges. *Power Eng. Int.* **2017**, *11*, 1782–1789.
27. Terzija, V.V. Adaptive Underfrequency Load Shedding Based on the Magnitude of the Disturbance Estimation. *IEEE Trans. Power Syst.* **2006**, *21*, 1260–1266. [[CrossRef](#)]
28. Anderson, P.M.; Mirheydar, M. An adaptive method for setting underfrequency load shedding relays. *IEEE Trans. Power Syst.* **1992**, *7*, 647–655. [[CrossRef](#)]
29. Rudez, U.; Mihalic, R. Monitoring the First Frequency Derivative to Improve Adaptive Underfrequency Load-Shedding Schemes. *IEEE Trans. Power Syst.* **2011**, *26*, 839–846. [[CrossRef](#)]
30. Laghari, J.A.; Mokhlis, H.; Karimi, M.; Abu Bakar, A.H.; Mohamad, H. A New Under-Frequency Load Shedding Technique Based on Combination of Fixed and Random Priority of Loads for Smart Grid Applications. *IEEE Trans. Power Syst.* **2014**, *30*, 2507–2515. [[CrossRef](#)]
31. Deb, N.; Papari, B.; Ozkan, G.; Badr, P.R.; Hoang, P.H.; Edrington, C.S. An Intelligent Load Shedding Scheme for the Micro-grid in Shipboard Power System Using Probabilistic Methods. In Proceedings of the 2020 Clemson University Power Systems Conference (PSC), Clemson, SC, USA, 10–13 March 2020.
32. Rudez, U.; Mihalic, R. Analysis of Underfrequency Load Shedding Using a Frequency Gradient. *IEEE Trans. Power Deliv.* **2011**, *26*, 565–575. [[CrossRef](#)]
33. Frigo, G.; Derviskadic, A.; Zuo, Y.; Paolone, M. PMU-Based ROCOF Measurements: Uncertainty Limits and Metrological Significance in Power System Applications. *IEEE Trans. Instrum. Meas.* **2019**, *68*, 3810–3822. [[CrossRef](#)]
34. Guzs, D.; Utans, A.; Sauhats, A.; Junghans, G.; Silinevics, J. Resilience of the Baltic power system when operating in island mode. In Proceedings of the 2020 IEEE 61th International Scientific Conference on Power and Electrical Engineering of Riga Technical University (RTUCON), Riga, Latvia, 5–7 November 2020; Institute of Electrical and Electronics Engineers (IEEE): Piscataway, NJ, USA, 2020; pp. 1–6.
35. Rubio, A.; Behrends, H.; Geißendörfer, S.; von Maydell, K.; Agert, C. Determination of the Required Power Response of Inverters to Provide Fast Frequency Support in Power Systems with Low Synchronous Inertia. *Energies* **2020**, *13*, 816. [[CrossRef](#)]
36. Siemens Power Technologies Inc. *PSS/E-34 Program Operational Manual*; Siemens Power Technologies Inc.: New York, NY, USA, 2019.

37. Operation Technology Inc. *ETAP Products & Solutions Comprehensive, Integrated Suite of Power System Software Modules from Design to Operation*; ETAP Electrical Power System Analysis Software; Operation Technology Inc.: Irvine, CA, USA, 1995.
38. Sauhats, A.; Svalova, I.; Svalovs, A.; Antonovs, D.; Utans, A.; Bochkarjova, G. Two-terminal out-of-step protection for mul-ti-machine grids using synchronised measurement. In Proceedings of the 2015 IEEE Eindhoven PowerTech, Eindhoven, The Netherlands, 29 June–2 July 2015.
39. Sauhats, A.; Utans, A.; Antonovs, D.; Svalovs, A. Angle Control-Based Multi-Terminal Out-of-Step Protection System. *Energies* **2017**, *10*, 308. [[CrossRef](#)]
40. Palensky, P.; Dietrich, D. Demand Side Management: Demand Response, Intelligent Energy Systems, and Smart Loads. *IEEE Trans. Ind. Inform.* **2011**, *7*, 381–388. [[CrossRef](#)]
41. Jabir, H.J.; Teh, J.; Ishak, D.; Abunima, H. Impacts of Demand-Side Management on Electrical Power Systems: A Review. *Energies* **2018**, *11*, 1050. [[CrossRef](#)]

Article

A Heuristic Algorithm for Combined Heat and Power System Operation Management

Muhammad Faisal Shehzad ^{1,*}, Mainak Dan ², Valerio Mariani ¹, Seshadhri Srinivasan ³, Davide Liuzza ⁴, Carmine Mongiello ⁵, Roberto Saraceno ⁶ and Luigi Glielmo ¹

- ¹ Group for Research on Automatic Control Engineering, Department of Engineering, University of Sannio, Piazza Roma 21, 82100 Benevento, Italy; vmariani@unisannio.it (V.M.); glielmo@unisannio.it (L.G.)
 - ² Interdisciplinary Graduate Programme, Nanyang Technological University Computational Intelligence Laboratory, Blk N4, B1a-02, Singapore 639798, Singapore; mainak001@e.ntu.edu.sg
 - ³ Berkeley Education Alliance for Research in Singapore, Singapore 138602, Singapore; seshadhri.srinivasan@bears-berkeley.sg
 - ⁴ Fusion and Technology for Nuclear Safety and Security Department, Italian National Agency for New Technologies, Energy and Sustainable Economic Development (ENEA), 00044 Rome, Italy; davide.liuzza@enea.it
 - ⁵ Energy Technologies and Renewable Sources Department, Italian National Agency for New Technologies, Energy and Sustainable Economic Development (ENEA), 80055 Portici, Italy; carmine.mongiello@enea.it
 - ⁶ AtenaTech srl, 00044 Rome, Italy; roberto.saraceno@atenatech.it
- * Correspondence: mshehzad@unisannio.it

Abstract: This paper presents a computationally efficient novel heuristic approach for solving the combined heat and power economic dispatch (CHP-ED) problem in residential buildings considering component interconnections. The proposed solution is meant as a substitute for the cutting-edge approaches, such as model predictive control, where the problem is a mixed-integer nonlinear program (MINLP), known to be computationally-intensive, and therefore requiring specialized hardware and sophisticated solvers, not suited for residential use. The proposed heuristic algorithm targets simple embedded hardware with limited computation and memory and, taking as inputs the hourly thermal and electrical demand estimated from daily load profiles, computes a dispatch of the energy vectors including the CHP. The main idea of the heuristic is to have a procedure that initially decomposes the three energy vectors' requests: electrical, thermal, and hot water. Then, the latter are later combined and dispatched considering interconnection and operational constraints. The proposed algorithm is illustrated using series of simulations on a residential pilot with a nanogenerator unit and shows around 25–30% energy savings when compared with a meta-heuristic genetic algorithm approach.

Keywords: combined heat and power; co-generation; energy storage system; energy management; heuristics; genetic algorithm; low-cost computing platform

Citation: Shehzad, M.F.; Dan, M.; Mariani, V.; Srinivasan, S.; Liuzza, D.; Mongiello, C.; Saraceno, R.; Glielmo, L. A Heuristic Algorithm for Combined Heat and Power System Operation Management. *Energies* **2021**, *14*, 1588. <https://doi.org/10.3390/en14061588>

Academic Editor: Adrian Ilinca

Received: 1 February 2021

Accepted: 9 March 2021

Published: 12 March 2021

Publisher's Note: MDPI stays neutral with regard to jurisdictional claims in published maps and institutional affiliations.



Copyright: © 2021 by the authors. Licensee MDPI, Basel, Switzerland. This article is an open access article distributed under the terms and conditions of the Creative Commons Attribution (CC BY) license (<https://creativecommons.org/licenses/by/4.0/>).

1. Introduction

Buildings equipped with multi-energy systems are an increasing trend due to the high energy efficiencies that could be achieved. In particular, the combined heat and power (CHP) systems that generate both electrical and thermal energy exploiting their inherent operating cycle [1,2] are vital components. There have been concerted efforts from building owners to replace single energy generators with higher efficiency CHP units. In comparison with traditional electrical and heat-only units, the CHP units can save 10–40% of the costs of generation, which means an equal amount of heat and electricity production with less fuel [3]. While this transition has increased CHP deployments across buildings (residential, commercial, and institutional), there are concerns regarding their return on investments. In addition, coordinating CHP units with roof-top solar, energy storage devices, and other components is important for building energy management.

The CHP economic dispatch (CHP-ED) that aims to minimize fuel cost/consumption respecting constraints (operating and physical) is seen as a promising solution to guarantee fast return on investments [4]. However, multi energy systems (MES) scheduling, due to nonlinearity and non-convexity, is a quite challenging optimization problem [5]. Solving CHP-ED problem requires specialized hardware and sophisticated algorithm/solvers with large computation resources, long solution time, and sensitivity to initial conditions, thereby making their adoption in buildings difficult. In general, the need for a scalable and simple scheduling approach for solving CHP-ED problems is widely recognized in industry (see, [6–9] and references therein) especially for the building level units. This investigation aims to propose one of such approaches for deploying CHP-ED problems on simple embedded hardware with minimum memory and computing power.

Contributions

The main contributions of the paper are:

1. A fast heuristic algorithm for single CHP plant to address residential CHP-ED problems. The main idea here is to decompose the problem into three parts: electrical, domestic hot water, and heat demands. Then, a suitable heuristic is designed to combine them:
2. A linear single CHP algorithm incorporating thermal and electrical demands and a holistic model for capturing the interactions among energy vectors in a building.
3. Illustrating the proposed heuristics on a nano-cogenerator and multi-energy systems in a building.

The paper is organized as follows: in Section 2, relevant papers from the literature will be revised; Section 3 presents the mathematical model of the CHP system and an evaluation criterion; Section 4 proposes a benchmarking optimization problem for the proposed heuristic method; finally, in Section 6, the results of some numerical experiments are showed.

2. Literature Review

The achievement of a stable economic growth where the possible increase of energy consumption and greenhouse gas emissions can be handled in a sustainable perspective is one of the main aspects the principal policy-makers are focused on today. In particular, the sustainable economic growth should be pursued with policies appealing also for emerging economies so as to maximize their impact worldwide. For instance, Larissa et al. [10] show that the aim of achieving a low carbon economy or a green economy is inherent with the concept of sustainable development. It also calls for preventing the depletion of natural resources, which should benefit future generations. The authors also believe that the adjusted net savings constitute one of the means to attain this aim. They highlight that the policy makers should promote new policies in accordance with the other elements of adjusted net savings, for the purpose of increasing the gross domestic product, consolidating a strong level of sustainable economic growth and reducing CO₂ emissions and greenhouse gas effects. Ioan et al. in [11] argue that the sustainable economic growth is a desirable goal for every economy, as it helps to implement the Paris Agreement on global warming [12]. Sustainable economy includes certain core principles such as the consumption of renewable and non-renewable resources without depriving society of future benefits, sustainable human development, sustainable investment, and innovation. Specifically, sustainable development means achieving development without environmental degradation. In this context, sustainable growth suggests a transformation of the brown economy into a green or low-carbon economy.

The energy sector is the main contributor to global warming with 42% share of greenhouse gas emissions [13]. To reduce the environmental impact of the energy sector, it is necessary to target not only the energy supply but also the energy end-use. Policies have been globally implemented to encourage the decarbonization of energy supply by incentivizing the switch to less polluting fuels (e.g., from coal to gas) and the deployment of wind and

solar renewable power plants [14]. Concerning the decarbonization of the energy end-use, instead, policies and incentives have been widely studied and already implemented in the industrial/commercial sector, while the residential sector is often not considered despite its potentially significant role in emissions reduction [15]. One option to reduce the carbon emissions associated with the electric demand of a residential facility is through on-site Variable Renewable Energy (VRE) generation. Renewable sources such as solar and wind could be exploited on-site to generate fuel-free electricity, reducing the annual energy costs and the CO₂ emissions [16]. However, electricity demand accounts only for around 30% of the total EU industrial energy consumption [17], while the remaining 70% consists of thermal energy demand at various temperatures. Heat is a relatively carbon intensive end-use since it mostly relies on fossil fuels: e.g., in 2000, the majority of the final consumption of heat in Europe was from oil (59%) and gas (24%). By 2018, the share of heat produced from gas increased to 40% and the share of heat from oil decreased to 42%, but, despite this switch, CO₂ emissions related to the heating sector increased by 6.4% [18].

Among the many, one possible solution for reducing the environmental impact of both electricity and heat demand is Combined Heat and Power (CHP). CHP is an efficient and cleaner way to generate electrical power and heat energy from a single fuel source. In order to utilize CHP units more efficiently, the economic dispatch problem is applied to determine the optimal combination of the power and heat sources' outputs to satisfy heat and power demand of a system, simultaneously, accounting for and operational constraints.

The CHP-ED approach presented in this research work complies fully with the sustainable energy development strategies that typically involve three major technological changes: energy savings, efficiency improvements in the energy production, and maximization of the integration of renewable energy sources via fossil fuels' usage reduction.

Existing approaches for solving CHP-ED problems could be broadly discerned into: (i) mathematical programming based techniques, (ii) heuristics, (iii) meta-heuristics, and (iv) hybrid techniques.

Mathematical programming and, in particular, linear programming (LP) models have been the traditional tool to model CHP-ED problems thanks to their ability to capture complex switching behaviors [19,20]. In addition, the mixed integer linear programming (MILP) technique has been used in [21] for scheduling CHP units in residential buildings. Steen et al. [20] apply the MILP technique to assess the viability of integrating the distributed energy resources with a thermal energy storage (TES) system. Wouters et al. [22] used MILP to identify the optimal design of the existing grid infrastructures through integration of renewable energy units and microgrids. In [23,24], residential application based energy management systems (EMSs) are presented. Ford et al. [25] show that home energy market products may help users to save energy through load shifting with the trade off of potential benefits comfort, convenience, and security. However, other mathematical programming approaches such as Benders decomposition [26], Lagrangian relaxation [27], branch-and-bound algorithms [28,29], and mixed-integer nonlinear programming [30] have also been studied for CHP-ED problems. The main objective in these works is to minimize the operational costs for meeting energy demand over the entire planning horizon [31]. However, their implementation is cumbersome.

This could be overcome by heuristic and meta-heuristic methods. In the past, such methods have shown promise as well for CHP-ED problem [32].

Rafique et al. [23] employs a genetic algorithm (GA) for a smart home energy management to obtain electrical and gas resources optimal scheduling. Instead, Allegrini et al. [33] developed a model based software tools that addresses district-level energy systems. Ahmadi et al. in [6] presented a multi-objective optimization technique which was solved using a GA-based fuzzy decision algorithm. Alomoush et al. [34] presented an improved stochastic fractal search algorithm to solve the CHP-ED optimization problem by satisfying different inequality and equality constraints and interdependent limits. The algorithm handled the constraints by penalizing infeasible solutions during the iterative

process, where the constrained CHP-ED problem is transformed into an unconstrained one. Nazari et al. [35] presented a “whale optimization algorithm” (WOA) for solving the CHP-ED problem; WOA is a new meta-heuristic approach for solving optimization problems, inspired by the social behavior of humpback whales. The authors proved WOA efficiency, feasibility, and capability of obtaining better solutions with respect to other meta-heuristics optimization techniques in terms of operational cost and its implementation ability at larger scales. Maleki et al. [36] propose a GA-based improved penalty function formulation to solve the CHP-ED problem. However, their applicability to EMS is arguable due to their solution times, and parameter initialization effects on the solution.

Hybrid algorithms combine meta-heuristics and mathematical approaches to solve the CHP-ED problem, but their complexity is still high. The heuristic based solvers provide advantages over existing approaches [37] in that they can treat the complex behaviors and reduce computational costs. Notwithstanding this, building the right heuristic is challenging, especially in the presence of operational and physical constraints. To the best of our knowledge, a heuristic approach which could be implemented on simple hardware has not been fully explored for the multi-vector scheduling problems for building applications.

3. System Description and Modeling

Figure 1 depicts the considered CHP system architecture along with the relevant energy flows of all the energy vectors involved. The system consists of a nano co-generation unit (CHP) which provides both electrical and thermal energy. The other thermal units consist of a thermal solar panel (TSP), a heat exchanger (HE), a thermal energy storage (TES) and a heat pump (HP). The electrical system comprises photo-voltaic panels (PVs), wind turbines (WTs), electrical storage systems (ESSs). Furthermore, the water pumps PM_1 , PM_2 , and PM_3 are reported as they either enable or disable the corresponding flow toward the downstream system and will be operated according to the heuristic strategy here developed. This section describes the model of the system used in this study. The total power required by the system is equal to the sum of the demands for electric, heating, and hot water powers. The description of the parameters, the electric powers, and the thermal power requests used in the proposed formulation are described in Tables 1–3.

Table 1. System model parameters.

Parameters	Description
Δt	Sampling time [h]
δ_{CHP}	ON-OFF state of the nano co-generation unit (CHP)
δ_{HP}	ON-OFF state of the heat pump (HP)
P_{CHP}	CHP Output Electrical power
\dot{Q}_{CHP}	CHP Output thermal power [kW]
σ_{CHP}	Operational state of the CHP
$P_{\text{CHP}}^{\text{max}}$	Rated power output of CHP [kW]
$\delta_{\text{PM}_1}(k)$	ON-OFF state of the Water Pump 1
$\delta_{\text{PM}_2}(k)$	ON-OFF state of the Water Pump 2
$\delta_{\text{PM}_3}(k)$	ON-OFF state of the Water Pump 3
$P_{\text{PM}_1}(k)$	Water Pump 1 rated electrical consumption [kW]
$P_{\text{PM}_2}(k)$	Water Pump 2 rated electrical consumption [kW]
$P_{\text{PM}_3}(k)$	Water Pump 3 rated electrical consumption [kW]
SOC_{ESS}	Electrical storage system (ESS) State of charge [kWh]
$\text{SOC}_{\text{ESS}}^{\text{min}}$	Minimum value of SOC_{ESS}
$\text{SOC}_{\text{ESS}}^{\text{max}}$	Maximum value of SOC_{ESS}

Table 1. Cont.

Parameters	Description
η_C	Charging efficiency of ESS
η_D	Discharging efficiency of ESS
$P_{ESS,Ch}$	ESS rated charging power [kW]
$P_{ESS,D}$	ESS rated discharging power [kW]
SOC_{HE}	State of charge of the heat exchanger [kWh]
$\dot{Q}_{HP \rightarrow HE}$	Heat pump to heat exchanger thermal power shunting [kW]
P_{RHE}	Electrical power of the thermal energy storage resistor [kW]
σ_{RHE}	Resistor heat-power ratio
$\dot{Q}_{HE \rightarrow TES}$	Thermal power flow from heat exchanger-thermal energy storage [kW]
SOC_{TES}	State of charge of thermal energy system [kWh]
$\dot{Q}_{HP \rightarrow TES}$	Heat pump to thermal energy storage thermal power flow [kW]
δ_{RTES}	ON-OFF state of the thermal energy storage resistor
δ_{RHE}	ON-OFF state of the heat exchanger resistor
σ_{RTES}	Heat-power ratio of the resistor associated with thermal energy storage
P_{RTES}	Electrical power of the thermal energy storage resistor [kW]
c_F	Fuel cost [€L^{-1}]
V_{HE}	Heat exchanger tank volume [L]
T_{HE}	Heat exchanger temperature [K]
T_{HE}^{set}	Set point temperature of the heat exchanger [K]
V_{TES}	Tank volume of the thermal energy storage [L]
T_{TES}	Thermal energy storage temperature [K]
T_{TES}^{set}	Set point temperature of the thermal energy storage [K]
\dot{Q}_{HP}^{min}	Heat pump minimum thermal flow [kW]
\dot{Q}_{HP}^{max}	Heat pump maximum thermal flow [kW]
T_{HP}	Heat pump temperature [K]
T_{amb}	Ambient temperature [K]

Table 2. Electric powers.

Power Forecasts	Description
P_{PV}	Solar power production [kW]
P_W	Wind power production [kW]
P_D	Electric demand [kW]

Table 3. Thermal powers.

Forecasts	Description
\dot{Q}_{TSP}	Thermal solar panel production [kW]
\dot{Q}_{DH}	Heat demand [kW]
\dot{Q}_{DHW}	Hot water demand [kW]

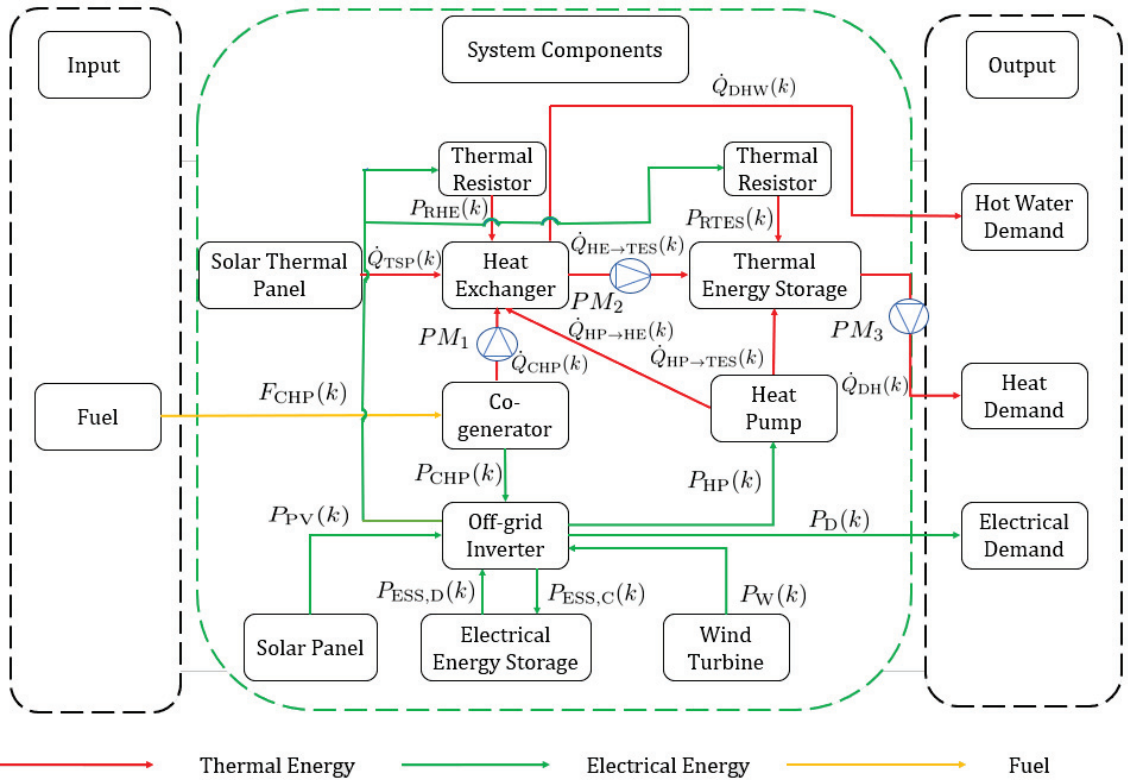


Figure 1. System Architecture. The yellow lines represent the gasoline (fuel) flows, and the green lines represent the electrical energy flows, while red lines represent the thermal energy flows.

3.1. Nano Co-Generation Unit

We let the ON-OFF state of the CHP at the time instant k be identified by the binary operating signal δ_{CHP} . Thus,

$$\delta_{CHP}(k) = 1 \implies P_{CHP}^{min} \leq P_{CHP}(k) \leq P_{CHP}^{max}, \tag{1}$$

where P_{CHP}^{max} and P_{CHP}^{min} are the maximum and minimum rated output powers of the CHP. When the CHP is in the ON state, the produced heat that is recovered through a water jacket from the exhaust output is

$$\dot{Q}_{CHP}(k) = \sigma_{CHP} \delta_{CHP}(k) P_{CHP}(k), \tag{2}$$

where $0 < \sigma_{CHP} < 1$ is the heat-to-power conversion ratio of the CHP. The water flow inside the water jacket is controlled by a water pump (PM_1), whose operation regulates the water flow from the CHP to the HE. Thus,

$$\delta_{CHP}(k) = 1 \iff \delta_{PM_1}(k) = 1, \quad \delta_{CHP}(k), \delta_{PM_1}(k) \in \{0, 1\}, \forall k, \tag{3}$$

where $\delta_{CHP}(k)$ is the logical variable used to model the state of the CHP, while $\delta_{PM_1}(k)$ is the PM_1 logical state variable. In other words, in order to use the available energy efficiently, PM_1 can be ON only if CHP is ON.

3.2. Electrical Storage System

The ESS is modeled by considering its state of charge $\text{SOC}_{\text{ESS}}(k)$ at each instant k . The dynamical model is

$$\text{SOC}_{\text{ESS}}(k+1) = \text{SOC}_{\text{ESS}}(k) + \left(\eta_C P_{\text{ESS},C}(k) - \frac{1}{\eta_D} P_{\text{ESS},D}(k) \right) \Delta t, \quad (4)$$

where $P_{\text{ESS},C}(k)$ is the charging power, $P_{\text{ESS},D}(k)$ is the discharging power, $\eta_C, \eta_D \in (0,1)$ are the charging and discharging efficiencies of the system, respectively. It has to be noted that the charging and discharging powers, and the storage capacity are bounded. The upper and lower limit can be depicted using the following simple constraints:

$$\begin{aligned} P_{\text{ESS},C}^{\min} &\leq P_{\text{ESS},C}(k) \leq P_{\text{ESS},C}^{\max}, \\ P_{\text{ESS},D}^{\min} &\leq P_{\text{ESS},D}(k) \leq P_{\text{ESS},D}^{\max}, \\ \text{SOC}_{\text{ESS}}^{\min} &\leq \text{SOC}_{\text{ESS}}(k) \leq \text{SOC}_{\text{ESS}}^{\max}, \end{aligned} \quad (5)$$

where the $\text{SOC}_{\text{ESS}}^{\min}$, and the $\text{SOC}_{\text{ESS}}^{\max}$ are the minimum and the maximum SOC_{ESS} within the range of 10% and 90%, respectively.

3.3. Heat Exchanger

In this study, the HE is storage, capable of supplying domestic hot water, and the water mixer is installed inside it. For the description of the SOC dynamics, we use a single-mass model [38], i.e.,

$$\frac{\text{SOC}_{\text{HE}}(k+1) - \text{SOC}_{\text{HE}}(k)}{\Delta t} = \dot{Q}_{\text{CHP}}(k) + \dot{Q}_{\text{TSP}}(k) + \dot{Q}_{\text{HP} \rightarrow \text{HE}}(k) + \delta_{\text{RHE}}(k) \sigma_{\text{RHE}} P_{\text{RHE}} - \dot{Q}_{\text{HE} \rightarrow \text{TES}}(k) - \dot{Q}_{\text{DHW}}(k) - \dot{Q}_{\text{HE,LOSS}}(k), \quad (6)$$

where $\text{SOC}_{\text{HE}}(k)$ is state of the charge of the HE (kWh), \dot{Q}_{DHW} is hot water demand (kW), $\dot{Q}_{\text{HE} \rightarrow \text{TES}}$ is the thermal power from the HE to the TES (kW), \dot{Q}_{CHP} is the thermal power output of the CHP (kW) at time instant k , $\dot{Q}_{\text{HP} \rightarrow \text{HE}}(k)$ is the transfer of the thermal power from the HP to the HE, P_{RHE} is the rated electrical power (kW) consumption by the resistor (RHE) if it is operating, i.e., $\delta_{\text{RHE}}(k) = 1, 0 < \sigma_{\text{RHE}} < 1$ is the power-to-heat conversion factor of the RHE and $\dot{Q}_{\text{HE,LOSS}}(k)$ is the loss term and depends upon the temperature difference between the HE and the ambient, and also on the heat loss coefficient and the surface area of the HE. The relation between $\text{SOC}_{\text{HE}}(k)$ and the temperature of the heat exchanger T_{HE} is given by

$$\text{SOC}_{\text{HE}}(k) = V_{\text{HE}} \rho_w C_w (T_{\text{HE}}(k) - T_{\text{HE}}^{\text{set}}), \quad (7)$$

where V_{HE} is the volume of the HE and $T_{\text{HE}}^{\text{set}}$ is the minimum set-point temperature. In addition, to maintain the minimum set-point temperature, the following constraint is imposed:

$$\text{SOC}_{\text{HE}}(k) \geq 0. \quad (8)$$

3.4. Thermal Storage System

Similar to the HE, the TES SOC is modeled as

$$\frac{\text{SOC}_{\text{TES}}(k+1) - \text{SOC}_{\text{TES}}(k)}{\Delta t} = \dot{Q}_{\text{HP} \rightarrow \text{TES}}(k) + \dot{Q}_{\text{HE} \rightarrow \text{TES}}(k) + \delta_{\text{RTES}}(k) \sigma_{\text{RTES}} P_{\text{RTES}} - \dot{Q}_{\text{DH}}(k) - \dot{Q}_{\text{TES,LOSS}}(k), \quad (9)$$

where $\text{SOC}_{\text{TES}}(k)$ is the state of charge of the TS (kWh), \dot{Q}_{DH} is the heat demand (kW), $\dot{Q}_{\text{HE} \rightarrow \text{TES}}$ is the thermal power from the HE to the TES (kW), \dot{Q}_{HP} is the thermal power output of the HP (kW), and $\dot{Q}_{\text{HP} \rightarrow \text{HE}}(k)$ is the transfer of the thermal power from the HP

to the TES, P_{RTES} is the rated electrical power (kW) consumption by the resistor (RTES) if it is operating, i.e., $\delta_{RTES}(k) = 1$, $0 < \sigma_{RTES} < 1$ is the power-to-heat ratio of the RTES and $\dot{Q}_{TES,LOSS}(k)$ is the loss and depends upon the temperature difference of the TES and the ambient, and also on the heat loss coefficient and the surface area of TES. Similar to the HE, the $SOC_{TES}(k)$ and T_{TES} relation is given by

$$SOC_{TES}(k) = V_{TES}\rho_w C_w(T_{TES}(k) - T_{TES}^{set}), \tag{10}$$

where V_{TES} is the volume of the TES and T_{TES}^{set} is the minimum set-point temperature. In addition, for the TES, the following constraint is imposed to maintain the minimum set-point temperature,

$$SOC_{TES}(k) \geq 0. \tag{11}$$

3.5. Heat Pump

The HP is operated by electricity and, considering its coefficient of performance (COP) and operating state $\delta_{HP}(k)$, is modeled as

$$\begin{aligned} \dot{Q}_{HP}(k) &= COP_{HP} \times P_{HP}(k), \\ \delta_{HP}(k)\dot{Q}_{HP}^{min} &\leq \dot{Q}_{HP}(k) \leq \delta_{HP}(k)\dot{Q}_{HP}^{max}, \quad \delta_{HP}(k) \in \{0, 1\}. \end{aligned} \tag{12}$$

In general, the COP_{HP} can vary according to the operating point of the HP as

$$COP_{HP} = \Psi[\dot{Q}_{HP}(k)], \tag{13}$$

where the nonlinear function $\Psi[\cdot]$ can be obtained by analyzing the P_{HP} v.s \dot{Q}_{HP} curve. However, we assume the COP value to be constant in the operating range considered.

3.6. Heat Pump Shunting between Heat Exchanger and Thermal Energy Storage

Both the HE and the TES can store thermal energy from the HP by proper shunting. The shunting operations are modeled by means of two binary signals denoted as $\delta_{HP \rightarrow HE}(k)$, $\delta_{HP \rightarrow TES}(k)$ and the auxiliary binary variable $\delta_{shunt}(k)$ as

$$\begin{aligned} \delta_{HP \rightarrow HE}(k) = 1 &\implies \dot{Q}_{HP \rightarrow HE}(k) = \dot{Q}_{HP}(k), \\ \delta_{HP \rightarrow TES}(k) = 1 &\implies \dot{Q}_{HP \rightarrow TES}(k) = \dot{Q}_{HP}(k). \end{aligned} \tag{14}$$

The following integer linear constraint denotes that only a single operation mode of the shunting is allowed at each time k :

$$\delta_{HP \rightarrow HE}(k) + \delta_{HP \rightarrow TES}(k) = \delta_{shunt}(k). \tag{15}$$

3.7. Power Balance

For benchmarking purposes, a GA optimization problem is also set up and presented later. The essence of the optimization model is to meet the thermal and electrical demands with renewable generation, using the CHP as a last option and, in case this happens, effectively exploiting the combined generation of heat and electrical power. In order to achieve a realistic optimal control policy, the following power balance equations must be satisfied at each time-step k :

$$\begin{aligned} P_D(k) &\leq P_{PV}(k) + P_W(k) + P_{CHP}(k) - P_{ESS,Ch}(k) + P_{ESS,Dis}(k) - P_{HP}(k) - P_{PM_1}\delta_{PM_1}(k) \\ &\quad - P_{PM_2}\delta_{PM_2}(k) - P_{PM_3}\delta_{PM_3}(k) - P_{RTES}\delta_{RTES}(k) - P_{RHE}\delta_{RHE}(k), \\ \dot{Q}_{DH}(k) &\leq \dot{Q}_{HP \rightarrow TES}(k) + \dot{Q}_{HE \rightarrow TES}(k) + \delta_{TES}(k)\sigma_{RTES}P_{RTES} + \frac{SOC_{TES}(k)}{\Delta t}, \\ \dot{Q}_{DHW}(k) &\leq \dot{Q}_{HP \rightarrow HE}(k) + \delta_{RHE}(k)\sigma_{RHE}P_{RHE} + \dot{Q}_{CHP}(k) + \dot{Q}_{TSP}(k) - \dot{Q}_{HE \rightarrow TES}(k) + \frac{SOC_{HE}(k)}{\Delta t}, \end{aligned} \tag{16}$$

where P_{PM_1} , P_{PM_2} , P_{PM_3} are the power consumptions of PM_1 , PM_2 and PM_3 , respectively.

4. Proposed Heuristics Formulation

The objective of the proposed heuristic energy dispatch strategy is to provide ON/OFF commands to the CHP system under investigation. The flow chart in Figure 2 describes the controller decision process.

The CHP system has to be operated the least possible without sacrificing the comfort in terms of electric, heat, and hot water. The overall problem is to decide how to effectively meet the electric and thermal demands of the commercial building by answering the following questions:

1. When should each equipment be switched on or off, and how much should it produce?
2. When should the electric and thermal storage be charged or discharged?

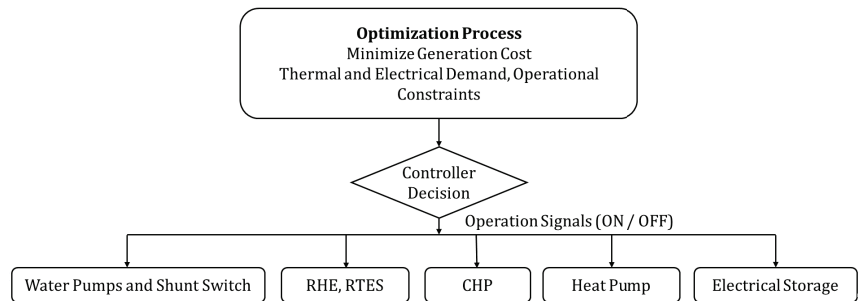


Figure 2. Energy management system schematic.

The CHP operation schedule is calculated with the proposed heuristic-based algorithm for heat, hot water, and electric demand and presented in the next subsections. It is worth mentioning that the heuristics developed for heat and hot water demand satisfactions consider the electrical energy consumption of the equipments i.e., the heat pump and the water pumps.

4.1. Heuristic Algorithm Module for Heat Demand Satisfaction

The heuristic algorithm is detailed in Figure 3 and described as follows:

- Step 1 The heat demand $\dot{Q}_{DH}(k)$ is first compared with the thermal energy stored in TES, by checking SOC_{TES} .
- Step 2 In case $\dot{Q}_{DH}(k)$ is not achievable with the available SOC_{TES} only, the algorithm is designed to set PM_2 to ON state, connecting HE with the TES so that both thermal storage are used.
- Step 3 If $\dot{Q}_{DH}(k)$ can not be satisfied even with HE and TES, the heat pump will be set to its ON state to cover the mismatch between the $\dot{Q}_{DH}(k)$ and the available thermal energy in the storage.
- Step 4 If the $\dot{Q}_{DH}(k)$ is not achieved with the available thermal power from heat pump, and thermal storage, the controller set the thermal resistor to ON state ($\delta_{RTES} = 1$).
- Step 5 As a last resort, if $\dot{Q}_{DH}(k)$ at a certain time is so large it can not be satisfied with the storage, the generation units, the thermal resistor, and the heat pump, the CHP will be set to ON state to meet the requested heat demand.

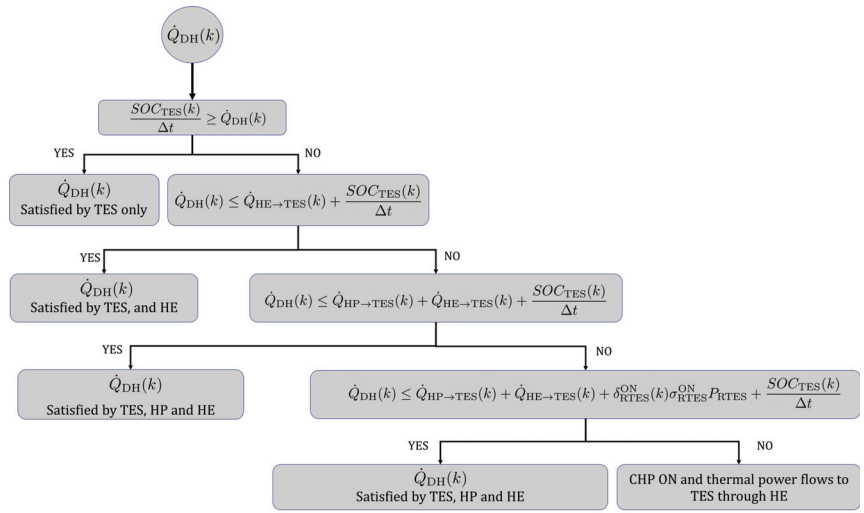


Figure 3. Heat demand satisfaction module.

4.2. Heuristic Algorithm Module for Hot Water Demand Satisfaction

The heuristic algorithm for hot water demand satisfaction is detailed in Figure 4 and described as follows:

- Step 1 The hot water demand $\dot{Q}_{DHW}(k)$ is first compared with the thermal solar panel generation $\dot{Q}_{TSP}(k)$, and the thermal energy stored in HE, by checking SOC_{HE} .
- Step 2 If $\dot{Q}_{DHW}(k)$ is not achievable with the available SOC_{HE} , and $\dot{Q}_{TSP}(k)$, the heat pump is set to ON state so that the additional thermal power is shunted towards HE to meet the required $\dot{Q}_{DHW}(k)$.
- Step 3 If $\dot{Q}_{DHW}(k)$ is not achieved with the available thermal power from heat pump and thermal storage, the controller sets the thermal resistor to ON state ($\delta_{RHE} = 1$).
- Step 4 In case $\dot{Q}_{DHW}(k)$ is achievable through the available energy from generation, storage, heat pump, and thermal resistor, the fuel cost of the CHP would be saved. Contrarily, CHP will be ON to fulfill the demand as a last resort.

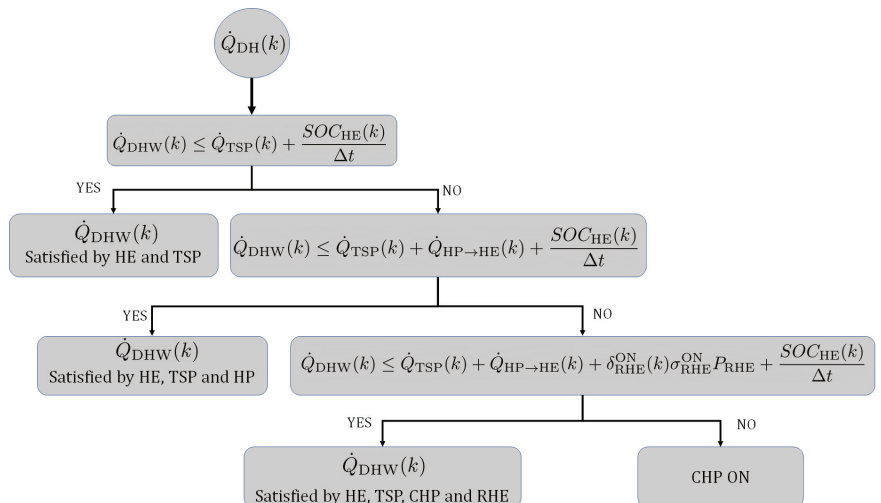


Figure 4. Hot water demand satisfaction module.

4.3. Heuristic Algorithm Module for Electric Demand Satisfaction

The heuristic algorithm for the electric demand satisfaction is showed in Figure 5. The objective is to minimize the usage of the CHP while satisfying all the system constraints and maximizing utilization of the power coming from the renewable sources. Since the nature of the renewable sources is intermittent, a backup battery is used for storing energy surpluses. The heuristic algorithm for electric demand satisfaction is described as follows:

- Step 1 At each time k , the available $P_{RES}(k)$ is first checked in order to meet electric demand $P_D(k)$, as well as the power needed to charge SOC_{ESS} to its maximum level.
- Step 2 In the second step, $P_{RES}(k)$ is compared with the electric demand $P_D(k)$ only. If $P_D(k)$ cannot be satisfied with it, the batteries act as a backup source in order to satisfy the power balance equation.
- Step 3 In case $P_D(k)$ cannot be met with the renewable sources as well as with the battery SOC_{ESS} , then the CHP is switched ON in order to meet that electric demands.

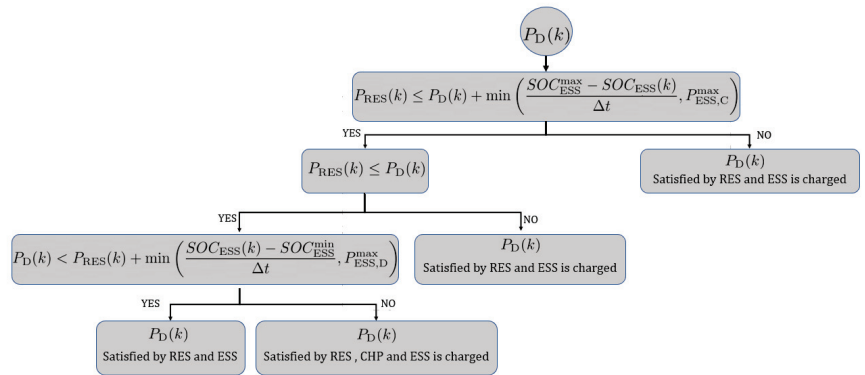


Figure 5. Electrical demand satisfaction module.

5. A GA-Solved Optimization Problem for Benchmarking

We compared the proposed heuristic approach with the performance of the popular meta-heuristic GA minimizing the power produced by the CHP, and hence its operation cost. The vector $\mathbf{u}(k)$ aggregates all the decision variables at time instant k , and is defined as

$$\mathbf{u}(k) = \left[\delta_{CHP}(k) \quad \delta_{HP}(k) \quad \delta_{RHE}(k) \quad \delta_{RTES}(k) \quad \delta_{PM_1}(k) \quad \delta_{PM_2}(k) \quad \delta_{PM_3}(k) \quad \delta_{HP \rightarrow TES}(k) \quad \delta_{HP \rightarrow HE}(k) \right]^T \tag{17}$$

Mathematically, the minimization problem computed at each time instant k is defined as

$$\begin{aligned} \min_{\mathbf{u}(k)} & P_{CHP}(k), \\ \text{s.t.} & \\ & \text{Constraints (4)–(11), (14)–(16),} \\ & \mathbf{u}(k) \in \{0, 1\}^9, \end{aligned} \tag{18}$$

where $P_{CHP}(k)$ represents the co-generator output power; assuming a constant price of the fuel and a constant efficiency of the CHP, such minimization is equivalent to minimizing the cost of CHP fuel.

GA is an evolution-based population direct search method which mimics the natural crossover and selection process [39–42] of a biological population to solve optimization problems.

Similar to other meta-heuristic optimization process, GA starts searching the solution space with a set of candidate solutions or seeds, otherwise known as population vectors. In our problem, we implement real-coded GA (RCGA), which improves the computational efficiency [41,42]. There exist different types of crossover and mutation strategies to generate off-spring vectors for subsequent generations and for preserving diversity within the candidate solutions. However, the practice shows that the choice of a certain type of techniques is largely based on experiments and dependent upon the problem specifications. In particular, the adaptive selection of a particular crossover or mutation from their ensemble is adopted to enhance the performance of RCGA. The selection of an off-spring from a particular cross-over or mutation is dependent upon the objective function value as well as the degree of constraint violation. For a detailed description and understanding of the working mechanism and principles of RCGA, the reader can refer to [41]. The algorithm takes into account the following steps:

- Step 1 Read the electric and thermal power requests, maximum number of iterations, and population size.
- Step 2 Generate an initial population P_0 . The chromosomes length is equal to the number of decision variables in Equation (17).
- Step 3 Check the constraints that correspond to the individuals in P_0 . Infeasible solutions are then removed from the solution space through the assignment of a large penalty cost.
- Step 4 Evaluate the “fitness function” for individuals in P_0 using the objective function in Equation (18). The population is then indexed by the iteration number i (i.e., population = P_i).
- Step 5 Generate a new pool of candidate solution P_{i+1} through the application of the operators selection, crossover, and mutation to P_i [42].
- Step 6 Check the constraints formulation for all the individuals mentioned in P_{i+1} .
- Step 7 Evaluate the objective function for all the individuals listed in P_{i+1} . The less constraint-violating solutions from P_i and P_{i+1} will be retained.
- Step 8 If the solution with the best objective value remains unchanged for a significant number of iterations, the algorithm goes to report the results at **step 9**, if not, it goes to **step 5**.
- Step 9 Report the results.

6. Simulations and Numerical Results

6.1. Simulation Setup

The parameters taken in this study for the controller setup are as follows: The fuel cost considered is assumed to be a constant, 1.54 [€/L]. Meanwhile, we take solar and wind power generations data with 1 h time resolution from literature. To generate power and heat, the default heat-power ratio of the CHP system under investigation is assumed to be 1:1. In this study, the proposed heuristic approach is implemented and compared with the standard GA meta-heuristic algorithm using MATLAB R2020a on a laptop with an Intel Core (TM) i7-7700 HQ 2.8 GHz processor and 16 GB of memory.

6.2. Test Runs

In order to prove the efficiency of the proposed heuristics, a series of test runs have been performed for a 24 h period. Specifically, extensive simulation scenarios have been conducted to compare the results obtained with the proposed heuristics against a genetic algorithm solver. Related histogram is reported showing the effectiveness of the proposed approach in energy cost saving. Before reporting such a cumulative comparison, two selected comparison scenarios among the ones considered are reported in details, to highlight the behaviors of the two different algorithms. It can be clearly seen from the simulations that both the thermal and the electric demands have always been satisfied either directly with the thermal panel, PVs, wind generator, with the stored electrical and thermal energy, or as a last resort with the CHP unit.

6.3. Example 1

Figure 6 depicts the electric and thermal generations data from the renewable sources (WTs, PVs, TSP) considered in this numerical example.

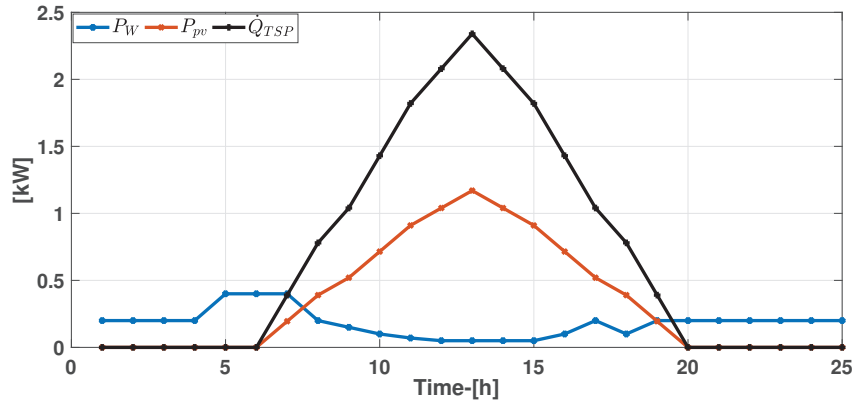


Figure 6. Thermal and electric power generation.

6.3.1. Heat Demand Satisfaction

In order to prove the efficacy of the implemented controller, the operational ON/OFF signals of the CHP system under investigation are shown for a case with frequent mismatch between available system thermal energy and the heat demand over the 24 h simulation. Figure 7 shows that the heat load through the proposed heuristic algorithm is met mostly with the thermal energy stored in the thermal energy storage tank, followed by the energy from the heat exchanger storage by switching on PM_2 or from the heat pump depending on the battery state of charge. In order to meet the demand, the Figure 7 top panel shows that the CHP unit is switched ON at hour 11 only, i.e., in one hour over 24 h simulations. Contrarily, the frequent switching of the CHP unit for heat load satisfaction through GA can be seen in Figure 7. It can be observed that the daily cost obtained by the proposed heuristic algorithm is 3.42 €, which is less than the one obtained with the GA 5.28 €. The heuristics performance is also more appealing than the performance of the GA algorithm, in terms of execution time, as it will be showed later in Section 6.5.

6.3.2. Hot Water Demand Satisfaction

Figure 8 shows the proposed heuristics and the GA for a hot water demand satisfaction simulation of the residential facility. It can be observed that the hot water demand is present for all 24 h of the day, while the available thermal power from solar thermal panel, as given in Figure 6, is only available between the hours 7–19. In that case, for the first 6 h, the hot water demand is met with the heat exchanger storage, as shown in Figure 8. It can be observed that the thermal energy level in the heat exchanger is at the minimum level between hours 9–10, 18–19, and 21 in the proposed heuristics simulations, while, for the GA, it is at the minimum between the hours 7, and 19–22. Therefore, the controller depending on the battery state of charge (SOC_{ESS}) switches the HP to ON for delivering mismatched thermal power. In conclusion, Figure 8 shows that, for all 24 h, the available thermal energy from the renewable resources, HE storage, and from HP is always greater than the requested demand. Thus, no CHP operations are seen towards hot water demand satisfaction.

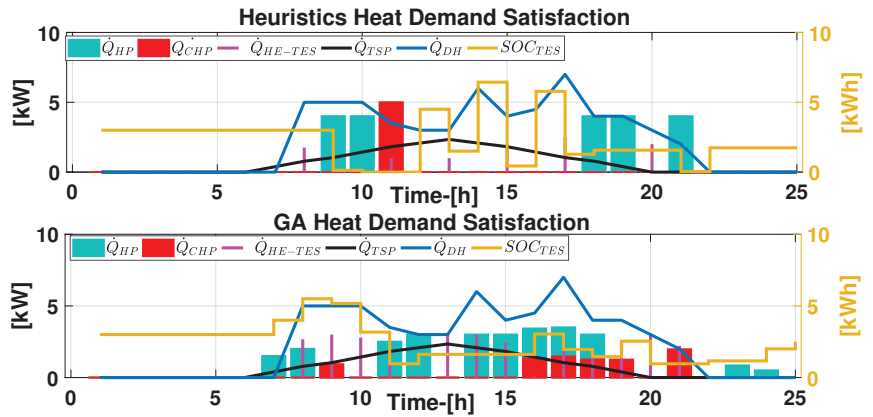


Figure 7. Heuristics and GA heat demand satisfaction numerical results.

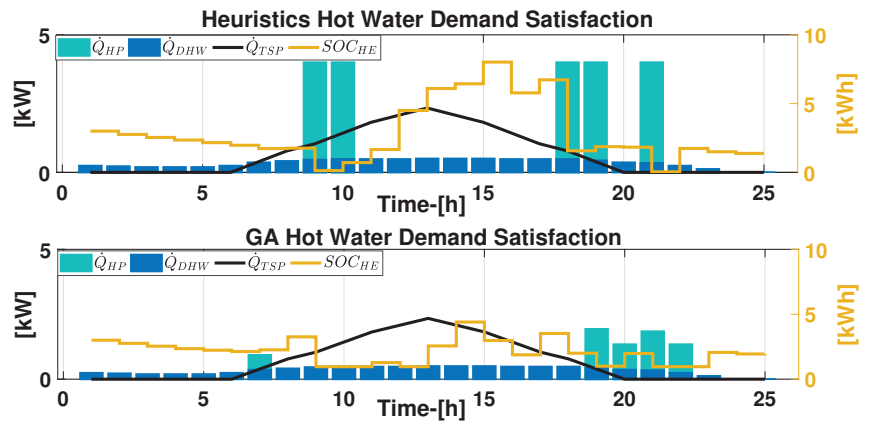


Figure 8. Heuristics and GA hot water demand satisfaction numerical results.

6.3.3. Electric Demand Satisfaction

To examine the effectiveness of the proposed heuristic algorithm for the electrical power demand satisfaction case, a 24 h electrical energy demand scenario has been considered. In Figure 9, it is possible to notice that, during the hours when solar or wind production is higher than the electric and thermal demands, both the heuristics and the GA controllers switch the batteries to charging state subject to the current level of SOC_{ESS} (Figure 9). As per the goal of the system, the priority is given to the power demand satisfaction with the renewable energy sources or with the batteries or a combination of both. In case the power demand is still higher than the electrical energy available in the system, then the controller switches the CHP unit to ON in order to balance the power equation.

Figure 9 shows the SOC_{ESS} . The batteries supply power to the electrical demand when there is low or nearly zero renewable energy resources. Furthermore, as HP is operated by electricity, the batteries also supply power to the heat pump that contributes to heat and hot water demand satisfaction as shown in Figure 7, and Figure 8, respectively. The controller switches the batteries to discharging mode during the hours with frequent mismatch between solar or wind generation and electric load demand. We stress that the electric demand for both the heuristics and the GA is met only with the system available electric energy.

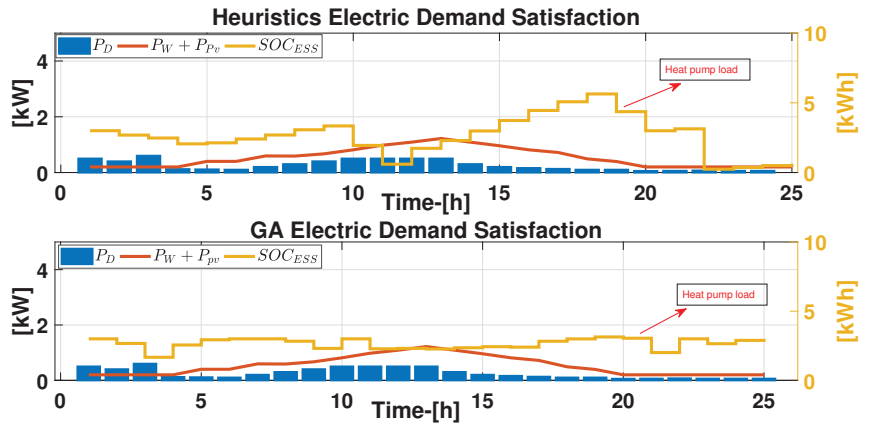


Figure 9. Heuristics and GA electric demand satisfaction numerical results.

6.3.4. Water Pumps

Figure 10 shows the water pumps PM_1 , PM_2 , and PM_3 switching states given by the heuristics and the GA algorithms. As shown in Figure 1, all three water pumps control the flow of hot water throughout the network. The water pump PM_1 is placed between the exhaust of CHP and HE. The water pump PM_2 is placed between HE and TES and is responsible for supplying hot water from HE to TES in case TES has storage scarcity. Similarly, the water pump PM_3 operates only when there is a heat demand signal.

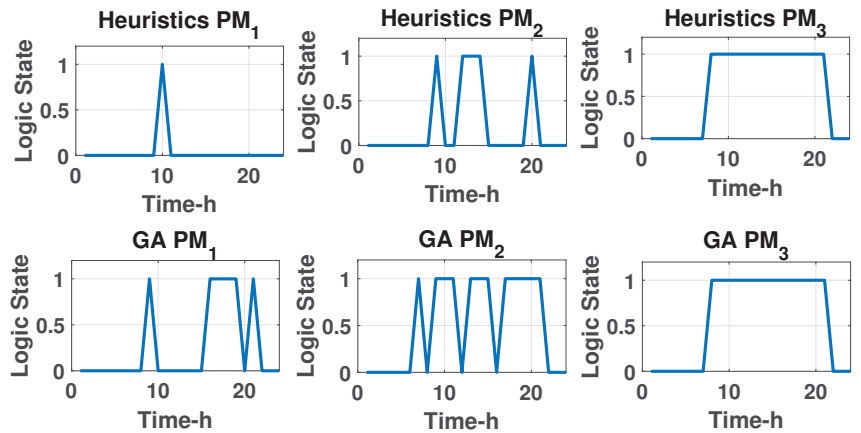


Figure 10. Heuristics and GA water pumps numerical results.

6.4. Example 2

In order to show the effectiveness of the proposed heuristics, a stressing plant scenario with limited availability of the renewable powers has been considered. In this scenario, the controller due to low renewable generations mostly relies on the energy available in the storage, or on the CHP unit that has to be switched ON in order to fulfill electric and thermal demands. The electric and thermal generation data from the renewable sources (WTs, PVs, TSP) considered are shown in Figure 11.

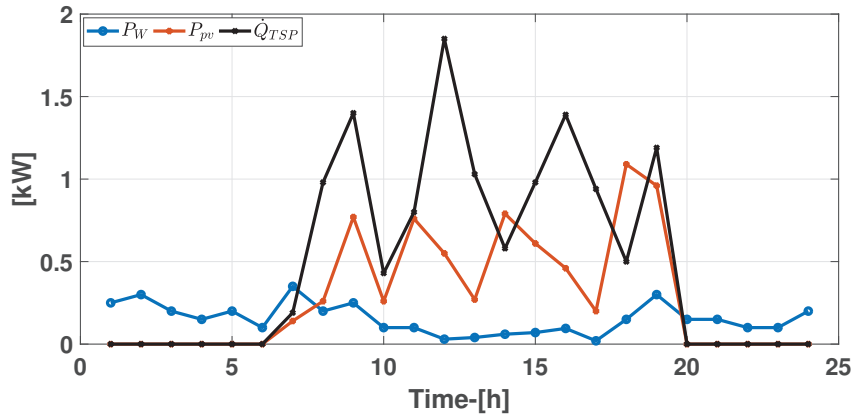


Figure 11. Thermal and electric power generation for Example 2.

6.4.1. Heat Demand Satisfaction

For the stressing plant scenario, the analysis has been conducted through simulations for a day with less renewable availability. As explained above, the purpose is to supply both the electric and thermal loads appropriately via exploiting the renewable production, the electric and thermal storage capacity, and the CHP unit.

Figure 12 shows that both the heuristics and the GA supply the heat load correctly. Initially, the heuristic algorithm switches the HP ON because of the hot water demand (detailed later in the next section). In the following hours, if the system available thermal energy for heat demand satisfaction is below the heat load, the shortfall is made up by switching ON the CHP unit, as can be seen during the hours 7, 11 and 17. On the other hand, the GA turns ON the CHP unit during the hours 6, 9–13, and 15 for heat load satisfaction, as can be seen in the panel below of Figure 12. It is observable that the cost obtained by the proposed heuristic algorithm for a day with limited renewable sources is 10.16 €, which is a slightly higher than the one obtained for the same day with the GA 9.80 €. However, the performance of the heuristics in terms of execution time is more appealing than that of the GA, as will be showed later in Section 6.5.

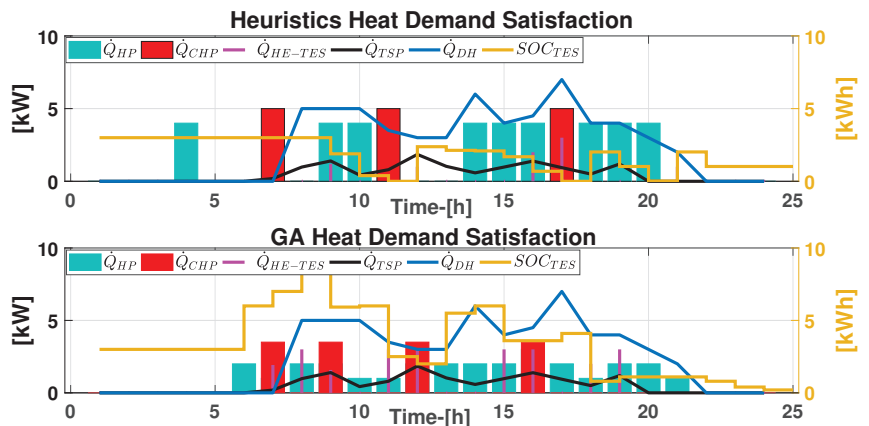


Figure 12. Heuristics and GA heat demand satisfaction numerical results for Example 2.

6.4.2. Hot Water Demand Satisfaction

The residential hot water demand satisfaction through the heuristics and the GA is reported in Figure 13. The hot water demand spans all 24 h of the day, while the renewable

sources are very limited. In order to supply the hot water load, during the first 3 h, both the control strategies exploited the heat exchanger storage SOC_{HE} . Any mismatch between the available system thermal energy and the hot water demand has been supplied by switching ON the (HP) depending on the battery state-of-charge SOC_{ESS} . It is also possible to notice that the heuristics algorithm relies on the HP less than the GA, thus resulting in more utilization of the renewable sources and the thermal storage. In this way, the heuristic algorithm saves the battery SOC_{ESS} for the future electric load, and at the same time avoids the conversion of the HP from electric to thermal, when possible. Figure 13 shows that the heuristics supplied the hot water demand by exploiting more the SOC_{HE} , and relied less on the HP operations. On the other hand, the GA frequently switched ON the HP in order to balance the mismatch between the \dot{Q}_{TSP} and the hot water demand. The frequent HP switching in GA resulting in more \dot{Q}_{HE-TES} supply than the heuristics for the heat demand satisfaction. In conclusion, with the proper coordination of both the storage (SOC_{HE} and the SOC_{HE}), and with the use of HP, both the heuristics and the GA supplied hot water demand correctly.

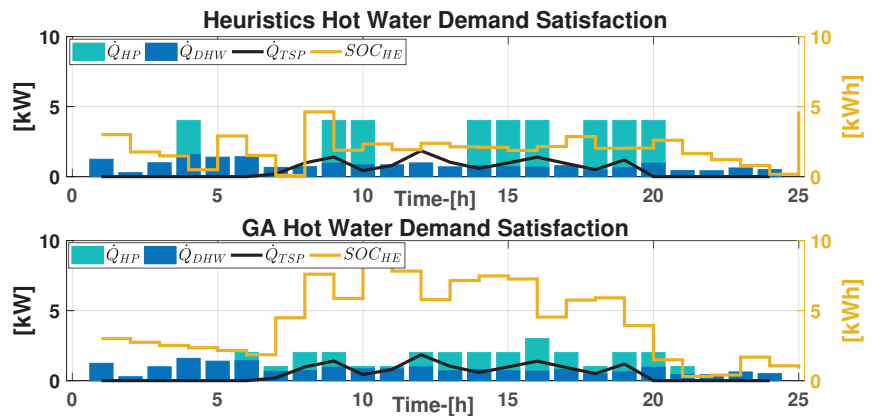


Figure 13. Heuristics and GA hot water demand satisfaction numerical results.

6.4.3. Electric Demand Satisfaction

Figure 14 shows the electric demand satisfaction for both control strategies. In the scenario at hand, the renewable data and the reference power demand are such that both exceeding and missing power are considered, with a power flow towards or from the storage. In order to show the effectiveness of the implemented heuristics, the unit commitment has been shown for a case with frequent imbalances between the reference demand and the limited available renewable power over the 24 h simulation. In Figure 14, it is possible to notice that the renewable power available from the wind and the photo voltaic are mostly less than the requested load. Therefore, in order to supply the electric load, both the heuristics and the GA controllers switch the batteries to discharging state subject to certain constraints on the battery bank SOC_{ESS} , and no CHP unit working is observed.

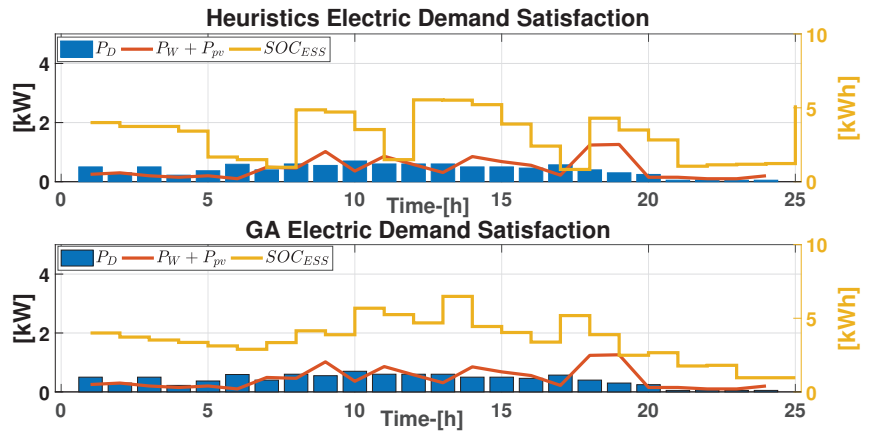


Figure 14. Heuristics and GA electric demand satisfaction numerical results.

6.4.4. Water Pumps

Similar to the previous example, Figure 15 shows the heuristics and the GA water pumps PM_1 , PM_2 , and PM_3 switching states. In comparison to Figure 10, the frequent switching of water pump PM_1 can be observed, as the absence of the renewable sources led the controllers to frequently operate the CHP unit in order to fulfill both the electric and the thermal demands.

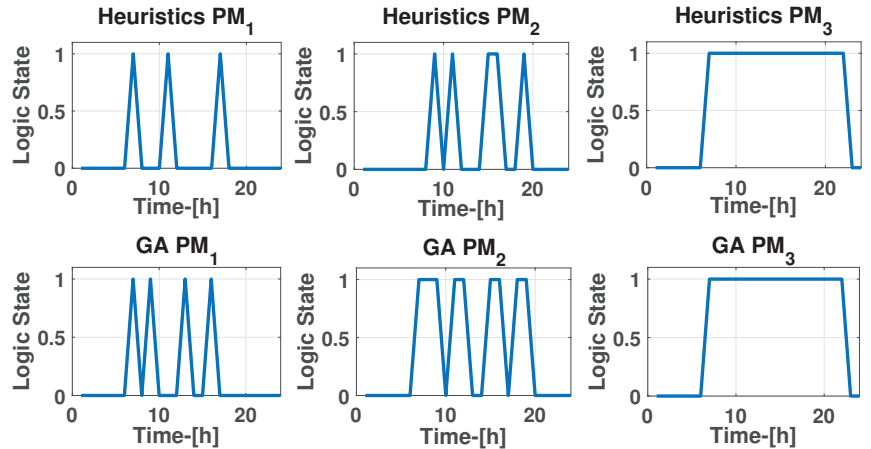


Figure 15. Heuristics and GA water pumps' numerical results.

6.5. Algorithms Comparison

This subsection summarizes the performance of the proposed heuristic algorithm and those of the GA. Fifty test runs of the system under study have been conducted over a 24 h simulation period. As representative examples, two of them have been reported in the previous sections. The obtained results are summarized in Table 4. In all the considered scenarios, both the heuristic and the meta-heuristic GA meet the electric and thermal demands of the residential facility. The heuristics and the GA cost per scenario is reported in Figure 16. Furthermore, the cost percentage gain of both approaches with respect to each other has also been reported in Figure 17. From Table 4, it is observable that the proposed heuristics in comparison with the optimally designed GA, competed reasonably well in terms of fuel costs minimization, despite the fact it uses a very simplified system model compared to the GA. Furthermore, the simulation time of the proposed

algorithm in all fifty scenarios is almost 300 times faster than the execution time taken by the GA. Hence, the proposed heuristic algorithm is deployable both on standard and low-performance hardware, contrary to a standard meta-heuristics strategy which cannot run on low-performance hardware.

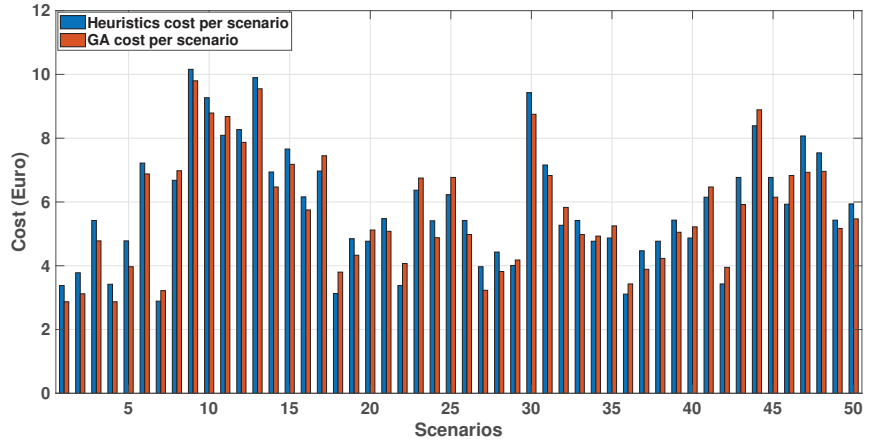


Figure 16. Heuristics and GA cost per scenario.

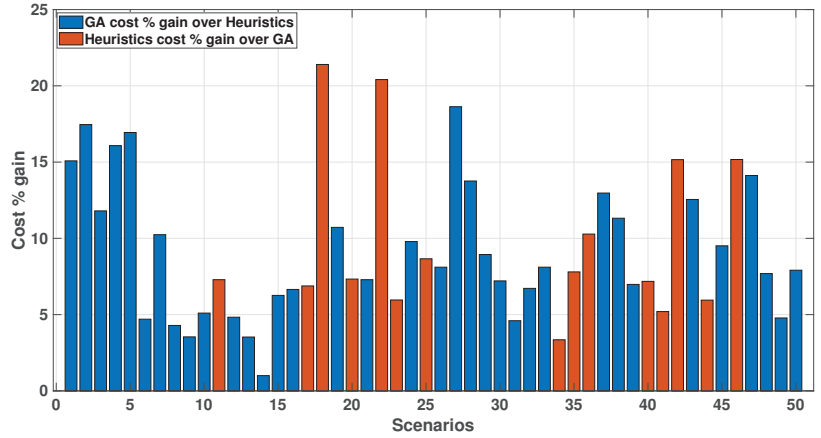


Figure 17. Cost percentage gain.

Table 4. Heuristics and GA test runs comparison. The CHP unit, the HP, and the thermal storage operating ranges considered in the test runs are 5 [kW], 4 [kW], and 10 [kWh], respectively. The average cost and the CPU time of the heuristics over 50 test runs are 6.48 €, and 0.45 s, respectively, while the average cost and the CPU time for the GA are 5.97 €, and 127.15 s, respectively.

Table Frame No. 1								
Algorithm	Values	Case 01	Case 02	Case 03	Case 04	Case 05	Case 06	Case 07
Heuristics	Cost Value €	3.38	3.78	5.42	3.42	4.78	7.22	3.22
	CPU Time (s)	0.42	0.40	0.50	0.41	0.43	0.44	0.39
GA	Cost Value €	2.87	3.12	4.78	2.87	3.98	6.87	2.89
	CPU Time (s)	123.12	120.72	120.1	123.15	123.75	122.45	121.05
Table Frame No. 2								
Algorithm	Values	Case 08	Case 09	Case 10	Case 11	Case 12	Case 13	Case 14
Heuristics	Cost Value €	6.98	10.16	9.27	8.09	8.27	9.90	6.94
	CPU Time (s)	0.41	0.40	0.49	0.42	0.42	0.41	0.41
GA	Cost Value €	6.68	9.80	8.79	8.68	7.87	9.55	6.47
	CPU Time (s)	127.13	120.72	122.10	121.05	124.70	123.75	123.75
Table Frame No. 3								
Algorithm	Values	Case 15	Case 16	Case 17	Case 18	Case 19	Case 20	Case 21
Heuristics	Cost Value €	7.16	6.16	6.97	3.13	4.85	4.77	5.48
	CPU Time (s)	0.42	0.41	0.50	0.41	0.44	0.41	0.38
GA	Cost Value €	7.18	5.75	7.45	3.80	4.33	5.12	5.08
	CPU Time (s)	124.02	120.27	119.51	122.65	120.75	121.95	123.75
Table Frame No. 4								
Algorithm	Values	Case 22	Case 23	Case 24	Case 25	Case 26	Case 27	Case 28
Heuristics	Cost Value €	3.38	6.378	5.41	6.23	5.42	3.97	4.43
	CPU Time (s)	0.38	0.49	0.50	0.44	0.43	0.40	0.41
GA	Cost Value €	4.07	6.75	4.88	6.77	4.98	3.23	3.82
	CPU Time (s)	112.12	121.52	119.01	129.55	118.47	125.95	121.05
Table Frame No. 5								
Algorithm	Values	Case 29	Case 30	Case 31	Case 32	Case 33	Case 34	Case 35
Heuristics	Cost Value €	4.01	9.43	7.16	5.27	5.42	4.78	4.87
	CPU Time (s)	0.37	0.44	0.45	0.49	0.39	0.44	0.44
GA	Cost Value €	4.18	8.75	6.83	5.83	4.98	4.93	5.25
	CPU Time (s)	130.12	121.92	116.10	114.50	121.05	123.45	126.32
Table Frame No. 6								
Algorithm	Values	Case 36	Case 37	Case 38	Case 39	Case 40	Case 41	Case 42
Heuristics	Cost Value €	3.11	4.47	4.77	5.43	5.22	6.15	3.97
	CPU Time (s)	0.41	0.40	0.40	0.49	0.53	0.40	0.42
GA	Cost Value €	3.43	4.07	4.23	5.05	4.87	6.47	3.43
	CPU Time (s)	121.21	120.27	125.10	121.57	123.50	119.73	120.67
Table Frame No. 7								
Algorithm	Values	Case 43	Case 44	Case 45	Case 46	Case 47	Case 48	Case 49
Heuristics	Cost Value €	6.77	8.39	6.77	5.93	8.08	7.54	5.43
	CPU Time (s)	0.46	0.46	0.50	0.49	0.42	0.49	0.42
GA	Cost Value €	5.92	8.89	6.15	6.83	6.93	6.96	5.17
	CPU Time (s)	113.42	118.20	119.56	123.59	121.67	120.50	121.95

7. Conclusions

This paper proposes a fast heuristic approach for solving the CHP-ED problem considering that the presence of multiple energy vectors through a novel was the computational efficient model of the system. The proposed heuristics were compared with Genetic Algorithm (GA), a meta-heuristic approach. The results show that the heuristic approach implies higher costs with respect to the GA; however, with the major benefit of being computationally simpler and faster so as to be run also on low-cost, low-performance platforms. Implementing the heuristics on an embedded hardware and studying implementation aspects are future paths for this investigation as well as the handling of renewable generation and load forecasts, to some extent, and the optimal tuning of the thresholds for improved performances.

Author Contributions: Conceptualization, L.G., D.L. and V.M.; methodology, M.F.S., M.D., V.M. and S.S.; software, M.F.S. and M.D.; validation, M.F.S., M.D., V.M. and S.S.; investigation, D.L., V.M. and S.S.; resources L.G., C.M. and R.S.; writing—original draft preparation, M.F.S., M.D., V.M. and S.S.; writing—review and editing, V.M., S.S., D.L., L.G.; supervision, V.M., S.S., D.L. and L.G.; project administration, L.G., C.M., R.S., D.L., V.M. and S.S.; funding acquisition, L.G., C.M. and R.S. All authors have read and agreed to the published version of the manuscript.

Funding: This work was partially funded by Regione Campania (FSE 2014/2020, D.G.R. n. 80 del 31/5/2016) and by Regione Lazio (POR FESR 2014/2020, Avviso pubblico n. 5, Bioedilizia e smart-building, determina n. G14229 del 30/11/2016).

Institutional Review Board Statement: Not applicable.

Informed Consent Statement: Not applicable.

Data Availability Statement: Not applicable.

Conflicts of Interest: The authors declare no conflicts of interest.

References

1. Caliano, M.; Bianco, N.; Graditi, G.; Mongibello, L. Economic optimization of a residential micro-CHP system considering different operation strategies. *Appl. Therm. Eng.* **2016**, *101*, 592–600. [[CrossRef](#)]
2. Yu, H.; Nord, L.O.; Yu, C.; Zhou, J.; Si, F. An improved combined heat and power economic dispatch model for natural gas combined cycle power plants. *Appl. Therm. Eng.* **2020**, *181*, 115939. [[CrossRef](#)]
3. Qaeini, S.; Nazar, M.S.; Varasteh, F.; Shafie-khah, M.; Catalão, J.P. Combined heat and power units and network expansion planning considering distributed energy resources and demand response programs. *Energy Convers. Manag.* **2020**, *211*, 112776. [[CrossRef](#)]
4. Pourghasem, P.; Sohrabi, F.; Abapour, M.; Mohammadi-Ivatloo, B. Stochastic multi-objective dynamic dispatch of renewable and CHP-based islanded microgrids. *Electr. Power Syst. Res.* **2019**, *173*, 193–201. [[CrossRef](#)]
5. Neyestani, M.; Hatami, M.; Hesari, S. Combined heat and power economic dispatch problem using advanced modified particle swarm optimization. *J. Renew. Sustain. Energy* **2019**, *11*, 015302. [[CrossRef](#)]
6. Ahmadi, P.; Almasi, A.; Shahriyari, M.; Dincer, I. Multi-objective optimization of a combined heat and power (CHP) system for heating purpose in a paper mill using evolutionary algorithm. *Int. J. Energy Res.* **2012**, *36*, 46–63. [[CrossRef](#)]
7. Olatomiwa, L.; Mekhilef, S.; Ismail, M.; Moghavvemi, M. Energy management strategies in hybrid renewable energy systems: A review. *Renew. Sustain. Energy Rev.* **2016**, *62*, 821–835. [[CrossRef](#)]
8. Maleki, A.; Rosen, M.A. Design of a cost-effective on-grid hybrid wind-hydrogen based CHP system using a modified heuristic approach. *Int. J. Hydrogen Energy* **2017**, *42*, 15973–15989. [[CrossRef](#)]
9. Barbieri, E.S.; Melino, F.; Morini, M. Influence of the thermal energy storage on the profitability of micro-CHP systems for residential building applications. *Appl. Energy* **2012**, *97*, 714–722. [[CrossRef](#)]
10. Larissa, B.; Maran, R.M.; Ioan, B.; Anca, N.; Mircea-Iosif, R.; Horia, T.; Gheorghe, F.; Ema Speranta, M.; Dan, M.I. Adjusted net savings of CEE and Baltic nations in the context of sustainable economic growth: A panel data analysis. *J. Risk Financ. Manag.* **2020**, *13*, 234. [[CrossRef](#)]
11. Ioan, B.; Malar Kumaran, R.; Larissa, B.; Anca, N.; Lucian, G.; Gheorghe, F.; Horia, T.; Ioan, B.; Mircea-Iosif, R. A panel data analysis on sustainable economic growth in India, Brazil, and Romania. *J. Risk Financ. Manag.* **2020**, *13*, 170. [[CrossRef](#)]
12. Rose, S.K.; Richels, R.; Blanford, G.; Rutherford, T. The Paris Agreement and next steps in limiting global warming. *Clim. Chang.* **2017**, *142*, 255–270. [[CrossRef](#)]
13. Casals, L.C.; Martinez-Laserna, E.; García, B.A.; Nieto, N. Sustainability analysis of the electric vehicle use in Europe for CO₂ emissions reduction. *J. Clean. Prod.* **2016**, *127*, 425–437. [[CrossRef](#)]

14. Acke, D. Zeroing In: Lessons from the European Climate Foundation's Roadmap 2050 Project. *IEEE Power Energy Mag.* **2014**, *12*, 42–49. [[CrossRef](#)]
15. Boden, T.A.; Marland, G.; Andres, R.J. *Global, Regional, and National Fossil-Fuel CO₂ Emissions*; Carbon Dioxide Information Analysis Center, Oak Ridge National Laboratory, US Department of Energy: Oak Ridge, TN, USA, 2009; Volume 10. [[CrossRef](#)]
16. Sgobba, A.; Meskell, C. On-site renewable electricity production and self consumption for manufacturing industry in Ireland: Sensitivity to techno-economic conditions. *J. Clean. Prod.* **2019**, *207*, 894–907. [[CrossRef](#)]
17. Kosmadakis, G. Estimating the potential of industrial (high-temperature) heat pumps for exploiting waste heat in EU industries. *Appl. Therm. Eng.* **2019**, *156*, 287–298. [[CrossRef](#)]
18. Capizzi, F.; Das, A.; Dauwe, T.; Moorkens, I.; Juhana, R. *Renewable Energy in Europe—2019*; European Environmental Agency-European Topic Centre on Climate Change Mitigation and Energy: Mol, Belgium, 2019.
19. Sun, J.; Li, Y. Social cognitive optimization with tent map for combined heat and power economic dispatch. *Int. Trans. Electr. Energy Syst.* **2019**, *29*, e2660. [[CrossRef](#)]
20. Steen, D.; Stadler, M.; Cardoso, G.; Groissböck, M.; DeForest, N.; Marnay, C. Modeling of thermal storage systems in MILP distributed energy resource models. *Appl. Energy* **2015**, *137*, 782–792. [[CrossRef](#)]
21. Li, Y.; Wang, J.; Zhao, D.; Li, G.; Chen, C. A two-stage approach for combined heat and power economic emission dispatch: Combining multi-objective optimization with integrated decision making. *Energy* **2018**, *162*, 237–254. [[CrossRef](#)]
22. Wouters, C.; Fraga, E.S.; James, A.M. An energy integrated, multi-microgrid, MILP (mixed-integer linear programming) approach for residential distributed energy system planning—A South Australian case-study. *Energy* **2015**, *85*, 30–44. [[CrossRef](#)]
23. Rafique, M.K.; Haider, Z.M.; Mehmood, K.K.; Saeed Uz Zaman, M.; Irfan, M.; Khan, S.U.; Kim, C.H. Optimal Scheduling of Hybrid Energy Resources for a Smart Home. *Energies* **2018**, *11*, 3201. [[CrossRef](#)]
24. Sanguinetti, A.; Karlin, B.; Ford, R.; Salmon, K.; Dombrovski, K. What's energy management got to do with it? Exploring the role of energy management in the smart home adoption process. *Energy Effic.* **2018**, *11*, 1897–1911. [[CrossRef](#)]
25. Ford, R.; Pritoni, M.; Sanguinetti, A.; Karlin, B. Categories and functionality of smart home technology for energy management. *Build. Environ.* **2017**, *123*, 543–554. [[CrossRef](#)]
26. Lin, C.; Wu, W.; Zhang, B.; Sun, Y. Decentralized solution for combined heat and power dispatch through benders decomposition. *IEEE Trans. Sustain. Energy* **2017**, *8*, 1361–1372. [[CrossRef](#)]
27. Sashirekha, A.; Pasupuleti, J.; Moin, N.; Tan, C.S. Combined heat and power (CHP) economic dispatch solved using Lagrangian relaxation with surrogate subgradient multiplier updates. *Int. J. Electr. Power Energy Syst.* **2013**, *44*, 421–430. [[CrossRef](#)]
28. Yokoyama, R.; Shinano, Y.; Wakayama, Y.; Wakui, T. Model reduction by time aggregation for optimal design of energy supply systems by a MILP hierarchical branch and bound method. *Energy* **2019**, *181*, 782–792. [[CrossRef](#)]
29. Nazari-Heris, M.; Mohammadi-Ivatloo, B. Application of heuristic algorithms to optimal PMU placement in electric power systems: An updated review. *Renew. Sustain. Energy Rev.* **2015**, *50*, 214–228. [[CrossRef](#)]
30. Kim, J.S.; Edgar, T.F. Optimal scheduling of combined heat and power plants using mixed-integer nonlinear programming. *Energy* **2014**, *77*, 675–690. [[CrossRef](#)]
31. Pattanaik, J.K.; Basu, M.; Dash, D.P. Heat Transfer Search Algorithm for Combined Heat and Power Economic Dispatch. *Iran. J. Sci. Technol. Trans. Electr. Eng.* **2020**, *44*, 963–978. [[CrossRef](#)]
32. Nguyen Trung, T.; Vo Ngoc, D. Improved particle swarm optimization for combined heat and power economic dispatch. *Sci. Iran.* **2016**, *23*, 1318–1334. [[CrossRef](#)]
33. Allegrini, J.; Orehounig, K.; Mavromatidis, G.; Ruesch, F.; Dorer, V.; Evins, R. A review of modelling approaches and tools for the simulation of district-scale energy systems. *Renew. Sustain. Energy Rev.* **2015**, *52*, 1391–1404. [[CrossRef](#)]
34. Alomoush, M.I. Optimal Combined Heat and Power Economic Dispatch Using Stochastic Fractal Search Algorithm. *J. Mod. Power Syst. Clean Energy* **2020**, *8*, 276–286. [[CrossRef](#)]
35. Nazari-Heris, M.; Mehdinejad, M.; Mohammadi-Ivatloo, B.; Babamalek-Gharehpetian, G. Combined heat and power economic dispatch problem solution by implementation of whale optimization method. *Neural Comput. Appl.* **2019**, *31*, 421–436. [[CrossRef](#)]
36. Maleki, A.; Rosen, M.A.; Pourfayaz, F. Optimal operation of a grid-connected hybrid renewable energy system for residential applications. *Sustainability* **2017**, *9*, 1314. [[CrossRef](#)]
37. Vögelin, P.; Koch, B.; Georges, G.; Boulouchos, K. Heuristic approach for the economic optimisation of combined heat and power (CHP) plants: Operating strategy, heat storage and power. *Energy* **2017**, *121*, 66–77. [[CrossRef](#)]
38. Celador, A.C.; Odriozola, M.; Sala, J. Implications of the modelling of stratified hot water storage tanks in the simulation of CHP plants. *Energy Convers. Manag.* **2011**, *52*, 3018–3026. [[CrossRef](#)]
39. Deb, K. *Multi-Objective Optimization Using Evolutionary Algorithms*; John Wiley & Sons: Hoboken, NJ, USA, 2001; Volume 16.
40. Goldberg, D.E. *Genetic Algorithms*; Pearson Education: Tamil Nadu, India, 2006.
41. Dan, M.; Srinivasan, S.; Sundaram, S. A Hybrid Cross-Entropy Guided Genetic Algorithm for Scheduling Multi-Energy Systems. In Proceedings of the 2018 IEEE Symposium Series on Computational Intelligence (SSCI), Bangalore, India, 18–21 November 2018; pp. 1807–1814.
42. Suresh, S.; Huang, H.; Kim, H.J. Hybrid real-coded genetic algorithm for data partitioning in multi-round load distribution and scheduling in heterogeneous systems. *Appl. Soft Comput.* **2014**, *24*, 500–510. [[CrossRef](#)]

Article

Modeling Control and Robustness Assessment of Multilevel Flying-Capacitor Converters

Roberto Zanasi and Davide Tebaldi *

“Enzo Ferrari” Department of Engineering, University of Modena and Reggio Emilia, Via Pietro Vivarelli 10 Int. 1, 41125 Modena, Italy; roberto.zanasi@unimore.it

* Correspondence: davide.tebaldi@unimore.it

Abstract: When performing AC/DC-DC/AC power conversions, multilevel converters provide several advantages as compared to classical two-level converters. This paper deals with the dynamic modeling, control, and robustness assessment of multilevel flying-capacitor converters. The dynamic model is derived using the Power-Oriented Graphs modeling technique, which provides the user with block schemes that are directly implementable in the Matlab/Simulink environment by employing standard Simulink libraries. The performed robustness assessment has led to the proposal of a divergence index, which allows for evaluating the voltage balancing capability of the converter using different voltage vector configurations for the extended operation of the converter, namely when the number of output voltage levels is increased for a given number of capacitors. A new variable-step control algorithm is then proposed. The variable-step control algorithm safely enables the converter extended operation, which prevents voltage balancing issues, even under particularly unfavorable conditions, such as a constant desired output voltage or a sudden load change. The simulation results showing the good performances of the proposed variable-step control as compared to a classical minimum distance approach are finally provided and commented in detail.

Keywords: multilevel flying-capacitor converter; dynamic modeling; robustness assessment; control; voltage balancing capability

Citation: Zanasi, R.; Tebaldi, D. Modeling Control and Robustness Assessment of Multilevel Flying-Capacitor Converters. *Energies* **2021**, *14*, 1903. <https://doi.org/10.3390/en14071903>

Academic Editor: Juri Belikov

Received: 21 February 2021

Accepted: 24 March 2021

Published: 30 March 2021

Publisher’s Note: MDPI stays neutral with regard to jurisdictional claims in published maps and institutional affiliations.



Copyright: © 2021 by the authors. Licensee MDPI, Basel, Switzerland. This article is an open access article distributed under the terms and conditions of the Creative Commons Attribution (CC BY) license (<https://creativecommons.org/licenses/by/4.0/>).

1. Introduction

The need of performing power conversion is present in a large variety of engineering fields. When focusing on electrical power conversions, the cases of DC/DC [1–3], AC/DC-DC/AC [4–6] power conversions can be distinguished. These types of power conversion find application in many areas, including smart grids [1,4,5], hybrid electric vehicles [7], and many others. The physical modeling of the employed power converter topology is of great importance, as it represents the starting point for understanding its dynamic behavior and developing an effective control strategy. This paper deals with the modeling, control and robustness assessment of multilevel flying-capacitor converters.

Multilevel topologies bring several advantages when compared to classical two-level converters, such as a significant distortion reduction in the output voltage waveform and in the drawn input current, a reduction of the dv/dt effect in the output voltage waveform, and the generation of a lower common-mode voltage [8,9]. Furthermore, transformerless grid-connected multilevel converters are largely used in applications, such as motor drives, solid-state power transformers, and photovoltaic systems, as they provide advantages, such as increased power, voltage ratings, and lower harmonic distortion [10,11]. In this latter type of converters, the development of suitable ground potentials models is important, as high ground potentials represents an issue that may affect the converter operation. This matter is addressed in [10,11], together with the creation of local grounding points limiting ground potentials and blocking ground leakage currents from flowing through the host grid grounding, and together with the testing of grounding circuits for the considered application. A vast array of different multilevel converter topologies have been proposed

over the years [8,10–12], including diode-clamped converters, flying-capacitors converters, cascaded H-bridge converters, etc. Together with the advantages and potentialities that are brought by multilevel converters comes the difficulty of having more power electronics devices to control. This has led to the development of different modulation algorithms and techniques having different trade-offs between the pros and cons [13,14].

When dealing with the modeling and control of multilevel converters, the choice of the employed modeling approach represents the first step. In [15], the modeling of the Modular Multilevel Matrix Converter (M^3C) is addressed in a matrix form defining voltage-current model and a power-capacitor voltage model, whereas, in [16], the modeling of a Modular Multilevel Converter is performed using a state-space model, which is next discretized using a forward Euler approximation. In this paper, we address the dynamic modeling of multilevel flying-capacitor converters using the Power-Oriented Graphs (POG) modeling technique [17], extending the modeling approach that was proposed in [12]. The POG technique is one of the main graphical formalisms for modeling physical systems, together with Bond Graphs [18] and Energetic Macroscopic Representation [18]. The POG technique is deemed effective, as it allows for building block diagrams that can be directly implemented in the Matlab/Simulink environment using blocks that are available in basic libraries, and to effectively control the power flows within the system [18]. The proposed approach provides a very compact continuous-time model of the considered multilevel converter which can be applied to other converter topologies as well, and establishes a straightforward way of computing the capacitor voltages and currents starting from the Insulated Gate Bipolar Transistors (IGBTs) switching states. The Readers are referred to [19] for applications of the POG technique to physical systems modeling in different energetic domains, where a web POG modeling program is presented, together with some examples.

Once the modeling is performed, the next step is represented by the control of the considered multilevel converter topology. The subject of multilevel converters control has been largely treated in the literature, by focusing on different converter topologies and aiming at different objectives, depending on the converter topology. In [20], the authors propose an interesting space-vector based approach for modeling modular multilevel converters for battery electric vehicles, showing that the traditional approach for achieving cell balancing can be seen as a special case of the proposed model. In [21], the control of modular multilevel converters is approached using model predictive control that is aided by disturbance observers with the objective of controlling the AC current and suppressing the circulating current in the converter. An asymmetric cascade H-bridge multilevel converter topology that is equipped with a predictive control strategy is instead proposed in [22]. The purpose of the latter is to minimize the converter commutations, while also exploiting the redundant states to equally distribute the load among the switches, thus equalizing their lifetime expectation. Focusing on multilevel topologies having floating capacitors involved in their operation, an important aspect is represented by the capacitors voltages balancing. If not properly controlled, the floating capacitors voltages may suffer from ripple [23], which would cause output voltage and current distortion, or even voltages trajectory divergence, thus further compromising the converter operation. An important distinction needs to be made between those multilevel converters having full floating capacitors voltage balancing capability and those not having it, due to topology limitations or lack of redundancy. This latter case is addressed in [23], where a new PWM method was proposed to improve the floating capacitors voltage balancing capability. Multilevel flying-capacitor converters have full floating capacitors voltage balancing capability if properly controlled and if the number of output voltage levels m equals the number of capacitors n plus one (i.e., the number of floating capacitors plus two). An analytical investigation of the voltage balancing characteristics of the flying capacitor converter while using the phase disposition PWM (PDPWM) modulation technique is presented in [24]. An interesting approach to ensure floating capacitors voltage balancing capability is presented in [25], where a modification of the carrier-redistribution PWM (CRPWM) is proposed in order to ensure a low output voltage harmonic content and low voltage ripple,

thanks to the symmetric disposition of carriers in every fundamental period. However, the main drawback that is associated with open-loop methods is that they aim at keeping the floating capacitors voltages as close to the desired value as possible, but do not consider the case of a voltage unbalance occurring because of some unfavorable conditions, such as a fault, for example. In this latter case, a closed-loop control solution is required, in order to drive the capacitors voltages trajectory back to the desired operating point, thus ensuring the correct operation of the converter. The multilevel flying-capacitor converter having a generic number n of capacitors can actually generate all the way up to 2^n output voltage levels, giving rise to what is called "extended operation" [26,27]. However, if the number of voltage levels m is greater than $n + 1$, then the multilevel flying-capacitor converter loses the property of full floating capacitors voltage balancing capability, and a suitable closed-loop control technique becomes paramount. An example of closed-loop control technique for the multilevel flying-capacitor converter in such operating condition using a "minimum distance" approach is proposed in [27]. However, to the best of our knowledge, there is no proposal in the literature of a metric allowing for performing the robustness assessment of multilevel flying-capacitor converters against the divergence of the flying capacitors voltage trajectory. This becomes especially crucial with the converter working in extended operation, namely with a number m of output voltage levels greater than $n + 1$ all the way up to 2^n . In this paper, we address: (a) the dynamic modeling of multilevel flying-capacitor converters; (b) the analysis of all the possible configurations of the converter in terms of capacitors voltage ratio allowing for the converter to work in extended operation; (c) the robustness assessment of multilevel flying-capacitor converters when working in extended operation and controlled using a classical minimum distance approach; (d) the proposal of a divergence index determining the degradation of the converter operation using a minimum distance control as the number of output voltage levels is increased for all of the possible capacitors voltages configurations; (e) the proposal of a new variable-step closed-loop control strategy for guaranteeing the best flying capacitors voltage balance in any extended operating condition; and, (f) the comparison of the proposed variable-step control strategy for multilevel flying-capacitor converters with a classical minimum distance control approach.

The remainder of the paper is organized as follows. Section 2 introduces the characteristics and basic properties of the POG modeling technique. Section 3, and the included subsections, address the dynamic modeling of the multilevel flying-capacitor converter. The main matrices and vectors of the model are introduced and described, together with some interesting properties that they exhibit. The model verification against the PLECS simulator is addressed in Section 3.4. Section 4 deals with the control of the multilevel flying-capacitor converter. In particular, Section 4.1 addresses the minimum distance algorithm, whereas Section 4.2 defines the basic configuration of the multilevel flying-capacitor converter. Section 4.3 describes the robustness assessment of the considered converter in extended mode using a minimum distance algorithm, whereas Section 4.4 proposes the new variable-step control algorithm. The converter simulation in extended mode with different dynamic loads is addressed in Section 5. Section 6 finally provides the conclusions of this work.

2. The POG Modeling Technique

The Power-Oriented Graphs (POG) technique [17,18] is a graphical modeling formalism that is based on the same energetic approach employed by the Bond Graph (BG) technique [18] using a different graphical notation. Power-Oriented Graphs are created using two elementary blocks, namely the elaboration block and the connection block, which are shown in Figure 1. The first block is employed for the modeling of all the physical elements storing and/or dissipating energy, whereas the second one is used for the modeling of all the physical elements performing energy conversion. The elaboration block describes static or dynamic physical elements, and is characterized by the transfer function (or matrix) $G(s)$ of the considered element. If the transfer function $G(s) = R$ is

constant, then the considered physical element is static, being characterized by the static relation between the input variable v_f and the output variable v_e or viceversa. The dynamic elements can be classified into two types:

- *across elements* D_e , having a flow variable v_f as input and an across variable v_e as output;
- *flow elements* D_f , having an across variable v_e as input and a flow variable v_f as output.

A flow power variable v_f is always defined in each point of the space, whereas an across power variable v_e is defined between two points. Table 1 provides a compact description of the dynamic and static elements, together with the across and flow variables, in the four typically considered energetic domains. The crossed circle in the upper part of the elaboration block in Figure 1 is a *summation node*, where the black spot on the right denotes that the power variable entering the summation node from that side has to be subtracted. The connection block is characterized by a coefficient (or matrix) K , which completely describes the energy conversion between the energetic domains.

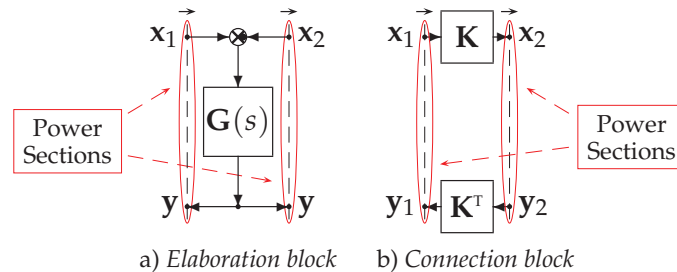


Figure 1. POG elementary blocks: *elaboration block* and *connection block*.

Table 1. Physical elements and power variables in the different energetic domains.

	Electrical	Mechanical Translational	Mechanical Rotational	Hydraulic
D_e	Capacitor C	Mass M	Inertia J	Hydraulic Capacitor C_I
v_e	Voltage V	Velocity \dot{x}	Angular Velocity ω	Pressure P
D_f	Inductor L	Spring E	Rotational Spring E	Hydraulic Inductor L_I
v_f	Current I	Force F	Torque τ	Volume Flow Rate Q
R	Resistor R	Friction b	Angular Friction b	Hydraulic Resistor R_I

One of the main characteristics of the POG modeling technique is the maintained direct correspondence between the power sections in the POG model, as highlighted by the red ellipses in Figure 1, and the power sections of the actual physical system. The scalar product $x^T y$ of the two power variables x and y in the considered power section has the physical meaning of *power flowing through the considered section*. The black oriented arrows placed at the top of each power section in the scheme of Figure 1 highlight the positive direction of the power flow through the considered section.

Any physical system that is modeled by means of the POG technique is characterized by the following POG state-space representation:

$$\begin{cases} \mathbf{L} \dot{\mathbf{x}} = \mathbf{A} \mathbf{x} + \mathbf{B} \mathbf{u} \\ \mathbf{y} = \mathbf{C} \mathbf{x} + \mathbf{D} \mathbf{u} \end{cases}$$

where \mathbf{L} is the energy matrix, \mathbf{A} is the power matrix, \mathbf{B} is the input matrix, \mathbf{C} is the output matrix, and \mathbf{D} is the input-output matrix. The energy matrix \mathbf{L} and power matrix \mathbf{A} describe the instantaneous energy E_s stored in the system and the instantaneous power P_d dissipated in the system, respectively:

$$E_s = \frac{1}{2} \mathbf{x}^T \mathbf{L} \mathbf{x}, \quad P_d = \mathbf{x}^T \mathbf{A}_s \mathbf{x},$$

where \mathbf{A}_s is the symmetric part of matrix \mathbf{A} .

3. Modeling of the n -Dimensional Multilevel Flying-Capacitor Converter

3.1. Physical System and Configuration Vectors

Let us consider the electric scheme of an n -dimensional Multilevel Flying-Capacitor Converter that is shown in Figure 2. The output voltage V_{out} is a function of the IGBTs activation signals $T_i \in \{0, 1\}$, for $i \in \{1, 2, \dots, n\}$. Let \mathbf{V}_c and \mathbf{T}_j denote the capacitors voltage column vector and the IGBTs signal row vectors, defined as follows:

$$\mathbf{V}_c = \begin{bmatrix} V_1 \\ V_2 \\ V_3 \\ \vdots \\ V_n \end{bmatrix}, \quad \begin{bmatrix} \mathbf{T}_0 \\ \mathbf{T}_1 \\ \mathbf{T}_2 \\ \mathbf{T}_3 \\ \vdots \\ \mathbf{T}_{m_c-2} \\ \mathbf{T}_{m_c-1} \end{bmatrix} = \begin{bmatrix} 0 & \dots & 0 & 0 & 0 \\ 0 & \dots & 0 & 0 & 1 \\ 0 & \dots & 0 & 1 & 0 \\ 0 & \dots & 0 & 1 & 1 \\ \vdots & \ddots & \vdots & \vdots & \vdots \\ 1 & \dots & 1 & 1 & 0 \\ 1 & \dots & 1 & 1 & 1 \end{bmatrix} \quad n=3 \Rightarrow \begin{bmatrix} \mathbf{T}_0 \\ \mathbf{T}_1 \\ \mathbf{T}_2 \\ \mathbf{T}_3 \\ \mathbf{T}_4 \\ \mathbf{T}_5 \\ \mathbf{T}_6 \\ \mathbf{T}_7 \end{bmatrix} = \begin{bmatrix} 0 & 0 & 0 \\ 0 & 0 & 1 \\ 0 & 1 & 0 \\ 0 & 1 & 1 \\ 1 & 0 & 0 \\ 1 & 0 & 1 \\ 1 & 1 & 0 \\ 1 & 1 & 1 \end{bmatrix}, \quad (1)$$

where $j \in \{0, 1, \dots, m_c - 1\}$, $m_c = 2^n$, and V_i are the voltages across the capacitors C_i . The electrical schemes that are reported in Figure 3 show how, for the case $n = 3$, the output voltage V_{out} is a function of the IGBTs signal vectors \mathbf{T}_j in the two cases $\mathbf{T}_j = \mathbf{T}_2 = [0 \ 1 \ 0]$ and $\mathbf{T}_j = \mathbf{T}_6 = [1 \ 1 \ 0]$.

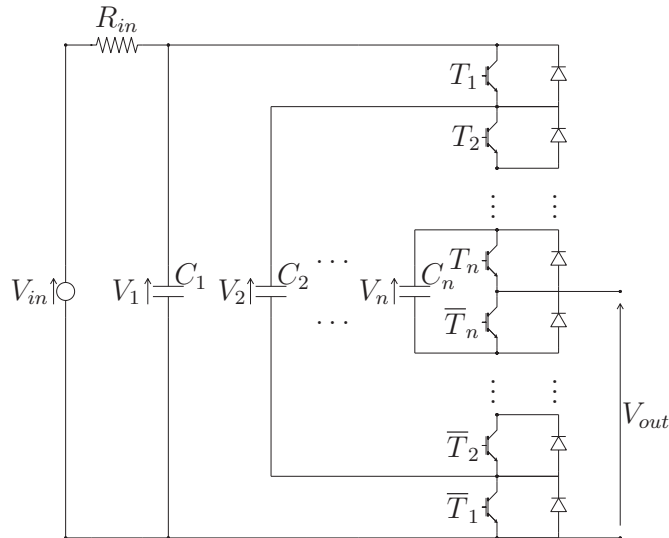


Figure 2. Electrical scheme of the n -dimensional Multilevel Flying-Capacitor Converter.

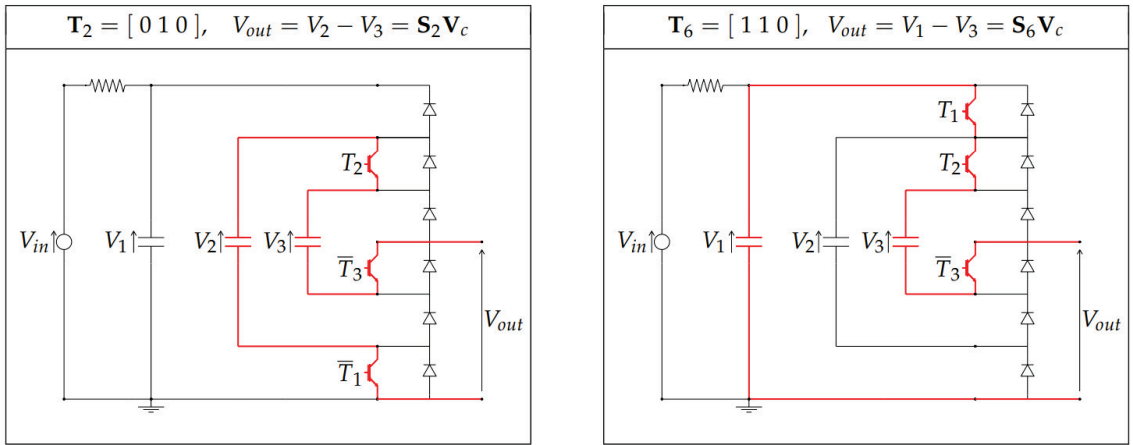


Figure 3. Electrical schemes showing how the output voltage V_{out} is obtained as a function of the Insulated Gate Bipolar Transistors (IGBTs) signal vectors T_i in the two cases $T_j = T_2 = [0\ 1\ 0]$ and $T_j = T_6 = [1\ 1\ 0]$.

One can easily verify that the output voltage V_{out} can always be expressed as follows:

$$V_{out} = S_j V_c, \tag{2}$$

where $S_j = [s_1\ s_2\ \dots\ s_n]$, for $j \in \{0, 1, \dots, m_c - 1\}$, are proper configuration vectors. In the two cases of Figure 3, for example, the output voltage V_{out} can be expressed as in (2) by using the following two configuration vectors: $S_2 = [0\ 1\ -1]$ and $S_6 = [1\ 0\ -1]$. Table 2 shows the relations between the IGBTs signal vectors T_j , the output voltage V_{out} and the configuration vectors S_j for the case $n = 3$, highlighting the connection between vectors T_j and S_j . One can verify that the following property holds.

Table 2. Relations between the IGBTs signal vectors T_j , the output voltage V_{out} and the configuration vectors S_j when $n = 3$.

T_j	$[T_1\ T_2\ T_3]$	V_{out}	$[s_1\ s_2\ s_3]$	S_j	V_{out} (5)	α_i
T_0	$[0\ 0\ 0]$	$S_0 V_c = 0$	$[0\ 0\ 0]$	S_0	0	0
T_1	$[0\ 0\ 1]$	$S_1 V_c = V_3$	$[0\ 0\ 1]$	S_1	$V_{in}/3$	1
T_2	$[0\ 1\ 0]$	$S_2 V_c = V_2 - V_3$	$[0\ 1\ -1]$	S_2	$V_{in}/3$	1
T_3	$[0\ 1\ 1]$	$S_3 V_c = V_2$	$[0\ 1\ 0]$	S_3	$2V_{in}/3$	2
T_4	$[1\ 0\ 0]$	$S_4 V_c = V_1 - V_2$	$[1\ -1\ 0]$	S_4	$V_{in}/3$	1
T_5	$[1\ 0\ 1]$	$S_5 V_c = V_1 - V_2 + V_3$	$[1\ -1\ 1]$	S_5	$2V_{in}/3$	2
T_6	$[1\ 1\ 0]$	$S_6 V_c = V_1 - V_3$	$[1\ 0\ -1]$	S_6	$2V_{in}/3$	2
T_7	$[1\ 1\ 1]$	$S_7 V_c = V_1$	$[1\ 0\ 0]$	S_7	V_{in}	3

Property 1. For $j \in \{0, 1, \dots, m_c - 1\}$, the components $s_i \in \{-1, 0, 1\}$ of the configuration vectors $S_j = [s_1\ s_2\ \dots\ s_n]$ can be obtained from the components $T_i \in \{0, 1\}$ of the IGBTs signal vectors $T_j = [T_1\ T_2\ \dots\ T_n]$, as follows:

$$s_i = \begin{cases} T_1 & \text{if } i = 1, \\ \bar{T}_{i-1} T_i - T_{i-1} \bar{T}_i & \text{if } i \in \{2, \dots, n\}, \end{cases} \tag{3}$$

or, equivalently, as follows:

$$s_i = \begin{cases} 1 & \text{if } T_i > T_{i-1}, \\ 0 & \text{if } T_i = T_{i-1}, \\ -1 & \text{if } T_i < T_{i-1}, \end{cases} \tag{4}$$

for $i \in \{1, 2, \dots, n\}$ and $T_0 = 0$.

As an example, the Reader can verify that Property 1 holds for all of the configuration vectors \mathbf{S}_j that are reported in Table 2 for the case $n = 3$. The second last column of Table 2 shows the values of the output voltage V_{out} corresponding to the following capacitors voltages V_i :

$$V_1 = V_{in}, \quad V_2 = \frac{2V_{in}}{3}, \quad V_3 = \frac{V_{in}}{3} \quad \Rightarrow \quad \mathbf{V}_c = \begin{bmatrix} V_{in} \\ \frac{2V_{in}}{3} \\ \frac{V_{in}}{3} \end{bmatrix}. \tag{5}$$

The last column of Table 2 shows the normalized values α_i , as defined in Section 3.3, used for representing the equally spaced values of the output voltage V_{out} in the case of $n = 3$ capacitors and $m = 4$ output voltage levels.

Let \mathbf{S}_M denote the matrix containing all of the possible configuration vectors \mathbf{S}_j , for $j \in \{0, 1, \dots, m_c - 1\}$:

$$\mathbf{S}_M = \begin{bmatrix} \mathbf{S}_0 \\ \mathbf{S}_1 \\ \vdots \\ \mathbf{S}_{m_c-1} \end{bmatrix}, \quad \text{if } n = 3 \quad \rightarrow \quad \mathbf{S}_M = \begin{bmatrix} \mathbf{S}_0 \\ \mathbf{S}_1 \\ \mathbf{S}_2 \\ \mathbf{S}_3 \\ \mathbf{S}_4 \\ \mathbf{S}_5 \\ \mathbf{S}_6 \\ \mathbf{S}_7 \end{bmatrix} = \begin{bmatrix} 0 & 0 & 0 \\ 0 & 0 & 1 \\ 0 & 1 & -1 \\ 0 & 1 & 0 \\ 1 & -1 & 0 \\ 1 & -1 & 1 \\ 1 & 0 & -1 \\ 1 & 0 & 0 \end{bmatrix}. \tag{6}$$

Matrix \mathbf{S}_M can always be rewritten in block matrix form as follows:

$$\mathbf{S}_M = \left[\begin{array}{c|c} \mathbf{0} & \mathbf{S}_{M0} \\ \hline \mathbf{1} & \mathbf{S}_{M1} \end{array} \right] \quad \text{if } n = 3 \quad \rightarrow \quad \mathbf{S}_M = \begin{bmatrix} 0 & 0 & 0 \\ 0 & 0 & 1 \\ 0 & 1 & -1 \\ 0 & 1 & 0 \\ \hline 1 & -1 & 0 \\ 1 & -1 & 1 \\ 1 & 0 & -1 \\ 1 & 0 & 0 \end{bmatrix}. \tag{7}$$

One can verify that the block matrices $\mathbf{S}_{M0}, \mathbf{S}_{M1} \in \mathbf{R}^{2^{n-1} \times (n-1)}$ satisfy the following property.

Property 2. Let \mathbf{S}_{M0}^j and \mathbf{S}_{M1}^j denote the j -th row of the block matrices $\mathbf{S}_{M0}, \mathbf{S}_{M1} \in \mathbf{R}^{2^{n-1} \times (n-1)}$ defined in (7). Matrix \mathbf{S}_{M1} can be obtained from matrix \mathbf{S}_{M0} , as follows:

$$\mathbf{S}_{M1}^j = -\mathbf{S}_{M0}^{2^{n-1}+1-j} \quad \text{for} \quad j \in \{1, 2, \dots, 2^{n-1}\}. \tag{8}$$

Equation (8) means that the rows of matrix \mathbf{S}_{M1} are equal, with opposite sign, to the rows of matrix \mathbf{S}_{M0} considered in reverse order.

From Property (2) and Equations (2) and (7), one can verify that the following property holds.

Property 3. If the output value $V_{out1} = \mathbf{S}_j \mathbf{V}_c$ is obtained using the configuration vector \mathbf{S}_j , then the following conjugate output value

$$V_{out2} = V_{in} - V_{out1} = \mathbf{S}_{m_c-j} \mathbf{V}_c$$

is obtained by employing the configuration vector \mathbf{S}_{m_c-j} , for $j \in \{0, 1, \dots, m_c - 1\}$ and $m_c = 2^n$.

3.2. Dynamic Model of the Multilevel Flying-Capacitor Converter

The dynamic model of the Multilevel Flying-Capacitor Converter shown in Figure 2 can be given by using the Power-Oriented Graphs (POG) scheme reported in Figure 4. The corresponding POG state-space equations are the following:

$$\begin{cases} \mathbf{C} \dot{\mathbf{V}}_c = \mathbf{A} \mathbf{V}_c - \mathbf{S}_j^T I_{out} + \mathbf{B} V_{in}, \\ V_{out} = \mathbf{S}_j \mathbf{V}_c. \end{cases} \quad (9)$$

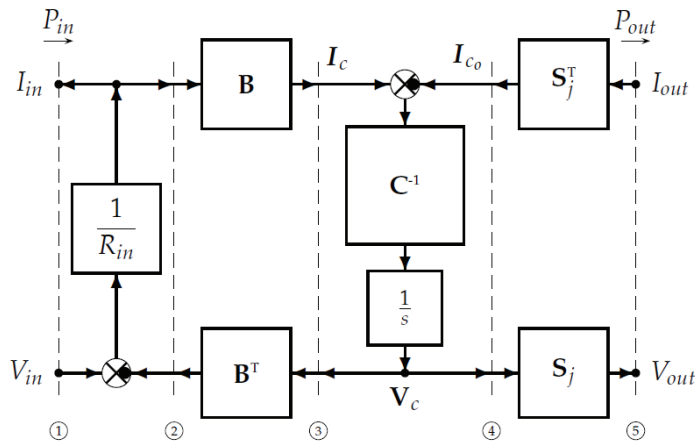


Figure 4. Power-Oriented Graphs (POG) model of the Multilevel Flying-Capacitor Converter.

Matrices \mathbf{C} , \mathbf{A} and vectors \mathbf{V}_c , \mathbf{S}_j^T and \mathbf{B} are defined, as follows:

$$\mathbf{C} = \begin{bmatrix} C_1 & 0 & \dots & 0 \\ 0 & C_2 & \dots & 0 \\ \vdots & \vdots & \ddots & \vdots \\ 0 & 0 & \dots & C_n \end{bmatrix}, \quad \mathbf{A} = \begin{bmatrix} -\frac{1}{R_{in}} & 0 & \dots & 0 \\ 0 & 0 & \dots & 0 \\ \vdots & \vdots & \ddots & \vdots \\ 0 & 0 & \dots & 0 \end{bmatrix}, \quad \mathbf{V}_c = \begin{bmatrix} V_1 \\ V_2 \\ \vdots \\ V_n \end{bmatrix}, \quad \mathbf{S}_j^T = \begin{bmatrix} s_1 \\ s_2 \\ \vdots \\ s_n \end{bmatrix}, \quad \mathbf{B} = \begin{bmatrix} \frac{1}{R_{in}} \\ 0 \\ \vdots \\ 0 \end{bmatrix}. \quad (10)$$

A representation such as the one that is shown in (9) and (10) highlights the following interesting features of the system:

- The energy matrix \mathbf{C} groups together the dynamic physical parameters C_i for $i \in \{1, 2, \dots, n\}$, namely the system capacitors.
- The power matrix \mathbf{A} and the input matrix \mathbf{B} contain the static physical parameter R_{in} , which is the system input resistance.
- The configuration vector \mathbf{S}_j contains the control signals that directly determine how the output current I_{out} is going to charge/discharge the capacitors through $I_{c0} = \mathbf{S}_j^T I_{out}$ and, at the same time, how the output voltage V_{out} is going to be generated from the capacitors voltages through (2).

Therefore, the proposed POG state-space model allows for the parameters within the system matrices to maintain their physical meaning, and also allows to emphasize the presence of

the configuration vector \mathbf{S}_j , representing the output of the two control algorithms that are addressed in Section 4.1 and Section 4.4. The POG block scheme that is shown in Figure 4 presents a graphical representation of the dynamic model of the considered system. The vertical dashed lines ①, ②, . . . , and ⑤ present in the POG scheme describe the system power sections: the product of the two power variables characterizing the power section has the physical meaning of "power flowing through the considered power section". The input power $P_{in} = V_{in} I_{in}$ flows through power section ① and the output power $P_{out} = V_{out} I_{out}$ flows through power section ⑤. The block scheme in between sections ① and ② describes the static equation of the input resistance R_{in} , the block scheme in between sections ② and ③ describes the interaction between the input resistance R_{in} and the capacitors C_i , and the block scheme in between sections ③ and ④ describes the dynamic equations of the capacitors C_i . Finally, the block scheme in between sections ④ and ⑤, which is characterized by the configuration vector \mathbf{S}_j , describes the interaction between the capacitors C_i and the output power section ⑤.

Remark 1. The first vectorial equation of system (9) can be rewritten as follows:

$$\dot{\mathbf{V}}_c = \mathbf{C}^{-1} \mathbf{A} \mathbf{V}_c - \underbrace{\mathbf{C}^{-1} \mathbf{S}_j^T}_{\dot{\mathbf{V}}_c^{out}} I_{out} + \mathbf{C}^{-1} \mathbf{B} V_{in}.$$

Vector $\dot{\mathbf{V}}_c^{out} = -\mathbf{C}^{-1} \mathbf{S}_j^T I_{out}$ is the component of the velocity vector $\dot{\mathbf{V}}_c$ which is due to the presence of the output current I_{out} . The direction of vector $\dot{\mathbf{V}}_c^{out}$ is completely defined by the configuration vector \mathbf{S}_j and by the values of the capacitors C_i .

Remark 2. The first scalar equation of system (9) can be rewritten as follows:

$$R_{in} C_1 \dot{V}_1 = V_{in} - V_1 - R_{in} s_1 I_{out}. \tag{11}$$

Because the value of the input resistance R_{in} is typically very low, from (11) it follows that $V_1 \simeq V_{in}$, that is the value of voltage V_1 tends to remain close to the input voltage value V_{in} . Hereinafter, the condition $V_1 = V_{in}$ will be assumed. This condition holds exactly if $R_{in} \rightarrow 0$, or if capacitor C_1 is replaced with a battery providing a constant voltage V_{in} .

3.3. Calculation of All the Configuration Voltage Vectors

An m -level Multilevel Converter is characterized by m different equally spaced values V_{oi} of the output voltage V_{out} :

$$V_{oi} = \frac{i V_{in}}{m - 1} \quad \text{for} \quad i = \{0, 1, \dots, m - 1\}. \tag{12}$$

In the following, the values V_{oi} in (12) will often be referred to by using the symbolic integer values α_i , defined as follows:

$$\alpha_i = \frac{V_{oi}}{K_m} = i \quad \text{where} \quad K_m = \frac{V_{in}}{m - 1}, \tag{13}$$

for $i = \{0, 1, \dots, m - 1\}$. From (13), it follows that the product $\alpha_i K_m$ directly gives the values of the corresponding equally spaced values V_{oi} of the output voltage V_{out} . All of the possible values V_{oi} of the output voltage V_{out} that can be obtained using a particular voltage vector \mathbf{V}_c can be expressed as follows:

$$\mathbf{V}_o = \mathbf{S}_M \mathbf{V}_c, \tag{14}$$

where \mathbf{S}_M is the matrix defined in (6). The considered Flying-Capacitor system acts properly as a Multilevel Converter only if vector $\mathbf{V}_o = [V_{o1}, V_{o2}, \dots, V_{om_c}]^T$ contains, among its components V_{oj} , all of the m different equally spaced values V_{oi} given in (12):

$$\forall i \in \{0, 1, \dots, m - 1\}, \exists V_{oj} \in \{V_{o1}, V_{o2}, \dots, V_{om_c}\} \mid V_{oj} = \frac{i V_{in}}{m - 1}. \quad (15)$$

Definition 1. Any voltage vector \mathbf{V}_c satisfying (14) and (15) will be called a " Configuration Voltage Vector of order m " for the Multilevel Flying-Capacitor Converter.

The problem of finding all the Configuration Voltage Vectors \mathbf{V}_c of order m for the considered Multilevel Flying-Capacitor Converter can be solved as follows. Dividing (14) by constant K_m , one obtains the following symbolic integer relation:

$$\mathbf{V}_L = \mathbf{S}_M \mathbf{V}_m \quad \text{where} \quad \mathbf{V}_L = \frac{\mathbf{V}_o}{K_m} \quad \text{and} \quad \mathbf{V}_m = \frac{\mathbf{V}_c}{K_m}. \quad (16)$$

A vector \mathbf{V}_m in (16) is a Configuration Voltage Vector of order m only if all the components V_{Lj} of vector $\mathbf{V}_L = [V_{L1}, V_{L2}, \dots, V_{Lm_c}]$, for $j \in \{1, 2, \dots, m_c\}$, are integer values $V_{Lj} \in \{0, 1, \dots, m - 1\}$ that satisfy the following relation:

$$\text{unique}(\{V_{L1}, V_{L2}, \dots, V_{Lm_c}\}) = \{0, 1, \dots, m - 1\}, \quad (17)$$

where "unique(S)" is a function providing a new set containing all the elements of set S which are different from each other.

Property 4. In (16), all of the components β_i of a Configuration Voltage Vector \mathbf{V}_m , for $i \in \{1, \dots, n\}$, are integer values satisfying $\beta_i \in \{0, 1, \dots, m - 1\}$:

$$\mathbf{V}_m = \begin{bmatrix} \beta_n \\ \beta_{n-1} \\ \vdots \\ \beta_1 \end{bmatrix} = \begin{bmatrix} m - 1 \\ \beta_{n-1} \\ \vdots \\ \beta_1 \end{bmatrix}, \quad (18)$$

where $\beta_{i+1} \geq \beta_i$ for $i \in \{1, 2, \dots, n - 2\}$. Furthermore, note that the top component β_n of vector \mathbf{V}_m is always given by $\beta_n = m - 1$.

The first statement of Property 4 holds true, because: (1) all of the components V_{Lj} of vector \mathbf{V}_L in (16) are integer values, see (17); and, (2) the configuration vectors $\mathbf{S}_1 = [0 \dots, 0, 0, 1]$, $\mathbf{S}_2 = [0 \dots, 0, 1, 0]$, $\mathbf{S}_3 = [0 \dots, 1, 0, 0]$, ..., $\mathbf{S}_{m_c} = [1, 0 \dots, 0, 0]$ are always present among the rows of matrix \mathbf{S}_M . The second statement of Property 4 holds true, because the top component β_n of vector \mathbf{V}_m is always equal to the first component V_1 of vector \mathbf{V}_c expressed in symbolic integer form: $\beta_n = V_1/K_m = V_{in}/K_m = m - 1$, see (13). This relation holds thanks to the assumption $V_1 = V_{in}$ made in Remark 2.

Thanks to Property 4, all of the Configuration Voltage Vectors \mathbf{V}_m of order m for the considered Multilevel Flying-Capacitor Converter can be found by making an exhaustive research in (18) for $\beta_i \in \{0, 1, \dots, m - 1\}$, and keeping all of the solutions \mathbf{V}_m that satisfy (16) and (18). Table 3 reports all of the Configuration Voltage Vectors \mathbf{V}_m for the case $n = 3$ and for $m \in \{4, 5, \dots, 8\}$. The total number N_c of Configuration Voltage Vectors for the case $n = 3$ is $N_c = 24$. Figure 5 shows a graphical representation of the normalized form

$\overline{\overline{\mathbf{V}}}_m$ of all the Configuration Voltage Vectors \mathbf{V}_m for the case $n = 3$. The normalized form $\overline{\overline{\mathbf{V}}}_m$ of the Voltage Vectors \mathbf{V}_m defined in (18) is obtained as follows:

$$\overline{\overline{\mathbf{V}}}_m = \frac{\mathbf{V}_m(2 : \text{end})}{m - 1} = \begin{bmatrix} \frac{\beta_{n-1}}{m-1} \\ \vdots \\ \frac{\beta_1}{m-1} \end{bmatrix} = \begin{bmatrix} \overline{\overline{V}}_2 \\ \vdots \\ \overline{\overline{V}}_n \end{bmatrix} \quad \text{if } n = 3 \quad \rightarrow \quad \overline{\overline{\mathbf{V}}}_m = \begin{bmatrix} \overline{\overline{V}}_2 \\ \overline{\overline{V}}_3 \end{bmatrix}, \quad (19)$$

meaning that the last $n - 1$ components of vector \mathbf{V}_m , from the second to the last one, are normalized by $m - 1$. Figure 5 clearly shows a symmetry with respect to the red straight line $\overline{\overline{V}}_3 = 1 - \overline{\overline{V}}_2$. This symmetry is strictly connected to Property 5 and Property 6, introduced in the following.

Table 3. All of the Configuration Voltage Vectors \mathbf{V}_m for the case $n = 3$ and $m \in \{4, 5, \dots, 8\}$.

m	4	4	4	5	5	5	6	6	6	6	6	7	7	7	7	7	7	8	8	8	8	8	8	
\mathbf{V}_m	3	3	3	4	4	4	5	5	5	5	5	6	6	6	6	6	6	7	7	7	7	7	7	
	1	2	2	3	3	3	2	3	3	4	4	4	3	3	4	4	5	5	3	3	5	6	5	6
	1	1	2	1	1	2	1	1	2	1	2	3	1	2	1	3	2	3	1	2	1	2	4	4
N_β	2	3	4	3	4	5	3	4	5	5	6	7	4	5	5	7	7	8	4	5	6	8	9	10

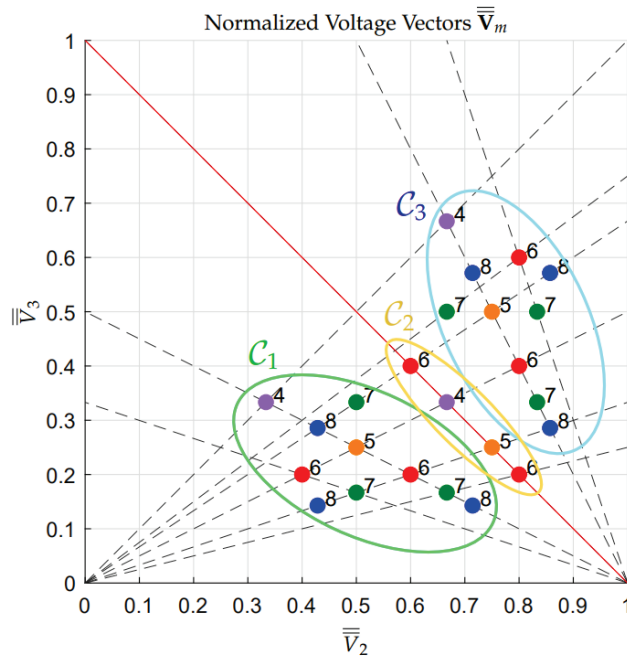


Figure 5. All the Configuration Voltage Vectors \mathbf{V}_m , in normalized form $\overline{\overline{\mathbf{V}}}_m$, for the case $n = 3$.

Property 5. For every Configuration Voltage Vector \mathbf{V}_m , there exists a Conjugate Configuration Voltage Vector \mathbf{V}_m^* , defined as follows:

$$\mathbf{V}_m = \begin{bmatrix} m - 1 \\ \beta_{n-1} \\ \vdots \\ \beta_2 \\ \beta_1 \end{bmatrix} \quad \Rightarrow \quad \mathbf{V}_m^* = \begin{bmatrix} m - 1 \\ m - 1 - \beta_1 \\ m - 1 - \beta_2 \\ \vdots \\ m - 1 - \beta_{n-1} \end{bmatrix}. \quad (20)$$

Furthermore, one can easily verify that $(\mathbf{V}_m^*)^* = \mathbf{V}_m$. This property directly follows from Property 3.

Property 6. Every Configuration Voltage Vector \mathbf{V}_m , see (20), is characterized by a configuration number N_β , defined as follows:

$$N_\beta = \sum_{i=1}^{n-1} \beta_i.$$

The set \mathcal{C} of all the Configuration Voltage Vectors \mathbf{V}_m can be divided into three different subsets, which are denoted by \mathcal{C}_1 , \mathcal{C}_2 , and \mathcal{C}_3 , defined as follows:

$$\mathcal{C}_1 = \{\mathbf{V}_m \in \mathcal{C} | N_\beta < m - 1\}, \quad \mathcal{C}_2 = \{\mathbf{V}_m \in \mathcal{C} | N_\beta = m - 1\}, \quad \mathcal{C}_3 = \{\mathbf{V}_m \in \mathcal{C} | N_\beta > m - 1\}. \quad (21)$$

The sets \mathcal{C}_1 and \mathcal{C}_3 are conjugate to one another: if $\mathbf{V}_m \in \mathcal{C}_1$, then $\mathbf{V}_m^* \in \mathcal{C}_3$ and vice versa. Furthermore, set \mathcal{C}_2 is conjugate to itself: if $\mathbf{V}_m \in \mathcal{C}_2$, then $\mathbf{V}_m^* = \mathbf{V}_m$.

Note: Table 3 has been given, for each number of output voltage levels m , in ascending order from left to right with respect to the configuration number N_β . Additionally, the colors that are present in Table 3 denote the subsets to which the Configuration Voltage Vectors \mathbf{V}_m belong: green color if $\mathbf{V}_m \in \mathcal{C}_1$, yellow color if $\mathbf{V}_m \in \mathcal{C}_2$, and blue color if $\mathbf{V}_m \in \mathcal{C}_3$. The same color notation has been adopted in Figure 5 to identify the subsets to which the normalized forms $\bar{\mathbf{V}}_m$ of the Configuration Voltage Vectors \mathbf{V}_m belong, which are highlighted by the colored ellipses.

The number N_c of Configuration Voltage Vectors \mathbf{V}_m for the case $n = 4$ is $N_c = 407$. Figure 6 shows a graphical representation of the normalized form $\bar{\mathbf{V}}_m$ of all the Configuration Voltage Vectors \mathbf{V}_m for the case $n = 4$. The considerations that are introduced in Property 5 and Property 6 also apply to the set of all the Configuration Voltage Vectors \mathbf{V}_m for the cases $n = 4$, $n = 5$, etc.

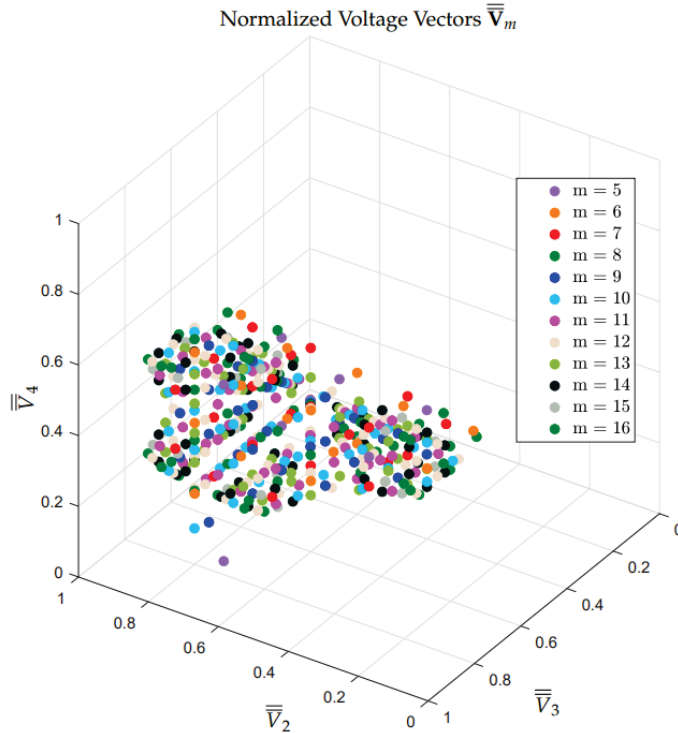
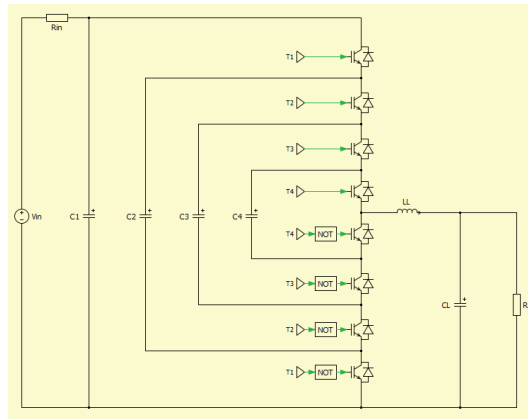


Figure 6. All of the Configuration Voltage Vectors \mathbf{V}_m , in normalized form $\bar{\mathbf{V}}_m$, for the case $n = 4$.

The number N_c of the Configuration Voltage Vectors \mathbf{V}_m increases very rapidly by increasing n , with a rate faster than exponential: $N_c = 24$ for $n = 3$, $N_c = 407$ for $n = 4$, $N_c = 14252$ for $n = 5$, $N_c = 1044305$ for $n = 6$, etc.

3.4. Model Verification

The model of the multilevel flying-capacitor converter proposed in Figure 4 has been tested in simulation against one of the most well-known platforms for the simulation of power electronics systems, namely PLECS, in order to perform a model verification. For this comparative simulations, the case $n = 4$ and $\mathbf{V}_m = [4 \ 3 \ 2 \ 1]^T$ has been considered to be a case study. Figure 7 reports the PLECS model and the system parameters. The initial and desired voltages for the multilevel converter capacitors can be determined by computing the voltage vector \mathbf{V}_c starting from the configuration voltage vector \mathbf{V}_m and using (13) and (16), namely $\mathbf{V}_c = [100 \ 75 \ 50 \ 25]^T$. The initial conditions of the RLC load are assumed to be equal to zero. The desired voltage V_d is assumed to be sinusoidal with an offset equal to $V_{in}/2$, a peak-to-peak amplitude equal to V_{in} and a frequency equal to 50 Hz. The simulation performed using the PLECS model in Figure 7 and the simulation performed using the Matlab/Simulink POG model in Figure 4 have both been performed applying the Minimum Distance Control described in Section 4.1.



V_{in}	100 [V]
R_{in}	0.1 [m Ω]
C_1	25 [mF]
C_2	33 [mF]
C_3	50 [mF]
C_4	100 [mF]
L_L	19 [mH]
C_L	50 [μ F]
R_L	10 [Ω]

Figure 7. PLECS implementation and parameters of the $n = 4$ multilevel flying-capacitor converter.

The results that are given by the PLECS model are shown in Figure 8. The comparison of these results with those given by the Matlab/Simulink POG model is reported in Figure 9.



Figure 8. Simulation results given by the PLECS model: output voltage V_{out} (upper subplot) and filtered voltage across C_L (lower subplot).

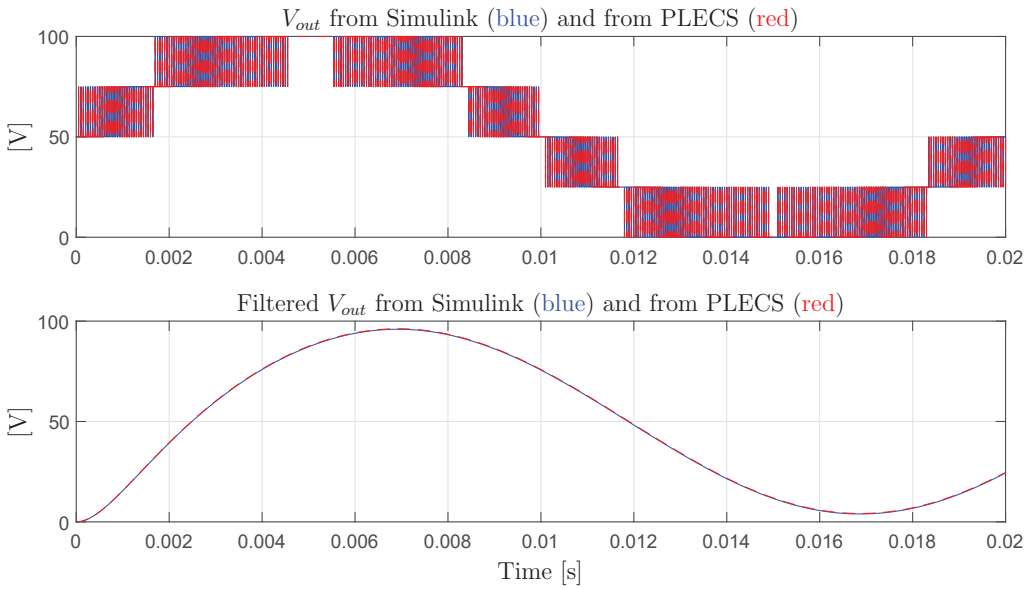


Figure 9. Comparison of the results given by PLECS and Matlab/Simulink: output voltage V_{out} (upper subplot) and filtered voltage across C_L (lower subplot).

The very good matching between the output voltage characteristics that are given by PLECS and by Matlab/Simulink in Figure 9 verifies the correctness of the proposed model of the multilevel flying-capacitor converter.

4. Control of the Multilevel Flying-Capacitor Converter

4.1. Minimum Distance Control

Figure 10 shows the typical scheme of a closed-loop Minimum Distance Control of a Multilevel Flying-Capacitor Converter. The first block of the scheme is the Output Level Generator. Let us consider the case of $m = 6$ output voltage levels, which will, therefore, be equally spaced between level “0” and level “ $m - 1 = 5$ ”. The black characteristic in Figure 11 shows the desired normalized voltage \tilde{V}_d multiplied by $m - 1$, in order to see it superimposed to the blue characteristic, namely the desired output voltage level α .

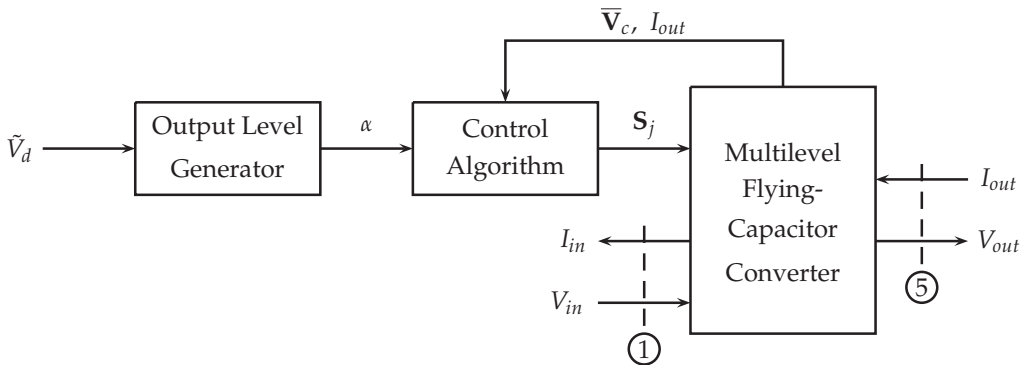


Figure 10. Typical scheme of a closed-loop Minimum Distance Control of a Multilevel Flying-Capacitor Converter.

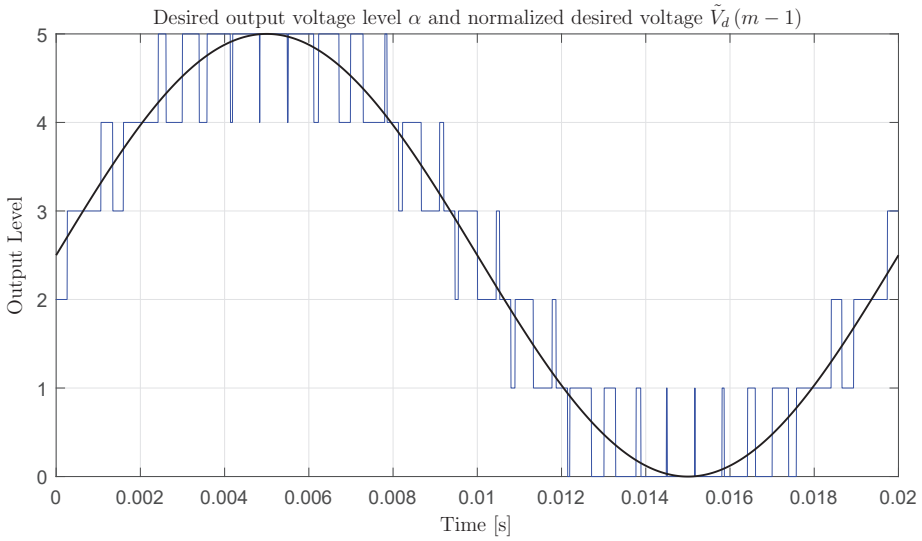


Figure 11. Desired output voltage level α superimposed to normalized desired voltage $\tilde{V}_d(m-1)$.

The Output Level Generator generates an integer value $\alpha \in \{0, 1, \dots, m-1\}$, which defines the desired output level to be applied at a certain time instant t_k :

$$\alpha = \sum_{h=0}^{m-1} (V_d \geq V_{cr_h}),$$

where $(V_d \geq V_{cr_h}) = 1$ if $V_d \geq V_{cr_h}$ and $(V_d \geq V_{cr_h}) = 0$ if $V_d < V_{cr_h}$. The second and third blocks in the scheme of Figure 10 are the Control Algorithm and the Multilevel Flying-Capacitor Converter. The latter is modeled using the POG block scheme that is shown in Figure 4. Indeed, it is possible to notice the correspondence between the power sections ① and ③ in Figures 4 and 10. The purpose of the Control Algorithm is to properly generate the Configuration Voltage Vector \mathbf{S}_j , which has a one-to-one correspondence with the IGBTs signal vector \mathbf{T}_j through Property 1, giving the desired output level α . This will be accomplished by exploiting the redundancy of Configuration Voltage Vectors \mathbf{S}_j generating the same desired output level α when available, as described in the remainder of this section. The Control Algorithm shown in Figure 10 is typically a "Minimum Distance Algorithm". Thanks to the assumption $V_1 = V_{in}$ made in Remark 2, the Minimum Distance algorithm only applies to the components V_2, V_3, \dots, V_n of the capacitors voltage vector \mathbf{V}_c . Let us denote, as $\bar{\mathbf{V}}_c = \mathbf{V}_c(2:n)$, $\bar{\mathbf{V}}_{m0} = K_m \mathbf{V}_m(2:n) = V_{in} \bar{\mathbf{V}}_m$ and $\bar{\mathbf{S}}_{Cj} = -\mathbf{S}_j(2:n) ./ \mathbf{C}(2:n)$, the following reduced vectors:

$$\bar{\mathbf{V}}_c = \begin{bmatrix} V_2 \\ V_3 \\ \vdots \\ V_n \end{bmatrix}, \quad \bar{\mathbf{V}}_{m0} = \begin{bmatrix} \frac{V_{in}\beta_{n-1}}{m-1} \\ \frac{V_{in}\beta_{n-2}}{m-1} \\ \vdots \\ \frac{V_{in}\beta_1}{m-1} \end{bmatrix}, \quad \bar{\mathbf{S}}_{Cj} = \begin{bmatrix} -\frac{s_{2j}}{C_2} \\ -\frac{s_{3j}}{C_3} \\ \vdots \\ -\frac{s_{nj}}{C_n} \end{bmatrix}, \quad (22)$$

where \mathbf{V}_m is the considered Configuration Voltage Vector that is introduced in (16), and \mathbf{S}_j is the j -th configuration vector defined in (10). The minimum distance algorithm tries to

keep the reduced voltage vector $\bar{\mathbf{V}}_c$ as close as possible to the desired reduced voltage vector $\bar{\mathbf{V}}_{m0}$. Let α be the desired output level to be applied at time t_k and let

$$\mathcal{S}_\alpha = \left\{ j \mid j \in [0, 1, \dots, m_c - 1] \wedge \mathbf{S}_j \mathbf{V}_c = \frac{\alpha V_{in}}{m - 1} \right\} \quad (23)$$

be the set of the indexes j of all the configuration vectors \mathbf{S}_j , which, for the considered Configuration Voltage Vector \mathbf{V}_m , provide the output level α . The Minimum Distance algorithm acts as follows:

1. At instant t_k , read the value of the reduced voltage vector $\bar{\mathbf{V}}_c(t_k)$;
2. For any $j \in \mathcal{S}_\alpha$, compute the new position $\bar{\mathbf{V}}_{cj}(t_k + T_W)$ of the reduced voltage vector $\bar{\mathbf{V}}_c$ at instant $t_k + T_W$, which is due to the application of the configuration vector \mathbf{S}_j :

$$\bar{\mathbf{V}}_{cj}(t_k + T_W) = \bar{\mathbf{V}}_c(t_k) + \underbrace{\bar{\mathbf{S}}_{Cj} I_{out} T_W}_{\Delta \bar{\mathbf{S}}_{Cj}} = \bar{\mathbf{V}}_c(t_k) + \Delta \bar{\mathbf{S}}_{Cj}, \quad (24)$$

where I_{out} is the value of the output current at instant t_k and T_W is the time for which the configuration vector \mathbf{S}_j is applied.

3. For any $j \in \mathcal{S}_\alpha$, compute the following distance vectors:

$$\Delta \bar{\mathbf{V}}_{cj} = \bar{\mathbf{V}}_{cj}(t_k + T_W) - \bar{\mathbf{V}}_{m0} \quad (25)$$

between points $\bar{\mathbf{V}}_{cj}(t_k + T_W)$ and the desired reduced Voltage Vector $\bar{\mathbf{V}}_{m0}$.

4. At instant t_k , apply the configuration vector \mathbf{S}_{j^*} , with $j^* \in \mathcal{S}_\alpha$, for which the norm of vectors $\Delta \bar{\mathbf{V}}_{cj}$ is minimized:

$$\mathbf{S}_{j^*} \text{ such that } |\Delta \bar{\mathbf{V}}_{cj^*}| \leq |\Delta \bar{\mathbf{V}}_{cj}| \text{ for } j \in \mathcal{S}_\alpha. \quad (26)$$

Figure 12 shows a graphical example of how the Minimum Distance algorithm works in the case of $n = 3, m = 4, \mathbf{V}_m = [3 \ 2 \ 1]^T$ when the desired output level is $\alpha = 1$. In this case, the distance vector $\Delta \bar{\mathbf{V}}_{cj}$ in (25) having the minimum norm is $|\Delta \mathbf{V}_{c4}|$, highlighted in magenta in the figure.

4.2. Basic Configurations

For any n -dimensional multilevel flying-capacitor converter, let us denote, as *Basic Configuration Voltage Vector*, the following Configuration Voltage Vector:

$$\mathbf{V}_m^* = [m-1 \ m-2 \ \dots \ 2 \ 1]^T, \quad (27)$$

occurring when $m = n + 1$.

Property 7. For any given n , the basic configuration voltage vector \mathbf{V}_m^* is the only configuration voltage vector for which the Minimum Distance algorithm is able to keep the reduced voltage vector $\bar{\mathbf{V}}_c$ in the neighborhood of the desired reduced voltage vector $\bar{\mathbf{V}}_{m0}^*$, for any value of the normalized desired voltage \tilde{V}_d and the output current I_{out} .

This property holds because the Basic Configuration Voltage Vector \mathbf{V}_m^* is the only one for which the number of possible configurations \mathbf{S}_j that are associated to the two adjacent levels of any desired voltage V_d are sufficient to guarantee that, at each PWM step, the distance between the reduced vector \mathbf{V}_c and the desired reduced voltage vector \mathbf{V}_{m0}^* is decreased for any value of the output current I_{out} . For any other Configuration Voltage Vector \mathbf{V}_m , it is always possible to find values for V_d and I_{out} causing the reduced vector \mathbf{V}_c to indefinitely diverge from the desired reduced voltage vector \mathbf{V}_{m0} .

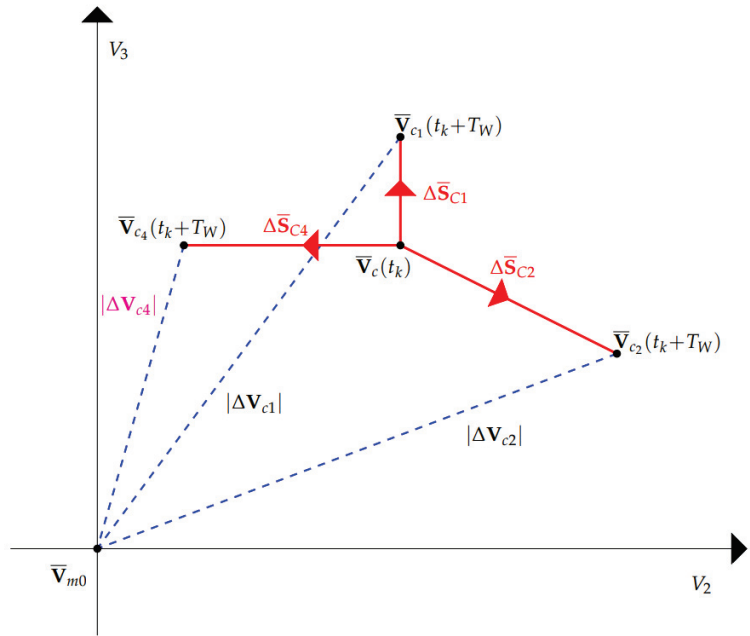


Figure 12. Calculations of the Minimum Distance algorithm in the case of $n = 3, m = 4, \mathbf{V}_m = [3 \ 2 \ 1]^T$ when the desired output level is $\alpha = 1$.

Figure 13 shows a first example of the validity of Property 7, for the case $n = 3$ and $\mathbf{V}_m^* = [3 \ 2 \ 1]^T$. In this figure, a certain number of trajectories in the space (V_2, V_3) starting from initial conditions that are distant from the desired reduced voltage vector $\bar{\mathbf{V}}_{m0}$ are shown. Red asterisks in the figure denote the considered initial conditions. The trajectories have been obtained using the Minimum Distance algorithm and using the following input signals:

$$V_d = \frac{V_{in}}{2} + \frac{V_{in}}{2} \sin(800\pi t), \quad I_{out} = 10 \text{ A}, \quad V_{in} = 1 \text{ V}. \quad (28)$$

The figure clearly shows that all of the trajectories asymptotically tend to the desired reduced voltage vector $\bar{\mathbf{V}}_{m0} = [0.66 \ 0.33]^T$.

A second similar example is given in Figure 14 for the case $n = 4$ and $\mathbf{V}_m^* = [4 \ 3 \ 2 \ 1]^T$. The three-dimensional trajectories in the space (V_2, V_3, V_4) have been obtained using the same input signals (28) that were used for the previous example. Even in this case, one can notice that all of the trajectories asymptotically tend to the desired reduced voltage vector $\bar{\mathbf{V}}_{m0} = [0.75 \ 0.5 \ 0.25]^T$.

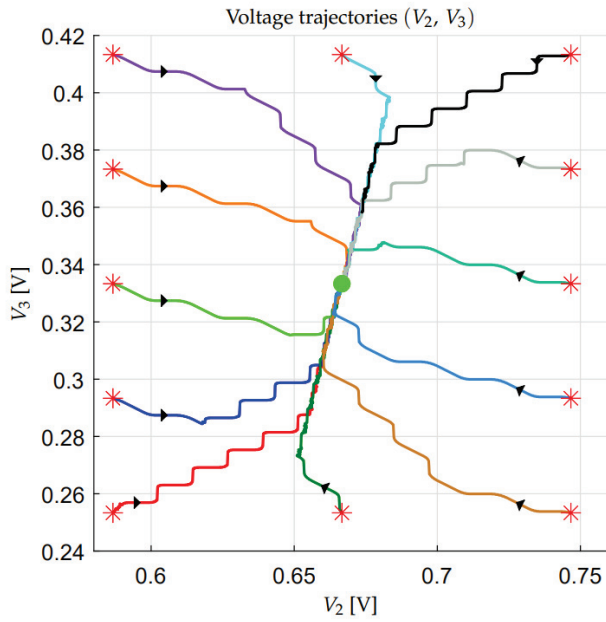


Figure 13. Stability of the Basic Configuration Voltage Vector $\mathbf{V}_m^* = [3 \ 2 \ 1]^T$ for $n = 3$.

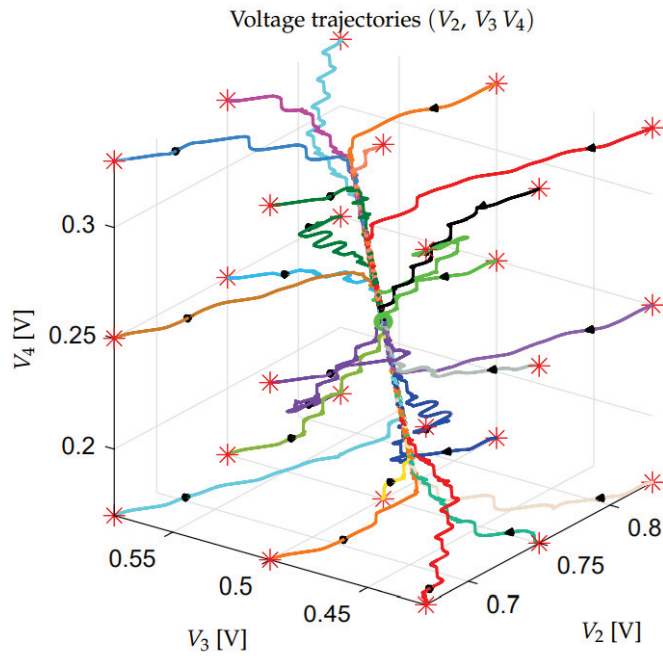


Figure 14. Stability of the Basic Configuration Voltage Vector $\mathbf{V}_m^* = [4 \ 3 \ 2 \ 1]^T$ for $n = 4$.

4.3. Robustness Assessment of the Configuration Voltage Vectors

All of the Configuration Voltage Vectors \mathbf{V}_m different from the basic one \mathbf{V}_m^* are characterized by divergent voltage trajectories under particularly unfavorable operating

conditions, as stated in Property 7. In Figures 15 and 16, for example, the voltage trajectories that are associated with two different Configuration Voltage Vectors \mathbf{V}_m in the space (V_2, V_3) for the case $n = 3$ are reported, starting from different initial conditions that are distant from the desired reduced voltage vector $\bar{\mathbf{V}}_{m0}$. The considered initial conditions are denoted by red asterisks in the figures. The trajectories shown in Figure 15 have been obtained using $\mathbf{V}_m = [5 \ 4 \ 3]^T$, $\bar{\mathbf{V}}_{m0} = [0.8 \ 0.6]^T$, $V_d = 0.3 \text{ V}$ and $I_{out} = 10 \text{ A}$. The trajectories in Figure 16 have been obtained using $\mathbf{V}_m = [5 \ 3 \ 2]^T$, $\bar{\mathbf{V}}_{m0} = [0.6 \ 0.4]^T$, $V_d = 0.7 \text{ V}$ and $I_{out} = 10 \text{ A}$. In both cases, after a transient, all of the trajectories tend to diverge along a particular direction, which is characteristic of the considered Configuration Voltage Vectors \mathbf{V}_m . One can verify that the same qualitative behavior is obtained for any \mathbf{V}_m different from the Basic Configuration Voltage Vector \mathbf{V}_m^* .

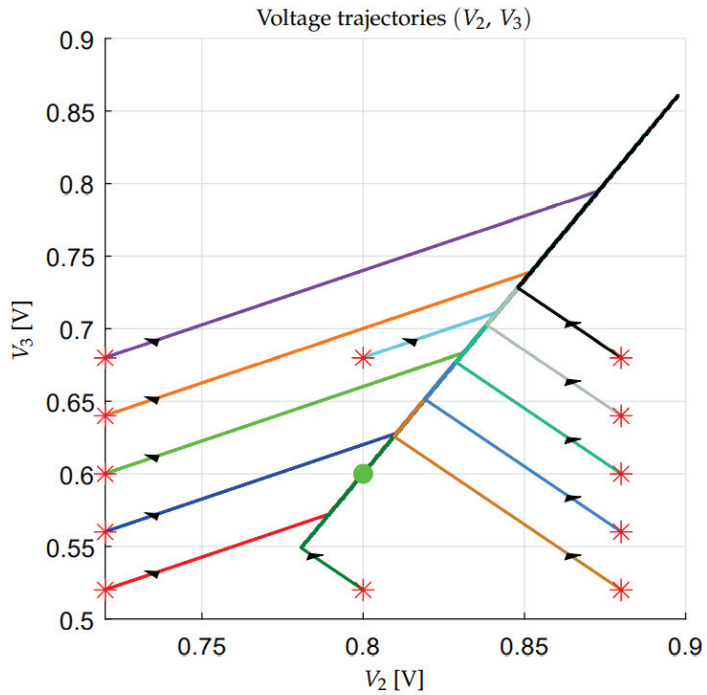


Figure 15. Instability of the Configuration Voltage Vector $\mathbf{V}_m = [5 \ 4 \ 3]^T$ when $V_d = 0.3$ and $I_{out} = 10 \text{ [A]}$.

From the previous considerations, the need to find a criterion to evaluate the degree of divergence of the different Configuration Voltage Vectors \mathbf{V}_m arises. For this purpose, a *Vectorial Divergence Function* $\vec{\mathbf{V}}_m(V_d)$ can be defined for each \mathbf{V}_m . Before giving the definition of this function, the following preliminary material needs to be introduced.

- Given the Configuration Voltage Vectors $\mathbf{V}_m = [m - 1 \ \beta_{n-1} \ \dots \ \beta_2 \ \beta_1]^T$ and the value of the last n -th capacitor C_n , let us choose the values of the remaining $n - 1$ capacitors C_1, C_2, \dots, C_{n-1} , as follows:

$$C_1 = \frac{\beta_1 C_n}{m - 1}, \quad C_2 = \frac{\beta_1 C_n}{\beta_{n-1}}, \quad \dots, \quad C_{n-2} = \frac{\beta_1 C_n}{\beta_3}, \quad C_{n-1} = \frac{\beta_1 C_n}{\beta_2}, \quad (29)$$

namely, each capacitor C_i is chosen inversely proportional to the components of vector \mathbf{V}_m .

- The Minimum Distance Algorithm that is given in Section 4.1 can be rewritten in an equivalent form by using the following Matlab-like function " $[S_j, \Delta \bar{V}] = \text{MDA}(\Delta \bar{V}, \alpha, I_{out}, T_W)$ ", which must be called providing $\Delta \bar{V} = \bar{V}_c(t_k) - \bar{V}_{m0}$:

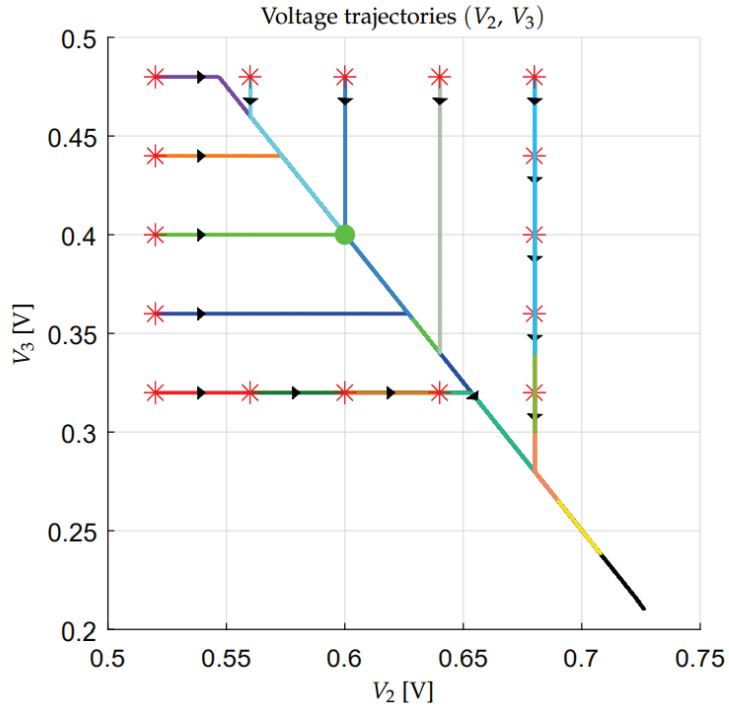


Figure 16. Instability of the Configuration Voltage Vector $\mathbf{V}_m = [5 \ 3 \ 2]^T$ when $V_d = 0.7$ and $I_{out} = 10[A]$.

```

function [S_j, ΔV̄] = MDA(ΔV̄, α, I_out, T_W)
Compute set S_α defined in (23);
Compute vectors S_Cj defined in (22) using (29);
for j ∈ S_α
    Compute ΔV̄_cj as follows, see (25):
    ΔV̄_cj = ΔV̄ + S_Cj I_out T_W;
end
Find j* ∈ S_α for which the norm of vectors ΔV̄_cj is minimized, as in (26);
Set S_j = S_j*;
Set ΔV̄ = ΔV̄_cj*;
    
```

Definition 2. Given a Configuration Voltage Vector \mathbf{V}_m , the corresponding Vectorial Divergence Function $\vec{V}_m(\vec{V}_d)$ is defined, by employing a Matlab-like notation, as follows:

$I_{out} = 1;$	% Function normalized with respect to I_{out}
$T_{PWM} = 1;$	% Function normalized with respect to time
$C_n = 1;$	% Function normalized with respect to C_n
for $\tilde{V}_d = (0 : 1/N_{Points} : 1)$	% N_{Points} of variable $\tilde{V}_d \in [0, 1]$
$V_D = \tilde{V}_d(m - 1);$	% N_{Points} of variable $V_D \in [0, m - 1]$
$\alpha_H = \text{ceil}(V_D);$	% Upper adjacent level
$\alpha_L = \text{floor}(V_D);$	% Lower adjacent level
$d_c = V_D - \alpha_L;$	% Duty cycle of the upper level
$\Delta\vec{V} = 0;$	% Zero initial condition
for $h = 1 : N_{Steps}$	% Repeat N_{Steps} times
$T_W = d_c T_{PWM}$	% Time interval of the upper level
$[\sim, \Delta\vec{V}] = \text{MDA}(\Delta\vec{V}, \alpha_H, I_{out}, T_W);$	% Upper level Minimum Distance Algorithm
$T_W = (1 - d_c) T_{PWM}$	% Time interval of the lower level
$[\sim, \Delta\vec{V}] = \text{MDA}(\Delta\vec{V}, \alpha_L, I_{out}, T_W);$	% Lower level Minimum Distance Algorithm
end	
$\vec{V}_m(\tilde{V}_d) = \Delta\vec{V}/N_{Steps};$	% Function \vec{V}_m is defined in point \tilde{V}_d
end	

The precision of calculation of function $\vec{V}_m(\tilde{V}_d)$ increases if the values of parameters N_{Points} and N_{Steps} increase. The Vectorial Divergence Function $\vec{V}_m(\tilde{V}_d)$ satisfies the following properties.

Property 8. The Vectorial Divergence Function $\vec{V}_m(\tilde{V}_d)$ of all the Basic Configuration Voltage Vectors \mathbf{V}_m^* is zero for any value of variable $\tilde{V}_d = [0 \ 1]$:

$$\vec{V}_m(\tilde{V}_d) = 0 \quad \text{for} \quad \tilde{V}_d = [0, 1].$$

This property holds as a direct consequence of Property 7.

Property 9. The Vectorial Divergence Function $\vec{V}_m(\tilde{V}_d)$ satisfies the following symmetry with respect to the value $\tilde{V}_d = 0.5$:

$$\vec{V}_m(\tilde{V}_d) = -\vec{V}_m(1 - \tilde{V}_d), \quad \text{for} \quad \tilde{V}_d \in [0, 0.5].$$

This property holds as a direct consequence of Property 3. Property 9 implies the symmetry of the Vectorial Divergence Function $\vec{V}_m(\tilde{V}_d)$ with respect to the origin. Figure 17 gives an example showing two different graphical representations of the Vectorial Divergence Function $\vec{V}_m(\tilde{V}_d)$ that is associated with all of the Configuration Voltage Vectors \mathbf{V}_m for the case $n = 3$, $N_{Points} = 400$ and $N_{Steps} = 200$. The left subplot shows the norm $|\vec{V}_m(\tilde{V}_d)|$ of the Vectorial Divergence Function versus $\tilde{V}_d \in [0, 0.5]$. The function $|\vec{V}_m(\tilde{V}_d)|$ has not been plotted for $\tilde{V}_d \in [0.5, 1]$, because of the symmetry defined in Property 9. The right subplot of Figure 17 shows the Vectorial Divergence Function $\vec{V}_m(\tilde{V}_d)$ on plane (V_2, V_3) . This subplot clearly shows the symmetry of function $\vec{V}_m(\tilde{V}_d)$ with respect to the origin, as stated in Property 9. The two digit numbers "m.i", which are present for each characteristic in the two subplots of Figure 17, denote the number m of output levels and the order i of the Configuration Voltage Vector \mathbf{V}_m of the nearby colored line, according to the order and the colors reported in Figure 18. The two subplots of Figure 17 clearly show that the norm $|\vec{V}_m(\tilde{V}_d)|$ of the Vectorial Divergence Function $\vec{V}_m(\tilde{V}_d)$ tends to increase with the number m of the output levels and, therefore, it can be used as a starting point to estimate the degree of divergence and, thus, the degradation of

the voltage balancing capability, associated to the corresponding Configuration Voltage Vector \mathbf{V}_m . For this purpose, let us define the following Divergence Index.

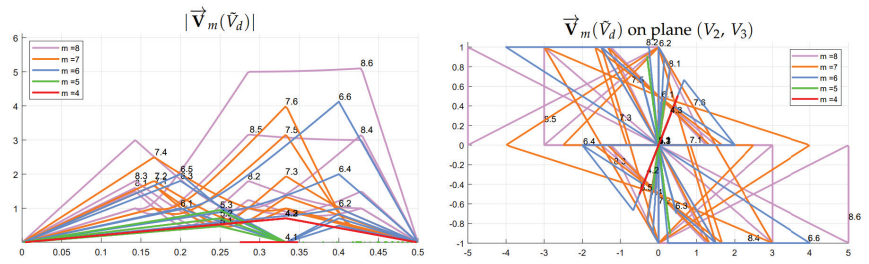


Figure 17. Left subplot: Norm $|\vec{\mathbf{V}}_m(\tilde{V}_d)|$ of the Vectorial Divergence Function vs $\tilde{V}_d \in [0, 0.5]$; Right subplot: Vectorial Divergence Function $\vec{\mathbf{V}}_m(\tilde{V}_d)$ on the plane (V_2, V_3) for all of the Configuration Voltage Vectors \mathbf{V}_m in the case $n = 3$.

Definition 3. The Divergence Index I_M of a Configuration Voltage Vector \mathbf{V}_m is defined as follows:

$$I_M = \max\left(|\vec{\mathbf{V}}_m(\tilde{V}_d)|\right),$$

namely as the maximum value of the norm $|\vec{\mathbf{V}}_m(\tilde{V}_d)|$ of the Vectorial Divergence Function $\vec{\mathbf{V}}_m(\tilde{V}_d)$.

The larger the Divergence Index I_M , the less robust is the corresponding Configuration Voltage Vector \mathbf{V}_m . Therefore, the Divergence Index I_M is inversely proportional to the degree of robustness of the corresponding Configuration Voltage Vector \mathbf{V}_m . For all of the Basic Configuration Voltage Vectors \mathbf{V}_m^* , the Divergence Index I_M is zero, according to Property 8. Index I_M can also be used to provide a new sorting for the Configuration Voltage Vectors \mathbf{V}_m having the same number m of output levels. Figure 18 shows the new sorting, in ascending order of the Divergence Index I_M for each vector \mathbf{V}_m having the same number m of output voltage levels. Therefore, the different Configuration Voltage Vectors \mathbf{V}_m having the same number m of output levels are sorted in decreasing degree of robustness when moving from left to right in Figure 18. The magenta line that is reported in Figure 18 is the Mean Index I_m of the Configuration Voltage Vectors \mathbf{V}_m . The Mean Index I_m is defined as the mean value of the norm $|\vec{\mathbf{V}}_m(\tilde{V}_d)|$ of the Vectorial Divergence Function $\vec{\mathbf{V}}_m(\tilde{V}_d)$: $I_m = \text{mean}\left(|\vec{\mathbf{V}}_m(\tilde{V}_d)|\right)$. Figure 18 clearly shows a strong correlation between the Divergence Index I_M and Mean Index I_m .

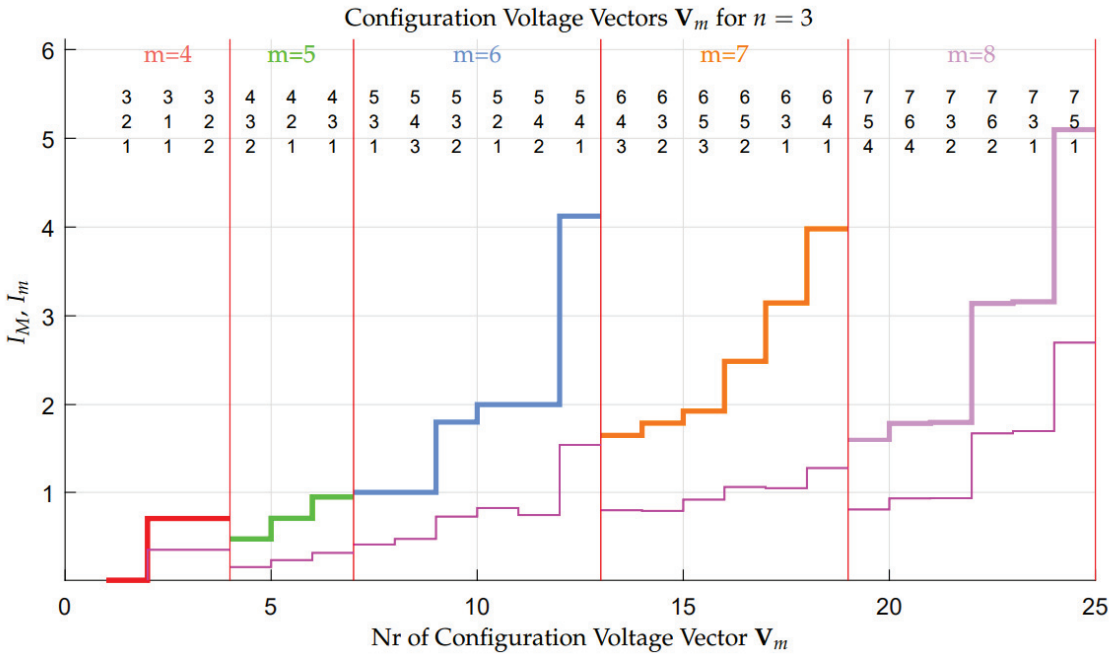


Figure 18. Configuration Voltage Vectors \mathbf{V}_m , for $n = 3$, sorted in ascending order with respect to the Divergence Index I_M .

In order to verify the correctness of the sorting proposed in Figure 18, all of the Configuration Voltage Vectors \mathbf{V}_m , for $n = 3$, have been tested in simulation using the three types of voltage signals V_d that are shown in Figure 19 (sinusoidal, triangular, and sawtooth) with $V_{in} = 1\text{ V}$, an offset equal to $V_{in}/2$, a peak-to-peak amplitude equal to V_{in} , a frequency equal to 50 Hz, an output current equal to $I_{out} = 1\text{ A}$, and capacitors C_i chosen as in (29) with $C_n = 1\text{ F}$. Figure 20 shows the results of these simulations, where the Divergence Index I_M (red characteristic, left vertical axis) is compared with the maximum norm $\max(|\Delta\bar{\mathbf{V}}|)$ of vectors $\Delta\bar{\mathbf{V}} = \bar{\mathbf{V}}_c(t) - \bar{\mathbf{V}}_{m0}$ obtained in simulation for the three types of the considered periodical signals (colored characteristics, right vertical axis). Two different reference axes have been used in Figure 20, because the Vectorial Divergence Function $\bar{\mathbf{V}}_m(\tilde{V}_d)$ and corresponding Divergence Index I_M have been computed using a constant normalized voltage $\tilde{V}_d \in [0, 1]$, whereas the maximum norms $\max(|\Delta\bar{\mathbf{V}}|)$ have been obtained in simulation using different signals, i.e., periodical normalized signals \tilde{V}_d with a non-zero frequency of 50 Hz. It can be shown that the two quantities I_M and $\max(|\Delta\bar{\mathbf{V}}|)$ would tend to be comparable only if the frequency of the periodical normalized signals \tilde{V}_d became equal to zero. Consequently, the Divergence Index I_M represents an upper boundary for the maximum norm index $\max(|\Delta\bar{\mathbf{V}}|)$, for each Configuration Voltage Vector \mathbf{V}_m . Furthermore, Figure 20 shows the good direct proportionality existing between the Divergence Index I_M and the maximum norm indices $\max(|\Delta\bar{\mathbf{V}}|)$ of the three considered signals. This good proportionality shows the effectiveness of using the Divergence Index I_M for evaluating the divergence characteristics of the different Configuration Voltage Vectors \mathbf{V}_m , which gives a direct measurement of their degree of robustness.

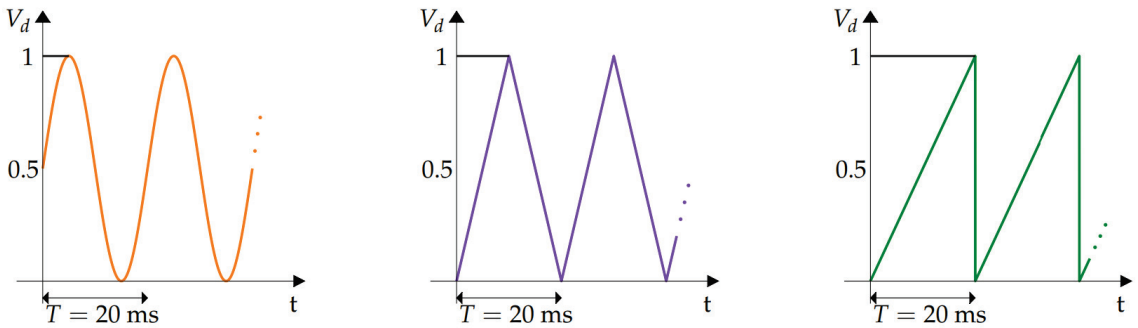


Figure 19. Desired voltage signals V_d for the comparisons in Figures 20 and 21.

Even for the case $n = 4$, all the Configuration Voltage Vectors \mathbf{V}_m have been tested in simulation by employing the same normalized periodical signals \tilde{V}_d used for the case $n = 3$, which are shown in Figure 19. Figure 21 reports the results of these simulations and the comparison between the Divergence Index I_M (red characteristic, left vertical axis) and the maximum norm indices $\max(|\Delta\bar{\mathbf{V}}|)$ (colored lines, right vertical axis). In this figure, the 407 Configuration Voltage Vectors \mathbf{V}_m of case $n = 4$ have been sorted with respect to the Divergence Index I_M . The upper part of the figure shows, for each $m \in [5, 6, \dots, 16]$, the Configuration Voltage Vector \mathbf{V}_m having the minimum Divergence Index I_M . The simulation results that are reported in Figure 21 show the good direct proportionality existing between the Divergence Index I_M and the maximum norm indices $\max(|\Delta\bar{\mathbf{V}}|)$, even in the case $n = 4$, and, therefore, the effectiveness of using the Divergence Index I_M for evaluating the divergence characteristics, i.e., the degree of robustness, of the different Configuration Voltage Vectors \mathbf{V}_m .

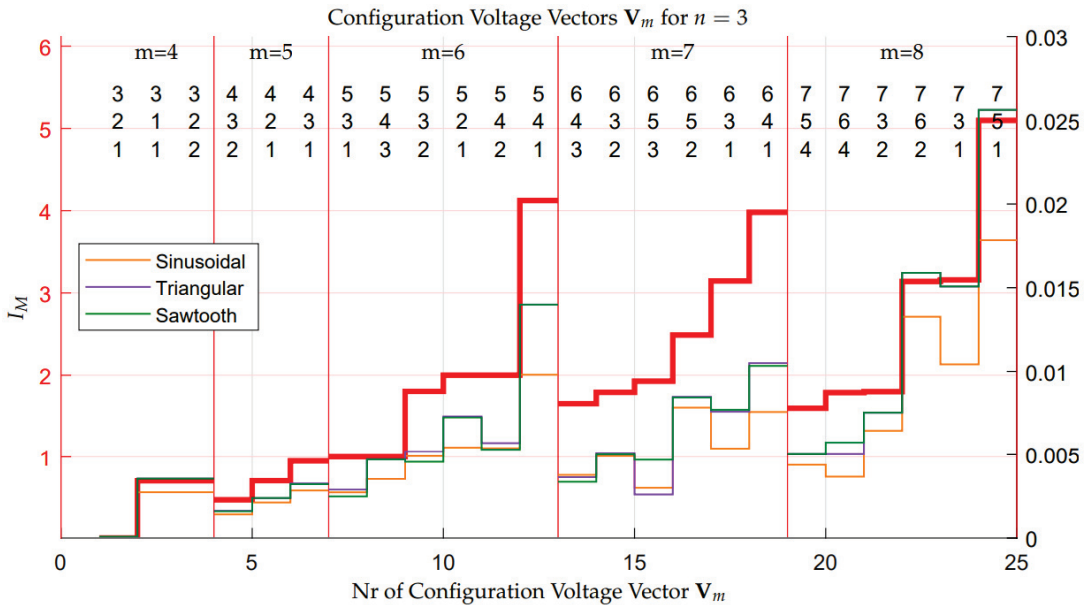


Figure 20. Comparison between the Divergence Index I_M and metric $\max(|\Delta\bar{\mathbf{V}}|)$, computed from simulation using three different \tilde{V}_d signals, for the Configuration Voltage Vectors \mathbf{V}_m in the case $n = 3$.

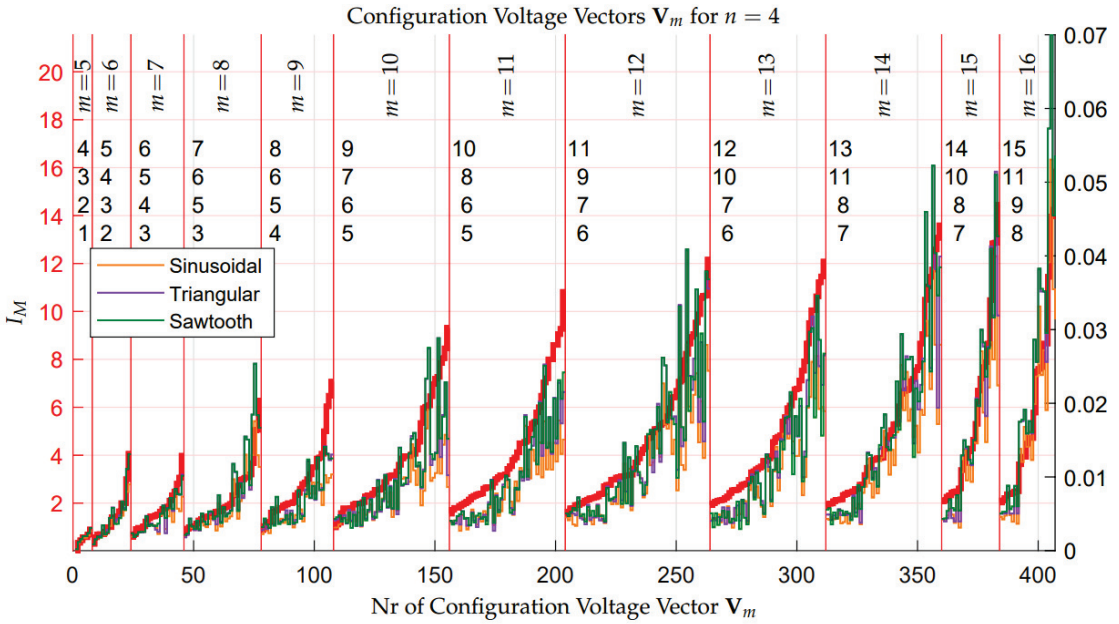


Figure 21. Comparison between the Divergence Index I_M and metric $\max(\Delta\bar{V})$, computed from simulation using three different \tilde{V}_d signals, for the Configuration Voltage Vectors \mathbf{V}_m in the case $n = 4$.

4.3.1. Minimum Distance Control: Stability Issues in Extended Operation

The analysis performed on the basis of the Vectorial Divergence Function $\vec{\nabla}_m(\tilde{V}_d)$ has shown that all of the Configuration Voltage Vectors \mathbf{V}_m , other than the basic one \mathbf{V}_m^* , are unstable with different degrees of divergence in some unfavorable conditions, such as constant desired voltage \tilde{V}_d , while using the Minimum Distance algorithm. Moreover, Figures 20 and 21 have shown that, for some periodical desired signal \tilde{V}_d with an average value equal to 0.5, the maximum distance $\max(\Delta\bar{V})$ of the voltage vector $\bar{\mathbf{V}}_c$ from the desired voltage vector $\bar{\mathbf{V}}_{m0}$ remains bounded. The amplitude of the maximum distance $\max(\Delta\bar{V})$ increases if the output current I_{out} increases, and it decreases if capacitor C_n or the frequency of the periodical signal \tilde{V}_d increase.

If $\bar{\mathbf{V}}_c$ remains in the vicinity of the desired voltage vector $\bar{\mathbf{V}}_{m0}$, then the multilevel converter works properly, providing an output signal V_{out} switching between equally spaced voltage values. On the contrary, if the maximum distance $\max(\Delta\bar{V})$ increases excessively, then the output values $S_M\mathbf{V}_c$ of the multilevel converter will no longer be equally spaced and the average value of the output switching signal V_{out} will no longer be equal to the desired signal $V_{in}\tilde{V}_d$. If this situation occurs, the multilevel converter cannot work properly, because it provides output signals that are not equal to the desired ones. The output voltage error $V_{err} = V_{out} - V_{in}\tilde{V}_d$ remains low and, therefore, acceptable, only if the maximum distance $\max(\Delta\bar{V})$ remains sufficiently low. Unfortunately, in practical applications, such as the electric motors control, it can happen that the desired voltage vector \tilde{V}_d does not have an average value equal to 0.5. In this condition, vector $\bar{\mathbf{V}}_c$ diverges from the desired voltage vector $\bar{\mathbf{V}}_{m0}$, which means that the output voltage error V_{err} increases excessively and the multilevel converter can no longer work correctly. Another destabilizing condition can be identified in a sudden load change. These two scenarios are considered in the following two simulation case studies:

(A) Let us consider the case of a constant output current $I_{out} = 1.1$ A and a sinusoidal desired voltage with an average value that is equal to 0.5: $\bar{V}_d = 0.5 + 0.5 \sin(393 t)$. Furthermore, the voltage signal is supposed to remain constant at the value $\bar{V}_d = 0.43$ for a short time interval $t \in [t_1 \ t_2]$, where $t_1 \simeq 32$ ms and $t_2 \simeq 72$ ms. Figure 22 shows the simulation results. The red characteristic in Figure 22 is the desired signal \bar{V}_d , the gray characteristic is the output switching signal V_{out} , whereas the blue characteristic is the average value of the output signal V_{out} . From the figure, it is evident that: (1) in the first part of the simulation, i.e., $t < t_1$, the multilevel converter works correctly, since the output switching levels are equally spaced and, thus, the output voltage error V_{err} is very low; (2) during the second part of the simulation, i.e., $t \in [t_1 \ t_2]$, the values of the output switching levels change considerably with respect to the desired ones, and they are no longer equally spaced. Therefore, the average value of the output signal V_{out} (blue characteristic) is no longer equal to the desired value \bar{V}_d (red characteristic); and, (3) in the third part of the simulation, i.e., $t > t_2$, the multilevel converter no longer works correctly, since the output signals (the gray and blue characteristics) are no longer equal to the desired one (the red characteristic). This is due to the fact that the trajectories of the reduced voltage vector \bar{V}_c have diverged from the desired value \bar{V}_{m0} because of the constant voltage \bar{V}_d . Moreover, the Minimum Distance algorithm is not able to force the reduced voltage vector \bar{V}_c to move back towards the desired voltage vector \bar{V}_{m0} after divergence has occurred.

(B) Let us consider the case of a sinusoidal desired voltage with an average value that is equal to 0.5: $\bar{V}_d = 0.5 + 0.5 \sin(393 t)$. The load current is supposed to be constant and equal to $I_{out} = 1$ A for $t < t_1 = 0.04$ s. Next, a sudden load change causing a current step is supposed to occur, causing I_{out} to jump from 1 A to 10.5 A for $t_1 \leq t < t_2 = 0.1$ s. The load operating condition giving $I_{out} = 1$ A is supposed to be reestablished for $t \geq t_2$. Figure 23 shows the simulation results. The characteristics color notation is the same as the one adopted in Figure 22. From Figure 23, it is evident that: (1) in the first part of the simulation, i.e., $t < t_1$, the multilevel converter works correctly, since the output switching levels are equally spaced, which means that the output voltage error V_{err} is very low; (2) for $t \in [t_1 \ t_2)$, the values of the output switching levels change with respect to the desired ones, and they are no longer equally spaced; and, (3) for $t \geq t_2$, the output voltage levels remain unequally spaced, due to the divergence of the trajectories of the reduced voltage vector \bar{V}_c from the desired value \bar{V}_{m0} caused by the sudden load change. Moreover, the Minimum Distance algorithm is not able to force the reduced voltage vector \bar{V}_c to move back towards the desired voltage vector \bar{V}_{m0} after the divergence has occurred.

Unfortunately, situations such as those that are shown in Figures 22 and 23 can happen for all of the Configuration Voltage Vectors \mathbf{V}_m , except for the basic one \mathbf{V}_m^* . This poses quite a limitation on the operation of the converter in the so-called "Extended Operation", namely for $\mathbf{V}_m \neq \mathbf{V}_m^*$ allowing to generate a number of output voltage levels $m > n + 1$ for the given n , since unpredictable undesired conditions may compromise the correct functioning of the multilevel converter.

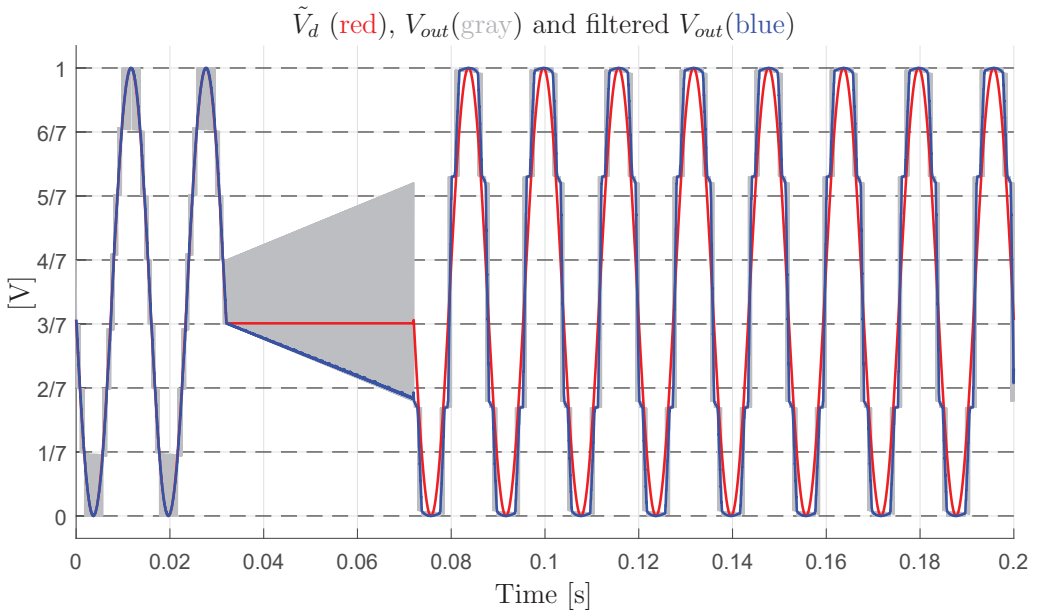


Figure 22. Deformation of the output voltage waveform in the extended operation of the converter with the Configuration Voltage Vector $\mathbf{V}_m = [7 \ 6 \ 2]^T$ caused by the voltage trajectory divergence in presence of a constant output voltage.

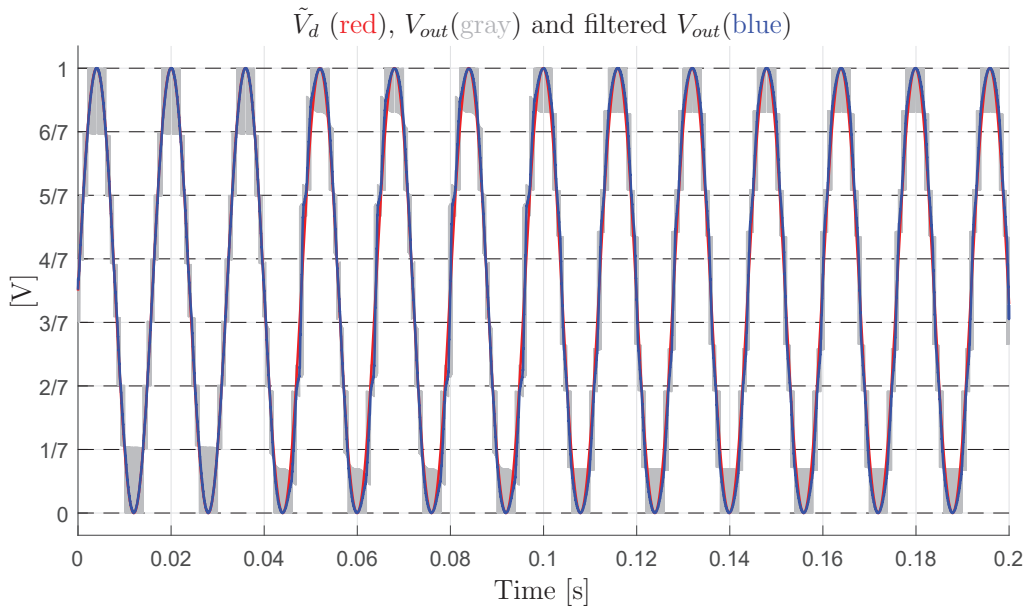


Figure 23. Deformation of the output voltage waveform in the extended operation of the converter with the Configuration Voltage Vector $\mathbf{V}_m = [7 \ 6 \ 2]^T$ caused by the voltage trajectory divergence in presence of a sudden load change.

4.4. Variable-Step Control of the Multilevel Flying-Capacitor Converter

To cope with the divergence problem described in the previous section, the use of a new solution based on the PWM physical scheme that is shown in Figure 24 is proposed.

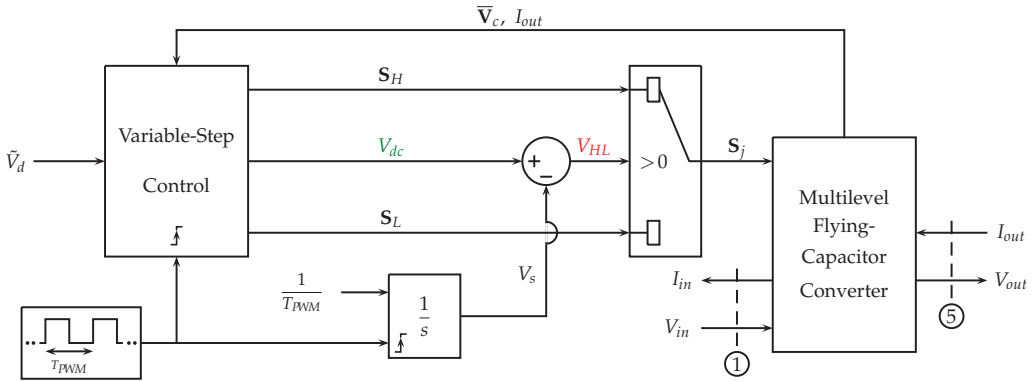


Figure 24. PWM physical scheme and Variable-Step Control of the Multilevel Flying-Capacitor Converter.

The basic elements of the new PWM scheme are the following:

- (a) a square wave signal having period T_{PWM} acting as a clock, which activates the Variable-Step Control and resets the integrator to the zero initial condition when the rising edge occurs;
- (b) an integrator with a constant input $\frac{1}{T_{PWM}}$ and a reset signal that is timed by the square clock. The output V_s of the integrator is a sawtooth signal which ranges from 0 to 1 within a time interval $t \in [t_r, t_r + T_{PWM}]$, where t_r is the reset time instant, see the black line in Figure 25;
- (c) the voltage V_{dc} that is provided by the Variable-Step Control block, defining the duty cycle of the high level of the PWM signal, namely the time interval T_H , see the green line in Figure 25;
- (d) the value of the signal $V_{HL} = V_{dc} - V_s$ determines the output of the selector and, thus, the configuration vector S_j , which is going to be applied to the multilevel converter during the next time interval: $S_j = S_H$ for a time interval T_H if $V_{HL} > 0$ and $S_j = S_L$ for a time interval $T_{PWM} - T_H$ if $V_{HL} < 0$;
- (e) at each activation time, the Variable-Step Control reads the input signal \tilde{V}_d and generates three output signals: S_H , V_{dc} and S_L . Using these signals, the Variable-Step Algorithm can decide the duty cycle d_c and the two levels $S_H V_c$ and $S_L V_c$ of the next PWM period;
- (f) let $V_H > V_d$ denote the voltage corresponding to configuration vector S_H and $V_L < V_d$ denote the voltage corresponding to configuration vector S_L . The duty cycle $d_c = T_H / T_{PWM}$ of the next PWM period, that is the ratio between the duration T_H of the higher level and the duration of the PWM period T_{PWM} , can be computed, as follows:

$$V_d = V_H d_c + V_L (1 - d_c) \quad \Leftrightarrow \quad d_c = \frac{V_d - V_L}{V_H - V_L}. \quad (30)$$

Using (30), the duty cycle d_c always guarantees that the average value of the PWM output voltage in the next period T_{PWM} is equal to the desired value V_d .

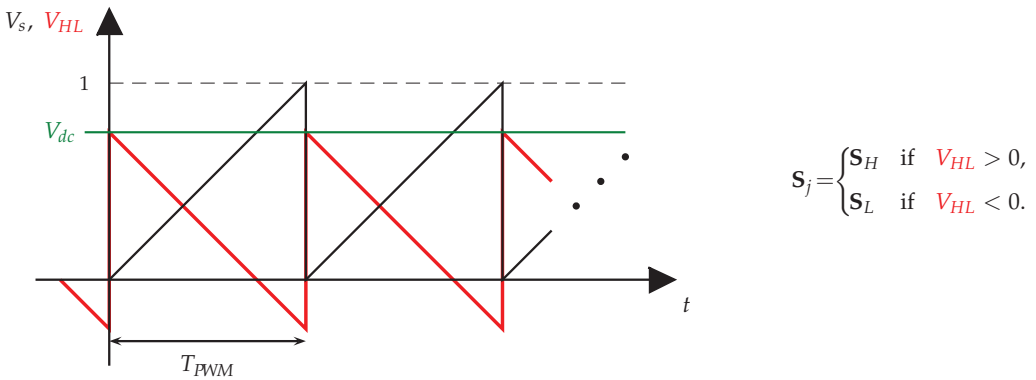


Figure 25. Scheme for the application of the configuration vectors S_{j_H} and S_{j_L} associated with the higher and lower level time intervals T_H and $T_{PWM} - T_H$.

Figure 26 provides the basic structure of the Variable-Step Control algorithm by means of a Matlab-like function called “Multi_Step_Algorithm(\dots)”. This function is called at each activation time providing the following input parameters: $\Delta\bar{V}$, \tilde{V}_d , I_{out} , T_{PWM} , N_s , V_{r0} . The “Multi_Step_Algorithm” attempts to keep the reduced voltage vector \bar{V}_c as close as possible to the desired reduced voltage vector \bar{V}_{m0} , see (22). The main features of the “Multi_Step_Algorithm” are the following:

```

function [SH, Vdc, SL] = Multi_Step_Algorithm(ΔV̄, V̄d, Iout, TPWM, Ns, Vr0)
1. VD = V̄d(m - 1); % Variable VD ∈ [0, m - 1]
2. αH0 = ceil(VD); % Initial upper adjacent level
3. Vdc = VD - floor(VD); % Voltage Vdc in Figure 24 and Figure 25
4. Nm = ∞; % Initialize minimum norm of ΔV̄cij
5. for Nsi = 1 : Ns % Nsi is the amplitude of the Step
6.     for k = 0 : Nsi - 1 % k is the up and down Shift
7.         αH = αH0 + k;   αL = αH - Nsi; % Current levels αH and αL
8.         Compute the new duty cycle dc; % As in (30)
9.         if (αH < m) && (αL ≥ 0) % αH, αL must not exceed boundaries
10.            Compute sets SαH and SαL; % Defined in (23)
11.            Compute vectors S̄CHi and S̄CLj; % Defined in (22)
12.            for i ∈ SαH % Cycle over indexes in SαH
13.                for j ∈ SαL % Cycle over indexes in SαL
14.                    ΔV̄cij = ΔV̄ + [S̄CHidc + S̄CLj(1 - dc)]IoutTPWM; % Distance vector
15.                    if norm(ΔV̄cij) < Nm % If |ΔV̄cij| < current minimum
16.                        Nm = norm(ΔV̄cij); % Set Nm to the current one
17.                        Set: SH = Si; SL = Sj; Vdc = dc; % Set the outputs
18.                    end
19.                end
20.            end
21.        end
22.    end
23.    if (Nm < norm(ΔV̄)) || (Nm < Vr0Nsi) % Nm < |ΔV̄| or < hypersphere radius
24.        return % Exit from the algorithm
25.    end
26. end

```

Figure 26. Matlab-like form of the Variable-Step Control algorithm.

- At each activation time t_k , the "Multi_Step_Algorithm" computes the two configuration vectors \mathbf{S}_H , \mathbf{S}_L and the duty cycle V_{dc} to be applied in the following PWM time interval $[t_k \ t_k + T_{PWM}]$: configuration \mathbf{S}_H will be applied in the first part of the PWM period when $V_{HL} = V_{dc} - V_s > 0$, while configuration \mathbf{S}_L will be applied in the second part of the PWM period when $V_{HL} < 0$, see Figure 25.
- The input N_s defines the maximum amplitude of the Step to be used in the algorithm, which is the *maximum level-to-level distance*. The **for** cycle at line 5 in Figure 26 defines the current value $N_{si} \in [1, 2, \dots, N_s]$ of the amplitude of the Step, i.e., the current level-to-level distance. The **for** cycle at line 6 defines the current value k of the up and down shift to be considered for the current amplitude N_{si} of the Step.
- At lines 7 and 8, the current values of the upper level α_H , the lower level α_L , and the duty cycle d_c are computed. If the current values of α_H and α_L are admissible, see condition at line 9, then the sets \mathcal{S}_{α_H} and \mathcal{S}_{α_L} of the admissible configuration vectors \mathbf{S}_{Hi} and \mathbf{S}_{Lj} and the corresponding vectors $\bar{\mathbf{S}}_{CHi}$ and $\bar{\mathbf{S}}_{CLj}$ are computed at lines 10 and 11.
- The two **for** cycles at lines 12 and 13 are used to compute the distance vector $\Delta \bar{\mathbf{V}}_{cij}$ for each possible combination of the configuration vectors \mathbf{S}_i and \mathbf{S}_j belonging to the two sets \mathcal{S}_{α_H} and \mathcal{S}_{α_L} . At line 14, the distance vector $\Delta \bar{\mathbf{V}}_{cij}$ is computed starting from the initial condition $\Delta \bar{\mathbf{V}}$ and adding the two terms $\bar{\mathbf{S}}_{CHi} d_c I_{out} T_{PWM}$ and $\bar{\mathbf{S}}_{CLj} (1 - d_c) I_{out} T_{PWM}$, due to the application of the configuration vectors \mathbf{S}_{Hi} and \mathbf{S}_{Li} in the first part $d_c T_{PWM}$ and in the second part $(1 - d_c) T_{PWM}$ of the PWM period T_{PWM} , respectively.
- If the norm of the distance vector $\Delta \bar{\mathbf{V}}_{cij}$ is smaller than the current minimum norm N_m , see line 15, then the algorithm updates the value of parameter N_m , see line 16, and it sets the values of the output variables \mathbf{S}_H , \mathbf{S}_L and V_{dc} equal to the values \mathbf{S}_i , \mathbf{S}_j and d_c of the current solution, see line 17.
- The "Multi_Step_Algorithm" ends its minimum distance vector search, see line 24, when one of the conditions at line 23 is verified, or when the maximum level-to-level distance N_s has been achieved. At line 23, the algorithm exits the search if the current minimum distance N_m is lower than the initial one, or if N_m is lower than radius $V_{r0} N_{si}$, where V_{r0} is the input basic radius and N_{si} is the current level-to-level distance. Radius $V_{r0} N_{si}$ represents the varying radius of an hypersphere in the $(n - 1)$ -dimensional space. Figure 27 shows the resulting circumferences with varying radius $V_{r0} N_{si}$ for the case $n = 3$.
- The "Multi_Step_Algorithm" introduces and uses the new concept of "*variable level-to-level distance*". This concept means that the algorithm can choose a higher level α_H and a lower level α_L that are not adjacent, see line 7 of the algorithm. The current level-to-level distance is denoted by variable $N_{si} \in [1, N_s]$. The new duty cycle d_c associated with the two levels α_H and α_L , computed in line 8, guarantees that the average value of the PWM output voltage in the next PWM period T_{PWM} will be equal to the desired value V_d .
- The ability to change the level-to-level distance allows the "Multi_Step_Algorithm" to keep the reduced voltage vector $\bar{\mathbf{V}}_c$ in the vicinity of the desired vector $\bar{\mathbf{V}}_{m0}$ even in extended operation and in presence of some particularly unfavorable operating conditions, such as normalized desired voltage \bar{V}_d having an average value different from 0.5.
- If the unfavorable conditions persist, the algorithm can enlarge the level-to-level distance N_{si} up to its upper boundary $N_s = m - 1$. This enlargement increases the number of the configuration vectors \mathbf{S}_j that the algorithm can use to keep vector $\bar{\mathbf{V}}_c$ in the vicinity of the desired vector $\bar{\mathbf{V}}_{m0}$, and to maintain the correct functioning of the multilevel converter. Furthermore, when the unfavorable conditions no longer occur, the "Multi_Step_Algorithm" has the ability to force the converter to go back to work as a normal multilevel converter switching between adjacent levels only, i.e., with a current level-to-level distance N_{si} equal to one.

- The example reported in Figure 28 shows all the possible combinations of levels α_H and α_L that can be obtained when $m = 6$, $N_{s_i} \in \{1, 2, 3, 4, 5\}$ and the desired voltage $V_D = (m - 1)\tilde{V}_d$ is in between levels “2” and “3”.

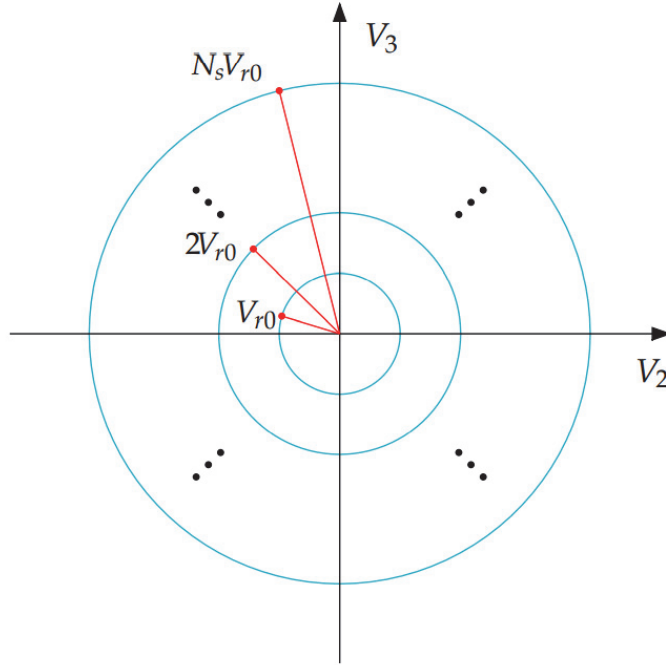


Figure 27. Circumference with varying radius $N_{s_i} V_{r0}$ in the two-dimensional space for the case $n = 3$.

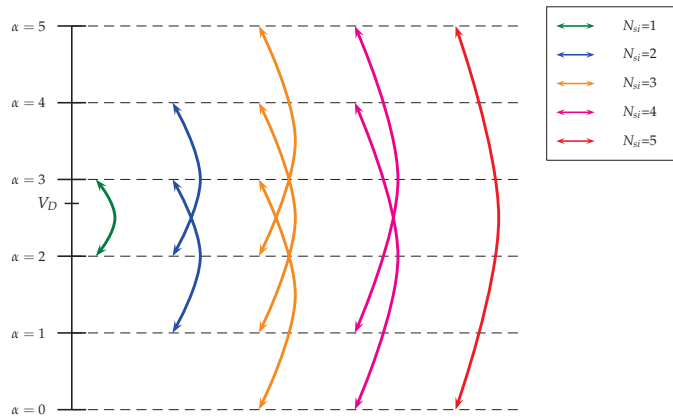


Figure 28. Possible combinations of higher and lower output voltage levels α_H and α_L as a function of the current level-to-level distance N_{s_i} for the case $m = 6$ and a desired voltage V_D in between “2” and “3”.

4.4.1. Variable-Step Control: Solution of the Stability Issues in Extended Operation

Section 4.3.1 has shown that the Minimum Distance Control is not capable of ensuring the correct operation of the multilevel flying-capacitor converter, in extended mode, under particularly unfavorable operating conditions, such as a desired voltage \tilde{V}_d , with an average value that is different from 0.5 or a sudden load change. Examples of this type are shown in Figures 22 and 23, respectively. On the contrary, the Variable-Step Control that was presented in the previous section is able to ensure the correct functioning of the multilevel converter, even under unfavorable operating conditions. To give some examples, reference is made to Figures 29 and 30, showing the simulation results obtained using the Variable-Step Control under the same operating conditions as those of the simulations in Figures 22 and 23, respectively, when the Minimum Distance Control was used instead. In Figures 29 and 30, the red characteristic is the desired signal \tilde{V}_d , the gray characteristic is the switching output signal V_{out} , and the green characteristic is the average value of the output signal V_{out} .

With reference to Figure 29, it is evident that: (1) in the first part of the simulation, for $t < t_1$, the multilevel converter works correctly in extended operation using the minimum level-to-level distance $N_{si} = 1$ and the output voltage error $V_{err} = V_{out} - V_{in}\tilde{V}_d$ remains low; (2) during the second part of the simulation, for $t \in [t_1 \ t_2]$, the current level-to-level distance N_{si} increases from 1 to 2, and the gray output variable V_{out} switches between levels $V_L = 2/7$ and $V_H = 4/7$. In this part of the simulation, the effectiveness of the Variable-Step Control comes into play, which prevents vector \bar{V}_c from diverging excessively from the desired reduced vector \bar{V}_{m0} , even in the presence of the unfavorable condition of a signal \tilde{V}_d constant and different from 0.5. On the other hand, in the simulation of Figure 22, the Minimum Distance Algorithm was not able to prevent the divergence of the vector \bar{V}_c , therefore compromising the correct functioning of the converter; (3) in the third part of the simulation, for $t > t_2$, the operating condition $N_{si} = 2$ is maintained until the distance between vectors \bar{V}_c and \bar{V}_{m0} is sufficiently reduced, namely until time instant $t_3 \simeq 176$ ms; and, (4) in the fourth part of the simulation, for $t > t_3$, the converter starts operating as a classical multilevel flying-capacitor converter in extended mode once again, setting the current level-to-level distance N_{si} back to 1. On the other hand, in the simulation of Figure 22, the Minimum Distance Algorithm was not able to force the vector \bar{V}_c to move back towards the desired vector \bar{V}_{m0} after the divergence occurred.

With reference to Figure 30, it is evident that: (1) in the first part of the simulation, for $t < t_1$, the multilevel converter works correctly in extended operation using the minimum level-to-level distance $N_{si} = 1$ and the output voltage error $V_{err} = V_{out} - V_{in}\tilde{V}_d$ remains low; (2) for $t \in [t_1 \ t_2]$, the current level-to-level distance N_{si} increases from 1 to 2, in order to prevent vector \bar{V}_c from diverging excessively from the desired reduced vector \bar{V}_{m0} as a consequence of the undesired sudden load change. On the other hand, in the simulation of Figure 23, the Minimum Distance Algorithm was not able to prevent the divergence of the vector \bar{V}_c , therefore compromising the correct functioning of the converter; (3) for $t \geq t_2$, the operating condition $N_{si} = 2$ is maintained until $t = t_3 \simeq 0.1039$ s, namely for the very short time interval that it takes for the distance between vectors \bar{V}_c and \bar{V}_{m0} to be sufficiently reduced; and, (4) for $t \geq t_3$, the converter starts operating as a classical multilevel flying-capacitor converter in extended mode once again, setting the current level-to-level distance N_{si} back to 1. On the other hand, in the simulation of Figure 23, the Minimum Distance Algorithm was not able to force the vector \bar{V}_c to move back towards the desired vector \bar{V}_{m0} after the divergence occurred.

The simulation results that are reported in Figures 29 and 30 clearly highlight the effectiveness of the proposed Variable-Step Control as compared with the classical Minimum Distance Control. This especially holds in those applications, such as the electric motors control, where it can happen that the desired voltage vector \tilde{V}_d does not have an average value equal to 0.5, or that an undesired sudden load change occurs. At the same time, it is desirable to have the converter operating in extended mode, because of all the advantages in the output voltage quality coming from a larger number of output voltage

levels without increasing the number of capacitors. The proposed Variable-Step Control aims at enabling the multilevel flying-capacitor converter operation in extended mode any time the operating conditions allow it, and it enlarges the level-to-level distance N_{si} only when strictly necessary to prevent the divergence of the flying capacitors voltages.

The Reader is invited to refer to the supplementary material in order to test and compare the Minimum Distance Control algorithm and the Variable-Step Control algorithm [28]. The Simulink model "Multilevel_Flying_Capacitor_Converter.mdl.slx" has been created with Matlab R2020b and it contains the dynamic model of the multilevel flying-capacitor converter with n capacitors given in Figure 4, as well as the implementation of both the Minimum Distance Control and the Variable-Step Control. The two algorithms are implemented in the Matlab functions "Distance_Control_0.m" and "Distance_Control_n.m", respectively. The main script that allows to control the simulations is named "Multilevel_Flying_Capacitor_Converter.m", where the system parameters that the user can set are reported and commented. Note that variables m and m_{ij} in the script "Multilevel_Flying_Capacitor_Converter.m" denote the number m of output levels and the order m_{ij} of the Configuration Voltage Vector \mathbf{V}_m , according to the orders that are reported in Figure 20 for the case $n = 3$ and in Figure 21 for the case $n = 4$.

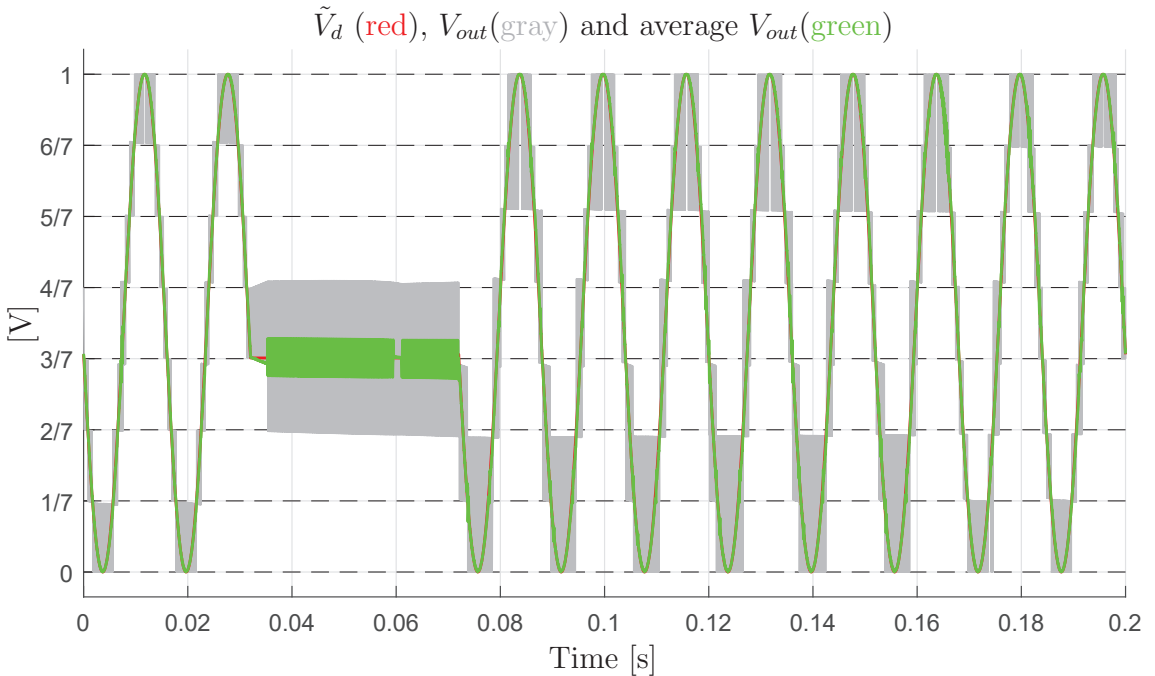


Figure 29. Non-Deformation of the output voltage waveform in the extended operation of the converter with the Configuration Voltage Vector $\mathbf{V}_m = [7 \ 6 \ 2]^T$, in the presence of a constant output voltage, thanks to the Variable-Step Control.

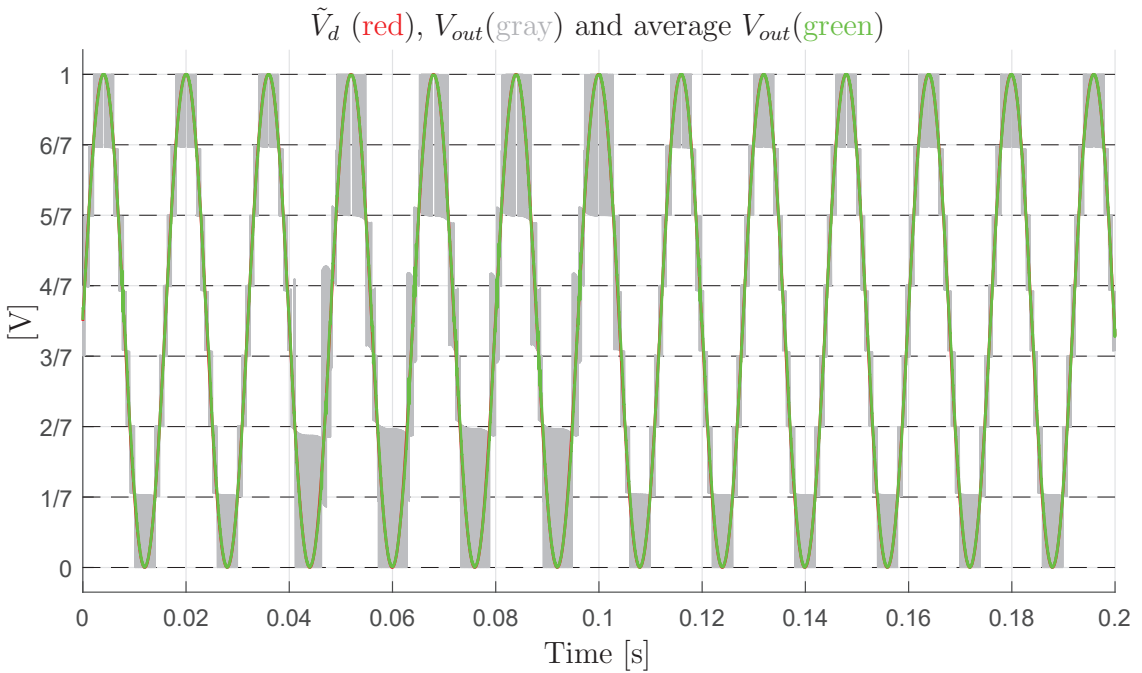


Figure 30. Non-Deformation of the output voltage waveform in the extended operation of the converter with the Configuration Voltage Vector $\mathbf{V}_m = [7 \ 6 \ 2]^T$, in the presence of a sudden load change, thanks to the Variable-Step Control.

5. Converter Testing with Dynamic Loads

This section deals with the simulation of the multilevel flying-capacitor converter with $n = 3$ in extended operation, while using the Configuration Voltage Vector $\mathbf{V}_m = [5 \ 4 \ 1]^T$, with several proposed load case studies. The considered load configuration is an RLC circuit, where a capacitor C_L and a resistor R_L are connected in parallel, and their parallel configuration is connected in series to an inductor L_L . The described load can be modeled using the POG block scheme that is shown in Figure 31 on the left. The transfer function $H(s)$ relating the output power variable I_{out} to the input power variable V_{out} is the following:

$$H(s) = \frac{I_{out}(s)}{V_{out}(s)} = \frac{sR_L C_L + 1}{s^2 R_L C_L L_L + sL_L + R_L} \tag{31}$$

The parameters values for the considered load case studies are shown in Figure 31 on the right, together with the converter parameters. As far as loads 1, 2 and 3 are concerned, the desired voltage V_d is assumed to be sinusoidal with an offset that is equal to $V_{in}/2$, a peak-to-peak amplitude equal to V_{in} and a frequency equal to 50 Hz. As far as load 4 is concerned, the desired voltage V_d is assumed to be constant and equal to 4.5 V. By focusing on the loads 1, 2, and 3, and using the parameters L_L , C_L , and R_L given in Figure 31, one can notice that they represent the cases of voltage V_{out} delayed by $\pi/4$ with respect to current I_{out} , current I_{out} delayed by $\pi/4$ with respect to voltage V_{out} , and current I_{out} in phase with voltage V_{out} , respectively. The initial conditions of the RLC load are assumed to be equal to zero. Figure 32 shows the simulation results in terms of output voltages V_{out} . The first three rows of subplots show the simulation results after the transient when the loads 1, 2 and 3 are considered. From the first three rows of subplots on the left-hand side, obtained using the Minimum Distance Control, it is possible to see that the average V_{out} characteristic exhibits different degrees of deviation from the desired voltage V_d . This is due to the fact

that the distance between vectors \bar{V}_c and \bar{V}_{m0} tends to increase, even if the average value of \hat{V}_d is equal to 0.5, i.e., the average value of V_d is equal to $V_{in}/2$. This can be explained by recalling that the output current I_{out} is not constant, as the load is dynamic, which means that the strength of the control action applied by the Configuration Vector S_j in (24) changes in time through I_{out} , which is a function of V_{out} . Without a loss of generality, it is possible to state that this makes the Voltage Configuration Vectors V_m different from the basic one V_m^* loose the full flying capacitors voltage balancing capability, i.e., to become unstable, even when the average value of the desired voltage V_d is equal to $V_{in}/2$. It follows that the distance between vectors \bar{V}_c and \bar{V}_{m0} will keep increasing, thus causing the output voltage levels to be increasingly unequally spaced. On the other hand, the subplots on the right-hand side show the very good matching between the average V_{out} characteristic and the desired voltage V_d when the converter is controlled using the Variable-Step Control. It follows that the Variable-Step Control is capable of handling the cases of non-constant output current I_{out} in extended operation as well, by increasing the current level-to-level distance N_{si} when necessary in order to prevent the divergence of vector \bar{V}_c from vector \bar{V}_{m0} . As an example of this, the voltage trajectories of the flying capacitors, namely the components of vector \bar{V}_c , are shown in Figure 33 for the case "Load 2" when the two different controls are used. From the figure, it is clearly possible to see that the Minimum Distance Control causes the divergence of vector \bar{V}_c (blue characteristic) from the desired vector \bar{V}_{m0} , which is highlighted by the red spot in the figure. Furthermore, the blue characteristic also shows that the strength of the control action applied by the Configuration Vector S_j in (24) is indeed not constant during the simulation, but it is a function of the output current I_{out} , since the length of the blue voltage trajectories in Figure 33 is not constant. On the other hand, the Variable-Step Control is indeed capable of ensuring the convergence of vector \bar{V}_c to the desired vector \bar{V}_{m0} .

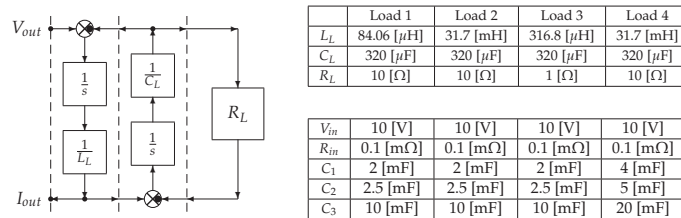


Figure 31. On the left: RLC load POG scheme; On the right: RLC load and converter parameters.

The fourth row of subplots presented in Figure 32 shows the case of constant desired voltage V_d with the load parameters identified by "Load 4" in Figure 31 on the right. The bottom-left subplot shows that the case of constant desired voltage $V_d \neq V_{in}/2$, namely $\hat{V}_d \neq 0.5$, is still the most severe one. This can be seen from the fact that the output voltage levels quickly become unequally spaced because of the divergence of vector \bar{V}_c from vector \bar{V}_{m0} . Furthermore, note that the average output voltage in the bottom-left subplot of Figure 32 tends to decrease, as a consequence of the divergence of the vector \bar{V}_c trajectories. Consequently, the output current I_{out} will also tend to decrease. This situation gives rise to an unstable loop: the more V_{out} decreases with respect to the desired value V_d , the lower the output current I_{out} , the weaker the control action applied by the Configuration Vector S_j in (24), the more severe the divergence of the \bar{V}_c trajectories from \bar{V}_{m0} . However, the bottom-right subplot of Figure 32 shows how the divergence of the \bar{V}_c trajectories from \bar{V}_{m0} is prevented by the Variable-Step Control, thanks to the increase of the current level-to-level distance N_{si} from 1 to 2, showing the effectiveness of the proposed Variable-Step Control.

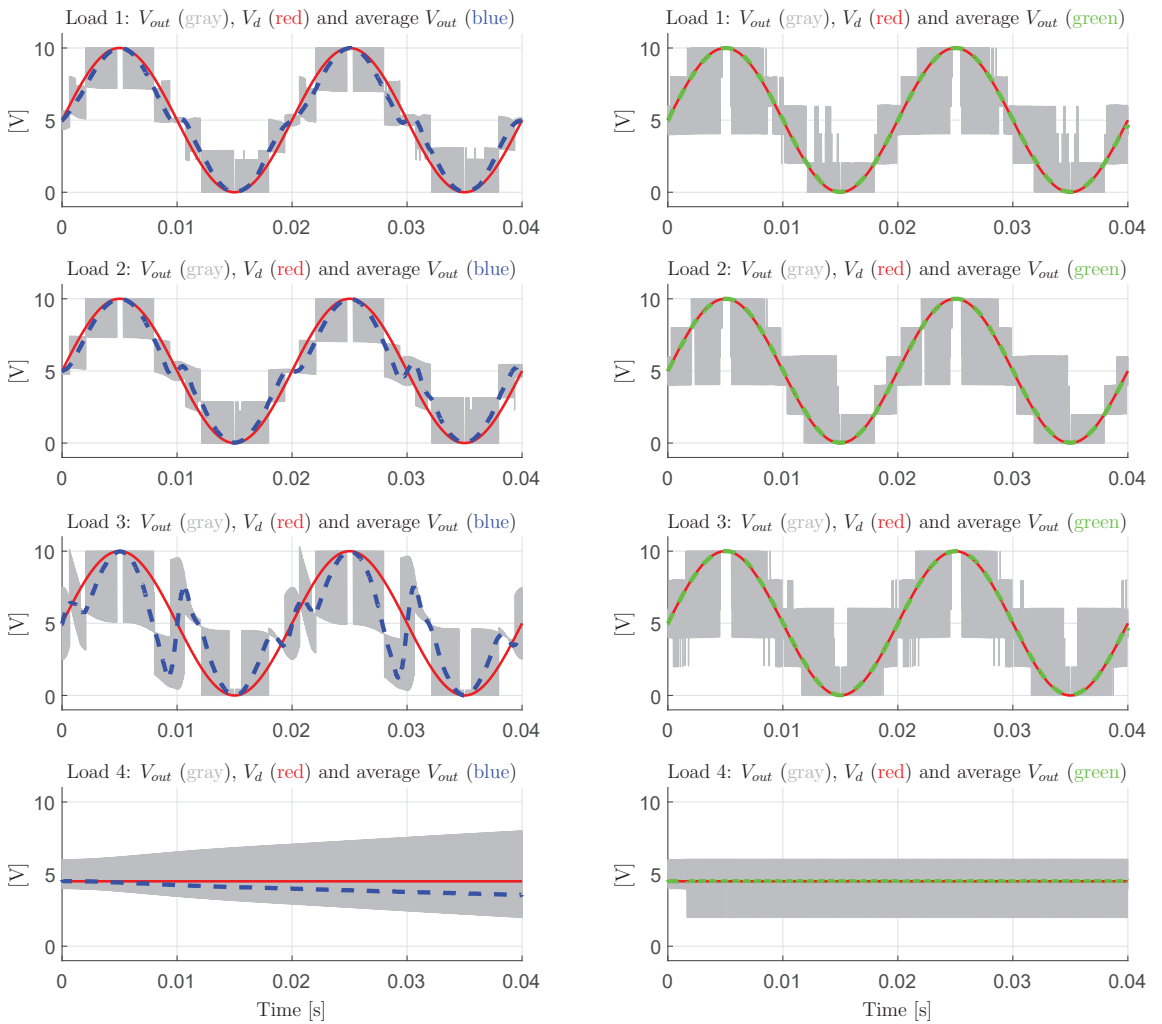


Figure 32. Left subplots: simulations using the Minimum Distance Control for $V_m = [5 \ 4 \ 1]^T$; Right subplot: simulations using the Variable-Step Control for $V_m = [5 \ 4 \ 1]^T$.

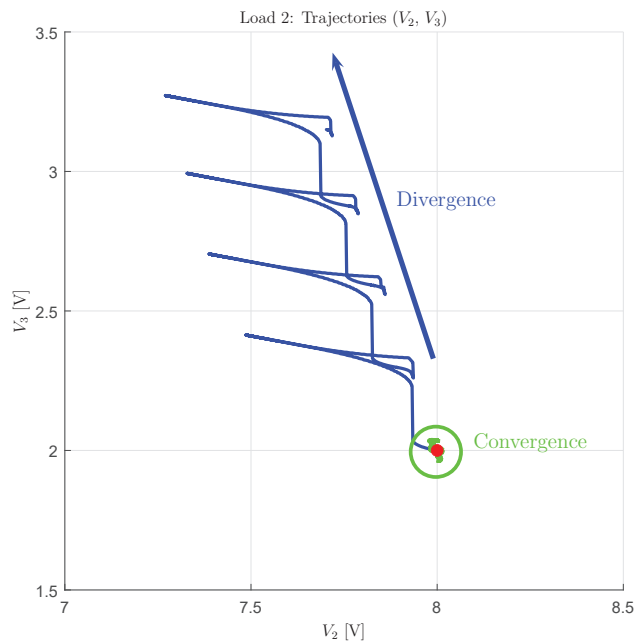


Figure 33. Voltage trajectories for the “Load 2” case using the Minimum Distance Control (blue) and the Variable-Step Control (green).

6. Conclusions

In this paper, the modeling, the control, and the robustness assessment of the multi-level flying-capacitor converter have been addressed. The main contributions of this paper are summarized in the following:

- the Power-Oriented Graphs modeling technique has been exploited to derive the system dynamic model of the n -dimensional converter, generating a POG model that can be directly implemented in Matlab/Simulink by employing standard Simulink libraries;
- a procedure for computing all the possible voltage vector configurations \mathbf{V}_m providing equally spaced levels of the output voltage V_{out} has been given;
- the robustness assessment of the converter operating in extended mode when using a Minimum Distance Control has been performed;
- a Divergence Index I_M has been introduced, which can be used as a metric for properly ordering the different Configuration Voltage Vectors on the basis of their voltage balancing capability in extended operation;
- a new Variable-Step Control algorithm has been proposed, allowing for the safe extended operation of the converter even under particularly destabilizing operating conditions, such as a constant desired output voltage or a sudden load change.

The good performances of the proposed control algorithm have finally been tested in simulation and compared with the results that are given by the classical Minimum Distance Control.

The next steps of the research work presented in this paper include the code optimization of the Variable-Step Control, in order to study and address its real-time implementation, as well as the investigation of the other potential benefits that the Variable-Step Control can bring. Additionally, the closed-loop stability analysis through the load can provide important criteria that the load must satisfy in order to ensure closed-loop stability. As far as the modeling part is concerned, the presented modeling procedure can be extended in order to show that it can also be easily applied to other converter topologies, such as the

diode-clamped topology. Furthermore, we are planning to address the analysis and the modeling of other multilevel converters, in order to perform their stability analysis and investigate the properties they exhibit, following the outlines introduced in this paper for multilevel flying-capacitor converters.

Author Contributions: Data curation, D.T. and R.Z.; Formal analysis, D.T. and R.Z.; Investigation, D.T. and R.Z.; Methodology, D.T. and R.Z.; Software, D.T. and R.Z.; Writing—original draft, D.T. and R.Z.; Writing—review & editing, D.T. and R.Z. All authors have read and agreed to the published version of the manuscript.

Funding: This research received no external funding.

Data Availability Statement: The supplementary material related to this study is available at the link provided in [28].

Conflicts of Interest: The authors declare no conflict of interest.

References

- Zanasi, R.; Cuoghi, S. Model of Soft-Switching Converter and Power Control of Grid-Connected Photovoltaic Systems. In Proceedings of the IECON Annual Conference of the IEEE Industrial Electronics Society, Melbourne, VIC, Australia, 7–11 November 2011; doi:10.1109/IECON.2011.6119518. [\[CrossRef\]](#)
- Wu, H.; Mu, T.; Ge, H.; Xing, Y. Full-Range Soft-Switching-Isolated Buck-Boost Converters With Integrated Interleaved Boost Converter and Phase-Shifted Control. *IEEE Trans. Power Electron.* **2016**, *31*, 987–999. [\[CrossRef\]](#)
- Azer, P.; Emadi, A. Generalized State Space Average Model for Multi-Phase Interleaved Buck, Boost and Buck-Boost DC-DC Converters: Transient, Steady-State and Switching Dynamics. *IEEE Access* **2020**, *8*, 77735–77745. [\[CrossRef\]](#)
- Zanasi, R.; Cuoghi, S. Model of Soft-Switching Converter and Power Control for Smart Grid Applications. In Proceedings of the IEEE PES Innovative Smart Grid Technologies, Perth, WA, Australia, 13–16 November 2011, doi:10.1109/ISGT-Asia.2011.6167073. [\[CrossRef\]](#)
- Al-Badi, A.H.; Ahshan, R.; Hosseinzadeh, N.; Ghorbani, R.; Hossain, E. Survey of Smart Grid Concepts and Technological Demonstrations Worldwide Emphasizing on the Oman Perspective. *Appl. Syst. Innov.* **2020**, *3*, 5. [\[CrossRef\]](#)
- Wu, B.; Narimani, M. *High-Power Converters and AC Drives*; Wiley-IEEE Press: Hoboken, NJ, USA, 2017.
- Quraan, M.; Tricoli, P.; D’Arco, S.; Piegari, L. Efficiency Assessment of Modular Multilevel Converters for Battery Electric Vehicles. *IEEE Trans. Power Electron.* **2017**, *35*, 2041–2051. [\[CrossRef\]](#)
- Rodriguez, J.; Lai, J.-S.; Peng, F.Z. Multilevel Inverters: A Survey of Topologies, Controls, and Applications. *IEEE Trans. Ind. Electron.* **2002**, *49*, 724–738. [\[CrossRef\]](#)
- Rodriguez Bernet, J.S.; Wu, B.; Pontt, J.O.; Kouro, S. Multilevel Voltage-Source-Converter Topologies for Industrial Medium-Voltage Drives. *IEEE Trans. Ind. Electron.* **2017**, *54*, 2930–2945. [\[CrossRef\]](#)
- Saleh, S.A.; Al-Durra, A.; Ahshan, R. Ground Potentials in Transformerless Grid-Connected Multi-Level Power Electronic Converters. In Proceedings of the 56th Industrial and Commercial Power Systems Technical Conference (I&CPS), Las Vegas, NV, USA, 29 June–28 July 2020. [\[CrossRef\]](#)
- Saleh, S.; Al-Durra, A.; Ahshan, R. On the Ground Potentials and Grounding Circuits of Transformerless Grid-Connected Multilevel Power Electronic Converters. *IEEE Trans. Ind. Appl.* **2020**, *56*, 6286–6297. [\[CrossRef\]](#)
- Zanasi, R.; Cuoghi, S. Dynamic Models of Multilevel Converters by using the Power Oriented Graph Technique. In Proceedings of the International Symposium on Power Electronics, Electrical Drives, Automation and Motion, Sorrento, Italy, 20–22 June 2012. [\[CrossRef\]](#)
- Rodriguez, J.; Franquelo, L.G.; Kouro, S.; León, J.I.; Portillo, R.C.; Prats, M.A.M.; Pérez, M.A. Multilevel Converters: An Enabling Technology for High-Power Applications. *Proc. IEEE* **2009**, *97*, 1786–1817. [\[CrossRef\]](#)
- Corzine, K.A.; Baker, J.R. Multilevel voltage-source duty-cycle modulation: Analysis and implementation. *IEEE Trans. Ind. Electron.* **2002**, *49*, 1009–1016. [\[CrossRef\]](#)
- Diaz, M.; Cardenas, R.; Ibaceta, E.; Mora, A.; Urrutia, M.; Espinoza, M.; Rojas, F.; Wheeler, P. An Overview of Modelling Techniques and Control Strategies for Modular Multilevel Matrix Converters. *Energies* **2020**, *13*, 4678. [\[CrossRef\]](#)
- Liu, M.; Li, Z.; Yang, X. A Universal Mathematical Model of Modular Multilevel Converter with Half-Bridge. *Energies* **2020**, *13*, 4464. [\[CrossRef\]](#)
- Zanasi, R. The Power-Oriented Graphs Technique: System modeling and basic properties. In Proceedings of the IEEE Vehicle Power and Propulsion Conference (VPPC), Lille, France, 1–3 September 2010. [\[CrossRef\]](#)
- Zanasi, R.; Geitner, G.H.; Bouscayrol, A.; Lhomme, W. Different energetic techniques for modelling traction drives. In Proceedings of the 9th International Conference on Modeling and Simulation of Electric Machines, Converters and Systems (ELECTRIMACS), Québec, QC, Canada, 8–11 June 2008.
- Zanasi, R. POG Modeler: The Web Power-Oriented Graphs Modeling Program. In Proceedings of the IFAC World Congress, Berlin, Germany, 11–17 July 2020.

20. Brando, G.; Dannier, A.; Spina, I.; Tricoli, P. Integrated BMS-MMC Balancing Technique Highlighted by a Novel Space-Vector Based Approach for BEVs Application. *Energies* **2017**, *10*, 1628. [[CrossRef](#)]
21. Liao, Y.; You, J.; Yang, J.; Wang, Z.; Jin, L. Disturbance-Observer-Based Model Predictive Control for Battery Energy Storage System Modular Multilevel Converters. *Energies* **2018**, *11*, 2285. [[CrossRef](#)]
22. Gaisse, P.; Muñoz, J.M.; Villalón, A.; Aliaga, R. Improved Predictive Control for an Asymmetric Multilevel Converter for Photovoltaic Energy. *Sustainability* **2020**, *12*, 6204. [[CrossRef](#)]
23. Tian, H.; Li, Y.W. Carrier-Based Stair Edge PWM (SEPWM) for Capacitor Balancing in Multilevel Converters With Floating Capacitors. *IEEE Trans. Ind. Appl.* **2018**, *54*, 3440–3452. [[CrossRef](#)]
24. McGrath, B.P.; Holmes, D.G. Enhanced Voltage Balancing of a Flying Capacitor Multilevel Converter Using Phase Disposition (PD) Modulation. *IEEE Trans. Power Electron.* **2011**, *26*, 1933–1942. [[CrossRef](#)]
25. Kang, D.-W.; Lee, B.-K.; Jeon, J.-H.; Kim, T.-J.; Hyun, D.-S. A Symmetric Carrier Technique of CRPWM for Voltage Balance Method of Flying-Capacitor Multilevel Inverter. *IEEE Trans. Ind. Electron.* **2005**, *52*, 879–888. [[CrossRef](#)]
26. Kou, X.; Corzine, K.A.; Familiant, Y.L. Full binary combination schema for floating voltage source multilevel inverters. *IEEE Trans. Power Electron.* **2002**, *17*, 891–897. [[CrossRef](#)]
27. Huang, J.; Corzine, K.A. Extended operation of flying capacitor multilevel inverters. *IEEE Trans. Power Electron.* **2006**, *21*, 140–147. [[CrossRef](#)]
28. Link of the Supplementary Material. Available online: http://dii.unimo.it/~zanasi/Personale/Suppl_M.zip (accessed on).

Article

The Use of a Real-Time Simulator for Analysis of Power Grid Operation States with a Wind Turbine

Zbigniew Kłosowski * and Sławomir Cieślík

Faculty of Telecommunications, Computer Science and Electrical Engineering, UTP University of Science and Technology, Kaliskiego 7, PL-85-796 Bydgoszcz, Poland; slawomir.cieslik@utp.edu.pl

* Correspondence: klosowski@utp.edu.pl

Abstract: The main issue in this paper is the real-time simulator of a part of a power grid with a wind turbine. The simulator is constructed on the basis of a classic PC running under a classic operating system. The proposed solution is expected and desired by users who intend to manage power microgrids as separate (but not autonomous) areas of common national power systems. The main reason for the decreased interest in real-time simulators solutions built on the basis of PC is the simulation instability. The instability of the simulation is due to not keeping with accurate results when using small integration steps and loss of accuracy or loss of stability when using large integration steps. The second obstacle was due to the lack of a method for integrating differential equations, which gives accurate results with a large integration step. This is the scientific problem that is solved in this paper. A new solution is the use of a new method for integrating differential equations based on average voltage in the integration step (AVIS). This paper shows that the applied AVIS method, compared to other methods proposed in the literature (in the context of real-time simulators), allows to maintain simulation stability and accurate results with the use of large integration steps. A new (in the context of the application of the AVIS method) mathematical model of a power transformer is described in detail, taking into account the nonlinearity of the magnetization characteristics. This model, together with the new doubly-fed induction machine model (described in the authors' previous article), was implemented in PC-based hardware. In this paper, we present the results of research on the operation states of such a developed real-time simulator over a long period (one week). In this way, the effectiveness of the operation of the real-time simulator proposed in the paper was proved.

Citation: Kłosowski, Z.; Cieślík, S. The Use of a Real-Time Simulator for Analysis of Power Grid Operation States with a Wind Turbine. *Energies* **2021**, *14*, 2327. <https://doi.org/10.3390/en14082327>

Academic Editors: Juri Belikov and Marco Pau

Received: 22 February 2021

Accepted: 13 April 2021

Published: 20 April 2021

Publisher's Note: MDPI stays neutral with regard to jurisdictional claims in published maps and institutional affiliations.



Copyright: © 2021 by the authors. Licensee MDPI, Basel, Switzerland. This article is an open access article distributed under the terms and conditions of the Creative Commons Attribution (CC BY) license (<https://creativecommons.org/licenses/by/4.0/>).

Keywords: power network simulation; real-time simulation; mathematical modeling of power systems; average voltages in the integration step method

1. Introduction

Modern state-of-the-art technology allows for the effective use of real-time simulators in solving many problems related to power systems operations. In the last dozen or so years, many good books [1–4], doctoral theses (including [5–7]) and articles in scientific journals (which will be cited further) have been written about real-time simulators of power systems. This proves that real-time simulators already have an established position in scientific publications, but due to their specificity, not all problems are already solved. This specificity results directly from the valuable advantages of this type of simulators, namely, the possibility of their cooperation with real devices (a regulator with a newly implemented algorithm, a master regulator controlling the entire farm or digital power protection) in real time.

The necessary condition for the correct operation of these simulators is obtaining simulation results at the same time as in their physical counterparts. An example of using a real-time simulator is shown in Figure 1.

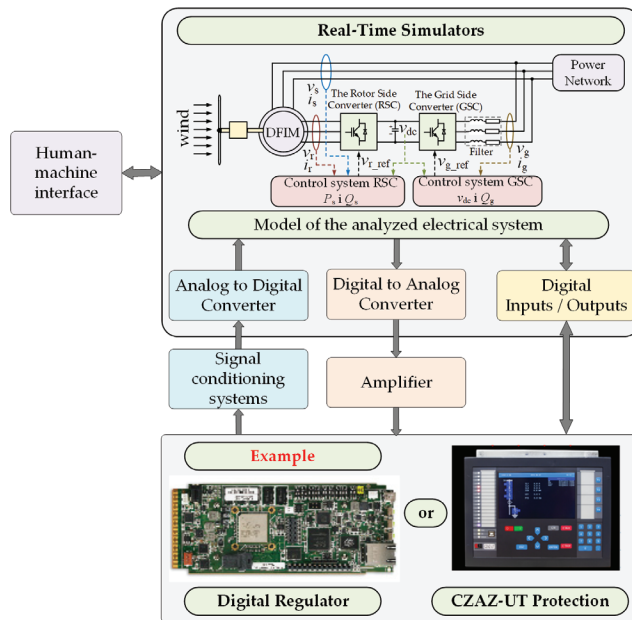


Figure 1. Schematic diagram of a real-time simulator.

A measurable effect of the development of real-time simulators in applications for analyzing the operation of power systems is a number of commercial solutions: RTDS (Real-Time Digital Simulator) [8,9] from the Canadian company RTDS Version 27 September 2020 submitted to Journal Not Specified Technologies and RT-LAB (Real-Time Laboratory) [10–12] from OPAL-RT Technologies. The cost of purchasing them is high; therefore, the scientific and research communities are using or looking for cheaper real-time simulators. This group includes simulators based on the DSP (Digital Signal Processor) [7,13–15], FPGAs (Field-Programmable Gate Array) [5,16–18] and classic personal computers [6,19–24].

Statements saying that the time of real-time simulators based on personal computers is over are often made on the basis of works from the end of the last century and are incorrect. Modern personal computers have high computing power and in many practical cases are a competitive solution, combining the technical requirements (of course with limitations as to the extent of the analyzed power system) and the cost of building a complete simulator. That is why such a simulator will be presented in this paper.

A real-time simulator is required to run steadily without interruption or to a scheduled shutdown in order to be able to run concurrently with external processes with an appropriate degree of adequacy, and to run with a constant time step. In order for these requirements to be met, appropriate numerical methods should be sought for the approximation of differential equations and for solving the equation systems of the developed mathematical model. In the above-mentioned publications on real-time simulators (excluding [20,22,24]) and in additional important books on mathematical modeling of power systems [25–27], two methods of approximating differential equations are proposed: backward Euler method and trapezoidal rule. The use of the backward Euler method involves a small integration step of the order of single μs , so the real-time simulator must have high computing power to be able to obtain the results of the calculations. The trapezoidal method allows one to increase the time step, but there is often a problem of numerical oscillations [5,27–29], which may lead to the loss of stability of the simulator operation. This state of knowledge has remained practically unchanged in the last several dozen years. A breakthrough in simulating the operating states of power and electromechanical systems is the use of a new method of approximation of differential equations in mathematical models of these

systems, which is systematically developed at the Institute of Electrical Engineering UTP University of Science and Technology in Bydgoszcz (Poland). The real-time simulator described in this article uses this method.

The essence of the method of approximating differential equations in mathematical models of electrical systems is the expansion of the used physical quantities into the Taylor series, but applied to the equations written for average voltages in the integration step. None of the publications listed above (excluding [20,22,24]) mention such a solution. The physical basis of the method was formulated in [30]. In the research conducted at the Institute of Electrical Engineering UTP University of Science and Technology in Bydgoszcz (Poland), this method is successfully used in real-time simulation. Examples of this can be found in [6,20,22,24,31–37].

The aim of the work, the results of which are presented in this article, was to develop a real-time simulator of the operation of a fragment of the power distribution network with a wind turbine, which will be characterized by stable operation for a relatively long time (at least one week) with appropriate accuracy of the results, taking into account various dynamic processes inside and outside the simulator. This problem was analyzed in detail in the unpublished doctoral dissertation [6]. The applied methods and their effectiveness allow us to state that stable real-time operation of a complex electrical system simulator is possible in a relatively long time, with a relatively long time step, while maintaining the appropriate accuracy of results.

The organization of this article is as follows. In Section 2, we present for the first time the theoretical advantage of using the average voltages in the integration step method in relation to using two other methods proposed in other publications for the RL circuit case. For this purpose, the amplitude and phase characteristics were determined for the system operator transmittances in discrete time $H(z)$ in relation to the solution accurate in continuous time $H(s)$ for three different methods used to analyze the RL circuit. The obtained characteristics were confirmed by example (average voltages in the integration step and trapezoidal rule methods) with practical simulation results that allow for proper interpretation and proof of the advantage of the applied method over two others. Section 3 describes the issues related to the mathematical modeling of a transformer, taking into account the nonlinear magnetization characteristics. The advantage of transient simulation with the use of the average voltages in the integration step method compared to the trapezoidal method was demonstrated. The transformer model was used in the model of a fragment of the power distribution network with a wind turbine, which is described in detail in Section 4. This model was implemented in a real-time simulator constructed by the Institute of Electrical Engineering UTP University of Science and Technology in Bydgoszcz (Poland) on the basis of a personal computer, running under the Windows operating system. The constructed simulator was tested, taking into account dynamic processes caused by events programmed inside the simulator, as well as events taking place in its real environment. The description and results of selected operating states of the simulator are presented in Section 5. The apparatus used, i.e., a real power network parameter analyzer, allowed us to obtain results confirming the stable operation of the simulator in a relatively long time (one week). Section 6 contains drawn conclusions.

2. Accuracy Assessment of the New Method for Approximation of Differential Equations

The accuracy of the applied method for approximation of differential equations is assessed using the method present in many publications [5,27,28,38]. This method consists of comparing the amplitude and phase characteristics of the transmittance ratio $H(z)$ for discrete equations in time to $H(s)$ for continuous equations in time as an exact solution. Additionally, the physical interpretation of the transient analysis is presented for an exemplary electrical circuit, the diagram of which is shown in Figure 2. The analyzed electrical circuit consists of a series connection of resistance R and inductance L , powered from an ideal source of sinusoidal voltage $v(t)$. The circuit parameters adopted in the

simulation: resistance $R = 0.1 \Omega$, inductance $L = 10 \text{ mH}$, voltage source amplitude $V_m = 300 \text{ V}$. The mathematical equation describing the two-terminal circuit is as follows:

$$v(t) = R \cdot i(t) + L \cdot \frac{di(t)}{dt} \tag{1}$$

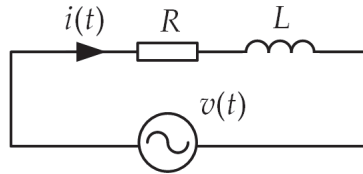


Figure 2. Electrical circuit diagram used to assess the accuracy of the differential equation approximation algorithm.

Three methods of approximation of the differential Equation (1) will be compared, namely, backward Euler method, trapezoidal method and the method based on average voltages in the integration step (acronym AVIS). Table 1 summarizes the operator transmittance $H(s) = \frac{I(s)}{V(s)}$ for the electric circuit shown in Figure 2 and the operator transfer functions $H(z) = \frac{I(z)}{V(z)}$ for these three methods in the application to the same circuit.

Table 1. Operator transmittances of the analyzed electrical circuit.

Rule	$H(s)$	$H(z)$
Backward Euler		$\frac{\Delta t \cdot z}{z \cdot (R \cdot \Delta t + L) - L}$
Trapezoidal	$\frac{1}{s \cdot L + R}$	$\frac{1}{\frac{R \cdot \Delta t \cdot z + 2 \cdot L \cdot z - 2 \cdot L}{\Delta t \cdot z} - \frac{2 \cdot L \cdot z + 2 \cdot L}{\Delta t \cdot z(z+1)}}$
AVIS		$\frac{z^{-1} - 1}{\omega \cdot \Delta t} \cdot \frac{z - \cos(\omega \cdot \Delta t)}{\sin(\omega \cdot \Delta t)}$
		$0.5 \cdot R + L \cdot \Delta t^{-1} + 0.5 \cdot R \cdot z^{-1} - L \cdot \Delta t^{-1} \cdot z^{-1}$

The operator transmittances $H(z)$ have been derived for the equation:

$$v(t_n) = R \cdot i(t_n) + L \cdot \frac{di(t_n)}{dt} \tag{2}$$

which is the transformation of Equation (1) to the discrete form.

The $\frac{H(z)}{H(s)}$ ratio for the considered integration methods is shown in Figures 3 and 4. In these figures, the frequency axis is labeled based on the per unit system, so the Nyquist frequency $\frac{1}{2 \cdot \Delta t} = \frac{1}{2}$.

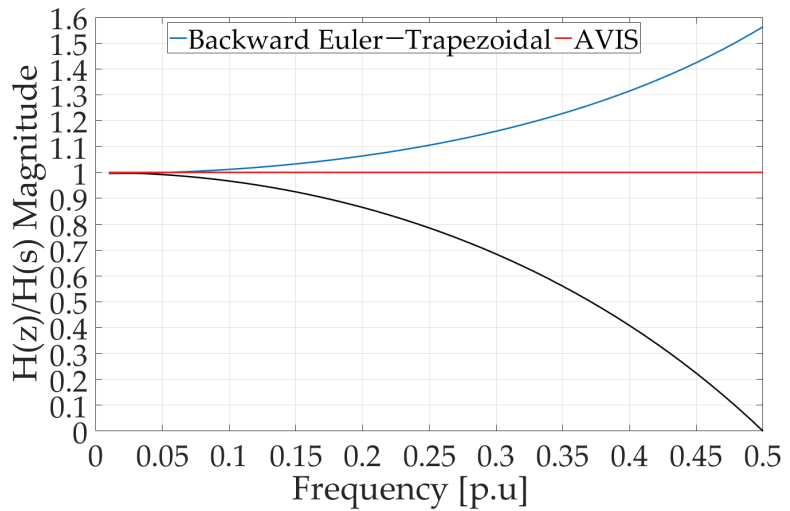


Figure 3. Amplitude frequency response of transmittance for considered numerical methods.

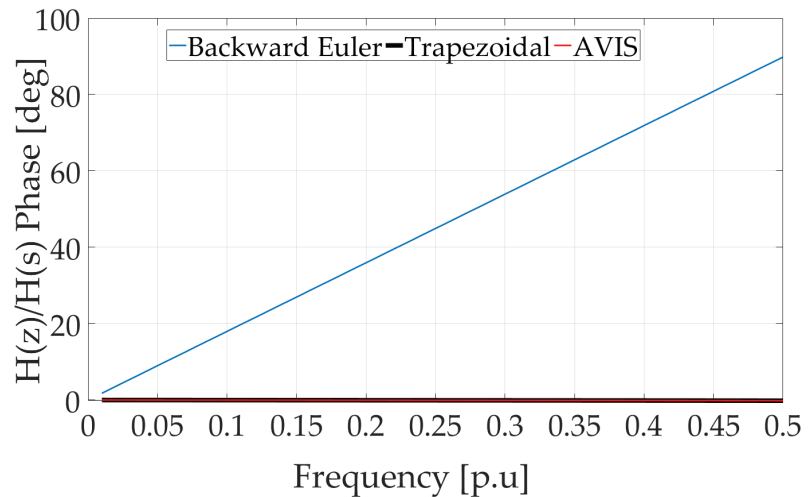


Figure 4. Phase frequency response of transmittance for considered numerical methods.

The analysis of the frequency characteristics presented in Figures 3 and 4 shows that the accuracy of the solution using the backward Euler and trapezoidal rule algorithms depends on the value of $f \cdot \Delta t$ (voltage frequency or integration step). As the value of $f \cdot \Delta t$ increases, the amplitude errors for both methods also increase. The phase error of the backward Euler method also increases with the increasing value of $f \cdot \Delta t$. The phase error of the trapezoidal method is close to zero in the entire range of $f \cdot \Delta t$ values under consideration. The conclusion is that the backward Euler method and the trapezoidal method gives fairly accurate answers up to $1/5$ of the value of $f \cdot \Delta t$.

Particularly noteworthy is the fact that the AVIS method used in this case is characterized by the amplitude and phase error close to zero, regardless of the $f \cdot \Delta t$ value in the entire range of the considered $f \cdot \Delta t$ values. This is a convincing proof of the advantage of the AVIS method, compared to the backward Euler and trapezoidal rule method.

To illustrate the obtained results in practice, a simulation of the transient state caused by connecting the RL terminal block to the AC voltage source was performed. The circuit parameters adopted in the simulation are: resistance $R = 0.1 \Omega$, inductance $L = 10 \text{ mH}$, voltage source amplitude $V_m = 300 \text{ V}$. Simulations were made with a constant integration step $\Delta t = 1 \text{ ms}$ for two values of the supply voltage frequency: 50 Hz and 150 Hz. Figure 5 shows the course of the current flowing in the circuit (Figure 2) after connecting the RL duplex to a voltage source with a frequency of 50 Hz. The current waveforms obtained using the three discussed methods of integration and the current waveform with the exact solution are shown. Additionally, Figure 6 shows a fragment (details can be seen) of this course in the time interval from 0.40 s to 0.42 s.

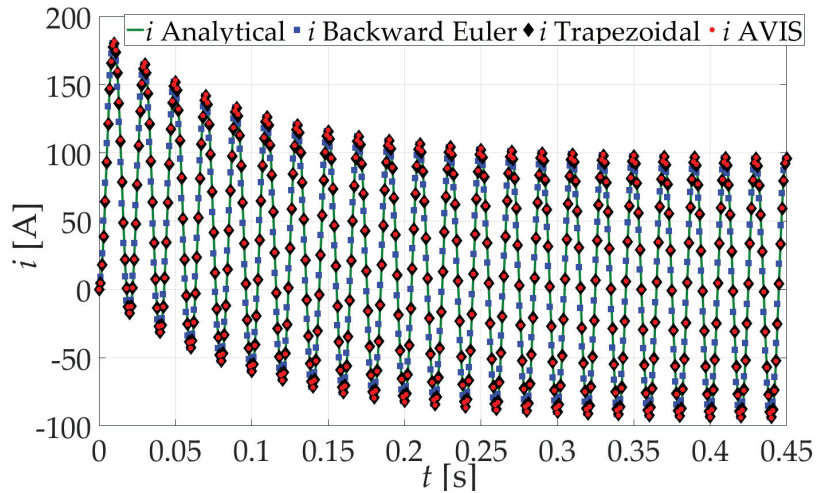


Figure 5. Current waveform caused by connecting the RL clamp to the voltage source with a frequency of 50 Hz.

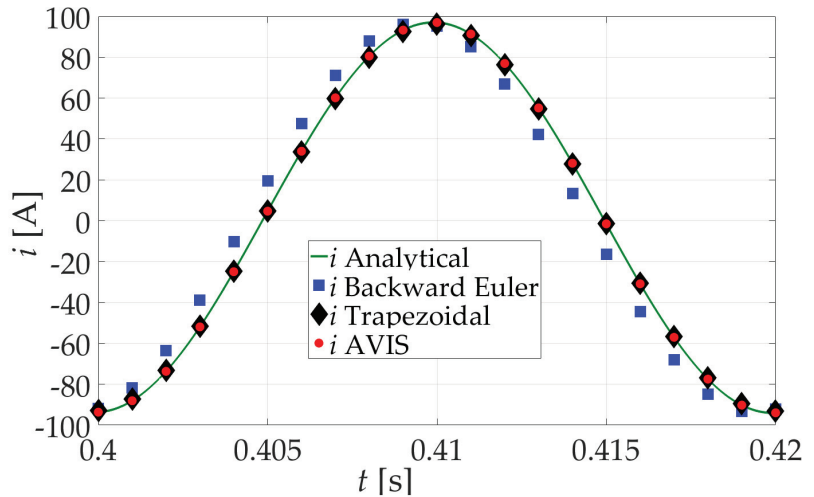


Figure 6. A section of the current waveform after connecting the RL double socket to a voltage source with a frequency of 50 Hz.

Figure 7 shows the course of the current flowing in the circuit after connecting the RL double socket to a voltage source with a frequency of 150 Hz. Additionally, Figure 8 shows a fragment of this course for the time from 0.40 s to 0.41 s.

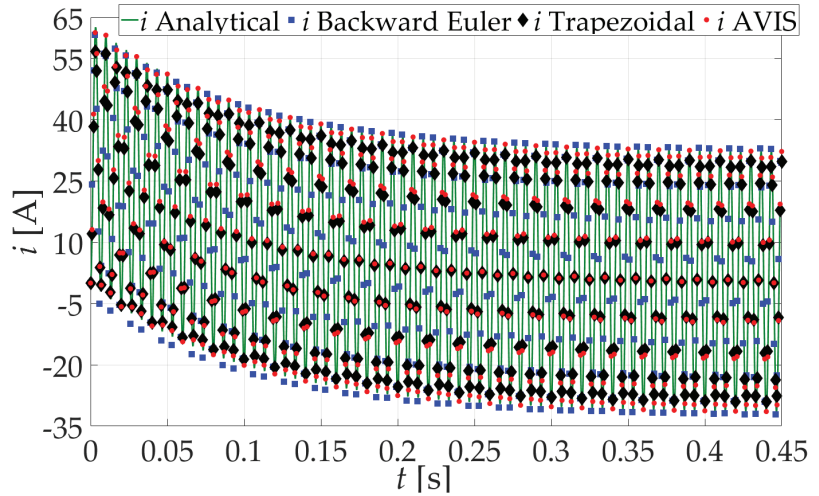


Figure 7. Current waveform caused by connecting the RL clamp to the voltage source with a frequency of 150 Hz.

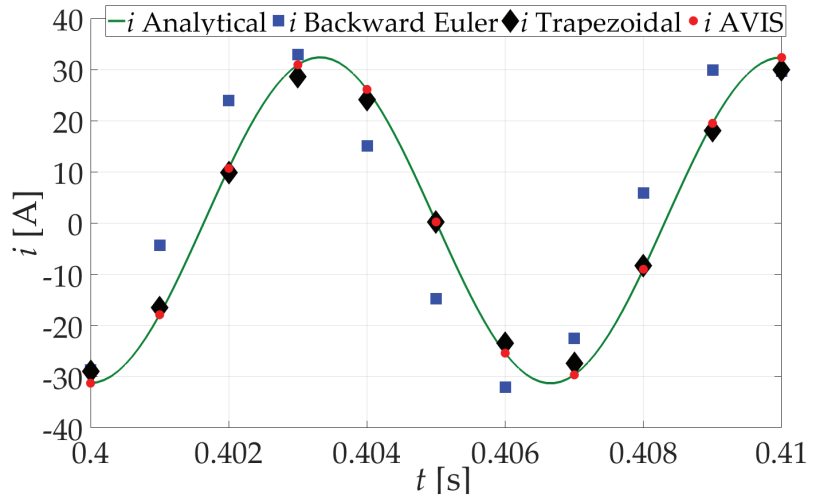


Figure 8. A section of the current waveform after connecting the RL double socket to a voltage source with a frequency of 150 Hz.

When analyzing the results of simulation experiments, it can be seen that for the integration step $\Delta t = 1$ ms, regardless of the frequency of the supply voltage, the most accurate results are obtained using the AVIS method for the approximation of differential equations. Discrete values of solutions coincide with the exact solution. This also confirms the correctness of the results presented in Figures 3 and 4. With the use of the trapezoidal method for a voltage excitation with a frequency of 50 Hz, the results are also satisfactory, but for a frequency of 150 Hz, there is clearly a difference in relation to the exact solution

(there is an amplitude error). The use of the backward Euler method in both cases (50 Hz and 150 Hz) causes clear differences in relation to the exact solution.

The analysis also shows that in the analyzed case, with the use of the backward Euler method, in order for the simulation results to be acceptable in terms of accuracy (the amplitude and phase error is small compared to the exact value), the integration step should be reduced ten times compared to the AVIS method. However, in the case of using the trapezoidal method, the integration step should be reduced twice as compared to the AVIS method. Reducing the integration step causes an increase in the time needed to simulate the transient states in the presented dipole. Increasing the computation time in order to obtain greater accuracy of results is not the right solution in the context of real-time simulators.

The results presented in this section clearly prove the advantage of the AVIS method used over the backward Euler and trapezoidal rule method, used by other authors in real-time simulation, for the simulation of an exemplary electric circuit.

3. Simulation of the Operating States of a Power Transformer

One of the elements frequently present in power grids is a transformer. The representation of the dynamics of transformer operation, mainly due to the nonlinearity of the magnetization characteristics and the core remagnetization process itself, is not a trivial issue, especially in the context of real-time simulation. This section presents the results of the test of the accuracy of simulation of transient states of the power transformer operation. Transient states during the transformer connection to the power grid and changes in the secondary side load of the transformer were analyzed.

When developing a mathematical model of a power transformer that would allow the simulation of various operating states, the electric multipoles method was used as a method of modeling complex electrical systems. An equivalent diagram of the power system, the test results of which are described in this section, with the division into structural elements is presented in Figure 9. The rated data is given in Table 2.

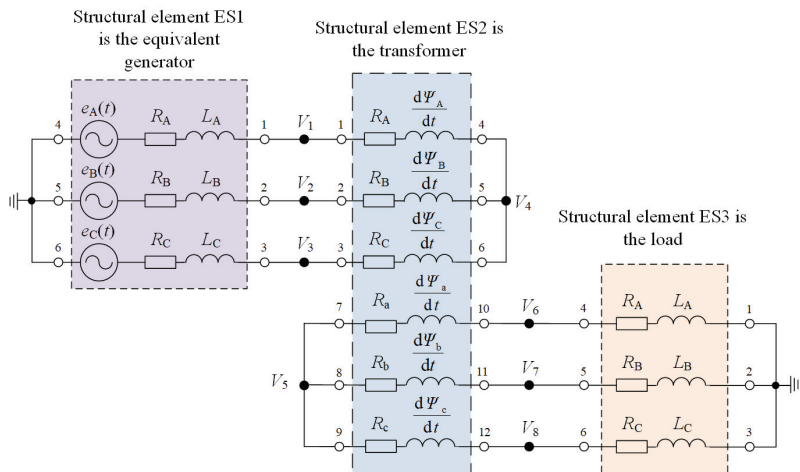


Figure 9. Equivalent diagram of the analyzed power system with division into structural elements.

Table 2. Nominal data of three-phase power transformer.

Rated power	10 kVA	Percentage impedance	3%
Rated voltage primary	380 V	Rated voltage secondary	340 V
Primary current	15 A	Secondary current	17 A
Load loss	220 W	No-load loss	70 W
No-load current	0.4 A	Frequency	50 Hz

A detailed mathematical model of a power transformer, developed by the authors of this article, is presented in [24]. When selecting the method of approximation of differential equations, it was taken into account that the developed model can be implemented in a simulator operating in real time. Therefore, the results obtained from such a simulation must be burdened with a small error at a relatively large integration step. It was assumed that the simulation would be performed with an integration step of 50 μ s.

The performed analysis of the accuracy of the obtained results from the simulation of transient states in the series junction RL (the previous section of this article) made it possible to find out that the results using the backward Euler method do not guarantee the appropriate accuracy. Only two methods were selected for the approximation of differential equations: the trapezoidal method and the method based on the average voltage in the integration step (AVIS). The iterative Gauss–Seidel method was used to solve systems of linear equations. Iterative methods (e.g., the Jacobi or Gauss–Seidel method) allow us to shorten the computation time compared to noniterative methods (e.g., LU decomposition or Gauss’s method) [15].

The comparison of the results obtained from the computer simulation with the integration step of 50 μ s is shown in Figure 10. The trapezoidal method was used to approximate the differential equations in the first simulation, while the AVIS method was used in the second one. The waveforms of the voltage in the L1 phase and the phase current in the L1 phase winding of the power transformer are presented. The following transformer operation states are presented: transformer switching on to the network, time from 0 s to 1.0 s, increasing the load, time from 1.0 s to 1.5 s and reducing the secondary side load of the transformer, time from 1.5 s to 2.0 s.

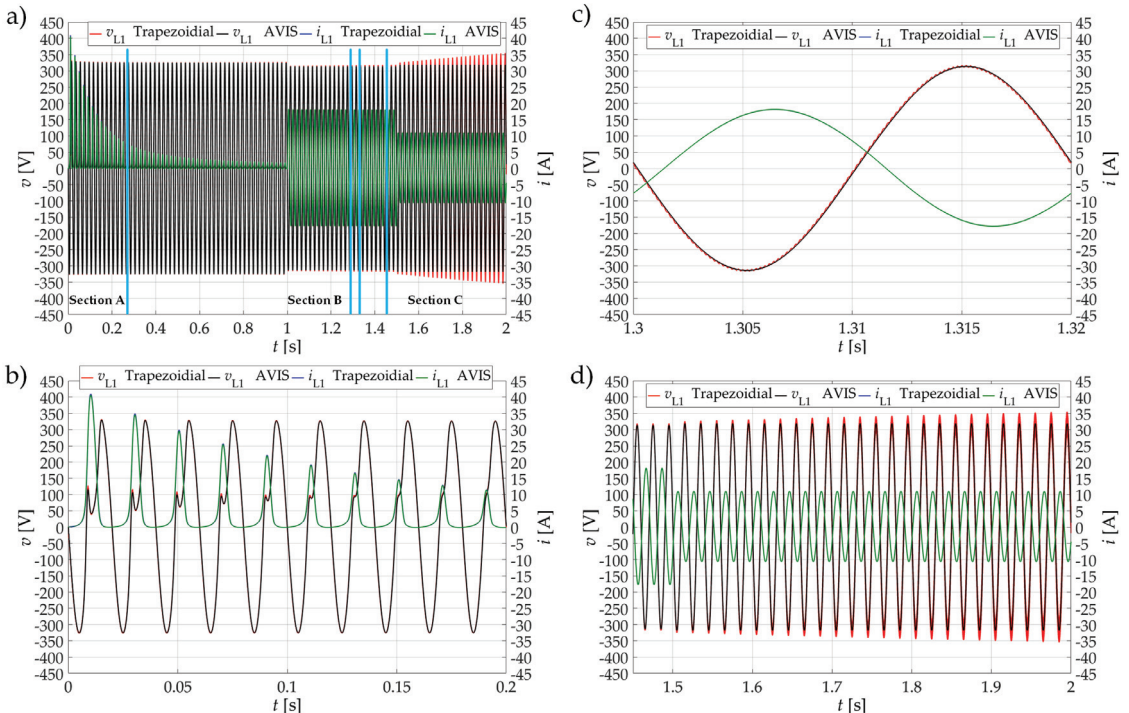


Figure 10. Time waveforms: (a) voltage in phase L1 and phase current in winding of phase L1 of a power transformer using the trapezoidal method and the AVIS method (three sections with details have been marked: (b) section A, (c) section B and (d) section C).

The presented simulation results with 50 μs step confirm that when both of the above-mentioned methods are used to approximate the differential equations, we obtain the same results (Figure 10b,c) for the two considered operating states: switching on and increasing the transformer load. The process caused by the reduction of the load on the secondary side of the transformer, when using the trapezoidal method, causes the simulation to lose stability (the initiation of this process is shown in Figure 10a,d). One of the main requirements for real-time simulators is stable operation over a relatively long time (several days) with various switching processes. Therefore, in the described simulation conditions, the trapezoidal method cannot be used. An effective solution in this case was the use of the AVIS method. The effect of using this method is visible in Figure 10a,d, where after reducing the load on the secondary side of the transformer, the simulation process is still stable. Obviously, the presented results for such a short time do not provide grounds for a general conclusion about the stability of the simulation in a relatively long time (several days). Therefore, the further part of this article presents the results of real-time simulation in the long term for the power grid, including transformer. Of course, the new AVIS method was used in these experiments.

4. Real-Time Simulator of a MV Power Line with a Wind Farm

4.1. Description of the Analyzed Case

The digital simulator is to map the operating states of the medium voltage power line, which supplies the technological park with two main power connections. A Vestas V90 wind turbine (WT) with a rated power of 1.8 MW is also connected to this line. Only this fragment of the MV power distribution network was considered, because its operation is managed by the technology park. The diagram of the analyzed medium voltage distribution line with a wind farm is shown in Figure 11.

Due to the experience in constructing real-time simulators at the Institute of Electrical Engineering UTP University of Science and Technology in Bydgoszcz (Poland), a simulator based on a personal computer was proposed. The simulator has implemented a mathematical model of the power system based on the connection of electric multipoles. A new method based on average voltages in the integration step (AVIS) was used to algebraize differential equations. This problem was the main goal of the doctoral dissertation [6].

In this article, the attention is focused on the experimental demonstration that the developed simulator based on a personal computer working under the MS Windows operating system can work stably with a constant time step for a relatively long time (several days), taking into account the switching and other processes taking place inside the simulator and in its technical environment.

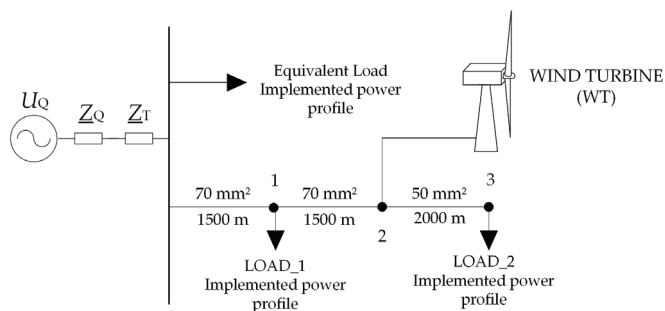


Figure 11. Diagram of the analyzed medium voltages distribution line with a wind farm.

The schematic diagram of the modeled wind turbine with the control system is shown in Figure 12. The electrical part of a wind turbine (WT) consists of the following main elements: a double-fed machine (DFIM); rotor side converter (RSC); mains side converter (GSC); LC filter; three-winding block transformer (TB); the converter control system from

the rotor side (RSC) and the converter control system from the network side (GSC). The characteristics of the control system were taken from the literature [9,39].

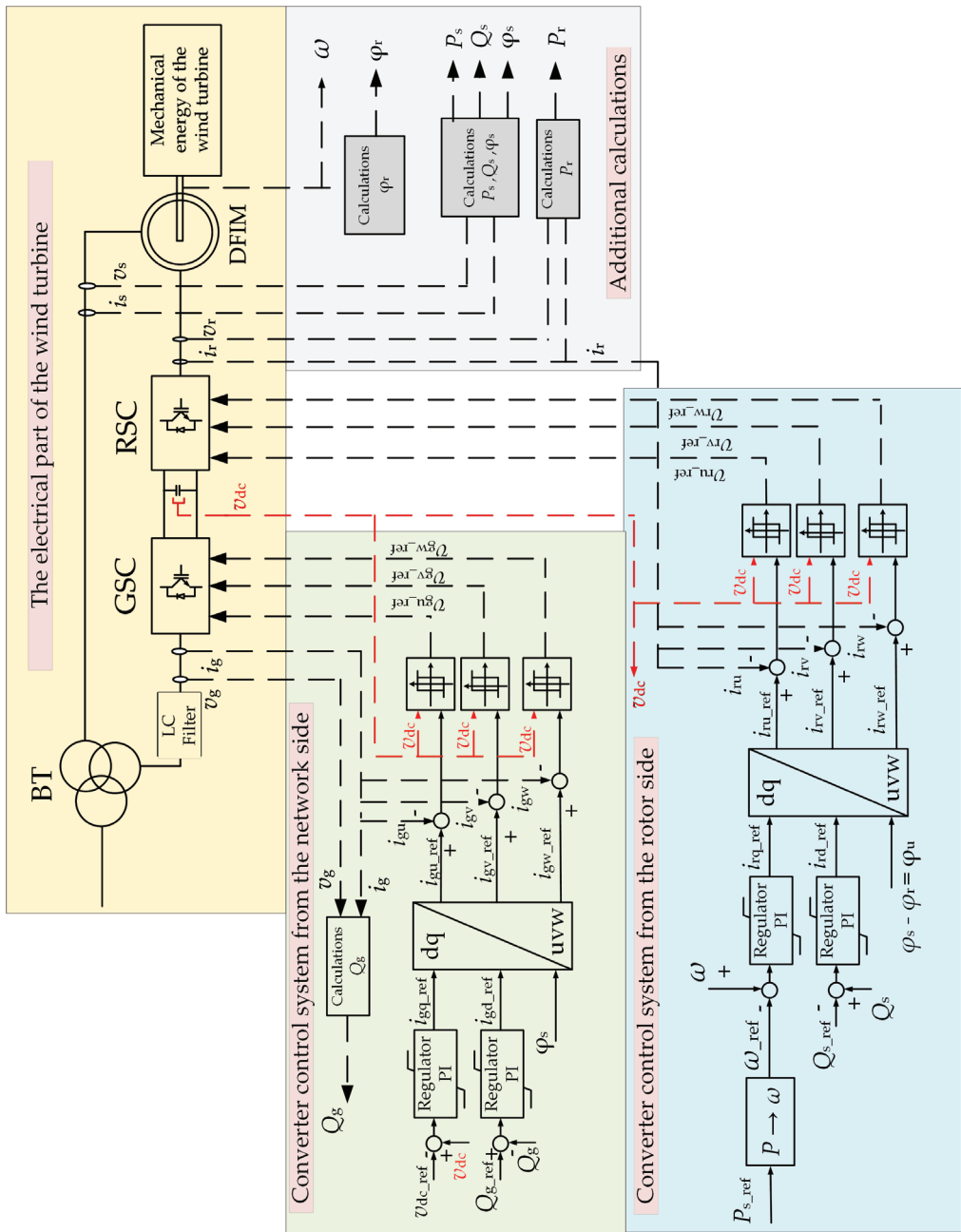


Figure 12. Schematic diagram of a wind turbine with a control system.

An equivalent diagram of the analyzed fragment of the MV power distribution network in the form of a connection system of electric multipole poles is shown in Figure 13. In this way, seventeen structural elements were distinguished, the names of which are written

directly in Figure 13. This diagram is the basis for the development of a mathematical model of this power system.

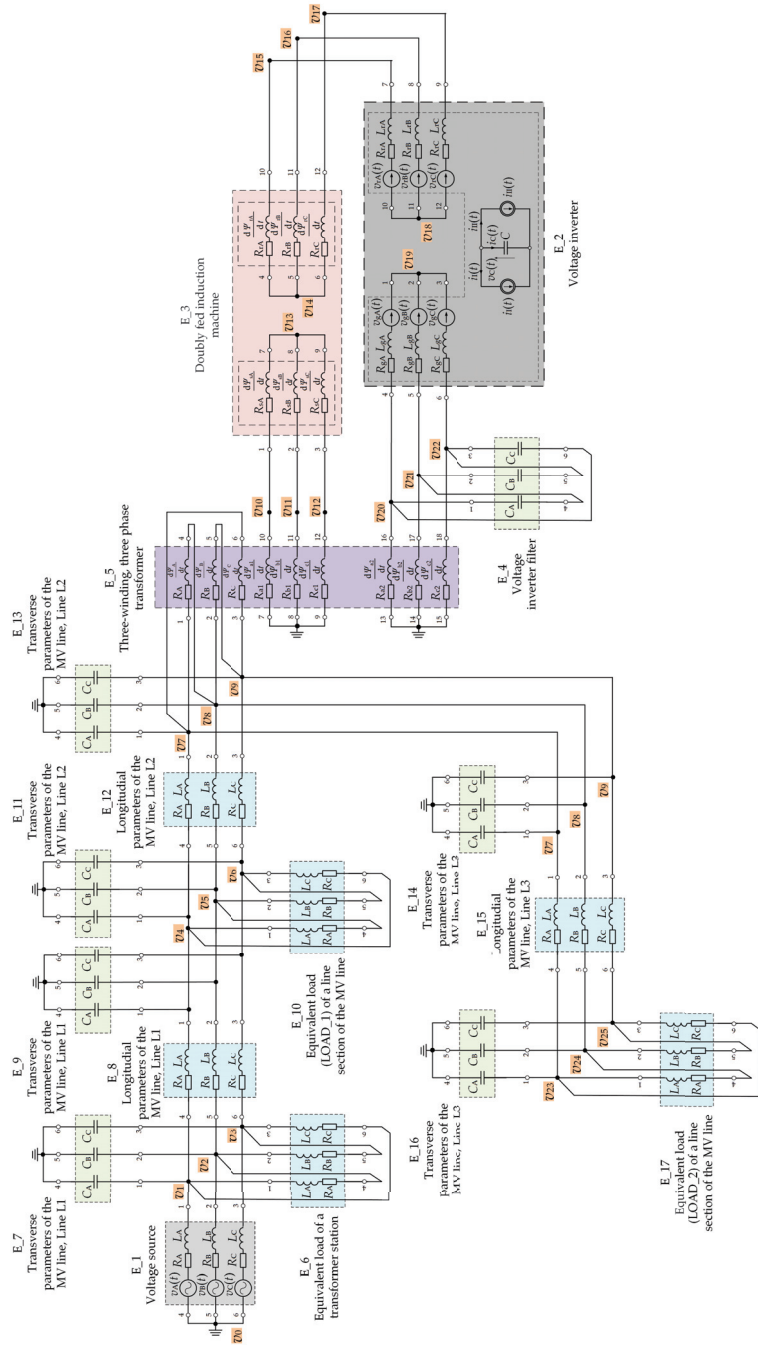


Figure 13. Equivalent diagram of the analyzed power system with the use of multipoles.

4.2. Mathematical Model of the Analyzed Network Fragment

The use of the AVIS method allows for a stable simulation of electrical systems in real time with a relatively large time step (200 μ s) while maintaining the appropriate accuracy of the results [31–35]. The iterative Gauss–Seidel method was used to solve the system of linear equations.

The basics of mathematical modeling of electrical systems using the above methods are presented in detail in the article [31] by the authors of this article. With regard to the power system considered here, the following structural elements are distinguished: a double-fed induction machine (DFIM), a detailed model of which is presented in [31]; three-winding transformer; power electronic converter, the detailed model of which is presented in [9,39,40] and the MV power line; three loads of electricity (LOAD_1, LOAD_2 and equivalent load) and a replacement energy source (replacement generator), detailed models of which are presented in [31]. Overhead power lines are modeled in the form of multipoles, where each phase of the line is modeled in the form of Π equivalent circuits with longitudinal (resistance and inductance) and transverse (capacitance) parameters. Electrical loads are also modeled in the form of multipoles where each phase is represented by longitudinal parameters (resistance and inductance).

Due to the fact that the mathematical models of some elements of the analyzed network fragment and the method of creating a mathematical model of the entire system have already been published by the authors of this article (as mentioned above), they will not be discussed here. In this section, only the mathematical model of a three-winding three-phase transformer (BT in Figure 12) will be detailed. Earlier in the work [24], the authors presented a mathematical model of a two-winding three-phase transformer that takes into account the nonlinearity of the core magnetization characteristics.

Using the mathematical modeling convention presented in [31], Figure 14 shows a diagram of a three-winding three-phase transformer as a structural element (eighteen-pole device).

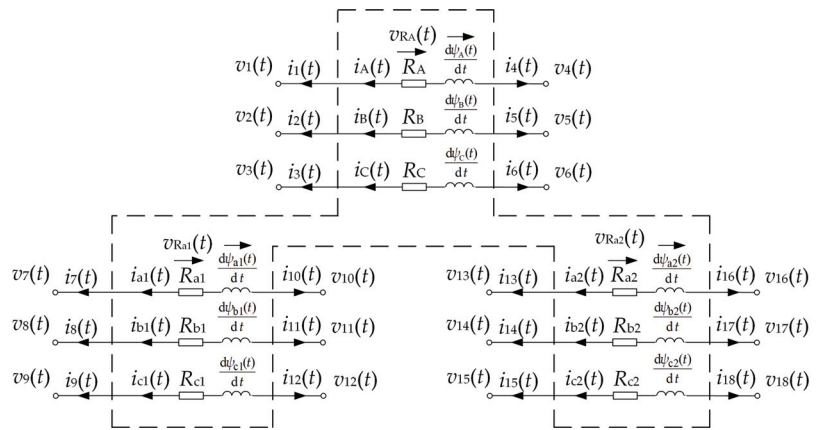


Figure 14. A diagram of a three-winding, three-phase transformer as an eighteen-pole device.

The three-winding, three-phase transformer consists of a three-column ferromagnetic core; on each column, there is placed one upper voltage winding (phase indexes A, B, C) and two lower voltage windings (phase indexes: a1, b1, c1 and a2, b2, c2, respectively). When creating the mathematical model of the transformer, the losses in the core, nonlinear magnetization characteristics and losses in structural elements were all taken into account. A suitable schematic diagram for one phase of the transformer is shown in Figure 15.

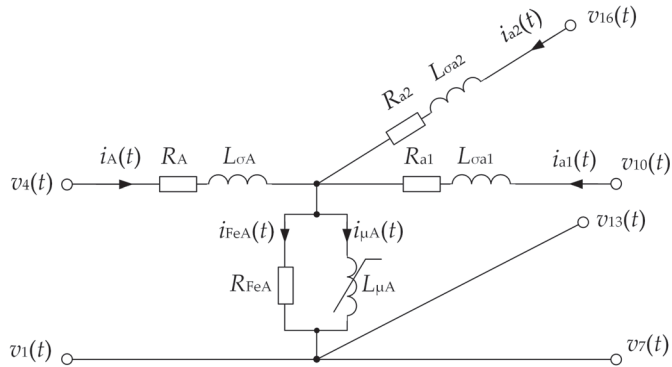


Figure 15. Schematic diagram for one phase of the transformer.

The electric circuit of the modeled transformer is described by the following matrix equation:

$$G \cdot v(t) - R \cdot i_g(t) - L_\sigma \cdot \frac{di_g(t)}{dt} - \frac{d\psi_\mu(t)}{dt} = 0, \tag{3}$$

where:

$$\psi_\mu(t) = \left[\psi_{\mu A}(t) \quad \psi_{\mu B}(t) \quad \psi_{\mu C}(t) \quad \frac{\psi_{\mu A}(t)}{n_1} \quad \frac{\psi_{\mu B}(t)}{n_1} \quad \frac{\psi_{\mu C}(t)}{n_1} \quad \frac{\psi_{\mu A}(t)}{n_2} \quad \frac{\psi_{\mu B}(t)}{n_2} \quad \frac{\psi_{\mu C}(t)}{n_2} \right]^T$$

is a column matrix of the instantaneous values of the main magnetic field fluxes associated with individual transformer windings,

$R = \text{diag}(R_A, R_B, R_C, R_{a1}, R_{b1}, R_{c1}, R_{a2}, R_{b2}, R_{c2})$ is a diagonal matrix of transformer phase winding resistance,

$i_g(t) = \left[i_A(t) \quad i_B(t) \quad i_C(t) \quad i_{a1}(t) \quad i_{b1}(t) \quad i_{c1}(t) \quad i_{a2}(t) \quad i_{b2}(t) \quad i_{c2}(t) \right]^T$ is a column matrix of instantaneous currents flowing through the windings of individual transformer phases,

$L_\sigma = \text{diag}(L_{\sigma A}, L_{\sigma B}, L_{\sigma C}, L_{\sigma a1}, L_{\sigma b1}, L_{\sigma c1}, L_{\sigma a2}, L_{\sigma b2}, L_{\sigma c2})$ is a diagonal matrix of the transformer phase winding dissipation inductance,

$v(t) = \left[v_1(t) \quad v_2(t) \quad \dots \quad v_{17}(t) \quad v_{18}(t) \right]^T$ is a column matrix of values of instantaneous potentials of winding terminals of individual phases of upper and lower voltages,

$$G = \begin{bmatrix} -1 & 0 & 0 & 1 & 0 & 0 & 0 & 0 & 0 & 0 & 0 & 0 & 0 & 0 & 0 & 0 & 0 & 0 \\ 0 & -1 & 0 & 0 & 1 & 0 & 0 & 0 & 0 & 0 & 0 & 0 & 0 & 0 & 0 & 0 & 0 & 0 \\ 0 & 0 & -1 & 0 & 0 & 1 & 0 & 0 & 0 & 0 & 0 & 0 & 0 & 0 & 0 & 0 & 0 & 0 \\ 0 & 0 & 0 & 0 & 0 & 0 & -1 & 0 & 0 & 1 & 0 & 0 & 0 & 0 & 0 & 0 & 0 & 0 \\ 0 & 0 & 0 & 0 & 0 & 0 & 0 & -1 & 0 & 0 & 1 & 0 & 0 & 0 & 0 & 0 & 0 & 0 \\ 0 & 0 & 0 & 0 & 0 & 0 & 0 & 0 & -1 & 0 & 0 & 1 & 0 & 0 & 0 & 0 & 0 & 0 \\ 0 & 0 & 0 & 0 & 0 & 0 & 0 & 0 & 0 & 0 & 0 & 0 & -1 & 0 & 0 & 0 & 1 & 0 \\ 0 & 0 & 0 & 0 & 0 & 0 & 0 & 0 & 0 & 0 & 0 & 0 & 0 & -1 & 0 & 0 & 1 & 0 \\ 0 & 0 & 0 & 0 & 0 & 0 & 0 & 0 & 0 & 0 & 0 & 0 & 0 & 0 & -1 & 0 & 0 & 1 \end{bmatrix}.$$

n_1 it is the transformer ratio of the phase voltage of the upper voltage winding and the phase voltage of the first low voltage winding,

n_2 it is the transformer ratio of the phase voltage of the upper voltage winding and the phase voltage of the second low voltage winding,

The transformer core is made of a ferromagnetic material, which is characterized by a magnetizing curve, showing the dependence of magnetic induction B on the strength of the magnetic field H , $B = f(H)$. This dependence is nonlinear because the relative magnetic permeability of the material from which the transformer core is made is determined by a nonlinear function $\mu_r = f(H)$. Consequently, the relationship between the main magnetic

flux associated with the winding of the respective phase and the magnetizing current of this phase is also nonlinear and corresponds to the following magnetizing characteristics:

$$\psi_{\mu j}(i_{\mu j}) = a_{0j} \cdot i_{\mu j} + a_{1j} \cdot \text{atan}(a_{2j} \cdot i_{\mu j}), \tag{4}$$

where: $j = A, B, C$ and a_{0j}, a_{1j}, a_{2j} . These are the coefficients of the approximating function that can be determined by carrying out the idling test.

Taking into account the magnetic characteristics of the main magnetic circuit (4), the matrix Equation (3) can be written as

$$\mathbf{G} \cdot \mathbf{v}(t) - \mathbf{R} \cdot \mathbf{i}_g(t) - \begin{bmatrix} L_{\mu d}(i_{\mu}) \\ n_1^{-1} \cdot L_{\mu d}(i_{\mu}) \\ n_2^{-1} \cdot L_{\mu d}(i_{\mu}) \end{bmatrix} \cdot \frac{d\mathbf{i}_{\mu}(t)}{dt} = \mathbf{0}, \tag{5}$$

where:

$\mathbf{i}_{\mu}(t) = [i_{\mu A}(t) \ i_{\mu B}(t) \ i_{\mu C}(t)]^T$ is a column matrix of instantaneous magnetizing currents for the respective phases,

$L_{\mu d}(i_{\mu}) = \text{diag}(L_{\mu dA}(i_{\mu A}), L_{\mu dB}(i_{\mu B}), L_{\mu dC}(i_{\mu C}))$ is a matrix of dynamic magnetic inductance of a ferromagnetic core

To simplify calculations, the matrix of dynamic magnetizing inductances in the Equation (5) has been replaced by a matrix of static inductances, which is determined by the formula:

$$L_{\mu s}(i_{\mu}) = \text{diag}(L_{\mu sA}(i_{\mu A}), L_{\mu sB}(i_{\mu B}), L_{\mu sC}(i_{\mu C})) = \text{diag}\left(\frac{\psi_{\mu A}(i_{\mu A})}{i_{\mu A}}, \frac{\psi_{\mu B}(i_{\mu B})}{i_{\mu B}}, \frac{\psi_{\mu C}(i_{\mu C})}{i_{\mu C}}\right). \tag{6}$$

The introduction of such a simplification enables finding an approximate solution without solving nonlinear equations. After introducing static inductance, the equation describing the electrical circuit of the modeled transformer takes the form of

$$\mathbf{G} \cdot \mathbf{v}(t) - \mathbf{R} \cdot \mathbf{i}_g(t) - \begin{bmatrix} L_{\mu s}(i_{\mu}) \\ n_1^{-1} \cdot L_{\mu s}(i_{\mu}) \\ n_2^{-1} \cdot L_{\mu s}(i_{\mu}) \end{bmatrix} \cdot \frac{d\mathbf{i}_{\mu}(t)}{dt} = \mathbf{0}. \tag{7}$$

The full mathematical model of a three-winding, three-phase transformer requires supplementing the matrix Equation (7) with equations describing the magnetic circuit. For this purpose, a surrogate diagram of the magnetic circuit of the modeled transformer was constructed, as shown in Figure 16.

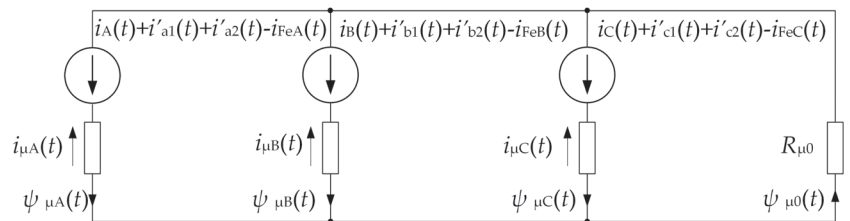


Figure 16. Schematic diagram of the magnetic circuit of the modeled transformer.

In the magnetic circuit, in addition to the main magnetic field fluxes, an additional magnetic flux is included, representing a part of the magnetic field that causes losses in the transformer structural elements, e.g., tank, cover, beams, flat bars and screws.

Using Kirchhoff's laws, the following system of matrix equations was created:

$$\begin{cases} \boldsymbol{\theta}_1 \cdot \mathbf{i}_G(t) + \boldsymbol{\theta}_2 \cdot \mathbf{i}_{d1}(t) + \boldsymbol{\theta}_3 \cdot \mathbf{i}_{d2}(t) - \mathbf{i}_{Fe}(t) - \mathbf{i}_\mu(t) - R_{\mu 0} \cdot \psi_{\mu 0}(t) \cdot \begin{bmatrix} 1 \\ 1 \\ 1 \end{bmatrix} = \mathbf{0} \\ \psi_{\mu 0}(t) = \psi_{\mu A}(t) + \psi_{\mu B}(t) + \psi_{\mu C}(t) \end{cases} \quad (8)$$

where:

$\mathbf{i}_G(t) = [i_A(t) \ i_B(t) \ i_C(t)]^T$ is a column matrix of instantaneous currents flowing through the upper voltage windings,

$\mathbf{i}_{d1}(t) = [i_{a1}(t) \ i_{b1}(t) \ i_{c1}(t)]^T$ is a column matrix of instantaneous currents flowing through the windings of the first low voltage,

$\mathbf{i}_{d2}(t) = [i_{a2}(t) \ i_{b2}(t) \ i_{c2}(t)]^T$ is a column matrix of instantaneous currents flowing through the windings of the second low voltage,

$\mathbf{i}_{Fe}(t) = [i_{FeA}(t) \ i_{FeB}(t) \ i_{FeC}(t)]^T$ is a column matrix of instantaneous currents causing iron losses,

$R_{\mu 0}$ is a constant reluctance for reproducing losses in transformer structural elements,

$\psi_{\mu 0}(t)$ it is a magnetic flux that represents the part of the magnetic field that causes losses in structural components,

$$\boldsymbol{\theta}_1 = \begin{bmatrix} 1 & 0 & 0 \\ 0 & 1 & 0 \\ 0 & 0 & 1 \end{bmatrix}, \boldsymbol{\theta}_2 = \begin{bmatrix} n_1^{-1} & 0 & 0 \\ 0 & n_1^{-1} & 0 \\ 0 & 0 & n_1^{-1} \end{bmatrix}, \boldsymbol{\theta}_3 = \begin{bmatrix} n_2^{-1} & 0 & 0 \\ 0 & n_2^{-1} & 0 \\ 0 & 0 & n_2^{-1} \end{bmatrix}.$$

The current that causes iron losses is determined by the following relationship:

$$\mathbf{i}_{Fe}(t) = \boldsymbol{\theta}_4 \cdot \frac{d\mathbf{i}_\mu(t)}{dt} = \text{diag}\left(\frac{L_{\mu sA}(i_{\mu A})}{R_{FeA}}, \frac{L_{\mu sB}(i_{\mu B})}{R_{FeB}}, \frac{L_{\mu sC}(i_{\mu C})}{R_{FeC}}\right) \cdot \frac{d}{dt} \begin{bmatrix} i_{\mu A}(t) \\ i_{\mu B}(t) \\ i_{\mu C}(t) \end{bmatrix} \quad (9)$$

where: $R_{FeA}, R_{FeB}, R_{FeC}$. These are the resistances reproductions of power losses in the iron of a magnetic transformer circuit.

Integrating the matrix Equation (7) in the range from t_n to t_{n+1} , and then dividing by $\Delta t = t_{n+1} - t_n$ and taking into account the formulas (14), (16), (20) and (21) in [31], this equation takes the following form:

$$\boldsymbol{\Lambda} \cdot \mathbf{i}_g(t_{n+1}) + \frac{1}{\Delta t} \cdot \mathbf{G} \cdot \mathbf{c}v + \boldsymbol{\Pi} - \frac{1}{\Delta t} \cdot \begin{bmatrix} L_{\mu s}(i_\mu(t_{n+1})) \\ n_1^{-1} \cdot L_{\mu s}(i_\mu(t_{n+1})) \\ n_2^{-1} \cdot L_{\mu s}(i_\mu(t_{n+1})) \end{bmatrix} \cdot \mathbf{i}_\mu(t_{n+1}) = \mathbf{0}, \quad (10)$$

where:

$$\boldsymbol{\Lambda} = \text{diag}\left(-\left(\frac{R_A}{m+1} + \frac{L_{\sigma A}}{\Delta t}\right), -\left(\frac{R_B}{m+1} + \frac{L_{\sigma B}}{\Delta t}\right), -\left(\frac{R_C}{m+1} + \frac{L_{\sigma C}}{\Delta t}\right), -\left(\frac{R_{a1}}{m+1} + \frac{L_{\sigma a1}}{\Delta t}\right), -\left(\frac{R_{b1}}{m+1} + \frac{L_{\sigma b1}}{\Delta t}\right), -\left(\frac{R_{c1}}{m+1} + \frac{L_{\sigma c1}}{\Delta t}\right), -\left(\frac{R_{a2}}{m+1} + \frac{L_{\sigma a2}}{\Delta t}\right), -\left(\frac{R_{b2}}{m+1} + \frac{L_{\sigma b2}}{\Delta t}\right), -\left(\frac{R_{c2}}{m+1} + \frac{L_{\sigma c2}}{\Delta t}\right)\right),$$

m is the number of terms included in the Taylor series in the mathematical description of branch currents [31],

$$\boldsymbol{\Pi} = -\frac{m}{m+1} \cdot \mathbf{R} \cdot \mathbf{i}_g(t_n) - \sum_{k=1}^{m-1} \left(\frac{\Delta t^k \cdot (m-k)}{(k+1)! \cdot (m+1)} \cdot \mathbf{R} \cdot \mathbf{i}_g^{(k)}(t_n)\right) + \frac{L_\sigma}{\Delta t} \cdot \mathbf{i}_g(t_n) + \frac{1}{\Delta t} \cdot \begin{bmatrix} L_{\mu s}(i_\mu(t_n)) \\ n_1^{-1} \cdot L_{\mu s}(i_\mu(t_n)) \\ n_2^{-1} \cdot L_{\mu s}(i_\mu(t_n)) \end{bmatrix} \cdot \mathbf{i}_\mu(t_n).$$

By making the appropriate mathematical transformations of the above relationships, you can write the formulas for the matrix \mathbf{A}_{Tr} and \mathbf{B}_{Tr} , that occur in the key form for the applied method of mathematical modeling of the external matrix equation of the analyzed transformer [31]:

$$\mathbf{i}_{Tr} + \mathbf{A}_{Tr} \cdot \mathbf{c}v_{Tr} + \mathbf{B}_{Tr} = \mathbf{0}. \quad (11)$$

These matrices have the following forms:

$$A_{Tr} = \begin{bmatrix} G_{Tr} \\ -G_{Tr} \end{bmatrix} \tag{12}$$

and

$$B_{Tr} = \begin{bmatrix} \Pi_{Tr} \\ -\Pi_{Tr} \end{bmatrix}, \tag{13}$$

where:

$$G_{Tr} = (\Lambda + Y(t_{n+1}) \cdot \Xi_{\mu}^{-1}(t_{n+1}) \cdot \Theta_5)^{-1} \cdot \frac{1}{\Delta t} \cdot G, \quad Y(t_{n+1}) = \frac{1}{\Delta t} \cdot \begin{bmatrix} L_{\mu S}(i_{\mu}(t_{n+1})) \\ \Pi_1^{-1} \cdot L_{\mu S}(i_{\mu}(t_{n+1})) \\ \Pi_2^{-1} \cdot L_{\mu S}(i_{\mu}(t_{n+1})) \end{bmatrix},$$

$$\Xi_{\mu}(t_{n+1}) = \begin{bmatrix} \xi_A & -R_{\mu 0} \cdot L_{\mu S B}(i_{\mu B}(t_{n+1})) & -R_{\mu 0} \cdot L_{\mu S C}(i_{\mu C}(t_{n+1})) \\ -R_{\mu 0} \cdot L_{\mu S A}(i_{\mu A}(t_{n+1})) & \xi_B & -R_{\mu 0} \cdot L_{\mu S C}(i_{\mu C}(t_{n+1})) \\ -R_{\mu 0} \cdot L_{\mu S A}(i_{\mu A}(t_{n+1})) & -R_{\mu 0} \cdot L_{\mu S B}(i_{\mu B}(t_{n+1})) & \xi_C \end{bmatrix},$$

$$\xi_j = -\frac{(m+1) \cdot L_{\mu S j}(i_{\mu j}(t_{n+1}))}{R_{Fej} \cdot \Delta t} - 1 - R_{\mu 0} \cdot L_{\mu S j}(i_{\mu j}(t_{n+1})), \text{ where } j = A, B, C;$$

$$\Theta_5 = [\theta_1 \quad \theta_2 \quad \theta_3],$$

$$\Pi_{Tr} = (\Lambda + Y(t_{n+1}) \cdot \Xi_{\mu}^{-1}(t_{n+1}) \cdot \Theta_5)^{-1} \cdot (\Pi(t_n) + Y(t_{n+1}) \cdot \Xi_{\mu}^{-1}(t_{n+1}) \cdot \Xi),$$

$$\Xi = \begin{bmatrix} m \cdot i_{FeA}(t_n) + \sum_{k=1}^{m-1} \left(\frac{\Delta t^{k \cdot (m-k)}}{(k+1)!} \cdot i_{FeA}^{(k)}(t_n) \right) + \frac{(m+1) \cdot L_{\mu S A}(i_{\mu A}(t_n))}{R_{FeA} \cdot \Delta t} \cdot i_{\mu A}(t_n) \\ m \cdot i_{FeB}(t_n) + \sum_{k=1}^{m-1} \left(\frac{\Delta t^{k \cdot (m-k)}}{(k+1)!} \cdot i_{FeB}^{(k)}(t_n) \right) + \frac{(m+1) \cdot L_{\mu S B}(i_{\mu B}(t_n))}{R_{FeB} \cdot \Delta t} \cdot i_{\mu B}(t_n) \\ m \cdot i_{FeC}(t_n) + \sum_{k=1}^{m-1} \left(\frac{\Delta t^{k \cdot (m-k)}}{(k+1)!} \cdot i_{FeC}^{(k)}(t_n) \right) + \frac{(m+1) \cdot L_{\mu S C}(i_{\mu C}(t_n))}{R_{FeC} \cdot \Delta t} \cdot i_{\mu C}(t_n) \end{bmatrix},$$

$$i_{Tr}(t_{n+1}) = \begin{bmatrix} i_1(t_{n+1}) & \cdots & i_3(t_{n+1}) & i_7(t_{n+1}) & \cdots & i_9(t_{n+1}) & i_{13}(t_{n+1}) & \cdots & i_{15}(t_{n+1}) \\ i_4(t_{n+1}) & \cdots & i_6(t_{n+1}) & i_{10}(t_{n+1}) & \cdots & i_{12}(t_{n+1}) & i_{16}(t_{n+1}) & \cdots & i_{18}(t_{n+1}) \end{bmatrix}^T,$$

$$c v_{Tr}(t) = \begin{bmatrix} \int_{t_n}^{t_{n+1}} v_1(t) \cdot dt & \int_{t_n}^{t_{n+1}} v_2(t) \cdot dt & \cdots & \int_{t_n}^{t_{n+1}} v_{17}(t) \cdot dt & \int_{t_n}^{t_{n+1}} v_{18}(t) \cdot dt \end{bmatrix}^T.$$

In order not to solve the system of nonlinear equations, the following algorithm of magnetic field inductance induction prediction was applied in each phase for a moment t_{n+1} :

- using the backward Euler method, a matrix of magnetizing currents is determined at the end of the integration step,
- knowing the values of the column matrix of magnetizing currents at the moment t_{n+1} determines the magnetic inductance of the magnetic circuit in each phase.

The principle of conservation of energy in a magnetic field results in the principle of magnetic flux continuity, which states that the products of current and inductance at times t_n and t_{n+1} should be equal. Determination of the magnetization inductance of the ferromagnetic core in each phase at the moment t_{n+1} based on the above method may cause this condition not to be met. Accordingly, based on the work [41,42] in the transformer model, this problem has been approximately solved. The algorithm that takes into account the continuity of the magnetic flux is as follows:

- the matrix of the current flowing through the transformer windings is calculated for the time instant t_{n+1} , using the Equation (11),
- for the magnetization inductance determined from the prediction described above, a matrix of estimated magnetizing currents is calculated in each phase $i_{\mu}^*(t_{n+1})$ using the appropriately transformed upper relationship in the Equation (8),
- the estimated magnetization inductances in each phase are calculated using the formula

$$L_{\mu S j}^*(i_{\mu j}^*(t_{n+1})) = \frac{\psi_{\mu j}(i_{\mu j}^*(t_{n+1}))}{i_{\mu j}^*(t_{n+1})}, \text{ where } j = A, B, C,$$

- the modified values of the magnetizing currents are calculated in each transformer phase in a way that ensures meeting the conditions arising from the fact that the products of current and inductance at times t_n and t_{n+1} are equal,
- values of corrected magnetizing currents and magnetizing inductance in each phase determined for time t_{n+1} are used in the next calculation step.

5. Experimental Studies of Real-Time Simulator Work

5.1. Description of the Experiment

Figure 17 is a schematic diagram of an experimental system that consists of a constructed simulator working in real time with a model of a wind power network, an external real system as an information source, e.g., about the current value of wind speed and a professional analyzer of the network parameters (PQ-Box 100). This section presents selected results of experiments that were the subject of research in the framework of a doctoral dissertation [6].

The simulator working with real time was built on the basis of a personal computer with an Intel six-core processor (Intel® Core™ i7 970 type) with a clock frequency of 3.20 GHz with a 32-bit Microsoft Windows operating system. The system bus speed is 1600 MHz. The platform has RAM memory (4.00 GB DDR3).

Communication between the environment and the simulator is bidirectional, using digital and analog signals. Advantech PCI-1712 card was used to introduce signals from the environment (e.g., wind speed, power, voltage, current) into the simulator. It is a multifunctional measuring card that allows the use of 16 analogue inputs and 16 digital inputs or outputs. The card is equipped with one analog-to-digital converter working with a resolution of 12 bits and a maximum sampling frequency of 1 MHz or 1 MS/s, which depends on the number of used analog inputs.

Advantech PCI-1724 card was used to output signals from the simulator to the environment (e.g., to terminals on the input signal strip of real controllers, protections). The card allows to activate 32 output channels. Each channel has a digital-to-analog converter working with a resolution of 14 bits in direct mode. This means that the sampling rate depends on the performance of the digital platform used.

The application implementing the simulation process (mathematical model and communication algorithms) was written using the C++ programming language. The application has been written in such a way that provides real-time simulation. When the application is launched, it receives the highest priority, which allows the application faster access to memory or PCI bus (cards with A/D converter or with D/A converters). Giving the application high priority partly solves the problem of proper allocation of resources between individual tasks and protection of allocated resources. Unfortunately, a fully satisfactory solution cannot be achieved using the Microsoft Windows operating system, because the system does not allow full control over the allocation of resources between individual tasks.

The experiment consisted of uninterrupted operation of the simulator during seven days. During that time, the PQ-Box 100 analyzer was connected at the point of common connection (PCC). To create real conditions for connecting the PQ-Box 100 analyzer to the analog outputs of the simulator, voltage and current amplifiers were turned on. The task of the amplifiers is to ensure the electrical compatibility of the simulator output circuits with the external electrical circuits of the real systems. In this case, the amplifiers at the output reproduce the secondary circuits of current and voltage transformers.

In the analysis of the work of the presented power system, the variability of wind speed values and the load variability of three loads identified in the modeled system were taken into account. Current values of wind speed were transmitted from the real external system, whereas the active and reactive power profiles of the loads were set in the form of appropriate schedules, entered into the simulator's memory.

In addition, random event simulation scenarios were prepared, which are listed in Table 3. These events were initiated in a mathematical model of the simulated system

during the experiment. The quantum of the simulator operation time during the experiment was 200 μ s.

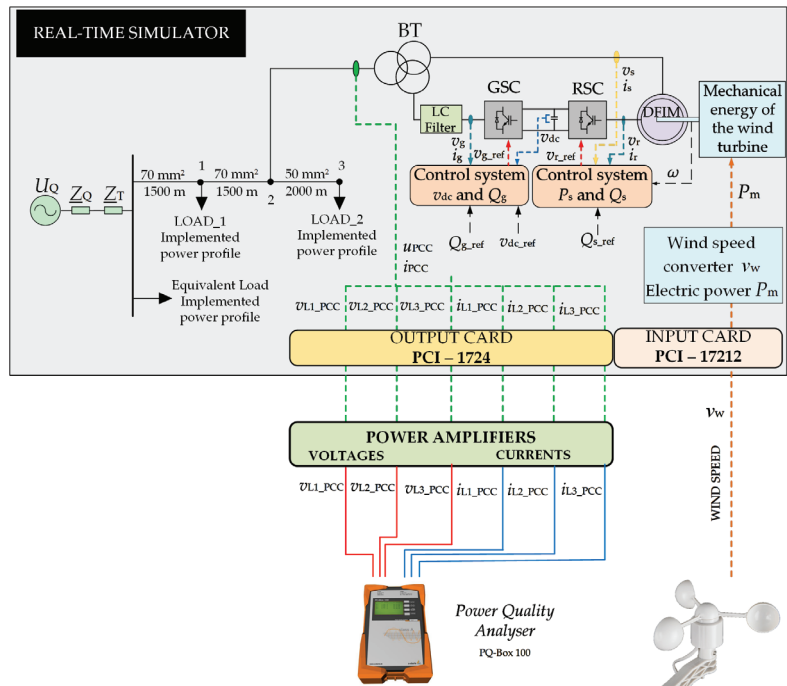


Figure 17. Diagram of the experimental system.

The purpose of experimental research was to verify the work stability of the developed real-time simulator, taking into account the processes caused by the normal operation of system components and including processes initiated by emergency events. The goal was also to check the interaction with the environment and timeliness (verification whether the simulator works with a fixed quantum of operation time).

Table 3. Schedule of random events of the power system operation.

Event Number	Date and Time of the Event	Duration of the Event	Description
1	17.10.2018, 1 ⁰⁰ p.m.	0.2 s	Short-circuit between L2 and L3 phases in LOAD_2
2	18.10.2018, 10 ⁰⁰ a.m.	1.0 s	Reduction of the supply voltage amplitude in the L1 phase (up to 60% of the output voltage)
3	19.10.2018, 8 ⁰⁰ a.m.	0.2 s	Short-circuit between L1 and L2 phases in LOAD_1
4	19.10.2018, 2 ⁰⁰ p.m.	0.15 s	Ground fault in the medium voltage line in phase L1. It occurred at the connection point of the wind turbine to the power grid
5	20.10.2018, 8 ⁰⁰ p.m.	0.15 s	Ground fault in the medium voltage line in phase L1. It occurred at the connection point of LOAD_2 to the power grid
6	21.10.2018, 7 ⁰⁰ p.m.	1.0 s	Reduction of the supply voltage amplitude in all three phases (up to 80% of the output voltage)

5.2. Test Results

After the experiment was completed, results were obtained that enable the analysis of the simulator’s work. First, the voltage frequency at the measuring point was analyzed during the experiment. The voltage frequency changes are shown in Figure 18. The average

frequency value recorded by the network parameter analyzer is 50.0003 Hz. The recorded voltage frequency values and the average value are proof that the developed simulator is stable throughout the experiment and that the quantum of the simulator's operation time has been correctly selected. If the quantum of the simulator's operation time was incorrect (if it was too long, the simulator could not keep up with the calculations), as a result of the simulator's operation, deviations from the value of 50 Hz would be recorded. A similar result would be obtained in the case of stability of the simulation. If there were any problems with stability, then the voltage frequency deviations from 50 Hz would also be recorded.

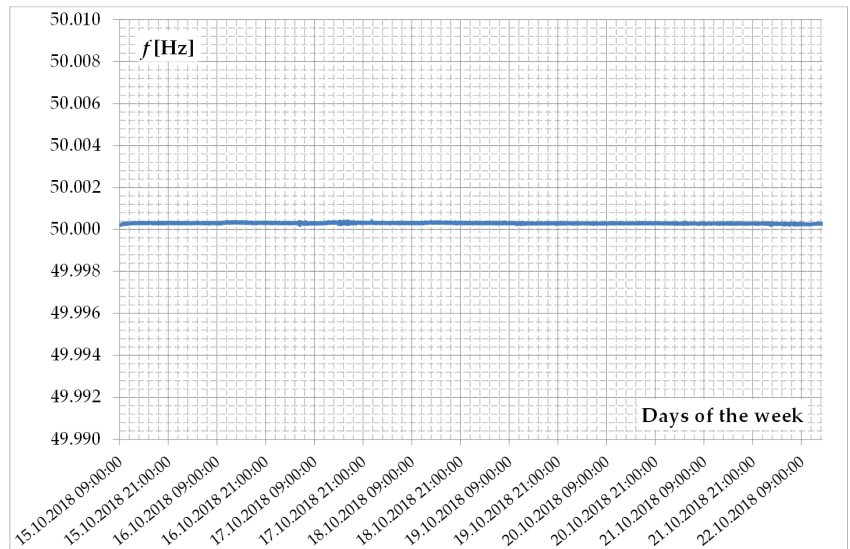


Figure 18. Frequency waveforms of the supply voltage during the experiment.

The course of effective values of phase-to-phase voltages in PCC is shown in Figure 19. When analyzing the course, it can be observed that changes in voltage values are caused by changing loads of three distinguished loads (active and reactive power profiles), changes resulting from changing wind speed (wind turbine operation) and changes caused by random events. Analyzing in detail the obtained waveforms and events recorded by the analyzer, it is possible to distinguish characteristic operating states, which are marked in Figure 19 by appropriate rectangles (red). The event numbers used in this figure correspond to the numbering used in Table 3.

Figure 20 shows the phase-to-phase voltage variability (L1-L2) at the connection point of the generating unit to the network, registered on 18 October 2018, taking into account the variability of active load power in the analyzed MV distribution network and changes in wind speed. Analyzing these waveforms, three characteristic states can be distinguished. The first of them lasts from 0⁰⁰ to 6⁰⁰ hours. During this period, the load works with relatively low power, while the wind turbine works with the rated power, because the wind speed exceeds 14 m/s. Thus, the voltage variation in the network is caused by changing values of load power, but to a relatively small extent.

The second state lasts from 6⁰⁰ to 18⁰⁰ hours. During this period, the wind speed still exceeds the value of 14 m/s, which means that the wind turbine still works at a rated power. However, at around 6⁰⁰ a.m., there was a clear increase in load power, which causes a decrease in the voltage value, which the analyzer registered. Further analyzing the voltage waveform during this period, it can be seen that at approximately 10⁰⁰ a.m., there was a short-term voltage reduction to approximately 15.75 kV. This is due to the decrease in the supply voltage amplitude in phase L1 planned in the scenario (Table 3) (Event no. 2).

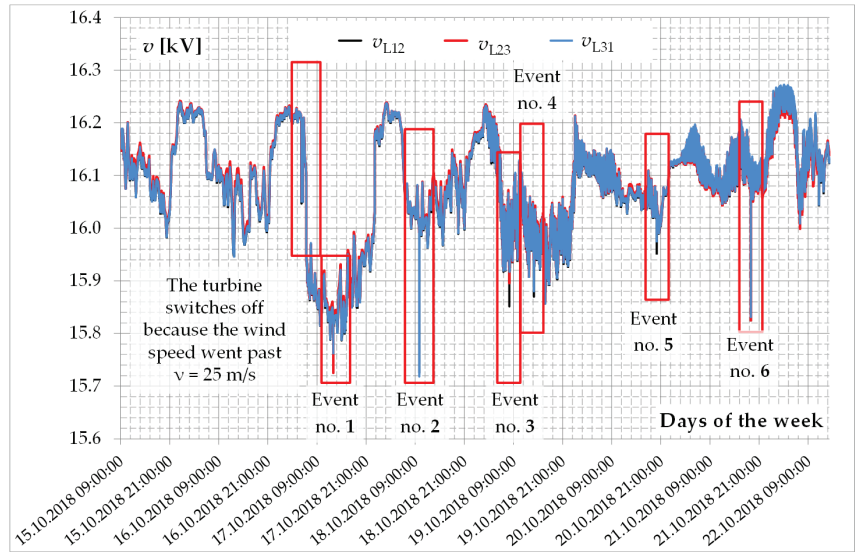


Figure 19. Waveforms of the effective value of phase-to-phase voltage in PCC during the experiment.

The third characteristic condition lasts from 6⁰⁰ p.m. to midnight. At this time, characteristic fluctuations of the RMS voltage value in PCC can be observed, which are caused by both load variability and wind turbine power variability, due to the fact that at wind speeds below 14 m/s, the turbine power varies according to its characteristics (Vestas V90). The slow voltage fluctuations, which are caused by the change in load power in the network, are superimposed by fast voltage fluctuations caused by the wind turbine.

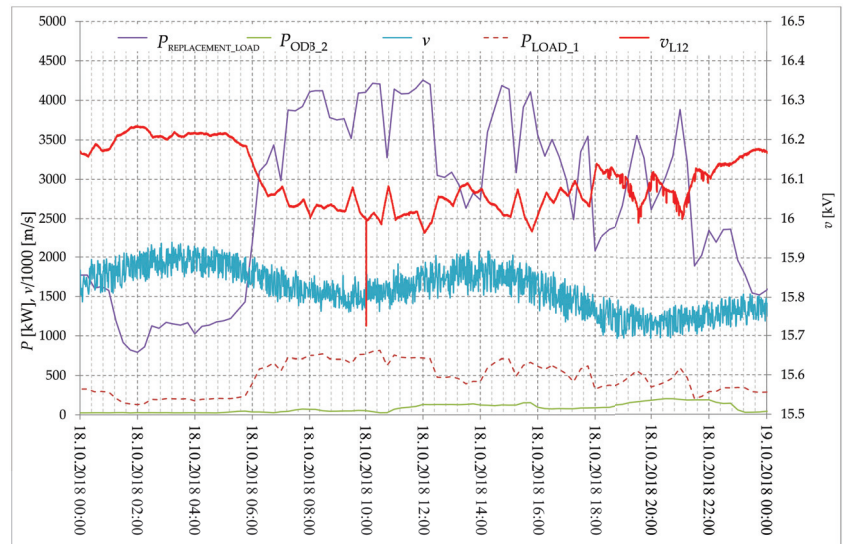


Figure 20. Waveforms of variation of the effective value of phase-to-phase voltage (L1-L2) in PCC from 18 October 2018, including active load power profiles and wind speed profile.

In further analysis, selected fragments of current waveforms and power generated by the wind turbine for MV distribution network (shown in Figures 21 and 22, respectively) will be considered in detail. From current waveforms, it can be seen that the effective values

of currents do not change when the generating unit is working with a constant power value (wind speed higher than the rated speed for Vestas V90 is 14 m/s). In the periods from 16 October 2018 from midnight and 18 October 2018 from 8⁰⁰ a.m., the wind turbine generate electricity with a nominal power of 1.8 MW.

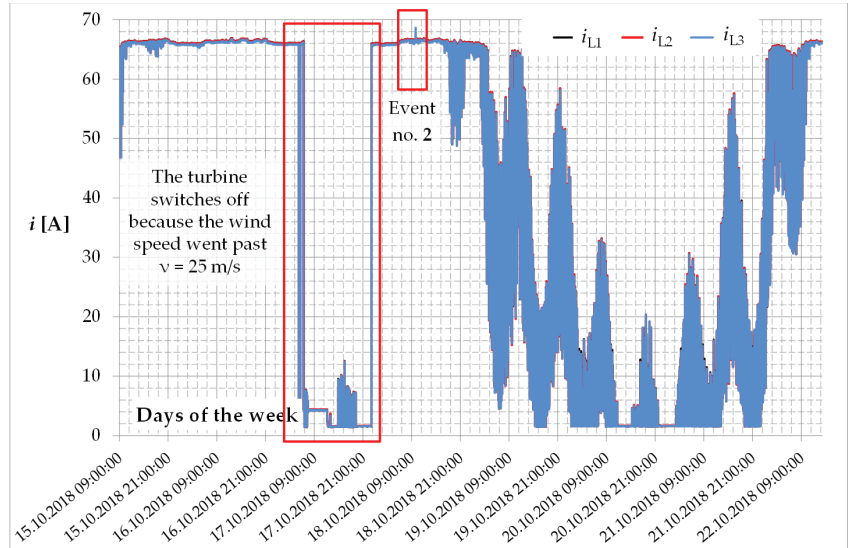


Figure 21. Waveforms of effective currents in PCC during the experiment.

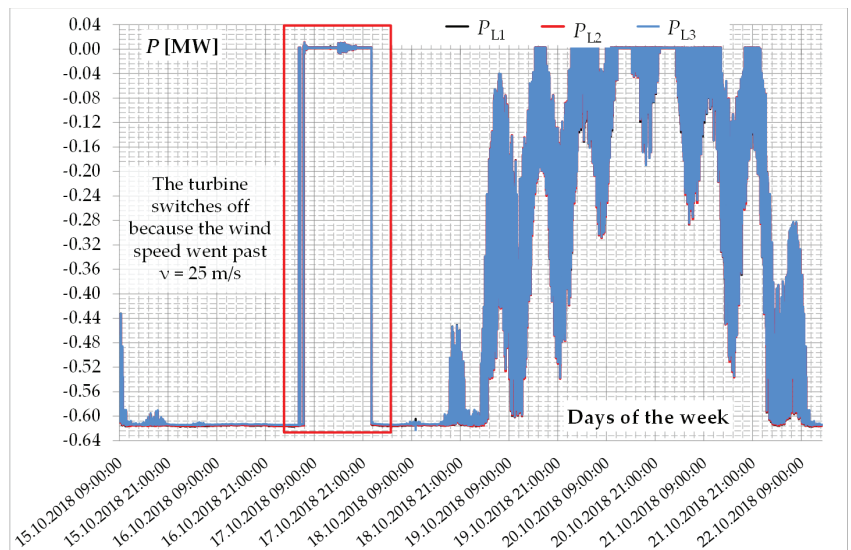


Figure 22. Active power generated by the generating unit during the experiment.

On 17.10.2018, the wind speed exceeded the maximum value for the operation of the wind turbine ($v > 25$ m/s); therefore, it was turned off. Of course, the value of active power decreased from 1.8 MW to 0 MW (Figure 22), and the effective current value decreased from 66.0 A to 4.0 A (Figure 21). Such changes have a large impact on the voltage value at the node connecting the generating unit to the network (PCC) (Figure 19), as mentioned earlier.

Figures 23 and 24 present waveforms of instantaneous voltages and currents recorded by the PQ-Box during a phase-to-phase short circuit. Figure 23 shows the phase-to-phase voltage waveforms at the generating unit connection node, while Figure 24 shows the waveforms of the block transformer line currents during the phase-to-phase short-circuit (between phases L1 and L2) in acceptance 1 (LOAD_1). The occurrence of a phase-to-phase short circuit in LOAD_1 caused an increase in the wire current in the MV windings of transforme of the generating unit in the L1 and L2 phases. Due to the relatively short fault time, the drawings show the waveforms that characterize the entire process.

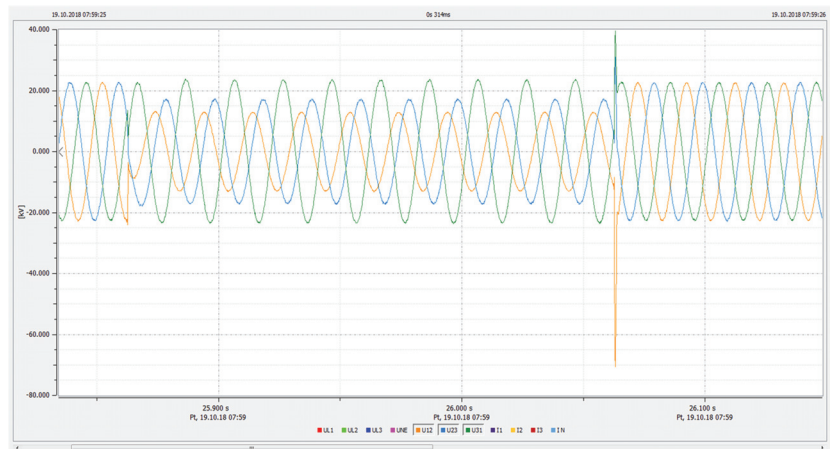


Figure 23. Waveforms of instantaneous phase-to-phase voltages values in PCC at the time of an interphase short-circuit in LOAD_1 (short-circuit between phases L1 and L2).

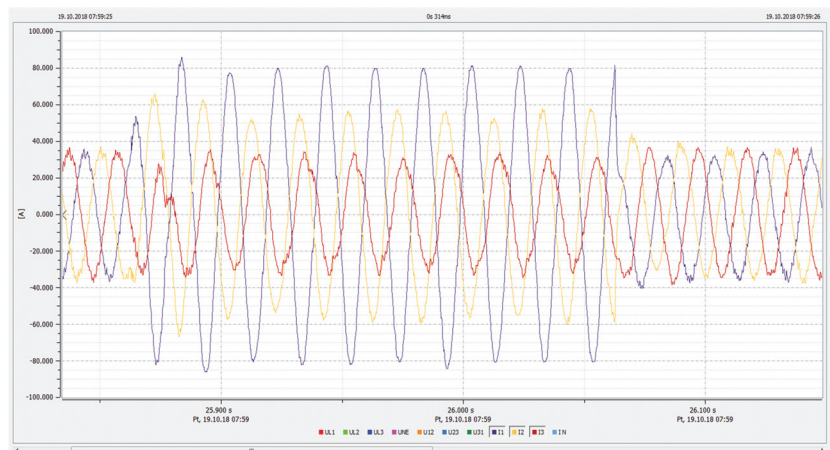


Figure 24. Waveforms of instantaneous values of the line currents of the generating unit's block transformer at the moment of an inte-phase short-circuit in LOAD_1 (short-circuit between phases L1 and L2).

Figure 25 shows the time history of phase-to-phase voltages in PCC and the wire currents of the wind turbine transformer on the MV side during normal operation (steady state). The generating unit works with rated power. The phase shift between phase-to-phase voltage and current is approximately $5/6\pi$. The asynchronous ring machine works as a generator. Analyzing the course, it can be observed that the quantum of the simulator

operation time was correctly selected. This is evidenced by the fact that the frequency of the presented signal is equal to 50 Hz.

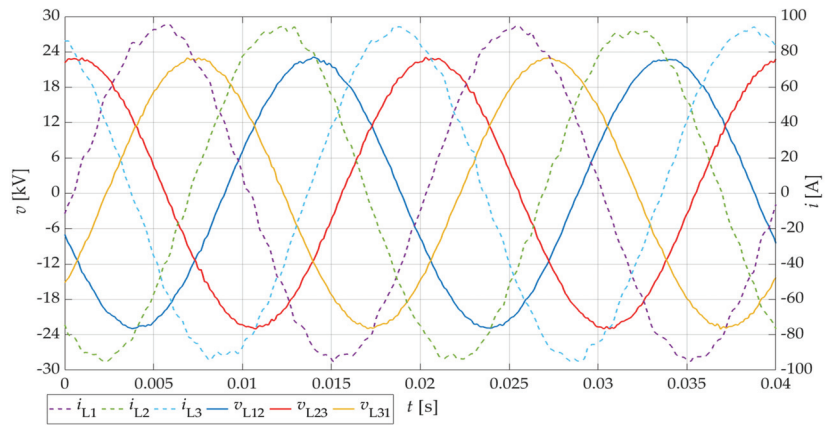


Figure 25. Waveforms of instantaneous values of line voltages and currents of a block transformer of a generating unit for normal operation (steady state, the generating unit worked with the rated power).

Finally, the option of automatically generating a report on the assessment of voltage (electricity) quality at the connection point of the generating unit to the MV distribution network was used, in accordance with the requirements of the PN-EN-50160 standard. This report is presented graphically in Figure 26. The horizontal line corresponds to the limit values for each parameter. Red bars are the parameter values that are not exceeded for 95% of the measurement time; dark blue bars are the maximum value from the set of values averaged during the measurement period. Analyzing the presented results, it can be stated that the quality parameters of electricity in accordance with the standard are met in the node connecting the generating unit to the MV network.

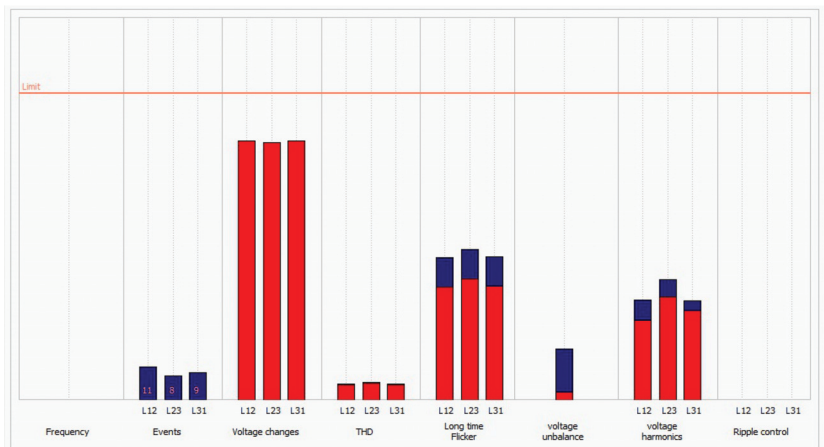


Figure 26. Final report on the assessment of voltage quality in PCC in accordance with PN-EN 50160.

6. Conclusions

The area of broadly understood real-time simulation is currently not fully developed. In the last few years, many good books and publications on this topic have been written. Limiting the applied methods of algebraizing differential equations in real-time simulators to only two (backward Euler and trapezoidal rule), introduced to real-time simulation at

the end of the last century, resulted in a tendency to reduce the integration step in order to maintain an appropriate level of accuracy of simulation results. This was considered the only right path in the development of real-time simulation, arguing that a standard personal computer is no longer sufficient for these applications. Work was developed towards the application of DSP, programmable logic circuits and graphics processors. In this regard, many researchers have obtained great results.

However, one should pay attention to the fact that in the future, the power industry will focus on managing local parts of the power systems [43]. From this, the following conclusions should be drawn:

- the demand for real-time simulators will increase, covering areas limited only to a part of the power system, i.e., MV power distribution networks or even only to single (or several) power lines,
- competitive solutions will be sought in terms of costs, both investment and operating costs,
- solutions that are uncomplicated in terms of installation and operation will be sought.

This leads to the conclusion that real-time simulators based on personal computers are going to be of great interest. This article and other work carried out at the Institute of Electrical Engineering UTP University of Science and Technology in Bydgoszcz (Poland) that are intended to meet the future expectations of conscious electricity users.

This article shows that:

- the use of the new AVIS method of algebraizing differential equations, which is based on average voltages in the integration step, allows real-time simulation with a large integration step of 0.2 ms in period of one week while maintaining appropriate accuracy of results,
- the comparison of frequency responses in the RL system with three methods (the known backward Euler and trapezoidal methods and the new AVIS method) in a wide frequency range up to the Nyquist frequency $\frac{1}{2T_s} = 0,5$ per unit showed that the AVIS method practically does not introduce magnitude or phase error, which is an advantage of this method over two others that are recommended by other authors,
- the effectiveness of the AVIS method allows for a “return” to real-time simulators based on personal computers,
- the use of the AVIS method for real-time simulation with integration step of 0.2 ms of a relatively complex power system (network fragment, three-winding transformer, double-powered induction machine and control system), implemented in the classic PC with classic operating system, allows for stable real-time simulations in a relatively long time (continuously for seven days), taking into account changes and events inside and outside the simulator.

It can also be stated that the real-time simulator solution proposed in this article, based on a personal computer with a classic operating system, may be a competitive solution to well-known commercial proposals. The advantage of this solution is definitely lower cost. In addition to the advantages, there are also some disadvantages. Globally, the disadvantage may be the limited size of the modeled power system. However, in the context of the above-mentioned efforts to manage the operation of local area fragments of power systems, this limitation is not necessarily a disadvantage. The disadvantage is the limitation of the possibility of reproducing physical processes and phenomena occurring inside power electronic converters. However, as shown in this article, in the analysis of power networks, this should not be a problem (unless we are interested in the processes inside the converter), because appropriate filters must be used anyway due to the quality of electricity.

Author Contributions: Conceptualization, Z.K. and S.C.; methodology, Z.K.; software, Z.K.; validation, Z.K. and S.C.; formal analysis, Z.K. and S.C.; investigation, Z.K. and S.C.; resources, Z.K.; data curation, Z.K.; writing—original draft preparation, Z.K.; writing—review and editing, S.C. All authors have read and agreed to the published version of the manuscript.

Funding: This research received no external funding.

Institutional Review Board Statement: Not applicable.

Informed Consent Statement: Not applicable.

Data Availability Statement: Not applicable.

Conflicts of Interest: The authors declare no conflict of interest.

Abbreviations

The following abbreviations are used in this manuscript:

AVIS Average Voltages in the Integration Step

References

1. Uriarte, F.M. *Multicore Simulation of Power System Transients*; The Institution of Engineering and Technology: London, UK, 2013.
2. Popovici, K.; Mosterman, P.J. *Real-Time Simulation Technologies. Principles, Methodologies and Applications*; CRC Press Taylor & Francis Group: Boca Raton, FL, USA, 2013.
3. Laplante, P.A. *Real-Time Systems Design and Analysis*, 3rd ed.; IEEE Press, Wiley-Interscience: New York, NY, USA, 2004.
4. Mughal, A.M. *Real Time Modeling, Simulation and Control of Dynamical Systems*; Springer International Publishing: Switzerland, Cham, 2016.
5. Bayoumi, M. An FPGA-Based Real-Time Simulator for the Analysis of Electromagnetic Transients in Electrical Power Systems. Ph.D. Thesis, Department of Electrical and Computer Engineering, University of Toronto, Toronto, ON, Canada, 2009.
6. Klosowski, Z. Real-Time Simulation of Electric Power Network with Wind Turbine. Ph.D. Thesis, Faculty of Electrical and Control Engineering, Gdańsk University of Technology, Gdansk, Poland, 2019. (In Polish)
7. Fajfer, M. Parallel computing in the simulation of the electric circuit with the use of DSP. Ph.D. Thesis, Faculty of Electrical Engineering, Poznań University of Technology, Poznan, Poland, 2019. (In Polish)
8. Adegbohun, F.R.; Lee, K.Y. Real-time modeling, simulation and analysis of a grid connected PV system with hardware-in-loop protection. In Proceedings of the North American Power Symposium (NAPS), Morgantown, WV, USA, 17–19 September 2017.
9. Kang, C.; Feng, X.; Yongjie, F.; Yuehai, Y. Comparative simulation of dynamic characteristics of Wind Turbine Doubly-Fed Induction Generator based on RTDS and MATLAB. In Proceedings of the International Conference on Power System Technology, Hangzhou, China, 24–28 October 2010.
10. Ofoli, A.R.; Altimania, M.R. Real-time digital simulator testbed using eMEGASim for wind power plants. In Proceedings of the 2017 IEEE Industry Applications Society Annual Meeting, Cincinnati, OH, USA, 1–5 October 2017.
11. Achary, S.B.; Mishra, S.; Kumar, A. Real time hardware in loop testing of single phase grid connected PV system. In Proceedings of the 2014 Eighteenth National Power Systems Conference (NPSC), Guwahati, India, 18–20 December 2014.
12. Dufour, C.; Abourida, S.; Belanger, J. InfiniBand-Based Real-Time Simulation of HVDC, STATCOM and SVC Devices with Custom-Of-The-Shelf PCs and FPGAs. In Proceedings of the 2006 IEEE International Symposium on Industrial Electronics, Montreal, QC, Canada, 9–13 July 2006.
13. Derouich, A.; Lagrioui, A. Real-Time Simulation and analysis of the Induction machine performances operating at flux constant. *Int. J. Adv. Comput. Sci. Appl.* **2014**, *5*. [[CrossRef](#)]
14. Umashankar, S.; Bhalekar, M.; Chandra, S.; Vijayakumar, D.; Kothari, D.P. DSP Based Real Time implementation of AC-DC-AC converter Using SPWM Technique. *Int. J. Electron. Commun. Electr. Eng.* **2013**, *3*, 96–113.
15. Fajfer, M. Medium voltage electrical system research using DSP-based real-time simulator. *Comput. Appl. Electr. Eng.* **2014**, *12*, 334–352.
16. Tarakanath, K.; Agarwal, V.; Yadav, P. Hardware in the loop simulation of direct synthesis based two degree of freedom PID control of DC-DC boost converter using Real Time Digital Simulation in FPGA. In Proceedings of the 2014 IEEE International Conference on Power Electronics, Drives and Energy Systems (PEDES), Mumbai, India, 16–19 December 2014.
17. Li, P.; Wang, Z.; Wang, C.; Fu, X.; Yu, H.; Wang, L. Synchronisation mechanism and interfaces design of multi-FPGA-based real-time simulator for microgrids. *IET Gener. Transm. Distrib.* **2017**, *11*. [[CrossRef](#)]
18. Estrada, L.; Vázquez, N.; Vaquero, J.; de Castro, Á.; Arau, J. Real-Time Hardware in the Loop Simulation Methodology for Power Converters Using LabVIEW FPGA. *Energies* **2020**, *13*, 373. [[CrossRef](#)]
19. Smolarczyk, A.; Kowalik, R.; Bartosiewicz, E.; Rasolomampionona, D. A simple real-time simulator for protection devices testing. In Proceedings of the 2014 IEEE International Energy Conference (ENERGYCON), Cavtat, Croatia, 13–16 May 2014.
20. Klosowski, Z. The analysis of the possible use of wind turbines for voltage stabilization in the power node of MV line with the use of a real-time simulator. *Przegląd Elektrotechniczny* **2015**, *1*, 20–27. (In Polish)
21. Cieślík, S. A PC-based real-time computer simulator of electric power system cooperated with real excitation system. In Proceedings of the XIX Symposium Electromagnetic Phenomena in Nonlinear Circuits, Maribor, Slovenia, 28–30 June 2006.

22. Plachytyna, O.; Kutsyk, A. A hybrid model of the electrical power generation system. In Proceedings of the 2016 10th International Conference on Compatibility, Power Electronics and Power Engineering (CPE-POWERENG), Bydgoszcz, Poland, 29 June–1 July 2016.
23. Espinoza, R.G.F.; Molina, Y.; Tavares, M. PC Implementation of a Real-Time Simulator Using ATP Foreign Models and a Sound Card. *Energies* **2018**, *11*, 2140. [[CrossRef](#)]
24. Klosowski, Z.; Cieřlik, S. Stability Analysis of Real-Time Simulation of a Power Transformer's Operating Conditions. *Acta Energetica* **2018**, *2*, 31–38.
25. Watson, N.R.; Arrillaga, J. *Power Systems Electromagnetic Transients Simulation*; Series 39; IET Power and Energy: UK, London, 2007.
26. Martinez-Velasco, J.A. *Transient Analysis of Power Systems: Solution Techniques, Tools and Applications*; IEEE Press Wiley: Chichester, UK, 2015.
27. Dommel, H.W. *Electromagnetic Transients Program Theory Book*; Bonneville Power Administration: Portland, OR, USA, 1995.
28. Marti, J.R.; Lin, J. Suppression of Numerical Oscillations in the EMTP. *IEEE Trans. Power Syst.* **1989**, *2*, 739–747. [[CrossRef](#)]
29. Araujo, A.E. Numerical Instabilities in Power System Transient Simulation. Ph.D. Thesis, Faculty of Graduate Studies Electrical Engineering, University of British Columbia, Vancouver, BC, Canada, 1993.
30. Plakhtyna, O. Numerical One-Step Method of Electric Circuits Analysis and Its Application in Electromechanical Tasks. *Sci. J. Khar'kov Tech. Univ.* **2008**, *30*, 223–225. (In Ukrainian)
31. Klosowski, Z.; Cieřlik, S. Real-Time Simulation of Power Conversion in Doubly Fed Induction Machine. *Energies* **2020**, *13*, 673. [[CrossRef](#)]
32. Klosowski, Z.; Plakhtyna, O.; Grugel, P. Applying the method of average voltage on the integration step length for the analysis of electrical circuits. *Zesz. Nauk. Elektrotechnika* **2014**, *17*, 17–31.
33. Plakhtyna, O.; Kutsyk, A.; Semeniuk, M.; Kuznyetsov, O. Object-oriented program environment for electromechanical systems analysis based on the method of average voltages on integration step. In Proceedings of the 2017 18th International Conference on Computational Problems of Electrical Engineering (CPEE), Kutna Hora, Czech Republic, 11–13 September 2017.
34. Plachytyna, O.; Bastian, B.; Kutsyk, A. Real time computer tester for automatic voltage regulators used in marine generators. *Ponzań Univ. Technol. Acad. J. Electr. Eng.* **2016**, *85*, 465–476.
35. Plachytyna, O.; Klosowski, Z.; Żarnowski, R. Mathematical model of DC drive based on a step-averaged voltage numerical method. *Przegląd Elektrotechniczny* **2011**, *87*, 51–56. (In Polish)
36. Plakhtyna, O.; Kutsyk, A.; Semeniuk, M. Real-Time Models of Electromechanical Power Systems, Based on the Method of Average Voltages in Integration Step and Their Computer Application. *Energies* **2020**, *13*, 2263. [[CrossRef](#)]
37. Plakhtyna, O.; Kutsyk, A.; Semeniuk, M. An analysis of fault modes in an electrical power-generation system on a real-time simulator with a real automatic excitation controller of a synchronous generator *Elektrotehniski Vestnik/Electrotech. Rev.* **2019**, *86*, 104–109.
38. Liu, J.; Wei, T.; Liu, J.; Wei, Z.; Hou, J.; Xiang, Z. Suppression of numerical oscillations in power system electromagnetic transient simulation via 2S-DIRK method. In Proceedings of the 2016 IEEE PES Asia-Pacific Power and Energy Engineering Conference (APPEEC), Xi'an, China, 25–28 October 2016; pp. 465–476.
39. Qiao, W. Dynamic modeling and control of double fed induction generators driven by wind turbines. In Proceedings of the IEEE/PES Power Systems Conference and Exposition, Seattle, WA, USA, 20 March 2009.
40. Wu, G.; Lee, K.Y.; Young, W. Modeling and control of power conditioning system for grid-connected fuel cell power plant. In Proceedings of the 2013 IEEE Power & Energy Society General Meeting, Vancouver, BC, Canada, 22–26 July 2013.
41. Ponick, B. Über den Einfluß der Hauptfeldsättigung auf Ausgleichsvorgänge elektrischer Antriebe und eine einfache Methode zu ihrer Berücksichtigung. *Archiv für Elektrotechnik* **1993**, *76*, 369–376. [[CrossRef](#)]
42. Ronkowski, M. *Circuits-Oriented Models of Electrical Machines for Simulation of Converter Systems*; Gdansk University of Technology: Gdansk, Poland, 1995.
43. Przychodzień, A. Virtual Power Plants—Types and Development Opportunities. *Rynek Energii* **2020**, *5*, 68–74. [[CrossRef](#)]

Low Frequency Damping Control for Power Electronics-Based AC Grid Using Inverters with Built-In PSS

Ming Yang¹, Wu Cao^{1,*}, Tingjun Lin¹, Jianfeng Zhao¹ and Wei Li²

- ¹ School of Electrical Engineering, Southeast University, Nanjing 210096, China; mingyang_ee@seu.edu.cn (M.Y.); 220192720@seu.edu.cn (T.L.); jianfeng_zhao@seu.edu.cn (J.Z.)
² NARI Group Corporation (State Grid Electric Power Research Institute), Nanjing 211106, China; liwei10@sgepri.sgcc.com.cn
* Correspondence: caowu_ee@seu.edu.cn

Abstract: Low frequency oscillations are the most easily occurring dynamic stability problem in the power system. With the increasing capacity of power electronic equipment, the coupling coordination of a synchronous generator and inverter in a low frequency range is worth to be studied further. This paper analyzes the mechanism of the interaction between a normal active/reactive power control grid-connected inverters and power regulation of a synchronous generator. Based on the mechanism, the power system stabilizer built in the inverter is used to increase damping in low frequency range. The small-signal model for electromagnetic torque interaction between the grid-connected inverters and the generator is analyzed first. The small-signal model is the basis for the inverters to provide damping with specific amplitude and phase. The additional damping torque control of the inverters is realized through a built-in power system stabilizer. The fundamentals and the structure of a built-in power system stabilizer are illustrated. The built-in power system stabilizer can be realized through the active or reactive power control loop. The parameter design method is also proposed. With the proposed model and suppression method, the inverters can provide a certain damping torque to improve system stability. Finally, detailed system damping simulation results of the universal step test verify that the analysis is valid and effective.

Keywords: low frequency damping; grid-connected inverter; power system stabilizer; power electronics-based AC power system

Citation: Yang, M.; Cao, W.; Lin, T.; Zhao, J.; Li, W. Low Frequency Damping Control for Power Electronics-Based AC Grid Using Inverters with Built-In PSS. *Energies* **2021**, *14*, 2435. <https://doi.org/10.3390/en14092435>

Academic Editor: Juri Belikov

Received: 22 March 2021
Accepted: 22 April 2021
Published: 24 April 2021

Publisher's Note: MDPI stays neutral with regard to jurisdictional claims in published maps and institutional affiliations.



Copyright: © 2021 by the authors. Licensee MDPI, Basel, Switzerland. This article is an open access article distributed under the terms and conditions of the Creative Commons Attribution (CC BY) license (<https://creativecommons.org/licenses/by/4.0/>).

1. Introduction

The power system has expanded and changed incessantly. There is a trend that conventional power systems are expected to be replaced by next-generation power systems. The grid-connected inverters are the crucial component that delivers renewable energy and energy storage to the grid. The grid-connected inverter should play a more critical role in the power system [1–6]. Due to the negative damping effect of the power system, the phenomenon of low frequency oscillations (LFOs) often occurs on the transmission lines with long distances, heavy loads or weak connections. The typical feature of low frequency oscillation is power swing and low frequency ranging between 0.1 and 2.5 Hz. The power regulation characteristic of inverter is different from that of synchronous generator. In the same power grid, the power regulation of inverters affects the swing characteristics of generator's power angle. Obviously, the research of the influence mechanism of inverter power regulation on generator torque, and the low frequency damping control is important for the system stability.

There have been many studies on the low frequency damping control. The power system stabilizer (PSS) in excitation system is used to generate the damping effect. The PSS suppresses LFOs through controlling electromagnetic torque variation. PSS in excitation system has been proved to be the most cost-effective damping control [7–10]. In power electronics-based AC grid, the proportion of synchronous generator capacity decreases.

The damping torque provided by the excitation system is not enough for LFOs suppression. Some power electronic devices such like unified power flow controller (UPFC), static var compensators (SVC), voltage source converter based high voltage direct current (VSC-HVDC) are researched to suppress the LFOs. The power electronic equipment can increase the system damping to inhibit oscillation [11–14]. References [15–19] analyze the impact of VSC control parameters on power system stability based on small-signal stability analysis. Reference [20] proposes a UPFC-based stabilizer that adopts a conventional PI controller and a lead-lag controller to produce the damping effect. Because of the UPFC covers active and reactive power controls with multiple time scales, the low frequency damping control parameters of UPFC are hard to design for most working condition. References [21,22] research the SVC with a damping controller. The damping control in SVC increases system damping by reactive power control. The influence of SVC's reactive power on generator is limited by distance and area. Reference [23–26] proposes VSC-HVDC damping strategies. These strategies are realized by adding angular velocity close loop control to the basic control of inverter. The damping control and the normal inverter control both regulate the active power. But the purpose of control is different. So, the two kinds of control are easy to affect each other, and the parameters are hard to design. For the situation that the virtual synchronous generator (VSG) control changes the regulation characteristic of inverter, references [27,28] investigates extra damping control in the VSG control. The damping capacity of inverter can not be fully utilized due to the limitation of virtual inertia control.

There are still some improvements as follows in the research of low frequency damping control in power electronic based AC grid.

(1) The capacity proportion of the UPFC and SVC is small in the power system. The damping effect of the UPFC and SVC is limited. The low frequency damping control should focus on the grid-connected inverters which have large proportion.

(2) These stability analyses mainly focus on the inverter itself. The correlation with generators in the power grid has not been considered enough. The influence of grid-connected inverter with normal active/reactive power control on the electromagnetic torque of the synchronous generator has little research. Using the mechanism of the influence to improve the dynamic safety and stability of the power system has not been fully considered.

(3) The different time scales controls are directly superimposed together in the inverters based on existing research. Without the detailed model for the interaction between inverters and generators, the control parameters are hard to set.

To improve the low frequency damping control and LFOs suppression, the main contributions of this paper are as follows:

(1) This paper investigates how grid-connected inverter with normal active/reactive power control influences the electromagnetic torque of the synchronous generator. The small-signal model for the impact of the output of the grid-connected inverter on the electromagnetic torque of the synchronous generator is proposed. The damping torque analysis is used to evaluate the effect of inverter on low frequency damping. The mechanism of grid-connected inverter providing positive damping is found. That can also be suitable for multi grid-connected inverters with same voltage and current control.

(2) The control time scale of the introduced damping control is adapted to the frequency range of LFOs. It is independent of the original fast control of the inverter. The method of introducing electromagnetic damping torque with built-in PSS to increase low frequency damping is proposed. The structure and parameter design method is also proposed. The additional electromagnetic damping control can be realized by the active power control or reactive power control of the inverter. Because of most of the inverters in power system output active power, the built-in PSS realized through the active power control are taken as the object of analysis. That is different from the excitation system's PSS. The difference between traditional PSS in excitation system and the proposed built-in PSS in inverter can be illustrated in Figure 1, where V_{ref} is the terminal voltage control reference value for excitation system, V_t is the terminal voltage value, E_{fd} is the excitation voltage,

P_{ref} is the active power control reference value for inverter, P is the active power actual value, Q_{ref} is the reactive power control reference value for inverter, Q is the reactive power actual value, $G_{i-P}(s)$ is the active power control, $G_{i-Q}(s)$ is the reactive power control, $G(s)$ is the excitation control.

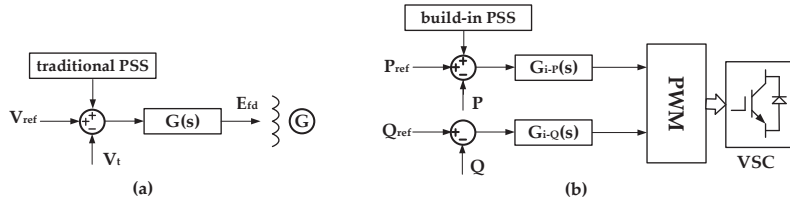


Figure 1. Traditional PSS in excitation system and the proposed built-in PSS in inverter. (a) Traditional PSS in excitation system; (b) the proposed built-in PSS in inverter.

(3) To verify the above analysis, two-part simulation is used. One part is about different damping torques' effect on single grid-connected inverter. The different damping torques are realized by using different parameters. The other part is about the effectiveness of the built-in PSS for dual paralleled grid-connected inverters.

The rest of this paper is organized as follows. Section 2 derives a small-signal model of the impact of the grid-connected inverter on electromagnetic torque of synchronous generator. The influence of inverter output on damping torque is analyzed. Section 3 provides a design for built-in PSS based on the small signal model. Section 4 gives the simulation result. The conclusions of this paper are presented in Section 5.

2. Modeling and Analysis

The study of the generator oscillation process shows that in most cases the generator rotor oscillation is related to the mechanical inertia time constant. The electrical angular velocity ($\Delta\omega$) and electrical acceleration ($\Delta\delta$) are used to describe the oscillations. The mechanical inertia time constant represents lower oscillation frequency and slower attenuation [29]. So, in the study of the process related to rotor oscillation, the fast process can be considered to be over. In the process of modelling, circuit impedance could be calculated under the situation of the rated frequency of power grid.

The electromagnetic torque of synchronous generator is used to increase low frequency damping because of its fast-changing characteristics. The power regulation of the grid-connected inverters affects the electromagnetic torque of synchronous generator. So, the influence of electromagnetic torque caused by inverter power regulation is the first problem to be clarified.

2.1. System Description

Figure 2 depicts the structure of a typical structure of power electronics-based AC power system. The power electronics-based AC power system has synchronous generators and multi inverters. The inverters have a considerable proportion of the transformation and consumption capacity in power grid. The normal control architecture of the inverter controller is shown in Figure 3, where P_{ref} is the d-axis control reference of active power, U_{dcref} is the d-axis control reference of DC voltage, Q_{ref} is the q-axis control reference of reactive power, U_{acref} is the q-axis control reference of AC voltage, i_{2dref} is the d-axis reference current value of inverter, i_{2qref} is the q-axis reference current value of inverter, i_{2d} is the d-axis current value of inverter, i_{2q} is the q-axis current value of inverter, U_{cd} is the d-axis component of system side voltage, U_{cq} is the q-axis component of system side voltage, Δv_d is the d-axis component variation of inverter side voltage, Δv_q is the q-axis component variation of inverter side voltage. $F_o(s)$ is the outer-loop control function of the inverter, $F(s)$ is the inner-loop control function of the inverter.

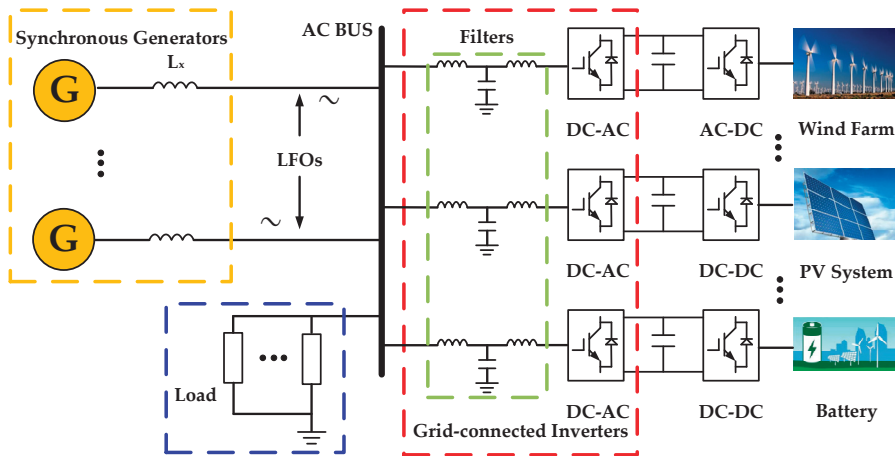


Figure 2. A typical set up of power electronics-based AC power system.

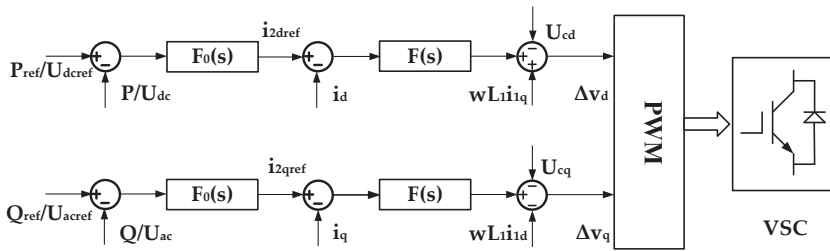


Figure 3. The typical control structure of the inverter.

The multi-inverters shown in Figure 2 can be considered as a controllable voltage source, connecting to the power grid with an LCL filter typically. The multi-generators can be equivalent as a voltage source with characteristics of synchronous generator. Figure 4 is the equivalent two-port network of the system shown in Figure 2, where U is the voltage of the generator, V is the voltage of the inverter, x_s is the contact inductive reactance, x_0 is the inductive reactance of load, r is the resistance of the load, x_1 and x_2 is the inductive reactance of LCL filter for the inverter and y_c is the admittance of LCL filter for the inverter.

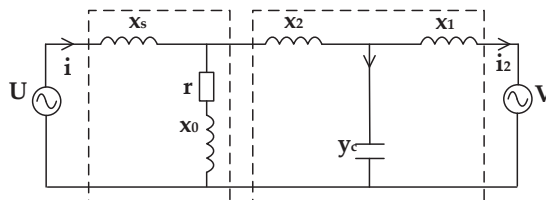


Figure 4. Two-port network for simplified power electronics-based AC power system.

The loop circuit equation of two-port network is shown in the following:

$$\begin{pmatrix} u \\ i \end{pmatrix} = \begin{pmatrix} z_{11}z'_{22} + z_{12}z'_{32} & z_{11}z'_{23} + z_{12}z'_{33} \\ z_{21}z'_{22} + z_{22}z'_{32} & z_{21}z'_{23} + z_{22}z'_{33} \end{pmatrix} \begin{pmatrix} v \\ i_2 \end{pmatrix} \quad (1)$$

where $z_{11}, z_{12}, z_{21}, z_{22}$ and $z'_{22}, z'_{23}, z'_{32}, z'_{33}$ are the impedance of two-port networks 1 and 2, respectively, i and i_2 are the currents of the line connected with the generator and the inverter, respectively.

Then, the current of the generator in dq synchronous frame is got as:

$$\begin{cases} i_d = y_1 u_d + y_2 u_q + y_3 v_d + y_4 v_q \\ i_q = y_5 u_d + y_6 u_q + y_7 v_d + y_8 v_q \end{cases} \quad (2)$$

where $y_1 \sim y_6$ represents the correlation impedance, v_d is the d-axis component of inverter side voltage, v_q is the q-axis component of inverter side voltage, u_d is the d-axis voltage of the generator, u_q is the q-axis voltage of generator.

2.2. System Modeling

Through Equation (2), the small-signal model of generator's current and voltage is derived as shown in Equation (3).

$$\begin{cases} \Delta u_d = x_q \Delta i_q \\ \Delta u_q = \Delta E'_q - x'_d \Delta i_d \\ \Delta i_d = y_1 \Delta u_d + y_2 \Delta u_q + y_3 \Delta v_d + y_4 \Delta v_q \\ \Delta i_q = y_5 \Delta u_d + y_6 \Delta u_q + y_7 \Delta v_d + y_8 \Delta v_q \end{cases} \quad (3)$$

where x'_d is the d-axis transient resistance of the generator, x_q is the q-axis resistance of the generator, i_d is the d-axis current of the generator, i_q is the q-axis current of generator, u_d is the d-axis voltage of the generator, u_q is the q-axis voltage of generator, E_q is the internal potential of the generator, Δ represents the micro change of electrical quantities.

The expression of Δi_d and Δi_q could be derived by eliminating Δu_d and Δu_q and illustrated as Equation (4):

$$\begin{cases} \Delta i_d = Z_1 \Delta E'_q + Z_2 \Delta v_d + Z_3 \Delta v_q \\ \Delta i_q = Z_4 \Delta E'_q + Z_5 \Delta v_d + Z_6 \Delta v_q \end{cases} \quad (4)$$

where $Z_1 \sim Z_6$ are the admittance coefficient which are derived through Equation (3).

A series equation of electromagnetic relation of the generator is shown as the following Equation (5) [7]:

$$\begin{cases} u_d = x_q i_q \\ u_q = E_q - (x_d - x'_d) i_d = E'_q - x'_d i_d \\ M_e = u_d i_d + u_q i_q = E_Q i_q \\ E'_q = E_Q - (x_q - x'_d) i_d \\ \frac{dE'_d}{dt} = \frac{1}{T'_{d0}} (E_{fd} - E_q) \\ u^2 = u_d^2 + u_q^2 \end{cases} \quad (5)$$

where E'_q is a hypothetical potential which is proportional to the flux of excitation system, M_e is the electromagnetic torque of the generator, E_Q is hypothetical potential behind x_q , E_{fd} is the excitation voltage, T'_{d0} is the time constant of the rotor when the stator is open-circuit.

The small-signal model of the generator is derived as:

$$\begin{cases} \Delta M_e = i_{q0} \Delta E'_q + i_{q0} (x_q - x'_d) \Delta i_d + E_{Q0} \Delta i_q \\ (1 + T'_{d0} s) \Delta E'_q = \Delta E_{fd} - (x_q - x'_d) \Delta i_d \\ \Delta u = \frac{u_{d0}}{u_0} x_q \Delta i_q + \frac{u_{q0}}{u_0} (\Delta E'_q - x'_d \Delta i_d) \end{cases} \quad (6)$$

where i_{q0} is the steady-state q-axis current of the generator, u_{d0} is the steady-state d-axis voltage of the generator, u_{q0} is the steady-state q-axis voltage of the generator, u_0 is the steady-state voltage of the generator, E_{Q0} is the hypothetical steady-state potential behind x_q .

The small-signal model of the synchronous generator with inverter’s voltage is derived in Equation (7) by substituting Equation (4) of Δi_d and Δi_q into Equation (6).

$$\begin{cases} \Delta M_e = K_1 \Delta E'_q + K_2 \Delta v_d + K_3 \Delta v_q \\ \Delta E'_q = K_4 \Delta E_{fd} - K_5 \Delta v_d - K_6 \Delta v_q \\ \Delta u = K_7 \Delta E'_q + K_8 \Delta v_d + K_9 \Delta v_q \\ \Delta E_{fd} = G(s) \Delta u \end{cases} \begin{cases} K_1 = i_{q0} + i_{q0}(x_q - x'_d)Z_1 - E_{Q0}Z_4 \\ K_2 = i_{q0}(x_q - x'_d)Z_2 + E_{Q0}Z_5 \\ K_3 = i_{q0}(x_q - x'_d)Z_3 + E_{Q0}Z_6 \end{cases} \quad (7)$$

$$\begin{cases} K_4 = \frac{1}{1 + (x_q - x'_d)Z_1 + T'_{d0}s} \\ K_5 = K_4(x_q - x'_d)Z_2 \\ K_6 = K_4(x_q - x'_d)Z_3 \end{cases} \begin{cases} K_7 = \frac{u_{d0}}{u_0} x_q Z_4 + \frac{u_{q0}}{u_0} - \frac{u_{q0}}{u_0} x'_d Z_1 \\ K_8 = \frac{u_{d0}}{u_0} x_q Z_5 - \frac{u_{q0}}{u_0} x'_d Z_2 \\ K_9 = \frac{u_{d0}}{u_0} x_q Z_6 - \frac{u_{q0}}{u_0} x'_d Z_3 \end{cases}$$

$G(s)$ represents the transfer function of the excitation system.

Consider the inverter control shown in Figure 3, the block diagram of the small-signal control model of the generator-inverter system can be obtained from the above analysis as Figure 5.

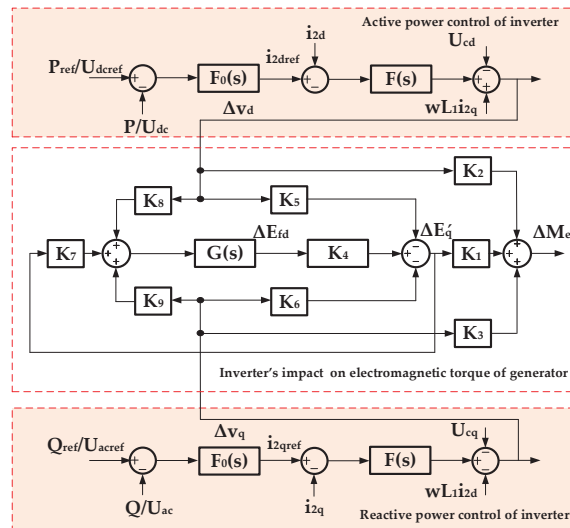


Figure 5. The small-signal model of the inverter output and the generator electromagnetic torque.

According to the control block diagram and the superposition principle, the transfer functions of $\Delta M_e / \Delta V_d$ and $\Delta M_e / \Delta V_q$ are obtained, respectively:

$$\begin{cases} \frac{\Delta M_e}{\Delta v_d} = \frac{(K_1 K_8 - K_2 K_7) G K_4 - K_1 K_5 + K_2}{1 - K_7 G K_4} \\ \frac{\Delta M_e}{\Delta v_q} = \frac{(K_1 K_9 - K_3 K_7) G K_4 - K_1 K_6 + K_3}{1 - K_7 G K_4} \\ G(s) = \frac{k_i + k_p s}{s} \end{cases} \quad (8)$$

where k_i is the integral time constant, k_p is the proportion coefficient.

The phase and amplitude difference between the output of the grid-connect inverter and the electromagnetic torque of the synchronous generator can be calculated by Equation (8). In this chapter, the small-signal model of the impact of the grid-connected inverter on electromagnetic torque of synchronous generator in power electronics-based AC power system has been deduced. The model reveals the relationship between the output power of the inverter and the generator torque. The model is the analysis basis of using the grid-connected inverter to increase low frequency damping.

According to the classical power system theory, a torque can be decomposed into two components, i.e., damping torque and synchronizing torque. The positive direction of the damping torque is in phase with the angular frequency $\Delta\omega$. The positive direction of the synchronizing torque is in phase with the angle $\Delta\delta$. The influence of normal control grid-connected inverter on low frequency damping mainly depends on the $\Delta\omega$ direction component of electromagnetic torque.

According to the Heffron-Philips model, the relationship between terminal voltage and power angle can be present as Equation (9).

$$\begin{cases} \Delta u = K_{5H-P}\Delta\delta + K_{6H-P}\Delta E_q' \\ K_{5H-P} = \frac{u_{d0}}{u_0} \frac{x_q}{x_q+x_l} U_L \cos \delta_0 - \frac{u_{q0}}{u_0} \frac{x'_d}{x'_d+x_l} U_L \sin \delta_0 \\ K_{6H-P} = \frac{u_{q0}}{u_0} \frac{x_l}{x'_d+x_l} \end{cases} \quad (9)$$

where $\Delta\delta$ is the power angle deviation, K_{5H-P} is the factor of $\Delta\delta$ in the Heffron-Philips model, K_{6H-P} is the factor of $\Delta E_q'$ in Heffron-Philips model, x_l is the line impedance and U_L is the voltage behind line impedance x_l .

According to Equation (9), Δu occurs when there is a disturbance of power angle. The variation of the active power of grid-connect inverter ΔP can be assumed to follow Δu . Moreover, the regulation of active power in the inverter is in the opposite direction of active power measurement variation. After a series of PI control, the phase of ΔM_e produced by grid-connect inverter lags the phase of $-\Delta u$. So, the torque phasor diagram under oscillation can be shown in Figure 6, where Δu is the component related to power angle, ΔM_{eD} is the damping torque component of ΔM_e , ΔM_{eS} is the synchronizing torque component of ΔM_e , θ_M represents the phase difference from the phase of $-\Delta u$ to the phase of ΔM_e . From Figure 6, it can be seen that the damping torque component of ΔM_e is negative. The negative damping reduces the damping of the system and makes it easier for the appearance of LFOs.

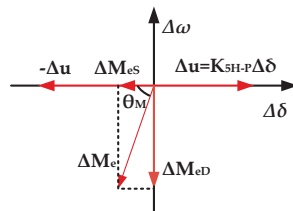


Figure 6. Torque phasor diagram during oscillation.

3. LFOs Suppression Strategy Using Inverter with Built-In PSS

3.1. The Control Structure of the Inverte with Built-In PSS

In order to increase low frequency damping, the grid-connected inverter needs to increase the torque in the positive direction of the axis $\Delta\omega$ to increase the damping torque. An extra torque ΔT can be introduced to provide positive synchronizing torque in the frequency range of LFOs. From Figure 4 and Equation (8), an additional control that passes the lead-lag correction component and inverter control loop can be introduced into the control loop of the grid-connected inverter to make the inverter produce positive damping torque.

To introduce the positive direction of the axis $\Delta\omega$, the active power or electric angular velocity on the interconnection line can be taken as the input of the additional control. Active power or angular velocity signal is introduced into the grid-connected inverter to produce positive damping, which is similar to the purpose of installing PSS on the excitation system. So, the additional control in the grid-connected inverter can use the experience of the structure of PSS to restrain LFOs. The grid-connected inverter is not willing to produce additional torque due to the normal power regulation of the generator, which will affect

its output capacity. Regarding the control structure of PSS2B, the acceleration power is used as the input signal. After the acceleration power input signal passes through a series of lead-lag components, the output phase is corrected to produce positive damping to suppress LFOs.

The built-in PSS structure for grid-connected inverter and application in the system is shown in Figure 7, where P_{ref} is the d-axis control reference of active power, U_{dcref} is the d-axis control reference of DC voltage, Q_{ref} is the q-axis control reference of reactive power, U_{acref} is the q-axis control reference of AC voltage. ω and P_e is the input signal, T_{W1} is the time constant of the first DC block component for input signal ω , T_{W2} is the time constant of the second DC block of input signal ω , T_{W3} is the time constant of the first DC block of input signal P_e , T_{W4} is the time constant of the second DC block for input signal P_e , K_{S2} is the gain coefficient of the integral component for input signal P_e , K_{S3} is a composite coefficient, T_6 is the time constant of the integral component for input signal P_e , K_{S1} is gain coefficient of regulating component, T_1 is the lead time constant of first lead-lag component, T_2 is the lead time constant of first lead-lag component, T_3 is the lead time constant of second lead-lag component, T_4 is the lag time constant of second lead-lag component, V_{BPSS} is the output of PSS for grid-connected inverter, V_{BPSS_max} is the upper limit of V_{BPSS} , V_{BPSS_min} is the lower limit of V_{BPSS} . V_{BPSS} is superimposed on the control target of the grid-connected inverter.

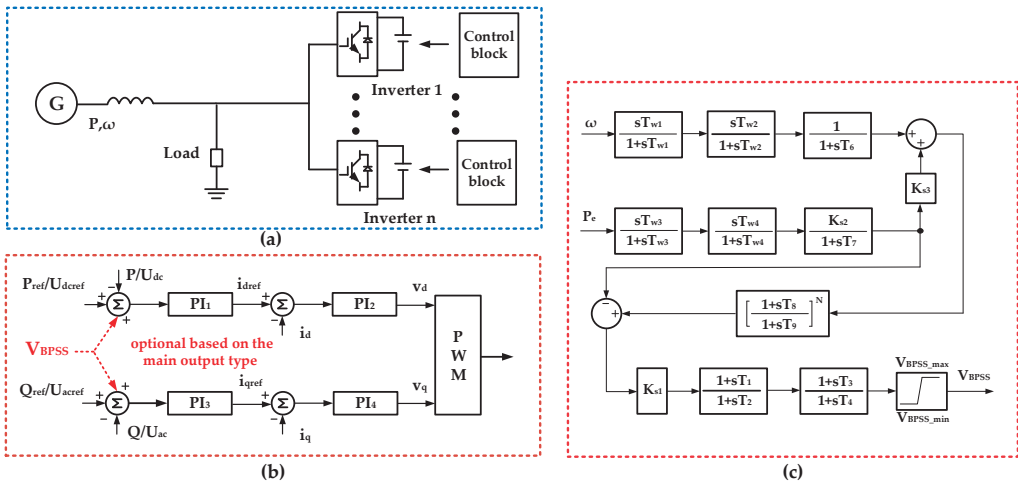


Figure 7. PSS control structure for grid-connected inverter and application in the system. (a) System structure; (b) superposition point of PSS output in the inverter control; (c) PSS control structure.

The additional electromagnetic torque is realized through the output of built-in PSS. The output of built-in PSS can be added with the reference of active power or reactive power in the control of grid-connected inverter. The superposition position is shown in Figure 7b, where The P_{ref}/U_{dcref} or Q_{ref}/U_{acref} in Figure 7b can be selected as the superimposed point according to the actual needs. When the grid-connected inverter output mainly active power, the built-in PSS shall be superposed on the corresponding active power control loop. When the grid-connected inverter output mainly reactive power, the built-in PSS shall be superposed on the corresponding reactive power control loop. The inverter damping torque control realized through active power control is different from the damping control of PSS realized through reactive power control of the generator.

3.2. Parameters Design Guideline for Built-In PSS

Different introduced extra torques have different damping effect. The angle between extra torque ΔT and $\Delta\omega$ axis and the amplitude of ΔT are the main factor determining damping torque. For the parameter tuning of built-in PSS, the lead-lag component parameters mainly determine the angle and K_{s1} determines the amplitude.

Undamped natural oscillation angular velocity is taken as the compensation point. The phase which the additional torque generated by built-in PSS lag to the input of the lead-lag components can be calculated through Equation (8). Then the parameters of the lead-lag components can be set according to the phase compensation demand. The other parameters of the filters in built-in PSS can use the design method of PSS which is used in excitation system.

As illustrated above, built-in PSS is superimposed on the reference of the outer-loop control. The additional control torque of built-in PSS has passed the control function $F_o(s)$ and $F(s)$. Then, the whole transfer function of additional torque of built-in PSS to electromagnetic torque of generator is shown as Equation (10).

$$\begin{cases} \frac{\Delta M_e}{\Delta\omega_{iPSS}} = \frac{\Delta M_e}{\Delta v_d} \cdot F_o(s) \cdot F(s) \\ F_o(s) = k_{po} + k_{io}/s \\ F(s) = k_{pi} + k_{ii}/s \end{cases} \quad (10)$$

where k_{po} is the proportion coefficient of the outer-loop control, k_{io} is the integral time constant of the outer-loop control, k_{pi} is the proportion coefficient of the inner-loop control, k_{ii} is the integral time constant of the inner-loop control.

According to the Heffron-Philips model, the undamped mechanical nature angular velocity of the rotor can be obtained through Equation (11).

$$\begin{cases} \omega_n = \sqrt{K_{1H-p}\omega_0/T_J} \\ K_{1H-p} = \frac{x_q - x_d'}{x_d' + x_s} i_{q0} u \sin \delta_0 + \frac{u \cos \delta_0}{x_q + x_s} E_{Q0} \end{cases} \quad (11)$$

where ω_n is the undamped mechanical nature angular velocity of the rotor, Δ_0 is the steady value of generator power-angle, ω_0 is the rated angular velocity, and T_J is the inertia constant of the generator.

When ω_n has been calculated, the phase of the whole system at the undamped mechanical nature angular velocity can be obtained through Equation (11). In order to produce positive damping torque and synchronous torque, the phase of additional damping torque should lead $\Delta\omega$ with phase 0~40 degrees. Then, compensatory angle ϕ_x of the lead-lag component of built-in PSS can be deduced.

The two lead-lag components of built-in PSS can adopt the same parameters. Then, T_1 is equal to T_3 , T_2 is equal to T_4 . As the inverter regulars very fast, the lag time constant T_2 is required to correspond with the speed. So, T_2 can be determined by reference to the regular time of inverter. The value of T_1 can be obtained according to the requirement of compensatory angle ϕ_x through Equation (12) as follow.

$$\phi_x/2 = \arctan T_1 \omega_n - \arctan T_2 \omega_n \quad (12)$$

When lead-lag component parameters are determined, KS1 can be determined by the critical gain method. The equivalent amplification factor of built-in PSS can be defined as AP, and its calculation formula is shown as Equation (13).

$$AP = K_{s1} \sqrt{\frac{1 + T_1^2}{1 + T_2^2}} \quad (13)$$

4. Verification

The classic step test of the generator terminal voltage is used to test low frequency damping. 5% step test of the generator terminal voltage is used in simulation and 3% step test of the generator terminal voltage is used in experiment. The damping effect of the built-in PSS can be observed in the process of the oscillation. The built-in PSS is a control for damping torque. So, the damping mechanism for multi-inverters with built-in PSS is same with the single inverter with built-in PSS. The simulation includes two parts. One part is about the different damping effects of different parameters of the built-in PSS. The other part is about the damping effects of dual paralleled grid-connected inverters with different built-in PSS situations. The experiment of generator-inverter system is also carried out to verify the damping control effect of the built-in PSS. The oscillation waveforms with and without built-in PSS in setting conditions are compared. The inverter can produce corresponding power oscillation which suppress the transmission power oscillation. The correctness of the analysis above is verified by the simulation and experimental result.

4.1. System Description and Setting

Simulation results based on PSCAD are provided to verify the analysis of built-in PSS. The simulation and experimental set up of a simplified power electronics-based AC power system is established as Figure 8. The two simulation parts uses single inverter and two paralleled inverters, respectively. The part with one inverter is used to verify the damping effects with different built-in PSS parameters. The part with two inverters is used to verify the damping effect of multi-inverters. The main parameters are shown in Table 1. The voltage of DC source is set as 400 V.

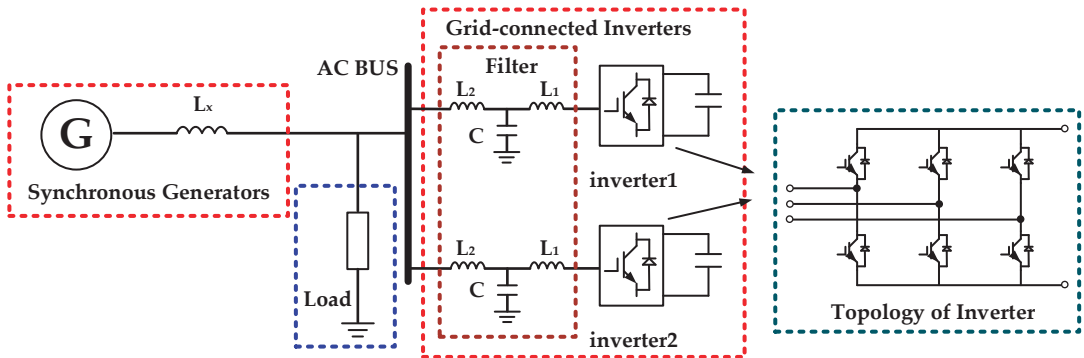


Figure 8. Simulation and experimental set up on PSCAD.

Table 1. Main parameters for simplified power electronics-based AC power system.

Parameters		Values
system impedance	L_s	0.1 mH
load	r	0.082 Ω
	L_0	0.082 mH
DC source	V_{dc}	400 V

Table 1. Cont.

Parameters		Values
Generator	x'_d	0.0361 Ω
	x_q	0.2238 Ω
	T'_{d0}	3.55
	i_{d0}	1093.7 A
	i_{q0}	1803.7 A
	u_{d0}	285.6726 V
	u_{q0}	117.17 V
	u_0	308.77 V
	E_{Q0}	361.96 V
	S_{base}	1 MVA
	U_{tbase}	20 kV
excitation system control	k_p	100
	k_i	60
LCL filter	L_1	0.2 mH
	L_2	0.04 mH
	C	15 μ F
Inverter control $F_0(s)$	k_{po}	4
	k_{io}	20
Inverter control $F(s)$	k_{pi}	4
	k_{ii}	100

4.2. Parameters Design

To make $T_1 \sim T_4$ positive, the output of built-in PSS is multiplied by -1 before adding to the reference value of active power control in this simulation, which results in a phase shift of 180° . According to the parameters of circuit and control function, the phase of ΔM_e lags the phase of $\Delta \omega_{BPSS}$ about $0 \sim 90^\circ$ in the frequency range of LFOs.

The output of built-in PSS is added with the output of d-axis control. The P_{ref} and Q_{ref} of the grid-connected inverter are set to be 0.4 MW and 0 MVar. According to the parameters of circuit and control function, ω_n can be calculated as 11.04 rad/s. From Figure 9 the phase of $\Delta M_e / \Delta \omega_{BPSS}$ at ω_n can be got as 75.1° .

Achieving $\Delta \omega_{BPSS}$ leading ΔM_e with 30° , this paper set compensatory angle ϕ_x of the lead-lag component of built-in PSS as 75° . According to the regulation time of the inverter, 0.01 can be taken as T_2 value. T_1 value can be derived through Equation (12). The parameters of built-in PSS are shown in Table 2. For see more details of the influence of built-in PSS, the limited output of built-in PSS is set quite lager as 20% of P_{ref} . In the actual project, the limit value should be according to the capacity of the inverter.

The bode diagram of $\Delta M_e / \Delta \omega_{BPSS}$ with and without compensation is shown in Figure 9. From the bode diagram, $\Delta \omega_{BPSS}$ leads ΔM_e 30 degree at the target frequency of LFOs. As the $\Delta \omega$ relevance vector is used as input, the phase of additional torque is 30 degrees lead of $\Delta \omega$ axis.

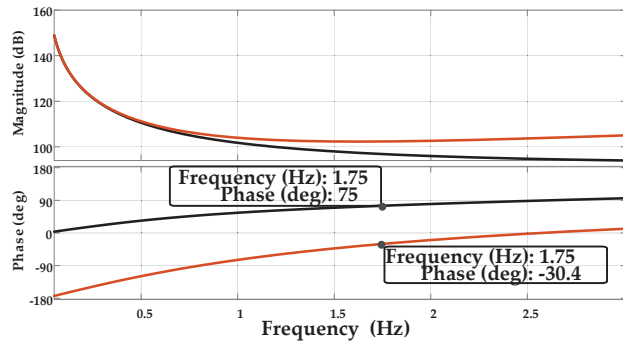


Figure 9. The bode diagram of $\Delta M_e / \Delta \omega_{BPSS}$ with and without compensation.

Table 2. Parameters of built-in PSS of inverter.

T_{w1}	T_{w2}	T_{w3}	T_{w4}	T_6	T_7	M
2	2	2	2	0	10	5
N	K_{s2}	K_{s3}	T_8	T_9	T_1	T_2
1	3.2	1	0.2	0.05	0.0868	0.01
T_3	T_4	K_{s1}	V_{BPSS_max}	V_{BPSS_min}		
0.0868	0.01	7.98	0.08 MW	-0.08 MW		

4.3. Damping Effects of Single Grid-Connected Inverter with Different Parameters

Case I is the situation that damping torques have same ϕ_x with different AP. Case II is the situation that damping torques have same AP with different ϕ_x . The simulation results are shown in Figure 10.

In case I compensatory angle ϕ_x of lead-lag component of built-in PSS is fixed as 75° , the damping torque diagram with different AP is shown in Figure 10a, where T_{BPSS0} is the damping torque of built-in PSS without phase compensation, T_{BPSS1} is the damping torque when $K_{s1} = 7.98$, T_{BPSS2} is the damping torque when $K_{s1} = 6$, T_{BPSS3} is the damping torque when $K_{s1} = 4$.

In case II AP of built-in PSS is fixed as 8.04, the damping torque diagram with different ϕ_x is shown in Figure 10a. Where T_{BPSS0} is the damping torque of built-in PSS without phase compensation, T_{BPSS1} is the damping torque when $\phi_x = 65^\circ$, T_{BPSS2} is the damping torque when $\phi_x = 75^\circ$, T_{BPSS3} is the damping torque when $\phi_x = 85^\circ$. Figure 10b shows the active power of generator in both cases; Figure 10c shows output of built-in PSS with various ϕ_x and AP; Figure 10d shows active power of grid-connected inverter in both cases; Figure 10e shows reactive power of grid-connected inverter in both cases; Figure 10f shows terminal voltage of generator in both cases.

For case I, from Figure 10b it can be seen that the bigger AP could produce larger positive damping torque. For case II, from Figure 10b the closer to the $\Delta\omega$ -axis could produce a larger positive damping torque. From Figure 10c,d it can be seen that larger output of the built-in PSS corresponds larger power fluctuation of inverter and larger positive damping torque. With the appropriate setting of K_{s1} and ϕ_x , the system damping can be increased. Under the action of built-in PSS, the active power fluctuation of inverter provides positive damping to the system. The verification results are consistent with the above theoretical analysis. Meanwhile, from Figure 10e,f, the damping regulation has little influence on terminal voltage of generator. The reason for that is that the built-in PSS in inverter is added to the active power control and the inverter adopts active and reactive power decoupling control strategy.

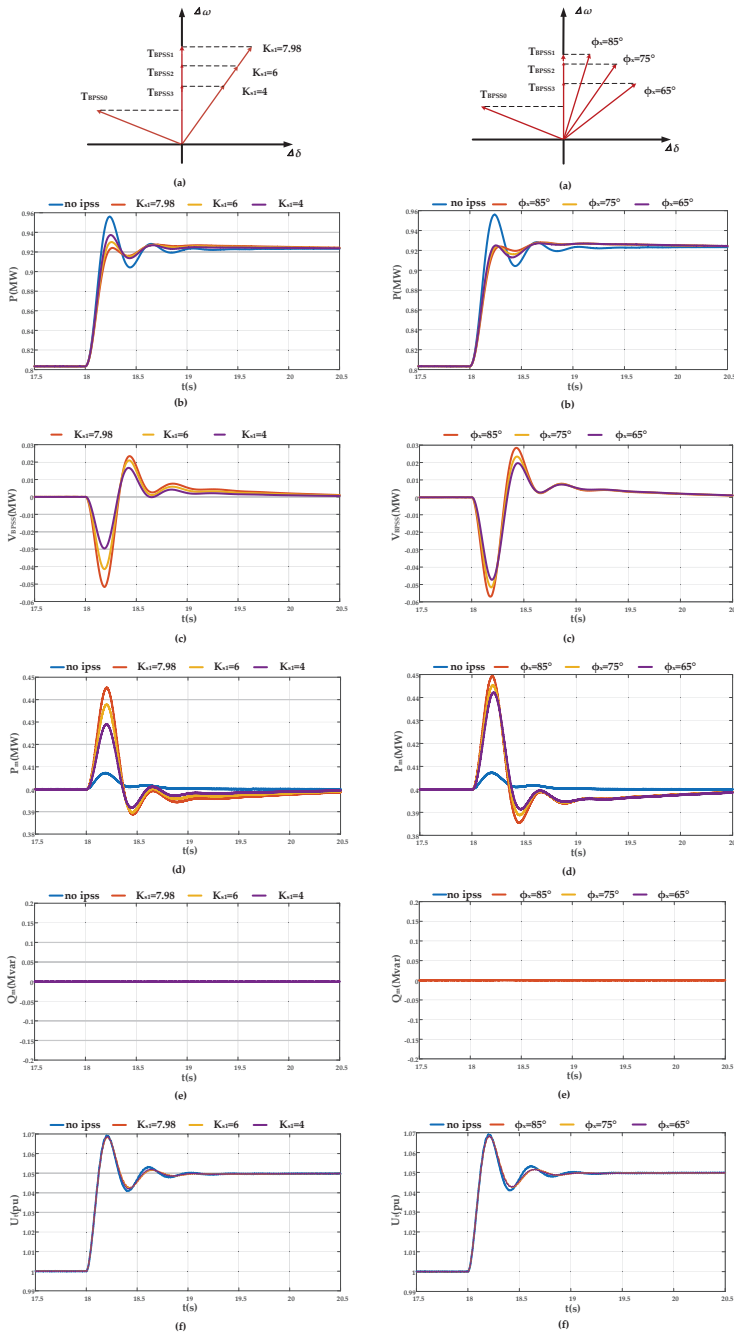


Figure 10. Simulation results of same ϕ_x with different AP (case I), same AP with different ϕ_x (case II). (a) Schematic diagram of damping torque with different AP and ϕ_x ; (b) active power of generator; (c) output of built-in PSS with various ϕ_x and AP; (d) active power of grid-connected inverter; (e) reactive power of grid-connected inverter; (f) terminal voltage of generator.

4.4. Damping Effects of Dual Paralleled Grid-Connected Inverters

More capacity of inverters to influence the electromagnetic torque of generator can present more damping effect. In this paper the situation of two inverters is taken as an example of multi-inverters connected with synchronous generator.

When the load is fixed, the different numbers of grid-connected inverters is set to realize the different distribution of active power between the inverter and the generator in the system shown in Figure 8. Figure 11 is the simulation result of two parallel grid-connected inverters system with different built-in PSS situations. The P_{ref} of the grid-connected inverter are set to be 0.4 MW and 0.2 MW, respectively. The Q_{ref} of the grid-connected inverter are set to be 0 MVar. The built-in PSS in both inverters adopts $K_{s1} = 6$ and same value as shown in Table 2 for the other parameters.

Three built-in PSS situations are simulated, case I: none of the inverters has built-in PSS; case II: only the larger output inverter has built-in PSS; case III: both of the inverters have built-in PSS. Figure 11a shows the fluctuation comparison of generator's active power under the three cases. From the figure it can be seen that better damping effect can be get by more inverters with built-in PSS. Figure 11b shows the active power of the larger output inverter under the three cases. Figure 11c shows the active power of the lower output inverter under the three cases. Figure 11d shows the output of built-in PSS in the inverters under the three cases. From Figure 11b–d, the active power fluctuation of the larger inverter can be reduced when two inverters have damping effect. The increasing of low frequency damping reduces the output of the built-in PSS of the inverter.

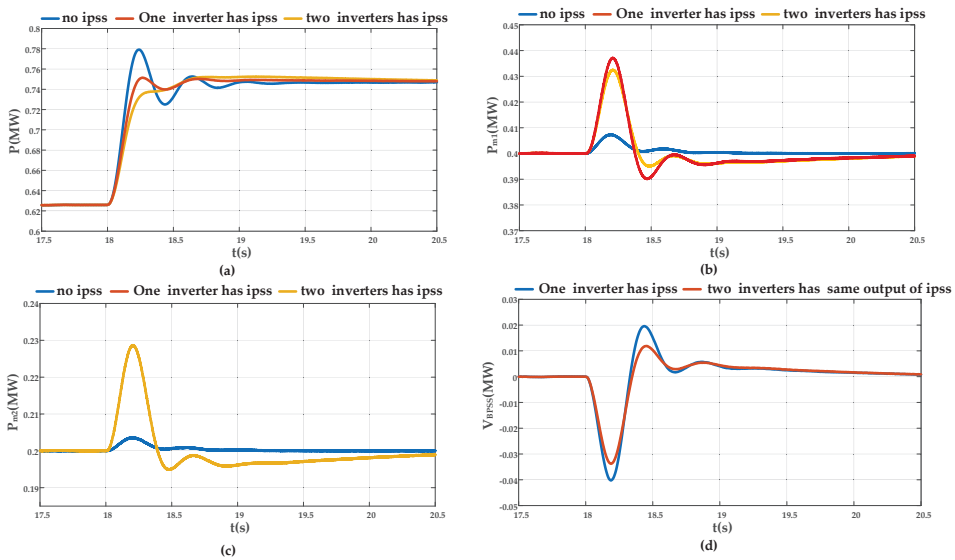


Figure 11. Simulation results of two parallel grid-connected inverters system with different built-in PSS situations, case I: none of the inverters has built-in PSS; case II: only the larger output inverter has built-in PSS; case III: both of the inverters have built-in PSS. (a) Active power fluctuation comparison of generator under the three cases; (b) active power of the larger output inverter under the three cases; (c) active power of the lower output inverter under the three cases; (d) output of built-in PSS in the inverters under the three cases.

4.5. Experimental Results

The experimental platform is consisted of one synchronous generator, two inverters and resistances. The structure of the system is same with the simulation system structure as shown in Figure 8. The experimental platform is shown in Figure 12. The parameters of the experimental platform are shown in Table 3. The two inverters all adopt same control

and built-in PSS. The excitation system and the inverters use the same control parameters as shown in Table 1.

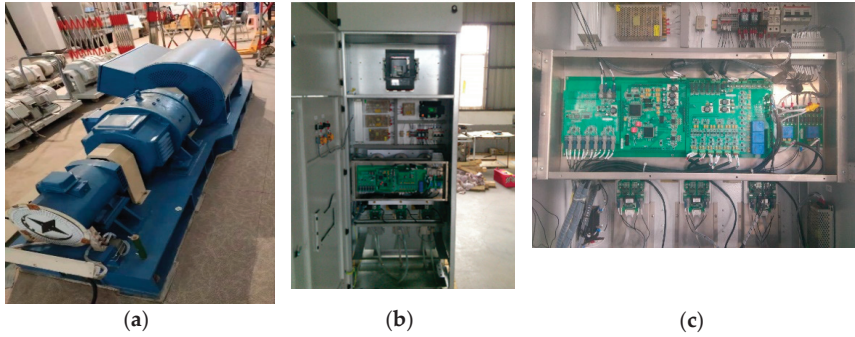


Figure 12. Experiment platform. (a) Synchronous generator; (b) inverter; (c) controller of the inverter.

Table 3. The parameters of the experimental platform.

Parameters		Values
Generator	S_{base}	30 kVA
	U_{tbase}	400 V
	x'_d	0.3556 pu
	x_q	1.0825 pu
	T'_{d0}	6.55
LCL filter	L_1	0.2 mH
	L_2	0.04 mH
	C	15 uF
load	r	2.4 Ω
DC source	V_{dc}	400 V

The parameters of built-in PSS are designed as the analysis above and shown in Table 4.

Table 4. Parameters of built-in PSS of inverter for experiment.

T_{w1}	T_{w2}	T_{w3}	T_{w4}	T_6	T_7	M
2	2	2	2	0	10	5
N	K_{s2}	K_{s3}	T_8	T_9	T_1	T_2
1	3.2	1	0.2	0.05	0.15	0.01
T_3	T_4	K_{s1}	V_{BPSS_max}	V_{BPSS_max}		
0.15	0.01	6.3	0.9 kW	-0.9 kW		

Three percent step of the generator terminal voltage test is used as the test condition. The active power waveforms of the generator under the system with and without built-in PSS are shown in Figure 13. To illustrate the damping effect of the built-in PSS with different parameters, the waveform of with built-in PSS 1 uses the parameters in Table 4 and the waveform of with built-in PSS 2 adopts the parameters in Table 4 except $T_1 = T_3 = 0.16$, $K_{s1} = 7.3$. The data of active power is recorded by controller of the inverter. The active power waveforms are obtained by using data processing software to process the recorded

data. From the comparison, the inverters with built-in PSS can increase the low frequency damping. The low frequency damping can be controlled through the adjusting of the parameters. The result is consistent with theoretical analysis above.

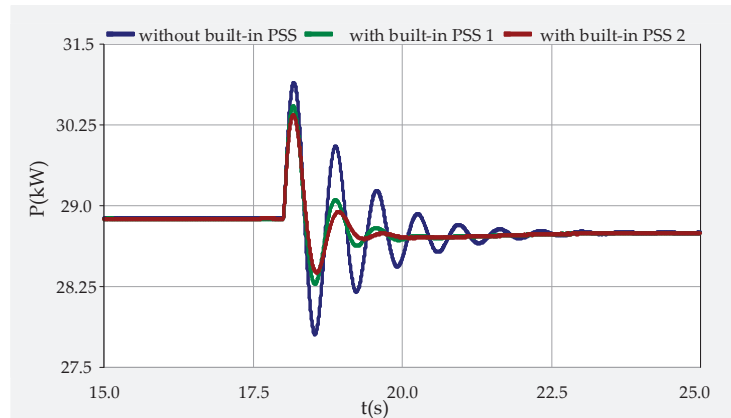


Figure 13. Active power waveform of the generator under the system with and without built-in PSS.

The oscillation information can be obtained through the input signals of the transmission active power and angular velocity. The lead-lag component compensates the phase shift caused by the power electronics-based AC grid. That makes the inverter can provide the corresponding active power variation to suppress the oscillation. The simulation and experimental result illustrate that the built-in PSS could increase low frequency damping with the proposed parameters design. The simulation and experimental results are consistent with the above theoretical analysis. The analysis is also suitable for multi parallel grid-connected inverters system in the power grid with synchronous generator characteristics.

5. Conclusions

Under the new situation that larger scale power electronics equipment and synchronous generator coexist in the power grid, making inverter participate in low frequency damping control is the key to enhancing system stability. In this paper, the low frequency damping control for power electronics-based AC power system using inverters with built-in PSS is analyzed. The model of the impact of the grid-connected inverter on the electromagnetic torque of the synchronous generator is researched and proposed. The model is the basis of increasing accurate positive low frequency damping torque through the grid-connected inverter. The built-in PSS of the inverter is used to introduce additional positive damping torque for the system. The structure of the built-in PSS is illustrated. Angular velocity and active power are used as input signals. Through lead-lag components, the built-in PSS makes inverter generate positive damping torque to increase low frequency damping. The built-in PSS control can be superposition to active power control or reactive power control loop of the inverter. The design method for the main parameter of built-in PSS is also proposed. Finally, the correctness of the theoretical analysis and the effectiveness of the built-in PSS is verified by the simulation and experiment.

Author Contributions: Conceptualization, W.C. and M.Y.; Data curation, M.Y.; Funding acquisition, J.Z.; Methodology, M.Y. and T.L.; Software, T.L.; Validation, W.L.; Writing—original draft, M.Y. and T.L.; Writing—review & editing, W.C. and M.Y. All authors have read and agreed to the published version of the manuscript.

Funding: This research was supported in part by the National Natural Science Foundation of China (Grant Number 51877042).

Institutional Review Board Statement: Not applicable.

Informed Consent Statement: Not applicable.

Data Availability Statement: Not applicable.

Conflicts of Interest: The authors declare no conflict of interest.

References

- Chompoobutrgool, Y.; Ghandhari, M.; Vanfretti, L. Survey on power system stabilizers control and their prospective applications for power system damping using synchrophasor-based wide-area systems. *Eur. Trans. Electr. Power* **2011**, *21*, 2098–2111. [\[CrossRef\]](#)
- Pogaku, N.; Prodanovic, M.; Green, T.C. Modeling, analysis and testing of autonomous operation of an inverter-based microgrid. *IEEE Trans. Power Electron.* **2007**, *22*, 613–625. [\[CrossRef\]](#)
- Qi, J.; Wu, Q.; Zhang, Y.; Weng, G.; Zhou, D. Unified residue method for design of compact wide-area damping controller based on power system stabilizer. *J. Mod. Power Syst. Clean Energy* **2020**, *8*, 366–375. [\[CrossRef\]](#)
- Zhong, Q.; Weiss, G. Synchronverters: Inverters that mimic synchronous generators. *IEEE Trans. Ind. Electron.* **2011**, *58*, 1259–1267. [\[CrossRef\]](#)
- Alipoor, J.; Miura, Y.; Ise, T. Stability assessment and optimization methods for microgrid with multiple VSG units. *IEEE Trans. Smart Grid* **2018**, *9*, 1462–1471. [\[CrossRef\]](#)
- Jiang, Q.; Li, B.; Liu, T. Large-scale power base's impact on low frequency oscillation characteristic in UHVAC power transmission system. *IEEE Access* **2019**, *7*, 56423–56430. [\[CrossRef\]](#)
- Kundur, P. *Power System Stability and Control*; McGraw-Hill: New York, NY, USA, 1994.
- Zhou, J.; Shi, P.; Gan, D.; Xu, Y.; Xin, H.; Jiang, C.; Xie, H.; Wu, T. Large-scale power system robust stability analysis based on value set approach. *IEEE Trans. Power Syst.* **2017**, *32*, 4012–4023. [\[CrossRef\]](#)
- Chen, H.; Yu, W.; Liu, Z.; Yan, Q.; Tasiu, I.A.; Han, Z. Low-frequency instability induced by hopf bifurcation in a single-phase converter connected to non-ideal power grid. *IEEE Access* **2020**, *8*, 62871–62882. [\[CrossRef\]](#)
- Zhou, J.; Ke, D.; Chung, C.Y.; Sun, Y. A computationally efficient method to design probabilistically robust wide-area PSSs for damping inter-area oscillations in wind-integrated power systems. *IEEE Trans. Power Syst.* **2018**, *33*, 5692–5703. [\[CrossRef\]](#)
- Xiong, L.; Zhuo, F.; Wang, F.; Liu, X.; Chen, Y.; Zhu, M.; Yi, H. Static synchronous generator model: A new perspective to investigate dynamic characteristics and stability issues of grid-tied PWM inverter. *IEEE Trans Power Electron.* **2016**, *31*, 6264–6280. [\[CrossRef\]](#)
- Yao, W.; Jiang, L.; Wen, J.; Wu, Q.H.; Cheng, S. Wide-area damping controller of FACTS devices for inter-area oscillations considering communication time delays. *IEEE Trans. Power Syst.* **2014**, *29*, 318–329. [\[CrossRef\]](#)
- Zhang, C.; Ke, D.; Sun, Y.; Chung, C.Y.; Xu, J.; Shen, F. Coordinated supplementary damping control of DFIG and PSS to suppress interarea oscillations with optimally controlled plant dynamics. *IEEE Trans. Sustain. Energy* **2018**, *9*, 780–791. [\[CrossRef\]](#)
- D'Arco, S.; Suul, J.A. Equivalence of virtual synchronous machines and frequency-droops for converter-based microgrids. *IEEE Trans. Smart Grid.* **2014**, *5*, 394–395. [\[CrossRef\]](#)
- Wen, B.; Boroyevich, D.; Burgos, R.; Mattavelli, P.; Shen, Z. Small signal stability analysis of three-phase AC systems in the presence of constant power loads based on measured D-Q frame impedances. *IEEE Trans. Power Electron.* **2015**, *30*, 5952–5963. [\[CrossRef\]](#)
- Amin, M.; Molinas, M. Small-signal stability assessment of power electronics based power systems: A discussion of impedance- and eigenvalue-based methods. *IEEE Trans. Ind. Appl.* **2017**, *53*, 5014–5030. [\[CrossRef\]](#)
- Wen, B.; Boroyevich, D.; Burgos, R.; Mattavelli, P.; Shen, Z. Analysis of D-Q small-signal impedance of grid-tied inverters. *IEEE Trans. Power Electron.* **2016**, *31*, 675–686. [\[CrossRef\]](#)
- Ashabani, M.; Mohamed, Y.A.R.I. Mohamed. Integrating VSCs to weak grids by nonlinear power damping controller with self-synchronization capability. *IEEE Trans. Power Syst.* **2014**, *29*, 805–813. [\[CrossRef\]](#)
- Kalco, G.O.; Adam, G.P.; Anaya-Lara, O.; Lo, S.; Uhlen, K. Small-signal stability analysis of multi-terminal VSC-based DC transmission systems. *IEEE Trans. Power Syst.* **2012**, *27*, 1818–1830. [\[CrossRef\]](#)
- Hassan, L.H.; Moghavvemi, M.; Almurib, H.A.; Muttaqi, K.M. A coordinated design of PSSs and UPFC-based stabilizer using genetic algorithm. *IEEE Trans. Ind. Appl.* **2014**, *50*, 2957–2966. [\[CrossRef\]](#)
- Zhang, K.; Shi, Z.; Huang, Y.; Qiu, C.; Yang, S. SVC damping controller design based on novel modified fruit fly optimization algorithm. *IET Renew. Power Gener.* **2017**, *12*, 90–97. [\[CrossRef\]](#)
- Zuo, J.; Li, Y.; Shi, D.; Duan, X. Simultaneous robust coordinated damping control of power system stabilizers (PSSs), static var compensator (SVC) and doubly-fed induction generator power oscillation dampers (DFIG PODs) in multi machine power systems. *Energies* **2017**, *10*, 565–588.
- Ahmed, M.; Vahidnia, A.; Datta, M.; Meegahapola, A. An adaptive power oscillation damping controller for a hybrid AC/DC microgrid. *IEEE Access* **2020**, *8*, 69482–69495. [\[CrossRef\]](#)
- Kerdphol, T.; Waranabe, M.; Hongesombut, K.; Mitani, Y. Self-adaptive virtual inertia control-based fuzzy logic to improve frequency stability of microgrid with high renewable penetration. *IEEE Access* **2019**, *7*, 76071–76083. [\[CrossRef\]](#)

25. Zhou, Y.; Liu, J.; Li, Y.; Gan, C.; Li, H.; Liu, Y. A gain scheduling wide-area damping controller for the efficient integration of photovoltaic plant. *IEEE Trans. Power Syst.* **2019**, *34*, 1703–1715. [[CrossRef](#)]
26. Wan, C.; Huang, M.; Tse, C.K.; Ruan, X. Effects of interaction of power converters coupled via power grid: A design-oriented study. *IEEE Trans. Power Electron.* **2015**, *30*, 3589–3600. [[CrossRef](#)]
27. Liu, J.; Miura, Y.; Ise, T. Comparison of dynamic characteristics between virtual synchronous generator and droop control in inverter based distributed generators. *IEEE Trans. Power Electron.* **2016**, *31*, 3600–3611. [[CrossRef](#)]
28. Huang, L.; Xin, H.; Wang, Z. Damping low-frequency oscillations through VSC-HVDC stations operated as virtual synchronous machines. *IEEE Trans. Power Electron.* **2018**, *34*, 5803–5818. [[CrossRef](#)]
29. Faraji, A.; Naghshbandy, A.H.; Baayeh, A.G. A hybrid coordinated design method for power system stabilizer and FACTS device based on synchro squeezed wavelet transform and stochastic subspace identification. *J. Mod. Power Syst. Clean Energy* **2020**, 1–10. [[CrossRef](#)]

Article

Mathematical Modeling of the Dynamics of Linear Electrical Systems with Parallel Calculations

Sławomir Cieslik

Faculty of Telecommunications, Computer Science and Electrical Engineering, UTP University of Science and Technology, 85-796 Bydgoszcz, Poland; slavcies@utp.edu.pl

Abstract: The dynamics of power systems is often analyzed using real-time simulators. The basic requirements of these simulators are the speed of obtaining the results and their accuracy. Known algorithms (backward Euler or trapezoidal rule) used in real-time simulations force the integration time step to be reduced to obtain the appropriate accuracy, which extends the time of obtaining the results. The acceleration of obtaining the results is achieved by using parallel calculations. The paper presents an algorithm for mathematical modeling of the dynamics of linear electrical systems, which works stably with a relatively large integration time step and with accuracy much better than other algorithms widely described in the literature. The algorithm takes into account the possibility of using parallel calculations. The proposed algorithm combines the advantages of known methods used in the analysis of electrical circuits, such as nodal analysis, multi-terminal electrical component theory, and transient states analysis methods. However, the main advantage over other algorithms is the use of the method based on average voltages in the integration step (AVIS method). The attention was focused on the presentation of the scientifically acceptable general principle offered to mathematical modeling of dynamics of linear electrical systems with parallel computations. However, the evidence of its effective application in the analysis of the dynamics of electric power and electromechanical systems was indicated in the works carried out by the team of authors from the Institute of Electrical Engineering UTP University of Science and Technology in Bydgoszcz (Poland).

Keywords: electrical system dynamics; power systems; dynamic behavior of power systems; power system simulation; AVIS method

Citation: Cieslik, S. Mathematical Modeling of the Dynamics of Linear Electrical Systems with Parallel Calculations. *Energies* **2021**, *14*, 2930. <https://doi.org/10.3390/en14102930>

Academic Editor: José Antonio Domínguez-Navarro

Received: 18 March 2021
Accepted: 7 May 2021
Published: 19 May 2021

Publisher's Note: MDPI stays neutral with regard to jurisdictional claims in published maps and institutional affiliations.



Copyright: © 2021 by the author. Licensee MDPI, Basel, Switzerland. This article is an open access article distributed under the terms and conditions of the Creative Commons Attribution (CC BY) license (<https://creativecommons.org/licenses/by/4.0/>).

1. Introduction

Mathematical models of complex electric power and electromechanical systems for transients simulation can be derived directly on the basis of mathematical descriptions of physical phenomena occurring in the elements of these systems or on the basis of equivalent diagrams containing the fundamental (ideal) elements of electrical circuits, including: resistors, inductors, capacitors, and sources. From the transients analysis point of view, the mathematical models consist of a set of first-order differential equations based on Kirchhoff's laws. This is a well-documented subject in electrical engineering texts.

The tensorial analysis of networks was developed in [1]. Rather than using nodes and edges in graphs to describe the circuit topology, the developed circuit definition using the space of the meshes was proposed. This approach was justified through topology considerations.

The application of efficient computational techniques to the solution of electromagnetic transient problems in systems of any size and topology is the actual scientific problem. The electric power system variables are continuous. The digital simulation is of course discrete. The main task in digital simulation is still the development of suitable methods for the solution of the differential and algebraic equations at discrete points. The diagram presented in Figure 1 shows the place of one-step integration methods in the analysis of the dynamics of electrical systems. The following publications were listed there: basic

Dommele's book [2], EMTP Theory Book [3], Araujo's Ph.D. thesis [4], Marti's publication [5] and Crow's book [6].

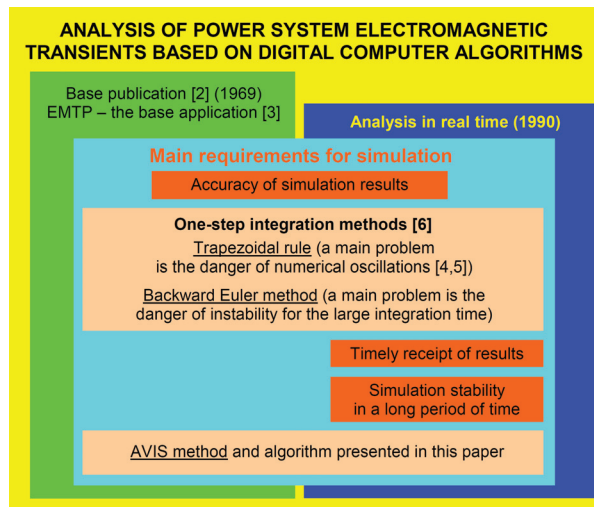


Figure 1. The place of one-step integration methods in the analysis of the dynamics of electrical systems.

The selection of an integration method and an algorithm is, in particular for the real-time mathematical modeling, an important and current scientific problem. The integration method for real-time simulation must be numerically stable, computationally efficient, and accurate enough for practical purposes.

The book [7] can be distinguished especially in the area of the parallel calculation in the real-time simulation of power system dynamics. The book [8] has a chapter on real-time simulation. A number of Ph.D. Thesis on real-time simulation were carried out, including [9–11].

The use of parallel calculations can significantly reduce the computation time. It is especially important in the case of real-time simulation and also simulation realized faster than real time (for example, the prediction of power system operating states). Real-time systems are widely used in the simulation of complex electric circuits [12]. In these kinds of systems, calculations for the given iteration of the discrete mathematical model of electrical system have to be done in the given integration time step [13]. This is an indispensable condition to be met with the requirements related to operation in real-time. Extracting individual processes is not a trivial problem. This subject in relation to electrical systems has been discussed in the literature. Methods such as wave relaxation [14] and domain decomposition [15,16] were used here. The main issue that occurs in the first case is the lack of guaranteed convergence for a general electric circuit. This caused the inhibition of using this method in simulating software of electrical systems. Scalability for algorithms based on the domain decomposition method is strictly limited in the case of increasing numbers of interface variables between extracted parts of the equation system [17].

The explanation of the parallelization of long-running power system simulations using existing desktop computer technology is presented in the book [7]. The topic of partitioning and evaluating runtime as a power system model with partitioned numerous times was discussed in this book. This book provides a fresh perspective on power system simulation to embrace multicore technology, including, among others: the power system model, time domain simulation, discretization, power apparatus models, network formulation, partitioning, and multithreading. In the topic of interest to us, from the point of view of this paper, tunable integration and root-matching were used in the book [7]. Tunable integration was used for stand-alone electrical branches and control blocks, and root-matching was

used for electrical branch pairs. Let us pay attention to a certain context of the solution proposed in this book. The choice of integration method typically depends on which power apparatus is included in the model. For example, the trapezoidal rule is recommended for networks where the voltages and currents are expected to be sinusoidal; the backward Euler method is recommended for networks where the voltages and currents are expected to be piecewise linear such as when power converters are present. Tunable integration was defined in [8], and it is an effective approach that benefits from the accuracy of trapezoidal integration and the stability of backward Euler integration. Therefore, it is expedient to look for new integration methods that will avoid the use of the tunable integration.

The answer to these problems is the new numerical one-step integration method and the resulting new mathematical models and new simulation algorithms that are used in the research carried out at the Institute of Electrical Engineering UTP University of Science and Technology in Bydgoszcz (Poland). Previously, no one wrote about this method, mathematical models, and algorithms in any of the above-mentioned publications. The essence of the new method is the use of the numerical discretization of electrical circuit equations, formulated for average voltage values [18]. The proposed method was successfully developed and used by the authors from IEE UTP for issues related to the analysis of complex power systems [19–22]. A survey of power systems analysis programs presented above did not mention the method based on average voltages in the integration step (AVIS method) even once.

The goal of this paper was the presentation of the scientifically acceptable general method for the mathematical modeling of the dynamics of linear electrical systems using parallel calculations. The new method for the mathematical modeling has an advantage over others known from the literature in that it allows for a stable simulation with a relatively large integration time step without losing the accuracy of the results. The original contributions of the author of this paper were the method of determining the areas of application of the proposed integration method, in which it has an advantage over other methods and the theory of mathematical modeling of dynamics of linear electrical systems using parallel calculations.

The organization of the article is as follows: (1) we present in detail the derivation and physical basis of the mathematical models of individual structural elements and the mathematical model of the generalized electrical system; (2) we present the method of separating the fragments of the mathematical model of the generalized electrical system into computational threads that can be implemented in parallel; and (3) we present, on a relatively simple example, the application of the mathematical modeling method proposed in this paper.

Section 1 of this paper presents the Introduction, which justifies the need to search for effective methods of the mathematical modeling of complex electrical systems, especially those that are to be used in real-time simulators. It has been shown that not everything is solved today in the area of the real-time simulation of the dynamics of power systems. The search for new stable simulation methods with a relatively large integration time step without losing the accuracy of the results is a current issue from the scientific point of view. The ability to perform computations in parallel is a way to speed up computation as expected in a real-time simulation. Section 2 defines the generalized electrical system and provides the basic terms and definitions used in the proposed method for the mathematical modeling of electrical systems. Mathematical relationships between physical quantities characteristic of a generalized electrical system are also presented. The mathematical model of the generalized branch of the electric circuit, based on the AVIS method, is presented in Section 3. The mathematical model of the generalized branch of the electric circuit was used to create mathematical models of the interconnecting structural elements, in which the terminals of the branches extend outside the structural element (a multi-term element). The advantage of the applied integration method (AVIS method) over others (backward Euler and trapezoidal rule) recommended in the literature is demonstrated in Section 4. The derivation and physical justification of the mathematical models of structural

elements with any internal structure are presented in Section 5. The mathematical basis for aggregating three structural elements into one equivalent element is presented in the Section 6. This is an example of the aggregation of multiple structural elements for which the external characteristics are known (the internal structure of the element does not have to be known) into one equivalent structural element. This manner is often used in modeling complex power structures. The mathematical bases and physical justifications presented in Sections 2, 3, 5, and 6 form the basis of the formulation of the algorithm of the mathematical modeling of linear electrical systems with parallel calculations. This algorithm is presented in Section 7. In Section 8, on a very simple example, the practical application of the algorithm resulting from the method proposed in this paper is shown. The conclusions are at the end of the paper.

The paper does not provide the implementation of the proposed method in a specific hardware solution of the simulator. A detailed description of the implementation of the proposed mathematical modeling method of electrical systems, due to its specificity (PC, DSP, FPGA, GPU), is beyond the scope of this paper.

2. Basic Terms and Definitions

The concept of a generalized electrical system is introduced here. Any electrical system consists of all of the elements needed to generate, distribute, and consume electrical energy. This system can be simplified as shown in Figure 2.

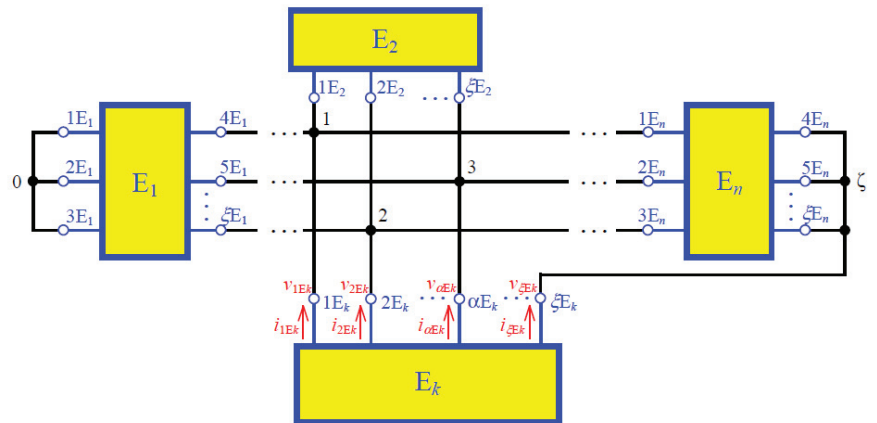


Figure 2. Schematic diagram of a generalized electrical system.

Definition 1. A generalized electrical system is an abstract object, consisting of abstract elements, that is characterized by suitable physical (electrical) and mathematically exact relationships among these elements.

The word “abstract” is understood in the sense of being a product of abstraction. That is, extracting characteristics or relations, i.e., formal relationships in a real object or event, or in a set of objects or events.

Generalized electrical system can be interpreted as the connection of *n* multi-terminal elements (E₁, E₂, ..., E_k, ..., E_n) in ζ + 1 nodes (0, 1, 2, 3, ..., ζ), as shown for example in Figure 2.

Physical (electrical) relationships, resulting directly from Definition 1, imply identifying physical quantities characteristic of nodes (black points in Figure 2) of this generalized electrical system as electric potentials. An electric potential of one of the nodes is taken as

a reference ($v_0 = 0$). Based on that, it is possible to introduce the vector of node electric potentials of the generalized electrical system, as follows:

$$v_S = [v_1 \quad v_2 \quad v_3 \quad \dots \quad v_\zeta]^T, \tag{1}$$

where v_S is the vector of the node electric potentials of the generalized electrical system, v_x is the electric potential of node x (where: $x = 1, 2, 3, \dots, \zeta$), and the symbol “T” in the superscript of the matrix notation means the transposition operation.

The essence of the new method of the integration of differential equations, which will be presented in detail in the next section, is to write down the equations for the average voltages in the integration step. Hence, in the mathematical models, the matrix of average electric potentials is used. Thus, the vector of average electric potentials in the integration step h for discrete time t_n has the following form:

$$\chi_S(t_n) = [\chi_1(t_n) \quad \chi_2(t_n) \quad \chi_3(t_n) \quad \dots \quad \chi_\zeta(t_n)]^T, \tag{2}$$

where $\chi_x(t_n) = \frac{1}{h} \cdot \int_{t_{n-1}}^{t_n} v_x(t)dt$ is the average electric potentials in the integration step of node x (where: $x = 1, 2, 3, \dots, \zeta$ and $h = t_n - t_{n-1}$).

Electrical systems naturally consist of separate multi-terminal elements interconnected with each other. Alternatively, it is also possible to carry out artificial extraction (decomposition) of the electrical system on the separate elements. Separate elements can be called structural elements of the analyzed electrical system (structural elements).

Definition 2. *The poles of each separate multi-terminal element (structural element) are the terminals (nodes) of this element that are available outside and allow direct electrical connection with other elements.*

These multi-terminal elements (structural elements) are known from electrical circuit theory as electric multipoles. Multipoles are introduced as elements with ordered external terminals (poles) consisting of a network and a family of terminal classes. The terminal classes are disjoint subsets of the node set of the corresponding network [23]. The rest of the nodes (after extraction of poles) in the structure of each structural element are named internal nodes of this element. Each structural element E_k in the general case is composed of g number of branches that are interconnected with each other. The branch is a set of interconnected ideal elements of electric circuits, which has only two terminals on the outside. Branches of the structural element E_k are interconnected in ζE_k number of poles (see Figure 2) and w number of internal nodes. Two vectors of external physical quantities are introduced for each structural element E_k , as follows:

$$v_{E_k} = [v_{1E_k} \quad v_{2E_k} \quad \dots \quad v_{\alpha E_k} \quad \dots \quad v_{\zeta E_k}]^T, \tag{3}$$

$$i_{E_k} = [i_{1E_k} \quad i_{2E_k} \quad \dots \quad i_{\alpha E_k} \quad \dots \quad i_{\zeta E_k}]^T, \tag{4}$$

where v_{E_k} and i_{E_k} are the vectors of the node (pole) potentials and currents of the external branches of structural element E_k (current directions in external branches of the structural elements are always oriented from inside the elements to the poles) and v_{xE_k} and i_{xE_k} are the electric potential of pole x and the current of the branch with pole x (where $x = 1, 2, \dots, \alpha, \dots, \zeta$) of structural element E_k (see Figure 2), respectively.

We consistently introduce the vector of average electric potentials of poles of structural element E_k in the integration step for discrete time t_n , as follows:

$$\chi_{E_k}(t_n) = [\chi_{1E_k}(t_n) \quad \chi_{2E_k}(t_n) \quad \dots \quad \chi_{\alpha E_k}(t_n) \quad \dots \quad \chi_{\zeta E_k}(t_n)]^T, \tag{5}$$

where $\chi_{xE_k}(t_n) = \frac{1}{h} \cdot \int_{t_{n-1}}^{t_n} v_{xE_k}(t)dt$ is the average electric potentials in the integration step of pole x of structural element E_k (where: $x = 1, 2, \dots, \alpha, \dots, \zeta$).

Definition 3. The external equation of the structural element is an equation in the following form (formulated for element E_k):

$$i_{E_k} + A_{E_k} \cdot \chi_{E_k} + B_{E_k} = 0. \tag{6}$$

Equation (6) is composed of matrices for which A_{E_k} is a square matrix of size $\zeta_{E_k} \times \zeta_{E_k}$ and B_{E_k} is the column matrix with ζ_{E_k} number of elements. Those matrices are described by parameters and physical quantities, which occur inside structural element E_k . The methods of the calculations of those matrices elements are introduced in next parts of this paper.

Dependencies between the pole potentials of structural element E_k and the nodal potentials of the analyzed electric system are described by equation:

$$v_{E_k} = C_{E_k}^T \cdot v_S, \tag{7}$$

where C_{E_k} is the incidence matrix of structural element E_k .

The same relationship is valid for the average pole potentials of the structural element E_k (Equation (5)) and the average nodal potentials of the analyzed electric system (Equation (2)), as follows:

$$\chi_{E_k} = C_{E_k}^T \cdot \chi_S. \tag{8}$$

Definition 4. The incidence matrix of the structural element is a matrix in which the number of rows is equal to the number (ζ) of independent nodes of the generalized electrical system and the column number is equal to the number (ζ) of poles of this structural element. The matrix element upon crossing the individual row and individual column is equal to one if the node with the number the same as the number of the row is connected to the pole with the number the same as the column number. In other cases, the matrix element is equal to zero.

Based on Kirchhoff’s current law for all independent nodes of the generalized system, the equation was obtained:

$$\sum_{k=1}^n (C_{E_k} \cdot i_{E_k}) = 0. \tag{9}$$

Substituting vectors of external branches’ currents determined from Equation (6) for each structural element into Equation (9) and taking into account Equation (8), we obtained the equation:

$$A_S \cdot \chi_S + B_S = 0, \tag{10}$$

where:

$$A_S = \sum_{k=1}^n (C_{E_k} \cdot A_{E_k} \cdot C_{E_k}^T) \text{ and } B_S = \sum_{k=1}^n (C_{E_k} \cdot B_{E_k}). \tag{11}$$

From Equation (11), it follows that the size of the matrix A_S is $\zeta \times \zeta$, and matrix B_S has ζ number of elements.

Taking into account Definition 2, which is related to the poles of structural element E_k , for the internal nodes (1, 2, ..., w) of this element, a vector of internal nodal potentials is written in the form of:

$$v_{iE_k} = [v_{1iE_k} \quad v_{2iE_k} \quad \dots \quad v_{wiE_k}]^T, \tag{12}$$

where v_{iE_k} is the vector of internal nodes potentials of structural element E_k (the symbol ‘‘i’’ indicates that it is about the internal value of the element) and v_{xiE_k} is an electric potential of internal node x (where: $x = 1, 2, \dots, w$) of structural element E_k .

We consistently introduce for the internal nodes (1, 2, ..., w) of structural element E_k a vector of internal nodal average potentials, in the following form:

$$\chi_{iE_k}(t_n) = [\chi_{1iE_k}(t_n) \quad \chi_{2iE_k}(t_n) \quad \dots \quad \chi_{wiE_k}(t_n)]^T, \tag{13}$$

where $\chi_{xiEk}(t_n) = \frac{1}{h} \cdot \int_{t_{n-1}}^{t_n} v_{xiEk}(t) dt$ is the average electric potentials in the integration step of internal node x (where: $x = 1, 2, \dots, w$).

For each branch (g) of structural element E_k , the branch’s voltages (as the differences of the electric potentials of the respective nodes of the branch) are written in the following vector:

$$v_{bEk} = [v_{1bEk} \ v_{2bEk} \ v_{3bEk} \ \dots \ v_{gbEk}]^T, \tag{14}$$

where v_{bEk} is the vector of the branch’s voltages of structural element E_k (the symbol “b” indicates that it is about the branches of the element) and v_{xbEk} is a voltage of branch x (where: $x = 1, 2, \dots, g$) of structural element E_k .

We consistently introduce for each branch (g) of structural element E_k the branch’s average voltages in integration step (as the differences of the average electric potentials of the respective nodes of the branch) the following form:

$$\chi_{bEk}(t_n) = [\chi_{1bEk}(t_n) \ \chi_{2bEk}(t_n) \ \chi_{3bEk}(t_n) \ \dots \ \chi_{gbEk}(t_n)]^T, \tag{15}$$

where $\chi_{xbEk}(t_n) = \frac{1}{h} \cdot \int_{t_{n-1}}^{t_n} v_{xbEk}(t) dt$ is the branch’s average voltages in integration step of branches x (where: $x = 1, 2, 3, \dots, g$).

The relation between the vector of branch voltages (14) and the vector of internal nodal potentials (12), as well as the vector potential of poles (3) of structural element E_k is given in the following equation:

$$v_{bEk} = M_{iEk}^T \cdot v_{iEk} + M_{pEk}^T \cdot v_{Ek}, \tag{16}$$

where M_{iEk} is the incidence matrix for internal nodes of structural element E_k and M_{pEk} is the incidence matrix for poles of structural element E_k .

The same relationship is valid for average voltages and electric potentials in the integration step, as follows:

$$\chi_{bEk} = M_{iEk}^T \cdot \chi_{iEk} + M_{pEk}^T \cdot \chi_{Ek}. \tag{17}$$

Definition 5. The incidence matrix for internal nodes of the structural element is a matrix in which the number of rows is equal to the number of internal nodes (w) and the column number is equal to the number of its branches (g). The matrix element in the n -th row and the m -th column is equal to: 0 if the terminals of the m -th branch are not connected with the n -th node, or -1 if the terminal of the m -th branch to which the branch current is supplied is connected to the n -th node, or 1 if the terminal of the m -th branch, from which the branch current flows, is connected to the n -th node.

Definition 6. The incidence matrix for poles of the structural element is a matrix in which the number of rows is equal to the number of poles (ξ_k) and the column number is equal to the number of its branches (g). The matrix element in the n -th row and the m -th column is equal to: 0 if the terminal of the m -th branch is not connected with the n -th pole, or -1 if the terminal of the m -th branch to which the branch current is supplied is connected to the n -th pole, or 1 if the terminal of the m -th branch, from which the branch current flows, is connected to the n -th pole.

Similar to the case of branch average voltages (15), also for each branch (g) of structural element E_k , branch currents are written in the following vector:

$$i_{bEk} = [i_{1bEk} \ i_{2bEk} \ i_{3bEk} \ \dots \ i_{gbEk}]^T, \tag{18}$$

where i_{bEk} is the vector of the branch currents of structural element E_k (the symbol “b” indicates that it is about the branches of the element) and i_{xbEk} is a current of branch x (where: $x = 1, 2, \dots, g$) of structural element E_k .

Therefore, for structural element E_k treated as an element of the generalized electric system, we can write the following matrix equations:

$$M_{iEk} \cdot i_{bEk} = 0, \tag{19}$$

$$i_{Ek} = -M_{pEk} \cdot i_{bEk}, \tag{20}$$

$$i_{bEk} = f(\chi_{bEk}). \tag{21}$$

Formula (21) is a characteristic of the individual branches as a vector relationship between current and average voltage.

Definition 7. The state equation system of the structural element is created using the following Equations (17) and (19)–(21).

The solution of the state equation system of structural element E_k is a set of values of the following vectors: χ_{iEk} , i_{bEk} , and χ_{bEk} , which meets all of the equations and describes the state of this structural element at given excitations, in this case the average values of the potentials of the poles of this element (matrix χ_{Ek}).

Definition 8. The structural element, the branches of which are described by the linear current–average voltage characteristic (21), is the linear structural element.

3. External Equation of the Generalized Linear Branch (Associated with the AVIS Method)

The generalized linear ε -th branch of the electric circuit of the k -th structural element is treated as a set of ideal elements connected with each other: independent voltage source, independent current source, inductor, resistor, and capacitor. Outside of this set, only two terminals are available (Figure 3).

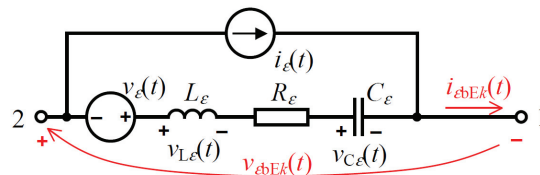


Figure 3. The generalized linear branch of the electric circuit.

Resistance R_ε of the resistor, inductance L_ε of the inductor, and capacitance C_ε of the capacitor are known. The source values of $v_\varepsilon(t)$ and $i_\varepsilon(t)$ are given in the forms of known analytical functions, e.g., in the following sinusoidal forms:

$$v_\varepsilon(t) = U_m \cdot \sin(\omega \cdot t + \psi_u) \text{ and } i_\varepsilon(t) = I_m \cdot \sin(\omega \cdot t + \psi_i), \tag{22}$$

where amplitudes U_m , I_m , initial phases ψ_u , ψ_i , and pulsation ω are known.

Based on [18] (for $m = 1$), for the ε -th branch of the k -th structural element, we can write the current–average voltage characteristics of the generalized linear branch, as follows:

$$i_{\varepsilon bEk}(t_n) = \alpha_\varepsilon \cdot \chi_{\varepsilon bEk} + \beta_\varepsilon, \tag{23}$$

where:

$$\alpha_\varepsilon = \left(\frac{R_\varepsilon}{2} + \frac{L_\varepsilon}{h} + \frac{h}{6 \cdot C_\varepsilon} \right)^{-1}, \tag{24}$$

$$\beta_\epsilon = \alpha_\epsilon \cdot \left\{ \frac{1}{h} \cdot \int_{t_{n-1}}^{t_n} v_\epsilon(t) dt + \frac{R_\epsilon}{h} \cdot \int_{t_{n-1}}^{t_n} i_\epsilon(t) dt - \left(\frac{R_\epsilon}{2} - \frac{L_\epsilon}{h} + \frac{h}{3 \cdot C_\epsilon} \right) \cdot i_{\epsilon bEk}(t_{n-1}) + \right. \\ \left. - v_{C\epsilon}(t_{n-1}) + \left(\frac{L_\epsilon}{h} + \frac{h}{6 \cdot C_\epsilon} \right) \cdot i_\epsilon(t_n) - \left(\frac{L_\epsilon}{h} - \frac{h}{3 \cdot C_\epsilon} \right) \cdot i_\epsilon(t_{n-1}) \right\}, \tag{25}$$

and

$$v_{C\epsilon}(t_n) = v_{C\epsilon}(t_{n-1}) + \frac{h}{2 \cdot C_\epsilon} \cdot i_{\epsilon bEk}(t_n) + \frac{h}{2 \cdot C_\epsilon} \cdot i_{\epsilon bEk}(t_{n-1}) - \frac{1}{C_\epsilon} \cdot \int_{t_{n-1}}^{t_n} i_\epsilon(t) dt. \tag{26}$$

4. Accuracy of the Integration Rules

The formulas for the AVIS method, presented in Section 3, and the commonly known formulas for the backward Euler and trapezoidal methods are the basis for assessing the accuracy of these integration methods. It should be noted here that we were interested in the integration methods proposed for real-time simulation. Therefore, many different integration methods used in the general approach to mathematical modeling of electrical systems were omitted here (this will be the subject of other publications).

For the purposes of this paper, the accuracy of an integration rule was assessed by considering its frequency response [3,5,9,24]. The frequency response of the integration for three rules in the discrete-time system $H(z)$ was compared with the exact frequency response of an integrator in the continuous-time system $H(s)$. Additionally, the results of the frequency responses comparison are illustrated with example waveforms for the selected branch of the electrical circuit.

For example, we considered the branch consisting of the following elements connected in series: a resistor, an inductor, and a capacitor, with the known parameters, respectively: resistance R , inductance L , and capacitance C . The branch was powered by a sinusoidal voltage source $v(t) = V_m \cdot \sin(2 \cdot \pi \cdot f \cdot t)$. Taking the supplying voltage as the input and the current as the output, $H(z)$ is the transfer function of the discrete time system, where $z = e^{j \cdot 2 \cdot \pi \cdot f \cdot h}$ (h is integration time step). Applying the above-mentioned three numerical integration methods to the integrator, appropriate transfer functions $H(z)$ were determined, which are listed in Table 1.

Table 1. Discrete-time transfer function $H(z)$ for the integration rules.

Integration Rule	Transfer Function $H(z)$
Backward Euler	$\frac{1}{R + \frac{L}{h} \cdot \frac{z-1}{z} + \frac{h}{C} \cdot \frac{z}{z-1}}$
Trapezoidal	$\frac{z+1}{R \cdot (z+1) + \frac{2L}{h} \cdot (z-1) + \frac{h}{2C} \cdot (z + \frac{4z}{z-1} + 1)}$
AVIS First Order	$\frac{\frac{1-z}{2 \cdot \pi \cdot f \cdot h} \cdot \frac{z - \cos(2 \cdot \pi \cdot f \cdot h)}{\sin(2 \cdot \pi \cdot f \cdot h)}}{\frac{R}{2} \cdot (z+1) + \frac{L}{h} \cdot (z-1) + \frac{h}{6C} \cdot \frac{z^2 + 4z + 1}{z-1}}$

The transfer function $H(s)$ of the consideration continuous-time system equals $\frac{1}{R+s \cdot L + \frac{1}{s \cdot C}}$.

Figures 4 and 5 show the accuracy as a function of frequency for the integration rules in Table 1 with the parameters presented in Table 2. Two sets of data were adopted, labeled as (1) and (2), respectively. The frequency axis is labeled in units of $\frac{1}{h}$ ($f_{pu} = f \cdot h$) up to the Nyquist frequency $\frac{1}{2h} = 0.5$.

Table 2. Parameters of the considered branch of the electrical circuit.

Parameter	V_m	R	L	C
Value of parameter (1)	320 V	100 Ω	300 mH	300 nF
Value of parameter (2)	320 V	10.0 Ω	150 mH	10.0 μ F

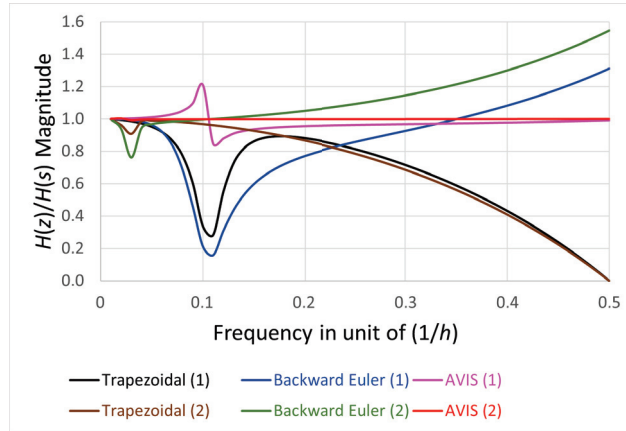


Figure 4. Magnitude ratio of the frequency response of the integration rules ($h = 0.2$ ms).

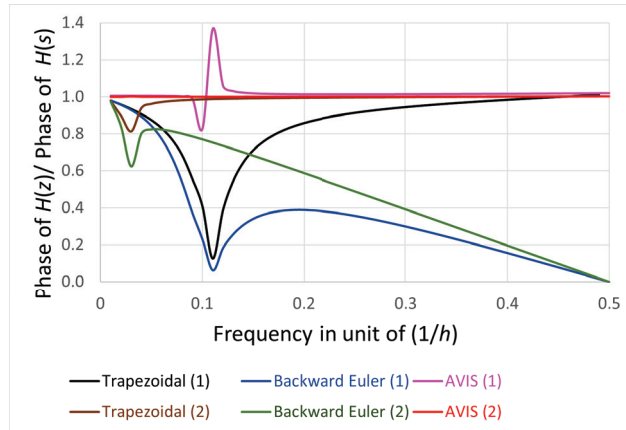


Figure 5. Phase ratio of the frequency response of the integration rules ($h = 0.2$ ms).

The “teeth” visible in the figures appear near the resonance frequencies (531 Hz for the first set and 130 Hz for the second set). The plots in Figure 4 show that the AVIS method gave very accurate magnitude responses for frequencies in the whole considered range. In addition, the AVIS method produced no phase distortion (excluding frequencies close to the resonance frequency for the first data set). This is clearly visible in the plots in Figure 5. The AVIS method was the best for the two sets of parameters considered here.

Figure 6 shows the current waveforms in the considered branch as the simulation results using three methods: backward Euler, trapezoidal, and AVIS, for the two data sets (see Table 2). These results are perfectly illustrated in the plots presented in Figures 4 and 5. For the second data set, it can be seen that the discrete values obtained from the simulation using the AVIS method (Figure 6c,d) coincided very precisely with the exact solution. Very good accuracy was also maintained at a frequency of 150 Hz (Figure 6c), close to the resonance frequency. For the first set, especially near the resonance frequency

(Figure 6a), the phase and amplitude shifts in the solution using the AVIS method are visible. However, the results obtained were acceptable in terms of accuracy. Taking into account the proximity of frequency to the resonance frequency, we achieved a satisfactory result when the difference of the simulation result with the exact solution did not exceed 20%. This difference should be determined close to the maximum values. It should be noted here that the most important effect of the real-time simulation near the resonance frequencies was the maintenance of stability. An error value greater than 20% can make the simulation unstable. The other two methods gave much worse results and were unacceptable in the context of real-time simulators.

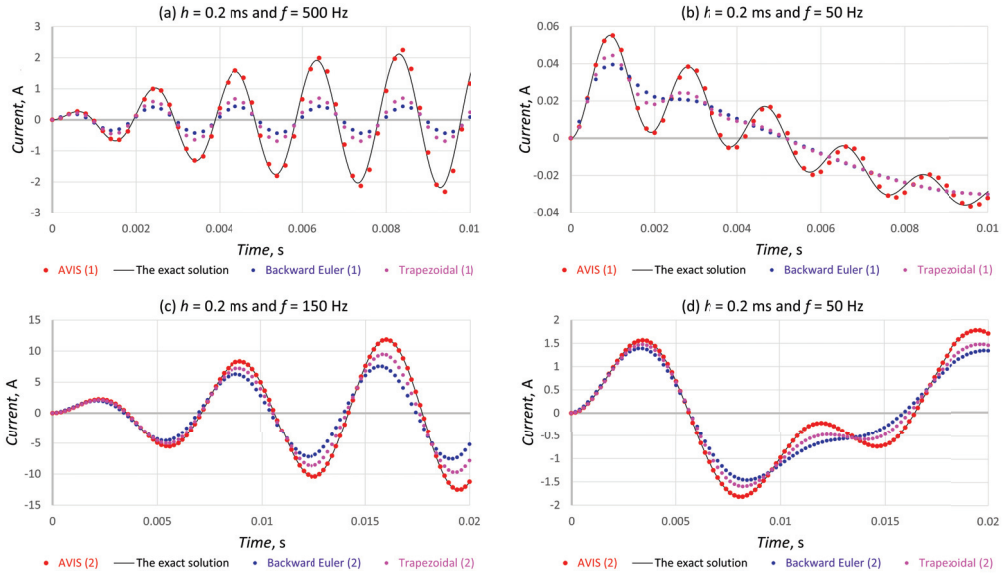


Figure 6. Current waveforms for different integration rules and for different data sets (according to Table 2).

The results presented in this section show the advantage of the proposed integration method in a real-time simulation over the other two proposed in the literature. Therefore, it is advisable to develop a new approach to the method of the mathematical modeling of the dynamics of linear electrical systems, with the possibility of parallel calculations. This is what is considered and proposed in the following sections of this paper.

5. External Equation of the Linear Electric Structural Element (Associated with the AVIS Rule)

First, an example of a three-phase structural element was considered, the schematic diagram of which is shown in Figure 7. The current–average voltage characteristic (Formula (21)) of this element takes the following form:

$$i_{bEk} = B_{bEk} + A_{bEk} \cdot \chi_{bEk}, \tag{27}$$

where:

$$i_{bEk} = [i_{1bEk} \ i_{2bEk} \ i_{3bEk}]^T \text{ and } \chi_{bEk} = [\chi_{1bEk} \ \chi_{2bEk} \ \chi_{3bEk}]^T; \tag{28}$$

$$A_{bEk} = \text{diag}(\alpha_{1Ek}, \alpha_{2Ek}, \alpha_{3Ek}) \text{ and } B_{bEk} = [\beta_{1Ek} \ \beta_{2Ek} \ \beta_{3Ek}]^T; \tag{29}$$

$$\alpha_{xEk} = \left(\frac{R_x}{2} + \frac{L_x}{h} + \frac{h}{6 \cdot C_x} \right)^{-1}; \ x = 1, 2, 3; \tag{30}$$

$$\beta_{xEk} = \alpha_{xEk} \cdot \left\{ \frac{1}{h} \cdot \int_{t_{n-1}}^{t_n} v_x(t) dt + \alpha_{xEk} \cdot \frac{R_x}{h} \cdot \int_{t_{n-1}}^{t_n} i_x(t) dt - \left(\frac{R_x}{2} - \frac{L_x}{h} + \frac{h}{3 \cdot C_x} \right) \cdot i_{xBk}(t_{n-1}) + v_{Cx}(t_{n-1}) + \left(\frac{L_x}{h} + \frac{h}{6 \cdot C_x} \right) \cdot i_x(t_n) - \left(\frac{L_x}{h} - \frac{h}{3 \cdot C_x} \right) \cdot i_x(t_{n-1}) \right\}; x = 1, 2, 3. \tag{31}$$

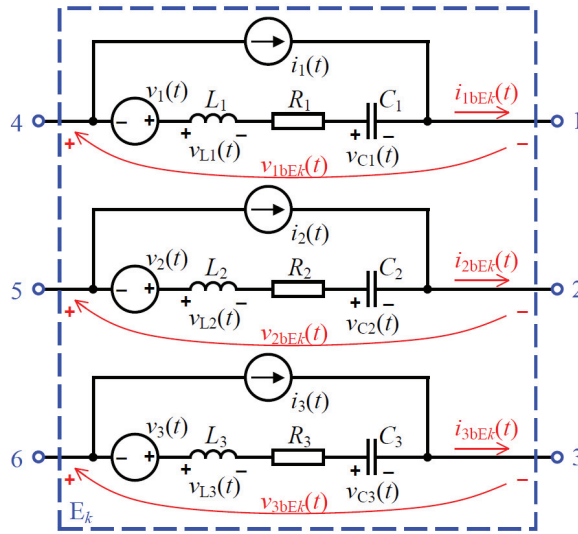


Figure 7. Structural element that reflects the three-phase element consisting of generalized linear branches.

It should be noted that matrix B_{bEk} (Equation (29)) contains values of individual physical quantities determined for the time t_{n-1} (so it is known from the previous integration step or initial conditions) and also values for time t_n , but there are values of voltage sources and current sources that are given by known algebraic equations.

Substitution Equation (17) into Equation (27) gives the following expression:

$$i_{bEk} = B_{bEk} + A_{bEk} \cdot M_{iEk}^T \cdot \chi_{iEk} + A_{bEk} \cdot M_{pEk}^T \cdot \chi_{Ek}, \tag{32}$$

which substituted into Formula (19) derives the following equation:

$$M_{iEk} \cdot B_{bEk} + M_{iEk} \cdot A_{bEk} \cdot M_{iEk}^T \cdot \chi_{iEk} + M_{iEk} \cdot A_{bEk} \cdot M_{pEk}^T \cdot \chi_{Ek} = 0. \tag{33}$$

By introducing:

$$G_{Ek} = M_{iEk} \cdot A_{bEk} \cdot M_{iEk}^T, \tag{34}$$

Equation (33) was transformed into the following form:

$$G_{Ek} \cdot \chi_{iEk} = -M_{iEk} \cdot B_{bEk} - M_{iEk} \cdot A_{bEk} \cdot M_{pEk}^T \cdot \chi_{Ek}. \tag{35}$$

It should be noted that matrix G_{Ek} is a nonsingular matrix with dimension $w \times w$. Taking this into account, it is possible to calculate the matrix of internal nodal average voltages of the structural element as follows:

$$\chi_{iEk} = -G_{Ek}^{-1} \cdot M_{iEk} \cdot B_{bEk} - G_{Ek}^{-1} \cdot M_{iEk} \cdot A_{bEk} \cdot M_{pEk}^T \cdot \chi_{Ek}. \tag{36}$$

Expression (32) gives the current vector of the internal branches of the structural element, so substitution of (36) into (32) derives the new form of Equation (32):

$$i_{bEk} = H_{Ek} \cdot B_{bEk} + H_{Ek} \cdot A_{bEk} \cdot M_{pEk}^T \cdot \chi_{Ek} \tag{37}$$

where:

$$H_{Ek} = 1 - A_{bEk} \cdot M_{pEk}^T \cdot G_{Ek}^{-1} \cdot M_{IEk} \tag{38}$$

The Formula (28) is substituted into (20), directly giving external matrix Equation (6) of the structural element in the following form:

$$i_{Ek} + M_{pEk} \cdot H_k \cdot A_{bEk} \cdot M_{pEk}^T \cdot \chi_{Ek} + M_{pEk} \cdot H_k \cdot B_{bEk} = 0. \tag{39}$$

Based on the matrices from Equation (6), it has the following form:

$$A_{Ek} = M_{pEk} \cdot H_k \cdot A_{bEk} \cdot M_{pEk}^T \text{ and } B_{Ek} = M_{pEk} \cdot H_k \cdot B_{bEk}. \tag{40}$$

The method of determining the external Equation (6) of a linear structural element with a general internal structure can be carried out on the example of a structural element with the schematic diagram shown in Figure 8.

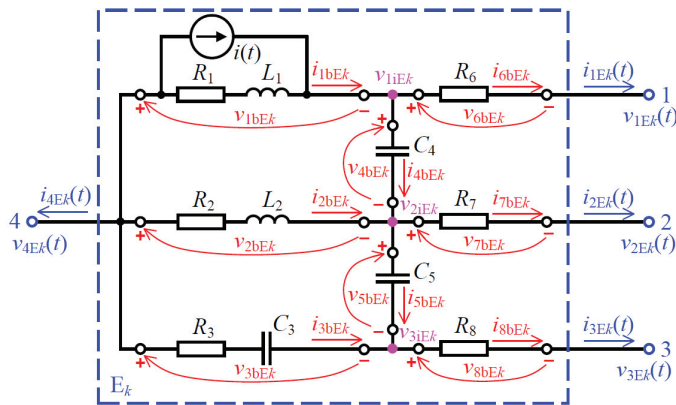


Figure 8. Schematic diagram of the internal structure of the example structural element.

Using the derived Formula (23) for the generalized linear branch of the electric circuit using the AVIS method for the considered structural element E_k , the characteristic (21) is described by Equation (27), so:

$$A_{bEk} = \text{diag}(\alpha_{1Ek}, \alpha_{2Ek}, \alpha_{3Ek}, \alpha_{4Ek}, \alpha_{5Ek}, \alpha_{6Ek}, \alpha_{7Ek}, \alpha_{8Ek}), \tag{41}$$

$$B_{bEk} = \begin{bmatrix} \alpha_{1Ek} \cdot \left\{ \frac{R_1}{h} \cdot \int_{t_{n-1}}^{t_n} i(t) dt - \left(\frac{R_1}{2} - \frac{L_1}{h} \right) \cdot i_{1bEk}(t_{n-1}) + \frac{L_1}{h} \cdot \left(i(t_n) - i(t_{n-1}) \right) \right\} \\ \alpha_{2Ek} \cdot \left(\frac{L_2}{h} - \frac{R_2}{2} \right) \cdot i_{2bEk}(t_{n-1}) \\ \alpha_{3Ek} \cdot \left(-\left(\frac{R_3}{2} + \frac{h}{3 \cdot C_3} \right) \cdot i_{3bEk}(t_{n-1}) - v_{C3}(t_{n-1}) \right) \\ \alpha_{4Ek} \cdot \left(-\left(\frac{R_4}{2} + \frac{h}{3 \cdot C_4} \right) \cdot i_{4bEk}(t_{n-1}) - v_{C4}(t_{n-1}) \right) \\ \alpha_{5Ek} \cdot \left(-\left(\frac{R_5}{2} + \frac{h}{3 \cdot C_5} \right) \cdot i_{5bEk}(t_{n-1}) - v_{C5}(t_{n-1}) \right) \\ -i_{6bEk}(t_{n-1}) \\ -i_{7bEk}(t_{n-1}) \\ -i_{8bEk}(t_{n-1}) \end{bmatrix}, \tag{42}$$

where:

$$\alpha_{1Ek} = \left(\frac{R_1}{2} + \frac{L_1}{h} \right)^{-1}, \alpha_{2Ek} = \left(\frac{R_2}{2} + \frac{L_2}{h} \right)^{-1}, \alpha_{3Ek} = \left(\frac{R_3}{2} + \frac{h}{6 \cdot C_3} \right)^{-1},$$

$$\alpha_{4Ek} = \frac{6 \cdot C_4}{h}, \alpha_{5Ek} = \frac{6 \cdot C_5}{h}, \alpha_{6Ek} = \frac{2}{R_6}, \alpha_{7Ek} = \frac{2}{R_7}, \alpha_{8Ek} = \frac{2}{R_8}. \quad (43)$$

By using Formulas (34) and (38), respectively, it is possible to get the matrices (40) and also Equation (6), which is the external equation of considered structural element E_k .

6. External Equation of the Structural Element as the Internal Connection of the Structural Elements with Known External Equations

In the real-time simulation of the operating states of complex electrical systems, it is useful to apply parallel computing in order to speed up the results of the calculations, without degrading the accuracy. The structural element extraction of the complex electrical system and using the previously described mathematical modeling method give the possibility to apply parallel computing in some parts of the computing process. At some stage of the calculations, it is necessary to solve the system of linear Equation (10) for the analyzed electrical system. Matrix A_S in Equation (10) is a sparse matrix for electrical systems with a high number of nodes (ζ). Even that feature does not enable a significant solving speedup of that equation system. This is due to issues with the effective parallelization of the procedure of solving systems of linear equations. The author of this paper proposed on the particular stage of the calculation process the aggregation of some structural elements' groups. This tends to replace a few structural elements in the given group by one structural element. This gives the opportunity to significantly reduce the electrical system nodes and reduce the number of equations in Equation (10), so it can speed up solving (even if the calculations are carried out sequentially in this part).

It was assumed that the considered electrical system consisted of structural elements for which the external equations of the form (6) were known. In the general case, the internal structures of the structural elements are not known. Due to that, the extraction of the internal branches of the structural elements being a product of aggregation was impossible. In this case, using only the pole average potentials of the aggregated structural elements and the currents of their external branches was required.

The method of determining the external Equation (6) of a linear structural element resulting from the aggregation of three structural elements, for which external equations are known, was considered on the example of a fragment of the electrical system with the schematic diagram shown in Figure 9.

The external equations of aggregated structural elements are known and have the form of Formula (6). The equivalent structural element E (including the aggregation of three $E_1, E_2,$ and E_3 structural elements) will have three poles and five internal nodes (Figure 9, right side). The vectors of the pole average potentials and currents of the external branches of the equivalent structural element E have the form of Formulas (5) and (4), respectively.

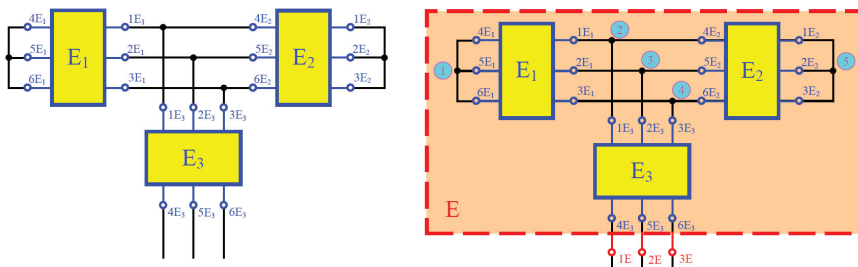


Figure 9. Schematic diagram of a fragment of the electrical system in which structural elements are aggregated and a diagram of the equivalent structural element.

For five internal nodes ($w = 5$), based on Formula (13), the vector of average potentials of these nodes is written as:

$$\chi_{iE} = [\chi_{1iE} \ \chi_{2iE} \ \chi_{3iE} \ \chi_{4iE} \ \chi_{5iE}]^T. \tag{44}$$

Formula (17) is written for branch average voltages, and in the aggregation of structural elements, it does not apply, because there is no reason to recognize, e.g., terminals $1E_1$ and $4E_1$ as terminals of the same branch. In the case of the aggregation of structural elements, the average potentials of their nodes (poles of aggregated structural elements) should be associated with the average potentials of the poles and internal nodes (Equation (44)) of the equivalent structural element, as follows:

$$[\chi_{E1} \ \chi_{E2} \ \chi_{E3}]^T = -M_{iE}^T \cdot \chi_{iE} - M_{pE}^T \cdot \chi_{E'}, \tag{45}$$

where the incidence matrix of internal nodes and the incidence matrix of poles are determined according to Definitions 5 and 6, respectively.

In this case, the vector of currents of the internal branches of the equivalent structural element E have the form:

$$i_{bE} = [i_{E1} \ i_{E2} \ i_{E3}]^T, \tag{46}$$

and taking into account the characteristics of aggregated structural elements, the following equation is obtained:

$$i_{bE} = B_{bE} - A_{bE} \cdot [\chi_{E1} \ \chi_{E2} \ \chi_{E3}]^T, \tag{47}$$

where:

$$A_{bE} = \begin{bmatrix} A_{E1} & 0 & 0 \\ 0 & A_{E2} & 0 \\ 0 & 0 & A_{E3} \end{bmatrix} \text{ and } B_{bE} = - \begin{bmatrix} B_{E1} \\ B_{E2} \\ B_{E3} \end{bmatrix}. \tag{48}$$

Substituting Equation (45) into Formula (47), the following formula is obtained:

$$i_{bE} = B_{bE} + A_{bE} \cdot M_{iE}^T \cdot \chi_{iE} + A_{bE} \cdot M_{pE}^T \cdot \chi_{E'}, \tag{49}$$

which, after substitution into Formula (19), gives exactly the same form as Equation (33). Using the same reasoning in the sequence of Formulas (33)–(40), we obtained formulas for matrices appearing in the external equation of the equivalent structural element E.

7. The Algorithm for the Mathematical Modeling of Linear Electrical Systems with Parallel Calculations

The method for the mathematical modeling of linear electrical systems presented above can be used to simulate the operating states of these systems with parallel calculations. This is particularly applicable in real-time simulators. The rest of this paper presents an example algorithm for using the proposed method to analyze a linear electrical system using parallel calculations.

The preparations for the simulation process were as follows:

1. Create an equivalent diagram of the modeled electrical system, and determine the values of the parameters of individual system components (in the proposed method, it is an electrical system as defined in Definition 1); determine the initial values of the individual physical quantities;
2. In the equivalent scheme, structural elements may already be naturally separated (in terms of circuit theory, they will be electric multi-poles), or these elements should be arbitrarily separated;
3. Identify and mark the nodes of the modeled electrical system (nodes in places where structural elements are connected with each other). Chose one of the identified nodes

- as the reference node. For the other nodes, formulate the vector of average potentials according to Equation (2);
4. Determine the poles of each extracted structural element, and formulate vectors according to Equations (4) and (5);
 5. Identify and mark internal nodes and branches of individual structural elements (if necessary). Formulate vectors defined by Formulas: (13), (15), and (18);
 6. Determine the values of the incidence matrix of individual structural elements according to Definition 4. Determine the values of the incidence matrix of individual structural elements according to Definitions 5 and 6 (if necessary).

If an electrical system with a fixed structure is considered, but the simulation process assumes changes in parameter values (e.g., change in switch resistance), then it is expedient to determine the values of the elements of the respective matrix and expressions for the case with closed switch resistance and the matrix for the case with open switch resistance (in the algorithm descriptions, these are matrices with the annotation “if necessary”). In the simulation process, appropriate matrices and expressions are used for the same structural element, but appropriate due to the condition of the switch (this speeds up the calculations, as it is not necessary to calculate the values of matrix elements during the simulation). The determined matrices and expressions can be stored in memory in the form of sets, as presented, for example, in Point 0.2 of the algorithm shown in Figure 10. The example algorithm for the computer simulation of the operating states of the electrical system using the proposed method with parallel calculations is shown in Figure 10.

Figure 11 shows an example algorithm for determining constant matrix and constant expressions for structural elements, which are described in Sections 3, 5 and 6 of this paper. It should be noted that the proposed method for the mathematical modeling of linear electrical systems with parallel calculations can be applied to virtually any system with any structure and also using other methods of integrating differential equations.

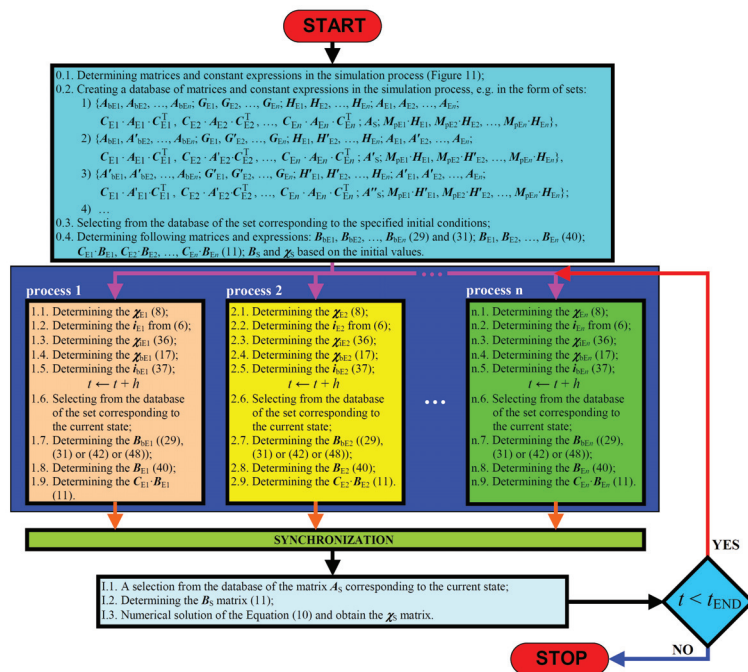


Figure 10. The example algorithm for the computer simulation of the operating states of the electrical system using the proposed theory with parallel calculations.

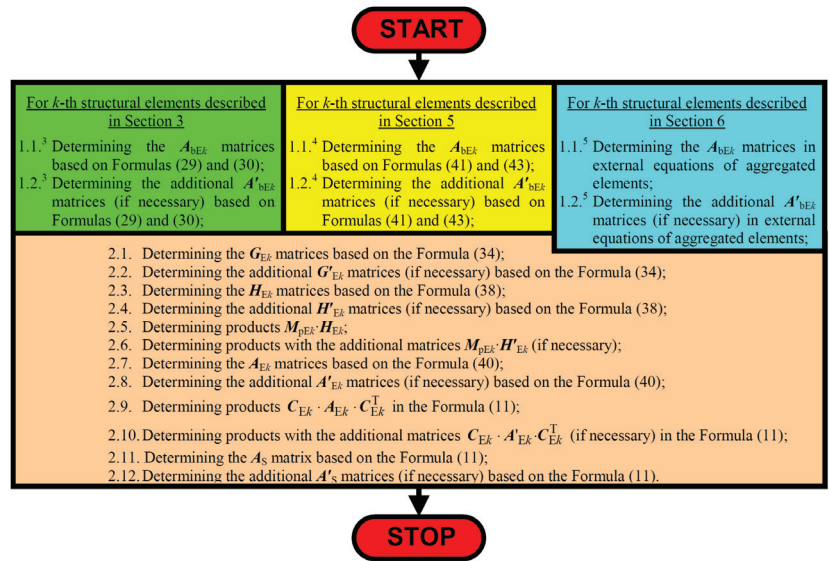


Figure 11. The example algorithm for determining constant matrix and constant expressions for structural elements described in Sections 3, 5 and 6.

The next section presents an example of using the proposed method to analyze the operating states of a linear electrical system.

8. The Example of Using the Proposed Method

The application of the method for the mathematical modeling of linear electric systems with parallel calculations proposed in this paper is shown on the example of a fragment of a MV power distribution network with distributed generation in one phase.

The equivalent diagram of the modeled electrical system is shown in Figure 12. The E₁ structural element is a substitute voltage source representing the power system, in the form of three independent branches (three phases), consisting of three series-connected ideal elements: voltage source, resistor, and inductor (based on Thevenin’s theorem).

The system nodes, marked in bold by 5, 6, and 7, represent busbars in the MV power substation. The E₂ structural element is an equivalent electric power receiver that contains a fragment of the network that is not modeled in detail. The E₃ structural element is a representation of a MV power line section that is derived from the power substation (from Busbars 5, 6, and 7). Element E₄ represents an unconventional electric power receiver, whose equivalent diagram is shown in Figure 8. The ideal current source in this element represents a single-phase generating unit (as a distributed generation) that uses renewable energy sources (e.g., a series of single-phase PV installations). The E₅ structural element is a representation of another section of the medium voltage power line that connects the E₄ load with the E₆ and E₇ loads. Structural elements E₆ and E₇ are representations of concentrated loads. The parameters of individual structural elements are summarized in Table 3.

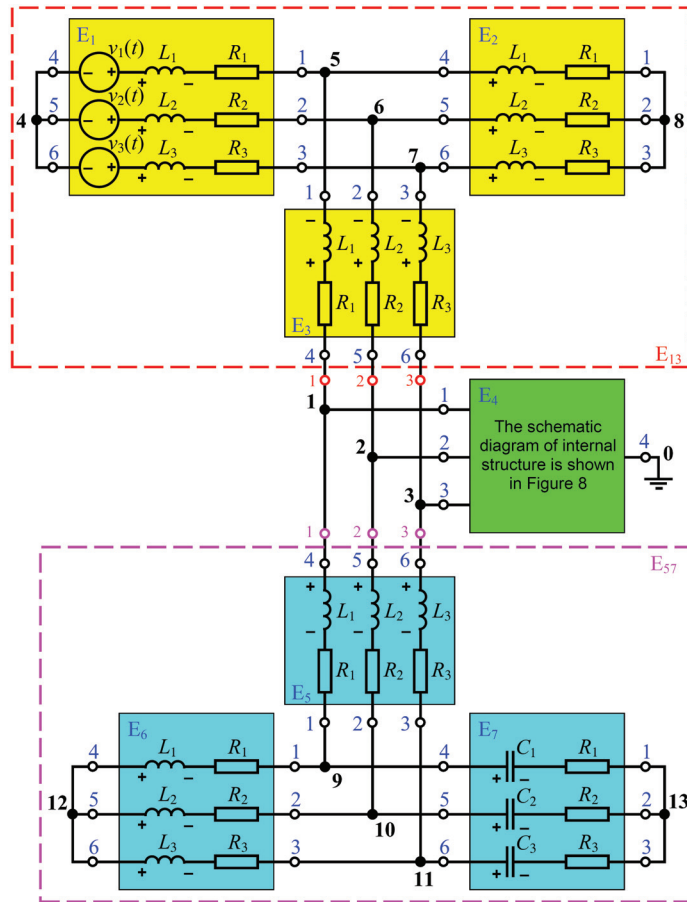


Figure 12. The equivalent diagram of a fragment of a MV power distribution network with distributed generation in one phase.

Table 3. Parameters of the structural elements of the modeled electrical system.

E ₂	E ₃	E ₅	E ₆	E ₇	
$R_1 = 2.64 \text{ k}\Omega$	$R_1 = 1.16 \text{ }\Omega$	$R_1 = 1.16 \text{ }\Omega$	$R_1 = 2.62 \text{ k}\Omega$	$R'_1 = 2.62 \text{ m}\Omega$	
$R_2 = 2.64 \text{ k}\Omega$	$R_2 = 1.16 \text{ }\Omega$	$R_2 = 1.16 \text{ }\Omega$	$R_2 = 2.62 \text{ k}\Omega$	$R'_2 = 2.62 \text{ m}\Omega$	
$R_3 = 2.64 \text{ k}\Omega$	$R_3 = 1.16 \text{ }\Omega$	$R_3 = 1.16 \text{ }\Omega$	$R_3 = 2.62 \text{ k}\Omega$	$R'_3 = 2.62 \text{ k}\Omega$	
$L_1 = 3.05 \text{ H}$	$L_1 = 122 \text{ mH}$	$L_1 = 120 \text{ mH}$	$L_1 = 1.05 \text{ H}$	$L'_1 = 10.5 \text{ }\mu\text{H}$	
$L_2 = 3.05 \text{ H}$	$L_2 = 122 \text{ mH}$	$L_2 = 120 \text{ mH}$	$L_2 = 1.05 \text{ H}$	$L'_2 = 10.5 \text{ }\mu\text{H}$	
$L_3 = 3.05 \text{ H}$	$L_3 = 122 \text{ mH}$	$L_3 = 120 \text{ mH}$	$L_3 = 1.05 \text{ H}$	$L'_3 = 1.05 \text{ H}$	
				$C_1 = 8.30 \text{ }\mu\text{F}$	
				$C_2 = 8.30 \text{ }\mu\text{F}$	
				$C_3 = 8.30 \text{ }\mu\text{F}$	
E ₁					
$R_1 = 163 \text{ m}\Omega$	$R_2 = 163 \text{ m}\Omega$	$R_3 = 163 \text{ m}\Omega$	$L_1 = 52.1 \text{ mH}$	$L_2 = 52.1 \text{ mH}$	$L_3 = 52.1 \text{ mH}$
$V_{m1} = 12.3 \text{ kV}$	$V_{m2} = 12.3 \text{ kV}$	$V_{m3} = 12.3 \text{ kV}$	$\psi_{V1} = 0 \text{ rad}$	$\psi_{V2} = -\frac{2\pi}{3} \text{ rad}$	$\psi_{V3} = \frac{2\pi}{3} \text{ rad}$
E ₄					
$R_1 = 2.02 \text{ k}\Omega$	$R_2 = 2.02 \text{ k}\Omega$	$R_3 = 8.02 \text{ k}\Omega$	$R_6 = 163 \text{ m}\Omega$	$R_7 = 163 \text{ m}\Omega$	$R_8 = 163 \text{ m}\Omega$
$L_1 = 14.1 \text{ H}$	$L_2 = 14.1 \text{ H}$	$C_3 = 10.8 \text{ }\mu\text{F}$	$C_4 = 1.20 \text{ }\mu\text{F}$	$C_5 = 1.20 \text{ }\mu\text{F}$	

Let us apply the algorithm proposed in Section 7 of this paper. The initial conditions are: the current value for each inductor and voltage on each capacitor. Thus, the following vectors are given:

$$\begin{aligned}
 \mathbf{i}_{bE1} &= [i_{1bE1}(t_0) \quad i_{2bE1}(t_0) \quad i_{3bE1}(t_0)]^T, \mathbf{i}_{bE2} = [i_{1bE2}(t_0) \quad i_{2bE2}(t_0) \quad i_{3bE2}(t_0)]^T, \\
 \mathbf{i}_{bE3} &= [i_{1bE3}(t_0) \quad i_{2bE3}(t_0) \quad i_{3bE3}(t_0)]^T, \mathbf{i}_{bE5} = [i_{1bE5}(t_0) \quad i_{2bE5}(t_0) \quad i_{3bE5}(t_0)]^T, \\
 \mathbf{i}_{bE6} &= [i_{1bE6}(t_0) \quad i_{2bE6}(t_0) \quad i_{3bE6}(t_0)]^T, \\
 \mathbf{v}_{CE7} &= [v_{C1E7}(t_0) \quad v_{C2E7}(t_0) \quad v_{C3E7}(t_0)]^T, \mathbf{i}_{bE4} = [i_{1bE4}(t_0) \quad i_{2bE4}(t_0)]^T, \\
 \text{and } \mathbf{v}_{CE4} &= [v_{C3E4}(t_0) \quad v_{C4E4}(t_0) \quad v_{C5E4}(t_0)]^T.
 \end{aligned}
 \tag{50}$$

The nodes of the modeled electrical system are marked in Figure 9 in bold: **0, 1, 2, ..., 13** (where $v_0 = 0$). Based on Equation (2), we have:

$$\chi_S = [\chi_1 \quad \chi_2 \quad \chi_3 \quad \chi_4 \quad \chi_5 \quad \chi_6 \quad \chi_7 \quad \chi_8 \quad \chi_9 \quad \chi_{10} \quad \chi_{11} \quad \chi_{12} \quad \chi_{13}]^T. \tag{51}$$

For individual structural elements, we write matrices based on Equations (4) and (5), respectively:

$$\begin{aligned}
 \chi_{Ek} &= [\chi_{1Ek} \quad \chi_{2Ek} \quad \chi_{3Ek} \quad \chi_{4Ek} \quad \chi_{5Ek} \quad \chi_{6Ek}]^T, \text{ where: } k = 1, 2, 3, 5, 6 \text{ and } 7; \\
 \chi_{E4} &= [\chi_{1E4} \quad \chi_{2E4} \quad \chi_{3E4} \quad \chi_{4E4}]^T; \\
 \mathbf{i}_{Ek} &= [i_{1Ek} \quad i_{2Ek} \quad i_{3Ek} \quad i_{4Ek} \quad i_{5Ek} \quad i_{6Ek}]^T, \text{ where: } k = 1, 2, 3, 5, 6 \text{ and } 7; \\
 \mathbf{i}_{E4} &= [i_{1E4} \quad i_{2E4} \quad i_{3E4} \quad i_{4E4}]^T.
 \end{aligned}
 \tag{52}$$

The potentials of internal nodes, the voltage at branch terminals, and the branch currents for the E_4 structural element are identical to the formulas presented in Section 5.

The incidence matrices (based on Definition 6) for poles of individual structural elements $E_1, E_2, E_3, E_5, E_6,$ and E_7 are the same. These matrices and incidence matrices (based on Definition 4) for individual structural elements of the modeled electrical system are easy to determine and are not presented here.

Then, the process of mathematical modeling of the states of operation of the analyzed electrical system proceeds in accordance with the algorithms shown in Figures 10 and 11.

Figure 13 presents examples of the simulation results of the analyzed electrical system (where: $f = 50.0$ Hz and $h = 0.2$ ms). Figure 13a,b shows the waveforms of the currents of structural element E_1 in a transient state caused by switching on ($t = 0$) of the three-phase supply voltage system. All initial conditions equal zero (all elements of vectors in (50) equal zero). Figure 13a shows the simulation results using the AVIS method and Figure 13b the results using the trapezoidal method. There were clear differences in the accuracy of the results, of course in favor of the AVIS method.

Figure 13c also shows the waveforms of the currents of structural element $E1$ characterizing a different transient operating state (using the AVIS method only). This state arose as a result of a simultaneous, significant reduction of the parameters values in two phases (L1 and L2) of the structural element E_6 (see Table 3). In this case, there was a short circuit (low impedance) between the system nodes: **9, 10,** and **12**. The short circuit occurred at $t = 50$ ms and ended at $t = 98$ ms. This is a kind of transient short circuit. At the end of the short circuit event, all parameters of the analyzed electrical system returned to their pre-short circuit values.

The same results can be obtained using the aggregation of structural elements, as described in Section 6 of this paper, with respect to elements $E_1, E_2,$ and E_3 (as equivalent element E_{13} ; Figure 9) and $E_5, E_6,$ and E_7 (as equivalent element E_{57} ; Figure 9).

The given results for the example system are only to illustrate the mathematical modeling method proposed in this paper. This simple example was deliberately chosen to achieve a clear effect. A detailed analysis of this example is not the subject of this paper.

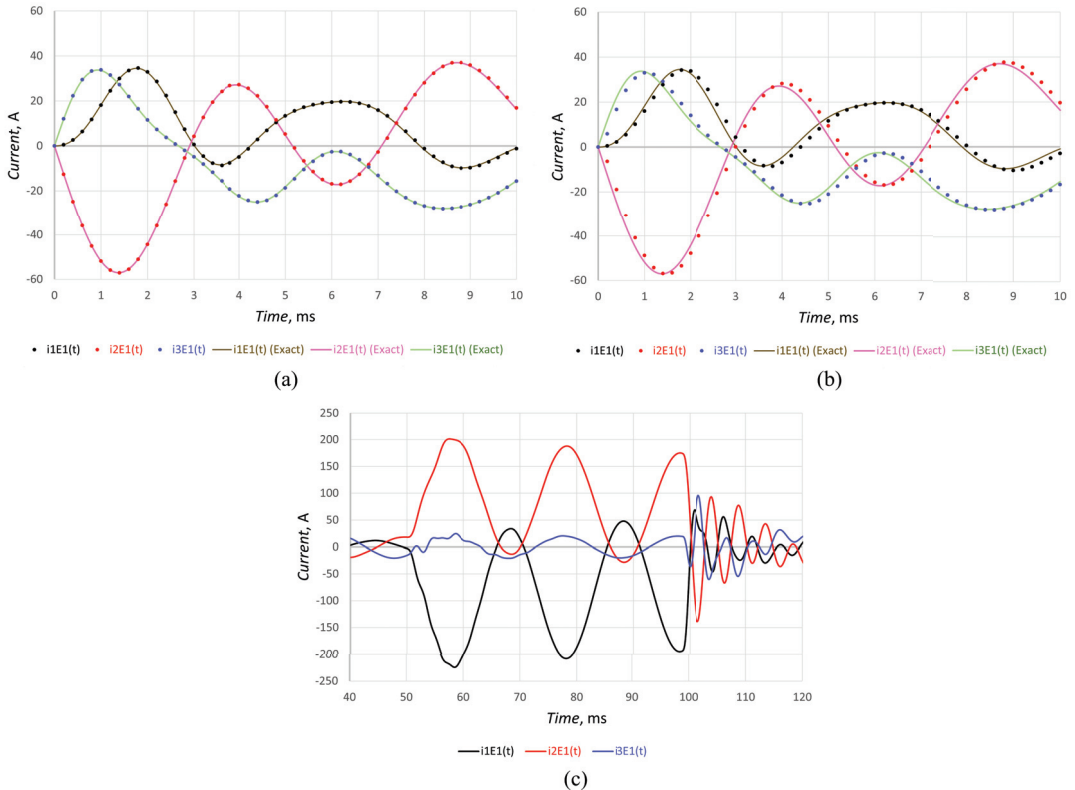


Figure 13. Waveforms of the currents of the structural element E_1 in a transient state caused by switching on of the three-phase supply voltage system ((a) the AVIS method and (b) the trapezoidal rule) and the currents of this structural element during the short circuit ((c) the AVIS method).

9. Conclusions

The development of modern real-time applications, in which complex electrical systems are modeled, is possible when finding a compromise between the accuracy and the time for obtaining results. The problem of accelerating the computational process in the simulation of the operating states of complex electrical systems is still valid. One of the interesting solutions is the use of parallel computations, which was also taken into account in the mathematical modeling method presented in this paper. Another important thread in this topic, poorly developed in the literature, is the use of numerical methods to solve differential equations in mathematical models of power systems with a relatively long integration time step. This was the method used in the solution presented in this paper.

This paper proposed the scientifically acceptable general principle offered to the mathematical modeling of linear electrical systems with parallel calculation. The presented method for the mathematical modeling of linear electrical systems is based on the use and appropriate conceptual approach of two methods known from the electrical circuits theory: methods of the analysis of electrical circuits using multi-terminal electrical components and the nodal method. The proposed method allows the distribution of calculations into individual processes that can be carried out in parallel and simultaneously. In this way, the

effect of accelerated calculations is obtained while maintaining the accuracy of the results. However, the main advantage over other algorithms is the use of the method based on average voltages in the integration step (AVIS method). The attention was focused on describing an ordered algorithm. However, the evidence of its effective application in the analysis of the dynamics of electric power and electromechanical systems was indicated in the works carried out by the team of authors from the Institute of Electrical Engineering UTP University of Science and Technology in Bydgoszcz (Poland).

The conclusions of the work described in this paper are as follows:

- This article alone presented the scientifically acceptable general principle offered to the mathematical modeling of dynamics of linear electrical systems with parallel computations. Appropriate formulas for mathematical modeling associated with the method of integrating differential equations based on average voltages in the integration step (AVIS method) were derived. The detailed derivation allowed a simple adaptation of the proposed algorithm to various other integration methods (e.g., backward Euler or trapezoidal methods). However, as was shown in this paper, the applied AVIS method gave the best results in the context of accuracy and the stability of operation in the considered cases.
- The advantage of the AVIS method used over the two other methods proposed in the literature was shown on the example of a series RLC connection. Comparing the frequency responses (magnitude and phase) for discrete and continuous (exact solution) values, the applied AVIS method gave the best results. It is necessary to note at this point that this result cannot be generalized to all cases. Even for the same structure of the electrical system, but for different parameters, the effect may be unsatisfactory. This does not diminish the advisability of using the proposed algorithm and the mathematical modeling method, even if it were only about specific cases.
- In the scientific work carried out at the Institute of Electrical Engineering UTP University of Science and Technology in Bydgoszcz (Poland), using the AVIS method, the problems of simulation stability were identified when there were very small capacitances in the analyzed system. In these cases, it usually helps to apply other known integration methods only to those branches of the circuit with these very small capacitances, of course sticking to the basics of the method, i.e., average voltages in the integration step. This thread will be considered in future publications.
- The proposed algorithm also allows for a partial solution to the problem of the inability to perform parallel calculations, e.g., to solve a system of linear equations. The method of the aggregation of structural elements of the analyzed system presented in this paper allows reducing the number of nodes occurring in an explicit manner, and consequently reducing the number of equations in the system that should be solved numerically (sequentially). In this way, the acceleration of the calculations (solutions of the system of equations) was achieved while maintaining the accuracy of the results.

The proposed algorithm has been verified in many works on real-time simulators of the operating states of complex electrical systems, e.g., [11,19–22]. This method also has interest for other researchers who analyze real-time management problems of complex electrical systems, including issues regarding procedures for the dispatcher switching off MV power lines in electric power deficit states [25] and research on the charging process of electric vehicle batteries [26].

The author is currently preparing a version of the proposed method for the mathematical modeling of the operating states of nonlinear electrical systems with parallel calculations.

Funding: This research received no external funding.

Institutional Review Board Statement: Not applicable.

Informed Consent Statement: Not applicable.

Data Availability Statement: Data available on request to the author.

Conflicts of Interest: The author declares no conflict of interest.

Abbreviations

The following abbreviations are used in this paper:

AVIS method	The integration method based on average voltages in the integration step
EMTP	The ElectroMagnetic Transients Program
IEE UTP	Institute of Electrical Engineering UTP University of Science and Technology in Bydgoszcz (Poland)
GPU	Graphics processing unit

References

1. Kron, G. *Tensors for Circuits*, 2nd ed.; Dover Publications: New York, NY, USA, 1959.
2. Dommel, H.W. Digital Computer Solution of Electromagnetic Transient in Single- and Multiphase Networks. *IEEE Trans. Power Appar. Syst.* **1969**, *4*, 388–399. [[CrossRef](#)]
3. Dommel, H.W. *Electromagnetic Transients Program Theory Book*; Bonneville Power Administration: Portland, OR, USA, 1995.
4. Araujo, A.E. Numerical Instabilities in Power System Transient Simulation. Ph.D. Thesis, Faculty of Graduate Studies Electrical Engineering, University of British Columbia, Vancouver, BC, Canada, 1993.
5. Marti, J.R.; Lin, J. Suppression of Numerical Oscillations in the EMTP. *IEEE Trans. Power Syst.* **1989**, *2*, 739–747. [[CrossRef](#)]
6. Crow, M. *Computational Methods for Electric Power System*, 3rd ed.; CRC Press: Boca Raton, FL, USA, 2016.
7. Uriarte, F.M. *Multicore Simulation of Power System Transients*; The Institution of Engineering and Technology: London, UK, 2013.
8. Watson, N.R.; Arrillaga, J. *Power Systems Electromagnetic Transients Simulation*, 1st ed.; The Institution of Engineering and Technology: London, UK, 2003.
9. Bayoumi, M. An FPGA-Based Real-Time Simulator for the Analysis of Electromagnetic Transients in Electrical Power Systems. Ph.D. Thesis, Department of Electrical and Computer Engineering, University of Toronto, Toronto, ON, Canada, 2009.
10. Fajfer, M. Concurrent Computing in the Simulation of the Electric Circuit with the Use of DSP. Ph.D. Thesis, Faculty of Electrical Engineering Poznań, University of Technology, Poznań, Poland, 2019. (In Polish)
11. Klosowski, Z. Real-Time Simulation of Electric Power Network with Wind Turbine. Ph.D. Thesis, Faculty of Electrical and Control Engineering Gdańsk, University of Technology, Gdańsk, Poland, 2019. (In Polish)
12. Estrada, L.; Vázquez, N.; Vaquero, J.; de Castro, Á.; Arau, J. Real-Time Hardware in the Loop Simulation Methodology for Power Converters Using LabVIEW FPGA. *Energies* **2020**, *13*, 373. [[CrossRef](#)]
13. Faruque, M.O.; Strasser, T.; Lauss, G.; Jalili-Maradi, V.; Forsyth, P.; Dufour, C.; Dinavahi, V.; Monti, A.; Kotsampopoulos, P.; Martinez, J.A.; et al. Real-Time Simulation Technologies for Power Systems Design, Testing and Analysis. *IEEE Power Energy Technol. Syst. J.* **2015**, *2*, 63–75. [[CrossRef](#)]
14. White, J.K.; Sangiovanni-Vincentelli, A. *Relaxation Techniques for the Simulation of VLSI Circuits*; Kluwer: Norwell, MA, USA, 1987.
15. Cox, P.F.; Burch, R.G.; Hocevar, D.E.; Yang, P.; Epler, B.D. Direct circuit simulation algorithms for parallel processing (VLSI). *IEEE Trans. Comput. Aided Des. Integr. Circuits Syst.* **1991**, *6*, 714–725. [[CrossRef](#)]
16. Frohlich, N.; Riess, B.M.; Wever, U.A.; Zheng, Q. A new approach for parallel simulation of VLSI circuits on a transistor level. *IEEE Trans. Circuits Syst. I Fundam. Theory Appl.* **1998**, *6*, 601–613. [[CrossRef](#)]
17. Thornquist, H.K.; Keiter, E.R.; Hoekstra, R.J.; Day, D.M.; Boman, E.G. A parallel preconditioning strategy for efficient transistor-level circuit simulation. In Proceedings of the IEEE/ACM International Conference on Computer-Aided Design—Digest of Technical Papers, San Jose, CA, USA, 2–5 November 2009; pp. 410–417.
18. Plakhtyna, O. Numerical One-Step Method of Electric Circuits Analysis and Its Application in Electromechanical Tasks. *Sci. J. Khar'kov Tech. Univ.* **2008**, *30*, 223–225. (In Ukrainian)
19. Klosowski, Z.; Cieślík, S. Real-time simulation of power conversion in doubly fed induction machine. *Energies* **2020**, *13*, 673. [[CrossRef](#)]
20. Klosowski, Z.; Cieślík, S. Stability Analysis of Real-Time Simulation of a Power Transformer's Operating Conditions. *Acta Energetica* **2018**, *35*, 31–38.
21. Plakhtyna, O.; Kutsyk, A. A hybrid model of the electrical power generation system. In Proceedings of the 10th International Conference on Compatibility, Power Electronics and Power Engineering (CPE-POWERENG), Bydgoszcz, Poland, 29 June–1 July 2016; pp. 16–20.
22. Plakhtyna, O.; Kutsyk, A.; Semeniuk, M. Real-Time Models of Electromechanical Power Systems, Based on the Method of Average Voltages in Integration Step and Their Computer Application. *Energies* **2020**, *13*, 2263. [[CrossRef](#)]
23. Reibiger, A. Networks, Multipoles and Multiports. In Proceedings of the Conference: Circuit Theory and Design (ECCTD), Dresden, Germany, 8–12 September 2013.
24. Liu, J.; Wei, T.; Liu, J.; Wei, Z.; Hou, J.; Xiang, Z. Suppression of Numerical Oscillations in Power System Electromagnetic Transient Simulation via 2S-DIRK Method. In Proceedings of the 2016 IEEE PES Asia-Pacific Power and Energy Conference (APPEEC), Xi'an, China, 2016; pp. 2230–2235.

25. Bieliński, K.S.; Bieliński, W. Procedures for dispatcher switching off of MV power lines in electric power deficit states (Procedury dyspozytorskiego wyłączenia linii średniego napięcia w stanach deficytu mocy). *Rynek Energii* **2010**, *6*, 38–45. (In Polish)
26. Bieliński, K.S.; Młodzikowski, P. Selected results of research on the charging process of electric vehicle batteries (Wybrane wyniki badań przebiegu procesu ładowania akumulatorów pojazdów elektrycznych). *Przegląd Elektrotechniczny* **2019**, *10*, 52–55. (In Polish)

Article

An RTDS-Based Testbed for Investigating the Impacts of Transmission-Level Disturbances on Solar PV Operation

Manisha Maharjan, Almir Ekic, Bennett Strombeck and Di Wu *

Department of Electrical and Computer Engineering, North Dakota State University (NDSU), Fargo, ND 58102, USA; manisha.maharjan@ndsu.edu (M.M.); almir.ekic@ndsu.edu (A.E.); bennett.strombeck@ndsu.edu (B.S.)

* Correspondence: di.wu.3@ndsu.edu

Abstract: The increasing penetration of renewable energy resources such as solar and wind via power electronic inverters is challenging grid dynamics, as well as grid planning, operation, and protection. Recently, the North American Electric Reliability Corporation (NERC) has reported a series of similar events of the unintended loss of solar generation in Southern California over a large geographic area following the transmission-level disturbances. These events highlight the importance of understanding the characteristics of the transmission-side disturbances propagating into the distribution systems and their impacts on the operation of inverter-based resources. In this paper, a real-time electromagnetic simulation testbed is constructed for real-time electromagnetic simulations to generate realistic transmission-level disturbances and investigate their impacts on the solar PV operation under different fault types and locations, solar penetration levels, and loading levels. Through the simulation analysis and grid strength assessment, it is found that the grid strength at points of integration (POIs) of solar PVs significantly affects the transient stability of solar generators. Particularly, undesirable transient stability events are more likely to occur at the weak POIs following the transmission-level disturbances. Moreover, undesirable transient stability events become severer when the transmission-level disturbance is closer to the weak POIs or the disturbances become more serious. Additionally, the impact of the transmission-level disturbances on the solar PVs at the weak POIs exacerbate with the increasing solar penetration levels and loading levels. Thus, it is important to study and develop new technologies for grid planning, operation, and protection in weak grid conditions to address the emerging issues of integrating the high penetration of solar PVs and other IBRs.

Citation: Maharjan, M.; Ekic, A.; Strombeck, B.; Wu, D. An RTDS-Based Testbed for Investigating the Impacts of Transmission-Level Disturbances on Solar PV Operation. *Energies* **2021**, *14*, 3867. <https://doi.org/10.3390/en14133867>

Academic Editor: Jesús Polo

Received: 14 May 2021
Accepted: 18 June 2021
Published: 27 June 2021

Publisher's Note: MDPI stays neutral with regard to jurisdictional claims in published maps and institutional affiliations.



Copyright: © 2021 by the authors. Licensee MDPI, Basel, Switzerland. This article is an open access article distributed under the terms and conditions of the Creative Commons Attribution (CC BY) license (<https://creativecommons.org/licenses/by/4.0/>).

Keywords: solar photovoltaics; transmission-level faults; grid strength; real-time simulation

1. Introduction

The electric power grid is undergoing a rapid change driven by the high penetration of renewable energy resources such as solar and wind via power electronic inverters. While these inverter-based resources (IBRs) can use power electronic controls to respond to grid disturbances nearly instantaneously and thus support grid reliability, they are challenging grid planning, operation, and protection [1]. The North American Electric Reliability Corporation (NERC) recently reported a series of similar events of the unintended loss of solar generation following the transmission-level disturbances that occurred from 2016 to 2020 in the Southern California region of the Western Electricity Coordinating Council's footprint [1–4].

- On 16 August 2016, the transmission system owned by Southern California Edison experienced thirteen 500 kV line faults, and the system owned by the Los Angeles Department of Water and Power experienced two 287 kV faults as a result of the fire. The most significant event resulted in the loss of nearly 1200 MW. There were no solar PV facilities de-energized as a direct consequence of the fault event; rather, the facilities ceased output as a response to the fault on the system [1].

- On 9 October 2017, the fire caused two transmission system faults near the Serrano substation, east of Los Angeles. The first fault was a normally cleared phase-to-phase fault on a 220 kV transmission line, and the second fault was a normally cleared phase-to-phase fault on a 500 kV transmission line. Both faults resulted in approximately 900 MW of solar PV generation loss [2].
- On 20 April 2018 and 11 May 2018, two similar events caused a loss of solar photovoltaic (PV) facilities in response to transmission line faults, though no generating resources were tripped as a consequence of either of the line outages [3].
- On 7 July 2020, the static wire on a 230 kV double circuit tower failed, causing a single-line-to-ground fault on both the #1 and #2 parallel circuits on the tower. The fault was cleared normally in about three cycles. In addition, a nearby 230 kV line relay incorrectly operated for an external fault. For this first fault event, approximately 205 MW of power reduction was observed at solar PV facilities in the Southern California region. After the #1 circuit was re-energized and held, the #2 line was re-energized and relayed back out due to a low-impedance three-phase fault that was cleared normally in 2.3 cycles. This second fault event experienced a larger 1000 MW reduction in solar PV output primarily due to the fact that it was a three-phase fault [4].

These similar events highlight the potential reliability impacts of IBRs including solar PV systems at both the distribution and transmission levels. Recently, these events have been investigated in [5–15]. To study the impact of IBRs on the bulk power systems, generic positive sequence dynamic stability simulations such as PSS/E are used with a simpler representation of IBRs and inverters in [5–7]. To more accurately capture the dynamics of the inverters' response to actual grid events using generic positive sequence stability models, reference [8] identifies the modeling deficiencies in generic inverter models. In [9–11], aggregated models of IBRs are used instead of individually detailed models of IBRs. Reference [12] presents a coupled simulation method, in which the transmission network is first initialized in a dynamic simulation platform and then the recorded response is passed to the distribution network, which is simulated in quasi-static time-series simulations. In [13–15], the impacts of inverter operating modes and inverter parameters on the transient stability of the bulk transmission system are studied. However, the existing works do not investigate the impact of the transmission-level disturbances on IBR operation, which is important for the operation of inverter-based resources. Additionally, these existing works usually use positive sequence stability models and simple inverter modeling for simulation analysis. Such models may not be used in electromagnetic transient simulations for modeling intricate details with different inverter controls and accurately evaluating the IBRs' response during abnormal events. In addition, the complete network topology of the transmissions system and the distribution system is ignored, which cannot be used for understanding the characteristics of the transmission-level disturbances propagating into the distribution systems.

To address these issues, a real-time electromagnetic simulation testbed is constructed based on a Real-Time Digital Simulator (RTDS) by integrating an IEEE standard transmission network into an IEEE distribution test feeder interfaced with solar PVs in multiple locations in this paper. With the testbed and grid strength assessment, the impact of the transmission-level disturbances on solar PV operation is investigated under different fault types and locations, solar penetration levels, and loading levels. The main contributions of the paper can be summarized as follows:

- (1) To generate realistic transmission-level disturbances and investigate their impacts on solar PVs in distribution systems, a real-time electromagnetic simulation testbed is constructed based on RTDS, which is developed by RTDS Technologies Inc. to solve the power system equations fast enough to realistically represent conditions in actual power grids [16].
- (2) The testbed has a full model of a transmission system, distribution system, and solar PVs. In the modeling of solar PVs, the detailed PV inverter controls are considered

in the distribution system with the comprehensive models of synchronous machines and excitation in the transmission system.

- (3) By using this testbed to investigate the impact of the transmission-level disturbances on solar PV operation under different fault types and locations, solar penetration levels, and loading levels, it is found that the grid strength at different POIs significantly affects the transient stability of solar PV operation. Particularly, at the weak POIs, undesirable transient stability events are more likely to occur under increasing solar penetration levels or decreasing loading levels following severe transmission-level disturbances.

The rest of this paper is organized as follows: Section 2 presents the detailed modeling of the testbed created using RTDS, including the transmission system, distribution system, and the PV systems and their inverter controls; in Section 3, the impact of transmission-level disturbances on solar PV operation in the distribution system is investigated by using the real-time testbed under different fault conditions, solar penetration, and loading levels, and Section 4 provides additional discussion on the impact of grid strength on solar PV responses under different scenarios; finally, Section 5 concludes the paper.

2. RTDS-Based Testbed

2.1. RTDS

To generate realistic transmission-level disturbances and investigate their impacts on solar PVs in distribution systems, a real-time electromagnetic simulation testbed is constructed based on RTDS, which is a commercially available digital real-time power system simulator. RTDS is developed by RTDS Technologies Inc. in Winnipeg, Canada, for the simulation and analysis of electromagnetic transients in electric power systems. RTDS can solve the power system equation fast enough to continuously produce output conditions that realistically represent conditions in actual power grids.

RTDS is generally composed of hardware and software, which is shown in Figure 1. The RTDS hardware includes processing and communicating cards, which are inserted in the unit and connected to a common plate located in the back of the RTDS. The processing cards have a parallel processing architecture customized to simulate with one or multiple processors for the equation solution for the power system and its components. The communicating cards are used to handle the communication between RTDS and its software installed on the guest computer. RTDS has additional dedicated interface cards that allow the physical and logical connection between the simulated power systems and actual devices. The RTDS software is a graphic interface software, RSCAD, which allows users to build, compile, execute, and analyze simulation cases. This software has a wide library of power system components, control, and automated protection systems, as well as a friendly user interface, which can make the assembly and analysis of a wide variety of electric AC and DC systems easier and integrated. As shown in Figure 1, users can use RSCAD software to build a model representing the power system and load this model to the RTDS for the electromagnetic transient simulation while obtaining the updated states of the simulated power system model for analysis.

2.2. RTDS-Based Representative Power System Model

With RTDS, a representative power system model is constructed for real-time electromagnetic simulations to investigate the impact of transmission-level disturbances on the IBR operation in distribution systems. This model includes complete transmission and distribution systems with solar PVs. Figure 2 shows the single-line diagram of the constructed power system model. The component details in the model are described below.



Figure 1. RTDS testbed.

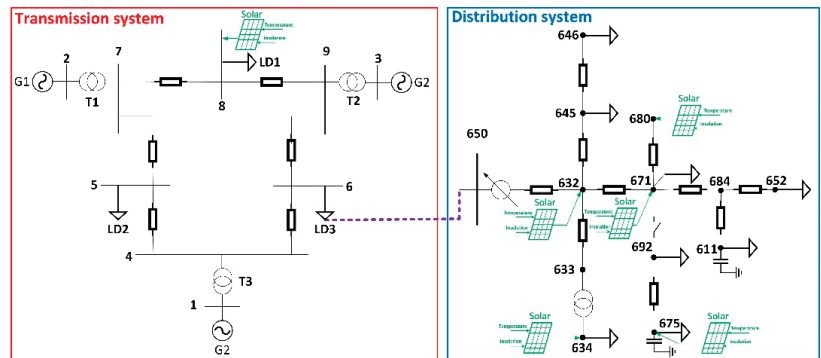


Figure 2. Single-line diagram of the constructed model for real-time electromagnetic simulation.

2.2.1. Transmission System

In the RTDS-based representative power system model, the transmission system is demonstrated by the IEEE 9 bus test system. In the system, its voltages include 230 kV at the transmission level and generator bus voltages of 16.5 kV, 18 kV, and 13.8 kV at buses 1, 2, and 3. The system is composed of three loads, three transformers, six transmission lines, and three synchronous generators with exciter and governor control systems. The system data can be found in [17]. The major electrical components used in the system include a hierarchy component box for the synchronous generator, the unified T-line model for the transmission line, and the dynamic load model.

- The synchronous generator and its excitation and governor systems are represented by a hierarchy component box. As shown in Figure 3a, this hierarchy component box includes the models of a synchronous machine and its excitation and governor systems. All the synchronous machine systems are modeled with a steam turbine, a governor system and an excitation system. The excitation system is modeled with an AC excitation type (EXAC1A) model. The time constants, regulators, and feedback gains are the input parameters for the excitation system. The machine is connected to the transmission system via a transformer.
- The transmission lines in the system are represented by the unified T-line model. As shown in Figure 3b, the unified T-line model is composed of three electrical

components: sending end, terminal end, and calculation box. The unified T-line model can be used for a Bergeron or a frequency-dependent phase model, but when required, either of these models can be collapsed into a simpler PI representation of a line. It is noted that in [9], the data are compensated for long line effects. The transmission lines in the RTDS simulation case are modeled using the Bergeron line model, which is simulated using distributed line parameters. Thus, the long line compensation was removed [15] to obtain the uncompensated data for the developed model.

- The load is represented by a dynamic load component in the transmission side of the network, which is shown in Figure 3c. The load model can be used to dynamically adjust the load to maintain real power and reactive power set points using variable conductance. Additionally, this model allows setting up the initial values and limits of real and reactive power absorbed by a load.

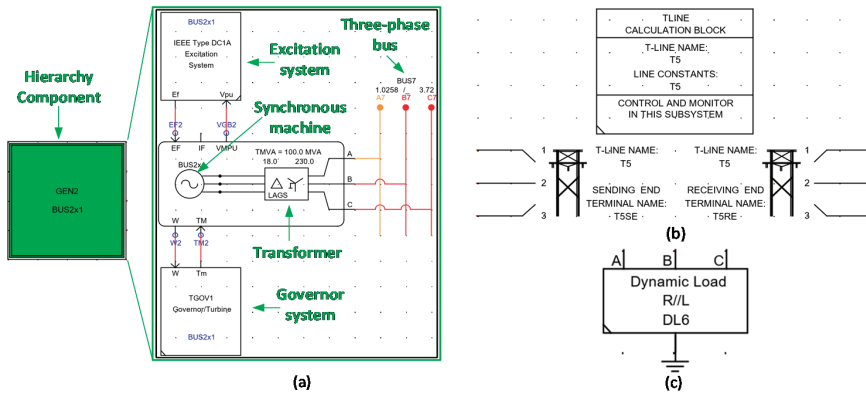


Figure 3. Modeling components used for constructing the transmission system in the real-time simulation testbed: (a) hierarchy component box for synchronous generator; (b) unified transmission line model; (c) dynamic load component.

2.2.2. Distribution System

In the RTDS-based representative power system model, the distribution system is modeled by the IEEE 13 bus test feeder, which includes a two-winding transformer model, the PI section line model, dynamic load model, and a hierarchy component box for the voltage regulator [18].

- In this system, a delta-wye transformer is connected to the transmission system, and it is represented by a two-winding, three-phase transformer model, which is shown in Figure 4a.
- The distribution line is represented by the PI section model in which a set of PI sections are connected in series, as shown in Figure 4b. It is noted that the PI section model requests the capacitance from the wire to the ground. The data given in [19] are the shunt capacitance matrix. Thus, the capacitance from the wire to the ground needs to be calculated from this matrix.
- The load in the system is represented by hierarchy component boxes. As shown in Figure 4c, different colored hierarchy component boxes include different connections of loads, which are modeled by the dynamic load component.

The voltage regulator has been adopted from the typical parameters used for the IEEE 13 bus test feeder. The voltage regulator is represented by a hierarchy component box. As shown in Figure 5, this hierarchy component box includes three single-phase two-winding transformers and the controls for the voltage regulator. For each phase, the regulator controls are represented by an individual hierarchy component box, in which there are the compensator circuit and the step voltage regulator control. This regulator is constructed based on reference [20].

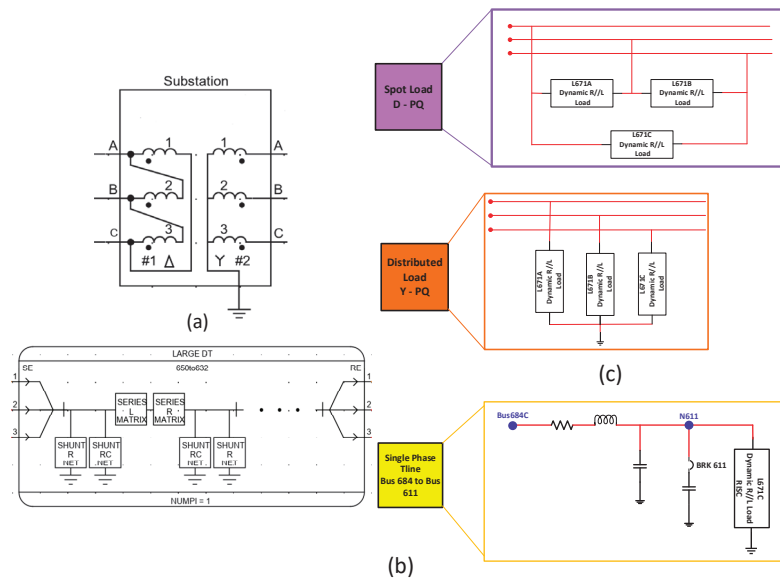


Figure 4. Modeling components used for constructing the distribution system in the real-time simulation testbed: (a) two-winding, three-phase transformer model; (b) PI section model for distribution lines; (c) hierarchy component boxes for loads.

2.2.3. Solar PV System

Solar PVs are integrated into the constructed transmission–distribution model. Each solar PV is modeled by the PV array component to supply the DC voltage for the converter. The converter is modeled using an average value model (AVM), and the AC side of the converter is connected to the feeder. Figure 6 shows the solar PV modeling components.

- A PV array model is used to represent the combination of individual solar cells into PV arrays to produce voltages and currents at the terminals of a PV array. The PV array generates power as a function of irradiation and temperature. The parameters of the PV array model can be modified to obtain a certain output power for the given irradiation and temperature. Each PV array has a temperature set to 25 °C and insolation to 1000 W/m² as input. This model can specify the parameters about how the cells are connected to form arrays. Additionally, this model can select different methods for estimating the maximum power point for a given insolation and temperature. The detailed parameters of the PV array are presented in Table 1.
- The AVM component models the averaged converter control dynamics developed by equivalent voltage and current sources. As shown in Figure 7, solar PV controls use the maximum power point tracking (MPPT) algorithm, which computes the DC voltage set point required for maximum power transfer based on the temperature and insolation levels of the PV array. This DC voltage set point then feeds into the outer loop DC-bus voltage control, which computes a corresponding real power set point. The real and reactive power is then fed into the inner current control loop operating in the *dq* reference frame and a set of three-phase modulation waveforms is synthesized. These modulation waveforms are then used in a carrier-based, sinusoidal pulse width modulation (SPWM) strategy to generate a corresponding set of firing pulses.

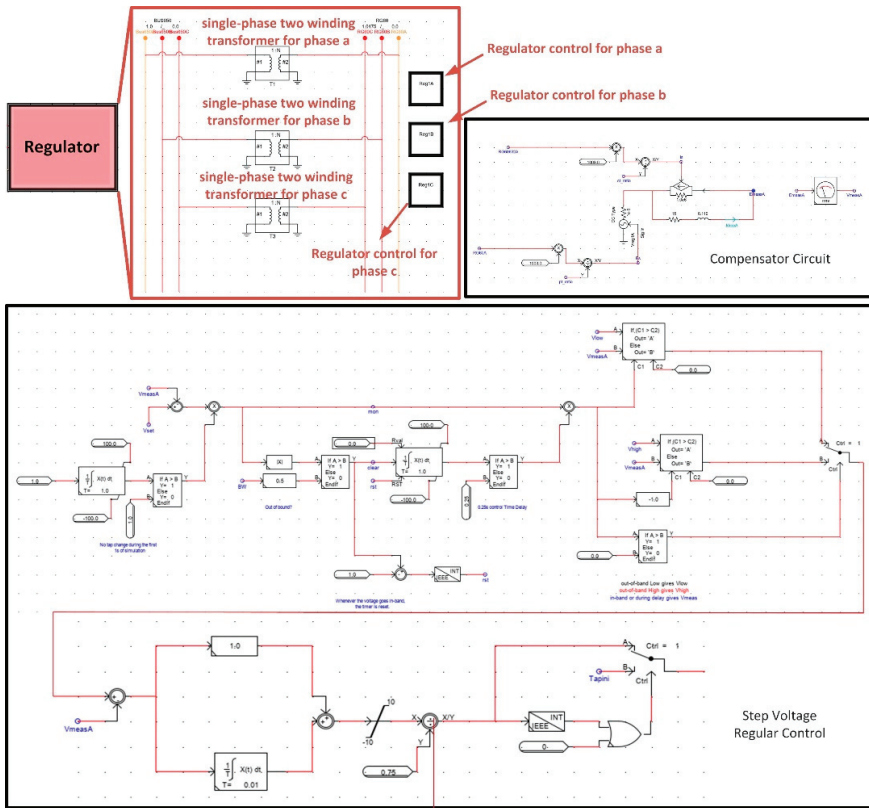


Figure 5. Voltage regulator used for constructing the distribution system.

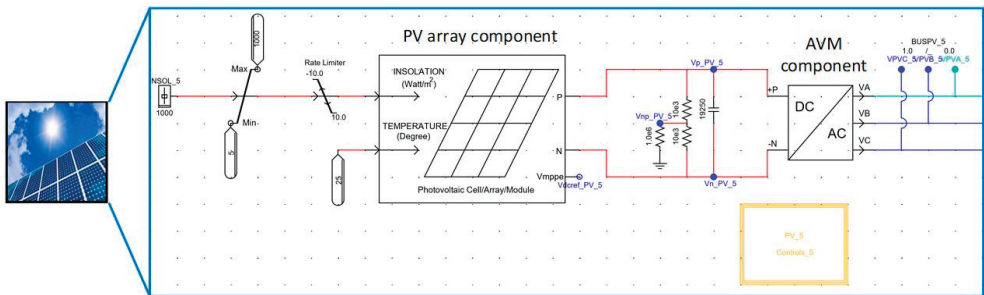


Figure 6. Components for solar PV system used in the variation model.

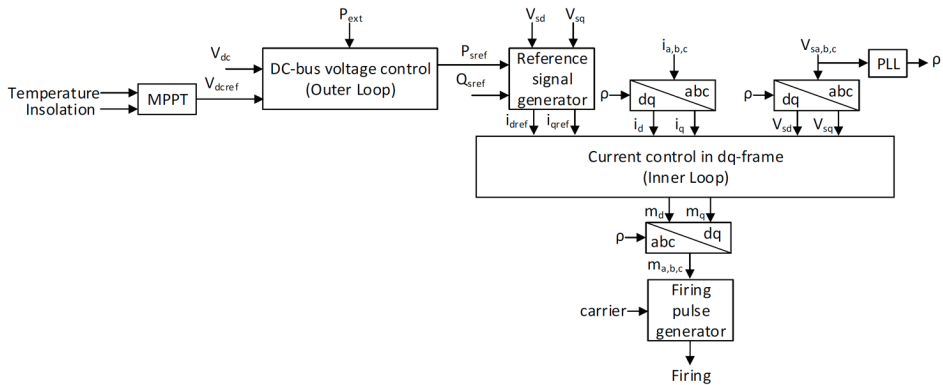


Figure 7. Block diagram of the inverter controls used for the PV system.

Table 1. Parameters for solar PV system.

Components	Parameters	Values
PV	Number of series cells	36
	Number of parallel strings	1
	Open-circuit voltage (Voc)	21.7 V
	Short-circuit current (Isc)	3.35 A
	Number of modules in series	115
	Number of modules in parallel	285
	Voltage at Pmax	17.4 V
DC link capacitor	Capacitance (C_{dc})	5 mF
Inverter	Filter resistance	1.0 mΩ
	Filter inductance	100 μH
High-pass filter	R_H	0.039 Ω
	L_H	7.874 μH
	C_H	2500 μF
Current control loop	k_{pi}	0.2
	k_{ii}	0.30675
PLL	k_{pPLL}	5
	k_{iPLL}	0.01

3. Impact Analysis of Transmission-Level Disturbances on Distributed Solar PV Operation

With the transmission–distribution model constructed in Section 3, the impact of transmission-level disturbances on the operation of distributed solar PVs is investigated using the real-time electromagnetic transient simulation testbed based on RTDS. The performance of the transmission–distribution model is tested by comparing RTDS simulation results with those from PSCAD/EMTDC in terms of steady-state simulation testing and dynamic simulation testing. The steady-state simulation testing is focused on power flow solutions while the transient simulation testing was centered on the dynamics of voltage and current in the model under different faulted scenarios. The consistent results between RTDS simulation and PSCAD/EMTDC confirm the correct function of the constructed model. Due to the page limitation, the comparison results are not shown here. In the following transient simulation analysis, the simulation is performed based on the Dommel algorithm. The simulation time step is 100 μs, and the simulation time is 0.2 s. The transmission–distribution model has 114 nodes. In the model, five cases below are considered.

3.1. Impact of Fault Types in Transmission System on Solar PV Operation

In this case, different fault types in the transmission system are generated to investigate their impacts on the operation of solar PVs in the distribution system. The fault is applied at bus 6 in the transmission system. Four types of faults are considered, including a three-phase fault, a single line-to-ground fault, a line-to-line fault, and a double line-to-ground fault. Each type of fault has the same occurring and clearing times when it is applied at bus 6. Following different types of faults, the voltage and current of each solar PV bus in the distribution system are observed to analyze the responses of the five solar PVs in the distribution system. Figures 8–11 demonstrate the voltage and current responses at solar PV buses 634 and 680 under the four types of faults at bus 6 in the transmission system.

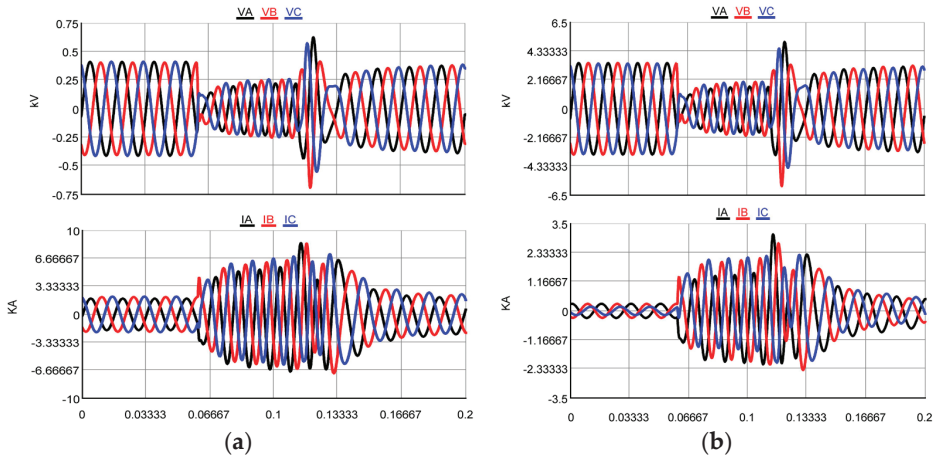


Figure 8. Three-phase fault applied at bus 6 in the transmission system of the testbed: (a) instantaneous voltage and current at bus 634; (b) instantaneous voltage and current at bus 680.

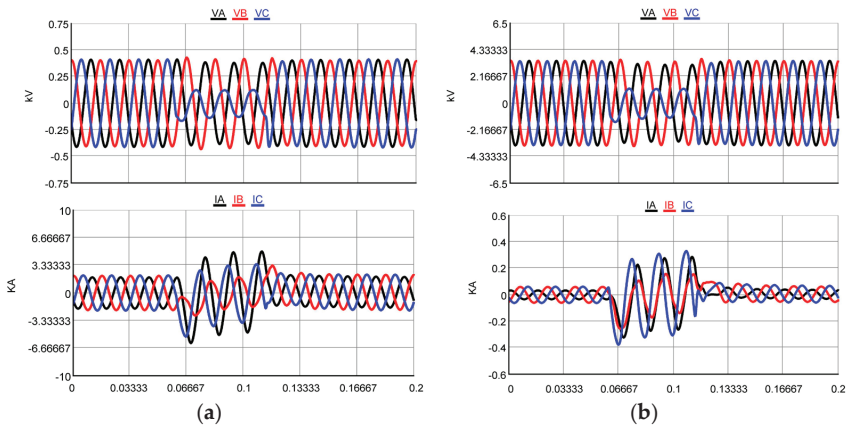


Figure 9. Single line-to-ground fault applied at bus 6 in the transmission system of the testbed: (a) instantaneous voltage and current at bus 634; (b) instantaneous voltage and current at bus 680.

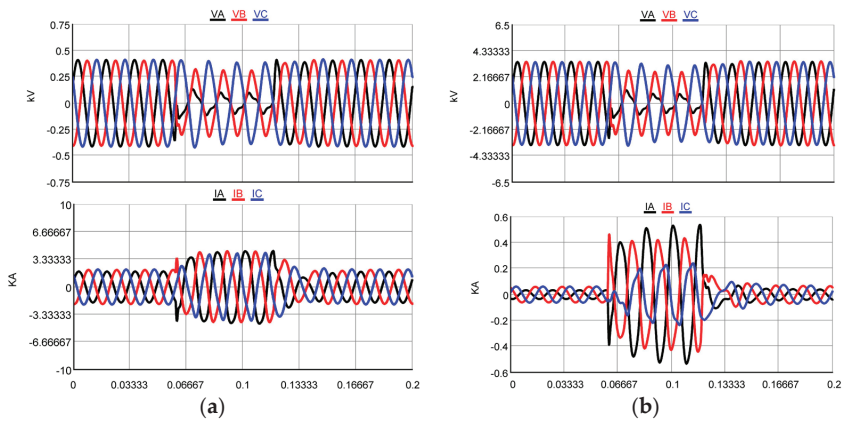


Figure 10. Line-to-line fault applied at bus 6 in the transmission system of the testbed: (a) instantaneous voltage and current at bus 634; (b) instantaneous voltage and current at bus 680.

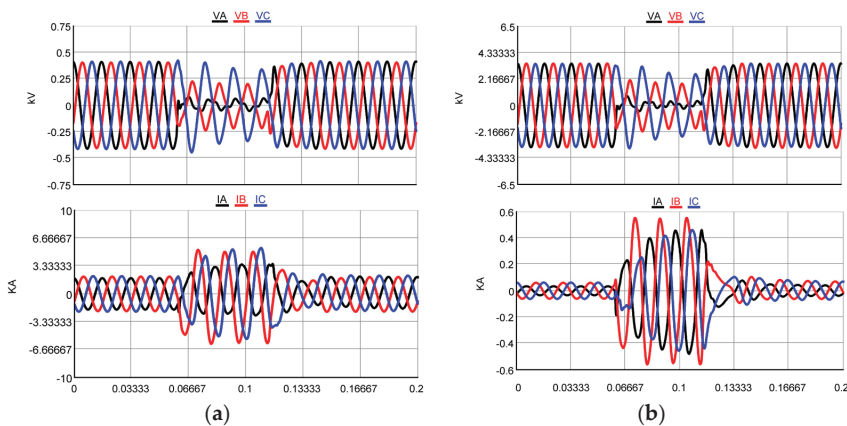


Figure 11. Double line-to-ground fault applied at bus 6 in the transmission system of the testbed: (a) instantaneous voltage and current at bus 634; (b) instantaneous voltage and current at bus 680.

It can be observed from Figures 8–11 that the three-phase fault has a more severe impact on the solar PV operation than the other three types of unsymmetrical faults; among those three types of unsymmetrical faults, the double line-to-ground fault has the most severe impact. As shown in Figure 8, the maximum transient voltage and current at solar PV bus 634 (or bus 680) following the three-phase fault are approximately 1.72 p.u. and 3.0 p.u. (1.75 p.u. and 17 p.u.), respectively, which are greater than those at bus 634 (or bus 680) following the other three types of unsymmetrical faults. Under a single line-to-ground fault, the maximum transient voltage at solar PV bus 634 (or bus 680) is smaller than 1.1 p.u., while the maximum transient current at solar PV bus 634 (or bus 680) is about 2.4 p.u. (6.8 p.u.). Under a line-to-line fault, the maximum transient voltage at solar PV bus 634 (or bus 680) is smaller than 1.0 p.u., and the maximum transient current at solar PV bus 634 (or bus 680) is about 2.0 p.u. (9.1 p.u.). Under a double line-to-ground fault, the maximum transient voltage at solar PV bus 634 (or bus 680) is still smaller than 1.0 p.u., and the maximum transient current at solar PV bus 634 (or bus 680) is about 2.0 p.u. (10.5 p.u.). The transient voltage of different phases at solar PV bus 634 (or bus 680) for these unsymmetrical faults is lower than the normal operating voltage. Compared to the

single line-to-ground fault and the line-to-line fault, the double line-to-ground fault on these solar PV buses is more severe.

3.2. Impact of Fault Locations in the Transmission System on Solar PV Operation

In this case, the impact of fault locations in the transmission system on the operation of solar PVs in the distribution system is investigated. To this end, another fault with the same fault occurring and clearing time of the fault transpired at bus 6 is applied at bus 7 in the transmission system. Still, four types of faults at bus 7, including a three-phase fault, a single line-to-ground fault, a line-to-line fault, and a double line-to-ground fault, are considered. Following different types of faults at bus 7, the voltage and current of each solar PV bus are observed to analyze the responses of the five solar PVs in the distribution system. According to the previous analysis, it is known that when the fault is applied at bus 6, the three-phase fault has the most severe impact on the solar PV operation. For comparison, Figure 12 shows the voltage and current responses at solar PV buses 634 and 680 under the three-phase fault at bus 7 in the transmission system.

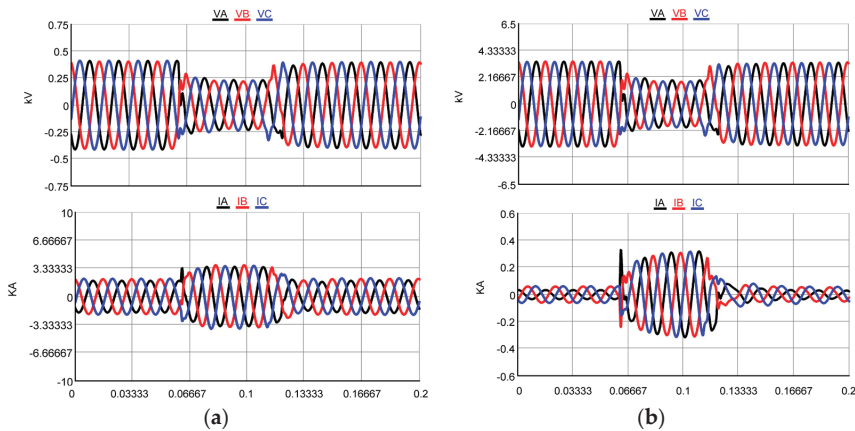


Figure 12. Three-phase fault applied at bus 7 in the transmission system of the testbed: (a) instantaneous voltage and current at bus 634; (b) instantaneous voltage and current at bus 680.

By comparing Figure 12 with Figure 8, it can be seen that when the fault location is moved far from the distributed solar PVs from bus 6 to bus 7 in the transmission system, the same fault has a less severe impact on solar PV operation. Since bus 7 is further than bus 6 in the transmission system for all solar PVs in the distribution system, the maximum transient voltage and current at bus 634 (or bus 680) following the three-phase fault at bus 7 is smaller than those at bus 634 (or bus 680) following the three-phase fault at bus 6. For example, the maximum transient voltage and current at bus 680 resulting from the fault at bus 7 is less than 1.0 p.u. and 5.67 p.u., respectively, but those resulting from the fault at bus 6 are 1.75 p.u. and 17 p.u. Thus, when the transmission-level fault location is closer to the solar PV buses, it has a substantial influence on solar PV operation in the distribution system.

3.3. Impact of Solar Penetration Levels on Solar PV Operation under Transmission-Level Faults

Under the identified severe transmission-level fault type and location, the impact of solar penetration level on solar PV operation is further investigated. More specifically, the penetration level of the integrated solar PVs is changed by decreasing the irradiance level from 1000 W/m^2 to 750 W/m^2 . Then, under the three-phase fault at bus 6 in the transmission system, Figure 13 shows the resulting voltage and current responses at solar PV bus 634 and bus 680 when solar PVs have the irradiance levels of 750 W/m^2 .

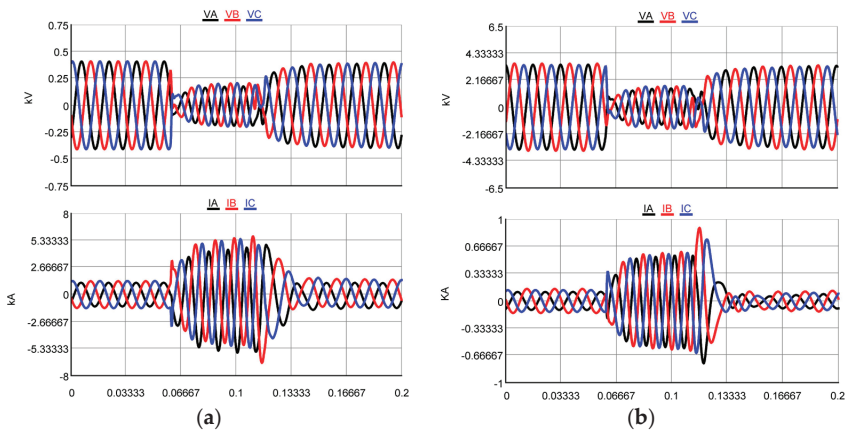


Figure 13. Three-phase fault applied at bus 6 in the transmission system of the testbed: (a) instantaneous voltage and current at bus 634 with 750 W/m^2 solar irradiance; (b) instantaneous voltage and current at bus 680 with 750 W/m^2 solar irradiance.

By comparing Figure 13 with Figure 8, it can be seen that the severity of the impact of transmission-level disturbance on solar PV operation decreases with solar penetration level. As shown in Figure 13, both the maximum transient voltage and current decrease with the solar penetration level due to the irradiance decrease to 750 W/m^2 from 1000 W/m^2 . For example, the maximum transient current is around 14.0 p.u. at solar PV bus 680 following the three-phase fault at bus 6 in the transmission system when all solar PVs in the distribution system have 750 W/m^2 solar irradiance, while the maximum current is increased to 17.0 p.u. at solar PV bus 680 resulting from the same fault when all solar PVs have 1000 W/m^2 solar irradiance. The maximum transient voltage in the case with 750 W/m^2 solar irradiance does not exceed the normal range but with 1000 W/m^2 solar irradiance has a peak of 1.75 p.u. for bus 680.

3.4. Impact of Loading Levels on Solar PV Operation under Transmission-Level Faults

Additionally, the impact of loading level on solar PV operation is investigated under the identified severe transmission-level fault type and location. In this case, the loading level is increased by four times its original loading level in the distribution system. Under the three-phase fault at bus 6 in the transmission system, the transient voltages and currents at the solar PV buses are investigated. For comparison, Figure 14 shows the resulting voltage and current responses at solar PV bus 634 and bus 680 after the loading is increased.

By comparing Figures 8 and 14, it can be seen that the maximum transient voltage and current at bus 634 and bus 680 following the transmission-level fault at bus 6 are decreased with the increased loading. For example, before the loading level is increased in the distribution system following the transmission-level fault at bus 6, the maximum transient currents at solar PV bus 634 and bus 680 are approximately 3.0 p.u. and 17 p.u., respectively; after the loading is increased in the distribution system following the same transmission-level fault, the resulting maximum transient voltage and current decreases to 2.8 p.u. and 16.2 p.u. at bus 634 and bus 680.

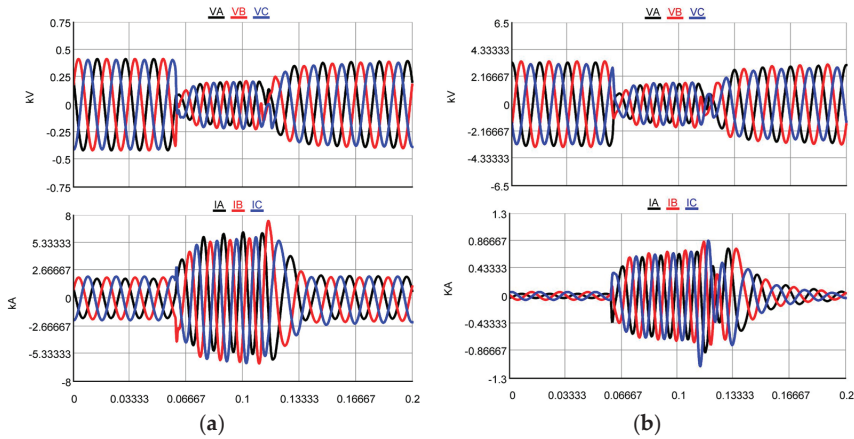


Figure 14. Three-phase fault applied at bus 6 in the transmission side of the testbed: (a) instantaneous voltage and current at bus 634 with increased loading; (b) instantaneous voltage and current at bus 680 with increased loading.

3.5. Impact of Grid Strength on Solar PV Operation under Transmission-Level Faults with Different Solar Penetration Levels and Loading Levels

To understand the relationship between the previous investigation results with grid strength, the impact of grid strength on the solar operation is further analyzed in the system. To assess grid strength, the site-dependent short circuit ratio (SDSCR) [21] is used, which considers the interaction among solar PVs interconnected through the power network. The SDSCR at any point of interconnection (POI) *i* is calculated using the following Equation (1):

$$SDSCR_i = \frac{|V_{R,i}|^2}{\left(P_{R,i} + \sum_{j \in R, j \neq i} \omega_{ij} P_{R,j} \right) |Z_{RR,ii}|} \quad \omega_{ij} = \frac{Z_{RR,ij}}{Z_{RR,ii}} \left(\frac{V_{R,i}}{V_{R,j}} \right)^* \quad (1)$$

where *R* is the set of all POIs connected to IBRs; *Z_{RR,ij}* is the (*i*th, *j*th) element in submatrix of bus impedance matrix that is only related to buses connected to IBRs; *V_{R,i}* is the voltage at POI *i*; *P_{R,j}* is the rated capacity or injected power from the IBR at POI *i*.

Based on the SDSCR defined in Equation (1), the grid strength at each POI of the solar PV in the distribution system in Figure 2 is evaluated. Table 2 lists the SDSCR values for the five POIs. If the SDSCR value is greater than 3, the grid is strong at the POI; if the SDSCR value is between 2 and 3, the grid is weak at the POI; if the SDSCR value is less than 2, the grid is very weak at the POI. Thus, it can be observed from Table 2 that buses 632, 634, and 675 are strong POIs since they have SDSCR values higher than 3. Bus 671 and 680 are the weak POIs as they have SDSCR values less than 3 but greater than 2.

Table 2. SDSCR values for solar PV buses in the distribution system.

Solar PV Buses	SDSCR Values
632	3.6346
634	3.3830
671	2.7768
675	3.0545
680	2.4765

4. Discussions

When comparing the evaluation results presented in Table 2 with the simulation results in Figures 8–14, the following conclusions can be obtained:

By comparing Table 2 with Figures 8–11, it is found that undesirable transient dynamics may be more likely to occur at weaker POIs under the same fault but different types. Moreover, the severity of the undesirable transient dynamics at the weaker POIs may increase with the fault type. Table 2 shows that bus 680 is weaker than bus 634. Comparing the maximum transient voltage and current at bus 634 with those at bus 680, it can be observed from Figures 8–11 that the maximum transient voltage and current at bus 634 are smaller than those at bus 680 following the same transmission-level fault with the four different types. For example, when the single line-to-ground fault occurred in the transmission system, Figure 9 shows that the maximum transient current at bus 634 is approximately 2.4 p.u., but the maximum transient current at bus 680 is approximately 6.8 p.u. Moreover, when the fault type is changed into the severest three-phase fault, Figure 8 shows that the maximum transient voltage and current at bus 634 are approximately 1.72 p.u. and 3 p.u.; however, the maximum transient voltage and current at bus 680 are approximately 1.75 p.u. and 17 p.u.

By comparing Table 2 with Figure 12, it is also found that under the same three-phase fault but different locations, weak POIs are more likely to have undesirable transient dynamics. As shown in Table 2, bus 680 is weaker than bus 634. By comparing the maximum transient voltage and current at bus 634 with those at bus 680 in Figures 8 and 12, it can be observed that when the three-phase fault is moved from bus 6 to bus 7 in the transmission system, the maximum current transient at bus 634 is decreased from 3 p.u. to 1.4 p.u.; the maximum current transient at bus 680 is decreased from 17 p.u. to 5.67 p.u. Additionally, even when the fault is far from the distribution system (at bus 7), weak bus 680 is still more likely to have an undesirable transient response than bus 634.

By comparing Table 2 with Figure 13, it is found that undesirable transient dynamics may be more likely to happen at weaker POIs under the increasing solar penetration level in the distribution system. Compared to bus 634, weak bus 680 has a more severe impact on solar PV operation following the same transmission-level fault. As shown in Figure 13, for bus 680, when the solar irradiance is 750 W/m^2 , the maximum transient current is 14 p.u.; as shown in Figure 8, when solar irradiance is increased to 1000 W/m^2 , the maximum transient current is 17 p.u. For bus 634, the maximum transient current is increased from about 2.2 p.u. to 3 p.u. when solar irradiance is increased from 750 W/m^2 to 1000 W/m^2 .

By comparing Table 2 with Figure 14, it is found that increasing the loading level in the distribution system may decrease the risk of undesirable transient dynamics at weaker POIs following the transmission-level disturbance. As shown in Figures 8 and 14, the severity of the impact of transmission-level disturbance on solar PV operation decreases with the increase in loading level in the distribution system. At the weak bus 680, this impact becomes relatively significant. Before increasing the loading level, the maximum transient current is 17 p.u. following the transmission-level fault at bus 6; the transient current is reduced to 16.2 p.u. following the same transmission-level fault when the loading level is increased. This change can improve grid strength at bus 680 and thus reduce the risk of undesirable transient dynamics of solar PV at bus 680.

5. Conclusions

In this paper, a real-time RTDS-based simulation testbed was presented to explore the impacts of realistic transmission-level disturbances on solar PV operation in the distribution system. The testbed includes detailed modeling of components in the transmission and distribution systems along with the detailed PV models and its inverter controls to capture the accurate dynamic behaviors of solar PVs in response to the transmission-level disturbances. The testbed was used in this paper to investigate the transient responses from the solar PV inverters under different transmission-level disturbances regarding different fault types and locations, solar penetration levels, and loading levels. It is found that the grid strength at the POIs of solar PV inverters significantly affects the transient response from the solar PV inverters following the transmission-level disturbances. At weaker POIs, the transient response is more sensitive to the disturbances. Such sensitivity becomes more significant

when the transmission-level disturbance is closer to the weak POIs or the disturbances become more severe. Additionally, the impact of the transmission-level disturbances on the solar PVs at the weak POIs exacerbate with the increasing solar penetration levels and loading levels. Thus, when an increasing number of IBRs are being integrated into the grid, it is important to study and develop new technologies for grid planning, operation, and protection in weak grid conditions to address the emerging issues of integrating the high penetration of solar PVs and other IBRs.

Author Contributions: Conceptualization, M.M., A.E. and D.W.; methodology M.M., A.E. and D.W.; software, A.E.; validation, M.M., A.E. and B.S.; formal analysis, M.M., A.E. and D.W.; investigation, A.E. and M.M.; resources, D.W.; data curation, A.E. and M.M.; writing—original draft preparation, M.M.; writing—review and editing, M.M., A.E., B.S. and D.W.; visualization, A.E. and M.M.; supervision, D.W.; project administration, D.W.; funding acquisition, D.W. All authors have read and agreed to the published version of the manuscript.

Funding: This material is based upon work supported by the US Department of Energy’s Office of Energy Efficiency and Renewable Energy (EERE) under the Solar Energy Technologies Office Award Number DE-EE0008772.

Institutional Review Board Statement: Not applicable.

Informed Consent Statement: Not applicable.

Data Availability Statement: The data presented in this study are available on request from the corresponding author.

Conflicts of Interest: The authors declare no conflict of interest.

References

1. North American Electric Reliability Corporation. *1200 MW Fault Induced Solar Photovoltaic Resource Interruption Disturbance Report*; North American Electric Reliability Corporation: Atlanta, GA, USA, 2016.
2. North American Electric Reliability Corporation. *900 MW Fault Induced Solar Photovoltaic Resource Interruption Disturbance Report*; North American Electric Reliability Corporation: Atlanta, GA, USA, 2018.
3. North American Electric Reliability Corporation. *April and May 2018 Fault Induced Solar Photovoltaic Resource Interruption Disturbances Report: Southern California Events: 20 April 2018 and 11 May 2018*; North American Electric Reliability Corporation: Atlanta, GA, USA, 2019.
4. San Fernando Disturbance Southern California Event: 7 July 2020 Joint NERC and WECC Staff Report. Atlanta, GA, USA, 2020. Available online: <https://www.nwpp.org/news/power-insights-podcast-episode-2-san-fernando-even> (accessed on 25 June 2021).
5. Kang, S.; Shin, H.; Jang, G.; Lee, B. Impact Analysis of Recovery Ramp Rate After Momentary Cessation in Inverter-based Distributed Generators on Power System Transient Stability. *IET Gener. Transm. Distrib.* **2020**, *15*, 24–33. [[CrossRef](#)]
6. Pierre, B.J.; Elkhatib, M.E.; Hoke, A. Photovoltaic Inverter Momentary Cessation: Recovery Process is Key. In Proceedings of the 2019 IEEE 46th Photovoltaic Specialists Conference (PVSC), Chicago, IL, USA, 16–21 June 2019.
7. Choi, N.; Park, B.; Cho, H.; Lee, B. Impact of Momentary Cessation Voltage Level in Inverter-Based Resources on Increasing the Short Circuit Current. *Sustainability* **2019**, *11*, 1153. [[CrossRef](#)]
8. Zhu, S.; Piper, D.; Ramasubramanian, D.; Quint, R.; Isaacs, A.; Bauer, R. Modeling Inverter-Based Resources in Stability Studies. In Proceedings of the 2018 IEEE Power & Energy Society General Meeting (PESGM), Portland, OR, USA, 5–10 August 2018.
9. Shin, H.; Jung, J.; Lee, B. Determining the Capacity Limit of Inverter-Based Distributed Generators in High-Generation Areas Considering Transient and Frequency Stability. *IEEE Access* **2020**, *8*, 34071–34079. [[CrossRef](#)]
10. Mather, B.; Ding, F. Distribution-connected PV’s response to voltage sags at transmission-scale. In Proceedings of the 2016 IEEE 43rd Photovoltaic Specialists Conference (PVSC), Portland, OR, USA, 5–10 June 2016; pp. 2030–2035.
11. Mather, B.; Aworo, O.; Bravo, R.; Piper, P.E.D. Laboratory Testing of a Utility-Scale PV Inverter’s Operational Response to Grid Disturbances. In Proceedings of the 2018 IEEE Power & Energy Society General Meeting (PESGM), Portland, OR, USA, 5–10 August 2018; pp. 1–5.
12. Kenyon, R.W.; Mather, B.; Hodge, B.-M. Coupled Transmission and Distribution Simulations to Assess Distributed Generation Response to Power System Faults. *Electr. Power Syst. Res.* **2020**, *189*, 106746. [[CrossRef](#)]
13. Shin, H.; Jung, J.; Oh, S.; Hur, K.; Iba, K.; Lee, B. Evaluating the Influence of Momentary Cessation Mode in Inverter-Based Distributed Generators on Power System Transient Stability. *IEEE Trans. Power Syst.* **2020**, *35*, 1618–1626. [[CrossRef](#)]
14. Li, C.; Reinmuller, R. Fault Responses of Inverter-based Renewable Generation: On Fault Ride-Through and Momentary Cessation. In Proceedings of the 2018 IEEE Power & Energy Society General Meeting (PESGM), Portland, OR, USA, 5–10 August 2018.

15. Pierre, B.J.; Elkhatib, M.E.; Hoke, A. PV Inverter Fault Response Including Momentary Cessation, Frequency-Watt, and Virtual Inertia. In Proceedings of the 2018 IEEE 7th World Conference on Photovoltaic Energy Conversion (WCPEC) (A Joint Conference of 45th IEEE PVSC, 28th PVSEC & 34th EU PVSEC), Waikoloa, HI, USA, 10–15 June 2018.
16. RTDS Technologies Inc. Available online: <https://www.rtds.com> (accessed on 25 June 2021).
17. Sauer, P.W.; Pai, M.A. *Power System Dynamics And stability*; Wiley Online Library: Hoboken, NJ, USA, 1998; Volume 101.
18. Kersting, W.H. *Distribution System Modeling and Analysis*; CRC Press: Boca Raton, FL, USA, 2017.
19. IEEE PES AMPS DSAS Test Feeder Working Group. Available online: <https://site.ieee.org/pes-testfeeders/resources/> (accessed on 25 June 2021).
20. Grainger, J.J.; Stevenson, W.D., Jr. *Power System Analysis*; McGrawHill: New York, NY, USA, 1994.
21. Wu, D.; Li, G.; Javadi, M.; Malyscheff, A.M.; Hong, M.; Jiang, J.N. Assessing impact of renewable energy integration on system strength using site-dependent short circuit ratio. *IEEE Trans. Sustain. Energy* **2017**, *9*, 1072–1080. [[CrossRef](#)]

Article

Converter-Driven Stability Analysis of Power Systems Integrated with Hybrid Renewable Energy Sources

Jianqiang Luo¹, Yiqing Zou¹, Siqi Bu^{1,2,3,*} and Ulas Karaagac¹

¹ Department of Electrical Engineering, The Hong Kong Polytechnic University, Kowloon 999077, Hong Kong; jianqiang.luo@polyu.edu.hk (J.L.); 18095429g@connect.polyu.hk (Y.Z.); ulas.karaagac@polyu.edu.hk (U.K.)

² Shenzhen Research Institute, The Hong Kong Polytechnic University, Shenzhen 518057, China

³ Research Institute for Smart Energy, The Hong Kong Polytechnic University, Kowloon 999077, Hong Kong

* Correspondence: siqi.bu@polyu.edu.hk

Abstract: Renewable energy sources such as wind power and photovoltaics (PVs) have been increasingly integrated into the power system through power electronic converters in recent years. However, power electronic converter-driven stability has issues under specific circumstances, for instance, modal resonances might deteriorate the dynamic performance of the power systems or even threaten the overall stability. In this work, the integration impact of a hybrid renewable energy source (HRES) system on modal interaction and converter-driven stability was investigated in an IEEE 16-machine 68-bus power system. In this paper, firstly, an HRES system is introduced, which consists of full converter-based wind power generation (FCWG) and full converter-based photovoltaic generation (FCPV). The equivalent dynamic models of FCWG and FCPV are then established, followed by linearized state-space modeling. On this basis, converter-driven stability analysis was performed to reveal the modal resonance mechanisms between different renewable energy sources (RESs) and weak grids in the interconnected power systems and the multi-modal interaction phenomenon. Additionally, time-domain simulations were conducted to verify the effectiveness of dynamic models and support the converter-driven stability analysis results. To avoid detrimental modal resonances, a multi-modal and multi-parametric optimization strategy is further proposed by retuning the controller parameters of the multi-RESs in the HRES system. The overall results demonstrate the modal interaction effect between the external AC power system and the HRES system and its various impacts on converter-driven stability.

Keywords: converter-driven stability; hybrid renewable energy source (HRES) system; multi-modal interaction; full converter-based wind power generation (FCWG); full converter-based photovoltaic generation (FCPV)

Citation: Luo, J.; Zou, Y.; Bu, S.; Karaagac, U. Converter-Driven Stability Analysis of Power Systems Integrated with Hybrid Renewable Energy Sources. *Energies* **2021**, *14*, 4290. <https://doi.org/10.3390/en14144290>

Academic Editor: Juri Belikov

Received: 3 May 2021

Accepted: 3 June 2021

Published: 16 July 2021

Publisher's Note: MDPI stays neutral with regard to jurisdictional claims in published maps and institutional affiliations.



Copyright: © 2021 by the authors. Licensee MDPI, Basel, Switzerland. This article is an open access article distributed under the terms and conditions of the Creative Commons Attribution (CC BY) license (<https://creativecommons.org/licenses/by/4.0/>).

1. Introduction

High penetration of converter-based power sources has become a popular trend due to its benefits in terms of environmental protection and social sustainability, especially the integration of wind power and photovoltaic (PV) solar energy in modern power systems [1,2]. The full converter-based wind generation (FCWG, e.g., permanent magnet synchronous generator (PMSG)) is more promising than doubly-fed induction generators (DFIGs) in new wind power applications [3]. As for PV solar energy, several generic PV system models based on the Type 4 wind turbine generator model have been introduced by Western Electric Coordinating Council (WECC) [4]. PV generation is modeled as an inverter-based generator associated with a variety of active power control reactive power control options.

Renewable energy sources are interconnected to the power system via flexibly controlled power electronic converters that might produce new stability issues due to the modal interactions between converter-based generators and the power system, such as converter-driven stability and resonance stability [5]. In particular, oscillation issues could

be induced by the modal interaction between converters and external AC power systems. The sub-synchronous resonance (SSR) was observed in ERCOT of United States [6], Hebei province of North China [7], London blackout in the United Kingdom [8], and sub-synchronous oscillation (SSO) in Xinjiang province of China [9]. Low-frequency power oscillations are normally caused by the modal interaction between the interconnection of power grids and the fast-response automatic voltage regulators (AVRs). It is generally understood that the occurrence of the oscillations is due to the lack of damping of power systems electromechanical oscillation modes (EOMs) [10,11]. An unusual transition in electromechanical dynamics is disclosed in [12], which indicates that an EOM may be dominated by FCWG dynamics and tuned into a quasi-EOM when the FCWG quasi-electromechanical state variables actively participate. The authors of [13] studied how system impedance and the parameters of the phase-locked loop (PLL) affect the dynamic behavior and the stability limits of the converters in HVDC applications.

Furthermore, increasingly power electronic converter-interfaced renewable energy sources introduce a challenge for converter-driven stability of the overall system [14]. Although the interconnection of power electronic converter-interfaced renewable generators and conventional power systems enhances the overall flexibility and controllability [15–17], the modal interactions of both transmission and distribution systems become complicated [18–20]. In contrast to the traditional synchronous generators (SGs), converter-based renewable energy sources have a major impact on power system converter-driven stability. The authors of [21] studied how the parameters of rotor current controllers have influences on the eigenvalues shift locus. Based on the dynamic modeling and analysis of traditional generators and converter-based DFIG, the impact on power system stability is the minimum under small-scale penetration of wind power generations [22]. However, when the wind power penetration level increases, the converter-driven stability of the overall power systems may be greatly affected. The authors of [23] conclude that the damping reduction of power system EOM may occur at weak interconnection lines and increased wind power penetration level. In multiple grid-interconnected PV generation systems, the coupling behavior between PLLs and near converters may make the system more vulnerable or even lose converter-driven stability [24,25].

In this work, a hybrid renewable energy source (HRES) system consisting of FCWG and FCPV was integrated into the same power system to study the complex modal interaction with external AC power systems and thus consequent impact on converter-driven stability. The main contributions of this paper are listed as follows:

1. Detailed dynamic models of FCWG and FCPV, including PMSG, PV generation unit, DC/DC converter and the associated control system, DC-link, grid side converter (GSC) and associated control systems, synchronous reference frame phase-locked loop (SRF-PLL), and the external AC power system are established. The linearized state-space models of each dynamic component, as well as the entire closed-loop system, are developed as the foundation of converter-driven stability analysis.
2. Based on the above models, modal analysis is conducted with different wind power and PV solar energy penetration levels in the IEEE 16-machine 68-bus system. Particularly, open-loop FCWG oscillation mode (FOM) and FCPV oscillation mode (POM) are tuned to be close to critical EOM in terms of frequency, which is the necessary condition of open-loop modal resonance.
3. Open-loop and closed-loop modal analysis is compared. Multi-modal interaction in the examined system with different renewable energy penetration levels is evaluated to analyze the essential resonance mechanism, which provides a theoretical indication to alleviate the negative effect caused by strong modal resonance.
4. To circumvent the malignant modal resonance and to enhance the converter-driven stability, a modal interaction optimization strategy was implemented to prevent potential modal resonance through carefully retuning the controller parameters of the HRES system. The overall converter-driven stability and dynamic performance of the entire system were improved thereafter.

2. Hybrid Renewable Energy Source (HRES) System

Wind power and PV solar energy have become prevalent renewable power sources and represent a gradually increasing share of generation in modern power systems. Consequently, these renewable energy sources also induce a long-lasting and complex impact on power system stability [26]. In this section, an HRES system is introduced to cover different types of renewable energy and their complex modal interaction with external AC power systems.

2.1. Configuration of FCWG

The typical topology of an FCWG is depicted in Figure 1.

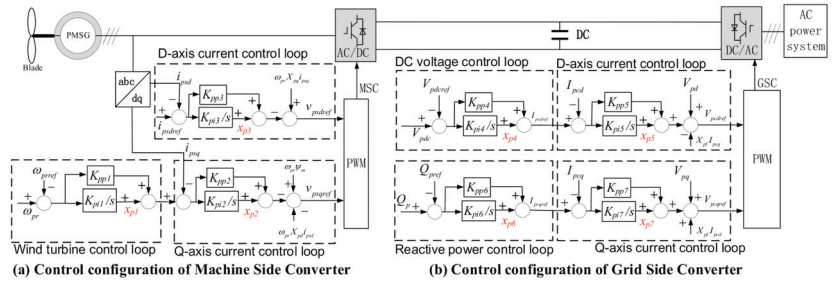


Figure 1. Physical configuration of an FCWG connected to the AC power system.

The FCWG consists of three parts: (1) the PMSG, the machine side converter (MSC), and the associated control system (as demonstrated in Figure 1a); (2) the DC-link, the grid side converter (GSC), and the associated control system (as shown in Figure 1b); and (3) the SRF-PLL (as presented in Figure 2), which is used to synchronize FCWG with the external power system.

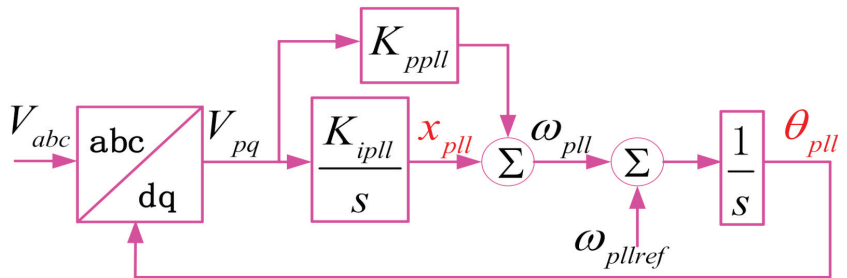


Figure 2. Block diagram of SRF-PLL.

2.2. Configuration of FCPV

A full converter-based photovoltaic generation (FCPV) farm interconnected to a power system is depicted in Figure 3, which consists of three main parts: (1) a PV generation unit, the DC/DC converter, and the associated control system; (2) the DC-link, GSC, and the associated control system; and (3) the SRF-PLL, which has the same DC control configuration and function as that of FCWG.

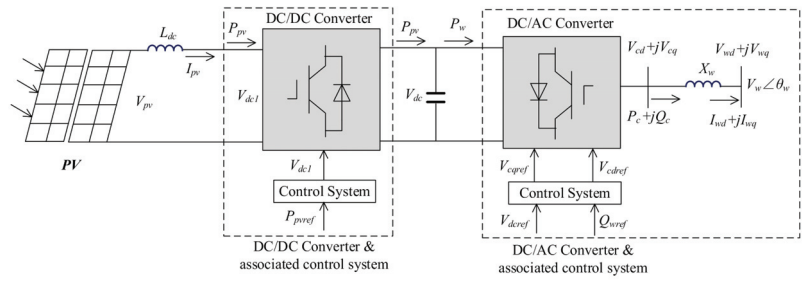


Figure 3. Physical configuration of an FCPV interconnected to the AC power system.

3. Dynamic Models of FCWG and FCPV

To elaborate the modal interaction mechanism, the external AC power system excluding the HRES dynamics is denoted as the open-loop system, while the entire system is the closed-loop system. Therefore, the impact of the HRES system can be quantified through open-loop and closed-loop modal analysis.

3.1. State-Space Model of FCWG

Dynamics equations of all FCWG components are derived in this section.

1. Modeling of PMSG

The PMSG can be represented by the following equations:

$$\begin{cases} \frac{d\psi_{psd}}{dt} = -\omega_0 R_{ps} i_{psd} - \omega_0 v_{psd} + \omega_0 \omega_{pr} \psi_{psq} \\ \frac{d\psi_{psq}}{dt} = -\omega_0 R_{ps} i_{psq} - \omega_0 v_{psq} - \omega_0 \omega_{pr} \psi_{psd} \end{cases} \quad (1)$$

$$\begin{cases} \psi_{psd} = X_{pd} i_{psd} - \psi_{pm} \\ \psi_{psq} = X_{pq} i_{psq} \end{cases} \quad (2)$$

where ψ_{psk} , v_{psk} , i_{psk} and X_{pk} ($k = d, q$) are the direct and quadrature axis flux, voltage, current, and reactance of stator winding, respectively. R_{ps} is the stator winding resistance, ω_b is the base angular speed in rad/s, ψ_{pm} is the flux linkage produced by the permanent magnet. ω_{pr} is the stator electrical angular speed, defined by: $\omega_{pr} = n_p \omega_m = \omega_m$, where $n_p = 1$ is the number of pole pairs of PMSG and ω_m is the mechanical (rotor) angular speed.

The motion equation of the wind turbine rotor is expressed as

$$H_{pr} \frac{d\omega_{pr}}{dt} = T_{pm} - T_{pe} \quad (3)$$

where H_{pr} is the inertia constant of the rotor, T_{pm} is the mechanical torque of the wind turbine, T_{pe} is the electrical torque of PMSG.

2. Modeling of MSC

From Figure 1a, the dynamics of MSC are derived as

$$\begin{cases} i_{psqref} = K_{pp1}(\omega_{pr} - \omega_{prref}) + x_{p1} \\ \frac{dx_{p1}}{dt} = K_{pi1}(\omega_{pr} - \omega_{prref}) \\ \frac{dx_{p2}}{dt} = K_{pi2}(i_{psqref} - i_{psq}) \\ \frac{dx_{p3}}{dt} = K_{pi3}(i_{psdref} - i_{psd}) \end{cases} \quad (4)$$

where x_{pk} ($k = 1, 2, 3$) are the state variables of PI controllers in MSC control loops. K_{ppk} and $K_{pi k}$ ($k = 1, 2, 3$) are the proportional and integral parameters shown in Figure 1a. X_{*ref} denotes the reference value of variable X_{*} , and such denotations are also applied to other variables in the following content.

3. Modeling of DC-link

The equation of the DC-link voltage is derived as

$$C_p V_{pdc} \frac{dV_{pdc}}{dt} = P_{ps} - P_{pc} \tag{5}$$

where C_p is the capacitance, V_{pdc} is DC voltage across the capacitor, P_{pc} is the active power output and expressed as

$$P_{pc} = V_{pcd} I_{pcd} + V_{pcq} I_{pcq} = V_{pd} I_{pcd} + V_{pq} I_{pcq} \tag{6}$$

where V_{pck} and I_{pck} ($k = d, q$) are the direct and quadrature axis output voltage and output current of GSC, respectively. V_{pd} and V_{pq} are the direct and quadrature axis voltage at the point of common coupling (PCC), respectively.

The line voltage equations across the filter reactance X_{pf} in Figure 1b is expressed as

$$\begin{cases} \frac{dI_{pcd}}{dt} = \frac{\omega_0}{X_{pf}}(V_{pcd} - V_{pd}) + \omega_0 I_{pcq} \\ \frac{dI_{pcq}}{dt} = \frac{\omega_0}{X_{pf}}(V_{pcq} - V_{pq}) - \omega_0 I_{pcd} \end{cases} \tag{7}$$

4. Modeling of GSC

A standard GSC configuration is shown in Figure 1b, and the mathematic equations are derived as

$$\begin{cases} \frac{dx_{p4}}{dt} = K_{pi4}(V_{pdc} - V_{pdcref}) \\ \frac{dx_{p5}}{dt} = K_{pi5}(I_{pcdref} - I_{pcd}) \\ \frac{dx_{p6}}{dt} = K_{pi6}(Q_p - Q_{pre}) \\ \frac{dx_{p7}}{dt} = K_{pi7}(I_{pcqref} - I_{pcq}) \end{cases} \tag{8}$$

where x_{pk} ($k = 4, 5, 6, 7$) are the state variables of PI controllers in GSC control loops. K_{ppk} and $K_{pi k}$ ($k = 4, 5, 6, 7$) are the proportional and integral parameters shown in Figure 1b. Q_p is the reactive power output of GSC and expressed as

$$Q_p = V_{pq} I_{pcd} - V_{pd} I_{pcq} \tag{9}$$

5. Modeling of PLL

From the block diagram of SRF-PLL shown in Figure 2,

$$\begin{cases} \frac{d}{dt} x_{pll} = K_{ipll} V_{pq} \\ \frac{d}{dt} \theta_{pll} = x_{pll} + K_{ppll} V_{pq} + \omega_{pllref} \end{cases} \tag{10}$$

where x_{pll} and θ_{pll} (i.e., phase angle) are the state variables of PLL dynamics, ω_{pllref} is the angular speed of PLL in rad/s, K_{ipll} and K_{ppll} are the integral and proportional parameters of the PLL controller, respectively.

By linearizing Equations (1)–(10) and combining them, the linearized state-space model of FCWG can be expressed as [3]

$$\begin{cases} \frac{d}{dt} \Delta \mathbf{X}_w = \mathbf{A}_w \Delta \mathbf{X}_w + \mathbf{B}_w \Delta \mathbf{V}_w \\ \Delta \mathbf{I}_w = \mathbf{C}_w \Delta \mathbf{X}_w \end{cases} \tag{11}$$

where $\Delta \mathbf{X}_w$ denotes all the state variables of FCWG (i.e., the differential state variables in equations above); \mathbf{A}_w , \mathbf{B}_w , \mathbf{C}_w are the state-space matrices after integrating all linearized differential equations; $\Delta \mathbf{V}_w$ and $\Delta \mathbf{I}_w$ denote the voltage variation and current variation at the PCC of FCWG in the common x-y coordinate.

3.2. State-Space Model of FCPV

1. Modeling of PV generation unit

According to the voltage-current characteristic of FCPV, the relation between the output voltage and current of an FCPV is expressed as [27]

$$V_{pv} = \frac{N_s n k T}{q} \ln \left(\frac{N_p I_{sc} I_r / 100 - I_{pv}}{N_p I_r} + 1 \right) \tag{12}$$

where V_{pv} and I_{pv} are voltage and current output respectively; T is the junction temperature, k is Boltzmann’s constant, N_s and N_p are the number of PV cells in series and parallel respectively, q is the charge of electron, n is the ideality factor, I_r is the irradiance, I_{sc} is the short-circuit current, I_0 is the saturation current.

Therefore, the output active power from an FCPV is expressed as

$$P_{pv} = V_{pv} I_{pv} \tag{13}$$

An inductance is used to limit the change of output current of the FCPV, and its dynamics can be derived as

$$\frac{dI_{pv}}{dt} = \frac{\omega_0}{L_{dc}} (V_{pv} - V_{dc1}) \tag{14}$$

where V_{dc1} is the input DC voltage of DC/DC converter.

2. Modeling of DC/DC converter

The control structure of DC/DC converter is shown in Figure 4. The DC/DC converter control system consists of two control loops, i.e., an outer active power control loop and an inner current control loop.

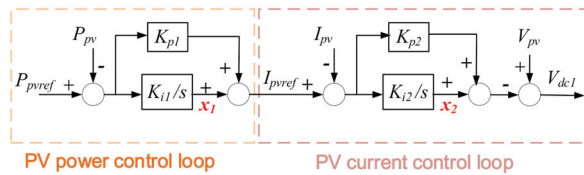


Figure 4. Control structure of DC/DC converter.

The dynamics of DC/DC converter control system can be written as

$$\begin{cases} \frac{dx_1}{dt} = K_{i1} (P_{pvref} - P_{pv}) \\ I_{pvref} = x_1 + K_{p1} (P_{pvref} - P_{pv}) \\ \frac{dx_2}{dt} = K_{i2} (I_{pvref} - I_{pv}) \\ V_{dc1} = -x_2 - K_{p2} (I_{pvref} - I_{pv}) + V_{pv} \end{cases} \tag{15}$$

where x_1 and x_2 are the state variables of PI controllers, K_{i1} and K_{p1} are the integral and proportional parameters of the active power controller, K_{i2} and K_{p2} are the integral and proportional parameters of the current controller.

3. Modeling of DC-link

Ignoring the power loss of converters, the dynamic equation of the DC capacitor is expressed as

$$C_{dc} V_{dc} \frac{dV_{dc}}{dt} = P_{pv} - P_w \tag{16}$$

where C_{dc} is DC capacitance, V_{dc} is the voltage across the capacitor, P_{pv} in the injected power from PV, and P_w is the output active power in DC-link and defined as

$$P_w = V_{wd}I_{wd} + V_{wq}I_{wq} \tag{17}$$

where I_{wd} and I_{wq} are the direct and quadrature axis output current of GSC, respectively; V_{wd} and V_{wq} are direct and quadrature axis voltage of PCC, respectively.

The dynamics of the filter inductor are expressed as

$$\begin{cases} \frac{dI_{wd}}{dt} = \frac{\omega_0}{x_w}(V_{cd} - V_{wd}) + \omega_0 I_{wq} \\ \frac{dI_{wq}}{dt} = \frac{\omega_0}{x_w}(V_{cq} - V_{wq}) - \omega_0 I_{wd} \end{cases} \tag{18}$$

where x_w is the inductance of the filter, V_{cd} and V_{cq} are direct and quadrature axis output voltage of DC/AC converter.

4. Modeling of GSC

The control structure of GSC is shown in Figure 5. GSC control system consists of four control loops: (1) the outer DC voltage control loop; (2) the inner direct axis current control loop; (3) the outer reactive power control loop; and (4) the inner quadrature axis current control loop.

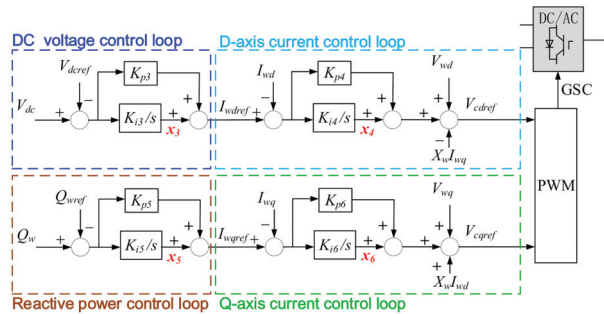


Figure 5. Control structure of GSC in FCPV.

The dynamics of GSC control system can be represented as

$$\begin{cases} \frac{dx_3}{dt} = K_{i3}(V_{dc} - V_{dcref}) \\ I_{wdref} = K_{p3}(V_{dc} - V_{dcref}) + x_3 \\ \frac{dx_4}{dt} = K_{i4}(I_{wdref} - I_{wd}) \\ V_{cdref} = K_{p4}(I_{wdref} - I_{wd}) + x_4 - X_w I_{wq} + V_{wd} \\ \frac{dx_5}{dt} = K_{i5}(Q_w - Q_{wref}) \\ I_{wqref} = K_{p5}(Q_w - Q_{wref}) + x_5 \\ \frac{dx_6}{dt} = K_{i6}(I_{wqref} - I_{wq}) \\ V_{cqref} = K_{p6}(I_{wqref} - I_{wq}) + x_6 + X_w I_{wd} + V_{wq} \end{cases} \tag{19}$$

where x_k ($k = 3, 4, 5, 6$) are the state variables of PI controllers, K_{pk} and K_{ik} ($k = 3, 4, 5, 6$) are the parameters of corresponding PI controllers. Q_w is the injected reactive power into power systems and expressed as

$$Q_w = V_{wq}I_{wd} - V_{wd}I_{wq} \tag{20}$$

5. Modeling of SRF-PLL

The same structure of the SRF-PLL shown in Figure 2 is applied in the FCPV and its dynamics are expressed as

$$\begin{cases} \frac{d}{dt}x_{pll2} = K_{ipll2}V_{wq} \\ \frac{d}{dt}\theta_{pll2} = x_{pll2} + K_{ppll2}V_{wq} + \omega_{pll2ref} \end{cases} \quad (21)$$

where all variables are similar to that of Equation (10). Accordingly, X_{*2} is used in (21) corresponding to X_* in (10).

Therefore, by linearizing Equations (12)–(21), the linearized state-space model of FCPV is obtained as

$$\begin{cases} \frac{d}{dt}\Delta X_{pv} = A_{pv}\Delta X_{pv} + B_{pv}\Delta V_{pv} \\ \Delta I_{pv} = C_{pv}\Delta X_{pv} \end{cases} \quad (22)$$

where ΔX_{pv} denotes all state variables of FCPV; A_{pv} , B_{pv} , C_{pv} are state-space matrices after integrating all the linearized differential equations. ΔV_{pv} and ΔI_{pv} denote the voltage variation and current variation at the PCC of FCPV in the common x-y coordinate.

3.3. Linearized Modeling of HRES System

Based on the linearized state-space models of FCWG in (11) and FCPV in (22), the linearized state-space model of an HRES system can be represented as

$$\begin{cases} \frac{d}{dt}\Delta X_{RES} = A_{RES}\Delta X_{RES} + B_{RES}\Delta V_M \\ \Delta I_M = C_{RES}\Delta X_{RES} \end{cases} \quad (23)$$

where

$\Delta X_{RES} = [\Delta X_{WG}^T \Delta X_{PVG}^T]^T$, $\Delta X_{WG} = [\Delta X_{w1}^T \Delta X_{w2}^T \dots \Delta X_{wM}^T]^T$, $\Delta X_{PVG} = [\Delta X_{pv1}^T \Delta X_{pv2}^T \dots \Delta X_{pvN}^T]^T$, $A_{RES} = \text{diag}[A_{WG} \ A_{PVG}]$, $A_{WG} = \text{diag}[A_{w1} \ A_{w2} \dots \ A_{wM}]$, $A_{PVG} = \text{diag}[A_{pv1} \ A_{pv2} \dots \ A_{pvN}]$, $B_{RES} = \text{diag}[B_{WG} \ B_{PVG}]$, $B_{WG} = \text{diag}[B_{w1} \ B_{w2} \dots \ B_{wM}]$, $B_{PVG} = \text{diag}[B_{pv1} \ B_{pv2} \dots \ B_{pvN}]$, $C_{RES} = \text{diag}[C_{WG} \ C_{PVG}]$, $C_{WG} = \text{diag}[C_{w1} \ C_{w2} \dots \ C_{wM}]$, $C_{PVG} = \text{diag}[C_{pv1} \ C_{pv2} \dots \ C_{pvN}]$; A_{wx} , B_{wx} , C_{wx} ($x = 1, 2, \dots, M$) are state matrices of the 1st to Mth FCWG, respectively; A_{pvx} , B_{pvx} , C_{pvx} ($x = 1, 2, \dots, N$) are state matrices of the 1st to Nth FCPV, respectively; ΔX_{wx}^T ($x = 1, 2, \dots, M$) and ΔX_{pvx}^T ($x = 1, 2, \dots, N$) denote the vector of all state variables of FCWGs and FCPVs, respectively; ΔV_M and ΔI_M are the voltage variation and current variation of the HRES system at PCCs. $\text{diag}[\]$ denotes either a diagonal matrix or a block diagonal matrix.

3.4. Entire Interconnected Power System

In the open-loop power system, the HRES system is modeled as a constant power source. Assume that the state-space model for N SGs in the AC power system is expressed as

$$\begin{cases} \frac{d}{dt}\Delta X_g = A_g\Delta X_g + B_g\Delta V_g \\ \Delta I_g = C_g\Delta X_g + D_g\Delta V_g \end{cases} \quad (24)$$

where $\Delta X_g = [\Delta X_{g1}^T \ \Delta X_{g2}^T \ \dots \ \Delta X_{gN}^T]^T$, $\Delta I_g = [\Delta I_{g1}^T \ \Delta I_{g2}^T \ \dots \ \Delta I_{gN}^T]^T$, $\Delta V_g = [\Delta V_{g1}^T \ \Delta V_{g2}^T \ \dots \ \Delta V_{gN}^T]^T$, $A_g = \text{diag}[A_{g1} \ A_{g2} \ \dots \ A_{gN}]$, $B_g = \text{diag}[B_{g1} \ B_{g2} \ \dots \ B_{gN}]$, $C_g = \text{diag}[C_{g1} \ C_{g2} \ \dots \ C_{gN}]$, $D_g = \text{diag}[D_{g1} \ D_{g2} \ \dots \ D_{gN}]$, ΔX_{gj}^T ($j = 1, 2, \dots, N$) denotes the vector of all state variables of the jth SG. ΔI_{gj}^T and ΔV_{gj}^T ($j = 1, 2, \dots, N$) are the current variation and voltage variation at connecting bus of jth SG. A_{gj} , B_{gj} , C_{gj} , and D_{gj} ($j = 1, 2, \dots, N$) denote state-space matrices of the jth SG.

The equation of the transmission network is expressed as

$$\begin{bmatrix} I_g \\ I_M \\ I_N \end{bmatrix} = Y \begin{bmatrix} V_g \\ V_M \\ V_N \end{bmatrix} = \begin{bmatrix} Y_{gg} & Y_{gw} & Y_{gn} \\ Y_{wg} & Y_{ww} & Y_{wn} \\ Y_{ng} & Y_{nw} & Y_{nn} \end{bmatrix} \begin{bmatrix} V_g \\ V_M \\ V_N \end{bmatrix} \quad (25)$$

where I_g and V_g denote the current injection and voltage at the connecting buses of all SGs; I_M and V_M denote the current injection and voltage at PCCs of the HRES system; I_N and V_N denote the current injection and voltage at other buses in the network; Y denotes the admittance matrix.

From Equations (24) and (25), the open-loop power system can be derived as

$$\begin{cases} \frac{d}{dt} \Delta X_g = A_{gs} \Delta X_g + B_{gs} \Delta I_M \\ \Delta V_M = C_{gs} \Delta X_g + d_{gs} \Delta I_M \end{cases} \quad (26)$$

where

$$\begin{aligned} A_{gs} &= A_g + B_g \left(Y_{ggN} - Y_{gwN} Y_{wwN}^{-1} Y_{wgN} - D_g \right)^{-1} C_g, \\ B_{gs} &= -B_g \left(Y_{ggN} - Y_{gwN} Y_{wwN}^{-1} Y_{wgN} - D_g \right)^{-1} Y_{gwN} Y_{wwN}^{-1}, \\ C_{gs} &= -Y_{wwN}^{-1} Y_{wgN} \left(Y_{ggN} - Y_{gwN} Y_{wwN}^{-1} Y_{wgN} - D_g \right)^{-1} C_g, \\ d_{gs} &= Y_{wwN}^{-1} + Y_{wwN}^{-1} Y_{wgN} \left(Y_{ggN} - Y_{gwN} Y_{wwN}^{-1} Y_{wgN} - D_g \right)^{-1} Y_{gwN} Y_{wwN}^{-1}, \\ Y_{ggN} &= \left(Y_{gg} - Y_{gn} Y_{nn}^{-1} Y_{ng} \right), Y_{gwN} = Y_{gw} - Y_{gn} Y_{nn}^{-1} Y_{nw}, \\ Y_{wgN} &= \left(Y_{wg} - Y_{wn} Y_{nn}^{-1} Y_{ng} \right), Y_{wwN} = \left(Y_{ww} - Y_{wn} Y_{nn}^{-1} Y_{nw} \right). \end{aligned}$$

From Equations (23) and (26), the closed-loop interconnected model of the power system can be derived as

$$\frac{d}{dt} \begin{bmatrix} \Delta X_g \\ \Delta X_{RES} \end{bmatrix} = \begin{bmatrix} A_{gs} & B_{gs} C_{RES} \\ B_{RES} C_{gs} & A_{RES} + B_{RES} d_{gs} C_{RES} \end{bmatrix} \begin{bmatrix} \Delta X_g \\ \Delta X_{RES} \end{bmatrix} \quad (27)$$

4. Methodology of Optimization Strategy

According to the modal superposition theory in [20], modal interaction can be categorized into three types: (1) weak interaction which indicates the HRES system interacts very slightly with the AC power system and thus the interaction effect can be ignored while studying converter-driven stability; (2) modal resonance that drives adjacent oscillation modes to move against each and thus impairs the system damping and threatens converter-driven stability; and (3) modal counteraction that implies that the HRES system interacts positively with AC power system and improves the system damping. It is worth mentioning that the negative modal resonance will jeopardize converter-driven stability and thus should be avoided, while the beneficial modal counteraction would be a favorable choice when integrating an HRES system.

To facilitate the positive interaction between the HRES system and the AC power system, an eigenvalue shift index (ESI) is utilized to quantitatively evaluate the effect of modal interaction on the critical EOM. Denote $\lambda_{olsysi} = \sigma \pm j\omega$ as the i th oscillation mode of the open-loop power system, $\lambda_{clsysi} = \hat{\sigma} \pm j\hat{\omega}$ as the i th oscillation mode of the closed-loop system. Hence, the modal interaction effect of the newly introduced HRES system is evaluated by $ESI = \Delta\lambda_{sys} = \lambda_{clsysi} - \lambda_{olsysi}$. According to the open-loop and closed-loop models in Section 3.4, modal analysis can be applied and thus provide a quantitative calculation for ESI.

If the real part of ESI, i.e., $Re(ESI) < 0$, demonstrates that the modal interaction is beneficial for the converter-driven stability. However, if $Re(ESI) > 0$, a detrimental impact regarding modal interaction is induced and deteriorates the converter-driven stability. To tackle this negative impact, a modal interaction optimization strategy can be implemented by tuning the control parameters of the HRES system. The optimization objective, as expressed in (28) is to obtain the largest modal shift in critical EOM towards the left half complex plane.

$$\text{Minimize } Re(ESI) = \text{real}(\Delta\lambda_{sysi}) \quad (28)$$

where $\Delta\lambda_{sysi}$ represents the eigenvalue shifts of interactive EOMs.

It should be pointed out that the modal interaction optimization should not sacrifice the dynamics of the HRES system at an unacceptable level. Since parameter tuning is performed in HRES controllers, it is necessary and feasible to guarantee a sufficient damping margin for the HRES system. In this study, the PLLs of FCWG and FCPV were identified to be key components to optimize the multi-modal interaction with two EOMs of AC power system, and thus this can be regarded as a multi-modal multi-parametric optimization problem. The multi-objective particle swarm optimization (MOPSO) algorithm was applied to tune the parameters of key controllers.

5. Case Study

5.1. Introduction of Test Power System

An IEEE 16-machine 68-bus system [28] with an HRES system connected at bus 8 is illustrated in Figure 6. The HRES system consists of an FCWG-based wind farm and an FCPV-based solar energy farm. To emulate different penetration levels, four operating condition cases were thoroughly studied to uncover the impact on converter-driven stability regarding the modal interaction between the HRES system and AC power system. Denote the active power outputs (in per unit with base $S_b = 100$ MVA) of FCWG and FCPV as P_{WG} and P_{PV} respectively. The four operating condition cases were: (1) Case 1: $P_{WG} = 0$, $P_{PV} = 0$; (2) Case 2: $P_{WG} = 0.5$ p.u., $P_{PV} = 0.5$ p.u.; (3) Case 3: $P_{WG} = 1.0$ p.u., $P_{PV} = 1.5$ p.u.; and (4) Case 4: $P_{WG} = 2.0$ p.u., $P_{PV} = 2.5$ p.u. Both FCWG and FCPV adopted reactive power control with constant power factor of 0.98. The test system was built on the Matlab R2020b platform via M-language programming.

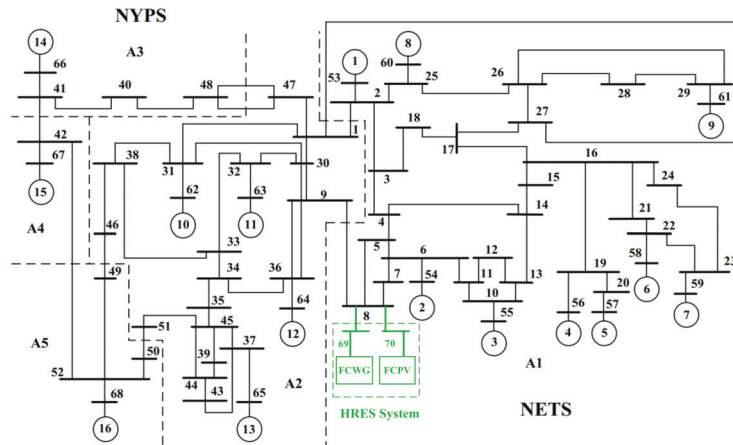


Figure 6. Configuration of test IEEE power system integrated with an HRES system.

The modal interaction can be either weak or strong. In a weak interaction case, the interaction impact can be ignored and the HRES system can be regarded as a constant power source. However, in strong interaction cases, the modal interaction between the HRES system and AC power system might have a considerable impact on the converter-driven stability and thus will be carefully addressed in the following analyses.

To begin with, open-loop modal analyses of the examined power systems with different wind power and PV solar energy penetration level were performed. Then, closed-loop modal resonance analyses of the closed-loop system and time-domain simulations were performed as supplementary verification. To mitigate the detrimental effect caused by strong modal interaction (i.e., modal resonance), the modal interaction optimization strategy was further adopted as well.

5.2. Converter-Driven Stability Analyses Considering Different Renewable Energy Penetration Levels

Based on the linearized state-space model the state matrix in Equation (26), the critical EOM of the open-loop power systems can be calculated, as exhibited in Table 1. The open-loop critical EOM of the power systems examined was slightly affected by different constant injected active power after ignoring the modal interaction of FCWG and FCPV. Since the open-loop EOM is mainly determined by the electromechanical dynamics of SGs in the AC power system, it had a relatively stable oscillation frequency (0.57 Hz–0.60 Hz) with a damping ratio (DR) around 2.9%. This was also confirmed by the electromechanical loop correlation ratio (ELCR) [12], which stayed at a very high level (36.80–37.50).

Table 1. Open-loop modal analysis regarding different renewable energy penetration levels.

Active Power from FCWG and FCPV (p.u.)	Open-Loop Critical EOM (λ_{opsys})	Frequency (Hz)	DR	ELCR
Case 1 (0, 0)	$-0.1064 \pm 3.6391 i$	0.5792	2.92%	36.80
Case 2 (0.5, 0.5)	$-0.1067 \pm 3.6694 i$	0.5840	2.91%	36.88
Case 3 (1.0, 1.5)	$-0.1068 \pm 3.7158 i$	0.5914	2.87%	37.08
Case 4 (2.0, 2.5)	$-0.1060 \pm 3.7790 i$	0.6014	2.80%	37.50

As shown in Table 2, when the renewable energy penetration level grew higher, the modal interaction became stronger. This is because the modal interaction between the HRES system and AC power system is negative (viz., modal resonance), and such interaction effect is further magnified in the cases with large active power output from the HRES system [20]. The decrease in DR manifests that the closed-loop critical EOM becomes weaker and less stable. For instance, in Case 4, the closed-loop critical EOM had a negative DR (-0.72%), which means that the system lost its converter-driven stability and became unstable.

Table 2. Closed-loop modal analysis regarding different renewable energy penetration levels.

Active power from FCWG and FCPV (p.u.)	Closed-Loop Critical EOM λ_{clsys}	Frequency (Hz)	DR	ELCR
Case 1 (0, 0)	$-0.1064 \pm 3.6391 i$	0.5792	2.92%	36.80
Case 2 (0.5, 0.5)	$-0.0527 \pm 3.6022 i$	0.5733	1.46%	2.9990
Case 3 (1.0, 1.5)	$-0.0105 \pm 3.5506 i$	0.5651	0.30%	1.8867
Case 4 (2.0, 2.5)	$0.0251 \pm 3.4917 i$	0.5557	-0.72%	1.4929

Participation factor analysis in Figure 7 illustrates that, in Case 1, since the active power of FCWG and FCPV were zero, they did not participate in the closed-loop critical EOM, and thus it stayed in the same position of the open-loop critical EOM. However, when the active power outputs of FCWG and FCPV increased, they began to actively interact with SGs and even became the dominant power sources (as shown in Case 3 and Case 4). A few very interesting and important findings are observed below. When we compare the active power outputs, although the total active power output of the HRES system (2.0 p.u. in Case 3 and 4.5 p.u. in Case 4 respectively) was less than one-tenth of the total active power of 13th and 15th SGs (45.91 p.u.), the HRES system had much larger participation factors for the critical EOM than that of the 13th and 15th SGs. It is also noteworthy that ELCR in Table 2 decreased significantly, which further indicates this critical EOM became less relevant to the electromechanical dynamics among SGs.

Through participation factor evaluation, it was also revealed that the closed-loop critical EOMs with oscillation frequencies between 0.55 Hz and 0.58 Hz were mainly dominated by PLL dynamics of the HRES system and electromechanical dynamics of the AC power system, respectively. Specifically, state variables related to PLL dynamics (i.e., Δx_{pll} , $\Delta \theta_{pll}$, Δx_{pll2} , $\Delta \theta_{pll2}$) and SG electromechanical dynamics (i.e., $\Delta \omega_K$, $\Delta \delta_K$, ($K = 1, 2, \dots, 16$)) were the most active components in these closed-loop EOMs.

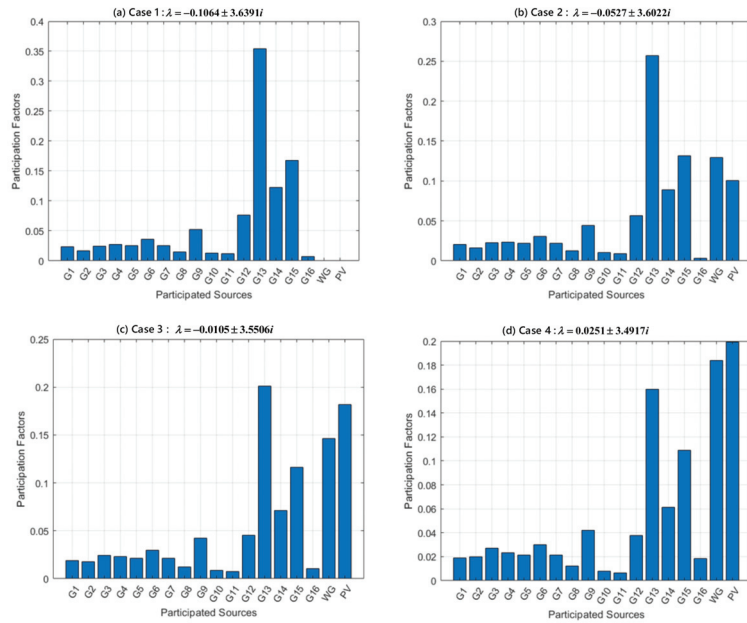


Figure 7. Participation factor analysis for closed-loop critical EOM (0.55 Hz–0.58 Hz). (a) Case 1; (b) Case 2; (c) Case 3; (d) Case 4.

It is worth mentioning that the integration of the HRES system not only affected the critical EOM, but also interacted with other EOMs with different intensity levels. Here we demonstrate the participation of HRES in another local EOM (0.65 Hz~0.67 Hz, mainly dominated by 14th and 16th SGs and denoted as EOM2) in Figure 8. In Case 4, the HRES system had a total participation factor larger than 0.2, and both FCWG and FCPV participated. It can be seen that the DR of EOM2 increased from 2.22% to 3.60%. In other words, the modal interaction effect on EOM2 was positive. Moreover, despite the large geographical/electrical distance between the HRES system and SGs (14th and 16th), great attention should be paid to their modal interaction, especially in the detrimental modal resonance cases. This also proves that the HRES dynamics can penetrate deeply into the local electromechanical dynamics. It further indicates that the interaction between the HRES system and AC power system can be multi-modal. In this study, two HRES oscillation modes and two EOMs were representative and involved in the modal interaction process.

Modal interaction also affects the oscillation modes of the HRES system. In this work, we investigated two critical oscillation modes of the HRES system, i.e., one from FCWG and the other from FCPV, which are denoted as FOM and POM respectively. It should be pointed out that there are 7 pairs of conjugated oscillation modes in FCWG and 5 pairs in FCPV. Only the two most active oscillation modes are listed and analyzed, and the other modes have a very limited interaction with the electromechanical dynamics and thus can be ignored in this study. The closed-loop modal analysis of the HRES system is presented in Table 3 (FCWG) and Table 4 (FCPV). The results of open-loop modal analysis are not listed separately here since they are almost the same as those of Case 1 in the closed-loop modal analysis. This is because the modal interaction impact is not considered in the open-loop modal analysis, and the power flow impact on modal shifts is minimal unless significant changes occur in the AC power system, as demonstrated in Table 1.

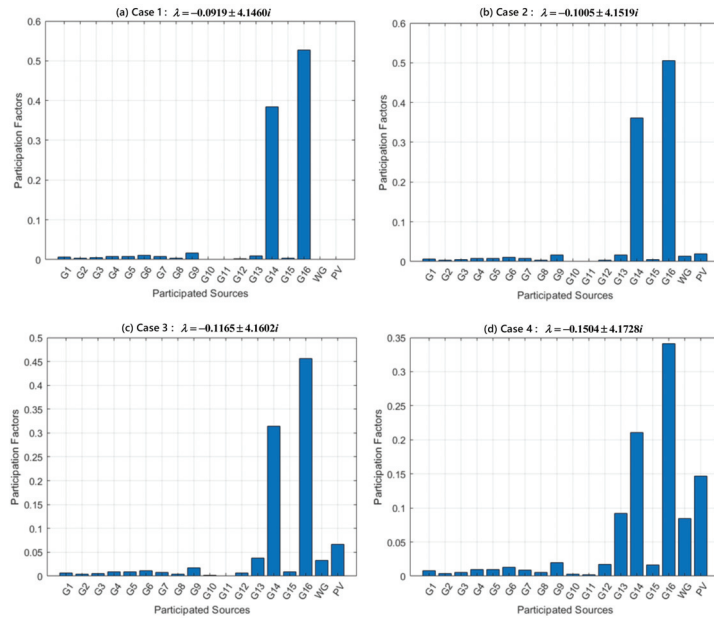


Figure 8. Participation factor analysis for closed-loop EOM2 (0.65 Hz~0.67 Hz). (a) Case 1; (b) Case 2; (c) Case 3; (d) Case 4.

Table 3. Closed-loop modal analysis of FOM (wind power).

Active Power from FCWG (p.u.)	Closed-Loop FOM λ_{clwg}	Frequency (Hz)	DR	ELCR
Case 1 (0)	$-0.0702 \pm 3.7456 i$	0.5961	1.87%	0
Case 2 (0.5)	$-0.0812 \pm 3.8706 i$	0.6160	2.10%	0.0482
Case 3 (1.0)	$-0.0783 \pm 3.9024 i$	0.6211	2.01%	0.0187
Case 4 (2.0)	$-0.0786 \pm 3.9446 i$	0.6278	1.99%	0.0122

Table 4. Closed-loop modal analysis of POM (PV).

Active Power from FCPV (p.u.)	Closed-Loop POM λ_{clpv}	Frequency (Hz)	DR	ELCR
Case 1 (0)	$-0.0748 \pm 3.8683 i$	0.6157	1.93%	0
Case 2 (0.5)	$-0.1083 \pm 3.9019 i$	0.6210	2.77%	0.2868
Case 3 (1.5)	$-0.1327 \pm 3.9710 i$	0.6320	3.34%	0.6820
Case 4 (2.5)	$-0.1297 \pm 4.0445 i$	0.6437	3.21%	1.4651

It can be seen in Tables 3 and 4 that both closed-loop FOM and closed-loop POM were improved with damping increase. Meanwhile, the corresponding oscillation frequencies also increased slightly. It is important to highlight that, in Case 4, the closed-loop POM has a large ELCR (**1.4651**), which is greater than 1. Thus, this POM can be recognized as an EOM, and its participation factor analysis is exhibited in Figure 9. Five SGs (12th–16th SGs) participate actively in this POM. Moreover, FCWG also has a large participation (larger than 0.1) in this POM, which indicates that FCWG and FCPV might interact with each other and affect their own dynamics.

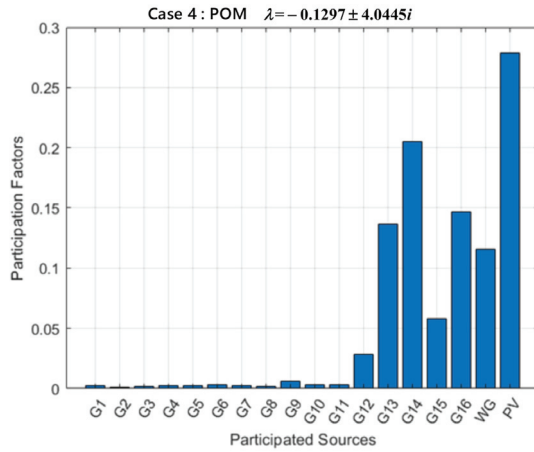


Figure 9. Participation factor analysis for closed-loop POM in Case 4.

To demonstrate the modal interaction effect discussed above, the modal shifts regarding four main interactive oscillation modes (i.e., Critical EOM, EOM2, FOM, and POM) from their open-loop location to closed-loop location are illustrated in Figure 10. λ_{clsysk} , $\lambda_{clsys2k}$, λ_{clwkg} , and λ_{clpvk} (case number $k = 1, 2, 3, 4$) denote the eigenvalues of four closed-loop oscillation modes in four cases, respectively. It should be noted that the open-loop location of the oscillation modes in all four cases was almost of the same as their closed-loop location of Case 1 (i.e., λ_{clsys1} , $\lambda_{clsys21}$, λ_{clwg1} , and λ_{clpv1}). This phenomenon can be evidenced the information in Table 1, as well as the nature of PLL oscillation modes of FCWG and FCPV. Hence, for better readability, the open-loop oscillation modes are not presented in Figure 10, and instead λ_{clsys1} , $\lambda_{clsys21}$, λ_{clwg1} , and λ_{clpv1} can be treated as the starting points of each modal shift. In other words, the modal shift of each oscillation mode due to the interaction is the eigenvalue movement from its starting point to the closed-loop oscillation mode. It is easy to conclude from Figure 10 that although EOM2 and POM were meliorated, the critical EOM was impaired and gradually shifted towards the unstable right half-plane.

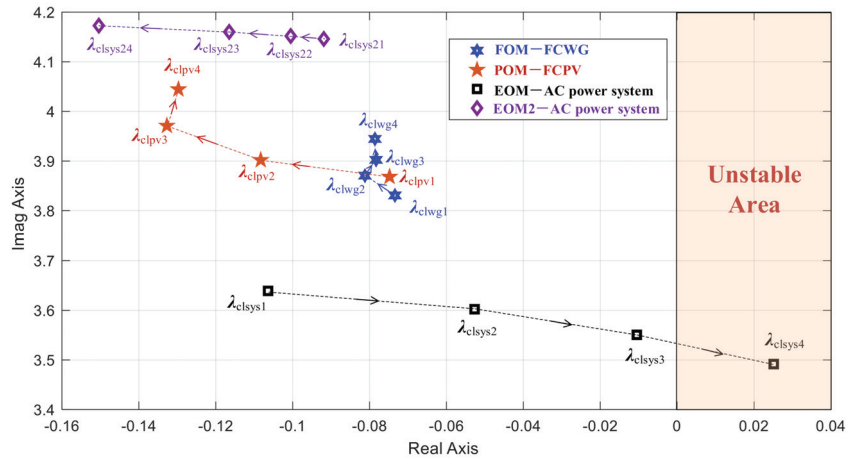


Figure 10. Modal shifts due to modal interaction in four cases.

To verify modal analysis results and further illustrate converter-driven stability visually, time-domain simulations were carried out. The simulation conditions were set as: a 5% step increase in the mechanical power of 1st SG occurs and subsequently drops to the original value after 100 ms. From the participation factor analysis in Figure 7, 13th and 15th SGs had the largest and second-largest participation factors in the AC power system, respectively. Hence, the rotor speed difference between 13th and 15th SG and active power of 15th SG were demonstrated. The DRs in Table 2 are also marked in the simulation results.

From Figures 11 and 12, modal interaction between the HRES system and AC power system had a negative impact on the closed-loop critical EOM. Especially in Case 4, the 13th and 15th SGs lost synchronism and the active power output of 15th SG became unstable. Therefore, the simulation results are consistent with the modal analysis above.

5.3. Modal Interaction Optimization to Enhance Converter-Driven Stability

A modal interaction optimization strategy was implemented to mitigate the detrimental effect of modal resonance and enhance the converter-driven stability. By tuning parameters of FCWG and FCPV, the open-loop critical FOM and POM can not only be relocated but also induce beneficial modal interactions with the AC power system. As a result, the strong multi-modal resonance was eliminated. In this study, PLL control parameters of FCWG and FCPV were identified as pivotal parameters related to strong modal resonance. Therefore, the modal interaction optimization strategy was performed to appropriately adjust these parameters. The modified parameters and corresponding modal analysis results are listed in Table 5. Compared with the original power system with inadequate damping, the closed-loop critical EOM after optimization gains significantly improved damping, and hence better converter-driven stability.

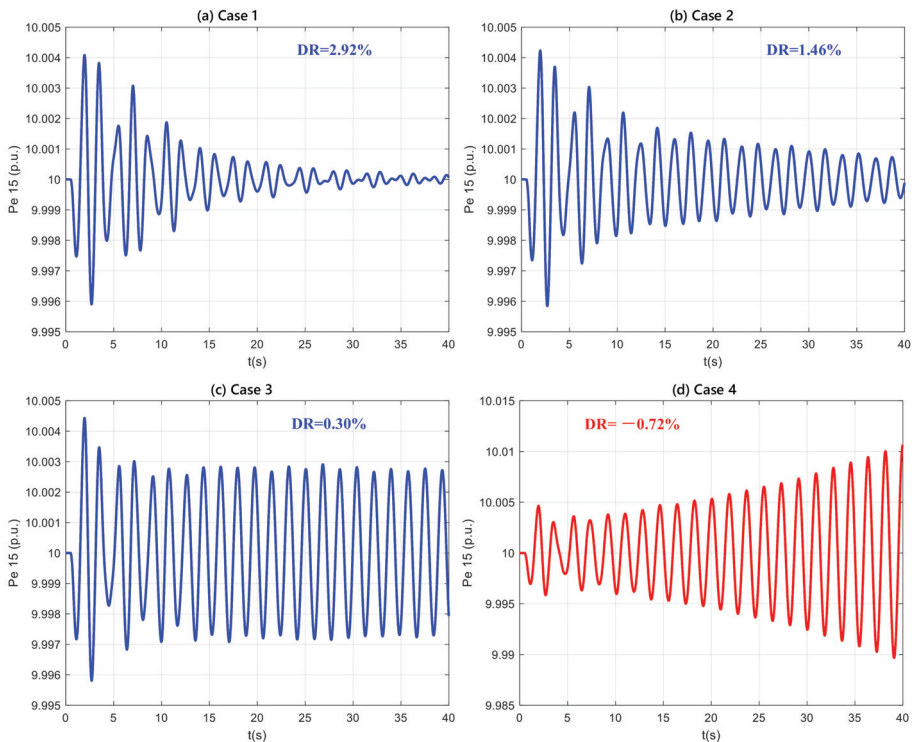


Figure 11. Rotor speed difference between 13th SG and 15th SG in four Cases. (a) Case 1; (b) Case 2; (c) Case 3; (d) Case 4.

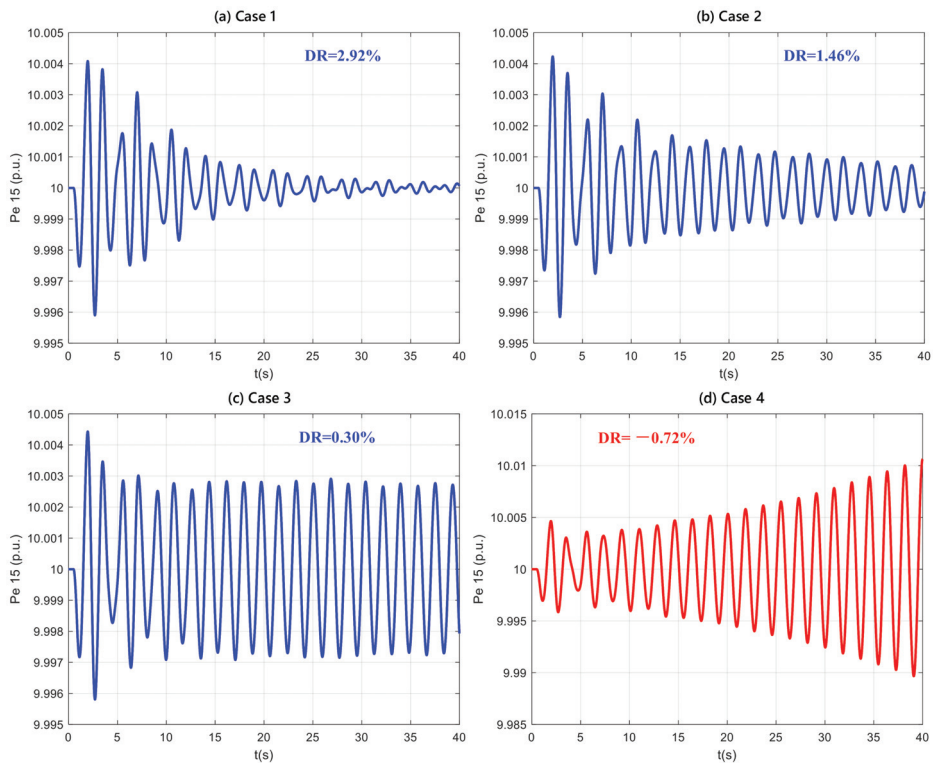


Figure 12. Active power output of 15th SG in four Cases. (a) Case 1; (b) Case 2; (c) Case 3; (d) Case 4.

Table 5. Parameter optimization of FCWG and FCPV.

Type	Original Control Parameters	Optimized Control Parameters
PLL control parameters of FCWG	$K_{pwg} = 0.15, K_{i wg} = 15,$	$K_{pwg} = 0.5631, K_{i wg} = 11.4376$
PLL control parameters of FCPV	$K_{ppv} = 0.16, K_{i pv} = 16$	$K_{ppv} = 0.3487, K_{i pv} = 16.3764$
Open-loop critical FOM (Freq., DR)	$-0.0776 \pm 3.9385 i$ (0.6268 Hz, 1.97%)	$-0.2731 \pm 3.3194 i$ (0.5283 Hz, 8.20%)
Closed-loop critical FOM (Freq., DR)	$-0.0786 \pm 3.9446 i$ (0.6278 Hz, 1.99%)	$-0.1388 \pm 3.2740 i$ (0.5211 Hz, 4.23%)
Open-loop critical POM (Freq., DR)	$-0.0792 \pm 3.9783 i$ (0.6332 Hz, 1.99%)	$-0.1725 \pm 4.0220 i$ (0.6401 Hz, 4.29%)
Closed-loop critical POM (Freq., DR)	$-0.1297 \pm 4.0445 i$ (0.6437 Hz, 3.21%)	$-0.1907 \pm 4.1088 i$ (0.6539 Hz, 4.64%)
Open-loop critical EOM (Freq., DR)	$-0.1060 \pm 3.7790 i$ (0.6024 Hz, 2.80%)	$-0.1060 \pm 3.7790 i$ (0.6024 Hz, 2.80%)
Closed-loop critical EOM (Freq., DR)	$0.0251 \pm 3.4917 i$ (0.5557 Hz, -0.72%)	$-0.1647 \pm 3.5897 i$ (0.5713 Hz, 4.58%)
Open-loop EOM2 (Freq., DR)	$-0.0934 \pm 4.1669 i$ (0.6632 Hz, 2.24%)	$-0.0934 \pm 4.1669 i$ (0.6632 Hz, 2.24%)
Closed-loop EOM2 (Freq., DR)	$-0.1504 \pm 4.1728 i$ (0.6641 Hz, 3.60%)	$-0.1323 \pm 4.1232 i$ (0.6562 Hz, 3.21%)

The modal shifts of system EOMs are also presented in Figure 13. Compared with the original system, in the optimized system, the closed-loop critical EOM moves towards the left half complex plane. Its DR increases from **-0.72%** to **4.58%**, which is quite a prominent improvement. It should also be highlighted that such a change is only brought by the

parameter tuning with the optimization strategy, while the operating condition remains the same. From the perspective of system operators, this method is very cost-effective since no additional control or devices involved.

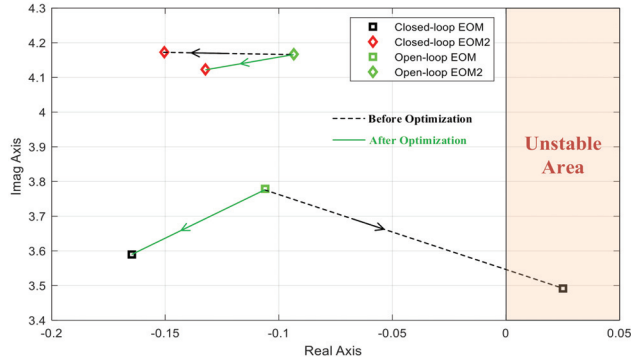


Figure 13. Modal shifts of system EOMs with/without optimization strategy.

The rotor speed difference between 13th and 15th SGs and active power of 15th SG are compared in Figure 14. The dynamic performance of the modified interconnected system was greatly improved. These results are in accordance with the DR indication of the closed-loop critical EOM in Table 5. Therefore, the implemented multi-modal and multi-parametric optimization strategy was found to be effective for reinforcing the converter-driven stability.

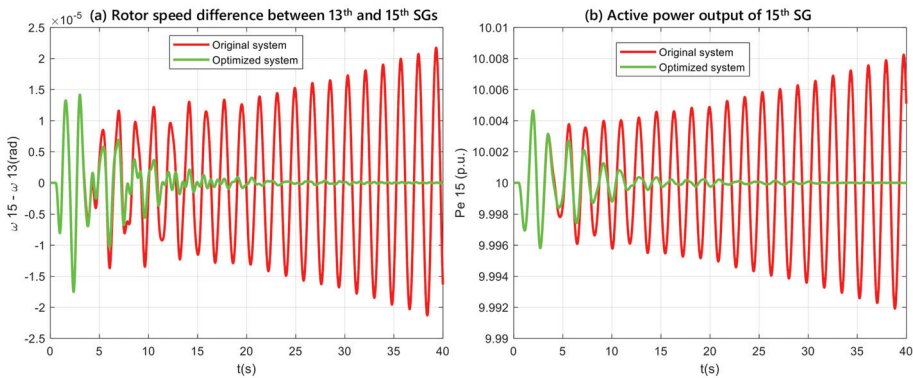


Figure 14. Comparison of simulation results in Case 4 before/after optimization. (a) Rotor speed difference between 13th and 15th SGs; (b) Active power output of 15th SG.

6. Discussion

In the above converter-driven stability analysis, various modal interaction conditions were thoroughly investigated by extensively evaluating the multi-modal interactions between the multi-RESs in the HRES system and AC power system. Several important findings are summarized as follows:

- (1) From the open-loop modal analysis of the external AC power system, with the increasing active power injection of RESs, the open-loop critical EOM was very slightly affected. Such minor variations are mainly due to the power flow impact since the modal interaction of the HRES system was excluded in the open-loop analysis.

- (2) For the closed-loop modal analysis, the overall impact of HRES integration was evaluated, considering both the power flow impact and modal interactions. Strong modal interaction occurred when the open-loop critical FOM and POM were close to the open-loop EOMs in terms of oscillation frequency. This is a necessary condition to induce strong modal interaction.
- (3) The multi-modal interaction involved oscillation modes of the multi-RESs in the HRES system and AC power system. The integration of the HRES system mainly affected two EOMs (i.e., one global critical EOM and one local EOM2). Strong modal interaction effects can be either positive or negative. For instance, in this study, the critical EOM deteriorated while the local EOM2 improved.
- (4) The HRES system could participate more actively in the critical EOMs even at a much lower active power output compared to SGs. The HRES dynamics could penetrate deeply into the local electromechanical dynamics regardless of their geographical/electrical distance.
- (5) The electromechanical dynamics of SGs might also participate in HRES oscillation modes (e.g., FOM and POM), which will lead to either positive or negative modal shifts in HRES oscillation modes. Their participation can also be quantified by ELCRs.
- (6) Apart from the interaction between SGs and HRES, FCWG and FCPV inside the HRES system can also interact with each other and participate in each other's dynamics. Therefore, it is necessary to coordinate their interaction (e.g., parameter tuning) and avoid the interior modal resonance.
- (7) An interesting phenomenon appears when electromechanical dynamics become quite active in an HRES oscillation mode, and thus this mode turns into an EOM. In Case 4, the closed-loop POM had an ELCR larger than 1, and hence it can be recognized as an EOM. Such phenomena usually happen at high HRES penetration levels.
- (8) As a negative strong modal interaction, modal resonance might dramatically degrade system damping and thus should be circumvented. An effective countermeasure is to implement the modal interaction optimization strategy to properly modify the key parameters of HRES controllers. With the optimization strategy adopted, not only can the detrimental effect of modal resonance be alleviated, but also a positive modal interaction (i.e., modal counteraction) can be achieved.

7. Conclusions

In this work, an IEEE benchmark power system with an HRES system was investigated regarding the converter-driven stability. The converter-driven stability issues studied are in the form of modal interaction between two subsystems (i.e., HRES system and AC power system). Therefore, we elaborately examined the detrimental modal resonance conditions to reveal the mechanisms of potential converter-driven instability issues.

The integration of the HRES system not only affected the power flow but also interacted with the external AC power system. Particularly, when modal resonance happened, the critical system EOM was forced to move towards the right half complex plane, and thus threatened the converter-driven stability. An extreme condition with a multi-modal interaction case was examined to evaluate the consequence of strong modal resonance. The DR of closed-loop critical mode was greatly weakened or even became negative. As a result, oscillations once being aroused due to unexpected disturbances cannot be effectively suppressed and may further propagate in the external AC power system.

To prevent this adverse phenomenon, a modal interaction optimization strategy was implemented. The converter-driven stability was remarkably enhanced after relocating critical modes of the HRES system and meliorating its modal interaction with the AC power system. Consistent with modal analysis, time-domain simulation results substantiate that the groups of SGs can maintain synchronism in disturbance conditions after optimization in the HRES system.

Author Contributions: J.L. completed the methodology, theory analysis, validation, and wrote the paper. Y.Z. conducted data analysis, simulations, and validation. S.B. supervised the research through-

out, acquired funding, coordinated the project, and revised & edited the paper. U.K. conducted validation. All authors have read and agreed to the published version of the manuscript.

Funding: This research was funded by National Natural Science Foundation of China for the Research Project (52077188), Guangdong Science and Technology Department for the Research Project (2019A1515011226), Hong Kong Research Grant Council for the Research Projects (25203917), (15200418) and (15219619), and Department of Electrical Engineering, The Hong Kong Polytechnic University for the Start-up Fund Research Project (1-ZE68).

Institutional Review Board Statement: Not applicable.

Informed Consent Statement: Not applicable.

Data Availability Statement: Not applicable.

Conflicts of Interest: The authors declare no conflict of interest.

References

- Quintero, J.; Vittal, V.; Heydt, G.T.; Zhang, H. The Impact of Increased Penetration of Converter Control-Based Generators on Power System Modes of Oscillation. *IEEE Trans. Power Syst.* **2014**, *29*, 2248–2256. [\[CrossRef\]](#)
- Badal, F.R.; Das, P.; Sarker, S.K.; Das, S.K. A survey on control issues in renewable energy integration and microgrid. *Prot. Control Mod. Power Syst.* **2019**, *4*, 8. [\[CrossRef\]](#)
- Luo, J.; Bu, S.; Zhu, J.; Chung, C.Y. Modal Shift Evaluation and Optimization for Resonance Mechanism Investigation and Mitigation of Power Systems Integrated With FCWG. *IEEE Trans. Power Syst.* **2020**, *35*, 4046–4055. [\[CrossRef\]](#)
- Elliott, R.T.; Ellis, A.; Pourbeik, P.; Sanchez-Gasca, J.J.; Senthil, J.; Weber, J. Generic photovoltaic system models for WECC—A status report, 2015. In Proceedings of the IEEE Power & Energy Society General Meeting, Denver, CO, USA, 26–30 July 2015; pp. 1–5.
- Hatziargyriou, N.; Milanović, J.; Rahmann, C.; Ajarapu, V.; Cañizares, C.; Erlich, I.; Hill, D.; Hiskens, I.; Kamwa, I.; Pal, B.S. *Stability Definitions and Characterization of Dynamic Behavior in Systems with High Penetration of Power Electronic Interfaced Technologies*; Technical Report No. PES-TR77; IEEE: Piscataway, NJ, USA, 2020; p. 42.
- Adams, J.; Pappu, V.A.; Dixit, A. Ercot experience screening for Sub-Synchronous Control Interaction in the vicinity of series capacitor banks, 2012. In Proceedings of the IEEE Power and Energy Society General Meeting, San Diego, CA, USA, 22–26 July 2012; pp. 1–5.
- Liu, H.; Xie, X.; Gao, X.; Liu, H.; Li, Y. Stability Analysis of SSR in Multiple Wind Farms Connected to Series-Compensated Systems Using Impedance Network Model. *IEEE Trans. Power Syst.* **2018**, *33*, 3118–3128. [\[CrossRef\]](#)
- Luo, J.; Bu, S.; Chung, C.Y. Design and Comparison of Auxiliary Resonance controllers for Mitigating Modal Resonance of Power Systems Integrated with Wind Generation. *IEEE Trans. Power Syst.* **2021**. [\[CrossRef\]](#)
- Zhan, Y.; Xie, X.; Liu, H.; Liu, H.; Li, Y. Frequency-Domain Modal Analysis of the Oscillatory Stability of Power Systems With High-Penetration Renewables. *IEEE Trans. Sustain. Energy* **2019**, *10*, 1534–1543. [\[CrossRef\]](#)
- Du, W.; Wang, H.F.; Bu, S. *Small-Signal Stability Analysis of Power Systems Integrated with Variable Speed Wind Generators*; Springer Nature: Cham, Switzerland, 2018.
- Du, W.; Bi, J.; Wang, H. Damping Degradation of Power System Low-Frequency Electromechanical Oscillations Caused by Open-Loop Modal Resonance. *IEEE Trans. Power Syst.* **2018**, *33*, 5072–5081. [\[CrossRef\]](#)
- Luo, J.; Bu, S.; Zhu, J. Transition from Electromechanical Dynamics to Quasi-Electromechanical Dynamics Caused by Participation of Full Converter-Based Wind Power Generation. *Energies* **2020**, *13*, 6270. [\[CrossRef\]](#)
- Zhou, J.Z.; Ding, H.; Fan, S.; Zhang, Y.; Gole, A.M. Impact of Short-Circuit Ratio and Phase-Locked-Loop Parameters on the Small-Signal Behavior of a VSC-HVDC Converter. *IEEE Trans. Power Deliv.* **2014**, *29*, 2287–2296. [\[CrossRef\]](#)
- Meegahapola, L.G.; Bu, S.; Wadduwage, D.P.; Chung, C.Y.; Yu, X. Review on Oscillatory Stability in Power Grids With Renewable Energy Sources: Monitoring, Analysis, and Control Using Synchronophasor Technology. *IEEE Trans. Ind. Electron.* **2021**, *68*, 519–531. [\[CrossRef\]](#)
- Morató, J.; Knüppel, T.; Østergaard, J. Residue-Based Evaluation of the Use of Wind Power Plants With Full Converter Wind Turbines for Power Oscillation Damping Control. *IEEE Trans. Sustain. Energy* **2014**, *5*, 82–89. [\[CrossRef\]](#)
- Knüppel, T.; Nielsen, J.N.; Jensen, K.H.; Dixon, A.; Østergaard, J. Power Oscillation Damping Capabilities of Wind Power Plant with Full Converter Wind Turbines Considering its Distributed and Modular Characteristics. *IET Renew. Power Gener.* **2013**, *7*, 431–442. [\[CrossRef\]](#)
- Haque, M.E.; Negnevitsky, M.; Muttaqi, K.M. A Novel Control Strategy for a Variable Speed Wind Turbine with a Permanent Magnet Synchronous Generator, 2008. In Proceedings of the IEEE Industry Applications Society Annual Meeting, Edmonton, AB, Canada, 5–9 October 2008; pp. 1–8.
- Jamehbozorg, A.; Radman, G. Small Signal Analysis of Power Systems with Wind and Energy Storage Units. *IEEE Trans. Power Syst.* **2015**, *30*, 298–305. [\[CrossRef\]](#)

19. Luo, J.; Bu, S.; Zhu, J. A Novel PMU-based Adaptive Coordination Strategy to Mitigate Modal Resonance between Full Converter-based Wind Generation and Grids. *IEEE J. Emerg. Sel. Top. Power Electron.* **2020**. [[CrossRef](#)]
20. Luo, J.; Bu, S.; Teng, F. An Optimal Modal Coordination Strategy based on Modal Superposition Theory to Mitigate Low Frequency Oscillation in FCWG Penetrated Power Systems. *Int. J. Electr. Power Energy Syst.* **2020**, *120*, 105975. [[CrossRef](#)]
21. Gautam, D.; Vittal, V.; Harbour, T. Impact of Increased Penetration of DFIG-Based Wind Turbine Generators on Transient and Small Signal Stability of Power Systems. *IEEE Trans. Power Syst.* **2009**, *24*, 1426–1434. [[CrossRef](#)]
22. Slootweg, J.G.; Kling, W.L. The impact of large scale wind power generation on power system oscillations. *Electr. Power Syst. Res.* **2003**, *67*, 9–20. [[CrossRef](#)]
23. Wen, B.; Boroyevich, D.; Burgos, R.; Mattavelli, P.; Shen, Z. Analysis of D-Q Small-Signal Impedance of Grid-Tied Inverters. *IEEE Trans. Power Electron.* **2016**, *31*, 675–687. [[CrossRef](#)]
24. Wang, L.; Lin, T.-C. Dynamic stability and transient responses of multiple grid-connected PV systems. In Proceedings of the 2008 IEEE/PES Transmission and Distribution Conference and Exposition, Chicago, IL, USA, 21–24 April 2008; pp. 1–6.
25. Teng, Y.; Zhang, X.; Fan, C.; Chen, X.; Zhang, R. Resonance Risk in Infirm-interconnected Grid Considering Photovoltaic Devices. In Proceedings of the 2018 International Conference on Power System Technology (POWERCON), Guangzhou, China, 6–8 November 2018; pp. 1004–1011.
26. Sun, J.; Li, M.; Zhang, Z.; Xu, T.; He, J.; Wang, H.; Li, G. Renewable Energy Transmission by HVDC Across the Continent: System Challenges and Opportunities. *CSEE J. Power Energy Syst.* **2017**, *3*, 353–364. [[CrossRef](#)]
27. Bi, J.T.; Du, W.; Wang, H.F. Aggregated dynamic model of grid-connected PV generation farms. In Proceedings of the International Conference on Renewable Power Generation (RPG 2015), Beijing, China, 7–18 October 2015.
28. Canizares, C.; Fernandes, T.; Geraldi, E.; Gerin-Lajoie, L.; Gibbard, M.; Hiskens, I.; Kersulis, J.; Kuiava, R.; Lima, L.; DeMarco, F.; et al. Benchmark Models for the Analysis and Control of Small-Signal Oscillatory Dynamics in Power Systems. *IEEE Trans. Power Syst.* **2017**, *32*, 715–722. [[CrossRef](#)]

Article

Multi-Mode Voltage Sag/Swell Generator Based on Three-Phase Inverter Circuit

Qiguo Han ¹, Xing Wang ¹, Pengfei Hu ^{2,*}, Maolin Wang ¹, Xu Luo ¹ and Weihua Hou ¹

¹ School of Automation, Hangzhou Dianzi University, Hangzhou 310018, China; hanqiguo@hdu.edu.cn (Q.H.); 142060135@hdu.edu.cn (X.W.); 161060079@hdu.edu.cn (M.W.); 172060059@hdu.edu.cn (X.L.); 181060076@hdu.edu.cn (W.H.)

² College of Electrical Engineering, Zhejiang University, Hangzhou 310027, China

* Correspondence: hpf@zju.edu.cn; Tel.: +86-13658095156

Abstract: The voltage ride through capability of the major auxiliary variable-frequency drive (VFD) in large thermal power plants is the key technical issue of power grid and source coordination. In order to test the high voltage ride through (HVRT) and low voltage ride through (LVRT) capability of the auxiliary VFD, it is necessary to develop a power supply to simulate different grid voltage sag and swell accurately. In this paper, a generator (VSSG) based on the common three-phase inverter circuit that can simulate multi-mode voltage sag/swell is proposed. The designed main circuit consisting of transformer, rectifier, DC split capacitors, three-phase inverter, and LC-filter can generate single-phase and three-phase voltage sag, swell, and phase angle jumping flexibly. The developed control strategies composed of the double closed-loop control and the neutral voltage balance control achieve accurate output, fast dynamic response, and step-less adjustment. Simulation and experiment results verify the multi-mode voltage simulation performances of the proposed VSSG, which can be effectively used to emulate power grid voltage sag and swell phenomena under the IEEE 1159 and IEC standards.

Citation: Han, Q.; Wang, X.; Hu, P.; Wang, M.; Luo, X.; Hou, W. Multi-Mode Voltage Sag/Swell Generator Based on Three-Phase Inverter Circuit. *Energies* **2021**, *14*, 6520. <https://doi.org/10.3390/en14206520>

Keywords: voltage sag/swell generator (VSSG); voltage sag; voltage swell; voltage phase angle jumping; three-phase inverter circuit

Academic Editor: Juri Belikov

Received: 11 September 2021

Accepted: 5 October 2021

Published: 11 October 2021

Publisher's Note: MDPI stays neutral with regard to jurisdictional claims in published maps and institutional affiliations.



Copyright: © 2021 by the authors. Licensee MDPI, Basel, Switzerland. This article is an open access article distributed under the terms and conditions of the Creative Commons Attribution (CC BY) license (<https://creativecommons.org/licenses/by/4.0/>).

1. Introduction

Voltage sag and swell are the common phenomena of power grid. Voltage sag is caused by grid short circuit, access of large capacity load and the dual power supply switching, etc. Additionally, voltage swell is caused by a reduction in large capacity load, a large capacitor compensator putting into operation and power system oscillation, etc. For a specific low-voltage electric equipment, it will encounter voltage sag/swell resulting not only from its own distribution system faults, but from faults propagated from transformers, power lines, and other loads in distance. Therefore, the diversity of the voltage sag/swell characteristics should be considered.

When the electric equipment encounters voltage sag or swell, its operation status is disturbed. Similar to the major auxiliary variable-frequency drives (VFD) in a large thermal power plant, to achieve operation coordination of the power grid and source, the high voltage ride through (HVRT) and low voltage ride through (LVRT) capability of the auxiliary VFD in the power plant need to be verified. Therefore, it is necessary to develop a power supply to simulate voltage sag/swell accurately, which is the basis and verification means for the HVRT and LVRT support equipment research [1–3]. At present most research is focused on the simulation of the grid voltage sag, i.e., voltage sag generator (VSG), which is mostly used in the field of wind power system test [4,5], power quality improvement in wind farm [6] and DC supply system [7], and other renewable energy systems [8–10].

The common VSG solutions can be categorized as shunt-impedance-based, synchronous-generator-based, transformer-based, and power-electronics-converter-based. The shunt-

impedance-based VSG [11–13] uses shunt and series impedances in its main circuit. The series impedance is used to suppress the current impact, and the shunt impedance is used to generate voltage sag. The voltage sag depth and duration are adjusted by controlling the shunt impedance value and its time of switching into the circuit. This method is simple and easy to implement, but it has the drawbacks of large energy consumption, low accuracy, and adjustment discontinuity. The synchronous-generator-based VSG can simulate the load side voltage sags by changing the exciting current, which has the drawbacks of slow response, only symmetrical faults emulation, relatively large weight, and high cost [14,15]. The transformer-based VSG is implemented by constructing the output voltage switchover of the autotransformer to simulate the actual grid voltage sag [16–19]. The switchover device usually uses contactor or the non-contact fast switch constructed by bidirectional thyristor or insulated gate bipolar transistor (IGBT). It is difficult to achieve precise control of voltage transient variation. Additionally, unexpected high impulse current and spike voltage are usually accompanied during the period of simulating voltage sag.

Comparatively, the power-electronics-converter-based grid voltage sag or swell generator deserves more attention, which is mostly on the basis of inverter circuit [5,20–25]. A comprehensive overview on cause classification of voltage sag and voltage sag emulators and applications is presented in [26]. With the improvement of topology and control scheme embedded, the voltage conversion can simulate all kinds of grid voltage sag or swell. This solution has many advantages over the foregoing solutions, such as quicker response, flexible control, and step-less output adjustment. The matrix-converter-based sag/swell generator is also a good solution [27–29], but its output modes are fewer than the inverter-based. In [24], a method using three single-phase inverters is proposed to achieve any phase voltage sag, but its circuit structure is relatively complex.

In view of the above, this paper presents a new voltage sag/swell generator (VSSG) based on the common three-phase inverter circuit and SPWM control, which can emulate multi-mode of voltage sag/swell and phase angle jumping. Corresponding technical performance and hardware structure comparison with other power-electronics-converter-based voltage sag/swell generator are shown in Table 1. Topology in [20,21] employs series transformer and auxiliary semiconductor devices, while topology in [22] employs four power legs. Comparatively, with simpler main circuit, more features and low cost, the VSSG proposed is a more perfect and practical than others.

Table 1. Comparison of various voltage sag/swell generators.

	Three Single-Phase-Inverters-Based [22]	3-Phase 3-Wire 4-Legs Inverter-Based [20,21]	Proposed 3-Phase 4-Wire Inverter with Neutral Control
Circuit structure	Complex	Less complex	Simple
No. of IGBT	12	8	6
Step-less adjustment	Yes	Yes	Yes
Angle jumping	No	No	Yes
Voltage Swell	No	No	Yes
Cost	High	High	Low

The rest of this paper is organized as follows. The grid voltage sag/swell features under different grid faults and fault propagation that need to be simulated are firstly introduced in Section 2. Section 3 presents the main circuit and its mathematical models of the proposed VSSG and Section 4 illustrates the designed control strategy. Simulation and experimental test results of the VSSG are depicted in Sections 5 and 6, respectively. Section 7 concludes the paper.

2. The Grid-Fault and Its Propagation

VSSG is designed to accurately simulate all kinds of faults in the power system. Therefore, it is necessary to consider the actual situation, i.e., the diversity of faults in the actual grid and the changes of fault features after propagation. The voltage sag/swell

features mainly include the amplitude of voltage sag/swell, sag/swell duration, fault frequency, and the voltage phase angle jump [30,31].

When line faults occur, the eigenvector diagrams of phase voltage at the point of common coupling (PCC) in relation to different neutral grounding modes are shown in Table 2. As the figures show in Table 2, the dotted line is the voltage amplitude and phase of each phase under normal condition, while the solid line indicates the voltage amplitude and phase corresponding to each phase fault.

Table 2. Phase voltage eigenvector diagram of different faults.

Fault Type	Neutral Effective Grounding	Neutral Non-Effective Grounding
Single-phase earthing		
Inter-phase short circuit		
Two-phase earthing		
Three-phase short circuit		

When fault propagates through transformer, the voltage eigenvector may change; it depends on the wiring form of the transformer. Take the Y/Δ-11-type transformer as an example: when the fault propagates through this type of transformer, the voltage zero sequence component cannot pass, which leads to the changes of phase voltage eigenvector as shown in Table 3.

Table 3. Voltage eigenvector change after fault propagation.

Fault Type (Neutral Ground)	Eigenvector Diagram of Original Fault	Eigenvector Diagram after Propagation through Transformer
Single-phase earthing (phase A)		
Inter-phase short circuit (phase B\C)		
Two-phase earthing (phase B\C)		

It can be seen from Tables 2 and 3, when fault occurs, the voltage vector is not only reflected in the amplitude variation, but also in the phase angle variation. It is required that the VSSG can simulate different kinds of voltage sag/swell features to test the HVRT and LVRT capability of the grid-connected equipment.

3. Main Circuit and Its Mathematical Model

As shown in Figure 1, the proposed VSSG main circuit consists of step-up transformer, uncontrolled rectifier bridge, DC split capacitors, three-phase inverter circuit and LC low-pass filter. The step-up transformer is used to provide voltage swell margin. The midpoint of DC split capacitors is connected to the neutral line of the AC side so that the AC output main circuit becomes a three-phase four-wire system.

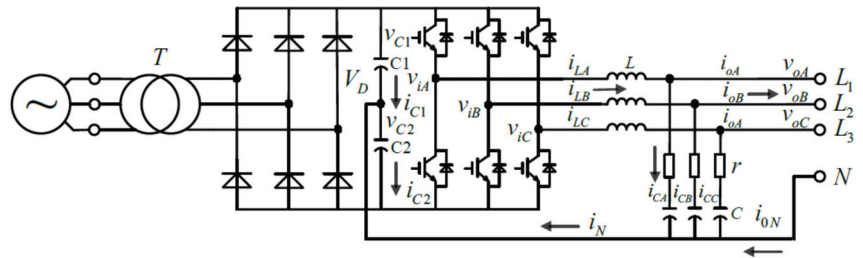


Figure 1. Main circuit of VSSG.

The symbols in Figure 1 and the following analysis are shown in Table 4.

Table 4. Symbols in the mathematical model.

Symbol	Meaning	Symbol	Meaning
L	filter inductor	v_{c1}	voltage on capacitor C1
C	filter capacitor	v_{c2}	voltage on capacitor C2
r	damping resistance	v_{oA}, v_{oB}, v_{oC}	three-phase output voltages
V_D	DC-link voltage	i_{oA}, i_{oB}, i_{oC}	three-phase output currents
i_{cA}, i_{cB}, i_{cC}	Currents in Filter capacitors	v_{iA}, v_{iB}, v_{iC}	three-phase output voltages before filter
i_{lA}, i_{lB}, i_{lC}	Currents through inductors	v_{rA}, v_{rB}, v_{rC}	three-phase modulation input voltages

The front circuit of the VSSG is composed of a step-up transformer and an uncontrolled rectifier. Under the ideal condition (the front circuit capacity satisfies the operation requirements and the AC supply voltage is stable), V_D is constant, and the neutral voltage deviation is controlled to ensure that N is zero potential. Each phase output may be controlled independently and not affected by each other, which is the precondition for any phase to simulate voltage sag/swell and phase angle shift as a real three-phase four-wire low-voltage power supply network.

The three phases coupling relationship in 3-phase 3-wire and 3-phase 4-wire inverter circuit can be illustrated using topologies in Figures 2 and 3, respectively.

It can be seen from Figure 2b that any phase voltage is affected by other two phases; there is a mutual coupling relationship between output voltages of 3 phases in the 3-phase 3-wire inverter circuit.

For a 3-phase 4-wire inverter circuit, by means of the neutral line connection and clamp control for the neutral voltage, the independence of each phase output circuit can be guaranteed as shown in Figure 3.

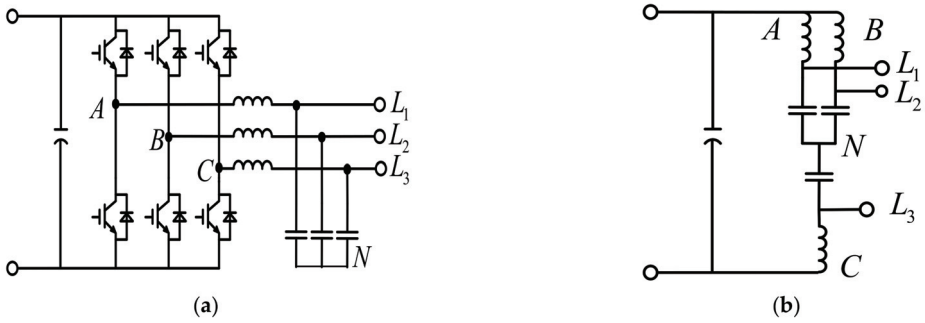


Figure 2. 3-phase 3-wire system topology. (a) Main circuit. (b) Simplified diagram of one working state.

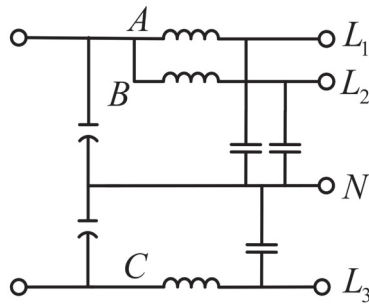


Figure 3. Simplified diagram of one working state of 3-phase 4-wire system topology.

Therefore, the main loop model of the VSSG proposed can be simplified to a single-phase inverter circuit as shown in Figure 4. The resistance r of the low-pass filter is used to damp oscillation. Due to its small value, resistance r can be ignored when analyzes the characteristics of the control system, and thus the relationships of phase current and voltage can be expressed as Equations (1)–(3) (take phase A as an example).

$$v_{iA} = v_{oA} + L \frac{di_{LA}}{dt} \tag{1}$$

$$i_{LA} = i_{CA} + i_{oA} \tag{2}$$

$$i_{CA} = C \frac{dv_{oA}}{dt} \tag{3}$$

From Equation (1) to Equation (3), the transfer function among v_{oA} , i_{oA} , and v_{iA} can be deduced as Equation (4).

$$v_{iA}(s) = (1 + LCs^2)v_{oA}(s) + Lsi_{oA}(s) \tag{4}$$

According to the principle of SPWM, the transfer function between the modulation wave input v_{rA} and output voltage v_{iA} of inverter side is a constant.

$$\frac{v_{iA}}{v_{rA}} = K_{PWM} \tag{5}$$

In the above inverter circuit, K_{PWM} is $V_D/2$. By adjusting the modulation ratio M in the control process, the amplitude of the modulation wave v_{rA} is adjusted, and finally the amplitude of v_{iA} is adjusted.

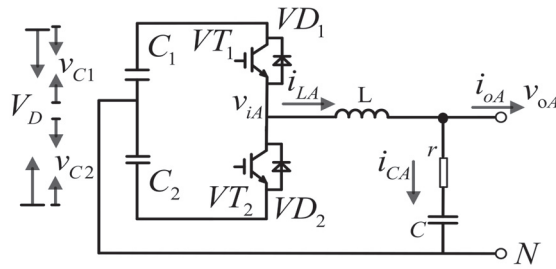


Figure 4. Equivalent single-phase inverter circuit.

Unlike the inverter with only voltage sag capability, the maximum modulation ratio ($M = 1$) in this case corresponds to the highest swell output voltage U_{hv} , and the modulation ratio at the rated voltage of 400 V is about $400/U_{hv}$.

According to Equations (4) and (5), the open-loop system structure of the inverter circuit is as shown in Figure 5.

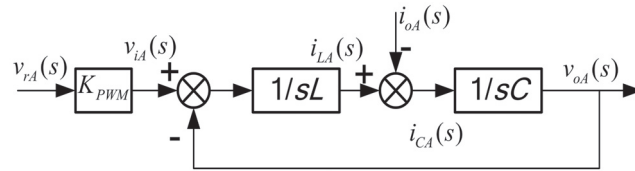


Figure 5. Single phase open loop block diagram of inverter.

The LC filter is designed according to the principles shown in Equations (6) and (7).

$$10f_r \leq f_c \leq f_s/10 \tag{6}$$

$$f_c = 1/(2\pi\sqrt{LC}) \tag{7}$$

where f_r is the fundamental frequency of VSSG output voltage, f_c is the resonant frequency of LC filter, and f_s is the switching frequency of inverter circuit.

The filter inductance is designed to control its voltage drop less than 3%, and to restrict the maximum current ripple in the meantime. The optimized design of the relevant parameters may be performed in combination with the Bode diagram of the corresponding transfer function, and details are not described herein.

4. Control Strategy

4.1. Main Control Strategy

For the inverter circuit above, the common dual closed-loop control strategy, namely the outer voltage control and the inner current control [32] is used. Corresponding control block diagram is shown in Figure 6.

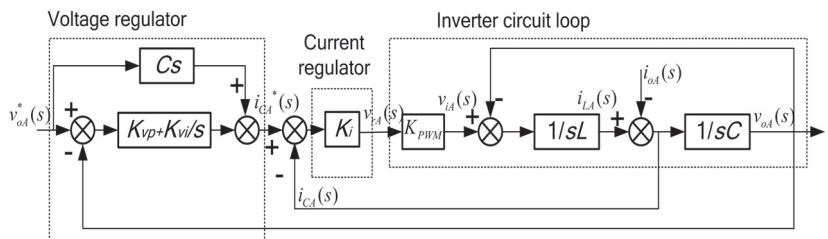


Figure 6. Double closed loop control strategy block diagram.

The control model in Figure 6 includes a current feedback inner loop, a voltage feedback outer loop and a voltage feedforward loop. The inner loop of the current is used to suppress the oscillation of LC filter and improve the dynamic characteristics of the whole system. The filter capacitor current i_{CA} is chosen as the control target, and the proportional controller can realize the expected control effect. K_i is the proportional gain in the current regulator. The voltage feedback outer loop is designed to ensure that the output voltage v_{oA} of VSSG follows the set value v_{oA}^* . The loop adopts the PI regulator, of which K_{vp} is the proportional gain and K_{vi} is the integral gain, while the PI regulator cannot realize no static error tracking control of the sine signal. Therefore, a load voltage feedforward loop is added to eliminate the error, and then the high precision tracking of the set value will be realized.

The transfer function from the set current value of inner loop to the feedback current value in Figure 6 can be written as:

$$i_{CA} = \frac{K_i K_{PWM} C s}{LCs^2 + K_i K_{PWM} C s + 1} i_{CA}^* - \frac{LCs^2}{LCs^2 + K_i K_{PWM} C s + 1} i_{oA} \tag{8}$$

The goals of the current controller are: (1) to reduce the impact of load current i_{oA} on the output voltage in the required frequency band, which is reflected in the Bode diagram that the load current gain is as small as possible near the power frequency; (2) to take into account the dynamic response performance of the overall power supply, which is reflected that the frequency band is as wide as possible in the Bode diagram. When $K_i = 5$, according to Equation (8), the relevant gain at frequency 50 Hz of the current loop is: $i_{CA}/i_{CA}^* = 1$, $i_{CA}/i_{oA} < 0.001$. By simulation, it is verified that the above parameters can meet the expected control effect of the current controller.

According to Figure 6, the transfer function from the set voltage value to the feedback voltage value of outer loop is:

$$v_{oA} = \frac{K_i K_{PWM} C s^2 + K_i K_{vp} K_{PWM} s + K_i K_{vi} K_{PWM}}{LCs^3 + K_i K_{PWM} C s^2 + (1 + K_i K_{vp} K_{PWM}) s + K_i K_{vi} K_{PWM}} v_{oA}^* - \frac{L s^2}{LCs^3 + K_i K_{PWM} C s^2 + (1 + K_i K_{vp} K_{PWM}) s + K_i K_{vi} K_{PWM}} i_{oA} \tag{9}$$

According to the Thevenin theorem, the above relational expression can be represented by the equivalent circuit depicted in Figure 7, where $G_c v_{oA}^*$ is a controllable voltage source, $Z(s)$ is the internal impedance of the inverter, and Z_L is equivalent impedance of the load.

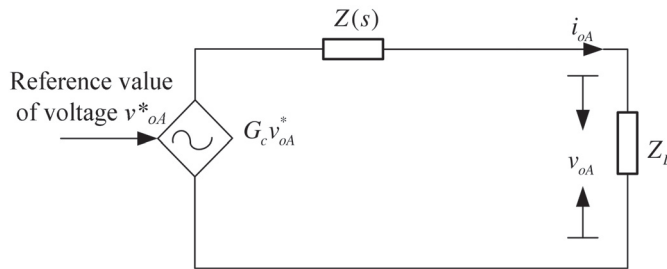


Figure 7. Thevenin’s equivalent circuit of VSSG closed loop control.

The equation in Figure 7 can be expressed as:

$$v_{oA} = G_c(s) v_{oA}^* - Z(s) i_{oA} \tag{10}$$

According to Equations (9) and (10), the closed-loop voltage gain $G_c(s)$ and the output impedance $Z(s)$ of the inverter are as follows:

$$G_c(s) = \frac{K_i K_{PWM} Cs^2 + K_i K_{vp} K_{PWM} s + K_i K_{vi} K_{PWM}}{LCs^3 + K_i K_{PWM} Cs^2 + (1 + K_i K_{vp} K_{PWM})s + K_i K_{vi} K_{PWM}} \quad (11)$$

$$Z(s) = \frac{Ls^2}{LCs^3 + K_i K_{PWM} Cs^2 + (1 + K_i K_{vp} K_{PWM})s + K_i K_{vi} K_{PWM}} \quad (12)$$

It can be seen from Equation (12) that the output impedance of the inverter under closed-loop control is not only affected by the filter parameters, but also related to the adopted control strategy.

The VSSG is a power generator, and it is used to simulate the actual grid power, for which the output impedance $Z(s)$ should be inductive near 50 Hz. Additionally, in order to suppress the high frequency harmonics of itself effectively, it should exhibit resistance characteristic in high frequency range.

The frequency-domain response curves of output impedance $Z(s)$ when the controller designed with different parameters are shown in Figure 8. Figure 8a shows the curves corresponding to different K_{vp} when $K_{vi} = 10$. The curves of b001, b01, b1, b10, and b100 are corresponding to 0.01, 0.1, 1, 10, and 100 of K_{vp} , respectively. Figure 8b shows the curves corresponding to different K_{vi} when $K_{vp} = 1$. The curves of b1, b10, b100, and b1000 are corresponding to 1, 10, 100, and 1000 of K_{vi} , respectively.

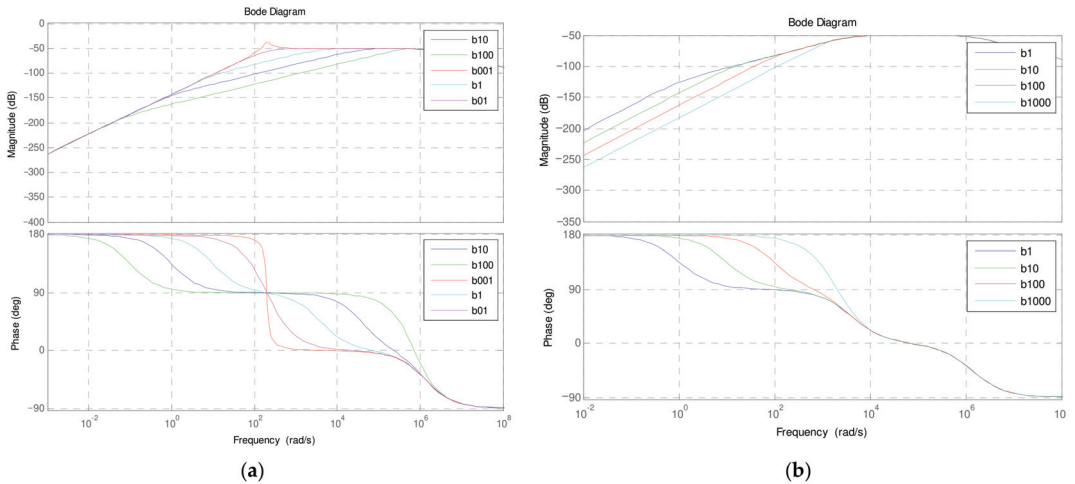


Figure 8. The frequency response curves of $Z(s)$ corresponding to different parameters. (a) The curves corresponding to different K_{vp} . (b) The curves corresponding to different K_{vi} .

It can be seen that when different parameters of the controller are applied, the output impedance characteristics exhibited are different at 50 Hz. Therefore, when selecting the specific parameters of the controller, it is necessary to comprehensively ensure that the output impedance is inductive at 50 Hz and is resistive at the high frequency range, so as to effectively suppress the harmonics of the switching frequency band and meet the requirements of the VSSG.

When $K_{vp} = 1$ and $K_{vi} = 10$, the frequency response curve of the transfer function $G_c(s)$ corresponding to the VSSG closed-loop control is shown in Figure 9.

In fact, due to the zero deviation of the neutral current and the physical parameters difference of the capacitor itself, there is a problem of midpoint voltage drift in VSSG DC

bus splitter capacitor, which will lead to the waveform distortion of output voltage and current, so the midpoint voltage drift must be controlled.

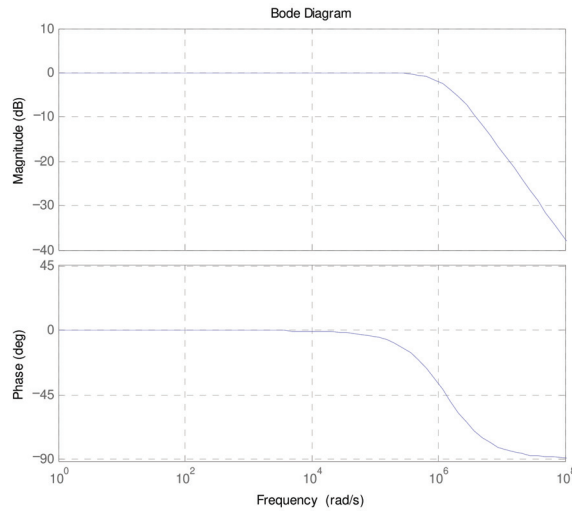


Figure 9. $G_c(s)$ frequency response curve.

4.2. DC Capacitor Voltage Deviation Control Strategy

For this VSSG, a split capacitor voltage deviation control is added to the control strategy to settle the midpoint voltage drift, as shown in Figure 10. Specifically, the split capacitor voltage deviation signal is added to the given current signal so that the current fluctuation will be compensated, and then the voltage of the split capacitors be balanced. The basic working principle is that, according to the difference of the split capacitor voltage, the inverter generates a small DC current to charge or discharge the positive/negative capacitor to adjust the potential of the N point. Its control strategy is a simple proportional control.

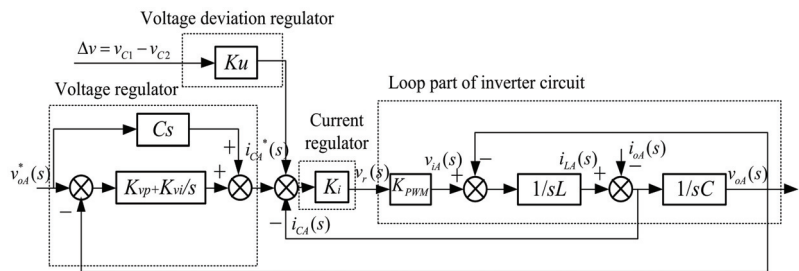


Figure 10. VSSG control block diagram with neutral voltage deviation control.

5. Simulation

In order to verify the feasibility of the VSSG scheme, the simulation model is built by Matlab/Simulink. The detail parameters of the simulation circuit are shown in Table 5, which are selected to match with the prototype as well as possible.

Specific simulation experiments are as follows:

- (1) Three-phase voltage synchronous swell and sag;
- (2) Single-phase voltage swell and sag;
- (3) Single-phase voltage swell, sag and phase angle jumping.

Table 5. Voltage eigenvector change after fault propagation.

Parameter	Value
DC-link Voltage, V_D	900 V
Switching Frequency, f_s	6 kHz
DC-link Capacitance, $C1/C2$	800 μ F
Filter Capacitance, C	250 μ F
Filter inductance, L	1.7 mH
Load Capacity	$8 + j6 \Omega$
Power Factor	0.8

The simulation results obtained are shown in Figure 11, the sag/swell duration is 50 ms (from 0.21 s to 0.26 s). It can be seen from Figure 11a,c that the VSSG can realize the simulation of three-phase voltage synchronous swell and sag, the transition time is short and the waveforms are not distorted. Figure 11b,d show the VSSG can also realize the simulation of single-phase voltage swell and sag, and the amplitude and phase of other phases remain unchanged. Figure 11e shows the VSSG can realize the simulation of single-phase phase angle jumping without interfering other phases. The independent voltage control for any phase is achieved. The above simulation results verified the feasibility of the VSSG design scheme.

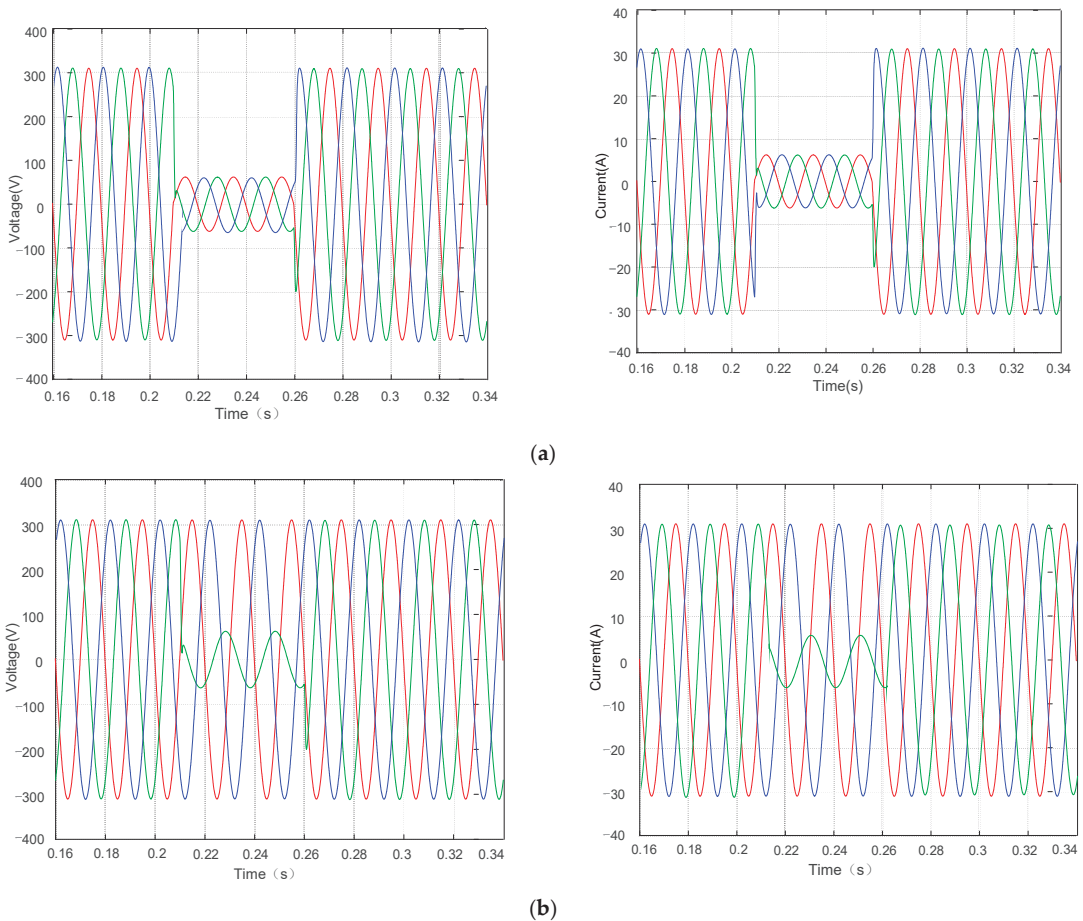
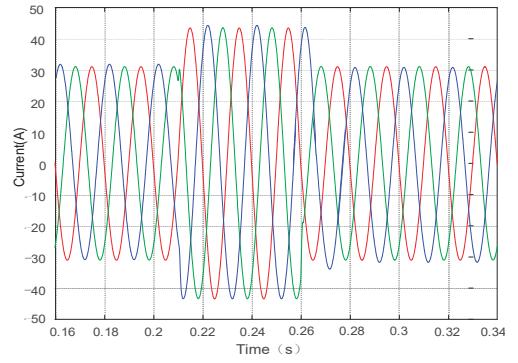
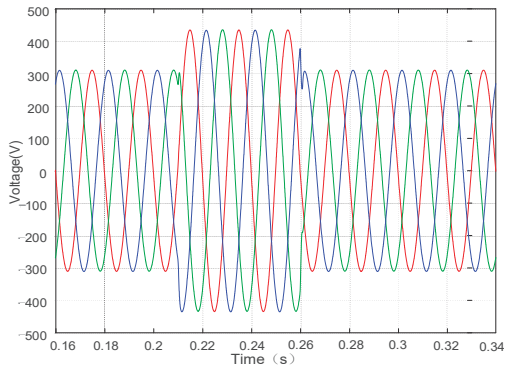
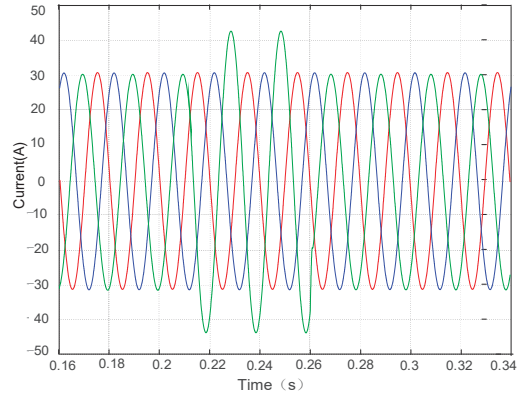
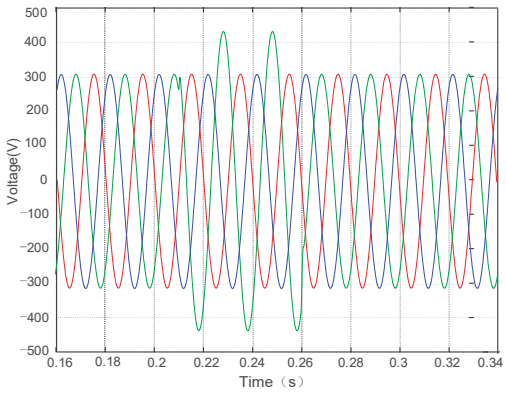


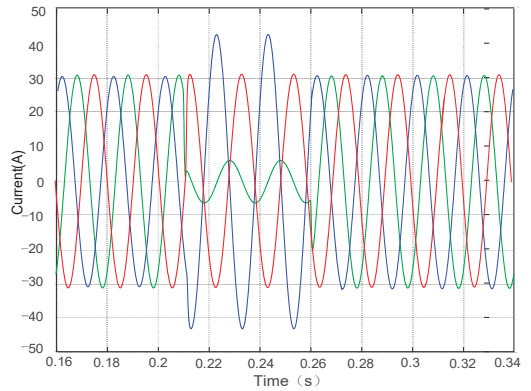
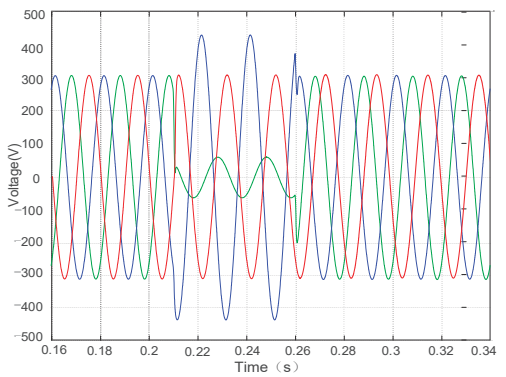
Figure 11. Cont.



(c)



(d)



(e)

Figure 11. Simulation voltage waveforms. (a) Three-phase sags to 20% (0.2 pu). (b) Single-phase sags to 20% (0.2 pu). (c) Three-phase swells to 140% (1.4 pu). (d) Single-phase swells to 140% (1.4 pu). (e) Phase A swells to 140% (1.4 pu), phase B sags to 20% (0.2 pu), and phase C phase angle jumping 60° .

6. Experimental Results

A test prototype is set up, which can support 11 kW constant power load with 400 V/25 A rated voltage/current. When the minimum output voltage is 20% of the rating, the maximum output current will increase to five times the rated value, i.e., 125 A. The designed maximum output voltage is 140% of the rated value, i.e., 560 V; the step-up transformer is an autotransformer. In order to make full use of DC voltage, the output voltage of the autotransformer is adjusted to 560 V. Table 6 shows the parameters of the test prototype.

Table 6. The test prototype parameters.

Component Name	Component Parameters	Max. Operating Parameters
Step-up Transformer	380 V/660 V/20 kVA	380/560 V/15 kVA
Rectifier Bridge	150 A/1200 VDC	25 A/760 VDC
Inverter Bridge	150 A/1200 VDC	125 A/760 VDC
DC-link Capacitance, C1/C2	800 μ F/450 VDC	800 μ F/440 VDC
Filter Capacitance, C	250 μ F/1000 VAC	250 μ F/560 VAC
Filter inductance, L	1.7 mH/150 A	1.7 mH/125 A

Figure 12 are the test output waveforms of a 5 kW load ($\cos \varphi = 0.8$). It can be observed from Figure 12, the generated voltage swell and sag by the VSSG can all achieve rapid response. The output voltage waveform can be completed to switch in a very short time. The voltage amplitude and phase of any phase can be fully controlled independently.

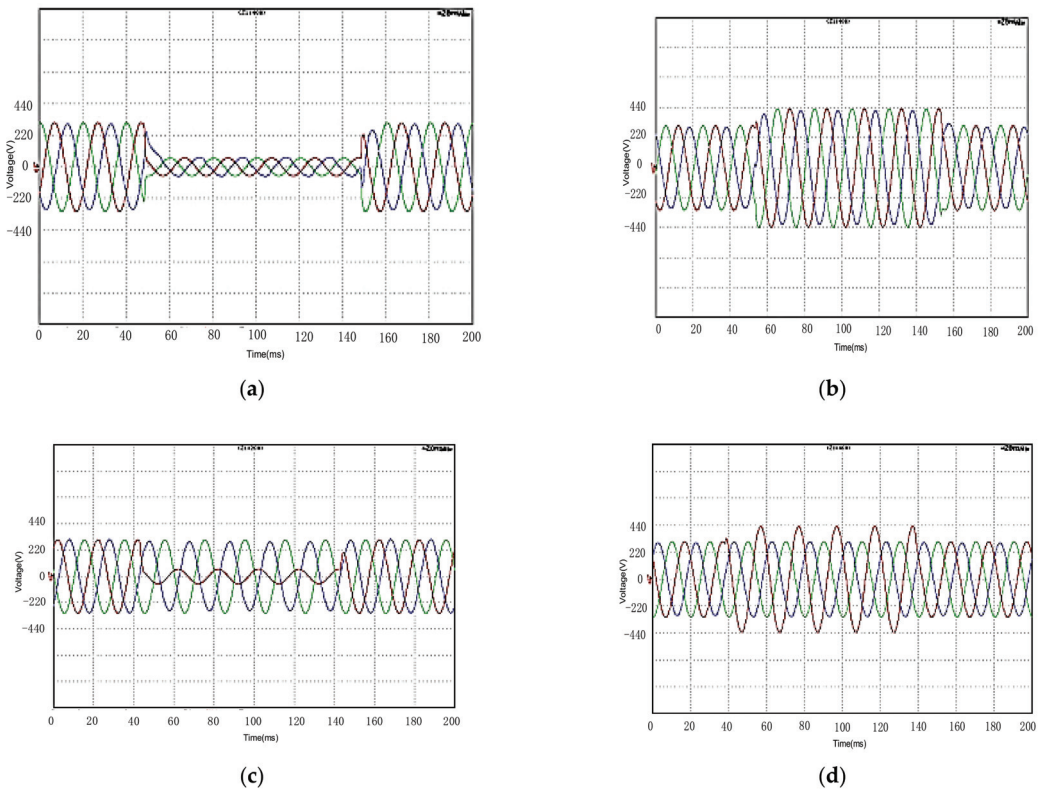
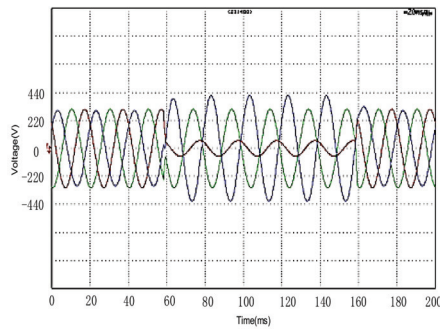


Figure 12. Cont.



(e)

Figure 12. Test waveforms. (a) Three-phase sags to 20% (0.2 pu). (b) Three-phase swells to 140%. (c) Single-phase sags to 20% (0.2 pu). (d) Single-phase swells to 140% (1.4 pu). (e) Phase A swells to 140% (1.4 pu), phase B sags to 20% (0.2 pu), and phase C phase angle jumping 60° .

From the above experiments, it is shown that the VSSG proposed in this paper can realize generating voltage swell, sag, and phase angle jumping of any phase, and also realize stepless adjustment within the set voltage range. The previous theoretical study is verified.

7. Conclusions

This paper proposes a multi-mode voltage sag/swell generator (VSSG) with a simple and reliable main circuit, which is based on the common three-phase inverter circuit and SPWM control. Cooperated with the designed control loops, the VSSG achieves to generate any kinds of voltage sag, swell, and phase angle jumping, and support step-less adjustment for voltage sag/swell depth, duration, and angle jumped. With high precision and fast response, the simulation and experimental results verify that it can accurately simulate the various types of power grid fault. Moreover, the VSSG is developed according to the standard of common multi-mode voltage sag/swell generator, which can simulate the power grid voltage sag and swell phenomena under IEEE 1159 and IEC standards. The VSSG has good practicality, which can be used as a power supply for testing various electrical equipment.

Author Contributions: Conceptualization, Q.H. and P.H.; Methodology, X.W.; Simulation, M.W.; Experiment test, X.L. and W.H.; Writing—original draft preparation, X.W.; Writing—review and editing, P.H.; and Funding acquisition, Q.H. All authors have read and agreed to the published version of the manuscript.

Funding: This research was funded by the Zhejiang Natural Science Foundation of China, Grant Number LY20E070004.

Conflicts of Interest: The authors declare no conflict of interest.

References

1. Tallam, R.M.; Lukaszewski, R.A. Voltage sag and unbalance generator for power quality testing of adjustable speed drives. In Proceedings of the IEEE Energy Conversion Congress and Exposition, Denver, CO, USA, 15–19 September 2013; pp. 4565–4571.
2. Xu, Y.; Lu, W.; Wang, K.; Li, C.; Aslam, W. Sensitivity of Low-Voltage Variable-Frequency Devices to Voltage Sags. *IEEE Access* **2018**, *7*, 2068–2079. [[CrossRef](#)]
3. Han, Q.; Zhu, K.; Shi, W.; Wu, K.; Chen, K. Research on the supercapacitor support schemes for LVRT of variable-frequency drive in the thermal power plant. In Proceedings of the EEEP 2017 The Second International Conference on Energy Engineering and Environmental Protection, Shanya, China, 20–22 November 2017; pp. 1–8.
4. Abdel-Baqi, O.; Nasiri, A. Series Voltage Compensation for DFIG Wind Turbine Low-Voltage Ride-Through Solution. *IEEE Trans. Energy Convers.* **2011**, *26*, 272–280. [[CrossRef](#)]

5. Zeng, R.; Nian, H.; Zhou, P. A three-phase programmable voltage sag generator for low voltage ride-through capability test of wind turbines. In Proceedings of the IEEE Energy Conversion Congress and Exposition (ECCE), Atlanta, GA, USA, 12–16 September 2010; pp. 305–311.
6. Liu, Q.; Li, Y. An Inductive Filtering-Based Parallel Operating Transformer with Shared Filter for Power Quality Improvement of Wind Farm. *IEEE Trans. Power Electron.* **2020**, *35*, 9281–9290. [[CrossRef](#)]
7. Liu, Q.; Li, Y.; Hu, S.; Luo, L. Power quality improvement using controllable inductive power filtering method for industrial DC supply system. *Control. Eng. Pract.* **2019**, *83*, 1–10. [[CrossRef](#)]
8. Hajizadeh, A.; Golkar, M.A.; Feliachi, A. Voltage Control and Active Power Management of Hybrid Fuel-Cell/Energy-Storage Power Conversion System under Unbalanced Voltage Sag Conditions. *IEEE Trans. Energy Convers.* **2010**, *25*, 1195–1208. [[CrossRef](#)]
9. Tafti, H.D.; Maswood, A.I.; Konstantinou, G.; Townsend, C.D.; Acuna, P.; Pou, J. Flexible Control of Photovoltaic Grid-Connected Cascaded H-Bridge Converters During Unbalanced Voltage Sags. *IEEE Trans. Ind. Electron.* **2018**, *65*, 6229–6238. [[CrossRef](#)]
10. Shabestary, M.M.; Mohamed, Y.A.I. Asymmetrical Ride-Through and Grid Support in Converter-Interfaced DG Units under Unbalanced Conditions. *IEEE Trans. Ind. Electron.* **2019**, *66*, 1130–1141. [[CrossRef](#)]
11. Gabe, I.J.; Gründling, H.A.; Pinheiro, H. Design of a voltage sag generator based on impedance switching. In Proceedings of the IECON 2011–37th Annual Conference on IEEE Industrial Electronics Society, Melbourne, VIC, Australia, 7–10 November 2011; pp. 3140–3145.
12. Chung, Y.H.; Kwon, G.H.; Park, T.B.; Lim, G.Y. Voltage sag and swell generator with thyristor controlled reactor. In Proceedings of the International Conference on Power System Technology, Kunming, China, 13–17 October 2002; pp. 1933–1937.
13. Yang, Y.; Blaabjerg, F.; Zou, Z. Benchmarking of Voltage Sag Generators. In Proceedings of the IECON 2012—38th Annual Conference on IEEE Industrial Electronics Society, Montreal, QC, Canada, 25–28 October 2012; pp. 943–948.
14. Collins, E.R.; Morgan, R.L. A three-phase sag generator for testing industrial equipment. *IEEE Trans. Power Deliv.* **1996**, *11*, 526–532. [[CrossRef](#)]
15. Kumsuwan, Y.; Boonmee, C.; Premrudeepreechacharn, S. Implementation of a 1-kVA programmable balanced three-phase voltage sag generator. In Proceedings of the 2009 6th International Conference on Electrical Engineering/Electronics, Computer, Telecommunications and Information Technology, Pattaya, Thailand, 6–9 May 2009; pp. 46–49.
16. Ma, Y.; Karady, G.G. A single-phase voltage sag generator for testing electrical equipments. In Proceedings of the 2008 IEEE/PES Transmission and Distribution Conference and Exposition, Chicago, IL, USA, 21–24 May 2009; pp. 1–5.
17. Wessels, C.; Lohde, R.; Fuchs, F.W. Transformer based voltage sag generator to perform LVRT and HVRT tests in the laboratory. In Proceedings of the 14th International Power Electronics and Motion Control Conference EPE-PEMC 2010, Ohrid, Macedonia, 6–8 September 2010; pp. T11–T18.
18. Senturk, O.S.; Hava, A.M. A Simple Sag Generator Using SSRs. *IEEE Trans. Ind. Appl.* **2012**, *48*, 172–180. [[CrossRef](#)]
19. İnci, M.; Demirdelen, T.; Tan, A.; Köroğlu, T.; Cuma, M.U.; Bayindir, K.Ç.; Tümay, M. A novel low cost sag/swell generator. In Proceedings of the 2015 IEEE 6th International Symposium on Power Electronics for Distributed Generation Systems (PEDG), Aachen, Germany, 22–25 June 2015; pp. 1–4.
20. Chung, Y.H.; Kwon, G.H.; Park, T.B.; Kim, H.J.; Moon, J.I. Voltage sag, swell and flicker generator with series injected inverter. In Proceedings of the IEEE Power Engineering Society General Meeting, San Francisco, CA, USA, 16 June 2005; pp. 1308–1313.
21. Chung, Y.H.; Kwon, G.H.; Park, T.B.; Kim, H.J.; Jeon, Y.S. Voltage sag and swell generator with series injected inverter for the KCPP. In Proceedings of the 2004 International Conference on Power System Technology, Singapore, 21–24 November 2004; pp. 1589–1594.
22. Oranpiroj, K.; Premrudeepreechacharn, S.; Ngoudech, M.; Muangjai, W.; Yingkayun, K.; Boonsai, T. The 3-phase 4-wire voltage sag generator based on three dimensions space vector modulation in abc coordinates. In Proceedings of the 2009 IEEE International Symposium on Industrial Electronics, Seoul, Korea, 5–8 July 2009; pp. 275–280.
23. Muangjai, W.; Premrudeepreechacharn, S.; Higuchi, K.; Oranpiroj, K.; Jantee, W. An implementation algorithm of a carrier-based PWM technique for three-phase four-leg voltage sag generator with microcontroller. In Proceedings of the 2013 IEEE 10th International Conference on Power Electronics and Drive Systems (PEDS), Kitakyushu, Japan, 22–25 April 2013; pp. 852–855.
24. Daychosawang, K.; Kumsuwan, Y. Balanced and unbalanced three-phase voltage sag generator for testing electrical equipment. In Proceedings of the IEEE 2014 11th International Conference on Electrical Engineering/Electronics, Computer, Telecommunications and Information Technology (ECTI-CON), Nakhon Ratchasima, Thailand, 14–17 May 2014; pp. 1–6.
25. Wu, K.; Han, Q.; Huang, X.; Quan, Y. Research on a Three-Phase Voltage Sag and Swell Generator Based on PWM Technology. *Power Electron.* **2015**, *49*, 56–58. (In Chinese)
26. Han, Y.; Feng, Y.; Yang, P.; Xu, L.; Xu, Y.; Blaabjerg, F. Cause Classification of Voltage Sag and Voltage Sag Emulators and Applications: A Comprehensive Overview. *IEEE Access* **2020**, *8*, 1922–1934. [[CrossRef](#)]
27. Cardenas, R.; Juri, C.; Pena, R.; Clare, J.; Wheeler, P. Analysis and Experimental Validation of Control Systems for Four-Leg Matrix Converter Applications. *IEEE Trans. Ind. Electron.* **2012**, *59*, 141–153. [[CrossRef](#)]
28. Díaz, M.; Cárdenas, R.; Soto, G. 4-wire Matrix Converter based voltage sag/swell generator to test LVRT in renewable energy systems. In Proceedings of the IEEE 2014 Ninth International Conference on Ecological Vehicles and Renewable Energies (EVER), Monte-Carlo, Monaco, 25–27 March 2014; pp. 1–10.
29. Díaz, M.; Cárdenas, R.; Rojas, F.; Clare, J. 3-Phase 4-wire matrix converter-based voltage sag/swell generator to test low-voltage ride through in wind energy conversion systems. *IET Power Electron.* **2014**, *7*, 3116–3125. [[CrossRef](#)]

30. Bollen, M.H.J. Algorithms for characterizing measured three-phase unbalanced voltage dips. *IEEE Trans. Power Deliv.* **2003**, *18*, 937–944. [[CrossRef](#)]
31. Didden, M.; de Jaeger, E.; D'Haeseleer, W.; Belmans, R. How to connect a voltage sag-measuring device: Phase to phase or phase to neutral. *IEEE Trans. Power Deliv.* **2005**, *20*, 1174–1181. [[CrossRef](#)]
32. Zhou, L.; Jian, X.; Zhang, K.; Shi, P. A High Precision Multiple Loop Control Strategy for Three Phase PWM Inverters. In Proceedings of the IECON 2006 32nd Annual Conference on IEEE Industrial Electronics, Paris, France, 6–10 November 2006; pp. 1781–1786.

Review

Probabilistic Optimization Techniques in Smart Power System

Muhammad Riaz ^{1,2}, Sadiq Ahmad ¹, Irshad Hussain ^{2,*}, Muhammad Naeem ¹ and Lucian Mihet-Popa ^{3,*}

¹ Department of Electrical and Computer Engineering, Wah Campus, COMSATS University, Wah 47040, Pakistan; m.riaz@uetpeshawar.edu.pk (M.R.); engrsadiqahmad@gmail.com (S.A.); mnaem@ciitwah.edu.pk (M.N.)

² Faculty of Electrical and Computer Engineering, University of Engineering and Technology Peshawar, Peshawar 25000, Pakistan

³ Faculty of Information Technology, Engineering and Economics, Oestfold University College, 1757 Halden, Norway

* Correspondence: ee.irshad@gmail.com (I.H.); lucian.mihet@hiof.no (L.M.-P.)

Abstract: Uncertainties are the most significant challenges in the smart power system, necessitating the use of precise techniques to deal with them properly. Such problems could be effectively solved using a probabilistic optimization strategy. It is further divided into stochastic, robust, distributionally robust, and chance-constrained optimizations. The topics of probabilistic optimization in smart power systems are covered in this review paper. In order to account for uncertainty in optimization processes, stochastic optimization is essential. Robust optimization is the most advanced approach to optimize a system under uncertainty, in which a deterministic, set-based uncertainty model is used instead of a stochastic one. The computational complexity of stochastic programming and the conservativeness of robust optimization are both reduced by distributionally robust optimization. Chance constrained algorithms help in solving the constraints optimization problems, where finite probability get violated. This review paper discusses microgrid and home energy management, demand-side management, unit commitment, microgrid integration, and economic dispatch as examples of applications of these techniques in smart power systems. Probabilistic mathematical models of different scenarios, for which deterministic approaches have been used in the literature, are also presented. Future research directions in a variety of smart power system domains are also presented.

Citation: Riaz, M.; Ahmad, S.; Hussain, I.; Naeem, M.; Mihet-Popa, L. Probabilistic Optimization Techniques in Smart Power System. *Energies* **2022**, *15*, 825. <https://doi.org/10.3390/en15030825>

Academic Editor: Abdelali El Aroudi

Received: 20 November 2021

Accepted: 19 January 2022

Published: 24 January 2022

Publisher's Note: MDPI stays neutral with regard to jurisdictional claims in published maps and institutional affiliations.



Copyright: © 2022 by the authors. Licensee MDPI, Basel, Switzerland. This article is an open access article distributed under the terms and conditions of the Creative Commons Attribution (CC BY) license (<https://creativecommons.org/licenses/by/4.0/>).

Keywords: probabilistic optimization; stochastic optimization; robust optimization; distributional robust optimization; chance constrained optimization; energy management; smart grid

1. Introduction

Energy demand is expanding in lockstep with global population expansion, resulting in a supply-demand mismatch. Increased generation capacity or load reduction can help close the demand-supply imbalance. Increased generation capacity is possible through the use of fossil fuels, which are costly and pollutant [1]. Enhancing generation capacity through the integration of renewable energy resources into the smart power system is beneficial. Load curtailment creates user displeasure, which can be mitigated by implementing appropriate demand-side policies. The integration of renewable energy supplies and variable load introduces a number of risks into the smart power system that must be handled. This article discusses uncertainty in a variety of sectors related to smart power systems. This is explained in greater detail below.

1.1. Smart Power System

Conventional grid electrical power is sent unidirectionally from a central power station to remote users. In 2000, a smart power system concept was established with the primary goal of integrating two-way communication into the infrastructure of a standard grid system. From the generating station to the consumers, a smart power system integrates

communication and information technology [2,3]. Consumers receive safe, robust, and high-quality power from a smart power system [4–6]. To transform a traditional grid into a smart power system, a scalable yet robust communication architecture is necessary [7]. In an electrical power system, the grid is composed of multiple energy generating, transmission, distribution, and control elements. The smart power system intelligently organizes and connects the traditional grid's elements previously stated [8–10].

In a smart power system, generating stations serve as the primary unit. Energy from renewable sources is required for new power plants since fossil fuels are becoming depleted and have other negative effects on the environment. Solar and wind energy have unpredictable output power since they are weather-dependent; as a result, the operation of smart power systems is affected as mentioned in [11–13]. Electrical power supply relies heavily on transmission systems because generating units are located distant from the end-users of the electricity. Climate change has a direct impact on the transmission system, resulting in issues such as wind and temperature stress. These uncertainties have a significant impact on the transmission system's performance and life expectancy [14].

Intelligent distribution systems are a critical component of a smart power system. It is composed of a variety of sensors and smart sensing mechanisms, as well as a sensor network that includes smart metres, distribution transformer management, and monitoring. Due to the usage of these sensors, a smart grid can monitor the health of the grid in real time and utilize the data to operate the grid in a reliable, secure, and stable manner, while also reducing costs and increasing energy efficiency. Sensors and actuators play a critical role in the energy management of smart power systems in this context [15,16]. Employing sensors for real-time monitoring helps to deal with the power management of distributed energy resources, such as distributed generators (DGs) [17] and electric vehicles [18], as well as to improve the smart grid's reliability as it makes the integration of renewable energy resources much more convenient and improves both the efficiency and reliability of smart power system [19,20]. Due to the integration of distributed generation, the smart distribution system is unpredictable. It may have uncertainty due to the fault resistance, the magnitude and model of the load, the faulted node, and the type of fault [21].

Energy management is a critical component of the advancement of smart power systems. It is applicable to a variety of smart power system domains, including microgrids, smart homes, and demand side management. Due to the unpredictable behaviour of renewable energy resources and loads, energy management challenges face an uncertainty challenge [22]. The complexity of unit commitment and economic dispatch problems increases with the inclusion of uncertainties [23,24]. It is necessary to investigate probabilistic optimization in order to formulate the influence of various types of uncertainty in intelligent power systems.

1.2. Related Work and Contributions

Numerous survey papers from the literature have been meticulously analysed and summarized for comparison in this review paper, as indicated in Table 1. In [25], the authors discussed stochastic optimization and offered architectures and solution techniques for single and multistage stochastic optimization. The architecture of stochastic and chance restricted optimization is demonstrated in [26]. Additionally, applications of stochastic and chance constrained optimization in a variety of industries have been summarized, including banking, transportation, telecommunications, and manufacturing. The [27] discusses stochastic and chance constrained optimization for intelligent power systems. Additionally, the authors addressed many variants of the above-mentioned optimization techniques' objective function and architecture. The authors of [28] described the architecture of robust optimization and highlighted its applications in a variety of fields, including structural design, circuit design, and wireless channel design. In [29] discusses the architecture and solution strategies for robust optimization. The authors discussed distributionally robust optimization, its architecture, and categorization of ambiguity sets in [30]. In [31], they discussed the design of single and two stage chance constrained optimization. This review

paper differs from the survey papers that are already available in the literature in a number of ways, which are detailed below.

- It gives a complete review of stochastic, robust, distributionally robust, and chance restricted optimization in the domain of smart power systems in a single survey study.
- An overview of numerous probabilistic optimization strategies, including their taxonomy, application examples, and solution algorithms is included in this survey study.
- Probabilistic mathematical models for various scenarios that can be used as a reference models in the field of smart power system have been developed.

Table 1. Summary of Related Survey Papers.

Ref.	SO	RO	DRO	CC	AR	TN	OF	SA	Smart Power System
[25]	✓				✓			✓	
[26]	✓			✓	✓				
[27]	✓			✓	✓		✓		✓
[28]		✓			✓				
[29]		✓			✓			✓	
[30]			✓		✓				
[31]				✓	✓				✓
Our Review Paper	✓	✓	✓	✓	✓	✓	✓	✓	✓

1.3. Organization of the Paper

This paper is organized as follows: Section 1 introduces the smart power system, its elements and related research contribution, while Section 2 covers the architecture and taxonomy of probabilistic optimization. Applications, objectives and solution algorithms of probabilistic optimization in various domains of smart power system are discussed in Section 3. Section 4 furnishes probabilistic mathematical models of various scenarios in smart power system. Then, future research directions and new challenges are discussed in Section 5, whereas Section 6 provides a brief summary of the whole article with concluding remarks.

2. Probabilistic Optimization

Stochastic programming is used to solve optimization problems in which the majority of the parameters are probabilistic [32]. Probabilistic optimization can make efficient use of information, both in terms of selecting evaluation points and the message they convey. It can handle many sorts of noise and adapts to various aspects of optimization issues. Unlike deterministic optimization, probabilistic optimization techniques discover the best solution for data with randomness [33]. As indicated in Figure 1, there are multiple probabilistic optimization categories: stochastic optimization, robust optimization, distributionally robust optimization, and chance-constrained optimization.

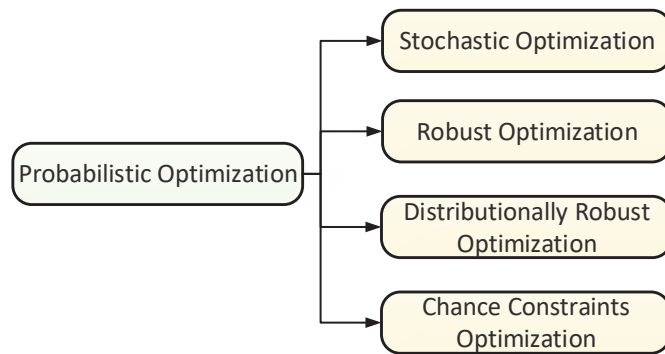


Figure 1. Classification of probabilistic optimization.

2.1. Stochastic Optimization

Stochastic optimization is critical for addressing uncertainty in optimization problems. Due to computing problems, uncertainty is typically disregarded in classical optimization, but breakthroughs in computational techniques now allow for the efficient handling of uncertainties [34]. Stochastic optimization is concerned with strategies for minimising or optimising an uncertain objective function. In contrast to deterministic optimization issues, stochastic optimization problems do not have a single solution. To solve the issue tractably, structural assumptions such as a constraint on the size of the choice variables, the result space, or convexity are required [35]. Traditionally, stochastic optimization modeled uncertainties as random variables with well-defined distributions [36].

2.1.1. Architecture of Stochastic Optimization

The objective function is typically optimized over the expected value of the uncertain parameters for the formulation of stochastic programming, as shown in Equation (1). Where x is the decision variable that belongs to set X , E_p is the expected value of the random variable ζ . Stochastic optimization is graphically represented in part *a* of Figure 2, where P is the probability distribution of random variable ζ . An exact distribution is required for the uncertainties, which cannot be estimated with the empirical data accurately [37]. Either all scenarios or scenarios with probability guarantees are feasible for the modeled solution. In stochastic optimization, sample-based techniques are commonly utilized due to the difficulty of obtaining the correct distribution of random variables. A greater sample size is utilized to get higher probability guarantees, increasing computing complexity [34].

$$\inf_x E_p\{f(x, \zeta)\} \quad (1)$$

$$s.t. \quad x \in X$$

The probability distribution determines the level of uncertainty in stochastic optimization. In basic scenarios, uncertainty is well known, but in practise, it is only partially unknown. The accuracy of stochastic optimization is influenced by the model specifics and availability of possible scenarios. If a stochastic framework is used for all scenarios, the problem becomes more difficult. A trade-off between number of scenarios and, computing time, and complexity is required [34].

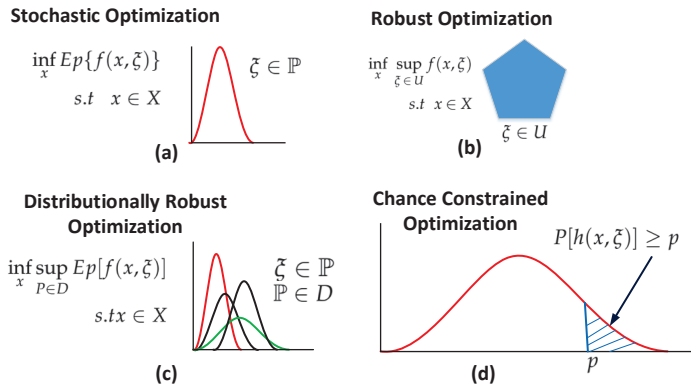


Figure 2. Graphical comparison of: (a) stochastic optimization; (b) robust optimization; (c) distributionally robust optimization; (d) chance constrained optimization.

2.1.2. Taxonomy of Stochastic Optimization

Stochastic optimization can be categorized into single stage problems and recourse problems. The recourse problems can be further classified into two stage and multistage problems as shown Figure 3 [25]. In single stage problems, a single but optimal decision is obtained where in recourse optimization problems, it is essential to know the probability distribution of the random variable in the first step, where the second step (correction of that decision) is being performed. In the two stage stochastic optimization the decision maker must make judgments in two stages (at two distinct times) for a given phenomenon with uncertainty. The first stage choice is critical since it must be made based on some random factors gleaned from previous experience or a survey.

Two-stage stochastic optimization problems may have fixed recourse or complete recourse. In case of fixed recourse, the first stage is prediction stage where in second-stage, fixed decision is done based on the results of the experiment [38]. Two-stage stochastic optimization problems will be considered as a complete recourse if, for every scenario, there always exists a viable second solution [33]. Multistage stochastic programming is an extension of two stage stochastic programming to the sequential realization of uncertainty. Majority of the real time problems lies in the domain of multistage stochastic optimization which entail a series of decisions in response to changing outcomes over time [35].

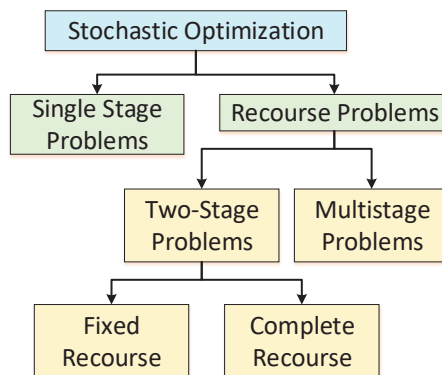


Figure 3. Taxonomy of stochastic optimization.

2.2. Robust Optimization

Robust optimization is a relatively new technique for optimising in the presence of uncertainty. Rather than using a stochastic model, it uses a deterministic, set-based uncertainty model. The robust optimization solution is valid for any specification of the uncertainty in a given set. The reason for robust optimization is that it accounts for both set-based uncertainty and computational tractability [28]. Robust optimization and the respective computational tools deal with optimization problems in which the information are indeterminate and belong to some set of uncertainty [39]. Robust optimization ensures that the worst-case scenario is realized, ensuring that the solution is both practical and optimal for a given set of uncertainties. Robust optimization is not chosen in some applications due to its conservative nature, however it is used in the power industry to preserve reliability. Robust optimization necessitates a considerable amount of knowledge about the uncertainty, such as its size and range [34].

2.2.1. Architecture of Robust Optimization

Robust optimization is a realization of worst-case parameters that belong to the uncertainty set. Worst case realization of robust optimization sometimes becomes unrealistic in practice [37]. The architecture of robust optimization is available in Equation (2), where x is the decision variable that belongs to set X , ζ is a random variable belonging to the uncertainty set U . Robust optimization can be graphically represented as shown in part *b* of Figure 2.

$$\inf_x \sup_{\zeta \in U} f(x, \zeta) \quad (2)$$

s.t. $x \in X$

2.2.2. Taxonomy of Robust Optimization

Robust optimization can be categorized as shown in Figure 4, and is discussed as follows.

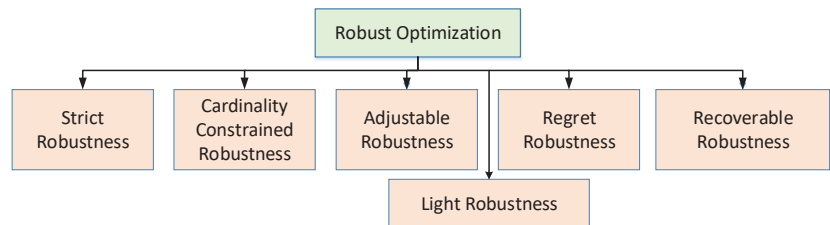


Figure 4. Taxonomy of robust optimization.

- **Strict robustness:** This optimization type is sometimes known as classic robust optimization, min–max optimization, absolute deviation, one-stage robustness, or simply robust optimization. It is treated, as the fundamental starting point in the area of robustness. A solution x is called strictly robust if it is feasible for all possible scenarios of uncertainty set U [40].
- **Cardinality constrained Robustness:** In cardinality constrained robustness, reduction in uncertainty’s space can relax strictness in robust optimization. Analyzing the worst-case scenario in robust optimization, it is improbable that all the uncertainty set parameters will change simultaneously. Hence, it restricts uncertainty space by varying some parameters while considering fixed values for the remaining [41].
- **Adjustable robustness:** In adjustable robustness, the uncertainty space of strict robustness gets relaxed by dividing uncertainty space into groups of variables such as here and now and wait-and-see. Variables from the here and now group must be evaluated

before the scenario $\zeta \in U$ is determined where variables from the wait-and-see group can be determined once the scenario ζ is known [42].

- Light robustness: In light robustness, relaxing the constraints in terms of quality can reduce the strictness of the robust optimization, rather than reducing the space of uncertainty. Light robustness develops a trade-off between quality and robustness of the solution [43].
- Regret robustness: In regret robustness, the objective function relaxes the problem. Rather than to minimize the worst case performance of the solution, regret robustness reduces the difference of objective function having the best solution and the objective function that would have been possible in a scenario [44].
- Recoverable robustness: Concept of recovery algorithm gets exploited in recoverable robustness and family of recovery algorithms which is represented by B . It provides the solution in two stages, such as adjustable robustness. A solution x is called recovery robust with respect to recovery algorithm A if for any probable situation $\zeta \in U$ an algorithm $A \in B$ exist such that when A is applied to the solution x and the scenario ζ makes a solution $A(x; \zeta) \in F(\zeta)$ [45].

2.3. Distributionally Robust Optimization

Distributionally robust optimization, also known as min–max stochastic programming, reduces the computational complexity of stochastic programming and conservative nature of robust optimization. It turns up optimal decisions for the worst-case probability distributions within a family of possible distributions, defined by specific characteristics such as their support vector and moments information [36]. As compare to stochastic programming, it is less dependent on the data having an exact probability distribution. Due to the incorporation of probability distribution and concept of ambiguity sets, the result becomes less conservative as compared to simple robust optimization [46].

2.3.1. Architecture of Distributionally Robust Optimization

A distributionally robust optimization or min–max stochastic programming model act as a bridge between robust and stochastic optimization. It usually takes the form, as shown in Equation (3). where x is the decision variable that belongs to set X , P is the probability distributions that belongs to an ambiguity set D , ζ is the random variable, and Ep is expected value of the random variable [37]. Distributionally robust optimization can be graphically represented as shown in part *c* of Figure 2. The random variable ζ belongs to probability distribution P where P itself belongs to ambiguity set D .

$$\inf_x \sup_{P \in D} Ep[f(x, \zeta)] \quad (3)$$

s.t. $x \in X$

2.3.2. Taxonomy of Distributionally Robust Optimization

Various categories of distributionally robust optimization (DRO) are shown in Figure 5 and are discussed as follows. DRO is a strong modeling paradigm for optimization under uncertainty that arises from the realization that the probability distribution of uncertain parameters of the the problem is uncertain in-itself. As a result the concept of ambiguity set arises which is defined as a set in which the modeler considers that the real distribution of the uncertain parameters of problem has uncertainty. Naturally, the ambiguity set's creation is critical to DRO's actual effectiveness. DRO can be classified on the basis of characteristics and specifications of ambiguity set which are described as follows [47].

1. Moment-based approach: The ambiguity set in moment based approach is the set of all probability distributions whose moments satisfy certain constraints [48,49].
2. Dissimilarity-based approach: The ambiguity set in this case is the set of all probability distributions whose dissimilarity to a nominal distribution is lower than or equal to a

given value. In this category, the choice of the dissimilarity function leads to couple of different variants which are as follows [47].

- (a) Optimal-transport-based (OTP) approach: The authors in [50,51] applied Wasserstein distance as a dissimilarity function which shows some nice statistical convergence properties.
- (b) ϕ -Divergences based approach: This group consist of all those techniques which uses ϕ -divergences such as Kullback–Leibler divergence, as was described in [52,53]. Approaches used in [54,55] are based on likelihood which also belongs to this category.

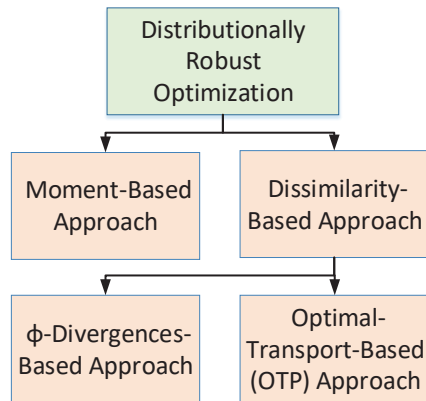


Figure 5. Taxonomy of distributionally robust optimization.

2.4. Chance Constrained Optimization

Chance constrained optimization solves the problems having constraints, in which finite probability get violated. As compared to conventional optimization problems, chance constrained optimization problems face a challenge when inequality function is not available explicitly. Hence, no suitable algorithmic or theoretical properties are evident, such as differentiation, continuity and concavity. A general solution method for chance constrained programming does not exist, but it depends on the interaction of decision and random variables in the constraint model [56].

2.4.1. Architecture of Chance Constrained Optimization

In general chance constrained optimization can be expressed as in inequality, as shown in Equation (4), where it can be graphically represented as shown in part *d* of Figure 2:

$$P[h(x, \xi)] \geq p \quad (4)$$

In Equation (4), ξ and x are random and decision vector, respectively, P is probability measure, $h(x, \xi) \geq 0$ represents a finite system of inequalities. $p \in [0, 1]$ is known as probability level and is chosen by decision maker for safety requirements [56].

2.4.2. Taxonomy of Chance Constrained Optimization

Chance constrained optimization problems can be categorized based on constraints involved as shown in Figure 6. It may have individual, joint, or mixed chance constrained. In individual chance-constrained optimization problems, each element of the stochastic inequality system is transformed into several chance constrained in a unique way where in joint chance-constrained optimization problems, the probability is considered over the stochastic inequality system as a whole. Chance constrained optimization in Equation (4) can be expressed as an individual and joint chance-constrained, as shown

in Equations (5) and (6), respectively, [56]. Mixed chance constrained optimization problems may comprise numerous multivariate chance constrained [57]. Individual chance constrained are simple but unreliable compared to joint chance constrained; hence joint chance constrained are used to guarantee the decision at a given probability level [56].

$$P[h_j(x, \xi)] \geq 0 \geq p_j (j = 1, 2, 3, \dots, m) \tag{5}$$

$$P[h_j(x, \xi)] \geq 0 (j = 1, 2, 3, \dots, m) \geq p \tag{6}$$

Based on the constraints involved in chance constrained optimization problems, it may be linear random vector, separated random vector, coupled random vector, or decision vector. Most important model of chance constrained system is linear random vector. Linear random vector is shown in Equation (4) where the constraint h may adopt different form such as expressed in Equations (7) and (8).

$$h(x, \xi) = g(x) - A \cdot \xi \tag{7}$$

$$h(x, \xi) = A(\xi)g(x) - b \tag{8}$$

where $A(\xi)$ and A are stochastic and deterministic matrices, respectively, b is a constant vector of suitable size, g is the function of decision vector x , The model shown in Equations (7) and (8) represents separated and coupled random vector, respectively. In isolated random vector, random vector and decision vector appear separated while combined in the coupled vector model. The random vector may be continuous, discrete, independent or correlated [56].

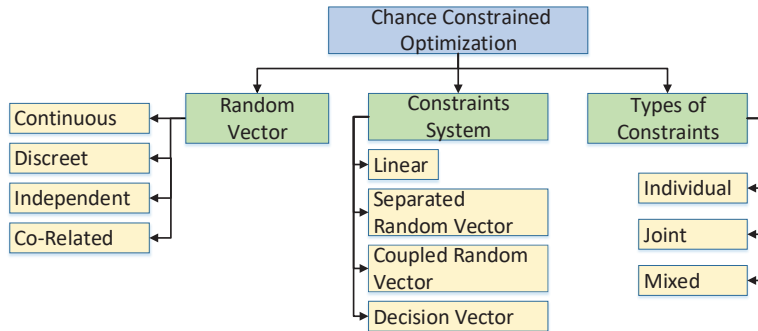


Figure 6. Taxonomy of chance constrained optimization.

3. Applications, Objectives and Solution Algorithms of Probabilistic Optimization

3.1. Applications, Objectives and Solution Algorithms of Stochastic Optimization

Applications of stochastic optimization shown in Table 2. Microgrid energy management problems might be seen as having uncertainty in plug-in electric vehicles and distributed renewable energy supplies [58]. The authors in [59] used stochastic dynamic programming to analyse smart home energy management with uncertainty in plug-in electric vehicles. The optimization problem is approached as non-linear programming, and the distribution of electric power among various smart home components is optimized.

The energy management problem of a smart thermal grid with aquifer thermal energy storage is solved using a stochastic model predictive control framework. Mixed-integer quadratic programming is used to solve the problem. The developed model is used to capture the aquifer’s injection and extraction imbalances, as well as the undesired mutual interaction of aquifer thermal energy storage and smart thermal grid [60]. The problem of probabilistic optimal power dispatch for microgrid is defined as non-linear programming. The operating cost is minimized through particle swarm optimization, and the optimization

problem is handled appropriately [61].

In day-ahead transmission network planning, a probabilistic model is utilized to schedule demand response. For the best demand response scheduling, network security and consumer economic factors are applied. Thermal units and renewable energy resources have been modeled, and the problem has been formulated using mixed-integer linear programming [62]. Residential appliances use real-time demand response management with stochastic and robust optimization. The mathematical model is developed using mixed-integer linear programming, and the electricity bill is reduced as compared to flat rate [63].

The probabilistic model has better performance to solve the smart power system economic dispatch problem as compared to the negative load reduction model for various cases [23]. Economic operation of future distribution grid is discussed, and the stochastic model is developed to find the optimal operation of small-scale energy resources and load [64]. Non-linear programming is used to develop mathematical model of the system as described in [23,64].

A stochastic model is utilized to reconfigure the distribution grid and model distributed photovoltaic generation in this study. The distribution grid is operated at its most cost-effective level, and different constraints such as power balance and power flow limits are met. The grid's reliability and stability have also been improved, which is an important component of incorporating renewable energy sources. Mixed-integer second-order cone programming is used to solve the optimization problem [65].

The stochastic optimization method is used to solve a unit commitment problem with a demand response that is uncertain. It is demonstrated that by taking the uncertainty of demand response into account in a probabilistic manner, generating capacity may be enhanced [66]. The model was created to deal with uncertainty in the unit commitment problem while minimizing the system's operating costs. To acquire an efficient solution for the system, parallelization and decomposition strategies are applied [67]. The integration of storage devices and a high penetration of renewable energy resources is demonstrated in a unit commitment and economic dispatch model. It is concluded that the consideration of storage devices to reduce operational cost is quite effective. Linear programming is used to formulate optimization problem in [66,67], where in [24] mixed-integer linear programming is applied.

For day-ahead optimal power flow, stochastic optimization is used, which can help to improve economic benefits. The uncertainties of wind power and load are incorporated into DC optimal power flow. The problem is expressed as a mixed integer linear programming problem that is solved using the two-point estimation approach. To determine the ideal number of switching each hour, a framework based on probability decisions is designed, taking into account risk cost and economic rewards [68].

Table 2. Applications of stochastic optimization and its problem type.

References	Applications	LP	NLP	MILP	MISOCP	MIQP
[59]	HEM		×			
[61]	MEM		×			
[68]	OPF			×		
[62,63]	DRM			×		
[23,64]	ED		×			
[24,66]	UC	×		×		
[60]	STG					×
[65]	RDG				×	

3.2. Applications, Objectives and Solution Algorithms of Robust Optimization

In a smart power system, robust optimization has a variety of applications with dynamic objectives. Table 3 shows the applications, and Table 4 summarizes the objectives.

3.2.1. Smart Grid Energy Management

One of the most common applications of robust optimization is smart grid energy management. Robust optimization can be used to model uncertainty in several parameters. To maximize social welfare, the problem is described as mixed integer linear programming and solved using a consensus algorithm and an optimal control technique [69].

3.2.2. Microgrid Energy Management

The energy management system for single and three-phase balance microgrids is designed using robust convex optimization. The problem is formulated as a mixed integer second-order cone programming [70]. Microgrid energy management takes into account the characteristics and constraints of the system. The system is mathematically modeled using mixed-integer nonlinear programming, which is subsequently linearized using the Lyapunov optimization approach [71]. For microgrid energy management, two-stage adaptive robust optimization is employed while taking into account the uncertainties of renewable energy resources. In both isolated and grid connected modes, the problem is formulated as mixed integer linear programming, and the total operating cost of the system is minimized. The column and constraint creation algorithm efficiently solves the problem [72]. Energy and frequency management of microgrid accomplishes a reliable and robust solution where total cost of the system is minimized by solving mixed integer linear programming using information gap decision theory [73,74].

Microgrid planning uses two-stage robust optimization to reduce operating and maintenance costs, investment costs, emissions, and fuel costs. The composition of a microgrid takes into account both renewable energy sources and dispatchable distributed generation. The key sources of uncertainty are intermittent renewable energy resources and time-varying load, which can be effectively managed by using robust optimization. The column and constraint creation approach aids in the solution of the mixed integer linear programming problem [75]. Scenario-based robust optimization is applied to minimize the microgrid's social benefit cost by accounting for uncertainty in load and renewable energy resources. Taguchi's orthogonal array generates scenarios, which are then verified using Monte Carlo simulations [76]. Distributed generation, distributed storage, and distributed economic dispatch are used to manage energy in the microgrid. The Lagrangian relaxation and dual decomposition method is used to reduce the net cost of a microgrid [77].

3.2.3. Unit Commitment

A security constraint unit commitment for the power grid considering the uncertainties in supply and demand is performed. Total operation cost is minimized, and the solution to the problem is achieved by applying the bender's decomposition and column generation methods [78]. The overall cost of the system gets minimized by applying various algorithms in different domains [79,80]. Unit commitment problem is solved by Benders' decomposition algorithm [81,82], column and constraints generation algorithm [83,84] and Lagrangian decomposition method [85]. Integrated electricity and heating system is scheduled by column and constraints generation algorithm [86]. Multistage robust optimization is applied for unit commitment, considering the uncertainties of wind power and demand response. The sole objective is to maximize social welfare and to satisfy various constraints. It is being solved by using bender's decomposition algorithm to achieve unit commitment in an optimal robust way [87].

3.2.4. Demand Side Management

The demand side is scheduled using robust optimization, which takes into account the uncertainty in manually operated appliances. The problem is formulated as quadratic programming [88], where nonlinear programming is used in [89] to minimize the cost of electricity. Commercial building appliances are scheduled in an ideal method to account for the impact of uncertainties. To minimize the cost of power, the optimization problem is framed as a mixed integer linear programming problem.

3.2.5. Smart Home

The robust index method is applied to handle the uncertainties of household load scheduling and minimize the customer discomfort. The problem is mathematically formulated as a mixed integer linear programming which has been solved by using branch and bound algorithm [90]. The proposed model schedules renewable energy resources at the production part and controls the smart home consumption part. An optimal solution achieved, along with the reduction in computational time and electricity cost. Meta-heuristic algorithm is applied to solve the mixed integer linear programming problem [91].

3.2.6. Plugin Electric Vehicles

Bidirectional dispatch coordination of plugin electric vehicles in a power grid restrains the generation cost. The problem is formulated as a mixed integer linear programming and solved by using heuristic approach [92].

Table 3. Applications of robust optimization and its problem Type.

Ref.	Applications	LP	NLP	MIP	MILP	MINLP	MIBLP	MISOCP	MIQP	QP
[69]	SGEM				×					
[70–73,75]	MEM				×	×		×		
[90,91]	HEM				×					
[88,89,93]	DSM		×		×					×
[92,94]	PEV				×				×	
[67,78,83–85,87,95–104]	UC	×	×	×	×		×		×	
[105]	SGTD				×					

3.3. Applications, Objectives and Solution Algorithms of Distributionally Robust Optimization

When considering energy storage, distributed generators, and wind turbines, distributionally robust chance constrained programming is used for energy management of an islanded microgrid. However, using an analytical method, the overall generation cost is minimized [106]. The generation frequency is managed appropriately via quadratic programming, and the generation cost is also curtailed [107].

The unit commitment problem with uncertainty in wind output power is solved via distributionally robust optimization. The MILP optimization problem is solved using an analytical method, and conservatism is reduced by using distribution information. [46,108]. Distance-based distributionally robust optimization is modeled for a unit commitment by using Kullback Leibler divergence. This model handles uncertainties of wind power in the form of an ambiguity set. The problem is arranged as mixed integer non-linear programming and is solved by using bender decomposition and the iterative method. Computational complexities are handled by decomposition method while the iterative algorithm guarantees the global conservatism [109]. The unit commitment problem is solved by Benders' decomposition algorithm [110].

Table 4. Objectives of robust optimization and its solution algorithms.

Ref.	Objectives	CCG	AM	LDR	IPEA and MH	HE	BD	TOA	DD and IGDT	MPC and FPIM	BB	LM	QP	MCS	LOM and BMLM	IM
[92,106,107]	Minimize Generation Cost	×				×										
[89,91]	Minimize Electricity Cost	×			×											
[76]	Minimize Social Benefits Cost						×							×		
[73,77]	Minimize Microgrid Net Cost							×				×				
[90]	Minimize Comfort Violation										×					
[72,78,85,111]	Minimize Operation Cost	×				×			×							
[67,71,75,81–84,86,98,110]	Minimize Overall Cost	×	×			×					×	×		×	×	×
[93]	Minimize Electricity Payment	×											×			
[69,87]	Maximize Social Welfare					×									×	
[75]	Maximize Profits	×														

The authors in [112] applied distributionally robust optimization to solve energy and reserve dispatch problem. It is shown that distributionally robust optimization is a suitable technique for reserve dispatch to fill the gap between stochastic and adjustable robust optimization. Strategic aggregation is offering regulation capacity on behalf of a group of distributed energy resources. Two stage stochastic optimization and distributionally robust chance constrained optimization are utilized for handling the uncertainties in day-ahead and hour-ahead schemes, respectively, [113]. The authors in [114] applied distributionally robust optimization to solve the power flow problem.

3.4. Applications, Objectives and Solution Algorithms of Chance Constrained Optimization

Chance constrained optimization can be applied to a smart power system by considering applications with diverse objectives. Applications and objectives of chance constrained optimization in smart power system are shown in Tables 5 and 6, respectively.

3.4.1. Microgrid Energy Management

Chance constrained optimization for microgrid energy management is used, where uncertainties are considered in various parameters. Electricity cost of microgrid is minimized by using linear programming while satisfying the energy balance constraint [115]. In [116], chance constrained optimization is applied to handle the uncertainties in power exchange between microgrid and macro-grid where overall cost of the system is minimized by using mixed integer linear programming. Chance constrained stochastic cone programming is applied to plan microgrid network and overall system's cost is minimized. To obtain the solution for the problem, it uses second-order cone programming (SOCP), bi-linear Benders decomposition method, Jensen's inequalities, and Pareto-optimal cuts [117]. Chance constrained optimization is used for the optimal operation of microgrid having uncertainties where the problem is formulated as a mixed-integer non-linear programming [118].

3.4.2. Distributed Energy Management

In the distribution system, chance constrained optimization helps in the operation and planning of the energy storage system. Overall cost of the system is minimized by using mixed integer linear programming [119,120]. Chance constrained optimization is used to handle the uncertainties that are due to photo-voltaic and batteries. Line losses in the distribution system are reduced by formulating the problem as second order cone programming and solved by analytic method [121,122]. Overall cost of the system is minimized in distributed energy management problem by using mixed integer linear programming [123]. In [124], the authors presented feasibility and profit based planning for the integration of distributed generation. The problem is mathematically formulated as a mixed integer bi-linear programming.

3.4.3. Demand Side Management

Uncertainties due to the consumption pattern and variation in consumers response to the price signal are modeled by chance constrained optimization. The problem is mathematically formulated as non-linear programming to minimize the electricity price and being solved by interior point method [125]. In [126], the authors considered uncertainties due to the interruptable load and consumer response. Penalty to the consumers and variations due to the interrupt-able load are minimized using non linear programming.

3.4.4. Smart Distribution Network

Joint chance constrained optimization handles the high penetration of distributed generator in a distribution network. The support vectors classifier (SVC) identifies zero probability constraints while sampling is done by Monte Carlo Simulations. Overall system cost is reduced by using non-linear programming to formulate the problem [127]. In [128], the authors minimized planning cost where the problem is being formulated as mixed integer non linear programming.

3.4.5. Home Energy Management

Chance constrained optimization for home energy management to optimize the operation of appliances is used. The model to formulate the uncertainties due to electricity prices and fluctuating loads is used. The problem is mathematically modeled as mixed-integer linear programming and being solved by using particle swarm optimization and two-point estimation method [129].

3.4.6. Unit Commitment

The chance constrained two stage stochastic program minimizes the overall generation cost, whereas sample average approximation helps in solving the mixed integer linear programming problem [130]. Spinning reserve cost gets minimized in an uncertain controllable load by using chance constrained optimization. The problems are mathematically formulated as linear programming which are being solved by applying the analytic method and scenario base analysis in [131] and in [132], respectively. Overall system's cost gets minimized by applying the ranking algorithm, and the iterative method in unit commitment problem using mixed integer linear programming [123]. The authors in [133] applied analytic method to satisfy the constraints in unit commitment problem. Operating cost is minimized by formulating the unit commitment problems as mixed integer programming and mixed integer second order cone programming in [134,135], respectively. Overall cost of the system is minimized in [136] using mixed integer quadratic programming and non-linear programming in [137].

3.4.7. Economic Dispatch

Economic dispatch problem is formulated as a linear programming problem in [138]. Active power losses are minimized in thermostatically controllable load, where Spatio temporal and dual decomposition algorithm solve the problem [139]. The pay-off gets maximized, and the problem is solved by applying linear regression and iterative method [140]. Dispatch coordination for plug-in electric vehicles are modeled as a mixed integer quadratic programming [141].

Table 5. Application of chance constrained optimization and its problem type.

Ref.	Applications	LP	NLP	MIP	MILP	MINLP	MIBLP	MISOCP	SOCp	MIQP
[115–118,142,143]	MEM	×	×		×	×		×		
[129]	HEM				×					
[119–121,123,124]	DEM				×		×		×	
[127,128]	SDN		×			×				
[125,126]	DSM		×							
[141]	PEV									×
[138]	ED	×								
[130,131,133–137,144]	UC	×	×	×	×			×		×
[145]	GEM		×							
[146]	OPF		×							
[147]	OPGF		×							

Table 6. Objectives of chance constrained optimization and the solution algorithms.

Ref.	Objectives	SA	AM	SBM	IPM	HE	BD and DE	HABC	POC	DD	SA	SVM	LR and IM	MDP	MCS	MDP	ADMM
[106,130]	Minimize Generation Cost	x	x														
[133]	Constraints Satisfaction		x														
[131,132]	Minimize Reserve Cost							x							x		
[125]	Minimize Signal Price			x													
[142]	Minimize Electricity Cost					x											
[115,118,134,135]	Minimize Operating Cost						x			x							
[116,117,119,120,123,127,136,144,148]	Minimize Overall Cost	x	x						x							x	
[121]	Minimize Thermal line losses																
[128]	Minimize planning cost										x						
[139]	Minimize Active Power Losses									x					x		
[140]	Maximize payoff												x				
[145]	Minimize Dispatch cost																x
[149]	Minimize Social cost																x

4. Mathematical Models for Various Scenarios

This review paper presents probabilistic mathematical models of diverse scenarios for better understanding of scientists and researchers. Researchers have, however, presented deterministic mathematical models in the literature.

4.1. Scenario 1: Energy Management

In [150], the authors presented an energy management model for a residential compound having N number of consumers, as shown in Figure 7. Each consumer has a set of appliances A , which includes seasonal, shift-able and non shift-able appliances. The system has some given parameters, but some parameters are to be determined.

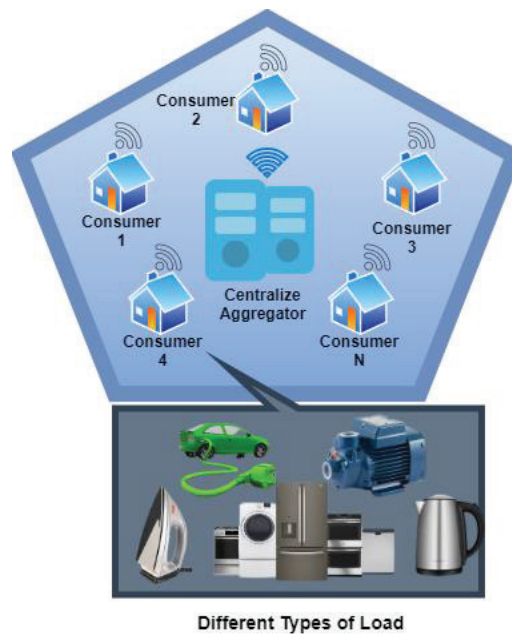


Figure 7. Residential compound.

Given Parameters:

- Total number of consumers N in residential compound
- Set of appliances A for each consumers
- Each appliances has a time dependent power profile $P_a^{t,n}$
- Each appliances operating time t_a^n
- Scheduled starting time t_s^n
- Human interaction factor for a certain time $H_a^{t,n}$
- Price tariff C^t
- Load shedding factor L^t

Parameters to be determined for each time slot

- To switched on a set of appliances
- Each consumer electricity consumption cost

A deterministic model of the system is shown in Equation (14), where the appliances are scheduled in such a way so that it reduces the consumer’s electricity cost. To turn on the given appliance we have introduced binary decision variable as shown in Equation (9).

$$X_a^{t,n} = \begin{cases} 1 & \text{if the } a\text{th appliances of the } n\text{th} \\ & \text{consumer is switch on at the } t\text{th time slot.} \\ 0 & \text{otherwise} \end{cases} \quad (9)$$

The a th appliance of the n th consumer requires t_a^n minutes to operate. To accomplish the task, the scheduling time begins at $t = t_s^n$ and ends at $t = t_a^n + t_s^n$. The decision variable $X_a^{t,n}$ would be 1 for the complete number of t_a time slots to ensure continuous operation of the appliance. Hence, the contiguous constraint is represented in mathematical form as shown in Equation (10).

$$\begin{aligned} \sum_{t=t_s^n}^{t_s^n+t_a^n} X_a^{t,n} &= t_a^n, \quad \forall a, n \\ t_a^n + t_s^n &\leq T \quad \forall a, n \end{aligned} \quad (10)$$

Certain appliances require human involvement to operate, hence human interaction factor (HIF) is considered. The human interaction factor is represented by the symbol $H_a^{t,n}$ and is mathematically modeled as shown below.

$$H_a^{t,n} = \begin{cases} 1 & \text{if the } n\text{th consumer is available to operate the} \\ & a\text{th appliance at the } t\text{th time slot.} \\ 0 & \text{otherwise} \end{cases}$$

The operation of a washing machine, for example, necessitates the presence of consumers. As a result, the human interaction factor $H_a^{t,n}$ will be 1 for a given time interval to correctly operate the washing machine. By inculcating the impact of HIF factor, the Equation (10) becomes as shown in Equation (11).

$$\sum_{t=t_s^n}^{t_s^n+t_a^n} X_a^{t,n} H_a^{t,n} = t_a^n, \quad \forall a, n \quad (11)$$

Another concern related with residential energy management is the lack of energy owing to a variety of factors, particularly in rural locations, such as maintenance etc. We introduce the load shedding (LS) factor L^t to address the load shedding issue and the lack of electricity.

$$L^t = \begin{cases} 1 & \text{if the electricity is available for the whole time.} \\ 0 & \text{otherwise} \end{cases}$$

With the addition of load shedding factor, Equation (11) can be rewritten as shown in Equation (12).

$$\sum_{t=t_s^n}^{t_s^n+t_a^n} X_a^{t,n} H_a^{t,n} L^t = t_a^n, \quad \forall a, n \quad (12)$$

Another thing to consider, while building an effective residential energy management system, is the willingness and preferences of consumers (CP). There are times when it is ideal for a particular appliance to turn on, but the consumer is unwilling to operate or switch it on. As a result, we add another input variable, $\lambda_a^{t,n}$ to respond to consumer preferences.

$$\lambda_a^{t,n} = \begin{cases} 1 & \text{if the } n\text{th consumer wants to operate the } a\text{th} \\ & \text{appliance at the } t\text{th time slot.} \\ 0 & \text{otherwise} \end{cases}$$

With the consideration of consumer preference Equation (12) can be expressed as shown in Equation (13)

$$\sum_{t=t_s^n}^{t_s^n+t_a^n} X_a^{t,n} H_a^{t,n} L^t \lambda_a^{t,n} = t_a^n, \quad \forall a, n \tag{13}$$

$$\min_{X_a^{t,n} \in \{0,1\} \forall a,n} \sum_{n=1}^N \sum_{a \in A} \sum_{t=1}^T X_a^{t,n} C^t E_a^{t,n}$$

subject to

Contiguous Constraint

$$C_1 : \sum_{t=t_s^n}^{t_s^n+t_a^n} X_a^{t,n} = t_a^n, \quad \forall a, n, t$$

LS and contiguous constraint

$$C_2 : \sum_{t=t_s^n}^{t_s^n+t_a^n} X_a^{t,n} H_a^{t,n} L^t = t_a^n, \quad \forall a, n, t$$

$$C_3 : \sum_{t=t_s^n}^{t_s^n+t_a^n} X_a^{t,n} H_a^{t,n} L^t \lambda_a^{t,n} = t_a^n, \quad \forall a, n, t$$

CP, LS, HIF and Contiguous Constraint

(14)

Considering that various parameters in Equation (14) have uncertainty such as total energy consumed $E_a^{t,n}$ and human interaction factor $H_a^{t,n}$. Uncertainty in $E_a^{t,n}$ is ζ_e^t while ζ_h^t is the uncertainty in $H_a^{t,n}$. To handle these uncertainties various probabilistic models are as follows.

4.1.1. Stochastic Optimization Model

Stochastic Optimization model is shown in Equation (15) where $\mathbb{E}_{\zeta_e^t}(E_a^{t,n}, \zeta_e^t)$ is the expected value of energy consumed at time T by each appliance of n^{th} consumer. Constraints C_1 in Equation (15) will remain same as shown in Equation (14). $[\mathbb{E}_{\zeta_h^t}(H_a^{t,n}, \zeta_h^t)]$ in C_2 and C_3 represent the expected value of human interaction factor.

$$\min_{X_a^{t,n} \in \{0,1\} \forall a,n} \sum_{n=1}^N \sum_{a \in A} \sum_{t=1}^T X_a^{t,n} C^t [\mathbb{E}_{\zeta_e^t}(E_a^{t,n}, \zeta_e^t)]$$

subject to

LS and contiguous constraint

$$C_2 : \sum_{t=t_s^n}^{t_s^n+t_a^n} X_a^{t,n} [\mathbb{E}_{\zeta_h^t}(\zeta_h^t H_a^{t,n})] L^t = t_a^n, \quad \forall a, n, t$$

$$C_3 : \sum_{t=t_s^n}^{t_s^n+t_a^n} X_a^{t,n} [\mathbb{E}_{\zeta_h^t}(\zeta_h^t H_a^{t,n})] L^t \lambda_a^{t,n} = t_a^n, \quad \forall a, n, t$$

CP, LS, HIF and Contiguous Constraint

(15)

4.1.2. Robust Optimization Model

Robust optimization model is shown in Equation (16), where ζ_e^t and ζ_h^t are the uncertainty factors. Constraint C_1 is not effected by the uncertainty factor, hence it will remain same as Equation (14). Constraints C_2 and C_3 are effected by the uncertainty factor and are shown in Equation (16). Equality symbol in C_2 and C_3 are replaced by inequality symbol which shows that worst case scenario are satisfied.

$$\begin{aligned}
 & \min_{X_a^{t,n} \in \{0,1\}, \forall a,n} \sum_{n=1}^N \sum_{a \in A} \sum_{t=1}^T \left(\max_{\zeta_e^t, \zeta_h^t \in \mathcal{U}} X_a^{t,n} C^t(\zeta_e^t E_a^{t,n}) \right) \\
 & \text{subject to} \\
 & \quad \underbrace{\text{LS and contiguous constraint}} \\
 & C_2 : \sum_{t=t_s^n}^{t_s^n+t_a^n} X_a^{t,n} (\zeta_h^t H_a^{t,n}) L^t \geq t_a^n, \forall a, n, t, \zeta_h^t \in \mathcal{U} \tag{16} \\
 & C_3 : \sum_{t=t_s^n}^{t_s^n+t_a^n} X_a^{t,n} (\zeta_e^t H_a^{t,n}) L^t \lambda_a^{t,n} \geq t_a^n, \forall a, n, t, \zeta_h^t \in \mathcal{U} \\
 & \quad \underbrace{\text{CP, LS, HIF and Contiguous Constraint}}
 \end{aligned}$$

Transforming min–max problem in (16) into minimization problem gives Equation (17)

$$\begin{aligned}
 & \min_{\Theta_a^{t,n}, X_a^{t,n} \in \{0,1\}, \forall a,n} \sum_{n=1}^N \sum_{a \in A} \sum_{t=1}^T \Theta_a^{t,n} \\
 & \text{subject to} \\
 & \quad \underbrace{\text{Contiguous Constraint}} \\
 & C_1 : \sum_{t=t_s^n}^{t_s^n+t_a^n} X_a^{t,n} = t_a^n, \forall a, n, t \\
 & \quad \underbrace{\text{LS and contiguous constraint}} \\
 & C_2 : \sum_{t=t_s^n}^{t_s^n+t_a^n} X_a^{t,n} (\zeta_h^t H_a^{t,n}) L^t \geq t_a^n, \forall a, n, t, \zeta_h^t \in \mathcal{U} \\
 & C_3 : \sum_{t=t_s^n}^{t_s^n+t_a^n} X_a^{t,n} (\zeta_e^t H_a^{t,n}) L^t \lambda_a^{t,n} \geq t_a^n, \forall a, n, t, \zeta_h^t \in \mathcal{U} \\
 & \quad \underbrace{\text{CP, LS, HIF and Contiguous Constraint}} \\
 & C_4 : X_a^{t,n} C^t(\zeta_e^t E_a^{t,n}) \leq \Theta_a^{t,n}, \forall a, n, t, \zeta_e^t, \zeta_h^t \in \mathcal{U}
 \end{aligned} \tag{17}$$

4.1.3. Distributionally Robust Optimization Model

Distributionally robust model for the system is shown in (18) where P_e^t and P_h^t are the probability distributions of uncertainty in total energy consumed $E_a^{t,n}$ and human interaction factor $H_a^{t,n}$. D is the ambiguity set and $\mathbb{E}_{\zeta_e^t}(\zeta_e^t E_a^{t,n})$ is the expected value of energy consumed at time T . Constraints C_2 and C_3 are effected by the uncertainty factors and are shown in Equation (18). Equality symbol in C_2 and C_3 are replaced by the inequality symbol which shows that worst case scenario are satisfied.

$$\begin{aligned}
 & \min_{X_a^{t,n} \in \{0,1\} \forall a,n} \sum_{n=1}^N \sum_{a \in A} \sum_{t=1}^T \max_{(P_e^t, P_h^t) \in \mathcal{D}} X_a^{t,n} C^t [\mathbb{E}_{\xi^t}(\zeta_e^t E_a^{t,n})] \\
 & \text{subject to} \\
 & \quad \underbrace{\text{LS and contiguous constraint}} \\
 & C_2 : \sum_{t=t_s^n}^{t_s^n+t_a^n} X_a^{t,n} [\mathbb{E}_{\xi_h^t}(\zeta_h^t H_a^{t,n})] L^t \geq t_a^n, \forall a, n, t, \xi_h^t \in \mathcal{U} \\
 & C_3 : \sum_{t=t_s^n}^{t_s^n+t_a^n} X_a^{t,n} [\mathbb{E}_{\xi_h^t}(\zeta_h^t H_a^{t,n})] L^t \lambda_a^{t,n} \geq t_a^n, \forall a, n, t, \xi_h^t \in \mathcal{U} \\
 & \quad \underbrace{\text{CP, LS, HIF and Contiguous Constraint}}
 \end{aligned} \tag{18}$$

4.1.4. Chance Constrained Optimization Model

Chance constrained optimization model is shown in Equation (19), where ζ_e^t and ζ_h^t are uncertainty factor in total energy consumed and human interaction factors. The confidence level for constraints C_2 and C_3 are γ_1 and γ_2 , respectively, where $\gamma_1, \gamma_2 \in [0, 1]$.

$$\begin{aligned}
 & \min_{X_a^{t,n} \in \{0,1\} \forall a,n} \sum_{n=1}^N \sum_{a \in A} \sum_{t=1}^T X_a^{t,n} C^t (\zeta_e^t E_a^{t,n}) \\
 & \text{subject to} \\
 & \quad \underbrace{\text{LS and contiguous constraint}} \\
 & C_2 : \mathbb{P} \left(\sum_{t=t_s^n}^{t_s^n+t_a^n} X_a^{t,n} (\zeta_h^t H_a^{t,n}) L^t \geq t_a^n \right) \leq \gamma_1, \forall a, n, t \\
 & C_3 : \mathbb{P} \left(\sum_{t=t_s^n}^{t_s^n+t_a^n} X_a^{t,n} (\zeta_h^t H_a^{t,n}) L^t \lambda_a^{t,n} \geq t_a^n \right) \leq \gamma_2, \forall a, n, t \\
 & \quad \underbrace{\text{CP, LS, HIF and Contiguous Constraint}}
 \end{aligned} \tag{19}$$

4.2. Scenario 2: GHG Emission Control Microgrid

Authors in [151] have considered a system as shown in Figure 8. The deterministic mathematical model is developed for unified demand side management, as shown in Equation (20). The objective function is to minimize overall cost of the system including electricity consumption cost $f_c(E_{n,a}^t)$ and carbon dioxide emission cost $f_{CO_2}(E_{n,a}^t)$. The parameter $\alpha_1 \in [0, 1]$ helps in selecting the priorities setting for job operation. Various system's constraints are operation time constraints, appliances continuous operation constraint, consumer preference constraint, human interaction constraint and load shedding constraint, peak clipping, and appliances priority constraint. Let the system has uncertainty in overall energy consumption $E_{n,a}^{k,t}$ and is represented by ξ . Various probabilistic models are formulated to show the impact of uncertainty on the deterministic mathematical model of the system.

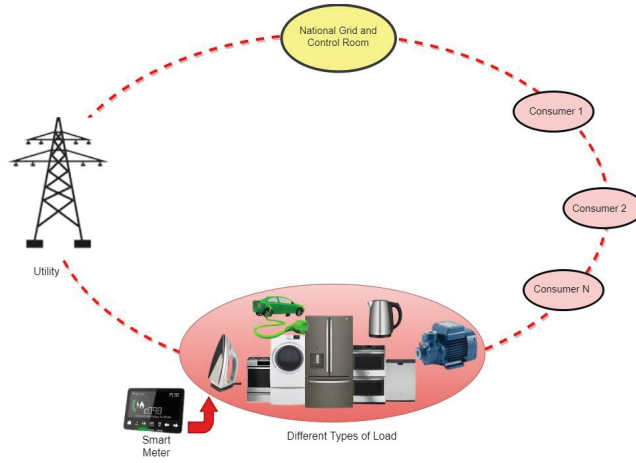


Figure 8. Residential compound architecture.

Deterministic Problem

$$\min_{X_{n,a}^{k,t} \in \{0,1\} \forall k,n,t,a} \sum_{k=1}^K \sum_{n=1}^N \sum_{a \in A_n} \sum_{t=1}^T \left[\begin{array}{c} \text{Total Cost} \\ \alpha_1 \underbrace{f_c(E_{n,a}^{k,t})}_{\text{Electricity cost function}} + (1 - \alpha_1) \underbrace{f_{CO_2}(E_{n,a}^{k,t})}_{\text{Emission cost function}} \end{array} \right] X_{n,a}^{k,t} \quad (20)$$

subject to:

$$C1 : \underbrace{\sum_{n=1}^N \sum_{a \in A_n} X_{n,a}^{k,t} E_{n,a}^{k,t}}_{\text{Peak clipping constraint}} \leq \alpha_4 \gamma^{k,t}, \quad \forall k, t$$

Operation time constraint

$$C2 : \sum_{t=1}^T X_{n,a}^{k,t} = t_a^k, \quad \forall k, n, a$$

$$C3 : \sum_{t=t_{n,a}^k}^{t_{n,a}^k + t_{n,a}^k - 1} X_{n,a}^{k,t} \geq t_a^k \alpha_5, \quad \forall k, n, a$$

Appliances time continuity constraint

$$C4 : X_{n,a}^{k,t} = X_{n,a}^{k,t} (\lambda_{n,a}^{k,t})^{\alpha_6} (H_{n,a}^{k,t})^{\alpha_3} (L^t)^{\alpha_2}, \quad \forall k, n, a, t$$

Consumer preferences, human interaction and load shedding factors consideration constraint

$$C5 : \sum_{a \in \beta_i} X_{n,a}^{k,t} \leq 1, \quad \forall \text{shiftable appliances}, k, t, \{i = 1, 2, 3, \dots, I\}$$

Appliances priorities constraint

4.2.1. Stochastic Optimization Model

Stochastic model for the system could be witnessed by Equation (21), where $\alpha_1 \mathbb{E}_{\xi} f_c(E_{n,a}^{k,t})$ is the expected value of electricity cost and $(1 - \alpha_1) \mathbb{E}_{\xi} f_{CO_2}(E_{n,a}^{k,t})$ is the expected value of CO₂ emission cost. Furthermore, the Constraints C₂ – C₅ are not affected by considering the uncertainty hence they will remain the same as given in Equation (20). In Constraint C₁ the expected value of energy consumption ($\mathbb{E}_{\xi}(\xi E_{n,a}^t)$ at time T is less than certain peak value.

Stochastic Problem

$$\min_{X_{n,a}^{k,t} \in \{0,1\} \forall k,n,t,a} \sum_{k=1}^K \sum_{n=1}^N \sum_{a \in A_n} \sum_{t=1}^T \left[\overbrace{\left(\alpha_1 \underbrace{\mathbb{E}_{\xi} f_c(E_{n,a}^{k,t}, \xi)}_{\text{Electricity cost function}} + (1 - \alpha_1) \underbrace{\mathbb{E}_{\xi} f_{CO_2}(E_{n,a}^t, \xi)}_{\text{Emission cost function}} \right)}^{\text{Total Cost}} X_{n,a}^{k,t} \right]. \quad (21)$$

subject to:

$$C1 : \underbrace{\sum_{n=1}^N \sum_{a \in A_n} X_{n,a}^{k,t} (\mathbb{E}_{\xi}(\xi E_{n,a}^t))}_{\text{Peak clipping constraint}} \leq \alpha_4 \gamma^{k,t}, \quad \forall k, t$$

4.2.2. Robust Optimization Model

In the robust minimization model, which is shown in Equation (22), where the uncertainty ξ in total energy consumed $E_{n,a}^{k,t}$ belongs to an uncertainty set U . $\alpha_1 f_c(\xi E_{n,a}^{k,t})$ shows the impact of uncertainty on total electricity cost where $(1 - \alpha_1) f_{CO_2}(\xi E_{n,a}^{k,t})$ shows the impact of uncertainty on carbon emission cost. The constraint C₁ is affected by the uncertainty ξ which shows that maximum energy consumption having uncertainty should be less than a certain peak value. Constraints C₂ to C₅ will remain same as in Equation (20). The problem in Equation (22) is a maximization problem that can be converted into a minimization problem as shown in Equation (23).

Robust Problem

$$\min_{X_{n,a}^{k,t} \in \{0,1\} \forall k,n,t,a} \sum_{k=1}^K \sum_{n=1}^N \sum_{a \in A_n} \sum_{t=1}^T \left(\max_{\xi \in U} \left(\alpha_1 f_c(\xi E_{n,a}^{k,t}) + (1 - \alpha_1) f_{CO_2}(\xi E_{n,a}^{k,t}) \right) X_{n,a}^{k,t} \right). \quad (22)$$

subject to:

$$C1 : \underbrace{\sum_{n=1}^N \sum_{a \in A_n} X_{n,a}^{k,t} (\xi E_{n,a}^{k,t})}_{\text{Peak clipping constraint}} \leq \alpha_4 \gamma^{k,t}, \quad \forall k, t, \xi \in U$$

Robust Problem 1

$$\min_{W_{n,a}^{k,t}, X_{n,a}^{k,t} \in \{0,1\} \forall k,n,t,a} \sum_{k=1}^K \sum_{n=1}^N \sum_{a \in A_n} \sum_{t=1}^T W_{n,a}^{k,t}. \quad (23)$$

subject to:

$$C1 : \underbrace{\sum_{n=1}^N \sum_{a \in A_n} X_{n,a}^{k,t}(\xi E_{n,a}^{k,t})}_{\text{Peak clipping constraint}} \leq \alpha_4 \gamma^{k,t}, \quad \forall k, t, \xi \in \mathcal{U}$$

$$C2 : \left(\alpha_1 f_c(\xi E_{n,a}^{k,t}) + (1 - \alpha_1) f_{CO_2}(\xi E_{n,a}^{k,t}) X_{n,a}^{k,t} \right) \leq W_{n,a}^{k,t} \quad \forall k, t, \xi \in \mathcal{U}$$

4.2.3. Distributionally Robust Model

Distributionally robust optimization model is shown in Equation (24), where P_{ξ} shows the probability distributions of uncertainty factor ξ that belongs to an ambiguity set D . $\alpha_1 f_c \mathbb{E}_{\xi}[(\xi E_{n,a}^{k,t})]$ is the expected value of uncertain electricity cost, where $(1 - \alpha_1) f_{CO_2} \mathbb{E}_{\xi}[(\xi E_{n,a}^{k,t})]$ is the expected value of uncertain CO₂ emission cost. Constraint C₂ to C₅ will remain same as shown in Equation (20) while C₁ shows the expected of energy consumption is less than a certain peak value.

Distributionally Robust Problem

$$\min_{X_{n,a}^{k,t} \in \{0,1\} \forall k,n,t,a} \sum_{k=1}^K \sum_{n=1}^N \sum_{a \in A_n} \sum_{t=1}^T \left(\max_{P_{\xi} \in D} \left(\alpha_1 f_c \mathbb{E}_{\xi}[(\xi E_{n,a}^{k,t})] + (1 - \alpha_1) f_{CO_2} \mathbb{E}_{\xi}[(\xi E_{n,a}^{k,t})] \right) X_{n,a}^{k,t} \right). \tag{24}$$

subject to:

$$C1 : \underbrace{\sum_{n=1}^N \sum_{a \in A_n} X_{n,a}^{k,t} \mathbb{E}_{\xi}(\xi E_{n,a}^{k,t})}_{\text{Peak clipping constraint}} \leq \alpha_4 \gamma^{k,t}, \quad \forall k, t, \xi \in \mathcal{U}$$

4.2.4. Chance Constrained Optimization Model

The Chance constrained model is shown in Equation (25), where the only affected constraint is C₁. It shows that probability of violating peak clipping limit is less than a certain predefined value, i.e., α . However, Constraint C₂ – C₅ will remain the same as given by Equation (20).

Chance Constrained Problem

$$\min_{X_{n,a}^{k,t} \in \{0,1\} \forall k,n,t,a} \sum_{k=1}^K \sum_{n=1}^N \sum_{a \in A_n} \sum_{t=1}^T \left[\underbrace{\left(\alpha_1 \underbrace{f_c(E_{n,a}^{k,t}, \xi)}_{\text{Electricity cost function}} + (1 - \alpha_1) \underbrace{f_{CO_2}(E_{n,a}^{k,t}, \xi)}_{\text{Emission cost function}} \right)}_{\text{Total Cost}} X_{n,a}^{k,t} \right]. \tag{25}$$

subject to:

$$C1 : \mathbb{P} \left(\underbrace{\sum_{n=1}^N \sum_{a \in A_n} X_{n,a}^{k,t}(\xi E_{n,a}^{k,t})}_{\text{Peak clipping constraint}} \leq \alpha_4 \gamma^{k,t} \right) \leq \alpha, \quad \forall k, t$$

4.3. Scenario 3: Energy Trading Model for Microgrid System

In Figure 9, the network of a microgrid is shown where different sources of generation are considered, e.g., PV cells, small wind turbines and utility. Furthermore, Figure 9

shows that microgrids are connected to each other and with utility. Based on defined tariff, the microgrids can exchange energy with each other as well as with utility. Cost per unit of self-generation is usually low as compared to energy procure from utility and from other microgrids. The system model shown in Figure 9 has a total of V microgrids connected with each other and with utility. N is the total number of consumers on each microgrid, and each consumer has a set of shiftable and non-shiftable appliances. The appliances are operated in such a way so that the self-generation of microgrid v can fulfill the energy demand; if the energy generated by microgrid v is not enough to meet its energy demand than microgrid v will procure energy from other microgrids. If the other microgrids do not have extra energy to sell it to microgrid v than they will procure energy from the utility.

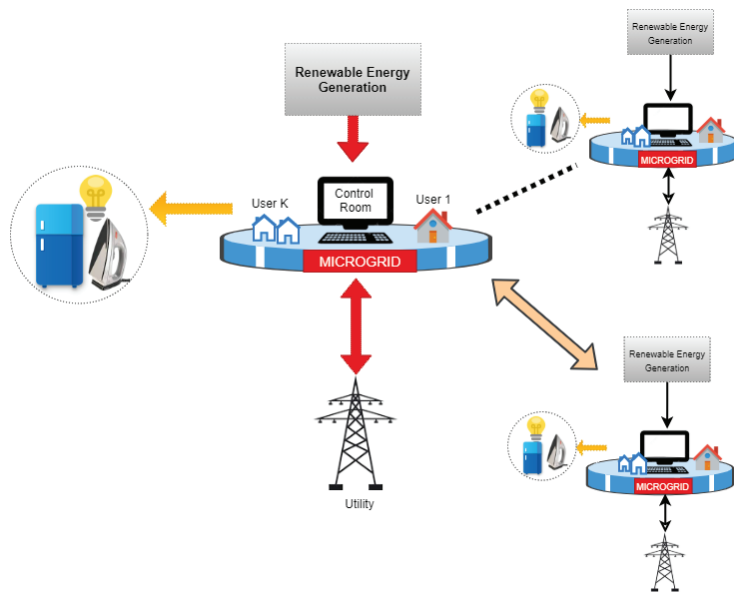


Figure 9. System model for scenarios 3 and 4.

The deterministic mathematical model for the energy trading module in the microgrid system as shown in Equation (26), where the objective function minimizes the overall cost of the system as well as to satisfy various constraints. Positive sign with the decision variables shows that the energy is either generated by the microgrid itself or it sells the extra energy to other microgrids or utility, where negative signs represents that the energy is purchased from the utility or from other microgrids. Peak generation constraint defines the maximum generating capacity of the microgrid. Maximum purchase of energy from utility or from other microgrids are represented by peak purchase constraint. Various other constraints are peak generation constraint, peak purchase from other microgrids and utility, appliances priority constraint, no self sell/purchase constraint, either to sell or purchase constraint. Let the energy generated by microgrid v has the uncertainty ζ_g . To model the impact of uncertainty factor ζ_g over the system, various probabilistic models are shown as follows.

Deterministic Problem

$$\begin{aligned}
 & \min_{\substack{E_v^{t,\mu}, E_n^{t,g}, E_{v,\mu}^t \\ E_{w,v}^t, E_{v,w}^t, X_{v,a}^{t,n} \in \{0,1\} \\ \forall v,n,t,a}} \\
 & \sum_{t=1}^T \sum_{v=1}^V \left(C(E_v^{t,\mu}) + C(E_v^{t,g}) - C(E_{v,\mu}^t) + \sum_{w=1}^V (C(E_{w,v}^t) - C(E_{v,w}^t)) \right) \\
 & \text{S.t.} \quad \text{Peak Generation Constraint} \\
 & \quad C1 : \quad \overbrace{0 \leq E_v^{t,g} \leq E_v^{t,g,max}} \quad \forall v, t \tag{26} \\
 & \quad \text{Peak Purchase from Microgrids} \\
 & \quad C2 : \quad \overbrace{0 \leq E_{w,v}^t \leq E_{w,v}^{t,max}} \quad \forall v, w, t \\
 & \quad \text{Peak Purchase from Utility} \\
 & \quad C3 : \quad \overbrace{0 \leq E_v^{t,\mu} \leq E_v^{t,\mu,max}} \quad \forall v, t \\
 & \quad \text{Appliances Priority Constraint} \\
 & \quad C4 : \quad \overbrace{\sum_{a \in \beta_1} X_{v,a}^{t_1,n} + \sum_{a \in \beta_2} X_{v,a}^{t_2,n} \leq 1} \quad \forall \{t_1 < t_2\}, n, v \\
 & \quad \text{No Self Sell/Purchase} \\
 & \quad C5 : \quad \overbrace{E_{v,v}^t = 0} \quad \forall v, t \\
 & \quad \text{Either Sell or Purchase Constraint} \\
 & \quad C6 : \quad \overbrace{E_{v,w}^t \times E_{w,v}^t = 0} \quad \forall t, v, w
 \end{aligned}$$

4.3.1. Stochastic Optimization Model

The stochastic optimization model could be represented such as in Equation (27), where the $C[\mathbb{E}_{\xi_g}(E_v^{t,g}, \xi_g)]$ is the expected value of the energy generated by microgrid v . The only constraint that is affected by considering uncertainty is C_1 , while the rest of the constraints will remain the same as Equation (26) witnesses it. The factor $\mathbb{E}_{\xi_g}(\xi_g E_v^{t,g})$ in constraint C_1 shows that expected value of uncertain generation supposed to be less than certain defined value.

Stochastic Problem

$$\begin{aligned}
 & \min_{\substack{E_v^{t,\mu}, E_n^{t,g}, E_{v,\mu}^t \\ E_{w,v}^t, E_{v,w}^t, X_{v,a}^{t,n} \in \{0,1\} \\ \forall v,n,t,a}} \\
 & \sum_{t=1}^T \sum_{v=1}^V \left(C(E_v^{t,\mu}) + C[\mathbb{E}_{\xi_g}(E_v^{t,g}, \xi_g)] - C(E_{v,\mu}^t) + \sum_{w=1}^V (C(E_{w,v}^t) - C(E_{v,w}^t)) \right) \\
 & \text{S.t.} \quad \text{Peak Generation Constraint} \\
 & \quad C1 : \quad \overbrace{0 \leq \mathbb{E}_{\xi_g}(\xi_g E_v^{t,g}) \leq E_v^{t,g,max}} \quad \forall v, t \tag{27}
 \end{aligned}$$

4.3.2. Robust Optimization Model

Robust optimization model is shown in Equation (28), where $C(\xi_g E_v^{t,g})$ show the energy generated by microgrid v having uncertainty ξ . The constraint C_1 which is effected by considering uncertainty, shows that the energy generated by microgrid v at time t varies in an uncertain manner but it should be less than a certain maximum value. The min-max problem of Equation (28) can be transformed into minimization problem as shown in Equation (29).

Robust Problem

$$\begin{aligned}
 & \min_{\substack{E_v^{t,\mu}, E_n^{t,g}, E_{v,\mu}^t \\ E_{w,v}^t, E_{v,w}^t, X_{v,a}^{t,n} \in \{0,1\} \\ \forall v,n,t,a}} \\
 & \sum_{t=1}^T \sum_{v=1}^V \max_{\xi_g \in \mathcal{U}} \left(C(E_v^{t,\mu}) + C(\xi_g E_v^{t,g}) - C(E_{v,\mu}^t) + \sum_{w=1}^V (C(E_{w,v}^t) - C(E_{v,w}^t)) \right) \\
 & \text{Peak Generation Constraint} \\
 \text{s.t.} \quad & C1 : 0 \leq \xi_g E_v^{t,g} \leq E_v^{t,g,max} \quad \forall v,t, \xi_g \in \mathcal{U}
 \end{aligned} \tag{28}$$

Robust Problem 1

$$\begin{aligned}
 & \min_{Z_v^n, X_{v,a}^n \in \{0,1\} \quad \forall v,n,t,a} \sum_{t=1}^T \sum_{v=1}^V Z_v^t \\
 & \text{Peak Generation Constraint} \\
 \text{s.t.} \quad & C1 : 0 \leq \xi_g E_v^{t,g} \leq E_v^{t,g,max} \quad \forall v,t, \xi_g \in \mathcal{U} \\
 & C2 : \left(C(E_v^{t,\mu}) + C(\xi_g E_v^{t,g}) - C(E_{v,\mu}^t) + \sum_{w=1}^V (C(E_{w,v}^t) - C(E_{v,w}^t)) \right) \leq Z_v^t \\
 & \quad \forall v,t, \xi_g \in \mathcal{U}
 \end{aligned} \tag{29}$$

4.3.3. Distributionally Robust Optimization

Distributionally robust model is shown in Equation (30), where the P_g indicates the probability distributions of uncertainty in energy generated by microgrid v . $\mathbb{E}_g(\xi_g E_v^{t,g})$ is the expected value of the energy generated by microgrid v at time t . The constraint C_1 is effected by considering the uncertainty while the constraints C_2 to C_6 will remain same as shown by Equation (26).

Distributionally Robust Problem

$$\begin{aligned}
 & \min_{\substack{E_v^{t,\mu}, E_n^{t,g}, E_{v,\mu}^t \\ E_{w,v}^t, E_{v,w}^t, X_{v,a}^{t,n} \in \{0,1\} \\ \forall v,n,t,a}} \\
 & \sum_{t=1}^T \sum_{v=1}^V \max_{P_g \in \mathcal{D}} \left(C(E_v^{t,\mu}) + C\mathbb{E}_g(\xi_g E_v^{t,g}) - C(E_{v,\mu}^t) + \sum_{w=1}^V (C(E_{w,v}^t) - C(E_{v,w}^t)) \right) \\
 & \text{Peak Generation Constraint} \\
 \text{s.t.} \quad & C1 : 0 \leq \mathbb{E}_g(\xi_g E_v^{t,g}) \leq E_v^{t,g,max} \quad \forall v,t, \xi_g \in \mathcal{U}
 \end{aligned} \tag{30}$$

4.3.4. Chance Constrained Optimization Model

The chance constrained model is shown in Equation (31), where constraint C_1 shows that the probability of violating the peak generation limit is less than a certain predefined value. Constrain from $C_2 - C_6$ will remain same as shown in Equation (26).

Chance Constrained Problem

$$\begin{aligned}
 & \min_{\substack{E_v^{t,\mu}, E_n^{t,g}, E_{v,\mu}^t \\ E_{w,v}^t, E_{v,w}^t, X_{v,a}^{t,n} \in \{0,1\} \\ \forall v,n,t,a}} \\
 & \sum_{t=1}^T \sum_{v=1}^V \left(C(E_v^{t,\mu}) + C(E_v^{t,g}, \xi_g) - C(E_{v,\mu}^t) + \sum_{w=1}^V (C(E_{w,v}^t) - C(E_{v,w}^t)) \right) \\
 & \text{Peak Generation Constraint} \\
 \text{s.t.} \quad & C1 : \mathbb{P} \left(0 \leq \xi_g E_v^{t,g} \leq E_v^{t,g,max} \right) \leq \zeta \quad \forall v,t
 \end{aligned} \tag{31}$$

4.4. Scenario 4: Joint Energy Management and Trading for Microgrid System

In this section, energy management and energy trading models are collectively considered, where the deterministic model of the system is formulated and described in [152]. The system model for joint energy management and trading is shown in Figure 9. Various energy management constraints such as energy balance constraint, peak clipping constraint, and operation time constraint have been considered in addition to energy trading constraints that are mentioned in scenario 3. Let the applied model in [152] have uncertainty in various parameters such as energy generated ($E_v^{t,g}$) by microgrid is v and base-load (B_v^t) on microgrid v . The uncertainty in $E_v^{t,g}$ and B_v^t are represented as ζ_g and ζ_l , respectively. The objective function and various constraints such as energy balance constraint, peak clipping constraint and peak generation constraint are effected by considering uncertainty in energy generation and base-load. The remaining constraints of the system will remain the same as shown in [152]. To show the impact of uncertainty, various probabilistic optimization schemes are applied as follows.

Deterministic Problem

$$\begin{aligned}
 \min_{\substack{E_v^{t,u}, E_v^{t,g}, E_{v,u}^t, \\ E_{w,v}^t, E_{v,w}^t, X_{v,a}^{t,n} \in \{0,1\} \\ \forall v,n,t,a}} & \sum_{t=1}^T \sum_{v=1}^V \left(C(E_v^{t,u}) + C(E_v^{t,g}) - C(E_{v,u}^t) + \sum_{w=1}^V (C(E_{w,v}^t) - C(E_{v,w}^t)) \right) \quad (32) \\
 \text{s.t.} & \quad \overbrace{C1: E_v^{t,u} + E_v^{t,g} + \sum_{w=1}^V E_{w,v}^t = \sum_{w=1}^V E_{v,w}^t + E_{v,u}^t + B_v^t + \sum_{a \in A^n} X_{v,a}^{t,n} \Gamma_{v,a}^{t,n}}^{\text{Energy Balance Constraint}} \quad \forall v, w, n, t \\
 & \quad \overbrace{C2: \sum_{t=t_a^n}^{t_a^n + t_a^n} (X_{v,a}^{t,n} H_{v,a}^{t,n} L_{v,a}^{t,n} \Lambda_{v,a}^{t,n} + B_v^t) \leq \gamma^t}^{\text{Peak Clipping Constraint}} \quad \forall n, a, v \\
 & \quad \overbrace{C3: \sum_{t=t_a^n}^{t_a^n + t_a^n} X_{v,a}^{t,n} H_{v,a}^{t,n} \Gamma_{v,a}^{t,n} \Lambda_{v,a}^{t,n} = t_a^n}^{\text{Operation Time Constraint}} \quad \forall n, a, v \\
 & \quad \overbrace{C4: 0 \leq E_v^{t,g} \leq E_v^{t,g,max}}^{\text{Peak Generation Constraint}} \quad \forall v, t \\
 & \quad \overbrace{C5: 0 \leq E_{w,v}^t \leq E_{w,v}^{t,max}}^{\text{Peak Purchase from Microgrids}} \quad \forall v, w, t \\
 & \quad \overbrace{C6: 0 \leq E_{v,u}^t \leq E_{v,u}^{t,max}}^{\text{Peak Purchase from Utility}} \quad \forall v, t \\
 & \quad \overbrace{C7: \sum_{a \in \beta_1} X_{v,a}^{t_1,n} + \sum_{a \in \beta_2} X_{v,a}^{t_2,n} \leq 1}^{\text{Appliances Priority Constraint}} \quad \forall \{t_1 < t_2\}, n, v \\
 & \quad \overbrace{C8: E_{v,v}^t = 0}^{\text{No Self Sell/Purchase}} \quad \forall v, t \\
 & \quad \overbrace{C9: E_{v,w}^t \times E_{w,v}^t = 0}^{\text{Either Sell or Purchase Constraint}} \quad \forall t, v, w
 \end{aligned}$$

4.4.1. Stochastic Optimization Model

In stochastic optimization, the expected value of uncertain parameters is considered. The stochastic mathematical model of the considered system is given by Equation (33). Where, in Equation (33) the $\mathbb{E}_{\zeta_g}[C(E_v^{t,g}, \zeta_g)]$ shows the expected value of total cost of the energy generated by microgrid v , where in constrains $\mathbb{E}_{\zeta_g}(\zeta_g E_v^{t,g})$ is the expected value of

the energy generated by microgrid v and $\mathbb{E}_{\zeta_l}(\zeta_l B_v^t)$ is the expected value of the base load on the microgrid v .

Stochastic Problem

$$\begin{aligned}
 & \min_{\substack{E_v^{t,\mu}, E_n^{t,g}, E_{v,\mu}^t \\ E_{w,v}^t, E_{v,w}^t, X_{v,a}^{t,n} \in \{0,1\} \\ \forall v,n,t,a}} \\
 & \sum_{t=1}^T \sum_{v=1}^V \left(C(E_v^{t,\mu}) + \mathbb{E}_{\zeta_g} [C(E_v^{t,g}, \zeta_g)] - C(E_{v,\mu}^t) + \sum_{w=1}^V (C(E_{w,v}^t) - C(E_{v,w}^t)) \right) \tag{33} \\
 \text{S.t.} \quad & \overbrace{C1 : E_v^{t,\mu} + \mathbb{E}_{\zeta_g} [\zeta_g E_v^{t,g}] + \sum_{w=1}^V E_{w,v}^t = \sum_{w=1}^V E_{v,w}^t + E_{v,\mu}^t + \mathbb{E}_{\zeta_l} [\zeta_l B_v^t] + \sum_{a \in A^n} X_{v,a}^{t,n} L_{v,a}^{t,n}}^{\text{Energy Balance Constraint}} \quad \forall v, w, n, t \\
 & \overbrace{C2 : \sum_{t=i_a^{s,n}}^{i_a^{e,n} + t_a^n} (X_{v,a}^{t,n} H_{v,a}^{t,n} L_{v,a}^{t,n} L_{v,a}^t \lambda_{v,a}^{t,n} + \mathbb{E}_{\zeta_l} [\zeta_l B_v^t]) \leq \gamma^t}^{\text{Peak Clipping Constraint}} \quad \forall n, a, v \\
 & \overbrace{C4 : 0 \leq \mathbb{E}_{\zeta_g} (\zeta_g E_v^{t,g}) \leq E_v^{t,g,max}}^{\text{Peak Generation Constraint}} \quad \forall v, t
 \end{aligned}$$

4.4.2. Robust Optimization Model

Robust optimization considers a worst-case scenario for the system. It is assumed that the uncertainty factor ζ_g can take values 0.9 – 1.0 and the uncertainty factor ζ_l can varies from 1.0 – 1.2. The robust mathematical model for the system considered is shown in Equation (34). Equality constraint C_1 is changed to inequality constraint, which ensures that the load balancing constraint should be satisfied in the worst case. The problem in Equation (34) is a min–max problem that can be converted into a minimization problem, as shown in Equation (35).

Robust Problem

$$\begin{aligned}
 & \min_{\substack{E_v^{t,\mu}, E_n^{t,g}, E_{v,\mu}^t \\ E_{w,v}^t, E_{v,w}^t, X_{v,a}^{t,n} \in \{0,1\} \\ \forall v,n,t,a}} \\
 & \sum_{t=1}^T \sum_{v=1}^V \max_{(\zeta_g, \zeta_l) \in \mathcal{U}} \left(C(E_v^{t,\mu}) + C(\zeta_g E_v^{t,g}) - C(E_{v,\mu}^t) + \sum_{w=1}^V (C(E_{w,v}^t) - C(E_{v,w}^t)) \right) \tag{34} \\
 \text{S.t.} \quad & \overbrace{C1 : E_v^{t,\mu} + \zeta_g E_v^{t,g} + \sum_{w=1}^V E_{w,v}^t \geq \sum_{w=1}^V E_{v,w}^t + E_{v,\mu}^t + \zeta_l B_v^t + \sum_{a \in A^n} X_{v,a}^{t,n} L_{v,a}^{t,n}}^{\text{Energy Balance Constraint}} \quad \forall v, w, n, t, (\zeta_g, \zeta_l) \in \mathcal{U} \\
 & \overbrace{C2 : \sum_{t=i_a^{s,n}}^{i_a^{e,n} + t_a^n} (X_{v,a}^{t,n} H_{v,a}^{t,n} L_{v,a}^{t,n} L_{v,a}^t \lambda_{v,a}^{t,n} + \zeta_l B_v^t) \leq \gamma^t}^{\text{Peak Clipping Constraint}} \quad \forall n, a, v, \zeta_l \in \mathcal{U} \\
 & \overbrace{C4 : 0 \leq \zeta_g E_v^{t,g} \leq E_v^{t,g,max}}^{\text{Peak Generation Constraint}} \quad \forall v, t, \zeta_g \in \mathcal{U}
 \end{aligned}$$

$$\begin{aligned}
 & \min_{\substack{Y_v^t, X_{v,a}^{t,n} \in \{0,1\} \\ \forall v,n,t,a}} \sum_{t=1}^T \sum_{v=1}^V Y_v^t \tag{35} \\
 \text{s.t.} \quad & \overbrace{C1: E_v^{t,\mu} + \zeta_g E_v^{t,g} + \sum_{w=1}^V E_{w,v}^t \geq \sum_{w=1}^V E_{v,w}^t + E_{v,\mu}^t + \zeta_l B_v^t + \sum_{a \in A^n} X_{v,a}^{t,n} L_{v,a}^{t,n}}^{\text{Energy Balance Constraint}} \quad \forall v, w, n, t, (\zeta_g, \zeta_l) \in \mathcal{U} \\
 & \overbrace{C2: \sum_{t=s_a^n}^{s_a^n+t_a^n} (X_{v,a}^{t,n} H_{v,a}^{t,n} L_{v,a}^{t,n} L_v^t \lambda_{v,a}^{t,n} + \zeta_l B_v^t) \leq \gamma^t}^{\text{Peak Clipping Constraint}} \quad \forall n, a, v, \zeta_l \in \mathcal{U} \\
 & \overbrace{C4: 0 \leq \zeta_g E_v^{t,g} \leq E_v^{t,g,max}}^{\text{Peak Generation Constraint}} \quad \forall v, t, \zeta_g \in \mathcal{U} \\
 & C5: C(E_v^{t,\mu}) + C(\zeta_g E_v^{t,g}) - C(E_{v,\mu}^t) + \sum_{w=1}^V (C(E_{w,v}^t) - C(E_{v,w}^t)) \leq Y_v^t \quad \forall v, w, n, t, (\zeta_g, \zeta_l) \in \mathcal{U}
 \end{aligned}$$

4.4.3. Distributionally Robust Optimization

Mathematical model for distributionally robust optimization is shown in Equation (36), where P_g and P_l are the probability distributions for the uncertain parameters ζ_g and ζ_l , respectively. ζ_g and ζ_l represent uncertainty in energy generated and base load on microgrid v at time t , respectively. $\mathbb{E}_g[E_v^{t,g}, \zeta_g]$ is the expected value of energy generated by microgrid v at time t , where $\mathbb{E}_l[\zeta_l B_v^t]$ is the expected value of base load on microgrid V . Constraints C_1 to C_3 are effected by considering uncertainty while the constraints C_4 to C_5 will remain same as in Equation (32).

Distributionally Robust Problem

$$\begin{aligned}
 & \min_{\substack{E_v^{t,\mu}, E_v^{t,g}, E_{v,\mu}^t \\ E_{w,v}^t, E_{v,w}^t, X_{v,a}^{t,n} \in \{0,1\} \\ \forall v,n,t,a}} \sum_{t=1}^T \sum_{v=1}^V \max_{(P_g, P_l) \in \mathcal{D}} \left(C(E_v^{t,\mu}) + C(\mathbb{E}_g[E_v^{t,g}, \zeta_g]) - C(E_{v,\mu}^t) + \sum_{w=1}^V (C(E_{w,v}^t) - C(E_{v,w}^t)) \right) \tag{36} \\
 \text{s.t.} \quad & \overbrace{C1: E_v^{t,\mu} + \mathbb{E}_g[\zeta_g E_v^{t,g}] + \sum_{w=1}^V E_{w,v}^t \geq \sum_{w=1}^V E_{v,w}^t + E_{v,\mu}^t + \mathbb{E}_l[\zeta_l B_v^t] + \sum_{a \in A^n} X_{v,a}^{t,n} L_{v,a}^{t,n}}^{\text{Energy Balance Constraint}} \quad \forall v, w, n, t, (\zeta_g, \zeta_l) \in \mathcal{U} \\
 & \overbrace{C2: \sum_{t=s_a^n}^{s_a^n+t_a^n} (X_{v,a}^{t,n} H_{v,a}^{t,n} L_{v,a}^{t,n} L_v^t \lambda_{v,a}^{t,n} + \mathbb{E}_l[\zeta_l B_v^t]) \leq \gamma^t}^{\text{Peak Clipping Constraint}} \quad \forall n, a, v, \zeta_l \in \mathcal{U} \\
 & \overbrace{C4: 0 \leq \mathbb{E}_g[\zeta_g E_v^{t,g}] \leq E_v^{t,g,max}}^{\text{Peak Generation Constraint}} \quad \forall v, t, \zeta_g \in \mathcal{U}
 \end{aligned}$$

4.4.4. Chance Constrained Optimization Model

Mathematically speaking, in chance constrained optimization, the probability of satisfying certain constraints should be above a certain predefined level, improving the confidence level of the solution [153,154]. The mathematical model of chance constrained optimization is available in Equation (37). α and β are the confidence level for energy balance and peak clipping constraints, respectively, where $\alpha, \beta \in [0, 1]$.

Chance Constrained

$$\begin{aligned}
 & \min_{\substack{E_v^{t,\mu}, E_n^{t,g}, E_{v,\mu}^t, \\ E_{w,v}^t, E_{v,w}^t, X_{v,a}^{t,n} \in \{0,1\} \\ \forall v,n,t,a}} \\
 & \sum_{t=1}^T \sum_{v=1}^V \left(C(E_v^{t,\mu}) + C(E_v^{t,g}, \zeta_g) - C(E_{v,\mu}^t) + \sum_{w=1}^V (C(E_{w,v}^t) - C(E_{v,w}^t)) \right) \tag{37} \\
 \text{S.t.} \quad & \underbrace{C1 : \mathbb{P} \left(E_v^{t,\mu} + \zeta_g E_v^{t,g} + \sum_{w=1}^V E_{w,v}^t = \sum_{w=1}^V E_{v,w}^t + E_{v,\mu}^t + \zeta_l B_v^t + \sum_{a \in A^n} X_{v,a}^{t,n} L_{v,a}^{t,n} \right)}_{\text{Energy Balance Constraint}} \leq \alpha \quad \forall v, w, n, t \\
 & \underbrace{C2 : \mathbb{P} \left(\sum_{t=t_a^n}^{t_a^n + t_a^n} (X_{v,a}^{t,n} H_{v,a}^{t,n} L_{v,a}^{t,n} L_v^t \lambda_{v,a}^{t,n} + \zeta_l B_v^t) \geq \gamma^t \right)}_{\text{Peak Clipping Constraint}} \leq \beta \quad \forall n, a, v \\
 & \underbrace{C4 : \mathbb{P} \left(0 \leq \zeta_g E_v^{t,g} \leq E_v^{t,g,max} \right)}_{\text{Peak Generation Constraint}} \leq \zeta \quad \forall v, t
 \end{aligned}$$

5. Challenges and Future Research Directions

After a comprehensive survey on the smart power system (having uncertainties in numerous domains), it is recommended to focus on limitations and challenges due to these uncertainties and improve the smart power system’s performance. These limitations and challenges arise in various segments of smart power system such as microgrid energy management, home energy management, demand side management, renewable energy resources, energy storage system, unit commitment, economic dispatch and transmission system.

5.1. Microgrid Energy Management

A microgrid is an essential and significant part of a smart power system. It is operated both in grid connected as well as in an isolated mode. Microgrid energy management problems’ accuracy is seriously affected by the uncertainties in various factors such as renewable energy resources, plug-in electric vehicle and load, etc. Research papers studied have considered uncertainties in few aspects at a time. Hence, it open doors for researchers to model microgrid energy-management problems in a comprehensive way, where uncertainties in all factors affecting microgrid operation can be considered. Furthermore, a model can be developed where the various techniques can be applied in a combined way. The impact of environmental conditions can also be considered in microgrid energy management.

5.2. Demand Side Management

Demand side management plays a critical role in the energy optimization of a smart power system. Demand-side management mainly deals with the consumers’ end; hence, the uncertainties at the consumers end have severe impact on the smart power system’s performance. Various components that cause uncertainties at consumers’ end are manually operated appliances, renewable energy generation, electric vehicle and distributed energy storage devices, inelastic load demand, etc. Therefore, it is an open research direction in the smart power system area to develop a model that can consider the impact of uncertainties caused by the sources mentioned above.

5.3. Integration of Distribution Energy Resources

One of the most significant elements of the smart power system is distributed energy resources. Wind and solar energy are considered prominent example of distributed energy resources. The output power of these sources is seriously affected by the weather condition, which causes uncertainty. Due to the integration of DER with the smart power system, the smart power system’s performance is affected by the uncertainties. The various

model used in the literature have considered a single source of uncertainty; hence, it is an open research area to comprehensively develop a model that can completely handle the uncertainty of distributed energy resources. Furthermore, various optimization techniques that can handle uncertainties can be considered in a combined way to improve the model's performance.

5.4. Smart Home

To increase consumers' participation and user comfort, reducing peak demand and consumer electricity bill, it is required to introduce a smart home concept in a smart power system. Various components of a smart home are renewable energy resources, battery storage system and load. Uncertainties are caused by generating resources due to their weather dependent nature. Load have uncertainties either due to its weather dependent behaviour as well as because of the random interaction of human. The impact of these uncertainties on the power system can be developed comprehensively in future research.

5.5. Unit Commitment

Unit commitment is an optimization problem that determines the generating units' operation schedule at certain time intervals with changing loads under different systems' constraints and environmental conditions. Unit commitment plays a vital role in the economic operation of a smart power system. Hence, to minimize the smart power system's operation cost, it is required to consider all factors affecting the unit commitment problems. The complexity of the unit commitment optimization problems increases with the inclusion of uncertainties in the system parameters. Uncertainties in unit commitment problems are due to the integration of renewable energy resources, power flow-ability of a transmission line, forecasted errors in load, unexpected generator outages etc. It can be considered a future research area to develop a unified unit commitment model that can handle all factors having uncertainties.

6. Conclusions

It is a known fact that real time problems of smart power systems have uncertainties and can be handled only by probabilistic optimization. This review paper has been focused on various aspects of probabilistic optimization in smart power system. Various techniques such as stochastic optimization, robust optimization, distributionally robust optimization, and chance constrained optimization have been thoroughly studied in this paper to deal with such type of uncertainties. From the analysis of different concrete study cases, it is observed that stochastic optimization is providing a reliable solution, however its computational cost is high. In worst case condition, robust optimization has a lower computational cost, but it offers a conservative and cautious solution. The solution of distributionally robust optimization is less conservative than robust and has a lower computational cost than stochastic optimization. Chance constrained optimization deals with problems, where finite probability is being violated. These techniques can be further categorized on the basis of the uncertainty involved. Various applications of the mentioned optimization approach in the area of smart power system have been discussed. Future directions of these techniques with reference to smart power system have been summarized. It has been concluded that these techniques must be used in combination to deal with new challenges of smart power system for achieving fruitful outcomes.

Author Contributions: Conceptualization, M.R. and M.N.; methodology, M.N. and S.A.; software, M.R. and I.H.; validation, M.R., I.H. and L.M.-P.; formal analysis, M.R. and M.N.; investigation, S.A. and I.H.; resources, I.H. and M.N.; data curation, S.A. and M.N.; writing—original draft preparation, M.R.; writing—review and editing, S.A. and I.H.; visualization, L.M.-P.; supervision, M.N. and L.M.-P. All authors have read and agreed to the published version of the manuscript.

Funding: This research received no external funding.

Institutional Review Board Statement: Not applicable.

Informed Consent Statement: Not applicable.

Data Availability Statement: Not applicable.

Acknowledgments: The authors are extremely thankful to anonymous reviewers for enhancing the quality of this paper via their valuable comments.

Conflicts of Interest: The authors declare no conflict of interest.

Abbreviations

The following abbreviations are used in this manuscript:

MEM	Micro-grid Energy Management
HEM	Home Energy Management
DER	Distributed Energy Management
SDN	Smart Distribution Network
DSM	Demand Side Management
PEV	Plugin Electric Vehicles
ED	Economic Dispatch
UC	Unit Commitment
STG	Smart Thermal Grid
MEO	Micro-grid Economic Operation
RDG	Reconfiguration of Distribution Grid
OPF	Optimal Power Flow
ERD	Energy and Reserve Dispatch
ESS	Energy Storage System
SPDA	Scenario Partition and Decomposition Algorithm
CCDCGP	Chance Constrained dependent chance goal programming
FMEA	Failure-Mode-and Effect analysis
IPEA	Inter-generation Projection Evolutionary Algorithm
IGDT	Information Gap Decision Theory
MPC	Model Predictive Control
FPIM	Fuzzy Prediction Interval Model
SPD	Scenario Partition and Decomposition
BMLM	Big-M Linearization Method
LOP	Lyapunov Optimization Method
CCG	Column-and-Constraint Generation
AM	Analytic Method
LDR	Linear Decision Rule
MH	Math-Heuristic
BD	Benders Decomposition
TOA	Taguchis Orthogonal Array
DD	Dual Decomposition
BB	Branch-and-Bound
LM	Lagrangian Multiplier
QP	Quadratic Programming
MCS	Monte Carlo Simulation
IM	Iterative Method
SAA	Sample Average Approximation
SBM	Scenario Based Method
IPM	Interior Point Methods
DE	Differential Evolution
HABC	Hybrid Artificial Bee Colony

POC	Pareto-optimal cuts
DD	Dual Decomposition
SA	Sensitivity Analysis
SVM	Support Vector Machine
LR	Linear Regression
MDP	Markov Decision Process
SO	Stochastic Optimization
RO	Robust Optimization
CCO	Chance Constrained Optimization
DRO	Distributional Robust Optimization
SA	Solution Algorithms
OF	Objective Function
FRD	Future Research Directions
GEM	Grid Energy Management
TPEM	Two-Point Estimate Method
OPGF	Optimal Power Gas Flow
SGTD	Smart Grid Tariff Design
HE	Heuristic
CC	Chance Constrained
AR	Architecture
TN	Taxonomy

References

- Martins, F.; Felgueiras, C.; Smitkova, M.; Caetano, N. Analysis of fossil fuel energy consumption and environmental impacts in European countries. *Energies* **2019**, *12*, 964. [[CrossRef](#)]
- Kabalci, E.; Kabalci, Y. Introduction to Smart Grid Architecture. In *Smart Grids and Their Communication Systems*; Springer: Berlin/Heidelberg, Germany, 2019; pp. 3–45.
- Ahmed, S.; Gondal, T.M.; Adil, M.; Malik, S.A.; Qureshi, R. A survey on communication technologies in smart grid. In Proceedings of the 2019 IEEE PES GTD Grand International Conference and Exposition Asia (GTD Asia), Bangkok, Thailand, 19–23 March 2019; pp. 7–12.
- Bruno, S.; Lamonaca, S.; La Scala, M.; Rotondo, G.; Stecchi, U. Load control through smart-metering on distribution networks. In Proceedings of the 2009 IEEE Bucharest PowerTech, Bucharest, Romania, 28 June–2 July 2009; pp. 1–8.
- Momoh, J.A. Smart grid design for efficient and flexible power networks operation and control. In Proceedings of the 2009 IEEE/PES Power Systems Conference and Exposition, Seattle, WA, USA, 15–18 March 2009; pp. 1–8.
- Khan, N.; Riaz, M. Reliable and Secure Advanced Metering Infrastructure for Smart Grid Network. In Proceedings of the 2018 International Conference on Computing, Electronic and Electrical Engineering (ICE Cube), Quetta, Pakistan, 12–13 November 2018; pp. 1–6. [[CrossRef](#)]
- Nafi, N.S.; Ahmed, K.; Gregory, M.A.; Datta, M. A survey of smart grid architectures, applications, benefits and standardization. *J. Netw. Comput. Appl.* **2016**, *76*, 23–36. [[CrossRef](#)]
- Ahmad, S.; Ahmad, A.; Naeem, M.; Ejaz, W.; Kim, H.S. A compendium of performance metrics, pricing schemes, optimization objectives, and solution methodologies of demand side management for the smart grid. *Energies* **2018**, *11*, 2801. [[CrossRef](#)]
- Malik, S.A.; Gondal, T.M.; Ahmad, S.; Adil, M.; Qureshi, R. Towards optimization approaches in smart grid a review. In Proceedings of the 2019 2nd International Conference on Computing, Mathematics and Engineering Technologies (iCoMET), Sukkur, Pakistan, 30–31 January 2019; pp. 1–5.
- Hussain, I.; Samara, G.; Ullah, I.; Khan, N. Encryption for End-User Privacy: A Cyber-Secure Smart Energy Management System. In Proceedings of the 2021 22nd International Arab Conference on Information Technology (ACIT), Muscat, Oman, 21–23 December 2021; pp. 1–6. [[CrossRef](#)]
- Shakeel, S.R.; Takala, J.; Shakeel, W. Renewable energy sources in power generation in Pakistan. *Renew. Sustain. Energy Rev.* **2016**, *64*, 421–434. [[CrossRef](#)]
- Mosaad, M.I.; Abu-Siada, A.; Ismaiel, M.M.; Albalawi, H.; Fahmy, A. Enhancing the Fault Ride-through Capability of a DFIG-WECS Using a High-Temperature Superconducting Coil. *Energies* **2021**, *14*, 6319. [[CrossRef](#)]
- Tawfiq, A.A.E.; El-Raouf, M.O.A.; Mosaad, M.I.; Gawad, A.F.A.; Farahat, M.A.E. Optimal Reliability Study of Grid-Connected PV Systems Using Evolutionary Computing Techniques. *IEEE Access* **2021**, *9*, 42125–42139. [[CrossRef](#)]
- Hlalele, T.; Du, S. Analysis of power transmission line uncertainties: Status review. *J. Elect. Electron. Syst.* **2016**, *5*, 1–5. [[CrossRef](#)]
- Delle Femine, A.; Gallo, D.; Landi, C.; Lo Schiavo, A.; Luiso, M. Low power contactless voltage sensor for low voltage power systems. *Sensors* **2019**, *19*, 3513. [[CrossRef](#)]
- Alonso, M.; Amaris, H.; Alcalá, D.; Florez R, D.M. Smart sensors for smart grid reliability. *Sensors* **2020**, *20*, 2187. [[CrossRef](#)]

17. Rojas-Delgado, B.; Alonso, M.; Amaris, H.; de Santiago, J. Wave power output smoothing through the use of a high-speed kinetic buffer. *Energies* **2019**, *12*, 2196. [[CrossRef](#)]
18. Vazquez, R.; Amaris, H.; Alonso, M.; Lopez, G.; Moreno, J.I.; Olmeda, D.; Coca, J. Assessment of an adaptive load forecasting methodology in a smart grid demonstration project. *Energies* **2017**, *10*, 190. [[CrossRef](#)]
19. Ng, C.H.; Logenthiran, T.; Woo, W.L. Intelligent distributed smart grid network-Reconfiguration. In Proceedings of the 2015 IEEE Innovative Smart Grid Technologies-Asia ISGT ASIA, Bangkok, Thailand, 3–6 November 2015; pp. 1–6.
20. Hussain, I.; Ullah, M.; Ullah, I.; Bibi, A.; Naeem, M.; Singh, M.; Singh, D. Optimizing Energy Consumption in the Home Energy Management System via a Bio-Inspired Dragonfly Algorithm and the Genetic Algorithm. *Electronics* **2020**, *9*, 406. [[CrossRef](#)]
21. Mora-Flórez, J.J.; Herrera-Orozco, R.A.; Bedoya-Cadena, A.F. Fault location considering load uncertainty and distributed generation in power distribution systems. *IET Gener. Transm. Distrib.* **2015**, *9*, 287–295. [[CrossRef](#)]
22. Miceli, R. Energy management and smart grids. *Energies* **2013**, *6*, 2262–2290. [[CrossRef](#)]
23. Hasan, Z.; El-Hawary, M. Load reduction probabilistic model for smart grid network economic dispatch problem. In Proceedings of the 2017 IEEE Electrical Power and Energy Conference (EPEC), Saskatoon, SK, Canada, 22–25 October 2017; pp. 1–7.
24. Bakirtzis, E.A.; Simoglou, C.K.; Biskas, P.N.; Bakirtzis, A.G. Storage management by rolling stochastic unit commitment for high renewable energy penetration. *Electr. Power Syst. Res.* **2018**, *158*, 240–249. [[CrossRef](#)]
25. Li, C.; Grossmann, I.E. A Review of Stochastic Programming Methods for Optimization of Process Systems under Uncertainty. *Front. Chem. Eng.* **2020**, *2*, 34. [[CrossRef](#)]
26. Birge, J.R. State-of-the-art-survey Stochastic programming: Computation and applications. *INFORMS J. Comput.* **1997**, *9*, 111–133. [[CrossRef](#)]
27. Reddy, S.S.; Sandeep, V.; Jung, C.M. Review of stochastic optimization methods for smart grid. *Front. Energy* **2017**, *11*, 197–209. [[CrossRef](#)]
28. Bertsimas, D.; Brown, D.B.; Caramanis, C. Theory and applications of robust optimization. *SIAM Rev.* **2011**, *53*, 464–501. [[CrossRef](#)]
29. Beyer, H.G.; Sendhoff, B. Robust optimization—A comprehensive survey. *Comput. Methods Appl. Mech. Eng.* **2007**, *196*, 3190–3218. [[CrossRef](#)]
30. Rahimian, H.; Mehrotra, S. Distributionally robust optimization: A review. *arXiv* **2019**, arXiv:1908.05659.
31. Küçükyavuz, S.; Jiang, R. Chance-Constrained Optimization: A Review of Mixed-Integer Conic Formulations and Applications. *arXiv* **2021**, arXiv:2101.08746.
32. Rao, S.S. *Engineering Optimization: Theory and Practice*; John Wiley & Sons: Hoboken, NJ, USA, 2009.
33. Birge, J.R.; Louveaux, F. *Introduction to Stochastic Programming*; Springer Science & Business Media: Berlin/Heidelberg, Germany, 2011.
34. Hedman, K.; Korad, A.; Zhang, M.; Dominguez-Garcia, A.; Jiang, X. *The Application of Robust Optimization in Power Systems*; Final Report to the Power Systems Engineering Research Center; PSERC Publication: Chandigarh, India, 2014; pp. 6–14.
35. Hannah, L.A. Stochastic optimization. *Int. Encycl. Soc. Behav. Sci.* **2015**, *2*, 473–481.
36. Goh, J.; Sim, M. Distributionally robust optimization and its tractable approximations. *Oper. Res.* **2010**, *58*, 902–917. [[CrossRef](#)]
37. Shang, C.; You, F. Distributionally robust optimization for planning and scheduling under uncertainty. *Comput. Chem. Eng.* **2018**, *110*, 53–68. [[CrossRef](#)]
38. Ahmed, H. Formulation of Two-Stage Stochastic Programming with Fixed Recourse. *Br. Int. Exact Sci. (BloEx) J.* **2019**, *1*, 18–21. [[CrossRef](#)]
39. Ben-Tal, A.; Nemirovski, A. Robust optimization—methodology and applications. *Math. Program.* **2002**, *92*, 453–480. [[CrossRef](#)]
40. Ben-Tal, A.; El Ghaoui, L.; Nemirovski, A. *Robust Optimization*; Princeton University Press: Princeton, NJ, USA, 2009; Volume 28.
41. Bertsimas, D.; Sim, M. The price of robustness. *Oper. Res.* **2004**, *52*, 35–53. [[CrossRef](#)]
42. Ben-Tal, A.; Goryashko, A.; Guslitzer, E.; Nemirovski, A. Adjustable robust solutions of uncertain linear programs. *Math. Program.* **2004**, *99*, 351–376. [[CrossRef](#)]
43. Schöbel, A. Generalized light robustness and the trade-off between robustness and nominal quality. *Math. Methods Oper. Res.* **2014**, *80*, 161–191. [[CrossRef](#)]
44. Kouvelis, P.; Yu, G. *Robust Discrete Optimization and Its Applications*; Springer Science & Business Media: Berlin/Heidelberg, Germany, 2013; Volume 14.
45. Carrizosa, E.; Goerigk, M.; Schöbel, A. A biobjective approach to recoverable robustness based on location planning. *Eur. J. Oper. Res.* **2017**, *261*, 421–435. [[CrossRef](#)]
46. Xiong, P.; Jirutitijaroen, P.; Singh, C. A distributionally robust optimization model for unit commitment considering uncertain wind power generation. *IEEE Trans. Power Syst.* **2017**, *32*, 39–49. [[CrossRef](#)]
47. Esteban-Pérez, A.; Morales, J.M. Partition-based Distributionally Robust Optimization via Optimal Transport with Order Cone Constraints. *arXiv* **2019**, arXiv:1903.01769.
48. Xin, L.; Goldberg, D.A. Time (in) consistency of multistage distributionally robust inventory models with moment constraints. *Eur. J. Oper. Res.* **2021**, *289*, 1127–1141. [[CrossRef](#)]
49. Liu, Q.; Wu, J.; Xiao, X.; Zhang, L. A note on distributionally robust optimization under moment uncertainty. *J. Numer. Math.* **2018**, *26*, 141–150. [[CrossRef](#)]

50. Esfahani, P.M.; Kuhn, D. Data-driven distributionally robust optimization using the Wasserstein metric: Performance guarantees and tractable reformulations. *Math. Program.* **2018**, *171*, 115–166. [[CrossRef](#)]
51. Shafieezadeh-Abadeh, S.; Kuhn, D.; Esfahani, P.M. Regularization via Mass Transportation. *J. Mach. Learn. Res.* **2019**, *20*, 1–68.
52. Namkoong, H.; Duchi, J.C. Stochastic Gradient Methods for Distributionally Robust Optimization with f-divergences. *NIPS* **2016**, *29*, 2208–2216.
53. Bayraksan, G.; Love, D.K. Data-driven stochastic programming using phi-divergences. In *The Operations Research Revolution*; INFORMS: Oslo, Norway, 2015; pp. 1–19. [[CrossRef](#)]
54. Duchi, J.C.; Glynn, P.W.; Namkoong, H. Statistics of robust optimization: A generalized empirical likelihood approach. *Math. Oper. Res.* **2021**, *46*, 835–1234. [[CrossRef](#)]
55. Xie, W. On distributionally robust chance constrained programs with Wasserstein distance. *Math. Program.* **2021**, *186*, 115–155. [[CrossRef](#)]
56. Van Ackooij, W.; Zorghi, R.; Henrion, R.; Möller, A. Chance constrained programming and its applications to energy management. In *Stochastic Optimization-Seeing the Optimal for the Uncertain*; IntechOpen: London, UK, 28 February 2011.
57. Gassmann, H.I.; Schweitzer, E. A comprehensive input format for stochastic linear programs. *Ann. Oper. Res.* **2001**, *104*, 89–125. [[CrossRef](#)]
58. Liu, J.; Rizzoni, G.; Yurkovich, B. Stochastic energy management for microgrids with constraints under uncertainty. In Proceedings of the 2016 IEEE Transportation Electrification Conference and Expo (ITEC), Dearborn, MI, USA, 27–29 June 2016; pp. 1–6.
59. Wu, X.; Hu, X.; Yin, X.; Moura, S.J. Stochastic optimal energy management of smart home with PEV energy storage. *IEEE Trans. Smart Grid* **2016**, *9*, 2065–2075. [[CrossRef](#)]
60. Rostampour, V.; Keviczky, T. Energy management for building climate comfort in uncertain smart thermal grids with aquifer thermal energy storage. *IFAC-PapersOnLine* **2017**, *50*, 13156–13163. [[CrossRef](#)]
61. Nikmehr, N.; Najafi-Ravadanegh, S. Probabilistic optimal power dispatch in multi-microgrids using heuristic algorithms. In Proceedings of the 2014 Smart Grid Conference (SGC), Tehran, Iran, 9–10 December 2014; pp. 1–6.
62. Kopsidas, K.; Kapetanaki, A.; Levi, V. Optimal demand response scheduling with real-time thermal ratings of overhead lines for improved network reliability. *IEEE Trans. Smart Grid* **2016**, *8*, 2813–2825. [[CrossRef](#)]
63. Chen, Z.; Wu, L.; Fu, Y. Real-time price-based demand response management for residential appliances via stochastic optimization and robust optimization. *IEEE Trans. Smart Grid* **2012**, *3*, 1822–1831. [[CrossRef](#)]
64. Nikmehr, N.; Ravadanegh, S.N. Optimal power dispatch of multi-microgrids at future smart distribution grids. *IEEE Trans. Smart Grid* **2015**, *6*, 1648–1657. [[CrossRef](#)]
65. Trpovski, A.; Melo, D.F.R.; Hamacher, T.; Massier, T. Stochastic optimization for distribution grid reconfiguration with high photovoltaic penetration. In Proceedings of the 2017 IEEE International Conference on Smart Energy Grid Engineering (SEGE), Oshawa, ON, Canada, 14–17 August 2017; pp. 67–73.
66. Wang, Q.; Wang, J.; Guan, Y. Stochastic unit commitment with uncertain demand response. *IEEE Trans. Power Syst.* **2012**, *28*, 562–563. [[CrossRef](#)]
67. Blanco, I.; Morales, J.M. An efficient robust solution to the two-stage stochastic unit commitment problem. *IEEE Trans. Power Syst.* **2017**, *32*, 4477–4488. [[CrossRef](#)]
68. Dehghanian, P.; Kezunovic, M. Probabilistic decision making for the bulk power system optimal topology control. *IEEE Trans. Smart Grid* **2016**, *7*, 2071–2081. [[CrossRef](#)]
69. Xu, Y.; Yang, Z.; Gu, W.; Li, M.; Deng, Z. Robust real-time distributed optimal control based energy management in a smart grid. *IEEE Trans. Smart Grid* **2015**, *8*, 1568–1579. [[CrossRef](#)]
70. Giraldo, J.S.; Castrillon, J.A.; López, J.C.; Rider, M.J.; Castro, C.A. Microgrids energy management using robust convex programming. *IEEE Trans. Smart Grid* **2018**, *10*, 4520–4530. [[CrossRef](#)]
71. Hu, W.; Wang, P.; Gooi, H.B. Toward optimal energy management of microgrids via robust two-stage optimization. *IEEE Trans. Smart Grid* **2016**, *9*, 1161–1174. [[CrossRef](#)]
72. Guo, Y.; Zhao, C. Islanding-aware robust energy management for microgrids. *IEEE Trans. Smart Grid* **2016**, *9*, 1301–1309. [[CrossRef](#)]
73. Rezaei, N.; Ahmadi, A.; Khazali, A.H.; Guerrero, J.M. Energy and frequency hierarchical management system using information gap decision theory for islanded microgrids. *IEEE Trans. Ind. Electron.* **2018**, *65*, 7921–7932. [[CrossRef](#)]
74. Ullah, H.; Khan, M.; Hussain, I.; Ullah, I.; Uthansakul, P.; Khan, N. An Optimal Energy Management System for University Campus Using the Hybrid Firefly Lion Algorithm (FLA). *Energies* **2021**, *14*, 6028. [[CrossRef](#)]
75. Wang, Z.; Chen, B.; Wang, J.; Kim, J.; Begovic, M.M. Robust optimization based optimal DG placement in microgrids. *IEEE Trans. Smart Grid* **2014**, *5*, 2173–2182. [[CrossRef](#)]
76. Xiang, Y.; Liu, J.; Liu, Y. Robust energy management of microgrid with uncertain renewable generation and load. *IEEE Trans. Smart Grid* **2015**, *7*, 1034–1043. [[CrossRef](#)]
77. Zhang, Y.; Gatsis, N.; Giannakis, G.B. Robust energy management for microgrids with high-penetration renewables. *IEEE Trans. Sustain. Energy* **2013**, *4*, 944–953. [[CrossRef](#)]
78. Ye, H.; Li, Z. Robust security-constrained unit commitment and dispatch with recourse cost requirement. *IEEE Trans. Power Syst.* **2015**, *31*, 3527–3536. [[CrossRef](#)]

79. Ullah, I.; Hussain, I.; Uthansakul, P.; Riaz, M.; Khan, M.N.; Lloret, J. Exploiting multi-verse optimization and sine-cosine algorithms for energy management in smart cities. *Appl. Sci.* **2020**, *10*, 2095. [[CrossRef](#)]
80. Ullah, I.; Hussain, I.; Singh, M. Exploiting Grasshopper and Cuckoo Search Bio-Inspired Optimization Algorithms for Industrial Energy Management System: Smart Industries. *Electronics* **2020**, *9*, 105. [[CrossRef](#)]
81. Gögler, P.; Dorfner, M.; Hamacher, T. Hybrid Robust/Stochastic Unit Commitment With Iterative Partitions of the Continuous Uncertainty Set. *Front. Energy Res.* **2018**, *6*, 71. [[CrossRef](#)]
82. Zhao, C.; Guan, Y. Unified stochastic and robust unit commitment. *IEEE Trans. Power Syst.* **2013**, *28*, 3353–3361. [[CrossRef](#)]
83. Wang, C.; Liu, F.; Wang, J.; Qiu, F.; Wei, W.; Mei, S.; Lei, S. Robust risk-constrained unit commitment with large-scale wind generation: An adjustable uncertainty set approach. *IEEE Trans. Power Syst.* **2016**, *32*, 723–733. [[CrossRef](#)]
84. Velloso, A.; Street, A.; Pozo, D.; Arroyo, J.M.; Cobos, N.G. Two-Stage Robust Unit Commitment for Co-Optimized Electricity Markets: An Adaptive Data-Driven Approach for Scenario-Based Uncertainty Sets. *IEEE Trans. Sustain. Energy* **2019**, *11*, 958–969. [[CrossRef](#)]
85. Li, Z.; Shahidehpour, M.; Wu, W.; Zeng, B.; Zhang, B.; Zheng, W. Decentralized multiarea robust generation unit and tie-line scheduling under wind power uncertainty. *IEEE Trans. Sustain. Energy* **2015**, *6*, 1377–1388. [[CrossRef](#)]
86. Zhou, H.; Li, Z.; Zheng, J.; Wu, Q.; Zhang, H. Robust Scheduling of Integrated Electricity and Heating System Hedging Heating Network Uncertainties. *IEEE Trans. Smart Grid* **2019**, *11*, 1543–1555. [[CrossRef](#)]
87. Zhao, C.; Wang, J.; Watson, J.P.; Guan, Y. Multi-stage robust unit commitment considering wind and demand response uncertainties. *IEEE Trans. Power Syst.* **2013**, *28*, 2708–2717. [[CrossRef](#)]
88. Zazo, J.; Zazo, S.; Macua, S.V. Robust worst-case analysis of demand-side management in smart grids. *IEEE Trans. Smart Grid* **2016**, *8*, 662–673. [[CrossRef](#)]
89. Du, Y.F.; Jiang, L.; Li, Y.; Wu, Q. A robust optimization approach for demand side scheduling considering uncertainty of manually operated appliances. *IEEE Trans. Smart Grid* **2016**, *9*, 743–755. [[CrossRef](#)]
90. Wang, C.; Zhou, Y.; Wu, J.; Wang, J.; Zhang, Y.; Wang, D. Robust-index method for household load scheduling considering uncertainties of customer behavior. *IEEE Trans. Smart Grid* **2015**, *6*, 1806–1818. [[CrossRef](#)]
91. Melhem, F.Y.; Grunder, O.; Hammoudan, Z.; Moubayed, N. Energy management in electrical smart grid environment using robust optimization algorithm. *IEEE Trans. Ind. Appl.* **2018**, *54*, 2714–2726. [[CrossRef](#)]
92. Bai, X.; Qiao, W. Robust optimization for bidirectional dispatch coordination of large-scale V2G. *IEEE Trans. Smart Grid* **2015**, *6*, 1944–1954. [[CrossRef](#)]
93. Xiao, J.; Xie, J.; Chen, X.; Yu, K.; Chen, Z.; Li, Z. Energy cost reduction robust optimization for meeting scheduling in smart commercial buildings. In Proceedings of the 2017 IEEE Conference on Energy Internet and Energy System Integration (EI2), Beijing, China, 26–28 November 2017; pp. 1–5.
94. Hajebrahimi, A.; Kamwa, I.; Delage, E.; Abdelaziz, M. Adaptive Distributionally Robust Optimization for Electricity and Electrified Transportation Planning. *IEEE Trans. Smart Grid* **2020**, *11*, 4278–4289. [[CrossRef](#)]
95. Lorca, A.; Sun, X.A. Multistage robust unit commitment with dynamic uncertainty sets and energy storage. *IEEE Trans. Power Syst.* **2016**, *32*, 1678–1688. [[CrossRef](#)]
96. Gupta, A.; Anderson, C.L. Statistical bus ranking for flexible robust unit commitment. *IEEE Trans. Power Syst.* **2018**, *34*, 236–245. [[CrossRef](#)]
97. Bertsimas, D.; Litvinov, E.; Sun, X.A.; Zhao, J.; Zheng, T. Adaptive robust optimization for the security constrained unit commitment problem. *IEEE Trans. Power Syst.* **2012**, *28*, 52–63. [[CrossRef](#)]
98. Mahboubi-Moghaddam, E.; Nayeripour, M.; Aghaei, J.; Khodaei, A.; Waffenschmidt, E. Interactive robust model for energy service providers integrating demand response programs in wholesale markets. *IEEE Trans. Smart Grid* **2016**, *9*, 2681–2690. [[CrossRef](#)]
99. Jiang, R.; Wang, J.; Guan, Y. Robust unit commitment with wind power and pumped storage hydro. *IEEE Trans. Power Syst.* **2011**, *27*, 800–810. [[CrossRef](#)]
100. Morales-Espana, G.; Lorca, A.; de Weerd, M.M. Robust unit commitment with dispatchable wind power. *Electr. Power Syst. Res.* **2018**, *155*, 58–66. [[CrossRef](#)]
101. Chen, Y.; Liu, F.; Wei, W.; Mei, S.; Chang, N. Robust unit commitment for large-scale wind generation and run-off-river hydropower. *CSEE J. Power Energy Syst.* **2016**, *2*, 66–75. [[CrossRef](#)]
102. Cho, Y.; Ishizaki, T.; Ramdani, N.; Imura, J.I. Box-based Temporal Decomposition of Multi-period Economic Dispatch for Two-stage Robust Unit Commitment. *IEEE Trans. Power Syst.* **2019**, *34*, 3109–3118. [[CrossRef](#)]
103. Jiang, R.; Wang, J.; Zhang, M.; Guan, Y. Two-stage minimax regret robust unit commitment. *IEEE Trans. Power Syst.* **2013**, *28*, 2271–2282. [[CrossRef](#)]
104. Lee, C.; Liu, C.; Mehrotra, S.; Shahidehpour, M. Modeling transmission line constraints in two-stage robust unit commitment problem. *IEEE Trans. Power Syst.* **2013**, *29*, 1221–1231. [[CrossRef](#)]
105. Carroll, P. Exploring Smart Grid Time-of-Use Tariffs using a Robust Optimisation Framework. In Proceedings of the 2020 International Joint Conference on Neural Networks (IJCNN), Glasgow, UK, 19–24 July 2020; pp. 1–6.
106. Shi, Z.; Liang, H.; Huang, S.; Dinavahi, V. Distributionally robust chance-constrained energy management for islanded microgrids. *IEEE Trans. Smart Grid* **2018**, *10*, 2234–2244. [[CrossRef](#)]

107. Sasaki, Y.; Yorino, N.; Zoka, Y.; Wahyudi, F.I. Robust stochastic dynamic load dispatch against uncertainties. *IEEE Trans. Smart Grid* **2017**, *9*, 5535–5542. [[CrossRef](#)]
108. Prabakaran, S.; Ramar, R.; Hussain, I.; Kavin, B.P.; Alshamrani, S.S.; AlGhamdi, A.S.; Alshehri, A. Predicting Attack Pattern via Machine Learning by Exploiting Stateful Firewall as Virtual Network Function in an SDN Network. *Sensors* **2022**, *22*, 709. [[CrossRef](#)]
109. Chen, Y.; Guo, Q.; Sun, H.; Li, Z.; Wu, W.; Li, Z. A distributionally robust optimization model for unit commitment based on Kullback–Leibler divergence. *IEEE Trans. Power Syst.* **2018**, *33*, 5147–5160. [[CrossRef](#)]
110. Zhao, C.; Jiang, R. Distributionally robust contingency-constrained unit commitment. *IEEE Trans. Power Syst.* **2017**, *33*, 94–102. [[CrossRef](#)]
111. Valencia, F.; Collado, J.; Sáez, D.; Marín, L.G. Robust energy management system for a microgrid based on a fuzzy prediction interval model. *IEEE Trans. Smart Grid* **2015**, *7*, 1486–1494. [[CrossRef](#)]
112. Wei, W.; Liu, F.; Mei, S. Distributionally robust co-optimization of energy and reserve dispatch. *IEEE Trans. Sustain. Energy* **2015**, *7*, 289–300. [[CrossRef](#)]
113. Zhang, H.; Hu, Z.; Munsing, E.; Moura, S.J.; Song, Y. Data-driven chance-constrained regulation capacity offering for distributed energy resources. *IEEE Trans. Smart Grid* **2018**, *10*, 2713–2725. [[CrossRef](#)]
114. Jabr, R.A. Distributionally robust CVaR constraints for power flow optimization. *IEEE Trans. Power Syst.* **2020**, *35*, 3764–3773. [[CrossRef](#)]
115. Liu, J.; Chen, H.; Zhang, W.; Yurkovich, B.; Rizzoni, G. Energy management problems under uncertainties for grid-connected microgrids: A chance constrained programming approach. *IEEE Trans. Smart Grid* **2016**, *8*, 2585–2596. [[CrossRef](#)]
116. Zachar, M.; Daoutidis, P. Microgrid/microgrid energy exchange: A novel market structure and stochastic scheduling. *IEEE Trans. Smart Grid* **2016**, *8*, 178–189. [[CrossRef](#)]
117. Cao, X.; Wang, J.; Zeng, B. Networked Microgrids Planning Through Chance Constrained Stochastic Conic Programming. *IEEE Trans. Smart Grid* **2019**, *10*, 6619–6628. [[CrossRef](#)]
118. Yang, Z.; Wu, R.; Yang, J.; Long, K.; You, P. Economical operation of microgrid with various devices via distributed optimization. *IEEE Trans. Smart Grid* **2015**, *7*, 857–867. [[CrossRef](#)]
119. Akhavan-Hejazi, H.; Mohsenian-Rad, H. Energy storage planning in active distribution grids: A chance-constrained optimization with non-parametric probability functions. *IEEE Trans. Smart Grid* **2016**, *9*, 1972–1985.
120. Cai, Y.; Huang, G.; Yang, Z.; Lin, Q.; Tan, Q. Community-scale renewable energy systems planning under uncertainty. An interval chance-constrained programming approach. *Renew. Sustain. Energy Rev.* **2009**, *13*, 721–735. [[CrossRef](#)]
121. Ayyagari, K.S.; Gatsis, N.; Taha, A.F. Chance constrained optimization of distributed energy resources via affine policies. In Proceedings of the 2017 IEEE Global Conference on Signal and Information Processing (GlobalSIP), Montreal, QC, Canada, 14–16 November 2017; pp. 1050–1054.
122. Hussain, I.; Khan, F.; Ahmad, I.; Khan, S.; Saeed, M. Power loss reduction via distributed generation system injected in a radial feeder. *Mehran Univ. Res. J. Eng. Technol.* **2021**, *40*, 160–168. [[CrossRef](#)]
123. Zhao, C.; Wang, Q.; Wang, J.; Guan, Y. Expected value and chance constrained stochastic unit commitment ensuring wind power utilization. *IEEE Trans. Power Syst.* **2014**, *29*, 2696–2705. [[CrossRef](#)]
124. Cao, X.; Wang, J.; Zeng, B. Distributed Generation Planning Guidance Through Feasibility and Profit Analysis. *IEEE Trans. Smart Grid* **2018**, *9*, 5473–5475. [[CrossRef](#)]
125. Dorini, G.; Pinson, P.; Madsen, H. Chance-constrained optimization of demand response to price signals. *IEEE Trans. Smart Grid* **2013**, *4*, 2072–2080. [[CrossRef](#)]
126. Niu, W.; Li, Y. Uncertain optimization decision of interruptible load in demand response program. In Proceedings of the 2014 IEEE Innovative Smart Grid Technologies-Asia (ISGT ASIA), Kuala Lumpur, Malaysia, 20–23 May 2014; pp. 675–679.
127. Baker, K.; Bernstein, A. Joint Chance Constraints in AC Optimal Power Flow: Improving Bounds through Learning. *IEEE Trans. Smart Grid* **2019**, *10*, 6376–6385. [[CrossRef](#)]
128. Arasteh, H.; Vahidinasab, V.; Sepasian, M.S.; Aghaei, J. Stochastic System of Systems Architecture for Adaptive Expansion of Smart Distribution Grids. *IEEE Trans. Ind. Inform.* **2018**, *15*, 377–389. [[CrossRef](#)]
129. Huang, Y.; Wang, L.; Guo, W.; Kang, Q.; Wu, Q. Chance constrained optimization in a home energy management system. *IEEE Trans. Smart Grid* **2016**, *9*, 252–260. [[CrossRef](#)]
130. Wang, Q.; Guan, Y.; Wang, J. A chance-constrained two-stage stochastic program for unit commitment with uncertain wind power output. *IEEE Trans. Power Syst.* **2011**, *27*, 206–215. [[CrossRef](#)]
131. Li, B.; Vrakopoulou, M.; Mathieu, J.L. Chance constrained reserve scheduling using uncertain controllable loads Part II: Analytical reformulation. *IEEE Trans. Smart Grid* **2017**, *10*, 1618–1625. [[CrossRef](#)]
132. Vrakopoulou, M.; Li, B.; Mathieu, J.L. Chance constrained reserve scheduling using uncertain controllable loads Part I: Formulation and scenario-based analysis. *IEEE Trans. Smart Grid* **2017**, *10*, 1608–1617. [[CrossRef](#)]
133. Peralta, J.; Pérez-Ruiz, J.; De la Torre, S. Unit commitment with load uncertainty by joint chance-constrained programming. In Proceedings of the 2013 IEEE Grenoble Conference, Grenoble, France, 16–20 June 2013; pp. 1–6.
134. Zhang, Y.; Wang, J.; Zeng, B.; Hu, Z. Chance-constrained two-stage unit commitment under uncertain load and wind power output using bilinear benders decomposition. *IEEE Trans. Power Syst.* **2017**, *32*, 3637–3647. [[CrossRef](#)]

135. Sundar, K.; Nagarajan, H.; Roald, L.; Misra, S.; Bent, R.; Bienstock, D. Chance-Constrained Unit Commitment with N-1 Security and Wind Uncertainty. *IEEE Trans. Control. Netw. Syst.* **2019**, *6*, 1062–1074. [[CrossRef](#)]
136. Li, Z.; Jin, T.; Zhao, S.; Liu, J. Power system day-ahead unit commitment based on chance-constrained dependent chance goal programming. *Energies* **2018**, *11*, 1718. [[CrossRef](#)]
137. Chen, D.; Hou, S.; Gong, N.; Zhang, W.; Li, H. A Chance-Constrained Two-Stage Stochastic UC Considering Uncertain Renewable Energy Output Furthermore, Demand Response. In Proceedings of the 2018 IEEE Innovative Smart Grid Technologies-Asia (ISGT Asia), Singapore, 22–25 May 2018; pp. 419–424.
138. Wang, Z.; Shen, C.; Liu, F.; Wu, X.; Liu, C.C.; Gao, F. Chance-constrained economic dispatch with non-Gaussian correlated wind power uncertainty. *IEEE Trans. Power Syst.* **2017**, *32*, 4880–4893. [[CrossRef](#)]
139. Hassan, A.; Mieth, R.; Chertkov, M.; Deka, D.; Dvorkin, Y. Optimal load ensemble control in chance-constrained optimal power flow. *IEEE Trans. Smart Grid* **2018**, *10*, 5186–5195. [[CrossRef](#)]
140. Li, B.; Wang, X.; Shahidepour, M.; Jiang, C.; Li, Z. DER Aggregators Data-Driven Bidding Strategy Using the Information Gap Decision Theory in a Non-Cooperative Electricity Market. *IEEE Trans. Smart Grid* **2019**, *10*, 6756–6767. [[CrossRef](#)]
141. Li, R.; Wu, Q.; Oren, S.S. Distribution locational marginal pricing for optimal electric vehicle charging management. *IEEE Trans. Power Syst.* **2013**, *29*, 203–211. [[CrossRef](#)]
142. Zare, M.; Niknam, T.; Azizpanah-Abarghoee, R.; Ostadi, A. New stochastic bi-objective optimal cost and chance of operation management approach for smart microgrid. *IEEE Trans. Ind. Inform.* **2016**, *12*, 2031–2040. [[CrossRef](#)]
143. Daneshvar, M.; Ivatloo, B.M.; Abapour, M.; Asadi, S.; Khanjani, R. Distributionally Robust Chance Constrained Transactive Energy Framework for Coupled Electrical and Gas Microgrids. *IEEE Trans. Ind. Electron.* **2020**, *68*, 347–357. [[CrossRef](#)]
144. Pozo, D.; Contreras, J. A chance-constrained unit commitment with an nK security criterion and significant wind generation. *IEEE Trans. Power Syst.* **2012**, *28*, 2842–2851. [[CrossRef](#)]
145. Wang, B.; Dehghanian, P.; Zhao, D. Chance-constrained energy management system for power grids with high proliferation of renewables and electric vehicles. *IEEE Trans. Smart Grid* **2019**, *11*, 2324–2336. [[CrossRef](#)]
146. Tang, K.; Dong, S.; Ma, X.; Lv, L.; Song, Y. Chance-Constrained Optimal Power Flow of Integrated Transmission and Distribution Networks with Limited Information Interaction. *IEEE Trans. Smart Grid* **2020**, *12*, 821–833. [[CrossRef](#)]
147. Yang, L.; Xu, Y.; Gu, W.; Sun, H. Distributionally Robust Chance-constrained Optimal Power-Gas Flow under Bidirectional Interactions Considering Uncertain Wind Power. *IEEE Trans. Smart Grid* **2020**, *12*, 1722–1735. [[CrossRef](#)]
148. Soltani, N.Y.; Nasiri, A. Chance-constrained Optimization of Energy Storage Capacity for Microgrids. *IEEE Trans. Smart Grid* **2020**, *11*, 2760–2770. [[CrossRef](#)]
149. Guo, Z.; Pinson, P.; Chen, S.; Yang, Q.; Yang, Z. Chance-Constrained Peer-to-Peer Joint Energy and Reserve Market Considering Renewable Generation Uncertainty. *IEEE Trans. Smart Grid* **2020**, *12*, 798–809. [[CrossRef](#)]
150. Ahmad, S.; Naeem, M.; Ahmad, A. Low complexity approach for energy management in residential buildings. *Int. Trans. Electr. Energy Syst.* **2019**, *29*, e2680. [[CrossRef](#)]
151. Ahmad, S.; Naeem, M.; Ahmad, A. Unified optimization model for energy management in sustainable smart power systems. *Int. Trans. Electr. Energy Syst.* **2020**, *30*, 1–19. [[CrossRef](#)]
152. Ahmad, S.; Alhaisoni, M.M.; Naeem, M.; Ahmad, A.; Altaf, M. Joint energy management and energy trading in residential microgrid system. *IEEE Access* **2020**, *8*, 123334–123346. [[CrossRef](#)]
153. Zaman, S.; Khan, L.U.; Hussain, I.; Mihet-Popa, L. Fast Computation of Highly Oscillatory ODE Problems: Applications in High-Frequency Communication Circuits. *Symmetry* **2022**, *14*, 115. [[CrossRef](#)]
154. Zaman, S.; Hussain, I.; Singh, D. Fast Computation of Integrals with Fourier-Type Oscillator Involving Stationary Point. *Mathematics* **2019**, *7*, 1160. [[CrossRef](#)]

Article

Generalized Control of the Power Flow in Local Area Energy Networks

Paolo Tenti¹ and Tommaso Caldognetto^{2,*}

¹ Department of Information Engineering, University of Padova, 35131 Padova, Italy; paolo.tenti@unipd.it

² Department of Management and Engineering, University of Padova, 36100 Vicenza, Italy

* Correspondence: tommaso.caldognetto@unipd.it

Abstract: Local area energy networks (E-LANs) are cyber-physical systems whose physical layer is a meshed low-voltage microgrid fed by a multiplicity of sources, i.e., utilities, energy storage systems, and distributed power sources. The cyber layer includes distributed measurement, control, and communication units, located at end-user premises, as well as centralized supervision and dispatchment control. As compared with standard microgrid, the E-LAN encompasses the ability for end-users to actively contribute to the operation of the microgrid while acting as independent energy traders in the electrical market. Operational goals include active contribution of end-users to power sharing, loss reduction, voltage stability, demand response, fault identification and clearing, isolation of sub-grids for maintenance, islanding, and black start. Economic goals include the possibility, for each end-user, to decide in every moment, based on convenience, how his energy and power capacity is shared with other users, e.g., for demand response or to trade energy in the electric market. This paper introduces a comprehensive theoretical approach of E-LAN control to achieve all the above operational goals while providing a high level of dynamic protection against faults or other events affecting the system functionality, e.g., overloads or fast transients. It shows that meshed microgrids are the necessary infrastructure to implement the desired functionalities.

Keywords: control of distributed energy resources; power flow control; microgrids; distributed electronic power converters; demand response

Citation: Tenti, P.; Caldognetto, T. Generalized Control of the Power Flow in Local Area Energy Networks. *Energies* **2022**, *15*, 1416. <https://doi.org/10.3390/en15041416>

Academic Editor: Juri Belikov

Received: 30 December 2021

Accepted: 10 February 2022

Published: 15 February 2022

Publisher's Note: MDPI stays neutral with regard to jurisdictional claims in published maps and institutional affiliations.



Copyright: © 2022 by the authors. Licensee MDPI, Basel, Switzerland. This article is an open access article distributed under the terms and conditions of the Creative Commons Attribution (CC BY) license (<https://creativecommons.org/licenses/by/4.0/>).

1. Introduction

The future of electric systems is characterized by the increasing participation of end-users to fill the gap between energy demand and supply while ensuring the flexibility needed to face and to exploit the increasing complexity, decentralization, and interconnection of power systems. While in the first phase of the green energy transition the end-users acted as distributed investors and renewable energy suppliers, in future they will gain a role as market players, either individually or in aggregated form [1,2]. This was explicitly envisioned by the European Union within the 2019 directive “Clean Energy for All Europeans” that states “Consumers are the drivers of the energy transition” and “Consumers and communities will be empowered to actively participate in the electricity market” [3].

A first step in this direction is represented by virtual power plants (VPPs) [4] that are cloud-based distributed power plants that aggregate the capacities of heterogeneous distributed energy resources for the purposes of enhancing power generation, as well as trading or selling power on the electricity market.

With this approach, end-users virtually commit their energy resources to an aggregator that gathers consumers for the purpose of negotiating the rate for generation service from electric system operators. In this way, the participation of end-users to the electric market is indirect. Moreover, since there is no physical interaction among virtually connected users, their resources cannot be exploited to improve the performance and extend the functionality of electrical systems.

Today, the aggregation of users within virtual power plants (VPPs) is already a reality in several instances [5,6], and helps improving the flexibility of the electric system in the low-end section.

A completely different approach relies on local area energy networks (E-LANs) that aggregate the users within a microgrid and coordinate their operation to improve the electric performances, extend the grid functionalities, and allow participation of end-users to the electric market either individually or within energy communities [7].

In principle, each user may decide, time by time, which part of his capacity (stored energy, active and reactive power) can be shared with the rest of the E-LAN to improve local performance (e.g., voltage stabilization, loss reduction, power sharing, stress reduction) or to meet system-level requirements (e.g., demand response, power factor at the point of common coupling with utility, transition from on-grid to off-grid operation, fault clearing, etc.). The remaining capacity can be used for private needs, e.g., smoothing of domestic power absorption or trading energy in the market [2,8].

The E-LAN controller manages the available resources to pursue the needed functionalities, properly prioritized, with a best-fit approach. Obviously, the envisioned flexibility of operation calls for energy storage capacity, either distributed or clustered.

From the above considerations it follows that, unlike traditional microgrids, E-LANs represent a special type of cyber-physical systems where the physical layer (the microgrid) is thoroughly interconnected with the cyber layer [9]. Energy and data processing proceed indissolubly, and the implementation of the above functionalities require, on one side, fast and precise control of the power flow in each section of the microgrid and, on the other side, fast and precise implementation of the control algorithms, either distributed or centralized.

The fundamental asset of E-LANs is the capacity to implement the power steering, i.e., to exploit every available control agent to drive the power flow in every section of the microgrid. This requires meshed architectures and a suitable number of controlling entities distributed within the microgrid.

In the following, we will approach the problem at large, discussing the properties of meshed grids at first, then deriving the input–output equations valid for any type of grid structure and distribution of power sources, and finally proposing an optimum control approach that ensures all needed functionalities while allowing dynamic tuning of users' behavior and parameters.

2. Meshed Grids: Motivation and Basic Equations

2.1. Motivation

Traditionally, electric plants use radial structure, where any pair of nodes are linked by a single path. This results in simple design, because the current stress in each feeder can easily be predicted in every operating condition. Moreover, selective protection against faults is effectively achieved by operating the upstream protection devices (e.g., circuit breakers or fuses). Figure 1 shows the evolution of a distribution network, from the purely unidirectional radial structure (Figure 1a) fed via the connection to an upstream—typically medium voltage—distribution grid, to a situation where the radial grid is permeated by distributed generators (DGs) enabling bidirectional power flow (Figure 1b), to the most advanced solution that makes use of meshed grids (Figure 1c) to improve the flexibility of power flow control and the robustness of the electrical service. In practice, adopting a radial structure for the microgrid makes it impossible to drive the power through different paths, thus making the power steering unfeasible.

Meshed grids, instead, in presence of a suitable number of control agents (i.e., power electronics converters [10,11]), allow both power steering and autonomous participation of end-users to the electric market [12]. In this context, control agents correspond to energy sources equipped with grid-tied inverters able to control the active and reactive power exchange with the grid.

Synergistic operation of control agents enables the following functionalities:

- Control of the power flow throughout the microgrid (power steering).

- Consensus-based exploitation of any available energy sources (power sharing, smart energy storage).
- Mitigation of useless circulation of active and reactive currents.
- Stabilization of voltage profiles
- Compensation of load unbalance.
- Electronic fault clearing.
- Demand response.
- Off-grid operation.
- Autonomous energy trading by end-users who can decide, time by time, which portion of their resources is shared with the energy community.

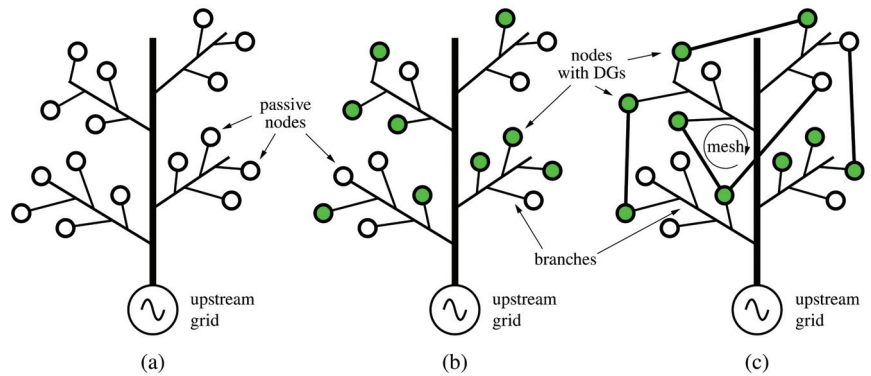


Figure 1. Different kinds of distribution networks. (a) Radial with passive nodes; (b) radial with distributed generators (DGs); (c) meshed with DGs.

Modern electricity scenarios foresee the possibility of trading the above operational functionalities as services for the upstream grid and therefore achieve economic benefits. In order to manage the system complexity and ensure a modular organization of E-LAN control, this typically involves the integration of economic and market layers in control hierarchy [2,13].

2.2. Basic Equations

The basic equations relating the voltages and currents in a microgrid are those determined by Kirchhoff’s principles [14], which are reported below to define the nomenclature used herein.

Let \mathbf{A} be the incidence matrix describing the graph of the microgrid. \mathbf{A} is an integer matrix with K rows (K being the number of grid branches, i.e., lines connecting pairs of nodes) and N columns (N being the number of all grid nodes but node 0 associated to voltage reference V_0). The generic element a_{kn} of matrix \mathbf{A} is -1 if branch k begins in node n , $+1$ if branch k ends in node n , 0 otherwise. Connections to reference node 0 are neglected.

In the following, to determine voltage relations that do not depend on the selected reference V_0 , we will refer to node voltage deviations \mathbf{u} in place of node voltages \mathbf{v} (for generic node n , voltage deviation is: $\mathbf{u}_n = \mathbf{v}_n - V_0$).

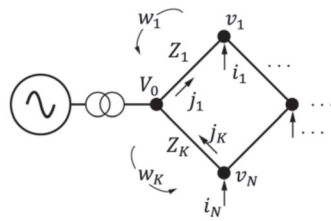
Based on matrix \mathbf{A} definition, the relation among node voltage deviations \mathbf{u} and branch voltages \mathbf{w} obeys the Kirchhoff’s law for voltages (KLV) and is expressed by

$$\mathbf{w} = \mathbf{A} \mathbf{u}, \tag{1a}$$

Similarly, the relation among branch currents \mathbf{j} and node currents \mathbf{i} (i.e., the currents entering network nodes) obeys the Kirchhoff law for currents (KLC) and is expressed by:

$$\mathbf{i} = \mathbf{A}^T \mathbf{j}, \tag{1b}$$

where superscript T means matrix transpose. The meaning of the used nomenclature is sketched in Figure 2, which refers to the nodes and links of a single mesh.



Explanation of nomenclature:

$u_n = v_n - V_0$: voltage deviation at node n

i_n : current entering network at node n

w_n voltage across branch n

j_n : current flowing in branch n

Z_n : impedance of branch n

Figure 2. Nomenclature for the nodes and branches of a single mesh.

The considerations reported hereafter hold both for DC and AC grids. In the latter case, we refer to sinusoidal operation where currents and voltages are represented by phasors in the complex domain. For the sake of simplicity, we will only treat the case of AC grids. In the case of DC grids, the complex variables and matrices will be substituted by real quantities.

In radial grids, matrix \mathbf{A} is invertible, thus the inverse of Equation (1) is easily obtained. Instead, in meshed grids the actual distribution of currents among the grid branches depends on their impedances; similarly, for the relation between branch voltages and node voltages. Letting \mathbf{Z} be the diagonal matrix of branch impedances, expressed as complex numbers, the relation among branch voltages \mathbf{w} and branch currents \mathbf{j} is

$$\mathbf{w} = \mathbf{Z} \mathbf{j} \Leftrightarrow \mathbf{j} = \mathbf{Z}^{-1} \mathbf{w}, \tag{2}$$

The relation among node currents \mathbf{i} and node voltage deviations \mathbf{u} , is:

$$\mathbf{i} = \mathbf{Y} \mathbf{u} \Leftrightarrow \mathbf{u} = \mathbf{Y}^{-1} \mathbf{i}, \tag{3a}$$

where \mathbf{Y} is the nodal admittance matrix, given by

$$\mathbf{Y} = \mathbf{A}^T \mathbf{Z}^{-1} \mathbf{A} \tag{3b}$$

Let us define the pseudo-inverse \mathbf{B} of matrix \mathbf{A} as

$$\mathbf{B} = \mathbf{Y}^{-1} \mathbf{A}^T \mathbf{Z}^{-1} \implies \mathbf{B} \mathbf{A} = \text{identity}, \tag{4}$$

We can now introduce the inverse of relations (1) as

$$\mathbf{u} = \mathbf{B} \mathbf{w}, \tag{5a}$$

$$\mathbf{j} = \mathbf{B}^T \mathbf{i}, \tag{5b}$$

The above set of complex equations allows a complete analysis of the microgrid operation for any given set of voltages and currents fed at the network nodes by the loads and sources connected therein.

3. Low-Voltage E-LAN: Structure and Input/Output Equations

The concept scheme of a low-voltage E-LAN is shown in Figure 3.

The E-LAN includes a LV distribution network with K branches, each one characterized by its length and impedance, and N nodes, where loads and sources are connected. The equations of the distribution network are those derived in the previous section.

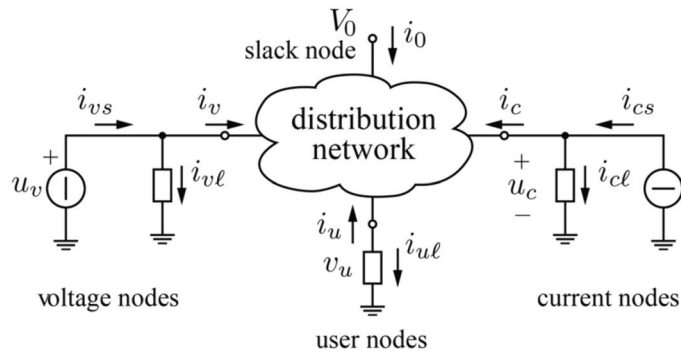


Figure 3. Concept scheme of E-LAN.

3.1. Node Classification

As shown in Figure 3, the nodes are classified in three groups:

- *Voltage nodes*, fed by voltage sources that can be uncontrollable (e.g., the secondary-side voltages of step-down transformers fed by the medium-voltage distribution system) or controllable (e.g., the voltages fed by voltage-driven converters interfacing energy sources with the distribution network). The voltage reference node normally corresponds to the point of common coupling (PCC) with the utility, where the network is fed by a nearly constant voltage V_0 which sets the amplitude and phase reference for any other grid voltages. This node is also called slack node, for its property to fill the gap between the power absorbed by the loads and that generated by the sources. In case of multiple PCCs, the most powerful node can be chosen as the voltage reference. Controllable voltage nodes may be used as voltage-forming units in case of off-grid operation and voltage-tracking units in case of on-grid operation. They are often interfacing the grid with the energy storage systems located in the proximity of the PCCs called utility interfaces (UIs).
- *Current nodes*, fed by current sources, namely, power sources tied to the distribution network by current-controlled converters. This definition generally applies to distributed renewable sources that, usually, operate as current sources that do not directly alter the voltage at their point of connection, to prevent instabilities in the distribution network.
- *Load nodes*, feeding purely passive loads.

Both voltage nodes and currents nodes can tie to passive loads in addition to the sources.

In the following, the analysis will be carried out with reference to a single-phase low-voltage microgrid, although it was developed for the general case of three-phase four-wire networks. In practice, as will be shown in the simulation section, actual loads and sources can be either single-phase or three-phase, their connection to the grid being phase-to-neutral, phase-to-phase, three-phase three-wires, or three-phase four-wires. The types of connection will be considered in the optimization procedure by introducing a suitable set of constraints on the amplitude and phase of the load and source currents.

3.2. Simplifying Assumptions

To simplify the analysis of low-voltage E-LANs, we observe that they extend over limited areas, with a number of users that cannot exceed few tens to comply with the power ratings of low-voltage distribution transformers. Considering the nearly resistive impedance of the LV distribution cables, we may assume that all voltages at grid nodes are nearly in phase with the reference voltage, their deviation being a few percent of the reference value.

Therefore, if we consider that all voltage phasors lie on the real axis, we may assume that the real components of the node currents correspond to active currents, while the imaginary components correspond to reactive currents.

Moreover, since node voltages are very close to the reference value, we may represent constant-power loads as constant-current loads.

The above assumptions introduce some inaccuracy, of course, but linearize the analysis of E-LAN operation, making it possible to find an explicit solution for the control problem. In fact, the nonlinear power-flow approach can be replaced by a linear current-flow approach that allows much easier analysis and reduced computational effort.

3.3. Node Selection

Let \mathbf{u} and \mathbf{i} be, respectively, the voltage deviations at the grid nodes and the corresponding currents entering the grid. We may express the electrical quantities at the voltage nodes as

$$\mathbf{u}_v = \mathbf{K}_v \mathbf{u}, \mathbf{i}_v = \mathbf{K}_v \mathbf{i}, \tag{6a}$$

where \mathbf{K}_v is the voltage node selector, i.e., an $N_v \times N$ integer matrix (with coefficients 0 or 1) that selects the N_v elements of vectors \mathbf{u} and \mathbf{i} corresponding to the node voltages. Similarly, for the N_c current nodes and the N_\downarrow load nodes, we can write

$$\mathbf{u}_c = \mathbf{K}_c \mathbf{u}, \mathbf{i}_c = \mathbf{K}_c \mathbf{i}, \tag{6b}$$

$$\mathbf{u}_\downarrow = \mathbf{K}_\downarrow \mathbf{u}, \mathbf{i}_\downarrow = \mathbf{K}_\downarrow \mathbf{i}, \tag{6c}$$

Given the voltages and the currents at the various types of nodes, the total node voltages and currents can be reconstructed by the reverse equations:

$$\mathbf{u} = \mathbf{K}_v^T \mathbf{u}_v + \mathbf{K}_c^T \mathbf{u}_c + \mathbf{K}_\downarrow^T \mathbf{u}_\downarrow, \mathbf{i} = \mathbf{K}_v^T \mathbf{i}_v + \mathbf{K}_c^T \mathbf{i}_c + \mathbf{K}_\downarrow^T \mathbf{i}_\downarrow, \tag{7}$$

The current terms in (6) are conventionally entering the grid. In practice, voltage and current sources can also feed loads connected to the same nodes; thus, the total currents fed by the sources are

$$\mathbf{i}_{vs} = \mathbf{i}_v + \mathbf{i}_{v\downarrow}, \mathbf{i}_{cs} = \mathbf{i}_c + \mathbf{i}_{c\downarrow}, \tag{8}$$

3.4. Input–Output Equations

From the above considerations, it turns out that the input variables, determining the operation of the distribution network, are voltages \mathbf{u}_v impressed at voltage nodes, currents \mathbf{i}_c impressed at current nodes, and load currents \mathbf{i}_\downarrow . The output variables are currents \mathbf{i}_v entering the grid at voltage nodes, voltages \mathbf{u}_c at current nodes, and voltages \mathbf{u}_\downarrow at load nodes. We define, for convenience, user currents \mathbf{i}_s and user voltages \mathbf{u}_s as

$$\mathbf{u}_s = \begin{vmatrix} \mathbf{u}_c \\ \mathbf{u}_\downarrow \end{vmatrix}, \mathbf{i}_s = \begin{vmatrix} \mathbf{i}_c \\ -\mathbf{i}_\downarrow \end{vmatrix}, \tag{9a}$$

Letting \mathbf{K}_s be the corresponding node selector, the input–output equations can therefore be expressed as

$$\begin{vmatrix} \mathbf{i}_v \\ \mathbf{u}_s \end{vmatrix} = \mathbf{H} \begin{vmatrix} \mathbf{u}_v \\ \mathbf{i}_s \end{vmatrix} = \begin{vmatrix} \mathbf{H}_{vv} & \mathbf{H}_{vs} \\ \mathbf{H}_{sv} & \mathbf{H}_{ss} \end{vmatrix} \begin{vmatrix} \mathbf{u}_v \\ \mathbf{i}_s \end{vmatrix}, \tag{9b}$$

where hybrid matrix \mathbf{H} is the input–output transfer matrix. It can be evaluated starting from the partitioned form of Equation (3a):

$$\begin{vmatrix} \mathbf{i}_v \\ \mathbf{i}_s \end{vmatrix} = \begin{vmatrix} \mathbf{Y}_{vv} & \mathbf{Y}_{vs} \\ \mathbf{Y}_{sv} & \mathbf{Y}_{ss} \end{vmatrix} \begin{vmatrix} \mathbf{u}_v \\ \mathbf{u}_s \end{vmatrix}, \left\{ \begin{array}{l} \mathbf{Y}_{vv} = \mathbf{K}_v \mathbf{Y} \mathbf{K}_v^T \\ \mathbf{Y}_{vs} = \mathbf{K}_v \mathbf{Y} \mathbf{K}_s^T \\ \mathbf{Y}_{sv} = \mathbf{K}_s \mathbf{Y} \mathbf{K}_v^T \\ \mathbf{Y}_{ss} = \mathbf{K}_s \mathbf{Y} \mathbf{K}_s^T \end{array} \right\}, \tag{9c}$$

In (9c) it is interesting to note that if one or more nodes change their operating mode, matrix \mathbf{Y} remains the same, while selection matrices \mathbf{K} change.

Now, combining (9b) and (9c), we easily derive the expression of matrix \mathbf{H} as

$$\mathbf{H} = \begin{bmatrix} \mathbf{H}_{vv} & \mathbf{H}_{vs} \\ \mathbf{H}_{sv} & \mathbf{H}_{ss} \end{bmatrix}, \left\{ \begin{array}{l} \mathbf{H}_{vv} = \mathbf{Y}_{vv} - \mathbf{Y}_{vs} \mathbf{Y}_{ss}^{-1} \mathbf{Y}_{sv} \quad \mathbf{H}_{vs} = \mathbf{Y}_{vs} \mathbf{Y}_{ss}^{-1} \\ \mathbf{H}_{sv} = -\mathbf{Y}_{ss}^{-1} \mathbf{Y}_{sv} \quad \mathbf{H}_{ss} = \mathbf{Y}_{ss}^{-1} \end{array} \right\}, \quad (9d)$$

Observe that the computation of all submatrices of \mathbf{H} requires only one matrix inversion (\mathbf{Y}_{ss}^{-1}).

4. Control Variables

As mentioned before, the input variables determining network operation are voltages \mathbf{u}_v impressed at voltage nodes, and currents \mathbf{i}_s impressed at user nodes. Generally, these variables are not fully controllable. Thus, we can split the input variables in noncontrollable terms (superscript $\bar{}$) and controllable terms (superscript $\tilde{}$):

$$\mathbf{u}_v = \bar{\mathbf{u}}_v + \tilde{\mathbf{u}}_v, \quad (10a)$$

$$\mathbf{i}_s = \bar{\mathbf{i}}_s + \tilde{\mathbf{i}}_s \quad (10b)$$

In practice, controllable terms may occur only for a limited set of input variables. Let \mathbf{K}_d be the selector of those voltages, among $\tilde{\mathbf{u}}_v$, whose phasor can be controlled on the real (direct) axis, and \mathbf{K}_q the selector of those voltages that can be controlled on the imaginary (quadrature) axis. Let \mathbf{u}_d be the controllable voltage terms along the direct axis, and \mathbf{u}_q the controllable voltage terms along the quadrature axis; similarly to (7), we may express voltages $\tilde{\mathbf{u}}_v$ as

$$\tilde{\mathbf{u}}_v = \mathbf{K}_d^T \mathbf{u}_d + \mathbf{K}_q^T \mathbf{u}_q \Rightarrow \mathbf{u}_v = \bar{\mathbf{u}}_v + \mathbf{K}_d^T \mathbf{u}_d + \mathbf{K}_q^T \mathbf{u}_q, \quad (11a)$$

Similarly, we define \mathbf{K}_a as the selector, among $\tilde{\mathbf{i}}_s$, of current terms \mathbf{i}_a that can be controlled on the real axis (active currents, corresponding to the active power entering the grid at the corresponding nodes), and \mathbf{K}_r as the selector of terms \mathbf{i}_r that can be controlled on the imaginary axis (reactive currents, corresponding to the reactive power). We may therefore express currents $\tilde{\mathbf{i}}_s$ as

$$\tilde{\mathbf{i}}_s = \mathbf{K}_a^T \mathbf{i}_a + \mathbf{K}_r^T \mathbf{i}_r \Rightarrow \mathbf{i}_s = \bar{\mathbf{i}}_s + \mathbf{K}_a^T \mathbf{i}_a + \mathbf{K}_r^T \mathbf{i}_r, \quad (11b)$$

Accordingly, the input variables for E-LAN control become real quantities $\mathbf{u}_d, \mathbf{u}_q, \mathbf{i}_a, \mathbf{i}_r$. Let \mathbf{x} be the real vector of control inputs:

$$\mathbf{x} = \begin{bmatrix} \mathbf{u}_d \\ \mathbf{u}_q \\ \mathbf{i}_a \\ \mathbf{i}_r \end{bmatrix}, \quad (11c)$$

By means of Equations (9) and (11) we can express all node voltages and currents in the form

$$\mathbf{u} = \mathbf{u}^0 + \mathbf{F}_u \mathbf{x}, \mathbf{i} = \mathbf{i}^0 + \mathbf{F}_i \mathbf{x}, \quad (12a)$$

While \mathbf{x} is a real vector, the other variables represent phasors in the complex plane. Constant matrices \mathbf{F} are complex and depend on grid structure and node types. Quantities with superscript 0 refer to the situation when all control inputs vanish (zero state).

Similarly, considering Equations (1a) and (5b), we can express branch voltages and currents as

$$\mathbf{w} = \mathbf{w}^0 + \mathbf{F}_w \mathbf{x}, \mathbf{j} = \mathbf{j}^0 + \mathbf{F}_j \mathbf{x}, \quad (12b)$$

The above expressions show that all relations between input and output variables are linear equations in the complex domain.

5. Optimum Control

Taking advantage of the linearity of control equations, we may approach the E-LAN control problem as a constrained optimum problem in L^2 space. For this purpose, we define a cost function that represents the grid performance from various perspectives. Then, we introduce a set of constraints that circumscribe the desired operating conditions.

5.1. Cost Function

The performances that we wish to optimize relate to voltage stability, energy efficiency, thermal stress of feeders, power stress of sources, and current stress of electronic power converters.

We therefore optimize a cost function φ including three weighted additive terms:

$$\varphi = \varphi_{loss} + \varphi_{stress} + \varphi_{dev} \quad (13a)$$

- Term φ_{loss} accounts for total power loss, including transformer loss, distribution loss in feeders, and conversion loss in power converters.
- Term φ_{stress} accounts for current stress in feeders, active power stress in sources, and apparent power stress in grid-tied converters.
- Term φ_{dev} accounts for total rms voltage deviation at grid nodes.

All terms of the cost function can be expressed as quadratic functions of control inputs. Overall, the cost function can be expressed in the quadratic form

$$\varphi = a_\varphi + \mathbf{x}^T \mathbf{b}_\varphi + \mathbf{x}^T \mathbf{C}_\varphi \mathbf{x}, \quad (13b)$$

where coefficient a_φ , vector \mathbf{b}_φ , and matrix \mathbf{C}_φ are constant real quantities, depending on network parameters and zero state variables. In particular, \mathbf{C}_φ is a positive definite matrix.

5.2. Constraints

The E-LAN operation is normally analyzed under different conditions (operation modes) that depend on the daily variations of source and load power, on the state of charge of energy storage systems, and on specific requirements on the power flow, either stationary (e.g., relating to power balance, reactive power compensation, demand response) or dynamic (e.g., transition to and from islanding, black start, electronic fault clearing). In both single-phase (or DC) and three-phase applications, pursuing the desired operation modes implies constraints of the power flowing at specific network gates. Thanks to linearity of control equations, such power constraints can be expressed as a system of linear equations:

$$\boldsymbol{\psi} = \mathbf{b}_\psi + \mathbf{C}_\psi \mathbf{x}, \quad (14)$$

where vector \mathbf{b}_ψ and matrix \mathbf{C}_ψ are real, because the constraints on real and imaginary axes are considered separately.

As mentioned before, the constraints set by the types of connection of single-phase and three-phase loads and sources are also considered in (14) to allow an accurate representation of the actual grid operation.

5.3. Solution

The constrained optimum control problem can be solved in explicit form by the Lagrange multipliers method. Let $\boldsymbol{\lambda}$ be the vector of Lagrange multipliers, the solving system is

$$\begin{cases} \frac{\partial \varphi}{\partial \mathbf{x}} + \frac{\partial \boldsymbol{\psi}}{\partial \mathbf{x}} \boldsymbol{\lambda} = 0 \\ \boldsymbol{\psi} = 0 \end{cases}, \quad (15a)$$

Solving the system gives the optimum control variables as

$$\mathbf{x} = -\frac{1}{2}\mathbf{C}_\varphi^{-1}\left(\mathbf{C}_\psi^T\mathbf{C}_\lambda^{-1}\mathbf{b}_\lambda + \mathbf{b}_\varphi\right), \text{ with : } \begin{cases} \mathbf{C}_\lambda = \mathbf{C}_\psi\mathbf{C}_\varphi^{-1}\mathbf{C}_\psi^T \\ \mathbf{b}_\lambda = 2\mathbf{b}_\psi - \mathbf{C}_\psi\mathbf{C}_\varphi^{-1}\mathbf{b}_\varphi, \end{cases} \quad (15b)$$

Note that the solution only requires the inversion of two reduced-order matrices, namely \mathbf{C}_φ and \mathbf{C}_λ , to obtain the result in a single computation step.

Overall, the proposed approach is computationally efficient and can be adapted to any networks, irrespective of their structure and complexity. Further, it can be used to analyze the E-LAN operation in any operating conditions and with flexible definition of the performance function to be optimized.

6. Problem of Silent Nodes

The correct application of the above optimum control approach would require complete monitoring of the currents and voltages at any grid nodes. In actuality, this may be impossible or impractical, since at residential premises only rms voltage and active power are metered; junction nodes are not monitored at all; voltage phase is rarely measured, etc. In this section, we introduce an estimation methodology of network voltages and currents that allows implementation of the optimum solution even if monitoring applies to a limited set of nodes or electric quantities.

For the sake of simplicity, although not strictly necessary, we keep the assumption that all node voltages are real quantities, in phase with voltage reference V_0 . Let \mathbf{v}^m be the vector of measured node voltages, and \mathbf{v}^s be the vector of voltages at silent nodes, where measurement is not available. Similarly, define \mathbf{i}_a^m and \mathbf{i}_r^m as the vectors of measured active (real) and reactive (imaginary) currents entering grid nodes, and \mathbf{i}_a^s and \mathbf{i}_r^s the corresponding quantities at silent nodes. The problem is to estimate the unknown quantities at silent nodes given the quantities measured at monitored nodes. Let $\mathbf{\Gamma} = \mathbf{Y}^{-1}$ be the nodal impedance matrix of the network. Recalling that voltages \mathbf{v} and currents \mathbf{i}_a and \mathbf{i}_r are real quantities, letting ι be the imaginary unit and \mathcal{R} the real operator, we can write:

$$\mathbf{v} = \mathbf{\Gamma} \mathbf{i} \Rightarrow \begin{vmatrix} \mathbf{v}_m \\ \mathbf{v}_s \end{vmatrix} = \Re\left(\begin{vmatrix} \mathbf{\Gamma}_m \\ \mathbf{\Gamma}_s \end{vmatrix} \mathbf{i}\right) = \mathcal{R}\left(\begin{vmatrix} \mathbf{\Gamma}_m \\ \mathbf{\Gamma}_s \end{vmatrix} \left(\begin{vmatrix} \mathbf{i}_a^m \\ \mathbf{i}_a^s \end{vmatrix} + \iota \begin{vmatrix} \mathbf{i}_r^m \\ \mathbf{i}_r^s \end{vmatrix}\right)\right), \quad (16a)$$

Considering only the equations related to measured voltages \mathbf{v}_m , from (16a), we obtain

$$\mathbf{v}_m = \mathcal{R}\left(\begin{vmatrix} \mathbf{\Gamma}_{ma}^m & \mathbf{\Gamma}_{ms}^m \\ \mathbf{\Gamma}_{ma}^s & \mathbf{\Gamma}_{ms}^s \end{vmatrix} \begin{vmatrix} \mathbf{i}_a^m \\ \mathbf{i}_a^s \end{vmatrix} + \iota \begin{vmatrix} \mathbf{\Gamma}_{mr}^m & \mathbf{\Gamma}_{ms}^m \\ \mathbf{\Gamma}_{mr}^s & \mathbf{\Gamma}_{ms}^s \end{vmatrix} \begin{vmatrix} \mathbf{i}_r^m \\ \mathbf{i}_r^s \end{vmatrix}\right), \quad (16b)$$

where $\mathbf{\Gamma}_{ma}^m$ and $\mathbf{\Gamma}_{ms}^m$ are the submatrices of $\mathbf{\Gamma}_m$ that correspond to measured and nonmeasured active currents, and similarly $\mathbf{\Gamma}_{mr}^m$ and $\mathbf{\Gamma}_{ms}^m$ correspond to measured and nonmeasured reactive currents. Given the above submatrices, we can develop Equation (16b) to extract its real part, and then express the unknown quantities \mathbf{i}_a^s and \mathbf{i}_r^s as a function of measured quantities \mathbf{v}_m , \mathbf{i}_a^m , \mathbf{i}_r^m in the following form:

$$\mathbf{D} \begin{vmatrix} \mathbf{i}_a^s \\ \mathbf{i}_r^s \end{vmatrix} + \mathbf{e} = 0, \quad \begin{cases} \mathbf{D} = \mathbf{D}(\mathbf{\Gamma}_m) \\ \mathbf{e} = \mathbf{e}(\mathbf{\Gamma}_m, \mathbf{v}_m, \mathbf{i}_a^m, \mathbf{i}_r^m) \end{cases}, \quad (16c)$$

Matrix \mathbf{D} depends only on network parameters, while vector \mathbf{e} depends on measured quantities, too. Equation (16c) cannot be solved by inversion of matrix \mathbf{D} that, generally, has not full rank. We can therefore find a solution with Moore–Penrose pseudo-inverse approach, which finds the unknown currents which meet the network equations and minimize their total rms value. Given the estimates of currents \mathbf{i}_a^s and \mathbf{i}_r^s , unknown voltages \mathbf{v}_s can then be determined from the lower part of Equation (16a).

Obviously, the estimation is affected by an inaccuracy that is as higher as smaller is the number of monitored nodes. This approach, however, allows application of optimum

control in any situations. Several tests demonstrated that the errors on the control variables are quite limited in all practical cases where at load nodes only the active power is measured, while at source nodes both active and reactive power are measured together with the line voltage.

A different approach must be adopted for the estimation of load currents, which are input quantities for the optimum control. In this case, each load current is independent, and the evaluation is carried out by assuming that the unknown loads share the total power in the same proportion observed for the average of measured loads.

7. Application Example and Performance Assessment

A comprehensive simulation code (SUSI³, Smart Users & Sources Integration, Interconnection and Interplay) was developed to allow the analysis of the above control approach in networks of high complexity while offering a full set of options regarding the following:

- Network architecture and ratings (e.g., topology, distribution line impedances, current ratings of feeders, grid voltage and frequency, tolerance on impedance values).
- Types, connection, power and energy ratings, control ability, and operating constraints for any given categories of loads and sources.
- Daily profiles of source power generation and load absorption.
- Dynamic pricing of energy.
- Definition of case studies, in terms of operating conditions, control variables, node and branch constraints for power steering (e.g., active and reactive power flow at given network sections, phase power balance, power factor, saturation and tripping in case of overstress, etc.).
- Adjustment of cost function coefficients.

The simulation code provides a complete description of the grid operation in any selected operating conditions and timeframes (node quantities, branch quantities, aggregated power production and consumption for groups and categories of users and pricing, cumulative performance indexes such as power factor, unbalance factor, etc.).

Since the computation kernel is compact and efficient, the code can be implemented with fast simulation times even on standard desktop computers. For example, execution times considering networks with a hundred nodes is in the order of seconds if executed on a desktop PC with CPU Intel i5. This is compatible with typical power systems dynamics [15] and energy pricing variations [13].

7.1. The Considered Benchmark Network

As an example of application, the European low-voltage benchmark network proposed by CIGRE [16], shown in Figure 4, was considered. The network includes three sub-networks: residential, commercial, and industrial. The characteristics and parameters of loads, sources, and distribution feeders of the network are detailed in [16], and were considered for the simulation. Details on the considered network are reported in Appendix A, where, Table A1 specifies the type of feeders, Table A2 shows the connections among grid nodes, the characteristics of the loads tied to the grid, and the parameters of MV/LV transformers feeding the three sub-networks, and Table A3 specifies the characteristics of distributed energy sources.

As compared to the CIGRE benchmark network, wind turbines (WT), photovoltaic systems (PV), and distributed energy storage units (DES) similar to those proposed for the residential sub-network were added in the commercial and industrial sections, too. All distributed power sources, either RES (renewable energy sources) or DES, tie in to the grid by electronic power converters and perform as controllable current sources.

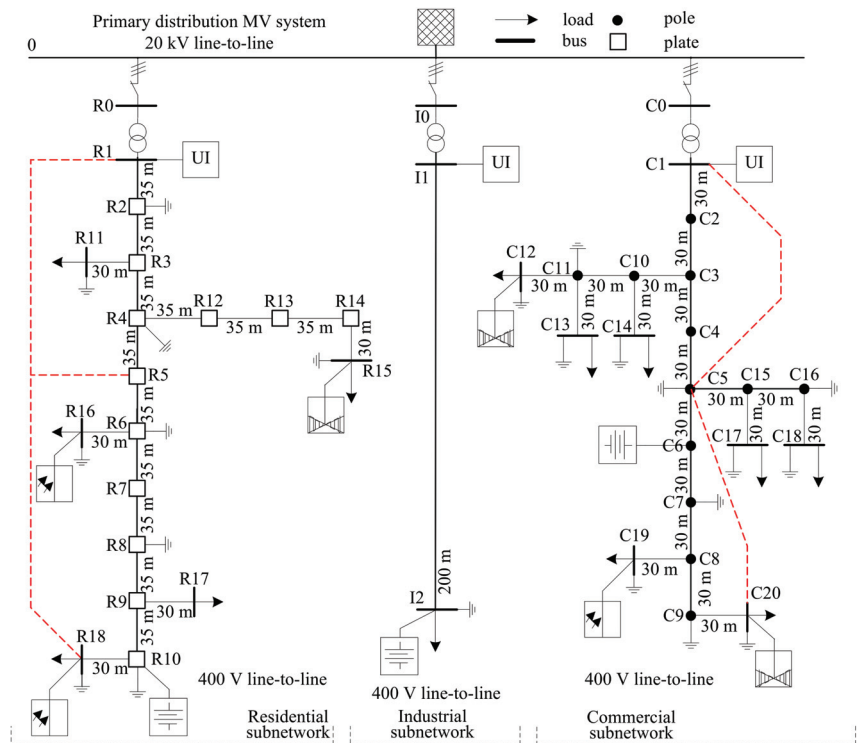


Figure 4. CIGRE European low-voltage network considered as application example.

To complement the network, we included the connecting lines shown in red color, that transform the original radial topology of each sub-network into a meshed one. In practice, this corresponds to duplicate the main power line in the cable duct.

Finally, utility interfaces (UIs) were added in each sub-network close to the PCC; these units, equipped with energy storage and three-phase PWM converters, perform as controllable voltage sources and act as voltage trackers during on-grid operation, and as voltage formers during off-grid operation [17–19]. Further to their voltage support action, these units allow reactive power and unbalance compensation in the proximity of each PCC, resulting in unity power factor at the utility terminals [20]. This action is possible thanks to the ability of three-phase grid-tied converters to exchange active power among the phases, and to generate compensating reactive power, without requiring net energy from the storage unit, the only limitation being due to the VA rating of the converter.

Utility interfaces and distributed energy storage units, as a whole, constitute the energy storage system (ESS).

We generally assume that load nodes only measure rms voltage and active power; RES and DES measure also reactive power for control purpose; finally, UIs measure voltage amplitude and phase, as needed to implement voltage tracking.

7.2. Radial versus Meshed Structure

A first set of simulation results are shown in Figure 5, where the network performances for radial and meshed topologies are compared. For this purpose, two quality indexes are considered. The first quality index is *total efficiency*, meant as the ratio between the total active power absorbed by loads and that generated by sources; all types of power loss (i.e., distribution, conversion, and generation loss) are considered in the computation. The second index is the *total voltage deviation*, meant as the cumulative rms value of the

differences between node voltages and the reference voltage. The upper part of the figure shows the daily profiles of the total active and reactive power absorbed by loads and the active power generated by renewable sources, computed according to typical CIGRE generation and consumption profiles. In this case, the ESS does not contribute to power generation, since DES and UIs are off. Moreover, RES converters do not generate reactive power. The lower part of the figure compares the performance of the radial and meshed configurations. As expected, for the given behavior of loads and sources, the meshed configuration provides better efficiency and lower voltage deviation, thanks to the multiple paths offered to the power to flow.

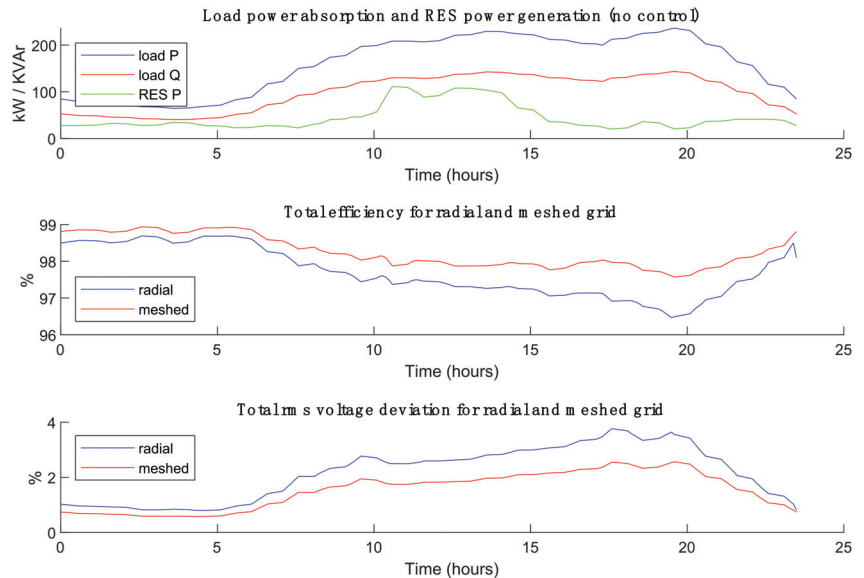


Figure 5. Comparison of quality indexes for radial and meshed network.

In the following, we will refer to the meshed topology, which—in addition to better performance indexes—allows full exploitation of the optimum control potentiality described above.

7.3. Impact of Reactive Power Control

Figure 6 aims at showing the effects of reactive power control, according to different techniques, which are referred to as Case 1–3 and discussed in the following. The above performance factors are considered again as indicators of the quality of performance.

- Case 1 refers to local reactive power compensation, when the converters interfacing the RES with the grid generate reactive power to compensate local loads. Obviously, the actual compensation capacity is limited by the VA rating of the converters. In this case, the control is merely local, and the central optimum control is not involved. The upper figure shows the reactive power sharing between utility and RES. The utility supplies the remaining reactive power, not locally provided by RES converters.
- In Case 2, the local reactive power compensation is complemented with the compensating action performed by ESS converters driven by the central optimum controller. The reactive power fed by the utility drops, evidently, the major burden of compensation being taken by the ESS. Note that the total reactive power fed by utility, DER, and ESS exceeds that required by the loads, and this is due to the optimum control that, in order to minimize the voltage deviation, creates a local injection of reactive power

- at network nodes. As a result, while total efficiency remains almost the same as in Case 1, the voltage deviation reduces significantly.
- Finally, in Case 3, all controllable converters (RES and ESS) are driven by the central optimum controller. The reactive power sharing among utility, RES, and ESS changes considerably from the previous cases, since the reactive power required for RES vanishes, and the compensation task is substantially committed to ESS, with a minor contribution from the utility. The result is a significant improvement of total efficiency, while voltage deviation is similar to Case 2.

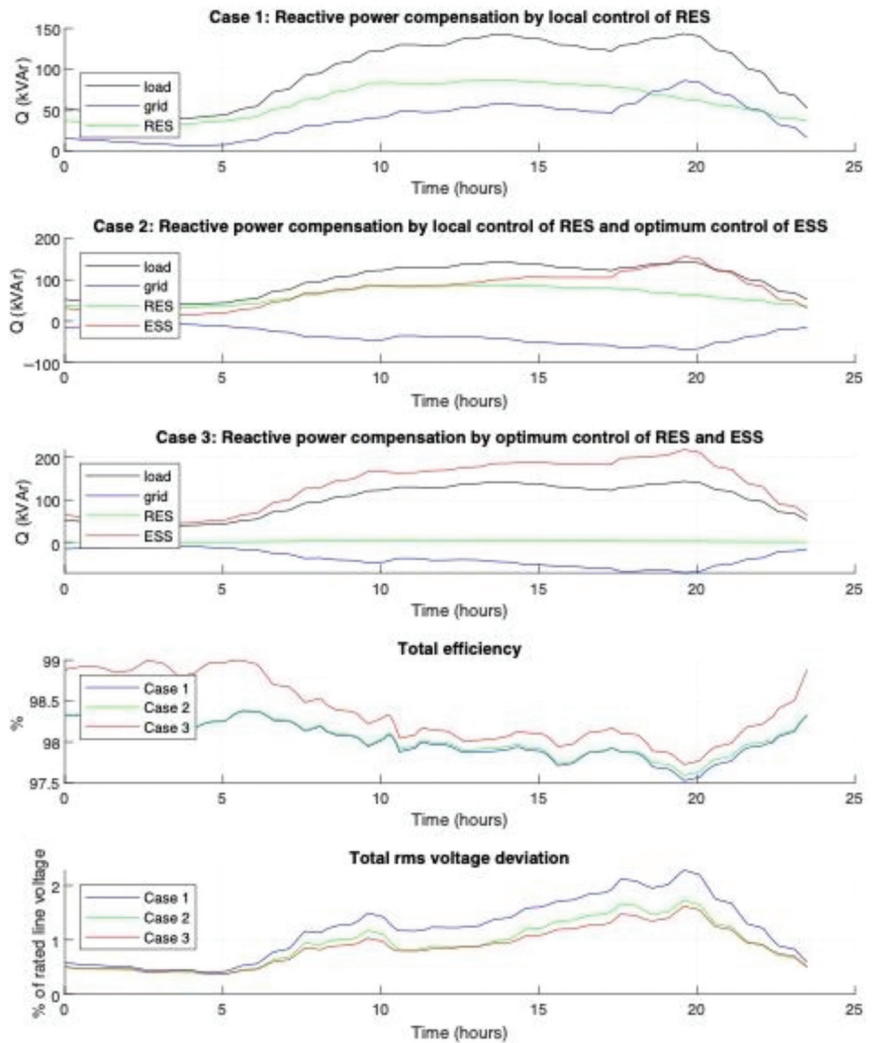


Figure 6. Results obtained considering different reactive power control methods.

Overall, this figure demonstrates that a suitable control of reactive power can significantly improve the network operation in terms of stability of the voltage profiles and reduction of power losses in the entire network.

7.4. Hybrid Control Operation

Figure 7 shows the daily network operation with hybrid control, i.e., local control of reactive power of RES units, whose active power is determined by renewable energy generation, and optimum control of all units equipped with energy storage (UIs and DES). Under regular operation, each ESS unit targets the nominal state of charge (SoC), while during transients they feed or store energy to suit network needs. At all times, the control ensures unity power factor at PCC, that is, balanced absorption of active power and no reactive power in all phases, and optimization of the global performance according to the selected cost function. During the daytime, load and source power profiles keep the same behavior shown in Figure 5. The regular operation is suspended three times, to suit the utility request:

- From 5 a.m. to 7 a.m., the network turns to islanded (i.e., off-grid) operation; correspondingly, the energy balance is ensured by the ESS, whose cumulative state of charge drops from 95% to 53% of the reference value for UIs, and from 95% to 72% for DES. Afterwards, the network returns to regular (i.e., on-grid) operation, and each ESS unit recharges at nominal SoC. This implies an extra power absorption from the utility for about 2.5 h, along which the recharge power of ESS is limited to 50% of rated power to preserve the lifetime of the batteries.
- From 10 a.m. to 11 a.m. and from 5 a.m. to 6 p.m., the power absorption of the network is reduced to 50% to halve the power fed by the utility. In this case, the utility and the ESS share the power demand of the network, and the cumulative SoC of batteries drops—to 70% in the first timeslot, and to 60% the second—and is recovered in the following recharge phases.

The lower part of the figure shows the behavior of the quality factors. The total efficiency keeps higher than 97.5% in all conditions, with an average value of 98%. The total rms voltage deviation keeps less than 2.5%, with an average value of 1.15%.

Overall, the figure shows the extreme flexibility of operation of the proposed control method, which allows effective exploitation of all the available resources while ensuring optimum performances from various perspectives: energy efficiency, voltage stability, thermal stresses in feeders, power stress of sources, and current stress of grid-tied converters.

Note, finally, that in the above examples, the utility requirements are met by exploiting only DES and UIs, the other sources being unaffected. In actuality, end users can individually decide on their participation to power control, as will be shown in the following.

7.5. Specific Features of the Proposed Control

The flexibility demonstrated by the previous examples derives from the methodological approach that pursues the optimization of a set of performance indexes while obeying a certain number of constraints. A proper selection of these constraints allows adaptation of E-LAN behavior to suit conditions that may considerably widen the usual range of operation of microgrids. Let us emphasize these aspects with reference to the previous examples.

- (a) *Active contribution of end-users to power-sharing.* Figure 6 shows the benefit of exploiting reactive power control by grid-tied inverters interfacing the distributed energy sources. In spite of the considerable improvement in terms of voltage stability, this ability is often disregarded, since inverters normally operate at unity power factor. In actuality, this feature can be implemented at local control level, that is, with limited modification of the inverters control algorithm. The contribution of end-users to active power balance could also be determinant; however, it is disregarded in Figure 7, where the total power demand halves (in intervals 11–12 a.m. and 5–6 p.m.) thanks only to the energy support provided by the common energy storage system (UIs and DES). In general, we may assume that the energy storage units installed at end-user premises are used to alleviate the energy bill of each individual prosumer. With the proposed approach, in fact, each end-user may decide how much of its power capacity is shared

with the rest of the microgrid to meet the objectives of centralized control and how much is kept available for local goals. Let us assume that every user node of the network of Figure 5 is equipped with an energy storage unit rated to meet the local power need for about two hours. This capacity is exploited to reduce the energy bill, by locally feeding the loads in those time intervals when the cost of energy is set high, specifically, +50% in the intervals 10–12 a.m. and 3–4 p.m.

Figure 8 shows the total load power absorption of end-users, together with the power locally fed by their energy storage units. The total power fed by the grid vanishes in the above intervals when the loads are fed at the expense of the locally stored energy. The state of charge of local energy storage is then recovered during the night, when the cost of energy drops by 50%. Overall, this causes, for end users, a net saving of energy bill of about 15%.

- (b) *Demand response.* This highly rewarding feature is inherently allowed by the proposed control approach and requires a tight coordination of the power flow from the various energy sources to fix the energy exchange between the microgrid and the utility at the given contractual levels. This necessarily requires a central management of some energy sources (e.g., the utility interfaces), together with the capacity, allowed by three-phase grid-tied inverters, to provide active and reactive power balance among the supply phases. In this way, the power can be exchanged with the utility at unity power factor, as happens in Figure 7 at all times.
- (c) *Fault identification and clearing.* The ability to control the power flow in each specific line of the microgrid requires a coordination of the voltages and currents fed by the grid-tied inverters and is another relevant feature of the proposed control approach. Within reasonable limits, this allows to clear the current in a faulty line by controlling the surrounding energy sources. The faulty line can then be isolated by operating disconnectors at no-load, thus allowing safe servicing. In Figure 7, this capability turns out to be useful during the islanding phase (i.e., 5–7 a.m.) for the lines connecting the microgrid to the utility but can be extended to isolate any other line of the grid.
- (d) *Isolation of sub-grids for maintenance.* This feature extends the previous one to a sequential isolation of more lines, to progressively disconnect an entire sub-grid.
- (e) *Black start.* This feature lies on the presence of utility interfaces at the secondary side of the step-down transformers interfacing the microgrid with the mains. As mentioned before, the UIs perform as voltage sources that are synchronized with the mains during on-grid operation, while they operate as independent voltage sources in off-grid conditions. During the black start, the E-LAN is firstly started up at no load by activating the UIs as voltage sources. The loads are then progressively activated, their power being fed by the ESS. Finally, after a synchronization with the mains voltage, the microgrid reconnects with a controlled ramp-up of the currents at PCC. This behavior is shown in Figure 7 at the end of the islanding phase (i.e., 5–6 a.m.).

7.6. Granularity and Robustness of Control

The proposed simulation spans over 24 h, to show various operating modes that may happen along a typical day. In theory, the granularity of control can reduce to a single period of the line voltage, since the analysis based on phasor representation requires integration of electrical quantities over a line period. In general, the sampling frequency of control must be adapted to the dynamics of controlled quantities (see, e.g., [15]). During transients (e.g., transition from off-grid to on-grid operation), the control quantities should be updated frequently, to prevent overstresses, while during regular operation, the control cycle can slow down to adapt to load variations. From this perspective, the presence of local energy storage smoothing the power steps allows running the central control at a slower timescale, resulting in less electrical stresses and improved robustness of control. Typically, various communication solutions are available with adequate performance when timescales of seconds are considered [21,22].

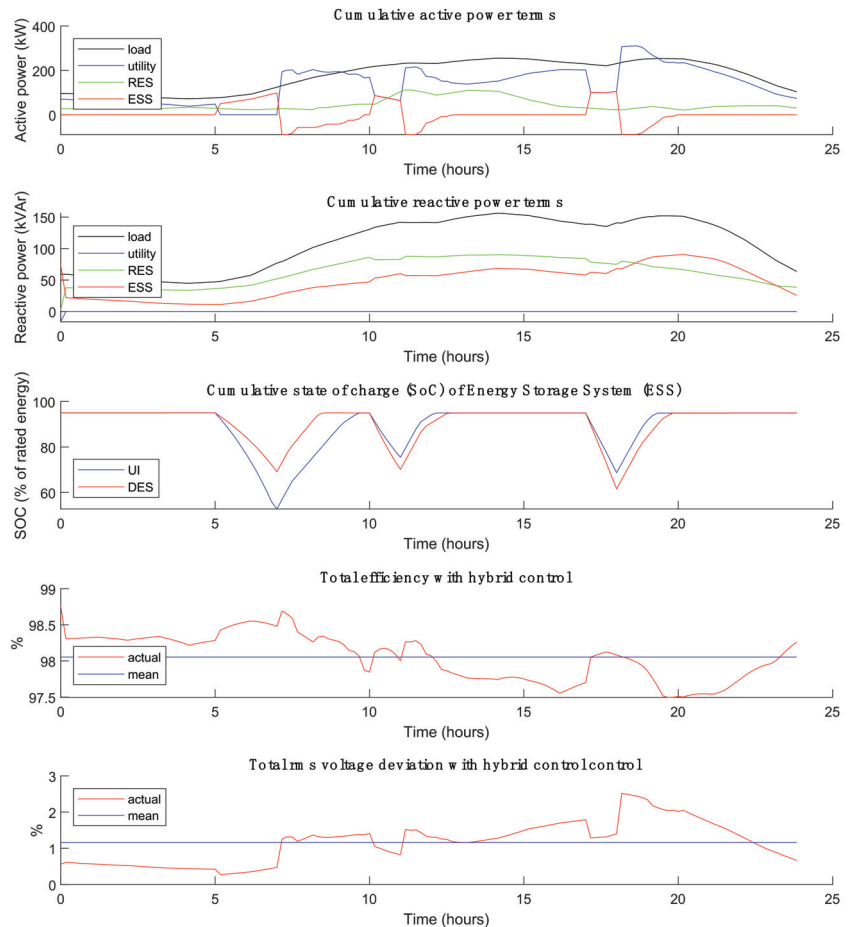


Figure 7. Results obtained with hybrid control.

7.7. Scalability of the Approach

The sample network of Figure 5 includes 55 nodes and 59 branches, representing the typical complexity of LV microgrids fed by MV/LV transformers. In actuality, the proposed control methodology can manage much more complex networks, since the computation algorithm is devised to minimize the number of matrix inversions in each computation step. In particular, only two matrix inversions are required, the size of the matrices being determined by the number of control variables, irrespective of the microgrid complexity.

The approach is scalable not only to handle larger microgrids but also to extend the analysis to the MV domain, where each E-LAN can be considered a single controllable end-user plugged into the MV distribution grid. In this sense, we can extend our analysis from the domain of LV E-LANs to that of MV E-WANs (wide area energy networks) that would set a completely new area of application for microgrid integration and coordination. Even in this case, the involved computation complexity remains practicable, allowing the extension of the optimum control approach to larger high-power networks.

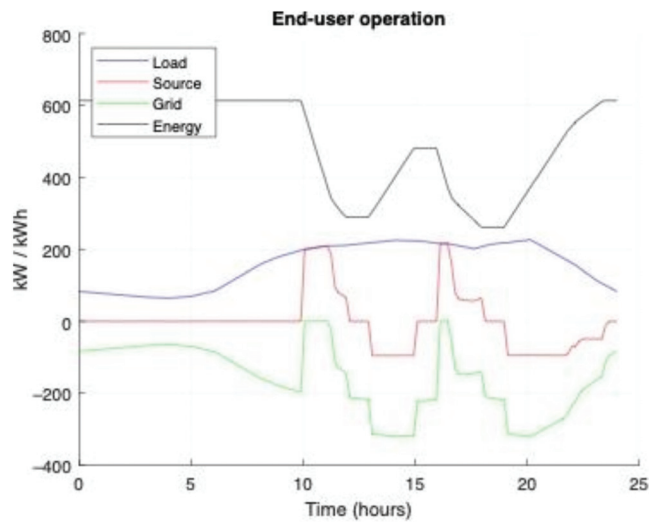


Figure 8. End-users' power and energy behavior in the scenario of Section 7.5a. End-users are equipped with energy storage units rated to feed the local load power for about two hours. Cost of energy is assumed to increase by 50% in the interval 10–12 a.m. and 3–4 p.m., and to halve during night.

8. Conclusions

Under the pressure of recent and incoming directives, the electric market is evolving toward an increasing use of renewable energy sources. A considerable part of these sources will be owned by end-users, who will substantially support the cost for greener electric power systems while aiming at enhancing their role in the energy market. This was already envisioned by the European Union, that plans for 2030 an independent and cost-driven participation of end-users to the electrical market. This sets a great challenge for the reorganization of the energy market, as well as for electric power systems that shall implement substantial technological and structural innovations.

The basic aggregations of the future electric systems will be the microgrids that embrace communities of neighboring end-users and potentially allow, on one side, significant improvement of the electrical performance and, on the other side, direct and independent (or aggregated) participation of end-users to the electric market. To make this possible, however, novel approaches to microgrid design and control shall be adopted.

In this paper, a comprehensive approach to analyze and control meshed microgrids is presented, which aims primarily at the power steering, i.e., the control of active and reactive power in every section of the microgrid. This allows, first, a significant improvement of microgrid performances by taking advantage of the controllability of distributed power sources. Second, power steering means that every user can decide, at any moment, which part of his energy resources can be shared within the microgrid and which is kept for local needs or for trading energy in the market [23].

The developed approach is applicable to AC and DC microgrids of any structure and complexity, irrespective of the nature and variety of end users tied to the microgrid. It sets a solid theoretical basis for future development of user-oriented electrical systems.

Author Contributions: Conceptualization, P.T. and T.C.; methodology, P.T.; software, P.T.; validation, P.T. and T.C.; formal analysis, P.T.; resources, P.T. and T.C.; data curation, P.T., T.C.; writing—original draft preparation, P.T.; writing—review and editing, P.T. and T.C.; project administration, P.T. and T.C. All authors have read and agreed to the published version of the manuscript.

Funding: This research received no external funding.

Institutional Review Board Statement: Not available.

Informed Consent Statement: Not available.

Data Availability Statement: Data available on request.

Conflicts of Interest: The authors declare no conflict of interest.

Appendix A

Details of the application example considered in Sect. are reported in this appendix. In particular, Table A1 specifies the type of feeders, Table A2 shows the connections among grid nodes, the characteristics of the loads tied to the grid, and the parameters of MV/LV transformers feeding the three sub-networks, and Table A3 specifies the characteristics of distributed energy sources.

Table A1. Parameters of the cables used in the application example in Section 7.

Cable Type	Effective Area (mm ²)	R Phase Wire (Ω /km)	L Phase Wire (mH/km)	R Neutral Wire (Ω /km)	L Neutral Wire (mH/km)	Rated Current (A _{rms})
UG1	240	1.63E−01	4.33E−01	4.90E−01	1.50E+00	430
UG2	150	2.66E−01	4.81E−01	7.33E−01	1.81E+00	325
UG3	120	3.26E−01	5.03E−01	8.60E−01	2.01E+00	290
UG4	25	1.54E+00	6.56E−01	2.33E+00	4.63E+00	120
UG5	35	1.11E+00	6.21E−01	1.93E+00	4.03E+00	145
UG6	70	5.69E−01	5.54E−01	1.29E+00	2.75E+00	215
OH1	50	3.87E−01	9.39E−01	6.89E−01	1.50E+00	172
OH2	35	5.24E−01	9.77E−01	8.38E−01	1.56E+00	145
OH3	16	1.15E+00	1.05E+00	1.84E+00	1.69E+00	93
I1	150	2.66E−01	4.81E−01	7.33E−01	1.81E+00	325

Table A2. Details about the connections among grid nodes, the characteristics of the loads tied to the grid, and the parameters of MV / LV transformers feeding the three sub-networks considered in the application example in Section 7.

Residential Subnetwork										Commercial Subnetwork										MV/LV Transformers (Yn)		
Line	Node from	Node to	Length (m)	Cable type	Line	Node from	Node to	Length (m)	Cable type	Name	Node from	Node to	kW	kVA	Conn	Vcc						
R1	R1	R2	35	UG1	C1	C1	C2	30	OH1	RT	R0	R1	500	5%								
R2	R2	R3	35	UG1	C2	C2	C3	30	OH1	CT	C0	C1	300	6%								
R3	R3	R4	35	UG1	C3	C3	C4	30	OH1	IT	I0	I1	150	2%								
R4	R4	R5	35	UG1	C4	C4	C5	30	OH1	Residential loads												
R5	R5	R6	35	UG1	C5	C5	C6	30	UG6	Node	Node	kW	kVA	Conn	Random term vs. CIGRE profile							
R6	R6	R7	35	UG1	C6	C6	C7	30	OH2	R11	R11	13	8	Yn	±40%							
R7	R7	R8	35	UG1	C7	C7	C8	30	OH2	R15	R15	60	38	Yn	±40%							
R8	R8	R9	35	UG1	C8	C8	C9	30	OH2	R16	R16	46	30	Yn	±40%							
R9	R9	R10	35	UG1	C9	C3	C10	30	OH2	R17	R17	4.25	2.65	3n	±40%							
R10	R3	R11	35	UG4	C10	C10	C11	30	OH2	R18	R18	40	25	Yn	±40%							
R11	R4	R12	35	UG2	C11	C11	C12	30	OH3	Commercial loads												
R12	R12	R13	35	UG2	C12	C11	C13	30	OH3	C12	C12	17	10.5	Yn	±30%							
R13	R13	R14	35	UG2	C13	C10	C14	30	OH3	C13	C13	6.8	4.2	Yn	±30%							
R14	R14	R15	30	UG3	C14	C5	C15	30	OH3	C14	C14	21.5	13	Yn	±30%							
R15	R6	R16	30	UG6	C15	C15	C16	30	OH3	C17	C17	13.5	8.5	Yn	±30%							
R16	R9	R17	30	UG4	C16	C15	C17	30	OH3	C18	C18	6.8	4.2	Yn	±30%							
R17	R10	R18	30	UG5	C17	C16	C18	30	OH3	C19	C19	21.5	13	Yn	±30%							
R18	R1	R5	140	UG1	C18	C8	C19	30	OH3	C20	C20	17	10.5	Yn	±30%							
R19	R5	R18	200	UG1	C19	C9	C20	30	UG4	Industrial loads												
I1	I1	I2	200	UG2	C20	C1	C5	120	UG1	I2	I2	60	37	Yn	20%							
					C21	C5	C20	150	UG1													

Table A3. Characteristics of the distributed energy resources considered in the application example in Section 7.

Type	Node	Inverter Rating (kVA)	Rated/Max Power (kW)	Rated Energy (kWh)	Random Term vs. CIGRE Profile
PV unit	R16	5	4		±20%
	R18	4	3		±20%
	C14	25	20		±20%
	C19	25	20		±20%
	I2	60	50		±20%
Wind turbine	R5	7	5.5		±30%
	C12	25	20		±20%
	C20	25	20		±20%
Energy storage	R10	35	15/30	30	
	C6	35	15/30	30	
	I3	35	15/30	30	
Utility interface	R1	120	50/100	100	
	C1	120	50/100	100	
	I1	80	35/70	70	

References

- Silva, V.A.; Aoki, A.R.; Lambert-Torres, G. Optimal Day-Ahead Scheduling of Microgrids with Battery Energy Storage System. *Energies* **2020**, *13*, 5188. [\[CrossRef\]](#)
- Agostini, M.; Bertolini, M.; Coppo, M.; Fontini, F. The Participation of Small-Scale Variable Distributed Renewable Energy Sources to the Balancing Services Market. *Energy Econ.* **2021**, *97*, 105208. [\[CrossRef\]](#)
- Union, P.O. of the E. *Clean Energy for All Europeans*; European Union: Brussels, Belgium, 2019; p. 24.
- Plancke, G.; De Vos, K.; Belmans, R.; Delnooz, A. Virtual Power Plants: Definition, Applications and Barriers to the Implementation in the Distribution System. In Proceedings of the 2015 12th International Conference on the European Energy Market (EEM), Lisbon, Portugal, 19–22 May 2015; pp. 1–5.
- Poplawski, T.; Dudzik, S.; Szelag, P.; Baran, J. A Case Study of a Virtual Power Plant (VPP) as a Data Acquisition Tool for PV Energy Forecasting. *Energies* **2021**, *14*, 6200. [\[CrossRef\]](#)
- Subramanya, R.; Yli-Ojanperä, M.; Sierla, S.; Hölltä, T.; Valtakari, J.; Vyatkin, V. A Virtual Power Plant Solution for Aggregating Photovoltaic Systems and Other Distributed Energy Resources for Northern European Primary Frequency Reserves. *Energies* **2021**, *14*, 1242. [\[CrossRef\]](#)
- Abedini, H.; Caldognetto, T.; Mattavelli, P.; Tenti, P. Real-Time Validation of Power Flow Control Method for Enhanced Operation of Microgrids. *Energies* **2020**, *13*, 5959. [\[CrossRef\]](#)
- Simmini, F.; Caldognetto, T.; Bruschetta, M.; Mion, E.; Carli, R. Model Predictive Control for Efficient Management of Energy Resources in Smart Buildings. *Energies* **2021**, *14*, 5592. [\[CrossRef\]](#)
- Mazumder, S.K.; Kulkarni, A.; Sahoo, S.; Blaabjerg, F.; Mantooth, H.A.; Balda, J.C.; Zhao, Y.; Ramos-Ruiz, J.A.; Enjeti, P.N.; Kumar, P.R.; et al. A Review of Current Research Trends in Power-Electronic Innovations in Cyber-Physical Systems. *IEEE J. Emerg. Sel. Topics Power Electron.* **2021**, *9*, 5146–5163. [\[CrossRef\]](#)
- Matevosyan, J.; MacDowell, J.; Miller, N.; Badrzadeh, B.; Ramasubramanian, D.; Isaacs, A.; Quint, R.; Quitmann, E.; Pfeiffer, R.; Urdal, H.; et al. A Future With Inverter-Based Resources: Finding Strength From Traditional Weakness. *IEEE Power Energy Mag.* **2021**, *19*, 18–28. [\[CrossRef\]](#)
- Buticchi, G.; Lam, C.-S.; Ruan, X.; Liserre, M.; Barater, D.; Benbouzid, M.; Gomis-Bellmunt, O.; Paja, C.; Kumar, C.; Zhu, R. The Role of Renewable Energy System in Reshaping the Electrical Grid Scenario. *IEEE Open J. Ind. Electron. Soc.* **2021**, *2*, 451–468. [\[CrossRef\]](#)
- Zafeiratou, I.; Prodan, I.; Lefèvre, L. A Hierarchical Control Approach for Power Loss Minimization and Optimal Power Flow within a Meshed DC Microgrid. *Energies* **2021**, *14*, 4846. [\[CrossRef\]](#)
- Simmini, F.; Agostini, M.; Coppo, M.; Caldognetto, T.; Cervi, A.; Lain, F.; Carli, R.; Turri, R.; Tenti, P. Leveraging Demand Flexibility by Exploiting Prosumer Response to Price Signals in Microgrids. *Energies* **2020**, *13*, 3078. [\[CrossRef\]](#)
- Balabanian, N.; Bickart, T.A. *Electrical Network Theory*; Wiley: New York, NY, USA, 1969; ISBN 978-0-471-04576-2.
- Ela, E.; O'Malley, M. Studying the Variability and Uncertainty Impacts of Variable Generation at Multiple Timescales. *IEEE Trans. Power Syst.* **2012**, *27*, 1324–1333. [\[CrossRef\]](#)

16. CIGRE Task Force C6. 04.02. In *Benchmark Systems for Network Integration of Renewable and Distributed Energy Resources*; International Council on Large Electric Systems: Paris, France, 2014.
17. Caldognetto, T.; Tenti, P. Microgrids Operation Based on Master–Slave Cooperative Control. *IEEE J. Emerg. Sel. Top. Power Electron.* **2014**, *2*, 1081–1088. [[CrossRef](#)]
18. Rosso, R.; Wang, X.; Liserre, M.; Lu, X.; Engelken, S. Grid-Forming Converters: Control Approaches, Grid-Synchronization, and Future Trends—A Review. *IEEE Open J. Ind. Applicat.* **2021**, *2*, 93–109. [[CrossRef](#)]
19. Caldognetto, T.; Abedini, H.; Mattavelli, P. A Per-Phase Power Controller for Smooth Transitions to Islanded Operation. *IEEE Open J. Power Electron.* **2021**, *2*, 636–646. [[CrossRef](#)]
20. Wang, J.; Zhou, N.; Ran, Y.; Wang, Q. Optimal Operation of Active Distribution Network Involving the Unbalance and Harmonic Compensation of Converter. *IEEE Trans. Smart Grid* **2019**, *10*, 5360–5373. [[CrossRef](#)]
21. Burgos, R.; Sun, J. The Future of Control and Communication: Power Electronics-Enabled Power Grids. *IEEE Power Electron. Mag.* **2020**, *7*, 34–36. [[CrossRef](#)]
22. Dambrauskas, P.; Syed, M.H.; Blair, S.M.; Irvine, J.M.; Abdulhadi, I.F.; Burt, G.M.; Bondy, D.E.M. Impact of Realistic Communications for Fast-Acting Demand Side Management. *CIREN-Open Access Proc. J.* **2017**, *2017*, 1813–1817. [[CrossRef](#)]
23. Shezan, S.A.; Hasan, K.N.; Rahman, A.; Datta, M.; Datta, U. Selection of Appropriate Dispatch Strategies for Effective Planning and Operation of a Microgrid. *Energies* **2021**, *14*, 7217. [[CrossRef](#)]

Review

23 Years of Development of the Solar Power Generation Sector in Spain: A Comprehensive Review of the Period 1998–2020 from a Regulatory Perspective

Sergio Coronas *, Jordi de la Hoz, Àlex Alonso and Helena Martín

Electrical Engineering Department, Escola d'Enginyeria de Barcelona Est, Polytechnic University of Catalonia, 08019 Barcelona, Spain; jordi.de.la.hoz@upc.edu (J.d.l.H.); alexandre.alonso.traveset@upc.edu (À.A.); m.helena.martin@upc.edu (H.M.)

* Correspondence: sergio.coronas@upc.edu

Abstract: Spain has become one of the leading countries in the world in promoting electricity generation from renewable energy sources (RES), due to their positive socioeconomic and environmental impacts, through highly favorable regulatory frameworks and public incentives set by Spanish governments mainly during the first decade of 2000s, i.e., Royal Decree (RD) 2818/1998, RD 436/2004 and RD 661/2007. Conversely, the highly favorable regime applicable to RES, and specifically to solar power plants during the 1998–2008 promotion period turned into an extremely unfavorable scenario during the 2008–2020 cost-containment stage, characterized by the dismantling of the previous promotion schemes so as to reduce the skyrocketing electricity system tariff deficit, in which regulations such as RD 1578/2008, Royal Decree Law (RDL) 6/2009, RDL 14/2010, RDL 1/2012, Law 15/2012, RDL 9/2013, Law 24/2013 and RD 413/2014 stood out. Nonetheless, the Spanish renewable sector, and especially the solar power sector, has shown great dynamism in its energy policy in the period 1998–2020. This academic contribution provides a comprehensive review of the energy policy evolution for the whole solar power sector in Spain, specifically both solar photovoltaic (PV) and concentrating solar power (CSP) plants, over the last 23 years. Thus, considering both the boom in the solar power sector as well as the solar sector's bust, a survey of the different legislation in force during the 1998–2020 period, as well as of the existing academic literature dealing with this issue, is conducted to first contextualize and describe, and then carefully assess, the last 23 years of solar energy policy in Spain. In brief, the decisive role of the Spanish government in developing the RES sector, and especially the solar power sector, in recent years has been noted. In this vein, a good planning of the energy development model, the regulatory stability, the simplicity and agility of the corresponding administrative process, the appropriate design of support mechanisms, as well as security and predictability of support levels in the mid and long term, play an important role in providing certainty to all the stakeholders. During the 1998–2008 promotion stage, even with a stable, quite favorable and easily predictable RES support mechanism in place, the Spanish solar system behaved as an open-loop system without any control structure detecting and reacting to problematic situations. The fact that the Spanish government was compelled to implement ex-post measures during the period 2008–2020, seriously jeopardizing the viability of the power plants in operation, as well as compromising the legal-economic stability of the renewable energy sector, clearly indicated a malfunctioning of the energy policy control mechanism. In essence, it is hoped that the lessons extracted from this 23-year comprehensive review of the Spanish solar power sector pathway could be quite useful for other countries either in the initial development stage or fully immersed in the promotion of solar power sector or any other renewable technology.

Citation: Coronas, S.; de la Hoz, J.; Alonso, À.; Martín, H. 23 Years of Development of the Solar Power Generation Sector in Spain: A Comprehensive Review of the Period 1998–2020 from a Regulatory Perspective. *Energies* **2022**, *15*, 1593. <https://doi.org/10.3390/en15041593>

Academic Editor: Juri Belikov

Received: 15 January 2022

Accepted: 18 February 2022

Published: 21 February 2022

Publisher's Note: MDPI stays neutral with regard to jurisdictional claims in published maps and institutional affiliations.



Copyright: © 2022 by the authors. Licensee MDPI, Basel, Switzerland. This article is an open access article distributed under the terms and conditions of the Creative Commons Attribution (CC BY) license (<https://creativecommons.org/licenses/by/4.0/>).

Keywords: Spain; review; regulatory framework; energy policy; promotion; cost-containment; public support; renewable energy; solar PV; CSP

1. Introduction

1.1. Setting the Context

Power generation has been, and remains, a fundamental sector to bear in mind in any energy policy across the world aimed at reducing greenhouse gas (GHG) emissions in the fight against global warming [1–4]. In fact, the energy sector is the biggest emitter of global GHG emissions, responsible for almost 75% by 2020, while the electricity sector accounted for 36% of all energy-related carbon dioxide (CO₂) emissions [5]. In this regard, the development of electricity production through renewable energy sources (RES), and therefore the substitution and reduction of usage of fossil fuels (coal, oil and natural gas), is the mainstay of the decarbonization of the worldwide electricity sector towards a low-carbon and more sustainable economy. Furthermore, RES ensure the enhancement in national security of energy supply and energy self-sufficiency from imported fossil fuels, commonly characterized by complex geopolitical environments [2,3,6–8]. The share of fossil fuels in the global energy mix has remained at around 80% throughout recent decades [5].

The development of non-GHG-emitting and non-depletable RES has followed a significant and accelerating trend in the global energy sector as a policy-driven phenomenon over the last few decades. Accordingly, most of the advancement in the expansion of renewable technologies has been acquired due to strong country-specific public promotion policies and regulatory frameworks, coupled with ambitious RES goals, substantiated by their positive socioeconomic and environmental impacts [3,4,7,9–16]. Indeed, RES policies are presently the rule rather than the exception. Specifically, nearly all countries worldwide had in place RES support policies by the end of 2020 [4,16].

The conversion of the power generation sector has been one of the cornerstones of the European Union (EU) energy policy in recent decades, giving rise to an intense legislative activity in the different European countries. First focusing on the liberalization of the electricity sector, one of the most highly regulated economic activities, and later curtailing the environmental impact of electricity production by promoting RES [8,17].

Spain has not been an exception in the EU market, but an especially relevant case, as it has been one of the world's leading countries in promoting RES through highly favorable public subsidies and legal-economic frameworks. Thus, resulting in a significant expansion of renewable technologies for electricity generation in the last two decades, particularly wind and solar energy [3,8,18]. Spain is in a particularly advantageous position with the most plentiful solar resource in the entire EU [15,19,20]. In this respect, Spain ranked seventh-highest for the share of electricity production from solar in 2019 among the International Energy Agency (IEA) countries [21].

From the 1990s, the national energy policy priority for the different Spanish governments was to support RES given its potential benefits related to environmental protection aligned with the EU policies, heightened awareness within society of the fight against global warming, job creation, diversification of the energy mix and decrease in energy reliance on fossil-fuel imports [8,22–24]. In particular, the Spanish energy system has always been characterized by its high dependence on imports for fossil fuels, i.e., Spain's national production only has covered about one quarter of total energy supply over the last two decades [2,19,21,25].

Several international institutions pointed to the Spanish RES development system as a successful story. Nevertheless, there have also been some shadows in the Spanish experience with the public support to RES, and especially to solar technologies, related to the substantial increase of its promotion costs [26–30]. Spain has experienced numerous legislative changes in the regulation of RES since the 1990s, receiving worldwide attention in recent years. Specifically, the last 23 years of the solar power generation sector can be divided into two periods with opposite goals, i.e., the 1998–2008 promotion period, characterized by quite favorable support mechanisms for the development of solar power plants, and the 2008–2020 containment period, marked by the dismantling of the previous promotion schemes so as to lessen the disproportionate solar power support costs to the electricity system, giving rise to highly unfavorable conditions for these renewable assets.

As for the 1998–2008 promotion period, Spain implemented a special regime (SR) promotion mechanism for RES, prompting high deployment levels of electricity generation from renewable technologies in that period. Specifically, the Spanish government introduced a feed-in promotion scheme, i.e., feed-in tariff (FIT) and feed-in premium (FIP), which were the most widespread RES promotion mechanism in the EU, and the most significant regarding the amount of support awarded at that time [1,3,8,22,24,29,31,32]. By way of example, almost all the new solar photovoltaic (PV) capacity in the EU was installed by means of FIT schemes during that period [33].

It is important to highlight that after a favorable promotion policy and public subsidies for solar technology especially in the second half of the 1998–2008 period, Spain suffered an unprecedented PV boom between 2007 and 2008 under Royal Decree (RD) 661/2007 framework, putting the country's solar PV sector as a global role model of technological advancement and installation rates. By that time, more than 70% of all European grid-connected solar PV facilities were in Spain, which is the biggest solar PV market [9,20,23,24,34–37]. Regarding the dispatchable concentrating solar power (CSP), which is regarded by the Spanish government as a strategic technology [8], the foundations for the subsequent 2011–2012 CSP bubble were laid during the latter part of the 1998–2008 period, due to the generous incentives for this technology. Since then, Spain has become the world leader in installed CSP capacity followed by the United States, although the progress in those two countries stalled in 2013 and 2015, respectively [10,38–40]. In the wake of the proactive RES policies deployed by the Spanish governments during the 1998–2008 promotion period, the electricity produced in Spain through fossil fuels fell considerably from 74% in 2000 to 52% in 2012 [41].

Administratively set feed-in pricing policies, specifically FIT and FIP, have remained as the most widely adopted form of renewable power support worldwide until 2017, when competitive auctions became the main RES promotion mechanism [4]. Furthermore, FIT has been regarded as the most successful mechanism for fostering the RES development in the EU, as demonstrated by the experiences in Germany, Spain and Denmark, among others [3,7,26,42]. Likewise, many other European countries have also implemented feed-in policies to support RES, such as Austria, the Czech Republic, France, the Netherlands, Italy, Portugal and Switzerland [42,43]. Notwithstanding the effectiveness of the incentive-based feed-in instrument, it has had a major drawback concerning its associated cost-burden, generally transferred to electricity consumers through their bills, in countries with significant raises in RES deployment and especially for high-cost renewable technologies. In fact, solar booms have only taken place in countries using FIT mechanisms. Consequently, the cutback of RES promotion costs by reversing the previously set supports and dismantling the renewable energy policies has become a policy priority and a major concern in many countries all over the world, such as Spain, France, Italy and Czech Republic [3,10,11,16,17,27,28,34,44,45].

As for the 2008–2020 containment period, the Spanish RES feed-in policy began to be dismantled by means of retroactive cost-containment measures until it was totally repealed by the electricity reform enacted in 2013, specifically the Spanish electricity sector (SES) Law 24/2013, in an attempt to tackle the overrun cost derived from the excessive RES support incentives (mostly related to solar PV promotion), and therefore the growing tariff deficit of the electricity system [3,15,18,29,30,36,45,46]. During that period, the Spanish solar PV sector suffered a significant bust, becoming the first European country to experience a clear boom-and-bust cycle in the solar PV sector. Therefore, Spain moved from a prominent position in the global market concerning the cumulative installed solar PV power, to an insignificant status with the PV sector virtually paralyzed until the 2017 RES auctions under RD 413/2014 framework [23,35,36,47]. Similarly, with no new capacity additions since 2013, Spain's share of global CSP capacity in operation dropped from a peak of almost 80% in 2012 to just under 40% by the end of 2020 [4]. The new market-based RD 413/2014 legislative framework for RES relied on an auction support mechanism, which

has recently been considered a cost-effective worthy option to induce further investments in RES without excessive costs for electricity consumers [17,32].

Spain has seen notable decarbonization of the electricity sector, as the share of electricity production from fossil fuels diminished from 56% in 2009 to 41% in 2019, while electricity production from RES increased from 24% in 2009 to 38% in 2019, ranking thirteenth highest in terms of the share of RES that year among the IEA countries [21].

1.2. State of the Art

There is wide agreement in the academic literature regarding the need for public policies to encourage RES advancement [13]. Presently, despite the increasing cost competitiveness of RES, their continued expansion remains dependent on policy support [16]. Accordingly, numerous articles have focused on the study of RES promotion policies, both from a general and country-specific point of view. In this vein, Spain has become one of the countries in the world that has attracted more attention for becoming one of the most successful countries concerning the public development of energy generation from RES during the 1998–2008 period [48]. Moreover, the continuous and considerable regulatory changes suffered by the Spanish RES sector over the last 23 years, and specifically by the solar power sector that experienced a relevant boom-and-bust cycle, may also have acted as a pole of attraction for the academia.

The legal–economic policy regulating the Spanish RES sector over the last 23 years, and specifically the solar power system, can be divided into two major phases, namely a first promotion stage from 1998 to 2008 and a second containment stage from 2008 to 2020, as explained in the body of this review.

As regards the Spanish country-specific study of the 1998–2008 RES promotion period, Arocena et al. [49] analyzed the regulatory reform in the Spanish electricity industry carried out by the first Law 54/1997 of the power sector. The factors giving rise to quite different diffusion rates of two key RES technologies in Spain, i.e., wind and solar PV, during the period 1994–2003 were assessed in [50], showing that economic and institutional factors played decisive roles in fostering or inhibiting diffusion during that period. In turn, an integrated assessment of one of the most successful policy schemes in Europe, i.e., the Spanish FIT system under RD 2818/1998 during the 1999–2003 period, was provided by [22]. Del Río [48] overviewed the RES promotion legislation in Spain during the period 1998–2007 and assessed the major differences and enhancements of the three main FIT promotion schemes existing in that period, i.e., RD 2818/1998, RD 436/2004 and RD 661/2007. Similarly, de la Hoz et al. [9] provided an authoritative review of the evolution of grid-connected PV power plants in Spain during the period 1998–2008, by analyzing the different legal, economic and technical frameworks affecting solar PV technology from a control theory point of view. Meanwhile the deployment process of a PV facility under RD 436/2004 and RD 661/2007 and its connection to the Spanish electricity network was assessed from an administrative and legal-economic perspective in [19]. Ciarreta et al. [6] overviewed the evolution of the European and the Spanish legislation until 2009 regarding the RES promotion in a context of electricity market liberalization, and studied the impact of the FIT promotion scheme for fostering RES on the oligopolistic Spanish power market under RD 661/2007, while also discussing economic implications of alternative support systems. Schallenberg-Rodríguez and Haas [31] assessed and compared the two alternative support options for RES, namely fixed FIT and premiums, which coexisted at the same time in Spain during the 1998–2009 analysis period, and evaluated their achievement bearing in mind the cap and floor mechanism introduced by RD 661/2007. Likewise, Salas and Olias [25] showed the Spanish solar PV technology status by 2007 taking into account the different support frameworks, as well as the outlook for the coming years. Meanwhile the socioeconomic impacts of increasing the installed CSP capacity in Spain under the provisions of the renewable energy plan (REP) 2005–2010 were estimated in [51].

Other works analyzed the transition from the highly favorable RES promotion legislation existing in Spain over the second half of the 1998–2008 period to the adverse RES

cost-containment legal framework, with drastic and sometimes retroactive regulatory cuts, thereafter. Specifically, Ortega et al. [42] provided a comparative assessment between the socioeconomic and environmental gains of RES deployment in Spain during the period 2002–2011, in terms of reduction of CO₂ emissions and fossil-fuel imports, and the RES public support costs granted through the FIT system. The public acceptance issue of RES was addressed in [52] by analyzing the Spanish solar PV case during the period of both greater expansion and contraction of that sector, i.e., from 2004 to 2010. In turn, del Río and Mir-Artigues [26] provided a summary of the patterns of the Spanish solar PV FIT scheme and its design features during the period 1998–2011, therefore considering the PV boom-and-bust cycle, and identified some implications for the successful and cost-effective expansion of solar PV in Spain. Likewise, a comprehensive review of the 2007–2010 solar PV boom-and-bust in Spain was provided in [23], by assessing in detail the 1998–2012 Spanish solar energy policy. Meanwhile Martín et al. [10] carried out a thorough analysis of the Spanish CSP evolution in the period 1998–2013, by means of a detailed overview of all the regulatory and economic legislations governing the development of the CSP technology. Furthermore, it used basic control theory standards to ease the identification of the major drivers behind the bubble-like behavior shown by the CSP technology. Additionally, Talavera et al. [35] undertook an economic profitability and cost assessment of grid-connected PV systems in Spain since 1998 to 2014 based on the internal rate of return (IRR), the net present value (NPV) and the levelized cost of electricity (LCOE), to identify the impact of the changing and confusing legislations applicable to the solar PV technology in that period on the PV investments. Similarly, Lomas et al. [36] analyzed an operating solar PV facility commissioned in Spain in 2007 from an economic and energy standpoint to analyze the impact of the evolution of the Spanish RES policy during the 2007–2015 period on its investment profitability as well as on its energy generation. In turn, the divergent performance in Germany and Spain of PV grid-connected systems regarding their legislation, profitability and diffusion was analyzed in [47], by reviewing the development of FIT supports and by assessing the cost effectiveness of different kinds of facilities through the IRR for the period 2004–2014. Meanwhile the economic and financial performance of Spanish solar PV energy generation firms over the period 2006–2015 was analyzed in [12], based on a longitudinal sample of around 5469 enterprises from the sector. Likewise, Blanco-Díez et al. [24] first reviewed the evolution of the Spanish RES regulatory framework, to subsequently analyze the economic effects of the retroactive legislative changes on the Spanish PV energy sector between 2004 and 2014, namely RD 436/2004, RD 661/2007 and RD 413/2014. Fernández-González et al. [37] analyzed how institutional changes in the Spanish solar PV sector during the period 2004–2018 affected its structure, by computing its degree of concentration and stability based on data from 5353 firms from the solar PV sector. Meanwhile San Miguel and Corona [39] reviewed the different regulatory frameworks affecting CSP technology in Spain between 1998 and 2015, to later evaluate the economic viability of CSP under those legislations based on the discounted cash flows, the IRR, the NPV and the LCOE.

As for the Spanish country-specific analysis of the 2008–2020 RES containment period, the financial return to the Spanish power system of the latest installed solar PV facilities under RD 1578/2008 saturation mechanism was analyzed by Azofra et al. [53], relied on the incentives perceived and the savings produced for the power market. It also presented alternative scenarios for the implementation of solar PV power in the Spanish network through a temporary redistribution of the power plants that prompted the Spanish 2007–2008 PV boom. De la Hoz et al. [27] described the 2008–2010 regulatory framework for grid-connected PV power plants resulting after the Spanish 2007–2008 PV boom as well as the development of the solar PV sector for that period, and assessed the control performance in terms of basic control theory standards. Likewise, de la Hoz et al. [28] provided a methodology for calculating the overrun cost to the Spanish power system as a result of the large overshoot of the solar PV power goals under RD 661/2007, to later assess the savings achievable by the retroactive cost-containment energy policy issued in the period 2010–2012

as well as the profitability reduction that those retroactive measures could cause on the PV facilities based on the NPV and the IRR. Meanwhile Mir-Artigues et al. [11] assessed the effects of the 2008–2013 cost-containment measures, implemented by the Spanish government after the 2007–2008 PV boom, on the net cash flows and cost effectiveness of PV facilities. Fernández-González et al. [41] assessed the consequences of eliminating the FIT mechanism for solar PV plants in 2012, due to the excessive budgetary burden involved in maintaining that FIT scheme and after many years of institutional volatility, based on a longitudinal sample of 5354 companies from the solar PV sector. In turn, del Río et al. [29] described in detail the main elements of the new Spanish renewable electricity support scheme under RD 413/2014 enacted in 2014 and provided a brief analysis of its main shortcomings. De la Hoz et al. [46] first analyzed RD 413/2014 legal–economic framework for RES electricity generators in Spain by means of a detailed overview and formulation of RD 413/2014 economic model, to subsequently put the spotlight on its effects on the economic performance of the pre-existing grid-connected PV facilities relied on the treasury, the IRR and the NPV. The impact of RD 413/2014 retroactive electricity support scheme on the cost effectiveness of the Spanish solar PV facilities was assessed in [18]. Similarly, de la Hoz et al. [30] assessed RD 413/2014 economic and regulatory framework for RES in Spain as well as its significant impact on the financial performance of the CSP plants based on the treasury, the NPV and the IRR, by means of a detailed overview and formulation of RD 413/2014 remuneration scheme. Likewise, Coronas et al. [54] analyzed the economic feasibility of the Spanish CSP plants under RD 413/2014 framework, based on the IRR, the NPV, the payback period and the LCOE, from a probabilistic perspective using the discounted cash flow-Monte Carlo method. Meanwhile del Río [32] contextualized and assessed the design elements used in the first (January 2016) and second (May 2017) RES auctions under RD 413/2014 in Spain, putting them in the context of international experiences, and analyzed the outcomes obtained in both auctions. Finally, the policy dismantling process of RES policies in two of the pioneer EU countries in supporting RES, i.e., Spain and Czech Republic, was assessed by [16].

1.3. Justification and Main Contributions of the Review

Spain has developed and implemented a great range of actions on promoting RES. Still, it has also been distinguished for becoming one of the most active countries applying cost-containment mechanisms on RES. Perhaps, it could explain why the Spanish legal and economic frameworks, specifically those applied to solar technology power plants, have been widely discussed in the scientific literature.

Nevertheless, to the best of the authors' knowledge, a detailed and complete review of the last 23 years of energy policy regulating the whole solar sector in Spain, namely both PV and CSP technologies, has not been conducted in the academic literature thus far.

In this regard, this academic contribution makes a thorough review of the development of solar energy policy in Spain during the period 1998–2020. This study covers from the enactment of the first SES Law 54/1997 [55], which ushered the process of progressive liberalization of the power sector, until 2020 with the validity of the new SES Law 24/2013 [56] and RD 413/2014 legal–economic framework for RES [57]; but prior to the recent approval of the new economic regime for RES enacted by RD 960/2020 in November 2020 [58]. Moreover, this review integrates and assesses all the relevant information from previously published research works, allowing the readers to enjoy a global vision concerning the most significant insights on the solar energy policy in Spain during the period 1998–2020.

This 23-year comprehensive review of the Spanish solar power sector pathway may be of great interest to any reader in general or specialist immersed in this thematic area who wants to know in considerable detail the trajectory of the solar sector development in Spain from 1998 to 2020 from a regulatory approach. Similarly, this work can be extremely useful for other countries either in the initial development stage or fully immersed in the promotion of solar power sector or any other renewable technology.

After this introduction, the rest of the review is organized as follows. In Section 2, the Spanish solar energy policy is contextualized during the period 1998–2020 based on the different REPs established in the country, as well as the corresponding European directives in which they are supported. Section 2 indicates the goals set in Spain for the development of PV and CSP technologies throughout the analysis period, as well as the actual results obtained, but without going into detail about the reasons for these results in the Spanish solar power sector. Then, Section 3 provides a detailed review of the different legislations that have taken place in Spain in the 1998–2020 period for the regulation of energy production by RES facilities, and specifically, by solar power plants. The analysis period has been divided into four subperiods according to the purposes of the legislation in force, i.e., the 1998–2004 subperiod, the 2004–2008 subperiod, the 2008–2013 subperiod and the 2013–2020 subperiod, to clearly identify and describe the different phases of the evolution of solar energy policy in Spain. Hereafter, Section 4 carries out a critical analysis of the different legislation that has regulated the Spanish RES sector, and specifically the solar power sector, during the period 1998–2020 based on the results and conclusions obtained from the existing literature analyzing this topic. In this case, the assessment has been divided into two clearly differentiated subperiods, i.e., the 1998–2008 promotion stage and the 2008–2020 containment stage. Lastly, conclusions are drawn in Section 5.

2. The Spanish Solar Energy Policy—Contextualization, Main Goals and Results

The development of renewable energies in Spain began to obtain positive results in the 1990s, as a consequence of a strategic energy policy to promote and support the generation of electricity through RES, whose starting point is in the 1980s with the enactment of Law 82/1980, on energy conservation [59], which mainly promoted the hydroelectric production.

The renewable energy power plants were integrated into the SR group, apart from conventional generation facilities, to boost their development by means of economic incentives, which constituted a financial support allowed and encouraged by the EU, given the importance attached to this type of electricity production. The SR concept was regulated in Spain since 1980 and consolidated by RD 2366/1994 [60], on the electricity generation by hydraulic, cogeneration and other RES facilities, and Law 40/1994 [61], on the organization of the national power system.

In December 1999, in response to the commitment emanating from the SES Law 54/1997 [55] enacted two years earlier, the REP for the 10-year period 2000–2010 [62] was approved in Spain. Its final objective was to promote and support electricity production from RES to achieve the major goals of the Spanish energy policy, i.e., the diversification of primary energy sources to ensure the security of supply, the efficient use of available energy resources and the respect to the environment.

In general terms, the REP 2000–2010 set the goal of reaching 12% of the primary energy consumption from RES in Spain by 2010, taking into account that this percentage was of 6.3% in 1998. The same overall target set in the White Paper for a Community Strategy and Action Plan for renewable energies by the European Commission in November 1997 [63].

As regards the solar power sector, the REP 2000–2010 set the goal of adding 135 MW of new solar PV capacity (115 MW connected to the grid and 20 MW isolated) and the first 200 MW of CSP capacity by 2010 [62].

In September 2001, two years after the enactment of the REP 2000–2010, it was approved the Directive 2001/77/CE with the aim of promoting the electricity generated from RES in the EU [64]. The Directive 2001/77/CE required Member States to instituted national indicative goals for the consumption of electricity generated from RES in terms of percentage of electricity consumption. It established an objective of reaching a 22% share of RES in the final electricity consumed in the EU as a whole by 2010. For Spain, this value was set at 29.4%. Likewise, it also considered the indicative goal set by the White Paper of reaching 12% of the total primary energy consumption with RES in 2010 [64].

In May 2003, it was issued the Directive 2003/30/CE on the promotion of the use of biofuels or other renewable fuels in transport [65]. It established the goal of reaching a 5.75% market share of biofuels in the transport sector in 2010.

At the halfway point of the REP 2000–2010, the global growth in renewable energies was significantly lower than expected. Specifically, at the end of 2004 only 28.4% of the global increase foreseen for the presence of RES in the Spanish energy system had been fulfilled. In this regard, only three RES were evolving satisfactorily: wind energy, biofuels and biogas. In contrast, other renewable technologies such as solar were developing well below the pace necessary to achieve the targets established [66].

Moreover, the strong growth in the Spanish energy intensity in the period 2000–2004 was an additional compelling reason to the REP 2000–2010 to meet the RES targets set for 2010 [66].

Accordingly, the REP 2000–2010 was reviewed in August 2005 by the 5-year REP 2005–2010 [66], with the aim of reinforcing the major goals of the Spanish energy policy, increasing the security and quality of the electricity supply and improving the respect for the environment. With this review, the goal was to uphold the agreement to cover at least 12% of total energy consumption with RES in 2010, as well as reaching 29.4% of electricity production with renewables (Directive 2001/77/CE) and using 5.75% of biofuels in transport (Directive 2003/30/CE) for that year [66].

The REP 2005–2010 set new targets to be met for the different renewable sectors by 2010. Regarding the solar sector, the goal for the accumulated installed power of both PV and CSP increased, from 144 MW to 400 MW (93% of grid-connected PV systems and 7% of isolated facilities) and from 200 MW to 500 MW, respectively [66].

In April 2009, the Directive 2009/28/CE on the promotion of the use of energy from RES entered into force [67]. It amended and repealed the Directive 2001/77/CE and the Directive 2003/30/CE. The Directive 2009/28/CE established binding national objectives, which for Spain coincided with those of the EU as a whole (20% of gross final energy consumption from RES by 2020 and 10% in the transport sector). The Directive 2009/28/CE was part of the so-called European Energy and Climate Change Package, which included as objectives for 2020 the known “20–20–20” targets, i.e., a 20% share of renewable energies in the EU’s final energy consumption, a 20% improvement in energy efficiency and a 20% reduction in GHG emissions compared to 1990 levels [67].

Once the period of validity of the REP 2005–2010 was exhausted and according to the mandates of RD 661/2007, which regulated the power generation activity under the SR, and Law 2/2011 on Sustainable Economy, the new REP for the period 2011–2020 was approved in November 2011 [68]. The REP 2011–2020 proposed a 20.8% share of renewable energies in the gross final energy consumption of Spain in 2020, reaching a 11.3% share of RES in the transport consumption in that same year, thus exceeding the mandatory minimum goals established for Spain in the Directive 2009/28/CE. The 20.8% share of RES in the gross final energy consumption represented the 39% of the total electricity consumption [68].

The REP 2011–2020 set new non-binding targets to be met for the different renewable sectors by 2020. As for the solar power sector, it established as goals for the accumulated capacity and the energy generated by 2020, 7250 MW and 12,350 GWh, respectively, for the solar PV technology, and 4800 MW and 14,378 GWh, respectively, for the CSP sector [68].

Figures 1 and 2 show the progression of the Spanish solar power sector in the period 1998–2020 for PV and CSP technology, respectively, in terms of installed capacity and produced energy. In both figures the targets set by the different REPs, namely REP 2000–2010, REP 2005–2010 and REP 2011–2020, are compared with the actual results obtained. Additionally, the period of validity of each REP has been marked in both figures.

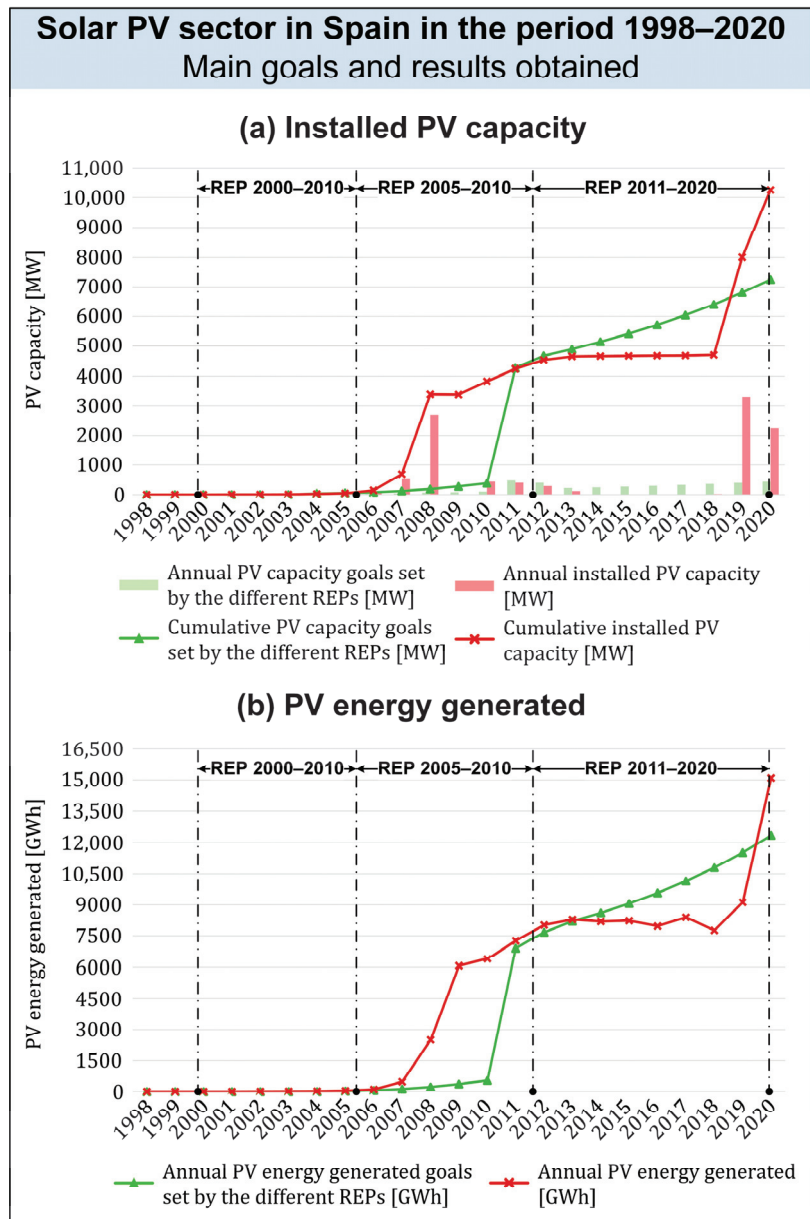


Figure 1. Evolution of the solar PV sector in Spain in the period 1998–2020 in terms of: (a) installed PV capacity; (b) PV energy generated. Source: self-elaboration based on [62,66,68,69].

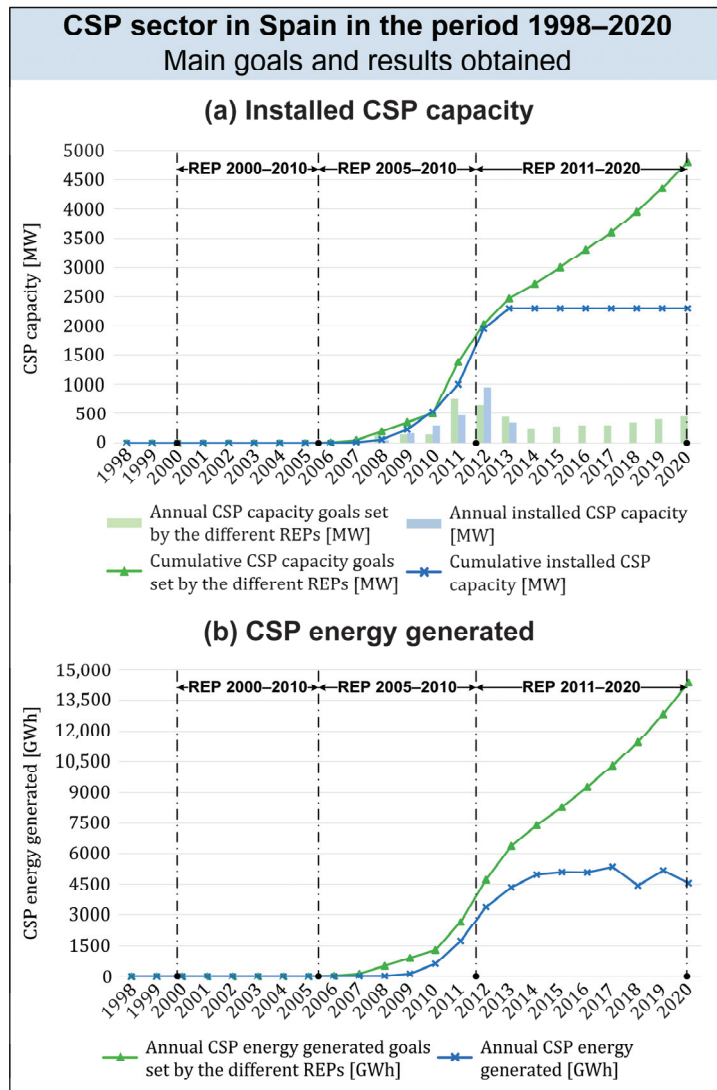


Figure 2. Evolution of the CSP sector in Spain in the period 1998–2020 in terms of: (a) installed CSP capacity; (b) CSP energy generated. Source: self-elaboration based on [62,66,68,69].

In Figure 1a, the cumulative PV capacity goals set by the different REPs are represented with a green solid line with triangle symbols, while the actual cumulative installed PV capacity is plotted by a red solid line with cross symbols. In turn, the annual PV capacity targets set by the different REPs are represented with green-colored vertical bars, while the actual annual installed PV capacity is plotted with red-colored vertical bars. In Figure 1b, the annual PV energy generated goals set by the different REPs are shown using a green solid line with triangle symbols, while the actual annual PV energy generated is represented by a red solid line with cross symbols.

The same pattern is followed in Figure 2 where the Spanish CSP sector is analyzed. In this case, the green color is kept to show the targets set by the different REPs for the CSP technology, but the color used to depict the actual results of this technology is changed to blue.

On the one hand, before describing and analyzing the period in detail taking into account the different regulatory frameworks in force, the following first lessons can be learned from Figure 1 regarding the evolution of the Spanish solar PV sector in the period 1998–2020:

- In the period 1998–2004, i.e., the period of validity of the REP 2000–2010, the foundations of the Spanish energy regulation regarding the promotion of RES began to be laid, but the solar PV sector did not evolve as planned. In this period, the cumulative installed PV capacity and the energy generated went from 1.5 MW and 1.1 GWh, respectively, in 1998, to 22.8 MW and 16.9 GWh, respectively, in 2004, far from the REP 2000–2010 forecasts. Even so, at the end of 2004 there were a total of 3266 PV facilities in Spain, compared to the 12 existing in 1998;
- The period 2005–2010, i.e., the period of validity of the REP 2005–2010, stood out for the existence of a very favorable legal–economic framework for PV facilities in Spain, in line with the PV energy promotion policy of the period 1998–2004. The moderate growth of the years 2005–2006 gave way to what is known as the “Spanish solar PV boom” in the years 2007–2008. In this 5-year period, the cumulative installed PV capacity and the energy generated increased to 3829.7 MW and 6073 GWh, respectively, by 2010, well above the REP 2005–2010 forecasts. At the end of 2010 there were a total of 54,949 PV plants in Spain, reaching a 2.3% share of solar PV energy in the energy demand;
- In the period 2011–2020, i.e., the period of validity of the REP 2011–2020, a series of regulatory containment frameworks were approved. From 2010 to 2013 the solar PV sector continued to increase its cumulative installed PV capacity but with a progressive downward trend until the stagnation of this technology in the years 2014–2018. At the end of the period, i.e., years 2019–2020, there was a new boom higher than that of 2007–2008 as a result of the call for new auctions for the solar PV technology. In this period, the cumulative installed PV capacity and the energy generated increased to 10,254.8 MW and 15,092.9 GWh, respectively, in 2020, well above the REP 2011–2020 forecasts. At the end of 2020 there were a total of 61,543 PV facilities in Spain, reaching a 6.1% share of solar PV energy in the energy demand.

On the other hand, as regards the evolution of the Spanish CSP sector in the period 1998–2020, the following first lessons can be learned from Figure 2:

- At the end of the period 1998–2004, i.e., the period of validity of the REP 2000–2010, there were no CSP plant in operation or in the construction stage in Spain;
- In the period 2005–2010, i.e., the period of validity of the REP 2005–2010, the first CSP facilities were put into operation as a result of the existence of a more favorable legislation for CSP in Spain. Since the commissioning of the first CSP plant in 2007, the sector began a continuous growth until the end of the period. In this 5-year period, the cumulative installed CSP capacity and the energy generated went from 11 MW and 7.6 GWh, respectively, in 2007, to 531.9 MW and 620.9 GWh, respectively, in 2010, quite close to the REP 2005–2010 forecasts. At the end of 2010 there were a total of 13 CSP facilities in Spain, compared to the 1 existing in 2007, reaching a 0.2% share of solar CSP energy in the energy demand;
- At the beginning of the period 2011–2020, i.e., the period of validity of the REP 2011–2020, and more specifically in the years 2011–2012, there was the boom of the Spanish CSP sector. Since then, 2013 was the last year in which commercial CSP capacity was installed in Spain due to the series of regulatory containment frameworks that were approved. In this period, the cumulative installed CSP capacity and the energy generated increased to 2299.4 MW and 4542.6 GWh, respectively, in 2020, well below the REP 2011–2020 forecasts. At the end of 2020 there were a total of 50 CSP plants in Spain, reaching a 1.8% share of solar CSP energy in the energy demand.

3. Overview of the 1998–2020 Legal–Economic Frameworks for the Solar Power Plants in Spain

The Spanish solar power sector has suffered continuous and considerable changes in its regulation in the period 1998–2020 since the enactment of the SES Law 54/1997, denoting a great dynamism and in turn generating high uncertainty in the electricity sector.

In Figure 3 the different legislations regulating the solar sector in Spain during the period 1998–2020 have been plotted chronologically. The European directives are displayed in purple-colored boxes, the Spanish rules in blue-colored boxes and the REPs in green-colored ones. In turn, the different legislative changes have been grouped into four regulatory subperiods according to their purposes, to correctly overview and understand the Spanish solar energy policy development in the 1998–2020 period.

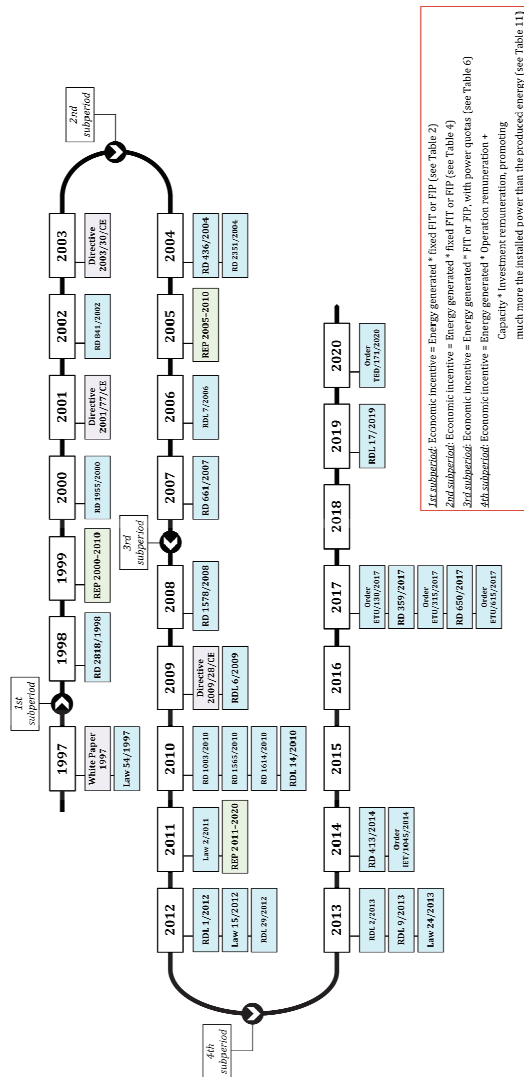


Figure 3. Timeline with the different legislations governing the Spanish solar power sector from 1998 to 2020. Source: self-elaboration.

3.1. The 1998–2004 Subperiod: Laying the Foundations of the Spanish Solar Power Sector

As background to the 1998–2004 subperiod, it is worth highlighting the enactment of the SES Law 54/1997 [55] in November 1997, which set a new operating model for producers of electricity based on free competition in Spain, while seeking to enhance energy efficiency and decrease the energy consumption as well as the GHG emissions. It also incorporated the targets set by the White Paper [63] for 2010, later included in the REP 2000–2010.

The SES Law 54/1997 distinguished two different groups of energy producers, namely those that were part of the SR, which enjoyed of a certain legal and economic singularity, compared to those that were part of the ordinary regime, i.e., conventional technology plants. Specifically, the generation activity under the SR included the production facilities with a capacity not exceeding 50 MW using as primary energy renewable energy, waste or cogeneration. In turn, all those generation power plants that had been authorized, as well as its characteristics and, especially, its power capacity, should be enrolled in the administrative registry of electricity production plants created by the SES Law 54/1997 [55].

Finally, the SES Law 54/1997 required the enactment of a decree adapting the functioning of the SR to the new regulation, namely RD 2818/1998, which was approved in December 1998 [70]. Then, with the enactment of RD 2818/1998, subsequently amended first by RD 1955/2000 [71] of December 2000, and later by RD 841/2002 [72] of August 2002, started what could be considered to be the first regulatory subperiod in which the rules and guidelines set by SES Law 54/1997 began to be developed. During the 1998–2004 subperiod, the foundations of the Spanish electricity production sector from RES, and more specifically of the Spanish solar power sector, were laid by means of the corresponding legislation. That first subperiod was extended until the first part of 2004 when the adoption of a new legal framework, namely RD 436/2004 [73], updated the legal–economic regime of the electricity generation activity under the SR.

Tables 1 and 2 provide a detailed overview of the main features of the different regulatory frameworks and economic regimes, respectively, in force for solar power plants in Spain in the period 1998–2004, namely RD 2818/1998 and its revisions by RD 1955/2000 and RD 841/2002.

Table 1. Major characteristics of the different regulatory frameworks in force for the Spanish solar power systems in the period 1998–2004. Source: self-elaboration based on [70–72].

Legislation	Main Characteristics
RD 2818/1998 of December 1998 [70]	
Subject	Development of Law 54/1997 with the aim of creating a favorable framework to promote energy generation facilities included in the SR without incurring in discriminatory situations that could curtail free competition. However, setting differentiated situations for those power systems that contributed more effectively to the achievement of the goals established
Previous regulations repealed or modified	Derogation of RD 2366/1994
RES goals	12% of primary energy consumption from RES by 2010
SR group for solar technology	All power plants with a capacity not exceeding 50 MW using solar energy as primary energy were sorted in the group b.1, not distinguishing between PV or CSP technologies
Economic regime	<ul style="list-style-type: none"> > Two remuneration options for the electricity produced by the SR generation facilities: <ul style="list-style-type: none"> (a) A fixed regulated tariff different from the pool price, i.e., a fixed FIT (b) A premium on top of the electricity pool price, i.e., a FIP, plus an additional complement for reactive energy > Both incentive mechanisms were set without time limit for the solar technology > Review of premiums and prices every 4 years according to the evolution of the market electricity price, the participation of power plants in the coverage of demand and its effect on the power system technical management > See Table 2 for a detailed summary of RD 2818/1998 economic scheme for the solar power plants

Table 1. Cont.

Legislation	Main Characteristics
Administrative features	–
Other issues	The solar facilities included in group b.1 of the SR could incorporate all the energy produced into the grid, as long as the 12% share of RES in the total energy demand was not reached
RD 1955/2000 of December 2000 [71]	
Subject	Inclusion of power plants only using solar thermal energy as primary energy in group b.3 of the SR together with those using tidal, wave, geothermal and hot and dry rocks energies
Previous regulations repealed or modified	Amendment of RD 2818/1998
RES goals	–
SR group for solar technology	b.1 for solar PV technology plants and b.3 for CSP technology facilities (with an installed capacity not exceeding 50 MW)
Economic regime	See Table 2 for a detailed summary of the changes introduced by RD 1955/2000 in RD 2818/1998 economic scheme for the solar power plants
Administrative features	–
RD 841/2002 of August 2002 [72]	
Subject	New classification for the SR solar facilities set by RD 2818/1998
Previous regulations repealed or modified	Amendment of RD 2818/1998 and suppression of the modifications introduced by RD 1955/2000 concerning the CSP plants
RES goals	–
SR group for solar technology	b.1.1 for solar PV facilities and b.1.2 for CSP plants (with an installed power not exceeding 50 MW)
Economic regime	See Table 2 for a detailed summary of the changes introduced by RD 841/2002 in RD 2818/1998 economic scheme for the solar power plants
Administrative features	–
Other issues	Unlike both RD 2818/1998 and RD 1955/2000, RD 841/2002 stated that fuel could be used to keep the temperature of the heat storage system of CSP facilities in subgroup b.1.2 during interruption periods of power production

Table 2. Major characteristics of the different economic regimes in force for solar power systems in Spain in the period 1998–2004. Source: self-elaboration based on [70–72].

Legislation	Technology	SR Group	Rated Power	Remuneration Options		Time Limit	Review and Update
				FIT	FIP ¹		
				Regulated Tariff [cEUR/kWh]	Premium [cEUR/kWh]		
RD 2818/1998	Solar PV	b.1	$P \leq 5$ kW	39.6668	36.0607	No	For both FIT and FIP options: <ul style="list-style-type: none"> No annual update Review every 4 years
			$P > 5$ kW	21.6364	18.0304		
	Solar CSP	b.1	$P \leq 5$ kW	39.6668	36.0607	No	
			$P > 5$ kW	21.6364	18.0304		
RD 1955/2000	Solar PV	b.1	$P \leq 5$ kW	39.6668	36.0607	No	For both FIT and FIP options: <ul style="list-style-type: none"> No annual update Review every 4 years
			$P > 5$ kW	21.6364	18.0304		
	Solar CSP	b.3	Any	6.7313	3.2755	No	
RD 841/2002	Solar PV	b.1.1	$P \leq 5$ kW	39.6668	36.0607	No	For both FIT and FIP options: <ul style="list-style-type: none"> No annual update Review every 4 years
			$P > 5$ kW	21.6364	18.0304		
	Solar CSP	b.1.2	Any	–	12.0202	No	

¹ This table only shows the values of the FIP components fully established in a regulatory manner, i.e., the premiums. Thus, the electricity market price and the reactive energy complement must be added to this economic parameter to obtain the total FIP of the power plant.

3.2. The 2004–2008 Subperiod: Ratifying the Unwavering and Forceful Commitment to Solar Power Projects in Spain

The second regulatory period began with the approval of RD 436/2004 in March 2004 [73], which derogated both RD 2818/1998 and RD 841/2002. The 2004–2008 subperiod was characterized by an extremely favorable economic framework for RES facilities, and especially for solar power plants, first under RD 436/2004 [73] and later under RD 661/2007 [74], which repealed RD 436/2004. Thus, ratifying the Spanish government its strong commitment to the development and deployment of solar power plants.

Tables 3 and 4 provide a comprehensive overview of the main features of the different regulatory frameworks and economic regimes, respectively, in force for the Spanish solar power facilities in the period 2004–2008, namely RD 436/2004 and RD 661/2007.

Table 3. Major characteristics of the different regulatory frameworks in force for solar power systems in Spain in the period 2004–2008. Source: self-elaboration based on [73,74].

Legislation	Main Characteristics
RD 436/2004 of March 2004 [73]	
Subject	Setting the methodology for systematizing and updating the legal–economic regime of the power generation activity in the SR
Previous regulations repealed or modified	Derogation of RD 2818/1998 and RD 841/2002
RES goals	<ul style="list-style-type: none"> ➤ As for the whole RES sector, 29.4% of electricity generation and 12% of total energy consumption from RES by 2010, without increasing the cost of production of the Spanish electricity system ➤ As for the solar power sector, 150 MW of solar PV and 200 MW of CSP eligible for the initial remuneration
SR group for solar technology	b.1.1 for solar PV facilities and b.1.2 for CSP facilities (with an installed capacity not exceeding 50 MW)
Economic regime	<ul style="list-style-type: none"> ➤ Two remuneration options for the electricity produced by the SR generation facilities: <ol style="list-style-type: none"> (a) The sale of their electricity production to a distribution company receiving a fixed FIT for all periods (b) The sale of its electricity production to the daily market receiving a premium plus an incentive on top of the electricity market price, i.e., a FIP ➤ Regardless the chosen electricity selling option, all solar power plants would also perceive a complement for reactive energy ➤ The chosen selling option should be kept for a minimum period of 1 year ➤ Both remuneration mechanisms were indexed to the yearly average electricity tariff (AET), which for 2004 had a value of 7.2072 cEUR/kWh. The AET was established as a relationship between the expected costs necessary to remunerate the electricity supplying activities and the forecast, for the same period considered, of the final energy demand determined by the Spanish government [75] ➤ After the first 25 years of receipt of any of the remuneration mechanisms, those public subsidies were reduced for the solar technology ➤ The first revision of FIT, premiums, incentives and complements was set for 2006. Thereafter, these economic parameters would be reviewed every 4 years, unless subgroup b.1.1 reached 150 MW of installed capacity or subgroup b.1.2 reached 200 MW ➤ The reviews would be made according to the evolution of the costs associated with the generation technologies, the participation degree of the SR in the energy production and its technical-economic management of the system. Moreover, the revisions would apply only to facilities coming into operation after the entry into force of the agreed revisions, thus eliminating their retroactive character ➤ See Table 4 for a detailed summary of RD 436/2004 economic scheme for the solar power plants

Table 3. Cont.

Legislation	Main Characteristics
Administrative features	From the end of 2005 until the approval of RD 661/2007 it was required a guarantee of 2% of the facility budget to request access to the transmission grid, but not for the distribution grid. The guarantee would be canceled when the petitioner obtained the commissioning certificate for the facility
Other issues	<ul style="list-style-type: none"> ➤ The CSP facilities in subgroup b.1.2 could use auxiliary equipment consuming fuels, i.e., propane or natural gas, only to maintain the heat storage system temperature. The annual fuel consumption, only during periods of interruption of electricity generation, for CSP facilities receiving a FIT should be less than 12% of their power generation. Otherwise, that percentage would raise to 15%, without any time-limit of fuel use, for CSP plants selling electricity to the pool ➤ At the end of 2004, RD 2351/2004 [76] modified the provisions on fuel usage for CSP plants belonging to the subgroup b.1.2 initially made by RD 436/2004. RD 2351/2004 enabled the use of any kind of fuel to maintain the heat transfer fluid temperature in the CSP facilities to compensate for the lack of solar irradiation that could compromise the expected supply of electricity. Thus, eliminating the requirement of fuel usage only during the periods of interruption of power production, while maintaining the percentages regarding the generation of electricity from fuel depending on the remuneration option chosen by the CSP facility
RD 661/2007 of May 2007 [74]	
Subject	Regulation of some technical issues to contribute to the expansion of SR technologies, safeguarding the safety of the power system and guaranteeing its quality of supply, as well as to minimize restrictions on production
Previous regulations repealed or modified	Suppression of RD 436/2004
RES goals	<ul style="list-style-type: none"> ➤ As for the whole RES sector, 29.4% of electricity generation and 12% of total energy consumption from RES by 2010 ➤ As for the solar power sector, 371 MW of solar PV and 500 MW of CSP
SR group for solar technology	b.1.1 for solar PV plants and b.1.2 for CSP facilities (with an installed capacity not exceeding 50 MW)
Economic regime	<ul style="list-style-type: none"> ➤ The basic regulatory structure of the SR was maintained by RD 661/2007. Nevertheless, based on Royal Decree Law (RDL) 7/2006 [77], which set that the AET future revisions would not apply to the remuneration of RES under the SR, it definitively decoupled the SR remuneration from the AET, ensuring a reasonable remuneration to the owners of the SR power plants for their investments ➤ Two remuneration options for the electricity produced by the SR generation facilities: <ul style="list-style-type: none"> (a) A fixed FIT for all periods (b) A premium on top of the electricity market price, i.e., a FIP ➤ RD 661/2007 bounded the FIP, i.e., the sum of the electricity pool price and the premium, between an upper boundary and a lower boundary. The new cap and floor system protected the promoter of the power plants under the FIP remuneration option when the income derived from the pool price was too low, and eliminated the premium when the pool price was high enough to ensure the coverage of its costs, thus removing irrationalities in the remuneration of technologies, whose costs were not directly linked to oil prices in international markets ➤ Regardless of the selected electricity selling option, all solar power plants would also receive a complement for reactive energy. This complement was set as a percentage, in accordance with the power factor with which the energy was delivered, of the value of 7.8441 cEUR/kWh, which would be reviewed annually ➤ The chosen selling option should be kept for a minimum period of 1 year ➤ After the first 25 years of receipt of any of the remuneration mechanisms, those public subsidies were reduced for the solar technology ➤ The FIT, premiums, complements and upper and lower bounds set by RD 661/2007 would be updated annually taking as a reference the rise in the consumer price index (CPI) minus 25 basis points (BP) until 31 December 2012, and 50 BP thereafter. However, in 2010, the year in which the REP 2005–2010 was expected to end, a review of these economic parameters was expected, which would be evaluated according to the variation in costs associated with each technology, the participation degree of the SR in the production of energy and its incidence in the technical-economic management of the system, ensuring a reasonable return. From then on, reviews would be carried out every 4 years

Table 3. Cont.

Legislation	Main Characteristics
Economic regime	<ul style="list-style-type: none"> ➤ The revisions of the regulated tariff as well as the upper and lower bounds would not affect the facilities whose commissioning certificate had been granted before 1st January of the second year after that in which the revision was carried out ➤ See Table 4 for a detailed summary of RD 661/2007 economic scheme for the solar power plants ➤ An additional mechanism to set the maintenance period of the regulated tariffs and premiums was established by RD 661/2007. Accordingly, once 85% of the power goal of a technology was reached, a maximum period of not less than 1 year would be set. During this period, those power plants properly enrolled in the administrative register of generation plants under the SR would be entitled to the corresponding premiums or regulated tariffs under RD 661/2007
Administrative features	<ul style="list-style-type: none"> ➤ RD 661/2007 requested guarantees to process the access both to the distribution grid as well as to the transmission grid. For the PV facilities these guarantees were of 500 EUR/kW, while for the CSP plants were of 20 EUR/kW. The guarantee would be canceled when the petitioner obtained the commissioning certificate for the facility ➤ It established priority of access and connection to the electricity network of RES power plants
Other issues	RD 661/2007 admitted the option of hybridization of different fuels and/or technologies. Among the technologies that could participate in hybridizations was CSP (subgroup b.1.2), but not solar PV (subgroup b.1.1)

3.3. The 2008–2013 Subperiod: The Containment of the Spanish Solar Power Sector

In August 2007, i.e., 3 months after entering into force RD 661/2007, 85% of the installed PV power target for 2010 was exceeded. Specifically, 1000 MW of installed PV capacity had already been reached in May 2008.

In accordance with the remuneration maintenance mechanism set by RD 661/2007 [74], as of August 2007, once 85% of the installed PV power target had been reached, the maximum period of not less than 1 year began to count. Once this transition period was over, the remuneration model established by RD 661/2007 for solar PV technology plants in subgroup b.1.1 would be reviewed and updated. Accordingly, RD 1578/2008 was approved in September 2008 [78].

With RD 1578/2008 of September 2008 began the containment stage of the Spanish solar power sector, which would later be extended to the rest of the RES power sector.

Prior to the containment stage, the SR regulation did not establish sufficient mechanisms that allowed the planning of the power plants, nor the amount and the time limit of their remuneration premiums and therefore the effect on the costs attributed to the tariff scheme. Furthermore, the increasing impact of the SR remuneration on the tariff deficit, i.e., the lack of incomes of the electrical system to cover all its expenditures, could jeopardize the short-term sustainability of the electrical system, both from a technical perspective, also compromising the financial sustainability of the facilities already completed, and from an economic standpoint owing to its impact on the electricity tariff. Thus, unlike previous legislations aimed mainly at the development and promotion of RES, the new measures approved by the Spanish government as of 2009 would be mainly aimed at reducing the cost of the RES technologies to the electricity system.

Accordingly, in May 2009 RDL 6/2009 [79] came into effect. The measures envisaged in RDL 6/2009, through the creation of a register of pre-allocation of remuneration (RPAR), allowed knowing the facilities that were projected, as well as those that met the conditions to be executed and access the electrical system with all legal provisions, its capacity and the effect on the costs of the electricity tariff and its schedule. It established the principle of sufficiency of access tolls to cover all the costs of the regulated activities as of 2013, so that from then on, no tariff deficit could appear. As solar PV technology had its specific framework, namely RD 1578/2008, these power plants were not affected by RDL 6/2009.

Table 4. Major characteristics of the different economic regimes in force for solar power systems in Spain in the period 2004–2008. Source: self-elaboration based on [73,74].

Legislation	Technology	SR Group	Rated Power	Remuneration Options			Time Limit	Review and Update
				FIT Regulated Tariff [cEUR/kWh]	Premium [cEUR/kWh]	FIP ¹ Incentive [cEUR/kWh]		
RD 436/2004	Solar PV	b.1.1	$P \leq 100$ kW	575% of AET	–	–	First 25 years	For both FIT and FIP options: <ul style="list-style-type: none"> • Annual update according to AET • Review in 2006 and thereafter every 4 years or when reaching 150 MW
				460% of AET	–	–	Thereafter	
	300% of AET	250% of AET	10% of AET	First 25 years				
	240% of AET	200% of AET	10% of AET	Thereafter				
RD 661/2007	Solar CSP	b.1.2	Any	300% of AET	250% of AET	10% of AET	First 25 years	For both FIT and FIP options: <ul style="list-style-type: none"> • Annual update according to AET • Review in 2006 and thereafter every 4 years or when reaching 200 MW
				240% of AET	200% of AET	10% of AET	Thereafter	
	44.0381	–	–	First 25 years				
	35.2305	–	–	Thereafter				
RD 661/2007	Solar PV	b.1.1	$100 \text{ kW} < P \leq 10$ MW	41.7500	–	–	First 25 years	For both FIT and FIP options: <ul style="list-style-type: none"> • Annual update according to CPI • Review in 2010 and thereafter every 4 years or not less than 1 year after reaching 85% of 371 MW
				33.4000	–	–	Thereafter	
	22.9764	–	–	First 25 years				
	18.3811	–	–	Thereafter				
RD 661/2007	Solar CSP	b.1.2	Any	26.9375	25.4000	–	First 25 years	For both FIT and FIP options: <ul style="list-style-type: none"> • Annual update according to CPI • Review in 2010 and thereafter every 4 years or not less than 1 year after reaching 85% of 500 MW
				21.5498	20.3200	–	Thereafter	

¹ This table only shows the values of the FIP components fully established in a regulatory manner, i.e., the premiums and the incentives. Thus, the electricity market price and the reactive energy complement must be added to these economic parameters to obtain the total FIP of the facility.

The Resolution of 19 November 2009 of the State Secretariat for Energy [80] published the ordering of the projects presented to the RPAR for electrical energy production facilities provided for in RDL 6/2009. The electrical management system allowed the incorporation of 3100 MW of capacity from new renewable facilities per year, until 2014, without compromising the technical-economic sustainability of the electrical system. Thus, it was necessary to defer the commissioning of the registered facilities.

The entry into operation of the registered CSP power plants was distributed in four successive steps until the end 2013 according to the following accumulated deployment rate: (a) step 1: 850 MW, (b) step 2: 1350 MW, (c) step 3: 1850 MW and (d) step 4: rest of registered power under the provisions of RDL 6/2009 [80].

The growth in the number of generation facilities from RES, cogeneration and waste under the SR had been very important until 2010, becoming especially noteworthy for wind, solar PV and CSP technologies that reached and even exceeded the installed power targets set for that year. Thus, Spain became one of the leading countries in the expansion of these technologies. This growth occurred thanks to the existence of a predictable, stable and solid legal-economic support mechanism.

In this context, the management experience accumulated as a result of the application of the SR legal framework, advised the redefinition of certain concepts and the adaptation of procedures to the evolution of the sectors under the SR. Thus, the support regime should be adapted, preserving the legal certainty of investments and the principle of reasonable return to correct the imbalance revealed between production costs and the value of premiums.

Moreover, since the approval of RDL 6/2009, there had been a set of supervening circumstances such as the drop in the electricity demand because of the Spanish recession, the reduction of market prices due to the fragile international economic situation or the increase in the electricity production from RES due to favorable weather conditions, with a direct impact on the electricity system tariff deficit. That contextual situation did not have symmetrical effects in all the electricity sectors. Although the ordinary regime (conventional power plants) saw their operating hours and revenues reduced because of the fall in prices on the wholesale market, the SR generators were awarded under its specific regime that ensured selling the electricity produced through its preferential entry into the system.

Accordingly, five prominent regulations for the SR power plants and, specifically, for the solar power sector, were enacted by the Spanish government in 2010, i.e., RD 1003/2010 [81], RD 1565/2010 [82], RD 1614/2010 [83], RDL 14/2010 [84] and Law 2/2011 [85].

However, the measures adopted until then were not sufficient, putting at risk the final goal of suppressing the tariff deficit as of 2013 set by RDL 6/2009. The tariff deficit constituted a barrier for the adequate development of the electricity sector as a whole and in particular for the continuation of the policies to promote electricity production from RES. Thus, the complex economic and financial situation made it necessary to approve new containment measures in 2012, namely RDL 1/2012 [86], Law 15/2012 [87] and RDL 29/2012 [88].

Tables 5 and 6 provide a comprehensive summary of the main features of the different regulatory frameworks and economic regimes, respectively, in force for the Spanish solar power plants in the period 2008–2013. In turn, Table 7 shows the reference equivalent operating hours for CSP technology facilities established by RD 1614/2010, while Tables 8 and 9 display the reference equivalent operating hours for PV facilities established by RDL 14/2010 and the specific reference equivalent operating hours for PV plants under RD 661/2007 until 31 December 2013, respectively. The reference equivalent operating hours for the PV plants were classified according to the solar climatic zone where the PV facilities were located as well as by technology, whereas the equivalent operating hours for the facilities under RD 661/2007 until 31 December 2013 were classified only by technology.

Table 5. Major characteristics of the different regulatory frameworks in force for solar power systems in Spain in the period 2008–2013. Source: self-elaboration based on [78,79,81–88].

Legislation	Main Characteristics
RD 1578/2008 of September 2008 [78]	
Subject	Setting the new economic framework for PV plants which obtained their definitive registration in the administrative register of the SR production facilities after 29 September 2008
Previous regulations repealed or modified	Amendment of RD 661/2007 for PV facilities in subgroup b.1.1 which obtained their definitive registration in the administrative register of the SR production facilities after 29 September 2008
RES goals	–
SR group for solar technology	Type I for roof-mounted or façade-mounted PV facilities, which in turn are subdivided into (a) subtype I.1 for those up to 20 kW of rated power and (b) subtype I.2 for those beyond 20 kW of rated power, and type II for ground-mounted PV plants and not included in type I
Economic regime	<ul style="list-style-type: none"> ➤ The new regulated tariff for the first call set by RD 1578/2008 for subtype I.1 PV plants under this remuneration option was set to 34.00 cEUR/kWh, while for subtype I.2 and type II PV facilities it was set to 32.00 cEUR/kWh. The regulated tariff for subtype I.1 facilities could never be less than that for subtype I.2 PV plants ➤ The values of the regulated tariff corresponding to the facilities enrolled in the RPAR associated with subsequent calls would be calculated based on the values of the previous call. If during two successive calls, 50% of the power quota for a type or subtype was not reached, the tariff for the next call could be increased by the same proportion that would be cut if the quota were covered ➤ For each call for registration in the RPAR, power quotas were established, consisting of base powers, and where appropriate, additional powers transferred, for each type of PV plant. For the first-year calls, the base powers were 66.75 MW for type I PV facilities (10% for subtype I.1 and 90% for subtype I.2) and 33.25 MW for type II PV plants ➤ The power quotas corresponding to the second and subsequent year calls would be calculated taking as a reference the base powers of the calls corresponding to the previous year, increasing or reducing them by the same cumulative percentage rate that reduced or increased, respectively, the remuneration corresponding to the calls held during the previous year. The mechanism for the transfer of additional power to the base power for the next call was established when some or all the power quotas of a call were not covered ➤ For type II facilities, extraordinary additional power quotas of 25 MW for 2009 and 15 MW for 2010 were established per call ➤ The rationalization of remuneration was considered necessary and, therefore, the new framework for PV plants modified the economic regime downwards, following the expected technology evolution, with a long-sighted prospect. Just as an insufficient remuneration would make investments unfeasible, a disproportionate remuneration could have a considerable impact on the costs of the electricity system ➤ The regulated tariff applicable to a PV facility would be kept for a maximum of 25 years from the commissioning date or the registration of the facility in the RPAR

Table 5. Cont.

Legislation	Main Characteristics
Economic regime	<ul style="list-style-type: none"> ➤ The new FIT established by RD 1578/2008 would be updated annually taking as a reference the rise in the CPI minus 25 BP until 31 December 2012, and 50 BP thereafter, as of 1st January of the second year after the call in which they were set. However, RD 1578/2008 contemplated the modification of the remuneration of the activity of production of electrical energy through solar PV technology in 2012, given the technological evolution of the sector and the market as well as the performance of the remuneration regime ➤ See Table 6 for a detailed summary of RD 1578/2008 economic scheme for the solar PV facilities
Administrative features	<ul style="list-style-type: none"> ➤ To be entitled to the remuneration defined in RD 1578/2008, it was necessary to register, in advance, the facility projects in the RPAR. There were four annual calls to be able to register in this RPAR, while the maximum power of the PV facilities enrolled in the RPAR could not exceed 2 MW for type I facilities and 10 MW for type II plants ➤ RD 1578/2008 also requested guarantees to process the access both to the distribution grid as well as to the transmission grid. These guarantees were of 50 EUR/kW for subtype I.1 PV plants and of 500 EUR/kW for subtype I.2 and type II PV facilities. The guarantee would be canceled when the petitioner obtained the corresponding commissioning certificate for the power plant
Other issues	<ul style="list-style-type: none"> ➤ A new definition of power capacity was set to streamline the implementation of large plants on land belonging to a multiplicity of owners, in such a way as to avoid the division of a single facility into several smaller ones to obtain a more favorable remuneration framework ➤ It proposed a new mechanism for setting the annual power target that would evolve upwards in a coordinated manner with technological improvements, instead of using the total cumulative power
RDL 6/2009 of May 2009 [79]	
Subject	Control of the implementation of new power plants under the SR
Previous regulations repealed or modified	-
RES goals	-
SR group for solar technology	b.1.2 for CSP facilities (PV plants in subgroup b.1.1 not affected)
Economic regime	<ul style="list-style-type: none"> ➤ In the case that the SR projects enrolled did not cover the power objective, RD 661/2007 economic framework would be kept until the goal was reached. However, if the power goal was exceeded, RD 661/2007 remuneration would be applied to all the enrolled projects, but would not be extended beyond ➤ A new regulatory and economic framework would be enacted for the power plants enrolled in the administrative RPAR once RD 661/2007 remuneration regime in force had been exhausted
Administrative features	<ul style="list-style-type: none"> ➤ Under RDL 6/2009, the registration in the RPAR had to be a necessary prerequisite for the granting of the right to the economic regime established in RD 661/2007. The facilities would be registered chronologically in the administrative RPAR until the power objective foreseen in each group and subgroup was met ➤ To get the enrolment in the RPAR a series of requirements should be fulfilled: an access point to the electrical network for all the installed power, the administrative authorization of the power plant, the construction permit, sufficient financial resources to assume at least 50% of the project investment, a purchase agreement for a minimum of 50% of the equipment value and a new guarantee of 100 EUR/kW for the CSP case

Table 5. Cont.

Legislation	Main Characteristics
Administrative features	<ul style="list-style-type: none"> ➤ The facilities registered in the RPAR would have a maximum period of 36 months from their notification date, to be definitively enrolled in the administrative register of generation power plants under the SR and to start the sale of energy. Otherwise, the economic right associated with the inclusion in the RPAR would be revoked ➤ Those facility projects which upon the enactment of RDL 6/2009 met the established requirements would have a period of 30 days from the day of coming into force of this framework to apply for registration in the RPAR. Likewise, they would have 30 additional days to deposit the corresponding guarantee. Once the fulfillment of the prerequisites of the power plant projects had been verified, they would be registered in the RPAR
RD 1003/2010 of August 2010 [81]	
Subject	Setting the procedure to improve the accreditation process of the different PV plants under RD 661/2007 and RD 1578/2008 remuneration frameworks, thus taking a further step in improving the efficiency of the remuneration framework corresponding to each PV facility based on its specific characteristics
Previous regulations repealed or modified	Amendment of RD 661/2007 and RD 1578/2008
RES goals	–
SR group for solar technology	–
Economic regime	–
Administrative features	<ul style="list-style-type: none"> ➤ All those PV plants under RD 661/2007 economic regime could make the request to renounce this remuneration scheme within a maximum period of 2 months from the enactment of RD 1003/2010. Thus, losing the right to perceive the regulated tariff or the premium set by RD 661/2007. However, it would entail the automatic inclusion of the PV facility in the conditions of the economic regime of the first call corresponding to the facilities registered in the RPAR regulated by RD 1578/2008 ➤ For the proper monitoring of the SR facilities without the right to a regulated tariff or premium, the registry of the SR without premium remuneration was established. The facilities registered in the register of SR without premium remuneration could participate in the administrative procedure for the pre-allocation of remuneration regulated in RD 1578/2008
RD 1565/2010 of November 2010 [82]	
Subject	Regulation and modification of certain issues related to the power generation activity under the SR
Previous regulations repealed or modified	Amendment of RD 661/2007 and RD 1578/2008
RES goals	–
SR group for solar technology	It modified the classification set by RD 1578/2008 for solar PV facilities. It specified that there should be a contracted power supply point inside the PV facility for at least 25% of its nominal power to be included in type I. Furthermore, PV plants located on greenhouse structures and on roofs of irrigation ponds were expressly excluded from this type I
Economic regime	<ul style="list-style-type: none"> ➤ It suppressed the values of the regulated tariffs set for SR facilities in subgroup b.1.1 under RD 661/2007 as of the twenty-sixth year ➤ It also carried out a remarkable shrinkage of the regulated PV tariff for the first call of the RPAR as of the entry into force of RD 1565/2010. Specifically, the regulated tariffs set by RD 1578/2008 for PV plants were reduced by 5% for subtype I.1, 25% for subtype I.2 and 45% for subtype II. The percentage of reduction of the tariff values would not be considered for the computation of the power quotas for the following year

Table 5. Cont.

Legislation	Main Characteristics
Economic regime	<ul style="list-style-type: none"> ➤ It established the option of granting an additional specific remuneration to innovative CSP projects for an aggregate total of 80 MW by means of a tender procedure ➤ See Table 6 for a detailed summary of the changes introduced by RD 1565/2010 in both RD 661/2007 and RD 1578/2008 economic schemes for the solar power facilities
Administrative features	-
Other issues	<ul style="list-style-type: none"> ➤ A power plant should be made up of new and unused main equipment to be included in the SR. Moreover, the SR facilities should have the necessary electrical energy measurement equipment, before injecting electricity into the grid ➤ It redefined the concept of substantial modifications of power plants that would imply losing the entitlement to the RD 661/2007 remuneration
RD 1614/2010 of December 2010 [83]	
Subject	Regulation of certain economic aspects for power plants of wind and CSP technologies, as well as resolution of some inefficiencies in the application of the previous RDL 6/2009 for those technologies
Previous regulations repealed or modified	-
RES goals	-
SR group for solar technology	-
Economic regime	<ul style="list-style-type: none"> ➤ It limited the equivalent operating hours at rated power eligible for the RD 661/2007 regulated tariff or premium for wind and CSP facilities (see Table 7). If the established equivalent operating hour limits were exceeded, in annual computation, the owners of the power plants should return the amounts received in excess, as a regulated tariff or premium, within a maximum period of 3 months ➤ It set that the CSP technology facilities under RD 661/2007 could only opt for the regulated tariff as the remuneration option for selling their electricity in the first 12 full months after the date of commissioning. Accordingly, the CSP plants in operation would receive the regulated tariff from 1 January 2011 and those under construction since their date of commissioning. During the 12-month period, the percentage of electricity production from fuel could rise to 15% ➤ For CSP plants under RD 661/2007, the revisions of the tariffs, premiums and lower and upper bounds would not affect either the power plants definitively enrolled in the administrative register of generation power plants under the SR, or those registered in the RPAR under RDL 6/2009
Administrative features	-
RDL 14/2010 of December 2010 [84]	
Subject	Urgently undertake the correction of the power sector tariff deficit
Previous regulations repealed or modified	Amendment of RD 661/2007
RES goals	-
SR group for solar technology	-
Economic regime	<ul style="list-style-type: none"> ➤ It limited the equivalent operating hours at rated power of PV plants. Thus, those solar PV technology facilities would be entitled to receive each year its recognized economic regime until reaching the reference number of equivalent operating hours (see Tables 8 and 9) ➤ It forced all power generators to pay a 0.5 EUR/MWh toll for the electricity fed into the distribution and transmission grids, from 1 January 2011 onwards

Table 5. Cont.

Legislation	Main Characteristics
Economic regime	<ul style="list-style-type: none"> ➤ It modified the reference period from which the regulated tariff received by PV power plants in subgroup b.1.1 under this remuneration option set by RD 661/2007 had to be updated. Specifically, it increased the reference term from the first 25 years to the first 28 years ➤ See Table 6 for a detailed summary of the changes introduced by RDL 14/2010 in RD 661/2007 economic scheme for the solar power plants
Administrative features	-
Law 2/2011 of March 2011 [85]	
Subject	Promotion of a sustainable economic development by means of the transposition into the Spanish legislation of the Directive 2009/28/CE energy goals. Furthermore, setting of the REP 2011–2020 elaboration
Previous regulations repealed or modified	Amendment of RD 661/2007 and RDL 14/2010 as for the solar PV technology plants
RES goals	Minimum 20% share of RES in the final energy consumption by 2020
SR group for solar technology	-
Economic regime	<ul style="list-style-type: none"> ➤ The reference period for the application of the regulated tariff set for the facilities in subgroup b.1.1 of RD 661/2007 under this remuneration scheme was modified again, increasing from the first 28 years to the first 30 years ➤ See Table 6 for a detailed summary of the changes introduced by Law 2/2011 in RD 661/2007 economic scheme for the solar power plants
Administrative features	-
Other issues	It specified that in the event of modifying the equivalent operating hours for the PV plants by the Spanish government, those changes would only affect power plants that were not in operation at the time of the entry into force of the corresponding new modification legislation
RDL 1/2012 of January 2012 [86]	
Subject	Suppression of the economic incentives for electricity production facilities under the SR and the suspension of the RPAR procedure for the granting of the economic regime
Previous regulations repealed or modified	Amendment of RD 661/2007 and RD 1578/2008
RES goals	-
SR group for solar technology	-
Economic regime	<ul style="list-style-type: none"> ➤ It temporarily suppressed the economic incentives of RD 661/2007, i.e., regulated tariffs, premiums, complements and upper and lower bounds, for the new SR power plants ➤ It provisionally suspended the registration procedure in the RPAR under RDL 6/2009 as well as under RD 1578/2008 for PV plants that had submitted their application to the 2012 calls. RDL 1/2012 also revoked the pre-allocation calls for 2012 and subsequent years for the PV facilities under RD 1578/2008. Thus, the new SR facilities would have to sell the energy produced to the power network at the wholesale electricity price ➤ These measures would not affect neither operating plants nor those already registered in the RPAR under RDL 6/2009 or under RD 1578/2008 as for the PV technology plants
Administrative features	The SR facilities registered in the RPAR finally choosing not to carry out the power plant could renounce the registration in the RPAR without this implying the execution of the guarantees they had deposited, within a maximum period of 2 months from the enactment of RDL 1/2012, provided that the period for the final registration and sale of energy had not expired

Table 5. Cont.

Legislation	Main Characteristics
Law 15/2012 of December 2012 [87]	
Subject	Harmonization of the Spanish tax system with a more efficient and respectful use regarding the environment and sustainability
Previous regulations repealed or modified	-
RES goals	-
SR group for solar technology	-
Economic regime	<ul style="list-style-type: none"> ➤ It added a new 7% tax on the gross revenues for the electricity generated, measured in power plant busbars, by all electricity producers in the Spanish electrical system to favor the budgetary balance of the system ➤ It removed tax exemptions for the energy products used in the power production ➤ It eliminated the premium economic regime for electricity attributable to the use of a fuel in a production power plant using any of the non-consumable renewable energies as primary energy, except in the case of hybrid facilities between RES non-consumables and consumables ones
Administrative features	-
RDL 29/2012 of December 2012 [88]	
Subject	Implementation of some measures to reduce the electricity system tariff deficit
Previous regulations repealed or modified	-
RES goals	-
SR group for solar technology	-
Economic regime	-
Administrative features	<ul style="list-style-type: none"> ➤ It established that the premium economic regime for SR generation facilities registered in the RPAR would become inapplicable if those facilities were not fully completed by the expiration of the deadline set to be definitively enrolled in the administrative register of generation power plants in SR ➤ The power plant would be considered fully completed if it had all the elements, equipment and infrastructure that were necessary to produce energy and deliver it into the electrical system and whose characteristics corresponded to the approved execution project

Table 6. Major characteristics of the different economic regimes in force for solar power systems in Spain in the period 2008–2013. Source: self-elaboration based on [78,82,84,85].

Legislation	Technology	SR Group	Rated Power and/or Facility Type	Remuneration Options			Review and Update	
				FIT Regulated Tariff [cEUR/kWh]	FIP ¹			
					Premium [cEUR/kWh]	Incentive [cEUR/kWh]		Time Limit
RD 1578/2008 modified by: -RD 1565/2010	Solar PV	b.1.1	Subtype I.1 $P < 2$ MW	34.0000 (first call under RD 1578/2008)/0.95*FIT first call (RD 1565/2010)	-	-	25 years maximum	<ul style="list-style-type: none"> Annual update according to CPI FIT of subsequent calls calculated by means of RD 1578/2008 equations Review in 2012
			Subtype I.2 $P < 2$ MW	32.0000 (first call under RD 1578/2008)/0.75*FIT first call (RD 1565/2010)	-	-	25 years maximum	
	Solar PV	b.1.1	Type II $P < 10$ MW	32.0000 (first call under RD 1578/2008)/0.55*FIT first call (RD 1565/2010)	-	-	25 years maximum	
			$P \leq 100$ kW	44.0381	-	-	First 28 years (RDL 14/2010)/First 30 years (Law 2/2011)	For both FIT and FIP options: <ul style="list-style-type: none"> Annual update according to CPI Review in 2010 and thereafter every 4 years or not less than 1 year after reaching 85% of 371 MW
RD 661/2007 modified by: -RD 1565/2010 -RDL 14/2010 -Law 2/2011	Solar PV	b.1.1	$100 \text{ kW} < P \leq 10$ MW	0 (RD 1565/2010)	-	-	Thereafter	
			$10 \text{ MW} < P \leq 50$ MW	41.7500	-	-	First 28 years (RDL 14/2010)/First 30 years (Law 2/2011)	
	Solar CSP	b.1.2	Any	0 (RD 1565/2010)	-	-	Thereafter	For both FIT and FIP options: <ul style="list-style-type: none"> Annual update according to CPI Review in 2010 and thereafter every 4 years or not less than 1 year after reaching 85% of 500 MW
				22.9764	25.4000	-	-	First 28 years (RDL 14/2010)/First 30 years (Law 2/2011)
				21.5498	20.3200	-	Thereafter	

¹ This table only shows the values of the FIP components fully established in a regulatory manner, i.e., the premiums and the incentives. Thus, the electricity market price and the reactive energy complement must be added to these economic parameters to obtain the total FIP of the facility.

Table 7. Reference equivalent operating hours for CSP power plants set by RD 1614/2010. Source: self-elaboration based on [83].

CSP Technology	Reference Equivalent Operating Hours per Year
Stirling	2350
Fresnel	2450
Saturated steam tower	2750
Parabolic trough without storage	2855
Parabolic trough with 4 h storage	3450
Parabolic trough with 7 h storage	3950
Parabolic trough with 9 h storage	4000
Salt tower with 15 h storage	6450

Table 8. Reference equivalent operating hours for PV power plants set by RDL 14/2010. Source: self-elaboration based on [84].

Solar PV Technology	Reference Equivalent Operating Hours per Year				
	Zone I	Zone II	Zone III	Zone IV	Zone V
One-axis solar tracking facility	1602	1770	1940	2122	2279
Two-axis solar tracking facility	1664	1838	2015	2204	2367
Fixed facility	1232	1362	1492	1632	1753

Table 9. Reference equivalent operating hours for PV power plants under RD 661/2007 until 31 December 2013 set by RDL 14/2010. Source: self-elaboration based on [84].

Solar PV Technology	Reference Equivalent Operating Hours per Year
One-axis solar tracking facility	1644
Two-axis solar tracking facility	1707
Fixed facility	1250

3.4. The 2013–2020 Subperiod: A New Paradigm for the Spanish Solar Power Sector

From 1998 to 2013, economic incentives for power generation power plants using RES, cogeneration and waste had amounted to more than 50,000 M EUR, increasing by more than 800% from 2005 to 2013, when premiums for these facilities reached approximately 9000 M EUR.

Premiums for renewable, cogeneration and waste technologies had been mainly financed by electricity consumers through their bills. In addition, and as of 1 January 2013, part of those RES public support costs was financed by the Spanish General State Budgets, with the income derived from the levies included in Law 15/2012.

Following with the cost-containment measures approved until 2012, RDL 2/2013 [89] was enacted in February 2013 to continue mitigating the electricity system deficit. Subsequently, it was approved RDL 9/2013 [90] in July 2013, which introduced the specific principles on which a new regulatory and economic regime for the SR power plants would be based. Thus, laying the foundations of the new paradigm for the Spanish RES power sector, and specifically for the solar power sector, which unlike the cost-containment measures approved until then, dismantled the previous regulatory and economic framework.

As a result of the failure of the numerous legal measures enacted in recent years to remove the tariff deficit, The new SES Law 24/2013 of December 2013 [56] established as two of its major objectives the recovery of the long-lost economic and financial stability of the power sector and the suppression of the undesirable regulatory dispersion existing in such a relevant economic sector. Then, the new legislation for the generation power plants from RES was governed by RD 413/2014 of June 2014 [57], which implemented the fundamentals already included in RDL 9/2013 and incorporated in Law 24/2013.

During the 2015–2017 period, given the need to comply with the binding objectives established in the Directive 2009/28/CE on the promotion of the use of energy from RES by 2020, it was necessary to boost the penetration of new renewable capacity in the Spanish electrical system. Thus, three RES auctions under RD 413/2014 framework were called in Spain.

The assignment of the specific remuneration regime and the standard value of the initial investment would be determined through a competitive tendering to introduce the most cost-efficient RES projects into the Spanish electricity system. It was a mechanism providing an incentive to the investment on the capital expenditures of the project (EUR/MW) so that it always achieved the reasonable profitability (Russia was the unique country to provide investment-based support as in Spain [32]). Thus, the products to be auctioned would be the installed power with the right to receive the specific remuneration regime, obtaining as a result of the auction a percentage of reduction of the standard value of the initial investment of the standard facility that they were willing to waive for installing the power plant. The projects offering higher discounts with respect to the standard values of the facilities, and therefore causing a lower cost overrun in the system, were awarded until the maximum established power quota was reached.

The first RES auction was held on 14 January 2016 and according to RD 947/2015 [91] and the Order IET/2212/2015 [92] of October 2015, the call was only set for the allocation of the specific remuneration regime under RD 413/2014 to new facilities for the electricity generation from biomass in the peninsular power system (200 MW awarded) and from wind technology (500 MW awarded). The allocation of the specific remuneration regime was carried out through a technology-specific auction procedure geographically neutral.

In April 2017, RD 359/2017 [93] and the Order ETU/315/2017 [94] approved a second technology-neutral call for the concession of the specific remuneration regime under RD 413/2014 up to a maximum of 3000 MW of installed power for new electricity production facilities from wind, PV and non-PV and wind technologies of group b located in the peninsular electricity system (geographically neutral). The allocation of the specific remuneration regime was determined by a static auction method with a uniform pricing rule. The Resolutions of 10 April 2017 of the State Secretariat for Energy [95,96] established the procedure and rules of the auction according to RD 359/2017 and Order ETU/315/2017, and called the auction for 17 May 2017.

That second RES auction established the following minimum and maximum values of the offered percentage of reduction of the standard value of the initial investment of the reference type facility, respectively: 0% and 63.43% for wind, 0% and 51.22% for solar PV, and 0% and 99.99% for the rest of technologies of group b [95]. Meanwhile, the amount of the economic guarantee requested as a prerequisite for participation in the auction would be of 60 EUR/kW (gradually recovered) [93,94].

The second auction carried out on 17 May 2017 resulted in the allocation of 3000 MW of renewable power plants at no cost to the consumers at least during the first regulatory period, as the successful bidders offered the maximum possible discount for the standard value of the initial investment. Specifically, 2979.664 MW were awarded to wind plants, only 1.037 MW for solar PV technology and 19.299 MW for the rest of group b technologies, mainly biomass [97]. Only 16 kW of wind technology and 21 kW of solar PV of the total of 3000 MW awarded were not finally enrolled in the registry of the specific remuneration regime in a pre-allocation state [98]. The cost attributable to the organization of the auction would be borne by those participants who were awarded in the auction through a rate of 0.08 EUR/kW [95].

In June 2017, RD 650/2017 [99] and the Order ETU/615/2017 [100] approved a new technology-neutral call for the concession of the specific remuneration regime under RD 413/2014 up to a maximum of 3000 MW of installed power for new electricity production facilities from wind and solar PV technologies located in the peninsular electricity system (geographically neutral). The granting of the specific remuneration regime was determined by a static auction method with a uniform pricing rule.

That third RES auction established the following minimum and maximum values of the offered percentage of reduction of the standard value of the initial investment of the reference type facility, respectively: 0% and 87.08% for wind, and 0% and 69.88% for solar PV [101]. Furthermore, that call included the possibility of increasing the power quota with the power of all those bids with the same extra cost as the last bid awarded, provided that the extra cost for the system was null and less than the value set in the confidential clause of the resolution calling for the auction [99].

The remuneration parameters of the standard facilities applicable to this new call, the mechanisms for assigning the specific remuneration regime, as well as the other aspects established for the proper holding of the auction would be those set in the previous Order ETU/315/2017. Likewise, the procedure and rules of the auction would be those established in the previous Resolution of the State Secretariat for Energy of 10 April 2017 [100]. In turn, the Resolution of 30 June 2017 of the State Secretariat for Energy [101] called the auction for 26 July 2017 under the provisions of RD 650/2017.

The third auction carried out on 26 July 2017 resulted in the allocation of 5036.921 MW of renewable power plants at no cost to the consumers at least during the first regulatory period, as the successful bidders offered the maximum possible discount for the standard value of the initial investment. Specifically, 1127.818 MW were awarded to wind technology and 3909.103 MW for solar PV technology [102]. All the awarded power was finally enrolled in the registry of the specific remuneration regime in a pre-allocation state [103]. The cost attributable to the organization of the auction would be borne by those participants who were awarded in the auction through a rate of 0.08 EUR/kW [101].

Already in November 2019, RDL 17/2019 [104] adopted urgent measures for the necessary adjustment of the remuneration parameters affecting the electricity system. As regards production facilities from RES, cogeneration and waste that were entitled for a premium remuneration upon the enactment of RDL 9/2013, various arbitration procedures were pending resolution accumulating large claims for the damages allegedly caused by the retroactively cuts in RES subsidies based on an alleged breach of the Energy Charter Treaty.

Tables 10 and 11 provide a comprehensive summary of the main features of the different regulatory frameworks and economic regimes, respectively, in force for the Spanish solar power plants in the period 2013–2020.

Table 10. Major characteristics of the different regulatory frameworks in force for solar power systems in Spain in the period 2013–2020. Source: self-elaboration based on [56,57,89,90,104].

Legislation	Main Characteristics
RDL 2/2013 of February 2013 [89]	
Subject	Adoption of urgent cost reduction measures to continue mitigating the electricity system deficit
Previous regulations repealed or modified	Amendment of RD 661/2007
RES goals	–
SR group for solar technology	–
Economic regime	<ul style="list-style-type: none"> ➤ It established that all those methodologies for updating remuneration linked to the CPI should replace it with the CPI at constant taxes without unprocessed food and energy products since 1 January 2013, to use a more stable index not affected by the volatility of the prices of unprocessed foods or fuels for domestic use ➤ Bearing in mind the volatility of the electricity pool price, the premium on top of the electricity market price was set to 0 cEUR/kWh and its upper and lower bounds were removed for all the SR facilities under RD 661/2007. Thus, guaranteeing a reasonable profitability for these facilities and avoiding an over-remuneration at the same time

Table 10. Cont.

Legislation	Main Characteristics
Economic regime	➤ It set that the premium economic regime should be based solely on the regulated tariff option, without prejudice to the fact that the SR facilities could freely sell their energy in the pool without perceiving a premium
Administrative features	–
RDL 9/2013 of July 2013 [90]	
Subject	To ensure the financial stability of the power sector in Spain
Previous regulations repealed or modified	<ul style="list-style-type: none"> ➤ Derogation of RD 661/2007, RD 1578/2008 and the RPAR mechanism for SR facilities of RDL 6/2009 ➤ Amendment of the SES Law 54/1997 to introduce the standards on which a new regulatory and economic regime for the SR power plants would be based
RES goals	–
SR group for solar technology	–
Economic regime	<ul style="list-style-type: none"> ➤ The previous remuneration options, namely the regulated tariff and the premium on top of the electricity market price, were superseded by the electricity market price plus an additional specific remuneration for offsetting the investment and operating costs that could not be regained with the revenues from the sale of energy in the market ➤ The specific remuneration would change in accordance with the typology of the SR power plants and would be such that an “efficient and well-managed” plant could acquire a reasonable return of investment along its regulatory useful life allowing it to cover costs and compete on an equal basis with all other technologies on the electricity pool ➤ For the specific remuneration computation, the standard income from the sale of electricity in the pool, the standard operating costs and the standard value of the initial investment for an “efficient and well-managed” facility would be considered throughout its useful life ➤ Only the costs and investments established by provisions enforceable to the entire Spanish territory and those responding solely to the electricity generation activity would be considered for the computation of the specific remuneration ➤ The reasonable return was defined, before taxes, at the average yield during determined period of the 10-year Spanish bonds in the secondary market plus an appropriate differential ➤ The specific remuneration parameters could be reviewed every 6 years ➤ For the particular issue of those SR power plants eligible for a premium economic regime before RDL 9/2013 effective date, the average yield of the 10-year Spanish bonds would be computed over the last 10 years and a differential of 300 BP would be added (amounting to 7.398%) ➤ Although the future regulatory and economic framework was deployed, the remuneration of these SR power plants would be temporarily paid as defined in RD 661/2007 and RD 1578/2008, but it would be recalculated afterwards in accordance with the new legislation. As an exception, the innovative CSP projects awarded under RD 1565/2010 maintained its specific remuneration regime

Table 10. Cont.

Legislation	Main Characteristics
Administrative features	To qualify for the new economic regime for the SR facilities, the enrolment in the specific remuneration regime register managed by the Spanish government became mandatory. Those SR facilities not enrolled in that registry would receive, exclusively, the market price
Other issues	An “efficient and well-managed” facility was understood as a plant with the necessary resources to conduct its activity, with the same costs as for an efficient facility in the same activity and considering the corresponding income and a reasonable benefit for the performance of its functions
Law 24/2013 of December 2013 [56]	
Subject	Setting of the power sector regulation so as to ensure the supply of electricity and to adjust it to the consumers’ needs in terms of efficiency, security, transparency, objectivity and at the lowest cost
Previous regulations repealed or modified	<ul style="list-style-type: none"> ➤ Repeal almost entirely the SES Law 54/1997, while partially repealed RDL 14/2010 and RDL 2/2013 ➤ Amendment of Law 15/2012
RES goals	–
SR group for solar technology	–
Economic regime	<ul style="list-style-type: none"> ➤ The standards of RDL 9/2013 for the remuneration of the generation power plants from RES were integrated, even though new items to adjusting the remuneration to the cyclic situation of the economy and to the power sector needs were added ➤ The new RES generation power plants would qualify for a specific remuneration only on certain exceptional basis set by the Spanish government, namely when there was an obligation to comply with energy objectives derived from EU rules or when their introduction implied a decrease in energy costs and external energy dependency ➤ The specific remuneration would be granted by a competitive procedure ➤ The conditions, technologies or group of specific facilities that could participate in the competitive competition mechanism would be established by RD ➤ The average yield of the 10-year Spanish bonds for the first regulatory period of the new power plants would be computed over the three months prior to the enactment of RDL 9/2013 and a differential of 300 BP would be added ➤ The remuneration parameters would be reviewed at the beginning of the 6-year regulatory periods, except the regulatory useful life and the standard value of the initial investment. In turn, some of these regulatory parameters could also be adjusted at the 3-year half-periods ➤ For the production activities from RES, cogeneration and waste in the specific remuneration regime, the first regulatory period began on RDL 9/2013 effective date and ended on 31 December 2019, while the first regulatory half-period began on RDL 9/2013 enactment date and ended on 31 December 2016 ➤ The remunerations received by the existing SR power plants before the enactment of RDL 9/2013 would not prompt any complaint even if the reasonable return set in the new economic legislation for their regulatory useful life was overstepped

Table 10. Cont.

Legislation	Main Characteristics
Administrative features	-
Other issues	<ul style="list-style-type: none"> ➤ It removed the SR concept and referred instead to generation power plants with specific remuneration ➤ It regulated the provisional closure of generation power plants ➤ It set regulatory periods of 6 years and regulatory half-periods of 3 years ➤ It established the priority criteria for access and dispatch of electricity from RES facilities, while the share of electricity produced from fuels would not receive the specific remuneration, but only the market price
RD 413/2014 of June 2014 [57]	
Subject	Development of the fundamentals already included in RDL 9/2013 and incorporated in Law 24/2013
Previous regulations repealed or modified	<ul style="list-style-type: none"> ➤ It suppressed the RPAR under RD 1578/2008 and under RDL 6/2009, the RPAR for SR experimental facilities under RD 1565/2010, as well as the registry of the SR without premium remuneration under RD 1003/2010 ➤ It repealed RD 1565/2010 and RD 1614/2010
RES goals	-
SR group for solar technology	The generation power plants using solar energy as primary energy continued to belong to group b.1 (PV plants in subgroup b.1.1 and CSP facilities in subgroup b.1.2)
Economic regime	<ul style="list-style-type: none"> ➤ Generation facilities would be obliged to make financial offers to the electricity market operator for each programming period either directly or through an agent ➤ Once the RES facilities exceeded its regulatory useful life under RD 413/2014 economic regime, they would no longer receive the specific remuneration, i.e., the remuneration for the investment and the remuneration for the operation. However, these facilities could remain in operation, perceiving exclusively the remuneration obtained from the sale of electricity in the pool. In turn, RES facilities that, even within their regulatory useful life, would have reached a reasonable profitability level, would have a return on investment equal to zero and would keep the return on operation during their regulatory lifetime ➤ The annual income perceived from the specific remuneration regime under RD 413/2014 by a facility whose number of equivalent operating hours in a given year did not exceed the minimum number of equivalent operating hours of the corresponding standard facility, would be reduced and would be null if it did not exceed the operating threshold defined for that facility type ➤ A classification of standard facilities would be established based on technology, installed power, year of commissioning, electrical system, as well as any other segmentation deemed necessary for the application of the remuneration regime. Each standard power plant defined was identified by a different code. In turn, the remuneration parameters for each standard facility under RD 413/2014 economic regime were set by the Spanish government through Ministerial Orders. The Order IET/1045/2014 of June 2014 [105], the Order ETU/130/2017 of February 2017 [106] and the Order TED/171/2020 of February 2020 [107], defined these remuneration parameters for the first, second and third half-periods, respectively ➤ For the PV power plants (subgroup b.1.1) under RD 413/2014, a total of 91 standard facilities ranging from IT-00001 to IT-00091 were defined. Regarding CSP technology (subgroup b.1.2), a total of 20 standard facilities ranging from IT-00601 to IT-00620 were set ➤ See Table 11 for a detailed summary of RD 413/2014 economic scheme for the solar facilities ➤ For a comprehensive overview of the economic model related to the solar facilities under RD 413/2014 regulatory framework the interested reader is addressed to [46] for the solar PV technology and to [30] for the CSP technology

Table 10. Cont.

Legislation	Main Characteristics
Administrative features	<ul style="list-style-type: none"> ➤ Generation facilities under RD 413/2014 should be compulsorily registered in definitive state in the administrative register of electricity generation power plants (first section for facilities whose installed power is greater than 50 MW and second section for facilities whose installed power is equal to or less than 50 MW) ➤ For the perception of the specific remuneration regime under RD 413/2014, it should be a necessary condition that the facilities were enrolled in operation state in the registry of the specific remuneration regime. For registration in the specific remuneration regime registry in a pre-allocation state, namely prior to the operation state, the facilities should deposit an economic guarantee
Other issues	<ul style="list-style-type: none"> ➤ The installed power would correspond to the maximum active power that a production unit could reach. As for the PV plants, the installed power would be the sum of the maximum unit powers of the solar PV modules of the power plant ➤ It would be a necessary condition for obtaining the specific remuneration regime that the facility was made up of new and unused main equipment
RDL 17/2019 of November 2019 [104]	
Subject	Adoption of immediate measures for the necessary adjustment of the remuneration parameters affecting the power system
Previous regulations repealed or modified	–
RES goals	–
SR group for solar technology	–
Economic regime	<ul style="list-style-type: none"> ➤ It established at 7.09% the value of the reasonable profitability applicable from the second regulatory period onwards for the standard facilities under RD 413/2014 legal–economic framework ➤ Exceptionally, for those generation facilities that were entitled for a premium remuneration upon the entry into force of RDL 9/2013, the value of the reasonable profitability set for the first regulatory period, i.e., 7.398%, could not be reviewed during the next two consecutive regulatory periods as of 1 January 2020. Thus, guaranteeing economic certainty to these facilities with a reasonable profitability of 7.398% during the 2020–2031 period, higher than the 7.09% established during the 2020–2025 period, and avoiding the uncertainty of the 2026–2031 period. However, these facilities could renounce this exception before 1 April 2020, thus a reasonable profitability of 7.09% for them being applicable ➤ The measure would not be applicable when an arbitration procedure based on the modification of the special remuneration regime operated after RD 661/2007 had previously been initiated on the profitability of these facilities, including those derived from the entry into force of RDL 9/2013, and its implementing regulations. Conversely, the aforementioned facilities could benefit from the exceptional regime when it was accredited before 30 September 2020, the early termination of the arbitration procedure and the waiver of its restart or its continuation, or the waiver of the receipt of compensation that had been recognized as a consequence of such procedures
Administrative features	–
Other issues	New standard facilities were created for those power plants under the new reasonable profitability of 7.09%, with identical technical and economic characteristics as those under the 7.398% profitability, except for the reasonable return applicable to them. The new standard facility codes to which a profitability of 7.09% was applied for solar PV technology were comprised between IT–20001 and IT–20091, while for CSP technology they were comprised between IT–20601 and IT–20620 [107]

Table 11. Major characteristics of the different economic regimes in force for solar power systems in Spain in the period 2013–2020. Source: self-elaboration based on [56,57,90].

Legislation	Technology	SR Group	Facility Type	Remuneration Option	Time Limit	Review and Update
				Specific Remuneration ¹		
RD 413/2014 (in accordance with RDL 9/2013 and Law 24/2013)	Solar PV	b.1.1	91 standard facilities ranging from IT-00001 to IT-00091 based on technology, installed power, year of commissioning and electrical system	For the first regulatory period: <ul style="list-style-type: none"> • Reasonable return for existing facilities of 7.398% • Reasonable return for new facilities: average yield during the last 3 months plus a differential of 300 BP 	Regulatory lifetime (30 years)	Review every 6-year regulatory period and/or each 3-year regulatory half-period
	Solar CSP	b.1.2	20 standard facilities ranging from IT-00601 to IT-00620 based on technology, installed power, year of commissioning and electrical system	For the first regulatory period: <ul style="list-style-type: none"> • Reasonable return for existing facilities of 7.398% • Reasonable return for new facilities: average yield during the last 3 months plus a differential of 300 BP 	Regulatory lifetime (25 years)	Review every 6-year regulatory period and/or each 3-year regulatory half-period

¹ The remuneration option established by RD 413/2014 framework in accordance with RDL 9/2013 and Law 24/2013 consisted of the electricity market price plus an additional specific remuneration, fully established in a regulatory manner, compensating for the investment and operating costs that could not be regained with the revenues from the sale of electricity in the market. The specific remuneration was awarded by competitive procedures.

4. Assessment of the 1998–2020 Energy Policy for the Solar Power Plants in Spain

4.1. Analysis of the 1998–2008 Promotion Stage

4.1.1. Concerning the Solar PV Technology Sector

First, the 1998–2004 subperiod was characterized by a stable remuneration system for PV facilities in group b.1 under RD 2818/1998 legal–economic framework. However, the solar PV generation technology did not develop as expected in the REP 2000–2010 with a 135 MW PV capacity target to be added for 2010, owing to the relatively low support levels and the uncertainty for investors related to the support annual updating [26]. Specifically, only 22.8 MW of PV capacity was put into operation at the end of 2004.

Subsequently, the 2004–2008 subperiod was marked by a much more favorable economic framework under RD 436/2004 and RD 661/2007 for PV facilities.

RD 436/2004 increased the regulated tariff, with respect to RD 2818/1998, by 4.5% for facilities up to 5 kW of installed power and by 91.5% for plants beyond 5 kW and up to 100 kW, while eliminating the possibility of FIP for these PV assets. Although PV plants above 100 kW almost kept the same value for both the FIT and the premium on top of the electricity pool price, incorporating an extra incentive to the FIP remuneration option. In all cases taking into account a time limit of 25 years from which the incentives and premiums would be reduced.

In this regard, the cumulative PV capacity installed in Spain at the end of 2006 was 145.6 MW, i.e., in just 2 years under RD 436/2004 the cumulative PV capacity was multiplied by 6.4, ensuring RD 436/2004 150 MW PV capacity target.

Although the evolution of the cumulative PV capacity installed under RD 436/2004 was quite positive, it was decided to modify the economic scheme again through RD 661/2007. This new economic framework eliminated the FIP option for all PV facilities (and it consequently lowered the risk related to the PV remuneration scheme, since the PV support levels were not linked to the electricity prices [26]), and, in turn, increased the FIT by 6.3% for plants up to 100 kW, by 93% for facilities above 100 kW and up to 10 MW, and by 6.3% for plants beyond 10 MW and up to 50 MW. Thus, over-incentivizing the PV plants unnecessarily led to a higher financial burden for the final consumers. In terms of the promotion of increasingly competitive solar PV energy, inflated rewards were considered

potentially detrimental to competition and cost reduction, thus discouraging technological research into this type of technology [12].

Even though periodic adjustments and revisions of the economic scheme were established by the different frameworks, the PV system behaved similar to an open-loop system during the whole period 1998–2008, in which the incentives were decoupled from the compliance level of the PV capacity goals set [9].

In 2007–2008, with the first symptoms of the economic crisis, the solar PV sector was seen as a safe and economically profitable business for investors due to its attractive RD 661/2007 economic framework with high internal rates of return (actual internal rates of return for projects were estimated to have been between 10% to 15%, as opposed to the targeted rate of 5% to 9% [23]) and very small risks [9]. The end of the Spanish housing market boom led professional as well as non-professional investors to shifted capital from the real estate sector to the power sector in the pursuit of cost-effective investment opportunities in a business legally implemented by the public administration and with high premiums [11,41].

Furthermore, other factors contributed to the great expansion of the solar PV sector in Spain in the 2007–2008 period, such as the ease of accessing low-interest loans to finance projects (75% of the 20,000 M EUR invested in this business came from national or foreign banks), the non-implementation of subsidy degression measures in order to lessen support in line with the evolving costs of solar PV projects, the modular and easy-to-install features of solar PV (particularly regarding the smaller facilities), the repowering of PV facilities with more efficient equipment while maintaining their nominal capacity, quick permit provisions, poor coordination between regional and national authorities and the favorable EUR/USD exchange rate since 2006 until 2008, fostering imports of solar PV cells and modules due to the stronger euro [23,26,41,47]. These extraordinary conditions attracted an enormous amount of capital, including investments from many small investors who, relying on government guarantees, did not doubt to use their family savings or become indebted by mortgaging their family assets. Financial expenses in this period raised as the number and amount of bank loans awarded to the sector increased considerably [12,41].

In addition, RD 661/2007 announced a transition mechanism that would be applied once it reached 85% of the PV capacity target (371 MW). This mechanism generated high uncertainty in the solar PV sector about its entering into force and duration. As a result, it acted as a “call for investment” before the highly favorable remuneration scheme finished. For example, to maintain the same IRR as before the approval of the new economic framework, it would have been necessary to reduce the solar PV production cost from 6.3 EUR/Wp to 0.5 EUR/Wp [9].

Consequently, the cumulative PV capacity installed in Spain at the end of 2008 was 3397.8 MW (545 MW and 2707 MW of new PV power were installed in 2007 and 2008, respectively), far above the 400 MW PV capacity goal set by REP 2005–2010 for 2010. Turning Spain into the second country in Europe with the largest cumulative installed PV capacity, with investments in the Spanish solar PV market accounting for more than 40% of the world’s total solar power plants in 2008 [9,11]. A total of 80% of that increase was due to the rise in capacity deployed by facilities with capacity lower than 100 kW (most of these plants being solar parks), and the remaining 20% took place in the segment from 100 kW to 10 MW, which was the one which experienced the greatest rise in remuneration [26].

Although the 1998–2008 promotion policies did not reduce the LCOE of PV systems installed during that period, they had an enormous impact on the maturity of solar PV technology making the country a leader within the PV market. This fact was reflected afterwards with a strong reduction in its unitary prices [35,36].

In this vein, Spain suffered a diffusion solar PV bubble between June 2007 and September 2008, in which the PV power plants were conceived more as investment products rather than environmental awareness-raising and commitment issues. Even banks included such systems in their product portfolios offered to their clients [36]. In addition, later, a profitability bubble between 2009 and 2011. Paradoxically, when PV incentives decreased between

2009 and 2012, cost effectiveness rocketed owing to the even stronger reduction of PV system prices. The spike in profitability was not accompanied, however, by a consequent expansion because of the cost-containment measures enacted in that period in Spain [47].

It is also important to stress that the on-roof PV systems promotion mechanism initially established by RD 2818/1998 was one of the greatest obstacles to its development. In this regard, the economic framework set by RD 2818/1998 guaranteed a more beneficial remuneration for small plants with a rated power up to 5 kW (subsequently, RD 436/2004 updated this rated power limit to 100 kW), with the incorrect assumption that roof-mounted PV systems would be those with the smallest installed powers. This ill-defined control scheme, relating the incentives to the rated power rather than to the PV facility type, was not corrected until the approval of RD 661/2007 [9].

This loophole allowed the segmentation of the ground-based PV facilities into modules of 5 kW under RD 2818/1998 or 100 kW under RD 436/2004 eligible for the highest premiums while benefiting of the lower costs of large facilities, giving rise to the so-called solar parks. Thus, boosting cost effectiveness above the levels intended by the regulation. More than 90% of the total PV capacity installed in the 2007–2008 period was some type of solar park, while 65% of the installed PV capacity in that period belonged to solar parks of more than 10 MW of total size divided into units of up to 100 kW [9,27,47].

This fact generated a high uncertainty and contributed to the failure of on-roof PV systems development, as less than 10% of the PV plants in Spain were located on a roof, as well as to the unbalanced development of the whole solar PV sector. Thereupon, although around 80–90% of the Spanish PV plants were located on ground, virtually 100% of them benefited from the incentives originally thought for on-roof PV systems [9,27,47].

The Spanish administrative process related to the commissioning of a solar PV power plant was lengthy because of the requirement to acquire different licenses, the processing of which involved the contact of up to three administrative layers at a local, provincial and autonomous level, in addition to a degree of unwillingness and even philistinism and lack of coordination between competent authorities. In this respect, the same procedure could have different results within the same autonomous community, owing to the specific understanding of the regulation of each administrative body. Specifically, it could take several years from the moment that a stakeholder decided to enter the PV electricity generation business until the facility network connection and the activity final commissioning [19,108].

Lastly, the costs of the power system associated with the remuneration of the solar PV sector raised significantly over the latter part of the 1998–2008 promotion stage. The solar PV sector represented a small share of RES in Spain and, simultaneously, an important portion of the total cost of RES promotion [26]. Figure 4 shows the evolution of the annual costs resulting from the public support devoted to the solar PV sector development in Spain during the period 1998–2020 using a red solid line. In addition, the amount of the specific remuneration costs related to the investment remuneration (see the purple-colored vertical bars in Figure 4) and the operation remuneration (see the yellow-colored vertical bars in Figure 4) are also plotted from 2014 when the new RD 413/2014 legal-economic framework came into force.

As can be seen in Figure 4, during the 1998–2004 subperiod, the solar PV development costs followed a fairly smooth growth, increasing from 0.08 M EUR in 1998 to 2.53 M EUR in 2003. Otherwise, as of the approval of RD 436/2004 and RD 661/2007, these public support costs of the solar PV sector began to take an increasing spiral. Thus, in 2004, the solar PV sector costs increased by 143% compared to the previous year reaching 6.15 M EUR.

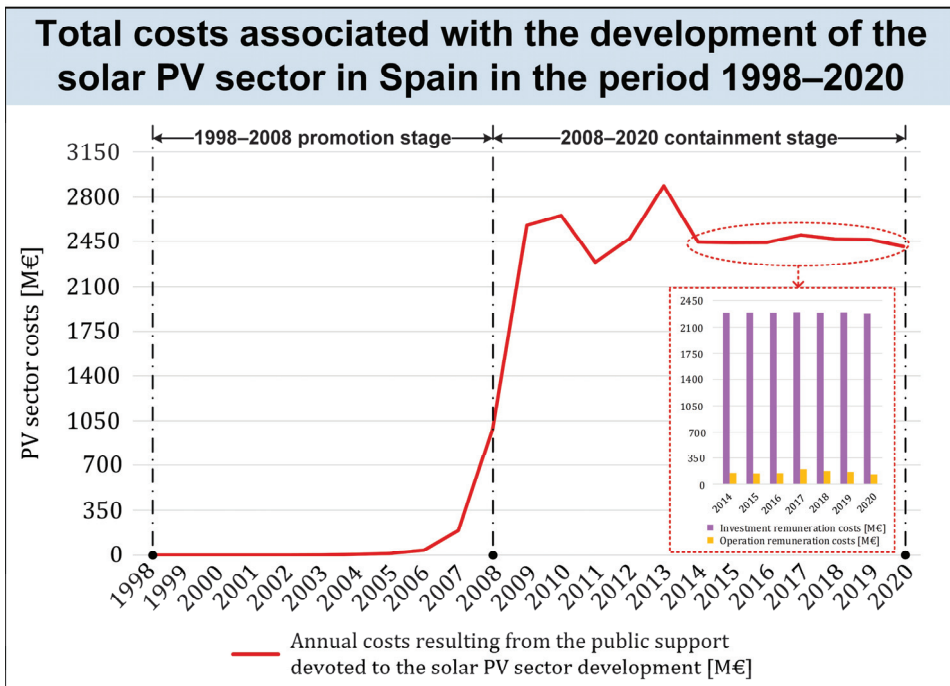


Figure 4. Evolution of the annual costs associated with the Spanish solar PV sector development in the period 1998–2020. Source: self-elaboration based on [69].

Table 12 presents a comparison between the real annual development costs of the Spanish solar PV sector and those expected by the REP 2005–2010 during the period 2005–2010. During the validity period of RD 436/2004, the public support costs of the solar PV sector increased at an annual rate of 130–185%, almost doubling the costs expected by REP 2005–2010. However, during the period 2007–2008, with the enactment of RD 661/2007, the solar PV development costs grew by around 400% annually, quadrupling in 2007 and multiplying by almost 12 in 2008 the costs anticipated by the REP 2005–2010. In this respect, around 80% of the total cost of all the solar PV systems under RD 661/2007 corresponded to the PV facilities installed in 2008 [28].

Furthermore, the 600 M EUR increase in the solar PV sector public support costs for 2008 over the previous year foreseen by the Spanish government was widely exceeded. Specifically, as denoted in Table 12, an increase of almost 800 M EUR was obtained, which in turn represented an increase around 4.9% on the consumers electricity tariff [27].

Table 12. Comparison between the real annual development costs of the Spanish solar PV sector and those expected by the REP 2005–2010 during the period 2005–2010. Source: self-elaboration based on [66,69].

Year	Real PV Costs [M EUR]	PV Costs Expected by the REP 2005–2010 [M EUR]
2005	14.00	9.42
2006	39.89	22.67
2007	191.75	46.56
2008	984.80	85.01
2009	2579.14	134.92
2010	2656.29	200.84

4.1.2. Concerning the CSP Technology Sector

First, the 1998–2004 subperiod was characterized by continuous changes in the economic framework of CSP technology facilities. Initially they were in the same remuneration group as the solar PV plants, namely group b.1, under RD 2818/1998. Later they became part of group b.3 under RD 1955/2000 with reductions in its incentives of 70–80% under the FIT option and 80–90% under the FIP option. In addition, finally, RD 841/2002 defined its own remuneration subgroup within the b.1 solar technology group, i.e., the subgroup b.1.2, which only allowed them to access the FIP remuneration scheme.

In this regard, in addition to the high uncertainty introduced by the continuous changes in the remuneration scheme, hindering the decision-making in the mid and the long term, the low level of remuneration caused that no CSP plant was put into operation in this subperiod. However, the REP 2000–2010 set a CSP capacity target of 200 MW for 2010.

Thereupon, the 2004–2008 subperiod was characterized by a much more favorable economic framework for CSP facilities. RD 436/2004 once again allowed CSP facilities to access the FIT remuneration option, in addition to incorporating an extra incentive to the premium on top of the electricity pool price option. In this sense, at the end of 2004 there were already three CSP projects in progress totaling 110 MW, as well as other initiatives in the development stage totaling 325 MW [10]. In short, with the remuneration system defined in RD 436/2004, RD 436/2004 200 MW capacity target and the 500 MW capacity goal set by REP 2005–2010 for 2010 were insured.

Even though only one CSP plant of 11.02 MW had just been put into operation, the economic framework was once again modified through RD 661/2007. This new economic scheme increased the incentives for CSP facilities by around 20% under the FIT option and around 30% under the FIP option, though the established capacity targets were virtually assured. Thus, over-incentivizing the CSP plants unnecessarily led to a higher financial burden for the final consumers.

Although periodic adjustments and revisions of the economic scheme were established, as in the solar PV sector, the CSP system also behaved similar to an open-loop system during the whole period 1998–2008, in which the incentives were decoupled from the compliance level of the CSP capacity goals set [10].

In addition, as for the PV plants, RD 661/2007 announced a transition mechanism to be applied once 85% of the 500 MW CSP capacity target had been reached, generating high uncertainty in the CSP sector about its date of entering into force and its duration, as well as a call for investment before the highly favorable remuneration scheme finished. Consequently, 4100 MW of CSP capacity had requested access to the grid by 2007 and 15,563 MW by 2009 [10]. Furthermore, a second CSP plant of 49.90 MW entered in operation at the end of 2008 totaling 60.92 MW of installed CSP capacity in Spain, which represented an increase in the cumulative installed CSP capacity of 453% with respect to the previous year. A CSP bubble was taking shape.

In Spain, the absence of a social backlash against the technology seemed to be related to CSP deployment being a win–win for most local actors due to its environmental and socioeconomic benefits [38].

In conclusion, the costs of the power system associated with the remuneration of the CSP sector started to increase at the end of the 1998–2008 promotion stage. Figure 5 depicts the evolution of the annual costs resulting from the public support devoted to the CSP sector development in Spain during the period 1998–2020 using a blue solid line. In addition, the amount of the specific remuneration costs related to the investment remuneration (see the purple-colored vertical bars in Figure 5) and the operation remuneration (see the yellow-colored vertical bars in Figure 5) are also plotted from 2014 when the new RD 413/2014 legal–economic framework came into force.

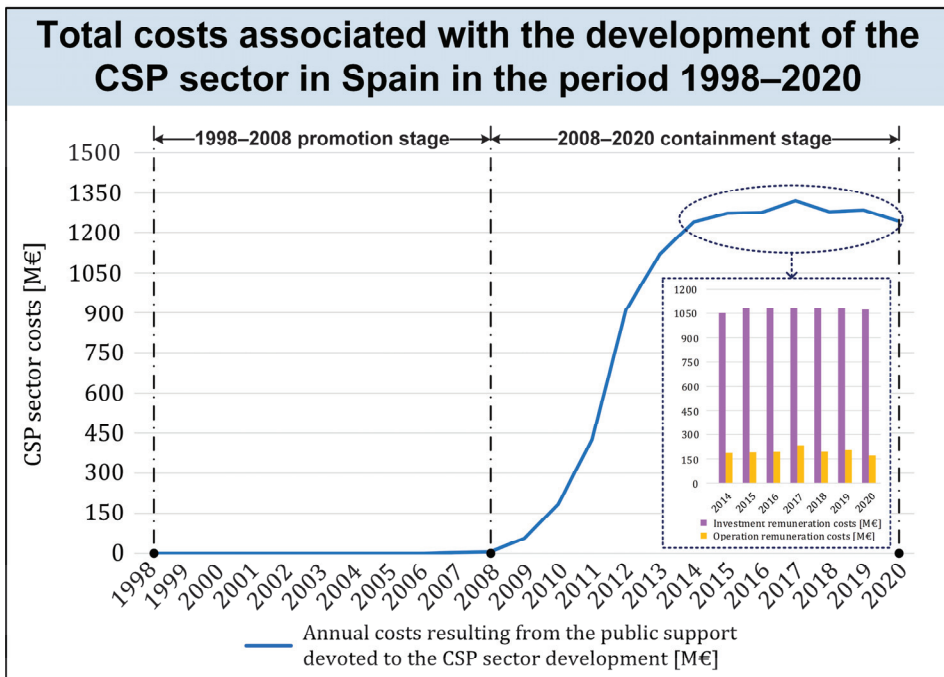


Figure 5. Evolution of the annual costs associated with the Spanish CSP sector development in the period 1998–2020. Source: self-elaboration based on [69].

As can be observed in Figure 5, during the 1998–2006 period no CSP plant was put into operation in Spain, thus the development costs of the CSP sector were zero. In 2007, the first 11.02 MW CSP plant was put into operation with public support costs for the CSP sector of 3.07 M EUR. In turn, with the commissioning of a second 49.90 MW CSP plant in 2008, those costs increased by 96% to 6.02 M EUR.

4.2. Analysis of the 2008–2020 Containment Stage

4.2.1. Concerning the Solar PV Technology Sector Containment Stage and RD 1578/2008

The 2008–2013 subperiod was characterized by the implementation of different measures to first control the Spanish PV boom that took place in 2007–2008 and then, to reduce the economic impact on the power sector of existing and future PV plants, ensuring its economic sustainability.

First, RD 1578/2008 was approved as a control structure aimed at adapting the remuneration scheme for new PV facilities once RD 661/2007 PV power targets had been largely exceeded due to the solar PV boom. It established a saturation mechanism through the creation of the RPAR that limited the total new PV power installed in the electricity system, as shown in Figure 6. Thus, the PV power finally awarded for registration in the RPAR was not allowed to exceed the quarterly power calls, which varied according to the system evolution. Given the small quotas legislated and the delay in their allocation, many awarded PV projects were delayed in their implementation as installed capacity [27,41]. However, the saturation mechanism could create an overheating of the market and boom-and-bust cycles if the capacity was provided on a first-come-first-served basis as in the Spanish case [44].

Figure 6 depicts the evolution of the solar PV technology under RD 1578/2008 control structure during the 3-year 2009–2011 period, in which a total of 12 power calls were carried out for each type of PV plant, i.e., 4 calls per year.

On the one hand, the first column of graphs shows the PV power awarded per call (see the green-colored vertical bars in Figure 6), as well as the PV power admitted but not awarded due to the full coverage of the quotas established (see the orange-colored vertical bars in Figure 6), the PV power not admitted due to the existence of formal defects (see the red-colored vertical bars in Figure 6) and the maximum PV quota established (see the black dashed line in Figure 6) for each PV plant typology, i.e., subtype I.1, subtype I.2 and type II.

On the other hand, the second column of graphs depicts the cumulative PV power awarded as the calls progressed (see the green solid line in Figure 6), as well as the maximum cumulative PV quota established (see the blue-colored vertical bars in Figure 6) for each type of PV facility, namely subtype I.1, subtype I.2 and type II.

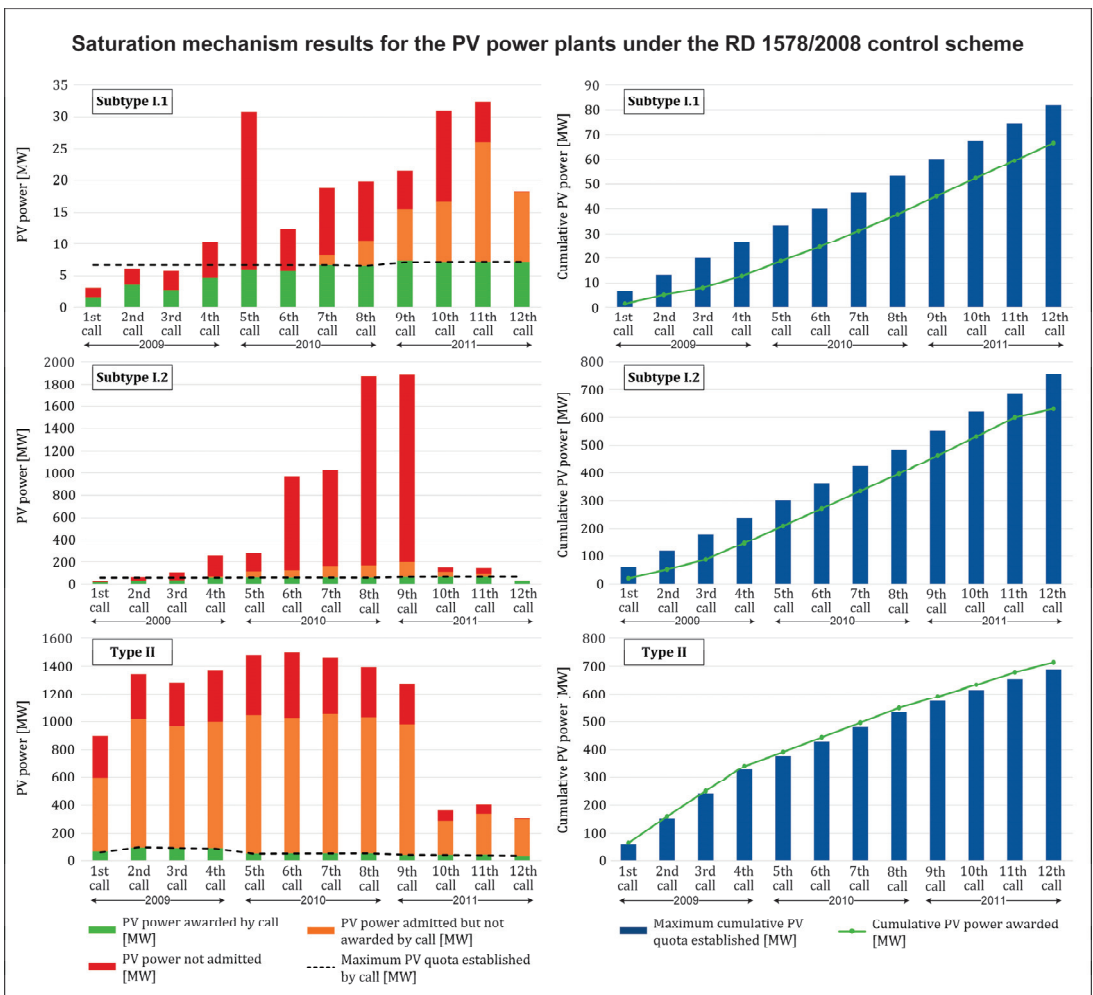


Figure 6. Evolution of the solar PV technology under RD 1578/2008 control structure during the period 2009–2011. Source: self-elaboration based on [69].

During the 3-year 2009–2011 period under RD 1578/2008 saturation mechanism, 66.7 MW of cumulative PV power for subtype I.1 (4.73% of the total awarded PV power), 630.9 MW for subtype I.2 (44.70% of the total awarded PV power) and 713.65 MW for type II (50.57% of the total awarded PV power) were awarded in the different power calls, as shown in Figure 6.

By contrast, without the control mechanism established by RD 1578/2008, the cumulative PV power awarded during the same period would have been 119.8 MW for subtype I.1, 1169.57 MW for subtype I.2 and 9655.18 MW for type II (see Figure 6). Obtaining, in this case, an excess in the cumulative PV power awarded with respect to the maximum cumulative PV quota established of 46.38% for subtype I.1, 54.63% for subtype I.2 and 1301.17% for type II.

Hence, the saturating effect of RD 1578/2008 RPAR was an effective mechanism to guarantee the stability and predictability of the PV system. It could be estimated that 125–171 M EUR for subtype I.2 and 615–842 M EUR for type II was saved for the Spanish electricity sector at the end of 2010 [27].

Furthermore, RD 1578/2008 corrected the previous decoupling of the regulated tariff and the compliance degree of the power goals, putting an end to the former open-loop control for new PV plants. Accordingly, it adjusted the annual power goals of each PV system type as a function of the regulated tariff, offsetting the rise in power targets with the decrease of its remuneration, as seen in Figure 7. Thus, limiting the economic impact on the power system of the new PV power plants, but without waiving the PV investment. Specifically, in the most likely scenario of full coverage of all the power calls, a FIT annual reduction of approximately 10% was obtained [27].

As the support levels evolution depended on the market reaction, it mitigated the asymmetric information problem related to technology costs common in the past (the Spanish government failed to estimate the costs of solar PV as well as their evolution and, thus, higher support levels than necessary were provided [44]). Thus, allowing the market to reveal the true costs of the technology [26]. However, the flexible degression tariff mechanism under RD 1578/2008 introduced uncertainty to investors, since they did not know exactly the level of support a period before they invested [26,44].

Figure 7 plots the evolution of the solar PV technology under RD 1578/2008 control structure during the 3-year 2009–2011 period in terms of the cumulative PV power awarded (see Figure 7a) and the eligible FIT for the PV power awarded (see Figure 7b), for each type of PV plant, i.e., subtype I.1 (see the dark-blue solid lines in Figure 7), subtype I.2 (see the light-blue solid lines in Figure 7) and type II (see the green solid lines in Figure 7).

As observed in Figure 7, during the 2009–2011 period, as the cumulative PV power awarded increased in a certain type of PV plant, the FIT decreased for that type of facility. Specifically, the cumulative PV power awarded during the 2009–2011 period increased from 1.67 MW to 66.70 MW for subtype I.1, from 20.92 MW to 630.90 MW for subtype I.2 and from 66.11 MW to 713.65 MW for type II. However, the FIT was reduced from 34 cEUR/kWh to 27.38 cEUR/kWh for subtype I.1 (19.47% of reduction), from 32 cEUR/kWh to 19.32 cEUR/kWh for the subtype I.2 (39.63% of reduction) and from 32 cEUR/kWh to 12.5 cEUR/kWh for type II (60.94% of reduction).

In addition, RD 1578/2008 control structure could have also contributed to the growth of rooftop PV plants, representing 49.43% of the new PV facilities with a total of 697.6 MW awarded during the 2009–2011 period.

Therefore, after a total of 2707.34 MW of PV power had been put into operation in 2008, there was a slowdown in installed PV capacity of almost one year, from October 2008 until practically November 2009, due to the increase in the administrative complexity and cueing procedures resulting from the enactment of RD 1578/2008 RPAR. Since then, the different calls under RD 1578/2008 control mechanism caused the commissioning of 1248.36 MW of new PV power in the 2009–2013 period. Thus, at the end of 2013, the cumulative PV power in Spain was 4646.15 MW, representing an increase of 36.74% compared to the cumulative PV power in 2008.

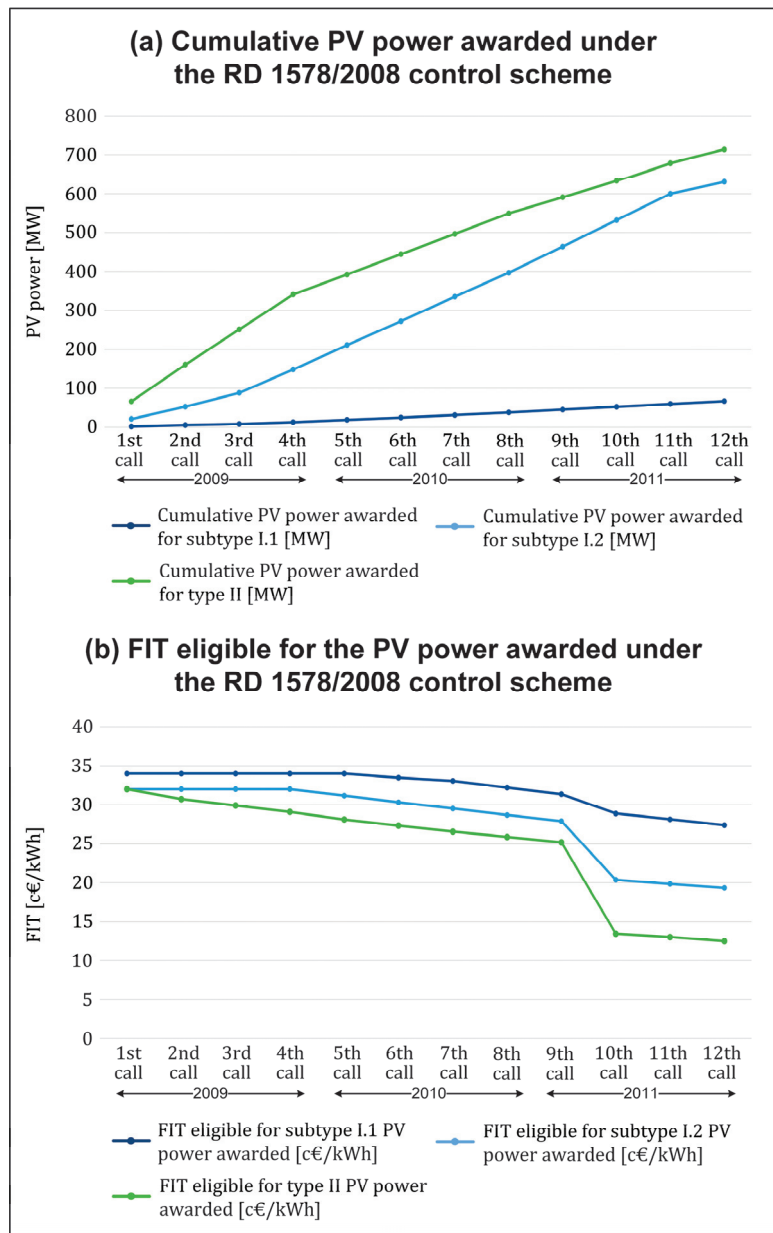


Figure 7. Evolution of the solar PV technology under RD 1578/2008 control structure during the period 2009–2011 in terms of: (a) the cumulative PV power awarded; (b) the FIT eligible for the PV power awarded. Source: self-elaboration based on [69].

Containment Stage and Retroactive Energy Policy from 2010 to 2012

Subsequently, the Spanish government enacted a retroactive energy policy in the period 2010–2012 to lessen the financial burden to the electricity system. The promotion cumulative cost of PV systems was expected to be less than 499.4 M EUR at the end of the period 2005–2010. However, at the end of 2010, this cost was, at least, 6802.8 M EUR, which

raised the Spanish power tariff deficit and, consequently, the electricity tariff charged to consumers [27].

The 2010–2012 energy policy changed the cost effectiveness of the PV power plants by impacting on their income and on their operating cost. The new energy measures representing savings to the electricity sector resulted in minor revenue for the power plants. However, the measures introducing new incomes for the electricity system were directly translated into an increment of their operating cost [28].

RD 1578/2008 did not regulate the PV cost-containment expressly. Thus, in 2010, 3 new rules entered into force to amend the inefficient cost control scheme, namely RD 1003/2010, RD 1565/2010 and RDL 14/2010.

The first saving action, introduced by RD 1003/2010, was the possible shrinkage of the PV power under RD 661/2007 depending on the existing fraud detection, which would imply the exclusion of the PV facilities involved from the remuneration framework of RD 661/2007. Thus, entailing a decrease on the final cumulative cost overrun [28].

RD 1565/2010 imposed a drastic decrease of the regulated tariffs applied to PV systems under RD 1578/2008 (note that about 80% of all PV facilities installed at that moment in Spain fell under RD 661/2007 [26]). The accumulated FIT reductions reached 32.3% for subtype I.1 PV systems, 52.5% for subtype I.2 and 68.8% for type II, respectively, regarding the conditions established by RD 661/2007. Thus, this control measure represented an annual saving of around 140 M EUR and countered the cost increment of approximately 138 M EUR per year provoked by the experienced growth in generation capacity [27].

RDL 14/2010 limited the operating time eligible for premium of PV facilities under both RD 661/2007 and RD 1578/2008. Then, the electricity generated exceeding that threshold should be sold at the wholesale market, thus reducing its revenues. This control measure prevented the consolidation of the experimented increase in generation capacity and therefore, future cost deviations. However, it could limit the efficient functioning of existing plants as well as the development of more efficient solar PV technologies, because it discouraged improvements in efficiency as a path to increase income [26,27]. With the enactment of RDL 14/2010, the government planned to decrease the expenditures of the power sector by 4600 M EUR in 3 years, namely from 2011 to 2013. Half of this amount was expected to come from the reduction of the PV plants revenues, representing an annual saving of 740 M EUR for consumers [11,26].

Moreover, measures were also implemented to increase the income of the electricity system under the 2010–2012 energy policy. Specifically, RDL 14/2010 obligated all power generators to pay a 0.5 EUR/MWh toll for the electricity fed into the distribution and transmission grids [84], and Law 15/2012 added a 7% tax on the gross revenues for the electricity generated by all electricity producers in the Spanish electrical system [87]. The solar PV sector claimed that the 0.5 EUR/MWh grid access charge reduced the revenues of ground-mounted PV facilities by 0.2% and those of roof facilities by 0.3%, while the RES generators receiving support through FIT could not pass the amount of this 7% fee to customers and, therefore, should assume the additional costs fully [11].

According to [11], the 7% generation charge had the greatest impact among the 2010–2012 containment measures, followed by RDL 2/2013 change in the tariff-updating mechanism, RDL 14/2010 generation cap, RD 1565/2010 shortening of the support period and the 0.5 EUR/MWh grid access charge. However, the rise of the support period length under RDL 14/2010, first, and under Law 2/2011, later, improved the profitability of the PV plants.

The urgent need to decrease the skyrocketing Spanish power tariff deficit forced the government to approve RDL 1/2012 in 2012, which cancelled economic incentives for all new RES power plants. Still, the main problem of regulating the Spanish solar PV industry by that moment was how to deal with the overflowed cost caused by the control deficiencies of the previous legislations [27]. Numerous solar PV manufacture companies either had to close or merge because neither minimum returns nor capital amortization were guaranteed, and employment in the sector fell from a high of 41,700 reported jobs to fewer than 10,000

in 2012 [23,41]. Even though a public credit line was launched by the Spanish government in July 2011, with a variable interest rate and a repayment term of 7 years maximum, that initiative was not enough to replace the private financing [41].

As shown in Figure 4, during the 2008–2013 subperiod, the solar PV sector development costs followed a significant and sustained growth, increasing from 984.80 M EUR in 2008 to 2889.11 M EUR in 2013. In 2009, the solar PV costs increased by 162% compared to the previous year reaching 2579.14 M EUR (in that year solar PV received almost 60% of all support for renewable electricity in Spain, despite providing only 12% of its renewable electricity and almost 3% of the total electricity generation [11,23]). However, thereafter, due to the cost-containment retroactive energy policy measures, the evolution in costs stabilized with a downward trend. Thus, solar PV costs grew 3% in 2010, decreased 14% in 2011, and again grew 8% in 2012 and 17% in 2013.

Containment Stage and Retroactive Energy Policy from 2013 to 2020

The cost reduction capability of the 2010–2012 energy policy had not been enough. Thus, in 2013, RDL 9/2013 broke with the legal philosophy applied so far, which had introduced cost reducing measures without dismantling the established economic framework [28].

Therefore, the 2013–2020 subperiod, unlike the 2008–2013 subperiod, was characterized by the dismantling of the previous open-loop control structure for the whole solar PV sector. Thus, RDL 9/2013 laid the foundations for a new closed-loop control scheme, the financial sustainability of the electricity system being a declared objective. Subsequently, the SES Law 24/2013 and RD 413/2014 developed this new control mechanism for both new PV plants under RD 1578/2008 and existing ones under RD 661/2007. The new remuneration scheme set by RD 413/2014 reasonable profitability cost-containment mechanism caused a considerable profitability reduction in the PV plants with respect to the former frameworks.

Moreover, the intrinsic complexity of RD 413/2014 framework, with a great number of regulatory parameters and a high uncertainty associated with their future evolution, severely hampered understanding its effects on the economic performance of the PV systems in the mid and the long term [46].

It is also important to stress that even though the minimum threshold of operating hours imposed by RD 413/2014 to PV plants could have represented an opportunity to force the owner to keep their facilities at their optimum status and, therefore, generating as much energy as possible, RD 413/2014 established that minimum threshold below 50% of the average operating hours of a standard PV power plant in Spain. Consequently, some investors wondered if it was worth keeping the annual investment in operating and management protocols to acquire high energy yields provided that the minimum threshold was achieved, as the economic effort to optimally maintain the PV facility did not exceed the maximum threshold of operating hours and its corresponding revenues [36].

After implementing the containment measures in the Spanish solar PV sector through the different regulatory frameworks enacted, the PV economic investments changed from an attractive initial cost-effective scenario to a limited situation in terms of the original business plans [36]. In this regard, more than one third of the existing PV plants in that moment were bearing negative returns and liquidity problems (additionally damaged by the slow pace of the government's subsidy payments [36]), leading to many appeals and legal claims in the court against the Spanish State. Most of the producers were pushed to refinance their bank debt under more burdensome terms or to sale the PV plants to foreign investment groups. In turn, many small investors were indirectly forced to abandon their plans, i.e., canceling the annual expenditures on operating and management tasks, so they could divert those operational expenditures to their loan duties and overcome possible bankruptcy scenarios. In those bankruptcy scenarios, private equity or vulture funds ([36] stated that there could be a certain degree of government complicity with some powerful equity funds or energy companies) were discovering market opportunities, either by acquiring PV-related enterprises or buying large PV plants [12,18,35,36,46,53].

Spain dropped from second position among the EU countries in 2008, with 32.5% of generation, to fifth in 2015, with 5.1% of production. Similarly, there were 1942 companies in operation in the solar PV sector in 2008, while 848 companies had disappeared in 2014 over a 6-month period, constituting 44% of companies active in 2008 [12].

During the 2014–2018 period there was a significant stoppage in the commissioning of new PV power. Specifically, only 53 MW of PV capacity were installed in Spain. This trend changed in the 2019–2020 period with the installation of 3311.71 MW in 2019 and 2243.95 MW in 2020 of new PV capacity as a result of RD 413/2014 auctions carried out in 2017. Thus, at the end of 2020 the cumulative PV power installed in Spain was 10,254.78 MW, representing an increase of 118% compared to the cumulative PV power in 2018. Although the first 2007–2008 PV boom was led by small companies, this second boom is linked to larger companies [37].

As shown in Figure 4, during the 2013–2020 subperiod the development costs of the solar PV sector remained practically constant with annual variations between -15% and $+2.5\%$. The solar PV costs evolved from 2889.11 M EUR in 2013 to 2409.77 M EUR in 2020.

During the 2013–2020 subperiod, the investment remuneration represented 92–94% of the specific remuneration costs, while the operation remuneration only represented the remaining 6–8%, as shown in Figure 4.

4.2.2. Concerning the CSP Technology Sector

Containment Stage and Retroactive Energy Policy from 2010 to 2013

The 2008–2013 subperiod was characterized by the implementation of a set of concurrent saving measures to the existing control system to limit the CSP bubble that was taking shape and the associated overrun cost to the power sector. To that effect, first, RDL 6/2009 replicated the control structure defined by RD 1578/2008 for PV plants, to avoid that the solar PV boom and its economic impact on the electricity system could occur in other renewable sectors such as CSP or wind.

RDL 6/2009 established a saturation mechanism through the creation of the RPAR that limited the total CSP power installed in the system. In this way, it was possible to limit the CSP bubble generated under RD 661/2007. Accordingly, only 29% of the 15,563 MW of CSP capacity, which had requested access to the electricity network and had deposited the corresponding economic guarantees, finally applied for the RPAR (4499 MW). Furthermore, only half of the CSP power that applied to the RPAR was definitely awarded [10].

However, the almost 2440 MW of CSP capacity awarded and registered in the RPAR five-fold increased the 500 MW CSP capacity goal set by REP 2005–2010 for 2010. Thus, the entry into operation of the enrolled CSP power plants was distributed in four stages until the end 2013 to defer the overrun costs to the electricity system.

Thereupon, 471 MW were put into operation in the first phase (years 2009–2010), 467 MW in the second phase (year 2011), 951 MW in the third phase (year 2012) and the last 350 MW in the fourth phase (year 2013). This new yearly installed capacity represented an increase in the cumulative CSP capacity compared to the previous year of 281% reaching 232 MW in 2009, 129% reaching 532 MW in 2010, 88% reaching almost 1000 MW in 2011, 95% reaching 1950 MW in 2012 and 18% reaching almost 2300 MW in 2013.

In addition, other regulatory measures were implemented to decrease the soaring costs of the electrical system, such as RD 1614/2010, which limited the equivalent operating hours at rated power eligible for the regulated tariff or premium of RD 661/2007 for CSP facilities [83], or RDL 1/2012, which temporarily suppressed the economic incentives of RD 661/2007 as well as the registration procedure in the RPAR under RDL 6/2009 for new SR power plants [86].

Moreover, measures were also implemented to increase the income of the electricity system such as RDL 14/2010, which obligated all power generators to pay a 0.5 EUR/MWh toll for the electricity fed into the distribution and transmission grids [84], or Law 15/2012, which added a 7% tax on the gross revenues for the electricity generated by all electricity producers in the Spanish electrical system [87].

As shown in Figure 5, during the 2008–2013 subperiod, the development costs of the CSP sector followed a significant and sustained growth, increasing from 6.02 M EUR in 2008 to 1120.75 M EUR in 2013. In 2009, the CSP public support costs increased by 815% compared to the previous year reaching 55.13 M EUR. However, thereafter, due to the cost deferral mechanism incorporated by RDL 6/2009, the increase in development costs stabilized with a downward trend. Thus, CSP costs grew 234% in 2010, 132% in 2011, 113% in 2012 and 23% in 2013.

Containment Stage and Retroactive Energy Policy from 2013 to 2020

Then, the 2013–2020 subperiod, unlike the 2008–2013 subperiod, was characterized by the dismantling of the previous open-loop control structure. Thus, RDL 9/2013 laid the foundations for a new closed-loop control scheme where the cost to the electrical system was the controlled variable. Subsequently, the SES Law 24/2013 and RD 413/2014 developed this new control mechanism, adjusting the remuneration of the RES facilities to the needs of the Spanish power system. The remuneration parameters were periodically reviewed and updated, seeking a reasonable profitability for the RES facilities, in which were included the CSP plants, while maintaining the economic sustainability of the electrical system [10].

By the end 2013, 50 CSP facilities with 2299.5 MW of cumulative capacity were commercially operating in Spain, turning it into the world leader in terms of installed CSP capacity, followed by the United States. A total of ten out of the 60 initially envisaged facilities, as well as the innovative CSP project, were finally withdrawn due to the cuts in the CSP remuneration introduced by the latest regulatory changes. Specifically, the new legislation implied a 15% mean cut in the CSP remuneration, which added to the retroactive measures adopted in the previous years increased the cumulative cut to 50% [10,30].

Accordingly, one of the most significant problems for the CSP sector was the liquidity shortage and the decrease of their legitimate expectations in the income statement. Furthermore, RD 413/2014 legal–economic framework introduced an enormous complexity and uncertainty in the Spanish CSP sector remuneration mechanism. Thus, significantly hampering their economic assessment and decision-making in the mid and the long term, and reducing the Spanish project developers, with only engineering, procurement and construction firms remaining in the sector [10,30,38,54].

CSP is still considered an immature non-competitive technology with the absence of public support. The principal reason for the sluggish growth of CSP is notably related to its huge generation costs (the most relevant barrier of the CSP technology compared to conventional power plants and other RES technologies according to [38]). This situation is strongly illustrated in Spain, where the solar power sector came to complete stagnation when the recession forced the national government to shorten the subsidies that had prompted its rapid development several years earlier. The feasibility of this type of CSP facilities essentially depend on a sharp decrease in operating costs and a rise in income from electricity sales [39].

The size limit of 50 MW to be eligible for support in Spain was regarded as a limit to further innovation and cost reductions, since CSP projects needed to be relatively large to function properly while upsizing is a relevant source of cost reductions [38,40].

No new CSP plant was installed in Spain as of 2013. Thus, as shown in Figure 5, during the 2013–2020 subperiod the development costs of the CSP sector remained practically constant with annual variations between -3% and $+10\%$. The CSP public support costs evolved from 1120.75 M EUR in 2013 to 1244.46 M EUR in 2020, going through a peak of 1320.76 M EUR in 2017.

During the 2013–2020 subperiod, the investment remuneration represented 82–86% of the specific remuneration costs, while the operation remuneration only represented the remaining 14–18%, as shown in Figure 5.

5. Conclusions

This work provides a comprehensive review of the energy policy evolution for the whole solar power sector in Spain, namely both solar PV and CSP technologies, from 1998 to 2020. Thus, this review deals with the complete boom-and-bust cycle experienced by the Spanish solar power sector in the last 23 years.

Spain has become one of the most successful countries in the world in promoting electricity generation from RES, and specifically from the solar resource due to the great country-specific solar potential, through a highly favorable energy policy combined with strong public incentives set by Spanish governments mainly during the first decade of the 2000s. Nevertheless, the initial highly favorable regime applicable to solar power plants turned into an extremely unfavorable scenario during the second decade of the 2000s.

The Spanish solar power sector has suffered continuous and significant changes in its regulation, denoting a great dynamism in recent years. In this vein, a survey of the different legislation in force during the 1998–2020 period was first conducted to contextualize and describe the last 23 years of solar energy policy in Spain. Two major stages have been identified, namely the 1998–2008 promotion stage, which began with the enactment of the first SES Law 54/1997, and the 2008–2020 cost-containment stage, which ended with the approval of the new RD 960/2020 economic regime for RES. During the 1998–2008 promotion stage, a total of two REPs, two European directives and seven meaningful national regulations were implemented for the solar power sector. In turn, during the 2008–2020 cost-containment period, a total of one REP, one European Directive and up to 22 relevant national regulations were implemented for that renewable electricity production sector. As regards the promotion stage, the first part began by laying the foundations of the Spanish electricity production sector from RES, and more specifically from solar technologies, through RD 2818/1998 framework and its revisions, i.e., RD 1955/2000 and RD 841/2002. However, during the second half of that period the Spanish government ratified its unwavering and forceful commitment to the development of solar power plants by an extremely favorable economic framework for those facilities, first under RD 436/2004 and later under RD 661/2007.

As for the cost-containment stage, the first part was characterized by the enactment of a set of measures aimed at controlling the excessive growth of solar capacity, derived from the Spanish solar boom that was taking shape during the period 2007–2008, and its huge impact on the electricity system costs, namely RD 1578/2008, RDL 6/2009, RD 1003/2010, RD 1565/2010, RD 1614/2010, RDL 14/2010 and Law 2/2011. However, the measures adopted until 2011 were not sufficient, putting at risk the final goal of suppressing the tariff deficit, which emerged because of the mismatch between the income and the costs of the Spanish power system, as of 2013. Thus, new containment measures were approved in 2012, namely RDL 1/2012, Law 15/2012 and RDL 29/2012. However, during the second half of that period, and after the approval of RDL 2/2013 which continued to seek the electricity system tariff deficit mitigation in line with the previous measures, the Spanish government retroactively dismantled the previous promotion frameworks breaking with the cost-containment philosophy applied so far, to reduce the high economic burden to the Spanish power system ultimately paid by the end consumers. Thus, laying the foundations of a new paradigm for the entire Spanish renewable power sector, in which were included the solar power plants, by means of RD 413/2014 regulation, which built the fundamentals already included in RDL 9/2013 and integrated in Law 24/2013. During the second half of the cost-containment stage, three RES auctions under RD 413/2014 framework were called in Spain to comply with the RES binding European targets by 2020.

Subsequently, a survey of the most relevant existing academic literature dealing with this issue was conducted to carefully assess the last 23 years of solar energy policy in Spain based on their results and conclusions. In short, it is important to stress the decisive role of Spanish governments in promoting the solar power sector during the 1998–2008 period by providing a stable, quite favorable and easily predictable RES regulatory support mechanism quite attractive for investors. However, during the 1998–2008 promotion stage,

the Spanish solar system behaved as an open-loop system without any control structure adjusting public support levels to the RES generation costs and/or to the compliance degree of the targets set by the Spanish solar energy policy, leading to uncontrolled growth in RES capacity and, therefore, to large system cost increases ultimately affecting end consumers. One of the biggest lessons extracted from the Spanish solar experience is that the specific design elements of RES support schemes and not so much the instrument chosen were a major factor for their efficiency and well-functioning.

In Spain, cost-containment measures were applied from 2008 onwards after the renewable energy policy had been implemented and investments had been made. Therefore, the RES stakeholders that invested ex-ante in the RES electricity production sector under the favorable conditions set by the Spanish government saw ex-post how it retroactively changed the legislation and substantially reduced or even eliminated the profitability of such investments. The fact that the Spanish governments were forced to implement retroactive measures during the period 2008–2020, dismantling the previous legal–economic framework for RES, clearly indicated a malfunctioning of the energy policy control mechanism. The new retroactive closed-loop control mechanism developed by the SES Law 24/2013 and RD 413/2014 had a critical impact on the profitability of the existing solar facilities, and could even lead to the bankruptcy of these RES facilities. Furthermore, the high complexity and uncertainty of the new retroactive investment-based remuneration scheme awarded by competitive tenders, significantly hindered the economic assessment and decision-making of both new and existing solar power plants in the mid and the long term. Conversely, the new RD 413/2014 legal–economic scheme has not been subjected to substantial modifications after coming into effect in 2014, therefore introducing a period of considerable regulatory stability.

On balance, it is expected that the lessons extracted from this 23-year comprehensive review of the Spanish solar power sector pathway could be quite useful for other countries either in the initial development stage or fully immersed in the promotion of solar power sector or any other renewable technology. First, a simple but robust, stable and predictable development model in the mid and long term, combined with an administrative process as simple and agile as possible to prevent it from acting as a barrier for renewable energy stakeholders, is extremely important. Thus, providing investors with maximum legal–economic security and reliability. Furthermore, a good planning of the energy development model is fundamental, establishing how much energy can be assumed at the national level and at what price. Therefore, limiting the implementation of retroactive measures, as happened in the Spanish cost-containment stage, which can seriously jeopardize the viability of the power plants in operation, as well as compromising the legal–economic stability of the renewable energy sector, thus, generating distrust and uncertainty among investors. In this respect, it is important to highlight the great importance of designing robust and adequate renewable technology support schemes, as well as of its updating mechanisms, to provide investors with certainty and good predictability of the income statement of their renewable assets in the mid and long term. In such a way that open-loop models without any control structure detecting and reacting to problematic situations, as occurred during the Spanish promotion stage, should be avoided. In recent years, the price setting system of auction mechanisms has shown a high effectiveness when setting electricity prices by limiting the costs for the power system, greater than that established through legislation by country-specific governments.

Future works will cover a detailed comparison between the Spanish case and the pathways experienced in the development of the renewable power sector in other countries of the world, as well as an extensive criticism of the solar energy policies implemented in Spain over the last 23 years by describing and assessing in detail the political and management implications. In addition, the authors are considering undertaking a comprehensive review of the self-consumption solar photovoltaic sector.

Author Contributions: Conceptualization, S.C. and J.d.l.H.; methodology, S.C., J.d.l.H. and À.A.; validation, S.C., J.d.l.H., À.A. and H.M.; formal analysis, S.C. and J.d.l.H.; investigation, S.C.; data curation, S.C., À.A.; writing—original draft preparation, S.C.; writing—review and editing, S.C., J.d.l.H., À.A. and H.M.; visualization, S.C.; supervision, J.d.l.H. and H.M.; project administration, J.d.l.H. and H.M.; funding acquisition, S.C. All authors have read and agreed to the published version of the manuscript.

Funding: This research was funded by Agència de Gestió d'Ajuts Universitaris i de Recerca (AGAUR) and European Social Fund, grant number 2020FI_B2_00055.

Institutional Review Board Statement: Not applicable.

Informed Consent Statement: Not applicable.

Conflicts of Interest: The authors declare no conflict of interest. The funders had no role in the design of the study; in the collection, analyses, or interpretation of data; in the writing of the manuscript, or in the decision to publish the results.

Nomenclature

AET	Average electricity tariff
BP	Basis points
CO ₂	Carbon dioxide
CPI	Consumer price index
CSP	Concentrating solar power
EU	European Union
FIP	Feed-in premium
FIT	Feed-in tariff
GHG	Greenhouse gas
IEA	International Energy Agency
IRR	Internal rate of return
LCOE	Levelized cost of electricity
NPV	Net present value
PV	Photovoltaic
RD	Royal Decree
RDL	Royal Decree Law
REP	Renewable energy plan
RES	Renewable energy sources
RPAR	Register of pre-allocation of remuneration
SES	Spanish electricity sector
SR	Special regime

References

1. Del Río, P. Analysing future trends of renewable electricity in the EU in a low-carbon context. *Renew. Sustain. Energy Rev.* **2011**, *15*, 2520–2533. [CrossRef]
2. Dinçer, F. The analysis on photovoltaic electricity generation status, potential and policies of the leading countries in solar energy. *Renew. Sustain. Energy Rev.* **2011**, *15*, 713–720. [CrossRef]
3. Espinosa, M.P.; Pizarro-Irizar, C. Is renewable energy a cost-effective mitigation resource? An application to the Spanish electricity market. *Renew. Sustain. Energy Rev.* **2018**, *94*, 902–914. [CrossRef]
4. REN21. Renewables 2021 Global Status Report. Paris. 2021. Available online: https://www.ren21.net/wp-content/uploads/2019/05/GSR2021_Full_Report.pdf (accessed on 10 November 2021).
5. IEA. World Energy Outlook 2021. Paris. 2021. Available online: <https://iea.blob.core.windows.net/assets/888004cf-1a38-4716-9e0c-3b0e3fdbf609/WorldEnergyOutlook2021.pdf> (accessed on 10 November 2021).
6. Ciarreta, A.; Gutiérrez-Hita, C.; Nasirov, S. Renewable energy sources in the Spanish electricity market: Instruments and effects. *Renew. Sustain. Energy Rev.* **2011**, *15*, 2510–2519. [CrossRef]
7. Abdmouleh, Z.; Alammari, R.A.M.; Gastli, A. Review of policies encouraging renewable energy integration & best practices. *Renew. Sustain. Energy Rev.* **2015**, *45*, 249–262. [CrossRef]
8. Bianco, V.; Driha, O.M.; Sevilla-Jiménez, M. Effects of renewables deployment in the Spanish electricity generation sector. *Util. Policy* **2019**, *56*, 72–81. [CrossRef]

9. De la Hoz, J.; Boix, O.; Martín, H.; Martins, B.; Graells, M. Promotion of grid-connected photovoltaic systems in Spain: Performance analysis of the period 1998–2008. *Renew. Sustain. Energy Rev.* **2010**, *14*, 2547–2563. [[CrossRef](#)]
10. Martín, H.; de la Hoz, J.; Velasco, G.; Castilla, M.; García de Vicuña, J.L. Promotion of concentrating solar thermal power (CSP) in Spain: Performance analysis of the period 1998–2013. *Renew. Sustain. Energy Rev.* **2015**, *50*, 1052–1068. [[CrossRef](#)]
11. Mir-Artigues, P.; Cerdá, E.; del Río, P. Analyzing the impact of cost-containment mechanisms on the profitability of solar PV plants in Spain. *Renew. Sustain. Energy Rev.* **2015**, *46*, 166–177. [[CrossRef](#)]
12. Ibarloza, A.; Heras-Saizarbitoria, I.; Allur, E.; Larrea, A. Regulatory cuts and economic and financial performance of Spanish solar power companies: An empirical review. *Renew. Sustain. Energy Rev.* **2018**, *92*, 784–793. [[CrossRef](#)]
13. Liu, W.; Zhang, X.; Feng, S. Does renewable energy policy work? Evidence from a panel data analysis. *Renew. Energy* **2019**, *135*, 635–642. [[CrossRef](#)]
14. Marques, A.C.; Fuinhas, J.A.; Macedo, D.P. The impact of feed-in and capacity policies on electricity generation from renewable energy sources in Spain. *Util. Policy* **2019**, *56*, 159–168. [[CrossRef](#)]
15. Zafrilla, J.-E.; Arce, G.; Cadarso, M.-Á.; Córcoles, C.; Gómez, N.; López, L.-A.; Monsalve, F.; Tobarra, M.-Á. Triple bottom line analysis of the Spanish solar photovoltaic sector: A footprint assessment. *Renew. Sustain. Energy Rev.* **2019**, *114*, 109311. [[CrossRef](#)]
16. Görtler, K.; Postpischil, R.; Quitzow, R. The dismantling of renewable energy policies: The cases of Spain and the Czech Republic. *Energy Policy* **2019**, *133*, 110881. [[CrossRef](#)]
17. Trujillo-Baute, E.; del Río, P.; Mir-Artigues, P. Analysing the impact of renewable energy regulation on retail electricity prices. *Energy Policy* **2018**, *114*, 153–164. [[CrossRef](#)]
18. Mir-Artigues, P.; Cerdá, E.; del Río, P. Analysing the economic impact of the new renewable electricity support scheme on solar PV plants in Spain. *Energy Policy* **2018**, *114*, 323–331. [[CrossRef](#)]
19. Díez-Mediavilla, M.; Alonso-Tristán, C.; Rodríguez-Amigo, M.C.; García-Calderón, T. Implementation of PV plants in Spain: A case study. *Renew. Sustain. Energy Rev.* **2010**, *14*, 1342–1346. [[CrossRef](#)]
20. Girard, A.; Gago, E.J.; Ordoñez, J.; Muneer, T. Spain's energy outlook: A review of PV potential and energy export. *Renew. Energy* **2016**, *86*, 703–715. [[CrossRef](#)]
21. IEA. Spain 2021 Energy Policy Review. Paris. 2021. Available online: <https://iea.blob.core.windows.net/assets/2f405ae0-4617-4e16-884c-7956d1945f64/Spain2021.pdf> (accessed on 10 November 2021).
22. Del Río, P.; Gual, M.A. An integrated assessment of the feed-in tariff system in Spain. *Energy Policy* **2007**, *35*, 994–1012. [[CrossRef](#)]
23. Del Río, P.; Mir-Artigues, P. A Cautionary Tale: Spain's Solar PV Investment Bubble. International Institute for Sustainable Development, 2014. Available online: https://www.iisd.org/gsi/sites/default/files/rens_ct_spain.pdf (accessed on 3 September 2021).
24. Blanco-Díez, P.; Díez-Mediavilla, M.; Alonso-Tristán, C. Review of the Legislative Framework for the Remuneration of Photovoltaic Production in Spain: A Case Study. *Sustainability* **2020**, *12*, 1214. [[CrossRef](#)]
25. Salas, V.; Olias, E. Overview of the photovoltaic technology status and perspective in Spain. *Renew. Sustain. Energy Rev.* **2009**, *13*, 1049–1057. [[CrossRef](#)]
26. Del Río, P.; Mir-Artigues, P. Support for solar PV deployment in Spain: Some policy lessons. *Renew. Sustain. Energy Rev.* **2012**, *16*, 5557–5566. [[CrossRef](#)]
27. De la Hoz, J.; Martín, H.; Ballart, J.; Córcoles, F.; Graells, M. Evaluating the new control structure for the promotion of grid connected photovoltaic systems in Spain: Performance analysis of the period 2008–2010. *Renew. Sustain. Energy Rev.* **2013**, *19*, 541–554. [[CrossRef](#)]
28. De la Hoz, J.; Martín, H.; Ballart, J.; Monjo, L. Evaluating the approach to reduce the overrun cost of grid connected PV systems for the Spanish electricity sector: Performance analysis of the period 2010–2012. *Appl. Energy* **2014**, *121*, 159–173. [[CrossRef](#)]
29. Del Río, P.; Calvo-Silvosa, A.; Iglesias, G. The New Renewable Electricity Support Scheme in Spain: A Comment. *Renew. Energy Law Policy Rev.* **2015**, *6*, 17–24.
30. De la Hoz, J.; Martín, H.; Montalà, M.; Matas, J.; Guzman, R. Assessing the 2014 retroactive regulatory framework applied to the concentrating solar power systems in Spain. *Appl. Energy* **2018**, *212*, 1377–1399. [[CrossRef](#)]
31. Schallenberg-Rodríguez, J.; Haas, R. Fixed feed-in tariff versus premium: A review of the current Spanish system. *Renew. Sustain. Energy Rev.* **2012**, *16*, 293–305. [[CrossRef](#)]
32. Del Río, P. Designing auctions for renewable electricity support: The case of Spain. *Renew. Energy Law Policy Rev.* **2017**, *8*, 23–37.
33. Del Río, P.; Bleda, M. Comparing the innovation effects of support schemes for renewable electricity technologies: A function of innovation approach. *Energy Policy* **2012**, *50*, 272–282. [[CrossRef](#)]
34. Avril, S.; Mansilla, C.; Busson, M.; Lemaire, T. Photovoltaic energy policy: Financial estimation and performance comparison of the public support in five representative countries. *Energy Policy* **2012**, *51*, 244–258. [[CrossRef](#)]
35. Talavera, D.L.; Muñoz-Cerón, E.; Ferrer-Rodríguez, J.P.; Nofuentes, G. Evolution of the cost and economic profitability of grid-connected PV investments in Spain: Long-term review according to the different regulatory frameworks approved. *Renew. Sustain. Energy Rev.* **2016**, *66*, 233–247. [[CrossRef](#)]
36. Lomas, J.C.; Muñoz-Cerón, E.; Nofuentes, G.; de la Casa, J. Sale of profitable but unaffordable PV plants in Spain: Analysis of a real case. *Energy Policy* **2018**, *117*, 279–294. [[CrossRef](#)]
37. Fernández-González, R.; Arce, E.; Garza-Gil, D. How political decisions affect the economy of a sector: The example of photovoltaic energy in Spain. *Energy Rep.* **2021**, *7*, 2940–2949. [[CrossRef](#)]

38. Del Río, P.; Peñasco, C.; Mir-Artigues, P. An overview of drivers and barriers to concentrated solar power in the European Union. *Renew. Sustain. Energy Rev.* **2018**, *81*, 1019–1029. [[CrossRef](#)]
39. San Miguel, G.; Corona, B. Economic viability of concentrated solar power under different regulatory frameworks in Spain. *Renew. Sustain. Energy Rev.* **2018**, *91*, 205–218. [[CrossRef](#)]
40. Kiefer, C.P.; del Río, P. Analysing the barriers and drivers to concentrating solar power in the European Union. Policy implications. *J. Clean. Prod.* **2020**, *251*, 119400. [[CrossRef](#)]
41. Fernández-González, R.; Suárez-García, A.; Álvarez Feijoo, M.Á.; Arce, E.; Díez-Mediavilla, M. Spanish Photovoltaic Solar Energy: Institutional Change, Financial Effects, and the Business Sector. *Sustainability* **2020**, *12*, 1892. [[CrossRef](#)]
42. Ortega, M.; del Río, P.; Montero, E.A. Assessing the benefits and costs of renewable electricity. The Spanish case. *Renew. Sustain. Energy Rev.* **2013**, *27*, 294–304. [[CrossRef](#)]
43. Sarasa-Maestro, C.J.; Dufo-López, R.; Bernal-Agustín, J.L. Photovoltaic remuneration policies in the European Union. *Energy Policy* **2013**, *55*, 317–328. [[CrossRef](#)]
44. Del Río, P.; Cerdá, E. The policy implications of the different interpretations of the cost-effectiveness of renewable electricity support. *Energy Policy* **2014**, *64*, 364–372. [[CrossRef](#)]
45. Ciarreta, A.; Pizarro-Irizar, C.; Zarraga, A. Renewable energy regulation and structural breaks: An empirical analysis of Spanish electricity price volatility. *Energy Econ.* **2020**, *88*, 104749. [[CrossRef](#)]
46. De la Hoz, J.; Martín, H.; Miret, J.; Castilla, M.; Guzman, R. Evaluating the 2014 retroactive regulatory framework applied to the grid connected PV systems in Spain. *Appl. Energy* **2016**, *170*, 329–344. [[CrossRef](#)]
47. López Prol, J. Regulation, profitability and diffusion of photovoltaic grid-connected systems: A comparative analysis of Germany and Spain. *Renew. Sustain. Energy Rev.* **2018**, *91*, 1170–1181. [[CrossRef](#)]
48. Del Río, P. Ten years of renewable electricity policies in Spain: An analysis of successive feed-in tariff reforms. *Energy Policy* **2008**, *36*, 2917–2929. [[CrossRef](#)]
49. Arocena, P.; Kühn, K.-U.; Regibeau, P. Regulatory reform in the Spanish electricity industry: A missed opportunity for competition. *Energy Policy* **1999**, *27*, 387–399. [[CrossRef](#)]
50. Del Río, P.; Unruh, G. Overcoming the lock-out of renewable energy technologies in Spain: The cases of wind and solar electricity. *Renew. Sustain. Energy Rev.* **2007**, *11*, 1498–1513. [[CrossRef](#)]
51. Caldés, N.; Varela, M.; Santamaría, M.; Sáez, R. Economic impact of solar thermal electricity deployment in Spain. *Energy Policy* **2009**, *37*, 1628–1636. [[CrossRef](#)]
52. Heras-Saizarbitoria, I.; Cilleruelo, E.; Zamanillo, I. Public acceptance of renewables and the media: An analysis of the Spanish PV solar experience. *Renew. Sustain. Energy Rev.* **2011**, *15*, 4685–4696. [[CrossRef](#)]
53. Azofra, D.; Saenz-Diez, J.C.; Martínez, E.; Jiménez, E.; Blanco, J. Ex-post economic analysis of photovoltaic power in the Spanish grid: Alternative scenarios. *Renew. Energy* **2016**, *95*, 98–108. [[CrossRef](#)]
54. Coronas, S.; Martín, H.; de la Hoz, J.; García de Vicuña, L.; Castilla, M. MONTE-CARLO probabilistic valuation of concentrated solar power systems in Spain under the 2014 retroactive regulatory framework. *Renew. Sustain. Energy Rev.* **2021**, *138*, 110670. [[CrossRef](#)]
55. Law 54/1997, of 27 November. BOE no. 285, 28 November 1997. Available online: <https://www.boe.es/eli/es/l/1997/11/27/54> (accessed on 7 September 2021).
56. Law 24/2013, of 26 December. BOE no. 310, 27 December 2013. Available online: <https://www.boe.es/eli/es/l/2013/12/26/24> (accessed on 15 September 2021).
57. RD 413/2014, of 6 June. BOE no. 140, 10 June 2014. Available online: <https://www.boe.es/eli/es/rd/2014/06/06/413> (accessed on 15 September 2021).
58. RD 960/2020, of 3 November. BOE no. 291, 4 November 2020. Available online: <https://www.boe.es/eli/es/rd/2020/11/03/960> (accessed on 15 September 2021).
59. Law 82/1980, of 30 December. BOE no. 23, 27 January 1981. Available online: <https://www.boe.es/eli/es/l/1980/12/30/82> (accessed on 7 September 2021).
60. RD 2366/1994, of 9 December. BOE no. 313, 31 December 1994. Available online: <https://www.boe.es/eli/es/rd/1994/12/09/2366> (accessed on 15 September 2021).
61. Law 40/1994, of 30 December. BOE no. 313, 31 December 1994. Available online: <https://www.boe.es/eli/es/l/1994/12/30/40> (accessed on 15 September 2021).
62. Ministerio de Ciencia y Tecnología. Instituto para la Diversificación y Ahorro de la Energía, IDEA. Plan de Fomento de las Energías Renovables en España 2000–2010. 1999. Available online: https://www.idae.es/uploads/documentos/documentos_4044_PFER2000-10_1999_1cd4b316.pdf (accessed on 7 September 2021).
63. Energy for the Future: Renewable Sources of Energy. White Paper for a Community Strategy and Action Plan. European Commission. Communication from the Commission. COM(97)599 Final (26/11/1997). 1997. Available online: https://europa.eu/documents/comm/white_papers/pdf/com97_599_en.pdf (accessed on 7 September 2021).
64. Directive 2001/77/CE, of 27 September, 2001. Official Journal of the European Union, L 283. 27 October 2001. Available online: <https://www.boe.es/doue/2001/283/L00033-00040.pdf> (accessed on 7 September 2021).
65. Directive 2003/30/CE, of 8 May, 2003. Official Journal of the European Union, L 123. 17 May 2003. Available online: <https://www.boe.es/doue/2003/123/L00042-00046.pdf> (accessed on 7 September 2021).

66. Ministerio de Industria, Turismo y Comercio; Instituto para la Diversificación y Ahorro de la Energía, IDAE. Plan de Energías Renovables en España 2005–2010. 2005. Available online: https://www.idae.es/sites/default/files/documentos/publicaciones_idae/documentos_10359_plan_de_energias_renovables_2005_2010_9da32b5e.pdf (accessed on 7 September 2021).
67. Directive 2009/28/CE, of 23 April, 2009. Official Journal of the European Union, L 140. 5 June 2009. Available online: <https://www.boe.es/doue/2009/140/L00016-00062.pdf> (accessed on 7 September 2021).
68. Instituto para la Diversificación y Ahorro de la Energía, IDAE. Plan de Energías Renovables 2011–2020. Ministerio de Industria, Turismo y Comercio. November 2011. Available online: https://www.idae.es/sites/default/files/documentos/publicaciones_idae/documentos_11227_per_2011-2020_def_93c624ab.pdf (accessed on 7 September 2021).
69. CNMC. Energía. Estadísticas. Available online: <https://www.cnmc.es/estadisticas> (accessed on 7 September 2021).
70. RD 2818/1998, of 23 December. BOE no. 312, 30 December 1998. Available online: <https://www.boe.es/eli/es/rd/1998/12/23/2818> (accessed on 15 September 2021).
71. RD 1955/2000, of 1 December. BOE no. 310, 27 December 2000. Available online: <https://www.boe.es/eli/es/rd/2000/12/01/1955> (accessed on 15 September 2021).
72. RD 841/2002, of 2 August. BOE no. 210, 2 September 2002. Available online: <https://www.boe.es/eli/es/rd/2002/08/02/841> (accessed on 15 September 2021).
73. RD 436/2004, of 12 March. BOE no. 75, 27 March 2004. Available online: <https://www.boe.es/eli/es/rd/2004/03/12/436> (accessed on 15 September 2021).
74. RD 661/2007, of 25 May. BOE no. 126, 26 May 2007. Available online: <https://www.boe.es/eli/es/rd/2007/05/25/661> (accessed on 15 September 2021).
75. RD 1432/2002, of 27 December. BOE no. 313, 31 December 2002. Available online: <https://www.boe.es/eli/es/rd/2002/12/27/1432> (accessed on 15 September 2021).
76. RD 2351/2004, of 23 December. BOE no. 309, 24 December 2004. Available online: <https://www.boe.es/eli/es/rd/2004/12/23/2351> (accessed on 15 September 2021).
77. RDL 7/2006, of 23 June. BOE no. 150, 24 June 2006. Available online: <https://www.boe.es/eli/es/rdl/2006/06/23/7> (accessed on 15 September 2021).
78. RD 1578/2008, of 26 September. BOE no. 234, 27 September 2008. Available online: <https://www.boe.es/eli/es/rd/2008/09/26/1578> (accessed on 15 September 2021).
79. RDL 6/2009, of 30 April. BOE no. 111, 7 May 2009. Available online: <https://www.boe.es/eli/es/rdl/2009/04/30/6> (accessed on 15 September 2021).
80. Resolution of the State Secretariat for Energy of 19 November 2009. BOE no. 283, 24 November 2009. Available online: https://www.boe.es/diario_boe/txt.php?id=BOE-A-2009-18772 (accessed on 15 September 2021).
81. RD 1003/2010, of 5 August. BOE no. 190, 6 August 2010. Available online: <https://www.boe.es/eli/es/rd/2010/08/05/1003> (accessed on 15 September 2021).
82. RD 1565/2010, of 19 November. BOE no. 283, 23 November 2010. Available online: <https://www.boe.es/eli/es/rd/2010/11/19/1565> (accessed on 15 September 2021).
83. RD 1614/2010, of 7 December. BOE no. 298, 8 December 2010. Available online: <https://www.boe.es/eli/es/rd/2010/12/07/1614> (accessed on 15 September 2021).
84. RDL 14/2010, of 23 December. BOE no. 312, 24 December 2010. Available online: <https://www.boe.es/eli/es/rdl/2010/12/23/14> (accessed on 15 September 2021).
85. Law 2/2011, of 4 March. BOE no. 55, 5 March 2011. Available online: <https://www.boe.es/eli/es/1/2011/03/04/2> (accessed on 15 September 2021).
86. RDL 1/2012, of 27 January. BOE no. 24, 28 January 2012. Available online: <https://www.boe.es/eli/es/rdl/2012/01/27/1> (accessed on 15 September 2021).
87. Law 15/2012, of 27 December. BOE no. 312, 28 December 2012. Available online: <https://www.boe.es/eli/es/1/2012/12/27/15> (accessed on 15 September 2021).
88. RDL 29/2012, of 28 December. BOE no. 314, 31 December 2012. Available online: <https://www.boe.es/eli/es/rdl/2012/12/28/29> (accessed on 15 September 2021).
89. RDL 2/2013, of 1 February. BOE no. 29, 2 February 2013. Available online: <https://www.boe.es/eli/es/rdl/2013/02/01/2> (accessed on 15 September 2021).
90. RDL 9/2013, of 12 July. BOE no. 167, 13 July 2013. Available online: <https://www.boe.es/eli/es/rdl/2013/07/12/9> (accessed on 15 September 2021).
91. RD 947/2015, of 16 October. BOE no. 249, 17 October 2015. Available online: <https://www.boe.es/eli/es/rd/2015/10/16/947> (accessed on 15 September 2021).
92. Order IET/2212/2015, of 23 October. BOE no. 255, 24 October 2015. Available online: <https://www.boe.es/eli/es/o/2015/10/23/iet2212> (accessed on 15 September 2021).
93. RD 359/2017, of 31 March. BOE no. 78, 1 April 2017. Available online: <https://www.boe.es/buscar/doc.php?id=BOE-A-2017-3639> (accessed on 15 September 2021).
94. Order ETU/315/2017, of 6 April. BOE no. 84, 8 April 2017. Available online: <https://www.boe.es/eli/es/o/2017/04/06/etu315> (accessed on 15 September 2021).

95. Resolution of the State Secretariat for Energy of 10 April 2017. BOE no. 87, 29592–29595, 12 April 2017. Available online: <https://www.boe.es/buscar/doc.php?id=BOE-A-2017-4094> (accessed on 15 September 2021).
96. Resolution of the State Secretariat for Energy of 10 April 2017. BOE no. 87, 29596–29622, 12 April 2017. Available online: <https://www.boe.es/buscar/doc.php?id=BOE-A-2017-4095> (accessed on 15 September 2021).
97. Resolution of the Directorate General for Energy Policy and Mines of 19 May 2017. BOE no. 125, 26 May 2017. Available online: https://www.boe.es/diario_boe/txt.php?id=BOE-A-2017-5848 (accessed on 15 September 2021).
98. Resolution of the Directorate General for Energy Policy and Mines of August 1, 2017. BOE no. 185, 4 August 2017. Available online: https://www.boe.es/diario_boe/txt.php?id=BOE-A-2017-9317 (accessed on 15 September 2021).
99. RD 650/2017, of 16 June. BOE no. 144, 17 June 2017. Available online: https://www.boe.es/diario_boe/txt.php?id=BOE-A-2017-6940 (accessed on 15 September 2021).
100. Order ETU/615/2017, of 27 June. BOE no. 153, 28 June 2017. Available online: <https://www.boe.es/eli/es/o/2017/06/27/etu615> (accessed on 15 September 2021).
101. Resolution of the State Secretariat for Energy of 30 June 2017. BOE no. 156, 1 July 2017. Available online: https://www.boe.es/diario_boe/txt.php?id=BOE-A-2017-7632 (accessed on 15 September 2021).
102. Resolution of the Directorate General for Energy Policy and Mines of 27 July 2017. BOE no. 179, 28 July 2017. Available online: https://www.boe.es/diario_boe/txt.php?id=BOE-A-2017-8997 (accessed on 15 September 2021).
103. Resolution of the Directorate General for Energy Policy and Mines of 10 October 2017. BOE no. 247, 13 October 2017. Available online: https://www.boe.es/diario_boe/txt.php?id=BOE-A-2017-11737 (accessed on 15 September 2021).
104. RDL 17/2019, of 22 November. BOE no. 282, 23 November 2019. Available online: <https://www.boe.es/eli/es/rdl/2019/11/22/17> (accessed on 15 September 2021).
105. Order IET/1045/2014, of 16 June. BOE no. 150, 20 June 2014. Available online: <https://www.boe.es/eli/es/o/2014/06/16/iet1045> (accessed on 15 September 2021).
106. Order ETU/130/2017, of 17 February. BOE no. 45, 22 February 2017. Available online: <https://www.boe.es/eli/es/o/2017/02/17/etu130> (accessed on 15 September 2021).
107. Order TED/171/2020, of 24 February. BOE no. 51, 28 February 2020. Available online: <https://www.boe.es/eli/es/o/2020/02/24/ted171> (accessed on 15 September 2021).
108. De la Hoz, J.; Martín, H.; Martins, B.; Matas, J.; Miret, J. Evaluating the impact of the administrative procedure and the landscape policy on grid connected PV systems (GCPVS) on-floor in Spain in the period 2004–2008: To which extent a limiting factor? *Energy Policy* **2013**, *63*, 147–167. [CrossRef]

MDPI
St. Alban-Anlage 66
4052 Basel
Switzerland
www.mdpi.com

Energies Editorial Office
E-mail: energies@mdpi.com
www.mdpi.com/journal/energies



Disclaimer/Publisher's Note: The statements, opinions and data contained in all publications are solely those of the individual author(s) and contributor(s) and not of MDPI and/or the editor(s). MDPI and/or the editor(s) disclaim responsibility for any injury to people or property resulting from any ideas, methods, instructions or products referred to in the content.



Academic Open
Access Publishing

www.mdpi.com

ISBN 978-3-0365-6967-3